PL-TR-91-2208

AD-A241 325

PROCEEDINGS OF THE 13TH ANNUAL PL/DARPA SEISMIC RESEARCH SYMPOSIUM, 8-10 OCTOBER 1991

EDITORS:

James F. Lewkowicz
Jeanne M. McPhetres

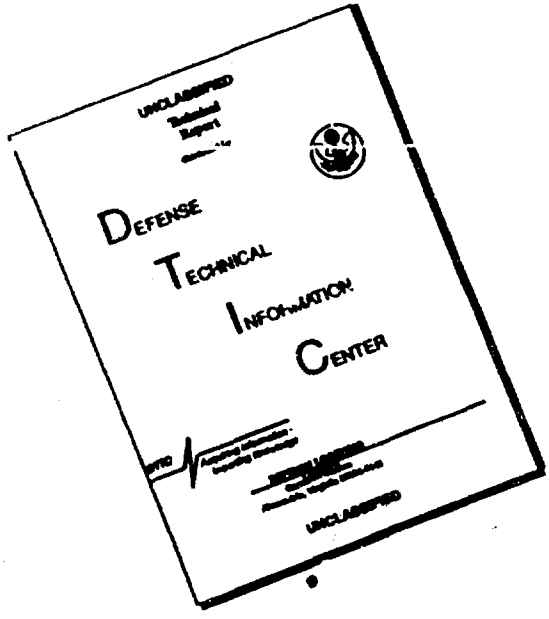
30 August 1991

APPROVED FOR PUBLIC RELEASE; DISTRIBUTION UNLIMITED

PHILLIPS LABORATORY
AIR FORCE SYSTEMS COMMAND
HANSCOM AIR FORCE BASE, MASSACHUSETTS 01731-5000

91-12541

DISCLAIMER NOTICE



THIS DOCUMENT IS BEST QUALITY AVAILABLE. THE COPY FURNISHED TO DTIC CONTAINED A SIGNIFICANT NUMBER OF PAGES WHICH DO NOT REPRODUCE LEGIBLY.

"This technical report has been reviewed and is approved for publication."

JAMES F. LEWKOWICZ
Branch Chief
Solid Earth Geophysics Branch
Earth Sciences Division

DONALD H. ECKHARDT
Director
Earth Sciences Division

This report has been reviewed by the ESD Public Affairs Office (PA) and is releasable to the National Technical Information Service (NTIS).

Qualified requestors may obtain additional copies from the Defense Technical Information Center. All others should apply to the National Technical Information Service.

If your address has changed, or if you wish to be removed from the mailing list, or if the addressee is no longer employed by your organization, please notify PL/IMA, Hanscom AFB, MA 01731-5000. This will assist us in maintaining a current mailing list.

Do not return copies of this report unless contractual obligations or notices on a specific document requires that it be returned.

REPORT DOCUMENTATION PAGE

Form Approved
OMB No. 0704-0188

Public reporting burden for this collection of information is estimated to average 1 hour per response, including the time for reviewing instructions, searching existing data sources, gathering and maintaining the data needed, and completing and reviewing the collection of information. Send comments regarding this burden estimate or any other aspect of this collection of information, including suggestions for reducing this burden, to Washington Headquarters Services, Directorate for Information Operations and Reports, 1215 Jefferson Davis Highway, Suite 1204, Arlington, VA 22202-4302, and to the Office of Management and Budget, Paperwork Reduction Project (0704-0188), Washington, DC 20503

1. AGENCY USE ONLY *(Leave blank)*	2. REPORT DATE	3. REPORT TYPE AND DATES COVERED
	30 August 1991	Scientific, Final

4. TITLE AND SUBTITLE
PROCEEDINGS OF THE 13TH ANNUAL PL/DARPA SEISMIC RESEARCH SYMPOSIUM, 8-10 OCTOBER 1991

5. FUNDING NUMBERS
PE 61102F
PR 2309
TA G2
WU 10

6. AUTHOR(S)
Editors: James F. Lewkowicz
Jeanne M. McPhetres

7. PERFORMING ORGANIZATION NAME(S) AND ADDRESS(ES)
Phillips Laboratory (LWH)
Hanscom AFB, MA 01731-5000

8. PERFORMING ORGANIZATION REPORT NUMBER
PL-TR-91-2208
ERP, No. 1093

9. SPONSORING / MONITORING AGENCY NAME(S) AND ADDRESS(ES)
DARPA/NMRO
3701 North Fairfax Drive
Arlington, VA 22203-1714

10. SPONSORING / MONITORING AGENCY REPORT NUMBER

11. SUPPLEMENTARY NOTES
This research was supported by DARPA under PE 62714E.

12a. DISTRIBUTION / AVAILABILITY STATEMENT
Approved for Public Release; distribution unlimited

12b. DISTRIBUTION CODE

13. ABSTRACT *(Maximum 200 words)*

These proceedings contain papers presented at the Thirteenth Annual Seismic Research Symposium held 8-10 October 1991, in Keystone, Colorado. This is the first year the symposium has been jointly sponsored by Phillips Laboratory and the Defense Advanced Research Projects Agency. In its capacity as a Technical Agent, the PL's Solid Earth Geophysics Branch (LWH) manages the DARPA Nuclear Monitoring Research Office's (NMRO) and its own Air Force funded basic research program in verification seismology. The scientific objectives of these programs are to improve the Air Force's capability to seismically detect, locate, identify and estimate the yield of underground nuclear explosions. The purpose of this symposium, which is organized annually by LWH, is to provide the sponsoring agencies an opportunity to review the research accomplished during the preceding year and outline areas of investigation for the coming year. For the researchers, it provides a forum for the exchange of scientific information, as well as an occasion to meet personally with the NMRO and LWH staff to discuss individual projects, ideas and results. In addition, the technical presentations

14. SUBJECT TERMS	15. NUMBER OF PAGES
underground nuclear explosion, seismic waves, regional seismology arrays, yield estimation, source coupling	552
	16. PRICE CODE

17. SECURITY CLASSIFICATION OF REPORT	18. SECURITY CLASSIFICATION OF THIS PAGE	19. SECURITY CLASSIFICATION OF ABSTRACT	20. LIMITATION OF ABSTRACT
UNCLASSIFIED	UNCLASSIFIED	UNCLASSIFIED	UL

serve as a means to inform representatives from other Government agencies about advances in seismic monitoring research, technologies and techniques as part of the important process of technology transition. The papers include studies on regional seismic wave propagation, attenuation and scattering, array processing and seismic techniques of yield estimation.

TABLE OF CONTENTS

PAGE

INVITED PRESENTATIONS*

Archambeau, Charles B. 1
Technical Issues Related to Test Ban Treaty Verification: Some Approaches to Current and Anticipated Future Problems

Bratt, Steven R. 2
Global Monitoring to Low Thresholds: Where We Stand

Given, Holly 3
Overview of Eurasian Seismic Stations and Networks

Kerr, Ann 13
Description of U.S. Participation in the Group of Scientific Experts Technical Test, April - June, 1991

Langston, Charles A. 14
Intraplate Earthquakes in Eurasia

Lay, Thorne 22
Yield Estimation, Free-Surface Interactions, and Tectonic Release at Novaya Zemlya

Richards, Paul G. 35
How can the Operation of Thousands of Seismic Stations (Carried out by Hundreds of Institutions in Tens of Countries) Best Be Focussed on Discrimination Research?

Ringdal, Frode 36
Lg as a Yield Estimation Tool

Robinson, Ambassador C. Paul 47
Seismology Issues in the Nuclear Talks between the U.S. and the U.S.S.R.

Simpson, David W. 48
Opportunities for Seismological Research in the USSR

DTIC COPY INSPECTED 4

Accession For
NTIS GRA&I
DTIC TAB
Unannounced
Justification
By
Distribution/
Availability Codes
Dist Special
A-1

POSTER PRESENTATIONS

PAGE

Ahrens, Thomas J.; **Duffy**, Thomas S.; and **Sekine**, Toshimori 49
Equation of State of Granitic Rock: A New Hysteretic Unloading Model

Amjad, M. and **Mitchell**, B.J. 57
Discrimination Studies Using Regional Phases in the Central United States

Barker, Jeffrey S. 64
Analysis of Regional Bodywave Phases from Earthquakes and Explosions in Eastern Asia

Baumgardt, Douglas R. 71
Design and Development of an Intelligent Event Identification System (ISEIS): Application to Regional Seismic Events in Eurasia

Bennett, T.J.; **Campanella**, A.K.; **Scheimer**, J.F.; and **Murphy**, J.R. 78
Regional Discrimination of Soviet Nuclear Explosions, Earthquakes and Mineblasts

Benz, H.M.; **Unger**, J.D.; **Leith**, W.; and **Ryaboy**, V. 85
The Norilsk DSS Profile in Northern Siberia: Interpretation of the Velocity Structure and Comparison with Basin and Range and New England Profiling Results

Burdick, L.J.; **Garnero**, E.J.; **Helmberger**, D.V.; and **Zhao**, L.S. 100
Regional and Upper Mantle Wave Propagation in the Soviet Union

Burdick, L.J.; and **Helmberger**, D.V. 108
Specialized Studies in Yield Estimation

Campillo, Michel and **Paul**, Anne 116
The Influence of the Lower Crustal Structure on the Early Coda of Regional Seismograms

Chapman, M.C.; **Bollinger**, G.A.; and **Sibol**, M.S. 138
Spectral Studies of the Elastic Wave Radiation from Appalachian Earthquakes and Explosions Explosion Source Spectra Modeling Using Blaster's Logs

PAGE

Cormier, Vernon F. 145
Ray Modeling of Lg Attenuation Across Mountainous Regions

Crusem, René and **Caristan**, Yves 152
Moment Tensor Inversion, Yield Estimation and Seismic Coupling Variability at the French Centre d'Experimentation du Pacifique

Der, Zoltan A.; **Shumway**, R.H.; **Baumgardt**, Douglas R.; **Hirano**, Michael R.; and **Worthington**, Eric A. 159
Broadband Studies of Seismic Sources at Regional and Teleseismic Distances Using Advanced Time Series Analysis Methods

Fielding, Eric J.; **Isacks**, Bryan L.; and **Barazangi**, Muawia 166
A Geological and Geophysical Information System for Eurasia

Fisk, M. D. and **McCartor**, G.D. 173
Simulated Seismic Wave Scattering in Random Media

Fisk, M. D.; **Wilson**, G. L.; **Gray**, H. L.; and **McCartor**, G. D. 180
A Constrained Bayesian Approach for Testing TTBT Compliance

Flatté, Stanley M.; **Xie**, Xiao-Bi; and **Zhang**, Tianrun 187
The Effect of Small-Scale Heterogeneities on Transmission Fluctuations for Teleseismic and Regional High-Frequency Propagation

Gaffet, Stéphane 194
An Attempt to Waveform Modelling - Influence of the Superficial Geological Structure

Gestermann, N.; **Harjes**, H.-P.; **Jost**, M.; **Schweitzer**, J. ; and **Wüster**, J. 204
Analysis of GERESS-Recordings during GSETT-2

Given, Holly 211
Heterogeneous Propagation and Blockage of Lg in the Caspian Sea - Caucasus Mountain Area of the USSR

Gupta, I.N.; **Lynnes**, C.S.; and **Wagner**, R.A. 218
Evidence for Rg-to-P Scattering in Teleseismic P-Coda and Rg-to-S Scattering in Regional Lg of East Kazakh Explosions and An Array Study of Effects of a Known Local Scatterer on Regional Phases

PAGE

Gurrola, Harold and **Minster**, J. Bernard 225
Single-Station Estimates of Crust and Upper Mantle Velocity Structure at Broadband IRIS/IDA Stations in the USSR

Harmsen, Steve; **Gomberg**, Joan; and **Richards**, Paul G. 237
Shallow Seismicity Following Selected Nuclear Explosions at the Nevada Test Site

Hedlin, Michael A.H.; **Minster**, J. Bernard; and **Orcutt**, John A. 241
Beam-stack Imaging of Scatterers near the NORESS Array

Helmberger, D.; **Dreger**, D.; **Zhao**, L.; **Kedar**, S.; **Woods**, B.; and **Harkrider**, D. 249
Source Retrieval from Regional Seismograms

Herrmann, R.B.; **Al-Eqabi**, G.I.; and **Hutchenson**, K. 261
Quantification of Small Explosions

Husebye, E.S. and **Ruud**, B.O. 268
Finite Difference Wavefield Synthetics - Understanding Seismic Source Discriminant Features

Israelsson, Hans 275
Analysis of Historical USSR Seismograms - RMS Magnitudes, Yields, and Depths of Explosions at the Semipalatinsk Test Range

Jih, R.-S.; **Lynnes**, C.S.; **Gupta**, I.N.; **Baumstark**, R.; **Wagner**, R.A.; and **Shumway**, R.H. 282
Explosion Source Size Determination, Discrimination and Spectral Characteristics

Johnson, Lane R. and **McEvilly**, T.V. 291
Characterization of Explosive Sources at Near Distances

Kennett, B.L.N. and **Bostock**, M.G. 297
Processes Contributing to the Coda of Regional Seismograms

Kennett, B.L.N. 305
The Distance Dependance of Regional Discriminants

Lacoss, R.T.; **Curtis**, S.R.; **Cunningham**, R.K.; and **Seibert**, M. 313
Seismic Phase and Event Labeling using Artificial Neural Networks

PAGE

Leonard, Michael A.; **Johnson**, Lane R.; and **McEvilly**, Thomas V. 320
Array Analysis of Regional Pn and Pg Wavefields from the Nevada Test Site

Malin, Peter and **Blakeslee**, Sam 327
A 2 Station and 2 Event Method for Near-Source Attenuation

McLaughlin, K.L.; **Stevens**, J.L.; **Barker**, T.G.; and **Shkoller**, B. 333
Investigations of Nonlinear Explosion Effects

Miller, S.A. and **Florence**, A.L. 339
Spherical Wave Propagation in Frozen Saturated Rock

Miller, S.A. and **Florence**, A.L. 348
Formation and Propagation of Love Waves from a P-Wave Source

Mitchell, Brian J. 354
Regional Variation of Q_{Lg} and its Frequency Dependence: Implications for Crustal Structure and Evolution

Murphy, J.R. 361
A New System for Seismic Yield Estimation Underground Explosions

Mykkeltveit, Svein; **Kvaerna**, Tormod; **Ringdal**, Frode; and **Fyen**, Jan 367
NORSAR Research on Regional Network Data Processing

Patnaik, Gagan B. and **Sereno**, Thomas J., Jr. 374
A Neural Network Approach to Initial Phase Identification from Three-Component Polarization Measurements

Pedersen, H. and **Campillo**, M. 380
Depth Dependance of Q Beneath the Baltic Shield Inferred from Modeling of Short Period Seismograms

Priestley, Keith F. and **Walter**, William R. 389
Studies of Seismic Data from Central Asia

Priestley, K.F.; **Cipar**, J.; **Yegorkin**, A.V.; **Pavlenkova**, N.I.; and **Martynov**, V. 396
Preliminary Analysis of the Western Norilsk - Lake Baikal Deep Seismic Sounding Profile

PAGE

Riviere-Barbier, Florence and **Grant**, Lori 403
Cluster Analysis Method Applied to Event Location

Ryaboy, V.; **Benz**, H.; **Unger**, J.; and **Leith**, W. 410
The Norilsk DSS Profile in Northern Siberia: An Analysis of the 2D Crustal Velocity Section Constructed by Soviet Seismologists

Schwartz, Susan Y. and **Lay**, Thorne 417
Analysis of the Effects of Eurasian Crustal and Upper Mantle Structure on Regional Phases using Broadband Seismic Data: Initial Phase

Stump, B.; **Reamer**, S. **Hinzen**, K.-G.; and **Min**, G. 424
Physical Constraints on Seismic Waves from Chemical and Nuclear Explosions

Sykes, Lynn R. 431
Yields of Nuclear Explosions at Azgir and Shagan River and Implications for Identifying Decoupled Tests in Salt

Thurber, Clifford H. and **Quin**, Howard R. 438
Teleseismic and Regional Seismic Event Location: Constraints from Master Events, Satellite Images, and Synthetic Seismograms

Toksöz, M.N.; **Mandal**, B.; **Gibson**, R.L., Jr.; and **Dainty**, A.M. 445
Research in Regional Seismology: The Effect of Anisotropy

Toksöz, M.N.; **Dainty**, A.M.; **Mandal**, B.; **Cheng**, N.; **Charrette**, E.E.; and **Schultz**, C. 453
Regional Seismograms: Attenuation and Scattering

Vermilye, Jan and **Scholz**, C.H. 461
Fracture Length and Aperture: A General Relationship

Vidale, John E. 468
Array Studies of Seismic Scattering

Vogfjörd, Kristin S.; **Yan**, Ben; and **Langston**, Charles A. 474
Composition of Short-Period Regional Phases Inferred from Fennoscandian Array Data

PAGE

Wagner, Gregory; **Clouser**, Robert; and **Langston**, Charles 481
Theoretical Studies of Scattering for Teleseismic P Waves and Regional S Waves

Wallace, Terry C. 488
Regional Distance Recordings of Large Mining Explosions in the Southwestern U.S.

Wallace, Terry C. 491
The Effects of Crustal Structure on Spectral Discriminates

Woods, B.B. and **Harkrider**, D.G. 497
NTS Surface Wave Magnitudes from a Regional Network

Wu, Francis T.; **Jones**, Alan L.; and **Ke**, Zhaoming 505
Velocity Structures of Different Tectonic Provinces of China

Young, Chris; **Chael**, Eric; and **Carter**, Jerry 512
Signal-to-Noise Enhancement with Depth in a Borehole near Amarillo, TX

Lynnes, C.S. and **Jih**, R.-S. 519
Regional Phase Propagation in Central Asia

Haupt, R.W.; **Martin**, III, R.J.; **Tang**, X. and **Dupree**, W.J. 526
Modulus Dispersion and Seismic Wave Attenuation Related to the Seismic Source Region

Harvey, Danny J. and **Hansen**, Roger A. 531
A Systematic Study of the Effects of Crust and Upper Mantle Structure on Regional Seismograms

***Hannon**, Willard J. 540
A View of the Department of Energy's Test Ban Verification Program

***Maxion**, Roy A. 541
What Machines Must Learn ... and Why

LATE SUBMISSIONS (Paper not included at time of press)

Archambeau, Charles B.; **Davies**, J.B.; and **Orrey**, Jeff
Modeling Seismic and Atmospheric Wave Fields Generated by Near Surface Sources

Callen, B.W.; **Fiedler**, R.; **Lamb**, F.K.; and **Sullivan**, J.D.
The Effect of Source Parameters on Hydrodynamic Yield Estimation

Duncan, Lewis M. and **Archambeau**, C.
Preliminary Investigations of Joint Seismic and Electromagnetic Methods for Nuclear Test Monitoring

Ferguson, John
University of Texas at Dallas, Contract No. F19628-89-K-0006

Lerner-Lam, Arthur L.; **Smith**, Walter H.F.; and **Simpson**, David W.
Satellite Images and Digital Terrain Analysis in Verification Research

Shearer, Peter; **Masters**, Guy; and **Orcutt**, John
Differential S-wave Travel Times from the ISC Data Set

Technical Issues Related to Test Ban Treaty Verification: Some Approaches to Current and Anticipated Future Problems

Charles B. Archambeau
Theoretical and Applied Geophysics Group
University of Colorado
Campus Box 449
Boulder, CO 80309

Contract No. F19628-90-K-0051

Abstract

In the past the 150 kt. test limitation has focused most of our attention on accurate yield estimation and on questions of structure and tectonic release effects that could bias yield estimates. In the future it is possible that the test yield limit could be lowered significantly; most probably to around 20 kt. initially and later to as low as 1 kt. With a test limit below about 10 kt. or so, decoupling tests could conceivably be conducted clandestinely and therefore, in order to properly monitor a low threshold treaty, it would be necessary to detect and discriminate seismic events in the m_b range from 2 to 4, as well as above $m_b \sim 4$. In this low magnitude range large industrial explosions would be observed as well as earthquakes and so it would be necessary to be able to distinguish possible decoupled tests from chemical explosions as well as earthquakes. In view of these possibilities, the research emphasis will probably need to shift to regional distance event monitoring using very high frequency (5-50Hz) seismic data, as well as the conventional broad-band data, in order to be able to identify the different kinds of seismic events. Further, yield estimation using regionally recorded data will be required. In this presentation I will summarize the need for very high frequency seismic data, how it will be useful in event identification and, lastly, whether we will be able to routinely obtain such data at regional distances in continental areas such as the U.S.S.R. In this regard, I will argue that very high frequency signals are commonly propagated with high efficiency because of crust-upper mantle wave guide effects and will show data and modeling results to support this contention. More broadly, the present status of regional event detection - identification using both seismic and non-seismic methods will be discussed, along with some ideas about methods that may be required in order to achieve good monitoring capability at very low event magnitudes.

Global Monitoring to Low Thresholds: Where We Stand

Steven R. Bratt
Science Applications International Corporation
Center for Seismic Studies
1300N. 17th Street, Suite 1450
Arlington, VA 22209

Contract # MDA903-91-C-0151

ABSTRACT

The potential capability of a seismic network for monitoring a low threshold (m_b 2.5) test ban treaty is a complex function of the source and path characteristics, network geometry, and the signal-to-noise threshold of the network's stations. However, the actual capability is best measured by the event bulletin produced. In other words, a network must accurately and efficiently process the data in order to effectively monitor, and this becomes increasingly difficult as the required threshold decreases. The goal of this study is to move beyond estimates of network detection thresholds based on simulations, and to use seismic bulletins to assess the actual ability of existing networks to detect, identify, and associate signals, then locate even small events. The prospect of a low yield threshold treaty and an increase in the number of nuclear-capable nations motivate this assessment, while the recent deployment of two prototype monitoring systems, the *Intelligent Monitoring System* (*IMS*) and the *Washington Experimental International Data Center* (*EIDC*), provide unique and salient databases.

Both the *IMS* and *EIDC* apply nearly-identical software to compute automated bulletins, which are then reviewed by an analyst and corrected as necessary. The *IMS* has been in operation since October 1989, and is now processing data from four arrays and a three component station in northern Europe. The *IMS* is locating 65 events per day; 85% are at regional distances and 75% of those are smaller than m_l 2.5. Approximately 40% of all non-noise phases detected by the system are associated with an event. The *Washington EIDC* was an integral part of the U.N. Conference on Disarmament's second Group of Scientific Experts Technical Test; a global effort to develop and test new concepts for an international cooperative system of seismic data exchange for monitoring nuclear explosion testing. Thirty-three countries and up to 59 globally-distributed stations (including the current *IMS* stations) participated in the test over 61 days in 1990 and 1991. The *EIDC* located about 64 events per day, 25% of which were smaller than m_b 2.5. About 40% of the observed phases were associated with an event.

Given these databases, the primary objectives of this work are to assess (1) the detection, association, and location capability of the *IMS* and *EIDC* systems, (2) the importance of arrays versus single stations, (3) the importance of automated processing, and (4) the prospects for monitoring a low threshold test ban treaty given today's technology. The overlap of contributing stations and operation time between the *IMS* and *EIDC* systems provides a unique cross-check of the capabilities of each. In addition, the *IMS* and *EIDC* bulletins are compared to those from other simultaneously-operating networks with potentially more complete and accurate bulletins for isolated regions to support the aforementioned assessments.

Overview of Eurasian Seismic Stations and Networks

Holly Given, Scripps Institution of Oceanography, UCSD

I. Introduction

Within the past five years, cooperative programs between various scientific and governmental organizations in the United States and the Soviet Union and China have yielded an unprecedented opportunity for the expansion of nuclear monitoring research, as well as basic seismological research, into the Eurasian continent. Under the Joint Seismic Program (JSP) between the Soviet Academy of Sciences, the IRIS consortium of universities, and the U.S. Geological Survey, state-of-the-art seismic systems have been deployed in wide parts of the USSR. Initiatives coordinated by the Nuclear Monitoring Office of the Defense Advance Research Projects Agency (DARPA) have contributed toward improving seismological facilities in Eurasia, particularly in the areas of data telemetry and the application of expert systems to network processing. These kinds of programs foster a more open policy toward the international exchange of seismic data, which has obvious and immediate implications for the feasibility of a program of global nuclear monitoring. Figure 1 shows a location map of the various seismological facilities in Eurasia to be discussed in this paper.

I. Broadband Installations and Data Telemetry

Perhaps the most predominant development in the last five years has been the establishment of broadband seismic stations in widely spaced areas of Eurasia. The basic component of each broadband station is the Steckeisen STS-1 broadband or extended-broadband three-component seismometer. The IRIS/IDA network, a collaboration between Project IDA at Scripps Institution of Oceanography and the IRIS Consortium, currently operates 6 broadband stations in the USSR under the Joint Seismic Program, located at Obninsk (OBN) near Moscow, Arti (ARU) in the Southern Ural Mountains, Kislovodsk (KIV) in the foothills of the Caucasus Mountains, Garm (GAR) in Tadjikistan, Ala-Archa (AAK) in Kirghizia, and Talaya (TLY) near Lake Baikal (Given, 1990). IRIS/IDA stations are continuously recorded at 20 samples per second with dual gain. The U.S. Geological Survey operates a broadband station at Garni (GNI) in Armenia. The Soviet group participating in the JSP has indicated that 6 more sites have been approved for future broadband installation by Project IDA and the USGS at Norilsk (NRI), Novosibirsk (NVS), and Yakutsk (YAK) in Siberia, Sakhalin Island (YSS), Lovozero (LVZ) on the Kola Peninsula, and Ashkabad (ASH) in Turkmenia (Figure 1). Noise surveys are currently being carried out at some of these sites. Also, installation of a broadband station at the Soviet scientific base at Novolazarevskaya, Antarctica, is being discussed under the Joint Seismic Program.

IRIS/IDA data from the USSR are currently archived in two places in the US, in addition to the central archive at Scripps Institution of Oceanography (SIO), where it is stored in CSS format. All data are sent to the IRIS Data Management Center (DMC) in SEED format, and also to the Center for Seismic Studies in Arlington, VA in CSS format. Data are typically shipped to CSS within one month of being received from the USSR. At SIO, IRIS/IDA data is archived on optical disk mass storage system manufactured by Epoch Systems. The cumulative amount of data from the USSR on the mass storage system, for 1989 and 1990, is approximately 34 Gigabytes.

As part of the experiment for the near-real time exchange of seismic waveform data by the GSE (Group of Scientific Experts), broadband seismic equipment with real-time digital telemetry capability was installed at three sites in China. The sites, HIA, LZH, and BJI, also host stations of the China Digital Seismographic Network, which was cooperatively established by the USGS and the State Seismological Bureau of China in 1986. Telemetry links have been established between the Chinese GSE stations and Beijing, and between Beijing and the data collection center at Scripps Institution of Oceanography. This will allow Chinese data to be

processed and stored simultaneously with IRIS/IDA data from the USSR, such that the two operations can viewed as one Eurasian network with comprehensive continental coverage.

Data telemetry from the IRIS/IDA USSR stations represents a major area of future work. During the GSE experiment, the Soviets provided real-time telemetry from stations ARU, GAR, and KIV into the Soviet data center at Obninsk using dedicated phone circuits and PDP-based communication utilities. A satellite link was established between Obninsk and the Center for Seismic Studies, as well as Scripps Institution of Oceanography. A planned upgrade to the IRIS/IDA stations in the USSR includes the installation of a Sun workstation, equipped with a communications board, at each field site that will read data records from the IRIS/IDA data logger and write CSS format files. Standard Unix utilities will then be used to transmit data files over Soviet telemetry lines to Obninsk, where they will be buffered and transmitted to Scripps in near-real time (Figure 2).

As a data collection center for globally telemetered data, SIO will serve as the gateway to processing routes such as the *Intelligent Monitoring System* (IMS), a knowledge-based processing system for detecting, locating, and identifying seismic events (Bache et al, 1990). IMS was designed primarily for use with array data at regional distances, but is being modified to accommodate the new facilities in the USSR. As one example of its applicability, we discuss a small series of intraplate earthquakes on May 28, 1990, in the Ural Mountains, approximately 150 km from the IRIS/IDA station ARU. In general, this is a very aseismic region of the USSR; however, many large PNEs ('peaceful nuclear explosions') have been sited in this area since the 1960's. Figure 3 shows a location map and filtered, vertical-component seismograms from the IRIS/IDA network. The two larger events were given in the PDE (Preliminary Determination of Epicenters) catalog with m_b=4.6. The ARU records are almost identical, indicating that the two events actually have the same location, although the PDE locations differ by about 80 km. Previous to any analyst review, the IMS detected and formed events for these two earthquakes in its automatic processing mode; however, it did not identify all phases that could be used for location. With analyst intervention, the events were located using the regional phases P_g, L_g at ARU; P_n, S_n at KIV; and S_n, L_g at OBN. As expected, the IMS locations are almost identical, and differ from the PDE locations by over 80 km in each case. The IMS also identified a small foreshock to the first event, detectable only at ARU, in approximately the same location. As the station separation in the USSR decreases with the addition of new broadband sites, routine application of regional processing packages such as IMS will yield increasingly accurate results.

Several other improvements to the basic IRIS/IDA station are under consideration. One would be to add one or more channels of strong motion instruments for stations sited in tectonically active areas, in order to record very close, large events on scale. For example, the Georgian earthquake of April 29, 1991 (Ms=7.0) just exceeded the range of the STS-1 seismometer at KIV, 180 km from the epicenter. Another suggestion has been to deploy three short-period seismometers in a triangular configuration around the broadband instrument, with a separation of some tens of meters, in order to improve short-period detection ability by introducing an effective beam gain, as well as to provide more accurate estimates of slowness and azimuth. The flexibility of the IRIS/IDA data logger is such that it could accommodate these improvements with no change to the basic hardware or software.

II. Regional Networks and Arrays

Regional networks and arrays have been established in the USSR under the Joint Seismic Program in areas of Armenia, Kirghizia, and the Caucasus Mountains. Many issues of regional seismology relevant to nuclear monitoring can be addressed with these facilities. Networks and arrays are shown in Figure 1 by open circles. In each case, they are located around one of the broadband stations.

The USGS, working with the Armenian Academy of Sciences, has been operating a dense, thirty-element array in Armenia about 30 km east of Yerevan since June 1990. The broadband station GNI lies within the array, which has a very small aperture (~500 m) and features 200 sps triggered recording of short-period (1 Hz) seismometers by the GEOS recording system (Borchert et al, 1985). It is planned to supplement the array with a 6-element telemetered regional network of 50 km approximate extent. Figure 4 shows records from the 10 vertical component sensors of a local earthquake. Data flow is into the USGS in Menlo Park.

A network in the Caucasus Mountains was installed jointly by Lamont-Doherty Geological Observatory and the Institute of Physics of the Earth of the Soviet Academy in August 1990. There are two components to the Caucasus network; a permanent network with plans for 6 telemetered stations (currently 4); and a set of 6 PASSCAL portable recorders that supplement the telemetered network. The broadband station KIV lies within the network's boundaries. The telemetered network sends 60 sample-per-second, three-component continuous data from 5 s seismometers to a central site, where data are detected and events saved to tape. The PASSCAL instruments, which were intended to supplement the telemetered network by expanding spatial coverage and responding to special events, are currently deployed to record seismicity associated with the Georgian earthquake of April 29, 1991. PASSCAL recording is on-site on 180 Mbyte disks of 1 sps continuous data, and 20 sps and 100 sps triggered recording. Data flow is into Lamont. In addition to the American equipment, the Soviets have developed a 6 station network using high quality analog telemetry with triggered digital recording in the same general area.

A regional network was recently installed in the Soviet republic of Kirghizia by Scripps Institution of Oceanography and the Kirghiz Institute of Seismology (August 1991). The 10-station, digitally telemetered Kirghiz network has a spatial extent of approximately 200 km with a station spacing of about 30 km. The network uses 3-component Steckeisen STS-2 broadband seismometers, and the telemetry provides synchronous sampling and transmission of both 20 sps continuous and 100 sps dual-gain triggered channels to a central site. Figure 5 shows the network configuration. Data flow will be into Scripps Institution of Oceanography.

III. Soviet Facilities

Access to Soviet geophysical data is becoming more available under joint projects. The Soviet Academy of Sciences maintains a national seismic network of over 30 analog stations with high-frequency (CKM-3) and broadband (CKD) sensors; these are shown in Figure 1. Data from this network, including records of weapons tests and PNEs, are now generally available; some has been obtained under an exchange with DARPA and under the Joint Seismic Program. An 'automatic' digitizing system, comprising a scanner for use with large-format originals and an interactive custom software package to digitize bitmaps, was developed under the Joint Seismic Program (Given et al, 1991); an example of its use with a regional analog record from the Soviet station FRU is shown in Figure 6. Information about other Soviet seismological observatories designed mainly for nuclear monitoring, such as Borovoye in northern Kazakhstan, is also becoming more publicly available, and access to these data outside the USSR is being explored by several groups.

IV. Concluding Remarks

When viewed together, the developments in seismological instrumentation and cooperation in Eurasia present a promising picture for nuclear monitoring research. Many direct results can be obtained from the new facilities, and seismologists who have studied the USSR for decades from an out-of-country vantage point now have the opportunity to corroborate their results directly on the Eurasian continent. It is hoped that the successful cooperation between the many groups and agencies will continue to result in high quality, publicly available seismic data.

Acknowledgements The author acknowledges contributions by, discussions with, and comments from Jonathan Berger, Frank Vernon, David Simpson, John Filson, Roger Borchert, Gary Glassmoyer, Art Lerner-Lam, Linda Carroll, Shane Ingate, Jeffrey Given, and Lian-She Zhao.

References

Bache, T.C., S.R. Bratt, J. Wang, R.M. Fung, C. Kobryn, and J.W. Given, The Intelligent Monitoring System, *Bull. Seismol. Soc. Am.* 80, 1833-1851, 1990.

Borchert, R.D., J.B. Fletcher, E.G. Jensen, G.L. Maxwell, J.R. VanSchaak, R.E. Warrick, E. Cranswick, M.J.S. Johnston, and R. McClearn, A general earthquake-observation system (GEOS), *Bull. Seismol. Soc. Am. 75,* 1783-1825, 1985.

Given, H.K., Variations in broadband noise at IRIS/IDA stations in the USSR with implications for event detection, *Bull. Seismol. Soc. Am. 80,* 2072-2088, 1990.

Given, H.K., D. Helmberger and L. Zhao, A new acquisition of seismograms from the USSR emphasizing digital storage, *EOS Trans. Am. Geophy. Union 72*, 190, 1991.

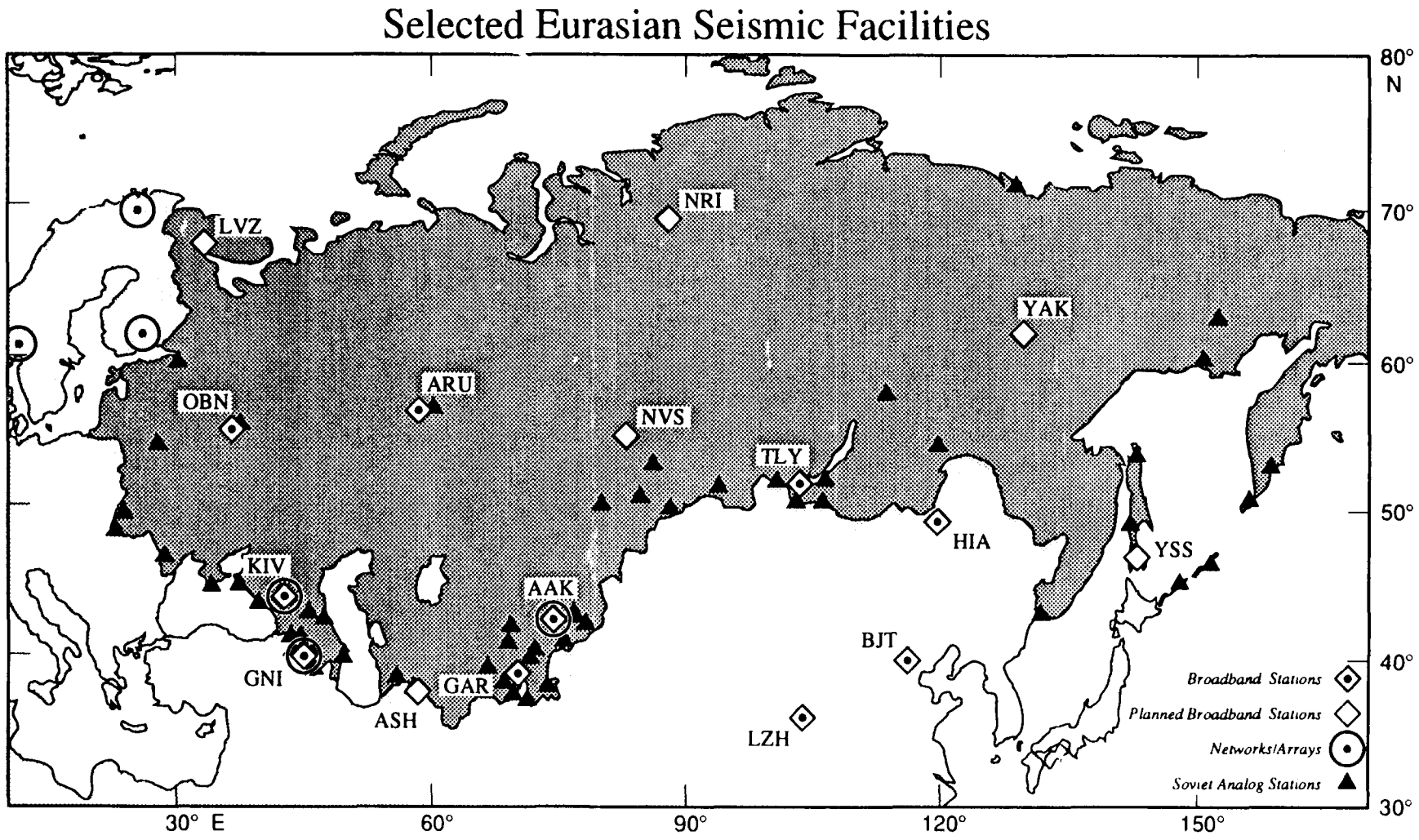
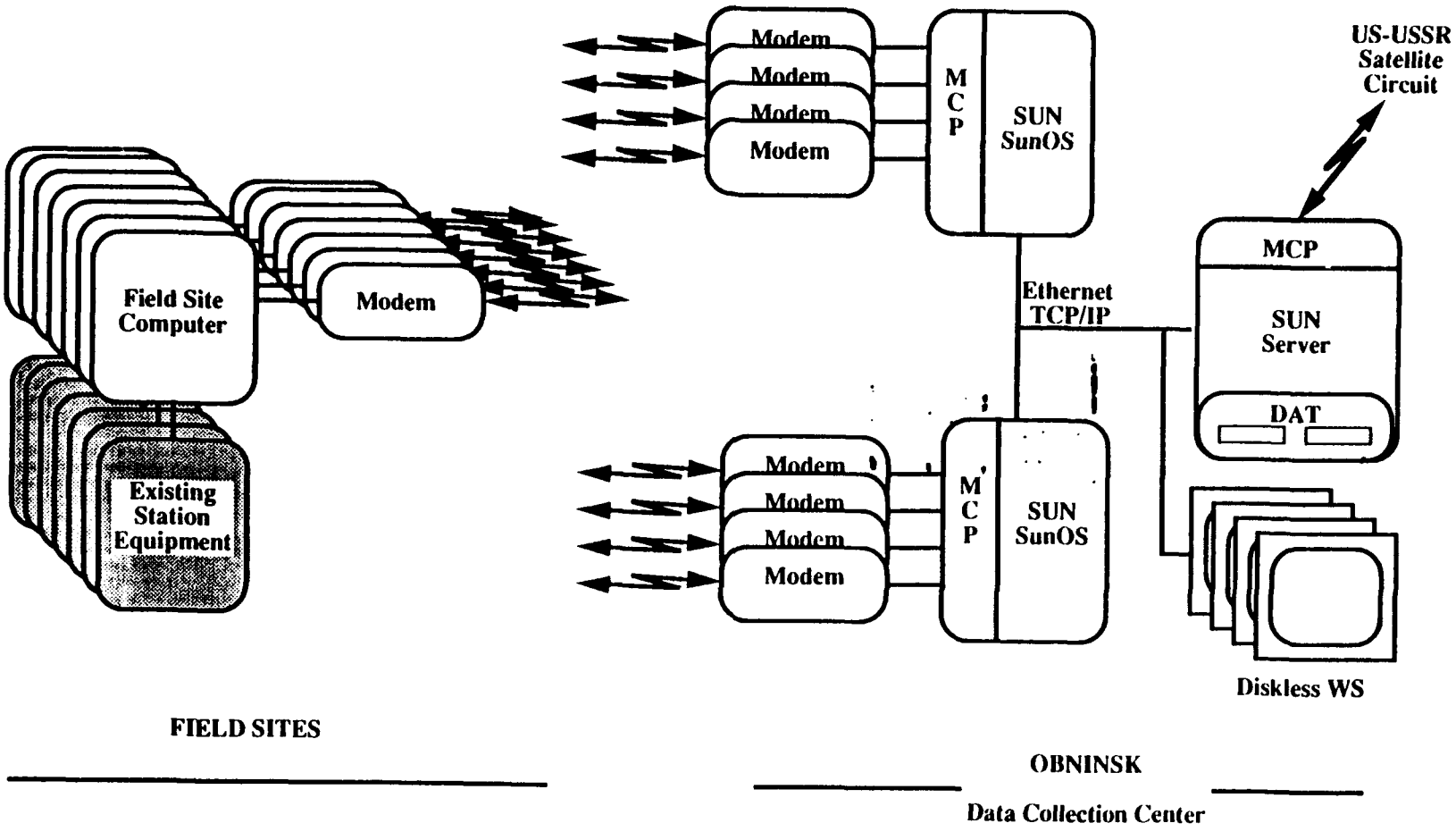
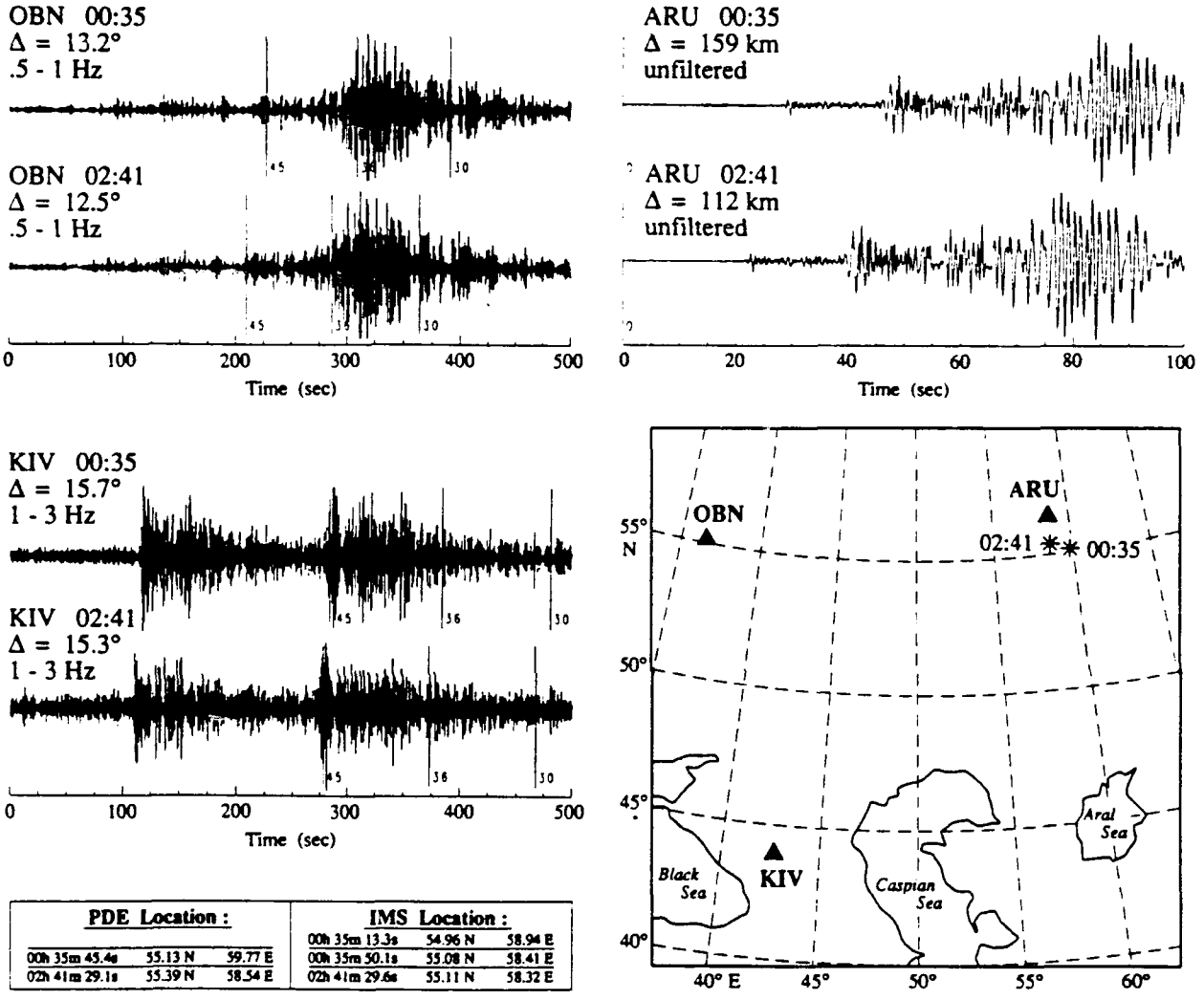


Figure 1. Location map of seismic facilities in Eurasia.



USSR Real Time Data Collection System

Figure 2. Schematic layout of planned telemetry between field sites and data collection center for IRIS/IDA broadband stations in the USSR.



PDE Location :			IMS Location :		
00h 35m 45.4s	55.13 N	59.77 E	00h 35m 13.3s	54.96 N	58.94 E
02h 41m 29.1s	55.39 N	58.54 E	00h 35m 50.1s	55.08 N	58.41 E
			02h 41m 29.6s	55.11 N	58.32 E

Figure 3. Map of two events in the Ural Mountains near ARU showing PDE locations and vertical seismograms recorded by IRIS/IDA stations. Records have been filtered in the passband shown to enhance regional phases. The ARU records are identical, indicating that the events actually have the same location. Arrival times of group velocities of 4.5, 3.6, and 3.0 km s^{-1} are shown on the KIV and OBN records; these times and the distances shown are with respect to the PDE locations. Table compares the PDE locations with those obtained by the *Intelligent Monitoring System*, which also identified a small foreshock in the same area.

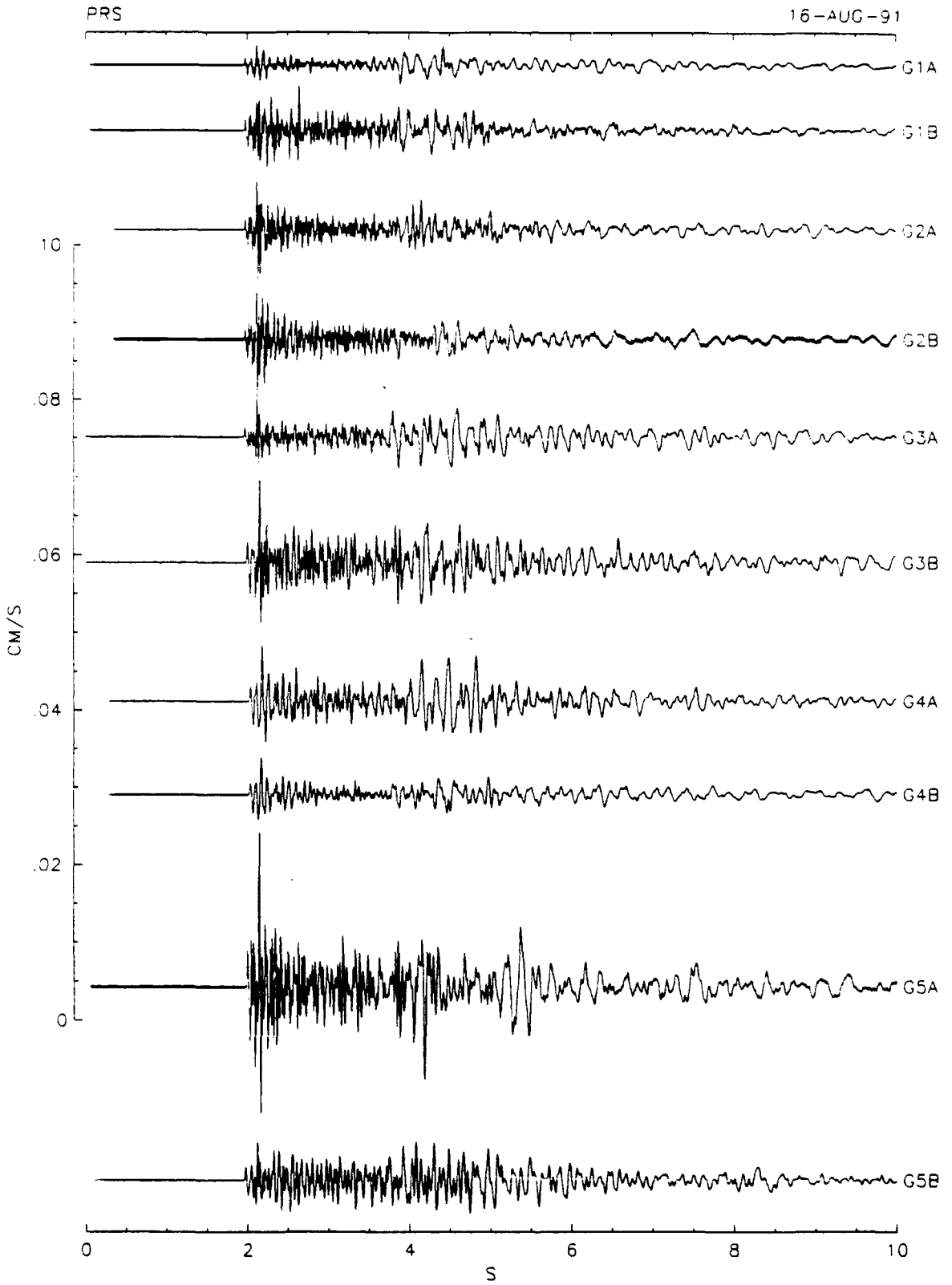


Figure 4. Records of a local earthquake from the high-frequency USGS small array in Armenia, colocated with the broadband station GNI. Most array elements lie in the same tunnel as the broadband station; array elements have a characteristic separation of tens of meters.

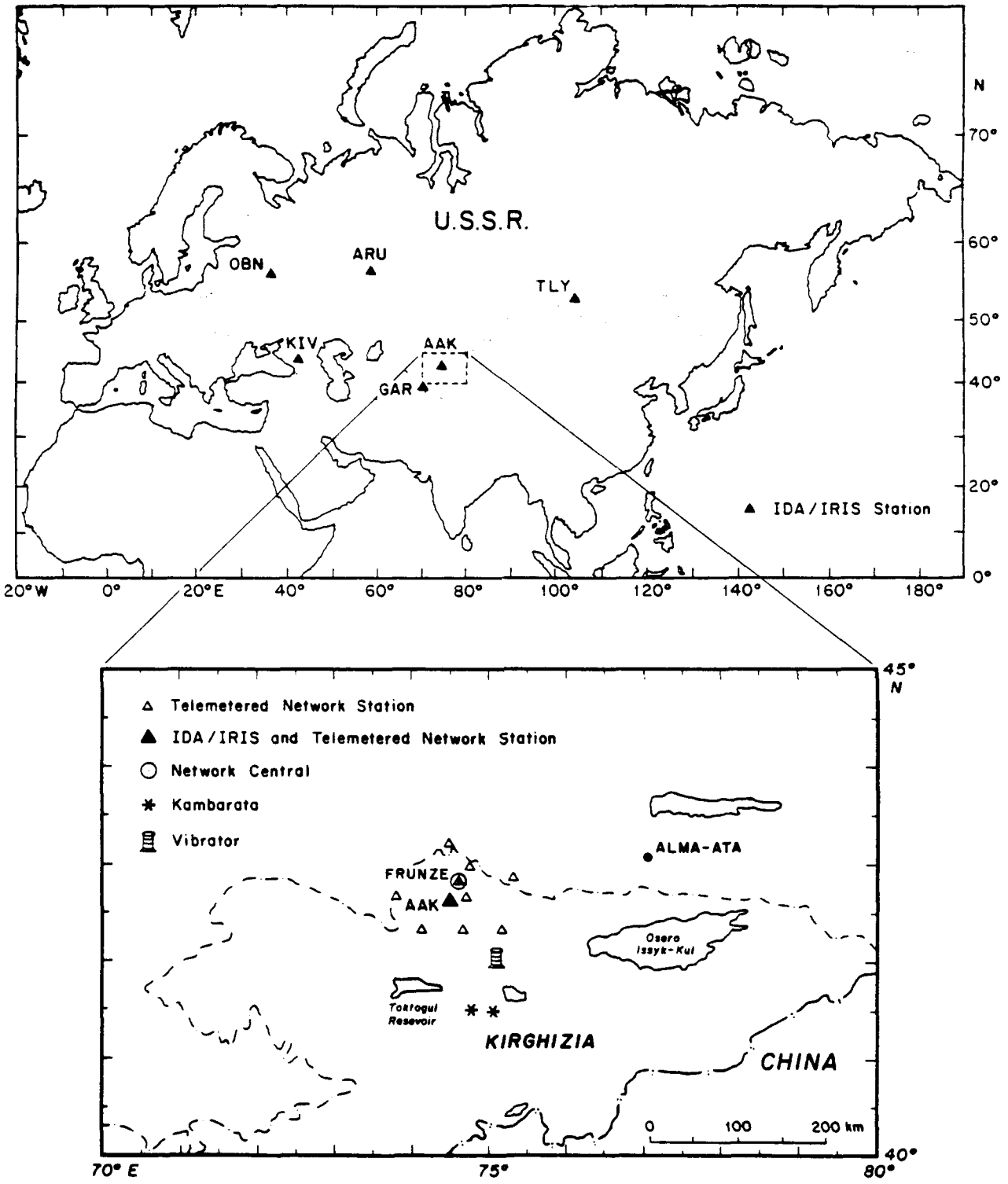


Figure 5. Location map of the digitally telemetered regional network in Kirghizia, around the broadband station AAK. The receiving site is in Frunze (Bishkek).

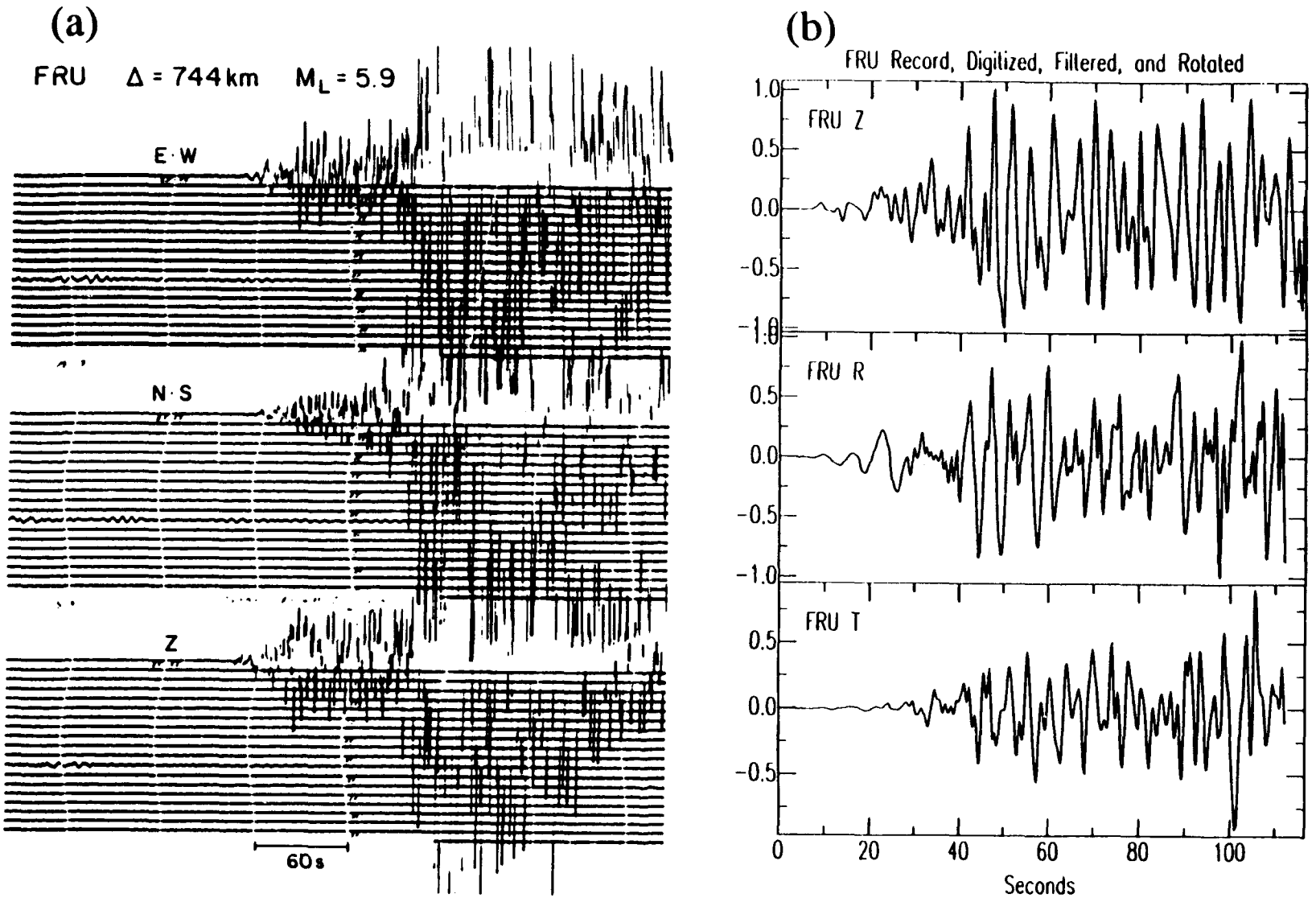


Figure 6. Example of a digitized time series (b) obtained from an analog record (a) of a regional earthquake recorded on a Soviet SKD seismometer using the prototype automatic digitizing system. The digitized traces have been filtered and rotated. Note the difference in time scales; only the portion of the record before the S arrival was digitized.

Description of U.S. Participation in the Group of Scientific Experts Technical Test, April - June, 1991

Ann U. Kerr (US GSE Delegation; Scripps Institution of Oceanography, LaJolla, CA. 92023; (619) 534-2103;kerr@beno.css.gov)

ABSTRACT

The Group of Scientific Experts is working to define an international system for the rapid exchange of seismic waveform and parameter data and their routine use in the preparation of daily event bulletins containing as many seismic events as possible. As part of its efforts to develop and test the technical concepts for this global system, the Group has undertaken a large scale multi-phase international experiment, called the Group of Scientific Experts Technical Test (GSETT-2). The last phase of this Test is a seven week experiment to be conducted from April 22, 1991 through June 9, 1991. The experiment will involve the collection of near-realtime data from a global network of stations and their transmission from National Data Centers in about thirty countries to International Data Centers in Australia, Sweden, Soviet Union and the U.S. An overview of the Technical Test and of the facilities being developed by DARPA to support U.S. participation is provided.

DARPA has undertaken several technical initiatives to develop each of the elements of the global system. They include high dynamic range seismic systems; distributed data centers incorporating knowledge based processing of seismic data, routine interactive analysis tools and rapid access to organized databases; and a communications network node, including dedicated links to Australia, Sweden and the Soviet Union.

The various phases of the experiment have provided considerable experience in the problems of international communications and the rapid processing and analysis of waveform data. The preliminary results of the experiment will be presented. Several bilateral experiments are also being conducted to provide new high quality data sources for the experiment and for research which will also be reviewed.

Intraplate Earthquakes in Eurasia

Charles A. Langston

Department of Geosciences
440 Deike Building
Pennsylvania State University
University Park, Pennsylvania 16802

Introduction

Plate tectonics has been a useful paradigm in tying together diverse geological and geophysical data particularly for those processes associated with the formation and destruction of the ocean basins. However, continental tectonic processes often seem much more complex and do not apparently abide by the same rules. Intraplate earthquakes are those events which are not associated with the standard plate tectonic elements of ridge spreading, transform faulting or subduction. Intraplate events which occur on continents pose serious problems to be solved in the fields of earthquake hazards assessment, the geodynamics of continental interiors and explosion verification research. The purpose of this short paper is to review some of the characteristics of Intraplate earthquakes which occur within continents and, in particular, examine what is known about seismicity within the Eurasian continent. Discrimination of underground nuclear explosions from earthquakes is predicated on knowing what the seismic signatures of the earthquakes are in a geographical region as well as knowing what the explosions look like. It is a challenge to seismology to characterize these earthquakes with the expected small amounts of data that will be available for events in many parts of Eurasia.

Intraplate Earthquakes

A simple definition of an Intraplate earthquake as being one that does not fall upon a plate boundary oversimplifies the observed complexity of continental tectonic structures. Many continents, such as North America and Eurasia, have several wide zones of active tectonic deformation which are not obviously related to plate tectonic elements. And even when Intraplate events do not fall in these active areas, the extensive geological history and complex structure of most any part of a continent must be considered to make any sense of earthquake occurrence.

A study by the Electric Power Research Institute (EPRI -Coppersmith et al, 1987; Johnston, 1989) suggested a regionalization of continental interiors to classify Intraplate seismicity in an attempt to correlate Intraplate seismicity with known geologic and tectonic structures. Continental interiors were divided into age provinces based on bedrock geology. Areas of recent tectonic activity were set aside as possibly being related to plate tectonic processes.

This classification is useful in earthquake hazards assessments of stable continental interiors but precludes, to a large extent, the obvious problems of seismicity in southern and southeast Asia which occurs over a wide area. Nevertheless, the EPRI study is a good place to start in analyzing possible seismicity in stable interiors where nuclear testing may be attempted.

Breaking continental terrains into Phanerozoic and Precambrian age groups, the EPRI results show that Intraplate earthquakes in stable continental interiors are a relatively minor contribution to world seismicity, producing less than 1% of the world's moment release (Johnston, 1989). Almost half of Intraplate events occur in Paleozoic and Mesozoic terrains and seem to be associated with regional compressional stresses reactivating old rift zone structures such as failed Aulocogens and rift structures associated with opening of the Atlantic. It was observed that stable areas outside of Europe in Eurasia were among the *least active* on earth. Thus, in the EPRI scheme of things, much of Soviet Eurasia is devoid of significant intraplate activity for events of magnitude 5.5 and greater. It remains to be seen, however, if smaller events are common. These possible small events, in combination with seismicity due to mining, may pose a problem in discrimination and detection in the monitoring of a comprehensive test ban.

Tectonics of Eurasia

Even though the stable interior of Eurasia has been seismically quiet, its overall tectonic framework is among the most complex and active in the world. The EPRI study suggested that much of southeastern Eurasia consists of a "distributed plate boundary"(Figure 1) due to the collision of India with Asia beginning in the Eocene (Molnar and Tapponnier, 1975). This is borne out by recent geological syntheses of the Soviet Union which show much of Asia consisting of a patch-work of accreted continental fragments and orogenic terrains (Zonenshain et al 1989; Zonenshain et al 1991; Figure 2). Although details of this process are poorly understood, the clear surface manifestations of earthquake producing structures and long history of major seismicity will undoubtably be the source of many future "Intraplate" earthquakes that will be of interest in verification research.

Figure 3 is from Molnar and Tapponnier(1975) and shows major elements of deformation within southeast Eurasia. The Himalayan frontal thrust marks the boundary of the plate interaction between India and Asia. Uplift of theTibetan plateau may either represent the effect of underthrusting of the Indian continental plate, which cannot be subducted due to its density, or pervasive crustal thickening due to regional plastic deformation and compression of Asian and Indian crust. Compressive stresses induced by the continental collision produce strike-slip faulting along major east-west striking faults within China. These stresses may also be inducing tensional rifting at Lake Baikal and in the Shansi area of China. Tension is produced perpendicular to the principal compressive stress direction.

The edge of the EPRI distributed-plate boundary is not well defined by exceptionally clear zones of seismicity or structures (Figure 1). For example, the area of the Kazakh test site, although not particularly seismically active, has had a few moderate earthquakes in the past, the most recent being November 12, 1990 (Ms 6.1). Zonenshain et al (1989) have synthesized a tectonic model of the Soviet Union based on mapped geologic structures, recognized tectonic terrains and loose trends in the seismicity (Figures 4 and 5). The southern plate boundaries defined by continental collision of the Arabian and Indian plates with Asia grade into a melange of micro-continental plates with mostly "diffuse" boundaries. Clearly, this kind of tectonic framework is a useful start in understanding the internal dynamics of Asia but the inherent fuzziness of inferred microplate boundaries suggests that there is room for fundamental contributions from detailed earthquake source mechanism studies.

Intraplate Seismicity and Verification Issues

The seismicity and structure of Eurasia are major research topics that will occupy hundreds of geoscientists for years to come. The fact that earthquakes will occur in many areas is a certainty. What is important here is the problem of identifying these future events as earthquakes. Currently, standard location methods are generally capable of locating moderate earthquakes to within only about 40 km in all spatial dimensions. Almost all earthquakes within Eurasia are confined to the crust or uppermost mantle (Chen, 1988) . Thus, location, and particularly source depth, cannot be currently used as a discriminant. Source depth is a particularly important discriminant, if available, since explosion emplacement depths can only be as great as a few kilometers. Fortunately, waveform modeling can be used to constrain source depth where wave propagation effects are well known such as for teleseismic body waves. These methods rely on differential measurements of traveltime between surface reflections and the direct wave and are not sensitive to precise epicentral locations. It may be possible to extend these modeling techniques to regional distances and higher frequencies although experience suggests that much will have to be learned about detailed wave propagation effects at regional distances.

The current political unrest in the Soviet Union suggests that the availability of seismic data will not dramatically improve in the near future, nor will the deployment of new seismic stations be expedited. It is my guess that the study of Eurasian seismic events will have to be performed with sparse data sets even for the moderately large events. Small events of interest will probably have only a few recordings. Discrimination of small earthquakes from explosions will probably be an important problem for some time to come, particularly if it turns out that small Intraplate earthquakes are common in the stable continental interior of Eurasia. The challenge to seismology will be to fully utilize these sparse data sets to determine source depth and orientation parameters for these earthquakes.

References

Chen, W.-P. (1988). A brief update on the focal depths of intracontinental earthquakes and their correlations with heat flow and tectonic age, *S.R.L., 59*, p.263-272.

Coppersmith, K.J., A.C. Johnston, A.G. Metzger and W.J. Arabasz(1987). Methods for assessing maximum earthquakes in the central and eastern United States, *Working Report, EPRI Research Project 2556-12,* Electric Power Research Institute,Palo Alto, California.

Johnston, A.C. (1989). The seismicity of 'stable continental interiors, in *Earthquakes at North-Atlantic Passive Margins: Neotectonics and Postglacial Rebound,* S. Gregersen and P.W.Basham editors, Kluwer Academic Publishers, p.299-327.

Molnar, P., and P. Tapponnier (1975). Cenozoic tectonics ofAsia: effects of a continental collision, *Science, 189,*p.419-426.

Zonenshain, L.P., J. Verhoef, R. Macnab and H. Meyers (1991). Magnetic imprints of continental accretion in the U.S.S.R., *EOS, 72,* 305.

Zonenshain, L.P., M.I. Kuzmin, L.M. Natapov, B. Page (ed)(1989). *Geology of the USSR: A plate tectonic synthesis,* AGU Geodynamics series, 242 pages.

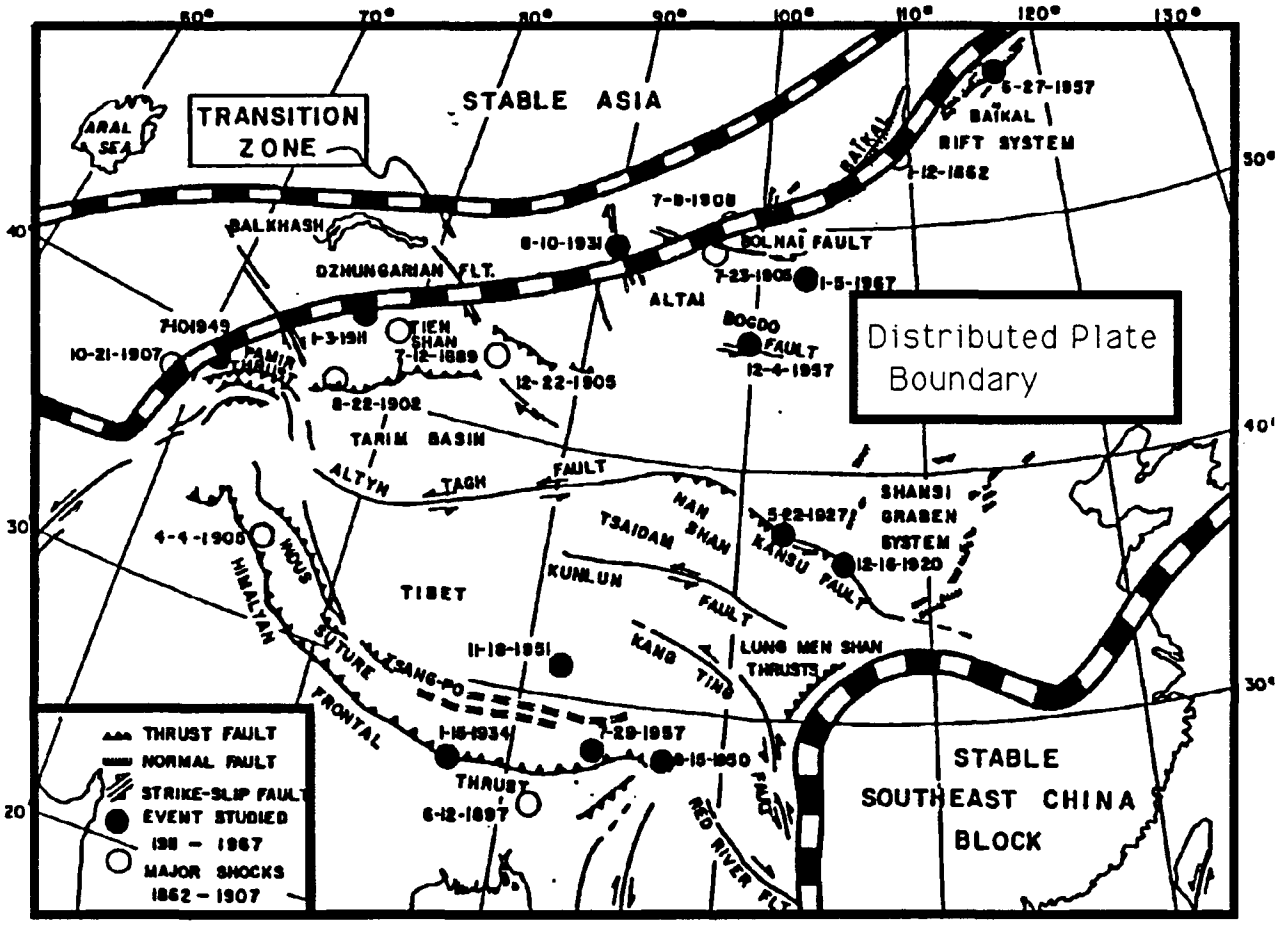


Figure 1 - Regionalization of central and south eastern asia in terms of of a distributed plate boundary and a transition zone to the stable interior of Asia. (from Coppersmith et al, 1987)

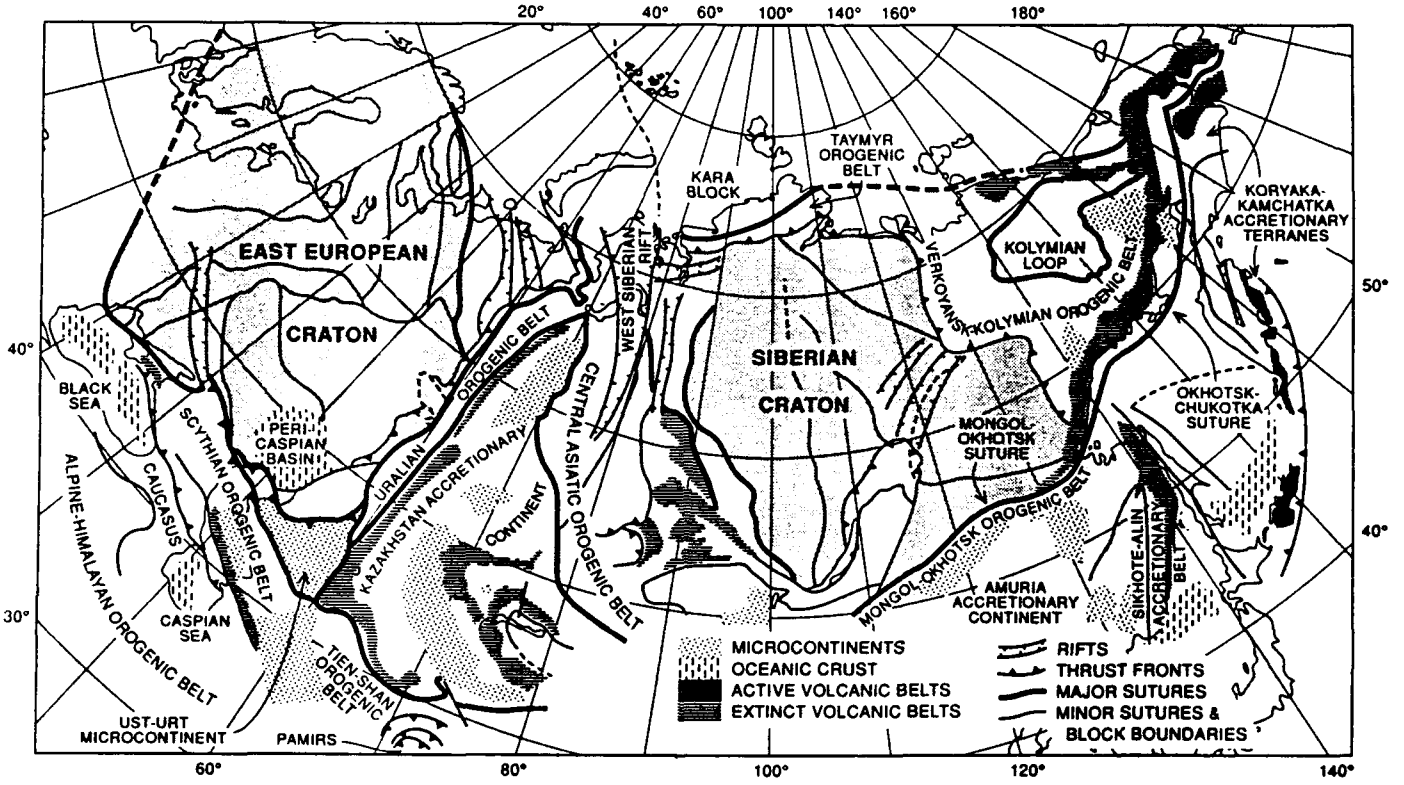


Figure 2: Major structural elements of the USSR (from figure 2 Zonenshain et al 1991).

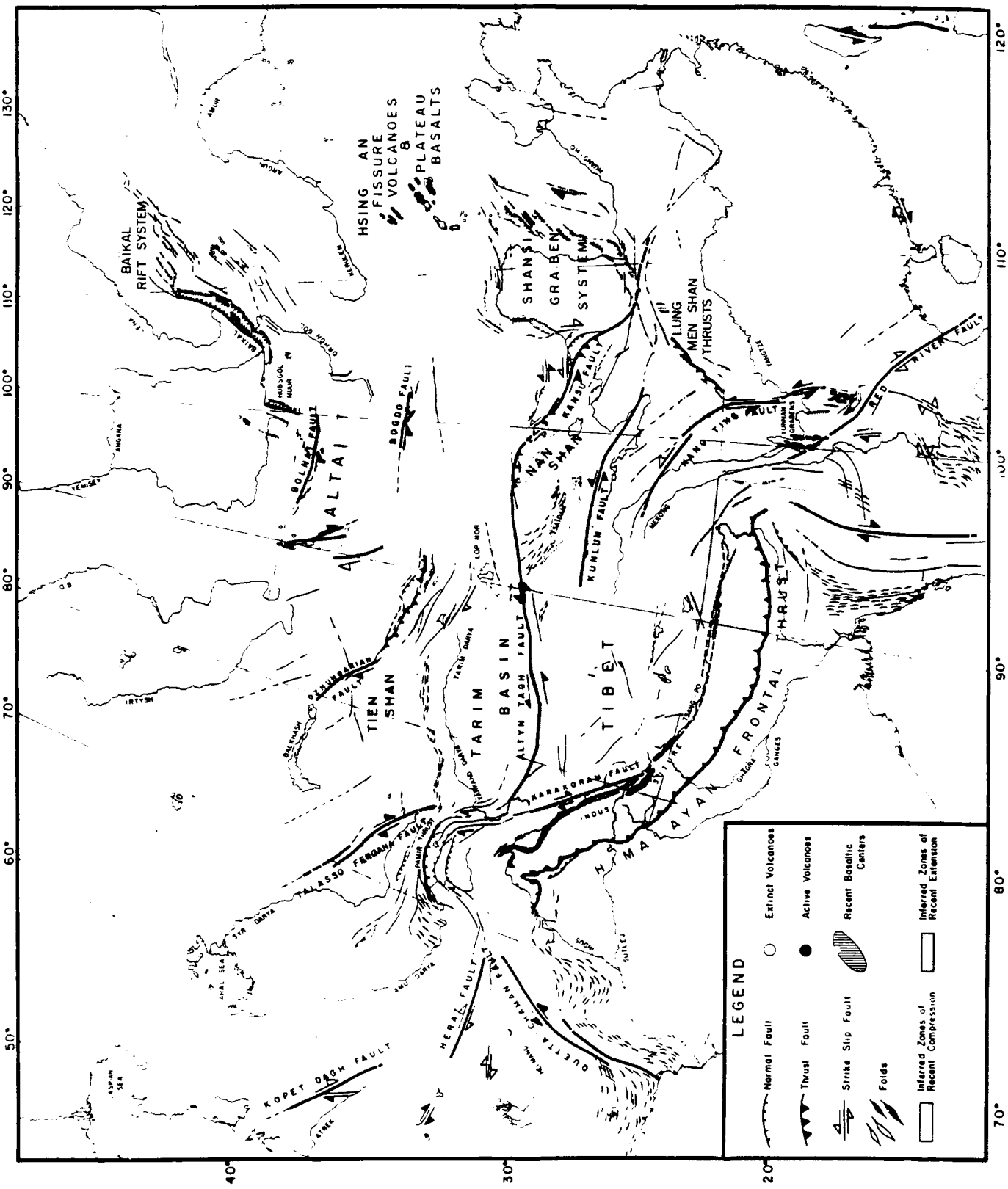


Figure 3: Tectonic map of Asia (from figure 4 of Molnar and Tapponnier, 1975).

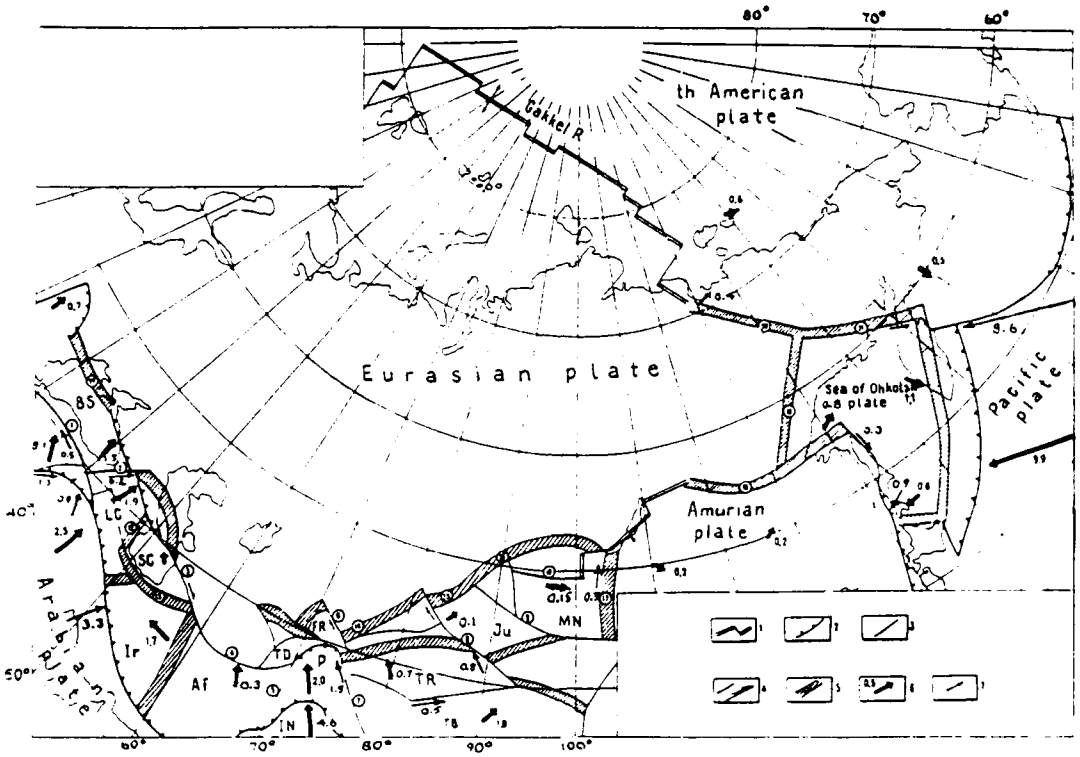


Fig. 184. Present plate boundaries within the USSR territory, after Zonenshain et al. [1983].
1, Spreading axis; 2, subduction zone; 3, transformn fault; 4, strike-slip fault; 5, diffuse plate boundary; 6, vector of plate motion with respect to Eurasia; 7, vector of relative plate motions along plate boundaries.
Plates and microplates: Af - Afghan, BS - Black Sea, FR - Fergana, IN - Indian, Ir - Iran, Ju - Junggar, LC - Lesser Caucasus, MN - Mongolian, P - Pamirs, SC - South Caspian, TB - Tibetan, TD - Tadjik, TR - Tarim.

Figure 4: Plate boundaries in the USSR (from figure 184 Zonenshain et al 1989).

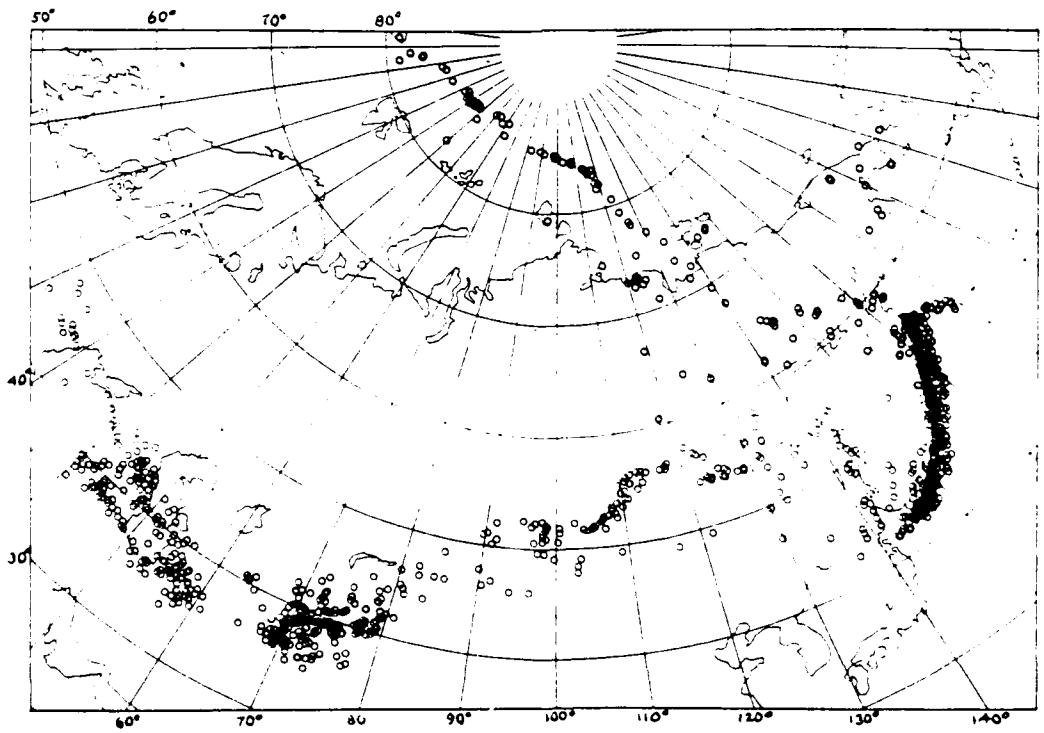


Fig. 185. Distribution of earthquake foci within the USSR territory for the period 1970 to 1985. All events of magnitude >4.5 are plotted after Lander (unpublished).

Figure 5: Earthquake epicenters within the USSR (from figure 185 Zonenshain et al 1989).

YIELD ESTIMATION, FREE-SURFACE INTERACTIONS, AND TECTONIC RELEASE AT NOVAYA ZEMLYA

Thorne Lay

Institute of Tectonics
University of California, Santa Cruz

Invited Review Paper

Objective: This unclassified review provides a summary of seismological constraints on explosion parameters for events at the Novaya Zemlya test site. The emphasis is on basic magnitude measurements and yield estimates, determinations of pP parameters and other near-source free-surface interactions, and analysis of tectonic release radiation. An extensive bibliography is included to facilitate future studies of the test site by researchers in the Phillips Laboratory/DARPA program.

Novaya Zemlya Test Information: A relatively small total number (<50) of underground explosions have been detonated at Novaya Zemlya since the first test on September 18, 1964; however, the largest underground Soviet tests are included in this population. Table 1 presents a fairly complete list of events at the test site, with magnitude determinations from a variety of sources. These include m_b determinations from the ISC and from Sykes and Ruggi (1988) [see also Sykes and Wiggins (1986)], and 'b' phase (first peak-to-first trough) magnitudes from Burger et al. (1986b) and Chan et al. (1988b), along with m_b^{Lg} (Nuttli, 1988) and M_S values (Sykes and Ruggi, 1988). Additional magnitude estimates from P and P'P' are available in Chan et al. (1988a,b) and Lilwall and Marshall (1986), with the latter study also giving precise relative locations and origin times of the events. The small events on October 27, 1973 may be aftershocks of the large test that day [Israelson et al. (1974) report 10 small events on this day], which are uncommon for this test site. For reference, the body wave magnitudes for the Amchitka explosion CANNIKIN (<5 Megatons) are from 0.1 to 0.3 magnitude units *lower* than the largest values in Table 1 [e.g. m_b^{ISC}=6.6; m_b^{ab} =6.73 for CANNIKIN (Lay and Welc, 1987)], while the M_S for Cannikin [5.69 (Marshall et al. (1979)] is 0.18 magnitude units *larger* than any of the Novaya Zemlya events, suggesting that the largest events have yields on the order of 3 to 5 Megatons.

The majority of events are located along the strait of Matochkin Shar, which separates the northern and southern Islands of Novaya Zemlya [see Leith et al. (1990) for a discussion of the geology], in what is usually referred to as the Northern subsite (events identified by N in Table 1). Folded carbonate and clastic formations appear to dominate in the region. Leith et al. (1990) report that analogous rocks in the northern Urals have seismic velocities from 4.3 to 5.1 km/sec; substantially higher than for the near-surface tuffs at NTS. Permafrost is likely to be substantial and year-round in the region, with depths of up to 900 meters in the mountains, which may increase near-source seismic velocities. A few events with a wide range of magnitudes have been located at the Southern subsite, near the southern end of the South Island of Novaya Zemlya (S in Table 1). It appears that no testing has occurred there since 1975. Leith et al.(1990) suggest that the nuclear tests at the northern site are primarily emplaced in near-horizontal tunnels, excavated into the steep mountain slopes. Burial depths can thus be inferred from topographic relief in conjunction with tunnel entrance locations, but the rough topography of the region and the difficulty of detecting the excavated material (Leith et al. 1990), complicates burial depth estimation by remote imaging techniques. Marginal or non-containment of the larger events seems very

Table 1. Large Novaya Zemlya Explosions

Event Date	Site	m_b^{ISC}	m_b^{S-R}	m_b^{ab}	m_b^{mle}	m_b^{Lg}	M_s^{S-R}	Y^{S-R}	Y^{DI}	Y^{BBL}	Y^{Lg}	Y^{Ms}
Sept. 18, 1964	N	4.2	4.3	—	—	4.37	—	2	2	-	2.5	-
Oct. 25, 1964	N	5.1	4.9	—	—	5.19	—	8	14	-	16.4	-
Oct. 27, 1966	N	6.4	6.39	6.38	6.306	6.45	4.7	422	770	600	644	415
Oct. 21, 1967	N	5.9	5.92	5.65	5.595	6.06	3.99	93	210	61	180	77
Nov. 7, 1968	N	6.1	6.02	5.83	5.845	6.17	4.30	119	310	110	253	160
Oct. 14, 1969	N	6.3	6.09	5.97	5.960	6.31	4.27	140	340	183	399	149
Oct. 14, 1970	N	6.6	6.60	6.72	6.648	6.75	5.02	1001	2100	1714	1970	888
Sept. 27, 1971	N	6.5	6.47	6.53	6.487	6.68	5.06	586	770	973	1500	976
Aug. 28, 1972	N	6.3	6.33	6.25	6.254	6.42	4.76	329	690	426	580	479
Sept. 12, 1973	N	6.8	6.78	6.84	6.699	6.89	5.26	2099	2700	2824	3510	1569
Sept. 27, 1973	S	5.9	5.95	5.52	5.474	5.95	3.74	100	210	36	129	42
Oct. 27, 1973	S	6.9	6.94	6.98	6.879	6.97	5.51	4055	3200	3886	4990	2841
Oct. 27, 1973	S#	4.2	—	—	4.007	—	---	-	-	-	-	-
Oct. 27, 1973	S#	4.8	—	—	3.854	—	---	-	-	-	-	-
July 22, 1974	S	—	—	—	—	—	—	-	-	-	-	-
Aug. 29, 1974	N	6.4	6.43	6.39	6.397	6.60	4.88	497	870	629	1110	636
Nov. 2, 1974	S	6.4	6.78	6.72	6.799	6.84	5.29	2099	1600	1624	2840	1685
Aug. 23, 1975	N	6.3	6.42	6.38	6.381	6.47	4.72	477	550	604	690	435
Oct. 18, 1975	S*	6.7	6.66	6.47	6.519	6.78	4.92	1281	1400	1166	2220	700
Oct. 21, 1975	N	6.6	6.43	6.35	6.348	6.43	4.78	497	700	554	600	502
Sept. 29, 1976	N	5.8	5.80	—	—	5.83	4.50	70	-	-	91	-
Oct. 20, 1976	N	5.1	5.10	—	4.353	5.24	3.40	13	-	-	19	-
Sept. 1, 1977	N	5.7	5.70	—	5.426	5.93	3.70	55	-	-	122	-
Oct. 9, 1977	N	4.6	4.60	—	—	4.99	—	4	-	-	10	-
Aug. 10, 1978	N	5.9	5.90	—	5.630	5.83	4.30	89	-	-	91	-
Sept. 27, 1978	N	5.6	5.60	—	—	5.69	4.50	44	-	-	61	-
Nov. 15, 1978	N	3.6	—	—	—	—	—	-	-	-	-	-
Sept. 24, 1979	N	5.7	5.70	—	—	5.79	4.50	55	-	-	81	55
Oct. 18, 1979	N	5.8	5.80	—	—	5.78	4.20	70	-	-	79	-
Oct. 11, 1980	N*	5.7	5.70	—	5.445	5.77	4.00	55	-	-	76	-
Oct. 1, 1981	N	6.0	6.00	—	5.492	5.91	3.80	113	-	-	116	-
Oct. 11, 1982	N	5.6	5.60	—	—	5.78	4.20	44	-	-	79	-
Aug. 18, 1983	N	5.9	5.90	—	5.531	5.99	4.10	89	-	-	145	-
Sept. 25, 1983	N	5.8	5.80	—	—	5.86	—	70	-	-	99	-
Aug. 26, 1984	N	3.8		—	—	—	—	-	-	-	-	-
Oct. 25, 1984	N	5.9	5.90	—	5.434	—	4.70	89	-	-	-	-
Aug. 2, 1987	N	5.8	5.80	—	-	—	—	70	-	-	-	-
May 7, 1988	N	5.6	5.60	—	—	—	-	-	-	-	-	-
Dec. 4, 1988	N	5.7	—	—	—	—	-	-	-	-	-	-
Oct. 24, 1990	N	5.4	—	—	—	—	-	-	-	-	-	-

possible aftershock; * Known Double Event

Key:

S is subsite N or S; m_b^{ISC} is from Bulletin of International Seismic Centre; m_b^{S-R} is from Sykes and Ruggi (1988); m_b^{ab} is from Burger et al. (1986b) ['b' phase] and Lay and Welc (1987); m_b^{mle} is from Chan et al. (1988b) ['b' phase]; m_b^{Lg} is from Nuttli (1988); M_s^{S-R} is from Sykes and Ruggi (1988); Y^{DI} is yield from Dahlman and Israelson (1977); Y^{S-R} is yield from Sykes and Ruggi (1988) m_b^{S-R} values; Y^{BBL} is yield from intercorrelation using Amchitka scaling from Burger et al. (1986b); Y^{Lg} is yield from Lg by Nuttli (1988); Y^{Ms} is yield from M_s^{S-R} from Sykes and Ruggi (1988).

plausible. Topography in the southern site is less pronounced and conventional drill hole emplacement is likely.

The large range of explosion size at the test site has required the development and application of station corrections in magnitude estimation, along with maximum likelihood procedures to overcome censoring difficulties caused by non-uniform network reporting (Burger et al., 1986b, McLaughlin et al., 1986; Chan et al. 1988b). Teleseismic body wave magnitude anomalies for the two Novaya Zemlya subsites exhibit very large azimuthal variations and strong relative patterns, so most procedures have treated events at the northern and southern subsites as separate populations despite their separation by less than 250 km (Butler and Ruff, 1980; Burger et al, 1986b; Chan et al. 1988a). This is also necessary for tectonic release analysis (Burger et al., 1986a).

Yield Estimates. Table 1 includes seismic yield estimates from a variety of sources, and shows the wide range of explosion yields at the two subsites. Note that factor of 2 discrepancies in yield estimates for the largest and smallest events are observed. The yield estimates from Dahlman and Israelson (1977) utilize a magnitude-yield calibration curve based on announced yields of PNE's. The yields from Sykes and Ruggi (1988) assume a Δm_b bias of 0.351 magnitude units relative to NTS and 0.027 relative to Amchitka. These are used to correct magnitudes for NTS and Amchitka events with announced yields to produce the Novaya Zemlya yield-scaling equation:

$$m_b = 4.9206 + 0.5597 \log_{10} Y$$

The estimated m_b biases are based on the spectral slope studies of Der et al. (1975a,b), which indicate a $\overline{\Delta t}^*$ of 0.26s for NTS relative to both Novaya Zemlya and Shagan River sites, with Amchitka having $\overline{\Delta t}^*$=0.02 s relative to Novaya Zemlya. [Empirically, $\Delta m_b \sim 1.35\ \overline{\Delta t}^*$, if the spectral slope estimates are inferred to give variations in absolute t*.] The 0.351 m_b bias is consistent with the 0.35± 0.5 magnitude unit M_s-m_b shift relative to NTS found by Sykes and Wiggins (1986), which is nearly the same as found for Kazakhstan data. Sykes and Wiggins (1986) also find little shift of M_s-m_b for Novaya Zemlya relative to Amchitka events, and it is commonly thought that both sites are relatively hard rock regions with comparable coupling effects. Burger et al. (1986b) used explosion strength estimates for the Novaya Zemlya events derived from waveform correlation procedures in an Amchitka event derived yield-scaling equation to produce the yield estimates given in Table 1. Their procedure assumed an average Δt^*=-0.25 s relative to their preferred value for NTS of 0.75 s (Burger et al., 1987). Chan et al. (1988) give source strength estimates from P and PcP spectral amplitude levels for many of these events as well. Additional work on yield estimation from body waves is reported in Murphy and O'Donnell (1988) and Murphy (1989). The yields from Nuttli are based on the quadratic equation derived for NTS events given by:

$$m_b^{Lg} = 3.943 + 1.124 \log_{10} Y - 0.0829 (\log_{10} Y)^2$$

This equation assumes that Lg scaling is transportable from NTS with no correction. Nuttli (1988) finds that m_b-m_b^{Lg} magnitude differences have a shift of 0.15 magnitude units relative to Shagan River tests. This could imply a reduced Δm_b relative to NTS of only 0.20 magnitude units, but it is also possible that the Lg excitation and attenuation properties are not fully transportable. Thus, the systematically higher yields obtained from Lg in Table 1 are not well understood. The yields calculated from M_s by Sykes and Ruggi (1988) utilize the equation:

$$M_s = 2.16 + 0.97 \log_{10} Y$$

which is based on a fit to data for events with known yields in hard rock or below the water table (Sykes and Wiggins, 1986). This equation gives an estimated yield for CANNIKIN of 4357 kt, significantly larger than the M_S-derived yield for any of the Novaya Zemlya events. Additional yield estimates based on surface waves have been given by Stevens and McLaughlin (1989) and Tucker et al. (1989). The apparent clustering of certain yield sizes at Novaya Zemlya has been discussed in the context of particular weapon types by Sykes and Wiggins (1986), Sykes and Davis (1987), and Sykes and Ruggi (1988).

It is clear from Table 1 that there are significant uncertainties in yields of the Novaya Zemlya events. Consider the simple comparison with event MILROW, an Amchitka test with an announced yield of ~1000 kt, with measured m_b^{ab}=6.27 (Lay and Welc, 1987) and M_S=5.05 (Marshall et al., 1979). Novaya Zemlya events with comparable values of M_S (October 14, 1970 and September 27, 1971) have m_b^{ab} differences relative to MILROW of 0.45 and 0.26 magnitude units respectively, and a suite of yield estimates ranging from 586 to 2100 kt. This discrepancy in yield estimates for Novaya Zemlya events based on body wave and surface wave comparisons with the Amchitka test site (which presumably should be a good analog according to the $\Delta\bar{t}$* studies and inferences about emplacement media) is not resolved. Cormier et al. (1991) have shown that slab effects may bias the Amchitka m_b's downward by about 0.1-0.4 magnitude units. This may in part account for the relatively large absolute t* (0.92 s at 1 Hz) estimated for the Amchitka site by Burdick et al. (1984), but it is still likely that the absolute t* level for Amchitka signals is higher than for Novaya Zemlya signals. [Note that the consistency in $\Delta\bar{t}$* measures of high frequency spectral slopes does *not* require common absolute t* values, see Burger et al (1987).] Thus, defocussing and attenuation beneath Amchitka may cause the m_b's to be significantly lower than for Novaya Zemlya events of the same yield, as is required for compatibility with the relatively low yield estimates in Table 1. This suggests that the consistency in M_S-m_b levels between Amchitka and Novaya Zemlya is fortuitous. Given the lack of tectonic release for Amchitka events, one must be concerned about the M_S values for Novaya Zemlya events being biased by either tectonic release or propagation differences.

Multiple Explosions. Double explosions, involving spatially offset events with nearly simultaneous detonation have been observed at both Novaya Zemlya subsites (October 18, 1975 at SNZ; Hurley, 1977; Subhash and Choudhury, 1979; Burger et al, 1986b, Chan et al., 1988a; and October 11, 1980 at NNZ; Lilwall and Marshall, 1986; Stewart and Marshall, 1988). The azimuthal interference pattern of these double arrivals has been resolvable given the good teleseismic azimuthal coverage provided by global seismic networks for the Novaya Zemlya source region. The yield estimates for these events may well be biased by the interference effects for both surface waves and body waves. Burger et al. (1986b) and Chan et al. (1988a) discuss additional events with unusual waveform or amplitude patterns that may possibly involve multiple explosions as well.

Propagation Complexities. The location of the test site on the islands of Novaya Zemlya appears to result in substantial waveform complexity for both teleseismic and regional phases. Teleseismic P waves from Novaya Zemlya events have often been found to have rather complex codas at stations that record simple signals for other explosion source regions (e.g. Hasegawa, 1971, Douglas et al., 1973). This led Greenfield (1971) to explore the effects of near-source Rayleigh wave to P wave scattering from the rough topography in the source region. More recent efforts to quantify near-source scattering include the work of McLaughlin and Jih (1987), where it is shown that Novaya Zemlya event P coda levels can be explained by *rms* velocity variations between 7 and 15% in the upper 3 km of the crust. Rough topography is more efficient at Rayleigh wave scattering than shallow heterogeneity and may dominate in Novaya Zemlya test site. While Lg phases

are observed at European and Soviet stations for Novaya Zemlya events (e.g. Nuttli, 1988; Israelson, in preparation), there is significant reduction of Lg amplitudes at the NORESS (20°) and ARCESS (10°) arrays, while Graefenburg (30°) records fairly clear Lg (Baumgardt, 1990, 1991). Blockage and scattering of Lg in the Barents Sea leg of the path may be responsible, with Baumgardt favoring blockage by Sn⇒Lg and Lg⇒Sn scattering due to variations in the sediment thicknesses in the Barents Sea. Sediment as thick as 15 km is found in some basins surrounding Novaya Zemlya. Such complexities may account for the anomaly in m_b-m_b^{Lg} behavior of Novaya Zemlya relative to Shagan River noted by Nuttli (1988), raising questions about the uncorrected transportability of the Lg-yield scaling formula to an island test site.

The distance of NORSAR from Novaya Zemlya (20°) causes the direct P phases at the array to be complicated by upper mantle triplications (Given and Helmberger, 1980; Given et al, 1988), and the associated amplifications have caused most NORSAR recordings to saturate except for the smaller events (Mykkeltveit, 1990). This fact, in combination with the reduced rate of testing at the site over the past 10 years, causes the modern digital seismogram data base for Novaya Zemlya events to be rather sparse, but the high quality data that are available (mainly from the AWRE arrays) favor a low t* source region (Der et al., 1985a,b; Israelson and Carter, 1991). Very few recordings of regional phases are available for the source region. This gives heightened importance to the historical Soviet station data sets that are being collected by DARPA, which will provide our primary regional phase experience with the source region. Long-period signals also encounter strong propagation complexities, particularly for paths crossing the Arctic Ocean. Lateral refraction, focussing, and multi-pathing are observed and can only be partially accounted for with existing tomographic or regionalized models (e.g. Teng and Aki, 1987; Zeng et al., 1989), so empirical M_S path corrections are also important. Efforts to study the surface waves for scalar moment and tectonic release estimation have drawn on empirical determination of the frequency dependent path transfer functions (Stevens and McLaughlin, 1989), but the small number of available events and the long propagation distances involved complicate this procedure. It is not fully established whether there may be any net bias of M_S levels caused by propagation effects relative to Amchitka or other test sites used to develop M_S-yield scaling relations.

Free Surface Interactions. Several studies have concentrated on the direct P signals and early P wave coda in an effort to constrain the near-source free surface interactions. This includes characterizing the pP lag time and amplitude as well as any later arrivals due to spall or tectonic release. As is true for other test sites, there has been substantial controversy over the interpretation of pP parameter estimates. Burdick and Helmberger (1979) were among the first to show that broadband ground motion deconvolution indicates strong pP arrivals for Novaya Zemlya events. They used forward modeling of the broadband ground motions with a von Seggern and Blandford source time function to estimate characteristics of the reduced displacement potential along with the pP arrival. Strong overshoot of the ground motion suggested that overshoot of the source function itself was needed in addition to a nearly elastic free surface reflection.

Additional evidence for strong pP reflections for Novaya Zemlya events was provided by analysis of short-period teleseismic signals using the intercorrelation method (Burger et al., 1985, 1986). This procedure involves waveform equalization between sets of observations at common stations for pairs of events. It utilizes a simple parameterization of the inter-event transfer function, typically as a two-spike model representing P and pP, along with a yield-varying source function model. Since the procedure involves waveform correlations, it tends to emphasize the lower frequency content of the signals, thus the pP parameters that are extracted are a low-pass filtered version of the actual arrivals. The timing and amplitude

of the pP arrivals can thus differ from results derived at higher frequency, but they do give appropriate characterizations of the low frequency energy to the extent that the two-spike model parameterization is appropriate. Strong spall or tectonic release processes that give rise to more complicated inter-event transfer functions may bias the results in complex ways. Burger et al. (1985, 1986b) give detailed results of their intercorrelation analysis of the Novaya Zemlya events, in which they use 566 teleseismic short period signals. The resulting pP delay time and relative amplitude estimates are listed in Table 2. The delay times for most of the events are similar to those found for the Amchitka events of comparable estimated yield, and vary from 0.55 to 0.74 s. While overshoot was included in the source model, the pP amplitudes are still large, comparable to the direct P arrivals, as suggested by Burdick and Helmberger (1979). This requires a nearly elastic reflection coefficient for the lower frequency energy, or possibly some constructive interference of near-source reverberations (see Burdick and Helmberger, 1979).

An alternate procedure for extracting the free surface interaction was used by Der et al. (1986, 1987) and Chan et al. (1988a). These studies used a maximum likelihood multichannel deconvolution of P and PcP phases recorded across short period arrays. Deconvolutions were performed for suites of events recorded at each array to develop separate source and propagation transfer functions. A total of 27 events at Novaya Zemlya have been analyzed. Examples of source time functions extracted using the three AWRE arrays GBA, EKA and YKA are shown in Figure 1 (Der et al., 1986). The source time functions are quite complex at YKA, suggesting that either there is strong nonisotropic radiation from the events, or that path effects have not been fully separated from the source functions. The YKA signals are too complex to identify pP, but the GBA and EKA signals suggest that pP is present, with a delay of about 0.35 s. In many signals, pP is followed by strong later arrivals. The presence of these additional arrivals, which are presumably associated with variable spall effects, may contaminate the intercorrelation procedure, but it is not clear what causes the azimuthal variability in the deconvolution results. Chan et al. (1988a) performed additional deconvolutions for the EKA and WRA arrays using PcP and Pdiff arrivals. These phases were on-scale for the larger events, for which P saturated the array. The EKA results were used to estimate pP lag times and relative amplitudes, with the values being listed in Table 2. Note that for the northern subsite the pP delay times are systematically shorter than indicated by intercorrelation, and the pP amplitudes are somewhat lower, while the results are more consistent for the southern subsite. The pP delay times exhibit a systematic increase with magnitude, as shown in Figure 2.

The pP delay times from multichannel deconvolution for the northern subsite are consistent with the relatively shallow burial depths expected for tunnel shots, along with the relatively high near-source velocities that are inferred from the geology. For pP delay times less than 0.2 s or so the tendency is to overestimate the delay when measuring peak-to-trough time differences in the ground motion (Der et al., 1987), so the short delay times in Figure 2 may be biased high. It is also possible that nonlinear effects near the shot point cause actual pP delay times to be less than predicted for an elastic structure. The longer pP delays inferred from the intercorrelation results are difficult to reconcile with shallow tunnel emplacement, and thus probably reflect the overall long-period characteristic of the free-surface interaction, including biasing effects of extra arrivals in the deconvolved traces. Since the pP reflection itself is complex and probably frequency dependent (Lay, 1991), the inconsistent delay times may also simply reflect the varying passbands of the different approaches. In terms of reliability for inferring burial depth, the higher frequency deconvolution technique is probably superior, but it has uncertainty due to bandwidth limitations and possible errors in the attenuation and source function parameterizations used in the deconvolution. For the southern test site the two methods give much more similar pP delays, which are longer than for comparable magnitude events at the northern site. The deconvolutions also tend to give simple source functions for the southern region (Der et al.,

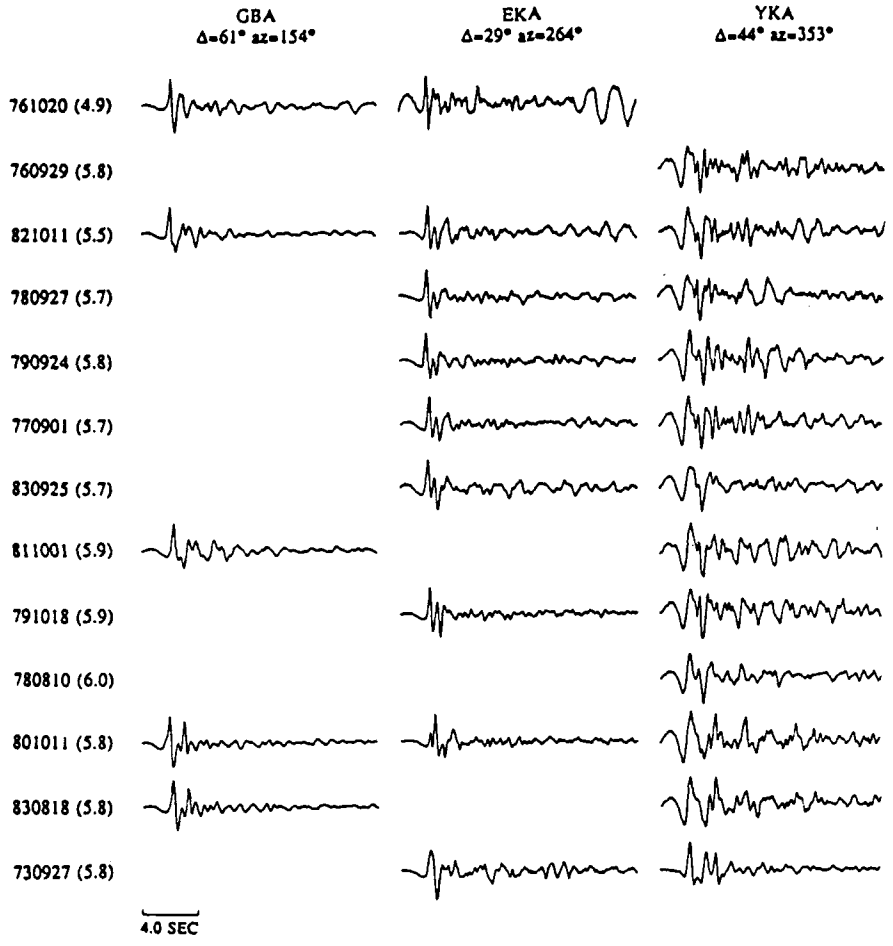


Figure 1. Source time function estimates for Novaya Zemlya events at three AWRE arrays. No source model has been removed from the traces. From Der et al. (1986).

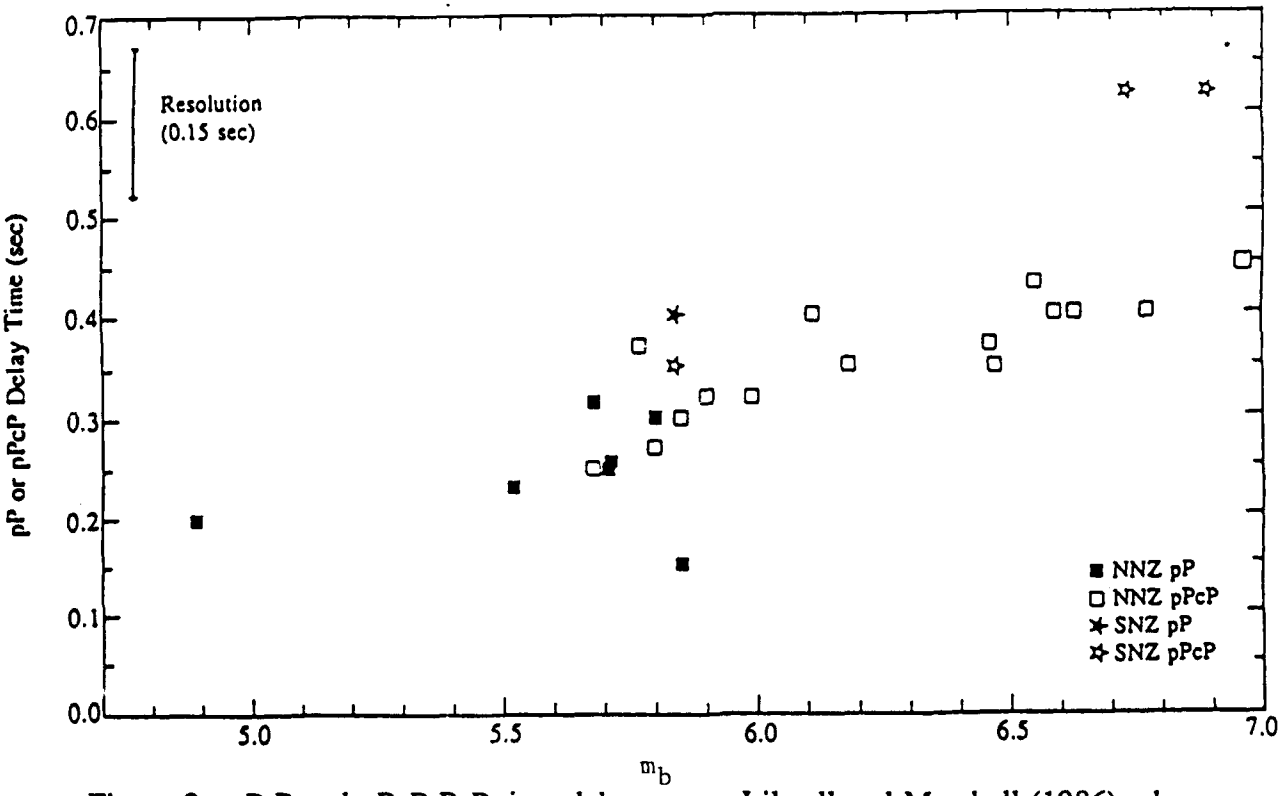


Figure 2. pP-P and pPcP-PcP time delays verus Lilwall and Marshall (1986) mb measured from P and PcP deconvolutions of Novaya Zemlya events recorded at EKA. Events at the southern Novaya Zemlya test site are indicated with stars, while boxes are for northern events. From Chan et al. (1988).

Table 2. pP Parameters Estimated for Large Novaya Zemlya Events

Event	pP-P*,sec	pP relative amp*	pP-P**,sec	pP relative amp**	Phase**
NNZ					
Oct. 27, 1966	0.74	-1.04	0.35	-0.35	PcP
Oct. 21, 1967	0.56	-0.80	0.30	-0.75	PcP
Nov. 7, 1968	0.58	-1.04	0.40	-1.10	PcP
Oct. 14. 1969	0.64	-1.00	0.35	-1.20	PcP
Oct. 14, 1970	0.65	-0.95	0.40	-0.75	PcP
Sep. 27, 1971	0.73	-1.06	0.40	-0.75	PcP
Aug. 28, 1972	0.66	-1.06	0.37	-0.7	PcP
Sep. 12, 1973	0.71	-1.15	0.45	-0.7	PcP
Aug. 29, 1974	0.71	-1.12	-	-	-
Aug. 23, 1975	0.62	-1.08	0.43	-1.0	PcP
Oct. 21, 1975	0.69	-1.05	0.40	-0.4	PcP
Sep. 29, 1976	-	-	0.37	-0.9	PcP
Oct. 20, 1976	-	-	0.20	-1.05	P
Sep. 1, 1977	-	-	0.25	-0.5	P
Sep. 27, 1978	-	-	0.33	-0.85	P
	-	-	0.25	-0.55	PcP
Sep. 24, 1979	-	-	0.30	-0.65	P
	-	-	0.50	-0.27	PcP
Oct. 11, 1982	-	-	0.60	-0.60	P
Sep. 25, 1983	-	-	0.90	-0.40	P
Oct. 25, 1984	-	-	0.32	-1.9	PcP
SNZ					
Sep. 27, 1973	0.55	-0.97	0.40	-1.45	P
			0.35	-1.80	PcP
Oct. 27, 1973	0.70	-1.18	0.62	-0.65	PcP
Nov. 02, 1974	0.58	-1.10	0.62	-0.75	PcP
Oct. 18, 1975	0.55	-0.95	-	-	-

*Burger et al. (1986b), **Chan et al. (1988)

1987), thus the intercorrelation procedure may intrinsically perform better than for the northern site. The longer delays at the southern test site are consistent with the interpretation that the events are emplaced in drill holes rather than tunnels, with more conventional burial depths. The short delays at the northern test site are probably responsible for some constructive interference that enhances the m_b values by as much as 0.2 magnitude units relative to comparable yield events at sites with deeper burial and weaker pP amplitudes (Der et al., 1987). This can help to reconcile some of the m_b discrepancies relative to the Amchitka events, which have large pP arrivals but much longer delay times (0.55-1.1 s).

One other approach that has provided estimates of pP parameters for Novaya Zemlya events is the spectral averaging method of Murphy and O'Donnell (1988) and Murphy (1989). This approach uses a spectral factorization of source and path terms for a suite of events recorded by a suite of globally distributed stations. The common source spectrum can then be modeled to infer source parameters. For a megaton size shot at Novaya Zemlya a delay time of 0.71 s and a pP relative amplitude of -0.2 were found. These numbers reflect the tendency for spectral averaging procedures to give pP delay times in good agreement with intercorrelation, but pP amplitudes that are substantially lower (Burdick, 1991). Burdick (1991) has shown that the particular spectral estimation procedure used in the spectral averaging method by Murphy intrinsically tends to underestimate the pP amplitudes due to spectral smoothing. Lay and Zhang (1991) performed spectral averaging for the same Novaya Zemlya signals that Burger et al. (1986b) modeled by intercorrelation, and found that the pP scalloping expected for strong pP reflections is indeed smoothed out by spectral carpentry effects. This suggests that pP parameters are best estimated from deconvolution methods, but as pointed out by Lay (1991) different deconvolutions weight different frequency bands, so all estimates of pP parameters need to be qualified by the associated bandwidth of the estimate.

Closely associated with the question of the pP behavior for Novaya Zemlya events is the nature of the early P wave coda. Several studies have characterized the energy partitioning into the early coda, as this holds the potential for constraining near-source information. Lay and Welc (1987) provide evidence that Novaya Zemlya events have an inverse relation between signal complexity and magnitude, with larger events having relatively simple waveforms, as was first noted by Davies (1970). The energy in the waveforms is concentrated earlier in the signals than for NTS and Amchitka events, reflecting the shorter pP delays and less pronounced spallation effects. The coda shows similar azimuthal patterns to the direct phases, indicating that much of the coda is generated near the source, as modeled by Greenfield (1971). The variation of complexity does not depend on tectonic release F-factor or pP amplitude, but does correlate with estimated pP delay time, suggesting a burial depth effect, perhaps associated with enhanced scattering of near-source surface waves for very shallow, small events. Lay (1987) showed that the complexity variations are primarily associated with the lower frequency content of the signals, with variations being strongest for periods of 0.4 to 0.8 s. Similar patterns are seen for events at both subsites. Lay and Zhang (1991) have used ratios of event-averaged spectra for P and P coda windows, and show that P waves from larger Novaya Zemlya events have relatively depleted high frequency content compared to the early coda, opposite to the observed behavior for NTS events. They suggest that since burial depth variations are likely to be fairly small at the northern site there may be a source volume effect by which larger sources excite relatively more high frequency energy in the coda (or depleted high frequency energy of the P wave). Modeling to test this idea is required.

Tectonic Release. Large long-period S waves have often been observed from Novaya Zemlya events (Given and Helmberger, 1980), along with large Love waves, so there has been much interest in quantifying the tectonic release characteristics of the test site to

determine its effect on m_b and M_S. Given the intrinsic ambiguities of surface wave modeling of tectonic release parameters, Burger et al. (1986a) and Cohee and Lay (1988) concentrated on the long-period body waves from the larger explosions. There appears to be little clearly identifiable effect of tectonic release on the teleseismic P waves, as recorded on either short-period or long-period records, but clear long-period SH and SV waves can be modeled for the larger events. For the October 27, 1973 and November 2, 1974 events at the southern test site, quantitative modeling of the SV waveforms appears to resolve the usual difficulty of distinguishing between vertical strike-slip and pure thrust solutions, with the strike-slip mechanism being favored (Cohee and Lay, 1988). F-factors of 1.0 are found for these events, with tectonic release moments of 3.2 10^{24} and 1.7 10^{24} dyne-cm respectively, with identical right-lateral vertical strike-slip mechanisms with a strike of 287°. The other large event at the southern site, on October 18, 1975, has a factor of 2 lower SH/P excitation, but the effect of this being a double event has not been fully explored.

It is apparent that the SH radiation pattern for the northern subsite is different than that from the south, but it is not clear what the best tectonic release mechanism is (Burger et al., 1986a). Acceptable fits to the SH waves can be obtained using oblique normal-faulting mechanisms with dips of 47° to 75° and slip angles of -65° to -20°, but these do not provide very good fits to the SV amplitude and waveform data. The ambiguity has not been resolved by subsequent detailed analysis of surface waves or by joint inversion of surface waves and body wave amplitudes and polarities (Tucker et al., 1989; 1990). Tucker et al. (1990) attempted to combine P waveform and SH polarity data with surface wave data in a joint inversion, but found for six northern events that they could not distinguish between an oblique normal mechanism and a thrust orientation. Both Burger et al. (1986a) and Tucker et al. (1990) found significant scatter in SV waves that is not understood, and exceeds that observed for events at the southern site. It is plausible that the unusual SV complexity, as well as the SH waves and Love waves, are in part caused by block faulting or scattering from the rough topography in the source region, leading to a failure to explain the data with a simple double-couple or moment-tensor model of tectonic release. Burger et al. (1986a) find about a factor of 3 variation in the SH/P ratios for the northern site, along with evidence for small changes in SH radiation patterns between events that requires either variable tectonic release or scattering effects. Tucker et al. (1989) also find evidence for event-to-event changes in the three surface wave source parameters that can be resolved by moment tensor inversion of surface waves.

Conclusions and Recommendations: There is still significant uncertainty in yield estimates for many of the early large events at Novaya Zemlya, with persisting questions regarding the relative confidence to be attached to yield estimates from m_b, Lg or M_S. Use of Amchitka as an analog site is complicated by inconsistencies in the body wave and surface wave measures. While m_b values for Novaya Zemlya events may be enhanced by short pP delays, and m_b values for Amchitka may be reduced by slab defocussing and strong attenuation, the discrepancies are not yet fully understood.

It appears that relatively strong pP arrivals are observed for Novaya Zemlya events, along with other free-surface complexities. The energy flux in the first 15 s of the waveforms shows variations that are not yet understood, with complexity decreasing with increasing yield, and relative enrichment of low frequency content of the early coda for small events and enrichment of high frequency content of the early coda for large events.

Tectonic release orientation at the northern subsite is still not well resolved, and the possibility of strong near-surface scattering needs to be fully explored. Attaining a quantitative understanding of the SV waves seems to be the most promising approach.

References: Studies of Seismic Waves From Novaya Zemlya Tests

Baumgardt, D. R. (1990). Investigation of teleseismic Lg blockage and scattering using regional arrays, *Bull. Seism. Soc. Am.* **80**, 2261-2281.

Baumgardt, D. R. (1991). High frequency array studies of long range Lg propagation and the causes of Lg blockage and attenuation in the Eurasian continental craton, *Technical Report PL-TR-91-2059(II)*, Phillips Laboratory, Hanscom Air Force Base, MA.

Burdick, L J. (1991). Resolution of the pP paradox at Novaya Zemlya, *Scientific Report No. 1, PL-TR-91-2042*, Phillips Laboratory, Hanscom Air Force Base, MA.

Burdick, L J., and D. V. Helmberger (1979). Time functions appropriate for nuclear explosions, *Bull. Seism. Soc. Am.* **69**, 957-973.

Burdick, L. J., T. Wallace, and T. Lay (1984). Modeling near-field and teleseismic observations from the Amchitka test site, *J. Geophys. Res.* **89**, 4373-4388.

Burger, R. W., T. Lay, C. G. Arvesen, and L. J. Burdick (1985). Estimating seismic yield, pP parameters and tectonic release characteristics at the Novaya Zemlya test site, *Technical Report, WCCP-R-85-03*, Woodward-Clyde Consultants, Pasadena, CA.

Burger, R. W., T. Lay, T. C. Wallace, and L. J. Burdick (1986a). Evidence of tectonic release in long-period S waves from underground nuclear explosions at the Novaya Zemlya test sites, *Bull. Seism. Soc. Am.* **76**, 733-755.

Burger, R. W., L J. Burdick, and T. Lay (1986b). Estimating the relative yields of Novaya Zemlya tests by waveform intercorrelation, *Geophys. J. R. Astr. Soc.* **87**, 775-800.

Burger, R. W., T. Lay, and L J. Burdick (1987). Average Q and yield estimates from the Pahute Mesa test site, *Bull. Seism. Soc. Am.* **77**, 1274-1294.

Butler, R., and L. Ruff (1980). Teleseismic short-period amplitudes: Source and receiver variations, *Bull. Seism. Soc. Am.* **70**, 831-850.

Chan, W. W., K. L. McLaughlin, R. K. Cessaro, M. E. Marshall, and A. C. Lees (1988a). Yield estimation of Novaya Zemlya explosions from short-period body waves, *Technical Report, TGAL-88-03*, Teledyne Geotech Alexandria Laboratories, VA.

Chan, W. W., K. L. McLaughlin, R.-S. Jih, M. E. Marshall, and R. A. Wagner (1988b). Comprehensive magnitude yield estimation for nuclear explosions: A maximum likelihood general linear model (MLE-GLM88), *Technical Report, TGAL-87-05*, Teledyne Geotech, Alexandria, VA.

Cohee, B. P., and T. Lay (1988). Modeling teleseismic SV waves from underground explosions with tectonic release: Results for Southern Novaya Zemlya, *Bull. Seism. Soc. Am.* **78**, 1158-1178.

Cormier, V. F., W. Kim, B. Mandal, and D. Harvey (1991). Effects of a descending lithospheric slab on yield estimates of underground nuclear tests, *Technical Report, PL-TR-91-2025*, Phillips Laboratory, Hanscom Air Force Base, MA.

Dahlman, O., and H. Israelson (1977). *Monitoring Underground Nuclear Explosions*, Elsevier Scientific Publishing Co., New York.

Davies, D. (1970). Some remarks on short-period discrimination, in *Papers Presented at the Woods Hole Conference on Seismic Discrimination*, Vol. **2**, National Technical Information Service, Springfield, VA, 147-159.

Der, Z., A. C. Lees, R. H. Shumway, T. McElfresh, and M E. Marshall (1986). Multichannel deconvolution of P waves at seismic arrays and three component stations, *Technical Report, TGAL-86-6*, Teledyne Geotech, Alexandria, VA.

Der, Z., A. C. Lees, W. W. Chan, R. H. Shumway, K. L. McLaughlin, E. Smart, T. W. McElfresh, and M. E. Marshall (1987). Maximum likelihood multichannel deconvolution of P waves at seismic arrays, *Technical Report TGAL-87-3*, Teledyne Geotech, Alexandria, VA.

Der, Z., T. McElfresh, R. Wagner, and J. Burnetti (1985). Spectral characteristics of P waves from nuclear explosions and yield estimation, *Bull. Seism. Soc. Am.* **75**, 379-390.

Der., Z., T. McElfresh, R. Wagner, and J. Burnetti (1985). Errata to "Spectral characteristics of P waves from nuclear explosions and yield estimation", *Bull. Seism. Soc. Am.* **75**, 1222-1223.

Douglas, A., P. D. Marshall, P. G. Gibbs, J. B. Young and C. Blamey (1973). P signal complexity re-examined, *Geophys. J. R. Astr. Soc.* **33**, 195-221.

Given, J. W., and D. V. Helmberger (1980). Upper mantle structure of northwestern Eurasia, *J. Geophys. Res.* **85**, 7183-7194.

Given, J. W., S. M. Ihnen, G. R. Mellman, and W. C. Tucker (1988). Discrimination studies using short-period P waves at upper mantle distances, *Technical Report, SGI-R-88-137*, Sierra Geophysics, Kirkland, WA.

Greenfield, R. J. (1971). Short-period P-wave generation by Rayleigh-wave scattering at Novaya Zemlya, *J. Geophys. Res.* **76**, 7988-8002.

Hasegawa, H. S. (1971). Analysis of teleseismic signals from underground nuclear explosions originating in four geological environments, *Geophys. J. R. Astr. Soc.* **24**, 365-381.

Hurley, R. W. (1977). Anomalous seismic signals from Novaya Zemlya, AWRE Report No. O 21/77, HMSO, London.

Israe'son, H., and J. Carter (1991). Analysis of high frequency seismic data, *Technical Report, PL-TR-91-2032*, Phillips Laboratory, Hanscom Air Force Base, MA.

Israelson, H., R. Slunga, O. Dahlman (1974). Aftershocks caused by the Novaya Zemlya explosion on October 27, 1973, *Nature* **247**, 450-452.

Lay, T. (1987). Analysis of near-source contributions to early P wave coda for underground explosions. 2. Frequency dependence, *Bull. Seism. Soc. Am.* **77**, 1252-1273.

Lay, T. (1991). The teleseismic manifestation of pP: Problems and paradoxes, AGU Monograph on Explosions Phenomenology, in press.

Lay, T., and J. L. Welc (1987). Analysis of near-source contributions to early P-wave coda for underground explosions. I. Waveform complexity, *Bull. Seism. Soc. Am.* **77**, 1017-1040.

Lay, T., and T. Zhang (1991). Near-source contributions to teleseismic P waves and P-wave coda for underground explosions, *Bull. Seism. Soc. Am.*, in press.

Leith, W., J. R. Matzko, and J. Unger (1990). Geology and image analysis of the Soviet Nuclear Test Site at Matochkin Shar Novaya Zemlya, U.S.S.R., *Proceedings of the 12th Annual DARPA/GL Seismic Research Symposium*, DARPA, Arlington, VA.

Lilwall, R. C., and P. D. Marshall (1986). Body wave magnitudes and locations of Soviet underground explosions at the Novaya Zemlya Test Site, *AWRE Report No O 17/86*, AWRE, MOD(PE), Blacknest, United Kingdom.

Marshall, P. D., D. L. Springer, and H.C. Rodean (1979). Magnitude corrections for attenuation in the upper mantle, *Geophys. J. R. Astr. Soc.* **57**, 609-638.

McLaughlin, K. L., and R.-S. Jih (1987). Finite-difference simulations of Rayleigh-wave scattering by shallow heterogeneity, *Scientific Report #1, AFGL-TR-87-0322*, Air Force Geophysics Laboratory, Hanscom Air Force Base, MA.

McLaughlin, K. L., R. O. Ahner and M. E. Marshall (1986). Maximum likelihood event magnitudes and Log(max/A) at the Novaya Zemlya and Degelen Test Sites, *Technical Report, TGAL-86-02*, Teledyne Geotech, Alexandria, VA.

Murphy, J. R. (1989). Further analyses of network averaged spectra with applications to Novaya Zemlya, *Technical Report, SSS-CR-89-9766*, S-Cubed, Reston, VA.

Murphy, J. R., and A. O'Donnell (1988). Further analysis of network averaged teleseismic P wave spectra with applications to yield estimation of Novaya Zemlya explosions, *Technical Report, SSS-CR-88-9766*, S-Cubed, Reston, VA.

Mykkeltveit, S. (1990). P-wave focusing effects at NORSAR for Novaya Zemlya explosions, In: NORSAR basic seismological research, *Scientific Report No. 7, GL-TR-90-0330*, Geophysics Laboratory, Hanscom Air Force Base, MA. pp. 21-31.

Nuttli, O. W. (1988). Lg magnitudes and yield estimates for underground Novaya Zemlya nuclear explosions, *Bull. Seism. Soc. Am.* **78**, 873-884.

Stevens, J. L., and K. L. McLaughlin (1989). Analysis of surface waves from Novaya Zemlya, Mururoa, and Amchitka test sites, and maximum likelihood estimation of scalar moments from earthquakes and explosions, *Technical Report, SSS-TR-89-9953*, S-Cubed, La Jolla, CA.

Stewart, R. C., and P. D. Marshall (1988). Seismic P waves from Novaya Zemlya explosions: Seeing double!, *Geophys. J.* **92**, 335-338.

Subhash, S. M. G., and M. A. Choudhury (1979). Coda power and modulation characteristics of a complex P signal from underground nuclear explosions, *Tectonophys.*, **53**, T33-T39.

Sykes, L. R., and D. M. Davis (1987). The yields of Soviet strategic weapons, *Scientific American* **256**, 29-37.

Sykes, L. R., and S. Ruggi (1988). Soviet nuclear testing, In: *Nuclear Weapons Databook*, **IV**, (T. B. Cochran et al., eds.), Washington, D.C..

Sykes, L. R., and G. C. Wiggins (1986). Yields of Soviet underground nuclear explosions at Novaya Zemlya, 1964-1976, from seismic body and surface waves, *Proc. Natl. Acad. Sci. USA* **83**, 201-205.

Teng, T., and K. Aki (1987). Surface wave ray tracing and Ms:Yield determination in a laterally heterogeneous earth, *Technical Report, AFGL-TR-87-0243*, Air Force Geophysics Laboratory, Hanscom Air Force Base, MA.

Tucker, W. C., G. R. Mellman, and J. W. Given (1989). Using long period surface waves to estimate the isotropic moment of underground explosions at Novaya Zemlya, *Technical Report SGI-R-89-141*, Sierra Geophysics, Kirkland, WA.

Tucker, W. C., G. R. Mellman, and M. Henry (1990). Estimation of explosion moments at Mururoa and tectonic release orientations at Novaya Zemlya, *Technical Report, SGI-R-90-143*, Sierra Geophysics, Kirkland, WA.

Wright, C., and K. J. Muirhead (1969). Longitudinal waves from the Novaya Zemlya nuclear explosion of October 27, 1967, recorded at the Warramunga Seismic Array, *J. Geophys. Res.* **74**, 2034-2048.

Zeng, Y., T. Teng, and K. Aki (1989). Surface wave ray tracing and Ms:yield determination in a laterally heterogeneous earth, *Technical Report, AFGL-TR-89-0065*, Air Force Geophysics Laboratory, Hanscom Air Force Base, MA.

HOW CAN THE OPERATION OF THOUSANDS OF SEISMIC STATIONS (CARRIED OUT BY HUNDREDS OF INSTITUTIONS IN TENS OF COUNTRIES) BEST BE FOCUSSED ON DISCRIMINATION RESEARCH ?

Paul G. Richards
Lamont-Doherty Geological Observatory and
Department of Geological Sciences,
Columbia University

For nearly twenty years, the most important technical issue for the United States in monitoring nuclear explosions has been estimation of explosion yield, particularly for nuclear weapons tests in the Soviet Union. U.S. capabilities in this area are now well understood, at least in the expert technical community, in the context of monitoring compliance with current treaties. The most obvious indicator of consensus in this area, is the lack of recent debate on technical questions of interpretation of the largest Soviet explosion m_b's — a situation very different from that which prevailed ten years ago.

In the 1990's, for seismologists, the most important technical issue in explosion monitoring is deemed by many to be an assessment of discrimination capability in the context of a follow-on to the Non-Proliferation Treaty.

These two issues present very different challenges in monitoring – differences that have implications for how monitoring can best be organized for different purposes. Yield estimation, whether for large or small explosions, if done well requires well calibrated stations and a coordinated effort that usually will require some type of centralized analysis. Discrimination too may best be done by a tightly directed effort, especially for those who must reach decisions promptly. But seismic stations are being installed at such a rapid rate in so many different parts of the world, and are being operated by so many different organizations, that detection and discrimination capabilities must surely vary quite substantially (and perhaps unpredictably) if ***all*** pertinent data can be brought to bear on a particular region after a period of a few months.

It is important to think of ways to maximize the amount of pertinent data. This paper will briefly review what has been achieved by several different organizations – and small groups of seismic stations – in monitoring seismicity at magnitude levels much smaller than those studied in the context of compliance with current nuclear testing treaties. In particular, examples will be given of the use of seismic stations acquiring regional data in areas of interest – areas with seismicity that is often assessed using only teleseismic data.

In answer to the title question, a case will be made for generating lists of problem events – seismic sources whose signals cannot easily be discriminated – as a mechanism for achieving three goals: (1) encouraging seismologists to contribute data that may help to discriminate events on the list; (2) training; and (2) helping to build consensus in the technical community, on what types of problem event are truly intractable with current data.

Lg AS A YIELD ESTIMATION TOOL

Frode Ringdal
NTNF/NORSAR, P.O. Box 51, 2007 Kjeller, Norway

Contract No. F49620-89-C-0038

Introduction

The seismic Lg wave propagates in the continental lithosphere and can be observed from large explosions as far away as 5000 km in shield and stable platform areas (Nuttli, 1973; Baumgardt, 1985). Lg is generally considered to consist of a superposition of many higher-mode surface waves of grup velocities near 3.5 km/s, and its radiation is therefore expected to be more isotropic than that of P waves. Thus, full azimuthal coverage is not essential for reliable determination of Lg magnitude. Furthermore, Lg is not affected by lateral heterogeneities in the upper mantle, which can produce strong focusing/defocusing effects on P-waves, and therefore contribute to a significant uncertainty in P-based m_b estimates.

In recent years, the Lg phase has emerged as maybe the most promising tool to obtain precise yield estimates by seismic means. The pioneering work by Otto Nuttli of Saint Louis University in the early 1970s first focused attention on using the Lg phase for seismic source size estimation, and Nuttli developed over the years a general technique for measuring Lg magnitude - m_b(Lg) - along any source-receiver path. He successfully applied this method to obtain excellent Lg-based yield estimates for NTS explosions, and also showed that the Lg phase could be used for teleseismic yield estimation at the main Soviet nuclear test sites.

Nuttli did his readings exclusively from analog seismograms, using a very sophisticated interactive analysis method. With the emergence of widespread digital recordings in the 1980s, the focus shifted to automatic digital processing, using in particular RMS measurements of digitally filtered traces (typically 0.6-3.0 Hz) in a fixed time window (typically 2 minutes). This method allowed reliable estimates to be made even at very low SNR, by using a noise compensation procedure. Assuming that independent yield estimates are available for calibration purposes, this method appears particularly well suited for TTBT monitoring of test sites of limited geographical extent.

Extensive research has been conducted by a number of scientists over the past decade investigating various aspects of Lg generation, propagation, attenuation and modelling. While recognizing the importance and impact of this work, it will lead too long to try to cover all of these topics in a brief review paper. I will therefore focus on the observational aspects of Lg as a tool for yield estimation. For a more extensive review of Lg related developments, reference is made to the paper by Hansen, Ringdal and Richards (1990).

In this paper a review is given of the Lg magnitude estimation methodology, and of results obtained with regard to yield estimation. Results are briefly summarized for each of three test sites: Nevada, Semipalatinsk and Novaya Zemlya. The paper is concluded with a short discussion of the capabilities and limitation of Lg as a yield estimation tool. Some very recent results are included, in particular regarding the use of Lg for Novaya Zemlya explosions.

Lg results at NTS

Much pioneering work on Lg waves was done in the 1970s and 1980s by Otto Nuttli of Saint Louis University. Thus, Nuttli (1973) proposed that "since Lg represents a higher-mode wave traveling with minimum group velocity" it would be appropriate to relate amplitude (A) and distance (Δ) via

$$A = K[\Delta^{-1/3}][(\sin\Delta)^{-1/2}]e^{-\gamma\Delta} \quad (1)$$

where K is governed by the source strength, and γ is the coefficient of anelastic attenuation. The quality factor Q is related to γ by the equation:

$$\gamma = (\pi f)/(QU) \quad (2)$$

where U is the group velocity.

With the goal of defining a magnitude scale, based on Lg observations Nuttli described in detail (Nuttli 1973, 1986a) a three-step procedure to obtain what he called an m_b(Lg) value for an earthquake or an explosion of interest. The three steps were as follows:

(i) γ was estimated for a particular source-receiver path;

(ii) equation (1) was used to predict an amplitude at one particular distance (he chose Δ corresponding to 10 km for reference); and

(iii) magnitude was assigned via the formula

$$m_b(Lg) = 5.0 + \log[\mathrm{A}(10\ \mathrm{km})/110]$$

where A(10 km) is the amplitude, in microns, resulting from (ii).

For 22 nuclear explosions below the water table at NTS, Nuttli (1986a) showed that his m_b(Lg) values, using only three WWSSN stations in the western U.S., were remarkably well correlated with the logarithm of announced yield. He proposed a best-fitting line through this magnitude-yield data, from which magnitudes had a standard deviation of only about 0.05. Patton (1988) developed computer-automated measures of Lg amplitude aiming at reporducing Nuttli's NTS results (see Fig. 1). Patton measured Lg amplitudes from digital seismograms in two ways -- by using the third-largest peak and by computing the RMS amplitude in the Lg time window -- and found very little difference (around 0.01 magnitude unit) in the amount of scatter about regression lines using the two measures. However, he found that standard deviations from best-fitting m_b(Lg) / log(yield) relations were low, 0.07-0.08 magnitude units, only if explosions were restricted to sub-regions of NTS (Pahute Mesa, northern Yucca Flat, southern Yucca Flat).

Lg results at Semipalatinsk

Based on the success in estimating yields for NTS explosions, Nuttli proceeded to apply the same magnitude-yield relation, together with Lg signals recorded at analog WWSN stations in Eurasia, to estimate the yields of nuclear explosions at the main Soviet test site (Shagan River, Semipalatinsk) (Nuttli 1986b). For the period 1978-1984, after the 150 kt Threshold Test Ban Treaty had gone into effect, his yield estimates for Shagan River explosions included twenty that exceeded the treshold, including one (1982 December 5) estimated by Nuttli to be about 300 kt. While acknowledging the pioneering work involved in these studies, it is clear that the generally low signal-to-noise ratios and the problematic data quality of these analog recordings made very precise mea-

surements impoissible to attain, a fact also recognized by Nuttli himself. Also, at the teleseismic distances for which Nuttli had Lg data, 1900-4400 km, yield estimates based on absolute measures of ground motion that have to be extrapolated back to 10 km are a severe test of the valicity of eq. (1), and, even if eq. (1) is appropriate, are very sensitive to errors in γ by 10-15% would result in yield estimates about two times too high.

In the first of a number of Lg studies undertaken by the NORSAR staff during the 1980s, Ringdal (1983) analyzed digital NORSAR Lg data of selected Semipalatinsk underground nuclear explosions. He found that when using NORSAR RMS Lg instead of P waves recorded at NORSAR to estimate source size, it was possible effectively to eliminate the magnitude bias relative to world-wide m_b observed at NORSAR between Degelen and Shagan River explosions. The method consisted of averaging log (RMS) values of individual NORSAR channels, filtered in a band 0.6-3.0 Hz in order to enhance Lg signal-to-noise ratio. Ringdal and Hokland (1987) expanded the data base, and introduced a noise compensation procedure to improve the reliability of measurement at low SNR values. They were able to idenify a distinct P-Lg bias between the northeast and southwest portions of the Shagan River test site (see Fig. 2), a feature that was confirmed by Ringdal and Fyen (1988) using Graefenberg array data. Ringdal and Marshall (1989) combined P and Lg based source size estimators to estimate the yields of 96 Shagan River explosions during 1965-1988, suing data on the cratering explosion 15 January 1965 as a reference for the yield calculations.

Hansen, Ringdal and Richards (1990) analyzed available data from stations in China and the Soviet Union, and found that RMS Lg of Semipalatinsk exploions measured at these stations showed excellent consistency (see Fig. 3). They concluded that for explosions at Semipalatinsk with good signal-to-noise ratio, m_b(Lg) may be estimated at single stations with an accuracy (one standard deviation) of about 0.03 magnitude unit. It is noteworthy that this high accuracy was consistently obtained for a variety of stations at very different azimuths and distances, even though the basic parameters remained exactly as originally proposed for NORSAR recordings (0.6-3.0 Hz bandpass filter, RMS window length of 2 minutes, centered at a time corresponding to a group velocity of 3.5 km/s).

A possibility to compare Lg and P magnitudes to published yields for Semipalatinsk explosions has recently emerged with the recent publication by Soviet scientists quoting yield estimates for a number of such explosion (Bocharov et al, 1989; see also Vergino, 1989a,b). Since these explosions were all conducted prior to 1973, there are very few available high-quality digital records of the events. Nevertheless, based on those NORSAR recordings that are available, the correspondence between log RMS Lg and log yield is excellent (Ringdal, 1990). A suite of analog recordings obtained from stations within the Soviet Union has recently been digitized and made available as part of bilateral US-USSR arrangements. Israelson (1991) has computed RMS Lg of these recordings and has found excellent correspondence with the yields published by Bocharov et al (1989).

Lg results at Novaya Zemlya

No yield data have so far been published from Soviet sources for explosions at the Novaya Zemlya test site. Thus an assessment of the Lg potential can only be made in an indirect way. Ringdal and Fyen (1991) compared NORSAR and Graefenberg RMS Lg for Novaya Zemlya explosions using the same procedure as earlier done for Semipalatinsk. Fig. 4 shows the propagation paths to the two arrays along with examples of recorded Novaya Zemlya explosions.

Fig. 5 shows the correspondence between RMS Lg at NORSAR and Grafenberg, and also compares various other source size estimators. Note that world-wide m_b corresponds extremely well with NORSAR P-coda magnitude, but correlates very poorly with either NORSAR or Grafenberg

RMS Lg. Note also that the RMS Lg correspondence between Grafenberg and NORSAR is excellent, with an orthogonal standard deviation of only 0.035. The scatter is further reduced (to 0.025) if we consider only events with at least 5 available GRF channels (Ringdal and Fyen, 1991). Thus, we obtain the same close correspondence between Lg observations from these two arrays for Novaya Zemlya explosions as has previously been observed for Semipalatinsk events.

With the current lack of independently obtained calibration data, it would be premature to draw any firm conclusions as to the relative accuracy of RMS Lg in estimating yields of these explosions. Nevertheless, it would appear that the close grouping in RMS Lg, especially seen for the NORSAR data, is unlikely to be a coincidence. It would seem reasonable to conclude that this group of explosions has very nearly the same yield, in spite of the divergence in m_b estimates. However, additional analysis, in particular including available Lg data from Soviet stations for this event set, should be performed in order to further test this hypothesis. Initial results from processing data from Soviet stations seem to give some support in this regard (Israelson, 1991).

Discussion

Most of the evidence for the "stability" of Lg magnitudes is indirect. By pairwise comparison of RMS Lg for a number of different source-receiver paths, it has been demonstrated that single-station RMS Lg can be used to estimate relative magnitude with a remarkably small scatter (0.02-0.03 in m_b units orthogonally). This was first shown for Semipalatinsk explosions, but has recently been confirmed also for explosions at Novaya Zemlya. The latter observation is particularly interesting, since many of the paths exhibited significant "Lg blockage" effects (Baumgardt, 1990). The Lg blockage is for example seen on NORSAR recordings, where the Lg phase is relatively weak compared to P and Sn.

NORSAR and Grafenberg array measurements of Lg waves from the Shagan River area have been demonstrated as being sufficiently precise to allow a systematic P-Lg magnitude bias to be identified between the NE and SW parts of that site. Available yield data from Soviet sources indicate that Lg magnitudes show better consistency with yield than does P-based magnitudes for explosions from this area. The reason for this P-Lg bias has been the subject of much discussion. The most likely explanation appears to be P-wave focusing/defocusing effects in the upper mantle underlying the source region.

A heuristic explanation for the apparently superior stability of Lg waves compared to P waves in measuring source size lies in the difference in the nature of the sampling of the seismic source for each of these phases. Teleseismic P waves sample only a very limited portion of the focal sphere, and are susceptible to strong focusing/defocusing effects in the upper mantle. Lg waves are composed of multiple rays that sample a larger portion of the focal sphere, and appear to have less significant focusing/defocusing effects along their propagation paths. In a sense, Lg waves "let the Earth do the averaging".

Still, there are many uncertainties remaining with regard to the potential of Lg as a yield estimator. The most significant question mark would appear to be the effects of full or partial "Lg blockage". As noted above, such blockage does not seem to have much effect on RMS Lg stability if the blockage structure is well removed from the source region (cf. NORSAR Lg blockage for Novaya Zemlya explosions). This is reasonable since the blockage effects would in this case be similar for all the events.

However, a different situation arises if full or partial "Lg blockage" structures are located within or in the immediate neighborhood of the test site. It is easy to see that the stability of Lg would be severely affected in such cases. In this connection, it is noteworthy that RMS Lg at NTS does not seem to show the same "stability" as at the two Soviet test sites (Richards, personal communica-

tion). It would seem likely that such local partial "blockage" effects at NTS might account for this difference

Lg waveforms cannot at present be modelled with the same quality of fit between synthetics and data that has been attained with other phases, and many aspects of Lg generation and propagation characteristics are still not well understood. Among topics that need further study are Lg blockage and scattering effects caused by tectonic heterogeneities and the effects of topography, near source geology and depth of burial on Lg excitation. Much challenging work therefore remains to be done in this field.

References

Baumgardt, D.R. (1985): Comparative analysis of teleseismic P coda and Lg waves from underground explosions in Eurasia, Bull. Seism. Soc. Am., 75, 1413-1433.

Baumgardt, D.R. (1990): Investigation of teleseismic Lg blockage and scattering using regional arrays, Bull. Seism. Soc. Am., Special Issue, 80, 2261-2281.

Bocharov, V.S., S.A. Zelentsov and V.I. Mikhailov (1980): Characteristics of 96 underground nuclear explosions at the Semipalatinsk test facility, Atomic Energy, 67, 3, 210-214 (in Russian).

Hansen, R.A., F. Ringdal and P.G. Richards (1990): The stability of RMS Lg measurements, and their potential for accurate estimation of the yields of Soviet underground nuclear explosions, Bull. Seism. Soc. Am., Special Issue, 80, 2106-2126.

Israelson, H. (1991): Manuscript in preparation.

Leith, W. (1987): Tectonics of eastern Kazakhstan and implications for seismic source studies in the Shagan River area. In: Papers presented at the 9th Annual DARPA/ AFGL Seismic Research Symposium, 15-18 June 1987, 34-37.

Nuttli, O.W. (1973): Seismic wave attenuation and magnitude relations for eastern North America, J. Geophys. Res., 78, 876-885.

Nuttli, O.W. (1986a): Yield estimates of Nevada test site explosions for eastern North America, J. Geophys. Res., 91, 2137-2151.

Nuttli, O.W. (1986b): Lg magnitudes of selected East Kazakhstan underground explosions, Bull. Seism. Soc. Am., 76, 1241-1251.

Patton, H.J. (1988): Application of Nuttli's method to estimate yield of Nevada test site explosions recorded on Lawrence Livermore National Laboratory's digital seismic system, Bull. Seism. Soc. Am., 78, 1759-1772.

Ringdal, F. (1983): Magnitudes from P coda and Lg using NORSAR data, In: NORSAR Semiann. tech. Summ., 1 Oct 1982 - 31 Mar 1983, NORSAR Sci. Rep. 2-82/83, Kjeller, Norway.

Ringdal, F. (1990): Detection and yield estimation studies, In: Semiann. Tech. Summ., 1 April - 30 September 1990, NORSAR Sci. Rep. 1-90/91, Kjeller, Norway.

Ringdal, F. and B.Kr. Hokland (1987): Magnitudes of large Semipalatinsk explosions using P coda and Lg measurements at NORSAR, In: Semiann. Tech. Summ., 1 Apr - 30 Sep 1987, NORSAR Sci. Rep. 1-87/88, Kjeller, Norway.

Ringdal, F. and J. Fyen (1988): Comparative analysis of NORSAR and Grafenberg Lg magnitudes of Shagan River explosions, In: Semiann. Tech. Summ., 1 Apr - 30 Sep 1988, NORSAR Sci. Rep. 1-88/89, Kjeller, Norway.

Ringdal, F. and P.D. Marshall (1989): Yield determination of Soviet underground nuclear explosions at the Shagan River Test Site, In: Semiann. Tech. Summ., 1 Oct 1988 - 31 Mar 1989, NORSAR Sci. Rep. No. 2-88/89, Kjeller, Norway.

Ringdal, F. and J. Fyen (1991): RMS Lg analysis Novaya Zemyla explosion recordings, In: Semiann. Tech. Summ., 1 Oct 1990 - 31 Mar 1991, NORSAR Sci. Rep. No. 2-90/91, Kjeller, Norway.

Vergino, E.S. (1989a): Soviet test yields, EOS, Trans. Am. Geophys. Un., 1511+, November 28.

Vergino, E.S. (1989b): Soviet test yields, Corrections and Additions, EOS, Trans. Am. Geophys. Un., 1569, December 26.

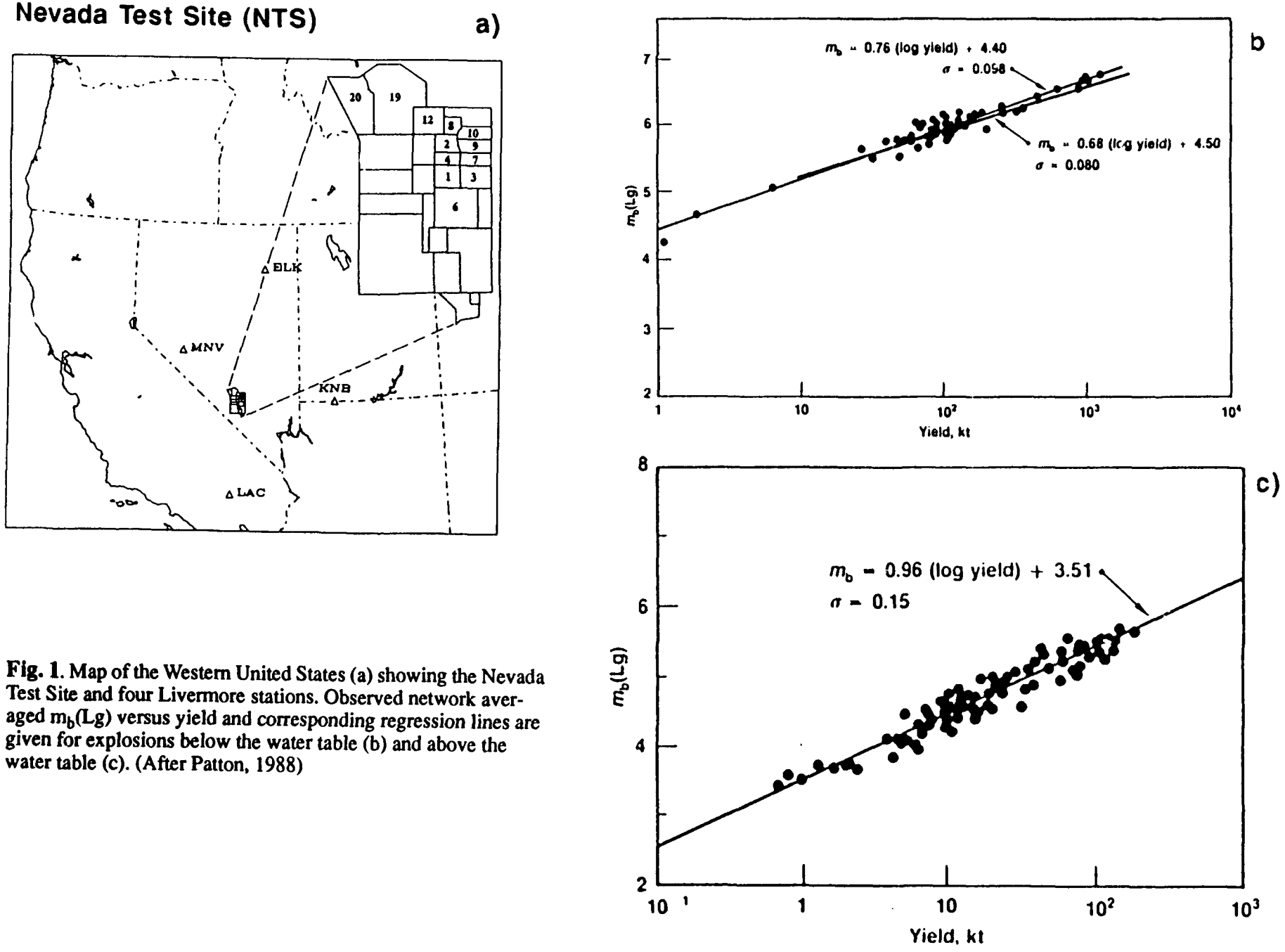
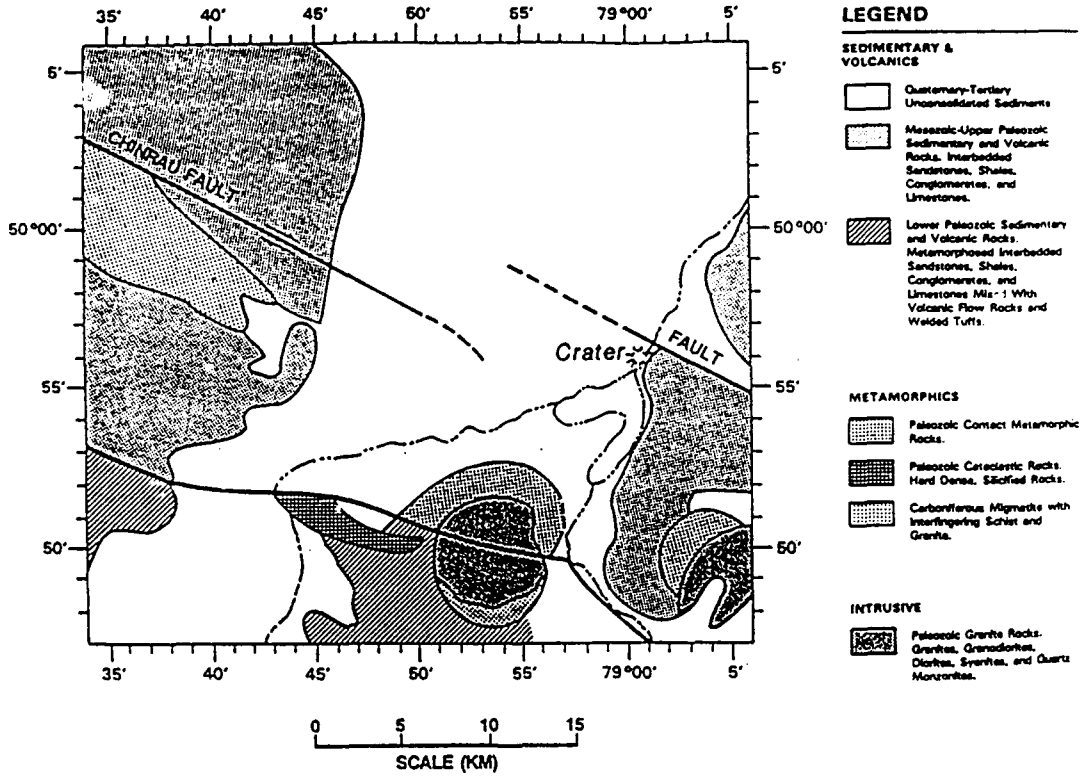


Fig. 1. Map of the Western United States (a) showing the Nevada Test Site and four Livermore stations. Observed network averaged m_b(Lg) versus yield and corresponding regression lines are given for explosions below the water table (b) and above the water table (c). (After Patton, 1988)

Shagan River Test Site, USSR



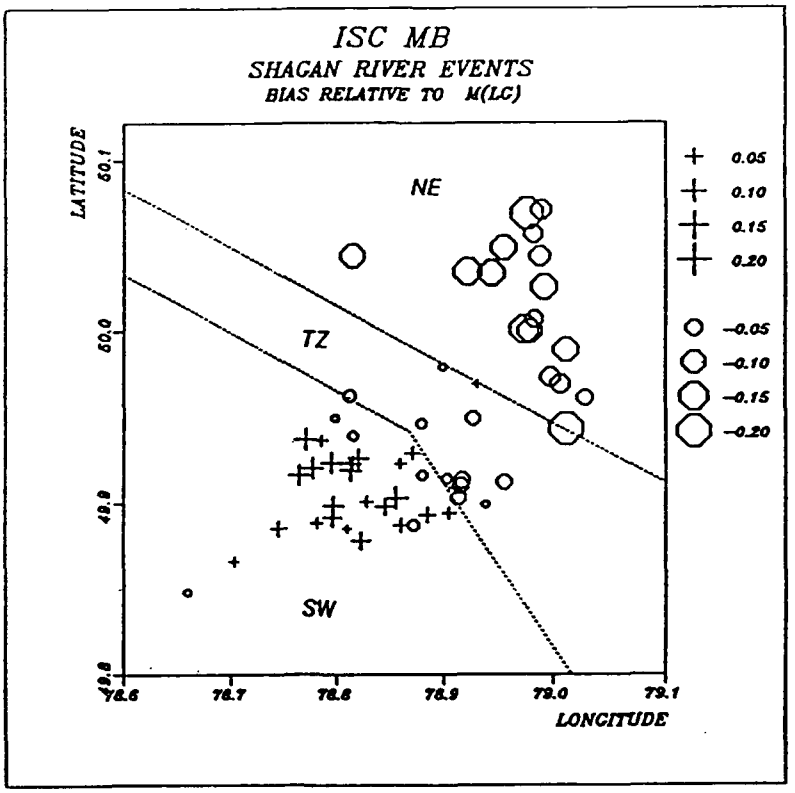


Fig. 2. Map of the Shagan River area (top), showing the surface geology (see Leith, 1987). The bottom figure illustrates the systematic P-Lg magnitude bias across the test site, and the correction with the observed faults. (After Ringdal and Marshall, 1989)

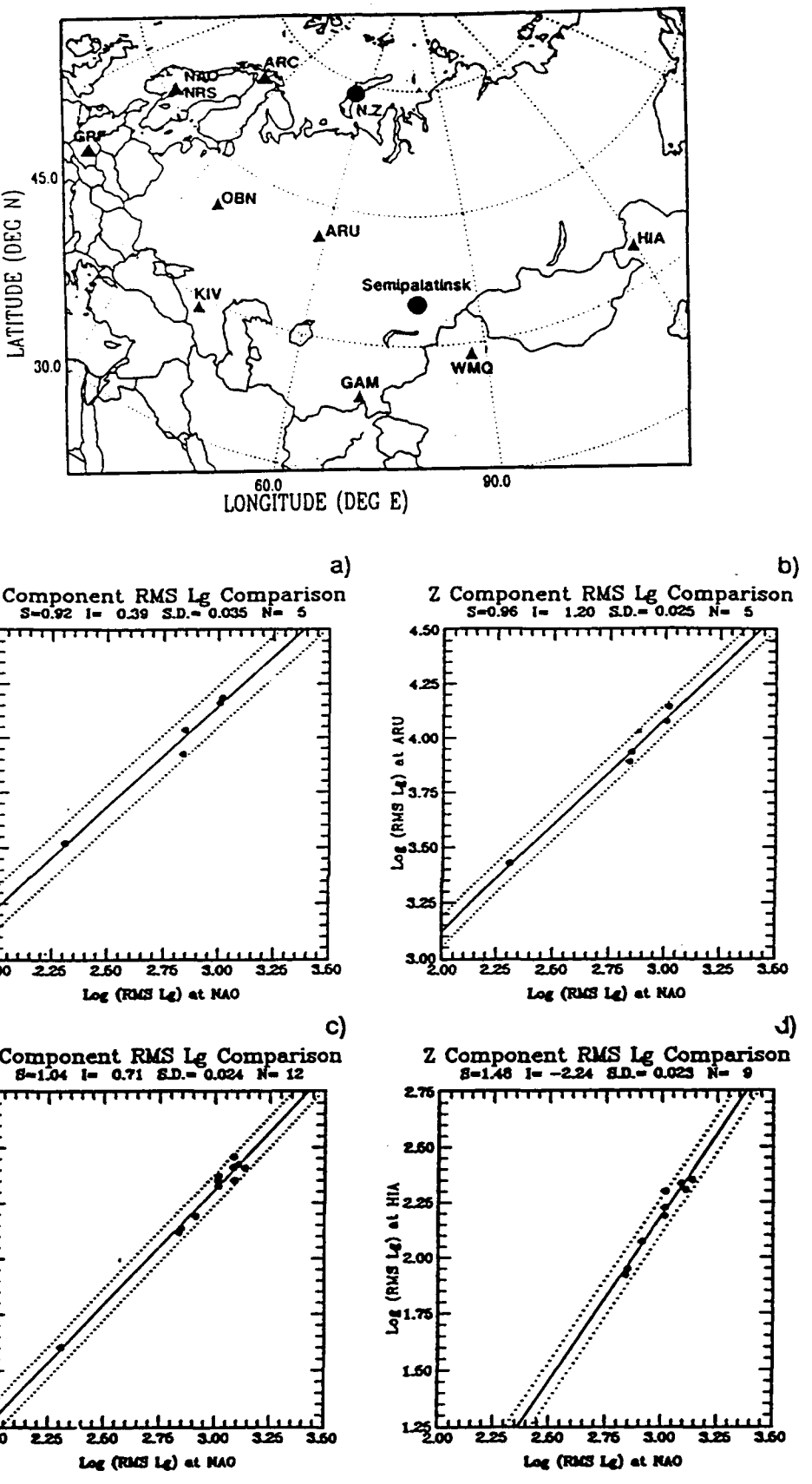
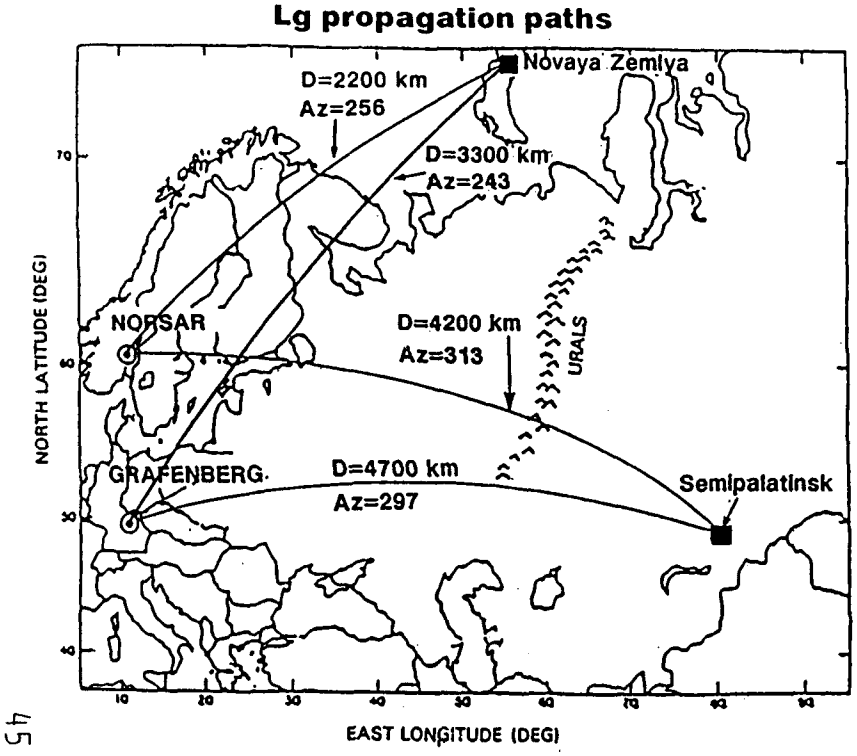
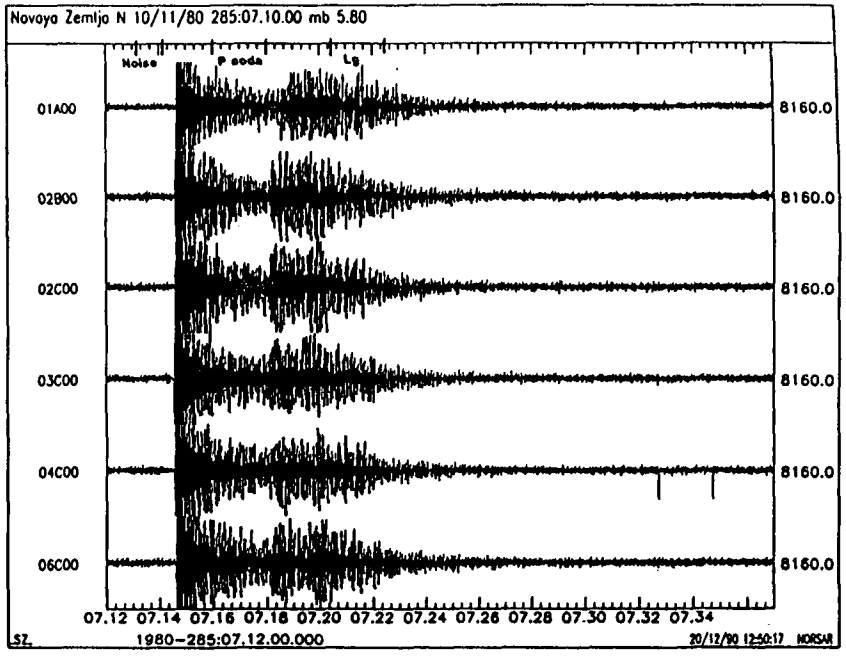


Fig. 3. The map at the top shows the location of stations analyzed in the study by Hansen, Ringdal and Richards (1990) (triangles) relative to the two main Soviet test sites. The bottom part, figures a)-d), shows the excellent RMS Lg correspondence between four of the stations in the USSR/ China and the NORSAR array for Shagan River explosions.





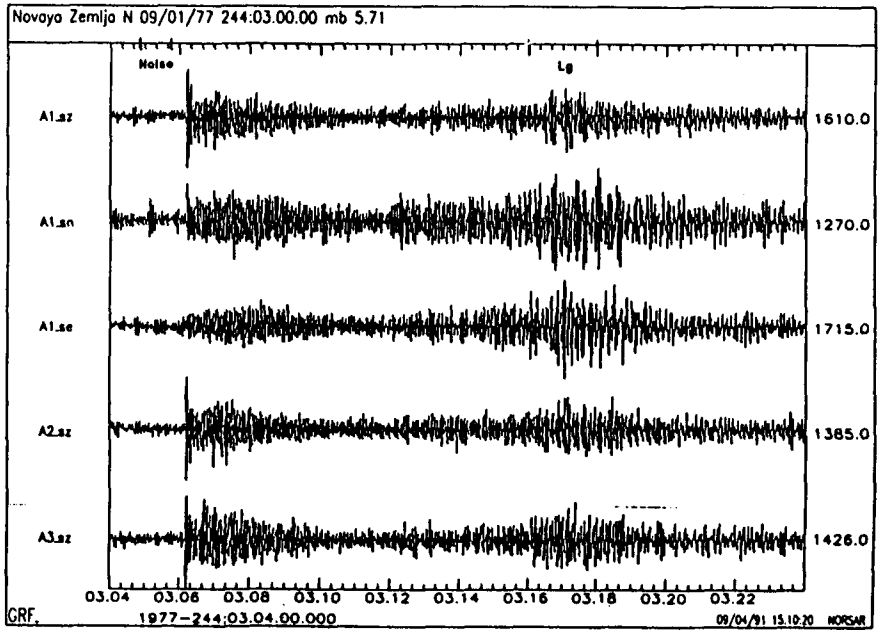


Fig. 4. a) Map showing the Lg propagation paths from the main Soviet test sites (Novaya Zemlya and Semipalatinsk) to the NORSAR and Grafenberg arrays. Typical recordings of explosions from Novaya Zemlya are shown for NORSAR (b) and Grafenberg (c). (After Ringdal and Fyen, 1991)

RMS Lg Novaya Zemlya - NORSAR and Graefenberg

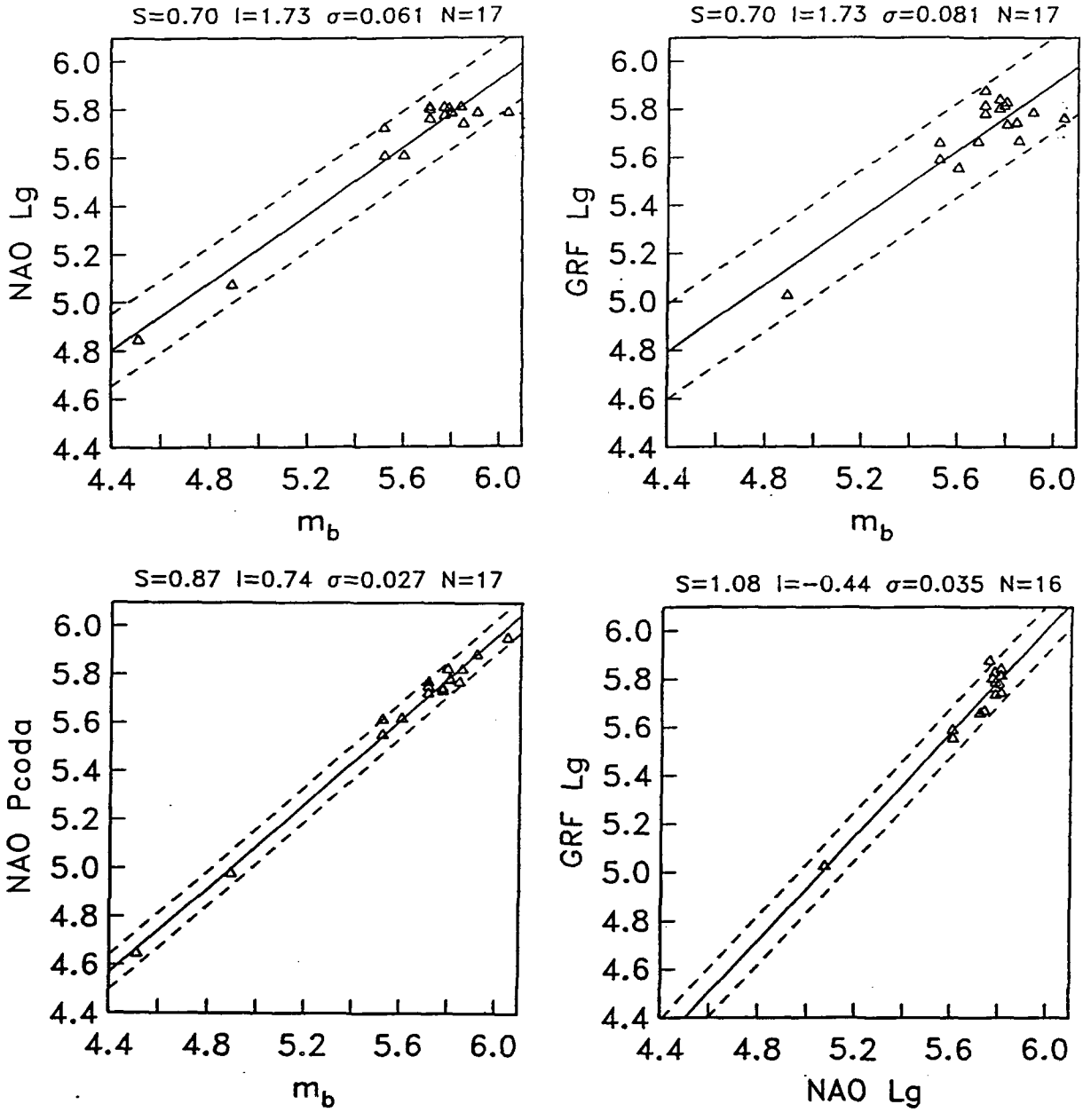


Fig. 5. Plots showing the correspondence between RMS Lg at NORSAR and Grafenberg and world wide m_b. Note that neither NORSAR nor GRF Lg correlates well with m_b ((a) and (b)), but they are mutually very consistent (d). Also note the excellent correspondence between m_b and NORSAR P-coda magnitude (c).

SEISMOLOGY ISSUES IN THE NUCLEAR TALKS BETWEEN THE U.S. AND THE U.S.S.R.

by

AMBASSADOR C. PAUL ROBINSON

Seismology was an integral part of the planning for and the negotiation of the new Protocols to the TTBT and PNET. The TTBT protocol now provides the right to make seismic measurements at three in-country seismic stations for nuclear tests where planned yields exceed 50 kilotons. In addition, the right to conduct on-site inspections or hydrodynamic yield measurements will also provide valuable data for use in seismic yield estimates of future tests.

This talk will communicate the negotiator's view of the key seismic issues the U.S. delegation faced and the role that seismic research played in the talks. It will also outline several seismic issues that need to be elucidated prior to subsequent negotiations on nuclear testing.

Opportunities for Seismological Research in the USSR

David W. Simpson
The IRIS Consortium
Suite 1440, 1616 North Fort Myer Dr.
Arlington, Virginia 22209

The Joint Seismic Program, a cooperative project between IRIS, the US Geological Survey and the Institute of Physics of the Earth of the Soviet Academy of Sciences, is now providing data from a network of GSN stations and arrays in the USSR and encouraging joint seismological studies between US and Soviet researchers. Broadband seismic stations of the GSN type, being installed at 15-20 sites throughout the USSR, provide data from both regional and teleseismic sources. More closely spaced arrays in Kirghizia, Armenia and the northern Caucasus are used to study the details of seismicity and structure in these more seismically active regions. Historical data are also being collected by digitizing records from the Soviet national seismic network of broadband analog instruments.

The proper interpretation of seismic data collected in the USSR, and their application to verification studies, will require a careful assessment of the influence of crustal structure on wave propagation and the variability of both natural and artificial sources from different regions. The USSR covers approximately 4.5 % of the earth's surface and represents almost 15 % of the continental land mass. Within its boundaries are found a wide variety of geological structures and tectonic environments. Although simple analogs for some parts of the Soviet Union can be found in other parts of the world, many of the structures are unique and an understanding of the details of regional variations in structure and sources will require the merging of a variety of data from local sources.

Although western access to many parts of the USSR has been restricted until recently, there is an extensive Russian literature on the geology, crustal structure and seismicity of Eurasia. Summaries of research activities in the USSR are frequently published in English journals and Russian journals in translation, but most of the detailed information is available only in limited-edition monographs, usually published by Academy or Institute publishing houses. Numerous maps with geological themes are also available, although most are at scales of 1:1 million or greater. Much of the interpretation of geological data has been heavily influenced by the long Soviet tradition of "fixist" theory, but basic data, where available, are usually sound. The Soviets were pioneers in the use of explosive sources for long range refraction and reflection studies. These Deep Seismic Sounding (DSS) profiles have been carried out through most of the major geological structures of the USSR.

Since the early 1960's the Institute of Physics of the Earth has been producing annual catalogs of earthquakes in the USSR. These catalogs are divided into geographic regions and are based on data from national and regional networks of seismograph stations. The catalogs are accompanied by articles with annual reviews of seismicity and details on the larger earthquakes in each region. The Central Asian catalog, for example, contains the locations of more than 43,000 earthquakes greater than magnitude 2.5 from 1962 to 1985. In contrast, only 7808 events are reported by ISC for the same area over the same period. Similar catalogs are available for all of the seismically active regions of the Soviet Union. These catalogs provide a wealth of information on both spatial and temporal variations in seismicity.

Various types of remotely sensed data and gridded data bases are also becoming available for the USSR. Multi-spectral satellite images from SPOT, Landsat and Soviet satellites allow resolution of features of geological interest on local and regional scales. Also becoming available are topographic data with resolution sufficient for use in structural mapping, merging with satellite images or preparing base maps for support of field work.

EQUATION OF STATE OF GRANITIC ROCK: A NEW HYSTERETIC UNLOADING MODEL

Thomas J. Ahrens, Thomas S. Duffy, and Toshimori Sekine*
Seismological Laboratory, Caltech 252-21, Pasadena, CA 91125

OBJECTIVE:

The Hugoniot curves for quartz and feldspars, the major mineral constitutents of granite, as well as the Hugoniot for granite, itself, demonstrate three distinct regimes within the shock pressure range (6-100 GPa) of interest to CORRTEX. Below ~6 GPa a quasielastic regime is observed. The elastic shock velocity for weathered granite [Sekine *et al.* 1991] which ranges from 5.65 to 6.44 km/sec is slightly greater than the zero-pressure longitudinal velocity of 5.36 ±0.10 km/sec. Above ~6 GPa, the Hugoniot elastic limit, the deformational regime is achieved. This regime represents a mixture of the low pressure phase and successively greater fractions of the high pressure phase. At 30 - 40 GPa the third high pressure phase regime is achieved. Release isentropes from regimes 1 and 3 lie close to the Hugoniot and can be described by a conventional Mie-Gruneisen equation of state. Our objective was to develop theoretical models for the release isentrope in the mixed phase regime based on the mixing of two Hugoniots for the low pressure phase regime and the high pressure regime in a range of pressure for the mixed phase regime. The approach assumes that the mass fraction of high pressure phase is frozen in the mixed phase during the release until the pressure drops down to a critical value represented by the relations P (GPa) = 32.2 - 85.5 V (cm^3/g) and P(GPa) = 19.3 - 77V (cm^3/g) for quartz and granite. Further release results in the formation of diaplectic glass and the final volumes of post-shock quartz and granite are given by the same relation V(cm^3/g) = 0.063M + 0.377 at ambient conditions, where M is the mass fraction of high pressure phase at the initial Hugoniot state.

RESEARCH ACCOMPLISHED:

We found that Hugoniots and equation of state parameters for quartz, feldspars and granite are quite similar. The release adiabat states measured for shocked quartz [Chhabildas & Miller 1985; Podurets, Simakov & Trunin 1976], feldspars [Ahrens, Peterson & Rosenberg 1969; Grady & Murri 1976] and granite [Swegle 1989; Swegle 1990] also show similar release paths, depending mainly upon the initial shock state. These release adiabats have been measured by independent methods: the impedance mismatch buffer method [Ahrens, Peterson & Rosenberg 1969; Podurets, Simakov & Trunin 1976], manganin transducer record [Grady &Murri 1976] and velocity interferometer (VISAR) [Chhabildas &Miller 1985; Swegle 1989].

Quartz has been studied widely under dynamic conditions. Figure 1 shows the release adiabats measured for quartz. The release adiabats from shocked quartz in the mixed phase regime are approximated by unloading paths in which the quantity of low and high pressure phase in the mixture is frozen down to about 8 GPa [Grady, Murri & Fowles 1974; Swegle 1989]. At this point, the volumes expand to the initial volume with further decreasing pressure.

The release adiabats from the stishovite regime, however, seem to occur along paths leading to less dense zero-pressure material than the zero-pressure density of the high-pressure form (stishovite), especially when the release pressure reaches within the mixed phase regime. It appears that a material with density of about 3.7 g/cm^3 is produced during the unloading process and may then revert to a diaplectic glass on further pressure release to ambient pressure and

---

* Permanent address: National Institute for Research in Inorganic Materials, Tsukuba, Ibaraki 305, JAPAN

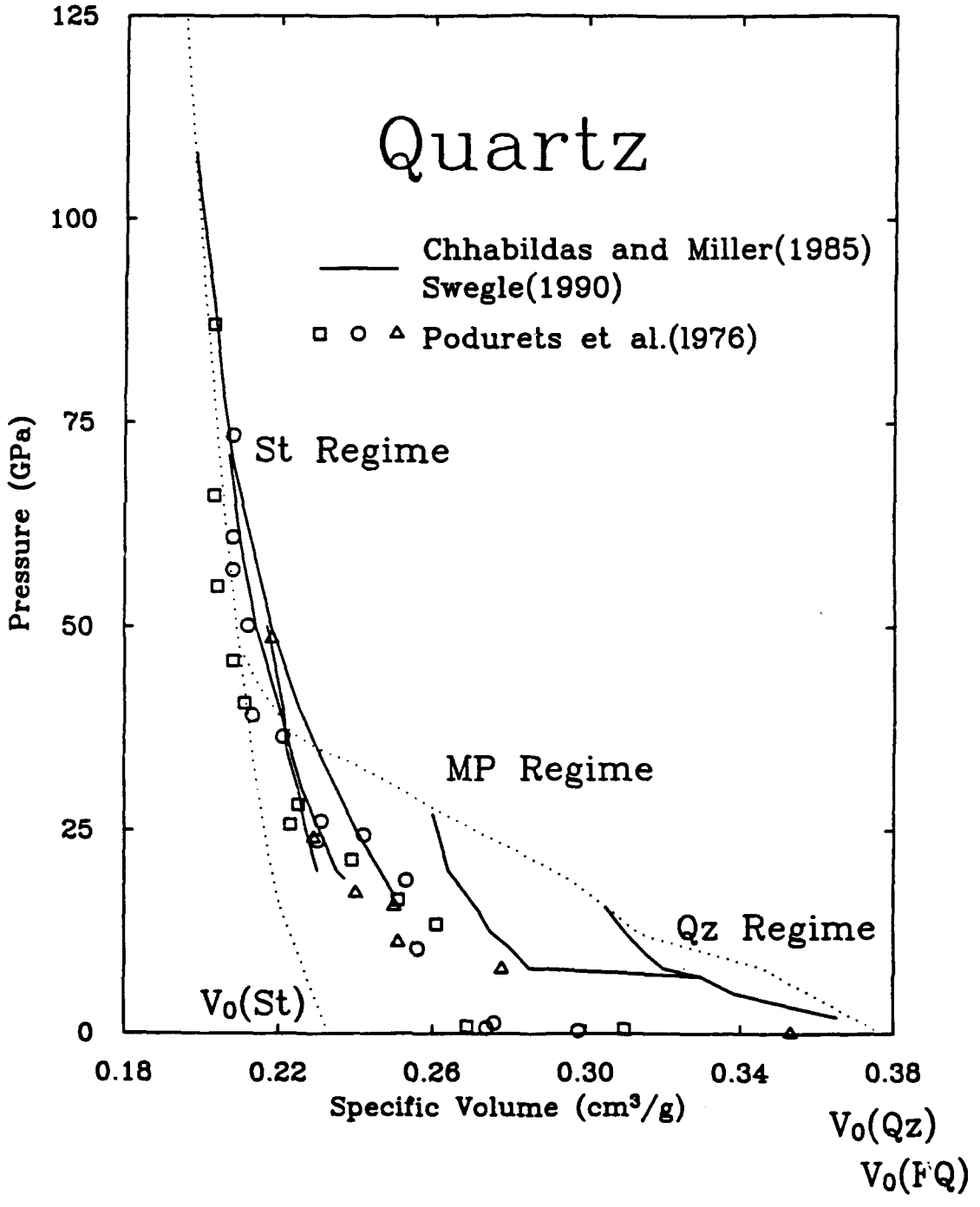


Fig. 1 Pressure-volume relations for quartz release paths. Data from Podurets, Simakov & Trunin [1976], Chhabildas & Miller [1985], and Swegle [1990]. St = stishovite, MP = mixed phase, Qz = quartz. FQ = fuzed quartz.

temperature as observed in the shock-recovery experiments on quartz. This apparent density, in fact, may represent a diaplectic glass with six-fold coordinated silicon with oxygen . We set the post-shock quartz density to be 2.27 g/cm^3 [Stöffler & Hornemann 1972]. It is interesting to note that the density ratio of this proposed material to stishovite is close to that of the fused silica glass to quartz. In this context, Chhabildas & Miller [1985] suggest that this material might represent a high density quartz liquid produced above the melting point during unloading.

Figure 2 displays calculations of release adiabats in the mixed phase regime based on the mixing of the two Hugoniots for the quartz regime and the stishovite regime over a range of pressure for the mixed phase regime. In this model, the mass fraction of stishovite is frozen in the mixed phase during the release state until the pressure drops down to a critical value represented by the relation P (GPa) = 32.2 - 85.5 V (cm^3/g) shown in Fig. 2. Further release causes the formation of diaplectic glass and the final volume of post-shock quartz is given by the relation V(cm^3/g) = 0.063M + 0.377 at ambient conditions, where M is the mass fraction of stishovite at the Hugoniot state. This model calculation is compared with the experimental data [Chhabildas &Miller 1985; Podurets, Simakov & Trunin 1976; Swegle 1990]. The calculated unloading curves in the mixed phase region were used to obtain Birch-Murnaghan parameters for the release curves. The zero-pressure densities were taken from the relative mass fraction of quartz (ρ_o = 2.65 g/cm^3) and stishovite (ρ_o = 4.29 g/cm^3). The bulk modulus increases with increasing stishovite fraction whereas the pressure derivative of the bulk modulus ranges from 8-10. Unloading from higher pressures in the stishovite regime leads to a lower apparent density of the high pressure phase as discussed above. This is consistent with initial transformation to stishovite followed by formation of glass at higher stresses [Kleeman & Ahrens 1973].

Figure 3 compares the calculated release paths in granite in the mixed phase regime with the experimental data which appears to behave in a similar manner as that proposed for quartz. The calculations are based on the mixing of the two Hugoniots for the low pressure (ρ_o=2.63 g/cm^3) and high pressure (ρ_o = 4.03 g/cm^3) regimes and the frozen mass fraction of the Hugoniots state down to a critical pressure. Below the critical pressure given by P(GPa) = 19.3 - 77 V (cm^3/g) the release paths are represented by straight lines on which the formation of diaplectic glasses proceeds.

The calculated post-shock temperatures using our formulation of the release isentropes for quartz and granite are shown in Fig. 4 For quartz, the maximum temperature achieved is 1673 K which is less than the 1 atm. melting temperature of SiO_2 (1996 K). We therefore infer that at pressures between 15-40 GPa both quartz and granite remain solid upon isentropic unloading. As discussed above, Chhabildas & Miller [1985] infer that release from pressures above 50 GPa results in a high-density quartz liquid. The transition energy associated with the transformation of the high pressure component to diaplectic glass can be estimated using the quartz to fused quartz transition energy (123 J/g) for the transforming high-pressure phase fraction. The effect of including this term is to produce a slight decrease in the calculated post-shock (and shock) temperature.

Also shown in Figure 4 are experimentally determined post-shock temperatures for quartz [Raikes & Ahrens 1979] and stishovite [Boslough 1988; Chhabildas &Miller 1985]. The present results are in good agreement with the highest pressure quartz data but are ~500 K colder than the stishovite data extrapolated to the top of the mixed phase region (~40 GPa). The results of Chhabildas & Miller [1985], and possibly Boslough [1988] as well, do not represent complete unloading and may therefore overestimate the residual temperature. The calculation of Wackerle [1962] based on the Mie-Gruneisen Equation predicts lower temperatures in the mixed phase region and a PT slope in the stishovite field which is much steeper than suggested by the experiments.

CONCLUSIONS AND RECOMMENDATIONS:

From the release adiabats in the mixed phase regime, a mixed Hugoniot model is applied and compared with experimental data. In this model, the release adiabats are calculated for the high-pressure and low-pressure phase mixture with the same mass fraction as at the Hugoniot state

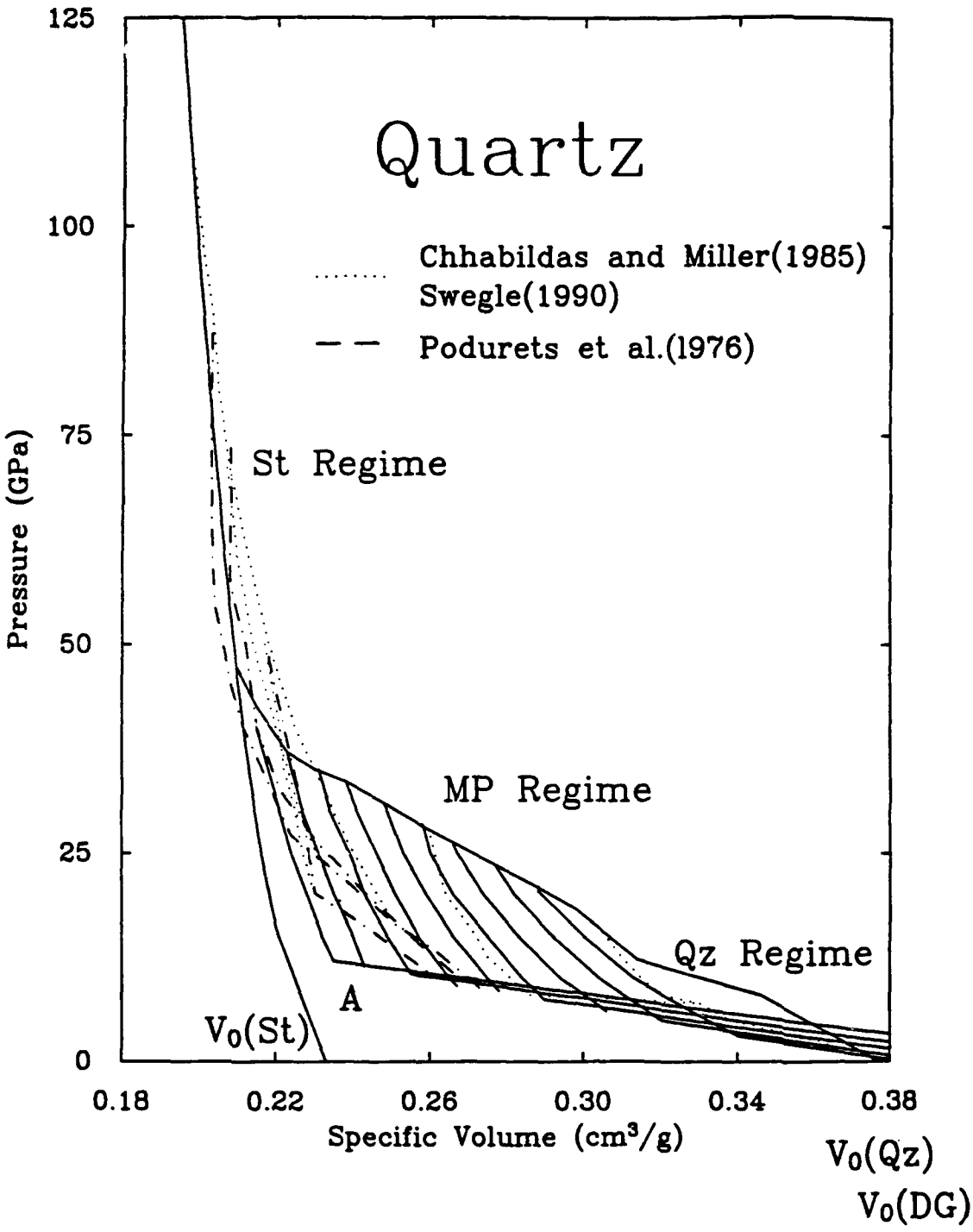


Fig. 2 Pressure-volume relations for quartz release paths. Dotted and broken curves illustrate experimental data, and solid curves illustrate Hugoniot curves and calculated release paths. Solid curves are computed based on mixed Hugoniots of quartz and stishovite regimes with mass fractions at 0.1 intervals for stishovite. Below the critical pressures, the release paths are modeled by straight lines. The zero-pressure volume of post-shock quartz shocked above some 50 GPa was taken to be 0.44 cm^3/g.

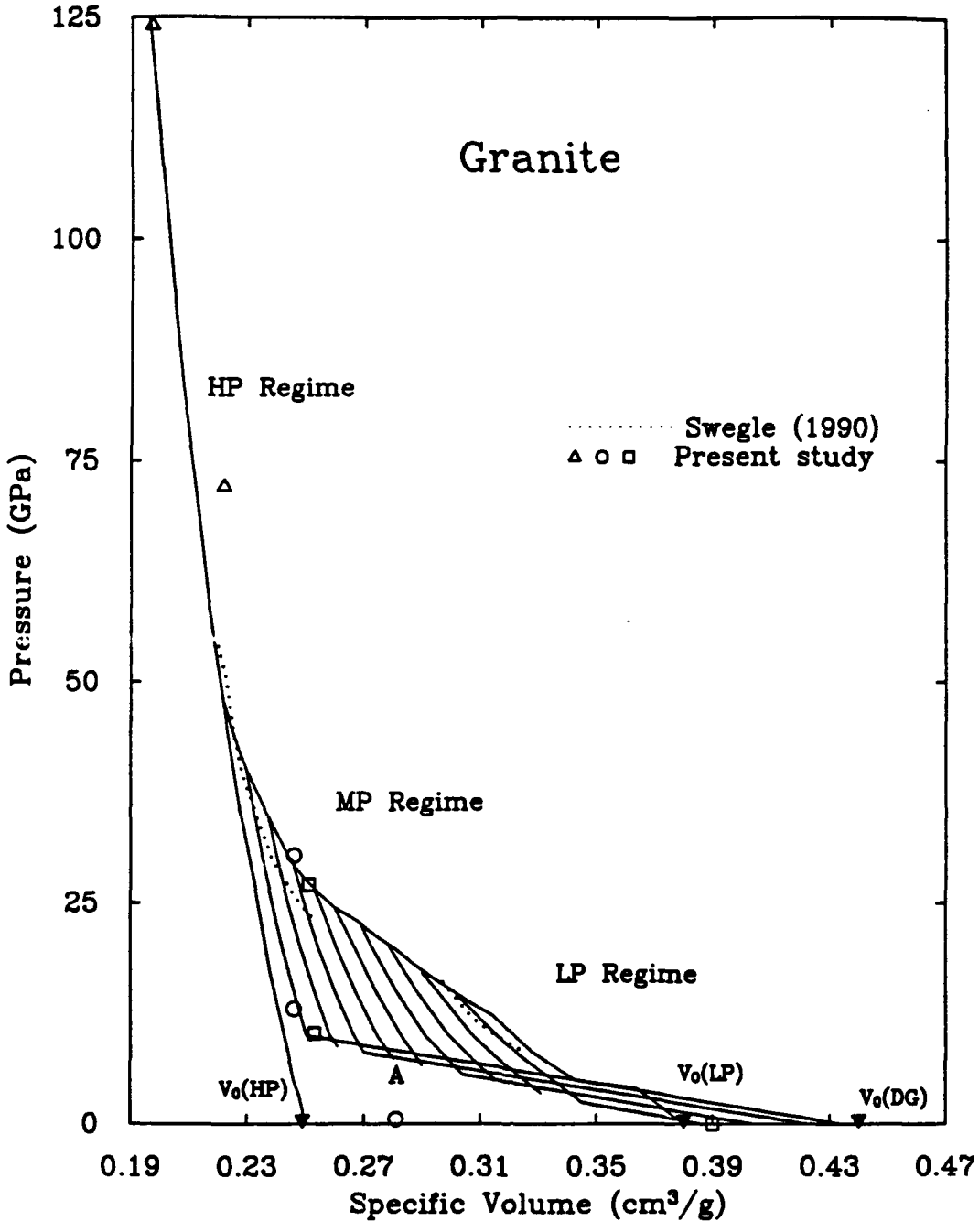


Fig. 3 Comparison of pressure-volume relations for measured granite release paths with the model calculations. HP = high-pressure, LP = low pressure, MP = mixed phase, and DG = diaplectic glass.

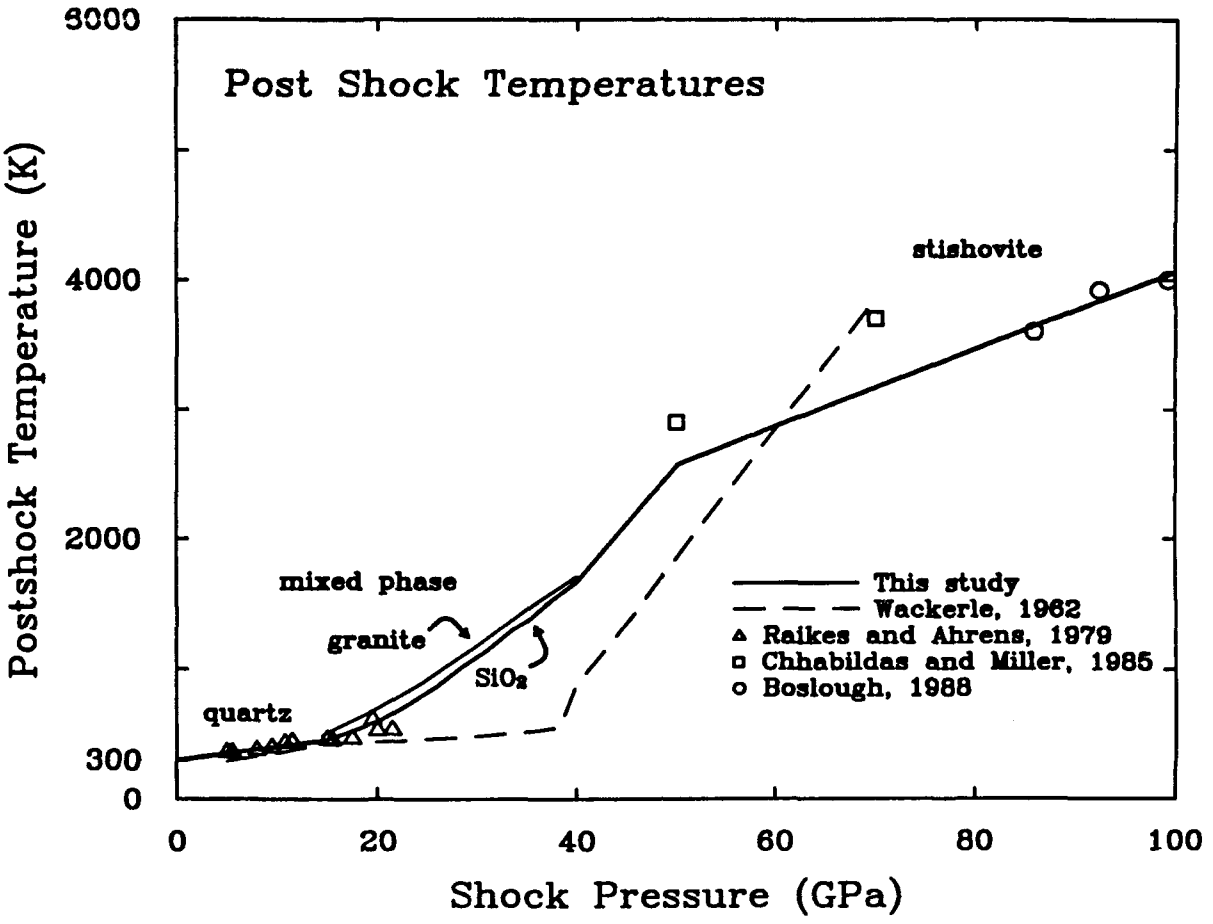


Fig. 4 Post-shock temperatures for quartz and granite plotted as a function of peak shock pressure. The heavy solid line represents preferred values for post shock temperatures in quartz between 0 and 100 GPa. Post shock temperatures calculated for granite in the mixed phase region are shown as the solid line. The data sets of Raikes & Ahrens [1979] and Boslough [1988] are from measurements of post-shock radiation. The data of Chhabildas & Miller [1985] represent calculated values determined from measured wave profiles and the Mie-Gruneisen equation. The dashed line is the calculation of Wackerle for SiO_2.

to critical pressures given by P(GPa) = 19.3 - 77 V (cm^3/g). Further releases below the critical pressures are associated with large volume changes related to formation of diaplectic glasses as quenched modifications of the high-pressure fractions. Based on the measurements of partially released states of granite as well as quartz shocked in the high-pressure regime (P > 50 GPa), it is proposed that the high-pressure form relaxes isentropically to a metastable, intermediate phase characterized by dense, highly-disordered material. This material is subsequently quenched to diaplectic glass. The inferred release curves from the mixed region for quartz yield Hugoniot temperatures which are considerably higher than those of Wackerle [1962], but are consistent with the data of Lyzenga, Ahrens & Mitchell [1983]. Moreover, the post shock temperatures predicted agree closely with the data of Raikes & Ahrens [1979] at low pressures and the data of Chhabildas & Miller [1985], and Boslough [1988] at higher pressures. These agreements lend further support to the release model developed here.

ACKNOWLEDGMENTS

We are grateful to Michael Long and Epaprodito Gelle for experimental assistance. Helpful comments were proferred by S. Peyton (S-Cubed). Research supported by AFGL (GL F19628-88-K-0034). Contribution #5053, Division of Geological and Planetary Sciences.

REFERENCES

Ahrens, T. J., Peterson, C. F. & Rosenberg, J. T., 1969. Shock compression of feldspars, *J. Geophys. Res.*, **74**, 2727-2746.

Boslough, M., 1988. Postshock temperatures in silica, *J. Geophys. Res.*, **93**, 6477-6484.

Chhabildas, L. C. & Miller, J. M., 1985, Release-adiabat measurements in crystalline quartz, Sandia National Laboratory, Albuquerque, N.M., SAND 85-1092,

Grady, D. E. & Murri, W. J., 1976. Dynamic unloading in shock compressed feldspar, *Geophys. Res. Lett.*, 472-474.

Grady, D. E., Murri, W. J. & Fowles, G. R., 1974. Quartz to stishovite: Wave propagation in the mixed phase region, *J. Geophys. Res.*, 332-338.

Kleeman, J. D. & Ahrens, T. J., 1973. Shock-induced transition of quartz to stishovite, *J. Geophys. Res.*, **78**, 5954-5960.

Lyzenga, G. A., Ahrens, T. J. & Mitchell, A. C., 1983. Shock temperatures of SiO_2 and their geophysical implications, *J. Geophys. Res.*, **88**, 2431-2444.

Podurets, M. A., Simakov, G. V. & Trunin, R. F., 1976. On the phase equilibrium in shock-compressed quartz and the kinetics of phase transitions, *Physics of the Solid Earth*, **12**, 419-424.

Raikes, S. A. & Ahrens, T. J., 1979. Post-shock temperatures of minerals, *Geophys. J. Roy. Astron. Soc.*, **58**, 717-748.

Sekine, T., Rubin, A. M., Duffy, T. S. & Ahrens, T. J., 1991. Shock compression and isentropic release of granite, *Geophysical J. I.*, (submitted).

Stöffler, D. & Hornemann, U., 1972. Quartz and feldspar glasses produced by natural and experimental shock, *Meteoritics*, **7**, 371-394.

Swegle, J. W., 1989, Irreversible phase transitions and wave propagation in silicate geologic materials, Sandia Natl. Laboratories, Albuquerque, NM, SAND 89-1443,

Swegle, J. W., 1990. Irreversible phase transition and wave propagation in silicate materials, *J. Appl. Phys.*, **68**, 1563-1579.

Wackerle, J., 1962. Shock-wave compression of quartz, *J. Appl. Phys.*, **33**, 922-937.

DISCRIMINATION STUDIES USING REGIONAL PHASES IN THE CENTRAL UNITED STATES

M. Amjad and B.J. Mitchell

Department of Earth and Atmospheric Sciences
Saint Louis University
St. Louis, MO 63103

OBJECTIVE

Recent deployments of seismographs inside the Soviet Union now permit seismologists to analyze phases recorded at regional distances from small earthquakes and explosions in that country. It is therefore possible to attempt to utilize those phases for discrimination purposes. The present study looks at regional phases recorded by digital stations in the central United States, a region which is geologically similar to the stable regions of central Asia, to see if those phases can successfully discriminate between earthquakes and explosions.

RESEARCH ACCOMPLISHED

Data Acquisition

Single station, three-component broadband seismograms from digital stations FVM and CCM in Missouri were used to examine the possibility of discriminating between small earthquakes and explosions in the central United States. Data were collected for events at epicentral distances between 5 and 340 km from FVM and between 134 and 417 km from CCM. Seismograms were obtained for 75 presumed explosions and 40 presumed earthquakes recorded by the station FVM from 1983 to 1988 and by 5 known earthquakes and 6 known explosions recorded at CCM in 1989 and 1990. The locations of the stations and events are shown in Figure 1. Since there is no explosion data from the seismically active New Madrid seismic zone, no earthquakes were selected from that region. The magnitudes of the explosions range from 1.9 to 3.4 and the magnitudes of the earthquakes from 1.1 to 3.9. Example vertical-component records at station FVM for some of the events appear in Figure 2.

We rotated the horizontal component records into radial and transverse components. The onsets of the Pg, Sg, Pn and Sn phases were then picked manually and a one-second window was used from the start of the phase selected for analysis. This window was applied to avoid contamination from closely following phases. For the Lg phase, a fixed velocity window from 3.60 km/sec to 3.00 km/sec was used. For each event, radial, transverse and vertical component signals were filtered to obtain records in the frequency ranges 0 to 2 Hz, 2 to 4 Hz, 4 to 6 Hz, 6 to 8 Hz, and 8 to 10 Hz, using a zero-phase, two-pole, time-domain Butterworth filter.

Ratios Between Different Phases

Amplitude ratios of various phases have been studied by several authors (e.g. Nuttli, 1981; Pomeroy *et al.*, 1982; Bennett and Murphy, 1986; Taylor *et al.*, 1989; Bennett *et al.*, 1989) with mixed results. In the present study, the ratios between different phases over the same frequency passband for the same component are calculated for Pg/Sg, Pg/Lg, Pg/Pn, Pg/Rg, Sg/Lg, Sg/Rg, Sg/Pn, Lg/Rg, Lg/Pn, and Rg/Pn phases. There are 10 possible ratios of different phases e.g. Pg/Sg for each frequency range. All these possible ratios for radial, transverse, and vertical components were determined as functions of distance and magnitude.

Although there is some suggestion of separation between earthquakes and explosions for some ratios in certain passbands, the separation is never clear-cut. The number of separated events vary from component to component for different phase ratios and for different frequency ranges. For instance, the ratio Sg/Rg indicates some separation at higher frequencies, whereas the ratio Pg/Rg inhibits better separation at low frequencies. In most cases, if there is separation, it tends to increase for higher frequency passbands of 6-8 Hz and 8-10 Hz. Our results generally indicate, however, that the ratio of different phases with respect to each other is not an effective discrimination criterion in the central United States.

Ratios of Different Passbands

Ratios between lower and higher frequencies for regional phases were studied by Murphy and Bennett (1987) and Taylor *et al.* (1988) and were found to be useful in many cases. Bennett *et al.* (1989), however, reported less effectiveness in some regions than in others. In this study, maximum amplitudes, rms values, maximum spectral amplitudes, mean spectral amplitudes, and rms spectral values of Pg, Sg, Pn phases, and values of maximum amplitudes of whole signal, of Lg and Rg phases were measured. These measurements are made for the whole signal (0-10 Hz), and for 0-2 hz, 2-4 Hz, 4-6 Hz, 6-8 Hz, and 8-10 Hz frequency passbands for radial, transverse and vertical components for all events. The 0-10 Hz/0-2 Hz, 0-10 Hz/2-4 Hz, 0-10 Hz/4-6 Hz, 0-10 Hz/6-8 Hz, 0-10 Hz/8-10 Hz, 0-2 Hz/2-4 Hz, 0-2 Hz/4-6 Hz, 0-2 Hz, 6-8 Hz, 0-2 Hz/8-10 Hz, 2-4 Hz/4-6 Hz, 2-4 hz/6-8 Hz, 2-4 Hz/8-10 Hz, 4-6 Hz/6-8 Hz, 4-6 Hz/8-10 Hz, and 6-8 Hz/8-10 Hz ratios for Pg, Sg, Lg, Rg, and Pn were calculated for radial, transverse and vertical components. These ratios indicated some separation between earthquakes and explosions could be obtained, with best results occurring for the Lg and Rg phases.

Figure 3 illustrates results for the Rg phase recorded at FVM. The low frequency ratio places most explosions below most earthquakes whereas the high-frequency ratio shows the opposite relation. There is some overlap which cannot be explained, but it is possible that some events have been misidentified. A difficulty with Rg is that, while it can be a large phase for explosions, it can also be readily absorbed on transmission through low-Q material. This seems to have occurred for several of the explosion events shown in Figure 2. Similar separations in ratios in Figure 3 were, however, also observed for Lg as recorded on all three components.

Amplitudes Versus Frequency

The most promising discriminant which we found relies on the variation of amplitudes with frequency. After correcting for instrument response, the amplitude decreases with increasing frequency is always greater than that for explosions. Figure 4 shows results for Lg waves using vertical-component recordings. Similar results were found for radial and transverse components of Lg and for all components of Rg.

CONCLUSIONS AND RECOMMENDATIONS

Using ratios of different passbands for the same phase is more promising than using ratios of different phases for the same passband in discriminating between earthquakes and explosions in the central United States. The variation of amplitudes with frequency between the 0-2 Hz and 6-8 Hz passbands, however, is the most promising discriminant for found in our study. It appears to apply to all phases, with best results likely to be obtained for the Lg and Rg phases.

REFERENCES

Bennett, T.J. and J.R. Murphy, Analysis of seismic discrimination capabilities using regional data from western United States events, *Bull. Seism. Soc. Am.*, *76*, 1069-1086, 1986.

Bennett, T.J., B.W. Barker, K.L. McLaughlin, and J.R. Murphy, Regional discrimination of quarry blasts, earthquakes and underground nuclear explosions, Final Report, GL-TR-89-0114, S-Cubed, La Jolla, CA, 1989.

Murphy, J., and T. Bennett, A discrimination analysis of short-period regional seismic data recorded at Tonto Forest Observatory, *Bull. Seism. Soc. Am.*, *72*, 1351-1366, 1982.

Nuttli, O.W., On the use of Lg waves in western and central Asia and their use as a discriminant between earthquakes and explosions, *Bull. Seism. Soc. Am.*, *71*, 249-262, 1981.

Pomeroy, P.W., W.j. Best, and T.V. McEvilly, Test ban treaty verification with regional data - a review, *Bull. Seism. Soc. Am.*, *72*, S89-S129, 1982.

Taylor, S.R., N.W. Sherman, and M.D. Denny, Spectral discrimination between NTS explosions and western United States earthquakes at regional distances, *Bull. Seism. Soc. Am.*, *78*, 1563-1579, 1988.

Taylor, S.R., M.D. Denny, E.S. Vergino, and R.E. Glaser, Regional discrimination between NTS explosions and western United States earthquakes, *Bull. Seism. Soc. Am.*, *79*, 1142-1176, 1989.

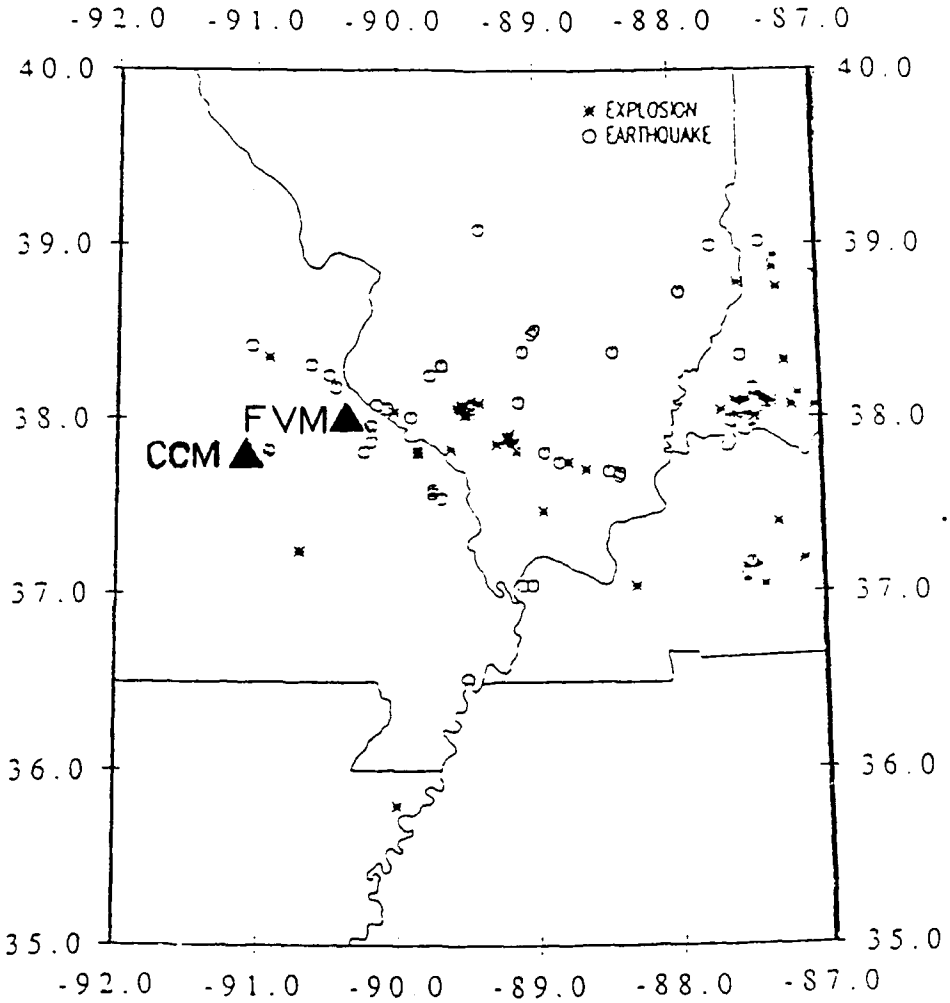


Figure 1. Map of area of study showing locations of seismic stations (FVM and CCM), explosions, and earthquakes.

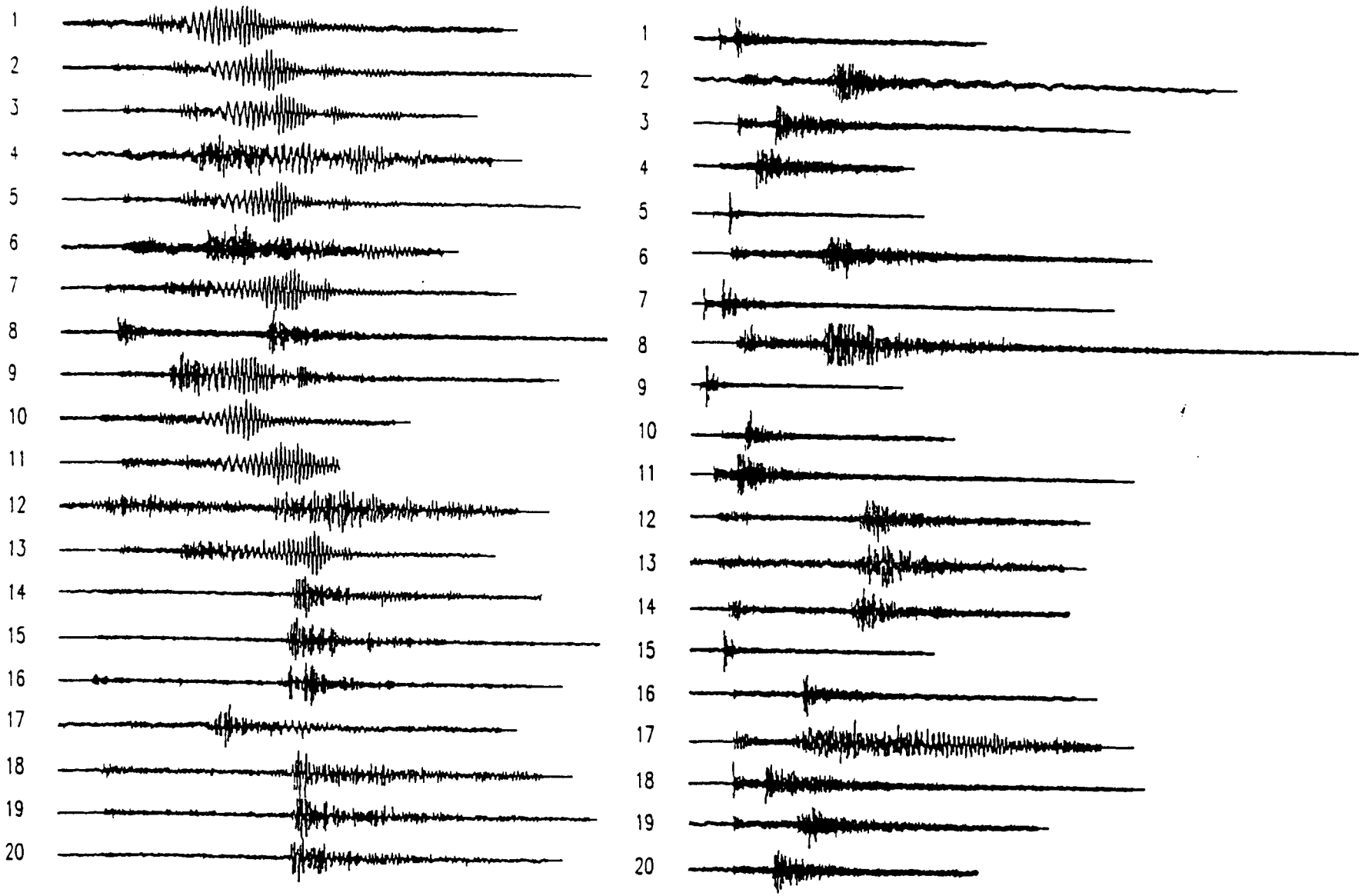


Figure 2. Example vertical-component seismograms generated by explosions (left) and earthquakes (right) as recorded at station FVM.

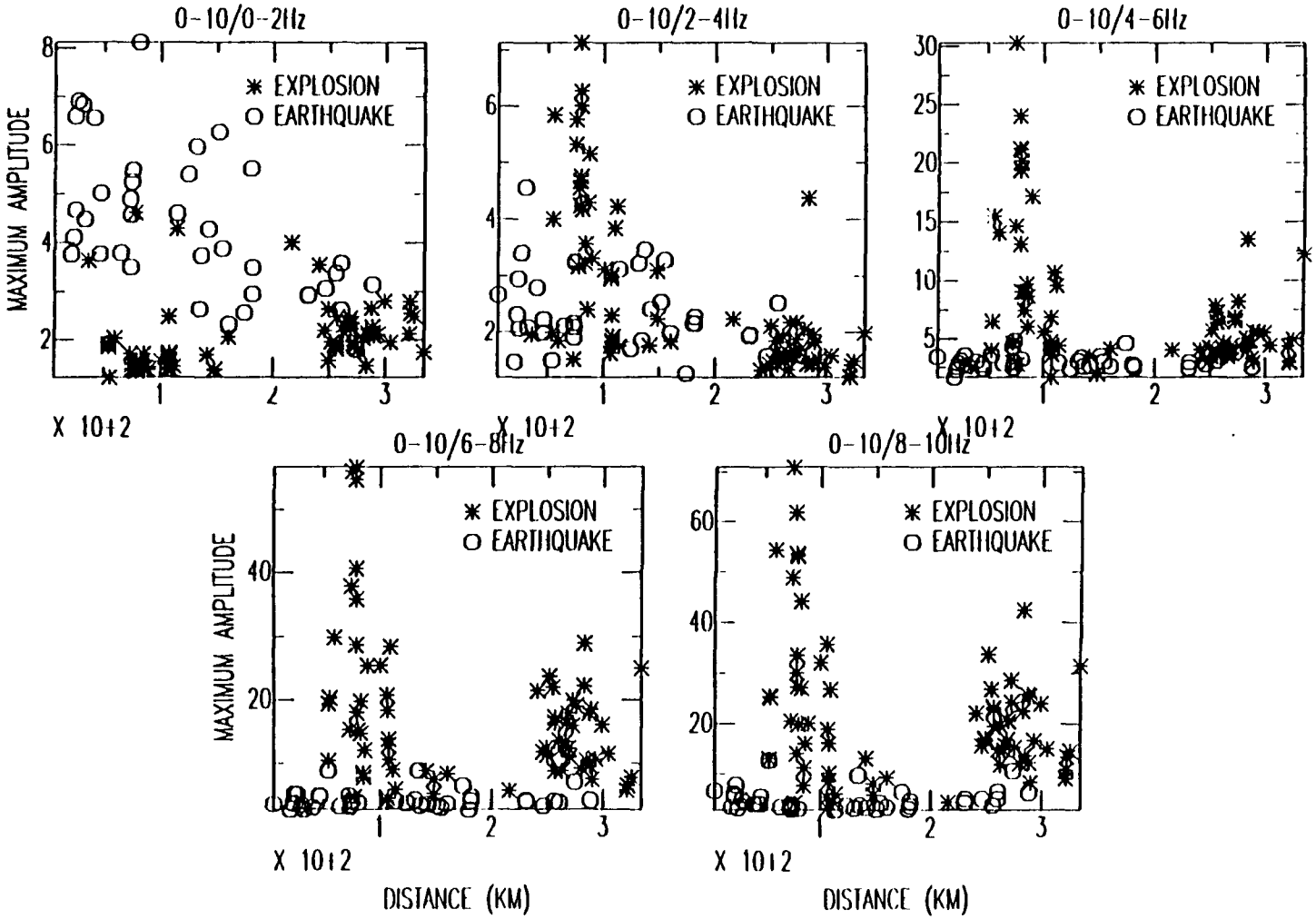


Figure 3. Ratios of Rg amplitudes at various frequencies versus distance as determined from vertical-component records.

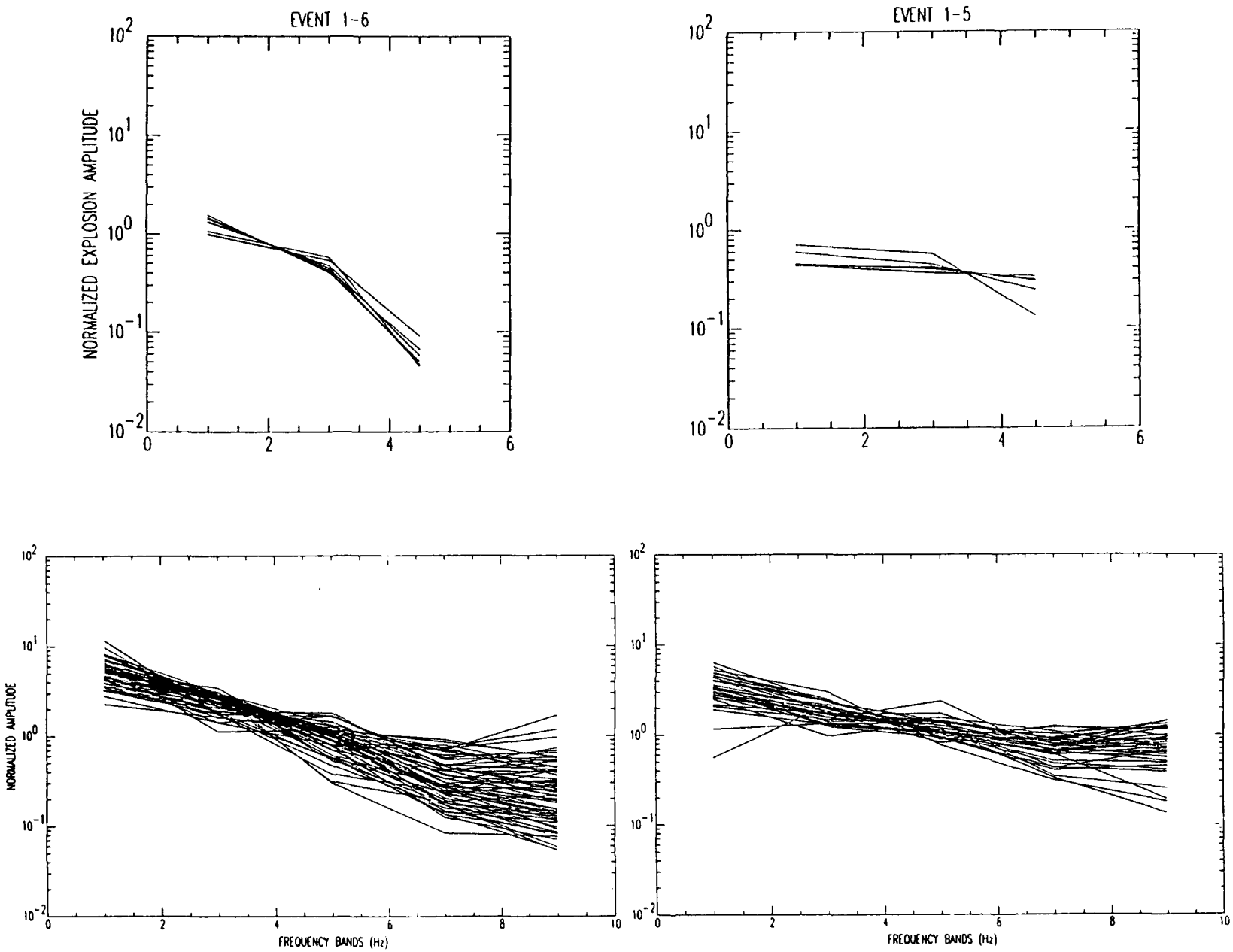


Figure 4. Normalized Lg amplitude variations for the vertical component after correcting for instrument response. (Top) Amplitude variations at CCM for explosions (left) and earthquakes (right). (Bottom) Amplitude variations at FVM for explosions (left) and earthquakes (right).

ANALYSIS OF REGIONAL BODYWAVE PHASES FROM EARTHQUAKES AND EXPLOSIONS IN EASTERN ASIA

Jeffrey S. Barker
State University of New York, Binghamton

CONTRACT NO: F19628-90-K-0042

OBJECTIVE:

The purpose of this study is to improve our understanding of the crustal waveguide phases, P_g and L_g, by modeling regional waveforms in eastern Asia. Burdick et al. (1989) have demonstrated that deterministic modeling of high-frequency P_n and P_g from NTS explosions can fit waveforms recorded on a regional network and provide valuable information on regional wave propagation characteristics. We wish to apply this sort of approach to regional waveforms from earthquakes and explosions in eastern Asia, making use of the recent high-quality, broad-band data recorded on the Chinese Digital Seismic Network (CDSN). Unfortunately the station spacing is quite sparse, so that for a given event, little correlation between stations may be made. Without independent information on crustal structure, there will remain a certain level of ambiguity in the identification of the arrivals that interfere to generate the P_n-P_g waveform.

In order to minimize this ambiguity, we begin by modeling broad-band P_n and P_g waveforms from profiles of earthquakes recorded at the CDSN station WMQ. This is not really the reciprocal experiment since the earthquakes have different depths, magnitudes and mechanisms. However, Wu (1990) showed that the P waveforms from these earthquakes have many similarities, and we may interpret these in terms of the moveout of specific crustal phases. By simultaneously modeling the waveforms from each of these earthquakes, we gain an understanding not only of regional P-wave propagation near WMQ, but also of the kinds of variations observed in the waveforms for different source depths and mechanisms. By modeling profiles along different azimuths or recorded at different stations, we may investigate the effect of different crustal structures, or the effect of lateral variations in structure. Finally, we may use this understanding to model high-frequency P_n-P_g waveforms from Kazakh explosions, or individual sources from other locations in eastern Asia.

RESEARCH ACCOMPLISHED:

As a first profile, we consider earthquakes along a line SW of WMQ (Figure 1 and Table 1), from the Tarim Basin and the Tienshan regions of western China. In a surface wave regionalization study (Wu et al., "Velocity structures of different tectonic provinces of China", this volume), these are considered to be within the same structural region, so lateral variations in crustal structure should be minimal. With one exception, these are shallow crustal earthquakes (depths 8-33 km) with thrust mechanisms. The exception is an event in the Pamir valley (87276) which occurred at a depth of 80 km. Since it is also our most distant event from WMQ, we will not consider it in the initial modeling, but only later to test the modeling at greater ranges and source depths. Broad-band seismograms from the other events have been processed to facilitate comparison with synthetic seismograms. This processing includes time integration (to ground displacement), a low-pass Butterworth filter (with a frequency of 2 Hz) in order to limit the frequency range to be computed, and a high-pass Butterworth filter (frequency 0.5 Hz) to reduce low-frequency drift in the synthetics. The resultant passband is comparable to the WWSSN short-period instrument, upon which most empirical studies of P_n and P_g have been based.

The first 40-50 sec of the vertical-component P waveforms are shown on the left side of Figure 2. Superimposed on the waveforms are travel-time curves appropriate for various P and S phases for a source at 30 km depth in a layered velocity structure model (discussed below). A number of features in the observed waveforms correlate with some of these predicted arrivals. In particular, for the closest event, P, pP and S may be identified. Beyond 400 km, P_n and P may be identified,

but P_MP is not a substantial arrival. In fact, for these mechanisms, sP_n and sP_MP may be seen as an elongated series of arrivals at 400-600 km and as distinct phases at 1200 km. Many other arrivals are present in the observed waveforms; the travel-time curves show only selected arrivals for a single source depth.

Other features are better modeled by computing synthetic seismograms for the appropriate range, depth and mechanism and comparing this with the observed waveform. In this paper, we cannot show these comparisons, but will present synthetic profiles and depth sections for discussion. The initial modeling uses generalized ray theory synthetics (Helmberger and Harkrider, 1978), which facilitates the identification of important phases, but cannot include all of the arrivals in the high-frequency P_n-P_g waveform. In all, 75 rays arriving as P waves are allowed, including up to three reverberations in the crust and mode conversions at the free surface and the Moho. More complete synthetics are computed using a frequency-wavenumber (F-K) integration technique (Barker, 1984). This method uses the compound matrix modification of the Haskell layer matrix method with Filon quadrature over wavenumber. Anelastic attenuation is included to move the poles off of the real-k axis. No wavenumber filtering is imposed, so the synthetics include S waves and surface waves in addition to the P wavetrain. These are computation-intensive synthetics, so we must limit the frequency band and time duration. The source parameters used in generating the synthetics are listed in Table 2. These include Harvard CMT mechanisms (published in the PDE) when available; otherwise an average mechanism is assumed. Source depths (again from the PDE) are sometimes questionable, so the synthetics are computed at 10, 20 and 30 km depths, and the depth closest to that reported for an event is used in the comparison. The velocity structure model assumed (Table 3) is based on the surface wave results of Feng and Teng (1983), modified so that the travel-time curves provide reasonable agreement to observed arrival times. A velocity gradient is included in the mantle so that P_n is modeled as a turning ray rather than as a head wave.

The profile of F-K synthetics for a source depth of 30 km is shown on the right side of Figure 2. The synthetics have been computed to 4 Hz and include the same Butterworth filters applied to the observed data. Although some wrap-around is apparent at the beginning of the traces, P_n and several later arrivals may be easily identified. The synthetics are somewhat simpler than the observed waveforms (compare with the left side of Figure 2), but many features are common. For example, at 400 km sP_n and sP_MP interfere to generate an elongated wavetrain. Although the travel-time curves are not shown, the second and third P-wave reverberations in the crust also arrive between 20-30 sec (reduced time) at this range. With increasing range, sP_n becomes the dominant phase, interfering with P_MP at 1200 km range. Higher-order crustal multiples (P_MPP_MP, S_MPP_MP, etc.) do not appear to play a dominant role in either the observed or synthetic waveforms for these earthquakes. Certainly the strength of the upgoing S wave that reflects from the free surface is dependent on the radiation pattern, and in this profile we are considering only earthquakes along a single azimuth and with comparable mechanisms. For near-surface isotropic sources (explosions), we would expect crustal multiples to dominate the waveform as Burdick et al. (1989) found for NTS. This is an example of how radiation pattern can cause substantial difference in the generation of the high-frequency P_n-P_g waveform, and may be exploited as a discriminant.

Since the P_n-P_g waveforms result from the interference of a number of phases which depart the source either upward or downward, it is instructive to see how this interference varies with changes in source depth. Shown in Figure 3 are observed vertical-component waveforms for two of the events in the SW profile, along with generalized ray synthetics computed for 10, 20 and 30 km source depths. The traces have been aligned on the P_n wave, so upward departing phases (such as sP_n) move out in time with increasing source depth, while downward departing phases (such as P_MP) remain stationary or move in. At 560 km range, this results in a crossing over of arrivals and a distinct variation in waveform with depth. At 1175 km, however, the phases are sufficiently separated in time that little interference occurs, and the effect of depth is simply to alter this time separation. The published depth for event 87005 is 17 km, although if the large phase 20 sec after P_n is interpreted as a combination of sP_CP and $s(P_n)_2$, a depth greater than 20 km (in our velocity

structure) is required. Similarly, event 87159 reportedly occurred at 10 km depth, and although many other arrivals are apparent in the observed waveform, the separation of sP_n and P_n suggests a depth closer to 30 km.

CONCLUSIONS AND RECOMMENDATIONS:

For the earthquake profile SW of WMQ, synthetic seismograms suggest that the high-frequency P_n-P_g waveform is dominated by S waves that depart the source upward, then reflect and convert to P waves at the free surface (e.g. sP_n). This is expected to be radiation pattern dependent, and should be investigated for earthquakes with other mechanisms and from different azimuths from WMQ. The interference of arrivals in the P_n-P_g wavetrain is also depth dependent. This makes waveform comparisons difficult for earthquakes at different depths, but once phases are identified through synthetic modeling, depth-dependent variations can contribute toward discrimination.

In future modeling, we intend to analyze waveforms for earthquakes along other azimuths from WMQ, as well as to other CDSN stations. The propagation paths for these profiles will likely be much more complex, since most other directions cross structural trends. We will make use of the surface wave regionalization results of Wu et al. (this volume) in determining structure models. It will be important to determine the effects of lateral variations in structure on the important crustal waveguide phases.

Finally, with our improved understanding of regional wave propagation to CDSN stations, including the effects of velocity structure, source depth and mechanism, we may model with confidence waveforms recorded at CDSN stations from Kazakh explosions. Figure 4 shows a comparison of broad-band P waveforms recorded at WMQ from five explosions at the Shagan River test site. The waveforms are extremely similar. Once Green's functions are computed to explain the regional wave propagation effects, details of the source function (including variations in shot depth and emplacment meduim) may be modeled.

REFERENCES:

Barker, J.S. (1984). A seismological analysis of the 1980 Mammoth Lakes, California, earthquakes, *PhD Thesis*, Pennsylvania State Univ.

Bennett, T.J., J.F. Scheimer, A.K. Campanella and J.R. Murphy (1990). Regional discrimination research and methodology implementation: Analyses of CDSN and Soviet IRIS data, *Scientific Report No. 4, GL-TR-90-0194*, Air Force Geophysics Laboratory.

Burdick, L.J., C.K. Saikia and D.V. Helmberger (1989). Deterministic modeling of regional waveforms from the Nevada Test Site, *Final Report, GL-TR-89-0196*, Air Force Geophysics Laboratory.

Feng, C.C. and T.L. Teng (1983). Three dimensional crust and upper mantle structure of the Eurasian continent, *J. Geophys. Res., 88*, 2261-2272.

Helmberger, D.V. and D.G. Harkrider (1978). Modeling earthquakes with generalized ray theory, in *Proc. IUTAM Symp.: Modern Problems in Elastic Wave Propagation*, J. Miklowitz and J. Achenback, eds., Wiley.

Wu, F.T. (1990). Studies of regional phases and discriminants in Asia, *Final Report, GL-TR-90-0017*, Air Force Geophysics Laboratory.

Table 1 - Earthquakes along the SW Profile from WMQ

Date	Time (GMT)	Lat. (°N)	Lon (°E)	R (km)	Az (°)	Depth (km)	m_b
10/6/87 (87279)	1306:20.3	43.44	88.55	82.0	302	32	4.8
12/17/87 (87351)	1217:25.0	41.94	83.20	421.9	59	33	5.1
8/5/87 (87217)	1024:21.0	41.36	82.11	534.1	57	33	4.8
1/5/87 (87005)	2252:46.5	41.96	81.32	559.6	66	17	5.9
1/24/87 (87024a)	0809:21.0	41.53	79.32	731.2	67	29	5.9
1/24/87 (87024b)	1340:40.0	41.44	79.25	740.5	66	33	5.2
6/8/87 (87159)	1330:36.0	39.79	74.69	1175.0	63	10	5.1
4/30/87 (87120)	0517:37.0	39.76	74.57	1178.3	63	8	5.7
10/3/87 (87276)	1100:03.3	36.45	71.44	1604.3	54	80	6.0

Compiled from PDE, Wu (1990), and Bennett et al. (1990).

Table 2 - Source Parameters for SW Profile

Date	R (km)	Az (°)	Depth[c] (km)	Strike[a] (°)	Dip[a] (°)	Rake[a] (°)	M_0[a] ($\times 10^{24}$ dyne-cm)
87279	82.0	302	30	220[b]	40[b]	65[b]	3.0[b]
87351	421.9	59	30	220[b]	40[b]	65[b]	3.0[b]
87005	559.6	66	20	226	21	47	4.1
87024a	731.2	67	30	268	45	107	20
87159	1175.0	63	10	298	27	91	.65

[a] Mechanisms are Harvard CMT solutions published in the PDE.
[b] No mechanism published. These vales are assumed.
[c] Approximate source depth used for synthetic profiles.

Table 3 - Structure Model for SW Profile Synthetics

V_P (km/s)	V_S (km/s)	Density (g/cm^3)	Thickness (km)	Q_P	Q_S
4.80	2.77	2.58	9.0	300	150
6.25	3.61	2.79	32.0	800	400
7.25	4.18	3.00	15.0	1000	500
8.00	4.62	3.33	20.0	1200	600
8.10	4.68	3.36	20.0	1200	600
8.20	4.73	3.40	40.0	1200	600
8.30	4.79	3.45	-	1200	600

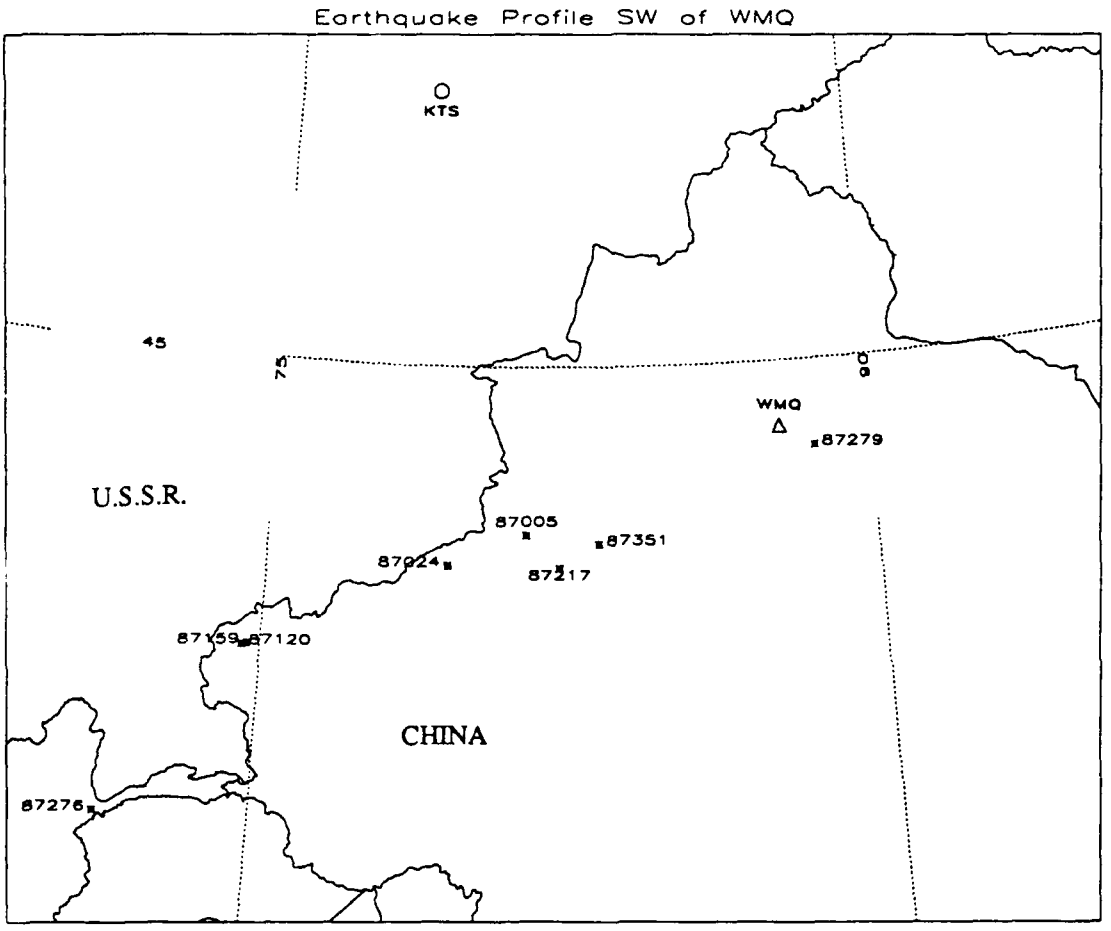


Fig. 1 Map of northwestern China showing the locations of earthquakes located along a profile SW of CDSN station WMQ. Also shown is the location of the Kazakh test site (KTS).

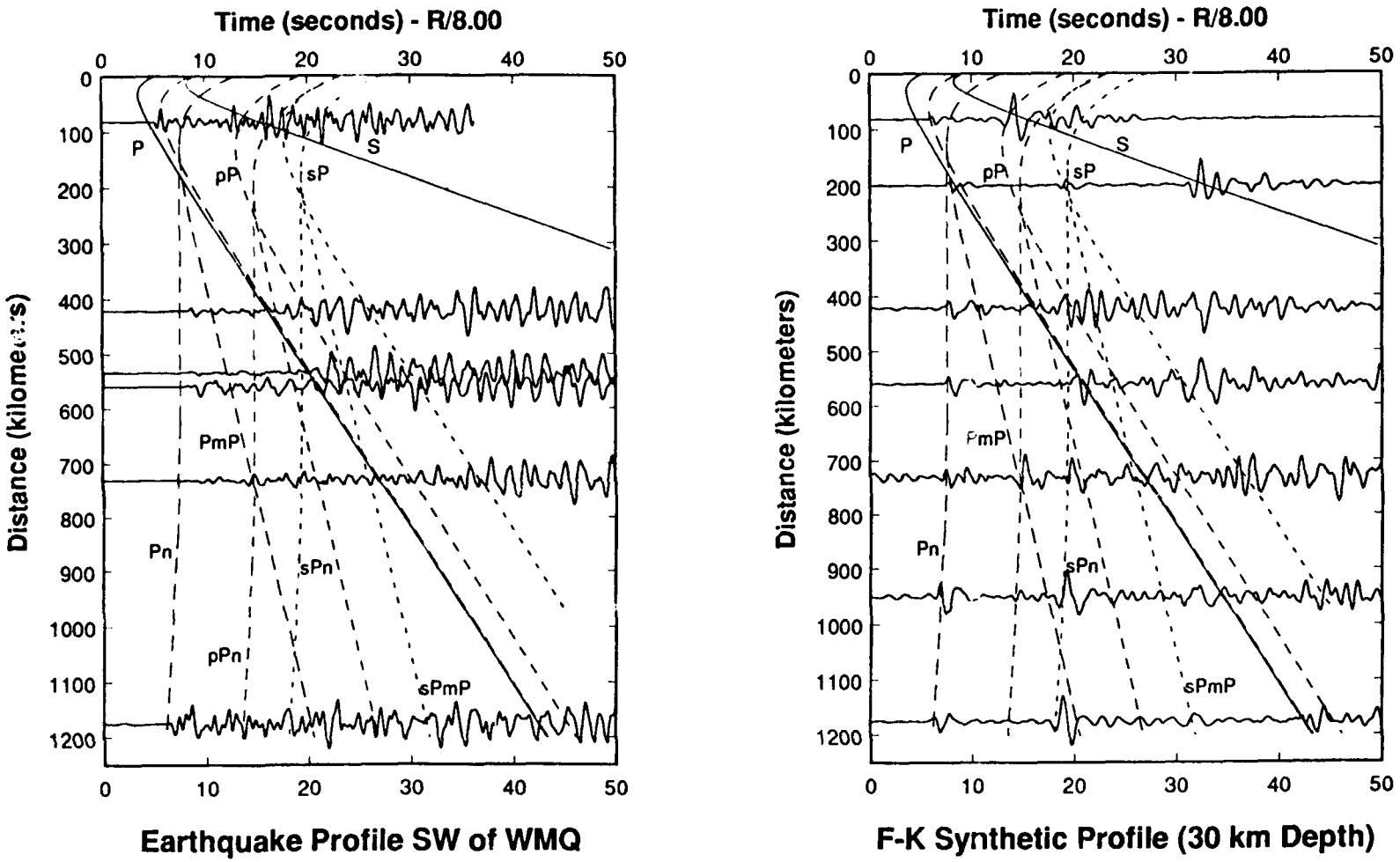


Fig. 2 (left) A profile of P_n-P_g waveforms from earthquakes to the SW recorded at WMQ. Also shown are travel-time curves for important phases computed for a source at 30 km depth in the velocity structure model in Table 3. Since the observed waveforms are from earthquakes at different depths, some waveforms have been time shifted slightly. (right) A profile of F-K synthetic seismograms for a sources at a depth of 30 km located SW of WMQ. Superimposed are the same travel-time curves as plotted on the observed data profile.

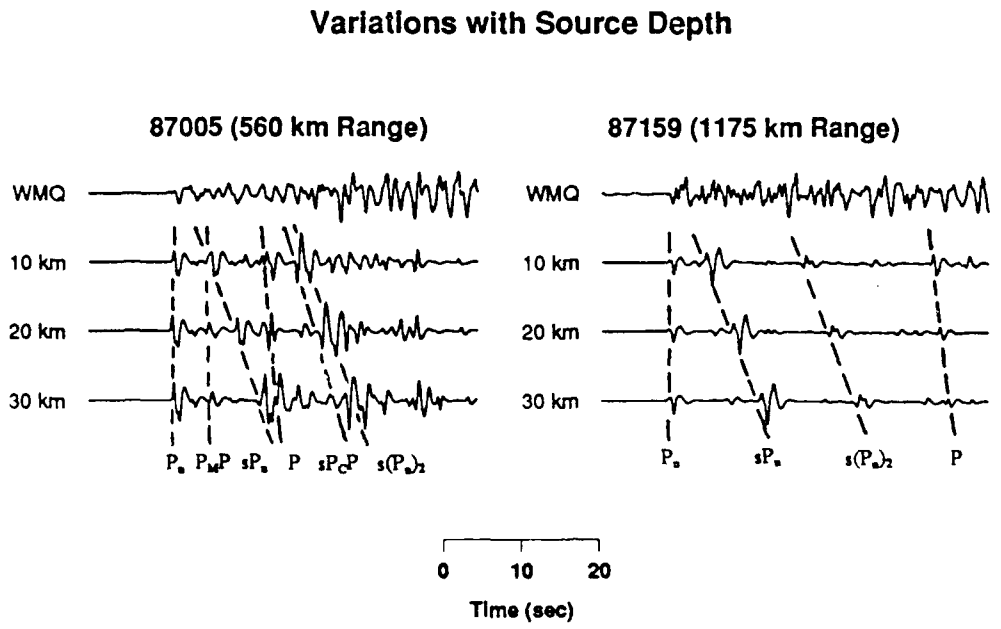


Fig. 3 Variations in P_n-P_g waveform due to changes in source depth. Shown at the top are observed waveforms from two earthquakes in the SW profile recorded at WMQ. Below each is a generalized ray synthetic seismogram computed for a source at 10, 20 or 30 km depth. Important phases are indicated.

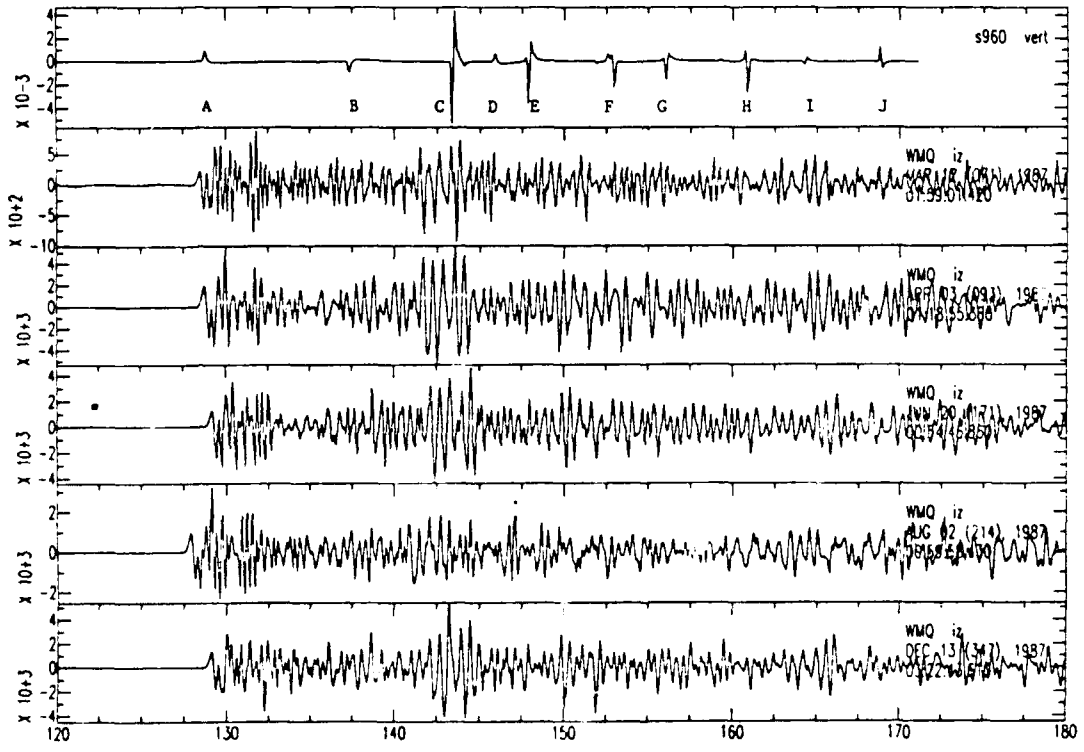


Fig. 4 A comparison of observed broad-band P waveforms at WMQ from Shagan River explosions. On the top is a generalized ray synthetic seismogram computed for an explosion source at a range of 960 km. Important phases are A: P_n; B: $(P_n)_2$; C: P_MP; D: $(P_n)_3$; E: $(P_MP)_2$; F: $(P_MP)_3$; G-J: phases including at least one traverse of the crust as S.

Design and Development of an Intelligent Event Identification System (ISEIS) Application to Regional Seismic Events in Eurasia

Douglas R. Baumgardt
ENSCO, Inc., 5400 Port Royal Road
Springfield, Virginia 22151

Under Contract No.:
F19628-90-C-0049

OBJECTIVE

The Intelligent Seismic Event Identification System (ISEIS) is a prototype research system for the systematic identification of seismic events from both regional and teleseismic seismic data using combined signal processing and artificial intelligence methods. A major goal of this project has been to develop a system which is flexible enough to easily incorporate new seismic knowledge and event identification techniques, as a result of event processing and event identification research. In addition to serving as the primary subsystem for event identification in the Nuclear Monitoring Research and Development (NMRD) system, ISEIS will also provide an analysis tool to support research efforts in seismic discrimination.

RESEARCH ACCOMPLISHED

A prototype of a research system for seismic event identification, with emphasis on the analysis of high-frequency regional, regional-array waveform data, has been developed. ISEIS consists of a variety of functions which process waveforms and parameters from seismic events detected and located by the front-end NMRD processes, extract important waveform features or measurements, apply "discriminants" in an expert system which reasons on the waveform features to characterize and identify the event, and displays the results in a number of different ways. The rules have been implemented in the C Language Production System (CLIPS), an expert system shell developed by NASA. A number of interactive graphics interfaces are available to display the results of the discrimination processing and to apply various signal-analysis functions (e.g., incoherent beam stacking, spectral analysis, continuous frequency-wavenumber analysis) for event characterization and research purposes. The discrimination processing of ISEIS can be done automatically or interactively. In the interactive mode, ISEIS relies on event locations and phase identifications determined by the NMRD systems, which are assumed to be stored in the CSS Version 3.0 database format (Anderson et al. 1990) and accessed through the Oracle RDBMS. In the automated mode, the user can change phase identifications, run any of the signal analysis and expert system processes, edit the discrimination rules, and view the results in many different ways. ISEIS is menu/mouse driven and uses the mouse for selection/deselection, dragging on waveforms, incoherent beams, and spectra, and Macintosh-style pull-down menus. ISEIS uses the X Window System for all graphics and the Oracle relational database for data acquisition and storage of discriminant processing results. The ISEIS system user interface and procedures are described in detail by Baumgardt (1991).

The ISEIS processing flow for a particular event consists of essentially three steps: *front-end signal analysis*, *feature extraction*, *discrimination processing*, and *results display*. The primary processing constituting *front-end signal analysis* is incoherent beam computation. Figure 1 (a) shows an example of incoherent beams computed in 8 filter bands, ranging from 0.5-2.5 Hz, primarily for *Rg* analysis, to 8.0-16 Hz. These beams provide the basic time domain measurements which are used in a number of subsequent discrimination processes, most importantly, *P*-to-*S* ratio discriminants. Phase measurements in the *feature extraction* process are made in "phase selection" time windows, such as

those shown in Figure 1(b). These windows can be set interactively by a "mouse drag" process or automatically from phase identifications already in the database. Average and maximum rms amplitudes are computed in each of the windows on all the incoherent-beam filter bands. Moreover, single-channel and/or array-averaged Fourier spectra are computed for each of the phase windows, which are used for the spectral-ratio discriminants and ripple-fire detection processing.

In *discrimination processing*, ISEIS makes decisions about the identity of seismic events using two artificial intelligence methods: *model-based reasoning* (MBR) or *case-base reasoning* (CBR). In MBR, rules are applied to the discrimination processing results, including seismic event parameters (e.g., location, depth) and waveform features (e.g., regional *P/S* ratios, *Lg* spectral ratios, spectral modulation analysis results for ripple-fire), to identify the event as a particular source type (i.e., nuclear explosion, earthquake, mine explosion, underwater explosion, unidentified), assuming that certain data-quality criteria (number of stations, signal-to-noise ratios) are met. In CBR, discriminant results for the events are compared to values of previous reference events in the same region, and the event is characterized in terms of how typical it is of previous events in the same region. A regionalization scheme has been developed where reference events are indexed in the database to specific geographic regions and are accessed in MBR for the regions closest to the event being identified.

Figure 2 shows an example of case-based reasoning, where an event located off the western Norwegian coast (CURRENT EVENT) is compared with other events in the same region and some onshore events. The numbers to the right of CF at the top of the plot in Figure 2(b) refer to the confidence of match of the feature (*Pn/Sn* ratio in the 4 to 6 Hz band against the average values of the reference events. The CURRENT EVENT matches the offshore earthquake group with a confidence of 0.84 which is higher than the match to the other regions. Thus, we would conclude that this event belongs to this earthquake group. Figure 3 shows another CBR scheme, called dynamic time warping (DTW) template matching, in which incoherent beams of entire regional codas are matched against reference events. If the coda shapes are similar, DTW gives a small distance of separation, whereas dissimilar events would have large separations. The best example of MBR in ISEIS is the Multiple Event Recognition System (MERSY), an example of which is shown in Figure 4, which uses the spectral/cepstral methods to identify ripple-fired explosions. Ripple-firing produces a time independent spectral scalloping which, in turn, produces cepstral peaks at consistent quefrencies for different phases. Thus, MERSY identifies mine blasts by assuming the "model" that most mine blasts are ripple-fired.

In *results displays*, ISEIS presents a three-tiered set of explanation displays for the results of discriminant processing on an event: *top-level spread sheet and map*, *intermediate-level text*, and *bottom-level data analysis*. As the user descends the tiers from the top to the bottom, the results are presented in a more data intensive manner. The *top-level spreadsheet/map* displays present an overview of the results of the event, along with other events being processed and/or reference events. This is accomplished by making use of color coding on a spreadsheet and in the use of symbols plotted on the map. This high-level display allows the quick evaluation of the results of the processing of several events at once on the spreadsheet and on the map. The *intermediate-level text* displays provide, in textual form, an explanation of the results of the status assessment and discriminant execution on any particular event. These explanations are reached by mousing on individual boxes in the spreadsheet display. Also, at this level, the user can view the trace of rule execution and edit the CLIPS rules themselves. The *bottom-level data analysis* displays provide the most detailed explanations of the processing results for the particular event.

In addition, various research processing functions are provided, which include spectrogram or sonogram and continuous frequency-wavenumber (fk) analysis. Sonograms display spectral power as a function of time and frequency and are useful for the analysis of time-independent modulations in ripple-fired mine explosions. Continuous fk analysis computes array-measured velocity, azimuth, and

f-statistic in moving time windows and displays templates of these features as a function of time. These templates are useful for phase identification and for characterization of the entire regional coda.

ISEIS is a distributed system, which means that different ISEIS subprocesses can be set up to run on several machines, and the different results displays may appear on any number of workstations. Currently, we are running ISEIS on three different platforms, a SUN Sparc 4/390 SparcServer, which displays the spreadsheet, intermediate and lower level displays, a SUN 3/160, which displays the map, and a Stardent 3000 minisupercomputer, which shares the main processing load with the Sparc 4 in addition to being used for special color 3d visualization displays of signal analysis results.

CONCLUSIONS AND RECOMMENDATIONS

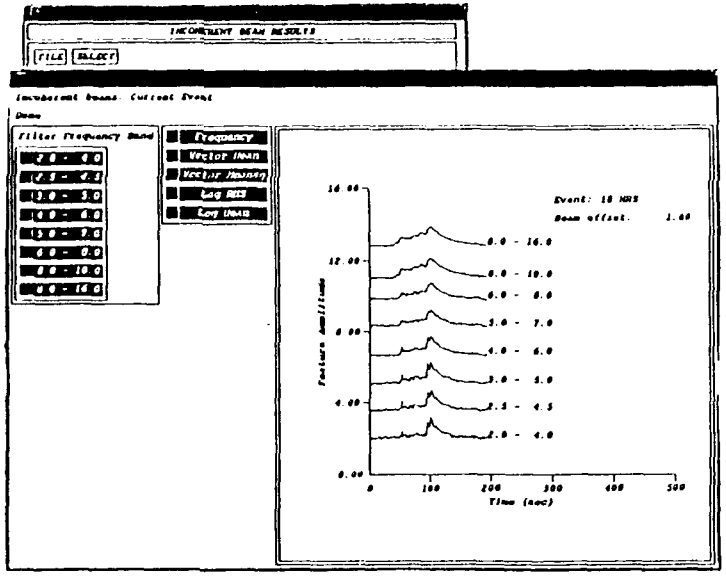
The ISEIS system has been tested on a limited database of over 100 regional seismic events from Scandinavia and Eurasia recorded at the NORESS and ARCESS. The current rules in ISEIS have been based on the analysis of an earthquake and explosion group in western Norway. The high-frequency *Pn/Sn* and *Pn/Lg* discriminant and ripple-fire detection using time-independent spectral modulations have so far proven to be the most effective discriminants for separating underwater and mine explosion and earthquake classes. As shown in Figure 5, the best separation of the classes of earthquakes and explosions using *Pn/Sn* and *Pn/Lg* ratios has been seen in the 8-16 Hz band, where earthquakes have much lower shear-wave amplitudes compared to mine explosions. We have also included a set of presumed underwater blasts, in the Stavenger offshore region of southern Norway, which seem to have the the highest amplitude ratios. We have continued this analysis into other regions of Eurasia, in order to develop more region-specific rules. Figure 6 shows the results of ISEIS analysis of seismic events recorded at ARCESS from earthquakes in the Spitzbergen region and explosions on the Kola Peninsula and Matochkin Shar. As in the case of the Scandinavian events, the greatest separation between the classes is obtained at high frequency. However, the regional amplitude-ratio discriminants are strongly affected by regional propagation effects, most notably the complete blockage of *Lg* waves and the partial blockage or attenuation of *Sn* waves, presumably in the Barents sedimentary basin, for the Matochkin Shar events (Baumgardt, 1990). However, Figure 6(b) shows that at comparable distances for ARCESS, the Spitzbergen earthquakes have much greater *Sn* excitation compared to the Matochkin Shar explosions. These results show the importance of taking propagation path effects into account in any attempt to use such waveform features in trying to identify seismic events. Continued evaluation of the system and enhancement of the discrimination rule-based on an expanded database are planned.

REFERENCES

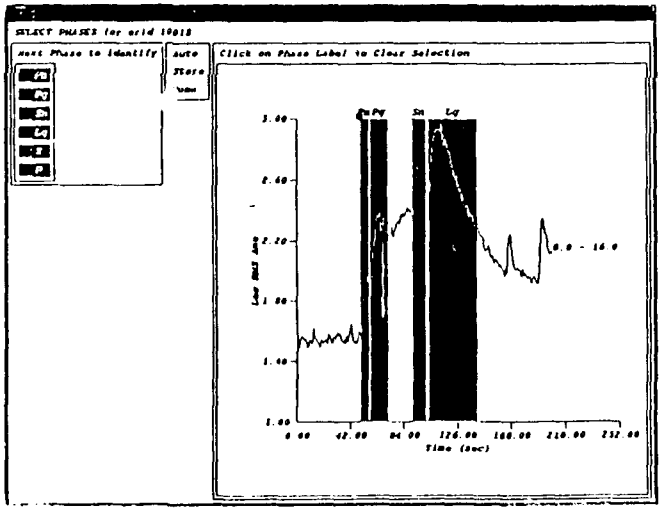
Anderson, J., W.E. Farrell, K. Garcia, J. Given, H. Swanger (1990). Center for Seismic Studies Version 3 database: schema reference manual, Technical Report C90-01, Center for Seismic Studies, Arlington, VA.

Baumgardt, D.R. (1990). Investigation of teleseismic *Lg* blockage and scattering using regional arrays, *Bull. Seism. Soc. Am.*, **80**, 2261-2281.

Baumgardt, D.R. (1991). *Intelligent Event Identification System: Reference Manual (Draft)*, ENSCO, Inc., Springfield, VA, May, 1991.

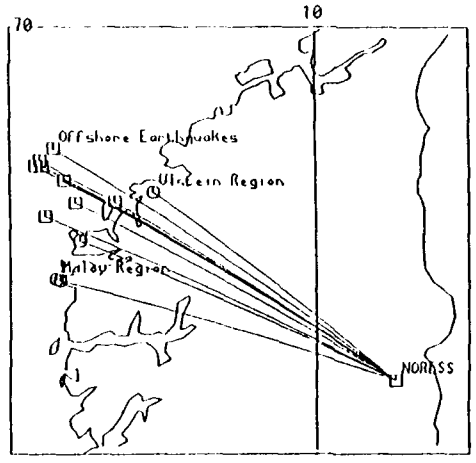


(a)

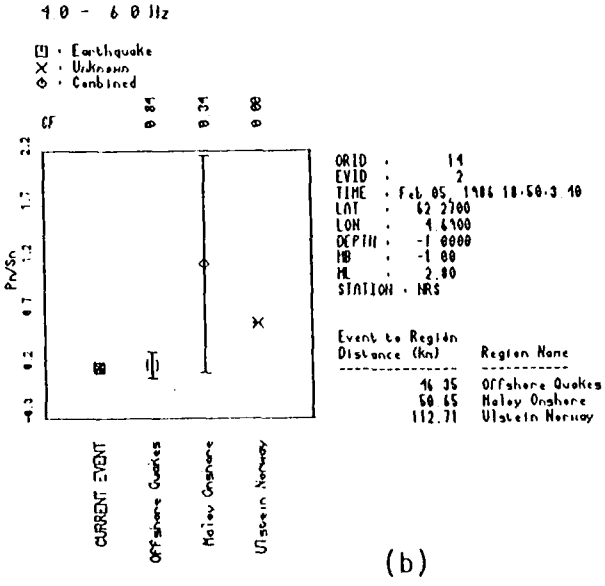


(b)

FIGURE 1: (a) ISEIS plot of incoherent beams in eight frequency bands. (b) Example of phase selection from the 8-16 Hz incoherent beam.



(a)



(b)

FIGURE 2: (a) Map showing locations of current event (arrow) and master event and propagation paths to NORESS. (b) Examples of CBR results for comparison of 4-6 Hz Pn/Sn ratios of an earthquake with reference events.

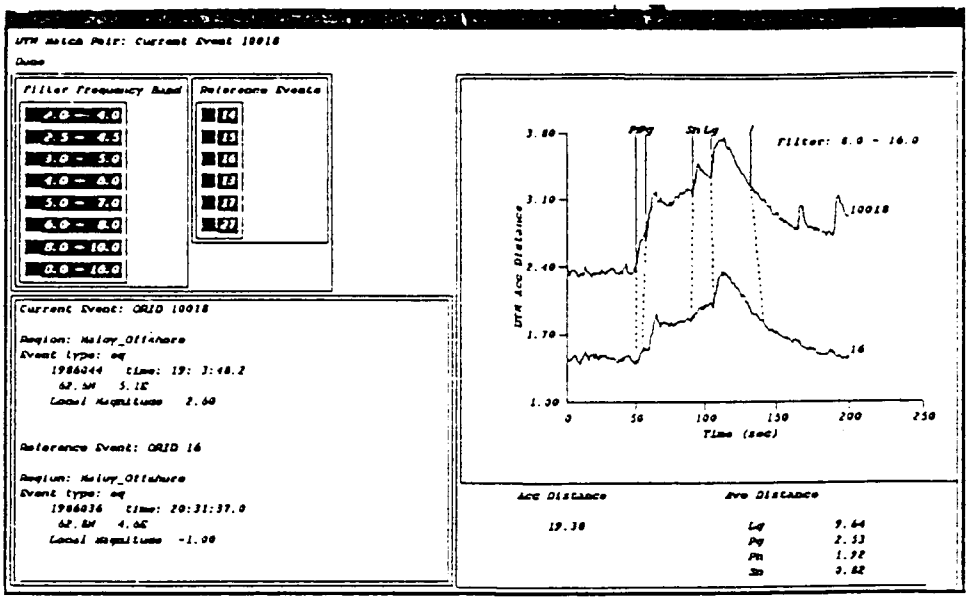


FIGURE 3: Example of DTW match between regional event codas of two western Norway earthquakes recorded at NORESS.

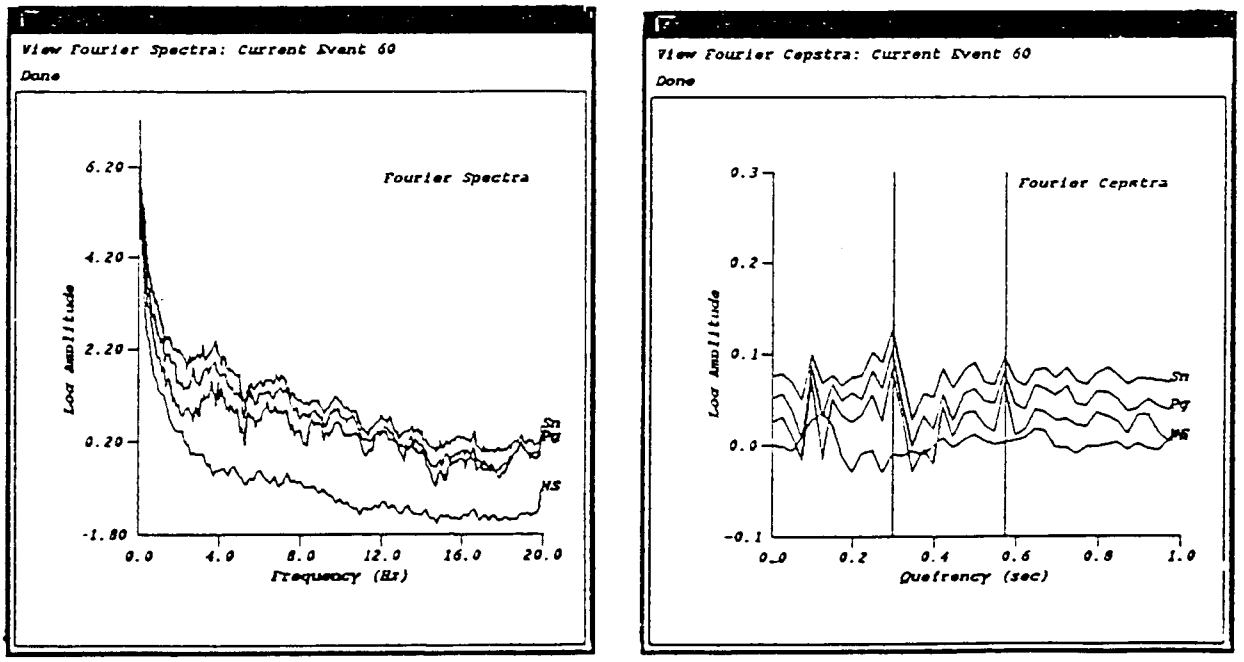
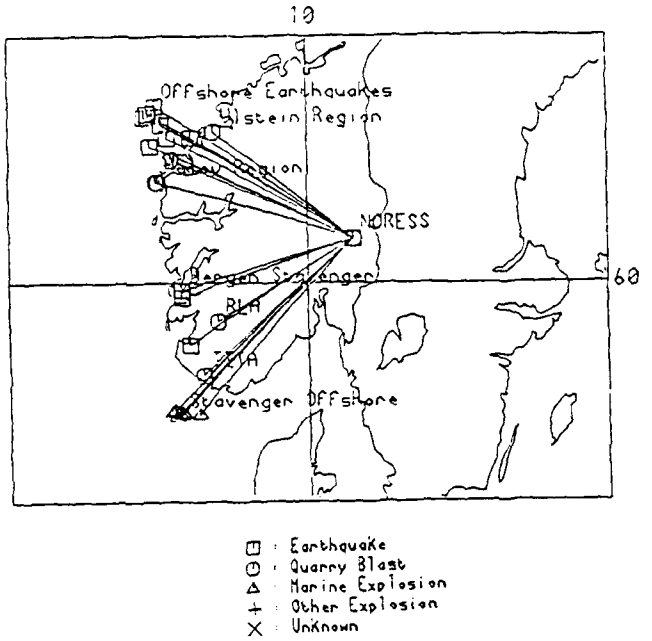
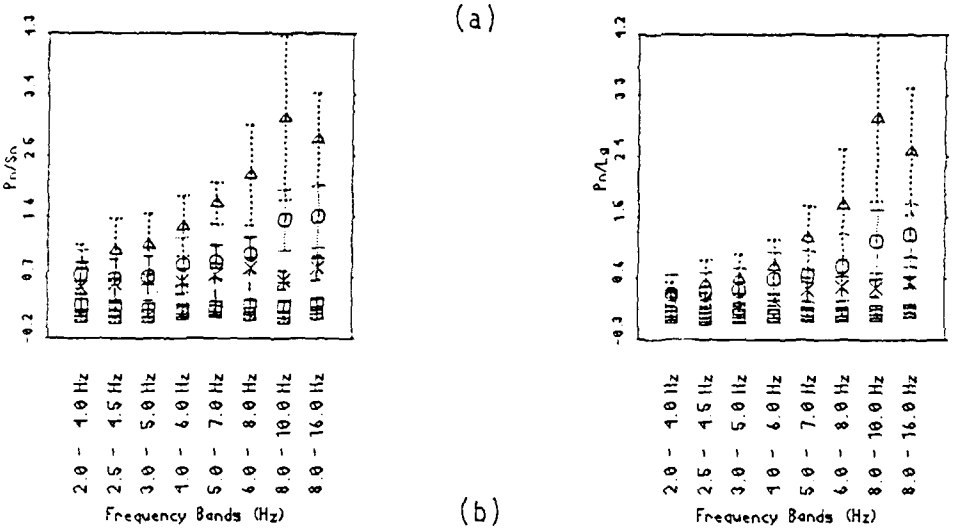


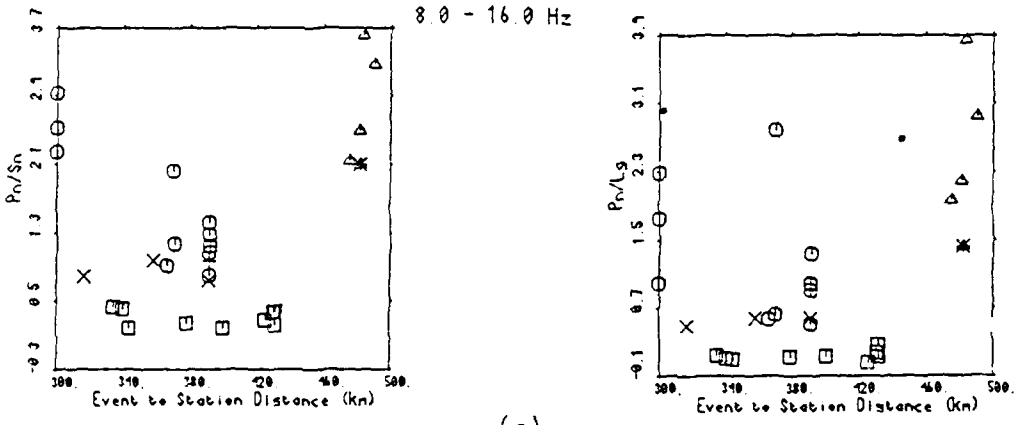
FIGURE 4: Fourier spectra (left) and cepstra (right), with peak selections from the ISEIS MERSY program, for a ripple-fired mine blast recorded at NORESS.



(a)

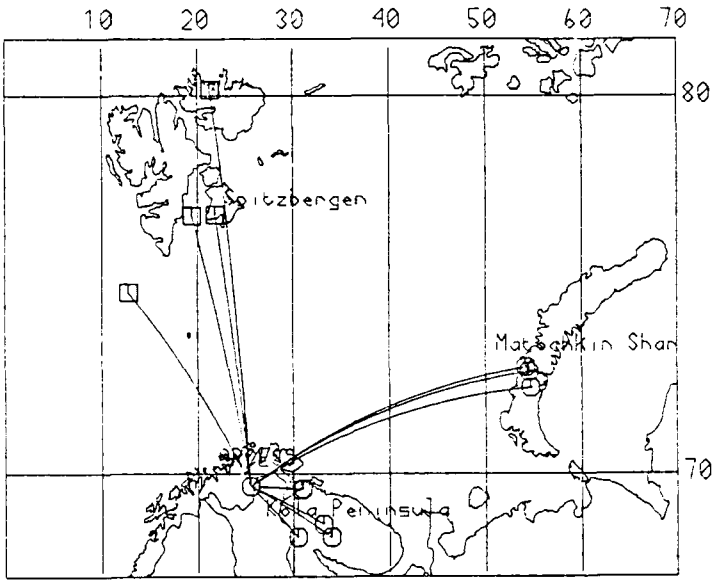


(b)

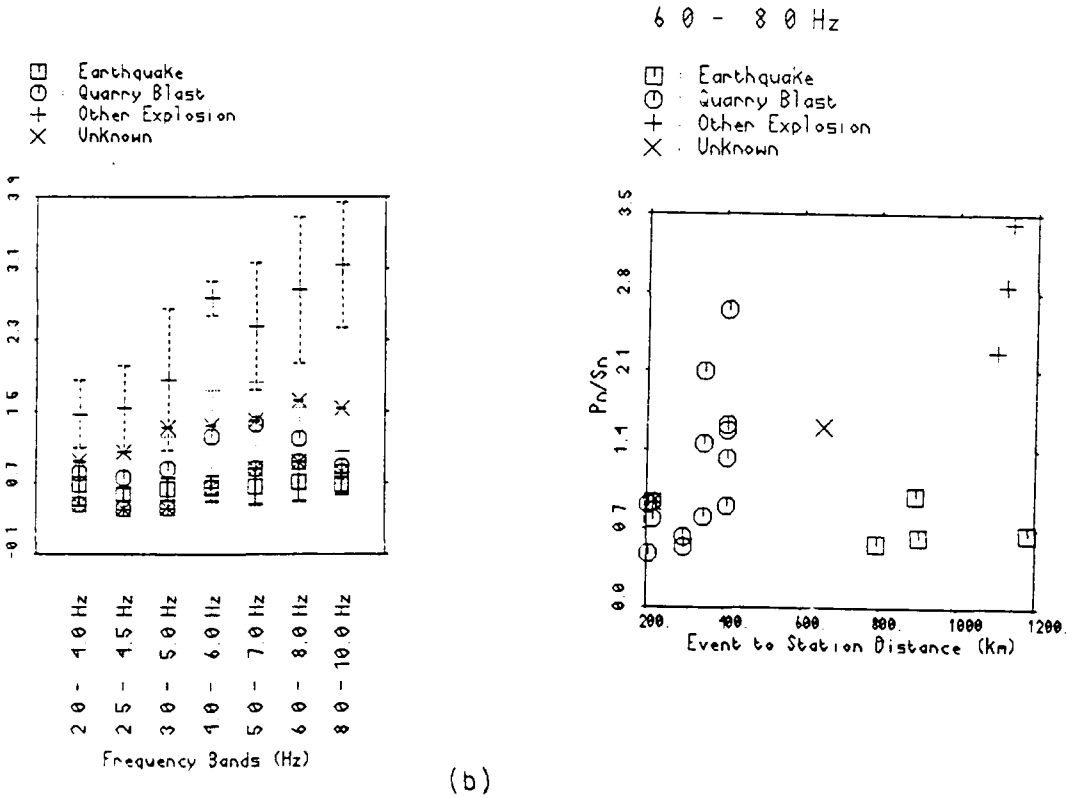


(c)

FIGURE 5: (a) Map showing propagation paths from western Norway events to NORESS. (b) Pn/Sn and Pn/Lg ratios plotted versus frequency. (c) Same ratios versus distance of event from NORESS.



(a)



(b)

FIGURE 6: (a) Propagation paths from explosions and earthquakes to ARCESS. (b) Plots of Pn/Sn ratios versus frequency (left) and distance (right).

Regional Discrimination of Soviet Nuclear Explosions, Earthquakes and Mineblasts

T. J. Bennett, A. K. Campanella, J. F. Scheimer and J. R. Murphy
S-CUBED
11800 Sunrise Valley Dr., Suite 1212
Reston, Virginia 22091
Contract No. F19628-89-C-0043

Objective

The goal of the research conducted under this contract has been to develop a seismic discrimination scheme utilizing the regional phase signals from events in the Soviet Union. Toward this goal we have been seeking to identify reliable regional discriminant measures for Soviet events and to develop a better understanding of how source and propagation factors within the region of interest affect these measurements. These analyses have focused on regional signals recorded at Soviet IRIS and CDSN stations from underground nuclear explosions and earthquakes. In addition, we have been investigating the problem of recognition of mineblasts in the Soviet Union utilizing primarily data from regional arrays in Scandinavia and northern Europe.

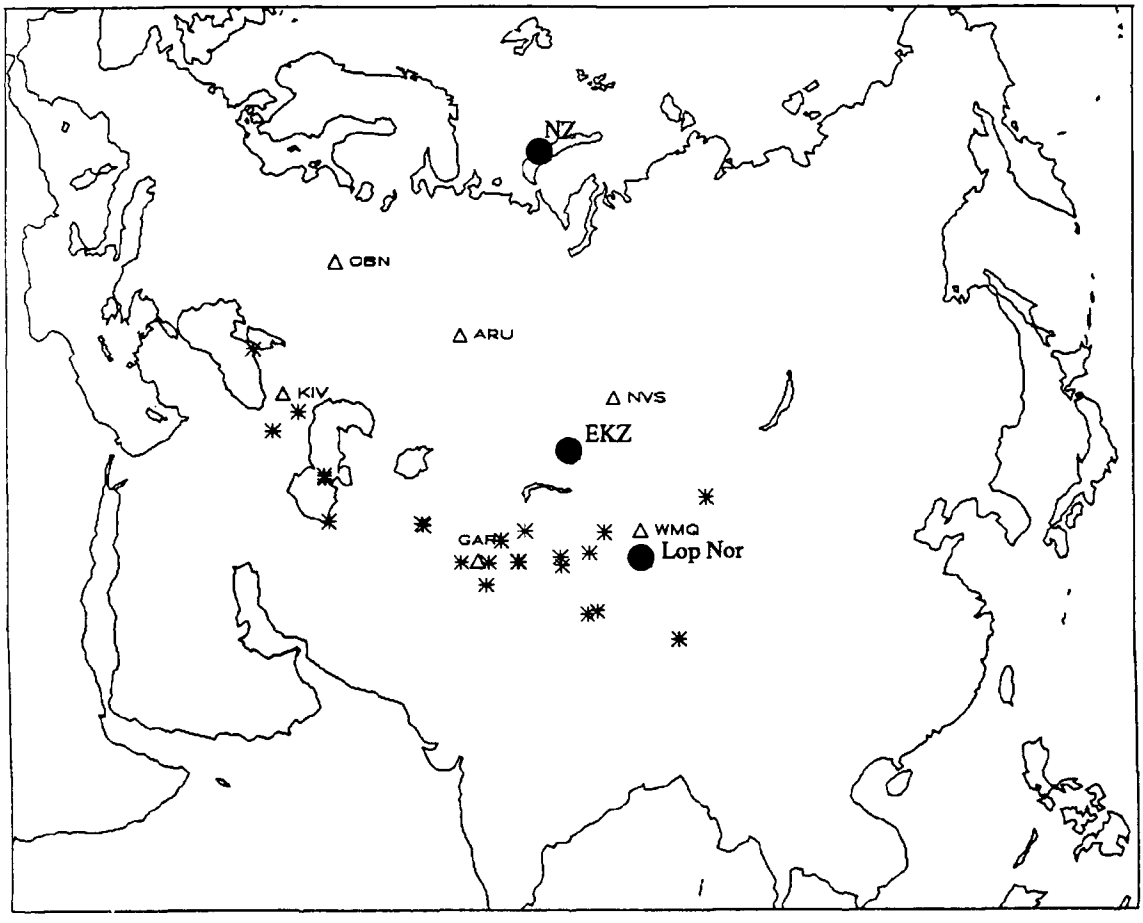
Research Accomplished

Over the past decade S-CUBED has been conducting a systematic research program aimed at improving regional seismic discrimination capability. In the course of this program, our research has produced several significant findings based on both empirical observations and theoretical analyses of regional seismic signals. We have investigated a variety of time-domain amplitude and spectral characteristics of regional signals and identified a number of features which appear to be diagnostic of source type as well as others which appear to be less promising for discrimination. Perhaps the most important findings of these studies was the identification of spectral differences in the regional L_g signals and in the L_g/P spectral ratios between underground nuclear explosions and earthquakes. Such differences were identified for Soviet events as well as for our original testbed of western U. S. events. Criticism regarding the influence of propagation effects on these results not withstanding, we continue to believe that source or near-source phenomena cause differences in the spectral behavior of regional phase signals for explosions and earthquakes. Our current research appears to support this conclusion. During the past year our research has focused on three areas. First, we have continued to analyze regional seismic signal characteristics recorded at the Soviet IRIS and CDSN stations. At past review meetings we reported on signal differences between Soviet explosions and earthquakes along the southern Soviet border recorded mainly at the regional Chinese stations. These data included 27 East Kazakh underground nuclear explosions and 32 earthquakes recorded primarily at station WMQ. During the past year our study has been directed more at regional events recorded at the Soviet IRIS stations as additional experience with the latter continues to develop. Figure 1 shows the locations of 22 earthquakes for which waveform data from the Soviet

IRIS stations have been retrieved and are being analyzed. The explosion database for the Soviet IRIS stations includes 11 East Kazakh nuclear tests in addition to one nuclear test at the Lop Nor site in China and one at the Novaya Zemlya test site, which are also shown on the map. For reference purposes we also show the locations of stations WMQ and NVS. NVS along with ARU and OBN have been sources of hand-digitized data for a number of historical Soviet explosions at East Kazakh and Novaya Zemlya which are being analyzed to improve understanding of propagation effects on regional signals for different areas of the Soviet interior.

In analyzing the database described above for WMQ, we found consistent differences in the L_g/P spectral ratios between the East Kazakh nuclear tests and the earthquakes. In particular, the L_g/P ratios were larger for the earthquakes over a broad frequency band with maximum differences occurring above about 2 Hz and some mixing of event types occurring at lower frequencies. It has been suggested subsequently by Frankel (1989) that this observation may have been influenced by propagation differences because the regional phases for the explosions and earthquakes followed different paths to WMQ. Furthermore, based on their results for events in the western U. S., Lynnes and Baumstark (1991) concluded that amplitude and spectral ratios of regional P and L_g phases were strongly influenced by path effects and show little dependence on source type. However, we do not believe that propagation effects alone can account for our observations for several reasons. First, in

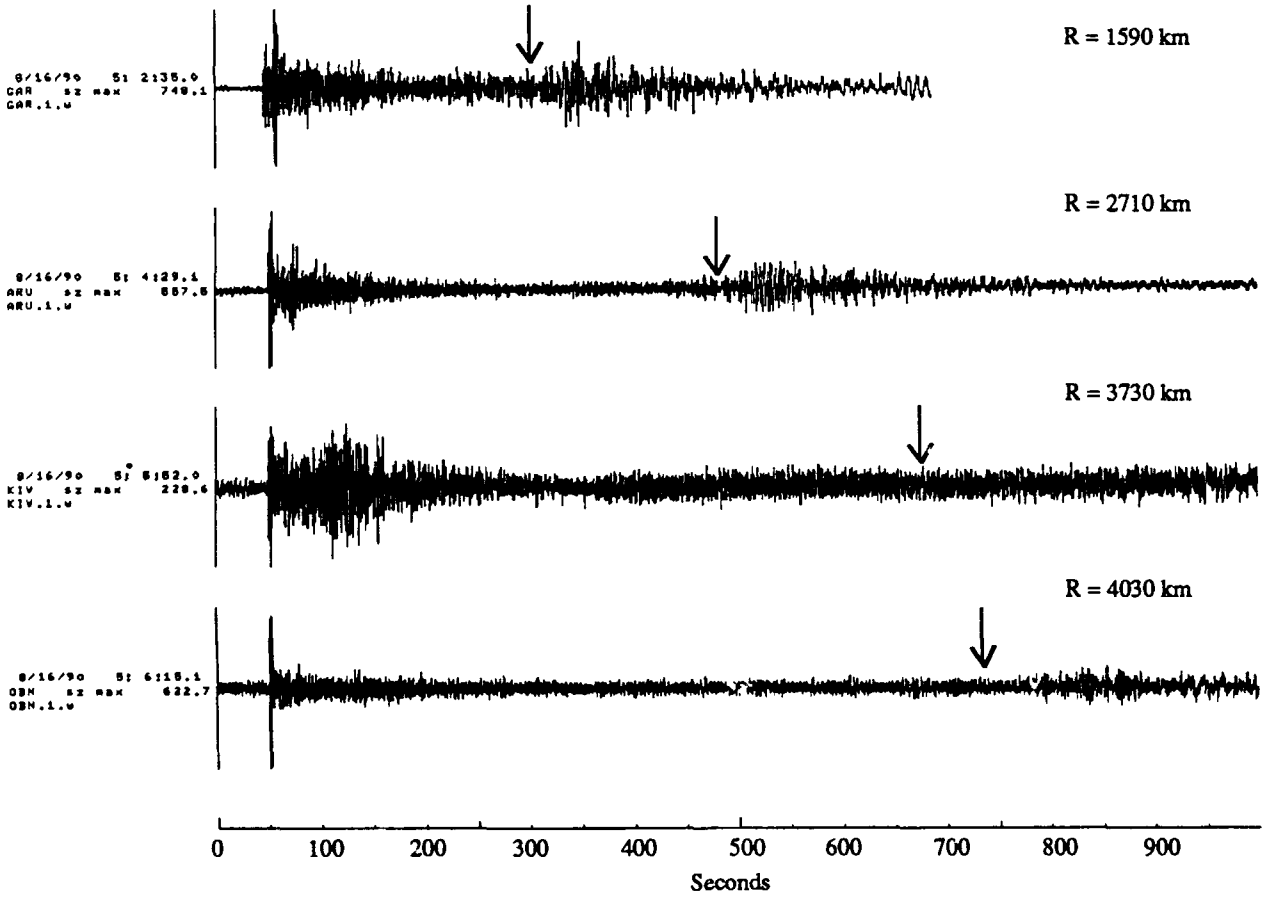
Figure 1: Locations of Stations and earthquakes used in analyses.



selecting earthquakes for analysis, although we could not pick events from the immediate source area of the explosions because of its aseismicity, we did pick earthquakes from a variety of azimuths surrounding WMQ. Therefore, the propagation effects for the earthquakes should have been averaged out to some degree and the results not strongly dependent on particular anomalous paths. Second, the result for the WMQ data is consistent with the behavior which we previously observed (cf. Murphy and Bennett, 1982; Bennett and Murphy, 1986) for regional phase spectral behavior for events in the western U. S. where the explosions and earthquakes were located in close proximity to one another.

To provide an additional test of the relative influence of propagation effects on the observed differences in the L_g/P spectral ratios, we have attempted to design an approximate reciprocal test using data from the August 16, 1990 underground nuclear explosion in Lop Nor, China recorded at the Soviet IRIS station GAR and two earthquakes (09/25/88 and 01/09/89) near GAR (viz. the nearest two earthquakes to GAR in Figure 1 above) recorded at station WMQ. As can be seen from Figure 1, the propagation paths for these events lie in close proximity. Figure 2 shows the vertical component records at all four Soviet IRIS stations for the Lop Nor explosion. The P phases, except at station OBN, appear relatively complex consistent with the expected behavior of regional P. The arrows on each record indicate a group velocity of 3.6 km/sec corresponding to the approximate start of the L_g window. L_g signals are apparent on the records at three of the four stations. Only at station

Figure 2: Regional phase signals at Soviet IRIS stations from Lop Nor nuclear explosion.



KIV is the L_g missing, as it appears to be buried in S coda. Figure 3 shows the vertical component records at GAR from the Lop Nor explosion and at WMQ from the two near-Garm earthquakes. For comparison we also show the GAR record for the East Kazakh JVE explosion which had a slightly shorter path length. Comparing the GAR records for the two explosions, there are apparent strong differences in the regional P and L_g signals which are most likely related to propagation differences. We are continuing to analyze this problem. On the positive side the comparison of the records for our reciprocal event sample also show clear differences in the relative excitation of the regional P and L_g signals between the earthquakes and explosion. In particular, for the broad-band records the L_g signals are much larger than P for the earthquakes while the L_g signal for the explosion is comparable to or weaker than P.

We have also investigated the L_g/P spectral ratios for the records from Figure 3. Fourier spectra were computed from a 25 second sample of the initial P and a 100 second sample of the L_g window for each record over a frequency band out to 10 Hz. Figure 4 shows the corresponding L_g/P spectral ratios. The L_g/P ratio for the East Kazakh explosion is seen to be generally larger than the corresponding ratio for the Lop Nor explosion. We would again attribute this difference to possible propagation differences to GAR for the two events. Comparing the reciprocal explosion and earthquake spectral ratios, the two earthquakes are seen to have fairly consistent L_g/P ratios which

Figure 3: Regional Signals for East Kazakh and Lop Nor explosion at GAR and for near-GAR earthquakes at WMQ

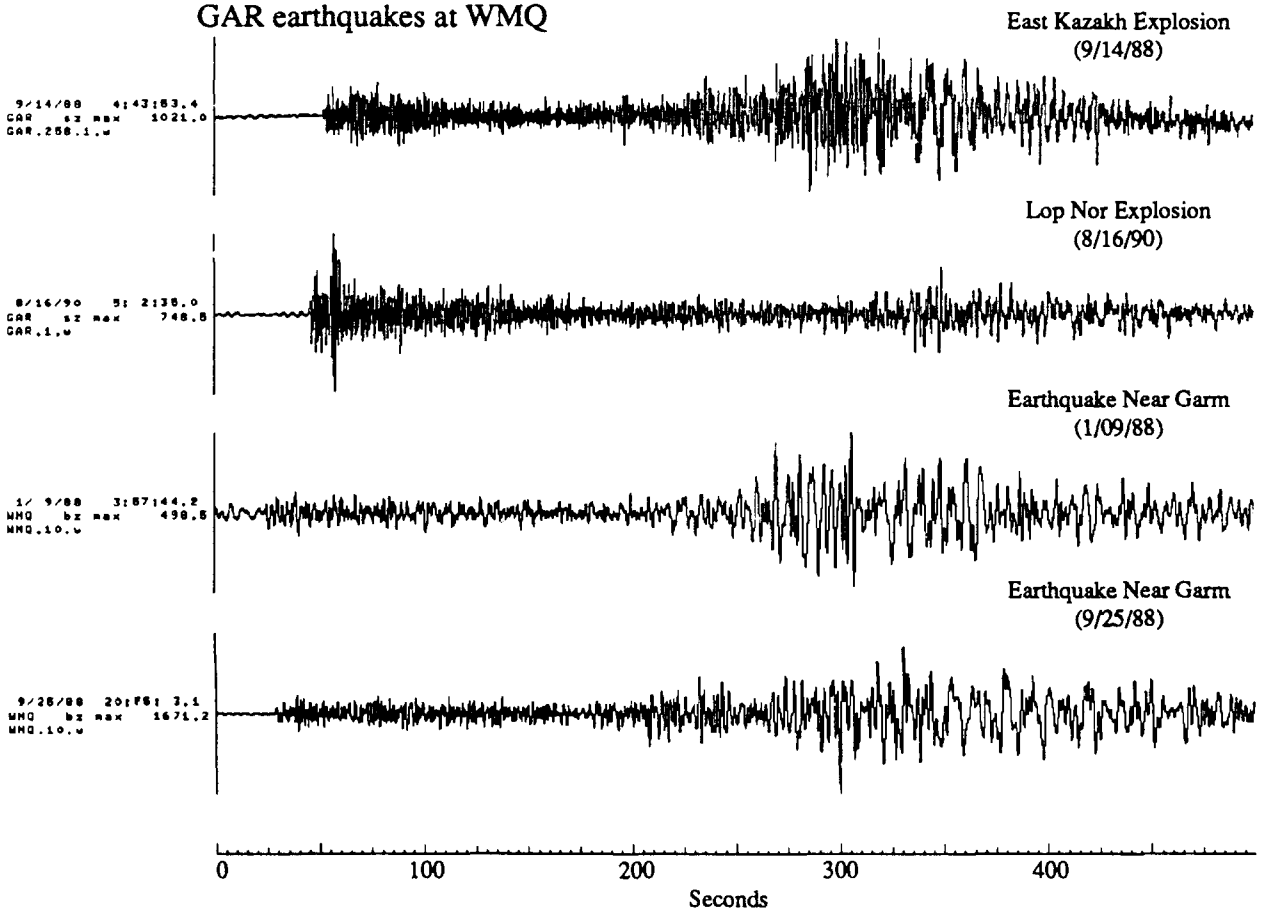
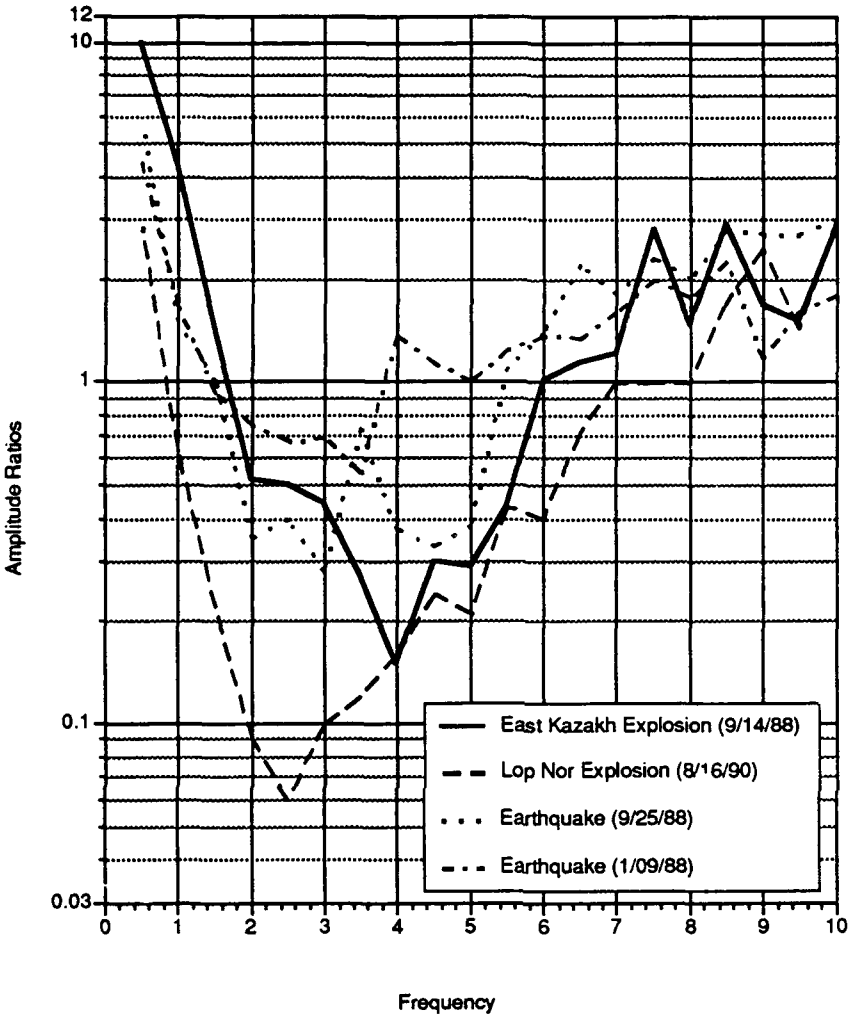


Figure 4: L_g/P Spectral Ratios for events from Figure 3.



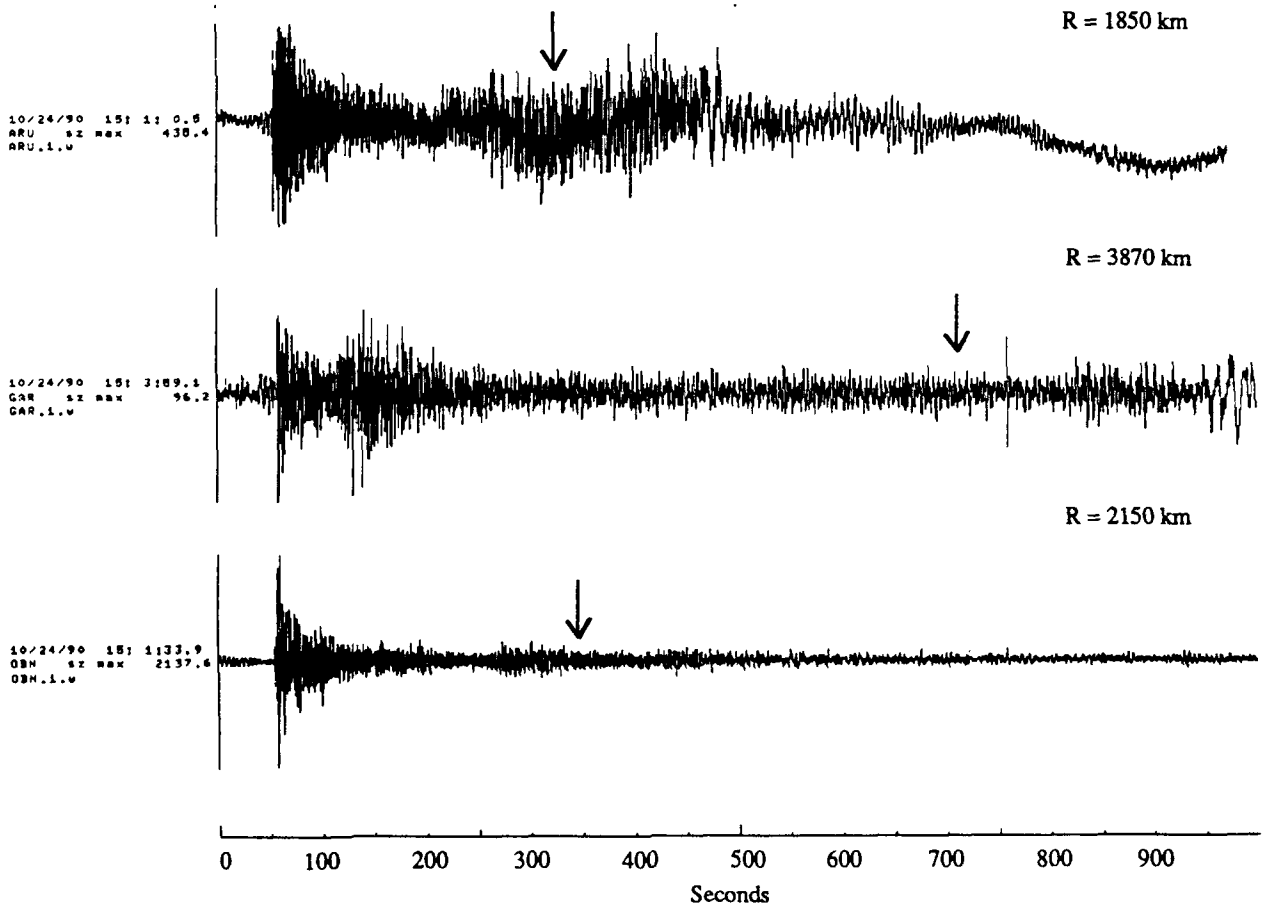
lie well above those of the Lop Nor explosion over a broad frequency band. In fact, the differences are up to a factor of ten in a frequency band between 2 and 3 Hz. We would conclude from this that the earthquakes and explosions produce significantly different L_g/P spectral ratios for approximately reciprocal paths. A reasonable explanation for this observation appears to be source differences in the excitation of regional phases from the two event types.

As noted above, we are continuing to use Soviet IRIS as well as hand-digitized station data to analyze regional phase propagation characteristics for other parts of the Soviet Union. Because the Soviet IRIS stations have been operating for only a few years, there has been little time to develop an experience base for seismic signals from events in different areas. In particular, the IRIS stations have recorded only one nuclear explosion (10/24/90) from the Soviet test site at Novaya Zemlya. Figure 5 shows the signals at these stations which are available for this explosion. The P signals are generally strong but complex. The L_g signals, whose starts are marked by the arrows at a 3.6 km/sec group velocity, are seen to be comparatively weak and barely rise above the coda. Only at station

ARU is the signal level in the L_g window large, and even there distinction between S-coda and L_g is ambiguous. Hand-digitized waveforms which have become available recently for a sample of East Kazakh and Novaya Zemlya explosions at stations ARU, OBN, NVS and other Soviet stations, provide a valuable supplement to our experience for regional phase propagation within the Soviet Union. Although these data are useful for only a rather limited frequency band, the signals are remarkably consistent. We are attempting to use the regional phase signals to develop effective attenuation along these additional propagation paths.

Another aspect of the current study of the Soviet IRIS station data has been an analysis of detection thresholds. Given (1990) conducted a thorough investigation of the background noise levels measured over an extended period of time at the IRIS sites. Based on these analyses and using an attenuation relationship developed for Scandinavia, she predicted detection thresholds in terms of magnitudes as a function of range for each station. We have used a somewhat similar approach except the noise was taken from the pre-P segments for nuclear explosions which were recorded at the stations and effective attenuation relations for L_g presented at last year's review meeting were used to represent attenuation for each station instead of the Scandinavian relationship. Using these we predict detection thresholds for 1 Hz Lg signals which are from 0.4 to 1.0 magnitude units greater than those reported by Given at comparable ranges.

Figure 5: Regional phase signals at Soviet IRIS stations from NZ nuclear explosion.



Finally, because mineblasts in the Soviet Union can represent a special problem for low-threshold discrimination, we have been reviewing data recorded at high-quality regional array stations from chemical explosions in the northwestern Soviet Union. The regional signals from these blasts show differences in relative amplitude and frequency content from event to event. In some cases these differences exist for events not separated by very large distances suggesting the behavior may be related to source differences associated with changes in shooting practice. We are systematically evaluating a sample of blasts from several different mining areas to better characterize the extent of this variability between events.

Conclusions and Recommendations

The results of analyses conducted to date of regional signal characteristics from nuclear explosions and earthquakes indicate that observed differences in L_g spectra and L_g/P spectral ratios cannot be explained simply as a propagation phenomenon. Although regional phase behavior is clearly influenced by propagation, we believe the measured spectral differences include an observable source component. The differences in the spectra appear to be caused by (1) the earthquake L_g signals being larger than comparable explosion signals over a fairly broad band, and (2) the explosion P signals having comparable or more high frequencies than the earthquakes. Development of more accurate knowledge of regional phase propagation characteristics within the Soviet Union could eventually provide the means to compensate for propagation effects to get more directly at source differences. Our analysis of noise conditions and attenuation for the Soviet IRIS stations indicates somewhat higher detection thresholds than those previously reported. Accurate assessment of regional seismic monitoring capability for the Soviet Union will require resolution of detection thresholds for an extensive geographical area. The extent of the commercial blasting discrimination problem for most areas of the Soviet Union is not well-defined and will need to be solved for lower threshold monitoring.

References

Bennett, T. J., and J. R. Murphy (1986), "Analysis of Seismic Discrimination Capabilities Using Regional Data from Western United States Events," *Bull. Seism. Soc. Am.*, 76, pp. 1069 - 1086.

Frankel, A. (1989), Personal Communication.

Given, H. K. (1990), "Variations in Broadband Seismic Noise at IRIS/IDA Stations in the USSR with Implications for Event Detection," *Bull. Seism. Soc. Am.*, 80, pp. 2072 - 2088.

Lynnes, C. S., and R. Baumstark (1991), "Spectral-Ratio and Phase-Ratio Discrimination in the United States," EOS, 72, p. 192.

Murphy, J. R., and T. J. Bennett (1982), "A Discrimination Analysis of Short-Period Regional Seismic Data Recorded at Tonto Forest Observatory," *Bull. Seism. Soc. Am.*, 72, pp. 1351 - 1366.

The Norilsk DSS Profile in Northern Siberia: Interpretation of the Velocity Structure and Comparison with Basin and Range and New England Profiling Results

H. M. Benz[1], J. D. Unger[2], W. Leith[2], and V. Ryaboy[3]
[1]U.S. Geological Survey, Menlo Park, CA
[2]U.S. Geological Survey, Reston, VA
[3]Center for Seismic Studies, Arlington, VA
Contract No. GLH0-6064

Objective

In the spring of 1991, the U.S. Geological Survey obtained digital Deep Seismic Sounding (DSS) data from the Ministry of Geology of the USSR. The refraction/wide-angle reflection profile acquired by the USGS was a NW-SE trending 220-km-long line that crosses the Norilsk uplift of northern Siberia. These data were modeled to determine the regional velocity structure of the transition zone between the Precambrian and Paleozoic portions of the Siberian platform. Modeling results are compared with results from comparable profiles recorded by the USGS in the Basin and Range and New England/New York region. The comparisons are used to illustrate similarities and differences in elastic wave propagation and crustal structure between the Eurasian and North American plates. Specifically, a comparison with the Basin and Range velocity structure is interesting because the Mesozoic and Cenozoic development of the Basin and Range crust is relatively youthful compared to the Siberian platform, which developed primarily during Precambrian and Paleozoic time. These comparisons are also helpful for understanding the differences in crust and upper mantle structure near seismic stations used to monitor nuclear explosions from the U.S. and Soviet test facilities.

Research Accomplished

Having only recently received the Norilsk DSS data, we have not had sufficient time to model completely the two-dimensional velocity structure beneath the Norilsk uplift. Consequently, we present generalized one-dimensional velocity models that we feel are representative of the velocity structure of the different regions investigated. Preliminary modeling of the Norilsk profile indicate that average upper and lower crustal velocity are 6.1 and 6.8 km s^{-1}, respectively, with an average crustal thickness of 40-42 km. P_n is typically a weak but observable phase with an average velocity of 8.2 to 8.3 km s^{-1}. These results differ significantly from interpretations of Basin and Range seismic refraction data [*Benz et al.*, 1990; *McCarthy et al.*, 1991], which indicate a thin crust (~30-km-thick) with average upper and lower crustal velocities of 6.0 and 6.5 km s^{-1}, respectively, and P_n velocities of 7.9 to 8.0 km s^{-1}.

Analysis of Pacific-Arizona Crustal Experiment (PACE) data show evidence for an upper mantle low-velocity zone (LVZ) that ranges from 38 to 49 km in depth with an estimated velocity of 7.5 km s^{-1}. Evidence for this LVZ is based on the observation of three upper mantle phases; two headwaves that are separated by ~1 sec, the first of which propagates above the LVZ and terminates abruptly at 275 km, and the second propagating beneath the LVZ, and a wide-angle reflection off the base of the LVZ. P_n is observed from 150 to 275 km with a velocity of 8.0 km s^{-1}, while the headwave below the LVZ is

observed from 200 to 370 km with a velocity of 8.2 km s^{-1}. The velocity within the LVZ represents a 5% velocity decrease relative to a Pn velocity of 8.0 km s^{-1}.

Regional Geology and Geophysics of the Basin and Range-- In the mid 1960's, the U.S. Geological Survey conducted reconnaissance refraction profiling of the Basin and Range Province and established that the crust is thin (< 32 km thick) with upper mantle P-wave velocities between 7.8 and 8.1 km s^{-1} [*Pakiser*, 1963; *Eaton*, 1963, *Hill and Pakiser*, 1966]. Reanalysis of these same data by *Prodehl* [1979] suggests a 29 to 35 km crust with a 7.9 km s^{-1} upper mantle velocity. Refraction surveys across northwestern Nevada using Nevada Test Site (NTS) explosions and quarry blasts showed evidence for an anomalously low P_n velocity of 7.8 km s^{-1} [*Stauber and Boore* , 1978] and anomalously thin crust of 20 km in northwestern Nevada [*Priestley et al.*, 1982]. Recent refraction results for northwestern Nevada [*Benz et al.*, 1990] indicates a crustal thickness of ~30 km and upper mantle velocities of 7.9-8.0 km s^{-1}, arguing against an anomalous crust and upper mantle. Province-wide, crustal thickness averages ~30 km and upper-mantle velocities range between 7.9 and 8.0 km s^{-1}.

The 1987 PACE seismic refraction profile crosses the southern Basin and Range onto the Basin and Range-Colorado Plateau transition zone. Evidence for this transition is seen in the crustal thickness, elevation, and related geophysical observations. Crustal thickness increases systematically from ~30 km in the southern Basin and Range [*McCarthy et al.*, 1991] to 40-45 km beneath the Colorado Plateau [*Roller*, 1965], and elevation increases steadily from about 1000 m at the south end of the profile to 1500-2000 m on the Colorado Plateau. Southern Basin and Range surface heat flow of 1.5-2.5 HFU is relatively high in comparison to Colorado Plateau heat flow of 0.75-1.5 HFU [*Lachenbruch and Sass*, 1978]. While the details may differ, the crustal structure of the southern Basin and Range exhibits, on average, properties similar to the Basin and Range average.

The 1987 PACE seismic experiment was designed to image the crust and upper mantle structure of the southern Basin and Range, including the Buckskin-Rawhide Mountain metamorphic core complex. The main objectives were achieved by recording the profile in three deployments; deployments 1 and 2, recorded in 1987, consists of a 180 km NE-SW trending line situated in the transition zone (Fig. 1), while the 1989 deployment extended the line 190 km northeastward onto the Colorado Plateau. Several shotpoints were re-shot during each deployments in order to increase the maximum recorded offset for the profile. Shots were spaced ~15-20 km apart and charge sizes ranged from 400 to 2700 kg.

We emphasis here modeling of amplitude and travel time variations of upper mantle P-wave phases observed in the PACE refraction data, primarily focusing on determining the depth-dependent velocity structure observed from shotpoint 20. A detailed two-dimensional P-wave velocity model for the southern Basin and Range has been determined from iterative travel time and amplitude modeling of selected shots [*McCarthy et al.*, 1991]. We restrict our analysis to the modeling of shotpoint 20 because it was the best recorded shot, recording prominent upper mantle phases, best represents the general features observed from the numerous shots recorded during the 1987-89 PACE experiment, and the modeling results from shotpoint 20 are sufficient to characterize the crust and upper mantle velocity structure of the southern Basin and Range. Shotpoint 20 was recorded to an offset of 370 km and was the only shot that clearly recorded correlatable upper mantle refractions and reflections. Reversed shots on the Colorado Plateau did not couple well and were not well recorded to distances beyond about 200 km (J. McCarthy, pers. comm., 1991).

Shown in Figure 2 are examples of the refraction data recorded during the 1987 deployment (Fig. 1). Each trace is low-pass filtered to 12 Hz and plotted trace normalized with a reducing velocity of 6.0 km s^{-1}. The P-wave phases easily recognized on the record section are the upper crustal headwave (P_g), the mid-crustal reflection (PcP), the Moho reflection (PmP), and upper mantle headwave (P_n). The P_g phase is observed and correlatable as a first arrivals to distances greater than 90 km. Large travel time variations of the P_g phase indicate large differences in near-surface velocity structure along the profile. On average, the velocity of the P_g phase is 6.0 km s^{-1}. The mid-crustal reflection is observed as a secondary arrival from ~30 (1.0 s reduced time) to ~120 km (0.5 s reduced time). This reflection closely following in time the P_g phase suggesting that the reflecting boundary is relatively shallow (<15-18 km). Modeling results of *McCarthy et al.* [1991] place the boundary at ~12 km beneath the center of the profile. The weak lower crustal reflection is observed from ~75 to 130 km at about 0.5 to 1.0 s in front of PmP. PmP is the most prominent secondary arrival and is observed from ~70 (~3.5 s reduced time) to 180 km (0.5 s reduced time). The lack of pre-critical energy (<80 km) is also suggestive of a transitional crust-mantle boundary [*Braile and Smith*, 1975].

Figure 3 shows an enlarged portion of the composite 1987-89 record section for shotpoint 20. Notice the clearly identifiable P_n phase that abruptly terminates at ~275 km. This phase is followed by a prominent later arrival (P_lP), which is interpreted as a wide-angle reflection off the base of an upper mantle low-velocity zone. Reflectivity synthetic seismograms will confirm this observation.

Regional Geology and Geophysics of the Norilsk Uplift--Since the early 1970's the Ministry of Geology of the USSR recorded tens of thousands of kilometers of Deep Seismic Sounding (DSS) data across much of the western Soviet Union and the southern Soviet republics (Fig. 4). Soviet DSS profiles range in length from 200 to 3000 km and are typically recorded by calibrated, three-component 2-Hz velocity transducers. A typical DSS profile is recorded with a station spacing that ranges from 2-5 km for the shorter lines (< 1000 km) to roughly 10-15 km station spacing for the longer lines (> 1000 km). All profiles are recorded using chemical explosions spaced approximately 30-40 km apart. Some of the longer DSS profiles used one or more PNE's to record to large offsets. Using standard recording parameters, Soviet seismology has collected an unprecedented amount of seismic data on the Eurasian continent.

The Norilsk DSS seismic data obtained by the USGS from the Ministry of Geology of USSR was a 220-km-long profile that crosses the Norilsk uplift in northern Siberia (see inset, Fig. 4). This profile consists of 9 shots recorded on calibrated three-component geophones spaced every 3 to 5 km apart. Shot spacing is approximately 40 km. Total record time at each station is 60 sec beginning approximately 5 sec before the first arrival P-wave and each seismogram is digitized at 0.02 sps. Four off-end shots provided additional wide-angle velocity controls on the sub-crustal structure beneath the Norilsk uplift. The profile lies in the transition zone between the Precambrian Siberian platform (northwest) and the Paleozoic Siberian platform within the Norilsk uplift. Regional DSS data in northern Siberia suggest crustal thicknesses that vary from 42 to 48 km (A. Egorkin, per. comm., 1991).

Figure 5 shows the P-wave record section for shotpoint 73 (Fig. 4). The record section shows that P_g and PmP are prominently observed crustal phases and correlatable for distances of tens of kms. Although not as prominent, a crustal reflection (P_lP) is observed from about 40 to 100 km that follows the P_g phase by about 0.5 s. We interpret

this phase as evidence of a shallow crustal low-velocity zone. The P_g phase is prominently observed as a first arrival to offsets of ~150 km. Apparent velocity of P_g is roughly 6.1 km s^{-1}. The wide-angle PmP phase is the most prominent reflection and it is observed from 100 km (4 sec) to distances of 200 km. Starting at about 160 km (3 sec) a possible upper mantle wide-angle reflection is observed to follow closely in time the PmP phase.

Modeling Results for PACE--Synthetic seismogram modeling of the mantle phases P_n and $P_{lv}P$ are used to determine the upper mantle velocity structure of the southern Basin and Range. We have choosen to use the one-dimensional reflectivity synthetic seismogram method in order to emphasize the general aspects of the velocity structure. The crustal velocity structure was obtained from the two-dimensional modeling results of *McCarthy et al.* [1991]. The synthetic source-time function was a Ricker wavelet with a peak frequency consistent with the observed data.

Shown in Figure 6 is a comparison of synthetic seismograms and observed seismic refraction data from shotpoint 20. The synthetic seismogram record sections were calculated using the alternative velocity models listed in Table 1a. A comparison of the observed and synthetic seismograms for Model 1 (7.5 km s^{-1} LVZ) show that the travel times and amplitudes of the prominent upper mantle P waves are in agreement to offsets of 370 km. The most significant features seen in the observed and synthetic seismograms are a marked decrease in P_n amplitude beyond about 250 km and a prominent reflection observed from about 250 to 370 km, which is delayed by about 1.0 sec relative to P_n. Synthetic seismograms for the alternative LVZ model (Model 2; 7.7 km s^{-1}) show comparable travel times, but the critical point on the wide-angle reflection off the base of the LVZ has moved from near 260 km (Model 1) to 300 km (Model 2). The observed critical point (Fig. 6) is less than 300 km and more likely near 240-260 km. Model 3 does not contain an upper mantle LVZ, but is defined by a first-order velocity increase at a depth of 50 km (Table 1a). A comparison shows that neither the amplitudes or travel times of P_n and $P_{lv}P$ phase are well modeled. Based on the comparisons shown in Figure 6 we favor Model 1.

Modeling Results for the Norilsk Uplift--Shown is Figure 7 is a comparison between reflectivity synthetic seismograms and observed seismic refraction data from shotpoint 73 (Fig. 4). The synthetic seismograms were computed using the velocity model listed in Table 1b. The preliminary model results show the synthetic seismograms match well both the travel times and relative amplitudes of the primary crust P-wave phases. The synthetic seismograms predict the significant amplitude decay of the P_g phase beyond 70-80 km. This amplitude decrease is due to the Pg phase bottoming into a shallow crustal (4.9 km) LVZ The base of the LVZ is defined by a prominent reflection ($P_{lv}P$) that is delayed relative to Pg by about 0.8 sec at a distance of 80 km. Preliminary synthetic seismogram modeling suggests a shallow crustal LVZ (5.1-km-thick) with an average velocity of 5.8 km s^{-1} (Table 1b). Modeling the travel time and amplitude of the PmP phase indicates a crustal thickness of ~42 km with an average low-crustal velocity of 6.8 km s^{-1}. P_n is observed as a weak phase with an apparent velocity of 8.38 km s^{-1}. While not all the details of the observed seismograms are well modeled, the synthetic seismogram comparison are adequate for defining a generalized velocity-depth structure for the Norilsk uplift. Determination of the detailed two-dimensional velocity structure of the Norilsk uplift requires modeling travel times and amplitudes of all shots along the Norilsk profile.

Comparison of the Velocity Structure between the Norilsk Uplift and Continental U.S.--In Figure 8, the generalized one-dimensional velocity-depth structure of the Norilsk uplift is

compared to the generalized one-dimensional velocity structure of the southern Basin and Range [*Benz et al.*, 1990; *McCarthy et al.*, 1991] and the eastern U.S. [*Hughes and Luetgert*, 1991]. This comparison is interesting considering the Basin and Range is a youthful, elevated crust that is being actively extended, while the crust beneath the Norilsk uplift and eastern U.S. were formed during Precambrian and Paleozoic times.

The most striking feature in Figure 8 is the similarity in crustal velocity gradient for the three regions, given the large difference in age, heat flow, and geologic development. The 42-km-thick crust beneath the Norilsk uplift is comparable to the 40-km-thick crust observed in the eastern U.S. The largest difference in crustal structure between these two regions is in the depth of the mid-crustal velocity discontinuity and evidence of a shallow upper crustal LVZ beneath the Norilsk uplift. For the eastern U.S. a mid-crustal velocity discontinuity is observed at a depth of ~15 km, while a mid-crustal discontinuity is not readily observed beneath the Norilsk uplift. Both the southern Basin and Range and eastern U.S. velocity models show upper mantle velocity variations. Although no upper mantle velocity discontinuities are shown in the Norilsik generalized velocity model (Fig. 8), the Norilsk refraction data do show a wide-angle reflection that may be indicative of shallow upper mantle velocity structure.

Recommendations

We recommend further travel time and amplitude modeling of the complete Norilsk profile to determine the two-dimensional velocity and attenuation structure beneath northern Siberia. This is particular important considering that the Norilsk region has been designated for a future IRIS broad-band station. Therefore, it is necessary to accurately determine the regional crust and upper mantle velocity structure to better understand regional body and surface wave observed at the future IRIS station.

References

Benz, H.M., R.B. Smith, and W.D. Mooney, Crustal structure of the northwestern Basin and Range province from the 1986 PASSCAL seismic experiment, *J. Geophys. Res.*, 95, 21823-21842, 1990.

Benz, H.M., J. McCarthy, and W.D. Mooney, Evidence for an upper mantle LVZ and an underlying 80-km-deep discontinuity from the 1987-89 PACE seismic refraction/wide-angle reflection data, *Eos Trans. AGU, 69*, p. 1323, 1990.

Braile, L.W., and R.B. Smith, Guide to the interpretation of crustal refraction profiles, *Geophys. J. R. Astr. Soc., 40*, 145-176, 1975.

Eaton, J.P., Crustal structure from San Francisco, California to Eureka, Nevada, from seismic refraction measurements, *J. Geophys. Res., 68*, 5789-5806, 1963.

Hill, D.P., and L.C. Pakiser, Crustal structure between the Nevada Test Site and Boise, Idaho, from seismic refraction measurements, in *The Earth beneath the Continents*, edited by J. S. Steinhart and T. J. Smith, *Am. Geophys. Union Mon.10*, 391-419, 1966.

Hughes, S. and J. Luetgert, Crustal structure of the western New England Appalachians and Adirondack mountains, *J. Geophys. Res.*, 1991, in press.

Lachenbruch, A.H., and J.H. Sass, Models of an extending lithosphere and heat flow in the Basin and Range province, in *Cenozoic Tectonics and Regional Geophysics of the Western Cordillera*, edited by R.B. Smith and G.P. Eaton, *Geol. Soc. Am. Memoir 152*, 209-250, 1978.

McCarthy, J., S.P. Larkin, G.S. Fuis, and R. Simpson, Anatomy of a metamorphic core complex: Seismic refraction and wide-angle reflection profiling in southeastern California and western Arizona, *J. Geophys. Res.*, 1991.

Pakiser, L.C., Structure of the crust and upper mantle in the western United States, *J. Geophys. Res., 68*, 5747-5756, 1963.

Priestley, K.F., A.S. Ryall, and G.S. Fezie, Crust and upper-mantle structure in the northwest Basin and Range province, *Bull. Seism. Soc. Am., 72*, 911-923, 1982.

Prodehl, C., Crustal structure of the western United States, *U. S. Geol. Surv. Prof. Pap.,1034*, 74 pp., 1979.

Roller, J.C., Crustal structure in the eastern Colorado Plateaus province from seismic-refraction measurements, *Bull. Seism. Soc. Am., 55*, 107-119, 1965.

Stauber, D.A., and D.M. Boore, Crustal thickness in northern Nevada from seismic refraction profiles, *Bull. Seism. Soc. Am., 68*, 1049-1058, 1978.

Table 1a (Southern Basin and Range)

Model 1		Model 2		Model 3	
Depth (km)	Vp (km s^{-1})	Depth (km)	Vp (km s^{-1})	Depth (km)	Vp (km s^{-1})
0.00	1.50	0.00	1.50	0.00	1.50
0.25	2.00	0.25	2.00	0.00	2.00
0.25	4.00	0.25	4.00	0.00	4.00
2.00	5.30	2.00	5.30	2.00	5.30
2.00	6.00	2.00	6.00	2.00	6.00
6.30	6.20	6.30	6.20	6.30	6.20
13.8	6.20	13.8	6.20	13.8	6.20
13.8	6.55	13.8	6.55	13.8	6.55
24.4	6.55	24.4	6.55	24.4	6.55
27.8	6.55	27.8	6.55	27.8	6.55
29.8	7.85	29.8	7.85	29.8	7.85
38.0	7.98	38.0	7.98	50.0	8.10
39.0	7.70	39 0	7.70	50.0	8.20
55.0	7.50	58.0	7.70	60.0	8.25
55.0	8.10	55.0	8.10		
60.0	8.15	60.0	8.15		

Table 1b

Norilsk Uplift		Eastern U.S.	
Depth (km)	Vp (km s^{-1})	Depth (km)	Vp (km s^{-1})
0.00	5.80	0.00	5.50
1.40	5.90	1.50	6.00
2.55	6.00	15.0	6.10
4.86	6.06	15.0	6.40
4.86	5.83	25.0	6.50
10.0	5.90	25.0	6.80
10.0	6.18	40.0	7.00
12.73	6.36	40.0	8.00
24.50	6.50	55.0	8.10
25.50	6.60	55.0	8.40
42.80	7.05		
45.40	8.38		
50.00	8.50		

Pacific to Arizona Crustal Experiment

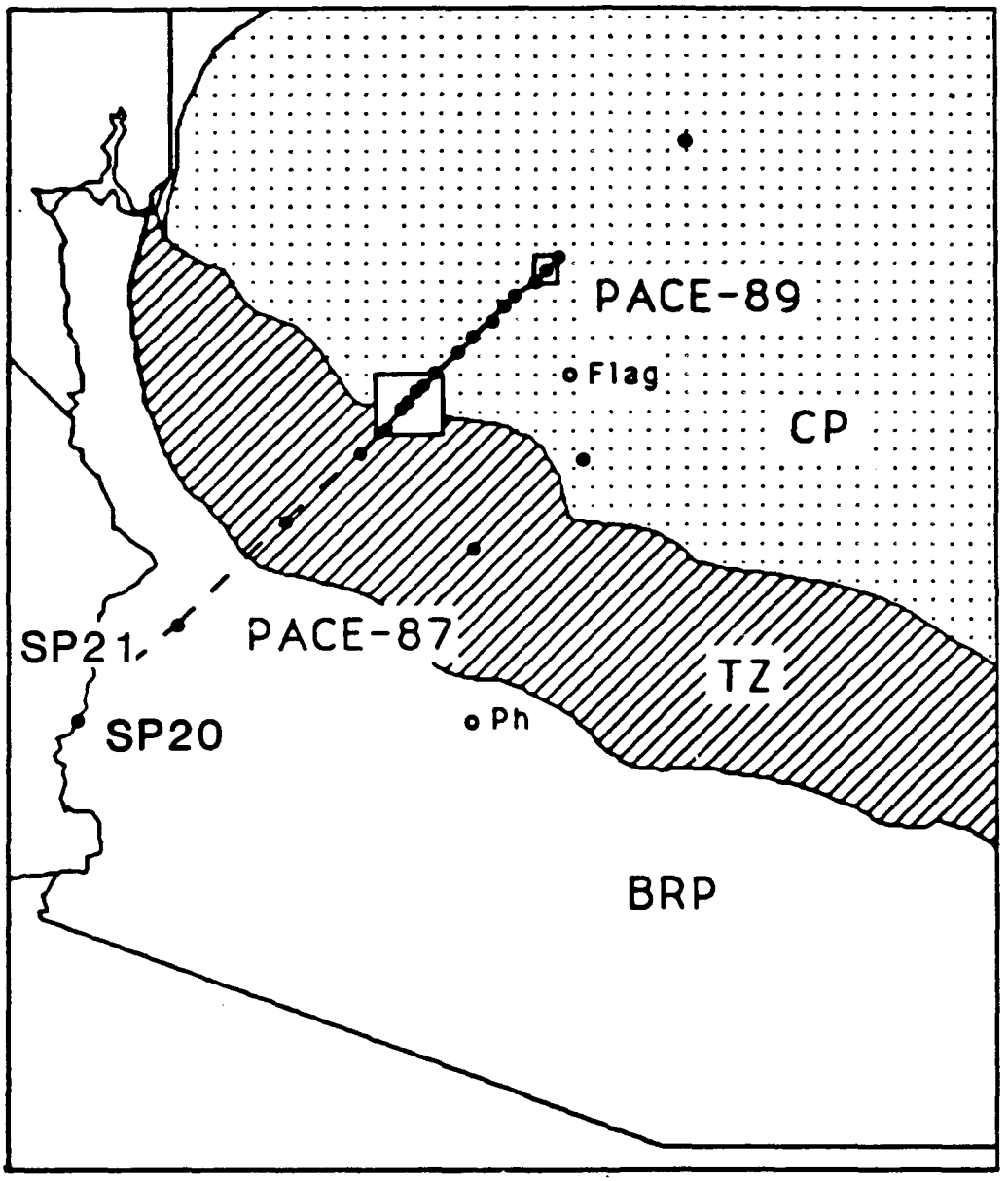


Figure 1. Location map of the 1987-89 PACE seismic transect. Circles are the principal shotpoints. The dash line is the location of the 1978 deployment and the solid line is the location of the 1989 deployment.

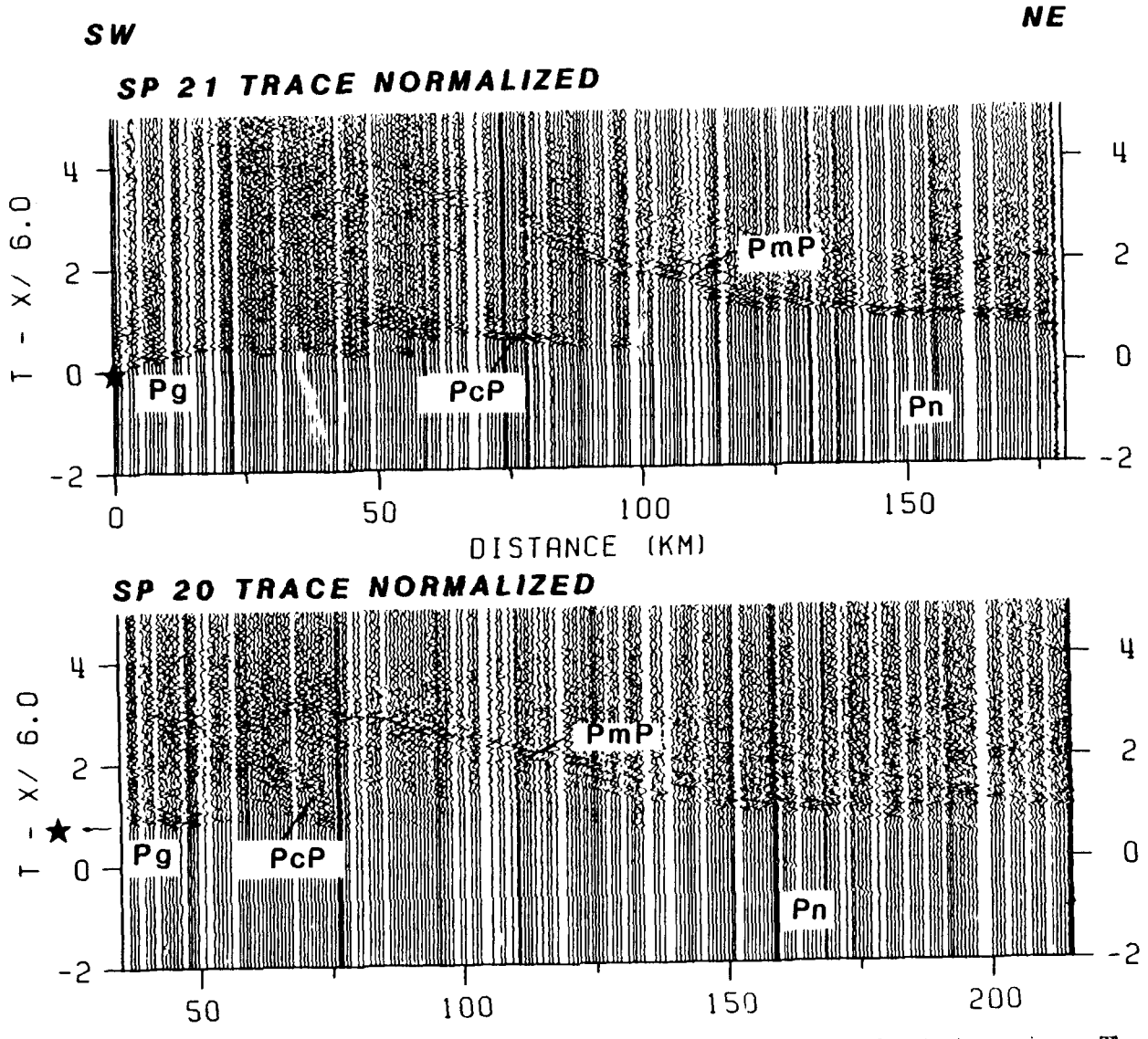


Figure 2. Trace normalized record sections from shotpoints 20 and 21 recorded during the 1987 PACE seismic experiment. These record sections show the principal crustal body wave phases typically recorded in the southern Basin and Range. Key to phase identifications: P_g, the diving or continuously refracted P wave in the crystalline upper crust; PcP, the wide-angle reflection from the mid-crustal discontinuity; PmP, the wide-angle reflection off the crust-mantle boundary (Moho); and P_n, the upper-mantle head wave.

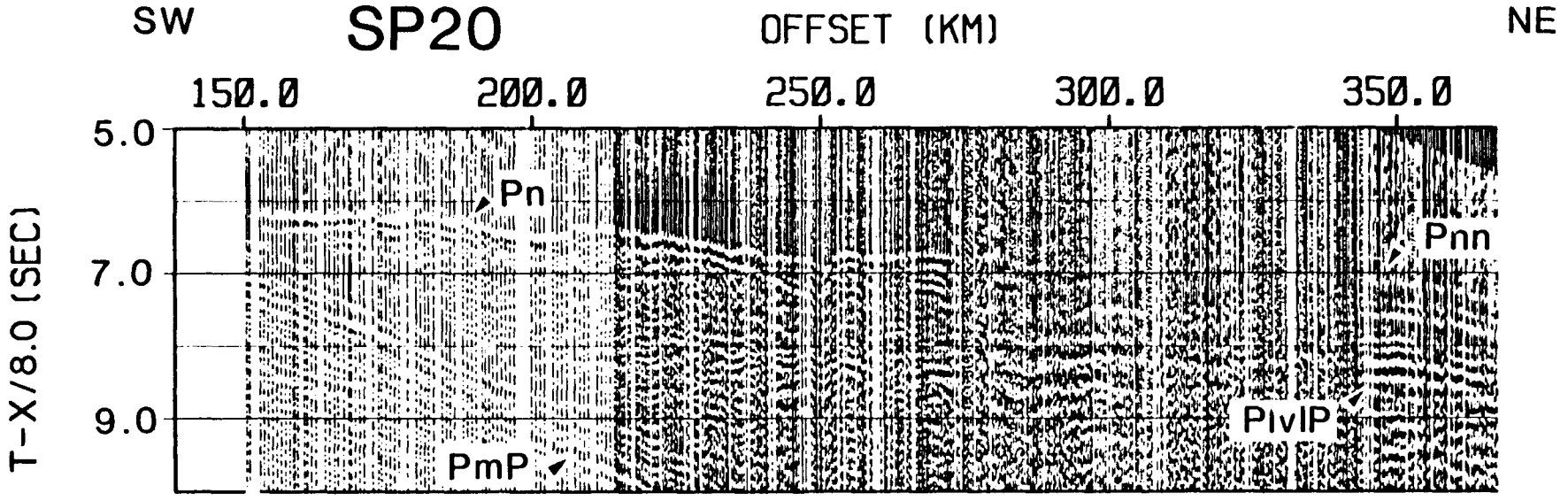


Figure 3. Shotpoint 20 trace normalized record section recorded during the 1987 and 1989 PACE experiment. This record section shows clearly observed upper mantle phases. Key to phase identifications: P_n, the upper-mantle head wave; PlvlP, the wide-angle reflection from the base of an upper mantle low-velocity zone; and P_{nn}, a weak upper mantle head wave.

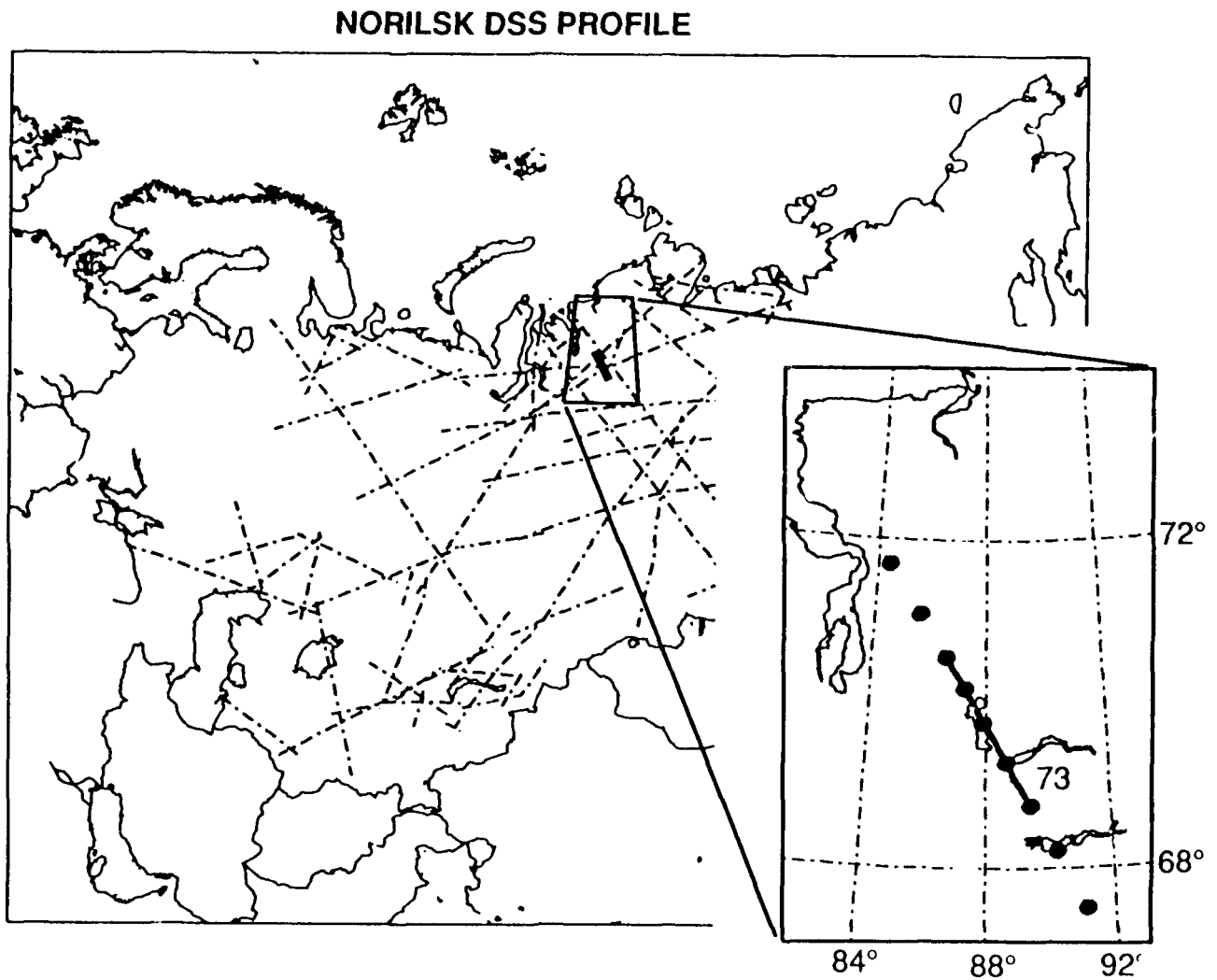


Figure 4. Location map of Soviet DSS lines (dashed) and the Norilsk profile (inset). Circles (inset) are the principal shotpoints.

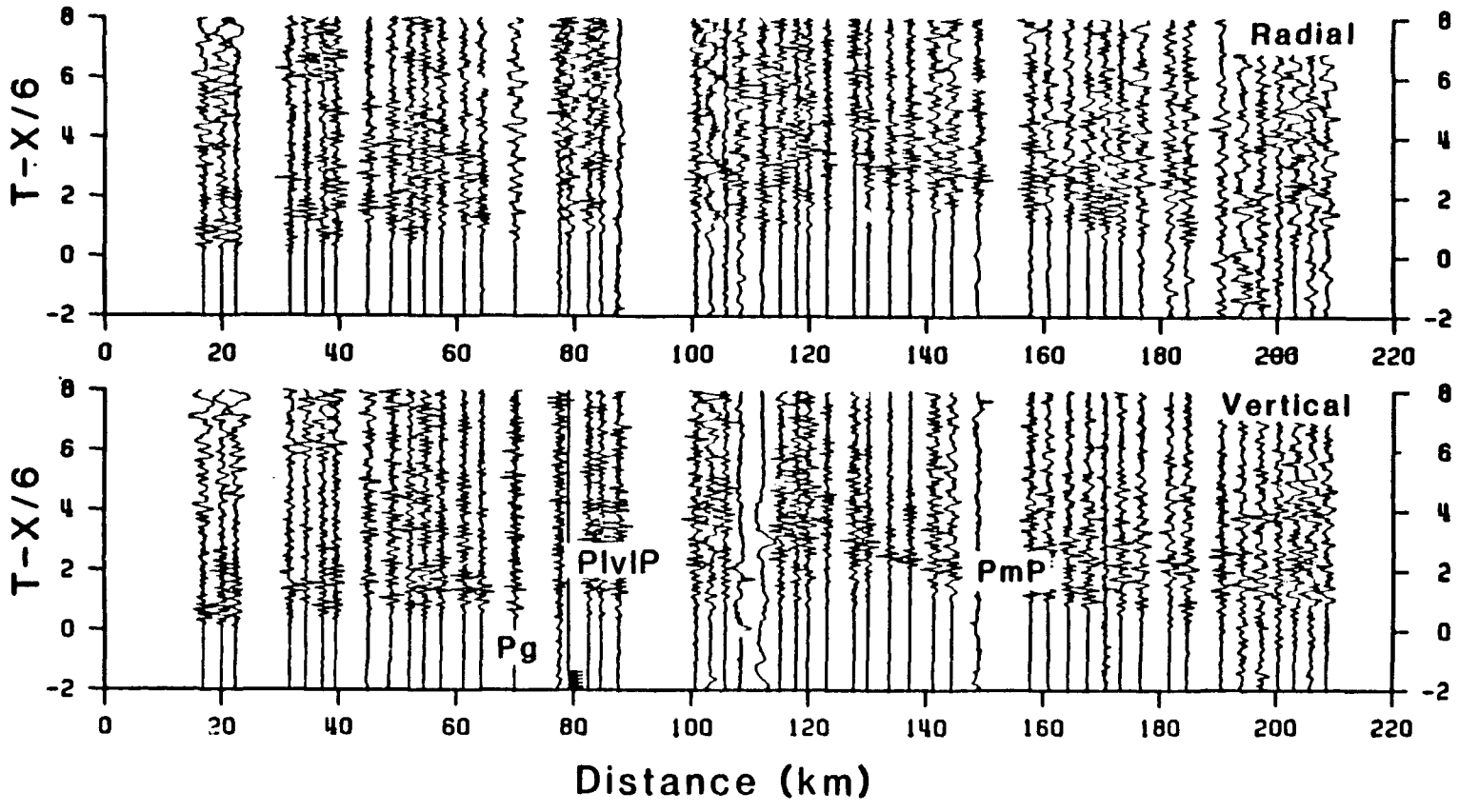


Figure 5. Trace normalized record sections from shotpoint 73 recorded during the Norilsk seismic experiment. Key to phase identifications: P_g, the diving or continuously refracted P wave in the crystalline upper crust; PlvlP, the wide-angle reflection from the base of a crustal low-velocity zone; and PmP, the wide-angle reflection off the crust-mantle boundary (Moho).

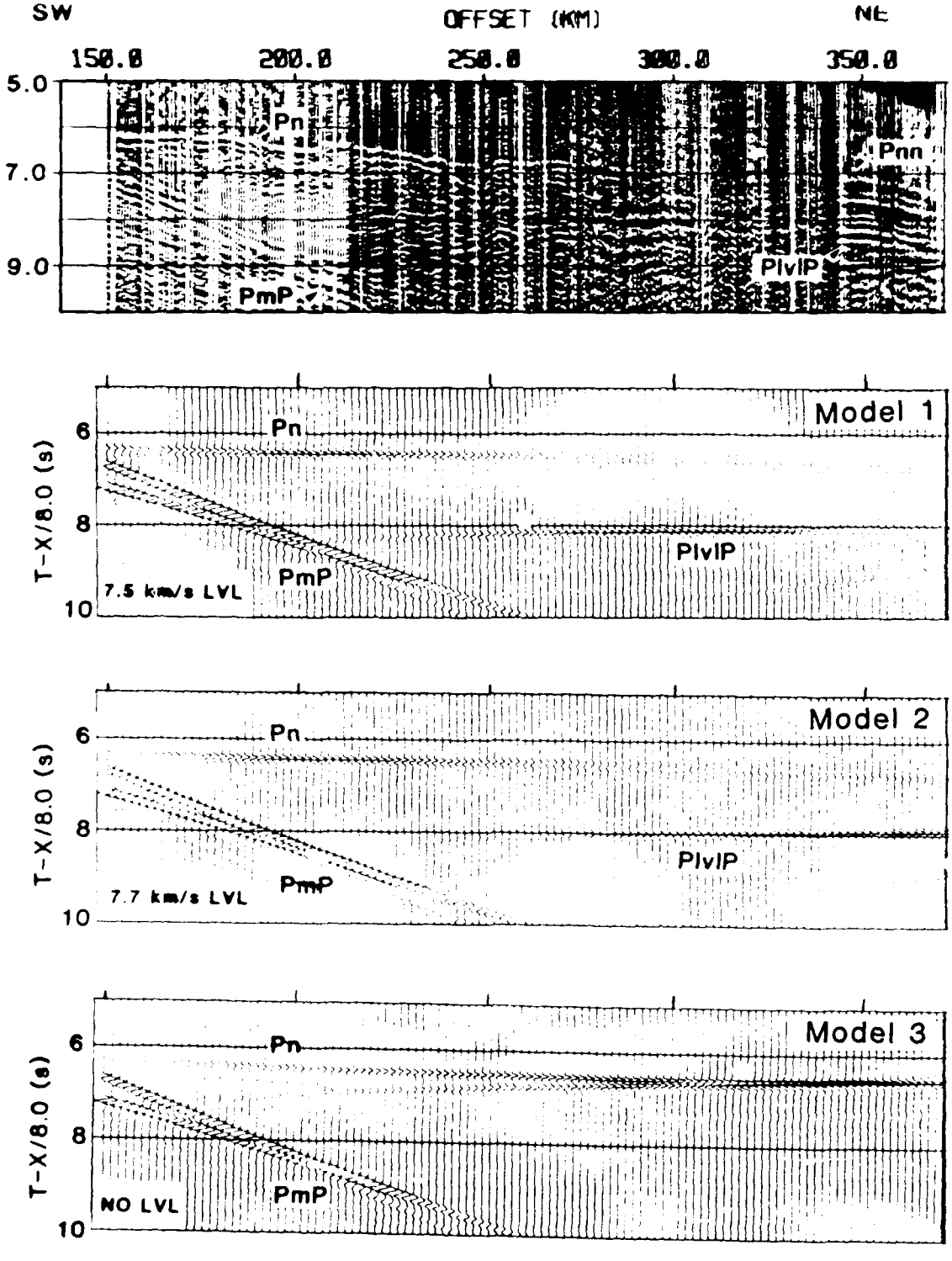


Figure 6. Comparison of the PACE shotpoint 20 seismic refraction data (top) and reflectivity synthetic seismograms for the velocity models listed in Table 1a. The dots mark the critical point for the wide-angle reflection from the base of the low-velocity zone (Models 1 and 2) and the model with a positive velocity discontinuity (Model 3).

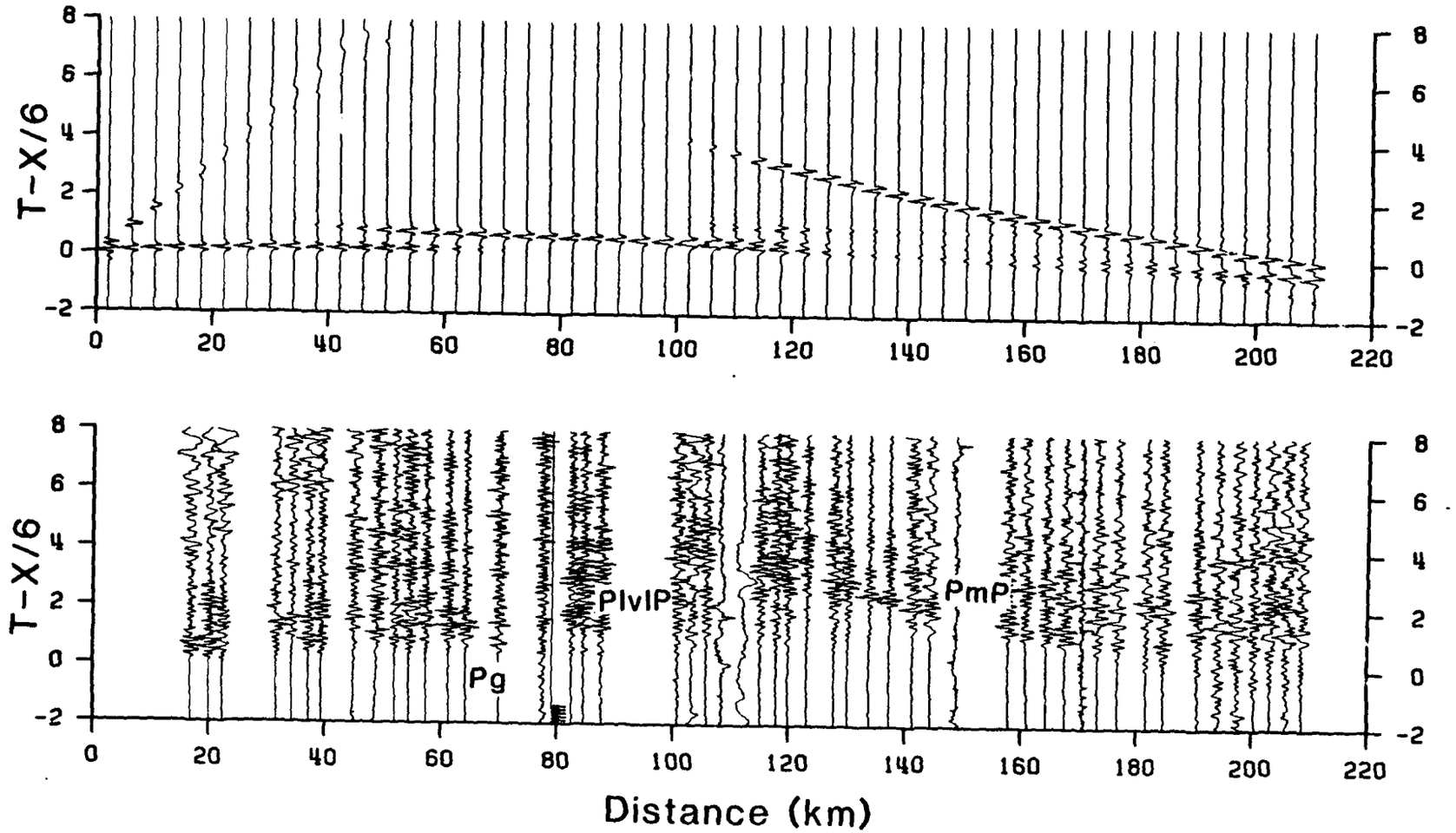


Figure 7. Comparison of Norilsk shotpoint 73 (bottom) and synthetic reflectivity synthetic seismograms (top). Synthetic seismograms were calculated using the velocity model listed in Table 1b.

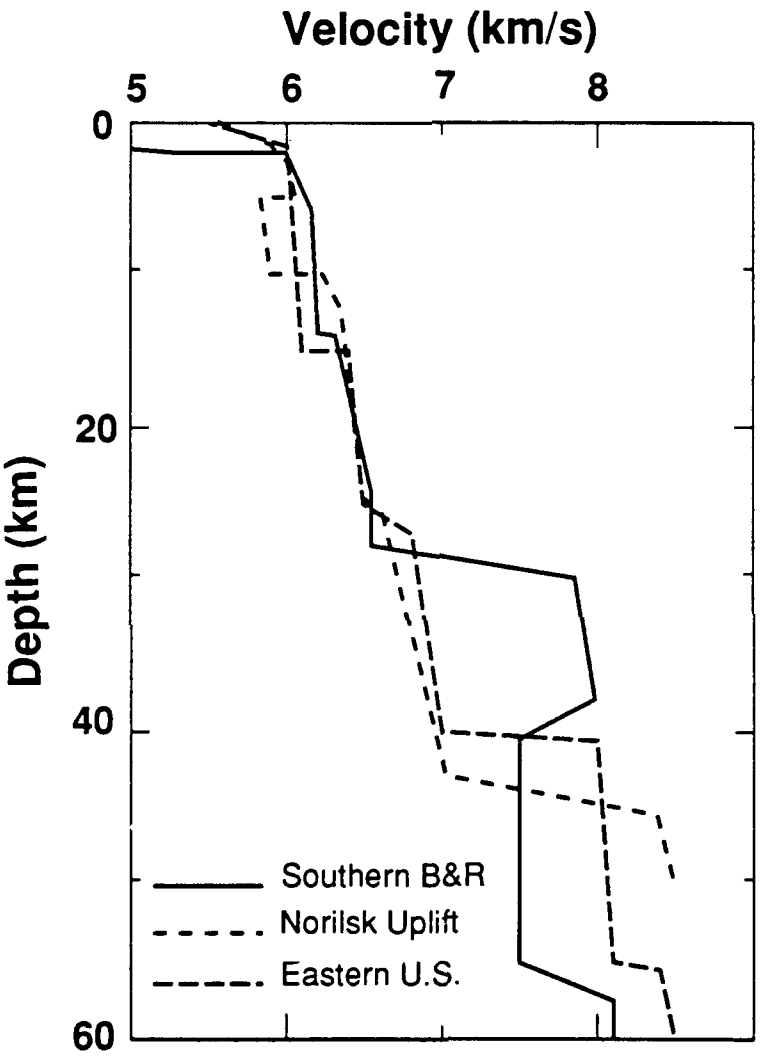


Figure 8. Generalized one-dimensional velocity-depth functions for the southern Basin and Range [*Benz et al.*, 1990; *McCarthy et al.*, 1991], eastern U.S. [*Hughes and Luetgert*, 1991], and the Norilsk uplift.

REGIONAL AND UPPER MANTLE WAVE PROPAGATION IN THE SOVIET UNION

by L. J. Burdick, E. J. Garnero, D. V. Helmberger and L. S. Zhao
Woodward Clyde Consultants
566 El Dorado Street
Pasadena, California 91101

Contract F19628-90-C-0194

OBJECTIVE

The time and frequency domains are equivalent displays of seismic trace information, though some qualities of the signal are more easily observed in one domain than the other. The relative frequency excitation of Lg, for instance, is most easily viewed in the frequency domain, but such waveform qualities as the sequence in which pulses arrive in the wave train or the sharpness of pulse onset are most easily observed in the time domain (Murphy and Bennett, 1982; Blandford, 1981). Because of the tremendous complexity of high frequency regional data, most attempts at using it for discrimination purposes have involved analysis of the frequency content of the various arrivals either through transforming selected windows or through multiple bandpass filtering. In this research effort, we are exploring the alternative of attempting to discriminate events using those waveform characteristics most easily observed in the time domain.

A second advantage of time domain analysis approaches is that they permit a deeper insight into the physical processes creating a seismic signal's character. For this reason, they can be more easily used to evaluate the transportability of a discriminant to varying geophysical and tectonic regimes. This is an especially important feature in the development of regional discriminants. The most prominent and successful spectral regional discriminants have been empirically developed. This means that they must be redeveloped and reverified in each new area. On the other hand, through rigorous time domain analysis such features as regional depth phases can be identified and used to discriminate. Discriminants based on such simple physical features as source depth should be transportable anywhere.

In North America, where all varieties of seismic data have been available for many years, complete models for the lithosphere and upper mantle have been developed for each tectonic regime. An important development of recent time has been the release of somewhat comparable, though limited, regional data from the Soviet Union. In the following, we describe two waveform analysis studies in which models for the lithosphere and upper mantle have been developed based on this data for the USSR. In each instance, the objective is to identify specific arrivals within the wave train with a particular emphasis on those phases which may be useful for discrimination. The first studies are of upper mantle arrivals from the Soviet data base. Comparable studies have been carried out in many other regions of the world, so we can compare the predictions of those models to the observed waveforms from the Soviet Union. P waves from the ranges of 10° to 30° are most sensitive to upper mantle structure and are used in the upper mantle study. Signals from 1° to 10° are generally designated as regional records and are used in our study of the crust and lithosphere in the Soviet Union.

RESEARCH ACCOMPLISHED

Upper Mantle Studies: Figure 1 is a map of the upper mantle study area. The data used in the study consisted of hand digitized signals from paper records which had recently been released by the Soviets. The sources were from the two major Soviet test sites at Novaya Zemlya and Semipalatinsk as shown in the figure. The ray paths sampled are also shown, and they indicate that the coverage of the central Asian platform is relatively complete. Not all of the paths have the appropriate length for upper mantle study, but all those within the 10° to 30° window were analyzed. It is worth noting that several of the stations used were later upgraded to digital IRIS stations including OBN, CHU (now Garm) and TLY.

The customary first step in an upper mantle study is to examine the travel time and slowness data if it is available. The latter has not yet been supplied for the Soviet Union and the travel time data is of limited quality. Exact origin times for the nuclear tests have not been released, so there is some feedback between the models used to locate the events and the values for origin time. We examined two possibilities to circumvent this problem. The first was to assume that events were detonated on the minute. However, we found a number of examples where this assumption appeared unreasonable. We therefore simply accepted the USGS origin times and examined the observations for consistent patterns which might be associated with tectonics. Figure 2 compares the observations to the predictions of model KCA, a stable continent structure model, which will be discussed further in the following. We identified paths as being shield-like or tectonic based on gross morphology. The tectonic paths identified were basically those to the south and east of Semipalatinsk. At short ranges, there is little difference between the types of paths, but there is a clear difference for those points near 16°. The slow values there for tectonic paths come primarily from Semipalatinsk events observed at station TLY. There is also a pattern of delayed arrivals for tectonic paths in the 25° to 35° range.

Short period observations of upper mantle triplications are known to be unstable because of lateral variations, and hand digitized records are very band limited in accuracy. We found that the best way to achieve stable results was to stack the observations. An illustration of the suppression of coda through stacking is shown in Figure 3. The observations are at station OBN from Novaya Zemlya events, and the reduction in noise after the direct arrival is clear. The initial pulse should contain a direct arrival and a reflection from the 650 km discontinuity. To interpret the data, we examined the predictions of several different upper mantle models. These included KCA (King and Calcagnile, 1976), S25 (LeFevere and Helmberger, 1989), K8 (Given and Helmberger, 1980) and T7 (Burdick and Helmberger, 1978). The first three are basically stable continent or shield models and the last is a tectonic continent model. The predictions of the two categories of models are quite different. Figure 4 illustrates a case in which the tectonic model fits a stacked record substantially better than the others. The map shows that this path to station TLY is to the east from the Semipalatinsk site. The second arrival is from the forward branch of the 400 km discontinuity. It is clear in both the predictions and the observations. Figure 5 shows an example in which the stable continent models are clearly more accurate. The secondary arrivals are formed from an interference of reflections from both upper mantle discontinuities. Again, there is little ambiguity in the greater accuracy of the preferred model. Table 1 lists the preferred model for each of the paths we studied.

TABLE 1.

STACKED TRACES LIST

Station Name	Delta (deg)	# Records in Stack	Source Region	Preferred Model
ARU	13.75	4	SEMIPALATINSK	KCA
TLY	15.72	14	" "	T7
ARU	17.09	9	NOVOYA ZEMLYA	K8
OBN	19.76	7	" "	KCA
NVS	21.91	5	" "	S25
BOD	22.01	4	SEMIPALATINSK	K8
BOD	22.49	3	" "	K8, T7
OBN	25.56	17	" "	K8, S25
BOD	27.44	9	NOVAYA ZEMLYA	K8
UZH	28.31	5	" "	none

Studies of the Crust and Lithosphere: In this section we report on modeling broadband seismograms from moderate-sized earthquakes at regional distances. Earlier efforts have demonstrated that long period motions (WWSSN) preceding the direct S arrival can be modeled reasonably well with a LAYER over a half space (mantle). These models require some modifications when we address broadband data; that is the additions of layers.

Some results from two regions, New England and near station GARM in the Soviet Union will be discussed. In Figure 6a we display the broadband motions from the Saguenay earthquake recorded at Harvard (HRV). The numbers indicate the absolute motion in (cm x 10^{-2}). Note that these motions would go off-scale on the standard WWSSN system which is easily verified by examining the WES station. The epicentral distance is 625 km and its source parameters are known from teleseismic studies (strike = 323°, dip = 165°, rake = 78°, depth = 28 km and moment = 5×10^{24} dyne cm). Figure 6b displays the comparison of observations with synthetics over the first 80 seconds of record as reported by Zhao and Helmberger (1991). In Figure 6c we show the results after convolving in a complex source time function proposed by Somerville et al. (1990). The zero to peak amplitude of the observed P_n is 0.01 mm. The later arrival is sP and is slightly larger. Note that phase pP is nodal for the above solution. Figure 6d shows the comparisons between these motions after a convolution with a short-period Wood-Anderson (Gain = 2800). The observed P_n is about 1.5 cm peak-to-peak. This phase would be very large if recorded on a standard (WWSS) short period instrument. To model the strength of this P_n requires a strong positive gradient at the top of the mantle, about 3% increase over a depth of 25 km (Zhao and Helmberger, 1991). Similar studies on California Earthquakes indicate weaker P_n's and much weaker S_n's (Dreger et al., 1991). This feature was modeled by a more uniform lithosphere which results in a faster short-period (P_n) decay with distance. Thus, it appears that short period amplitudes can be predicted from longer period (a few seconds) studies, which also seems to be the case in Garm.

Figure 7 displays the locations of the IRIS station at GAR along with some locations of recent earthquakes. The star to the south indicates a relatively large deep event, depth = 85 km, studied earlier by Helmberger, et al. (1990). They determined the crustal model displayed on the right. This model is similar to that found in Tibet which is the dark shaded area to the southeast.

We used the above model to estimate the synthetics for the path from GAR to the eastern event (star). The results are displayed in the lower portion of the figure. This event is listed as a M_b = 4.5. The distance is estimated to be 435 km as modeled and to be located at a depth of 20 km. The source parameters used in the synthetics are: strike = 315. dip = 39°, rake = 153°, $M_0 = 1.3 \times 10^{23}$ dyne cm and source duration of (0.5, 1.0, 0.5). The depth phase (sS_mS) is particularly obvious on the vertical components while the phase (S_mSS_mS) is very sharp on the tangential component.

Note that the phase S_mSS_mS is considerably sharper on the vertical observations than in the synthetics. Ray calculations indicate that this feature is caused by the complex nature of the receiver function as discussed in Zhao and Helmberger (1991) and is subject to the local receiver structure at GAR. This disparity can be fixed if all the observations at GAR show this feature. Nevertheless, the timing and general agreement between the synthetics and data indicates that layered models yield sufficiently acceptable fits to allow important estimates of event parameters such as depth, moment, etc. These parameters are needed in some of the recent discrimination methods involving $M_L : M_0$.

RECOMMENDATIONS AND CONCLUSIONS

Until recently it was generally assumed that t^* was uniformly low beneath the Soviet Union. Our preliminary results on in-country data indicates this assumption is an over simplification and that the southern edge is complicated with relatively slow upper mantle and irregular crustal thickness. These lateral variations have led to considerable difficulties in establishing precise locations using teleseismic data. These complex structures also make it difficult to estimate source strength from regional phases. Detailed studies of in-country observations, PNE's and earthquakes, could help clarify these issues. Our preliminary results demonstrate that calibrated paths (local layered crust) will allow depth phases to be identified and, thus, discrimination possible. Secondly, being able to identify phases in the time domain allows strength estimates of particular phases which prove very useful in high frequency/low frequency discriminants and yield estimation.

REFERENCES

Blandford, R. R., "Seismic discrimination problems at regional distances", in *Identification of Seismic Sources*, E. S. Husebye and S. Mykkelveit eds., D. Reidel Publishing Co., Dordrecht, The Netherlands, 695-740, 1981.

Burdick, L. J. and Helmberger, D. V., **"The upper mantle P velocity structure of the western United States", J. Geophys. Res.**, 83, 1699-1712, 1978.

Dreger, D. S., D. V. Helmberger, and L. Zhao, "Three-component waveform inversion of regional earthquakes", **Bull. Seism. Soc. Am.**, submitted, 1991.

Given, J. W. and D. V. Helmberger, "Upper mantle structure of Northwestern Eurasia", **J. Geophys. Res., 85**, 7183-7194, 1980.

Helmberger, D. V., L. Zhao, and D. S. Dreger, "Broad-band modeling of regional seismograms", 12th Annual DARPA/GL Symposium, Key West, Fl., Geophysics Lab., Hanscom AFB 01731-5000, 1990.

King, D. W. and G. Calcagnile, "P wave velocities in the upper mantle beneath Fennoseandia and Western Russia", **Geophys. J. R. Astr. Soc., 46**, 407-432, 1976.

LeFevre, L. V. and D. V. Helmberger, "Upper mantle P velocity structure of the Canadian shield", **J. Geophys. Res., 94**, 17749-17765.

Murphy, J. R. and T. J. Bennett, "A discrimination analysis of short period regional seismic data recorded at Toronto Forest Observatory", **Bull. Siesm. Soc. Am., 72**, 1351-1366, 1982.

Somerville, P. G., J. P. McLaren, C. K. Saikia, and D. V. Helmberger, "The 25 November 1988 Saguenay, Quebec, Earthquake: Source Parameters and the Attenuation of Strong Ground Motion, **Bull. Seism. Soc. Am., 80**, 1118-1143, 1990.

Zhao, L. S. and D. V. Helmberger, "Broadband modeling along a regional shield path, Harvard recording of the Saguenay Earthquake, **Geophys. J. Int., 105**, 301-312, 1991.

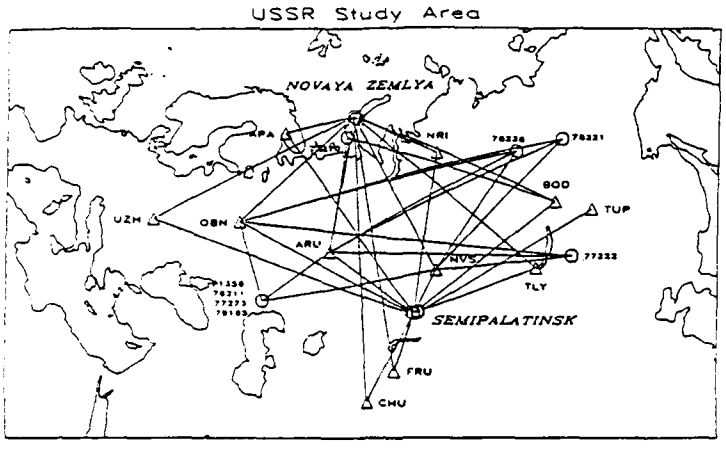


Figure 1. Map of Asia: 11 stations (triangles) and source regions used (circles.) The year and julian date are plotted next to the 8 events (PNEs) that are not in the two main source regions. Raypath coverage is good, adequately covering central Asia.

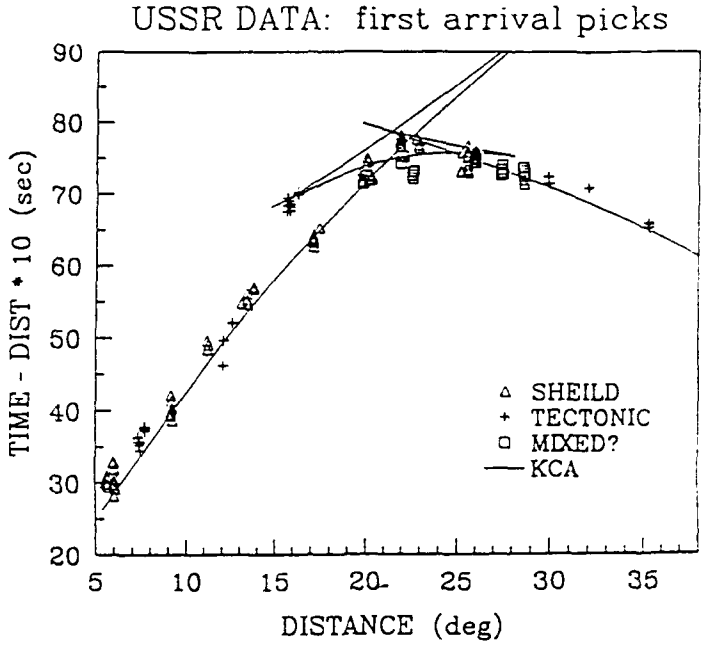


Figure 2. First Arrival Travel Times. First arrival picks made from only impulsive waveforms with good signal to noise ratio are shown here with the prediction of model KCA. Anomalies are clearly seen on this figure, e.g., at 15.7 degrees (station TLY) which is a slow tectonic path.

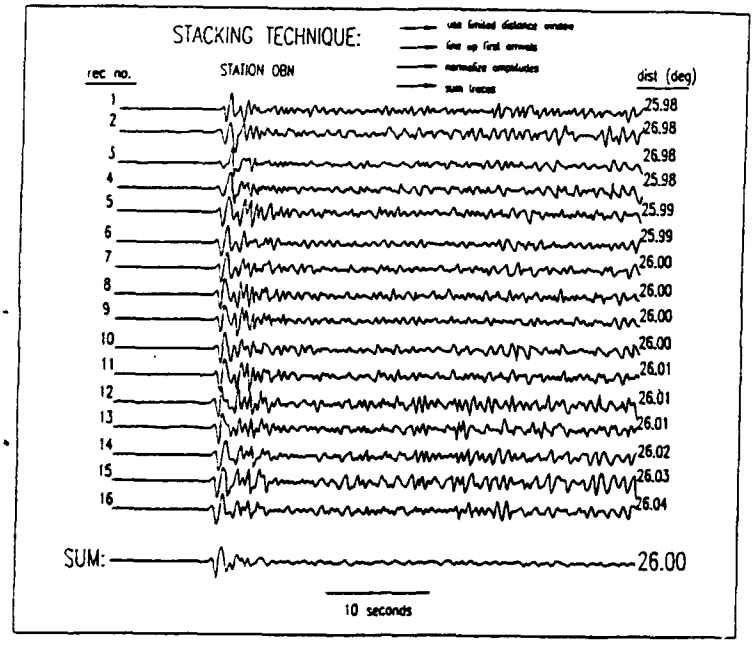


Figure 3. Stacking Technique. For a specific source region and station, which results in a very limited distance window, the first arrivals are lined up, all amplitudes are normalized, then the traces are summed. For the example given, the distance window is about 10 km. The resulting sum exhibits enhanced triplication arrivals and suppressed coda arrivals. This example is for station OBN recording Shagan events.

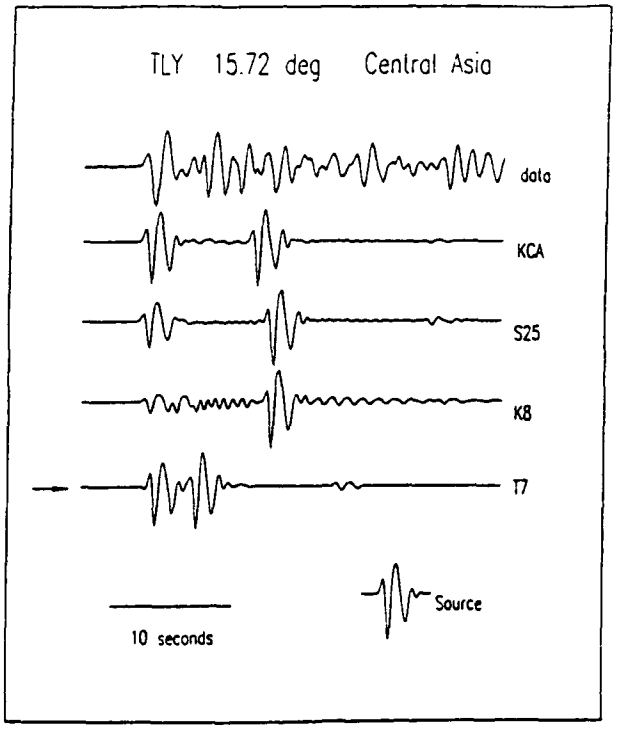


Figure 4. TLY from Central Asia, 15.72 deg. This path is believed to be a tectonic path. The low velocity zone in model T7 slows the direct arrival substantially so that the differential travel time between the direct and the 400 arrival is small. This feature is observed in the data stack trace.

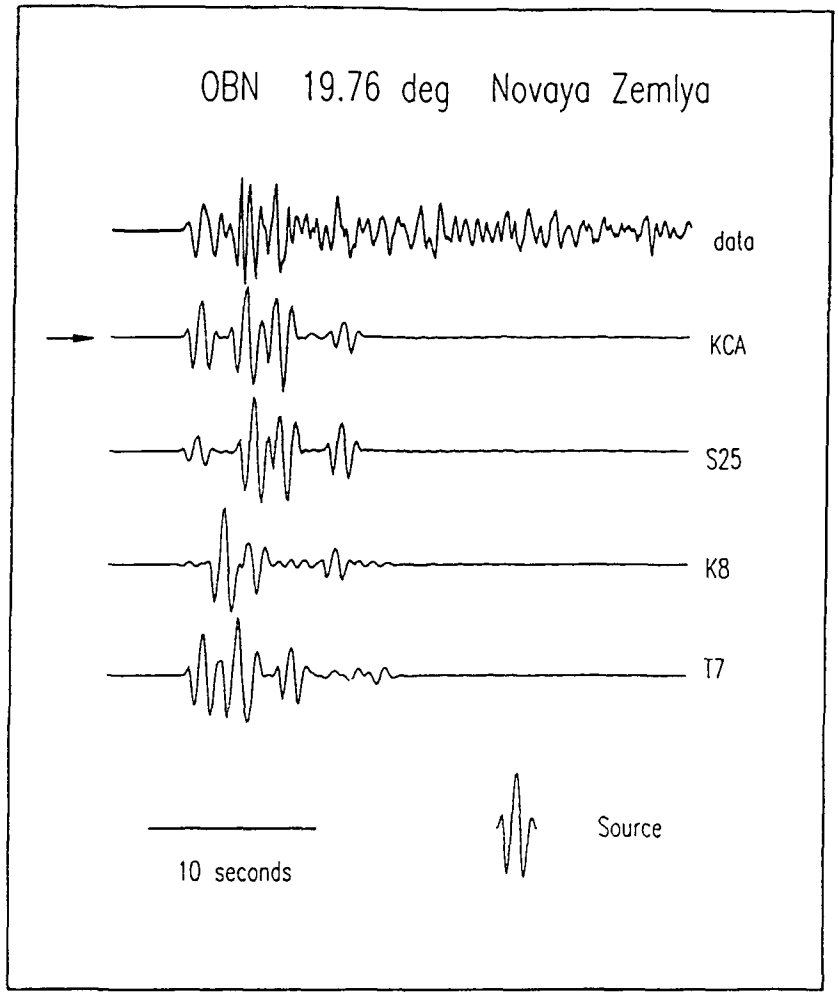


Figure 5. OBN from Novaya Zemlya, 19.76 deg. Model KCA does the best for differential times between the direct, 400 arrival and 670 arrival, though S25 does well with amplitude ratios.

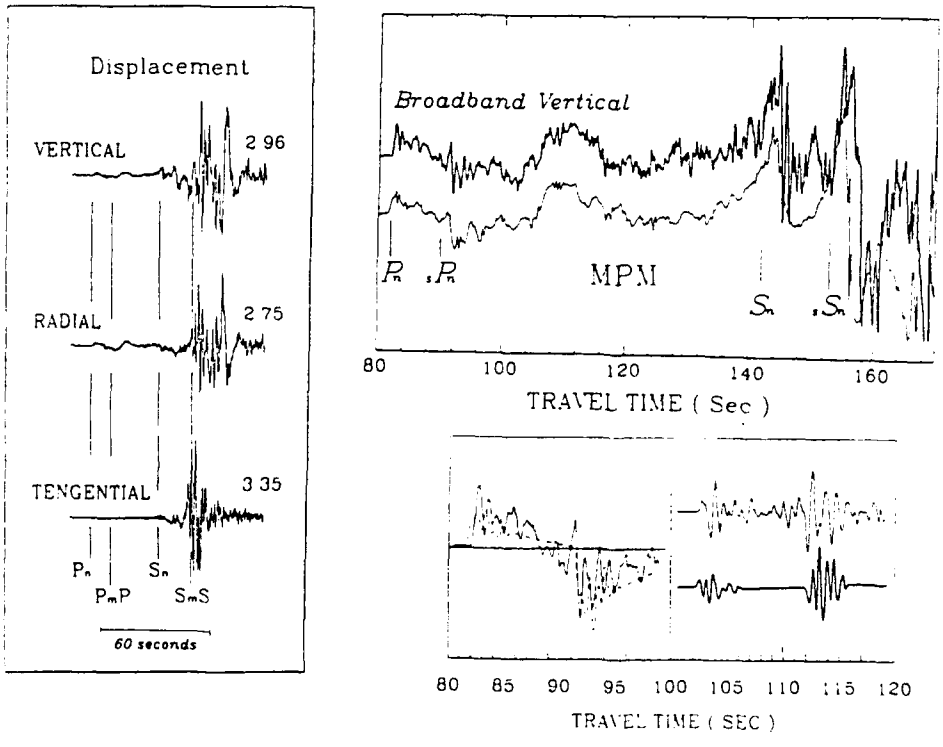
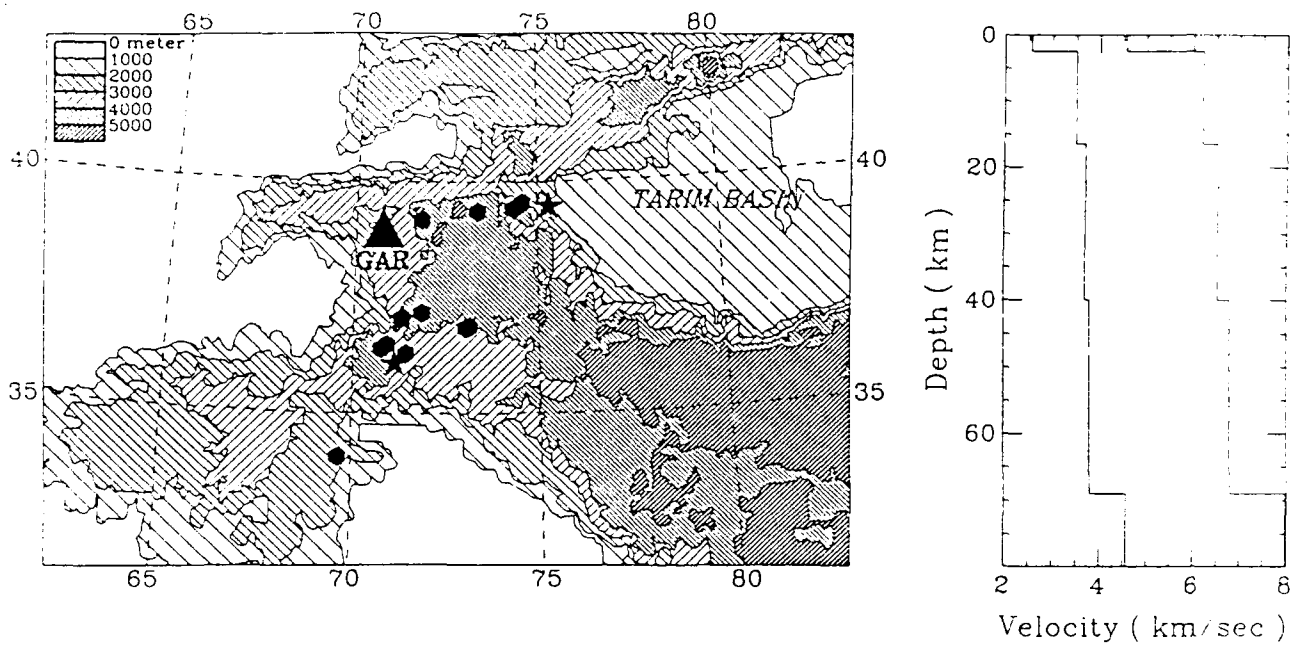


Figure 6. Displays broadband data obtained at HRV (a), with a blow-up portion (b) accompanied by a synthetic, enlarged some more (c) and a short-period band comparison in (d).



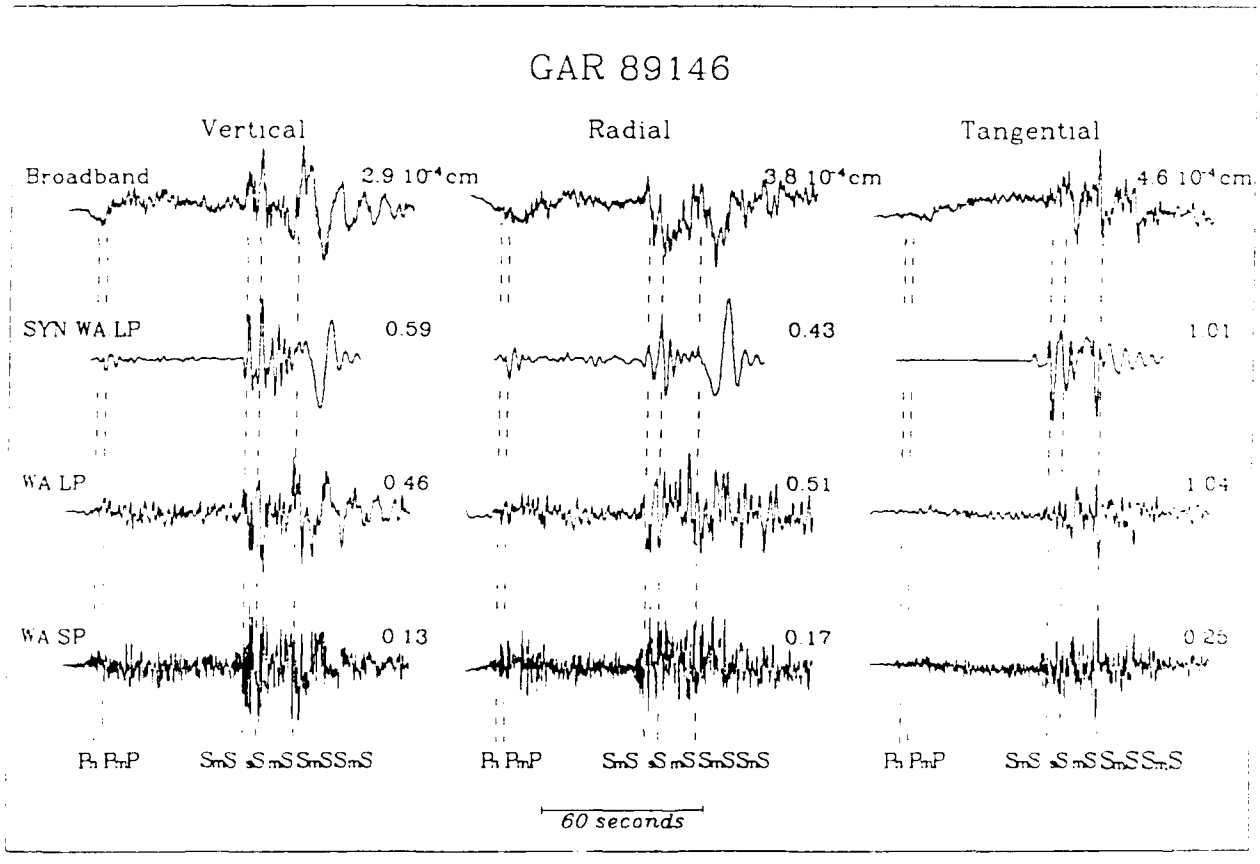


Figure 7. Map displays the GARM region where two events have been studied to date, indicated by stars. The structure on the right was obtained from an earlier study involving the calibration event to the south. The lower panel displays the comparison of synthetics generated from this model with observations of the event on the right (star). Note the clear identifications of depth phases.

Specialized Studies in Yield Estimation

by L. J. Burdick and D. V. Helmberger
Woodward Clyde Consultants
566 El Dorado Street
Pasadena, California 91101

Contract F19628-89-C-0216

OBJECTIVES

The scope of this project includes a number of separate specialized investigations directed at solving problems associated with yield estimation utilizing short and long period body waves. We here present the results of our research on several of them. In terms of short period body waves, these problems involve the effects of attenuation, pP and nonlinear effects such as spall on seismic amplitude and on m_b. We specifically discuss two studies which address a number of these issues. A common feature between them is that they both deal with the problem of regional Q values. It is obvious that at lower yields, which are most relevant to current treaty monitoring efforts, that regional observations will predominate in the data base. The effects of regional velocity structure on such observations have received much attention in other studies since they are very significant. The potential effects of Q and the interaction of Q with velocity structure have not been studied as completely, so we address those topics here.

The first study which is reported on is an attempt to generalize the relative waveform analysis procedure called intercorrelation, to regional teleseismic P_n waves. This approach has been used almost exclusively to analyze teleseismic data in the past. There is a current need to characterize the behavior and uncertainty in magnitude-yield relations down to body wave magnitudes which are as small as possible. Of course, the seismic data with good signal to noise for such small events will be restricted to regional distances. It has recently come to light that the P_n waveform in the western U.S. is highly stable and that it shows a strong variation with event size. Intercorrelation has been used to measure source function scaling for well coupled events below the water table down to magnitude 3.9. It has been established in a number of separate studies by many investigators that the behavior of pP from nuclear tests is not consistent with elastic reflection from a simple point compressional source. Direct observation of isolated pP_n appears to confirm this. Because of the relatively low attenuation of P_n with respect to teleseismic P, it is possible to isolate the direct P_n arrival from pP_n. The parameters of the source time function can be studied independently from this data using the intercorrelation approach. It was found that the relative yield of events could be reliably determined from the direct P_n wave shapes alone using the method.

The second investigation which has been undertaken involves modeling studies of broad band records from the recently released Soviet data base. The focus of the study is on the relationship of regional and upper mantle Q structure with estimates of explosion source RDP's. We correlate our results from the Soviet Union with those from U.S. tests off the Nevada test site such as GASBUGGY and RULISON.

RESEARCH ACCOMPLISHED

Intercorrelation of Regional P_n: The first study we will discuss is an attempt to take advantage of some recent observations made by Burdick et al. (1991) regarding the waveform of the onset of regional P_n. It appears clear that these waveforms are very directly comparable to those of teleseismic P. Rather than being true head waves, these arrivals seem to be turning rays in the uppermost mantle above the low velocity zone. At short times, they can be represented as a simple convolution of a source, Q and instrument operator just as teleseismic short period P can. However, because they never penetrate the low velocity zone, the effect of attenuation is tremendously reduced. Instead of t^* having a value of approximately 1.0 s, as it does for teleseismic P from NTS, it has a a value close to 0.1s; an order of magnitude change in the exponential. This allows the direct P to be separated from the pP through simple time domain windowing. Figure 1 shows some of the typical data from the Burdick et al. (1991) study. Observed deconvolved velocity waveforms from 4 Yucca Flat events as recorded at digital station MNV are shown in solid line. Almost 1.5 orders of magnitude are represented between the largest and smallest events. The frequency difference between them is clear even in the time domain. Synthetics computed using the Murphy (1977) source and an assumption of elastic pP behavior are shown as dashed lines. The observed and predicted pP arrivals are indicated by arrows. The observed arrivals are late and close to the elastic predictions in size, but in any case, in this representation it is simple to window out the distinct direct P arrival. In passing, we note that these observations lend additional credence to the intercorrelation results as opposed to the spectral averaging results. We also note that the Murphy (1977) predictions of change in frequency content between the largest and smallest event are not satisfactory. The predicted changes in time function are less extreme than the observed. The data available from LLNL is limited, but in reviewing it we did find signals from four Yucca Flat events below the water table. These were JORNADA, m_b = 5.9, BOUSCHET, m_b = 5.7, MUNDO, m_b = 5.4, and BORREGO, m_b = 3.9. Figure 2 compares the waveforms at common LLNL stations for the smallest and largest. The change in frequency content at all stations is dramatic. Under each complete P_n trace is a windowed trace where the window is a trapezoid with an 0.5 s lead a 1.0 s level beginning at estimated onset time and an 0.5 second fall. There are clearly waveform differenced between the stations, particularly at ELK, but the principle of intercorrelation is to characterize the changes in waveshape at fixed stations allowing for the possibility of complex path effects. The window should allow good spectral measurements up to frequencies of 1 hz.

The procedure for intercorrelation has been presented in most of the previous reports on it (Burger et al., 1986, Lay et al., 1984, Lay, 1985, 1991). The basic idea, however, is to choose a reference event and an estimated source function for it. If the signal includes pP, then pP parameters must also be included, but in this case, only direct P_n is present. We selected BORREGO and used the Murphy (1977) source. The procedure is then to find a source function for each other event which minimizes the differences between waveforms when a cross-convolution is performed. Since the depth of these events is known, the only free parameter is yield, and we simply stepped through yield values to find the yield values for the non-reference events which optimized a least squares norm. The yield of BORREGO was estimated to be 0.7 kt from the scaling relation of Yacoub (1984) based on WWSSN records (Network AA) of Pahute and Yucca events below the water table. Figure 3 shows the equalized waveforms for BORREGO and JORNADA. The fits are far from perfect, but the norm is a simple and objective least squares which is performed at the phase of

optimum correlation. It should also be noted that we are cross correlating waveforms from events differing by two orders of magnitude in size. There does seem to be some difference in the ratio of the first to second swings, particularly at ELKO which might indicate some difficulty with the amount of overshoot in the Murphy (1977) source over this range. In any event, we applied the procedure to all the events to predict the yield scaling behavior in Figure 4. The solid curve is the Yacoub (1984) line determined directly from m_b and yield and the data points were determined strictly from the change in frequency content of the P waves and the source scaling predictions. The correspondence between the data points and the line is strong enough to be very convincing though more data is clearly needed.

Studies of Q and Explosion Source Functions from Soviet Data: It would be hard to understate the importance of the recent Joint Verification Experiments in terms of treaty monitoring. However without some absolute RDP determination, we are still faced with the problems of trade-offs between bias due to t^* and source coupling differences. Thus, one of the key issues in yield estimation is the question of transportability. This subject was recently addressed by Burdick et al. (1991), with respect to explaining the behavior of U.S. PNE's; most notably those of GASBUGGY and RULISON. These events were overburied as were most of the Soviet PNE's; GASBUGGY (29 kt, h = 1.3 km, m_b = 5.3) and RULISON (40 kt, h = 2.6 km, m_b = 5.0). These events are inconsistent with current scaling laws in that GASBUGGY has a larger m_b than RULISON, even though it has a smaller yield. Murphy and Archambeau (1986) present evidence that the anomaly is principally caused by tectonic release associated with RULISON. They suggest that his release of tectonic energy was oriented in such as fashion as to destructively interfere with and reduce the amplitudes of the teleseismic short period P waves for RULISON. The magnitude of their proposed release is such that the amplitude of the tectonic P waves is roughly one half the amplitude of the explosion P waves. This requires a relatively high stress drop tectonic release as they maintain.

The clearest indication of the presence of non-explosion energy is the presence of significant Love waves. RULISON does show significant Love waves, but when they are modeled simultaneously with the Rayleigh waves only a low F factor is required. Burdick et al. (1991) conclude that using a modified scaling law, similar to that proposed by Lay et al. (1984), in which the overshoot parameter decreases with depth, can explain the anomaly. Their expression

$$\mathrm{Log}(B) = 0.57 - 0.97\,\mathrm{Log}(h)$$

in conjunction with the Helmberger-Hadley RDP scaling laws explains this anomaly without requiring short period tectonic release. However, his same expression predicts that under-buried explosions will have enhanced body wave magnitudes relative to M_S. This behavior is in agreement with observations of Soviet events at Shagan River relative to NTS (Stevens, 1986). He compared the largest 10 events with the smallest F factors at each test site where JVE's have occurred and obtains an M_S offset of 0.36 compared to a value of 0.39 predicted by the above expression. In short, overshoot can explain the surface wave behavior as well as the relative body wave magnitudes without large t^* biases between test sites. This conclusion agrees well with the work of Grand and Ding (1989) who find the attenuation bias between shields and oceanic rises to be relatively small, probably less than 1.0 s for S waves and .25 s for P waves.

This same formalism predicts relatively lower yield estimates for large Novaya Zemlya events than those made previously (Sykes and Wiggins, 1986) as well as explaining the $m_b : M_S$ relationship. Here it is supposed that small events are overburied while large events are underburied since they are assumed to be tunnel shots.

This study clearly illustrates the need for more accurate estimates of both regional and teleseismic Q. This goal may be possible, given the broad band data becoming available through the Soviet IRIS program. Figures 5 and 6 display observations from Hindu-Kush events at three stations; ARU (near the Urals), KIV (near the Caucuses) and OBN (near Moscow). The paths to OBN and ARU are mostly shield-like while the path to KIV is more tectonic in nature based on multiple S wave studies (Burdick et al., 1984). At present, only the source mechanism for the 1989 event is available (Helmberger et al., 1990). This thrust event was assumed to be at a depth of 80 km in generating the accompanying synthetics. The large second pulse, about 40 s behind the first arrival in the P wave train is caused by the depth phase sP. A similar phase, sS, follows direct S which is relatively nodal for station ARU. The source for the 1990 event is presently being investigated, but it appears to have a stronger sS.

These broad band synthetics were generated with reflectivity from models with very high Q values so that various t^* values could be investigated later. The results from applying a t^* of 1.0 s and 4.0 s, which correspond to normally assumed values for P and S, are plotted in Figure 5. The observed S wave at ARU requires a t^* between these values probably closer to 4.0 as displayed on the vertical component in Figure 6.

The observed S arrival at KIV appears to be late relative to SNA, probably in between SNA and TNA as predicted. The timing of OBN appears to be more compatible with SNA, but the later arrivals are larger. These same features were observed in the short-period P-wave data (Burdick et al., 1991)., and some upper mantle model modifications are required before the attenuation operator can be extracted. However, this broad band data appears to contain the needed information.

CONCLUSIONS AND RECOMMENDATIONS

The release of internal data from the Soviet Union obviously presents some great opportunities for solving some of the most long-standing yield estimation problems. However, interpretation of the data is still complex, and we continue to face the challenges of modeling the source RDP, determining its dependence on depth and separating source from propagation effects. Here we have focused on the influence of Q. We recommend that integrated Q, velocity and source models be developed for the Soviet Union which yield consistent values for regional and teleseismic t^*. The Soviet PNE program has been much more extensive than the U.S., and intensive studies of this data should yield important new insights into source scaling. We also recommend an intensive effort to obtain near field explosion data from the Soviet Union since data of this type has proved so valuable in interpreting U.S. data.

REFERENCES

Burdick, L. J., "Estimation of the frequency dependence of Q from ScP and ScS", **Geophys. J. R. astr. soc.**, **80**, 35-55, 1985.

Burdick L. J., C. K. Saikia and N. F. Smith, "Pn for the Nevada Test Site", AGU monograph on **Explosion Source Phenomenology**, (in press), 1991.

Burdick, L. J., E. J. Garnero, J. P. Mclaren, B. W. Woods, D. V. Helmberger and D. G. Harkrider, "Uncertainty in yield scaling at low yield". AFTAC Draft Report, 1991.

Burger R. W., T. X. Lay and L. J. Burdick, "Examining the relative yield of the Novaya Zemlya tests by waveform intercorrelation", **Geophys. J. R. astr. Soc., 87**, 775-800, 1986.

Grand, S. P. and X. Y. Ding, "Determination of Q as a function of depth and tectonic province', Final Report, EL-TR-89-0157, 1989.

Grand, S. P. and D. V. Helmberger, "Upper mantle shear structure of North America", **Geophys. J. R. astr. Soc., 76**, 399-438, 1984.

Lay, T. X., D. V. Helmberger and D. G. Harkrider, "Source models and yield scaling relations for underground nuclear explosions at Amchitka Island", **Bull. Seism. Soc. Am., 3**, 843-862.

LeFevre, L. V. and Helmberger, D. V., "Upper mantle P velocity of the Canadian Shield", **J. Geophys. Res., 94**, 1749-1765, 1989.

Lay T. X., "Estimating explosion yield by analytical waveform comparison", **Geophys. J. R. astr. Soc., 82**, 1,-31, 1985.

Lay T. X., "The teleseismic manifestation of pP: Problems and paradoxes", AGU Monograph on **Explosion Source Phenomenology**, (in press) 1991.

Lay T. X., L. J. Burdick and D. V. Helmberger, "Estimating the yields of the Amchitka tests by waveform intercorrelation", **Geophys. J. R. astr. Soc., 78**, 181-207, 1984.

Murphy, J. R., "Seismic source functions and magnitude determinations for underground nuclear detonations", **Bull. Seism. Soc. Am., 67**, 135-158, 1977.

Murphy, J. R. and C. B. Archambeau, "Variability in explosion body wave magnitudes: an analysis of the RULISON/GASBUGGY anomaly", **Bull. Seism. Soc. Am., 4**, 1087-1113, 1986.

Stevens, J. L., "Estimation of scalar moments from explosion generated surface waves", Bull. Seism. Soc. Am., **76**, 123-151, 1986.

Yacoub N. K., "Seismic network effect on yield estimation from body wave magnitude for NTS explosions", AFTAC-TR-84-2, (1984)

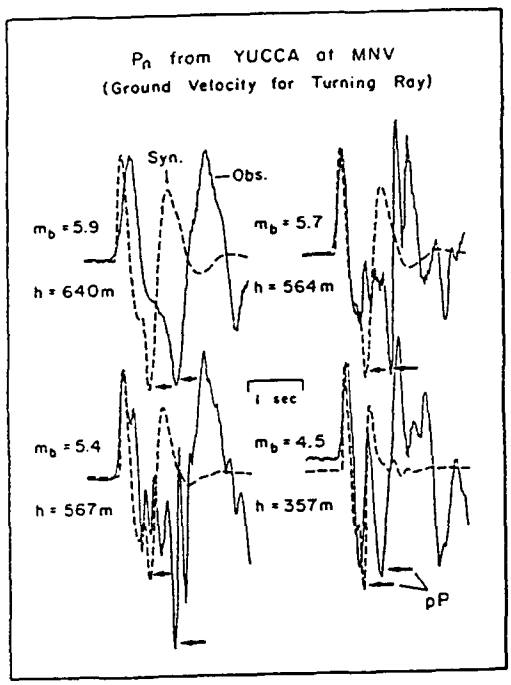


Figure 1. Observed versus synthetic waveforms for four Yucca events beneath the water table. The pP arrival is indicated by arrows. It is late and amplified in the data.

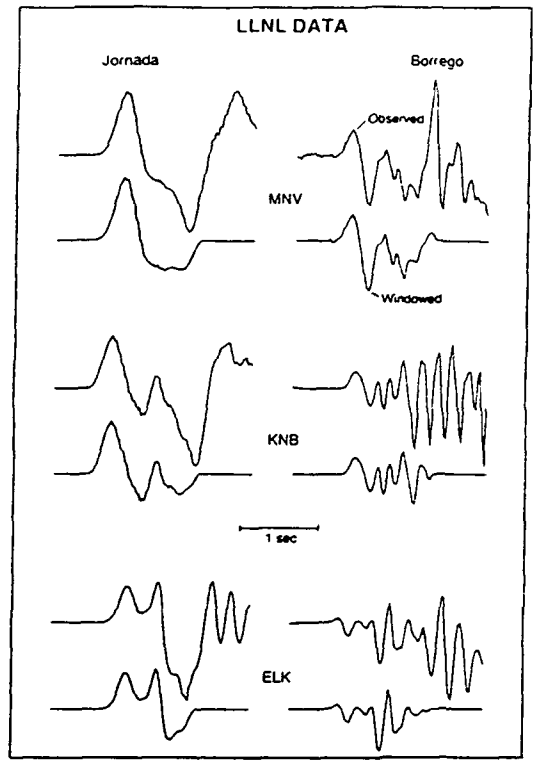


Figure 2. Observed deconvolved velocity waveforms for the Yucca events JORNADA and BORREGO. The initial signal is displayed over the windowed signal.

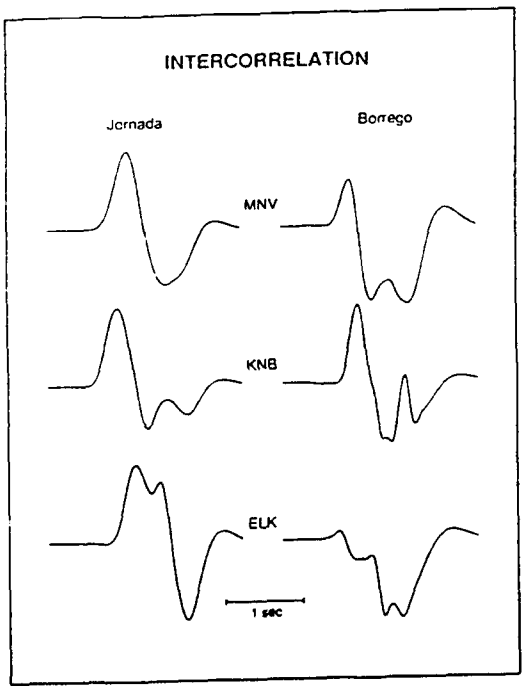


Figure 3. Intercorrelated waveforms for the two Yucca events JORNADA and BORREGO. These are the direct P_n waves only. The phase pP_n has been windowed out.

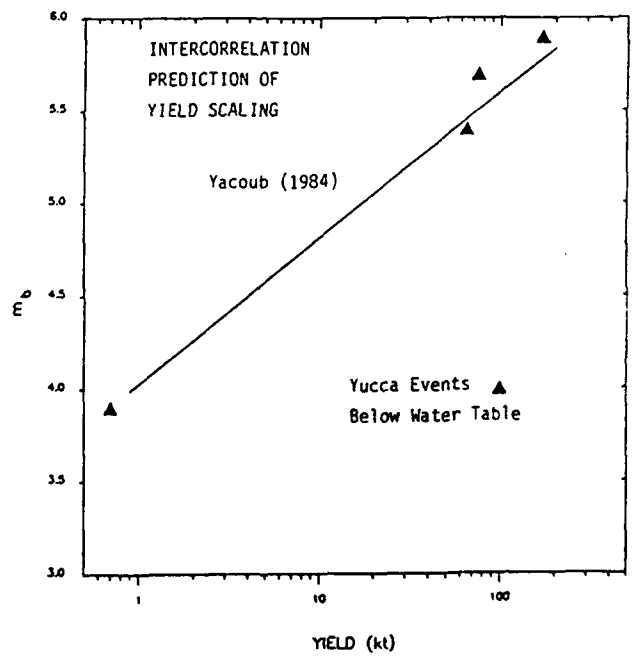


Figure 4. A comparison of yield scaling predictions based only on intercorrelation of direct P_n compared to a standard scaling law.

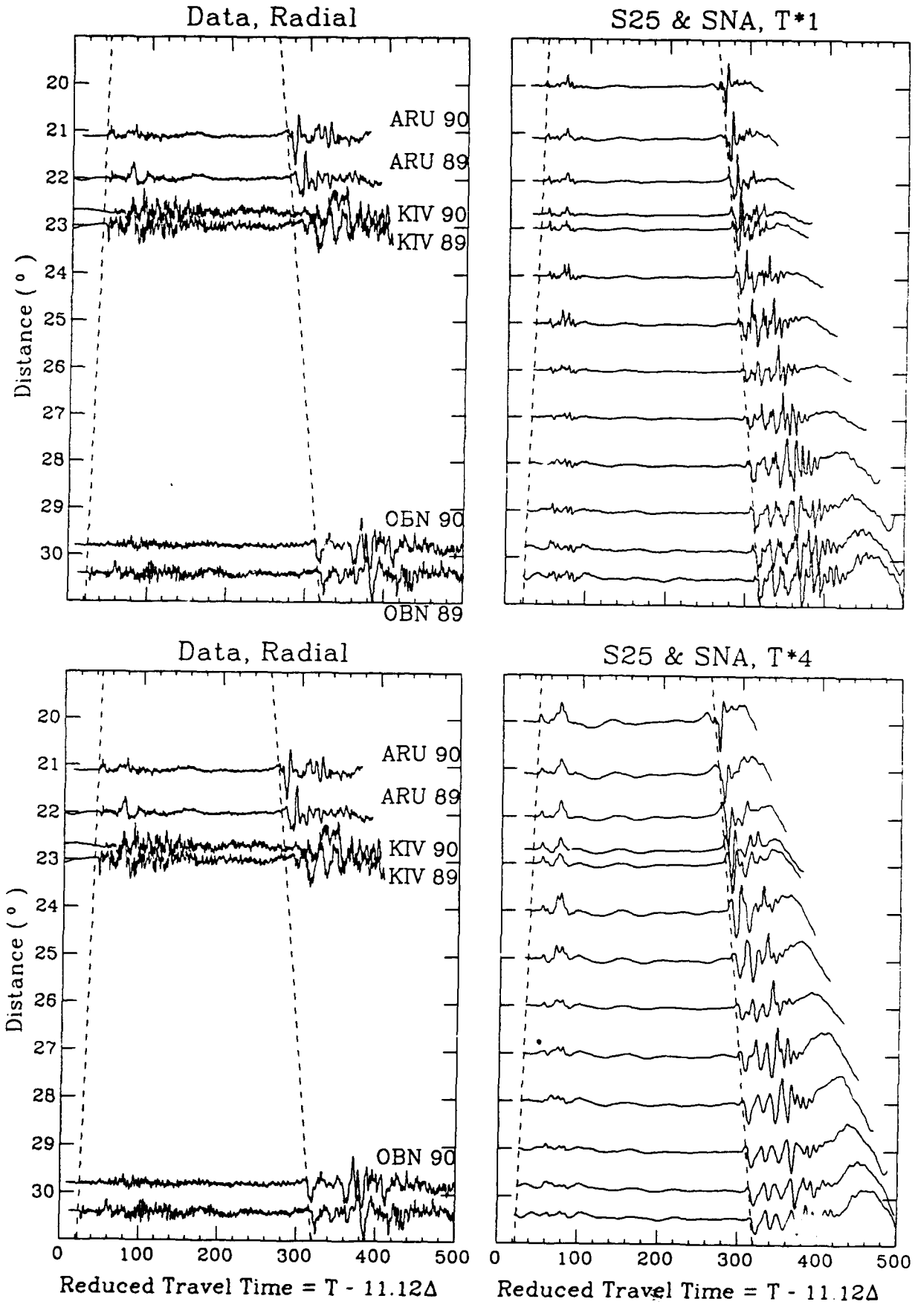


Figure 5. Observations of two Hindu-Kush events are displayed on the left with synthetics for pure-path shield models shown on the right; SNA (Grand and Helmberger, 1984) and S25 (LeFevre and Helmberger, 1989). The top panel displays synthetics for a $t^* = 1.0$ for both P and S while the results for $t^* = 4.0$ are given on the bottom.

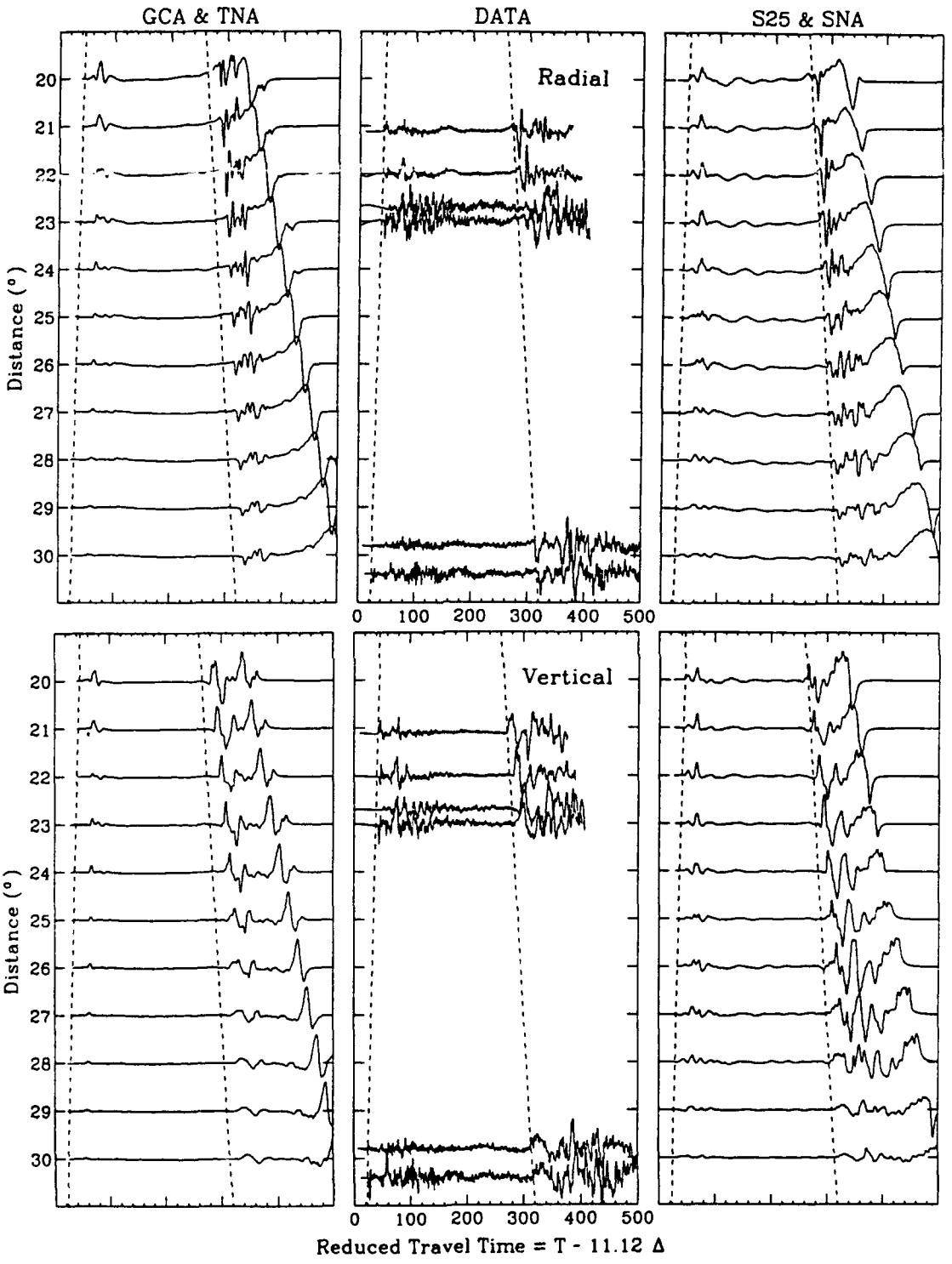


Figure 6. Comparison of the same data set as in Figure 6 with synthetics for both tectonic and shield models; TNA (see Figure 6) and GCA (Walck and Helmberger, 1985). A $t^* = 4.0$ was used in both sets of synthetics. These synthetics were run with reflectivity where the ray parameters are only appropriate for body waves. Thus the large, long-period later arrival is a truncation phase.

THE INFLUENCE OF THE LOWER CRUSTAL STRUCTURE ON THE EARLY CODA OF REGIONAL SEISMOGRAMS.

Michel CAMPILLO and Anne PAUL
Laboratoire de Géophysique Interne et Tectonophysique,
Université Joseph Fourier,
BP 53X, 38041 Grenoble cedex, France

May 1991

ABSTRACT

Numerous deep seismic reflection profiles recorded in Western Europe have revealed subhorizontal and energetic reflections in the lower continental crust. Since this heterogeneity appears to be quite strong and widespread over large areas, we propose to study its influence on the propagation of seismic regional phases by the mean of synthetic seismograms computed for a flat-layered earth model. The lower crustal layering induces a clear increase in the duration of the Pg and Lg phases on both the vertical and radial components beyond the group velocity of their terminations in a model with a homogeneous lower crust. The transverse component is weakly affected. The amplitude and the spectral content of the early Lg coda is strongly dependent on the distribution of layers thicknesses. The predominence of the low frequency components (below 2 Hz) observed in the Lg coda of real data is correctly accounted for with 1 km-thick layers in the lower crust. From particle motions at various depths and the analysis of the dispersion curves of normal modes, we hypothesize that the late arrivals result from the interaction of plate-type disturbances of the high impedance layers. These waves leak energy in the mantle at a weak rate. This mode of generation of the coda waves explains the puzzling observation that the spreading coefficient of Lg seems to be applicable to the early coda of regional seismograms. The influence of the *lamellae* on the average Q factor of the continental crust is also investigated. It shows that the lower crust layering does not account for the low values of the apparent Qs. Another origin has to be assumed for this strong attenuation, like scattering by randomly distributed heterogeneities.

objectives

Since the introduction of the coda method to measure apparent attenuation in the lithosphere by Aki and Chouet (1975), numerous measurements and applications have been carried out including the study of spatial (Singh and Herrmann, 1983) and temporal variations of the quality factor (Aki, 1985). The background of the method is the theory of single scattering in an elastic space with isotropically distributed inhomogeneities (see Sato, 1990). In this paper we shall also discuss the effect of crustal heterogeneities. However, the framework of our modeling is quite different since we consider the crust as a stack of flat layers. Although this representation is oversimplified, it allows to model easily the complete phenomenon of wave propagation, including multiple scattering. Furthermore, the fine structure of the crust in western Europe presents a distribution of heterogeneity which, by some aspects, is closer to a horizontal layering than to an isotropic distribution, especially in the lower crust.

We shall investigate the influence of the thin layering of the lower crust revealed by deep reflection profiles on the propagation of regional phases. In particular, we shall study the effect of the lamination on the duration of the seismograms and the consequences of this structure on the measurements of apparent attenuation using regional records in France. The influence of a series of thin layers with variable thickness on wave propagation has already been extensively investigated (e.g. Menke (1983), Mallick and Frazer (1990)). But the contexts were different from the study of regional phases presented in this paper.

Research accomplished

Some attenuation characteristics of regional phases

The regional phases Pg and Lg are one of the most characteristic features of the short period seismograms recorded in the continental domain. These waves are observed from distances as close as 150 km up to several thousand kilometers of epicentral distances. They disappear along oceanic pathes (Press and Ewing, 1952) and at some very strong structural boundaries (e.g. Ruzaikin *et al.* (1977), Kennett *et al.* (1985)). The interpretation of these arrivals as P and S waves multiply reflected within the crust is supported by the success of the numerical modeling of these phases (see Campillo, 1990 for a review of recent results). These models were based upon simple crustal structures as deduced from deep seismic soundings. For example, Bouchon (1982), Kim (1987) or Bertil *et al.* (1989) have presented realistic seismograms obtained with models consisting of a few flat homogeneous layers. However these computations fail to explain the long duration of observed seismograms. Figure 1 presents examples of records of vertical motion at stations of LDG (Laboratoire de Détection Géophysique) from an earthquake in the region of Lacq (southwestern France). The paths are purely continental and propagate through the hercynian province of Massif Central. They are compared to synthetic seismograms computed for a simple flat model consisting of 4 homogeneous layers.

All computations of synthetic seismograms presented in this paper are performed using the discrete wavenumber decomposition (Bouchon, 1981) associated with the reflection-transmission matrix technique of Kennett (1983). The source consists in a point strike-slip dislocation at 10 km depth. The receivers lie in an azimuth of 30 ° with respect to the fault plane. Seismograms are computed in the frequency range 0 to 10 Hz. The source function corresponds to an omega-square model with corner frequency at 1Hz and the seismograms are convolved with the LDG station response. The comparison between synthetics and records shows that the model succeeds in predicting the amplitudes and shapes of the energetic parts of both Pg and Lg. It fails, however, to fit the long progressive temporal decay of the amplitude of these phases as observed on actual seismograms.

Another striking observation is the decay of spectral energy with epicentral distance of the Lg phase. Campillo *et al.* (1985) have shown that the introduction of a frequency dependent quality factor for the whole crust allows to simulate the decay of spectral energy with distance. In their study of the attenuation of Lg in different group velocity windows, they also found that the computed apparent quality factors of the crust were almost identical for the windows 3.6-3.1 km/s, 3.1-2.6 km/s and 2.6-2.3 km/s.

However, the process of anelastic attenuation cannot account for the long duration of the coda. This suggests that scattering could be the cause of both frequency dependent attenuation and coda of the seismograms. This last interpretation is coherent with the frequency dependence of Qp and Qs and with the ratio Qs over Qp observed in France by Campillo and Plantet (1991). An intriguing result obtained in this last study is the correlation of a zone of strong attenuation with a zone of strong heterogeneity of the lower crust as revealed by a wide angle profile. This suggests that the intense scattering occurring in the heterogenous lower crust might be the cause of the attenuation anomaly.

The heterogeneity of the crust as displayed by deep reflection profiles

The heterogeneous character of the crust is clearly shown by deep seismic reflection experiments. One of the major results of vertical seismic reflection profiling in western Europe (Bois *et al.* (1988), Matthews (1986), Fuchs *et al.* (1987)) is the existence of a bright sub-horizontal seismic layering in the lower part of the continental crust. On the other hand, the upper crust is nearly transparent except for the shallow sedimentary layers. The nature and the origin of these lower crustal reflectors remain controversial (Warner, 1990a). However, the lateral coherency of the reflections suggests that the reflecting structures are mostly horizontal and very elongated in shape. Deep seismic reflection profiling thus provides the most reliable information of small scale crustal heterogeneities since the reflectivity is a direct observation of the fluctuations of the properties of the Earth that induce the scattering of seismic waves. In this paper we study the implications of the layering of the lower crust discovered over the last few years, on the characteristics of guided

wave propagation. As consisting of multiply reflected waves, Pg and Lg have to be affected by heterogeneities in the same way as the waves used in reflection seismics although the frequency ranges considered for these two domains are different. Moreover, the large amplitude of impedance contrasts that are probably associated with the layering, the large thickness of the heterogeneous zone and the lateral extent of the region affected in western Europe support the idea that the influence of the layering on Pg and Lg phases has to be considered. Some characteristics of the P-wave velocity structure of the lower crust are known as a result of the detailed analysis of reflection records. Particularly, one can evaluate the main features of acceptable distributions of velocity with depth such as the mean thickness of the layers or the mean velocity contrast between them. Such constraints have been obtained by modeling of wide-angle reflection data recorded in the Black Forest (Sandmeier and Wenzel, 1986) and in northern France (Paul and Nicollin, 1989), as well as from normal incidence data from the continental shelf off southwest Britain (Warner (1990b), Paul and Hobbs (1991)). These studies all lead to the same average thickness of 100 m for the reflective layering of the lower crust. They also show that the impedance contrasts required to explain the brightness of the reflections are as large as 20%, leading to velocity contrasts of at least 10% between high and low velocity layers. However, the frequency ranges considered for deep seismic reflection is 8 - 30 Hz while for the study of short period regional phases the domain of interest is 1 to 10 Hz. As a consequence, the scales of layer thicknesses which the wave are sensitive to can be different in the two domains. Therefore, the effect of the mean thickness has to be investigated by a series of numerical experiments.

Simulation of regional propagation

The first velocity model is presented in Figure 2. Below a 2 km-thick sedimentary layer (Vs=2.8 km/s) and a 13 km-thick homogeneous upper crust with Vs=3.58 km/s, the lower crust is made of alternating low and high velocity layers with an average thickness of 1 km. Thicknesses are chosen randomly in the range 900 to 1000 m. The P-wave velocity law is inspired from the model given by Sandmeier and Wenzel (1986), with alternations between 2 gaussian distributions with average values increasing linearly with depth. The gradients are chosen so that the energy reflected at normal incidence remains nearly constant with two-way traveltime, as observed in seismic data. At the moment, shear waves images of the reflective lower crust remain exceptional (Lüschen *et al.* (1990), Sandmeier and Wenzel (1990)). As a consequence, the S-wave velocity structure is poorly known and we had to assume a constant Vp/Vs ratio of 1.73. On Figure 2 are also displayed the synthetic seismograms corresponding to the simple 4-layer model and those obtained in presence of a laminated lower crust. The increase in duration due to the lamination is spectacular for both the radial and vertical components. The envelope of the transverse component, corresponding to pure SH case is almost

unsensitive to the presence of the laminated lower crust. The coda of Lg exhibits significant arrivals at group velocities as low as 2.3 km/s, while for the 4-layer reference model the lowest velocity observed was 2.9 km/s. Indeed the envelope of the late part of the Lg wavetrain shows some unrealistic features very different from the regular decay of actual seismograms. Nevertheless, it is important to note the drastic influence of the lamination on the duration of both Pg and Lg wavetrains. One may remark that this result is in contradiction with the assertion of Cormier *et al.* (1991) that the Lg wave train is almost unsensitive to the detail of the crustal structure and that its coda is controlled by the total thickness of the crust. We have checked in another model that the velocity structure of the sedimentary layer has a much smaller effect on the amplitude and the duration of the Pg and Lg codas.

Influence of the characteristics of the lamination

In order to study the influence of the distribution of velocities and thicknesses, we consider a series of models that correspond to different depth distributions of seismic velocity in the lower crust. The other characteristics (sedimentary layer, upper crust, Moho depth) remain the same as in the first model. Different velocity structures are depicted in Figure 3 with the corresponding synthetic vertical seismograms computed at a distance of 370 km and plotted as a function of group velocity. In each case, a time-frequency map of the distribution of spectral amplitude is also presented. It is evaluated by computing Fourier spectra in time-windows moving along the seismograms. The windows are 8.125 s wide. In each time-window, the total amount of spectral amplitude is evaluated by summing up the contribution of each frequency, yielding the curve of amplitude variation with time displayed along the top of the maps. The distribution of spectral amplitude with frequency is obtained in a similar way by summing up the contribution of each window for each frequency. It is depicted on the right-hand side of the maps. The first model (labelled 019 on the figure because it is made up of 19 layers) has 1 km thick laminations and is the one used for computing the seismograms presented in Figure 2. The time frequency map (Figure 3a) allows to visualize the specific distribution of energy of the late arrivals, i.e. for group velocity smaller than 2.9 km/s. Well organized wavetrains are present in individualized frequency bands. In the time-frequency domain they have a remarkable continuity between 3.2 and 2.3 km/s. For model 019 the dominant arrival lies in the band 1.5-2 Hz and exhibits a slight inverse dispersion. This type of well defined characteristics is much more difficult to see in the coda of Pg. Let us considerer now models with a thinner layering in the lower crust. In model 033 (Figure 3b), the layers have a mean thickness of 500m. Again the increase in duration with respect to the reference model is very clear. The energy map shows that the main contribution is within the frequency range 2-4 Hz. Another arrival can be seen at a frequency of about 8 Hz. This indicates that the frequency content of the late arrivals is inversely

proportional to the mean thickness of the layering. It is confirmed by the results obtained with model 121 (Figure 3c) where the average thickness of the layers is 100 m. In this case, the energy map shows that there is no generation of late arrivals for frequency lower than 8 Hz. The 3 models that we have just discussed present unimodal distributions of layer thicknesses. The influence of more realistic distributions has also to be tested.

In model 049 the lower crust is made up of layers with a bimodal distribution of thicknesses in the ranges 900-1100 m and 90-120 m. The velocity structure and the results of the computations are shown in Figure 3d. The patterns seen on the time-frequency plot are more complex and diffuse than in the previous examples. The arrival at about 2 Hz which was noticed for model 019 is present. The effect of mixing 2 scales of thicknesses is to spread the energy in the time-frequency domain. With model 031, the layer thicknesses are randomly distributed between 100m and 1000m. We present the results obtained in Figure 3e. The coda is well developed and reaches group velocities as low as 2.2 km/s, as in the case of the models with narrower distributions of thicknesses. Indeed in this case the energy is widespread in the time-frequency domain. On the seismograms, the decay of amplitude with time after the onset of Lg is more regular than in the previous examples, resulting in an envelope that seems more realistic. Model 031 corresponds to a particular draw of random thicknesses between 100 and 1000m. In order to check the importance of the details of the distribution, we set up a new model (model 035) with the same characteristics and we recalculated the synthetic seismograms. The results are presented in Figure 3 f. Indeed the wavefields obtained for models 031 and 035 present some differences but the overall characteristics are the same and in particular the envelopes of the coda are similar. On the other hand the details of the energy maps are different, showing that the spectral amplitude of the late arrivals changes rapidly from one draw to the other.

We have performed these different simulations in models with roughly the same statistical characteristics of layering in order to check what differences could be observed between records obtained for different paths in the same region. This indicates that the mean results obtained for a large number of paths will show only strong maxima of excitation of the early coda for frequencies corresponding to a range of thicknesses predominantly represented in the crust beneath most of the path.

We present in Figure 4 an example of energy map for a seismogram recorded in central France at approximately the same epicentral distance as the synthetics of Figure 4. It illustrates the predominance of the low frequency component in the later part of the Lg wavetrain. We computed the mean ratio of spectral amplitudes in the group velocity windows 3.6-3.1 and 2.6-2.3 km/s for a series of paths beneath central France and showed that the mean ratio decreases for frequencies smaller than 2 Hz (Campillo, 1990). This spectral behavior is independent of the nature of the soil beneath the stations. It indicates that, on the average, the early coda is mainly excited in a frequency range corresponding to layer thicknesses around 1 km. One must remember that we have no information for frequency less than 1 Hz.

Nature of the the late arrivals

We have shown that the presence of a laminated lower crust implies a duration of the regional seismograms much larger than the one predicted by a simple model having a homogeneous lower crust. It appears that the spectral characteristics of this early coda are closely related to the statistical properties of the stratification. We have not addressed yet the problem of the identification of the waves that form this slow wavetrain. To this aim we will consider the simplest case among those presented in the previous sections: model 019. We have seen that a specific mode of propagation exists for frequencies around 2 Hz with a group velocity that reaches 2.3 km/s. We have computed the particle motion on the surface and at depth for different group velocity windows at 530 km of epicentral distance. The amplitude spectrum of the seismograms is strongly dominated by the low frequency component around 1.5 Hz, as shown in Figure 3a. On Figure 5 (left) we present the particle motion computed in the group velocity window 3.45-3.40 km/s, which corresponds to the maximum amplitude of Lg. At the surface, the particle motions are complex and almost isotropic, indicating that Lg is made up of SV and SH waves propagating over a wide range of incidence angles. The same observation can be made at depths of 14 and 28 km. Beneath the Moho, at 34 km depth the motion becomes purely vertical and transverse as expected for vanishing SV and SH waves. If we consider now a time window in the wavetrain that appears only in presence of the laminated lower crust, the polarization is completely different. The particle motions computed in a window corresponding to group velocities between 2.70 and 2.65 km/s are displayed on Figure 5 (right). At the surface and in the upper crust the motion in the incidence plane is complex and does not indicate any type of linear polarization. As we observed previously, the transverse (SH) component is equal to zero. In the lower crust (28 km depth) the polarization becomes almost linear and vertical. When the Moho is reached, the direction of polarization changes suddenly and corresponds to a SV wave propagating downward in the lower half space with an angle of about 66 °. These polarization patterns indicate that the later arrivals that occur in presence of thin layering in the lower crust have a very distinct nature from the primary Lg (defined between 3.5 and 3.0 km/s). Before discussing further the nature of these waves, one must notice that the vertical polarization observed in the lower crust for group velocities between 2.70 and 2.65 km/s is a phenomenon limited to the mode of propagation observed at frequencies between 1 and 2 Hz. When considering frequencies higher than 4 Hz and the same group velocity, the polarization of the motion in the lower crust is observed to be no longer vertical but almost circular. On the other hand, the linear polarization of the waves propagating in the mantle is observed with the same angle regardless of the frequency considered. This last point suggests a leakage in the mantle of part of the energy of these "modes". To check this conclusion we use the framework of normal mode theory. The dispersion curves of normal modes are computed using the computer programs developped by Herrmann (1985) following the approach of Haskell (1953).

We consider first the 4-layer reference model with a homogeneous half space mantle. The dispersion curves of all the higher modes of rank greater than 6 are plotted in Figure 6a. The lower group velocity of the crustal modes is about 3.1 km/s. Considering now model 019 that includes a laminated lower crust, the dispersion curves presented in Figure 6b indicate a lower limit of group velocity at about 2.9 km/s. Nevertheless, group velocities lower than 3 km/s are reached by a small number of modes. It may be noticed that the contribution at 2.9 km/s occurs at a frequency of 1.8 Hz that is the dominant frequency of the late arrivals observed in our synthetics for this model. However, our numerical simulations have shown that energy can travel at velocities much lower than those computed for normal modes.

It is a usual practice to introduce a jump of wave velocities in the mantle to get modes representative of upper mantle propagation as Sn. We have verified that such a modification of the 4-layer reference model does not change the lower limit of the group velocity as shown in Figure 6c. On the contrary, when model 019 with a jump of velocity in the mantle is considered, the dispersion curves reach velocities smaller than 2.7 km/s (Fig. 6d). The locations of the minima of the group velocity, that correspond to Airy phases, give an image very close to the energy map obtained for the same model as presented in Figure 3a. In particular, the distribution of the minima indicates a slight inverse dispersion of the resulting energy wavetrain. These modes appear only in presence of the laminated lower crust *and* of the jump of velocity indicating that they are associated with the lamellae and that they are not normal crustal modes. After the observation of the polarization, this is another indication of the importance of leaky modes in the early coda. Their characteristics suggest that these modes result from the interaction of the plate type vibrations of the high impedance layers. We have checked that this effect does not exist for Love wave higher modes. This is in agreement with our previous noting that there is no coda produced by the lamination for the transverse component.

Apparent attenuation

With respect to the evaluation of Qs in the crust from actual seismograms, the important point is to evaluate the rate of amplitude decay of these modes. A perfectly elastic media has been assumed in our calculations. However, in order to perform the same analysis as we did with data (Campillo *et al.*, 1985, Campillo and Plantet, 1991), we studied the decay of spectral amplitude with epicentral distance for different group velocity with the synthetics computed for model 019. The seismograms were corrected for time domain geometrical spreading of Lg, as evaluated from numerical simulation in a reference model. We evaluated apparent Q values from linear regression of the logarithm of the amplitude with distance. Figure 7 shows the results of this processing for 2 time windows centred at group velocities of 3.3 km/s and 2.6 km/s. The first case (3.3 km/s) corresponds to the part of Lg with maximum amplitude regardless of the model considered. The results presented in Figure 7 (left) indicate that there is no measurable apparent

attenuation of Lg due to the excitation of low velocity modes in presence of lamination. The poor correlation is explained by the rapid variations of Lg amplitude due to interferences between multiply reflected S waves. Considering a window centred at a velocity of 2.6 km/s (Figure 7 (right)), the loss of energy of the late arrival leads to an apparent attenuation. The reader must keep in mind that the seismograms were corrected from the spreading of Lg. The values of Q that were computed are never smaller than 1000. The minimum values are not associated with the frequency ranges of the low velocity arrivals which were identified in Figure 3a. For example, at 2Hz where the maximum of amplitude occurs, the correlation coefficient is very small and the Q value very high, indicating that the spreading is very similar to the one of Lg.

Several conclusions can be drawn from this analysis. The decay of amplitude of Lg is not affected by the presence of the laminated lower crust in spite of the excitation of the slow waves. Surprisingly, the decay of the slow modes is close to the one of Lg. This means that the leakage of energy into the mantle is weak with respect to the geometrical spreading of a guided wave. In the frequency bands 1.5-2Hz or 4-5Hz, where significant energy travels at small group velocities (2.5 km/s), the values of the equivalent Q factor representing the leakage of energy are much larger than the average values measured for the crust in France (about 400 at 1.5 Hz and 640 at 4 Hz respectively). This mode of generation of the early coda is therefore coherent with the observation that the Q measurements made in different group velocity windows between 3.5 and 2.3 km/s lead to almost the same value even when the analysis assumes the same geometrical spreading regardless of the window considered (Campillo *et al.*, 1985).

Indeed this observation is not universal, no more than the existence of a laminated lower crust. It is recognized for example that the crust in shield areas is less reflective to the high frequency waves used in deep seismic reflection experiments than in paleozoic and mesozoic areas (Nelson, 1991). However, on the other hand the coda of Lg in shield areas is much less developed than for the seismograms recorded in France. This can be seen by comparing the data observed in Scandinavia and studied by Kim (1987) with those recorded in France and presented here. Our analysis is relevant for France, and as a matter of speculation for other regions where the reflective lower crust has been observed.

Conclusion

We have included present day knowledge of the structure of the lower crust in the models used to simulate the propagation of regional phases. A striking implication is the fact that taking into account the lamination of the lower crust increases considerably the duration of the wavetrain which begins with the onset of Lg. Numerical simulations predict arrivals of energy with group velocity as low as 2.3 km/s. This is in good agreement with the envelopes of seismograms recorded in France.

The study of the polarization of these waves and the modal representation of the wave field suggest that the late arrivals consist of plate vibration-like disturbances which leak energy in the mantle at a very weak rate. On the other hand, these modes show a decay of amplitude with distance which is close enough to the geometrical spreading of Lg to allow that the apparent quality factor deduced from these waves is close to the one obtained from Lg. This model is therefore in agreement with the observation that Qs for the crust is almost constant when measured in different group velocity windows assuming the spreading of Lg. Another result of this study is that the spreading of Lg is not affected by the presence of the thin layering of the lower crust, in spite of the generation of the coda.

Indeed the existence of a layered lower crust does not account for the observed values of the apparent quality factor and we have to assume that the loss of energy of the wavetrain observed in real data is due to anelastic attenuation or to the dispersive effect of scattering over randomly distributed inhomogeneities. After taking into account the findings of the present study, we maintain our previous conclusion (Campillo and Plantet, 1991) that random scattering very likely prevails for the attenuation of short period waves.

Our results illustrate the fact that the early coda of regional seismograms may be strongly affected by waves relevant from the multiple scattering theory as the slow arrivals discussed in this paper. We have verified that these waves exist also at distances smaller than the critical distance for the reflection on the Moho. Indeed we can emphasize the recommendation of Aki (1982) that the analysis of coda using single scattering theory is valid only for very large lapse time (larger than twice the S wave traveltime). According to our results, the early coda can contain wavetrains which exhibit an inverse dispersion that mimics the variation of prominant frequency expected from the effect of attenuation.

Acknowledgments: We thank Olivier Coutant who wrote the computer program used to generate the synthetic seismograms. This work was supported by Institut National des Sciences de l'Univers through "Action d'accompagnement ECORS" (INSU-CNRS, France) and by Advanced Research Projects Agency (USA). Part of the numerical simulations were performed at the Centre de Calcul Vectoriel pour la Recherche.

REFERENCES

Aki, K., Scattering and attenuation, *Bull. seis. Soc. Am.*, **72**, 319-330, 1982.

Aki, K., Theory of earthquake prediction with special reference to monitoring the quality factor of lithosphere by the coda method, *Earthq. Predict. Res.*, **3**, 219-230, 1985.

Aki, K. and B. Chouet, Origin of coda waves: source, attenuation and scattering effects, *J. Geophys. Res.*, **3**, 3322-3342, 1975.

Bertil, D., Bethoux, N., M. Campillo and B. Massinon, Modeling crustal phases in southeast France for focal depth determination, *Earth Planet. Sci. Let.*, **95**, 341-358, 1989.

Bois, C., Cazes, M., Hirn, A., Mascle A., Matte, P., Montadert, L., and Pinet, B., Contribution of deep seismic profiling to the knowledge of the lower crust in France and neighbouring areas, *Tectonophysics*, **145**, 253-275, 1988.

Bouchon, M., A simple method to calculate Green's functions for elastic layered media, *Bull. seis. Soc. Am.*, **71**, 959-971, 1981.

Bouchon, M., The complete synthesis of seismic crustal phases at regional distances, *J. Geophys. Res.*, **87**, 1735-1741, 1982.

Campillo, M., Plantet J.L., and Bouchon M., Frequency-dependent attenuation in the crust beneath Central France from Lg waves: data analysis and numerical modeling, Bull. seis. Soc. Am., **75**, 1395-1411, 1985.

Campillo, M., Propagation and attenuation characteristics of the crustal phase Lg, *Pure Appl. Geophys.*, **132**, 1-19, 1990.

Campillo, M., and Plantet J.L., Frequency dependence and spatial distribution of seismic attenuation in France: experimental results and possible interpretations, *Phys. Earth planet. Interiors*, in press, 1991.

Cormier, V.F., Mandal, B. and Harvey, D., Incorporation of velocity gradients in the synthesis of complete seismograms by the locked mode method, *Bull. seis. Soc. Am.*, in press, 1991

Fuchs, K., Bonjer, K.P., Gajewski, D., Lüschen, E., Prodehl, C., Sandmeier, K.J., Wenzel, F., and Wilhelm, H., Crustal evolution of the Rhinegraben area, 1. Exploring the lower crust in the Rhinegraben rift by unified geophysical experiments, *Tectonophysics*, **141**, 261-275, 1987.

Haskell, N.A., The dispersion of surface waves in multi-layered media, *Bull. seis. Soc. Am.*, **43**, 17-34, 1953.

Herrmann, R.B., Computer Programs in Seismology, University of Saint Louis, 1985.

Kennett, B.L.N., *Seismic wave propagation in stratified media*, Cambridge University Press, Cambridge, 1983.

Kennett, B.L.N., Gregersen, S., Mykkeltveit, S., and Newmark, R., Mapping of crustal heterogeneity in the North Sea Basins via the propagation of Lg waves, *Geophys. J. R. astr. Soc.*, **83**, 299-306, 1985.

Kim, W.Y., Modeling short period crsutal phases at regional distances for the seismic source parameter inversion, *Phys. Earth planet. Interiors*, **47**, 159-178,

1987.

Lüschen, E., Nolte, B., and Fuchs, K., Shear-wave evidence for an anisotropic lower crust beneath the Black Forest, southwest Germany, *Tectonophysics*, **173**, 483-493, 1990.

Mallick, S. and Frazer, L.N., Po/So synthetics for a variety of oceanic models and their implications for the structure of the oceanic lithosphere, *Geophys. J. Int.*, **100**, 235-253, 1990.

Matthews, D.H., Seismic reflections from the lower crust around Britain, in: *Nature of the lower continental crust*, J.B. Dawson, D.A. Carswell, J. Hall and K.H. Wedepohl (eds), Geol. Soc. London Spec. Publ., 24, Blackwell, Oxford, 11-22, 1986.

Menke, W., A formula for the apparent attenuation of acoustic waves in randomly layered media, *Geophys. J. R. astr. Soc.*, **75**, 5416-5422, 1983.

Nelson, K.D., A unified view of craton evolution motivated by recent deep seismic reflection and refraction results, *Geophys. J. Int.*, **105**, 23-35, 1991.

Paul, A., and Nicollin, F., Thin crustal layering in Northern France: observations and modelling of the PmP spectral content, *Geophys. J. Int.*, **99**, 229-246, 1989.

Paul, A., and Hobbs, R., Layers thicknesses in the lower crust: modelling and spectral analysis of BIRPS data, *4th Int. Symp. on Deep Seismic Reflection Profiling of the Continental Lithosphere spec. volume, AGU Geodynamics Series*, in press, 1991.

Press, F., and Ewing, M., Two slow surface waves across North America, *Bull. seis. Soc. Am.*, **42**, 219-228, 1952.

Ruzaikin, A.I., Nersesov, I.L., Khalturin, V.I. and Molnar P., Propagation of Lg and lateral variations of crustal structure in Asia, *J. Geophys. Res.*, **82**, 307-316, 1977.

Sandmeier, K.J., and Wenzel, F., Synthetic seismograms for a complex crustal model, *Geophys. Res. Lett.*, **13**, 22-25, 1986.

Sandmeier, K.J., and Wenzel, F., Lower crustal petrology from wide-angle P- and S-wave measurement in the Black Forest, *Tectonophysics*, **173**, 495-505, 1990.

Sato, H., Unified approach to amplitude attenuation and coda excitation in the randomly inhomogeneous lithosphere, *Pure Appl. Geophys.*, **132**, 93-121, 1990.

Singh, S.K. and R.B. Herrmann, Regionalization of crustal coda Q in the continental United States, *J. Geophys. Res.*, **88**, 527-538, 1983.

Warner, M., Basalts, water, or shear zones in the lower continental crust?, *Tectonophysics*, **173**, 163-174, 1990a.

Warner, M., Absolute reflection coefficients from deep seismic reflections, *Tectonophysics*, **173**, 15-23, 1990b.

FIGURE CAPTIONS

Figure 1: Comparison between real records of the Pg and Lg phases (traces 1, 3 and 5) of an earthquake in southwestern France and synthetics (traces 2, 4 and 6) obtained at similar epicentral distances with a 4-layer model.

Figure 2: Synthetic seismograms obtained between 170 and 570 km of epicentral distance for the 4-layer model with a homogeneous lower crust (top) and for a 19-layer model with layering at kilometric scale in the lower crust (bottom).

Figure 3: Time-frequency maps of spectral amplitude for synthetic seismograms obtained at 370 km epicentral distance with different lower crustal velocity structures. The velocity models are presented above the corresponding maps. The horizontal axis is scaled linearly with respect to the inverse of the group velocity. The seismograms are plotted at the same scale. The curve plotted along the top axis of each map is obtained by summing up the contributions of all the frequencies. The curve presented on the right-hand side is obtained by adding the contributions of all the time-windows. It is used as a normalization curve to compensate for the attenuation of high frequencies before plotting the contour levels on the maps.

Figure 4: Time-frequency map of spectral amplitude for a record of the same earthquake as in Fig. 1 at 386 km epicentral distance.

Figure 5: Particle motion obtained from synthetic seismograms computed at 530 km distance and at 4 different depths: 0, 14 28 and 34 km. The velocity model encludes 1 km-thick lower crustal layers. In the left-hand side, particle motions correspond to the primary Lg (group velocity between 3.45 and 3.40 km/s). In the right-hand side, lower group velocities (2.70 to 2.65 km/s) are considered to study the characteristics of the late arrivals which appear when the lower cust is layered.

Figure 6: Influence of the lower crust laminations on the normal modes dispersion curves. a: Result obtained with the 4-layer velocity model and a homogeneous half space mantle. b: Laminated lower crust with 1 km-thick layers and homogeneous half space mantle.c: 4-layer model with a velocity jump in the mantle. d: 19-layer model with a velocity jump in the mantle.

Figure 7: Results of the measurement of the apparent Q factor for model 019 from the decay of spectral amplitude with distance. The density of spectral energy is computed in a 8.125s-wide window centred on a group velocity of 3.3 km/s in the left-hand side and 2.6 km/s in the right-hand side. The variations of the Q-factor with frequency are presented on top. The curves in the middle show

the linear correlation coefficient for the linear regression used to measure Q. The bottom curves show the square root of the energy density for the seismogram at 170 km epicentral distance in the corresponding time window.

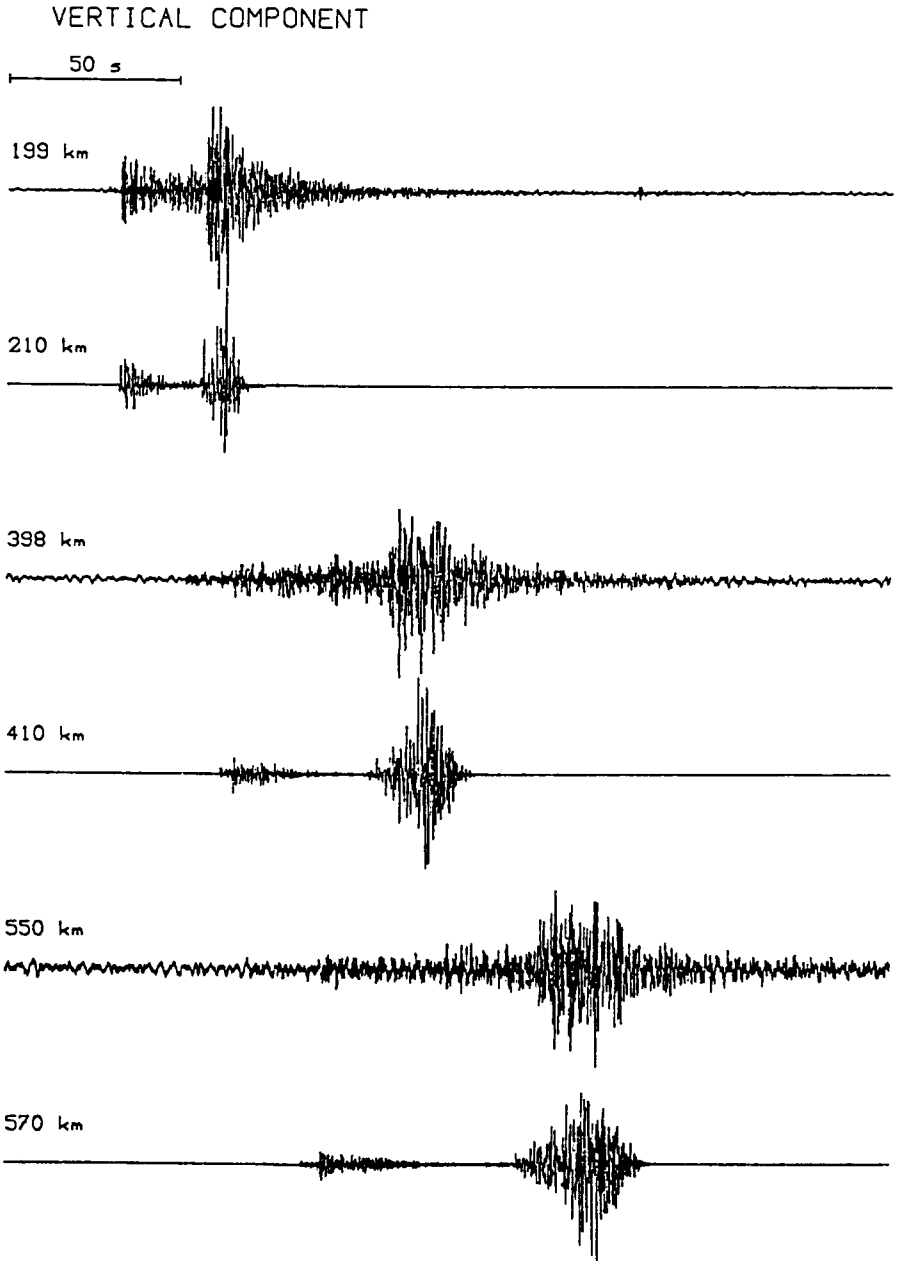

VERTICAL COMPONENT
50 s
199 km
210 km
398 km
410 km
550 km
570 km

Figure 1

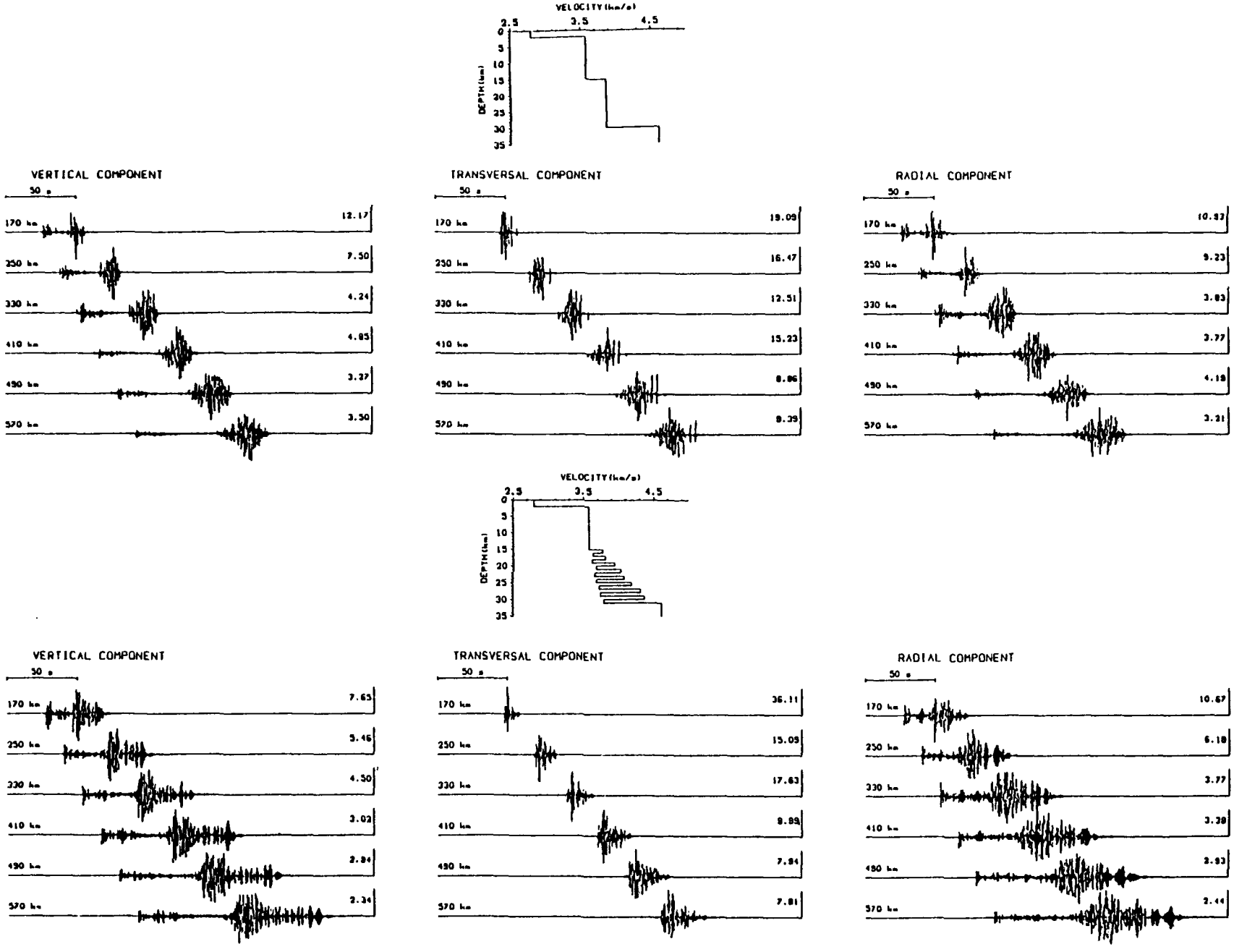

VELOCITY (km/s)
2.5
3.5
4.5
DEPTH (km)
VERTICAL COMPONENT
TRANSVERSAL COMPONENT
RADIAL COMPONENT
50 s
170 km
250 km
330 km
410 km
490 km
570 km
12.17
7.50
4.24
4.85
3.27
3.50
19.09
16.47
12.51
15.23
8.86
8.39
10.83
9.23
3.83
3.77
4.19
3.21
7.65
5.46
4.50
3.02
2.84
2.34
36.11
15.09
17.63
9.89
7.84
7.81
10.67
6.18
3.77
3.38
2.93
2.44

Figure 2

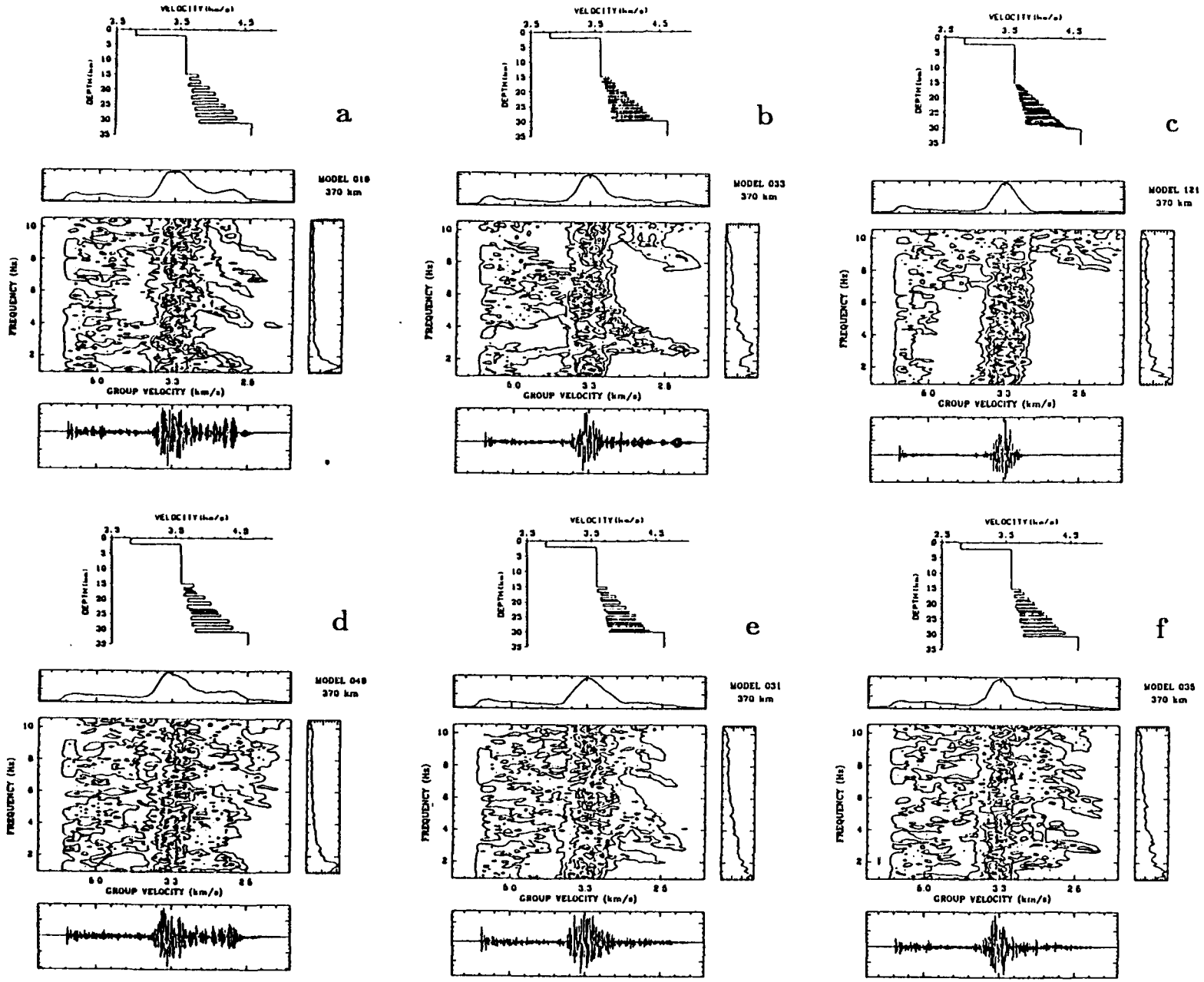

a
b
c
d
e
f
VELOCITY (km/s)
DEPTH (km)
MODEL 018
MODEL 033
MODEL 121
MODEL 048
MODEL 031
MODEL 035
370 km
FREQUENCY (Hz)
GROUP VELOCITY (km/s)

Figure 3

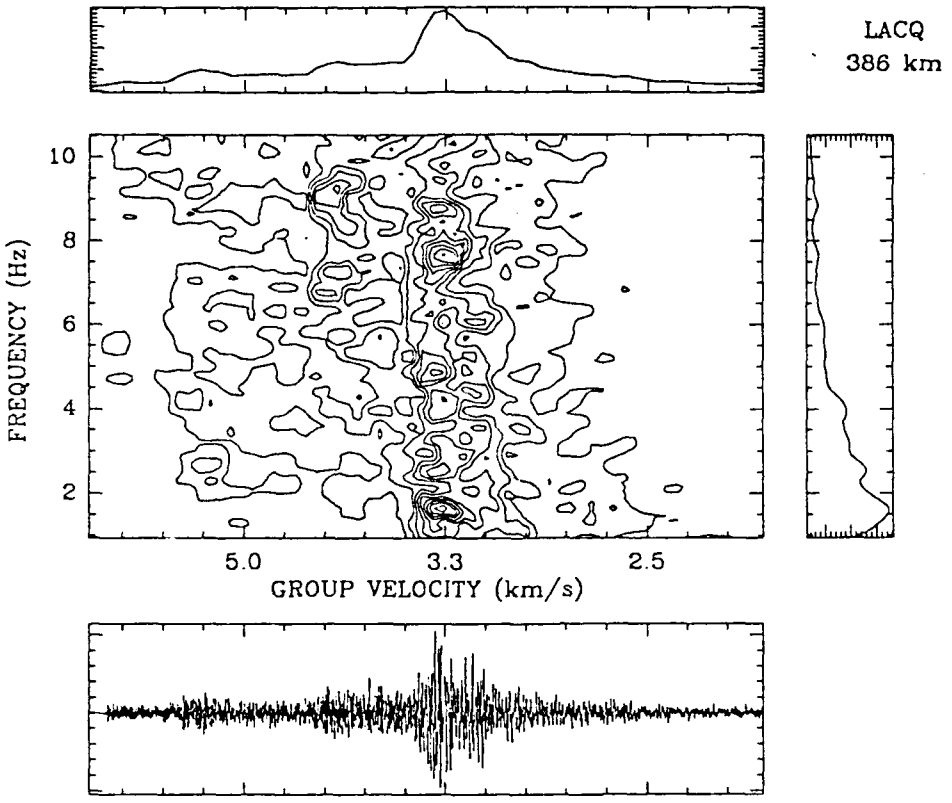
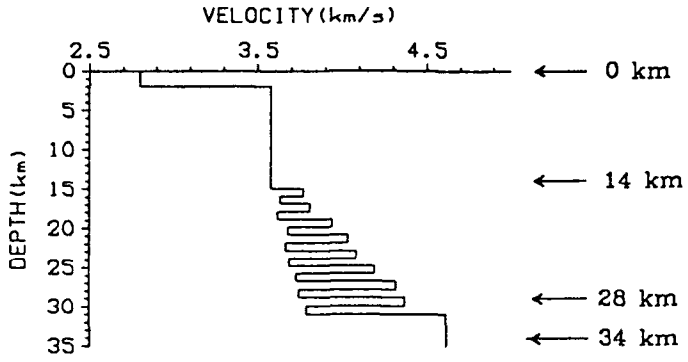
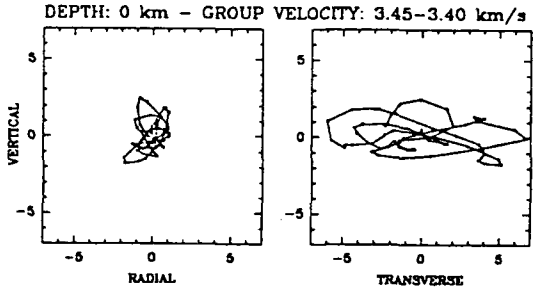
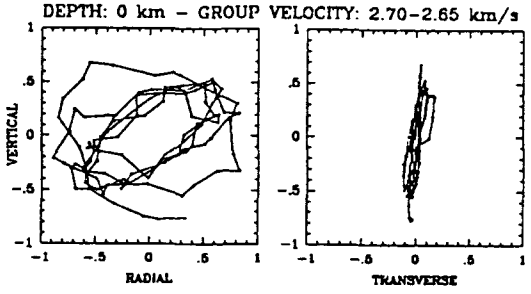
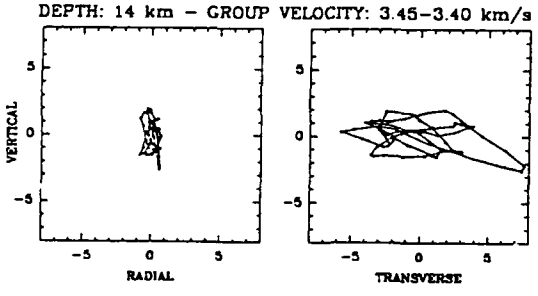


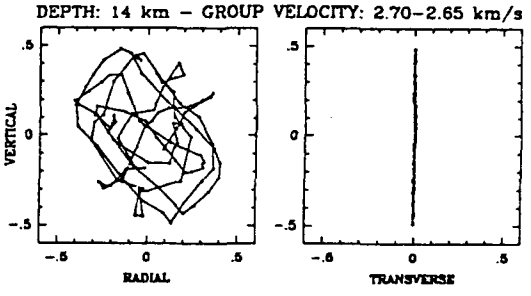
Figure 4

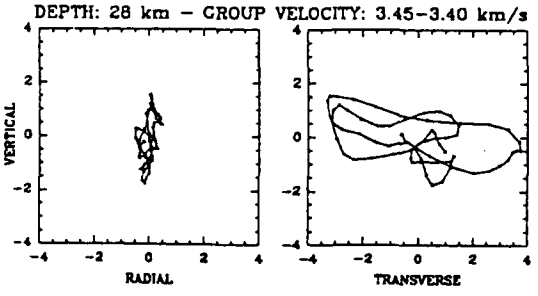

VELOCITY(km/s)
2.5
3.5
4.5
DEPTH(km)
0
5
10
15
20
25
30
35
0 km
14 km
28 km
34 km

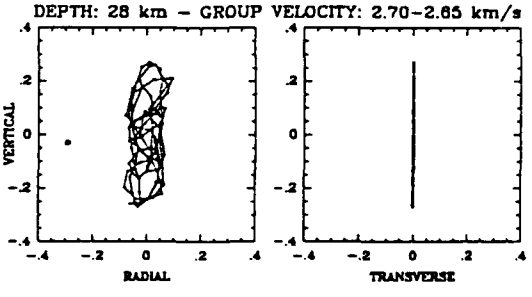

DEPTH: 0 km - GROUP VELOCITY: 3.45-3.40 km/s
VERTICAL
RADIAL
TRANSVERSE

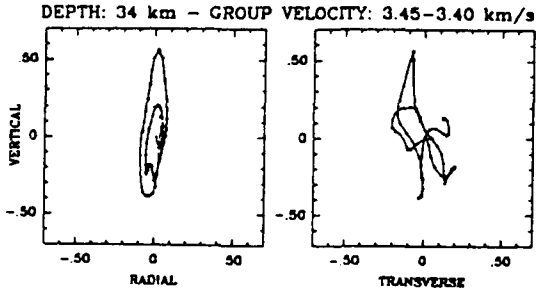

DEPTH: 0 km - GROUP VELOCITY: 2.70-2.65 km/s
VERTICAL
RADIAL
TRANSVERSE


DEPTH: 14 km - GROUP VELOCITY: 3.45-3.40 km/s
VERTICAL
RADIAL
TRANSVERSE


DEPTH: 14 km - GROUP VELOCITY: 2.70-2.65 km/s
VERTICAL
RADIAL
TRANSVERSE


DEPTH: 28 km - GROUP VELOCITY: 3.45-3.40 km/s
VERTICAL
RADIAL
TRANSVERSE


DEPTH: 28 km - GROUP VELOCITY: 2.70-2.65 km/s
VERTICAL
RADIAL
TRANSVERSE


DEPTH: 34 km - GROUP VELOCITY: 3.45-3.40 km/s
VERTICAL
RADIAL
TRANSVERSE

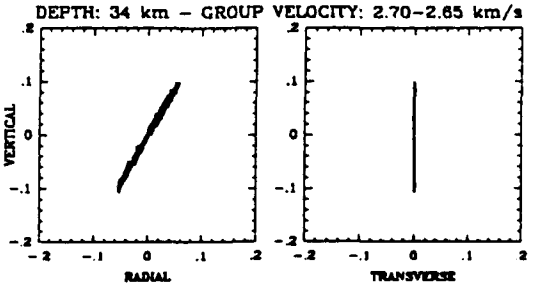

DEPTH: 34 km - GROUP VELOCITY: 2.70-2.65 km/s
VERTICAL
RADIAL
TRANSVERSE

Figure 5

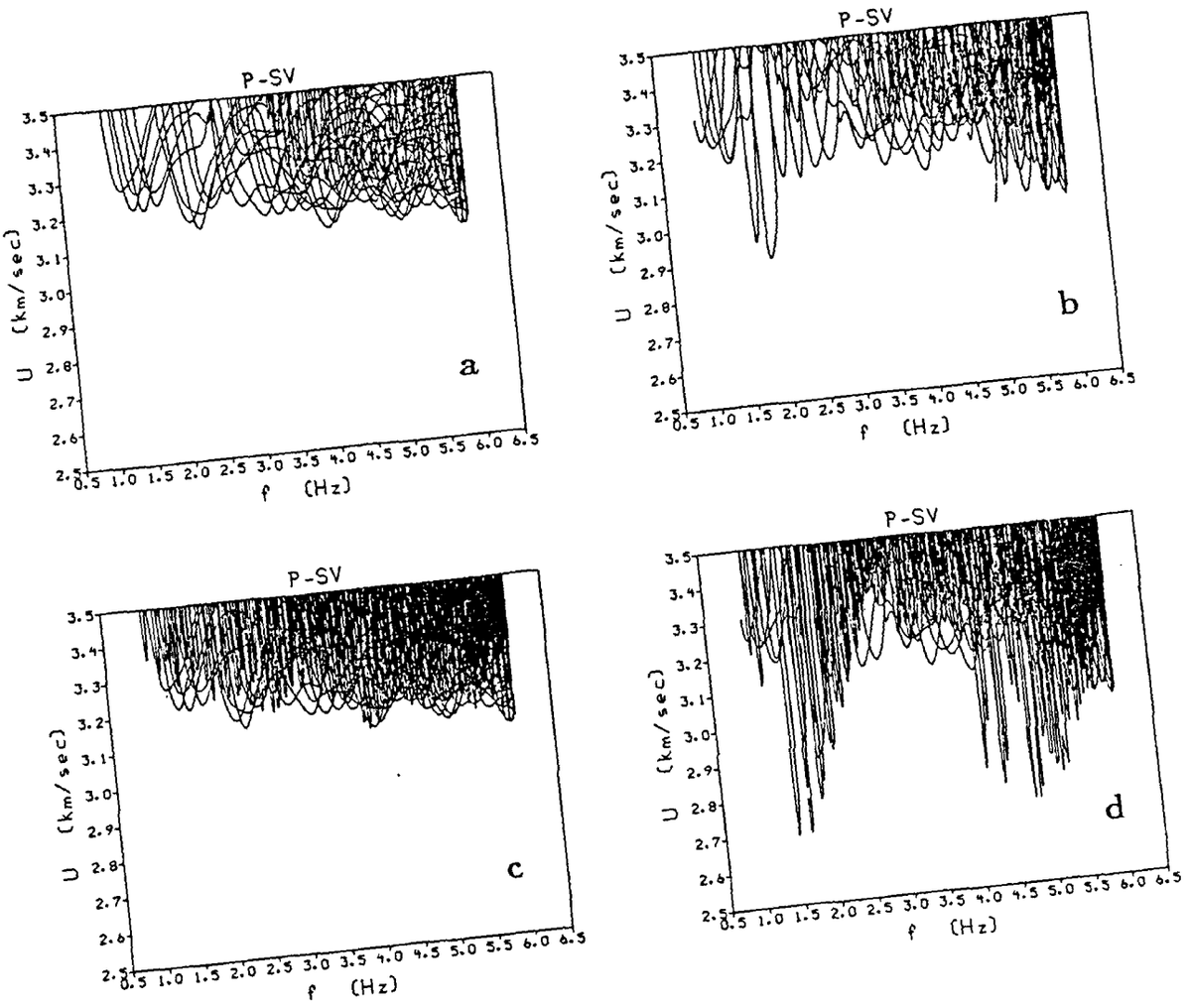


Figure 6

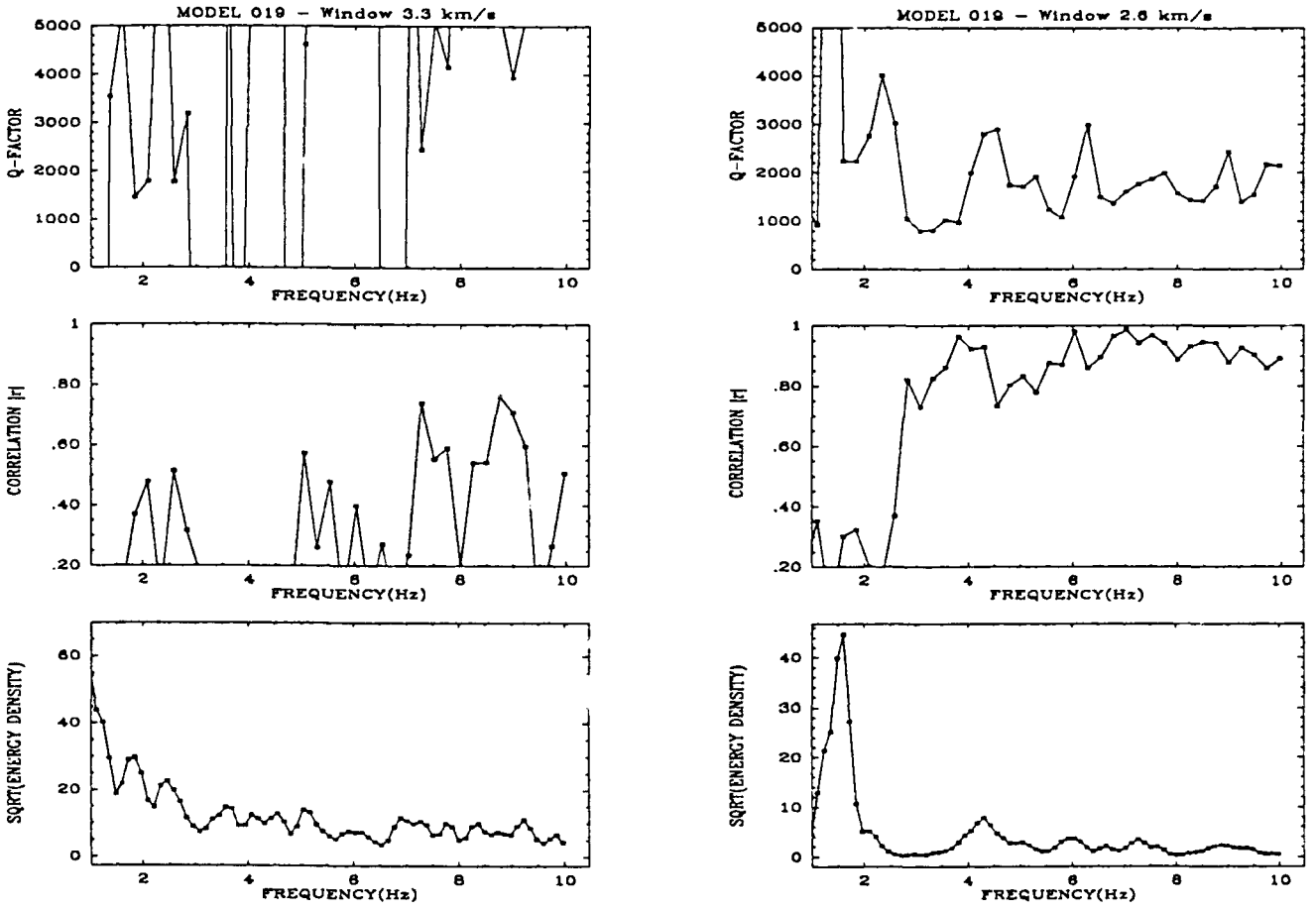

MODEL 019 – Window 3.3 km/s
MODEL 019 – Window 2.6 km/s
Q-FACTOR
CORRELATION |r|
SQRT(ENERGY DENSITY)
FREQUENCY(Hz)

Figure 7

SPECTRAL STUDIES OF THE ELASTIC WAVE RADIATION FROM APPALACHIAN EARTHQUAKES AND EXPLOSIONS - EXPLOSION SOURCE SPECTRA MODELING USING BLASTER'S LOGS

by
M. C. Chapman, G. A. Bollinger and M. S. Sibol
Virginia Polytechnic Institute
and State University
Blacksburg, Virginia 24061-0420

Contract No. F19628-90-K-0052
August 1991

OBJECTIVE

The objectives of this study are to model the observed spectra of seismic radiation from large industrial explosions using information obtained from blaster's logs and to compare the explosion spectra with those of small earthquakes occurring in the same source region.

RESEARCH ACCOMPLISHED

Data

The data set is derived from digital waveforms recorded by the Virginia Regional Seismic Network. Figure 1 shows the locations of the network stations, along with the locations of the four explosions and the epicenters of the two earthquakes employed in the study.

Explosion Spectral Modulation

Generally, surface mine or quarry blasting operations employ explosive charges in holes that are arranged spatially in one or more rows. The individual charges are usually fired in a time sequence designed to achieve objectives such as proper rock breakage, reduction of fly rock, and directed movement of the fractured rock mass away from the free face of the quarry. The time intervals (delays) between the individual subexplosions may be on the order of a few milliseconds to hundreds of milliseconds, depending on the application (Langefors and Kihlstrom, 1963; E.I. du Pont de Nemours & Co., 1978). For large mining explosions, similar to those studied here, a variety of different delays may be employed.

Baumgardt and Ziegler (1988), Smith (1989) and Hedlin et al (1990) discuss the origin of spectral modulations in regional seismograms of industrial explosions. Assuming that the explosion source-time function is a linear superposition of individual subexplosions (Stump and Reinke, 1988), we can model the explosion source by convolving a source wavelet S(t) with an impulse series W(t). In addition to the firing times of the subexplosions, W(t) must also incorporate the spatial distribution of the charge holes, the azimuth of the receiver, and the wave velocity of the material. The source-time function, A(t), for an explosion with n subexplosions observed at distances large in comparison to the dimension of the charge layout, is given by

$$A(t) = S(t) * W(t), \tag{1}$$

where

$$W(t) = \sum_{j=1}^{n} \alpha_j \delta(t-\tau'_j), \tag{2}$$

and

$$\tau'_j = \tau_j - (x_j \sin\theta + y_j \cos\theta)/V. \tag{3}$$

Here, $\delta(t)$ is the Dirac delta function, τ_j is the time of the j'th subexplosion defined relative to the time of the initial subexplosion, x_j and y_j are the coordinates of the j'th subexplosion in a coordinate system with origin at the location of the initial subexplosion. The constant α_j represents the amplitude of the subexplosion. The azimuth θ from origin to recording station is measured clockwise from the Y axis and V is the phase velocity. The amplitude spectrum $A(\omega)$ of the source-time function is given by

$$A(\omega) = |S(\omega)W(\omega)|, \qquad (4)$$

where

$$W(\omega) = \sum_{j=1}^{n} \alpha_j \exp(i\omega\tau'_j) \qquad (5)$$

Explosion Source Information

The explosions studied here were fired to remove the soil and rock overburden from coal seams. We obtained copies of the blaster's logs and have used the information contained therein to model the explosion source amplitude spectrum using equations 1 through 5.

The detail of information contained in the logs varied among the individual explosions. However, in all cases, the firing times of each charge could be ascertained. Other pertinent information contained in the logs included the distance between rows (burden) and between holes in a row (spacing), the types of millisecond delay connectors used (9,17,42 and 200 msec, in various combinations), the types of downhole delay blasting caps (450 or 500 msec), the total charge weight used for each hole, and the maximum weight per delay period. Important ambiguities in the logs involve the distribution of charge weight within some of the decked holes for 3 of the 4 explosions: also, the detonation velocity of the surface and downhole detonating cord is not specified. The copies of the blasting logs and other information, such as the orientation of the charge pattern with respect to North, were kindly furnished by the Kentucky Department of Mines and Minerals (written communication).

Observed Explosion Spectra versus Theoretical

The explosions studied here produced time independent spectral modulations. This phenomenon has been noted previously (see, e.g,. Baumgardt and Ziegler, 1988) from delay-fired explosions, and is an indication that the modulations are source related and not due to multipathing.

Figure 2 shows a sonogram for Explosion 2. It was created using an approach similar to that of Hedlin et al (1989). Note that the spectral peaks persist throughout the signal, from P onset to well within the Lg coda.

Figures 3 and 4 show the explosive charge pattern and the time series W(t) for two of the four explosions.

In Figures 5 through 8 we compare the acceleration amplitude spectra of Lg with theoretical spectra for each of the 4 explosions. All spectra have been corrected for instrument response and anelastic attenuation. The assumed quality factor is $Q=811f^{0.42}$ (Chapman and Rogers, 1989).

Figure 5 shows the vertical component Lg acceleration spectrum (20 sec window) at stations WMV,VWV, and CVL, in comparison with the theoretical source acceleration spectrum for Explosion 1. The observed spectra are plotted at frequencies where the signal/noise ratio exceeds 2. The theoretical model assumes an ω^2 amplitude spectrum for the source wavelet: hence, in equation (4),

$$|S(\omega)| = \frac{\omega^2}{1+(\frac{\omega}{\omega_c})^2} . \qquad (6)$$

Trial and error modeling indicates a corner frequency of 3 Hz ($\omega_c=6\pi$) for Lg. The amplitude of the subexplosions are scaled in proportion to charge weight: i.e., α in Equation (5) is charge weight in thousands of pounds. Note the good agreement between observed and theoretical spectra at frequencies less than about 7 Hz. The similarity of spectra at the three stations clearly demonstrates that the significant modulations at low frequency are path and site independent.

Various values for the phase velocity V were tested and it was found that 3000 m/sec gave good agreement for the Lg spectrum. The lower frequency parts of the theoretical spectrum (less than 5 Hz) are insensitive to velocity V and station azimuth θ. However, these parameters become increasingly important at higher frequencies, and must be taken into consideration.

A potential for error in the modeling of the high frequency spectrum exists because of uncertainty involving the detonation velocity and arrangement of the surface and downhole detonating cord. In the case of all four explosions, it is assumed that the time delays introduced by the detonating cord have negligable effect on the amplitude spectra at the relatively low frequencies where we have adequate signal/noise ratios. Modeling of the effect shows little impact on the spectra at frequencies less than 20 Hz if the detonation velocity is in excess of 6000 m/sec.

The Lg acceleration spectra for Explosions 2, 3 and 4 are shown in Figures 6 through 8. Although the exact charge weight distribution is in question for these explosions, the overall shape and the frequencies of peaks and troughs in the observed spectra match those of the theoretical spectra well. Again, the theoretical Lg spectra source wavelet corner frequency is 3 Hz, and the velocity assumed is 3000 m/sec.

The appearance of the spectra from all four explosions at frequencies less than about 7 Hz is readily explained in terms of two effects. The most obvious aspect of the spectra are the amplitude minima at approximately 1.2, 2.3 and 3.4 Hz. These are directly related to the apparent duration of the explosion sequence and coincide with the amplitude nulls in the amplitude spectrum of a boxcar (square wave) time function of duration T sec. The frequencies of the amplitude nulls are given by n/T, where n=1,2,3,... etc. The apparent duration T of Explosions 1 through 4 are 0.90,0.93,0.85 and 0.84 seconds, respectively.

The other major aspect of the observed spectra is the persistent strong amplitude peak near 5 Hz. This peak is the result of reinforcement due to a nominal row delay of 0.2 sec used in all of the explosions.

Earthquake Spectra

Two small earthquakes which occurred in eastern Kentucky provide an opportunity to compare spectra from known explosions and earthquakes over similar source-station paths (Figure 1). Figures 9 and 10 show the amplitude spectra of unclipped portions of the Lg phase from the earthquakes. Comparison with Figures 5 through 8 indicates that the earthquake acceleration spectra are much flatter than the explosion spectra, exhibiting larger amplitudes at high frequency (>6 Hz) relative to low frequency amplitudes (<6 Hz). Examination of the earthquake sonograms (Figures 11 and 12) shows no evidence of time independent spectral modulation.

CONCLUSIONS AND RECOMMENDATIONS

The surface mine explosions studied here produced signals at near regional distance featuring time independent spectral modulations of the type

previously reported by Baumgardt and Ziegler (1988), Smith (1989), Hedlin et al (1989), Baumgardt and Young (1990) and Hedlin et al (1990). The dominant features of the modulation are independent of recording site and source-station path. In contrast, natural earthquakes which occurred in the mine locale exhibit much flatter acceleration spectra, with substantially larger high frequency amplitudes, and show no evidence of time independent spectral modulation.

The explosion spectra were successfully reproduced at low frequency using a simple source model. The most obvious characteristics of the explosion spectra are amplitude minima controlled by the total duration of the explosion sequence, and amplitude reinforcement due to relatively long (0.2 sec) delays between the firing of multiple rows of explosives. The model spectra at low frequency are relatively insensitive to station azimuth and phase velocity. However, as frequency increases these parameters become important. Additionally, any random variation in the firing times of subexplosions strongly affects the high frequency spectrum. The agreement between the model Lg spectra and the observations is so good as to imply that for the study area at least, the Earth's transfer function for low frequency Lg waves is very simple: i.e., it acts primarily as an ideal low pass filter in terms of amplitude response.

REFERENCES

Baumgardt, D.R. and K.A. Ziegler (1988) Spectral evidence for source multiplicity in explosions: Application to regional discrimination of earthquakes and explosions. Bulletin Seismological Society America, 78 pp. 1773-1795.

Baumgardt, D.R. and G.B. Young, (1990) Regional seismic waveform discriminants and case-based event identification using regional arrays, Bulletin Seismological Society America, 80b, pp. 1874-1892.

Chapman, M.C. and M.J.B. Rogers (1989) Coda Q in the Southern Appalachians, Geophys. Res. Letters, 16, pp. 531-534.

E.I. du Pont de Nemours & Co. (1978) Blasters' Handbook, 16th Ed., du Pont Technical Services Section, Explosives Product Division, Wilmingtion, Delaware, 494 p.

Hedlin, M.A.H., J. B. Minster, and J.A. Orcutt (1989). The time-frequency characteristics of quarry blasts and calibration explosions recorded in Kazakhstan, USSR, Geophys. J. Int., 99 pp 109-121.

Hedlin M.A.H., J. B. Minster, and J.A. Orcutt (1990) An automatic means to discriminate between earthquakes and quarry blasts, Bulletin Seismological Society America, 80b, pp. 2143-2160.

Langefors, U. and B. Kihlstrom (1963) The Modern Technique of Rock Blasting, John Wiley and Sons, New York.

Smith, A.T. (1989) High-frequency seismic observations and models of chemical explosions: implications for the discrimination of ripple-fired mining blasts, Bulletin Seismological Society America 79 pp 1089-1110.

Stump, B.W. and R.E. Reinke (1988) Experimental confirmation of superposition from small scale explosions, Bulletin Seismological Society America, 78 pp. 1059-1073.

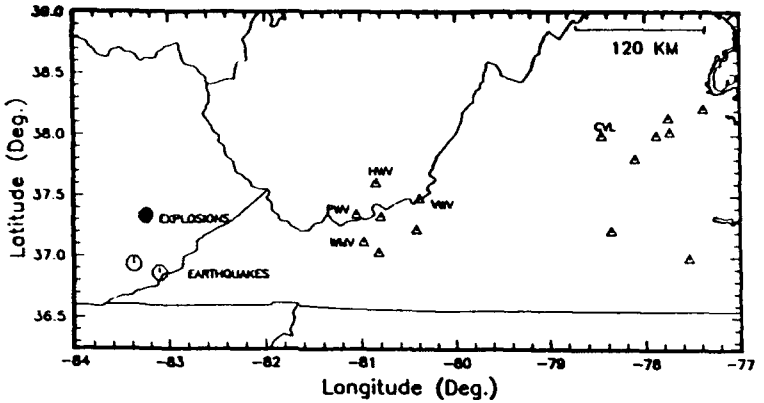


Figure 1: Location map showing network stations (open triangles) earthquake epicenters (open circles) and the location of four surface mine explosions (solid circle). Stations mentioned in the text are identified.

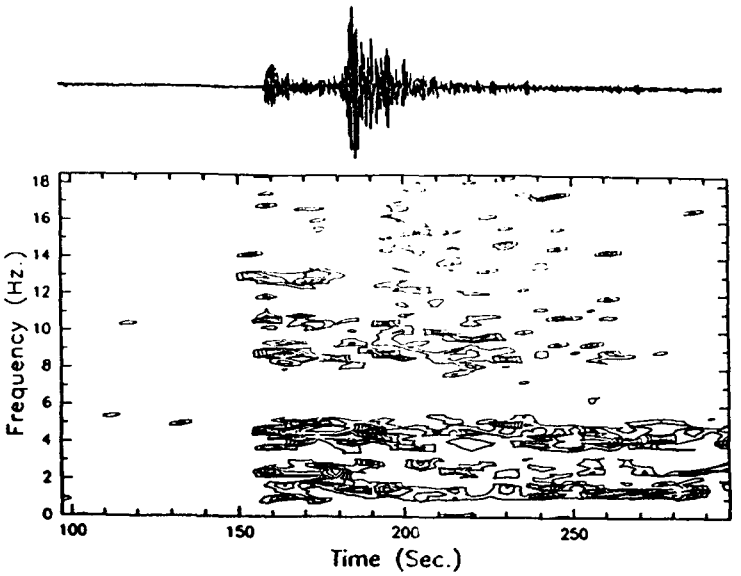


Figure 2: Time series (top) and sonogram (bottom) for Explosion 2.

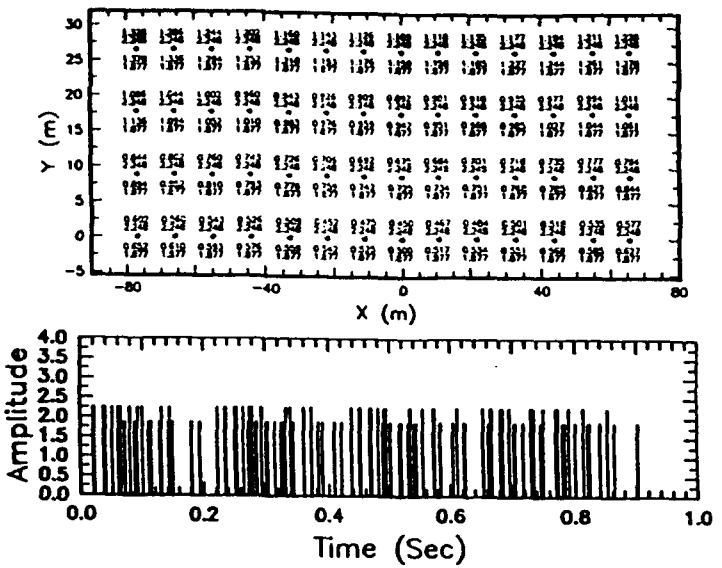


Figure 3: (Top) Charge pattern for Explosion 1 (plan view). Locations of each hole are indicated by small circles. Numbers above each circle indicate firing time (sec) of upper charge and charge weight (thousands of pounds), respectively. Numbers below circle refer to lower charge firing time and charge weight. (Bottom) Time series of Explosion 1, assuming station azimuth 307 deg, and phase velocity 3000 m/sec. Amplitude is charge weight in thousands of pounds.

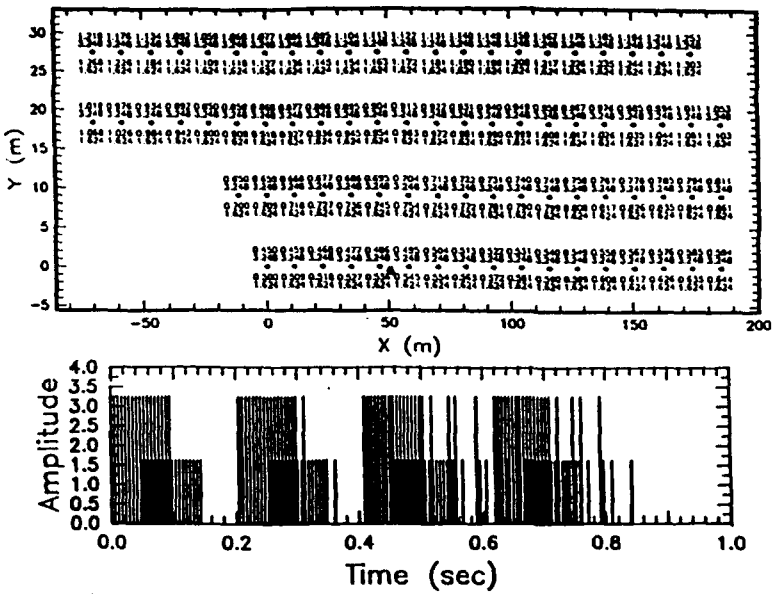


Figure 4: (Top) Charge pattern for Explosion 4 (plan view). Locations of each hole are indicated by small circles. Numbers above each circle indicate firing time (sec) of upper charge and charge weight (thousands of pounds), respectively. Numbers below circle refer to lower charge firing time and charge weight. (Bottom) Time series for Explosion 4, assuming station azimuth 125 deg and phase velocity 3000 m/sec. Amplitude is charge weight in thousands of pounds.

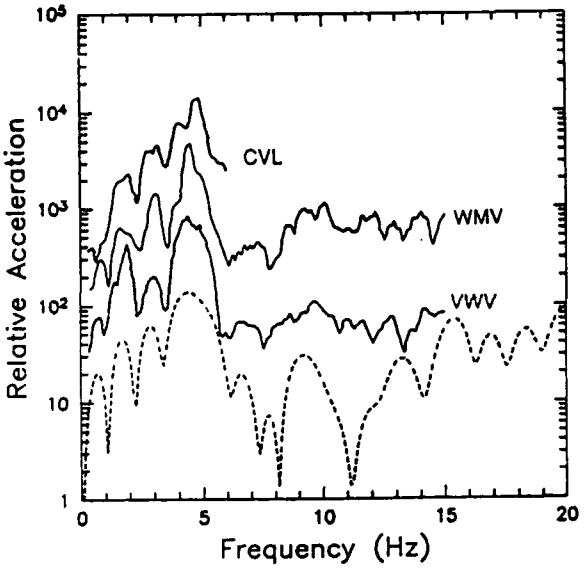


Figure 5: Solid lines show vertical component Lg acceleration spectra for Explosion 1 at stations CVL, WMV and VWV. Dashed line shows model spectrum. Amplitudes have been scaled to separate the spectra on the plot.

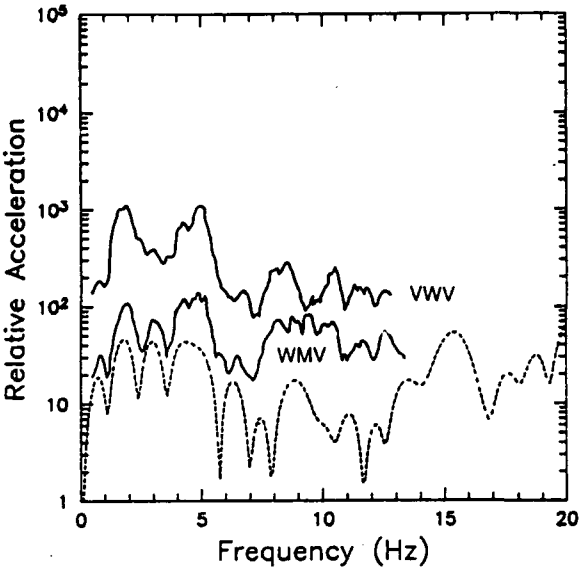


Figure 6: Solid lines show vertical component Lg acceleration spectra for Explosion 2, at stations VWV and WMV. Dashed line shows the model spectrum. Amplitudes have been scaled to separate the spectra on the plot.

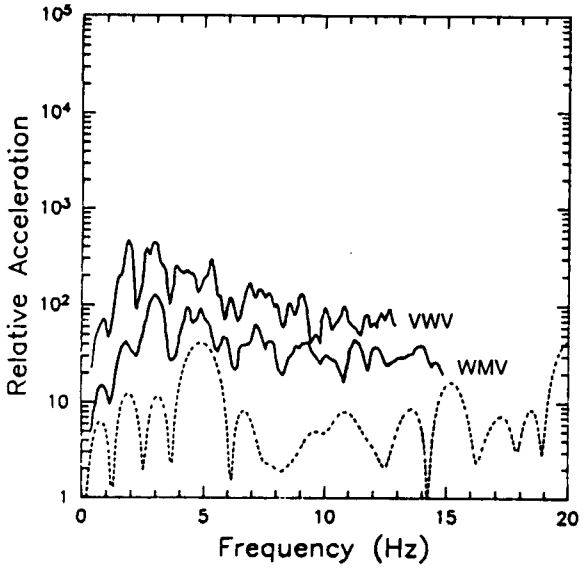


Figure 7: Solid lines show vertical component Lg acceleration spectra for Explosion 3, at stations VWV and WMV. Dashed line shows the model spectrum. Amplitudes have been scaled to separate the spectra on the plot.

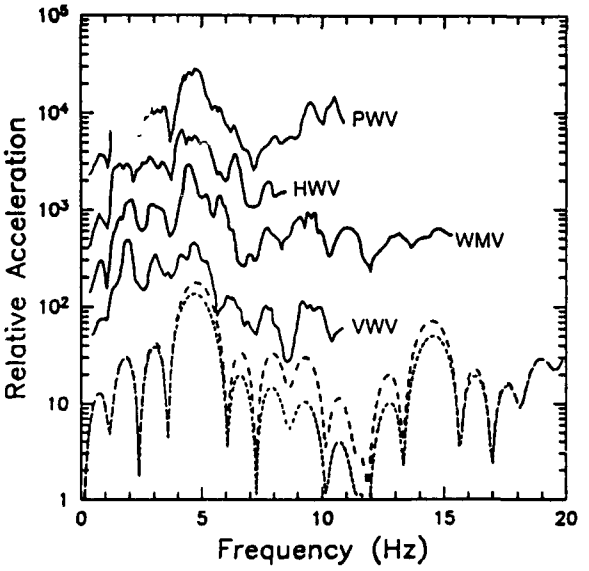


Figure 8: Solid lines show vertical component Lg acceleration spectra for Explosion 4, at stations PWV, HWV, WMV and VWV. Short dashed line shows the model spectrum, assuming that charges were decked. Long dashed line shows the model spectrum assuming that charges were not decked.

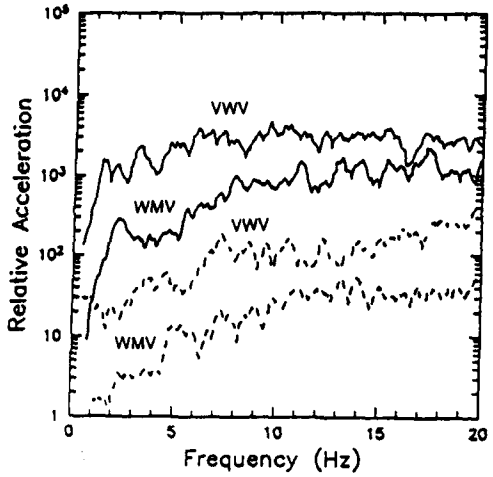


Figure 9: Solid lines show vertical component Lg acceleration spectra (unclipped) for the magnitude 3.5 Kentucky - Virginia border earthquake of November 27, 1987. Twenty second time windows were used, and the spectra were smoothed using a 4 point moving average filter. Dashed lines show the pre-P wave noise spectrum. The amplitudes have been scaled for separation on the plot: signal/noise ratios at the two stations are preserved.

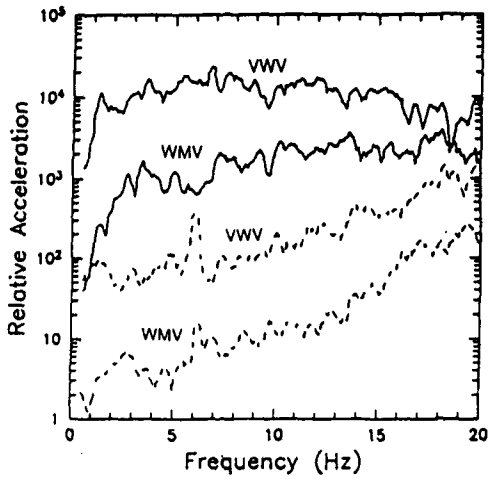


Figure 10: Solid lines show vertical component Lg acceleration spectra (unclipped) for the magnitude 4.0 Eastern Kentucky earthquake of August 17, 1990. Twenty second time windows were used and the spectra were smoothed using a 4 point moving average filter. Dashed lines show the pre-P wave noise spectrum. The amplitudes have been scaled for separation on the plot: signal/noise ratios at the two stations are preserved.

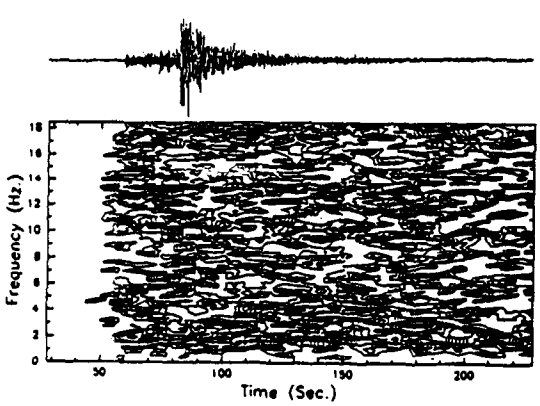


Figure 11: Time series (top) and sonogram (bottom) for the November 27, 1987 Kentucky - Virginia border earthquake.

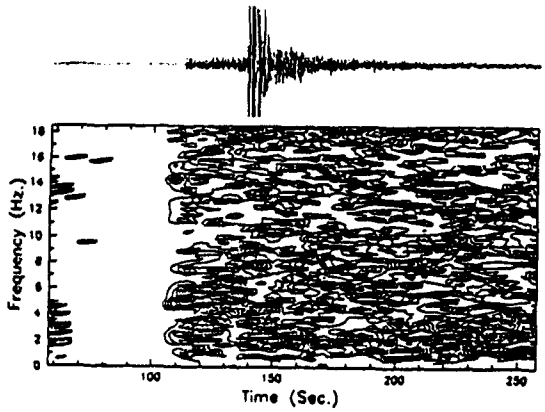


Figure 12: Time series (top) and sonogram (bottom) for the August 17, 1990 Eastern Kentucky earthquake.

RAY MODELING OF Lg ATTENUATION ACROSS MOUNTAINOUS REGIONS

Vernon F. Cormier
Department of Geology and Geophysics, Box U-45
University of Connecticut
Storrs, CT 06269-2045

Contract No. F19628-90-K-0043

OBJECTIVE

This paper summarizes a portion of a two year project titled "Crustal and Upper Mantle Gradients in the Vicinity of the Kazakh Test Sites and their Effects on Regional Discriminants." The objectives of this project are to investigate the effects of crustal structure, including the effects of velocity gradients, on the amplitude, frequency content, and decay with distance of regional seismic phases. To investigate the effects of velocity gradients, the locked mode method of seismogram synthesis is modified to incorporate the effects of velocity gradients within thick, vertically inhomogeneous layers. Crustal and upper mantle gradients in the vicinity of the Kazakh test sites will be modeled by comparing observed with synthetic seismograms computed by this method. The trial and error modeling will be supplemented by direct, linearized inversion of complete waveforms for crustal and upper mantle gradients. Particular emphasis will be placed on the effects of gradients on the Pn/Sn discriminant. Also included in this project is an effort to model the Lg phase by dynamic ray tracing and superposition of Gaussian beams in a laterally varying crustal waveguide. The effect of known surface topography and Moho topography inferred from the assumption of isostasy will be investigated for regional Lg paths from the Kazakh test sites.

RESEARCH ACCOMPLISHED

Locked Mode Synthesis with Gradient Layers. Cormier et al. (1991) describe the modifications of the locked mode method needed to incorporate gradients within layers. Initial testing of the effects of gradients confirms earlier work that found strong effects on interference head waves, Pn, and Sn. In a pass band of a SP-WWSSN seismograph, however, the synthetic seismograms of the first 10 Rayleigh modes (top of Figure 1) were found to be relatively insensitive to the details of crustal structure, including gradients within the crust. The gross characteristics of Lg in this pass band seem to be primarily sensitive to average crustal velocities and crustal thickness. Introduction of layers is not necessary unless there is compelling evidence for crustal discontinuities observed in the earlier time window of the regional seismograms in the form of refracted body waves and interference head waves.

Synthesis of Lg in 3-D Models by Dynamic Ray Tracing. Lg is synthesized as a sum of multiply critically reflected S waves in the crust (bottom of Figure 1). The crust has a constant P and S velocity overlying a homogeneous mantle. Topography of the Moho is

correlated with given or known surface topography under the assumption of Airy isostasy. The synthetics include geometric spreading and complex reflection transmission coefficients. Intrinsic attenuation, Lg/Sn interactions, and scattering by fine scale heterogeneities within the crust are ignored. The starting assumptions are essentially the same as those used by Kennett (1986) in identifying gross effects of crustal thickness on Lg by plotting the bounce points of critically reflected S waves in the crust. Here, however, waveforms are calculated and effects of geometric spreading are included by dynamic ray tracing (e.g., Červený, 1985).

Results obtained in experiments with a hypothetical mountain range found Lg transmission to be only weakly dependent on the angle of the path with respect to the strike of the mountain range (Figure 2), but more strongly dependent on the width of the crustal transition (Figure 3). Transmission across wider transition zones is more efficient because a shallower Moho dip reduces Lg leakage into the mantle. An upper bound on SV to SH conversion due to Moho topography was found for the case of sources and receivers within the mountain belt. The amount of SH energy, however, was too small to account for the equalization of Lg energy on all components of motion commonly observed from explosion sources.

In an experiment to test this approach against observed Lg data, we examined the data reported by Ruzaikin et al. (1977) for paths from receivers in the Tian Shan to sources in the Tibet Plateau (Figure 4). Source depths and radiation patterns are included from those published by Molnar and Chen (1983). Variations in Lg propagation are qualitatively predicted, including good agreement between observed and predicted Lg waveforms along paths having efficient transmission. The waveform agreement along weak paths is not as good. Transmission in the observed data is much weaker. We attribute the poorer comparison for the weak paths to the omission of intrinsic attenuation and/or basin interactions in the synthetic Lg's. Considering the results of Baumgardt (1991), the omission of basin interactions is probably the more serious effect. Since variations in surface topography are associated with strong variations in the distribution of sedimentary basins as well as with Moho topography, it is clear that Lg interactions with basins must be included in any ray based modeling. The omission of basin effects in forward modeling techniques may also explain the consistently greater mount of Lg blockage by mountain belts seen in observations compared to predictions.

CONCLUSIONS AND RECOMMENDATIONS

Details of crustal structure do not seem to have much of an effect on the peak amplitude and coda length of Lg in the frequency band up to 1 Hz. This result suggests that an adequate model to explain the gross features of Lg consists of a homogeneous crust having a thickness and average shear velocity representative of particular paths. Ray/beam modeling of Lg as a sum of multiply, critically reflected S waves demonstrates that Moho topography can have a profound influence on the efficiency of Lg propagation. Comparison of predicted with

observed Lg propagation suggest that near surface structure, such as sedimentary basins, must also be included together with Moho topography to completely explain the attenuation and efficiency of Lg propagation. Good qualitative comparison of Lg codas in the 1-2 Hz band along selected paths suggest that incorporation of finer scale three-dimensional structure in the Earth's crust may only be required to explain characteristics of Lg propagation in the frequency band above 1 Hz.

Future Lg work will be directed towards including the effects of basin structure in ray/beam modeling and the effects of finer scale crustal structure in ray/beam modeling. One possible approach would be to include the effects of fine scale structure by operators in in the (ω, k) domain estimated for individual S legs in the crust. These operators can be easily constructed in a plane layered crust. In a crust having fine scale variations in three dimensions, these operators can be estimated by finite difference calculations for single plane S waves incident at varying take-off angles on the Moho.

REFERENCES

Baumgardt, D.R., High frequency array studies of long range Lg propagation and the causes of Lg blockage and attenuation in the Eurasian continental craton, Final Report, PL-TR-91-2059(II), Phillips Laboratory, Hanscom AFB, MA, 1991.

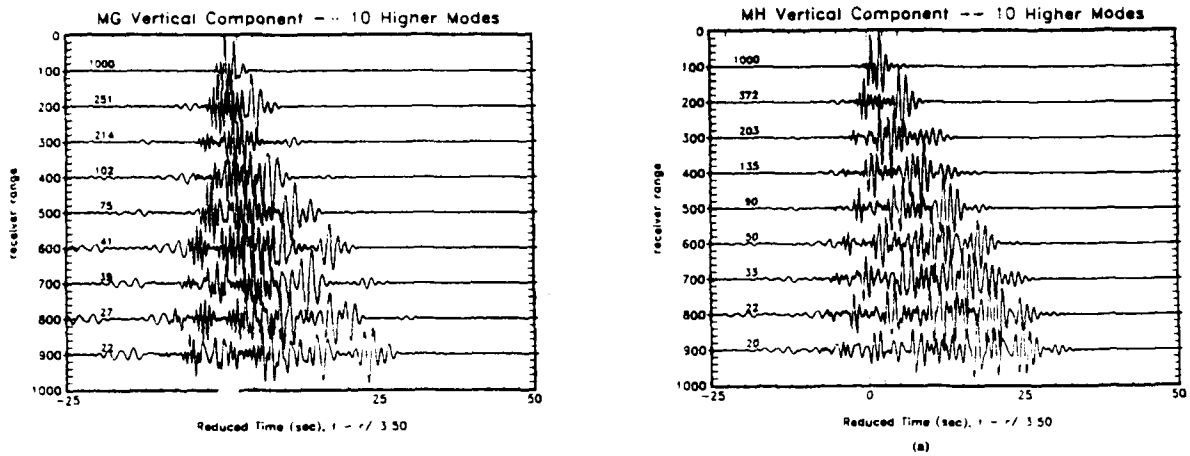
Cormier, V.F., B. Mandal, and D. Harvey, Incorporation of velocity gradients in the synthesis of complete seismograms by the locked mode method, *Bull. Seism. Soc. Am., 81*, 897-930, 1991.

Červený, V., The application of ray tracing to the propagation of shear waves in complex media, in *Seismic Exploration*, pp. 1-124, Treitel and Helbig, Vol. on Seismic Shear Waves, G. Dohr, ed., Geophysical Press, 1985.

Kennett, B.L.N., Lg waves and structural boundaries, *Bull. Seism. Soc. Am., 76*, 1133-1141, 1986.

Molnar, P., and W. Chen, Focal depths and fault plane solutions of earthquakes under the Tibetan Plateau, *J. Geophys. Res., 88*, 1180-1196.

Ruzaikin, A.I., V. Nersesov, V. Khalturin, and P. Molnar, Propagation of Lg and lateral variations in crustal structure in Asia, *J. Geophys. Res., 82*, 307-316, 1977.



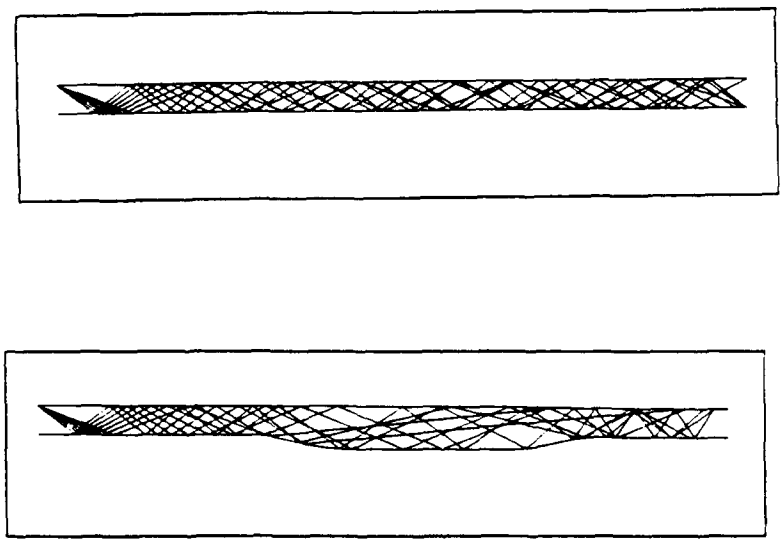
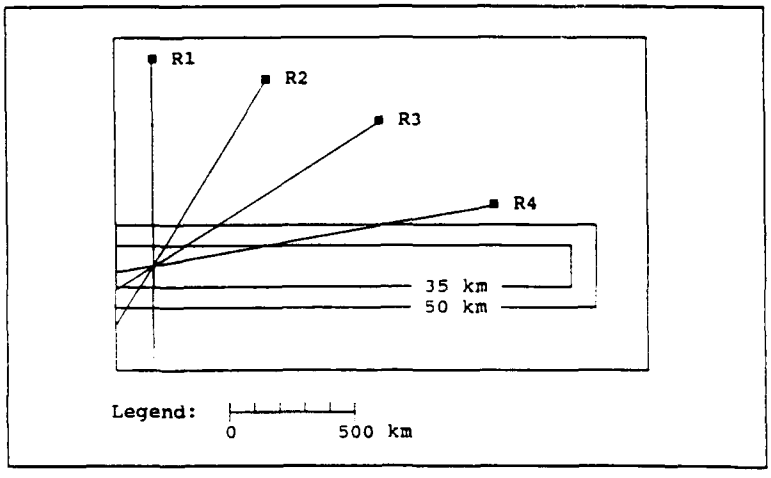


Figure 1: Above: A comparison of Lg waves synthesized by summing 10 Higher Rayleigh modes in two models of the crust. Model MH consist of two homogeneous layers. Model MG consists of a single crustal layer having a gradient. For details see Cormier et al., (1991). Below: ray paths of multiply, critically reflected S waves in a homogeneous plane layered crust (middle) and a crust having a deep root given by Airy compensation of topography. Surface topography in the botommost figure is not easily visible at the scale of the figure.



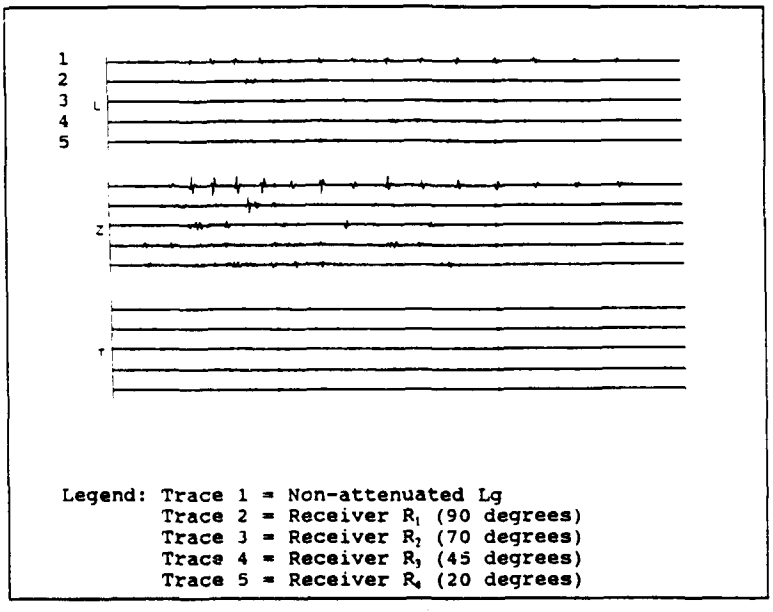
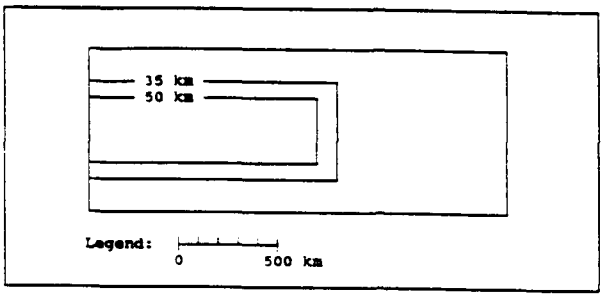
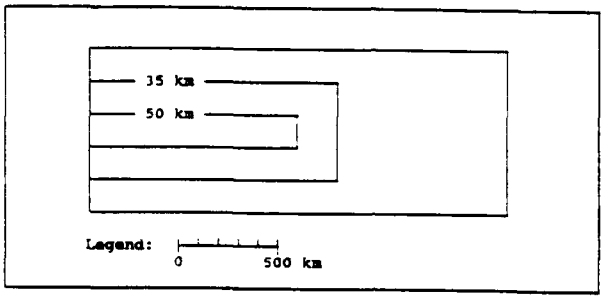


Figure 2: Above: effect of path angle of Lg with respect to the strike of a mountain range. R_1 is 90 degrees, R_2 is 70 degrees, R_3 is 45 degrees, and R_4 is 20 degrees. Receiver offset is 2000 km over all paths. Below: Synthetic seismograms from dynamic ray tracing of multiply, critically reflected S waves between the Moho and surface. All synthetics indicate strong attenuation and total energy is roughly the same for each of these paths.





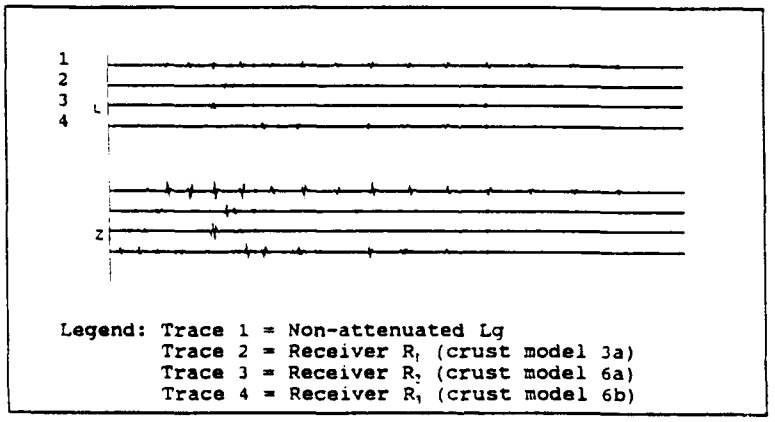
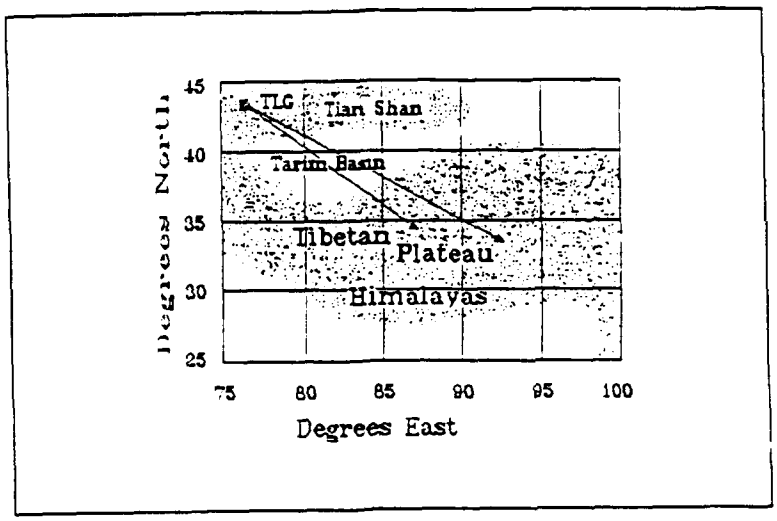
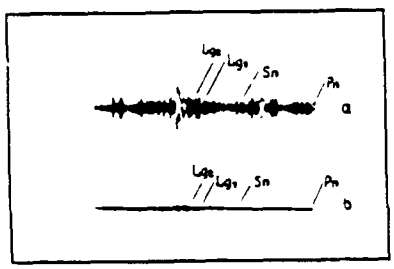
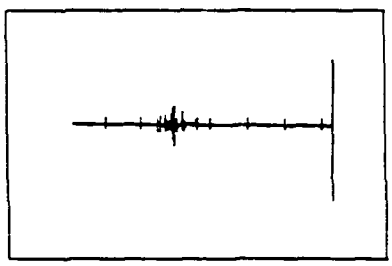
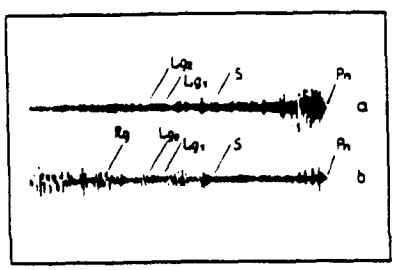


Figure 3: Above: effect of the width of crustal thickening and thinning. The The crust increases and decreases in thickness over transition regions of 100 km. (above) and 200 km (middle). Below: synthetic Lg wavetrains for a series of increasing transition zone widths of crustal thickness. Receiver offset is 2000 km in each case and the propagation paths are perpendicular to mountain strike. Weak Lg in traces 2 and 3 compared to strong Lg in trace 4 indicates that the width of the transition regions effects Lg efficiency more than does the overall width of a mountain root.









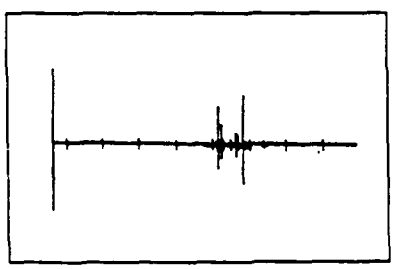


Figure 4: Above: map of Central Asia showing the propagation paths of two earthquakes modeled by ray methods. Shading highlights high mountainous regions of thickened crust. The left path gives a detectable Lg signal and is referred to as the strong path. Lg from the right earthquake is very weak. Middle: Central Asia strong path seismograms. The seismograms recorded from the left earthquake of the top figure show clear Lg energy in both the top (1.25-2.0 second period) and bottom (2.5-5.0 second) traces. The synthetic seismogram to the right of the observation figure compares well with the gross characteristics of the Lg coda. Bottom: Central Asia weak path seismograms. The seismograms are recorded at TLG from the right earthquake in the top figure. The synthetic seismogram of the weak path predicts energetic pulses that are not present in the actual recordings.

TITLE: MOMENT TENSOR INVERSION, YIELD ESTIMATION AND SEISMIC COUPLING VARIABILITY AT THE FRENCH CENTRE D'EXPERIMENTATION DU PACIFIQUE

AUTHORS: René CRUSEM and Yves CARISTAN

AFFILIATION: LABORATOIRE de DETECTION et de GEOPHYSIQUE
COMMISSARIAT A L'ENERGIE ATOMIQUE
BP 12 - 91680 BRUYERES-LE-CHATEL - FRANCE

CONTRACT N°: GRANT 90-0356

OBJECTIVE: to develop a precise and reliable yield estimation technique based on locally recorded waveform data (CRUSEM & CARISTAN 1991), which may be used for the Monitoring and Verification of underground nuclear tests.

RESEARCH ACCOMPLISHED:

DATA AND SEISMIC PROPAGATION MODEL

The three components of the surface ground velocity were digitally recorded at 100 Hz at four stations located within 8 to 22 km from about 50 buried nuclear tests at the French Centre d'Expérimentation du Pacifique (CEP). Typical seismograms and first motion hodograms are displayed in Figure 1. Figure 2 demonstrates that the first P-wave is off-azimuth and that back-azimuth residuals may exceed 30 degrees.

The procedure outlined by STUMP & JOHNSON (1977) was then followed: since the dimensions of the inelastic source region are small relative to the wavelengths and source-receiver distances of interest, the nuclear source is modeled by a second-order symmetric seismic moment tensor. The ground velocity at a given frequency is then the product of the moment rate tensor and the Green's functions of the medium.

For the CEP a 1D laterally-averaged horizontally-layered model was developed. It consists in four homogeneous layers (limestone, dolomite, aerial volcanic rock and submarine volcanic rock) overlying a basaltic bedrock (CRUSEM 1986). The flanks and the lagoon of the atoll were not modelled and no attenuation was introduced.

The Green's functions were calculated with a propagator-matrix technique using the discrete wavenumber summation of BOUCHON (1981). Real and synthetic data are shown for comparison in Figure 3 assuming a purely isotropic source. For these stations, the first seconds of the signal are well explained on the vertical components, but for later arrival times the fit is not so good. For the remaining stations the fit was even poorer and another seismic model should be used. Though this single 1D averaged model is clearly insufficient to explain the totality of the data, especially the observed tangential components, no three-dimensional model was used because knowledge of the true geological structure is incomplete and because computing complete Green's functions for fully 3D media is difficult. A more realistic approach used here is to introduce 'second order' corrections in an empirical and *a posteriori* manner.

UNKNOWNS AND DATA FOR THE INVERSION

Inverting for the whole moment rate tensor resulted in anisotropic source terms with maximum amplitudes comparable to the isotropic term (CRUSEM 1986) because the twelve signal components used for the inversion did not suffice to average out the effects of scatterring on lateral heterogeneities, so that the source terms were strongly biased by propagation effects (STUMP 1987). Also, the phase of the source was not well resolved, therefore the assumption was made that the spectral *amplitude* of the *isotropic* component of the moment rate tensor is the unique unknown of the inverse problem.

The data components which could not be satisfactorily explained by such a model were then discarded and, in practice, only the vertical records at two stations were used. A 10.24 seconds long time window was chosen on each record, and the seismograms were multiplied by a decreasing exponential function. This was required by the method used to compute the Green's functions and served also to reduce the sensibility of the deconvolved source to the late and poorly modeled arrivals. The spectra obtained when Fourier-transforming such a signal are termed 'pseudo-spectra'.

PSEUDO-SPECTRA OF THE DECONVOLVED SOURCE

The isotropic source term was obtained for each test using a linear deconvolution technique based on the stochastic inverse (JACKSON 1972). The inversion was done in 1.17 Hz wide overlapping spectral windows consisting in 13 discrete frequencies. In each window the modulus of the pseudo-spectrum was supposed to be constant so the problem was largely overdetermined and the inversion was quite stable. No comparison of real and synthetized seismograms was made since the phase of the source remained unknown. However in each spectral window 60 to 80 % of the data could usually be explained by the solution of the inverse problem. Figure 4 displays one representative example of the deconvolved source, whose shape is close to most published nuclear source models.

REDUCED DISPLACEMENT POTENTIAL AND YIELD ESTIMATION

The long period level of the (pseudo-)spectrum of the isotropic moment rate was converted to the static temporal value Ψ_∞ of the reduced displacement potential (MULLER 1973). For an overburied and fully coupled explosion in a given medium, Ψ_∞ is supposed to be only a function of $Yh^{-1/3}$ where Y is the yield and h is the depth of burial. Such a scaling law is close to the results obtained by LAY & al. (1984) at Amchitka Island, and is not too different from MUELLER & MURPHY (1971). Based on 20 nuclear tests with known radiochemical yield Y_r, the following mean regression was then obtained for the CEP:

$$Y_r\, h^{-1/3} \# K\, \Psi_\infty{}^{0.92\pm0.04} \qquad (1)$$

The fact that the exponent of Ψ_∞ in (1) is less than 1 may be due to contamination of the low frequency part of the pseudo-spectrum by the peak at corner frequency, or to differences between the pseudo-spectrum and the true spectrum.

Yields estimated using (1) are termed **apparent seismic yields** Y_{as}. Their standard error is close to 30%. The errors are not distributed normally because of systematic differences between the *models* used in this study and the *true* phenomena occuring in the geological media during a buried nuclear test.

GLOBAL COUPLING INDEX

In order to quantify these biases, the exponent of Ψ_∞ in (1) was supposed exact and independent of source and propagation-path properties, and a **global coupling index** I_{gc} was defined for each test by:

$$I_{gc} = (K\, \Psi_\infty{}^{0.92}) / (Y_r\, h^{-1/3}) = Y_{as} / Y_r \qquad (2)$$

Supposing further that source and propagation effects can be separated, I_{gc} is written in the form:

$$I_{gc} = I_s \cdot I_p + N \qquad (3)$$

where I_s is the **source-coupling index**, depending only on the source medium properties, I_p is the **apparent propagation index** depending on the differences between the 1D averaged seismic model and the real earth, and N is an unbiased noise term.

Since the decomposition in (3) is not unique, additional assumptions are necessary. First a regression analysis of I_{gc} over source media properties alone is performed and, supposing that propagation effects average out, this leads to the 'theoretical' source-coupling index I_s. An estimate of the propagation index I_p can then be computed on a source-by-source basis using (3). The next step consists in working on the geographical distribution of I_p in order to bring out some zoning of the site based on propagation effects alone. From these smoothed I_p values updated I_s values are then obtained using (3) again and the process is repeated until convergence is achieved.

SOURCE-COUPLING AND PROPAGATION INDEXES

The source media at the CEP are saturated and extremely heterogeneous, and no data are available below and laterally around the working point. However, total densities measured in the emplacement hole over several tens of meters above the working point rarely varied by more than 30%. So the total in situ density averaged over such a distance was chosen as *the* parameter to characterize the source medium. The regression analysis between source-coupling index and average density then results in a smooth exponentially decaying relation, with an overall variation of about a factor two and a standard deviation of 0.1.

The propagation index is found to vary between 0.7 and 1.8 at the CEP. Depending only on source-receiver distances, four different geographic zones of propagation could be distinguished. The standard deviation of the propagation index is less than 0.15 for each zone, except for one zone where only four tests were detonated.

DISCUSSION OF THE RESULTS

Once the seismic signals from a new test are available, Ψ_∞ is computed and an estimate of the apparent seismic yield Y_{as} is obtained. If the average working point density is known, a corrected **seismic yield** Y_s follows when taking into account the *a priori* estimated global coupling index I_{gc}:

$$Y_s = Y_{as} / I_{gc} \qquad (4)$$

This technique was calibrated against 20 reference nuclear tests and was then used in operational conditions for 30 other tests. This resulted in a clear increase in confidence, as shown in Figure 5: the standard error for the *corrected* yield estimates is 13%.

Source-coupling efficiency decreases when maximum material strength, air filled porosity or overburden pressure increase (LARSON 1982). At the CEP, low density media correspond to ductile clayey material and high density media correspond to basaltic rock; air filled porosity plays no role and, for volcanic hard rock, maximum material strength is related to density. So it is thought that source-coupling efficiency *can* be related to the *unique* total density. Since water is probably the best coupling material a high density medium (i.e. with low water content and high material strength) should have a lower source-coupling index, as is indeed indicated by our results.

Variations in apparent propagation effects at the CEP are consistent with body-wave magnitude anomalies documented for other test sites, for instance the Nevada test site (LYNNES & LAY 1990). As the wavelengths of interest are a few kilometers, the empirical geographic zoning obtained here should correlate with the gross three-dimensional geology of the CEP. In fact, two of the zones correspond to the main volcanic structures of the atoll, and one zone corresponds to a caldeira-like structure separating the two volcanoes. Also, the apparent propagation index is larger in the narrowest part of the site: this may be due to the focussing of seismic waves on the flanks of the atoll.

CONCLUSIONS AND RECOMMENDATIONS:

When using locally recorded data at a well calibrated and well known test site and taking into account empirical corrections for source-coupling and propagation-path effects, yield may be estimated by seismic methods with an uncertainty significantly less than 30% at the 95% confidence level. This is comparable to the accuracy obtained with CORRTEX (MORRISON 1987). Improvements of this method at the CEP are now dependent on increased knowledge of source and propagation medium properties.

One practical problem remains unsolved: since the contours of the empirical zones of propagation are not known precisely, the a priori estimated I_p may sometimes be ambiguous. Therefore further research based on numerical simulations of seismic wave propagation in heterogeneous 3D media is necessary to understand and quantify the relationships between our observations and the geological structure of the site.

Concerning source-coupling efficiency, BOCHAROV & al.(1988) have indicated that informations on coupling may sometimes be obtained from the high frequency characteristics (i.e. corner frequencies) of the source, or from it's location and depth of burial, but this was not observed at the CEP. Our empirical results should rather be confirmed and explained using hydro- and elasto-dynamic computer simulations.

REFERENCES:

BOCHAROV, V. S., M. N. GEORGIEVSKII, V. V. KIRICHENKO, and A. B. PESHKOV (1988). Estimation of the power of underground nuclear explosions taking account of their actual seismic efficiency, Sov. Atomic Energy 65, 653-659.

BOUCHON, M. (1981). A simple method to calculate Greens functions for elastic layered media, Bull. Seismol. Soc. Am. 71, 959-971.

CRUSEM, R. (1986). Simulation de signaux sismiques et étude de sources nucléaires souterraines par inversion de moments, Thesis, Ecole Centrale des Arts et Manufactures, Chatenay-Malabry, FRANCE.

CRUSEM, R. and Y. CARISTAN (1991). Moment tensor inversion, yield estimation and seismic coupling variability at the French Centre d'Expérimentation du Pacifique, Bull. Seismol. Soc. Am. (submitted).

JACKSON, D. D. (1972). Interpretation of inaccurate, insufficient and inconsistent data, Geophys. J. R. astr. Soc. 28, 97-109.

LARSON, D. B. (1982). Explosive energy coupling in geological material, Int. J. Rock Min. Sci. & Geomech. Abstr. 19, 157-166.

LAY, T., D. V. HELMBERGER, and D. G. HARKRIDER (1984). Source models and yield scaling relations of underground nuclear explosions at AMCHITKA ISLAND, Bull. Seismol. Soc. Am. 74, 843-862.

LYNNES, C. S. and T. LAY (1990). Effects of lateral velocity heterogeneity under the Nevada Test Site on short-period P-wave amplitude and travel times, PAGEOPH 132, 245-268.

MORRISON, D. C. (1987). Test Ban Compliance: is seismology enough?, Science 236, 383-386.

MULLER, G. (1973). Seismic moment and long-period radiation of underground nuclear explosions, Bull. Seismol. Soc. Am. 63, 847-857.

MUELLER, R. A. and J. R. MURPHY (1971). Seismic characteristics of underground nuclear detonations. Part. I. Seismic spectrum scaling, Bull. Seismol. Soc. Am. 61, 1675-1692.

STUMP, B. W. and L. R. JOHNSON (1977). The determination of source properties by the linear inversion of seismograms, Bull. Seismol. Soc. Am. 67, 1489-1502.

STUMP, B. W. (1987). Mathematical representation and physical interpretation of a contained chemical explosion in alluvium, Bull. Seismol. Soc. Am. 77, 1312-1325.

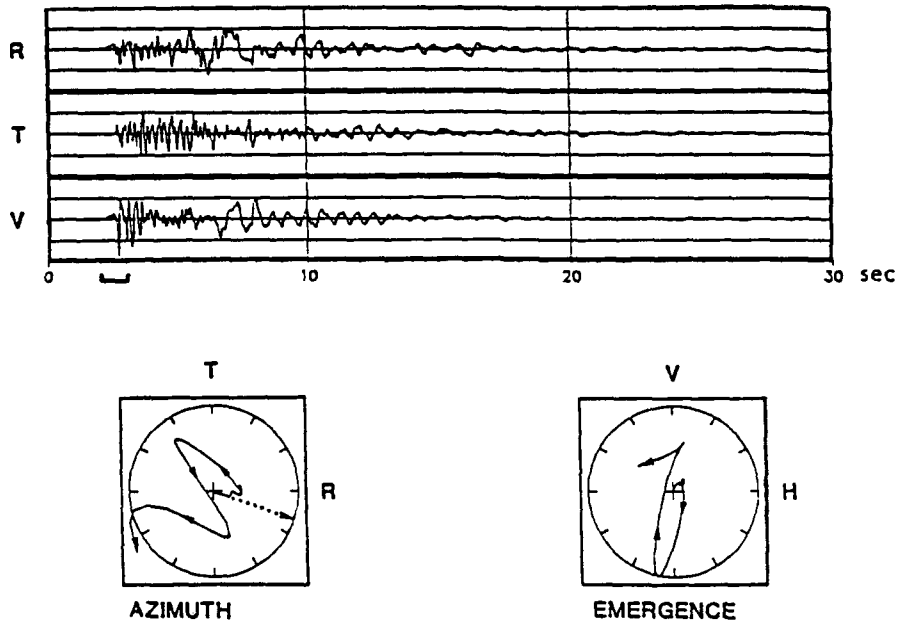


FIGURE 1: Ground motion velocity records and first motion hodograms for an underground nuclear explosion detonated at the CEP. The source-receiver epicentral distance was close to 8.5 km. The 3 components of data (Radial, Tranverse and Vertical) are shown at the same scale. The radial component is oriented towards the source and the window used for the hodograms is indicated. Note the prominent surface waves on the radial and vertical components at about 7 sec and the off-azimuth P-wave arrival.

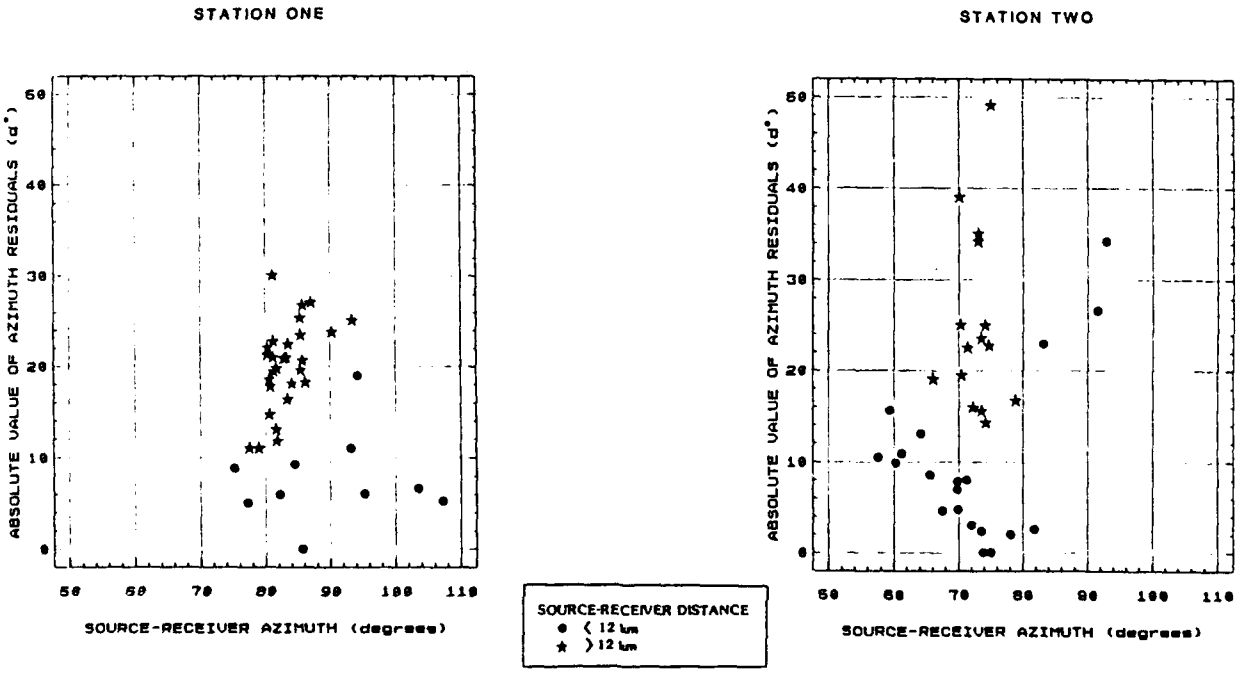


FIGURE 2: Variation of absolute values of P-wave back-azimuth residuals with source-receiver azimuth at stations ONE and TWO separated by 3 km. Back-azimuth residuals were estimated with a confidence of about 5 degrees. Source-receiver distance effects and recording-site effects are clearly observed.

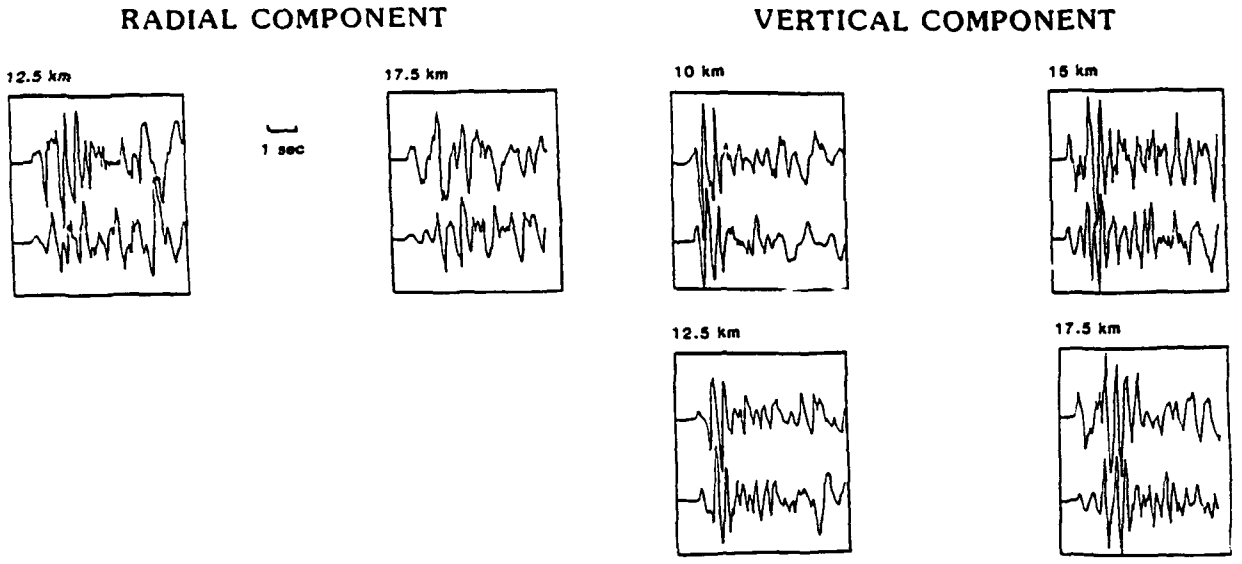


FIGURE 3: Comparison of the observed (upper trace) and synthetic (lower trace) velocity waveform data for stations ONE and TWO. Approximate source-receiver distances are indicated and the vertical scale is arbitrary. The real data are not for the same nuclear source while the source used for the synthetics is the same for all the plots. It's corner frequency is 2 Hz and it's high-frequency spectral slope is -3.

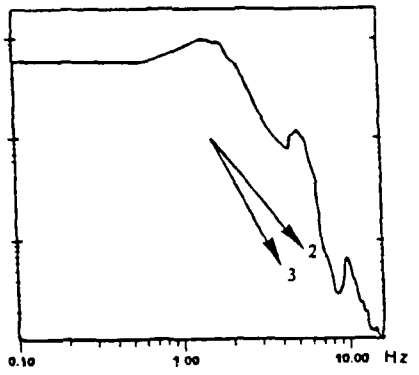


FIGURE 4: One example of the deconvolved isotropic component of the seismic moment rate tensor for an underground nuclear test detonated at the CEP. The modulus of the pseudo-spectrum smoothed over 1.17 Hz wide overlapping spectral windows is shown. Theoretical high-frequency spectral slopes of 2 and 3 are indicated.

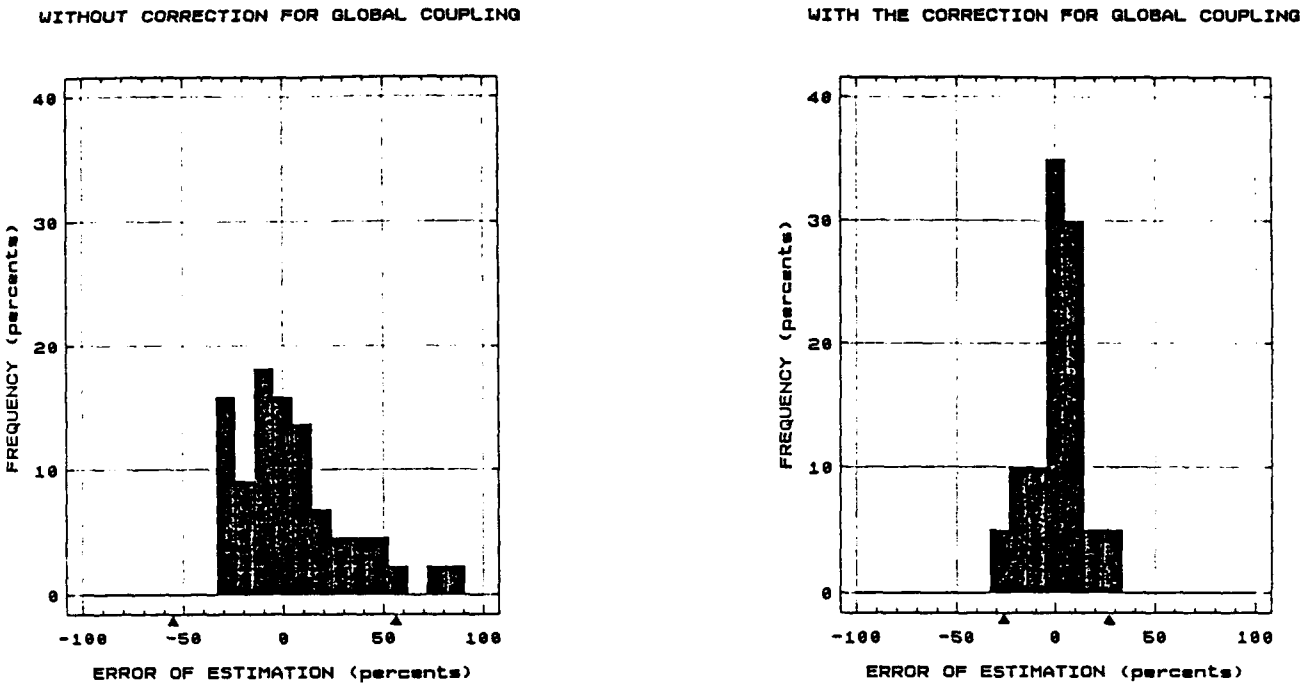


FIGURE 5: Comparison of the distribution functions of the yield estimation errors obtained without applying the corrections for source-coupling efficiency and propagation effects (left plot) and with these corrections (right plot). Errors are given in percents relative to the radiochemical yield. The two-sigma error bars are indicated (triangles).

BROADBAND STUDIES OF SEISMIC SOURCES AT REGIONAL AND TELESEISMIC DISTANCES USING ADVANCED TIME SERIES ANALYSIS METHODS

Zoltan A. Der, R.H. Shumway, Douglas R. Baumgardt
Michael R. Hirano and Eric A.Worthington
ENSCO, Inc., 5400 Port Royal Road
Springfield, Virginia 22151

Contract No.:
F19628-89-C-0030

OBJECTIVE

The objective of the work was to explore various new ways for utilizing and inverting seismic data by systematically exploiting the broadband information contained in the signals rather than attempting to model the often narrowband raw waveforms in the time domain. The emphasis is on information transmission capability in the sense defined by Shannon (Goldman, 1953). The study consist of four main parts. In the first, we explore applications of linear system (transfer function) methodologies to the analyses of sources of regional signals; in the second, we reevaluate various methods for estimating pP parameters from teleseismic P waves; in the third, we assess the spatial resolution obtainable from source studies; and in the fourth, we apply the findings for optimum filtering of regional and teleseismic records. The overall objective of all these studies is to improve our capabilities of seismic monitoring of nuclear explosions.

RESEARCH ACCOMPLISHED

Study of Regional Waveforms and Spectra

Under this task we endeavored to circumvent the difficulties of estimating reliable and realistic Green's functions for regional propagation paths. Instead of the forward modeling approach in which we attempt to model seismic traces, we regard the seismic recordings as outputs of single and multiple channel linear filter systems in which random time-series (Green's functions) are passed through short FIR sets of filters (moment tensor time functions). Multiple paths to various sensors in an array or small network are regarded as resulting in independent realizations of such processes. It turns out that even though we do not know either the Green's functions or the source time functions, and that we probably shall never know them well enough to model the details of seismic waveforms, it is possible to tests various scenarios in propagation and deduce some attributes of sources. The tools for such analyses consist of methods developed for analyzing linear systems, single- and multi-channel transfer functions and coherences.

A central theme of the techniques developed is spectral factorability, i.e., the fact that spectra of arrivals observed at a small array for a group of closely spaced events can be written as products of source and site response functions. This opens a way for relative studies of sources using recordings at multiple sites. The efficiency of factoring can be tested by comparing the original data traces with those reconstructed from the source and site spectral factors using various kinds of coherence measures.

Based on various considerations involving time series analysis, factorability and reciprocity, the following diagnostics, with respect to the analysis of seismic sources using array data, were postulated and can be summarized as follows:

a) Events with nearly identical waveforms - closely spaced events with identical mechanisms and source time functions.

b) Waveforms different but spectrally factorable, inter-event transfer functions can be characterized by short FIR filters and these are valid for *several* regional phases, inter-event coherences are high - closely spaced events with similar source mechanisms, but different source time functions.

c) Waveforms different but spectrally factorable, inter-event transfer functions are *not the same* for different regional phases, inter-event coherences are high for the same phases and spectral modulation patterns shift with the dominant phase velocities of the respective arrivals - events with similar source mechanisms, but different source time functions with sources of moderate spatial extent.

d) Waveforms different and spectrally factorable, but short FIR filters cannot describe the inter-event transfer functions (low inter-event coherences) - events with similar mechanisms, still grouped tightly, but not very closely spaced.

e) Not factorable, but high multiple coherences within a group of events - closely spaced events with different mechanisms.

f) Not factorable, low multiple coherences - different mechanisms and/or large spatial separations.

Our work, during the last two years, demonstrated that several of the expected properties described above are indeed exhibited by real data. In particular, the factorability concept, a key feature for the kinds of analyses we propose, is valid for the Pn and Lg phases recorded at regional distances at NORESS, as evidenced by comparisons of some reconstructed waveforms with actual Pn phases in *Figure 1*. We have also found that Pn waveforms of some event pairs at the Titania mine can be transformed into each other simultaneously at all sensors with simple common short FIR filters. For the same event pair a single short filter designed from the *whole seismogram* increased the waveform similarity expressed in terms of the site-averaged correlation coefficient from 0.04 to near 0.7. For other event pairs this could not be done, despite the fact that all would factor well for individual arrivals. Moreover, we have found that events at the Estonian mine, designated as E9, fell into two categories with respect to the effectiveness of factorability. The Lg phases from some events, while still located at the same mine, did not reconstruct well when factored with a group of others (*Figure 2*). On closer examination, we have found that these had slightly different Lg envelope shapes, a feature that was very subtle and could have gone unnoticed. This may point to a different modal composition for their Lg phases (and source mechanism).

An interesting phenomenon observed for several quarry blasts on the Kola Peninsula is spectral modulation that shifts with the average phase velocities of the respective arrivals (*Figure 3*) which seems to have an explanation under the item c) above. This seems to be the first observed indication of source multiplicity where the simultaneous sources are spatially separated. Inversion of such patterns for source spatio-temporal configurations requires multiple arrays at various azimuths from the source. Previously observed modulation patterns for Norwegian mines tended to be identical for the various arrivals indicating that the spectral modulation for those events was due to common temporal patterns of events at nearly the same location (Baumgardt and Ziegler, 1988).

Further Studies of the pP Problem

The basic motivation for determining parameters of secondary arrivals, such as pP in P waves from nuclear explosions, is to find out whether pP has any direct effect on the yield estimates derived from the data. Moreover, for inaccessible test sites, any information with regards to the circumstances for testing, such as source depth, may be useful. For instance, knowing the depth, one

may obtain indirect information about the source medium and coupling. Factors that complicate the inversion of P waves for pP parameters are the existence of receiver transfer functions, noise, bandwidth limitations due to Q and the possibility of additional phases (such as spall) in the P waves.

We have reevaluated several methods for the estimation of pP parameters. Spectral methods assume that the modulations in the shapes of P wave spectra are due to P-pP interference from which the pP delay times and amplitudes are determined by some kind of fitting procedure. Computing the spectra essentially discards the phase information in the signals and the underlying P+pP interpretation of the spectra has to be verified by some techniques that uses the appropriate phases. Intercorrelating (Lay, 1985) a suite of waveform pairs from two events recorded at common sites using pP parameters estimated from spectra shapes fails to equalize the waveforms (*Figure 4*) thus, indicating that spectral modulations are caused by arrival patterns more complex than simple P-pP interference. Comparing the similarity of waveforms for NTS events by using a coherence measure showed that the P-pP modulation models leaves 30-40% of the P wave energy unaccounted for.

Testing of the intercorrelation method using the pP results derived from a suite of narrowband WWSSN data for NTS events by Lay (1985) showed that these results account for somewhat more of the signal energy, but the results are statistically not significant because of the low time-bandwidth product of such data sets. It appears, thus, the simplistic P-pP interference model does adequately fit most NTS data.

For Kazakh events numerous studies reported spectral nulls at various frequencies, but it appears that most nulls are generally not consistent from site to site (*Figure 5*). The set of spectra shown for a Shagan event appears to have a reasonably consistent null only at 2 Hz. This would correspond to a pP delay of .5 sec, a value also consistent with some deconvolution results (Der et al, 1987) for Shagan. Similar tests for Degelen events failed to shown any consistent nulls. We are continuing our evaluation of pP results for various test sites including Novaya Zemlya.

Investigation of the Resolution of the Inversion of Spatial Structures of Seismic Sources

The inversion of the spatial structures of a seismic source can be formulated in a manner similar to F-K analysis (Baggeroer et al, 1988). Various types of algorithms were proposed for this purpose, many of which had been previously used in F-K analysis (Capon, 1969; Shumway, 1988). We have adopted Shumway's method (Shumway, 1988) and performed tests of the obtainable resolution for a typical problem of source inversion based on long period body waves. We have found that the resolution of the spatial details of sources in such studies is generally grossly overestimated and many results given in the literature may not be statistically significant (Der et al, 1991).

Optimum Processing of Array Data

Past attempts for increasing the S/N ratios of seismic signals by optimum array processing were frustrated by two factors:

a) Distortion of seismic signals by geologic structures near the receivers degraded the similarity of signals resulting in a loss of signal amplitude at beaming.

b) Nonstationarity of the background noise made it difficult to characterize the noise statistically using long noise samples.

Utilizing the fact that source and site spectral factors can be derived from large sets of seismograms, we attempted to reduce the signal loss in beaming by equalizing seismograms across

arrays. At the same time we also applied adaptive optimum filtering to reduce the problems associated with the second factor above (Booker and Ong, 1971).

We have found that 4-6 dB improvement over simple beam processor could often be achieved at NORESS and EKA. Such gains are worth the additional computational complexity in special application.

CONCLUSIONS AND RECOMMENDATIONS

The research presented in this paper describes various frequency domain methodologies for utilizing the full information allowable within the given S/N ratios in seismic signals. Broadband processing of regional seismograms has the potential to derive source diagnostics from details of waveforms not otherwise obtainable. The tools for such analyses are those developed for standard analyses of linear systems. Further analyses of the pP problem revealed that the P-pP model cannot adequately describe P wave seismograms from NTS, but may do so for the Shagan and Novaya Zemlya test sites. A methodology for inversion for the spatial configuration of large earthquakes was also developed. The results of these studies point to the inadequacy of the direct time domain waveform modeling methods and the necessity of more quantitative assessment of the reliability of source inversions.

REFERENCES

Baggeroer, A.B., W.A. Kuperman and H. Schmidt (1988). Matched-field processing: Source localization in correlated noise as an optimum parameter estimation problem. *J. Acoust. Soc. Am.*, **83**, 571-587.

Baumgardt, D.R. and K.A. Ziegler (1988). Spectral evidence for source multiplicity in explosions, application to regional discrimination of earthquakes and explosions, *Bull. Seism. Soc. Am.*, **78**, 1773-1795.

Booker, A. and C.Y. Ong (1971). Multiple constraint adaptive filtering. *Geophysics*, **36**, 498-509.

Capon, J. (1969). High resolution frequency-wavenumber analysis. *Proc IEEE*, **57**, 1408-1412.

Der, Z.A., R.H. Shumway and A.C. Lees (1987b). Multi-channel deconvolution of P waves at seismic arrays. *Bull. Seism. Soc. Am.* **77**, 195-211.

Der, Z.A., M.R. Hirano and R.H. Shumway (1990). Coherent processing of regional signals at small seismic arrays. *Bull. Seism. Soc. Am.*, **80**, 2161-2176.

Der, Z.A., R.H. Shumway and M.R. Hirano (1991). Time domain waveform inversion: A frequency domain view. How well do we need to match waveforms? *Bull. Seism. Soc. Am.*, (In press).

Goldman, S. (1953). *Information Theory*. Prentice Hall.

Lay, Thorne (1985). Estimating explosion yield by analytical waveform comparison. *Geophys. J.*, **83**, 1-30.

Murphy, J.R. (1989). Network averaged teleseismic P-wave spectra for underground explosions: Part II. Source characteristics of Pahute Mesa explosions. *Bull Seism. Soc. Am.*, **79**, 156-171.

Shumway, R.H. (1988). *Applied Statistical Time Series Analysis*. Prentice Hall.

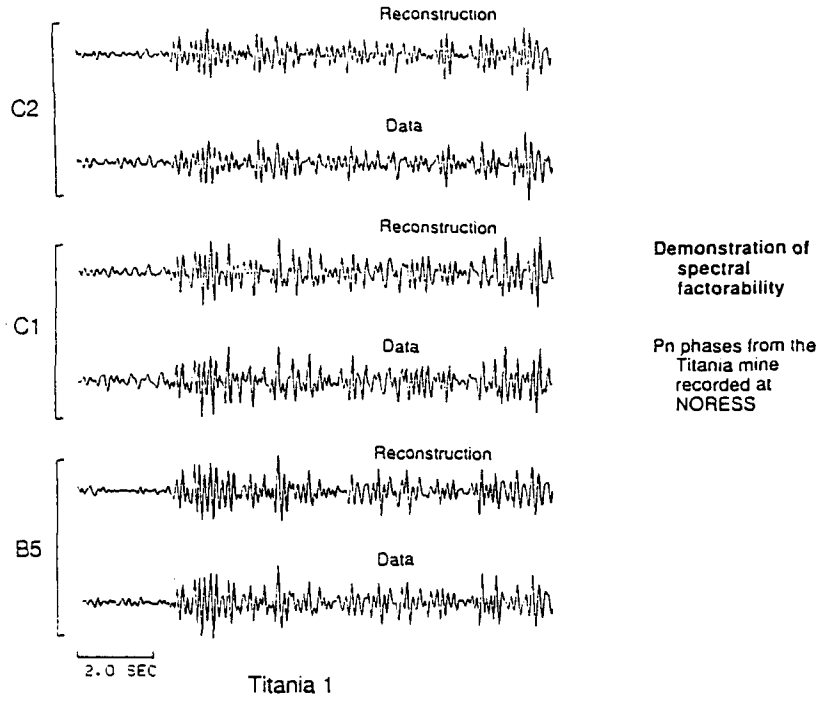


FIGURE 1: Selected reconstructed and data traces of Pn arrivals from the Titania1 event. The designation C2 refers to the second sensor in the C ring of NORESS, etc.

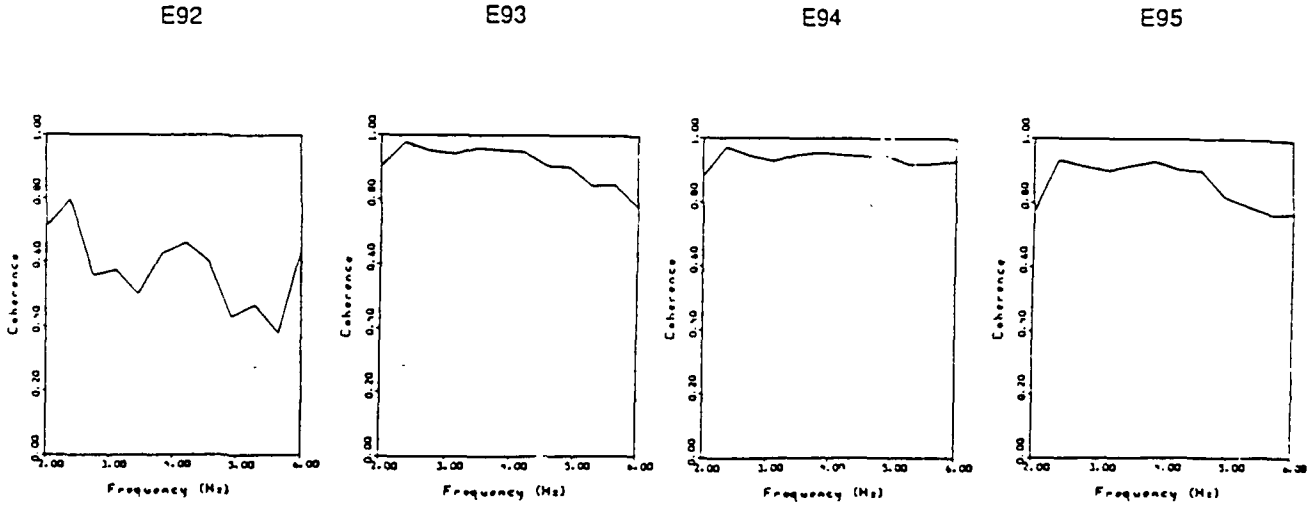


FIGURE 2: Site-averaged coherence results from the joint factorization of four E9 events with reconstructions of one event factors much less well than the others.

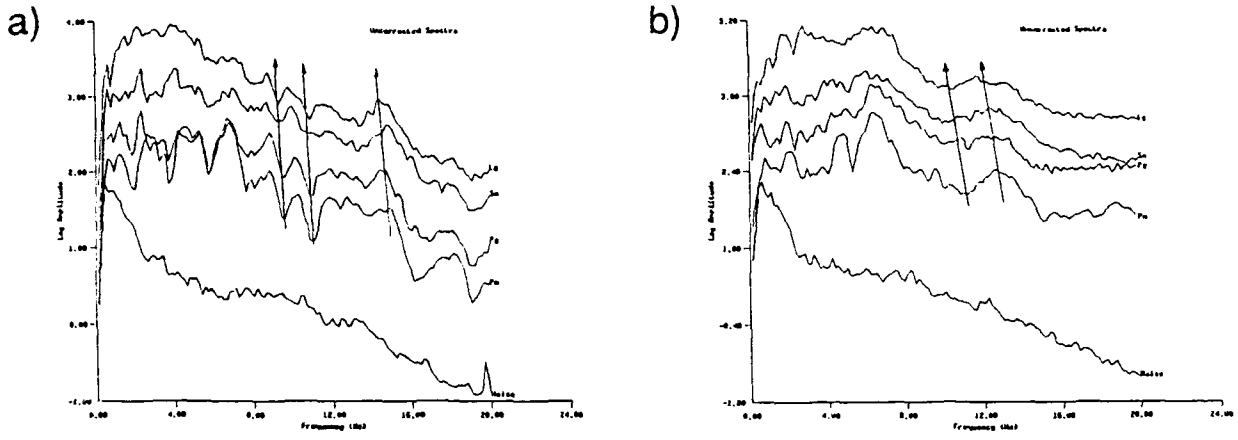


FIGURE 3: Phase velocity dependent frequency shifts in the modulation patterns of regional arrivals for two Kola pennisula events. a) 10 August 1990 event b) 13 February 1990 event.

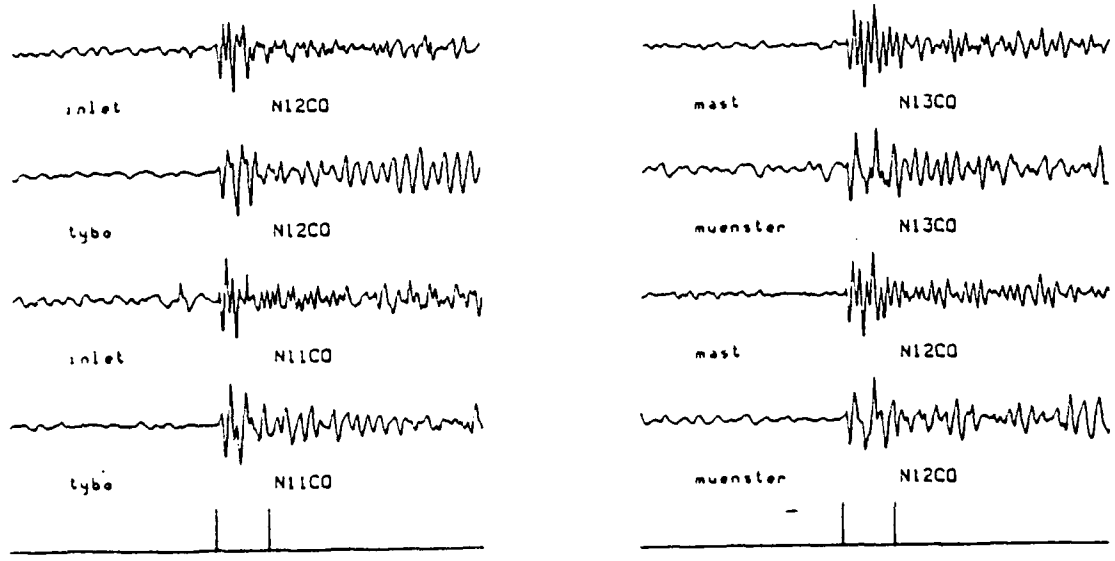


FIGURE 4: Waveform inter-correlation results at NORSAR using Murphy's (1989) pP parameters for Pahute Mesa events. The waveforms at the same sensors should be identical, but they are not, indicating that the P+pP model and/or the pP parameters are invalid.

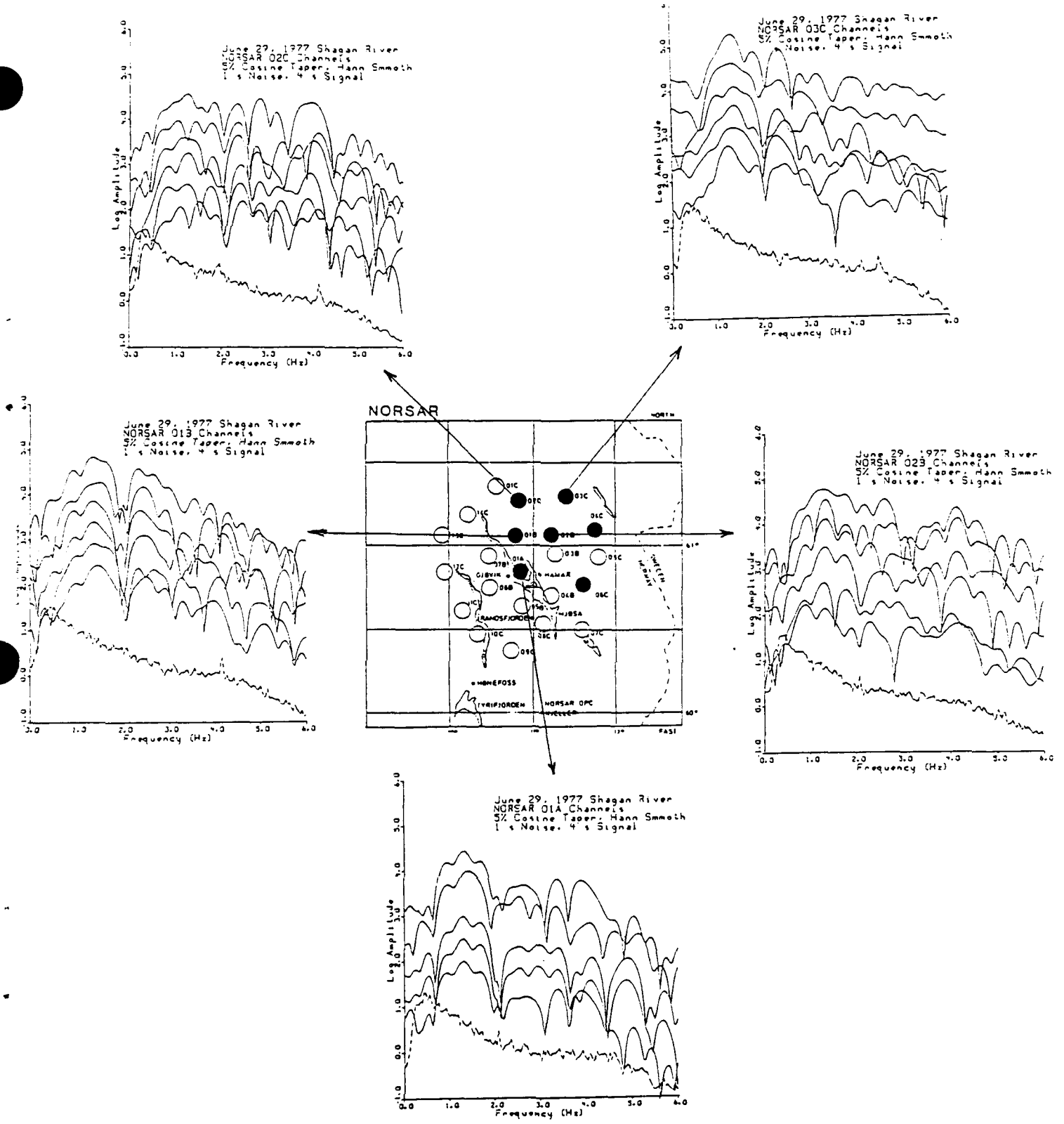


FIGURE 5: Spectra of the first five seconds of P waves from a Shagan explosion at NORSAR showing variability in the modulation patterns. Only the 2 Hz null can be substantiated.

A Geological and Geophysical Information System for Eurasia

Eric J. Fielding, Bryan L. Isacks, and Muawia Barazangi

Institute for the Study of the Continents (INSTOC)
Cornell University, Ithaca, NY 14853

Contract nos.: F19628-88-K-0035 (expired April 1991)
and F29601-91-K-DB08 (new DARPA contract)

OBJECTIVE:

The topography and crustal structure variations along seismic propagation paths and at the source and receiver sites are crucial information to understand the excitation and propagation of regional seismic phases and other aspects of the problems of verification and estimation of the yield. Our objective is to collect and organize available topographical, geological and geophysical datasets for Eurasia into a digital information system that can be accessed by display programs running at the Center for Seismic Studies (CSS) and by other DARPA researchers. The information system will be organized to extract and usefully display the information most relevant to verification and yield estimation. We plan to assemble all available digital datasets such as topography, satellite imagery, and crustal reflection and refraction profiles and digitization of available geological and geophysical information on sedimentary basins and crustal structure thicknesses.

RESEARCH ACCOMPLISHED:

We have begun work on a prototype of an interface to display information from our databases over network connections. We are building upon "widgets" from the Motif toolkit and the X Window System (X11R4) to create a user interface that is compatible with existing programs at CSS. The use of "widgets" or functional elements that communicate with the user and with the databases is an effective way to create an interface that is easy to use and easy to modify. Many modifications can be made via "resource" files that specify parts of the interface and properties of the widgets without recompiling the programs. This allows the user to customize much of the "look and feel" of the interface.

Special techniques are required to manage and analyze the large volumes of digital topography, satellite imagery, and geologic map data available for Eurasia. A large and detailed dataset covering almost the whole area of Eurasia is digital topography. We have completed the processing of the large digital topography dataset (DTED level 1; ~100 m resolution; the level available to us) that we requested under our previous contract and have received from the Defense Mapping Agency (DMA) during 1989, 1990, and 1991. This covers the high topography of the Himalayas, Tibet, the Hindu Kush, Pamirs, Tien Shan, Altai mountains, and Lake Baikal regions of Central Asia, including the Kazakhstan test site. We have also processed datasets that we received covering the southern part of Novaya Zemlya including the nuclear test site and most of the Atlas mountains in Morocco (Figure 1). We will be transferring the entire dataset, so far about 5 gigabytes (GB) to a 60 GB optical disk jukebox unit that we have ordered to provide nearly "on-line" access to any part of the data.

The dataset presently consists of 1556 "cells" for the central Asia data plus 23 cells for Novaya Zemlya and 89 cells for the Morocco area (see Figure 1) that each

cover a square degree with a spacing of 3 arc-seconds (1200 points per degree) in the latitude direction and in the longitude direction for the cells south of 50°N. The individual cells for the Central Asia dataset have been mosaicked together at the full resolution into 67 5° x 5° blocks (see Figure 2) and the Novaya Zemlya and Morocco cells have been mosaicked separately to allow analysis of moderately large areas. We have recently requested the DTED to cover all of western Eurasia, some 126 5° x 5° blocks covering the area between latitudes 25°N to 70°N and longitudes 10°W to 60°E as shown in Figure 1.

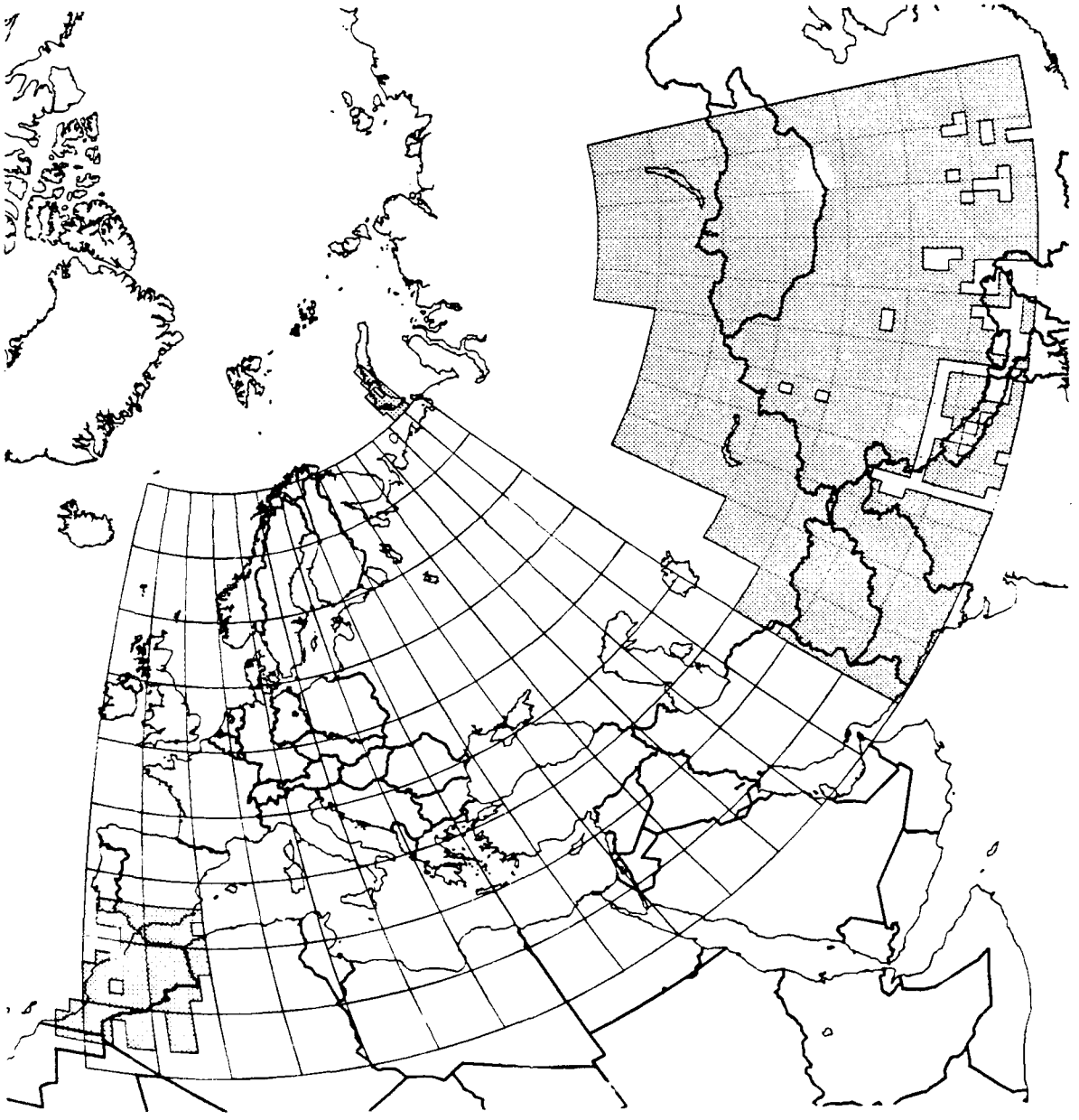


Figure 1. Map of Eurasia showing area covered by mosaics of digital topography for central Asia, Novaya Zemlya, Morocco and requested data. Coastlines are *black lines* and country borders are *dark gray lines*. DTED cells received during 1989, 1990, and 1991 are shown *filled medium gray with black outline*, cells missing from the data are visible as *blank areas* between filled cells. Central Asia 5° x 5° blocks are outlined by *medium gray lines*, and recently requested 5° x 5° blocks for western Eurasia are shown as *thin black lines*. Map is an azimuthal projection centered in north central Eurasia.

The next step in the processing, after the 5° x 5° degree mosaic files have been created, is the calculation of the mean, maximum, minimum, and total relief (max–min) for a set of different sized moving windows (from 20 x 20 to 600 x 600 points) applied to the full resolution data. This results in mosaics with resolutions from ~1 km to ~30 km. As described in more detail below, these derived data sets can be used for the interpretation of surface roughness on a variety of scales for comparison to the propagation paths of L_g. The calculations maintain the full range (maximums and minimums) of values in the original data but result in a more manageable dataset that can be stored on-line and manipulated for the whole area of coverage, *e.g.*, to generate topographic profiles along great-circle paths. The mosaics can also be used for display of larger areas and other uses for which lower resolution is adequate and for which the large volume of the full resolution data is a burden. We are seeking permission from the DMA to release these datasets derived from the DTED to other DARPA researchers through an Internet network interface.

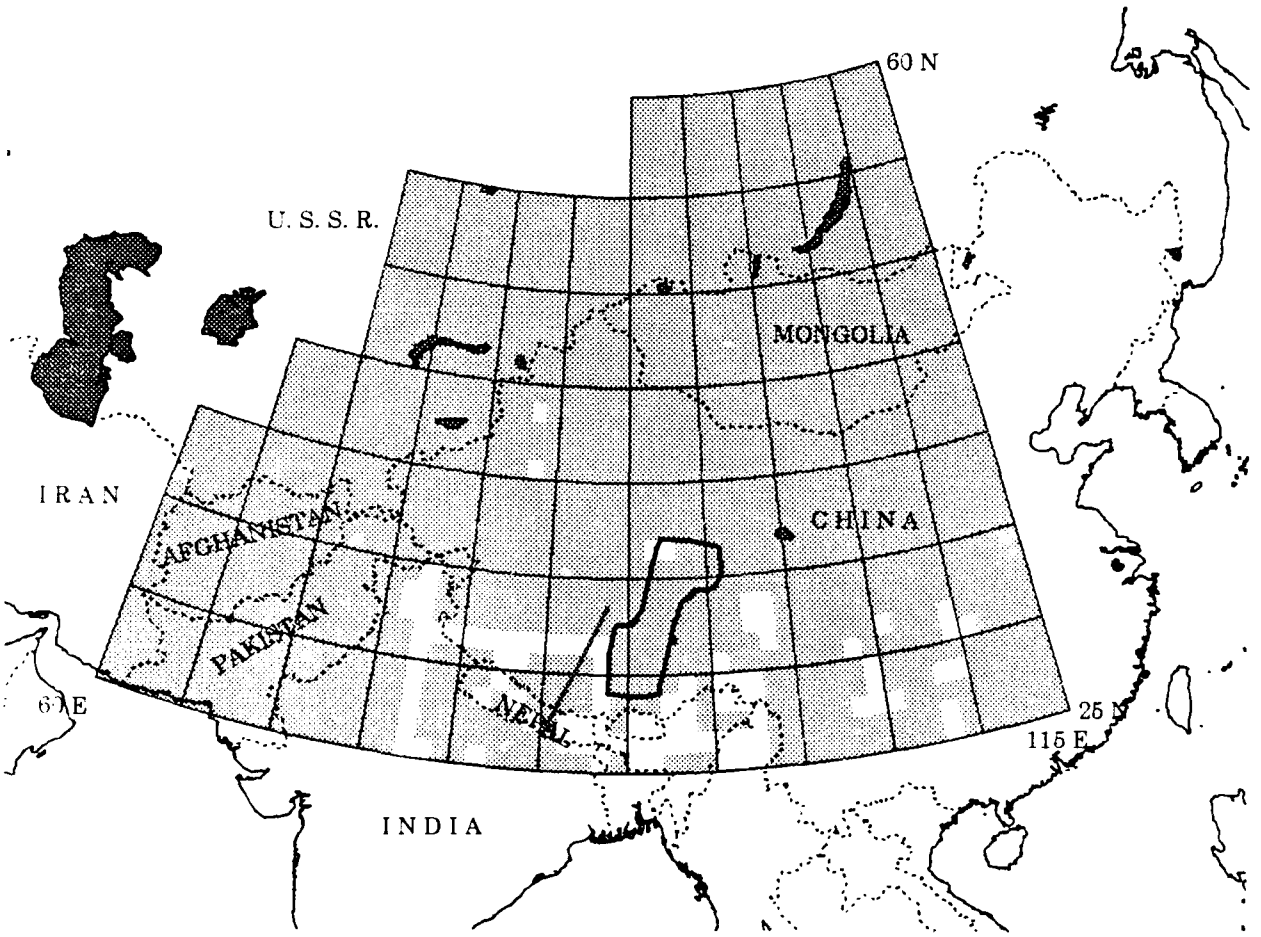


Figure 2. Overview map of Central Asia showing coverage of DTED cells received and location of digitized Geotraverse across Tibet. Received and processed cells are shown *filled medium gray* and cells missing from the data requested are visible as *blank white areas* between filled cells. Country borders are shown as *thin black dashed lines*. Seas and major lakes are *filled gray with black borders*. The great circle swath of Figure 3 is shown as a *thick grey line*. The outline of the geologic data digitized from the Geotraverse map of Figure 4 is shown as a *thick black line*.

Extreme surface roughness caused by fluvial and glacial erosion may significantly contribute to explaining the lack of propagation across high mountain ranges such as the Himalaya. Use of L_g amplitudes along such paths for discrimination or yield estimation could be invalid or require correction factors. The surface roughness images can be used to map out areas of significant relief. The calculated maximum and minimum value images maintain the full range of the original data but result in a more manageable dataset that can be stored on-line and manipulated for the whole area of coverage to generate topographic profiles along great-circle paths (see Figure 3). These profiles of topography in a swath along the propagation path of L_g from a given event show the amount of topographic relief at the surface that could contribute to scattering high-frequency energy. We have a program running to generate these great-circle projections of topography for any given great circle from our processed topography datasets. In most cases the reduced resolution mean elevation mosaics are used to reduce the volume of data that must be projected. One type of plot available is the minimum, maximum, and mean elevations for segments of a swath as shown in Figure 3.

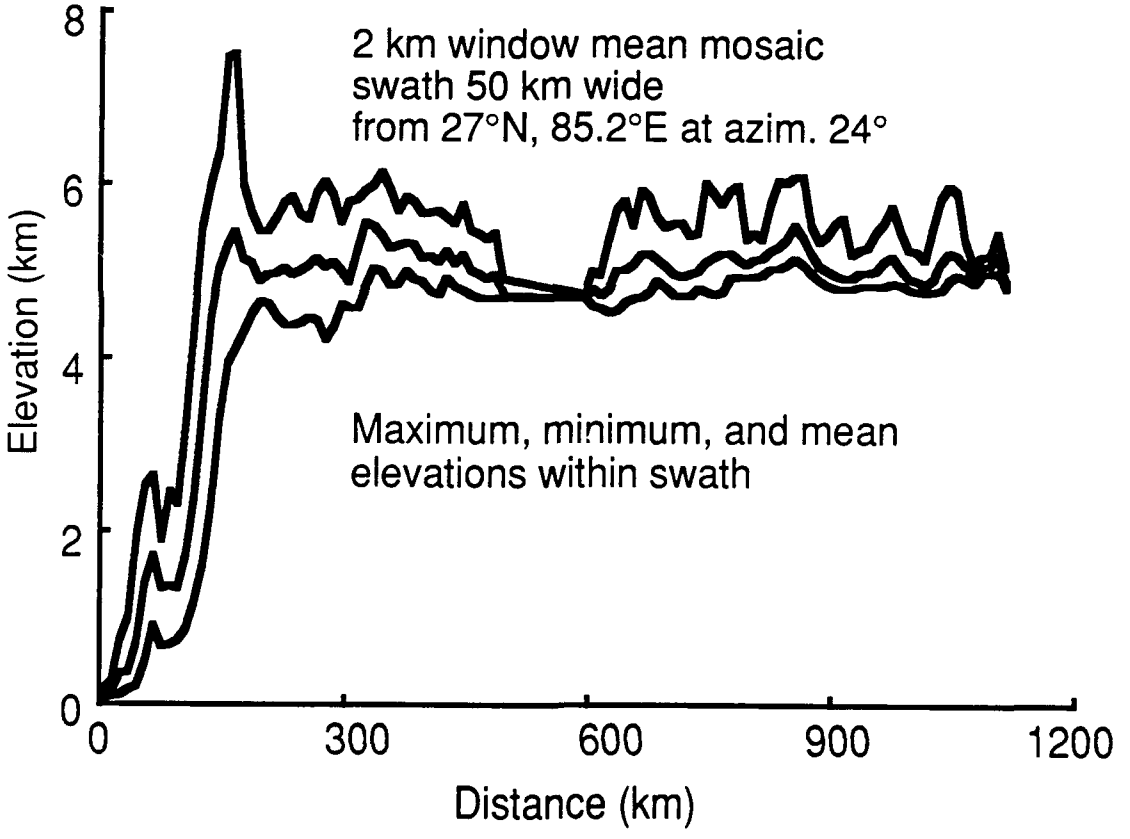


Figure 3. Topographic profiles along a swath centered on great circle path as shown in Figure 2, an example of one kind of display that we plan to include in our information system. Swath is 50 km wide, and maximum, minimum, and mean elevations from the 2 km window mean mosaic are projected into the plane of the great circle. Straight segments at about 500 km distance are due to a data gap. There is a large amount of vertical exaggeration, as seen in the elevation and distance scales plotted at the left and bottom, respectively. This is a path across the Himalaya along which L_g does not propagate efficiently.

We developed a methodology for the digitizing of polygons as opposed to line data (as previously used for faults and contour lines) to digitize maps with areal

units, such as geologic maps. The lines or "arcs" marking the boundaries between geologic units are digitized along with a "label" point for each geologic unit. Then the arcs are formed into polygons that each enclosed one unit. Polygons are assigned two or more "attributes" within ARC/INFO via their labels that include information on the interpreted age and type of rock for the unit. These attributes allow one to select rock units of a certain age and then color or otherwise mark the different rock units on a workstation display or on a hardcopy map (see Figure 4).

We have begun to digitize available geologic and tectonic maps for Eurasia. ARC/INFO provides powerful editing capabilities to correctly form and label the polygons that correspond to units on maps. We have also developed a method for digitizing contour maps and creating gridded databases in ARC/INFO. This will be used for digitizing geophysical maps such as crustal thickness. The ARC/INFO system provides a powerful "toolbox" for selecting and combining the various types of data and overlaying them on top of raster imagery.

We digitized one area of Central Asia where there is a relatively detailed and modern geologic map to compare with the digital topography, the "Geotraverse" along the only major road across Tibet (Kidd, 1988; Kidd and others, 1988). This 1:500,000 scale map is the most detailed available for any complete section across the plateau (see Figures 2 and 4). The wide variety of tectonic and geologic units from Paleozoic rocks and faults to Mesozoic deposits and sutures to Neogene deposits and active normal faults, combined with the arid to semi-arid climate made this an excellent place to calibrate our methodology. The topographic data along this section is relatively complete (almost no missing DTED cells within the area of the map) compared to other sections across the plateau.

We have acquired sets of maps of the Soviet Union, some with surrounding areas, with a variety of different kinds of geological and geophysical information at a scales of 1:7,500,000 and 1:10,000,000. The maps of crustal thicknesses (depth to Moho) and sedimentary basin depths (depth to seismic basement) are probably the most useful. The attributes capability of ARC/INFO, can record which contours are dashed (inferred or interpolated) and which are solid. We have begun to digitize the Moho depth map although its unusual map projection will require extra processing to convert the contours into geographic coordinates. After digitization and subsequent editing, regularly spaced grids of the crustal and sediment thickness values can be created from these preliminary maps. We hope to acquire some of the original data from which the geophysical maps were generated to better represent the actual control on the lithospheric structure. We have also begun to digitize a geologic map of the Soviet Union to provide information on the major crustal structures and blocks exposed at the surface.

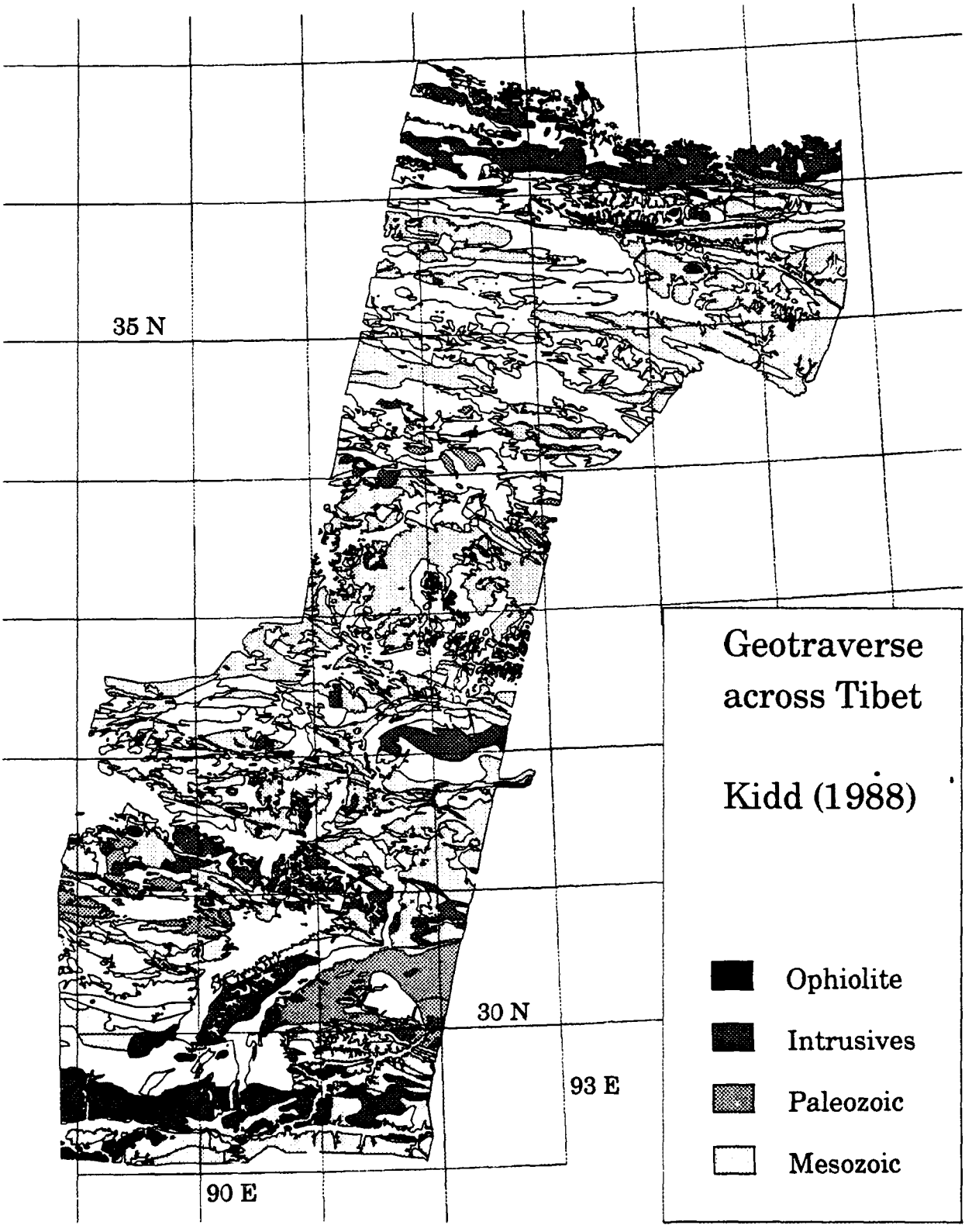


Figure 4. Map showing the digitized geology coverage of the Geotraverse across Tibet (see Figure 2 for location). Four geologic units are *filled with grays* according to the key. Overlain are the boundaries of the available topographic data as *thin dark gray lines*. This map contains about two thousand individual polygons, each with attributes of unit age and rock type. Map is a Lambert Conformal Conic projection.

CONCLUSIONS AND RECOMMENDATIONS:

The use of the inherently network-based X Window System and Motif for the user interface to our datasets allows a display in one location to access data in another location across the Internet (formerly called the ARPAnet). We plan to maintain our archive here at Cornell and provide CSS users and other DARPA researchers with programs to display the data at CSS. We are working with CSS personnel to enhance the interface and to acquire the most useful datasets. We find that it is much more efficient to build upon existing commercial GIS (ARC/INFO) and image processing packages for advanced processing and editing functions than to re-write these locally. We then add programs to access the data from these databases. A useful function will be to extract the lithospheric structure along a given swath, such as the great-circle propagation path of a regional seismic phase, and display information from our databases including topography, Moho and sedimentary basin depths, and geologic information.

References

Kidd, W.S.F., ed., 1988, Geological map of the Academica Sinica-Royal Society Geotraverse route across the Xizang-Qinghai (Tibetan) plateau, 1:500,000 scale, *Phil. Trans. R. Soc. Lond., A*, v. 327, (map pocket).

Kidd, W.S.F., Pan Y., Chang C., M.P. Coward, J.F. Dewey, A. Gansser, P. Molnar, R.M. Shackleton, and Sun Y., 1988, Geological mapping of the 1985 Chinese–British Tibetan (Xizang-Qinghai) Plateau Geotraverse route, *Phil. Trans. R. Soc. Lond., A*, v. 327, p. 287–305.

SIMULATED SEISMIC WAVE SCATTERING IN RANDOM MEDIA

M.D. Fisk, Mission Research Corporation
G.D. McCartor, Southern Methodist University
CONTRACT NO: F19628-89-C-0040

OBJECTIVE

A phase screen method to rapidly forward propagate vector elastic waves has been developed for the purpose of simulating seismic wave scattering relevant to monitoring issues. Phase screen calculations of elastic wave propagation in 2-D random media have been compared with finite difference results to assess the accuracy and relative speed of the new method. Phase screen simulation of seismic wave propagation in elastic random media has been used to: (1) analyze transmission fluctuations of incident P waves propagated through models of the crust and upper mantle beneath NORSAR; (2) examine the effect of random structure on the variances of two seismic magnitudes (m_b and pseudo-m_{Lg}) used for yield estimation.

RESEARCH ACCOMPLISHED

The phase screen method, developed by Fisk and McCartor (1989, 1991a), is an algorithm to rapidly forward propagate vector elastic waves, including P/S conversion. The medium is approximated by a sequence of thin screens, which only alter the phase (similar to ray theory), interspersed with uniform medium between the screens. Unlike simple ray theory, however, diffraction effects (*i.e.*, amplitude variation) are accumulated as a result of propagation through many screens. While this method is limited to moderate perturbations, it is very efficient, allowing for practical 3-D applications, and provides an excellent approximation to cases of interest. Like the finite difference method, this method may be used to generate synthetic seismograms at any gridpoint. Results of the method have been compared with considerable success to those of other calculational techniques. Fisk and McCartor (1991a) compared the results of the method with an exact (eigenmode-expansion) solution of an elastic wave in a 2-D laterally-layered structure. Even for wavelengths on the order of the length scale of the layers and velocity variation of 5%, the comparison was excellent.

In a collaborative study with the ERL at MIT, Fisk et al. (1991) compared phase screen and finite difference calculations for elastic waves in 2-D random media. We made use of the second-order scheme proposed by Kelly et al. (1976), and the absorbing boundary conditions proposed by Clayton and Engquist (1977). Eight

different random medium models were considered, including ones with constant and varying Poisson ratio. The same realization of the medium was used by both methods to compare the results directly. The average velocities used were $\bar{\alpha} = 5.5$ km/s and $\bar{\beta} = \bar{\alpha}/\sqrt{3}$. The source was a plane P wave of the Ricker wavelet type with a peak frequency of 2 Hz. Figure 1a shows a comparison of these solutions for a medium characterized by an exponential autocorrelation function with 5 km correlation length and 2% standard deviation in the velocities. Figure 1b shows a comparison for a medium characterized by a self-similar autocorrelation function with 5 km correlation length and 5% standard deviation in the velocities. The comparison is particularly good at early times when the effects of backscatter are negligible. (Since spurious large-amplitude boundary reflections were present in the finite difference synthetics, differences in the solutions at intermediate to late times could only partially be attributed to errors in the phase screen method.)

Execution times were compared for simulations on a CRAY-2 and an nCUBE parallel computer. Although the phase screen algorithm was developed on an ELXSI 6400, and only minimal efforts were made to optimize the code on the CRAY-2 and nCUBE computers, it was found to be roughly two orders of magnitude faster than the finite difference scheme for the 2-D models considered. An estimate, based on the number of operations in each algorithm, suggests that the phase screen method may be three orders of magnitude faster for comparable 3-D problems.

Phase screen simulation of vector wave propagation in elastic random media were also applied to two studies whose analytic and finite difference solutions are currently infeasible because of the strength of the scattering and the extent of the medium (see, Fisk and McCartor, 1991b). In the first study, we analyzed transmission fluctuations of incident plane P waves propagated through a 2-D version of the model proposed by Flatté and Wu (1988) for the crust and upper mantle beneath NORSAR. Analytic solutions exist for this problem, however, the approximations involved lead to results that are valid only for sufficiently weak fluctuations. As the strength of the perturbations increase, the commonly used Rytov approximation loses its validity. The scalar wave and parabolic approximations are also apt to break down in this case since moderately strong heterogeneities are likely to generate obliquely scattered waves and P/S conversion. Since the phase screen method for vector waves treats P/S conversion and wide-angle scattering, it is valid for stronger perturbations.

We compared simulated transverse coherence functions (TCF's) of the amplitude, phase and cross correlation, based on the vector wave method, to analytic and simulated results based on the parabolic approximation to the scalar wave equation to assess the validity of the approximations assumed, and the usefulness of numerical simulations for analyzing array and 3-component data. The incident wave in all

of these calculations was a 1 Hz normally incident plane P wave. Figure 2 shows the TCF's for this model with $\sigma = 0.5\%, 1.0\%, 2.0\%$. The solid, dashed, and dotted curves represent the simulated vector wave, simulated scalar wave, and analytic results, respectively. For wave speed perturbations $\leq 0.5\%$ the comparison of the three calculations is excellent. For $\sigma \geq 1.0\%$, however, the simulated results differ from the analytic results. For $\sigma = 2.0\%$ (Figure 2c), the simulated vector wave decorrelates at a somewhat smaller offset than the scalar wave. Figure 2c also shows TCF's of the horizontal component of the scattered vector wave which illustrate that the phase screen method for vector waves may be used to analyze 3-component data.

In the second study, we examined the effect of random structure on the variances of the direct P wave peak-to-peak amplitude, and the rms amplitude of the transverse component in the velocity window between the P and S wave speeds. The purpose of this study was to assess the conditions under which a particular seismic magnitude provides the most reliable estimate of yield. A large statistical ensemble of realizations (320 total samples of synthetic seismograms at 25 km intervals out to 200 km for each of eight models) was generated to compute statistically accurate variances. For all of the media considered here we assumed mean P and S wave velocities of $\bar{\alpha}$ = 6.0 km/s and $\bar{\beta}$ = 3.5 km/s, respectively. A Ricker wavelet with a peak frequency of 1 Hz was used as the initial pulse.

The standard deviations, given as percentages relative to the means, are plotted in Figure 3 for four models. These plots show that near the source the direct P wave amplitude has far less variation than the scattered phase, while away from the source the scattered phase has less variation. Perhaps the most interesting result of this study is that the standard deviation of the scattered phase at distances greater than 150 km is so insensitive to the model. The variance of the forward scattered P wave depends greatly on the strength of the large-scale heterogeneities.

CONCLUSIONS AND RECOMMENDATIONS

We believe that there are a significant number of problems in seismology that may necessitate the use of the phase screen method. Its tremendous efficiency allows for substantially longer propagation distances, more extensive parametric studies, ensemble averaging over realizations, and 3-D simulations to be considered. A future application relevant to the DARPA monitoring program is to analyze near-receiver scattering effects on 3-component data in order to optimize backazimuth estimates needed for event location. Numerical simulation for more realistic geological models should also be performed to investigate the variability of body waves, regional phases and P-coda to be used for yield estimation.

REFERENCES

Clayton, R. and B. Engquist (1977). Absorbing boundary conditions for acoustic and elastic wave equations, *Bull. Seismol. Soc. Am., 67,* 1529–1540.

Fisk, M. D., E. E. Charrette and G. D. McCartor (1991). A comparison of phase screen and finite difference methods for elastic waves in random media, submitted to *J. Geophys. Res.*

Fisk, M. D., and G. D. McCartor (1989). "The Phase-Screen Method for Elastic Waves and Seismic Discrimination", GL-TR-89-0330, ADA220771, Mission Research Corp.

Fisk, M. D., and G. D. McCartor (1991a). The phase-screen method for vector elastic waves, *J. Geophys. Res.*, 96, 5985–6010.

Fisk, M. D., and G. D. McCartor (1991b). Fluctuation Analysis of Elastic Waves in Random Media via Phase Screen Simulation, submitted to *J. Geophys. Res.*

Flatté, S. M., and R. S. Wu (1988). Small-scale structure in the lithosphere and asthenosphere deduced from arrival-time and amplitude fluctuations at NORSAR, *J. Geophys. Res.*, 93, 6601–6614.

Kelly, K. R., R. W. Ward, S. Treitel, and R. M. Alford (1976). Synthetic seismograms: A finite difference approach, *Geophysics*, 41, 2–27.

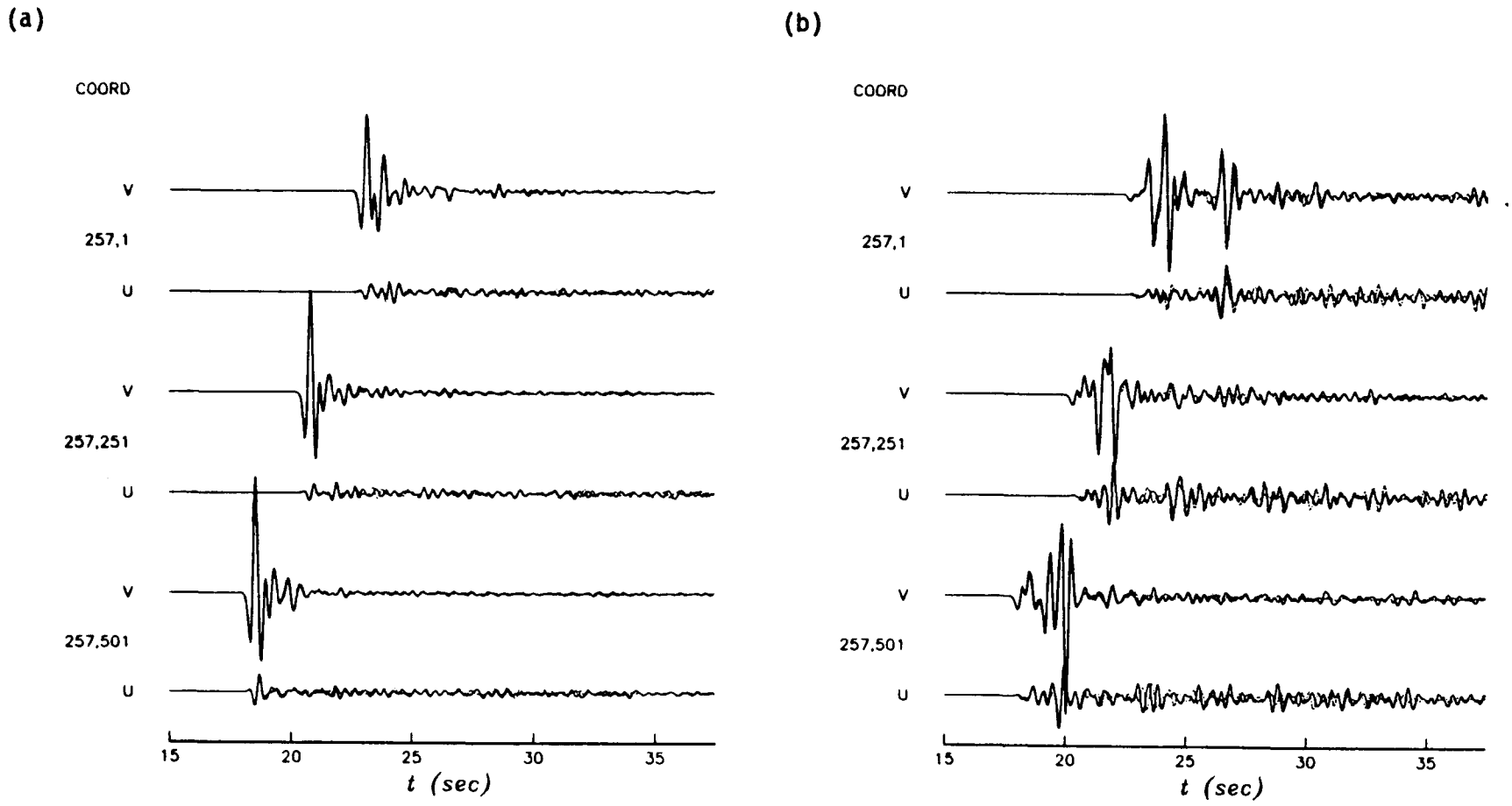


Figure 1. **Comparison of finite difference (solid) and phase screen (dotted) synthetics of the vertical (V) and horizontal (U) components of the displacement for (a) an exponential medium with 2% rms velocity perturbation; (b) a self-similar medium with 5% rms velocity perturbation.**

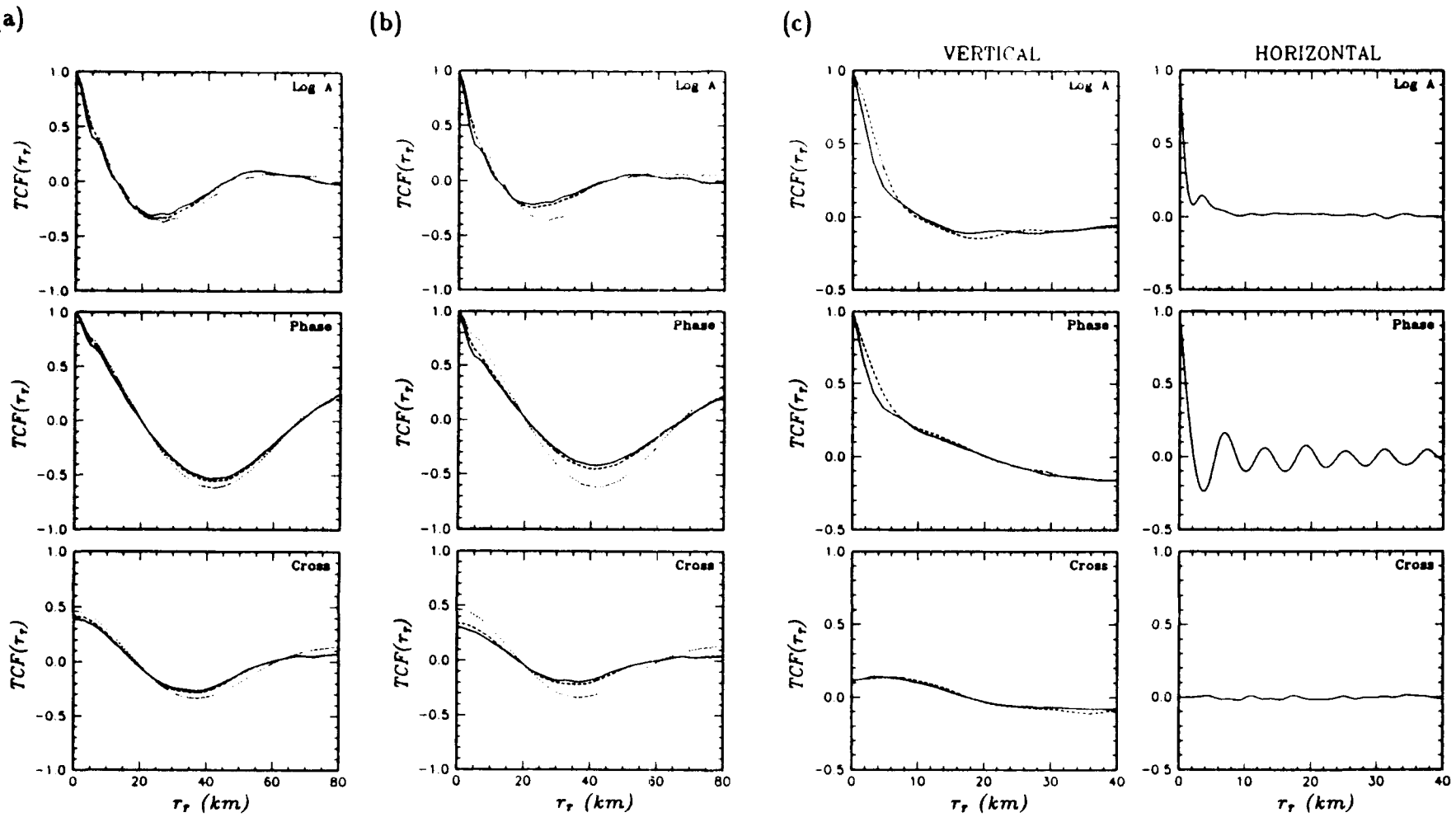


Figure 2. **TCF's of the log amplitude, phase and cross correlation computed for a P wave transmitted through a two-layer power-law model with rms velocity perturbations of (a) 0.5%, (b) 1.0% and (c) 2.0%. The solid, dashed, and dotted curves in (a) and (b) represent the results of the simulated vector (vertical component) wave and the simulated and analytic scalar waves, respectively. The TCF's in (c) are computed for the simulated (scalar and vector) vertical and (vector only) horizontal components.**

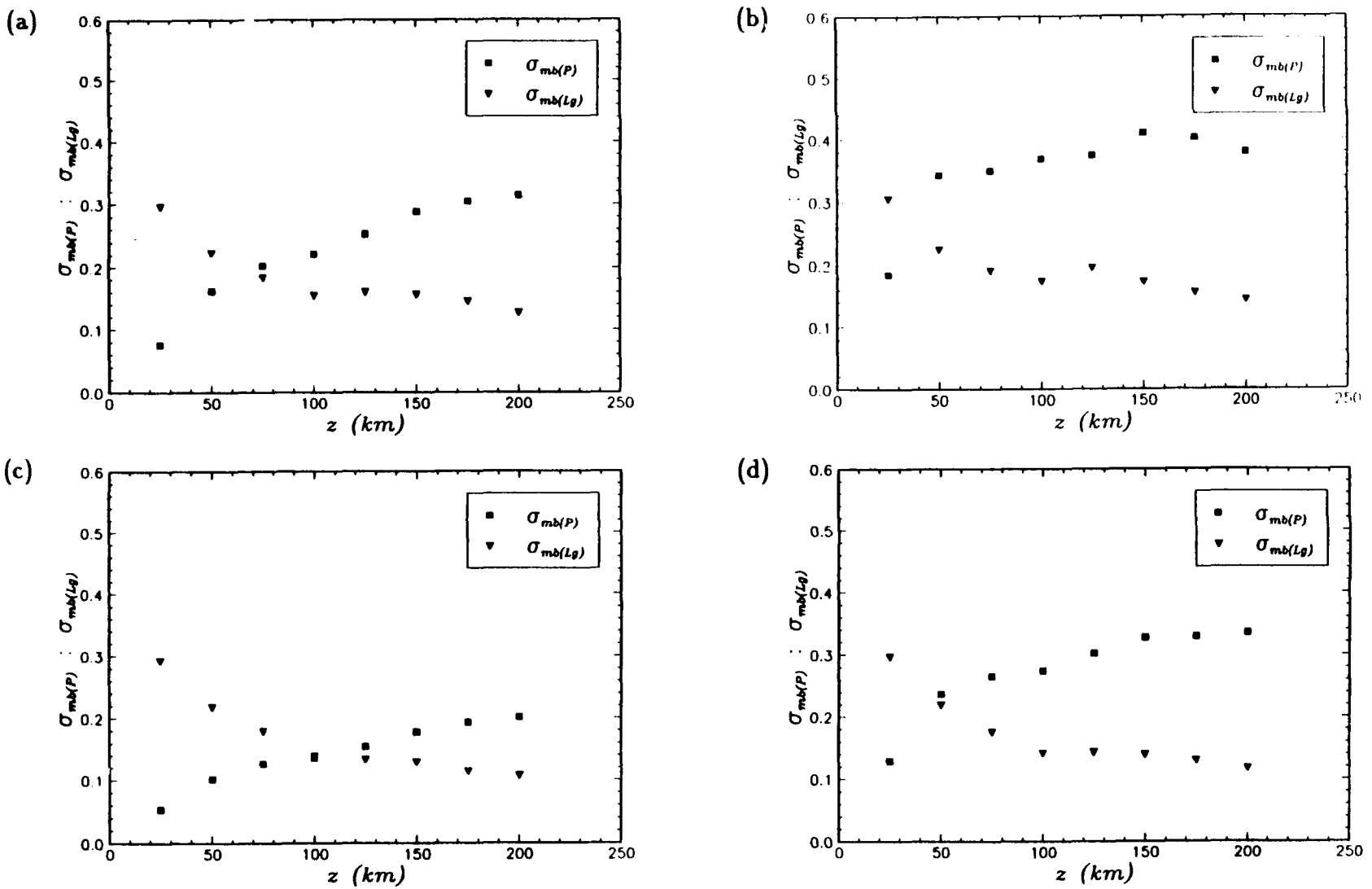


Figure 3. **Standard deviations (given as percentages relative to the means) of the direct peak-to-peak P wave amplitudes $\sigma_{mb(P)}$, and the rms transverse amplitudes $\sigma_{mb(Lg)}$ for an exponential medium with (a) 2%, (b) 5% rms velocity perturbations, and for a self-similar medium with (c) 2%, (d) 5% rms velocity perturbations.**

A CONSTRAINED BAYESIAN APPROACH FOR TESTING TTBT COMPLIANCE

M. D. Fisk and G. L. Wilson
Mission Research Corporation
Santa Barbara, CA

H. L. Gray and G. D. McCartor
Southern Methodist University
Dallas, TX

CONTRACT NO: F19628-90-C-0135

OBJECTIVE

A Bayesian approach is developed to improve estimates of the unknown parameters of the yield estimation problem. Our approach allows expert opinion to be used as prior information, similar to the approach suggested by Shumway and Der [1990]. In addition, we include information available from existing data for which the yields are unknown, as constraints on the mean and variance of the difference of the seismic magnitudes in the joint prior. We investigate the effect of such information on a test of compliance by comparing the power and F-number of this test with those based on classical statistics.

RESEARCH ACCOMPLISHED

Consider a linear model relating the seismic magnitudes $m_{1j} = m_b$, $m_{2j} = m_{Lg}$ to the log yield W_j, for the j-th event, of the form

$$\begin{aligned} & m_{ij} = A_i + B_i W_j + \epsilon_{ij}; \quad i = 1,2; \quad j = 1,\ldots,n \\ & E[\epsilon_{ij}] = 0 \\ & Var\ \epsilon_{ij} = \sigma^2_{\epsilon_i} \\ & Cov(\epsilon_{1j}, \epsilon_{2j}) = \rho(\epsilon_1, \epsilon_2)\sigma_{\epsilon_1}\sigma_{\epsilon_2}. \end{aligned} \tag{1}$$

Given n calibration events for which the yields are known, we consider the problem of estimating yield and establishing a compliance test for future events, under the assumption that the A_i and the covariance matrix of ϵ_{ij} are unknown, but sufficient information is available to define a joint Bayesian prior for these quantities. We also assume that the slopes are known, and hence *w.l.o.g.* set $B_1 = B_2 = 1$. (The generalization to other known values of the slopes is straightforward.)

In addition to using panel information to supply prior information, we will exploit the information contained in previous magnitude data for which the associated yields are unknown. These data sets will be referred to as "no-yield data." Let

$$E[m_{1j} - m_{2j}] = A_1 - A_2 \equiv \mu \tag{2}$$

$$Var(m_{1j} - m_{2j}) = \sigma_{\epsilon_1}^2 + \sigma_{\epsilon_2}^2 + \rho(\epsilon_1, \epsilon_2)\sigma_{\epsilon_1}\sigma_{\epsilon_2} \equiv \lambda^2. \tag{3}$$

Under the assumption that $B_1 = B_2 = 1$, these quantities are independent of the yield. Typically, large no-yield data sets are available, which may be used to provide excellent estimates of μ and λ^2.

We now define the random variables $\{A, \Sigma\} = \{a_1, a_2, \sigma_1, \sigma_2, \rho\}$ corresponding to the unknown parameters $\{A_1, A_2, \sigma_{\epsilon_1}, \sigma_{\epsilon_2}, \rho(\epsilon_1, \epsilon_2)\}$. Also, define the set of magnitudes for which the yields are known by $\vec{m}_k = (m_{11}, m_{21}, \ldots m_{1k}, m_{2k})$. The joint distribution of $\{A, \Sigma\}$ given $\vec{m}_n$ may be computed using Bayes' law as follows:

$$f(A, \Sigma | \vec{m}_n) = \frac{h(A, \Sigma) L(\vec{m}_n | A, \Sigma)}{\int h(A, \Sigma) L(\vec{m}_n | A, \Sigma)\, dA\, d\Sigma} \tag{4}$$

where h is the joint prior and L is the likelihood function for the data, $\vec{m}_n$, given values of A, Σ. Assuming (m_{1k}, m_{2k}) are bivariate normal, then

$$L(\vec{m}_n | A, \Sigma) = \prod_{k=1}^{n} \psi(m_{1k}, m_{2k}; A, \Sigma) \tag{5}$$

where

$$\psi(m_{1k}, m_{2k}; A, \Sigma) = \frac{1}{2\pi\sigma_1\sigma_2\sqrt{1-\rho^2}} \exp\left\{-\frac{1}{2(1-\rho^2)}\left(x_k^2 - 2\rho x_k y_k + y_k^2\right)\right\} \tag{6}$$

$$x_k = \frac{m_{1k} - W_k - a_1}{\sigma_1}; \qquad y_k = \frac{m_{2k} - W_k - a_2}{\sigma_2}$$

Thus, if $h(A, \Sigma)$ is available, f is completely determined.

Given a set of no-yield data, we impose the constraints (2) and (3) by replacing, in (4), the prior $h(A,\Sigma)$ with a new prior $h_c(A,\Sigma)$. If the no-yield data set is sufficiently large, then the constrained joint prior is given by

$$h_c(A,\Sigma) = \mathcal{N}\, h(A,\Sigma)\, \delta(a_1 - a_2 - \mu)\, \delta(\sigma_1^2 + \sigma_2^2 - 2\rho\sigma_1\sigma_2 - \lambda^2), \tag{7}$$

where $\mathcal{N}$ is a normalization constant, and $\delta(x)$ is the Dirac delta-function of distribution theory.

There are many distributions worth considering for $h(A,\Sigma)$. Here we will specify $h(A,\Sigma)$ as the product of sampling distributions (see, Anderson [1958]), where

$$\frac{a_i - \mu_{a_i}}{\sigma_{a_i}} \sim N(0,1) \tag{8}$$

$$\frac{\sigma_i^2}{\sigma_{0_i}^2}(N-1) \sim \chi^2(N-1) \tag{9}$$

$$\rho \sim \text{Approximately log normal.} \tag{10}$$

The parameters for these distributions may be given as panel estimates (*e.g.*, Nicholson et al. [1991]), or estimated from calibration data if available.

To test compliance of a future event we will use a linear combination of the seismic magnitudes $(0 < r < 1)$

$$m_r = r\, m_1 + (1-r)\, m_2 \tag{11}$$

Consider a $100\alpha\%$ significance level test of the null hypothesis, $H_0 : W \leq W_T$, versus the alternative, $H_1 : W > W_T$, of the form:

$$\text{Reject } H_0 \text{ if } m_r > T_\alpha, \tag{12}$$

where $W_T = \log 150$ is the treaty threshold and T_α satisfies

$$P[m_r > T_\alpha | \vec{m}_n, W = W_T] = \alpha. \tag{13}$$

Using the distribution of the parameters given the data and prior information obtained above, this expression may be written as

$$\int P[m_r > T_\alpha | A, \Sigma, W = W_T]\ f_c(A, \Sigma | \vec{m}_n)\ dA\ d\Sigma = \alpha \tag{14}$$

where

$$P[m_r > T_\alpha | A, \Sigma, W = W_T] = \int_{T_\alpha}^{\infty} dm_r\ \frac{1}{\sqrt{2\pi}\sigma_r} \exp\left[-\frac{1}{2}\left(\frac{m_r - a_r - W_T}{\sigma_r}\right)^2\right] \tag{15}$$

$$\begin{aligned} a_r &= r a_1 + (1-r) a_2 \\ \sigma_r^2 &= r^2\sigma_1^2 + (1-r)^2\sigma_2^2 + 2r(1-r)\rho\sigma_1\sigma_2 \end{aligned}$$

Once T_α is determined, the power of the test is defined to be the probability that the null hypothesis is rejected, *i.e.*, the power at $W = W_0$ is given by

$$\begin{aligned} \text{Power}(W_0) &= P\left[m_r > T_\alpha | \vec{m}_n, W = W_0\right] \\ &= \int P[T_\alpha | \vec{m}_n, W = W_0]\ P[m_r > T_\alpha; A_r, \sigma_{\epsilon_r} | W = W_0]\ dT_\alpha \end{aligned}$$

The expression for $P[m_r > T_\alpha; A_r, \sigma_{\epsilon_r} | W = W_0]$ is the same as (15) except that the parameters are the true parameters as in (1). In practice it is only possible to estimate the power, however, performing a simulation allows the true power to be computed. The F-number of the test is given by

$$F = 10^{W_F - W_T}, \tag{16}$$

where W_F is the value of the log yield at which the power is 0.5.

In order to assess the impact of imposing the prior information, particularly the constraints, it is useful to compare the power of the resulting Bayesian test with the power of analogous tests based on classical statistics. We will consider the following three 0.025 significance level tests:

test 1 = a test of hypothesis based on the assumption that the population parameters are completely known. This test will have the greatest power, however, it is infeasible.

test 2 = a test of hypothesis based on our constrained Bayesian approach and the assumption that the population parameters are unknown.

test 3 = a test of hypothesis based only on calibration data and the assumption that the population parameters are unknown.

The power of tests 1 and 3 may be computed by integrating a normal distribution and a non-central t-distribution, respectively, from the critical value to infinity (see Alewine et al. [1988] and Gray and Woodward [1990]).

Test 2 depends on the particular realization of data. Thus we have performed a simulation in which random samples of data are generated from a bivariate normal population, for $k = 1, \ldots, n$. The population parameters are considered to be the true values as in (1). We computed the average power and F-numbers for 100 realizations. Throughout our study we set $A_1 = 4.15$, $A_2 = 4.20$ and $r = 1/2$. We also set $\sigma_{\epsilon_1} = 0.05$ and consider the nine cases for all possible combinations of $\sigma_{\epsilon_2} = 0.05, 0.10, 0.15$ and $\rho(\epsilon_1, \epsilon_2) = 0, \pm 0.5$. For each case we consider $n = 3, 4, 5, 6, 10$ sample sizes of simulated calibration data.

Figure 1 shows the power of tests 1, 2 and 3 for a typical case, versus the true yield, denoted by solid, dashed and dotted curves, respectively. The corresponding F-numbers are given in the legends. There are several significant points to make concerning these results of this study (see Fisk et al. [1991]).

1. Test 2 is better than test 3 in all cases for $n \leq 6$. In a majority of the cases the increase in power of test 2 to test 3 is dramatic. For $n = 10$ the improvement is not as significant.
2. The power of test 2 is far less sensitive to the number of calibration events than the power of test 3. Thus the greatest relative increase in power of test 2 to test 3 occurs when n is the smallest.
3. The power of test 2 is less sensitive to the population parameters than the power of test 3.

CONCLUSIONS AND RECOMMENDATIONS

This study implies that for a fixed number of calibration events, no-yield magnitude data provide valuable information that may be used to improve the probability of detecting a violation. Alternatively, it implies that fewer calibration events

are needed if the constrained Bayesian approach is employed (test 2), in order to achieve the same F-number as for test 3. For example, if six CORRTEX events were needed to adequately calibrate a test site using only calibration data, then typically as few as three events would be adequate to obtain the same F-number using our approach.

Future work should treat the slopes as unknown if this approach is to have monitoring applications relevant to low yields. The assumption that μ and λ^2 are known exactly should also be relaxed so that our approach may be applied at Novaya Zemlya where the no-yield data set is relatively small. Other joint prior distributions are worth investigation as well. The robustness of the compliance test based on our approach should be studied when the assumptions concerning the parameters of the joint prior distribution are incorrect. This study would assess how the power of the test depends on the accuracy of panel estimates. We expect that the information provided by the constraints will correct for poor estimates and hence lead to a more robust test than a corresponding Bayesian test without the constraints.

REFERENCES

Alewine, R.W. III, H.L. Gray, G.D. McCartor and G.L. Wilson, Seismic Monitoring of a Threshold Test Ban Treaty (TTBT) Following Calibration of the Test Site with CORRTEX Experiments, AFGL-TR-88-0055, Air Force Geophysics Laboratory, Hanscom AFB, Massachusetts 01731, 1988.

Anderson, T.W., *An Introduction to Multivariate Statistical Analysis*, John Wiley & Sons, New York, 1958.

Fisk, M.D., H.L. Gray, G.D. McCartor and G.L. Wilson, A Constrained Bayesian Approach for Testing TTBT Compliance, MRC-R-1367, Mission Research Corporation, (Submitted to Phillips Laboratory for distribution) 1991.

Gray, H.L. and W.A. Woodward, Some Remarks on Compliance Testing, GL-TR-90-0282, Air Force Geophysics Laboratory, Hanscom AFB, Massachusetts 01731, 1990.

Nicholson W.L., R.W. Mensing, and H.L. Gray, Magnitude/Yield Modeling, Seismic Yield Estimation and Uncertainty Analysis, Pacific Northwest Laboratories, Unpublished, 1991.

Shumway, R.H. and Z.A. Der, Multivariate Calibration and Yield Estimation for Nuclear Tests, Unpublished, 1990.

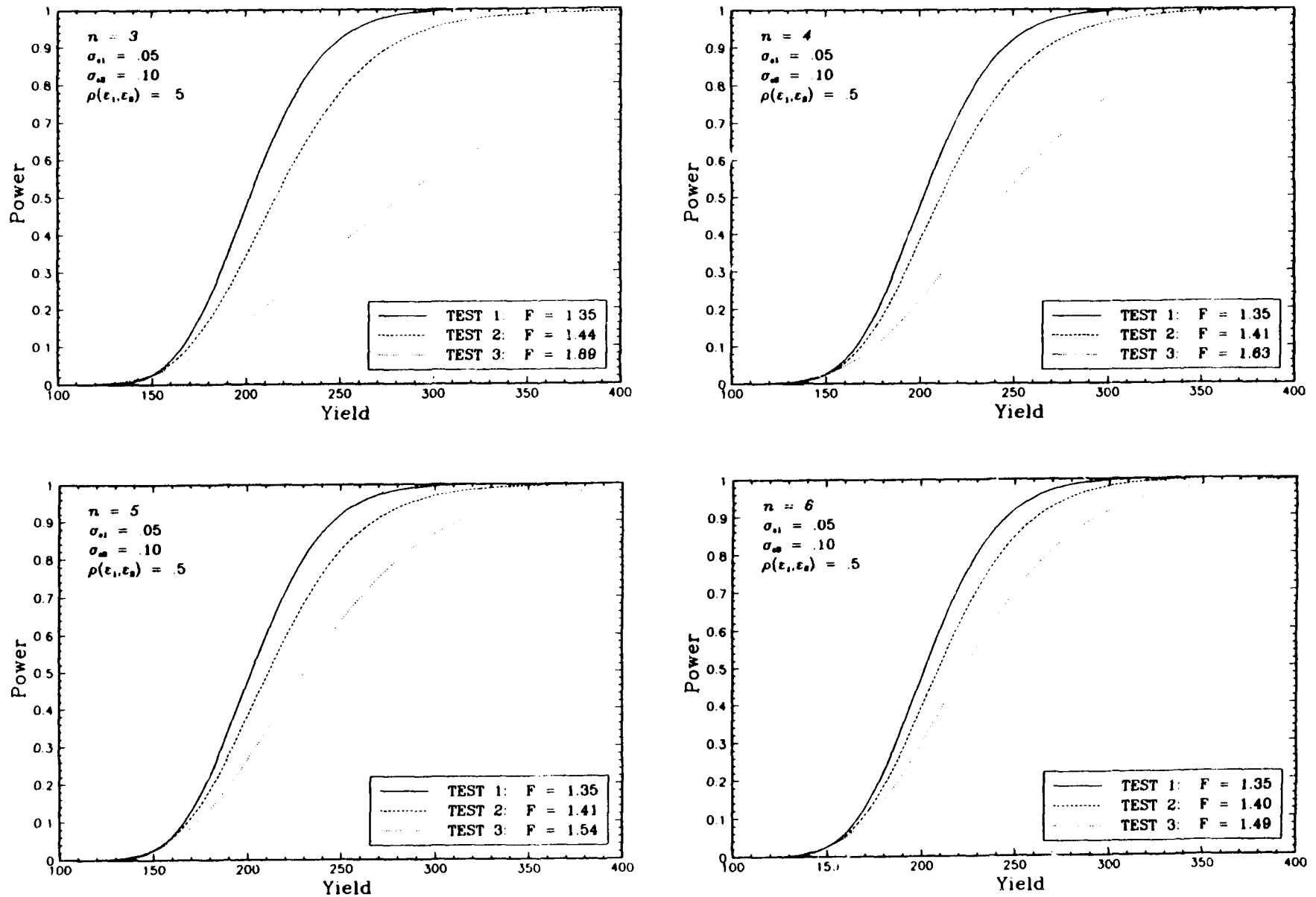


Figure 1. Power comparisons as a function of the yield for three tests of compliance.

The Effect of Small-Scale Heterogeneities on Transmission Fluctuations for Teleseismic and Regional High-Frequency Propagation

Stanley M. Flatté, Xiao-Bi Xie, and Tianrun Zhang

Institute of Tectonics, University of California, Santa Cruz, CA 95064

Contract No. F19628-89-K-0027

Objectives: Coherence Functions of Seismic Waves

1. Inhomogeneities in the crust and mantle, resulting from many different geophysical processes, have scales that range from grain size to continental scale. In other words, the inhomogeneities are very broad band in the spatial wavenumber domain. These inhomogeneities result in decoherence of waveforms, and this decoherence inhibits determinations of seismic source characteristics from waveform data. To investigate very broad band and probably anisotropic inhomogeneities, techniques which have broad band capability need to be used. The combination of data from arrays of different sizes can determine the coherence functions over a broad range of scales, and should give better constraints on any model of inhomogeneities. Teleseismic waves, which are near vertically incident on the array, carry information about variations in the horizontal direction while integrating in the vertical direction. They can therefore be used to investigate the power spectrum of inhomogeneities in the horizontal direction. Regional phases, which propagate near the horizontal in the crust, can give us some further information on the power spectrum. The purpose of our research is to develop techniques for combining data from large scale, coarse arrays like NORSAR with small-scale, fine arrays like NORESS for the purpose of determining coherence properties of seismic waves and their connection with crust and mantle inhomogeneities. We use both teleseismic and regional events in an attempt to obtain a three-dimensional view of the inhomogeneities.

2. Traditionally there are two approaches for investigating crust and mantle heterogeneities, i.e., deterministic and statistical. From the deterministic viewpoint people try to give a deterministic description for the structure, that is a seismic wavespeed field as a function of position. But the sparse distribution of stations and seismic sources limits this method to obtaining some information about the large scale inhomogeneity structure. By contrast, in the stochastic point of view people treat the inhomogeneities with a random model and try to use a few statistical parameters to describe the properties of the medium. These parameters include rms fluctuations in wavespeed, correlation functions or power spectra of the inhomogeneities, etc. The objective of our research in this area is to develop techniques for combining the two approaches to modelling inhomogeneities, to combine the advantages of both and if possible eliminate some of the disadvantages that occur in their individual usage.

Research Accomplishments

1. The Determination of Coherence Functions and Small Scale Inhomogeneities

Several statistical measurements can be determined from array data, e.g., rms fluctuations of travel time, log amplitude, and slowness, and various kinds of coherence functions. These measurements are strongly dependent on the size of the array, because the variations across an array are measured relative to the mean *within the array*, and the effect of variations with scale sizes larger than the array are not seen. In this research, we have developed a technique for combining the measurements from arrays of very different sizes, and we have applied the technique to the Transverse Coherence Function (TCF) of travel time determined from NORSAR and NORESS data.

Consider the arrival time of a seismic wavefront impinging on the surface of the earth. It is a random function of transverse position. The response of an array to a wavefront can be considered as a nonlinear band-pass spatial filter to the power spectrum of the random function, with its low-wavenumber cut-off proportional to the reciprocal of the array aperture and high-wavenumber cut-off proportional to the reciprocal of the smallest separation between sensors. The observed coherence function is the Fourier transform of the filtered power spectrum. The mean square travel-time fluctuation

corresponds to the integration of the filtered power spectrum. The mean-square slowness (tilt) corresponds to the integration of the filtered power spectrum weighted by the square of the wavenumber. The TCF of a coarse array spread over a large area is affected by inhomogeneities of all scales less than the array size, but since no small transverse separations are available in a coarse array, the TCF at small separations is not available. The problem is to use independent observations on a smaller fine-scale array to find the TCF at small separations. From the above relationships, the following formula can be derived connecting the coherence functions and various mean-square fluctuation measurements:

$$f_L(\rho) = 1 - \frac{\langle t_S^2 \rangle}{\langle t_L^2 \rangle}(1-f_S(\rho)) - \frac{1}{2}\frac{\langle \delta u^2 \rangle}{\langle t_L^2 \rangle}\rho^2 - \frac{\langle \varepsilon^2 \rangle}{\langle t_L^2 \rangle}(1-g(\rho)), \qquad (1)$$

where $f_L(\rho)$ and $f_S(\rho)$ are coherence functions for the large and small array respectively, $\langle t_L^2 \rangle$ and $\langle t_S^2 \rangle$ are mean square fluctuations for the large array and the small array, $\langle \delta u^2 \rangle$ is the mean square slowness fluctuation of the small array relative to the large array, $\langle \varepsilon^2 \rangle$ is the mean square value of the noise field, $g(\rho)$ is the normalized coherence function of the noise. Once these quantities are obtained $f_S(\rho)$ can be corrected to $f_L(\rho)$ or vice versa. In other words, by combining different observations (slowness, rms fluctuations, coherence functions etc.), we can construct a comprehensive coherence function, $f_L(\rho)$, where we have measurements of f_L at small values of ρ obtained from the data of the small array.

The Norwegian seismic array was originally composed of 22 subarrays with each subarray composed of 6 stations. The aperture of the original NORSAR is about 110 km. The separations between the subarrays are 15 to 20 km and the separations between the stations are about 3 kilometers. Since 1976, there are only 7 subarrays still work continuously, so that the aperture of NORSAR is reduced to about 80 km. Hereafter we will label the original NORSAR array as NORSAR and the reduced NORSAR as NORSAR-R. Also, we combine part of the NORSAR subarrays to form another array with an aperture around 50 km, which is called NORSAR-P. The distribution of the elements of these arrays is shown in Fig. 1. In 1983, centered on one of the NORSAR stations, i.e. N06C2, a high frequency small scale array, NORESS, was established. This array is composed of 25 stations with an aperture of 3 km and a minimum separation of 150 meters. The location of NORESS is also marked in Fig. 1.

Table. 1 Statistical Measurements from Different Arrays

array	aperture km	frequency Hz	t_{rms} sec.	$\log u_{rms}$	$slowness_{rms}$ $s \cdot km^{-1}$	reference
NORSAR	110	2.0	0.135*	0.41		Flatté & Wu, 1988
NORSAR	110	2.0	0.115			this work (subarray data)
NORSAR-R	80	2.0	0.064		$4.96 \cdot 10^{-3}$ **	this work (subarray data)
NORSAR-R	80	2.0	0.058	0.42		this work (station data)
NORSAR-P	50	2.0	0.043	0.37	$2.56 \cdot 10^{-4}$ ***	this work (station data)
NORESS	3	2.0	0.011	0.09	$2.23 \cdot 10^{-2}$ ***	this work (station data)

*) without subtracting the deterministic part, **) relative to NORSAR, ***) relative to NORSAR-R

For calculating coherence functions we follow the method of Flatté and Wu (1988). Coherence analysis is applied to NORSAR, NORSAR-R, NORSAR-P and NORESS. For comparison, Fig. 2a gives the transverse travel-time coherence functions for these arrays. Table 1 lists the rms values of travel time fluctuations, log-amplitude fluctuations and slowness fluctuations from these arrays. Subarray data means the old data used by Flatté and Wu (1988) and station data means more recent waveform data from NORSAR-R and NORESS. It is clear that, even in the same area, i.e. where the NORSAR array is located, the statistical quantities are quite different for arrays with different apertures, because each array is missing the effects of inhomogeneities that are larger than the array. For an array even as large as 100 km, the coherence function still has not reached its stable state, indicating that the inhomogeneities probably contain variations on scales larger than 100 km. Thus the structure under NORSAR is multiscaled.

Shown in Fig. 2b are the same coherence functions as those in Fig. 2a except that they are corrected with eq. (1). The NORSAR array is chosen as the reference array. The data listed in table 1 are used as the coefficients of eq. (1). Coherence functions from both the large arrays and small arrays are well corrected. Previous work (Flatté and Wu 1988) gave only the coherence functions with a smallest separation of 15 km, which is limited by the separation between subarrays. Here, by use of the observations from individual stations, the smallest separation for the coherence function (from NORSAR-R) has been reduced to 5 km.

Measurements show that the wavefront across NORESS is a plane wave within measurement errors, so that the only significant number from NORESS is the slowness relative to a larger array. Therefore we have used simultaneous events on NORSAR-R and NORESS to determine the mean-square slowness variation for a small array. The assumption of plane-wave tilts across NORESS combined with this mean-square slowness gives a specific functional form (a parabola) for the TCF at small separations. This measurement from NORESS is indicated by the shaded region near small separations in Fig. 2b. Also shown in this figure is the coherence function calculated from the inhomogeneity model determined by Flatté et al (1991) from data including this TCF with only the points at separations larger than 15 km. The theoretical curve is consistent with the observations, although no rapid drop near zero separation is clearly observed in the data.

Additional Information from Regional Phases

Regional phases propagate near the horizontal in the crust. If there is no scattering in the crust, the energy arrival in the slowness domain will be a clear peak indicating the direction from which the energy comes; otherwise the energy peak will be broadened in slowness and arrival time by the effect of the scattering. Records from high frequency regional arrays NORESS and ARCESS are used. First the array records are band pass filtered between 4 and 8 Hz to remove the noise. Then the records are beamformed in all possible directions to give the energy distribution in the slowness domain. The theoretical array response is obtained by a synthetic method. To avoid contamination from deterministic layered structure only azimuth variation of the energy distribution is used. This part of the work is in progress.

2. Statistical Observations Compared with Deterministic Observations

In the NORSAR area, both deterministic and stochastic investigations are carried out by many authors. Among these studies, three-dimensional deterministic structures under NORSAR were obtained by the standard tomographic method (e.g., Aki 1977, Christoffersson 1979, Thomson and Gubbins 1982). Most of the authors use block or grid wavespeed models with a block size or grid spacing of 20 km in horizontal and 20-50 km in vertical direction. These models cover an area of about 200 by 200 km. The average rms wavespeed perturbations of these models are approximately between 1.7-2.8 percent.

The stochastic structure under NORSAR has been investigated by Capon and Berteussen (1974) and Berteussen et al (1975). Recently, Flatté and Wu (1988) introduced a new idea of angular coherence function in addition to the widely used transverse coherence function. The additional information allows them to estimate the power spectrum of the inhomogeneity under the array as a function of depth. They obtained (see Flatté et al (1991)) a two-overlapping-layer model for lithospheric and asthenospheric heterogeneities underneath NORSAR, the upper layer with a flat power spectrum extending from the surface to about 200 km and a lower layer with a K^{-4} power spectrum extending from 15 to 250 km. The rms P-wave speed variations lie in the range 1-4 percent, with the uncertainty arising from lack of knowledge about the power spectrum in the k_z direction.

The spatial wavenumber band of the deterministic models depends on their block size and the scale of the model. For those models mentioned above, the horizontal wavenumber band lies between 0.06 km^{-1} and 0.16 km^{-1}. For statistical observation, the wavenumber band is between 0.06 km^{-1} and 0.3 km^{-1}. Most of the deterministic models give three-dimensional wavespeed structures from which a three-dimensional power spectrum can be calculated. But, as is well known, for near vertically incident teleseismic data the resolution along the vertical direction is poor. The Flatté-Wu model gives a power spectrum in the horizontal wavenumber domain, but determines only the zero vertical wavenumber

component. Taking these restrictions into account, we make comparisons between these two types of models in the horizontal wavenumber domain.

First, the linear trends of the deterministic velocity models are removed in individual layers, then the power spectra are calculated for each layer and averaged to give an average power spectrum of the model in the horizontal wavenumber domain. The power spectrum from the Flatté-Wu model, which is the three-dimensional power spectrum at $k_z = 0$, is modified to be compatible with the two-dimensional power spectrum from the deterministic models. Figure 3 gives the comparison between the deterministic models and two curves corresponding to the Flatté-Wu model with rms wavespeed fluctuations of 1 and 4 percent respectively and isotropy assumed. The different symbols represent various deterministic models. The two kinds of descriptions are overlapped in the wavenumber band between 0.06 km^{-1} and 0.16 km^{-1} . Within this band, their shapes are very similar. The absolute level of the statistical and deterministic models are both uncertain because of lack of vertical resolution, but their uncertainties have different characteristics. This is being investigated.

Conclusions and Recommendations

In the first part of this research, data from NORESS, NORSAR, and subsections of NORSAR were combined to form a picture of the Transverse Coherence Function (TCF) of travel time from separations of 150 meters up to 100 km. All the corrected TCF data are consistent with the Flatté et al (1991) model formed only from original NORSAR subarray-averaged data. To accomplish this result, a technique was developed for combining independent measurements from arrays of widely differing apertures. It is recommended that this approach be applied to other multiple-array data sets.

We have begun an investigation into the effect on regional waveforms of small-scale inhomogeneities. This work is in progress.

In the second part of this research, previously published deterministic (tomographic) models are compared with a stochastic inhomogeneity model in the wavenumber domain. Deterministic models give results in a lower wavenumber band while the stochastic model can extend to higher wavenumbers. It is shown that under NORSAR within the overlap wavenumber band the deterministic and stochastic results are consistent with each other. It is recommended that this comparison be investigated for possible insight into the lack of vertical resolution present in the data, and differently treated in the two approaches. In particular the comparison should include the possibility of anisotropy.

References

Aki, K., Christoffersson, A. and Husebye, E. S., 1977. Determination of the three-dimensional seismic structure of the lithosphere, *J. Geophys. Res.*, **82,** 277-296.

Berteussen, K.A., Christoffersson, A., Husebye, E.S., and Dahle, A., 1975. Wave scattering theory in analysis of *p* wave anomalies at NORSAR and LASA, *Geophys. J. R. astr. Soc.*, **42,** 403-417.

Capon, J., and Berteussen, K.A., 1974. A random medium analysis of crust and upper mantle structure under NORSAR, *Geophys. Res. Lett.*, **1,** 327-328.

Christoffersson, A., and Husebye, E. S., 1979, On three-dimensional inversion of P wave time residuals: option for geological modeling, *J. Geophys. Res.*, **84,** 6168- 6176.

Flatté , S.M., and Wu, R.S., 1988. Small scale structure in the lithosphere and asthenosphere deduced from arrival time and amplitude fluctuations at NORSAR, *J. Geophys. Res.*, **93:** 6601-6614.

Flatté , S.M., Wu, R.S., and Shen, Z.K., 1991. Nonlinear inversion of phase and amplitude coherence functions at NORSAR for a model of nonuniform heterogeneities, *Geophys. Res. Lett.*, **18,** 1269-1272.

Thompson, C. J., and Gubbins, D., 1982, Three-dimensional lithospheric modeling at Norsar: linearity of the method and amplitude variations from the anomalies, *Geophys. J. R. astr. Soc.*, **71,** 1-36.

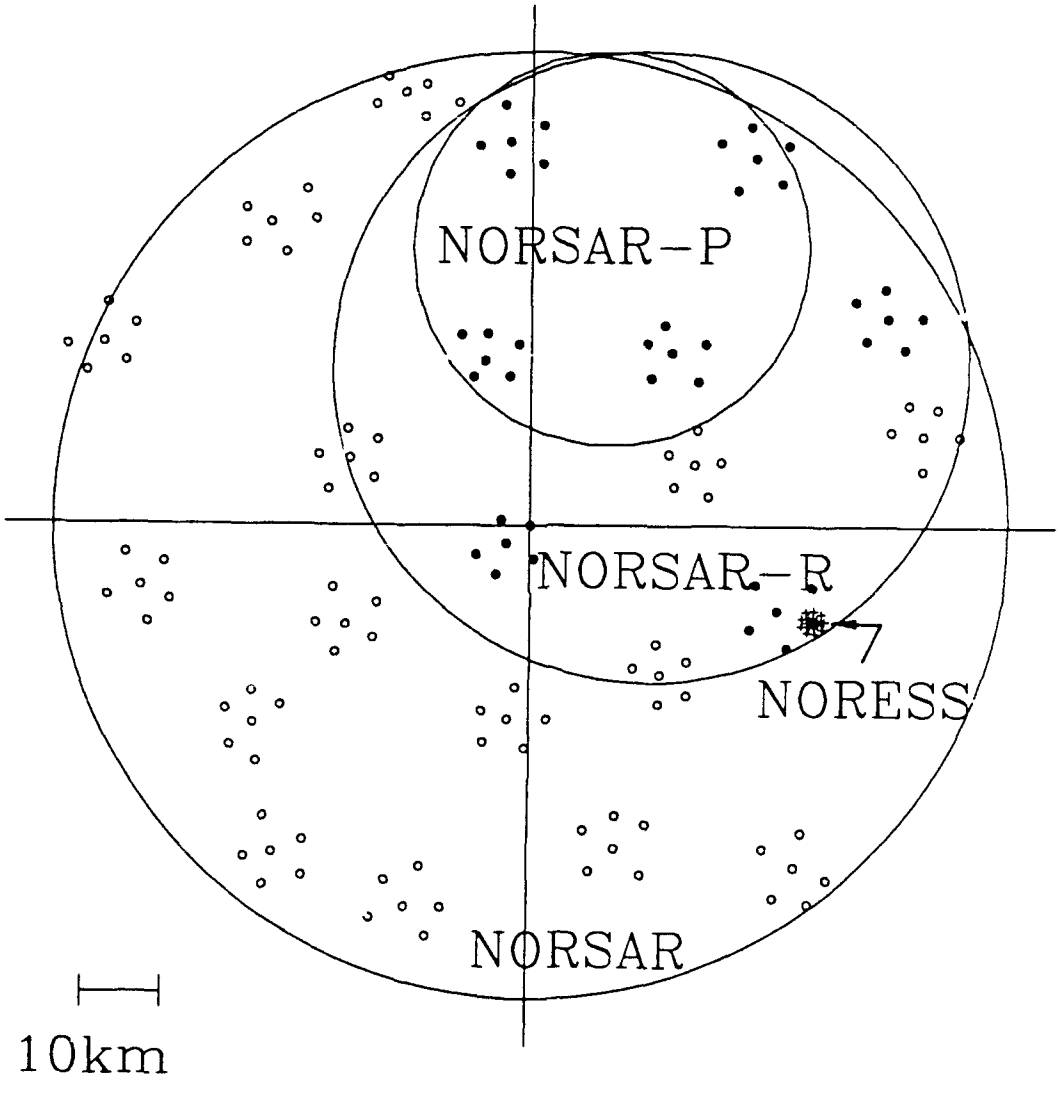


Figure 1. Array configurations for NORSAR, NORSAR-R, NORSAR-P and NORESS. The apertures of these arrays are approximately 110, 80, 50 and 3 kilometers.

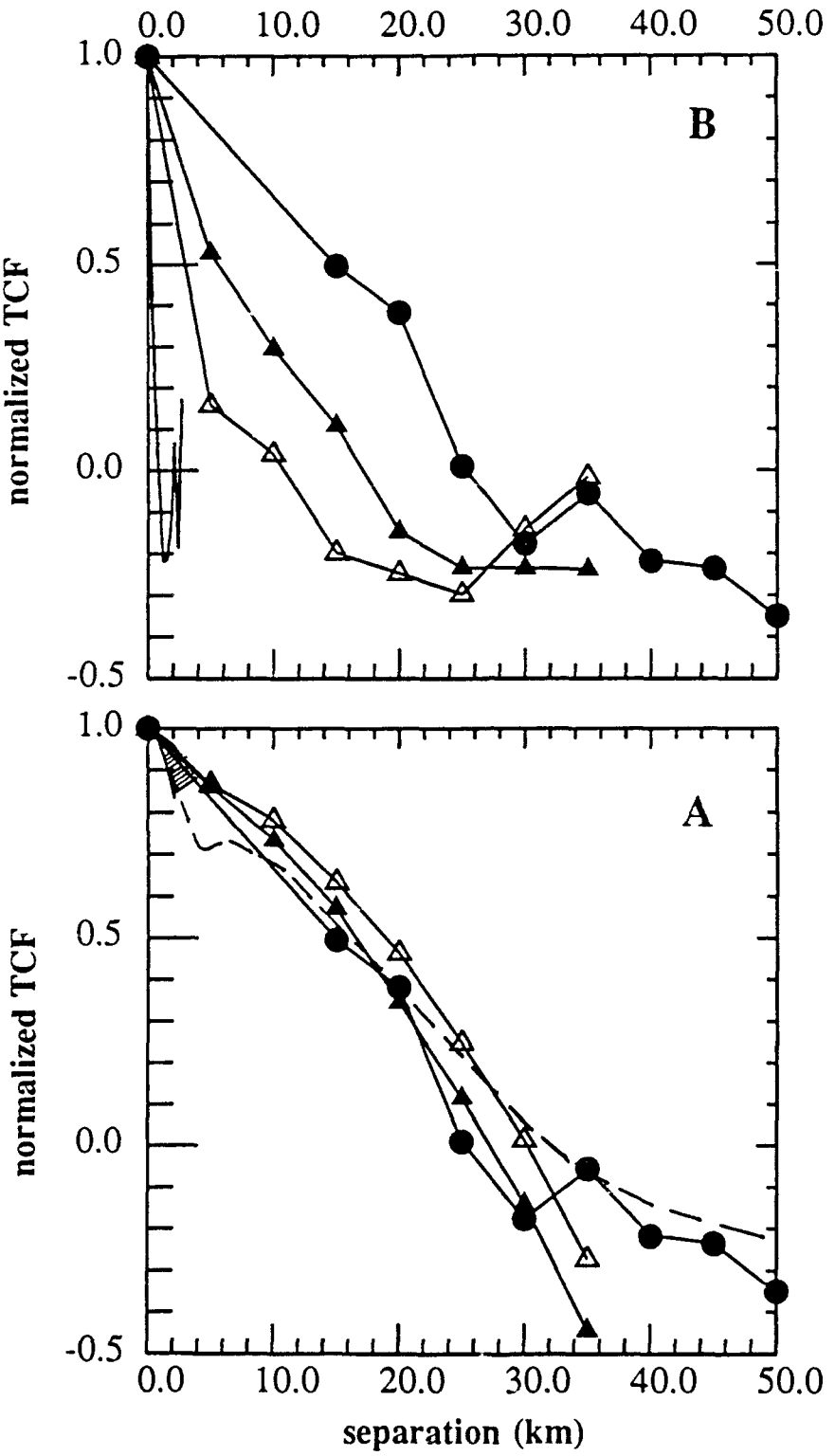


Figure 2. Transverse coherence functions, where the solid circles, solid triangles, open triangles and solid line are from NORSAR, NORSAR-R, NORSAR-P and NORESS respectively. a) The original observations; note that although these arrays are located in the same region, their coherence functions show quite different characteristics because of the inability of the TCF from an individual array to see the effects of inhomogeneities larger than the array. b) The same coherence functions, but after being corrected with equation (1). All the curves are reasonably consistent. The shaded region is from measurements of mean-square slowness of NORESS relative to NORSAR-R. The dashed line is the coherence function from the inversion of Flatté et al (1991).

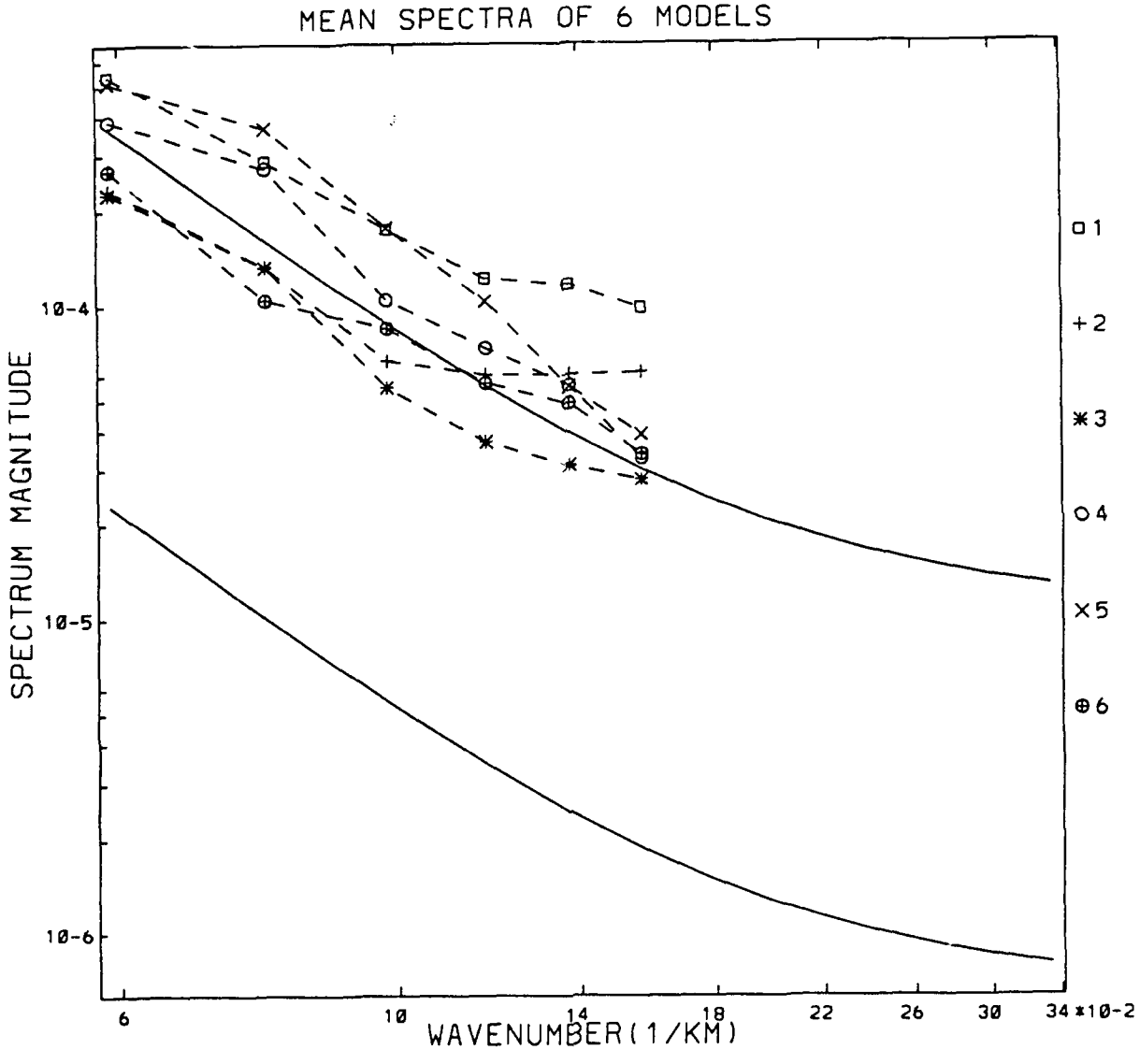


Figure 3. Comparison between a stochastic model and several deterministic models. The curves are from Flatté and Wu (1988) and correspond to assumed isotropy and to 1 and 4 percent rms wavespeed perturbations respectively. The symbols are from various published tomographic models: (1) Aki and Christofferssen (1977); (2-3) Christoffersson and Husebye (1979); (4-6) Thompson and Gubbins (1982).

An attempt to waveform modelling - Influence of the superficial geological structure

Stéphane Gaffet

Société Radiomana - 27, rue Claude Bernard - 75005 Paris - France

Grant No: 90 - 0356

Research accomplished

The aim of this work is to investigate the possibility we have to obtain a reliable synthetic representation of the displacement waveform recorded by the French Laboratoire de Détection et de Géophysique (L.D.G.) network for detonations occured in the central region of Yucca Flat, Nevada (Fig. 1, adapted copy from Ferguson, 1988). To hit this object we have in a first time integrated the discrete wavenumber boundary integral equation method (Bouchon and Aki, 1977; Gaffet and Bouchon 1991) into a powerful numerical algorithm which permit now to investigate any kind of non vertical subsurface or topographic structures. Having this tool, the major problem remains now in the definition of a realistic model of wave propagation and of source function for explosion.

The data we try to shape are summations of the displacements recorded over the whole L.D.G. network. These data allow us to consider a global almost flat receiver response (Lemenager, 1982) with an unknown magnification or attenuation that stays constant for all the events studied. The mantle path attenuations of the *P* and *pP* phases are assumed to be governed by the Futterman (1962) attenuation law. We now describe the model used to represent the central region of the Yucca Flat valley. The cross section oriented toward the France is roughly perpendicular to the main axis of the valley. Such an orientation justifies very well the use of a 2D model to compute the farfield synthetic seismograms. The figure 2 shows the corresponding cross section. The width of the valley equals approximately *12.6* km and the height *1* km. The display vertical exaggeration is *5:1*. The water table, *wt*, is issued from Doty and Thordarson (1983). It separates the dry, *DT*, and the wet, *WT*, tuff levels. Above these volcanic rocks stay superficial deposits, *SD*, whose base depth, *sd*, has been interpolated from drill holes data given by Fernald et *al.* (1968). Following Bouchon (1976), a superficial layer made up of fan alluvium, *FA*, has been introduced. Finally, the Tertiary-Paleozoic contact depth, *tp*, is derived from the works of Ferguson et *al.* (1988) and Ferguson (1988).

Table 1

Medium	α (*m/s*)	β (*m/s*)	ρ	ν
AL	700	330	1500	0.35
SL	1340	640	1770	0.35
DT	2140	1140	1790	0.30
WT	3000	1600	1790	0.30
PZ	4570	2640	2500	0.25

The elastic parameters of each medium sumed up in table 1 are those given by Ferguson (1988). α, β, ρ, and ν denote the *P* and SV velocities, the density and the

Poisson coefficient. No inelastic attenuation has been introduced in the aim to validate the numerical stability of the algorithm. *21* explosions have been selected which occured near the cross section as shown figure 1. The principal characteristics of these events are recalled in table 2. Their locations resulting from the projection onto the cross section are depicted figure 3. Four explosions are inside the dry tuff level (*e.g. Draughts*, *Tajo*, *Strake*, and *Texarkana*). The majority of them are below the water table. *Breton* assumed to be buried in the sediment deposit level is very close to the closing area of all the media near the horst Paleozoic structure.

Table 2

No	Latitude	Longitude	depth (m)	Date	m_b	Event name
1	37.0867	-116.0711	**483**	13 *Sep* 1984	5.0	**Breton**
2	37.0858	-116.0686	**500**	30 *Aug* 1988	5.0	**Bullfrog**
3	37.0831	-116.0661	**600**	22 *Mar* 1986	5.1	**Glencoe**
4	37.0797	-116.0514	**442**	27 *Sep* 1978	5.0	**Draughts**
5	37.0722	-116.0500	**701**	09 *Nov* 1977	5.7	**Sandreef**
6	37.0533	-116.0453	**600**	05 *Dec* 1985	5.7	**Kinibito**
7	37.0914	-116.0511	**640**	28 *Jan* 1982	5.9	**Jornada**
8	37.0658	-116.0464	**639**	01 *Mar* 1984	5.9	**Tortugas**
9	37.0608	-116.0453	**600**	13 *Aug* 1987	5.9	**Tahoka**
10	37.0889	-116.0492	**600**	13 *Oct* 1988	5.9	**Dalhart**
11	37.0728	-116.0458	**533**	14 *Apr* 1983	5.7	**Turquoise**
12	37.0786	-116.0439	**564**	12 *Jul* 1978	5.5	**Lowball**
13	37.0944	-116.0447	**564**	25 *May* 1977	5.3	**Crewline**
14	37.0947	-116.0361	**637**	03 *Jun* 1975	5.7	**Mizzen**
15	37.0692	-116.0303	**640**	04 *Feb* 1976	5.8	**Keelson**
16	37.0947	-116.0322	**640**	02 *Apr* 1985	5.7	**Hermosa**
17	37.0947	-116.0278	**594**	27 *Apr* 1977	5.4	**Bulkhead**
18	37.0739	-116.0197	**640**	27 *Sep* 1978	5.7	**Rummy**
19	37.0983	-116.0156	**500**	05 *Jun* 1986	5.3	**Tajo**
20	37.0867	-116.0069	**518**	04 *Aug* 1977	5.0	**Strake**
21	37.0767	-116.0006	**500**	10 *Feb* 1989	5.2	**Texarkana**

The observed signals are displayed figure 4 with their normalized amplitudes. A general observation can already be made. Taken as a whole, the amplitudes of the seismograms appear to be poorly correlated to the U.S.G.S. m_b magnitudes. For instance, the amplitude of *Tajo* (m_b = 5.3) is *2* times the one of *Jornada* and *Tortugas* (m_b = 5.9). Likewise, *Kinibito* and *Mizzen* have both m_b = 5.7 whereas the amplitude of *Mizzen* if *6* times the amplitude of *Kinibito*. Source effect or source site response ? Both reasons can be advanced to explain these observations.

The next step of this work concerns the waveform modelling. Following Bouchon (1976), we use the reciprocity theorem to compute the teleseismic displacement

diffracted by the Yucca Flat valley. The source function developped by Mueller and Murphy (1971) and Murphy (1977) is applied in a first time to model the synthetic seismograms shown figure 5. These seismograms correspond to the best waveforms obtained by fitting the relative amplitudes. Only the yield has been tuned to do this modelling. For it has the maximum observed relative amplitude, the choosen reference event is *Mizzen* (m_b = 5.7), and we arbitrarily fix its yield to be *150* kt. The table 3 summarizes the relative yields obtained. The media of burial are written in parenthesis. The relative yields are equal to the amplitude ratio for *Bullfrog*, *Glencoe*, *Draughts*, *Keelson*, *Hermosa*, *Bulkhead*, and *Rummy*, thus for these events the relative source site effect is not significant. For the events *Tajo*, *Strake*, and *Texarkana* (all in dry tuff) the relative amplitude is *25 %* greater than the relative yield. For all the other events, except *Breton* (staying in sediment deposits and for which the relative amplitude is *4* times the yield ratio), the relative amplitude is approximately *30 %* lower than the yield ratio.

Table 3

No	m_b	Yield ratio	Event name	No	m_b	Yield ratio	Event name
1	**5.0**	**0.01**	*Breton* (SD)	*12*	**5.5**	**0.33**	*Lowball* (WT)
2	**5.0**	**0.05**	*Bullfrog* (WT)	*13*	**5.3**	**0.21**	*Crewline* (WT)
3	**5.1**	**0.08**	*Glencoe* (WT)	*14*	**5.7**	**1**	*Mizzen* (WT)
4	**5.0**	**0.05**	*Draughts* (DT)	*15*	**5.8**	**0.47**	*Keelson* (WT)
5	**5.7**	**0.49**	*Sandreef* (WT)	*16*	**5.7**	**0.30**	*Hermosa* (WT)
6	**5.7**	**0.21**	*Kinibito* (WT)	*17*	**5.4**	**0.22**	*Bulkhead* (WT)
7	**5.9**	**0.41**	*Jornada* (WT)	*18*	**5.7**	**0.39**	*Rummy* (WT)
8	**5.9**	**0.44**	*Tortugas* (WT)	*19*	**5.3**	**0.55**	*Tajo* (DT)
9	**5.9**	**0.57**	*Tahoka* (WT)	*20*	**5.0**	**0.05**	*Strake* (DT)
10	**5.9**	**0.65**	*Dalhart* (WT)	*21*	**5.2**	**0.03**	*Texarkana* (DT)
11	**5.7**	**0.42**	*Turquoise* (WT)				

The signals presented figure 5 are *10* seconds long and include the L.D.G. short period seismometer response (Gaffet, 1990). The validity of the different fits is measured with the correlation coefficient computed over the first *5* seconds of signals. The comparison between observed and computed seismograms show two classes of events. The first one groups *Draughts*, *Sandreef*, *Kinibito*, *Jornada*, *Tortugas*, *Tahoka*, *Dalhart*, *Turquoise*, *Lowball*, *Crewline*, *Mizzen*, *Bulkhead*, and *Strake*. The second class contains all the other events. The first group shows waveforms which resemble closely to the observed ones. The longer duration of the ground motion observed in the central region (*i.e.* around *Tahoka*) is well reconstructed as well as the relative amplitudes of the two first troughs corresponding to the *P* and *pP* wave arrivals. The fourth peak that induces the duration lengthening arrives *4* seconds after the first arrival, this delay is very close to the one of the true seismograms. Unfortunately, the *pP* wave of *Jornada* to *Bulkhead* events arrive as far as *0.4* second earlier than the real one. This discrepancy should be explain by many parameters, *e.g.* the depth of burial may be too slight beneath the surface, the wave velocities used (Table 1) are maybe too large or the model should take into account laterally varying velocities as depicted by Johnson and McEvilly (1990). However that may be, this *pP* phase advance is the principal factor

that decreases the correlation coefficient.

The second class of events contains the seismograms with uncorrect *pP* over *P* trough amplitude ratio. The different phases received from *Keelson* and *Hermosa* appear to be not sufficiently delayed along the seismograms and show a too high predominant frequency. The first effect (also seen for *Mizzen*) can be described as a too earlier *pP* wave arrival inducing a fourth peak advance. The other events of this group have a good frequency behaviour. But while for *Breton*, *Bullfrog*, and *Glencoe* the *pP* - *P* delay is correct, the *pP* wave arrives earlier for *Rummy*, *Tajo*, and *Texarkana*.

Conclusion

We have shown in this work that explosion teleseismic seismogram waveforms are very sensitive to the shot location [illegible] event occured in the Yucca Flat Test Site, Nevada. We obtain a good correlation between the synthetic seismograms durations and the real ones. Compare for instance synthetic (Fig. 5) and real (Fig. 4) *Strake* and *Texarkana* or *Breton* and *Jornada* detonations. All the seismograms computed have been constrained by the observed relative amplitude. This constrain has been taken into account by adjusting the yield of the Mueller-Murphy source. On the one hand, this method leads us to realistic waveform for the majority of the *21* explosions studied. The misrepresentation between synthetic and real seismograms beeing then explained by lateral velocity variations. But on the other hand, this method induces unrealistic yield estimation basically for explosion occured in sediment deposit for which the real yield is certainly greater than the one found. Thus the explosion source used must be adapted to better take into account such media. An other problem must be considered which could also explain a part of the misrepresentation. This problem concerns the Mueller-Murphy source radiation for detonations that take place near interfaces (*i.e.* at distances smaller than the elastic radius). If we do not take into account this fact we can over- as well as underestimate the explosion yield. Thus if the shot location in a heterogeneous media plays a great role in shaping the seismograms, it appears necessary to take care of the detonation working to have the best possible source function as input into the diffracting heterogeneous media system. In fact we cannot consider the explosion as a point source because the elastic radius becomes important in comparison with the valley dimensions. Likewise the spherical elastic zone shape in a homogeneous space should be modified in presence of different media having different compaction properties which induce variations in the frequency content and in the amount of seismic energy radiated outside of the valley.

Bibliography

Bouchon, M. (1976). Teleseismic body wave radiation from a seismic source in a layered medium. *Geophys. J. R. astr. Soc.* **47**, 515-530

Bouchon, M. and K. Aki (1977). Discrete wave-number representation of seismic source wave fields. *Bull. Seism. Soc. Am.* **67**, 259-277

G. C. Doty and W. Thordarson (1983). Water table in rocks of cenozoic and paleozoic age, 1980, Yucca Flat, Nevada test site, Nevada. *Department of the Interior - United States Geological Survey*

Ferguson, J. F., R. N. Felch, C. L. V. Aiken, J. S. Oldow, and H. Dockery (1988). Models of the Bouguer gravity and geologic structure at Yucca Flat, Nevada. *Geophysics* **53**, 231-244

Ferguson, J. F. (1988). Body waves magnitude variation at Yucca Flat, Nevada. *Bull. Seism. Soc. Am.* **78**, 863-872

Fernald, A. T., G. S. Corchary, and W. P. Williams (1968). Surficial geologic map of Yucca Flat, Nye and Lincoln counties, Nevada. *Department of the Interior - United States Geological Survey*

Futterman, W. I. (1962). Dispersive body waves. *J. Geophys. Res.* **67**, 5279-5291

Gaffet, S. (1990). Simulation des mouvements du sol à distances locales et télésismiques en milieu hétérogène - Méthode et applications - *Thèse de Doctorat*, **Grenoble I**, 85pp

Gaffet, S. and M. Bouchon (1991). Source location and boundary shape effects on the *P-SV* near displacement field using a boundary integral equation - discrete wavenumber representation method. *Geophys. J. Int.* **107**, in press

Johnson, L. R. and T. V. McEvilly (1990). OSSY Source characterization - Summary report. *Master*, **LBL, University of California**, 33pp

Lemenager, C. (1982). Applications de techniques numériques du traitement du signal à la sismologie. *Thèse D. I.*, **Paris VI**, 150pp

Mueller, R. A. and J. R. Murphy (1971). Seismic characteristics of underground nuclear detonations. Part I: seismic spectrum scaling. *Bull. Seism. Soc. Am.* **61**, 1675-1692

Murphy, J. R. (1977). Seismic source functions and magnitude determinations for underground detonations. *Bull. Seism. Soc. Am.* **67**, 135-158

Murphy, J. R. and R. A. Mueller (1971). Seismic characteristics of underground nuclear detonations. Part II: elastic energy and magnitude determinations. *Bull. Seism. Soc. Am.* **61**, 1693-1704

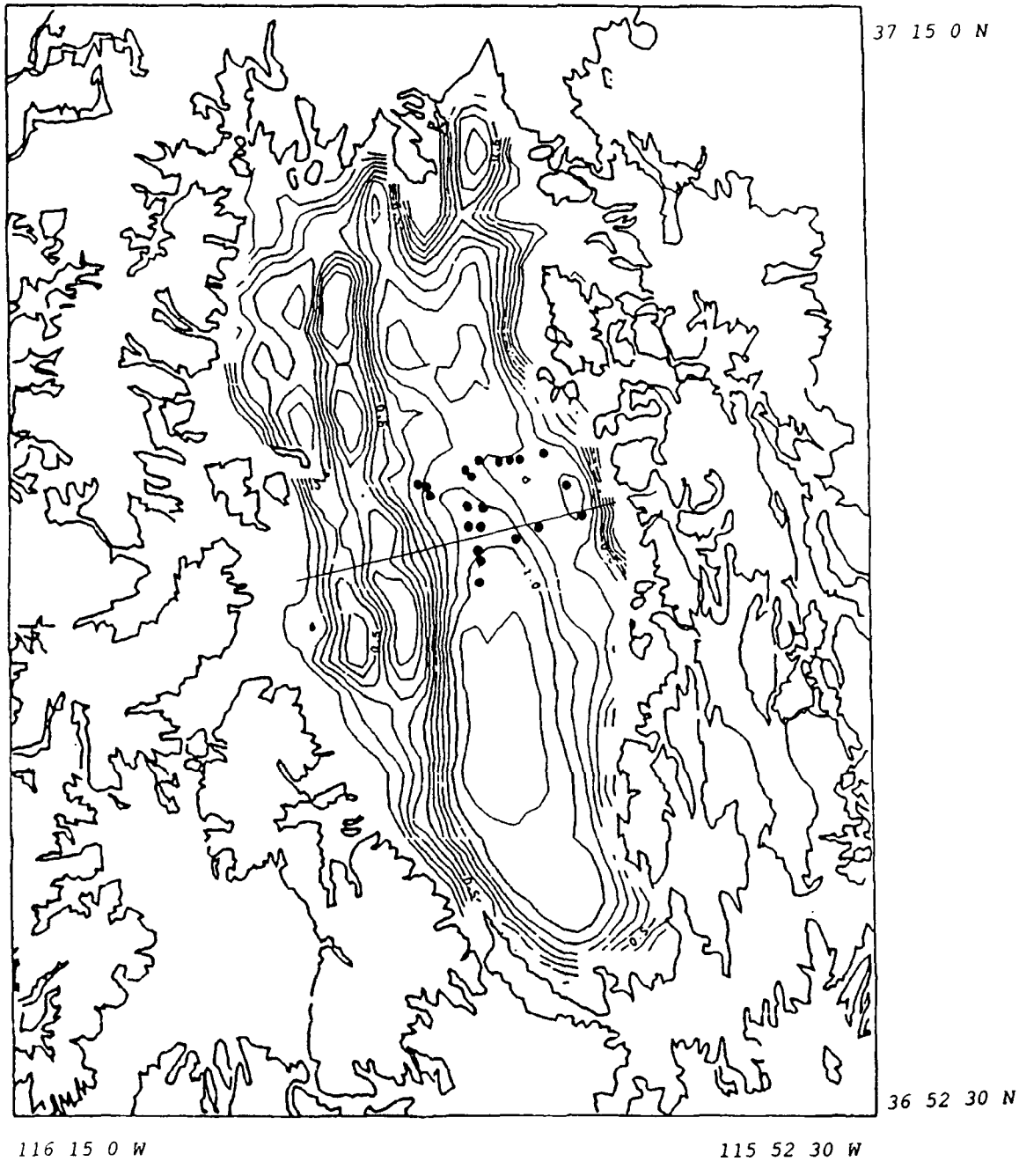


Fig. 1 Map of the Tertiary - Paleozoic contact depth in the Yucca Flat valley issued from Ferguson (1988). The locations of the explosions and of the cross section also plotted with the black circles and the bold line.

Yucca Flat cross-section

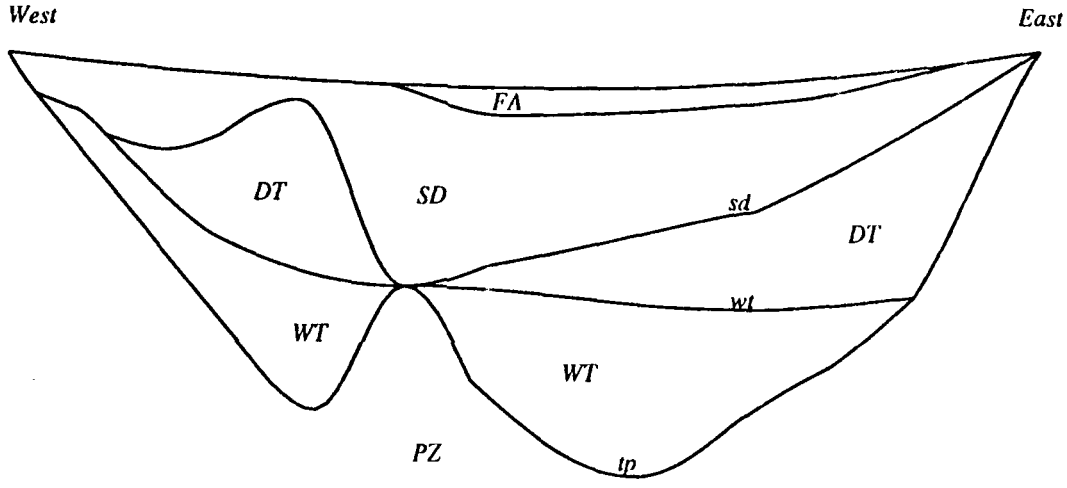


Fig. 2 Cross section model used for the calculations. See text for explanations of the different notations.

Yucca Flat cross-section and events selected

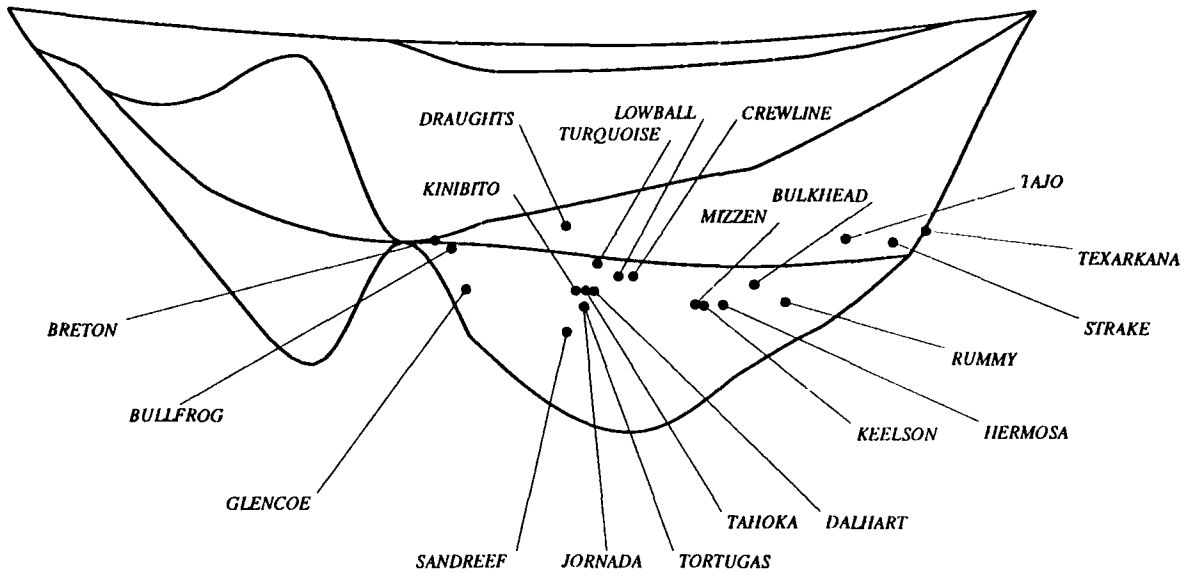


Fig. 3 Cross section and location of all the events studied.

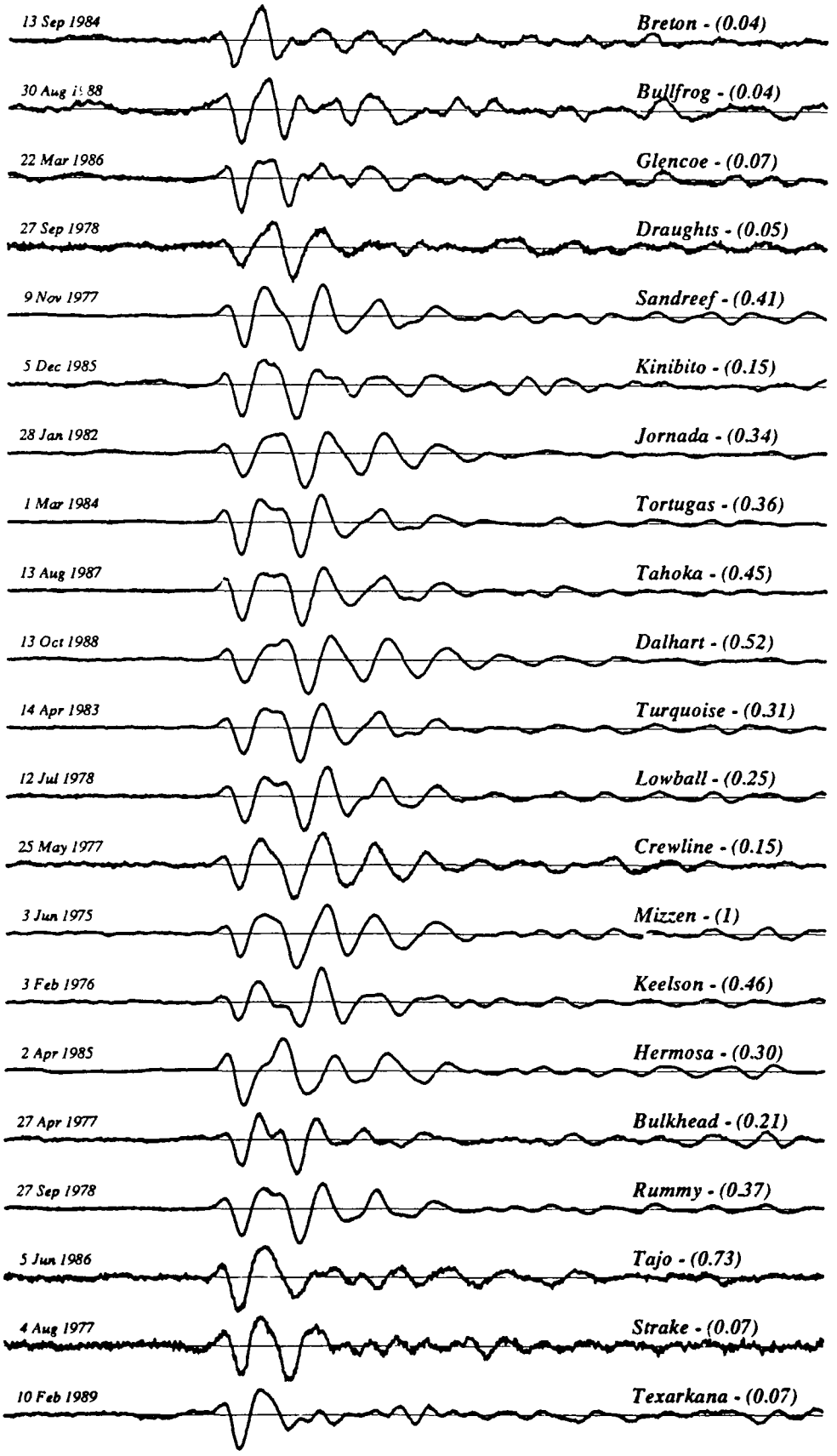


Fig. 4 Observed seismograms. The signals have been normalized and represent the mean seismograms observed during *20* seconds by the whole Laboratoire de Détection et de Géophysique network. The events displayed from the top to the bottom of the figure are located from the west part to the east part of the valley (See Fig. 3).

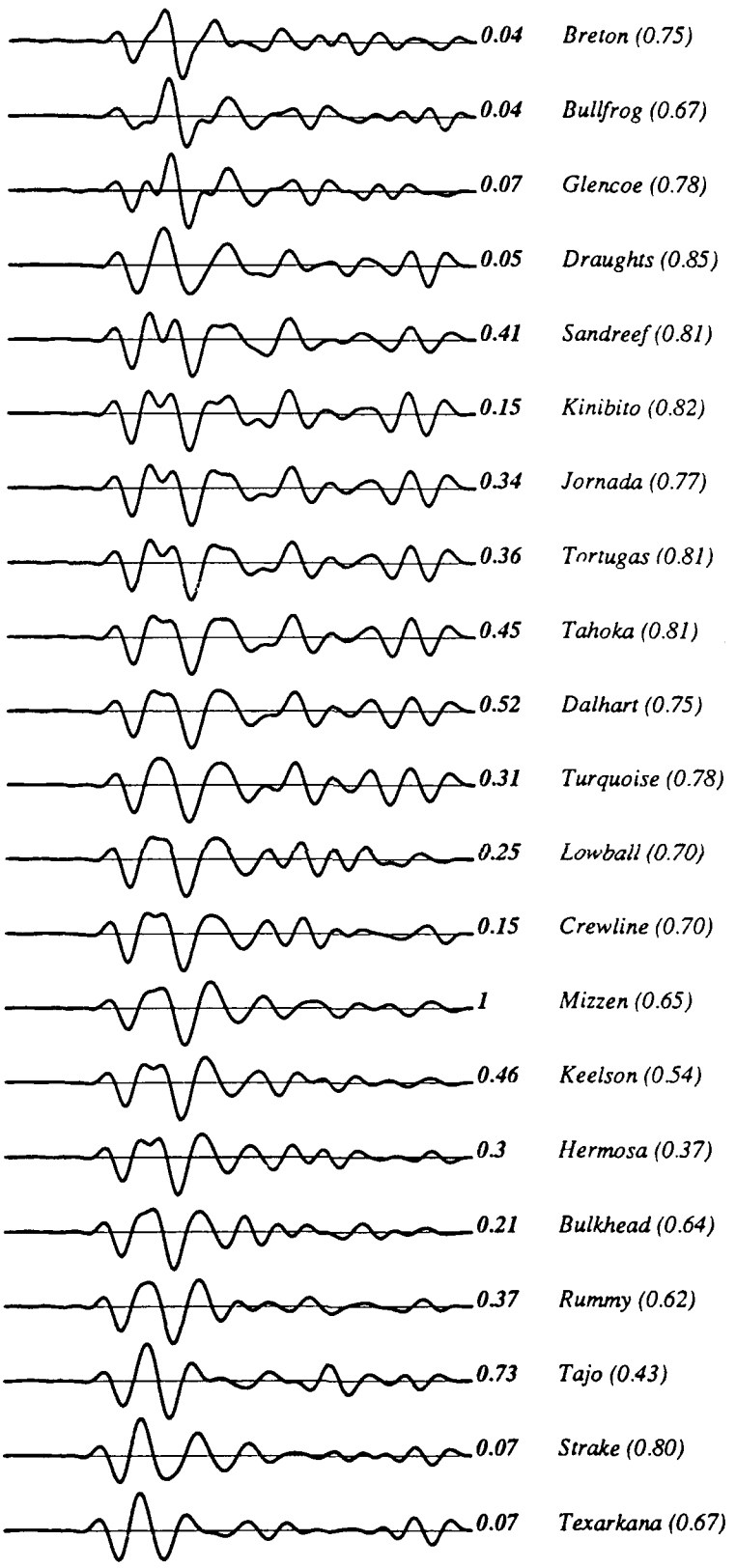


Fig. 5 Synthetic seismograms computed with the model displayed Fig. 2. The relative amplitudes as well as the corresponding event names are recalled. The time duration is *10* seconds. The numbers written in brackets are the correlation coefficients with the observed signals.

Analysis of GERESS-Recordings during GSETT-2

N. Gestermann, H.-P. Harjes, M. Jost, J. Schweitzer, and J. Wüster

Institute of Geophysics, Ruhr-University Bochum, Germany

Grant AFOSR-90-0189

Objective

The German Experimental Seismic System (GERESS) array project is a cooperative research program, jointly undertaken by Southern Methodist University Dallas, USA, and Ruhr-University Bochum in Germany. It is part of a multi-array network which includes NORESS, ARCESS, and FINESA in Scandinavia (Harjes, 1990). The objective of research activities carried out at the data center in Bochum was to analyze local, regional, and teleseismic waveforms recorded at GERESS. In this paper, results of this effort are presented for the period of April 22 - June 2, 1991 (Group of Seismic Experts Technical Test 2 (GSETT-2, phase 3)).

Research accomplished

During the GSETT-2 experiment, which took place from 22 April to 2 June 1991, GERESS data were extensively analyzed. The first step of this analysis consisted of an automatic detection algorithm based on a conventional short-term average (STA) over long-term average (LTA) technique. The STA/LTA detector worked on a set of filtered beams deployed at typical velocities of teleseismic and regional seismic phases. An onset was recognized if the STA/LTA ratio for a filtered trial-beam exceeded a threshold of 4.

For each detection, an interactive frequency-wavenumber (fk) analysis was carried out to estimate phase velocity and back-azimuth. From the slowness and back-azimuth of each phase, regional phases such as P_n, P_g, S_n, S_g, L_g, and R_g were identified in addition to teleseismic P-phase onsets.

Local and regional phases were associated to events using the RONAPP algorithm (Mykkeltveit and Bungum, 1984). From the arrival time differences of regional phases, the distance to the epicenter was determined from the Jeffreys-Bullen travel time tables. Together with the mean back-azimuth, the epicenter locations of local and regional events were determined.

From 22 April to 2 June 1991, GERESS reported 3795 phases and each report included back-azimuth, slowness, amplitude, and period, the latter two also measured manually. Of all reported phases, 33 % could be associated to Experimental International Data Center (EIDC) events, 27 % to own localized local or regional events, and 39 % were left as unassociatable phases. The array outage was about 8 %.

Because the bulletins of the international data centers (e.g. PDE, ISC, or EMSC) are not yet available, the contribution of GERESS can only be analyzed on the background of the GSETT-2 Final Event Bulletins (FEB). These bulletins were produced by the EIDCs under high time pressure and contain a few doubtful phase associations and events. We were not able to remove all misassociations from the FEBs, however the most obvious ones pertaining to GERESS were

addressed. These "cleaned" FEBs are used throughout this study as reference. GERESS contributed to 20 % of all event locations in these cleaned lists. After bulletins of international data centers become available, the work presented here will be extended.

a) Regional Distances

GERESS localized 682 events within a distance of 5°. Only 26 % appear for the same region in the FEBs published by the EIDCs (Fig. 1). Fig. 2 shows all regional FEB-epicenters to which GERESS contributed with phase readings.

Although Central Europe is an area of low natural seismicity, there is a high population of artificial seismic sources, mainly quarries and rock bursts. During working hours between Monday and Friday (and Saturday in the CSFR), significantly more events are located than in non-working hours or on weekends. Correcting for holidays, we obtained the following statistics: The highest rate of events per hour (1.1) was observed on Tuesdays, Wednesdays, and Thursdays; the rate is somewhat lower on Mondays and Fridays. On Saturdays the rate of events per hour decreased to 0.6, and reaches a minimum on Sundays (0.2). Addressing located events per time of day, we observed a strong increase in activity starting at about 7 am (all times in UT) and reaching a maximum at about 11 am. The number of events per hour generally follows a Gaussian distribution. A smaller peak between 3 to 4 am is interpreted as being caused by activities in the Polish copper mining area around Lubin. At this time of day, small explosions are detonated to trigger larger mining induced events for adjustment of the local stress field.

Local magnitudes were determined for GERESS from all localized local and regional events during GSETT-2. Because magnitude correction tables for the specific location of GERESS have not yet been determined, a systematic deviation of M_L magnitude values for GERESS cannot be precluded. The detection threshold for GERESS for certain azimuthal sectors can vary up to 0.5 magnitude units. The reason for this observed azimuthal variation of detection threshold is the variation of crustal structure around GERESS (f.e., the Alps, Molasse, Bohemian Massive). These structural features may lead to a virtual blockage of regional seismic phases in a certain distance range, in extreme cases. As an example, the Teisseyre-Tornquist-suture zone between north-eastern and south-western Europe apparently blocks regional waves of small events.

The Teisseyre-Tornquist line (Tornquist, 1911) defines a sharp boundary between the East European Platform and the Paleozoic Europe (as sketched in Figs. 1 and 2). Investigations show that the Moho discontinuity increases from a depth of about 25 - 35 km in Central Europe to a depth of about 45 - 50 km in the East European Platform. In the central section of the Teisseyre-Tornquist line (Poland) the Moho apparently reaches depths of more than 60 km (Meissner *et al.*, 1987) in a graben-like structure.

During GSETT-2 regional seismic phases from events, whose travel path crossed this suture zone, were not detected for epicentral distances smaller than 8.0°. Consequently, stations southwest of this suture are missing virtually all regional events from the Baltic area around Leningrad (compare Fig. 1 and Fig. 2). Vice versa, the detection capability of Scandinavian stations is lowered for events originating south of this suture zone. These observations lead to the assumption that this line virtually blocks regional seismic phases. In contrast, there has been no clear indication of a blockage of regional seismic energy across the deep roots of the Cenozoic orogenies (e.g., Alps, Pyrenees, Hellenides), which also show depths of the Moho greater than 60 km. We conclude that an increase of the Moho depth is not sufficient to explain the observed effective blockage of regional phases across the Teisseyre-Tornquist suture.

b) Teleseismic Distances

GERESS, designed as a regional array, also contributed remarkably to the teleseismic observations ($\Delta > 20^{\circ}$). GERESS onsets could be associated to more than 22 % of all events in the teleseismic distance range (Fig. 3). For example, GERESS observed about 100 aftershocks (m_b = 2.7 - 5.5) of the large Caucasus event of Apr. 29, 1991 (m_b = 6.2, $\Delta = 22^{\circ}$) out of a total number of 118 aftershocks (FEB). The good teleseismic detection capability of GERESS (Fig. 4) is caused mainly by the general low noise level at frequencies around 1 Hz and the application of advanced array techniques to teleseismic P and PKP onsets.

On the other hand, we clearly see that man-made noise (mining and industrial activity) increased during day time. This increased cultural noise diminished the detection capability for teleseismic events. Consequently, we observed less P-phases during general working hours and during this time of the day, the number of reported teleseismic onsets decreased by 30 % .

For addressing the teleseismic detection capability of GERESS, we assume that the network magnitudes as given in the FEBs are not systematically underestimated. After correcting for array outages, about 25 % of the teleseismic events in the magnitude range between 3.0 - 4.0 were observed at GERESS. For events distributed world-wide with magnitudes above 4.2, the detection capability of GERESS is above 50 %, and GERESS did not miss any event larger than m_b = 5.3.

Detection capabilities clearly decrease for distances beyond 90°, but begin to increase from about 120° for PKP phases. For distances between 140° to 155°, around the PKP caustic, the detection threshold is similar to that at about 90°. At $\Delta = 146^{\circ}$, the PKP caustic is at its maximum which enables GERESS to detect events between m_b = 3.5 - 4.0. This is the reason for the excellent monitoring capability of GERESS with respect to the French nuclear test sites in the Tuamotu Archipelago (Mururoa and Fangataufa) in the South Pacific. Three underground explosions from this test site were clearly recorded at GERESS during the GSETT-2 period.

For 356 events in the distance range between 20° and 100°, m_b values were calculated by the EIDCs using amplitudes and periods observed at GERESS. Therefore, it is possible to compare GERESS magnitudes with the FEB network magnitudes. A preliminary relation is given by:

$$m_b(\text{FEB}) = 0.86\ m_b(\text{GERESS}) + 0.63 \quad .$$

GERESS seems to have a slight negative magnitude residual with respect to the GSETT-2 network for magnitudes lower than 4.5 and a positive residual for events with larger magnitudes.

We cannot expect, that the GERESS array with its small aperture of about 4 km can observe slowness and azimuth for teleseismic phases with the same accuracy as larger arrays (e. g., Gräfenberg, NORSAR, Yellowknife). Therefore a point of general interest is: how good are the observed azimuth and slowness values and do the mislocation vectors show any systematic pattern?

To investigate this problem, we calculated the theoretical slowness and azimuth (from station to epicenter) values and their residuals for about 350 teleseismic events. To reduce the scatter in the data and the influence of observed slowness and azimuth errors at GERESS, we only used events, which had been localized with more than 15 defining phases.

A first analysis shows that the residuals for azimuth and relative slowness (i. e. $(p_{obs} - p_{theo})/p_{theo}$) increase with epicentral distance - as expected. The azimuth residuals are +/- 30° for distances less than 70° and increase rapidly to +/- 60° for larger distances. Only few observations (about 2 %) show residuals of more than +/- 90°. The observed relative slowness residuals show a similar pattern. We observe slowness variations of up to +/- 60 % for P- and P_{diff}-phases and an

increase of slowness variations to +/-100 % for PKP-phases.

If we plot these preliminary mislocation vectors in the slowness space, we see some systematic effects: The slowness observations - without the PKP_{DF} observations from the north-east - are rather too small than too large. How far this effect is caused or masked by the array transfer function, needs further investigations.

The mean value of the azimuth residuals is positive for observations from the north and northeast. For the azimuth range from 40° to 80° we observe negative residuals which change again to positive residuals for events directly from the east. For the azimuth range between 250° and 300°, we once again observe a change in the sign of the residuals from negative to positive. All other directions are not well constrained.

The GERESS mislocation vector field in slowness space shows a lot of similarities - especially for observations from the north and east - with the mislocation vectors of the Gräfenberg array (Faber *et al.*, 1986). These authors explained the mislocation of GRF with a lateral heterogeneous velocity structure in the crust and in the upper mantle under the GRF array and north-north-east from GRF under the Bohemian Massive. Either we see the same effects in GERESS mislocations by chance, or the mislocations of both arrays (the distances between seismometer vaults of GRF and GERESS range between 150 km and 205 km) are caused by commonly seen larger heterogeneous structures. This would require a reinterpretation of GRF mislocation vectors.

Conclusions and Recommendations

After one year of data recording and analysis it is obvious that GERESS is the most sensitive station in Central Europe for monitoring local, regional, and teleseismic seismicity as demonstrated by the results of the GSETT-2 experiment. During the time of the experiment, GERESS localized on average 16 events per day within a 5° distance. In addition, an average of 12 teleseismic events per day were observed.

GERESS shows an azimuthally varying detection capability which seems to be related to a major suture zone in Central Europe effectively blocking regional seismic energy. Further investigations on the physical nature of this wave propagation anomaly are required.

For teleseismic observations the GERESS array is not only very sensitive but also the observed magnitudes are in good agreement with network magnitudes. The observed slowness and azimuth values for P- and PKP-phases can be used for a first order event localization, with increasing error bars for larger distances. To increase the location capabilities it seems to be promising to further determine azimuth correction values.

Acknowledgement

The kind hospitality and support of the NORSAR staff during the stay of one of us (J. S.) for analyzing GERESS during GSETT-2 and also their help in implementing the NORSAR software package in Bochum is gratefully acknowledged.

Literature

Faber, S., J. Plomerová, V. Babuška (1986). Deep-seated lateral velocity variations beneath the GRF array inferred from mislocation pattern and P residuals, *J. Geoph.* **60,** 139-148.

Harjes, H.-P. (1990). Design and siting of a new regional array in Central Europe, *Bull. Seism. Soc. Am.* **80,** 1801-1817.

Meissner, R., T. Wever, E. R. Flüh (1987). The Moho in Europe - Implications for crustal development, *Ann. Geophys.* **5B,** (4), 357-364.

Mykkeltveit, S. and H. Bungum (1984). Processing of regional seismic events using data from small- aperture arrays, *Bull. Seism. Soc. Am.* **74,** 2313-2333.

Tornquist, A. (1911). Die Tektonik des tieferen Untergrundes Norddeutschlands, *Sitzungsberichte der königlich preussischen Akademie der Wissenschaften,* **38,** 27.7.1911, 822-836.

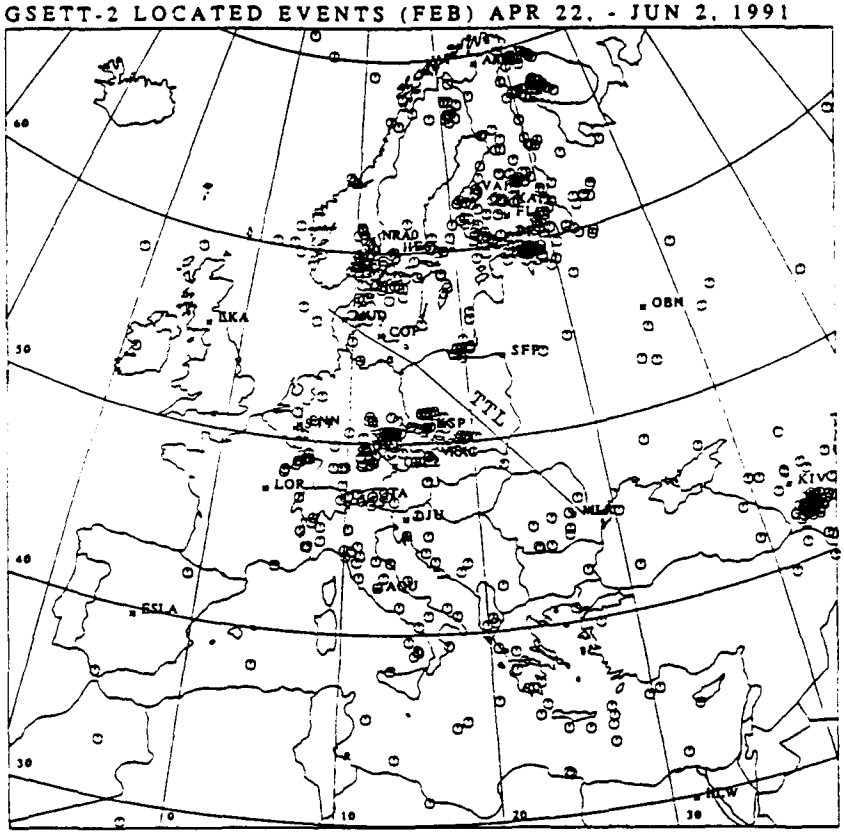


Fig. 1:
All European events localized by the EIDCs for GSETT-2, phase 3 from Apr. 22 to June 2, 1991. Notice the sketched Teisseyre - Tornquist line (TTL).

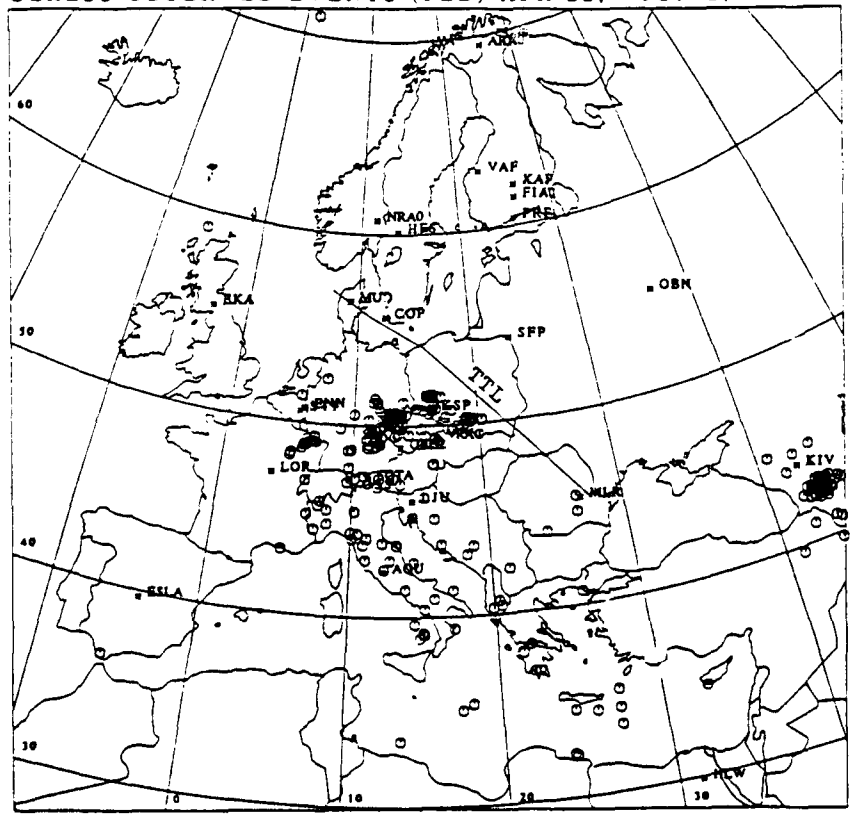


Fig. 2:
As Fig. 1, but now only for events seen by GERESS.

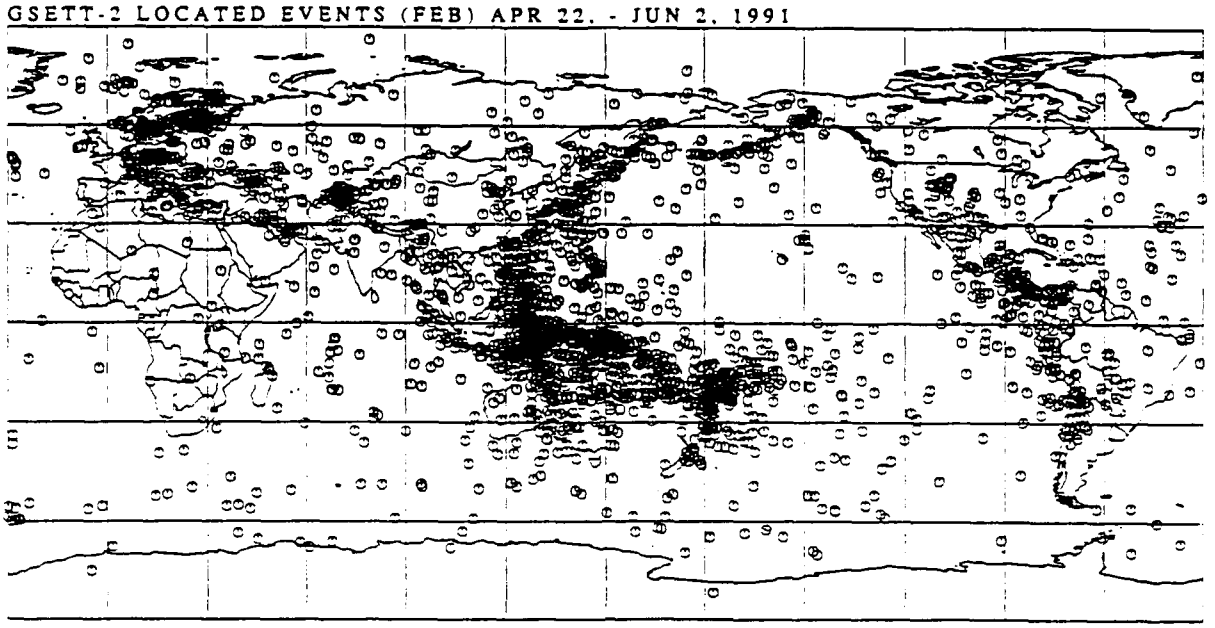


Fig. 3:
All events localized by the EIDCs for GSETT-2, phase 3 from Apr. 22 to June 2, 1991.

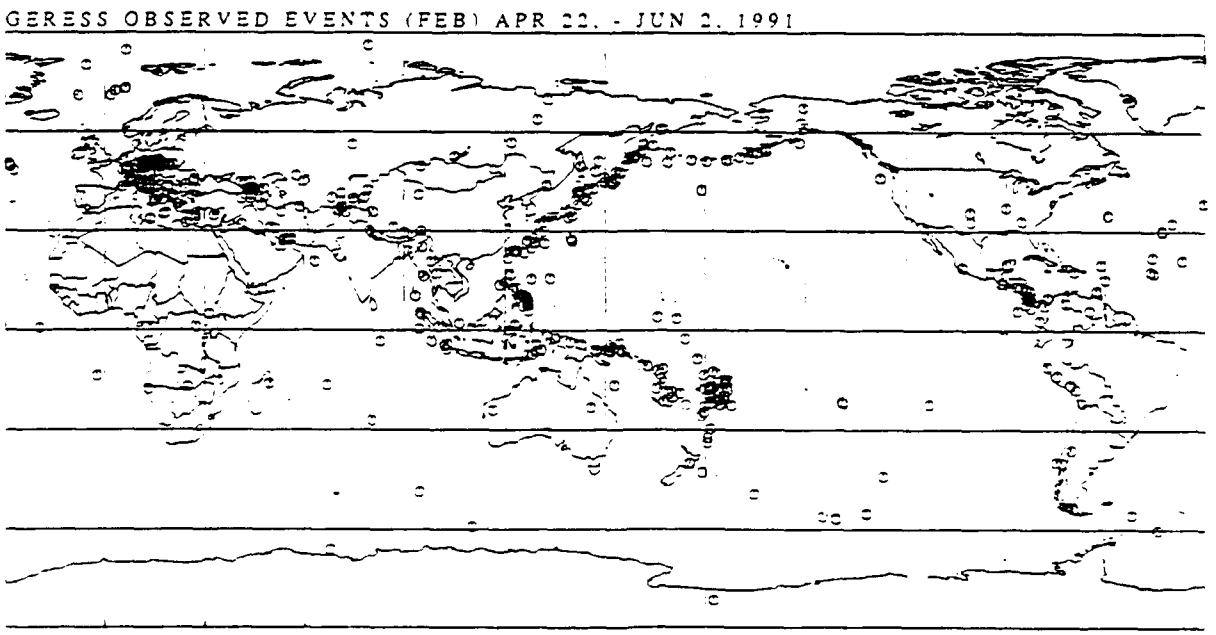


Fig. 4:
As Fig. 3, but now only for events seen by GERESS.

TITLE: Heterogeneous Propagation and Blockage of L_g in the Caspian Sea - Caucasus Mountain Area of the USSR

AUTHOR: Holly Given, Scripps Institution of Oceanography, UCSD

CONTRACT NUMBER: F19628-90-K-0045

OBJECTIVE: An observational study has been undertaken to document azimuthal variations in regional wave propagation at the broadband IRIS/IDA station KIV (Kislovodsk) in the USSR, with emphasis on the seismic phase L_g. KIV was chosen because of its location in an active seismic area. KIV has been routinely operating since February 1989, and has recorded many local, near-regional, and far-regional Eurasian earthquakes with depths in the crust from a wide azimuth range. KIV is sited in an interesting tectonic area of known variations in structure; it is located in the foothills of the Caucasus Mountains, between two inland seas, the Black Sea and the Caspian Sea, in a region rife with small-scale topographic and tectonic variation. Thus, it is possible to directly compare the character of regional phases at the same distance which propagate through different structures. Nuttli (1986) and many others noted that magnitudes inferred from the amplitude of the regional L_g phase from events in the same source region, as observed at a single station, are very stable measurements of the absolute size of the seismic event. However, many studies have shown that L_g amplitudes are very sensitive to structure, in particular, to abrupt changes in crustal structure that deviate from a slowly varying horizontally stratified structure (for example, Kennett and Mykkeltveit, 1984). Around KIV, the Caspian Depression, north of the Caspian Sea, has been noted in particular as a possible attenuating feature of L_g. This study attempts to refine such observations by looking at events which have propagated shorter distances, eliminating some of the possible causative features of diminished amplitudes. A more general objective is to document all obvious differences in regional phases observed at KIV, particularly where they can expand results from other regional studies of heterogeneous wave propagation, such as those of Kadinsky-Cade et al (1981) for the Turkish and Iranian Plateau area south of KIV.

RESEARCH ACCOMPLISHED: All events in the PDE catalog on the order of 9° to 15° from KIV, with global $m_b \leq 5.3$ and catalog depths of ≤ 33 km between the beginning of station operation (February 1989) and the end of 1990, were examined. Twenty nine events were deemed suitable for further study; their locations are shown in Figure 1. Geographic areas approximately equidistant at 15° from KIV include (clockwise from north) the southern Urals, western Kazakhstan, Iran, Jordan, Turkey and the Aegean Sea.

Different frequency bands of the earthquake seismograms were examined to enhance various regional phases. In order to have an overall comparative value for earthquake size, long-period surface waves (20 s - 10 s) were plotted and surface wave magnitudes were calculated from the KIV records. Three general zones of differing Rayleigh wave dispersion were observed in the long-period passband. Events 1-9 (see Figure 1), with back azimuths between 36° and 132°, show maximum Rayleigh wave amplitudes between group velocities of 2.5 - 2.0 km/s and sometimes slower; Rayleigh waves are very dispersed. This azimuth range includes the Caspian Depression and Caspian Sea. Events 10-20 from azimuths generally to the south of KIV (140° - 220°) show much less

dispersion, with Rayleigh waves arriving around 3.0 km/s. The third zone, events 21-29, with back azimuths from 239° to 265° (Turkey and the Aegean Sea), once again show slower Rayleigh waves centered around 2.5 km/s, but not as dispersed as zone 1. Figure 2 shows examples of these three characteristic patterns.

Records were bandpass filtered from .6-3 Hz to isolate L_g, and plots of the three-component RMS amplitude were made. This passband showed more variability with azimuth, particularly for L_g and S_n. Figure 3 shows smoothed three-component RMS amplitudes for all events except 1 and 23 (nearly identical to events 2 and 24), which were omitted due to space consideration. Markers denoting arrival times of velocities of 4.6, 3.6, and 3.0 km/s are shown. As a general statement, we can say that regional L_g is very poorly observed for most azimuths around KIV. Of the 29 earthquakes studied, only event 10 shows L_g amplitude above the S_n amplitude. Events 1-9 and 19, 20, and 29 were the only other events that showed any L_g energy, and this was small. There are also characteristic azimuths for which S_n is not observed. Events 11-18 (from Iran) and 21-28 (from southern Turkey) show no S_n or L_g energy at KIV, although many of these events have a prominent broadband S wave with energy peaked around periods of 5 - 2.5 s.

By looking at records of these earthquakes at other regional broadband stations, we can isolate whether the absence of a phase is in some way a characteristic of the earthquake or earthquake source region, or if it is a consequence of the path. Several of these events were recorded at similar distances at other IRIS/IDA stations. Events 1 and 2, from the southern Urals, show a clear S_n phase of extended duration at KIV, but no L_g. This path crosses the Caspian Depression north of the Caspian Sea, which has been suggested as a possible attenuating feature for L_g in studies that looked at events that had propagated to teleseismic distances (Baumgardt, 1991; Eissler et al, 1988). Figure 4 (top trace) shows the RMS amplitude for Event 2 at OBN, 13.2° away and to the west of the earthquake. The propagation path to OBN crosses the Russian Platform and should be fairly homogeneous. The OBN record shows a large L_g phase. This implies that the Caspian Depression has caused the blockage of L_g at KIV. Event 5's path to KIV crosses the Caspian Sea about mid-latitude. A large S_n phase, but a very low-amplitude and slow L_g phase, was observed at KIV from Event 5. Figure 4 (2nd trace) shows the RMS amplitude for event 5 at ARU, 16.6° north of the earthquake. L_g is the largest observed phase at ARU. Similarly, Event 8, whose path to KIV crosses the southern part of the Caspian Sea, shows a large L_g phase at GAR, 13.0° east of the earthquake (Figure 4, 3rd trace). Event 10 was recorded at two other IRIS/IDA stations, ARU and GAR. Event 10 was the only event for which L_g was the largest observed phase at KIV. Event 10's path to ARU crosses the Caspian Sea and part of the Caspian Depression along its long axis; its path to GAR crosses the area just south of the Caspian Sea. L_g is not observed at ARU or GAR for this earthquake. S_n is well observed at ARU, but only weakly observed at GAR from Event 10 (traces 4 and 5, Figure 4).

Four of the events from Iran (11-18) were recorded at GAR, approximately 18° to the northeast. None of these events showed any S_n or L_g energy in the .6-3 Hz passband at GAR, which is the same observation made for KIV.

CONCLUSIONS AND RECOMMENDATIONS: Clear zonations are seen in the behavior of regional phases for earthquakes near KIV. Both longer period Rayleigh waves (10-20 s) and shorter period (.6-3 Hz) phases S_n and L_g showed behavior that varies generally with

azimuth. Features associated with the Caspian Depression and the Caspian Sea cause complete blockage (Depression), and partial blockage or severe attenuation (Sea), of L_g. The S_n phase is not affected, implying that the causative features are in the crust. Earthquakes from the Iran/North Persian Gulf source area, however, show no high-frequency S_n phase at KIV or GAR. This could be a general feature of the source area, and implies that the uppermost mantle there is highly attenuating for shear waves, compared to the mantle north and east of the Caspian Sea. The detection threshold at KIV for events from the source area in Iran, in terms of global m_b, is in general higher than for events east of the Caspian, again implying that both the crust and mantle are more attenuating. Events crossing the Turkish Plateau to KIV show simliar behavior to those from Iran. These results are very similar to those of Kadinsky-Cade et al (1981), who delineated regions of S_n and L_g attenuation south of KIV in a comprehensive observational study using stations in Iran, Pakistan, and Turkey. This study will be able to fill in some of the boundaries of attenuating features that were beyond the resolution of their study.

Several possible complications from the use of earthquakes (vs. explosions) need to be addressed, such as the effect of source depth and the effect, if any, of the earthquake size and time function. Observation of the events at other regional stations is a powerful way to rule out such source effects. More earthquakes should be studied; it would be useful to look at a narrow azimuth range but step out in range from the station to watch the evolution of regional phases and place further bounds on the attenuating features.

References

Baumgardt, D.R., High frequency array studies of long range L_g propagation and the causes of L_g blockage and attenuation of the Eurasian continental craton, PL-TR-91-2059, ENSCO, Ins, Springfield, VA, 1991.

Eissler, H.K., M. Hedlin, J. Berger, F. Vernon, M. Kappus, D. Chavez, and R. Aster, Regional seismic observations of nuclear explosions inside the Soviet Union, *EOS Trans. Am. Geophys. Union 69*, 1321, 1988.

Kadinsky-Cade, K., M. Barazangi, J. Oliver and B. Isacks, Lateral variations of high-frequency wave propagation at regional distances across the Turkish-Iranian Plateaus, *J. Geophys. Res. 86*, 9377-9396, 1981.

Kennett, B.L.N., and S. Mykkeltveit, Guided wave propagation in laterally varying media - II. L_g waves in northwestern Europe, *Geophys. J. R. astr. Soc. 79*, 257-267, 1984.

Nuttli, O., L_g magnitudes of selected east Kazakh underground explosions, *Bull. Seismol. Soc. Am. 76*, 1241-1251, 1986.

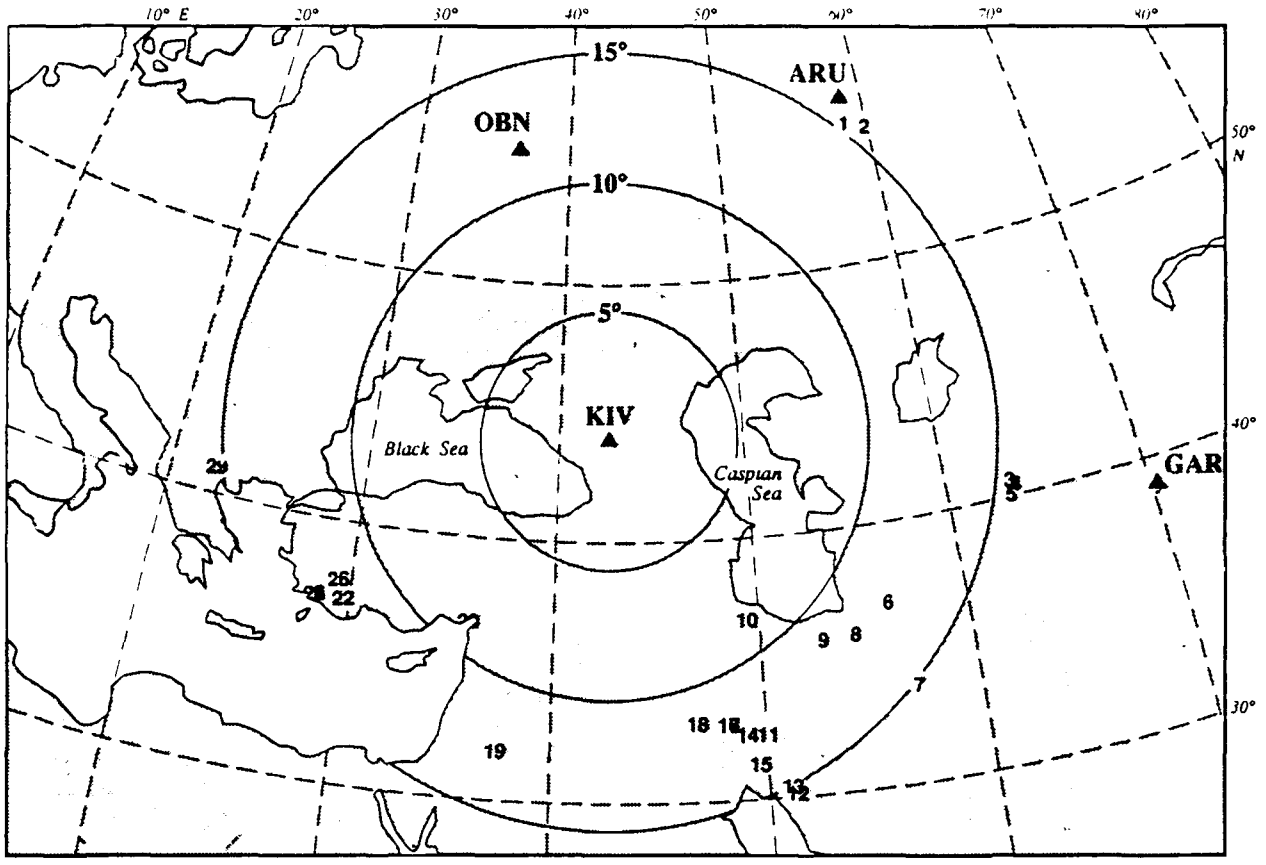


Figure 1. Study events near KIV.

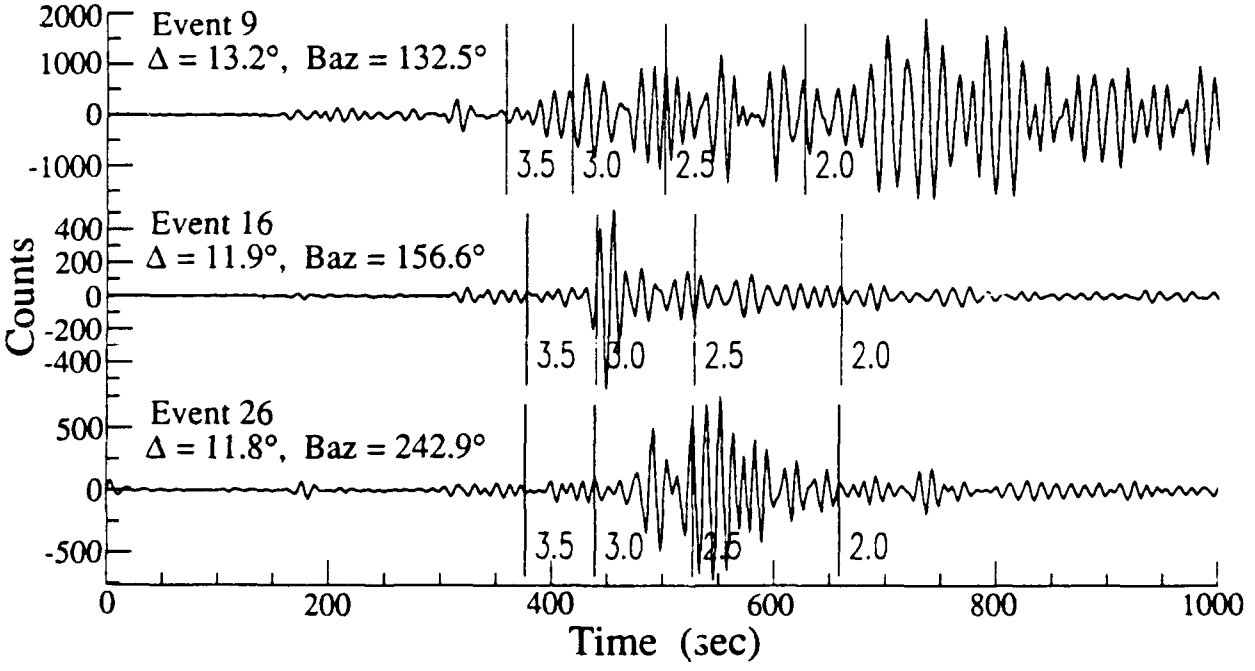


Figure 2. Bandpass filtered (20s - 10s) vertical seismograms from three events, showing the three general types of Rayleigh wave dispersion observed at KIV.

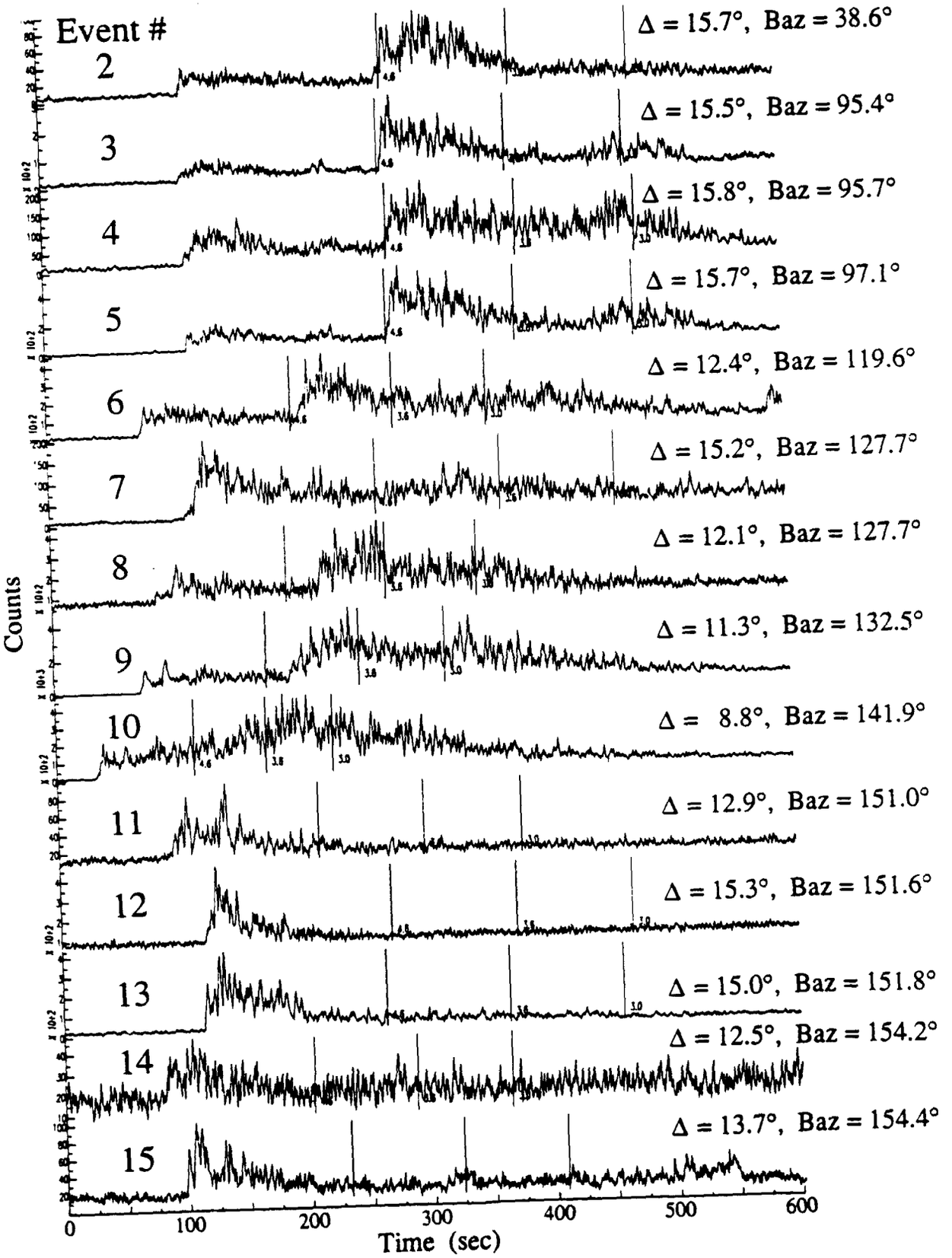


Figure 3. Smoothed three-component RMS amplitudes from .6-3Hz.

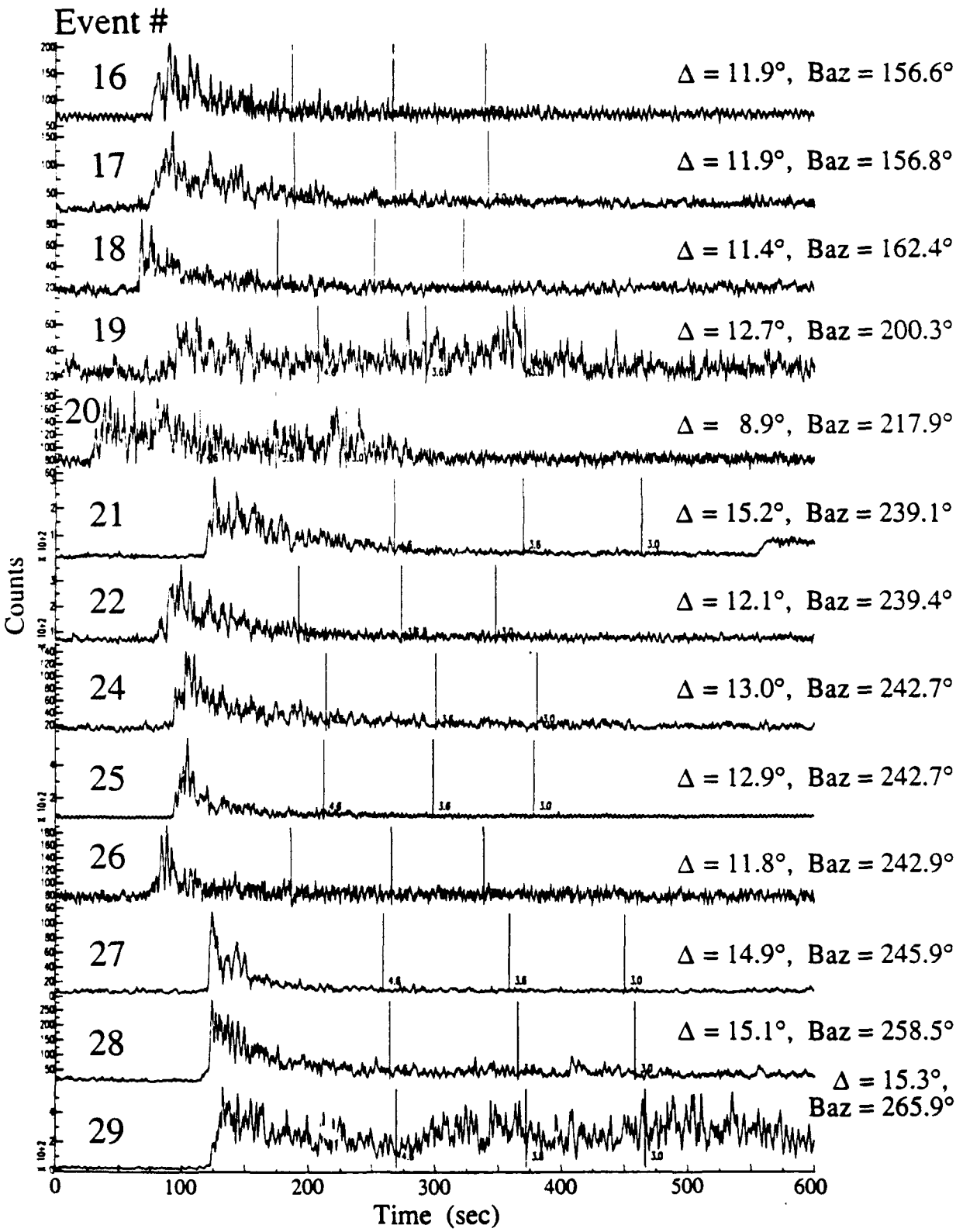


Figure 3 continued.

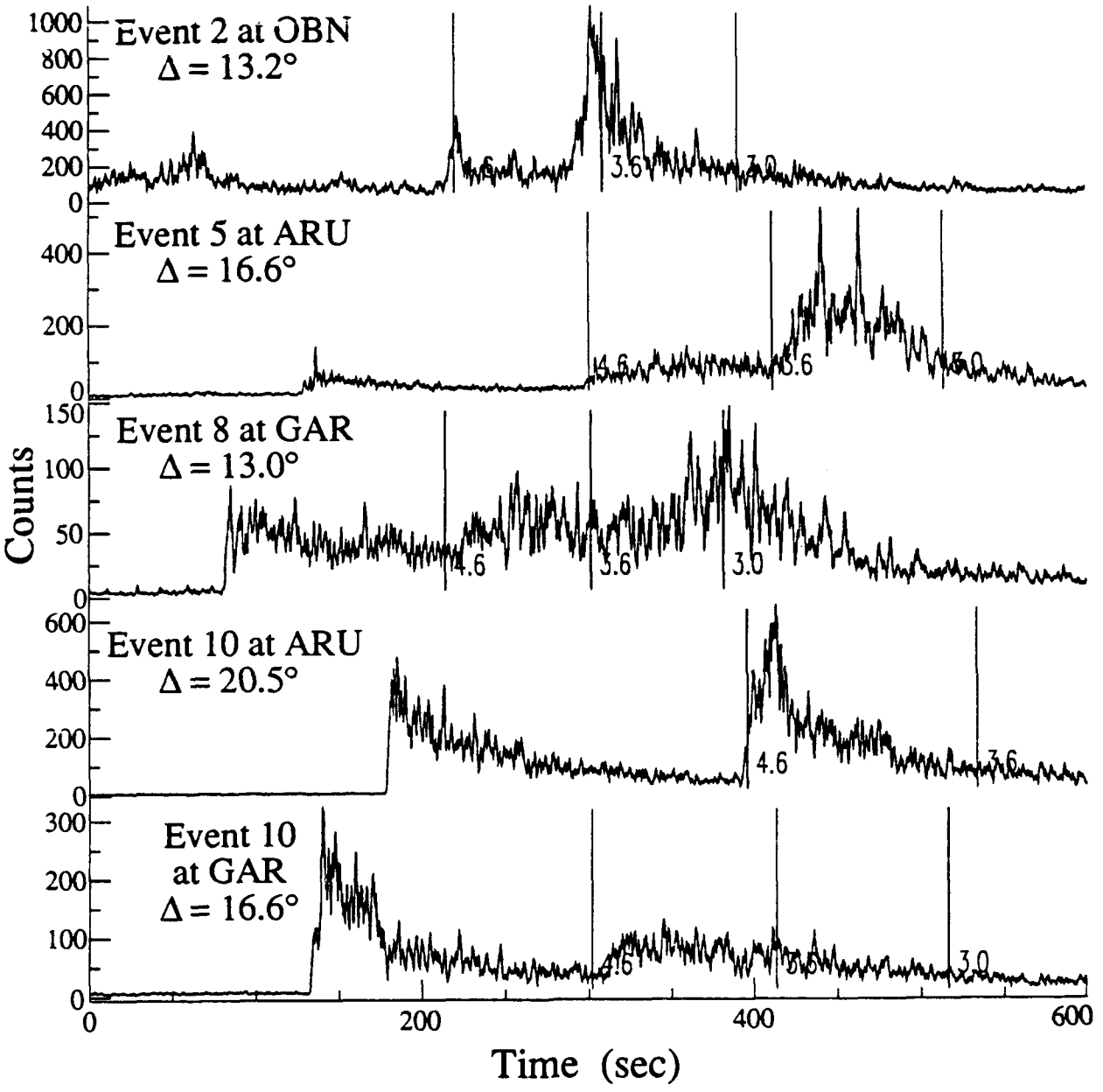


Figure 4. RMS amplitudes of selected KIV study events at other IRIS/IDA stations at regional distances. Arrival times corresponding to velocities of 4.6, 3.6, and 3.0 km/s are shown for reference. Note that these records are very different in character from the corresponding KIV records in Figure 3, indicating heterogeneous propogation of Lg.

(A) EVIDENCE FOR Rg-TO-P SCATTERING IN TELESEISMIC P-CODA AND Rg-TO-S SCATTERING IN REGIONAL Lg OF EAST KAZAKH EXPLOSIONS AND (B) AN ARRAY STUDY OF EFFECTS OF A KNOWN LOCAL SCATTERER ON REGIONAL PHASES

I. N. Gupta, C. S. Lynnes, and R. A. Wagner
Teledyne Geotech Alexandria Laboratory
314 Montgomery Street, Alexandria, VA 22314-1581
Contract No. F19628-89-C-0036

OBJECTIVE

(A) Analyze teleseismic and regional data from underground nuclear explosions in East Kazakh for the possibility that the low-frequency teleseismic P coda and Lg are generated by the scattering of explosion-generated Rg into P and S, respectively.

(B) Investigate the effects of a known prominent scatterer near NORESS on array recordings of the regional phases Pn, Pg, and Lg.

RESEARCH ACCOMPLISHED

(A) ORIGIN OF LOW-FREQUENCY P CODA AND REGIONAL Lg:

Previous studies of NTS explosions have indicated that the explosion-generated Rg contributes significantly to low-frequency arrivals following the direct P and pP (Gupta *et al.*, 1985, 1991b; Stead and Helmberger, 1988). Our analysis of teleseismic data from both Degelen and Shagan River (East Kazakh, USSR) underground nuclear explosions recorded at two seismic arrays suggests that the low-frequency teleseismic P coda is dominated by near-source scattering of fundamental-mode Rayleigh-to-P (Rg→P) scattering. Similarly, analysis of regional data from 14 Shagan River explosions recorded at the CDSN station, WMQ indicates that the low-frequency component of the observed Lg is probably due to the scattering of explosion-generated Rg into S.

For an explosion source with source function S(f) within a homogeneous half space, the fundamental-mode Rayleigh wave amplitude $R_g(f)$ is given by the expression (Hudson and Douglas, 1975):

$$R_g(f) = \frac{A\,\bar{\phi}(\omega)}{r^{0.5}\,\rho\,\alpha^{3.5}}\, f^{1.5}\, 10^{-4.4\frac{h}{\alpha}f} \qquad (1)$$

where $\bar{\phi}(\omega)$ is the Fourier transform of the source RDP $\phi(t)$, h is the shot depth, $\omega = 2\pi f$, α is the compressional-wave velocity of the shot medium, ρ is the density, r is the epicentral distance, A is a numerical constant, and a Poisson's ratio of 0.25 is assumed. The far-field P-wave displacement, in the frequency domain, may be written as (Hudson and Douglas, 1975):

$$P(f) = \frac{1}{4\,\pi\,\rho\,\alpha^3\,R}\,\omega\,\bar{\phi}(\omega) \qquad (2)$$

where R is the teleseismic source-receiver distance. If the source-receiver path and the medium velocity do not change, equations (1) and (2) yield

$$\frac{Rg \rightarrow P}{P}(f) = k\, C(f)\, f^{0.5}\, 10^{-4.4 \frac{h}{\alpha} f} \quad (3)$$

where k is a constant and C(f) denotes the scattering function Rg→P. Assuming that the low-frequency P-coda in teleseismic data is mainly due to the scattering of Rg, we replace Rg→P and P in equation (3) by P-coda and P, respectively, and obtain

$$\log \frac{P}{P\text{–coda}}(f) = 4.4 \frac{h}{\alpha} f - \log k - \log C(f) - 0.5 \log f \quad (4)$$

This shows that if we consider explosions for which the Rg→P-coda scattering function may be assumed to be the same (such as closely spaced explosions) and the frequency is kept fixed (i.e. for a narrow frequency band), a plot of log P/P-coda versus shot depth, h should have a slope of about 4.4 f/α. Observations of the spectra of Rg signals from both explosions and very shallow-focus earthquakes indicate the dominant energy in Rg to be confined to frequencies less than about 2 Hz and the most important parameter for the generation of Rg to be source depth (e.g. Kafka, 1990).

We first examined short-period, vertical component teleseismic P arrivals from 22 Degelen Mountain explosions recorded at 22 center element sensors of the NORSAR array, providing over 400 observations. Spectra and spectral ratios P/P-coda were obtained for each record by selecting a window length of 12.8 sec (beginning 4 sec before the onset of P) as the P-window and the following 25.6 sec signal as the P-coda, and applying Parzen taper to each. A correction for noise was made by selecting a sample of noise before the onset of P. All available amplitude ratios P/P-coda were used as input to a least squares inversion that separated the source and receiver terms. A plot of the source-term amplitude ratio P/P-coda versus shot depth for 8 Degelen explosions for which shot depths are known (Bocharov *et al.*, 1989) is shown in Figure A1a whereas a plot of the source term versus m_b (from P. D. Marshall, written communication, 1987) for all 22 shots is shown in Figure A1b. Assuming the P-wave velocity in the Degelen testing region to be about 4 km/sec (Bonham *et al.*, 1980), 4.4 f/α ≈ 1.4, if f is taken to be the average of 0.5 and 2.0 or 1.25 Hz. Good agreement between the mean slope expected from simple theory and observation (Figure A1a) suggests that the low-frequency P-coda is mainly due to the scattering of explosion-generated Rg. Results in Figure A1b, in which the 8 explosions used in Figure A1a have been identified, suggest generally larger P/P-coda for larger explosions and a dependence on shot depth that is likely to be similar to that in Figure A1a.

On the basis of the known locations of 8 Degelen shots (Bocharov *et al.*, 1989), Figure A1a includes results from three pairs of explosions (nos. 1 and 2, 3 and 6, and 4 and 8) that are within about 2 km of each other. Since differences in propagation paths are known to exert significant influence on various seismic arrivals, results from closely spaced seismic sources recorded at a common station should be considered more reliable than others. It is important to note that the slope from each of the three pairs of closely spaced shots in Figure A1a is nearly the same as that derived from the average of all (8) shots and is in good agreement with the theoretically expected value.

Results of similar analysis of 40 Shagan River explosions recorded at the EKA array are shown in Figure A1c in which the data points indicate a mean slope close to that in Figure A1b. A relationship between the average ratio P/P-coda and shot depth was obtained by converting the known m_b into shot depth by using empirical relationships based on the information on shot depths and yields recently released by Bocharov *et al.* (1989). These relationships, derived from the Shagan River and Koynstan (Murzhik) explosions are (R. S. Jih, written communications, 1990):

$$m_b = 0.690 \log Y + 4.605 \quad (5)$$

where Y is the yield in kt, and

$$\log h = 0.241 \log Y + 2.174 \quad (6)$$

where h is shot depth in meters. These two equations would indicate an explosion of $m_b = 6$ to have a yield of about 105 kt and a depth of 458 m. Using equations (5) and (6), one obtains

$$\log h = 0.349\ m_b + 0.567 \quad (7)$$

and a plot of the amplitude ratio P/P-coda versus estimated shot depth in km (Figure A1d) indicates a mean slope of 0.943. Assuming the P-wave velocity for the uppermost 0.5 km of the crust in the Shagan test site region to be 5 km/sec, $4.4\ f/\alpha \approx 1.1$. Good agreement between simple theory and observation (Figure A1d) again suggests the low-frequency P-coda to be due to the scattering of explosion-generated Rg. Figures A1c and A1d include results from 6 (including 2 from NE Shagan) pairs of explosions within less than 2 km of each other (identified by the letters A through F). The slope from each of the six pairs of shots in Figure A1d is nearly the same as derived from the average of all (40) shots and is in good agreement with the theoretically expected value.

Regional data from Shagan River explosions recorded at the CDSN station, WMQ (distance about 950 km) were analyzed to obtain the amplitude ratio Pn/Lg, averaged over the frequency range of 0.5-2.0 Hz (Gupta *et al.*, 1991a). Figure A1e shows a plot of this ratio versus m_b for 14 explosions from the southwest region of the Shagan River test site for which the assumption of the same Rg→S scattering function may be approximately valid. A plot of the amplitude ratio Pn/Lg versus estimated shot depth (Figure A1f) shows a mean slope of about 1.1, in excellent agreement with the slope expected from theory. Figures A1e and A1f include results from two explosions (nos. 1 and 2) that are within a few km of each other. Regional phases are extremely sensitive to differences in propagation paths (Blandford, 1981) so that results from seismic sources with nearly common paths should be given more weight than others. Note that the slope from the two closely spaced shots in Figure A1f is nearly the same as that derived from the average of all (14) shots and is in good agreement with the theoretically expected value. It seems therefore that the low-frequency Lg is generated by the scattering of explosion-generated Rg into S.

(B) EFFECT OF LOCAL SCATTERING ON REGIONAL PHASES:

Our recent f-k analyses of data from the high-frequency seismic array NORESS (Norway) first suggested the presence of a local scatterer about 25-30 km southwest of the array, in the region of Lake Mjosa near Skreikampen in Figure B1 (Gupta *et al.*, 1989; Gupta *et al.*, 1990a, 1990b). Soviet and U.S. nuclear explosions and an earthquake were used as the seismic sources, providing significantly different source-receiver azimuthal directions. Our deterministic location of a prominent scatterer near Skreikampen has been duplicated by later studies (e.g. Bannister *et al.*, 1990). We also located another scatterer about 10 km east of NORESS, near Bronkeberget in Figure B1 (Gupta *et al.*, 1989) and this too has been confirmed by later studies.

Our study of several regional events recorded at NORESS suggested that near-receiver scattering exerts significant influence on the regional phases Pn, Pg, and Lg by generating observable scattered arrivals (Gupta et al. 1990c). As an example, results from the earthquake of 1 April 1986 (56.42° N, 12.10° E, $m_b \approx 3.6$, distance 482 km, backazimuth 176°) are shown in Figures B2, and B3. As with teleseismic data, the use of residual seismograms derived by subtracting the beamed record from each

array channel provided an effective method for isolating the secondary source from the primary source. Figure B2a shows f-k results for the 6.4 sec long window with the largest amplitude Lg, $L_{g\,max}$. It indicates a phase velocity of about 3.7 km/sec and a backazimuth of about 169°. Knowing the location of the Skreikampen scatterer and assuming a group velocity of 3.5 km/sec for Lg, the scattered Lg-to-Rg arrival should arrive about 6 sec after $L_{g\,max}$; the corresponding normal f-k plot is shown in Figure B2b. F-k plots from residual seismograms provided the results shown in Figures B2c through B2f in which plots for both later windows (Figures B2d and B2f) clearly indicate the expected Lg-to-Rg arrivals along the two expected directions and with phase velocity appropriate for Rg. A comparison of the power on the normal and residual f-k plots suggests that the amplitude of the scattered Lg is not insignificantly small as compared to the on-azimuth Lg. For example, in the $L_{g\,max}$ + 6 sec window (Figure B2d), each of the two prominent scattered arrivals has an amplitude about 10% of that of the on-azimuth Lg (Figure B2b).

F-k plots were also obtained for 6.4 sec long windows containing the Pn, $P_{g\,max}$ and later arrivals. Results from normal and residual seismograms for the Pn and $P_{g\,max}$ windows are shown in Figures B3a and B3d, respectively. The residual f-k plots for the Pn + 6 sec and $P_{g\,max}$ + 6 sec windows indicated dominant arrivals from the south-west direction (Figures B3c and B3f) although the corresponding normal f-k plots (Figures B3b and B3e) suggested dominant arrivals directly from the source region. Considering the phase velocities and the various distances involved, it seems that the primary arrivals observed on the two residual plots in Figures B3c and B3f may be due to the scattering near Skreikampen of Pn-to-Rg and $P_{g\,max}$-to-Rg, respectively. In addition to the event of 1 April 1986, several other earthquake and explosion sources along various azimuthal directions to NORESS also provided evidence for scattered arrivals Pn→Rg, Pg→Rg, and Lg→Rg, originating mainly from the two scattering source regions near Skreikampen and Bronkeberget.

CONCLUSIONS AND RECOMMENDATIONS

(A) Analysis of a large amount of teleseismic and regional data from East Kazakh underground nuclear explosions suggests that the low-frequency teleseismic P coda and Lg are dominated by the near-source scattering of fundamental-mode Rayleigh (Rg) to P and S, respectively. An understanding of the generation of teleseismic P coda and low-frequency Lg from underground nuclear explosions provides useful source information, including improved methods for estimating shot depths. It will be useful to apply these techniques to more teleseismic and regional data and estimate shot depths of USSR explosions. Similar analysis should also be carried out for NTS explosions for which the near-source environment (including shot depth) are known but the shallow crustal structure is considerably more complex than in East Kazakh.

(B) F-k analyses of NORESS array recordings of teleseismic events have indicated a prominent secondary source about 25-30 km southwest of the array, in the region of Lake Mjosa, with large topographical relief. Both earthquake and explosion sources along various azimuthal directions to NORESS provide evidence for scattered arrivals Pn→Rg, Pg→Rg, and Lg→Rg, originating from the same region of Lake Mjosa. These scattered arrivals are observed with remarkable clarity and closeness to the expected arrival times and are rich in low frequencies, as expected for Rg. Their presence in various regional phases indicates that near-receiver scattering plays an important role in the composition of regional phases. Similar studies of the influence of discrete local scatterers on regional phases should be carried out for other arrays such as ARCESS and GERESS. The results will be useful in the understanding of various arrivals on regional seismograms.

REFERENCES

--------(A)--------

Blandford, R. R. (1981). Seismic discrimination problems at regional distances, in *Identification of Seismic Sources - Earthquake or Underground Explosions*, E. S. Husebye and S. Mykkeltveit, Editors, D. Reidel Publishing Co., Dordrecht, Holland, 695-740.

Bocharov, V. S., S. A. Zelentsoz, and V. N. Mikhailov (1989). Characteristics of 96 underground nuclear explosions at the Semipalatinsk test site, *Atomic Energy 67(3)*.

Bonham, S., W. J. Dempsey, and J. Rachlin (1980). Geologic environment of the Semipalatinsk area, U.S.S.R. *(Preliminary Report)*, U. S. Geological Survey, Reston, Virginia.

Gupta, I. N., R. R. Blandford, R. A. Wagner, and J. A. Burnetti (1985). Use of P coda for explosion medium and improved yield determination, in *The Vela Program*, A. U. Kerr, Editor, Executive Graphic Services, Virginia, 711-720.

Gupta, I. N., W. W. Chan, and R. A. Wagner (1991a). A comparison of regional phases from underground nuclear explosions at East Kazakh and Nevada Test Sites, *Bull. Seism. Soc. Am. 81* (in press).

Gupta, I. N., T. W. McElfresh, and R. A. Wagner (1991b). Near-source scattering of Rayleigh to P in teleseismic arrivals from Pahute Mesa (NTS) shots, *AGU Monograph on Explosion Source Phenomenology* (in press).

Hudson, J. A. and A. Douglas (1975). On the amplitudes of seismic waves, *Geophys. J. 42*, 1039-1044.

Kafka, A. L. (1990). Rg as a depth discriminant for earthquakes and explosions: a case study in New England, *Bull. Seism. Soc. Am. 80*, 373-394.

Stead, R. J. and D. V. Helmberger (1988). Numerical-analytical interfacing in two dimensions with applications to modeling NTS seismograms, *PAGEOPH 128*, Nos. 1/2, 157-193.

--------(B)--------

Bannister, S. C., E. S. Husebye, and B. O. Ruud (1990). Teleseismic P-coda analyzed by three-component and array techniques - deterministic location of topographic P-to-Rg scattering near the NORESS array, *Bull. Seism. Soc. Am. 80*, 1969-1986.

Gupta, I. N., C. S. Lynnes, R. S. Jih, and R. A. Wagner (1989). A study of teleseismic P and P coda from U.S. and Soviet nuclear explosions, paper presented at the 11th Annual DARPA/AFGL Seismic Research Symposium, San Antonio, Texas.

Gupta, I. N., C. S. Lynnes, and R. A. Wagner (1990a). Broadband f-k analysis of array data to identify sources of local scattering, *Geophys. Res. Lett. 17*, 183-186.

Gupta, I. N., C. S. Lynnes, T. W. McElfresh, and R. A. Wagner (1990b). F-k analysis of NORESS array and single-station data to identify sources of near-receiver and near-source scattering, *Bull. Seism. Soc. Am. 80*, 2227-2241.

Gupta, I. N., C. S. Lynnes, and R. A. Wagner (1990c). An array study of the effects of a known local scatterer on regional phases - preliminary results, *EOS 71 (17)*, 565 (abstract).

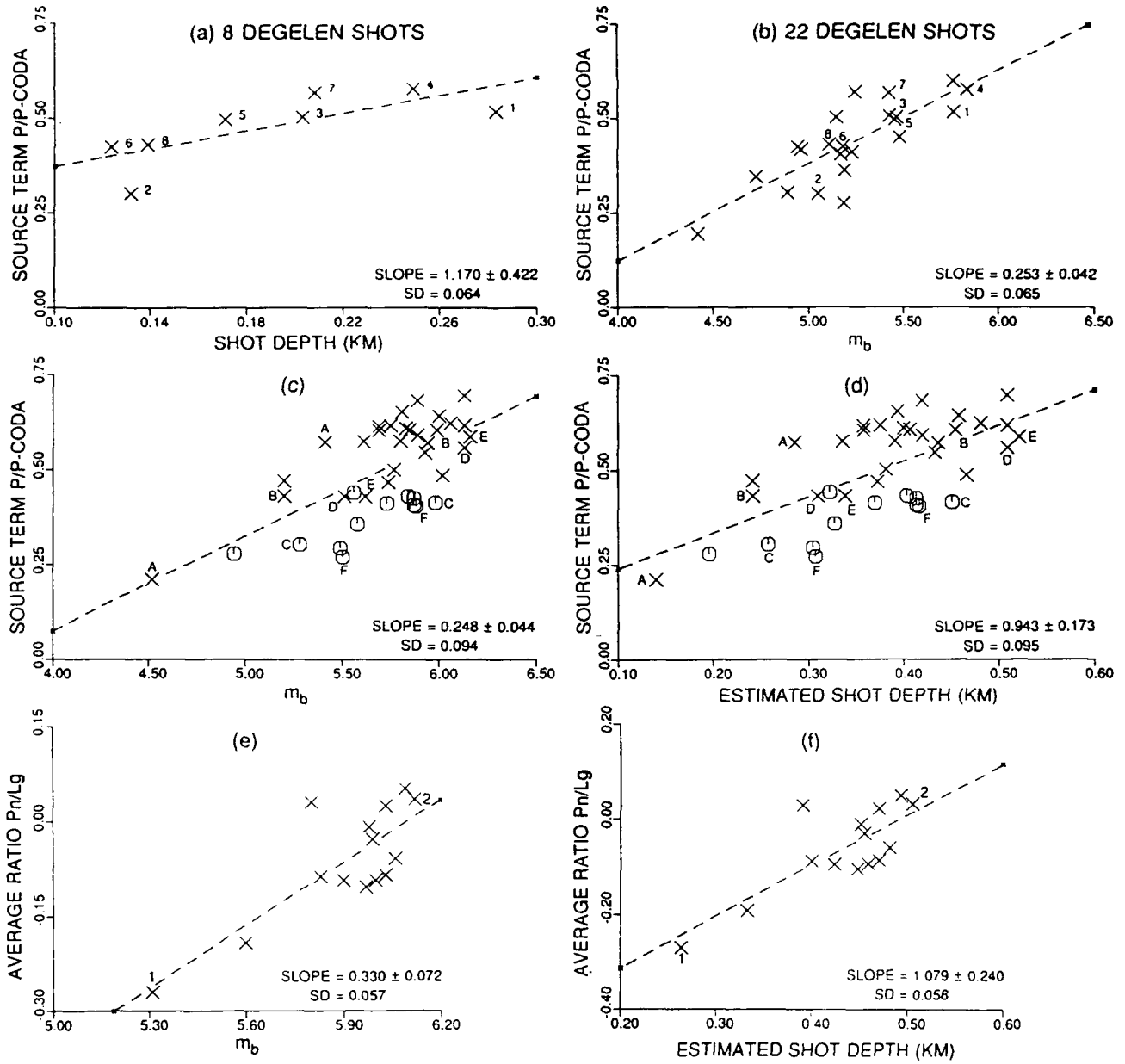


Figure A1. Source term amplitude ratio P/P-coda (log units), averaged over the frequency range of 0.5-2.0 Hz, derived from (a) 8 Degelen explosions recorded at NORSAR array versus known shot depths, (b) 22 Degelen explosions recorded at NORSAR array versus m_b, (c) 40 Shagan River explosions recorded at the EKA array plotted versus m_b; six pairs of closely spaced explosions are identified by the letters A through F and the SW and NE explosion populations are denoted by × and ○, respectively, and (d) the same data as in (c) plotted versus estimated shot depth. Average Pn/Lg amplitude ratio over the frequency range of 0.5-2.0 Hz from WMQ versus (e) m_b and (f) estimated shot depth for 14 explosions from the southwest Shagan test site. Data from two closely spaced shots (nos. 1 and 2) are identified. The least squares linear regression (dashed line), mean slope (with associated standard deviation), and one standard deviation of residuals (SD) are indicated on each plot.

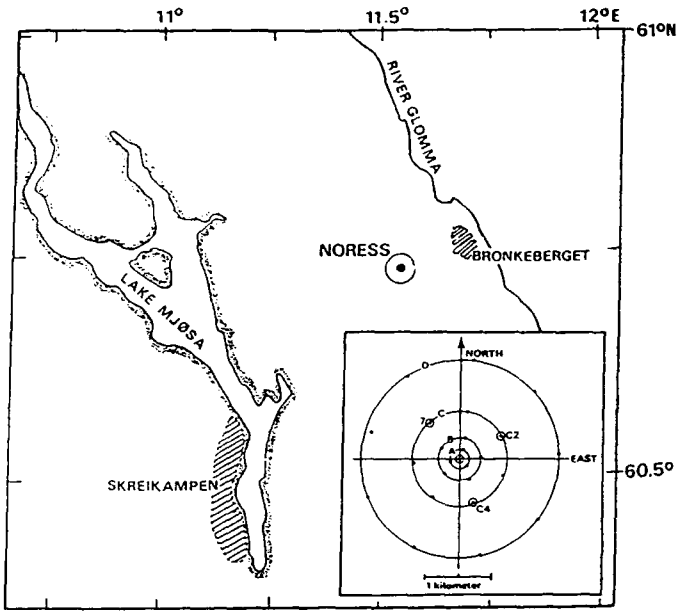


Figure B1. The general NORESS array region with the two scattering locations Skreikampen and Bronkeberget hatched. The array configuration is given in the lower right insert where encircled stations indicate three-component sites.

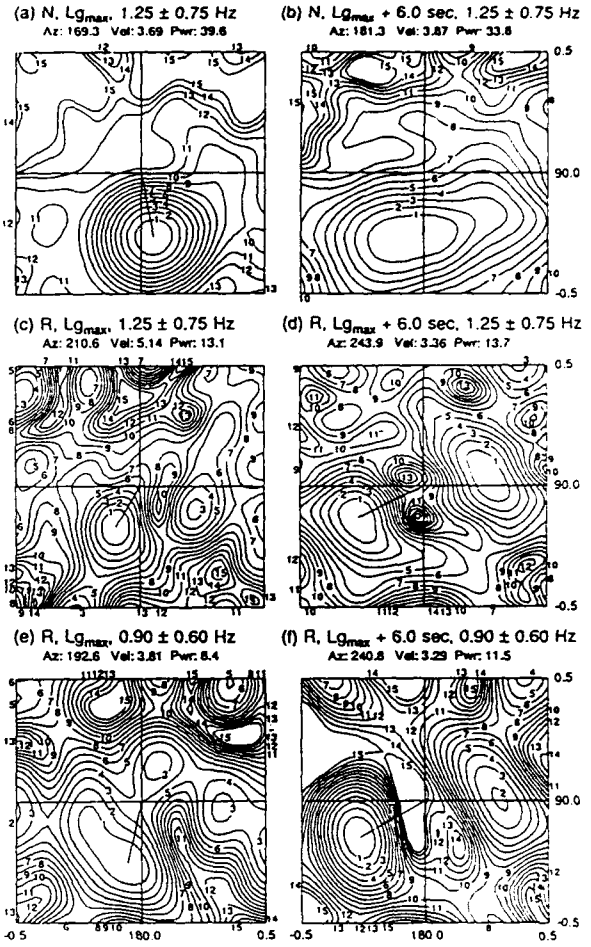


Figure B2. Frequency-slowness spectral estimates derived from NORESS records of the regional earthquake of 1 April 1986 with a maximum slowness of 0.5 sec/km and the use of Lg windows. The numbers on top of each plot indicate backazimuth (deg), phase velocity (km/sec), and signal power (dB), respectively of the highest-amplitude arrival which is shown connected to the plot origin. The signal windows and frequency passbands are indicated on each plot. Plots (a) and (b) are based on the use of normal (denoted by N) seismograms whereas (c) to (f) are derived from the residual (R) seismograms. Both (d) and (f) indicate prominent scattered arrivals from the directions of Skreikampen and Bronkeberget.

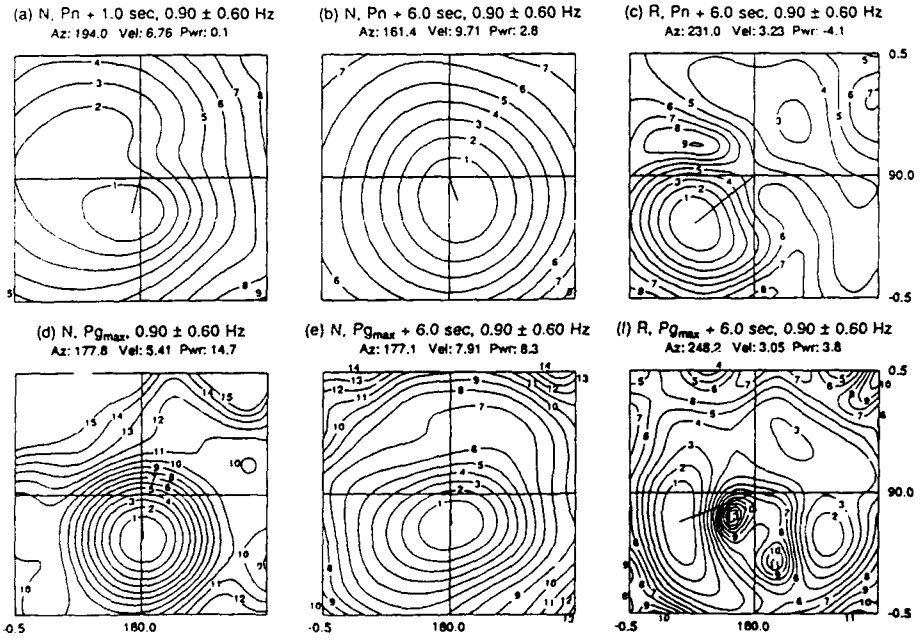


Figure B3. Similar to Figure B2 but based on the use of Pn and Pg windows. Plots (a), (b), (d), and (e) are obtained by using normal (N) seismograms. Plots (c) and (f), derived from residual (R) seismograms, indicate prominent scattered arrival from the direction of Skreikampen probably due to the scattering of Pn-to-Rg and $P_{g\,max}$-to-Rg, respectively.

Single-Station Estimates of Crust and Upper Mantle Velocity Structure at Broadband IRIS/IDA Stations in the USSR.

Harold Gurrola and J. Bernard Minster
(both at, IGPP, UCSD, La Jolla, Ca, 92093)
Tom Owens
(Geological Sciences, University of South Carolina)
Contract Number: F19628-90-K-0045

Objectives

The broad objective of our study is to determine the crustal and upper mantle structure beneath the Soviet IRIS stations at Arti (ARU), Garm (GAR), Kislovodsk (KIV), and Obninsk (OBN) by computing receiver functions. We are developing new techniques useful to our interpretation. We have adapted the velocity spectrum method, used extensively in processing seismic reflection data, in order to stack receiver functions from a wider range of ray parameters than conventionally stacked data. This technique is as much an interpretive tool as an aid in improving the signal to noise ratio of stacked receiver functions. We are also experimenting with different approaches to the deconvolution to improve the computation of receiver functions. The immediate objective of this paper is to report on the progress in developing these two techniques. In doing so, we give results of modeling receiver functions at OBN. We are in the early stages of exploring the deconvolution method, so we only show results using data from Piñon Flat (PFO), California because there is no surface layer there to generate a response which could be misinterpreted as an artifact of improper deconvolution.

What is a Velocity Spectrum Stack ?

The "velocity spectrum stack" (VSS) is a useful tool for stacking reflection data within a range of ray parameters in multichannel studies [e.g. *Yilmaz*, 1987]. The functional dependence of arrival times on ray parameter p, relative to a reference phase with ray parameter p_0 is called the "moveout". The "normal moveout correction" (NMO) then refers to the time adjustment necessary to correct the arrival time to what would have been observed from a vertically incident ray, irrespective of amplitude, assuming a given velocity structure. The "velocity spectrum stack" is a contour map of amplitudes across constant velocity stacks (produced by stacking the observed records after NMO using a uniform velocity) in the velocity-time plane [e.g. *Sheriff*, 1982]. A phase at a particular time on the receiver function is thus enhanced if the appropriate NMO correction is made. The enhancement will be most effective for a value of velocity matching the "true" mean velocity to that particular time delay (it is most appropriate at this point to think of the velocity structure as a function of time since arrival time is observed whereas depth will be computed after the velocity structure is determined) [*Yilmaz*, 1987]. Because of differences in the shape of their moveout curves, separate stacks must be produced for each of the prominent phases present in the receiver functions. Therefore, the velocity spectrum stacks can be used to distinguish between phases as well as to infer velocity structure.

Method

Figure 1 illustrates the geometry of the most significant type of phase observed in receiver function studies - the P to S conversion (Ps) generated when the wave crosses an interface - for a layer over a half space. The time delay for the Ps arrival relative to that of the P arrival $\Delta T_{Ps}(p)$ is given by:

$$\Delta T_{Ps}(p) = T_S + T_h - T_P \qquad (1)$$

$$\Delta T_{Ps}(p) = z\left(\sqrt{V_S^{-2} - p^2} - \sqrt{V_P^{-2} - p^2}\right) \qquad (2)$$

In the above equations: T_S, T_h and T_P are travel times along the paths labeled in Figure 1; V_S and V_p are the average S and P velocities in the layer, respectively; p is the ray parameter; and z is the depth to the interface. In terms of the relative vertical P travel time (ΔT_{PS0}) through the layer and the velocity ratio $r = V_p / V_S$, we have:

$$\Delta T_{PS}(T_{PS0},p,V_S,r) = \frac{r\Delta T_{PS0}}{r-1}\left(\sqrt{1 - p^2V_S^2} - \sqrt{r^{-2} - p^2V_S^2}\right) \qquad (3)$$

Note that this equation depends only on ΔT_{PS0}, p, Vs and an assumed value for r (which will be held constant for an entire velocity spectrum stack, e.g. $r=\sqrt{3}$ for a Poisson solid). Figure 2 depicts a set of synthetic receiver functions generated for a layer (V_P = 6.0 km/sec, V_S = 3.5 km/sec) over a half space (V_P = 8.0 km/sec, V_S = 4.6 km/sec) for a range of ray parameters. In this figure, we observe that the Ps phase is delayed with increasing ray parameter relative to the initial P-wave.

In figure 2, all phases (reverberations) following Ps are advanced in arrival time relative to the P arrival with increasing ray parameter. We take advantage of this difference in the shape of the moveout curve to distinguish reverberations from the Ps phase. Equation 4 gives the time delay (ΔT_{PPS}) for the PPS (a reverberation with two P legs and a final S leg) phase relative to the P arrival for a layer over a half space (depicted in figure 3):

$$\Delta T_{PPS}(T_{PPS0},p,V_S,r) = \frac{r\Delta T_{PPS0}}{r+1}\left(\sqrt{1 - p^2V_S^2} + \sqrt{r^{-2} - p^2V_S^2}\right) \qquad (4)$$

In like fashion, we can derive moveout equations for the PPP, PSS and SSS phases. However PPP and SSS have small amplitudes (even after stacking a very large number of events) so are usually of little significance in interpretations. PSS, on the other hand, has reversed polarity and is easily distinguishable from Ps and PPS, so it is sometimes a useful phase in the interpretation of receiver structure.

Constant velocity stacks are produced by averaging along the moveout curve the amplitudes of N receiver functions with various ray parameters.

$$S(T_{\Phi 0},V_s) = \frac{1}{N}\sum_{i=1}^{N} f_i\left\{\Delta T_{\Phi}(T_{\Phi 0},p_i,V_S,r)\right\} \qquad (5)$$

Where Φ is either Ps or PPS; $S(T_{\Phi 0},V_S)$ is the averaged amplitude at a given zero offset time and S-wave velocity; $f_i\{\Delta T_{\Phi}(T_{\Phi 0},p_i,V_S,r)\}$ is the amplitude of the i^{th} trace at the computed moveout time ($\Delta T_{\Phi}(T_{\Phi 0},p_i,V_S,r)$) for a given wave type (Φ). If the moveout time falls between two samples we linearly interpolate a value for $f_i\{\Delta T_{\Phi}(T_{\Phi 0},p_i,V_S,r)\}$. After producing constant velocity stacks for the range of all reasonable velocities, we contour the amplitudes in the velocity-time plane to produce the "velocity spectrum stack" (VSS). The Ps conversion or PPS reverberation on their respective velocity spectrum stacks will appear as positive ridges (negative for a velocity inversion) elongated parallel to the velocity axis. The velocity structure beneath a station can then be inferred by selecting the time and velocity of the highest amplitude on each ridge.

A Synthetic Example

Figure 4 depicts VSS produced for the Ps and PPS phases for the synthetic receiver functions shown in Figure 2. Upon inspection of the Ps stack (left) we observe good time resolution for Ps near 5 seconds but poor velocity resolution. This phase also appears on the PPS stack (right), but the peak is not as sharp and does not have as large an amplitude as on the Ps stack. PPS (at 18 sec) is only observed on the PPS stack and has much better velocity resolution than Ps. It is not surprising that we are able to pick V_S=3.5 km/sec (the velocity used to compute the synthetics in Figure 2) more accurately from PPS stack, since Figure 2 shows twice as much moveout for PPS than for Ps. We can use this velocity together with the approximate 4.8 sec arrival time on the Ps stack to compute the thickness of the layer (40 km; the arrival times on the VSS are zero offset arrival times, so equation (2) becomes $T_{PS}=z\{1/V_S - 1/V_P\}$).

Figure 5 depicts single stacks of the receiver functions shown in figure 2. The top stack has no moveout applied - the next three are stacked using the respective Ps, PPS, and PSS moveout curves (from top to bottom). In each case the respective velocity depth (time) function was picked by observation of the stacking amplitudes on the corresponding VSS (Figure 4). The P, Ps, PPS, and PSS arrivals are at 5, 10, 23 and 28 seconds respectively. Figure 5 clearly illustrates the fact that the various arrivals are greatly enhanced when stacked under the appropriate moveout curve. An added bonus is the annihilation of the reverberations (PPS and PSS) on the Ps stack and conversely the Ps phase is greatly diminished on the two reverberation stacks. We conclude that by producing the stacks with normal moveout we may observe arrivals that would otherwise be below noise levels and avoid mislabeling other phases.

Upper mantle discontinuities at the OBN IRIS/IDA station

We have computed receiver functions for the IRIS/IDA station OBN —located in Obninsk, USSR— using data collected in 1989-90 [*Gurrola et al.*, 1990a,b]. The station is equipped with a broadband three-component system with response nominally flat with respect to velocity from approximately 3 mHz to 5 Hz. We used teleseismic P and PP phases which, due to the uneven distribution of source regions during the one year period covered by the data, primarily sample the northeast and southeast quadrants at all sites. It was necessary to high-pass filter most of these data in order to counter the effects of occasional nonlinear noise problems at frequencies lower than 20 mHz.

The broad band receiver functions are dominated by reverberations in a shallow surface layer. In order to identify phases from deeper layers, we have reduced the contribution of the near surface layer by low-pass filtering these data with a phaseless Gaussian filter (centered at 0 Hz with a half power width of 0.6 Hz). The simplest model that we could construct which satisfies both the broad band and the high frequency data includes a low velocity surface layer of no more than 2.5 km thickness and a rather smoothly increasing velocity gradient to the 47 km deep MOHO [*Gurrola et al.*, 1990a,b, Figure 6].

VSS produced from OBN receiver functions exhibit clear arrivals from the upper mantle discontinuities. The top row of figure 7 depicts the Ps stacks computed from synthetics produced for the PREM P velocity structure modified to include the OBN crustal structure while preserving vertical travel time (left) and the Ps stacks computed from the observed data at OBN (right). The bottom row depicts the corresponding PPS stacks. We observe Ps and PPS phases from the MOHO at about 5 and 20 seconds respectively. The contour interval was chosen to illustrate best the upper mantle arrivals not observable on the individual receiver functions. As a result, the MOHO arrivals are not very sharp in these plots. If we had used the correct S-velocities for the PREM model, all arrivals would appear slightly sooner in time and lower in velocity, but we chose to use a uniform Poisson ratio because varying this ratio with depth would add another free parameter and complicate any interpretation.

The observed Ps phase from the 410 km discontinuity (at 42 seconds on the velocity spectrum stacks of Figure 7) exhibits much higher amplitude than the PREM synthetics. This is consistent with the larger velocity contrast for the 410 km discontinuity suggested by the K8 model of *Given and Helmberger* [1980]. The Ps arrival from the 670 km discontinuity is similar in amplitude on both the observed stacks and the PREM synthetics, which implies a similar velocity contrast, although this arrival appears slightly earlier and at a higher velocity in the observations. These observations indicate that the time delay between the 410 and 670 km discontinuities is smaller than observed in PREM, which is consistent with independent observations by *Vinnik* (personal comm., 1991).

We do not observe a 210 km discontinuity beneath OBN. The Ps phase from the 210 km discontinuity arrives just after the PPS from the MOHO for the PREM model making the peak at 20 seconds on the synthetic velocity spectrum stacks broader than observed in the data. The strong PPS arrival from the 210 km discontinuity observed at 75 seconds on the PREM VSS is not apparent in VSS computed from the observed receiver functions (Figure 7). These observations lead us to conclude that there is no 210 km discontinuity beneath OBN, at least not as pronounced as in PREM.

Problems Observed with the Existing Deconvolution Method

Receiver functions are typically produced by deconvolving the horizontal components recorded at a three-component seismic station with the vertical component. The deconvolution is usually performed by spectral division.

$$r = \frac{h\, v^*}{v\, v^* + w} \tag{6}$$

Where r is the Fourier transform of the receiver function. h and v are the Fourier transforms of the horizontal and vertical components of the seismogram respectively, * indicates complex conjugation, and w is a prewhitening function. The prewhitening is carried out by replacing the power level of vv^* by a water level anywhere that it falls below a specified value, usually a given fraction of the peak power level (Owens, 1983). By filling the troughs in the denominator of equation 6 we avoid spurious peaks that may appear in r and cause ringing in the receiver functions. Receiver functions are computed for a range of water levels, and the best water level is selected on an individual basis. Figure 8 depicts the results of deconvolution of a seismogram computed with water levels of 0.0, .00001, .001 and .1 times the peak power (top to bottom respectively). The signal retrieved with the lower water levels (top 2) is barely perceptible above the high frequency ringing. However with the .1 percent (.001) peak amplitude water level the signal becomes clear. With the next greater water level the signal begins to degrade once again. This hand selection of water levels is not only time consuming, but subjective and somewhat ad hoc. As a result, we are exploring deconvolution techniques that are more rigorous in the treatment of prewhitening and misfit.

Simultaneous Deconvolution

By casting the deconvolution as a linear inverse problem we are able to use more objective penalty functions than the somewhat random method of prewhitening described above. We can write the forward convolution problem as:

$$\mathbf{V}\,\mathbf{r} = \mathbf{h} \tag{7}$$

Where $\mathbf{r}$ (m components) is the receiver function, $\mathbf{h}$ (i components) is the horizontal component of the seismogram and V is composed of m columns each containing the vertical component of the seismogram (v with n components) padded with zeros to fill the columns to a length i. V is given as the i x m matrix:

$$\mathbf{V} = \begin{pmatrix} v_1 & 0 & \vdots & \vdots & \cdots & 0 \\ \vdots & v_1 & 0 & \vdots & \vdots & \vdots \\ v_n & \vdots & v_1 & \ddots & \vdots & \vdots \\ 0 & v_n & \vdots & \ddots & \vdots & \vdots \\ \vdots & 0 & v_n & \vdots & \vdots & \vdots \\ \vdots & \vdots & 0 & \ddots & v_1 & 0 \\ \vdots & \vdots & \vdots & \vdots & \vdots & v_1 \\ \vdots & \vdots & \vdots & \vdots & v_n & \vdots \\ \vdots & \vdots & \vdots & \cdots & 0 & v_n \end{pmatrix} \tag{8}$$

It is desirable to seek a solution for $\mathbf{r}$ in equation 7 in which the least square difference between the observations ($\mathbf{h}$) and predicted data ($\mathbf{Vr}$) have the appropriate misfit (in our case we will assume the expected misfit (T) is equal to the standard deviation of the pre-event noise). We therefore wish to impose the constraint:

$$\|\mathbf{V}\,\mathbf{r} - \mathbf{h}\|^2 - T^2 = 0 \tag{9}$$

The notation " $\|\mathbf{x}\|^2$ " in the above equation is a functional that yields a scalar equal to the sum of the square of the components of the vector $\mathbf{x}$. For the example given in this paper, we imposed an additional constraint to solve for the smallest least square sum of the amplitudes of the receiver function (U), where U is simply:

$$\|\mathbf{r}\|^2 = U \tag{10}$$

We can multiply equation 9 by a Lagrange multiplier (μ^{-1}) and add it directly to equation 10 in order to find a weighted solution that satisfies both constraints (*Constable et al.*,1987).

$$\|\mathbf{r}\|^2 + \mu^{-1}\{\|\mathbf{V}\,\mathbf{r} - \mathbf{h}\|^2 - T^2\} = U \tag{11}$$

By differentiating this equation with respect to **r** and setting the results equal to zero, we can solve for the vector **r** which yields the minimum value of U. (*Constable et al.*,1987; *Oldenburg et al.*, 1981):

$$\mathbf{r} = \left(\mathbf{I} + \mu^{-1}\,\mathbf{V}^T\mathbf{V}\right)^{-1}\mu^{-1}\mathbf{V}^T\mathbf{h} \tag{12}$$

I is the m x m identity matrix. In order to select the appropriate value for μ we perform repeated iterations through the inversion until we find a solution which satisfies the constraint given in equation 9.

To extend this method for the simultaneous deconvolution of several (N) events we modify equation 7 to read:

$$\begin{pmatrix} \mathbf{V}_1 \\ \mathbf{V}_2 \\ \vdots \\ \mathbf{V}_N \end{pmatrix}\mathbf{r} = \begin{pmatrix} \mathbf{h}_1 \\ \mathbf{h}_2 \\ \vdots \\ \mathbf{h}_N \end{pmatrix} \tag{13}$$

In which each $\mathbf{V}_N$, and $\mathbf{h}_N$ are the same as **V**, and **h**, defined above, for the N^{th} seismogram. Following the same steps outlined in equations 7 through 12 we arrive at the following relationship for **r**:

$$\mathbf{r} = \left(\mathbf{I} + \mu^{-1}\left(\mathbf{V}_1^T\,\mathbf{V}_2^T \cdots \mathbf{V}_N^T\right)\begin{pmatrix} \mathbf{V}_1 \\ \mathbf{V}_2 \\ \vdots \\ \mathbf{V}_N \end{pmatrix}\right)^{-1}\mu^{-1}\left(\mathbf{V}_1^T\,\mathbf{V}_2^T \cdots \mathbf{V}_N^T\right)\begin{pmatrix} \mathbf{h}_1 \\ \mathbf{h}_2 \\ \vdots \\ \mathbf{h}_N \end{pmatrix} \tag{14}$$

or

$$\mathbf{r} = \left(\mathbf{I} + \mu^{-1}\sum_{j=1}^{N}\mathbf{V}_j^T\mathbf{V}_j\right)^{-1}\mu^{-1}\sum_{j=1}^{N}\mathbf{V}_j^T\mathbf{h}_j \tag{15}$$

The solution to the simultaneous deconvolution (equation 15) requires no larger matrix inversion than for the inversion of a single seismogram, in fact it saves computer time over performing several inversions for each individual receiver function followed by conventional stacking. Figure 9 depicts a receiver function computed by the simultaneous time domain deconvolution of 23 events recorded at PFO (top) and the mean (stack) of 23 receiver functions computed individually by spectral division (bottom). The receiver function computed by simultaneous deconvolution appears to have broader frequency content whereas the stacked receiver function has larger amplitudes on almost all peaks. In the case of the initial positive peak (at 5 seconds), the stacked receiver function has greater amplitude, but the simultaneous deconvolution gives a much sharper peak and therefore has better resolution. The strong negative peak (at 6 seconds) on the stacked receiver function is almost impossible to model with any reasonable velocity model for PFO (*Baker*, 1991 *personal comm*), suggesting that the smaller amplitude observed in the simultaneous deconvolution may be a better estimate. For this example the deconvolution was performed with a simple smallest amplitude least squares constraint. We expect to improve further the simultaneous deconvolution by consideration of other inversion approaches (ie. Tarantola, 1982) or other norms such as the L_1 norm (Taylor, 1979; Debeye, 1990).

Conclusions

Through the use of velocity spectrum stacks we can stack data with different ray parameters, and directly infer the velocity structure beneath a seismographic station. This type of analysis can be used to distinguish between a Ps phase and a PPS reverberation based on the difference in the shape of their respective moveout curves. Through the analysis of velocity spectrum stacks produced for data from OBN, we have been able to identify upper mantle Ps conversions associated with the 410 and 670 km discontinuities that were not observable in the individual receiver functions. We have also obtained evidence that the 210 km discontinuity is not present beneath OBN.

The simultaneous deconvolution of seismograms to produce receiver functions appears to be a desirable alternative to the traditional deconvolution followed by stacking. Simultaneous deconvolution can only be performed on events with common ray parameter and back azimuth, and so it cannot replace the velocity spectrum technique as a means of stacking data from a wider range of ray parameters.

References

Constable, S.C., R.L. Parker, and C.G. Constable, 1987, Occam's inversion: A practical algorithm for generating smooth models from electromagnetic sounding data. *Philos. Trans. R. Soc. London Ser. A*, **266**, 123-192.

Debeye, H. W. J. and P. Van Riel, 1990, L_p-Norm Deconvolution. *Geophysical Prospecting*, **38**, 381-403.

Given, J.W. and D.V. Helmberger, 1980, Upper Mantle structure of northwestern Eurasia, Jour. of Geophy. Res., 85, 7183-7194.

Gurrola, H, J.B. Minster, and T. Owens, 1991, The use of Velocity Spectrum in the stacking of Receiver Functions, Geophy. Jour. Int. (in preparation).

Gurrola, H, J.B. Minster, and T. Owens, 1990a, Receiver Responses at IRIS/IDA Stations in the USSR, 12th annual Darpa/GL Seismic Research Symposium, Geophysical Laboratory Hanscom AFB. Mass.

Gurrola, H, J.B. Minster, and T. Owens, 1990b, Receiver Responses at IRIS/IDA Stations in the USSR, *EOS*, 71, 1450 (abstract, S21C-12).

Owens, T. J., S. R. Taylor, and G. Zandt, 1983, Isolation and Enhancement of the Response of Local Seismic Structure from Teleseismic Structure from Teleseismic P-waveforms, *internal report*, Lawrence Livermore Laboratory.

Sheriff, R.E., 1982, Encyclopedic Dictionary of Exploration Geophysics, Society of Exploration Geophysicist, Tulsa, Ok.

Tatantola, A. and Valette, B., 1982, Generalized nonlinear inverse problems solved using the least squares criterion. *Rev. Geophys. Space Phys.*, **20**, 219-232.

Taylor, H. L., C. B. Banks, and J. F. McCoy, 1979, Deconvolution with the L_1 norm. *Geophysics*, **44**, 39-52.

Vinnik, L.P., 1977, Detection of waves converted from P to SV in the mantle, *Physics of the Earth and Planetary Interiors*, **15**, 39-45.

Yilmaz, O., 1987, *Seismic data processing*. Society of Exploration Geophysicists, investigations in geophysics volume 2.

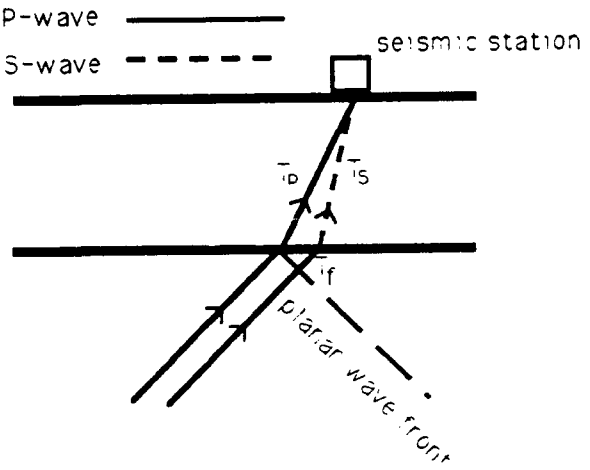


Figure 1, Ray paths for the Ps phase relative to the P phase for a layer over a half space. T_P and T_S are the travel times of the P and S phases with the same ray parameter through the layer respectively. T_h is the travel time differential in the half space for the two rays assuming a planar wave front.

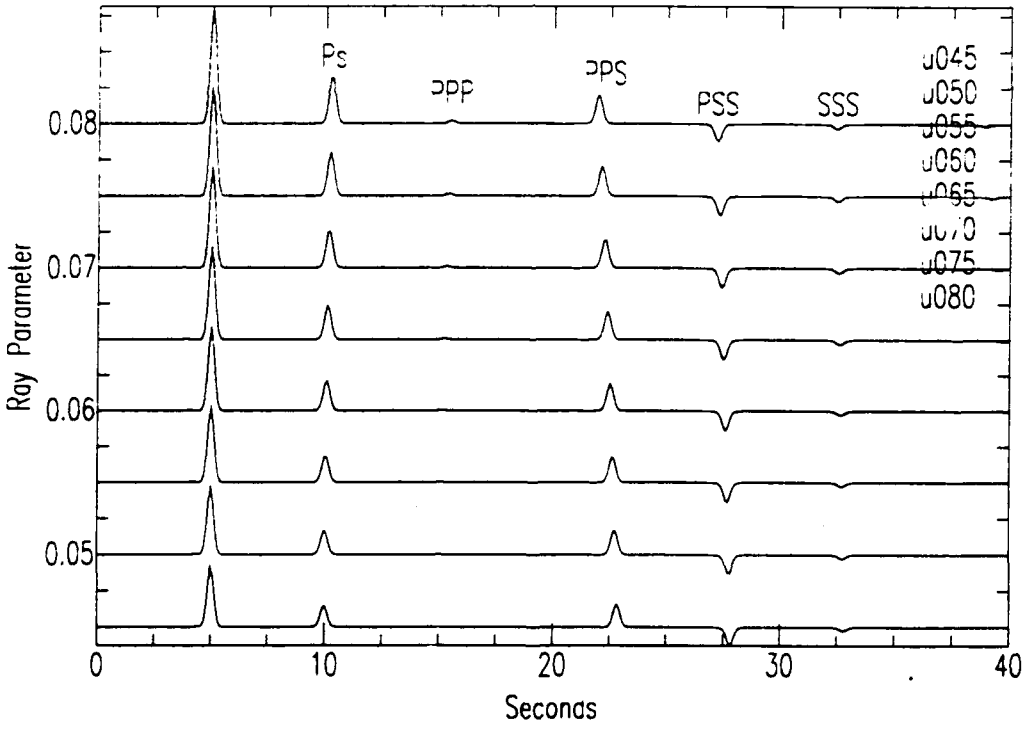


Figure 2, Seismic section of synthetic receiver functions computed for a layer (V_P=6.0 km/sec, V_S=3.5 km/sec) over a half space (V_P=8.0 km/sec, V_S=4.6 km/sec).

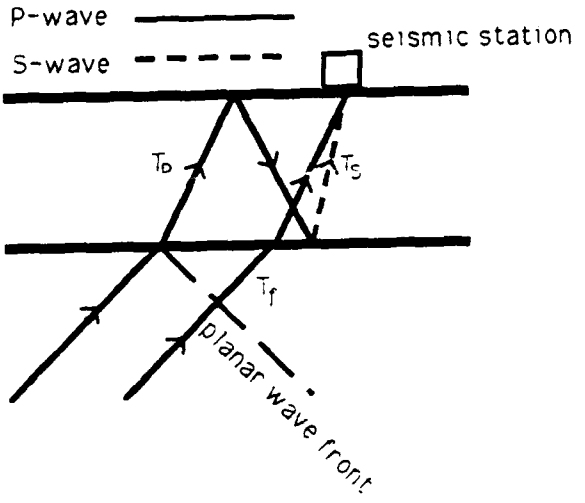


Figure 3, Ray paths for the PPS phase relative to the P phase for a layer over a half space. T_P and T_S are the travel times of the P and S phases with same ray parameter through the layer respectively. T_h is the travel time differential in the half space for the two rays assuming a planar wave front.

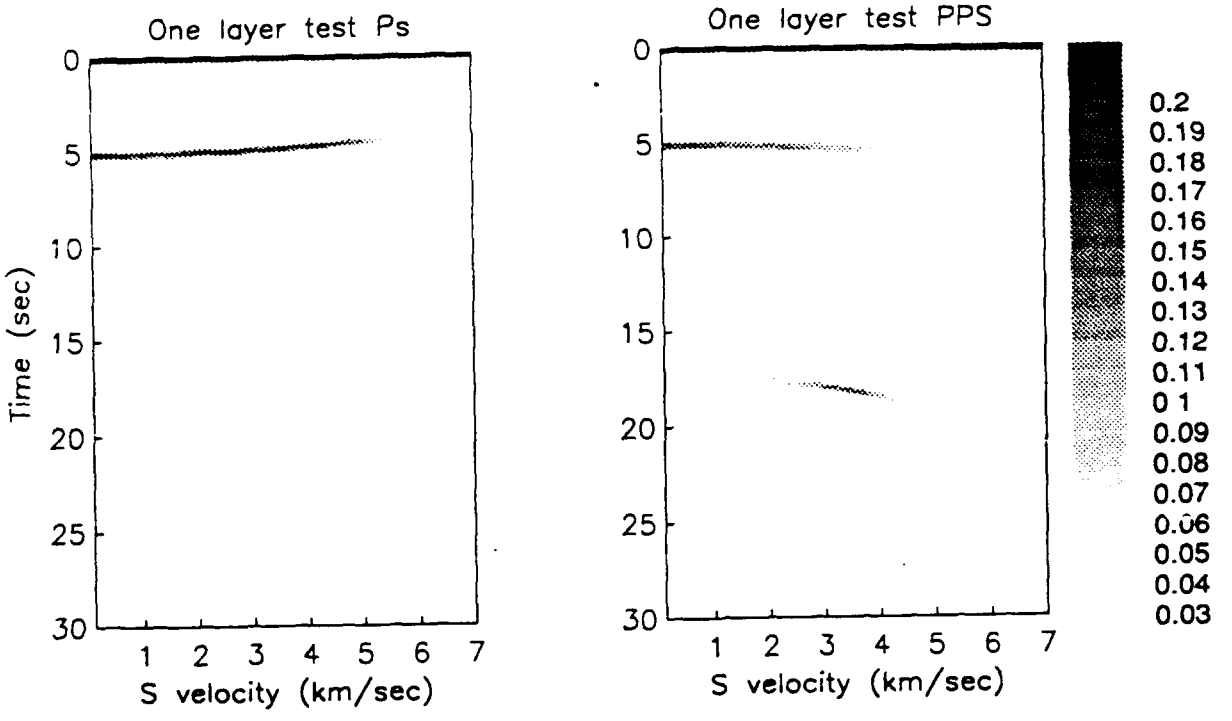


Figure 4, Velocity spectrum stacks produced from the synthetic receiver functions depicted in figure 2. Ps stacks are shown on the left and PPS stacks are on the right.

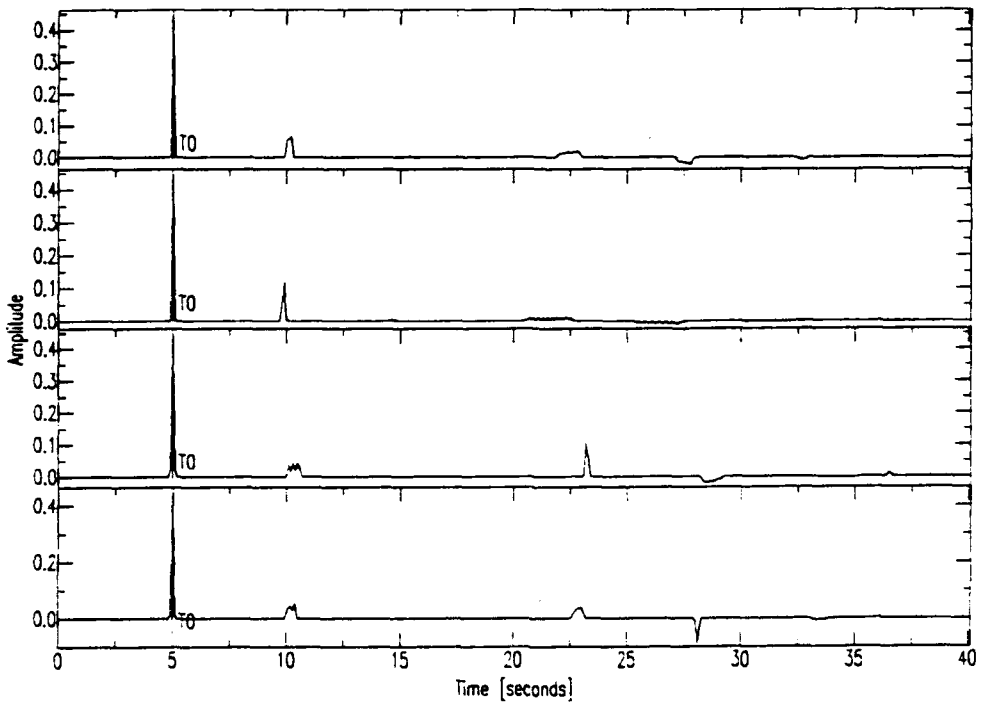


Figure 5, Stacks of the synthetic receiver functions depicted in figure 2. On top is a straight stack with no time correction applied. The bottom three receiver function stacks are computed after applying the appropriate normal moveout correction for Ps, PPS, and PSS respectively (from top to bottom).

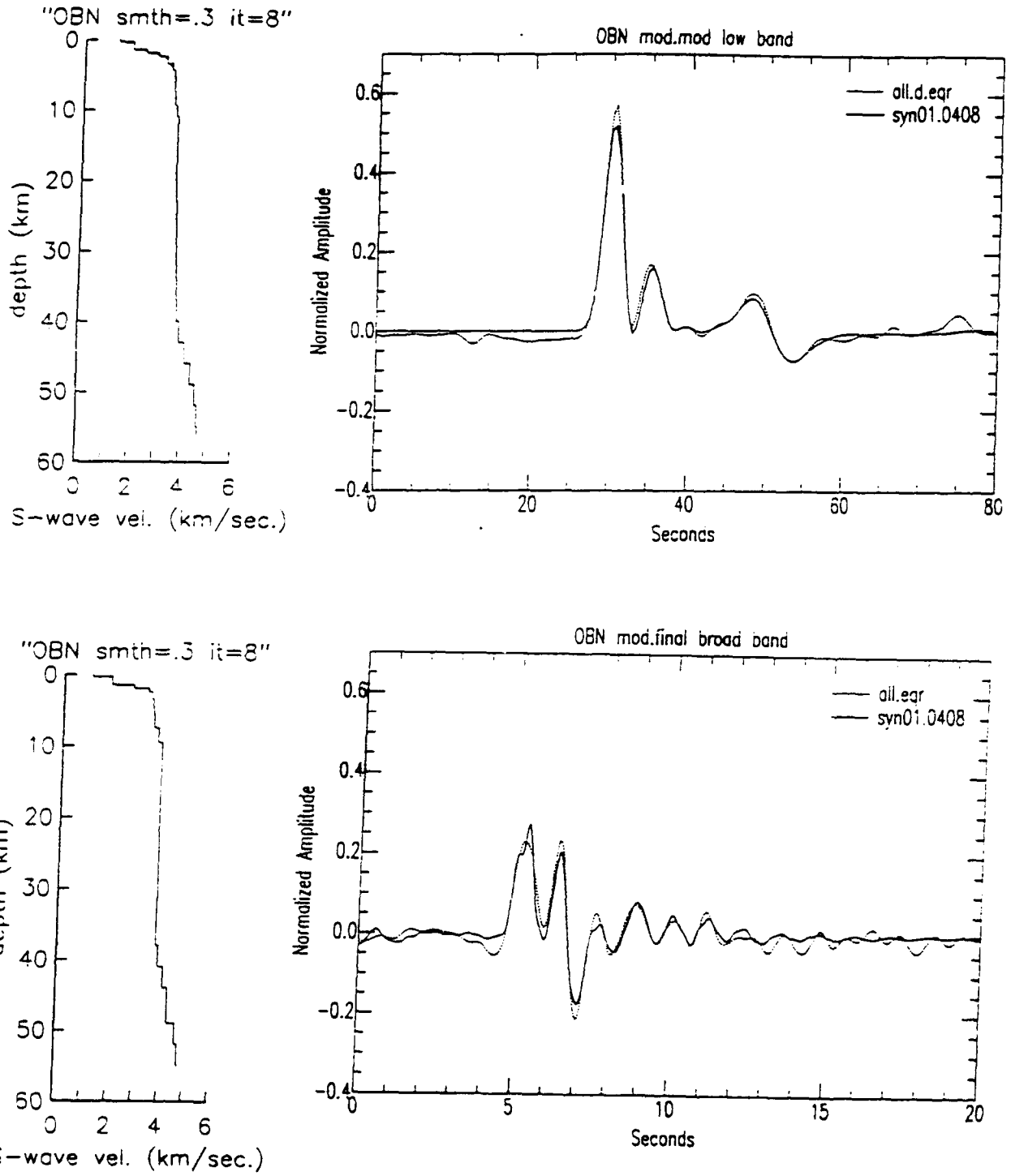


Figure 6. The synthetic (solid line) and observed (dashed line) receiver functions computed for the Soviet Seismographic station at Obninsk. The synthetics pertain to the crustal structure models depicted to the left of the respective receiver functions. The low pass filtered response is given on the top figure; the broad band results are on the bottom.

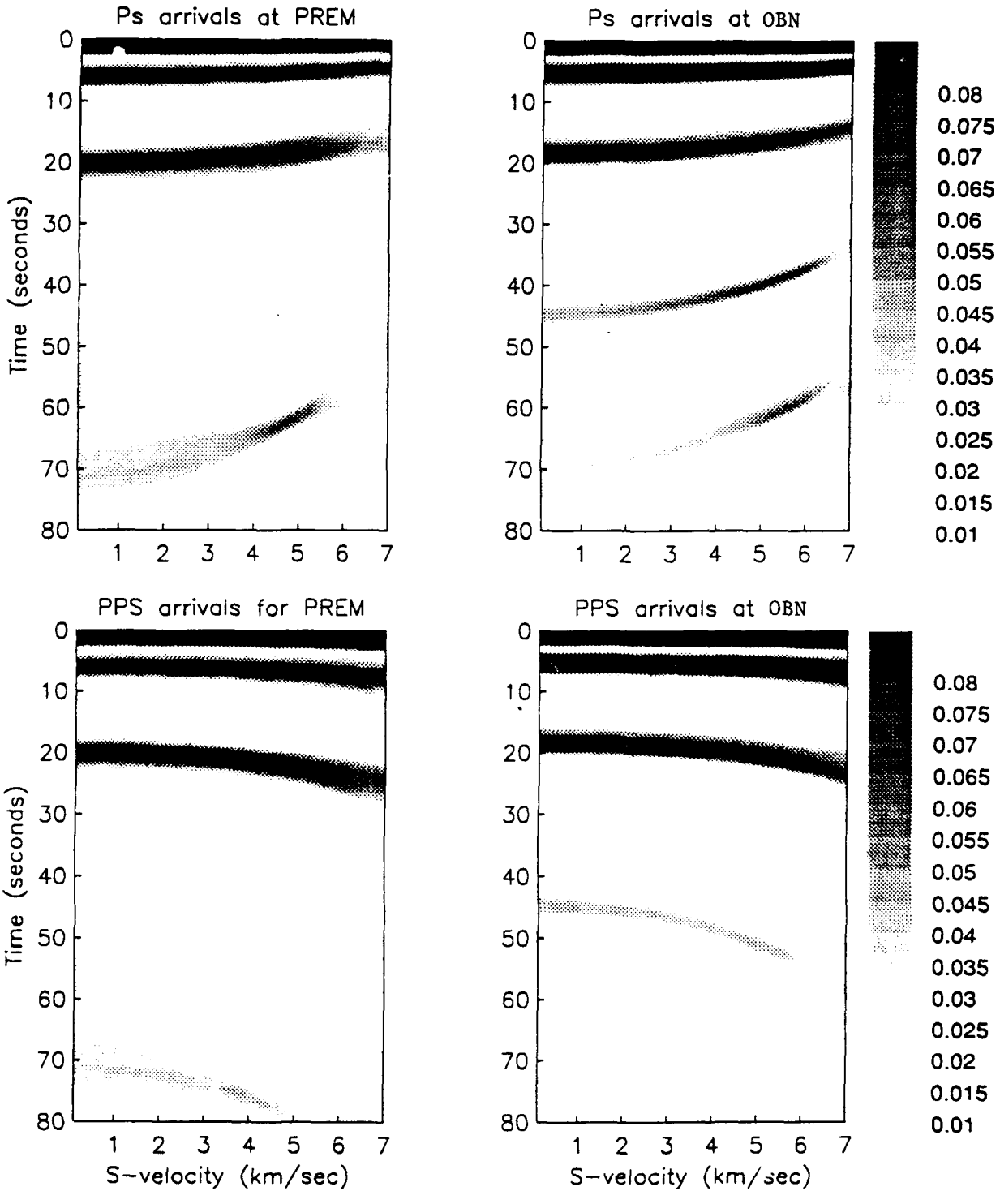


Figure 7. The two top Ps velocity spectrum stacks are produced from the synthetics computed from PREM (left) and receiver functions computed from observed data recorded at Obninsk (right). The two lower plots are the corresponding PPS stacks.

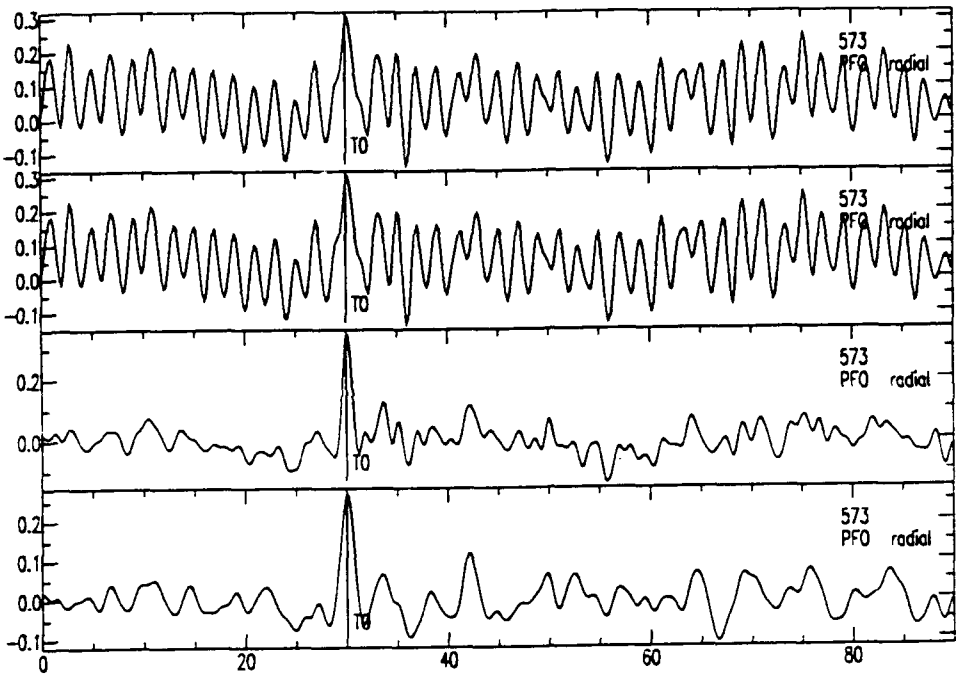


Figure 8. Receiver functions computed by spectral division using water levels of 0.0, 0.00001, 0.001 and 0.1 times the peak amplitude from top to bottom respectively.

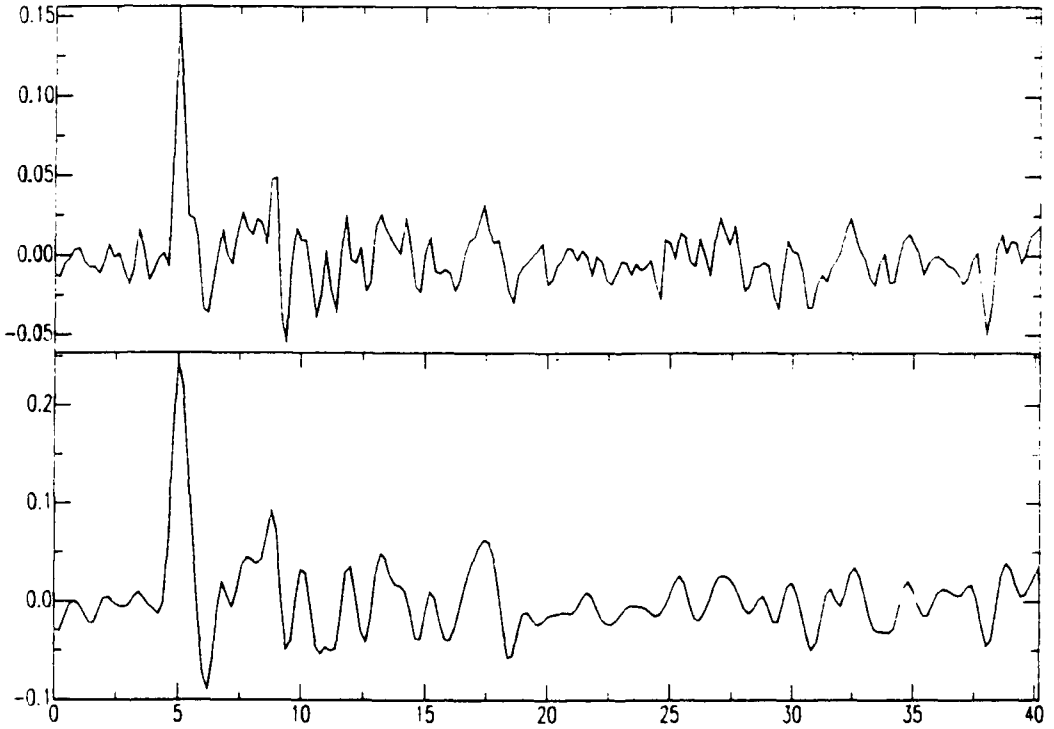


Figure 9. The top is a receiver function computed with a simultaneous time domain least squares deconvolution of 23 events. The bottom is a stack of 23 receiver functions (computed from the same 23 events as above) computed by spectral division (as in figure 8).

SHALLOW SEISMICITY FOLLOWING SELECTED NUCLEAR EXPLOSIONS AT THE NEVADA TEST SITE

Steve Harmsen[1], Joan Gomberg[1], and Paul G. Richards[2]

[1]U.S. Geological Survey, Geologic Division Branch of Geologic Risk Assessment
Denver, Colorado
[2]Lamont-Doherty Geological Observatory, and Department of Geological Sciences,
Columbia University

CONTRACT NO. F19628-90-K-0048

OBJECTIVE To characterize shallow seismicity following an underground nuclear explosion, thus helping to understand what could be achieved by on-site inspection of a region in which a suspicious event had occurred.

RESEARCH ACCOMPLISHED We have examined the list of preliminary locations of seismic events recorded by the Southern Great Basin Seismic Network (Nevada), and find many small events close to selected nuclear explosions, occurring days and months following the nuclear event.

We have concentrated on seismicity in the Silent Canyon Caldera (E. Pahute), following underground nuclear explosions in 1986-89. In particular, following LOCKNEY (magnitude 5.7, 1987 Sept 24) and up to the time of the next explosion in the region (COMSTOCK, 1988 June 2), we found eleven events occurring within ten km of the LOCKNEY shot point that were routinely located in the preliminary processing of network data.

In the network archive, we also found high quality digital data that had not been routinely processed, but which revealed the occurrence of about an order of magnitude more events. Many of these additional events, whose occurrence rate dropped with time post-LOCKNEY, exhibited a low frequency character that differed from the events routinely located as small earthquakes by the network. Many of the post-LOCKNEY events displayed a dilatational first motion at most of the stations at which first-motion could be determined. The same pattern, of some small earthquakes and more low frequency events, is observed following the smaller nuclear explosion AMARILLO (magnitude 4.9, 1989 June 27).

Figure 1 shows an example of what we would call a "small earthquake", and Figure 2 an example of a "low frequency event", both occurring post-LOCKNEY and in the vicinity of this shot. We note that Smith (1982) and Adushkin *et al.*(1990) have

also found it natural to describe seismicity following an underground nuclear explosion in terms of two separate types of events, one "high frequency" or "impulsive"; the other "low frequency" or "emergent", the presumption being that the latter type represents events associated with the cavity. These two previous studies used specially-deployed stations with a spacing of less than one km. Though SGBSN has a greater station spacing, it has the merit of having been in operation for a number of years, permitting statistics of explosion-aftershock occurrence to be acquired.

Even though, in our study, the low frequency events are also characterized by a lack of clear S arrivals, in many cases a sufficient number of first arrivals can be identified to enable hypocentral coordinates to be estimated. Preliminary analysis suggests that strong variations in the velocity structure must be modeled to achieve hypocenter location accuracies greater than 1-2 km. Some of the post-explosion seismic events obviously occur in almost exactly the same location, since they have very similar seismograms.

CONCLUSIONS and RECOMMENDATIONS Statistics of explosion-aftershock occurrence can and should be acquired.

REFERENCES

Adushkin, V.V., A.A. Spivak, M.M. Krekov, M.G. Starshina, and S.K. Daragan. Aftershocks of large-scale underground nuclear explosions, *Academ. Nauk CCCP Izvestiya: Fizika Zemlyi*, no. 9, pp 19-27 (in Russian), 1990.

Smith, A.T. and R.G. Geil. Microseismicity following an explosion, *Earthquake Notes*, **53**, no. 1, page 10, 1982.

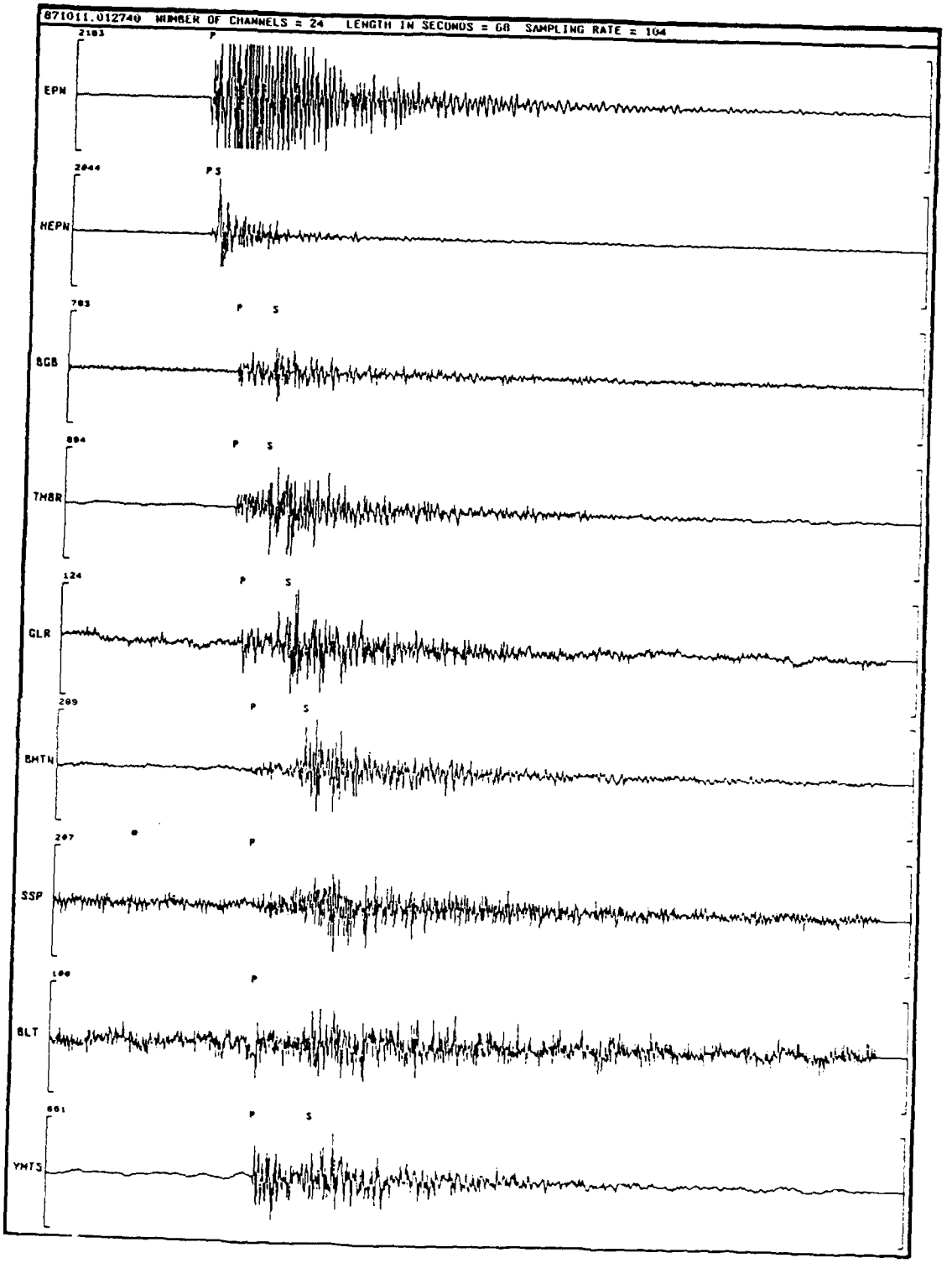


Figure 1. Seismograms of an event (traces start at 1987/10/11 01:27:40; 68 seconds displayed) that we would classify as a small earthquake, or "normal event." It has clear *S* arrivals, and was located in routine processing of SGBSN data. The closest station, EPN, is less than 10 km from the location of the LOCKNEY explosions.

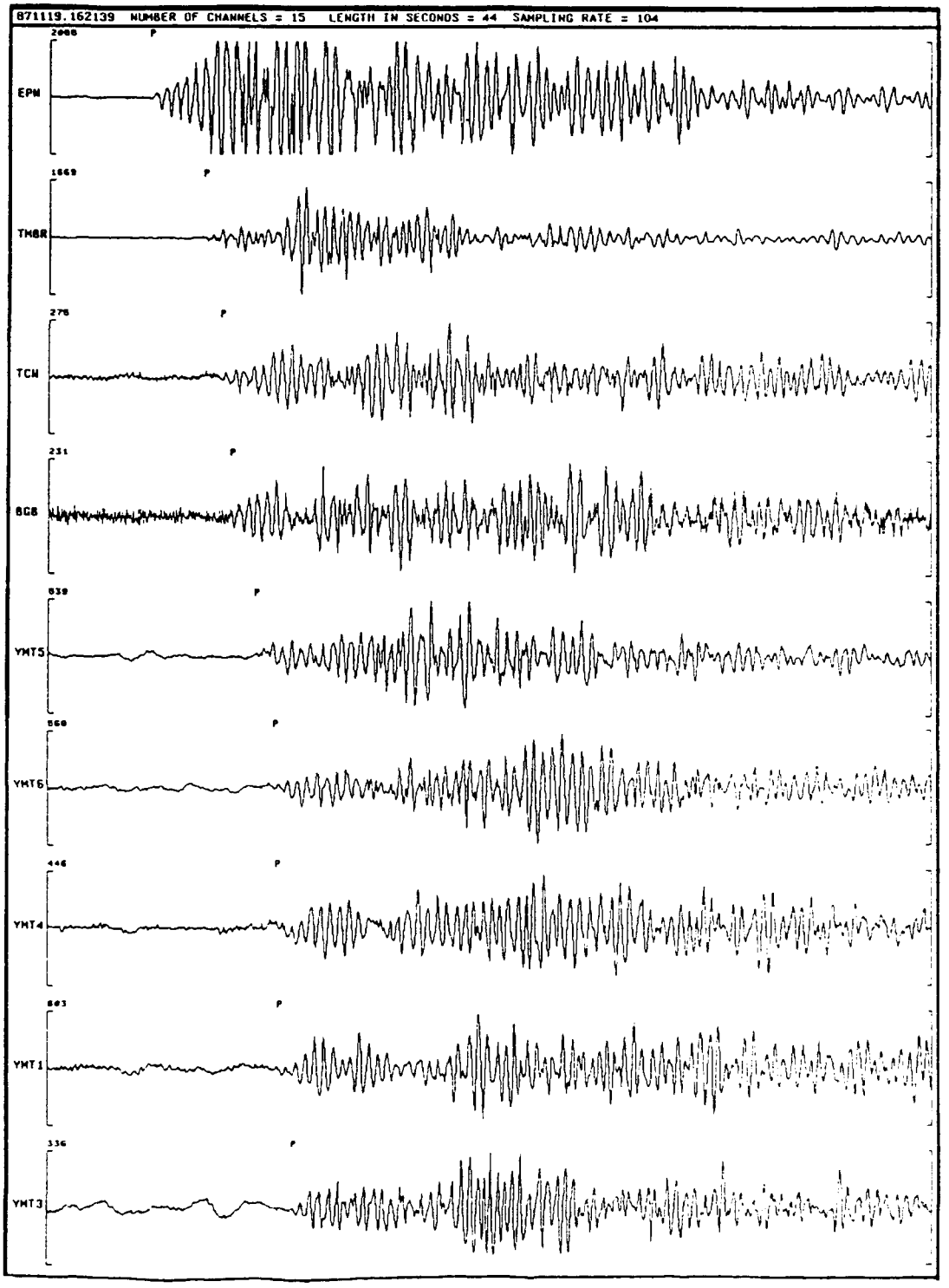


Figure 2. Seismograms (starting at 1987/11/19 16:21:39; 44 seconds displayed) of what we would classify as a "low-frequency" event. The order of first arrivals indicates that this event, like that of Figure 1, is close to the location of the LOCKNEY explosion.

Beam-stack imaging of scatterers near the NORESS array

Michael A.H. Hedlin, J. Bernard Minster and John A. Orcutt

Institute of Geophysics and Planetary Physics (A-025)
Scripps Institution of Oceanography, University of California at San Diego
La Jolla CA 92093 U.S.A.

Contracts No. F19628-89-K-0018 and F19628-88-K-0044

1. Objective

The research described in this report extends the analysis described in our previous DARPA/GL short paper (Hedlin, *et al.*, 1990) and in somewhat more detail by Hedlin, *et al.*, (1991). In short, we are interested in assessing the degree to which large topographic features or crustal heterogeneities are capable of contributing large, identifiable, seismic phases to coda recorded by nearby seismometers. The technique we have developed for this analysis relies on the existence of an array of sensors in the vicinity of these features. In essence, a hyperboloid-summation time migration is performed on the array recordings of distant primary events to enhance locally scattered phases. This technique is designed to accommodate simultaneously an arbitrarily large number of teleseisms. To date attention has been focused on the generation of Rg phases by incident P wave trains.

Since the last report, our work has centered on the analysis of synthetic scattered phases to quantify the gain in image quality we can expect from stacking a well distributed set of teleseisms. Further work has indicated that, due to the protracted nature of most teleseisms, deconvolution of the incoming wavefield from the event records should be done before spatial images of the scatterers can be produced. In this report we produce an image of the local scatterers based on the migration and stacking a suite of 31 teleseisms. Two prominent secondary sources of surface waves are inferred to exist 10 km to the east and 27 km to the southwest of the array. We compare this result with the local topography and find significant similarities. Our findings are largely consistent with those of Gupta *et al.*(1990a,b) and Bannister *et al.*(1990).

2. Research Accomplished

2.a The adaptation of hyperbola summation migration to small aperture array data

To describe the imaging technique, we adopt, for the time being, a simple model describing the origin of locally scattered waves - one in which a single omnidirectional point scatterer exists, is impulsively excited at a time t=0 and produces seismic motions that are recorded by an array of sensors located at the free surface (z=0; $x=x_j$, $y=y_j$) where j varies from 1 to N (the number of sensors in the array). Furthermore, we assume that the scattered energy propagates at a constant velocity, V, and there is no dispersion. Without loss of generality we place the scatterer at x=0,y=0 and find, using simple trigonometry, that the time t_j at which the scattered wavefront should pass the jth sensor is given by:

$$t_j = \frac{\sqrt{x_j^2 + y_j^2 + z_s^2}}{V} \tag{1}$$

or, defining $t_0 = (\frac{z_s}{V})$, the vertical travel time from the scatterer to the free surface, equation 1 becomes:

$$\frac{t_j^2}{t_0^2} - \frac{x_j^2}{t_0^2 V^2} - \frac{y_j^2}{t_0^2 V^2} = 1 \tag{2}$$

The surface in 3 dimensional space-time which describes the onset times predicted for energy arriving from the scatterer is a hyperboloid of revolution (whose axis of symmetry is the time axis). This surface is sketched in Figure 1. When the scatterer is located in the x-y plane the hyperboloid degrades to a circular cone with its apex located at the origin. If the space-time location of this sensor is outside the hyperboloid, the sensor cannot have been influenced by the scatterer. Conversely, if the sensor is located within the hyperboloid, the scattered wavefield will

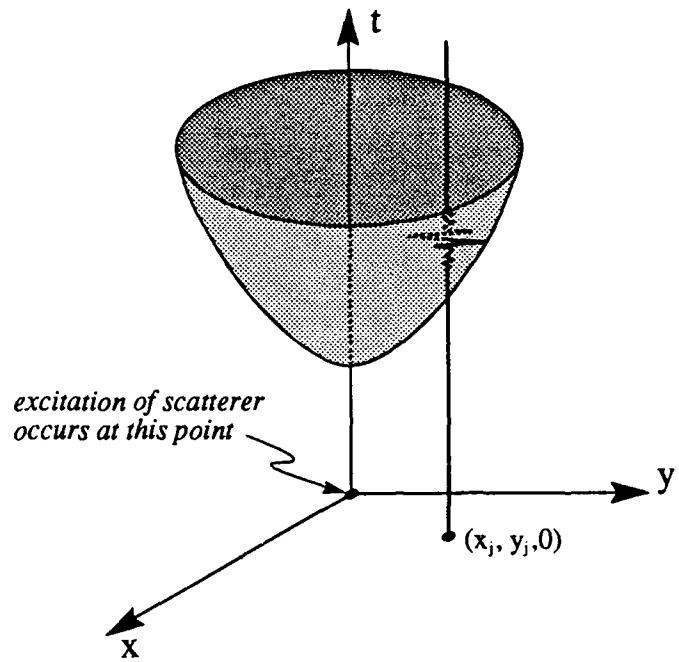


Figure 1 The surface in 3 dimensional space-time that describes the arrival times for energy originating at a subsurface scatterer and detected at the free-surface. In this schematic illustration, seismic motions recorded by a sensor located at $(x_j,y_j,0)$ are indicated by the vertical seismic trace. The hyperboloid intersects the vertical axis at the time $\frac{z_s}{V}$, where z_s is the depth of the scatterer, V is the velocity of the medium.

have already passed. Given this simple situation, to achieve the greatest enhancement of seismic motions caused by this source (at the expense of motions caused by secondary sources at other locations), and thus to achieve the best image of the source itself, one should sum the motions recorded by the sensors at times that will reposition each sensor in space-time onto the surface of the hyperboloid. This is a simple extension of the hyperbola summation migration method (Yilmaz, 1987) in seismic reflection.

2.b Processing details

To image a region of the crust, we subdivide the area into small segments and consider them individually, in sequence. It is assumed that a secondary source exists within the sub-area of current interest. Since the location of the hypothetical scatterer is known, the adoption of a slowness of propagation of the scattered waves, $\mathbf{p}_s$, allows the space-time hyperboloid to be defined. For each crustal sub-area being scanned, the recordings of the teleseismic event are summed after shifting them in time as required by the hyperboloid. In practice, since it is not known when, in absolute time, excitation occurs, the time axis is translated so that the onset time of the primary energy at the array occurs at t=0. Using elementary ray theory it is possible to estimate what time delay, τ, should exist between the arrival of the primary energy and the scattered phases originating at the hypothetical scatterer after excitation by the primary energy. Considering a single event-scatterer pair, the time offset, τ, between the arrivals of energy propagating directly from the source (at vector slowness $\mathbf{p}_i$) and via the scatterer (vector slowness $\mathbf{p}_s$) at a vector distance $\mathbf{R}_{as}$ from the array is given by:

$$\tau = \mathbf{R}_{as} \bullet (\mathbf{p}_i - \mathbf{p}_s) \tag{3}$$

It is possible to estimate $\mathbf{p}_s$ by considering a suite of broadly distributed events and computing a number of preliminary images while slowly varying this parameter and selecting the value that brings the image into the sharpest focus. The slowness of the incident energy, $\mathbf{p}_i$, is well constrained by fitting a least-squares best fit plane (in x-y-t space) to the first breaks on the array records. By systematically scanning the crustal volume about the array, we can generate an image which is interpreted as a map of local scatterers. To date, we have considered

scattering interactions excited by P waves, using both synthetic seismograms and recorded data.

In practice, there are a number of complicating factors that must be taken into account prior to constructing images of faint, local sources using synthetics or recorded data.

1) If the scattered field consists of dispersed surface waves, no single velocity, V, will allow a comprehensive description of the scattered wavefield. As a result, we choose to integrate over a span of time centered on the space-time hyerboloid which is defined by a velocity representative of the average speed of propagation of the surface wave energy. We have used integration time windows of up to 5 seconds in duration.

2) Based on the results of synthetic tests we have not attempted to use the full coherent, or phased, recordings. Because we are are dealing with dispersed energy, we have concluded that the trade-off between image resolution and stability can best be mitigated by migrating coherent records but converting the results to envelopes prior to integration in a method akin to incoherent beamforming (Ringdal *et al.*, 1975).

3) When considering the recorded data, it is immediately apparent that local scattered phases, excited by teleseismic energy, cannot be examined in the absence of this (primary) energy. It is necessary to mask the stronger primary source by suppressing the energy that has propagated directly from it. The method we have adopted to accomplish this, introduced by Gupta *et al.*(1990a), is known as beam correction and simply involves the coherent subtraction of the primary source beam from all the individual channels to yield residual seismograms.

4) The recorded signals are immersed in seismic noise, much of which - at NORESS - is microseismic energy originating in the North Sea (Fyen, 1986), and thus exists in a relatively low frequency band (0.1 to 1/3 Hz). Fortunately, the surface wave energy of interest exists, mainly, in the band from 0.5 to 3.0 Hz, and thus the signal to noise ratio (SNR) can be significantly improved by narrow band pass filtering the array records.

5) Since we are considering surface wave propagation, a gain proportional to $\sqrt{|R_{as}|}$ should be applied to compensate for amplitude loss due to cylindrical geometrical spreading.

6) Finally, a further complication, that exists only in the recorded data, is caused by the non-impulsive nature of most teleseisms - they consist of a protracted sequence of arrivals. To limit the impact of this we deconvolve an estimate of the incoming wavefield, obtained by beamforming for the primary source, from the individual array records. The deconvolution is treated as an inverse problem. We seek the deconvolved trace that produces an acceptable fit to the recorded data and has a reasonable degree of autocovariance (for further details see Hedlin, 1991).

2.c Analysis of synthetics - imaging resolution

Prior to analyzing data, we gauge the resolution of the imaging technique by analyzing infinitesimally small synthetic scatterers. In Figure 2 we display the image of a single point source located to the southwest of the array. The radial resolution is limited because we have employed time averaging of 5 s. The azimuthal resolution is limited because of the coherence of the surface waves and because we are employing envelopes of beams. Energy is spatially aliased away from the actual location of the scatterer to locations which share a common delay time. By manipulation of equation 3 it can be shown that scatterers which share a common delay time τ lie on a curve described by:

$$|\mathbf{R}_{as}| = \frac{\tau}{|\mathbf{p}_s| - |\mathbf{p}_i|cos(\theta)} \tag{4}$$

where θ is the angle between $\mathbf{p}_s$ and $\mathbf{p}_i$. When $\mathbf{p}_s$ is greater than $\mathbf{p}_i$ (eg. P to R_g scattering) this describes an ellipse with one focus at the center of the array, major axis pointing to the primary source and eccentricity proportional to $\mathbf{p}_s$. In this synthetic calculation the primary source was located directly beneath the array ($\mathbf{p}_i = 0$) and thus the curves of constant τ have degenerated into circles centered on the array. The same secondary source illuminated by a teleseism arriving from the north at a phase velocity of 15 km/s and imaged using 1 s of time averaging yields the result in Figure 3. The radial resolution is superior to that in Figure 2; however, the azimuthal resolution is worse - this image possesses more significant sidelobes.

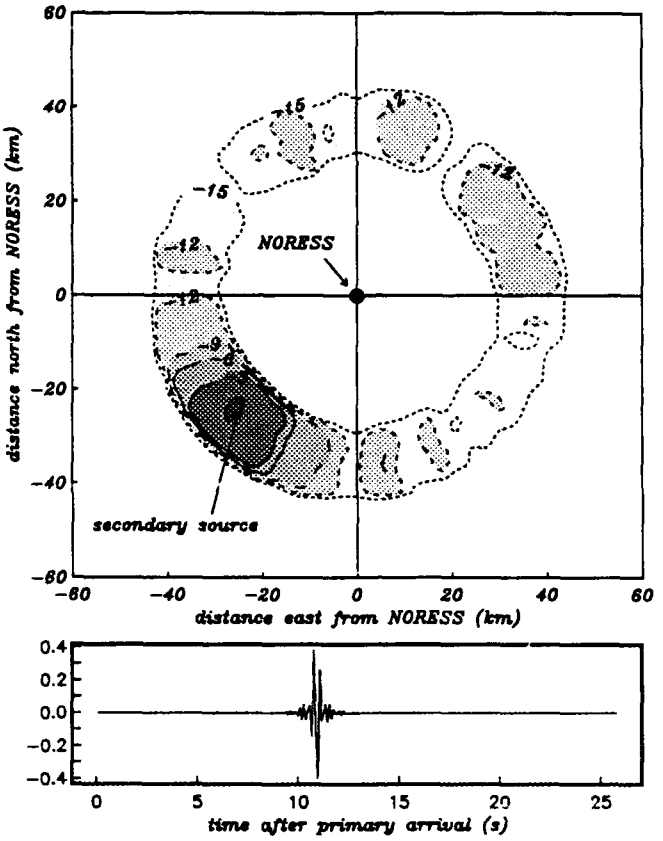


Figure 2 Image of a synthetic point source located 35 km from the array at a back azimuth of 225°. Wavenumber Integration was used to generate synthetic seismograms individually for each of the 25 vertical component sensors in the NORESS array (illustrated is the synthetic computed for the center station). In this, and all subsequent images, contour values indicate amplitudes in dB relative to the largest value in the image and cylindrical propagation of scattered wavefronts was assumed.

2.d Stacking to increase azimuthal resolution

Since energy is aliased along elliptical curves, that depend on the back azimuth to the primary event, it is possible to increase azimuthal resolution by stacking images obtained using a broadly distributed set of teleseismic events. To illustrate this point we have calculated the aliasing ellipses for a synthetic scatterer when it is illuminated by 30 teleseismic events that are uniformly distributed azimuthally. The results are displayed in Figure 4. This figure illustrates the enhancement of azimuthal resolution we can hope to attain via the stacking af a uniformly distributed suite of teleseismic events. In this figure, the more broadly spaced the ellipses are, the greater the suppression of amplitudes (originating at the secondary source) should be. Conversely, the more closely the curves are grouped, the greater the enhancement should be. All 30 ellipses are contained within a cyclic curve and converge at the location of the scatterer. Maximum enhancement of amplitudes will occur at this point. This figure illustrates that energy aliased to distant azimuths (greater than 45° from the secondary source) should be well dispersed. Unfortunately, all ellipses emanate from the secondary source location to the northwest and southeast - so we might expect local distortion of the character of the image of the point source. Specifically, it should become elongated to the northwest and southeast, and, if time averaging is used, somewhat blurred radially. The ellipses are slightly concentrated along the edges of the cyclic curve.

To further test the impact of stacking we repeat the calculation displayed in Figure 4 for all 30 teleseisms and arrive at the result displayed in Figure 5. As predicted the distant aliasing is reduced by a significant degree (beyond 45° the maximum amplitude in Figure 3 is roughly -10 dB, in Figure 5 it is reduced to -25 dB. At close azimuths the image is distorted to be elongate to the northwest and southeast and slightly wider radially - conditions predicted

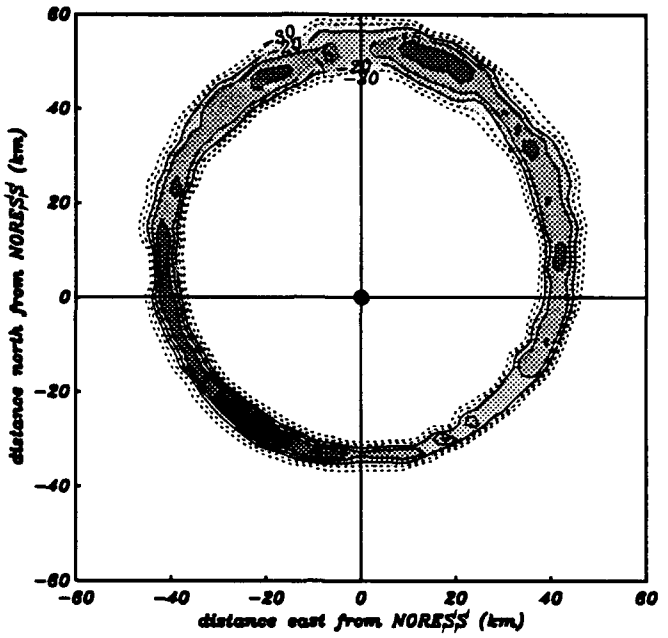


Figure 3 Image of a synthetic point source located 35 km from NORESS at a back azimuth of 225°. The secondary source is illuminated by a single impulsive teleseism arriving from the north at 15 km/s.

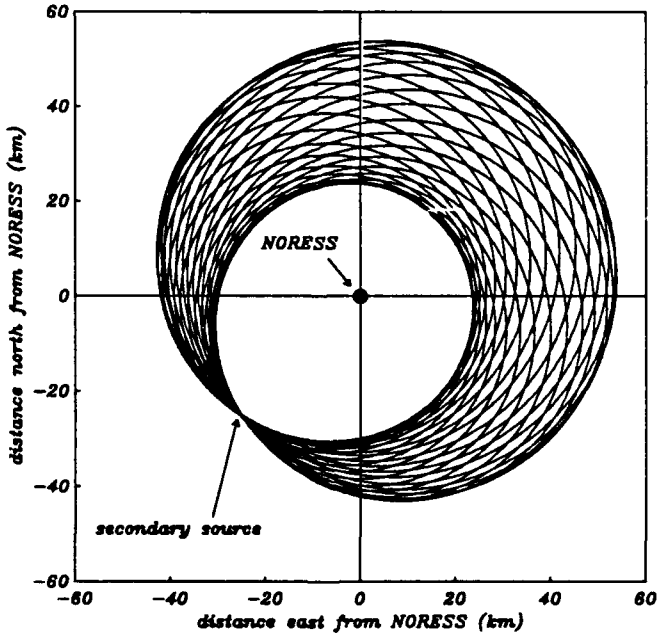


Figure 4 A suite of 30 ellipses computed using equation 3. A single point scatterer has been located 35 km from NORESS at a back azimuth of 225°. This scatterer is illuminated by 30 teleseismic events regularly spaced in back-azimuth. All teleseismic arrivals have a phase velocity of 15 km/s.

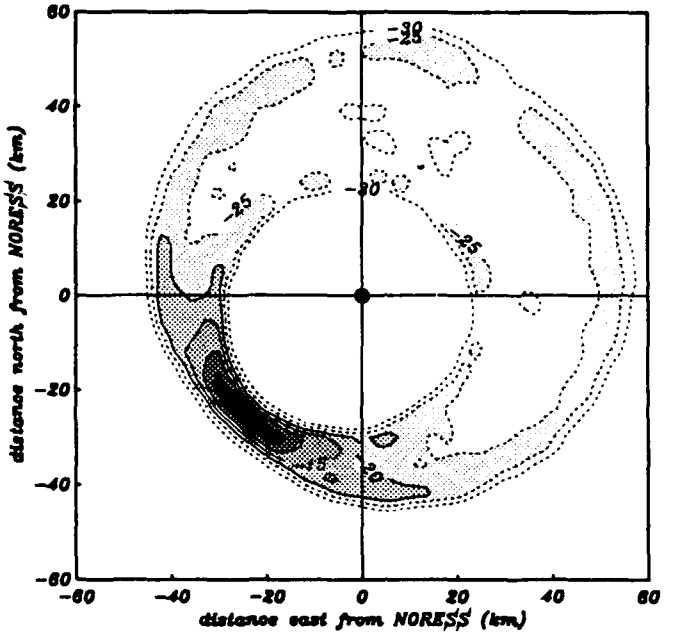


Figure 5 Image of a synthetic point source located 35 km from NORESS at a back azimuth of 225°. The secondary source is illuminated by 30 impulsive teleseisms arriving from all quadrants at 15 km/s.

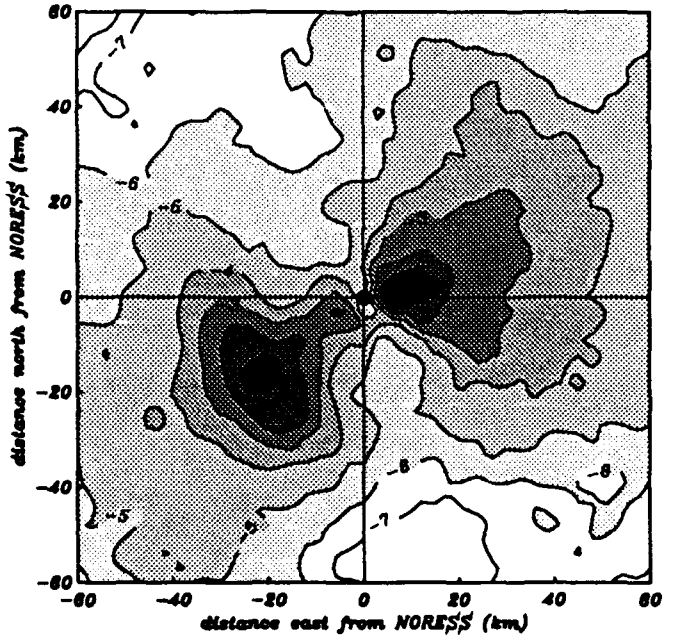


Figure 6 Final image of the scatterers in the vicinity of the NORESS array computed using deconvolved array recordings of 31 teleseismic earthquakes and nuclear explosions (see Table 4.1). A scattered wave velocity of .36 s/km was used.

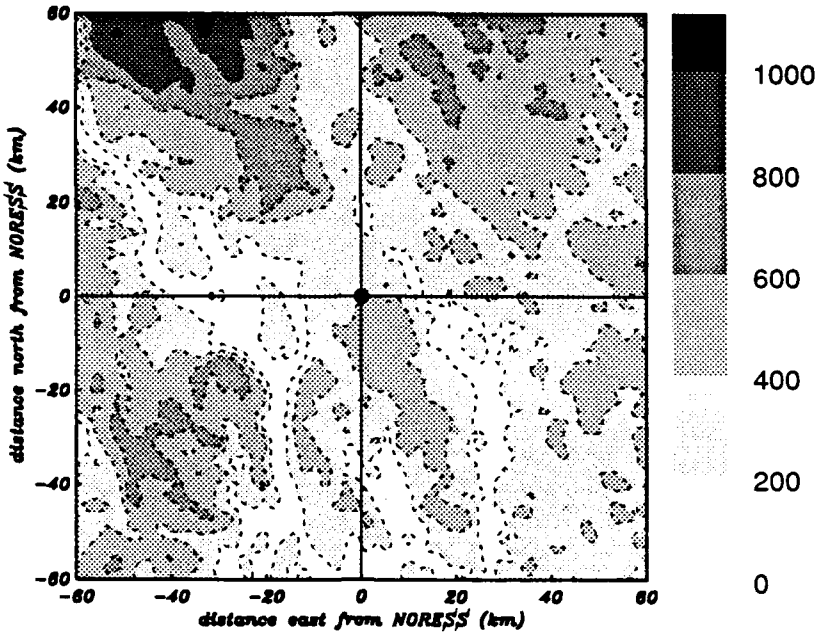


Figure 7 Topography near the NORESS array.

by Figure 4. Aliased energy has become slightly concentrated at the edges of the bounding cyclic curve. Despite these drawbacks, the synthetics reveal that image quality should be enhanced by stacking.

2.e Analysis of recorded data

When we apply this technique to a suite of 31 teleseismic events (listed in Hedlin, 1991) we obtain the image displayed in Figure 6. All events considered in this image have been deconvolved prior to migration and stacking. A focusing analysis. in which the velocity of scattered energy is gradually changed, suggests a reasonable velocity of secondary energy is .36 s/km - a result consistent with the findings of Lokshtanov *et al.*(1991). If we adopt this velocity, two local sources of seismic energy are strongly inferred to exist in the vicinity of the array. One roughly 27 km to the southwest and the other roughly 10 km to the east of the array. Examination of the topography near NORESS, Figure 7, reveals that the former feature does coincide with the southwest edge of lake Mjosa as the topography rapidly rises to from the bottom of the lake (depths not shown on this map) to the neighboring peak. The latter source appears to coincide with a small topographic feature but the coincidence is not striking suggesting the possibility of a subsurface source.

Conclusions and Recommendations

Our analysis of synthetics and a large suite of teleseisms recorded by the NORESS array indicates that two secondary sources are likely present in the vicinity of this array. These sources appear to be commonly excited by incoming teleseismic waves and generate identifiable phases at NORESS. A source 10 km to the east of the array coincides with only a slight topographic relief suggesting the presence of a buried source. A second source 27 km to the southwest coincides with dramatic topographic relief at the southwest edge of Lake Mjosa. This observation is in complete agreement with previous studies (Gupta *et al.*, 1990a,b; Bannister *et al.*, 1990). We are currently investigating the stability of our image, using Jacknife and Bootstrap error estimation techniques.

References

Bannister, S.C., Husebye, E.S. and Ruud, B.O., Teleseismic P coda analyzed by three-component and array tech-

niques: Deterministic location of topographic P-to-R_g scattering near the NORESS array. *Bull. Seismol. Soc. Am.* , **80B**, 1969-1986, 1990.

Fyen, J., NORSAR semiannual technical summary - 2-85/86. *48-59*, 1986.

Gupta, I.N., Lynnes, C.S., McElfresh, T.W. and Wagner, R.A., F-K analysis of NORESS array and single station data to identify sources of near-receiver and near-source scattering. *Bull. Seismol. Soc. Am.* , **80B**, 2227-2241, 1990a.

Gupta, I.N., Lynnes, C.S. and Wagner, R.A., Broadband F-K analysis of array data to identify sources of local scattering. *Geophys. Res. Lett.* , **17**, 183-186, 1990b.

Hedlin, M.A.H., Minster, J.B. and Orcutt, J.A. (1990). Beam-stack imaging of scatterers near a small aperture array. Contributed paper at "*12th annual AFGL/DARPA seism. Res. Symp*", held in Key West, FL.

Hedlin, M.A.H., *Seismic array observations of local scattering and regional mine explosions.* PhD thesis, University of California, San Diego, 1991.

Hedlin, M.A.H., Minster, J.B. and Orcutt, J.A., *Beam-stack imaging of scatterers near a small aperture array.* Geophysical Research Letters - in press, 1991.

Lokshtanov, D.E., Ruud, B.O. and Husebye, E.S., The upper crust low velocity layer; a Rayleigh (R_g) phase velocity study from SE Norway. *Terra Nova*, **3**, 49-56, 1991.

Ringdal, F., Husebye, E.S. and Dahle, A., P-wave envelope representation in event detection using array data. *Exploitation of Seismograph Networks, K.G. Beauchamp, Editor, Noordoff-Leiden*, 1975.

Yilmaz, O., *Seismic data processing.* Society of Exploration Geophysicists, Investigations in Geophysics, volume 2, 1987.

Source Retrieval from Regional Seismograms

D. Helmberger, D. Dreger, L. Zhao,
S. Kedar, B. Woods and D. Harkrider
California Institute of Technology

Contract Nos. F19628-90-K-0049
F19628-89-K-0028

Objective: Our primary objective is to develop techniques for discrimination and source strength estimation for small events. To retrieve source information from small events requires working with regional phases. This study addresses some significant progress in extracting such information from sparse broadband data (IRIS) of the type deployed in the Soviet Union.

Results: With the installation of the broad-band, high dynamic range IRIS instruments, it has become possible to compare the regional waveforms of earthquakes and explosions at magnitudes 3 to 6. These waveforms are similar for event sequences in many situations and can be inverted for source mechanism. We find that standard flat-layered models used in regional event location networks are sufficient for predicting and inverting the body waveforms at periods greater than a few seconds. Many times a single station is sufficient for this purpose in the case of earthquake sources.

This report will begin with some basic broadband observations of earthquakes and explosions and discussion of general characteristics. Some preliminary useful discriminants are discussed and tested in terms of (M_0 vs. M_L) plots and high frequency/low frequency ratios. This will be followed by some preliminary results for Soviet events.

1) Broadband Observation of Earthquakes and Explosions

A new digital system called TERRAscope has been recently installed in Southern California and we will use this data at these relatively dense stations to develop methods which can be transported and tested on Soviet data base.

(a.) Earthquakes

The first sizable event to be recorded by the array occurred on June 28, ML = 5.8. Figure 1 shows the location of the event and stations. Remarkably, four of the stations (GSC, ISA, PFO and SBC) were located at 159.2±0.7 km from the event. Observations from three of the stations namely GSC, ISA and PFO display strong similarities in waveform.

It is interesting to compare the broadband displacement data recorded at GSC, ISA and PFO with displacement synthetics as displayed in Figure 2 to demonstrate the usefulness of one-dimensional velocity model in explaining the data. This figure emphasizes the strengths and weaknesses of the various types of regional phases in determining source parameters. The synthetics were computed using a reflectivity method assuming the Socal velocity model, see figure 3, and the source parameters obtained from waveform inversion as discussed later. The data in this figure is plotted in absolute time, and the synthetics have been delayed 0.37 seconds in order to align them with the first arrival. In addition to P_n and S_n two important reflected arrivals in the synthetics are marked by vertical lines to aid in the identification of the phases. There is clearly very little variation in the P_n arrival times. The variation is less than 2% of the average P_n traveltime of 26.2 seconds. For S_n the variation is less than 3% of the average S_n traveltime of 44.6 seconds. There is also good agreement between the data and synthetic waveforms. The short-period phase sP_mP is well modeled for all of the stations. The short-period phase S_mS is a strong arrival in both the GSC and PFO data. The phase S_mS in the synthetics has the correct relative traveltime for station GSC, but arrives a little too late at PFO. The surface waves are relatively well modeled at stations GSC and PFO but they show the largest variation in arrival time. The best fits are for the longer period PL waves arriving between P_n and S_mS. The PL wave are composed of P to S and S to P converted head waves that

propagate along the top of the mantle, are relatively insensitive to short wavelength crustal heterogeneity (Helmberger and Engen, 1980; Wallace et al., 1981), and are therefore useful in determining the source parameters of earthquakes. We filtered the data with a Press-Ewing instrument response and inverted only the long-period crustal body waves from P_n to just after the S_mS arrival to minimize errors due to misalignment of the short-period body waves and the surface waves.

In sum, since the phases P_n, sP_mP, S_n, S_mS, sS_mS arrivals are dependent primarily on deeper crustal structure and show relatively small variations in absolute and relative timing for each of the stations the lower crust is probably fairly uniform. In contrast, the surface waves display the largest variations in traveltime and are subject to the lateral heterogeneity of the upper crust (Stead, 1989; Ho-Liu and Helmberger, 1989). Fine tuning the velocity model for each source-station path to better fit the short-period body wave phases and the surface waves will be addressed later in an aftershock-mainshock comparison study. We can usually treat events down to about magnitude 3 before long period noise dominates the signals, see Dreger and Helmberger (1991a).

We use the inversion method described in detail by Liu and Helmberger (1985), modified to invert local body waves recorded at a single station (Dreger and Helmberger, 1991a) and regional body waves (Dreger and Helmberger, 1991b). Generally, the method can be described as a least squares inversion, parameterized using an L2 norm. This parameterization allows the inversion to be sensitive to both the amplitudes and the waveforms. The method is non-linear and requires iteration on a starting model. Uniqueness of the solution is determined by using a number of starting models and graphically examine the model parameter space.

The inversion yields a strike of 235°, rake of 74°, dip of 50° and a seismic moment of 2.5 x 10^{24} dyne-cm. Figure 3 compares the data to synthetics calculated using these parameters for stations GSC, ISA and PFO. There is good agreement in amplitude and in waveform for all of the stations. Figure 3 shows the seismic moment as a function of error. There is a pronounced minima and the lowest errors were obtained with the seismic moment reported above. We tested the uniqueness of our solution by using a number of starting models to see if there is common convergence. The iterative process of the inversion serves to map out the error space and allows one to determine if the minima are global minima, see Dreger and Helmberger (1991b) for details.

A second example of earthquake data at a greater distance is displayed in figure 4. Figure 5 shows the location of this event, Lee Vining relative to Pasadena. The broadband data at Pasadena for this earthquake is displayed at the top of figure 4. Since this frequency band encompasses the frequency bands of conventional instruments we filter the data using the instrument responses of conventional instruments such as the short-period Wood-Anderson (WASP), long-period Wood-Anderson (WALP) and Press-Ewing (LP3090). Processing the data in this manner aids in the identification of the different phases in the data. Note that relatively long-period P_{nl} and S_{nl} arrivals are evident in the broadband displacement and LP3090 data as are the Love waves and the Raleigh waves. The long-period arrivals on the radial and vertical component, following the phase marked P_mP are the PL waves. The displacement data filtered with the WASP and WALP instrument responses highlights the shorter-period phases such as P_mP, LG and RG. The waveforms are generally well ordered in that they are composed of phases that can be modeled using simple one-dimensional plane layered models as in the earlier example. In many cases a simple layer over a halfspace model is adequate.

Two velocity models were used in the inversion, a layer over a half-space model (LHS) and one due to Jones and Dollar (1986), JD. The latter is used in locating Sierran earthquakes with stations located in Southern California.

The results are displayed in figure 6 where the event proves to be mostly strike-slip, θ =360°, λ=-154, δ=85° and a seismic moment of $3x10^{23}$erg s, see beach balls in figure 6. The best fits are obtained from using the JD model but both are adequate. Including GSC yield similar results, see Dreger et al. (1991). Generally we find that considerable adjustments in these models

are required to invert shorter period signals. Strategies for doing this are discussed in Dreger and Helmberger (1991b). It appears that the deeper the event the easier it is to obtain reasonable models. Conversely, shallow events are difficult, especially if they are in basins, see Ho and Helmberger (1989). The primary reason for this appears to be the scattering of energetic high frequency surface waves caused by the pinching out of basins and shallow geologic ridges, etc, see Helmberger et al. (199la). Introducing strong scatterers into the upper few kms of the crust, indeed, produces abundant coda. These features are particularly apparent in explosion data.

(b.) Broadband Explosion Data

A relatively large number of Streckeisen records of explosions are now available. Two examples are displayed in figure 7. The Kearsarge event, JVE, has a yield near 150 kt. The second example has a much smaller yield and was fired at Yucca Flats. This source region seems to produce the more complex records but all NTS events appear extremely complicated in the short period band (WASP) compared to earthquakes. The fundamental Rayleigh wave can be readily recognized and modeled at the longer periods, see Woods and Harkrider (1991) of this volume. Generally, the shape of the (3090) records appears constant at the various TERRAscope stations from the two subtest sites, Pahute and Yucca. It is important to note that the long period Rayleigh wave for small events, Shellbourne, can be easily identified on these high quality instruments whereas it would be very difficult to see a signal 3mm high on the older analog records. We are able to see the fundamental Rayleigh waves from some explosions as small as M_L=3(~1 kt) depending on the long period noise.

2) Discrimination

The most obvious differences between these explosion records and the earthquake records, see figure 6, is in frequency content. The amount of high frequency energy to low frequency is quite clear. Secondly, the relative strength of the short period P-wave energy to shear wave strength is much higher in these explosions than in the earthquake records, see figure 8a. Thus, it appears that these broadband records can be used to establish some meaningful criterion for discrimination.

Although there are many possible measures of their differences, two particular discriminants are presently being pursued. The easiest is simply computing the high frequency/low frequency ratio averaged over all three components. At this stage we assume the (WASP) and (3090) bands respectively. These ratios for explosions range from .58 (smallest) to .17 (largest) recorded to date. Applying this same ratio to earthquakes produces smaller values. For example, the Lee Vining event recorded at PAS (figure 4) yields (.03) while GSC produced (.01). this measure probably depends on distance since long periods (surface waves) decay more slowly than shorter periods (bodywaves). The above ratios are from about the same range so this is not an issue with these few measurements. Secondly, the paths from NTS to PAS are more likely to be higher attenuating than from Lee Vining; so that, this explanation can also be removed. Thus, it appears that this ratio differential reflects the differences in effective source excitation. The term "effective" is used to acknowledge the likelihood of additional amounts of short-period surface wave scattered energy in the source region. These issues can be easily addressed with future shots since the TERRAscope array is rapidly growing in size.

Another approach which is essentially an extension of the m_b:M_S discriminant to low yields is M_L vs. M_O. A plot of NTS explosions and Californian earthquakes is displayed in figure 8b. Again the two populations are quite distinct. This approach requires more effort in that the long period waveforms must be modeled to determine the event moment.

Recommendations and Conclusions

It appears that some useful discriminants can be constructed from regional phases. However, at this stage it is important to understand more about the various crustal waveguides that are controlling m_b (lower crust and upper mantle), M_L (crust) M_S (uppercrust) etc. While the inversion techniques discussed earlier prove effective in EUS, Helmberger et al. (1991b), considerably different crustal structure are encountered in southeast Asia, see figure 9. Many of

these earthquakes are apparently caused by the continental collision involving the India and Eurasia plates. Major strike-slip faults have allowed stable portions of Asia to move laterally to accommodate this changing stress field and have contributed to the broad zone of tectonic activity from the Pamirs to the Baikal rift. The 1500 km of crustal shortening across the convergence zone from the Russian Platform to the Indian Shield makes this zone interesting with a great deal of local crustal variation in thickness depending on the positions of the mini-plates and associated lithosphere. Epicentral depths of earthquakes are poorly determined because of this structural variation, see figure 10. However, many earthquakes are in the lower crust which produces relatively weak M_S. This is one of the reasons for the emphasize on the moment as opposed to surface waves. In short, a great deal more about broadband data from the IRIS network in the Soviet Union needs to be understood in terms of path vs. source before we can have confidence in the above discriminants. Nevertheless, it appears useful to apply the (hf/lf) and M_L vs. M_O) discriminants to a combination of PNE and earthquakes in the Soviet Union to test their validity.

References -

Dreger, D. and D. V. Helmberger, 1990. Broad-band modeling of local earthquakes, *Bull. Seism. Soc. Am.*, **80**, 1162-1179.

Dreger, D. and D. Helmberger, 1991. Complex faulting deduced from Broadband modeling of the February 28, 1990 Upland earthquake (M_L=5.5) *Bull. Seism. Soc. Am,* submitted.

Dreger, D. S., D. V. Helmberger, and L. Zhao , 1991. Three-component waveform Inversion of Regional Earthquakes, *Bull. Seism. Soc. Am.*, submitted

Helmberger, D. V., Engen, G. R., Grand, S.: Notes on wave propagation in laterally varying structure. *J. Geophys. Res.*, **58**, 82-91, 1985.

Helmberger, D., R. Stead, P. Ho-Liu, D. Dreger, 1991. Broadband modeling of regional seismograms; Imperial Valley to Pasadena, submitted to *Geophys. J. R. astr. Soc.*

Helmberger, D. V., L. S. Zhao, D. Dreger and V. LeFevre (1991). Exploration of the lower lithosphere; Northeastern United States, IASPEI, submitted

Ho-Liu, P. and D. Helmberger, 1989. Modeling regional love waves: Imperial Valley to Pasadena, *Bull. Seism. Soc. Am.*, **79**, 1194-1209.

Liu, H., and D. V. Helmberger. The 23:19 Aftershock of the 15 October 1979 Imperial Valley Earthquake: More Evidence for an Asperity, *Bull. Seism. Soc. Am.*, V. 75, 689-708, 1985.

Stead, R. J., Finite Differences and a Coupled Analytic Technique with Applications to Explosions and Earthquakes, *Ph.D. Thesis*, California Institute of Technology, Pasadena, California, 1989.

Wallace, T. C., Helmberger, d. V. and G. R. Mellman. A Technique for the Inversion of Regional Data in Source Parameter Studies, *J. Geophys. Res.*, 86, 1679-1685, 1981.

Zhao, L. S. and D. Helmberger, 1991a. A note on the Relocation of Tibetan Earthquakes, *Geophy. Res. Letters*, submitted

Zhao, L. S. and D. Helmberger, 1991b. Broadband modeling along a regional shield path, Harvard recording of the Saguenay Earthquake, *Geophy. J. Int.*, **105**, 301-312.

Zhao, L. S., D. V. Helmberger, and Harkrider, D. G., 1991. Shear-velocity structure of the crust and upper mantle beneath Tibetan and Southeastern China, *Geophys. J. Int.*, **105**, 713-730.

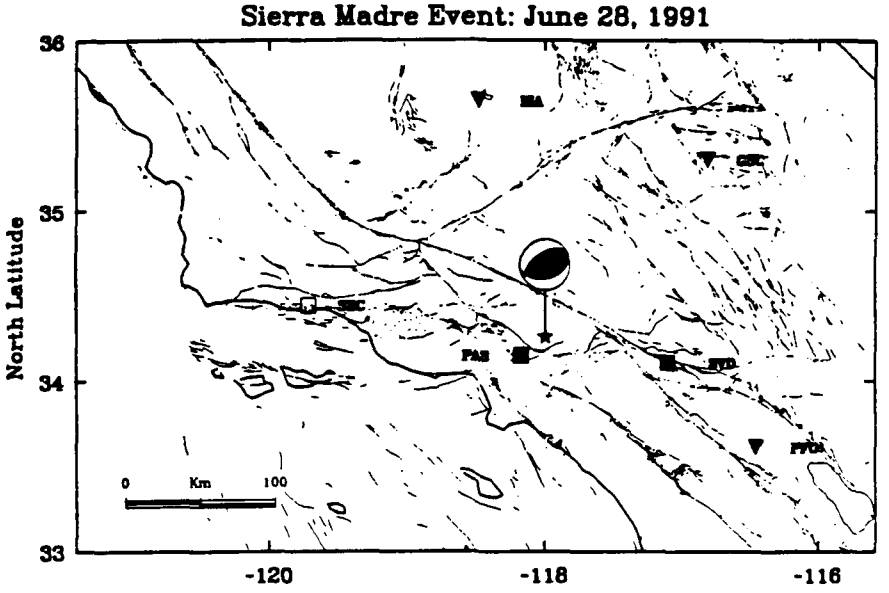


Figure 1. Location Map: The location of the Sierra Madre earthquake (star), and TERRAscope stations are plotted on the Fault Map of California (Jennings et al., 1975). Stations represented by solid inverted triangles were used in all of the inversions. Stations represented by solid squares were included in an additional inversion. Station SBC (open square) was not used in the inversion. A focal mechanism showing the results of the inversion is also plotted.

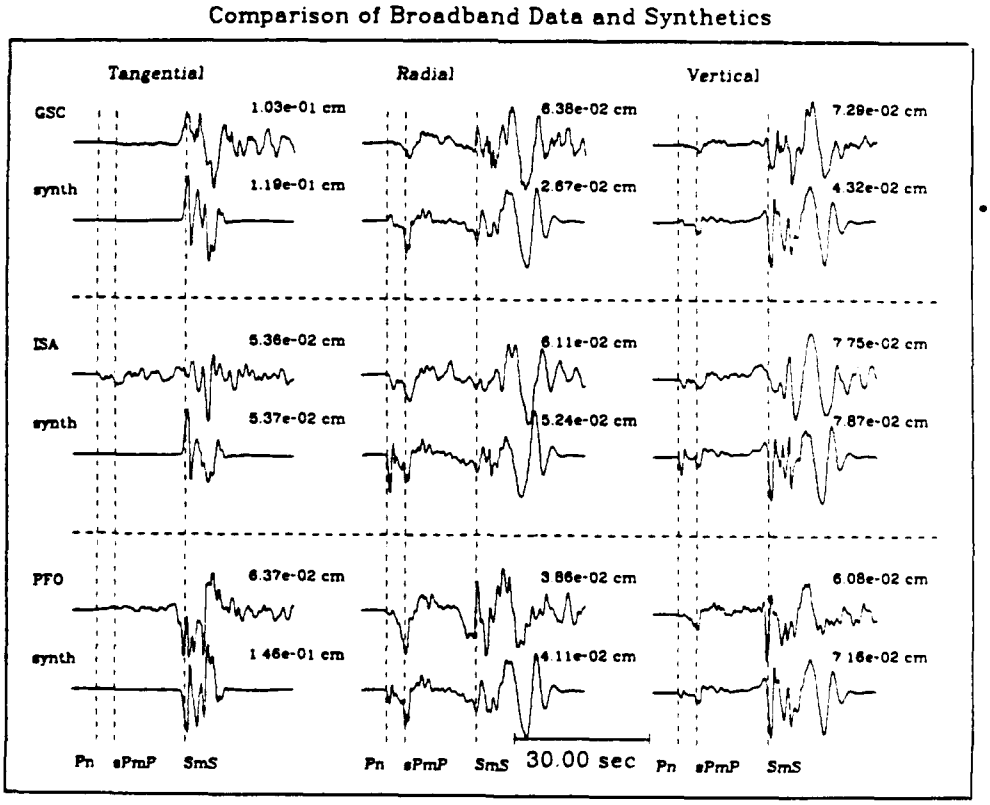
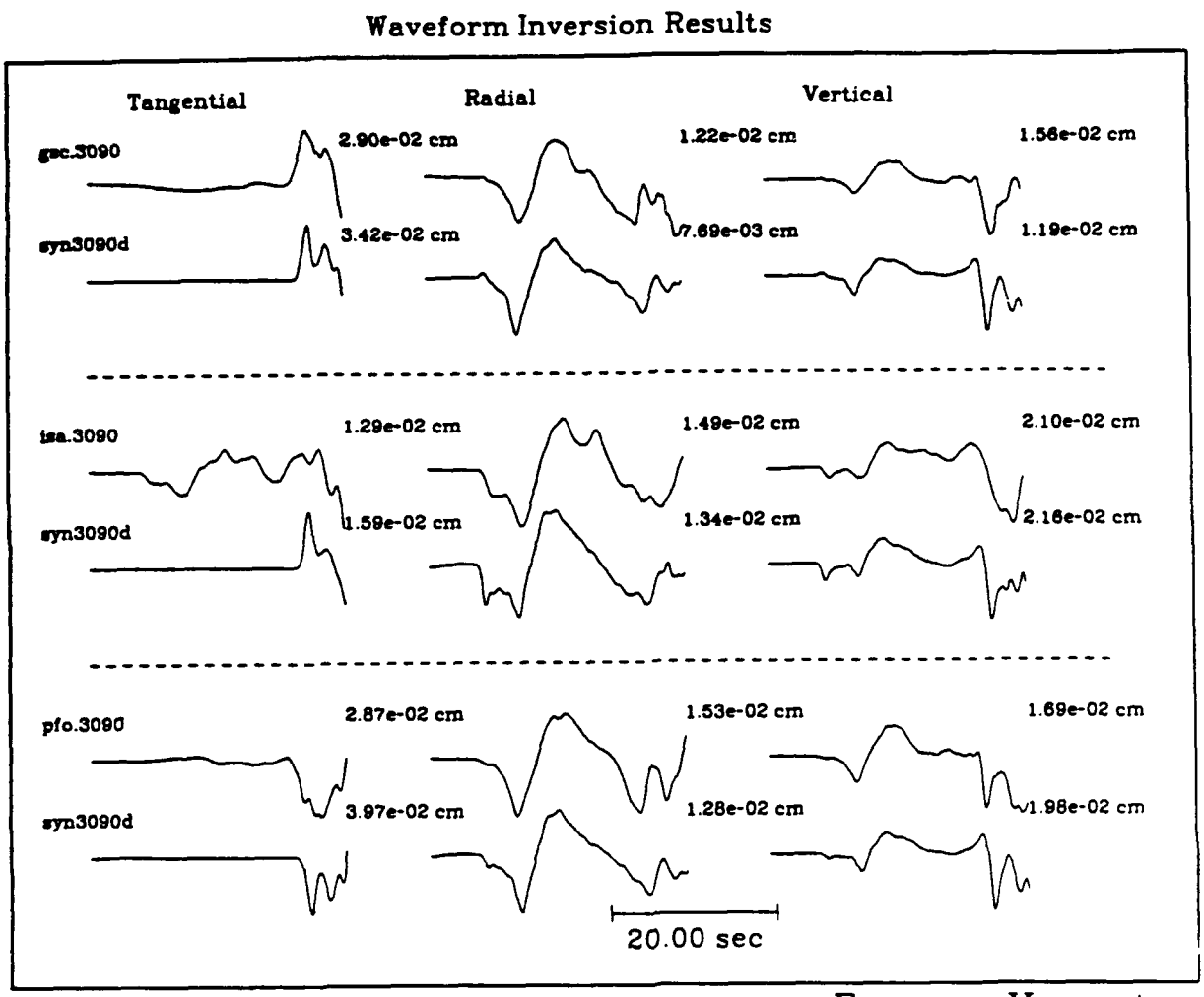


Figure 2. Comparison of broadband displacement seismograms to broadband displacement synthetic seismograms computed with the fault plane solution obtained by inverting the long-period body waves. Arrival times of key phases in the synthetics are marked by vertical lines. Amplitudes are ground displacement in centimeters.



$SoCal_R$			
V_p	V_s	ρ	Z
5.5	3.18	2.4	0.0
6.3	3.64	2.67	5.5
6.7	3.87	2.8	16.0
7.8	4.5	3.0	35.0

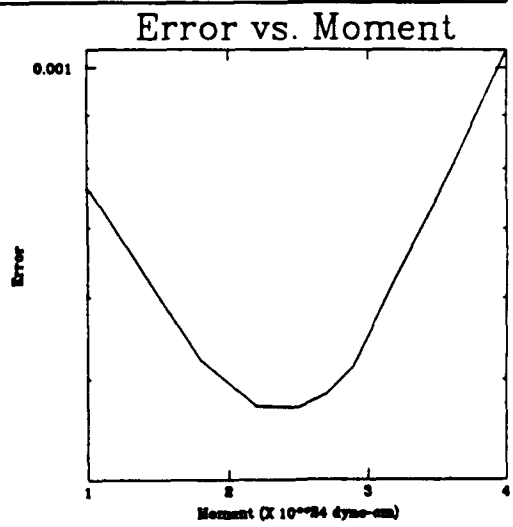


Figure 3. Results of three-component P_n-SmS waveform inversion using stations GSC, ISA and PFO. The data and synthetics have been filtered with the response of a Press-Ewing instrument with unit gain. Amplitudes are instrument amplitudes (unit gain) in centimeters. The velocity model used in the synthetics and moment estimation plot are included at the bottom.

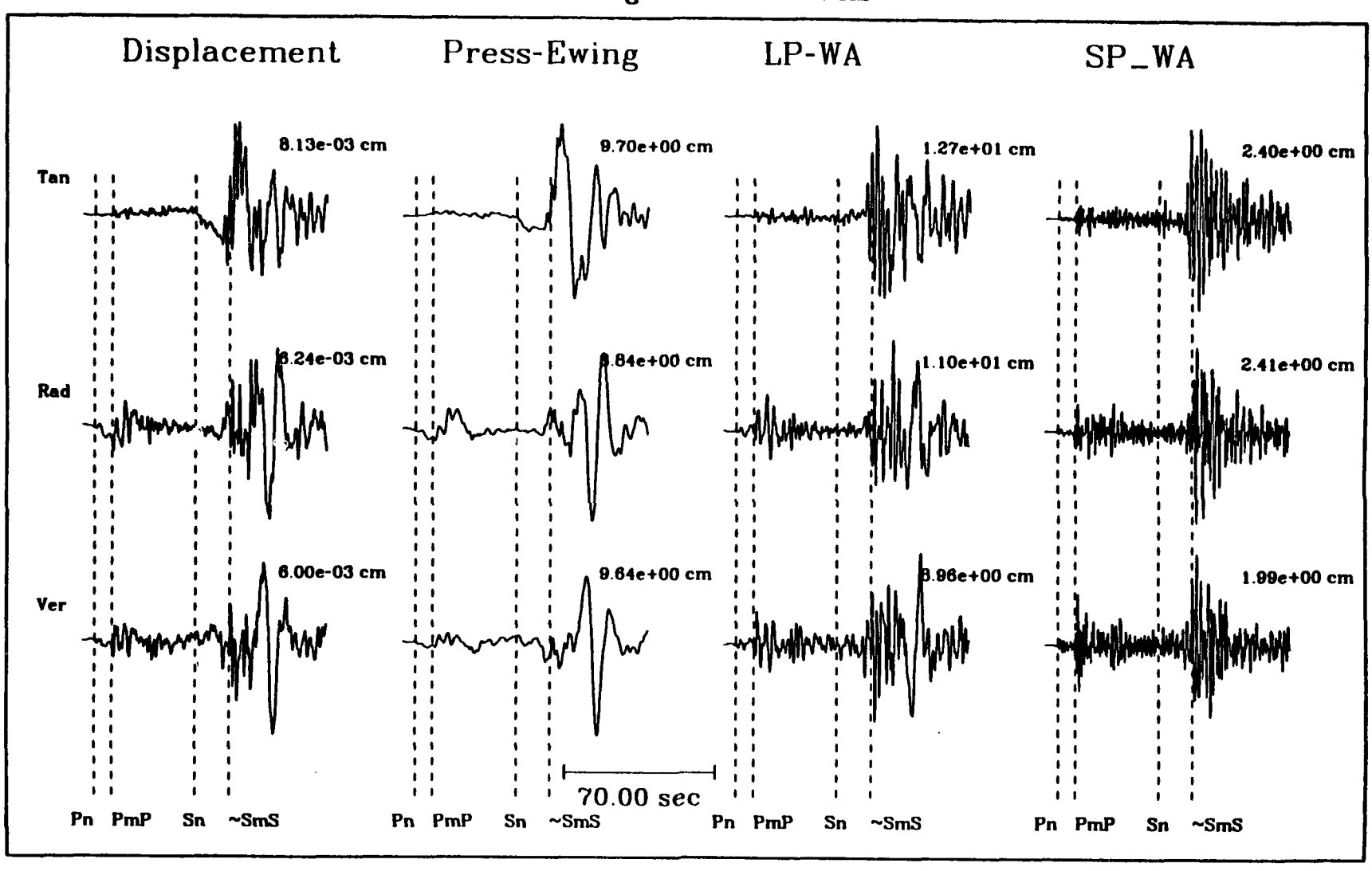


Figure 4. Three component displacement seismograms recorded at PAS. Simulated Press-Ewing, long-period Wood-Anderson (LP-WA), and short-period Wood-Anderson (SP-WA) instruments are also shown. Dashed lines mark the arrivals of the P_n, P_mP, S_n and S_mS phases. The long-period arrival following the phase marked P_mP on the displacement and Press-Ewing records is the P_L wave group. Displacement amplitudes and instrumental amplitudes are in centimeters.

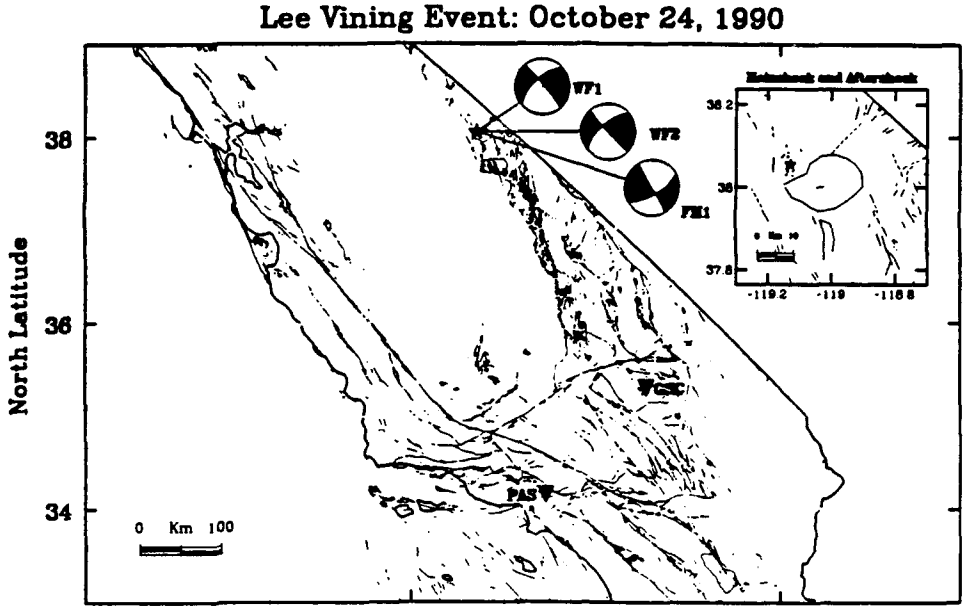


Figure 5. Location Map: The location of the Lee Vining earthquake (star), and the locations of the Pasadena (PAS) and Goldstone (GSC) stations (shown by inverted triangles) are plotted on the Fault Map of California (Jennings et al., 1975). The insert shows the location of the first 24 hours of aftershock activity. Focal mechanisms WF1 and WF2 were obtained by inverting with Green's functions computed with the JD and LHS models, respectively. Focal mechanism FM1 was obtained from first motion polarities (Horton, 1991).

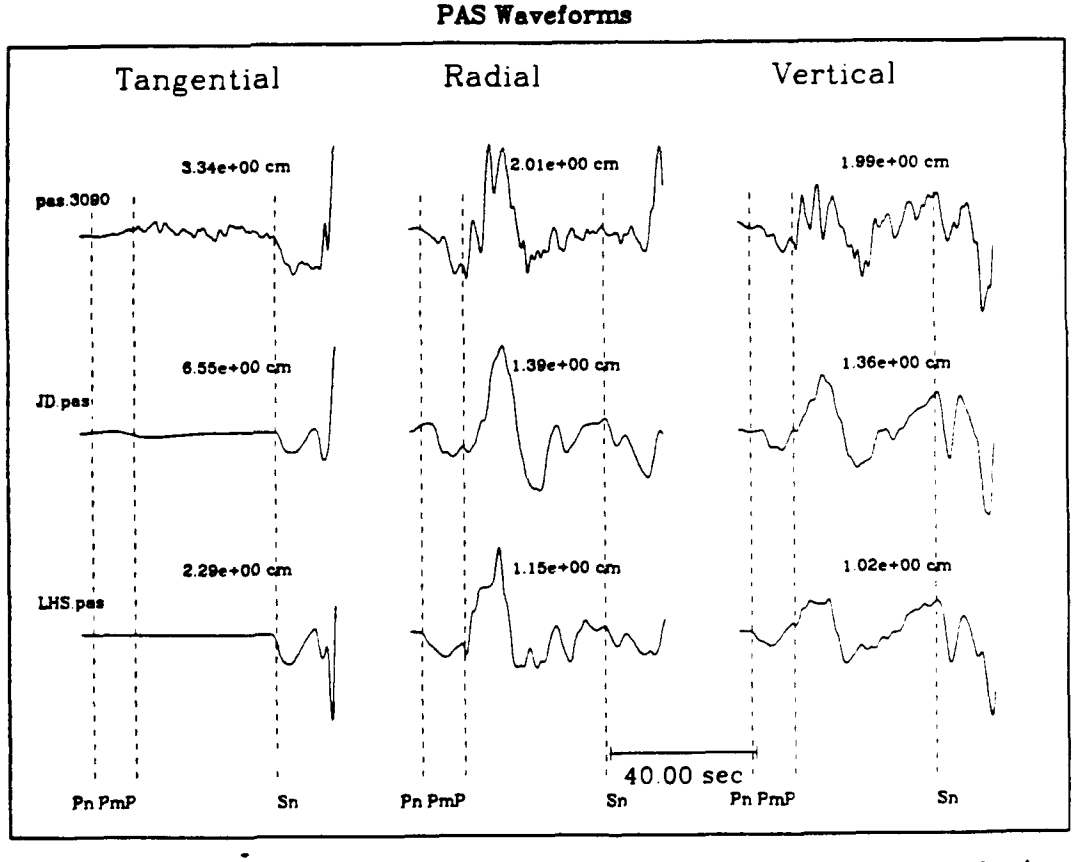


Figure 6. Comparison of the simulated Press-Ewing data and synthetics computed using the focal mechanisms determined from the inversion for station PAS.JD.pas are the synthetics computed using the JD velocity model and LHS.pas are the synthetics computed using the LHS velocity model. The phases P_n, P_mP and S_n are marked by the dashed lines. Amplitudes are instrumental amplitudes in centimeters.

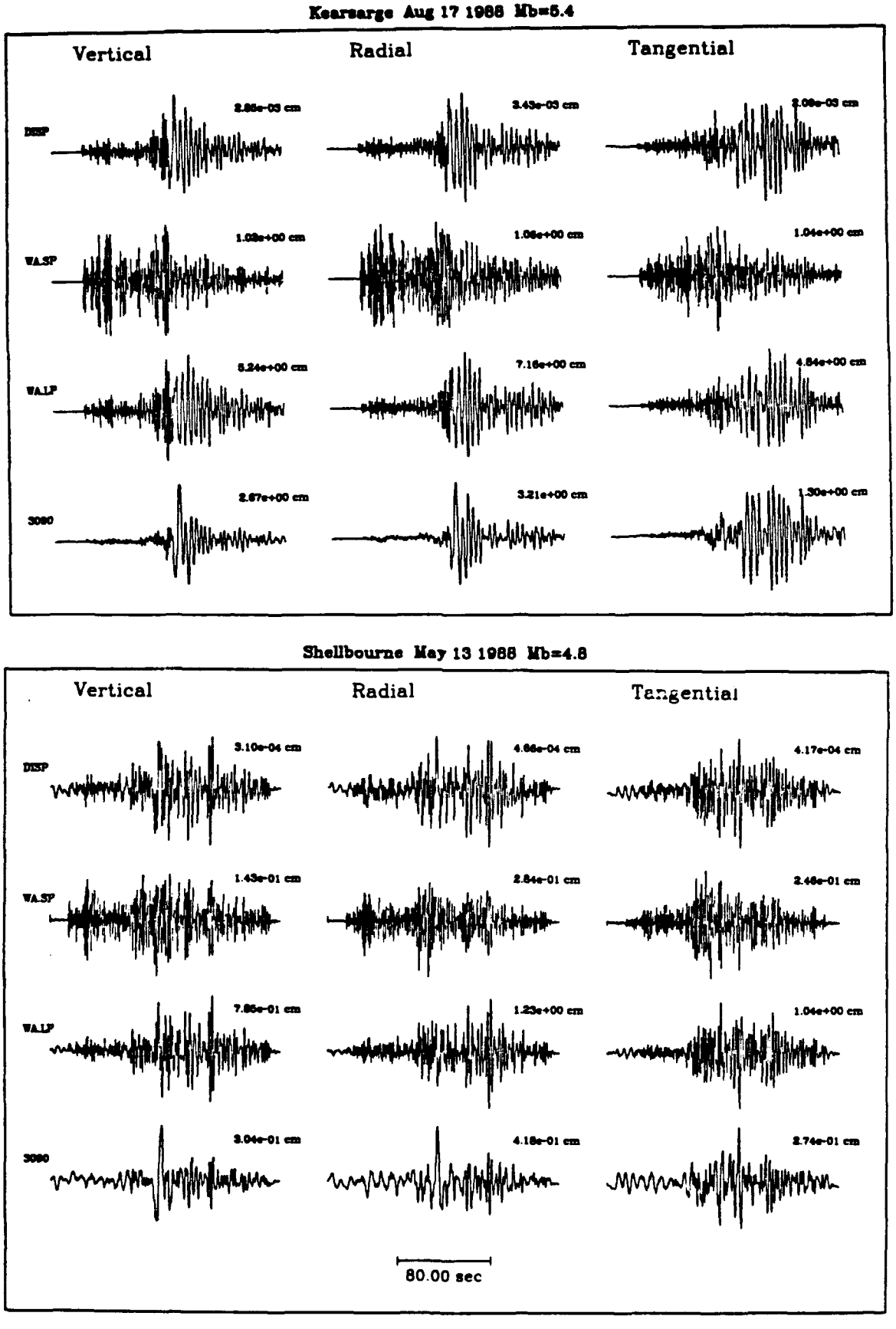


Figure 7. Comparison of broadband observations and various conventional responses for the JVE (Kearsarge, Pahute Mesa) with a smaller event Shellbourne (Yucca).

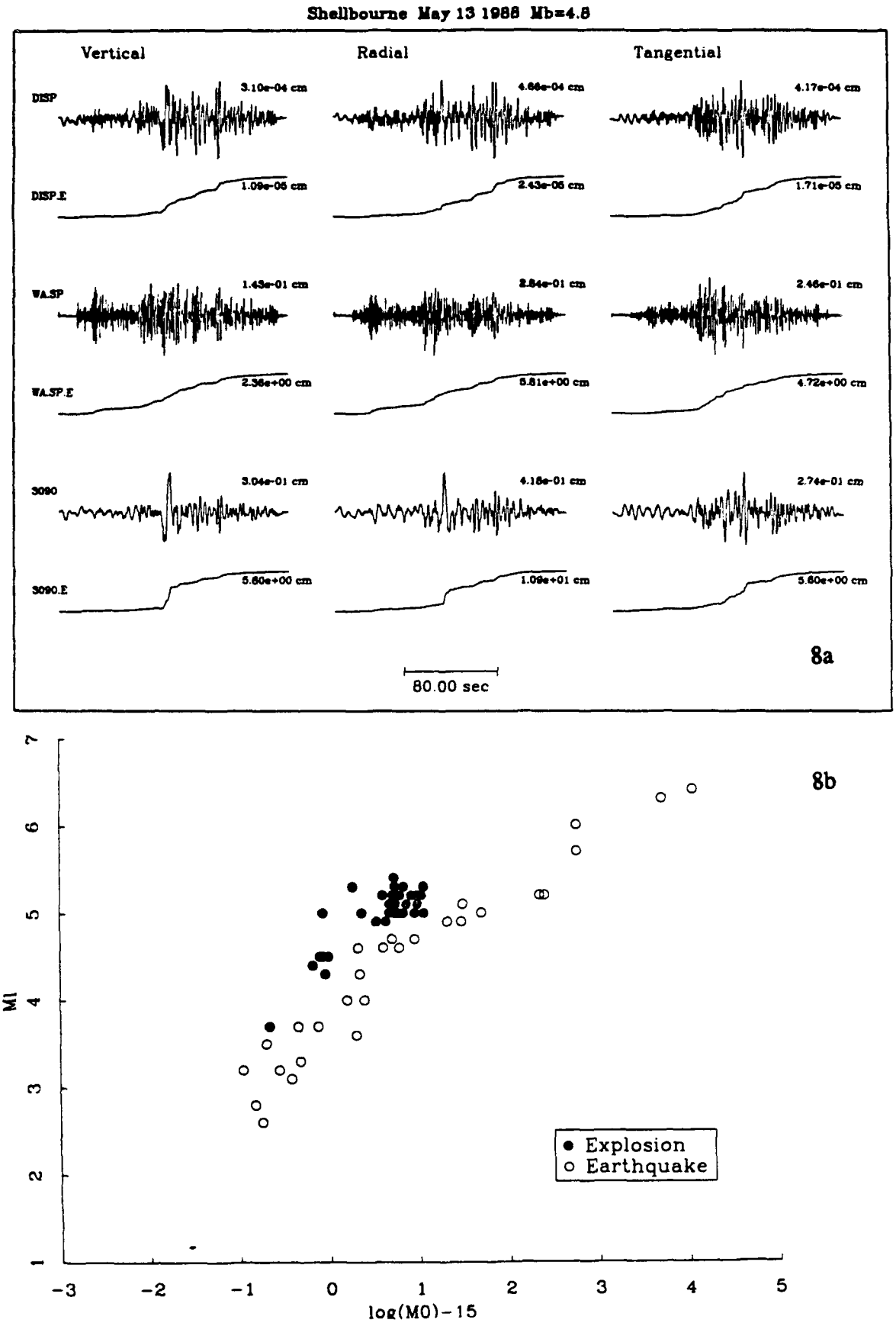
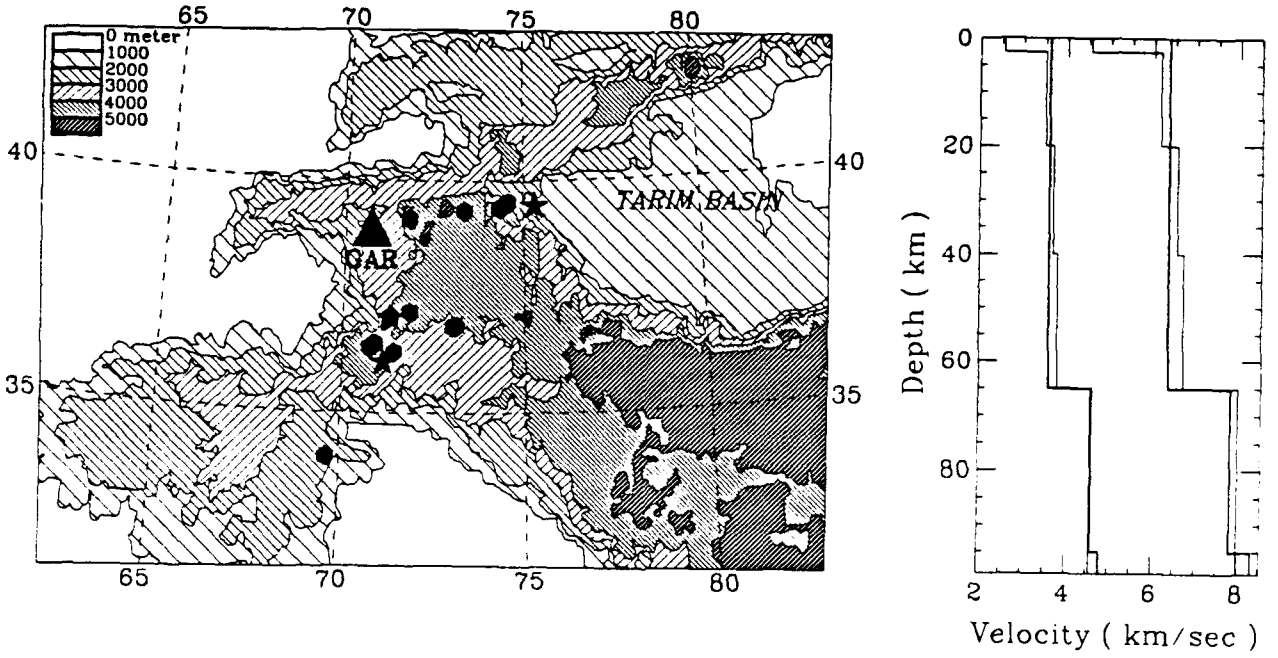


Figure 8. Figure 8a displays the accumulated energy plots for the various traces. The lower plot, 8b, displays the separation of the explosion and earthquake populations.



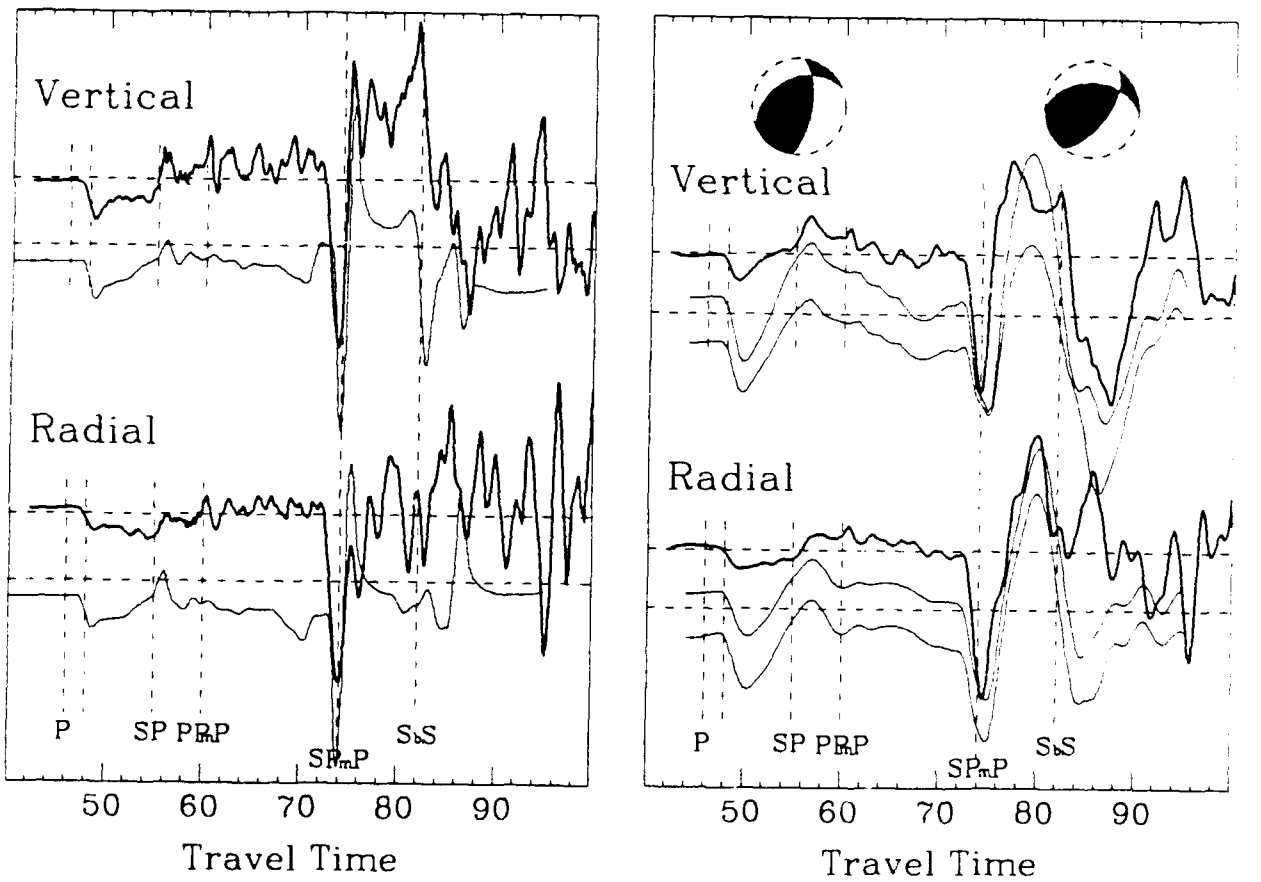
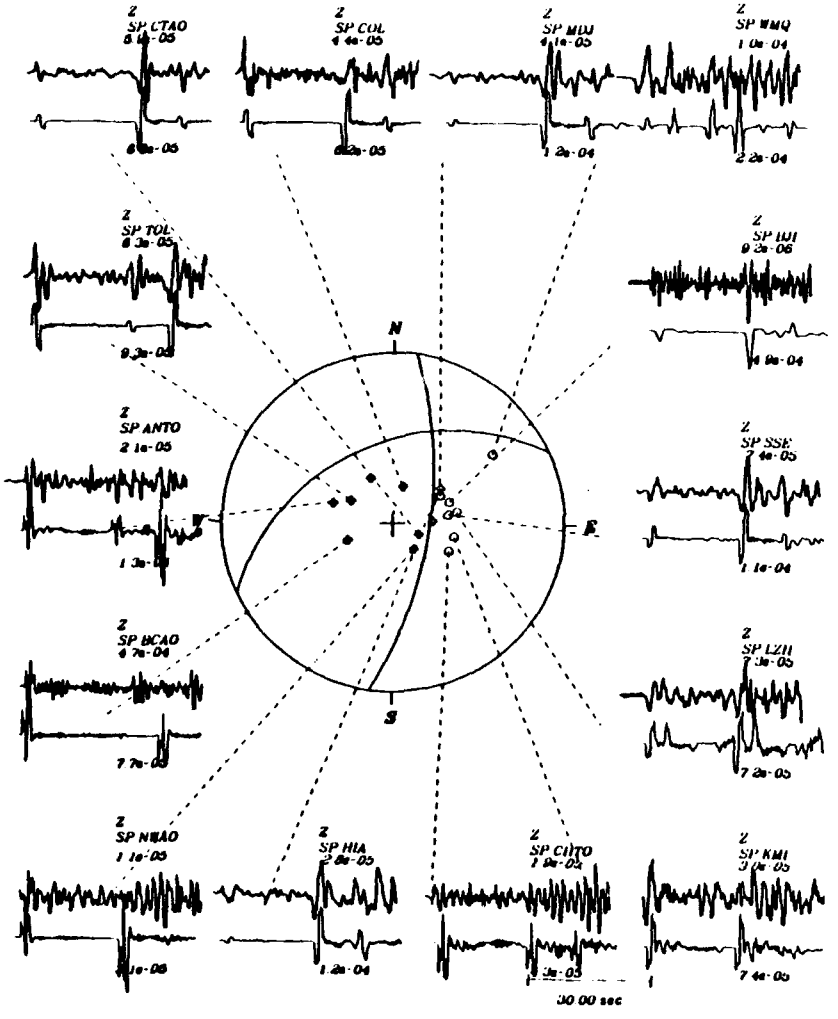
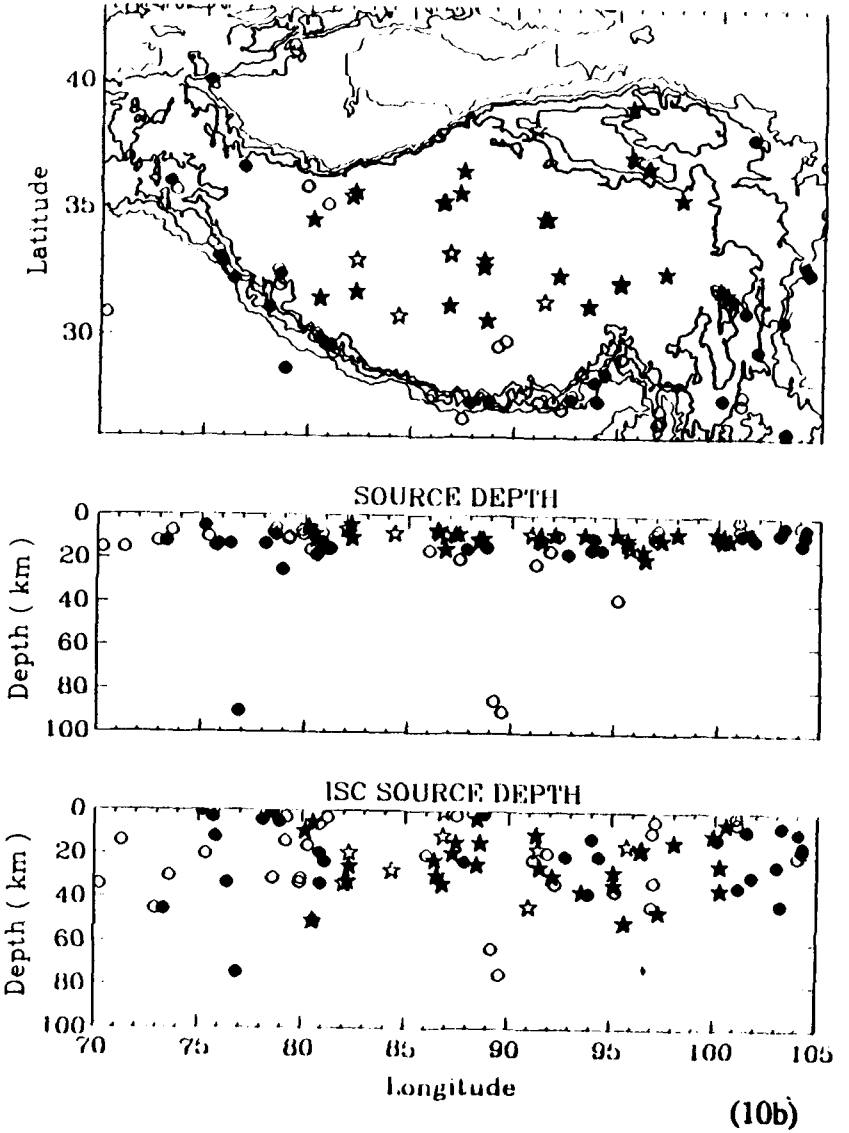


Figure 9. Top panel displays a map of the GARM region along with a proposed layered structure. Two sets of comparisons of observations and synthetics are given on the bottom. Synthetics on the left are for a layer over-a-half space where the layer is 65 kms thick. The comparisons on the right are appropriate for the upper layered structure. The top traces on the right are data, vertical and radial. The middle traces are assuming the teleseismic orientation, see figure 10. The bottom set of traces are the results after inversion with similar orientations.



(10a)



(10b)

Figure (10a) displays observed and synthetic short-period depth phases for an event beneath the Hindu-Kush region. The three panels in figure (10b) display the earthquake locations beneath Tibet before and after relocation.

TITLE: Quantification of small explosions

AUTHOR: R. B. Herrmann, G. I. Al-Eqabi and K. Hutchenson

Department of Earth and Atmospheric Sciences
Saint Louis University
3507 Laclede Avenue
St. Louis, MO 63103

CONTRACT: F19628-90-K-0040

OBJECTIVE: Investigation of yield estimators for small explosions

RESEARCH ACCOMPLISHED:

The primary focus has been on developing techniques for the estimation of isotropic moment, M_I, from fundamental mode surface-wave data with application to small explosions. Since the frequencies of interest are in the 0.5 - 5.0 Hz, range, path specific structure and anelastic attenuation must be defined before M_I can be estimated. To do this a robust technique for inferring the path effects from a single station recording of an explosion must be developed and then the methodology must be carefully tested before being routinely applied.

We have made extensive use of a USGS-GSC refraction survey in the state of Maine (Murphy and Luetgert, 1986; Murphy and Luetgert, 1987). Figure 1 presents the profiles analyzed. The profiles are interesting since they are either parallel or perpendicular to the structural trend of the Appalachian Mountains in the state.

We noted significant lateral changes in the moveout of the surface-wave train. Figure 2 shows some data acquired from Shot Point 6, in a direction toward Shot Point 7. The observed data have been bandpass filtered between 0.5 and 5.0 Hz. Lateral variation is seen in the observed surface-wave train, center, and also in the S-arrivals, bottom. While some of the S-wave arrival lateral variation could be attributed to an increase of velocity with depth, it occurs at the same places where the surface-wave moveout changes. The arrivals beyond 30 km are delayed, and cannot be explained by refracted arrivals. Other shot also show a strong correlation between the lateral variation in the surface-wave and S-wave arrivals.

By using a sequence of stacking techniques, visual examination, waveform modeling and cross-correlation techniques, a blocklike velocity model was derived (Keilis-Borok *et al*, 1989;a BNolet, 1990). Table 1 shows the model developed for this profile. This table shows the width of each block, and the shear-wave velocity values within each block. The same Q model is assumed for each separate velocity block.

One test of the model is to compare both the shape and amplitudes of synthetic time histories. The synthetic time histories are show at the top of Figure 2. The arrival times and waveform shapes are well modeled. Another test is to compare peak amplitudes of the synthetics and observed data in the time domain. This is shown in Figure 3, where the peak amplitudes resulting from different choices of bandpass filters are plotted. In this figure, the individual filter responses are shifted vertically for clarity. The synthetic data are given by solid curves and the observed data are given by the different symbols. This figure shows that the Q model of Table 1 can explain the spatial decay of amplitudes. One final check is the test of the assumption of a step source time function used in the synthetics, by computing M_I for each bandpass filter. If the assumption of the source time function shape is correct, then the isotropic moment estimates from the different bandpass filtered data sets should agree. Table 2 shows this comparison. The assumption of a step source time function is valid in the frequency range of 0.5-5.0 Hz for this data set. Higher or lower frequency information was not resolved in the data.

Table 1.
Four Velocity Models and Q_β Structure for
Region A, SP6 Positive Side (SE) Obtained from Waveform
Inversion, Two Station Phase Adjustment Followed by Dispersion Inversion.

Position(km)	Model-1 517 0.0-10.0	Model-2 517-519 10.0-12.0	Model-3 520-526 12.0-19.5	Model-4 526-533 19.5-29.0	Average model	Standard deviation	Q_α	Q_β
H km	β km/sec	β km/sec	β km/sec	β km/sec	β km/sec	σ_β km/sec		
0.250	2.4939	2.3808	2.6091	2.7411	2.5562	0.133810	84.0	42.0
0.250	3.0149	2.8335	3.0871	3.3590	3.0736	0.188894	163.0	81.0
0.250	3.1111	2.9546	3.2003	3.4813	3.1868	0.191414	320.0	160.0
0.250	3.1281	2.9881	3.1980	3.5310	3.2113	0.199446	378.0	189.0
0.250	3.1486	3.0154	3.2264	3.5772	3.2419	0.207765	381.0	190.5
0.250	3.1864	3.0387	3.2655	3.6006	3.2728	0.206011	394.0	197.0
0.250	3.2274	3.0533	3.3012	3.6006	3.2956	0.197741	426.0	213.0
0.250	3.2782	3.0587	3.3242	3.6006	3.3154	0.192804	485.0	242.5
0.500	3.3148	3.0566	3.3336	3.6006	3.3264	0.192460	582.0	291.0
0.500	3.3225	3.0458	3.3336	3.6006	3.3256	0.196202	762.0	381.0
0.500	3.3224	3.0315	3.3336	3.6006	3.3220	0.201333	1134.0	567.0
	3.4699	3.0161	3.3336	3.6006	3.3550	0.217274	2255.0	1127.0

Table 2. Estimation of M_I from filtered seismograms

Frequency band (Hz)	Isotropic Moment (dyne-cm)	Confidence Factor 1 σ
0.5-1.5	1.99E+18	1.06
1.5-2.5	2.11E+18	1.07
2.5-3.5	2.14E+18	1.06
3.5-4.5	1.77E+18	1.07
0.5-5.0	1.97E+18	1.09

We were able to perform this analysis on the data from eight shot points, estimating M_I and also Ψ_∞ for each shot. The Ψ_∞ was estimated using the density and compressional wave velocity at the source depth inferred from the surface-wave inversion. The results of this analysis are compared to other in published literature in Table 3. The comparison is also shown in Figures 4 and 5. Several features stand out. First, the present data set of chemical explosions includes only small yield events. Second, a trend for chemical explosions is not obvious due to the differences in the experiments, e.g., spall, whether shot point physical parameters were known, etc. The possible relationship between the chemical and nuclear explosion populations is not apparent given the lack of overlap.

CONCLUSIONS AND RECOMMENDATIONS:

1. From the standpoint of wave propagation, the lateral variations observed are large, some as large as 10%. Analysis and modeling of these data require new techniques.

2. Isotropic moment estimates show variability for nominally the same shot size. Further refinement is not possible since detailed information on shot emplacement and shot medium properties are not available to us. On the other hand these results good since the multichannel processing gave reliable estimates of dispersion and anelastic attenuation.

3. To further understand the relation between chemical and nuclear explosion yield estimates, it is necessary to obtain data in the 10 - 100 ton range. A coordinated field experiment to acquire such data from the shot point out to 300 km should be sponsored.

Table 3
Source Parameters of Nuclear (N) and Chemical (C) explosions

Type	ID	Y (*ton*)	M_l (*dyne–cm*)	Ψ_∞ (m^3)	Ref
C	KQ01	0.5	2.37e+18	0.46	(Johnson, 1989)
C	KQ03	0.45	1.78e+18	0.53	(Johnson, 1989)
C	KQ05	0.45	1.99e+18	0.87	(Johnson, 1989)
C	KQ08	0.17	0.79e+18	0.42	(Johnson, 1989)
C	KQ09	0.15	0.75e+18	0.27	(Johnson, 1989)
C	ST87	0.125	2.87e+16	0.28	(Stump, 1987)
C	ST87	0.125	1.35e+16	0.11	(Stump, 1987)
C	ST87	0.125	0.94e+16	0.07	(Stump, 1987)
N	GASBUGGY	29000	2.57e+22	6371	(Perret, 1972)
N	HARZER	107000	7.40e+22	27000	(Johnson, 1988)
N	CHANCELLOR	78000	5.70e+22	21000	(Johnson, 1988)
C	NRDC3	10.0	4.00e+19	3.27	(Given *et al*, 1990)
C	SP1+	1.0	1.85e+18	0.29	(Ghassan, 1991)
C	SP4+	1.0	1.42e+18	0.20	(Ghassan, 1991)
C	SP6-	1.0	2.87e+18	0.47	(Ghassan, 1991)
C	SP6+	1.0	1.99e+18	0.36	(Ghassan, 1991)
C	SP13-	1.0	1.49e+18	0.28	(Ghassan, 1991)
C	SP20+	1.0	2.27e+18	0.30	(Ghassan, 1991)
C	SP19-	1.0	2.39e+18	0.46	(Ghassan 1991)
C	SP19+	1.0	2.11e+18	0.35	(Ghassan, 1991)
N	NTSY-0.02	20	1.43e+19	11.0	(Bache, 1982)
N	NTSP-0.02	20	2.45e+19	9.6	(Bache, 1982)
N	NTSMM-60	60000	3.26e+22	25000	(Bache, 1982)

Data Source

KQ01, KQ03, KQ05, KQ08, KQ09. Inversion Kaiser quarry data with distance ranges of 70-600m by inversion of entire waveform for moment tensor elements. Low frequency level isotropic moment rates are used. Ψ_∞ taken from their Figure 40 moment tensor results.

SP1+, SP4+, SP6-, SP6+, SP13-, SP20+, SP19-, SP19+. Inversion of surface wave data from USGS refraction lines in Maine. The number indicates the shot point, and the plus (+) or minus (-) indicate whether the line went from the shot point to the next larger shot point (+), or to the next lower shot point number (-). A split recording spread was used. Q_β and shear-wave velocity profiles are determined. M_l is estimated by a regression of filtered synthetic and observed seismic traces over the entire data range. Filter bands of 0.5-1.5 Hz, 1.5-2.5 Hz, 2.5-3.5 Hz, 3.4-4.5 Hz, and 0.5-4.5 Hz were used to test the correctness of the assumption of a step source time function for the isotropic source. Ψ_∞ derived using the earth model derived, using $M_l = 4\pi\rho\alpha^2\Psi_\infty$.

STUMP. Ψ_∞ and M_l from 50-150m varying half-space, 50-75 m layered and 50-100 m layered models in his Table 3.

GASBUGGY. Ψ_∞ estimated from four RDP's in his Figure 7. M_l derived from each Ψ_∞ using $M_l = 4\pi\rho\alpha^2\Psi_\infty$ with ρ and α given in his Table 1. The yield is given at 29 kT in the paper.

HARZER and CHANCELLOR. Yield estimated from body wave, Ψ_∞ and M_l are an average of using four source models (Mueller-Murphy, von Seggern-Blandford, Helmberger-Hadley, and Haskell) (Johnson, 1988). Johnson (1988) notes the presence of spall.

NRDC3. M_0 estimated from vertical component Lg spectra published in Given *et al* (1990). Ψ_∞ derived using the earth model provided. Soreno (1990) estimated an explosion moment of 5.0E+20 dyne-cm for the calibration shot, no correction is made for free surface effects. This observation is not plotted, but would be a major outlier!

NTSY-0.02, NTSP-0.02, NTSMM-60. From Bache (1982) Ψ_∞ values for scaled 0.02 kT nuclear shots at Yucca (NTSY-0.02) and Pahute (NTSP-0.02) and for Mueller/Murphy wet tuff/rhyolite 60 kT (NTSMM-60). To obtain isotropic moment, ρ = 1.8 and 2.0 gm/cc and α = 2.4 and 3.5 km/sec for Yucca and Pahute, respectively (Bache *et al.*, 1978).

References

Bache, T. C. (1982). Estimating the yield of underground nuclear explosions, *Bull. Seism. Soc. Am.* 72 S131-S168.

Bache, T. C., W. L. Rodi, and D. G. Harkrider (1978). Crustal structures inferred from Rayleigh wave signatures of NTS explosions, *Bull. Seism. Soc. Am.* **68** 1399-1413.

Given, H. K., N. T. Tarasov, V. Zhuravlev, F. L. Vernon, J. Berger and I. L. Nersesov (1990). High-frequency seismic observations in Eastern Kazakhstan, USSR, with emphasis on chemical explosion experiments, *J. Geophys. Res.* **95**, 295-307.

Johnson, L. R. and M. A. Leonard (1989). Near-source observations of quarry explosions, in McEvilly, T. V., and L. R. Johnson (1989), *Regional studies with broadband data*, Geophysics Laboratory GL-TR-89-0224, pp 1-57.

Johnson, L. R. (1988). Source characteristics of two underground nuclear explosions, *Geophys J.* **95**, 15-30.

Keilis-Borok, V. I., A. L. Levshin, T. B. Yanovskaya, A. V. Lander, B. G. Bukchin, M. P. Barmin, L. I. Ratnikova, and E. N. Its (1989). *Seismic surface waves in a laterally inhomogeneous earth*, Kluwer Academic Publishers, Dordrecht.

Murphy, J. M. and J. H. Luetgert (1986). Data report for the Maine-Quebec cross-strike seismic-refraction profile, *U. S. Geological Survey Open-File Report 86-47*, Menlo Park, CA.

Murphy, J. M. and J. H. Luetgert (1987). Data report for the Maine along-strike seismic-refraction profiles, *U. S. Geological Survey Open-File Report 87-133*, Menlo Park, CA.

Nolet, G. (1990). Partitioned waveform inversion and two-dimensional structure under the network of autonomously recording seismographs, *J. Geophys. Res.* **95**, 8499-8512.

Perret, W. R. (1972). Gasbuggy seismic source experiments, *Geophysics* **37**, 301-312.

Soreno, T. J. (1990). Frequency-dependent attenuation in Eastern Kazakhstan and implications for seismic detection thresholds in the Soviet Union, *Bull. Seism. Soc. Am.* **80**, 2089-2105.

Stump, B. W. (1987). Mathematical representation and physical interpretation of a contained chemical explosion in alluvium, *Bull. Seism. Soc. Am.* **77**, 1312-1325.

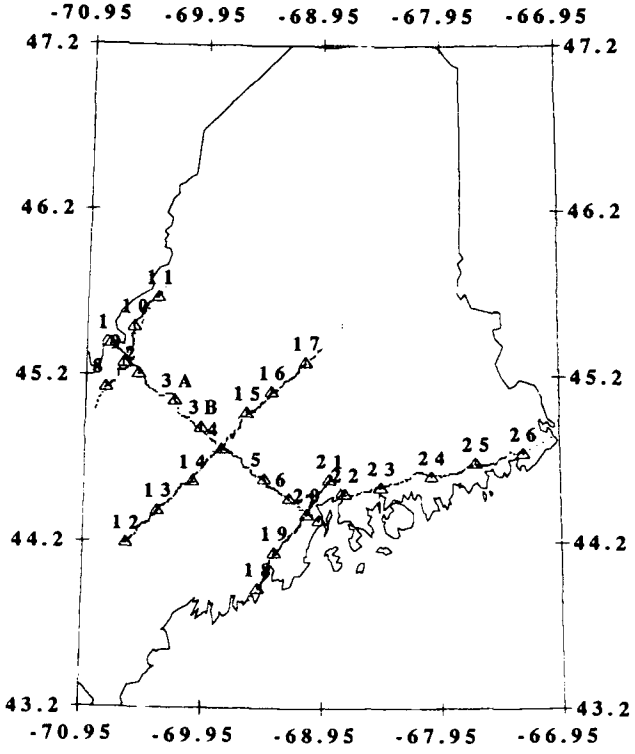


Figure 1. Location of shotpoints and observation points for the Maine refraction profiles.

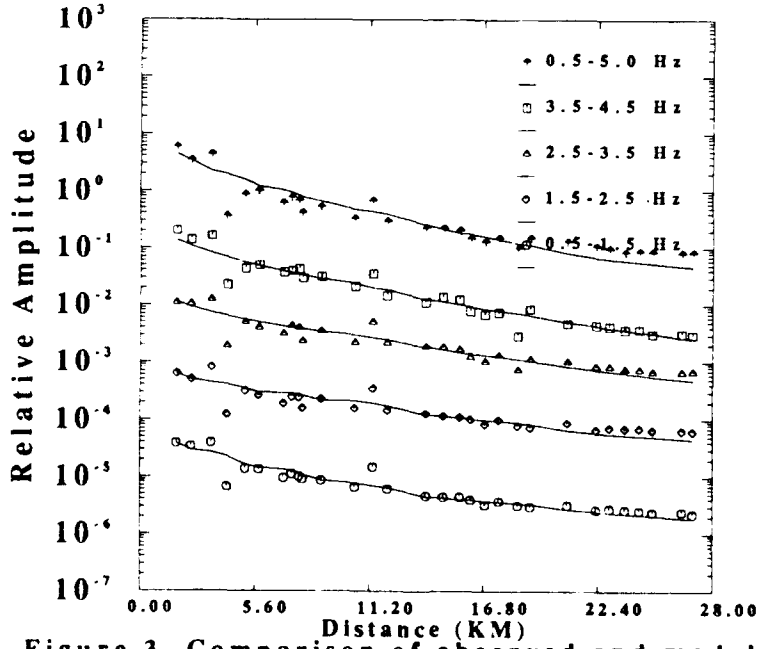


Figure 3. Comparison of observed and modeled filtered peak amplitudes in different frequency bands. (SP6+)

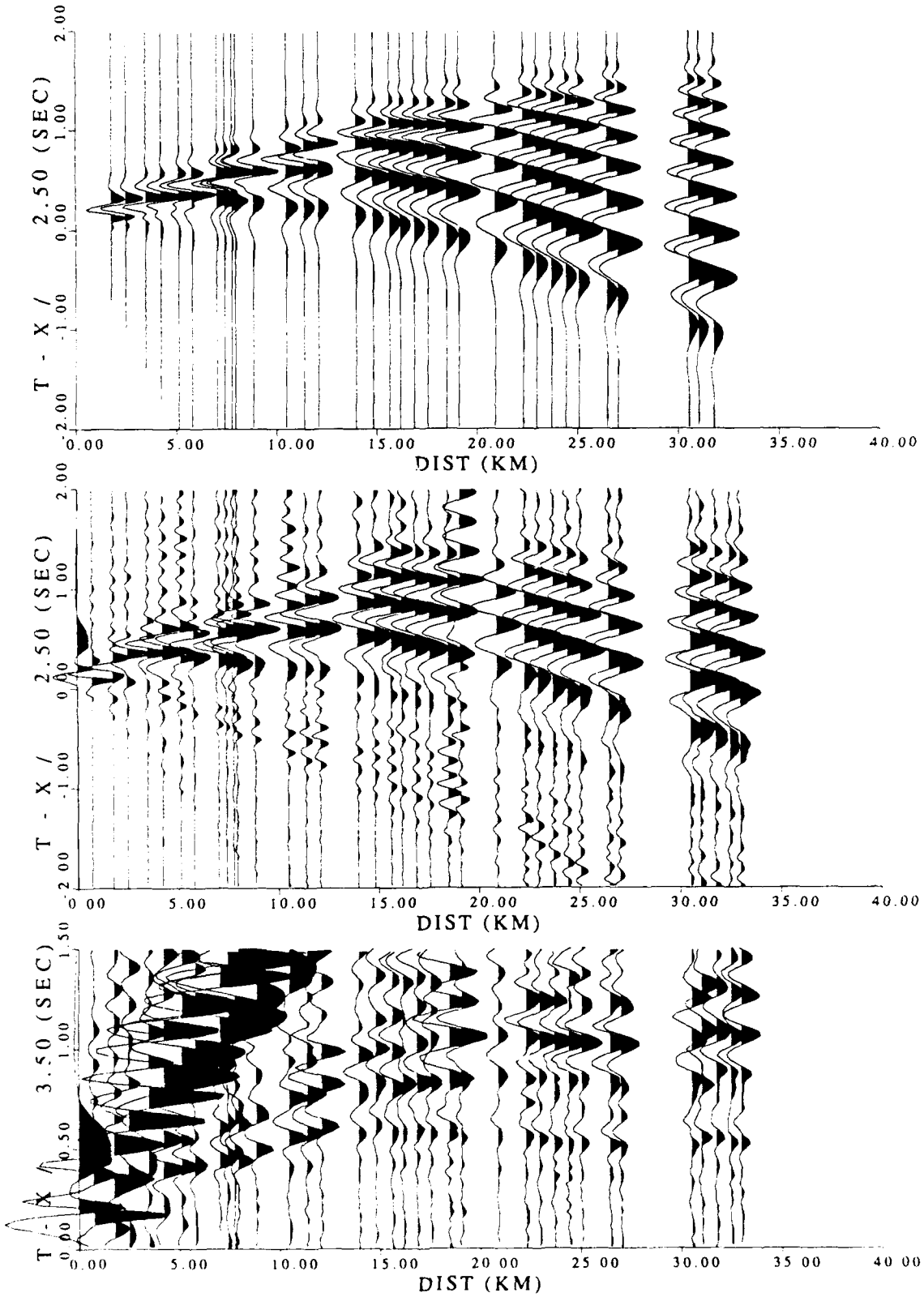


Figure 2. Seismograms from shot point 6. top) synthetic surface wave; center) observed surface wave; bottom) observed shear-wave arrivals

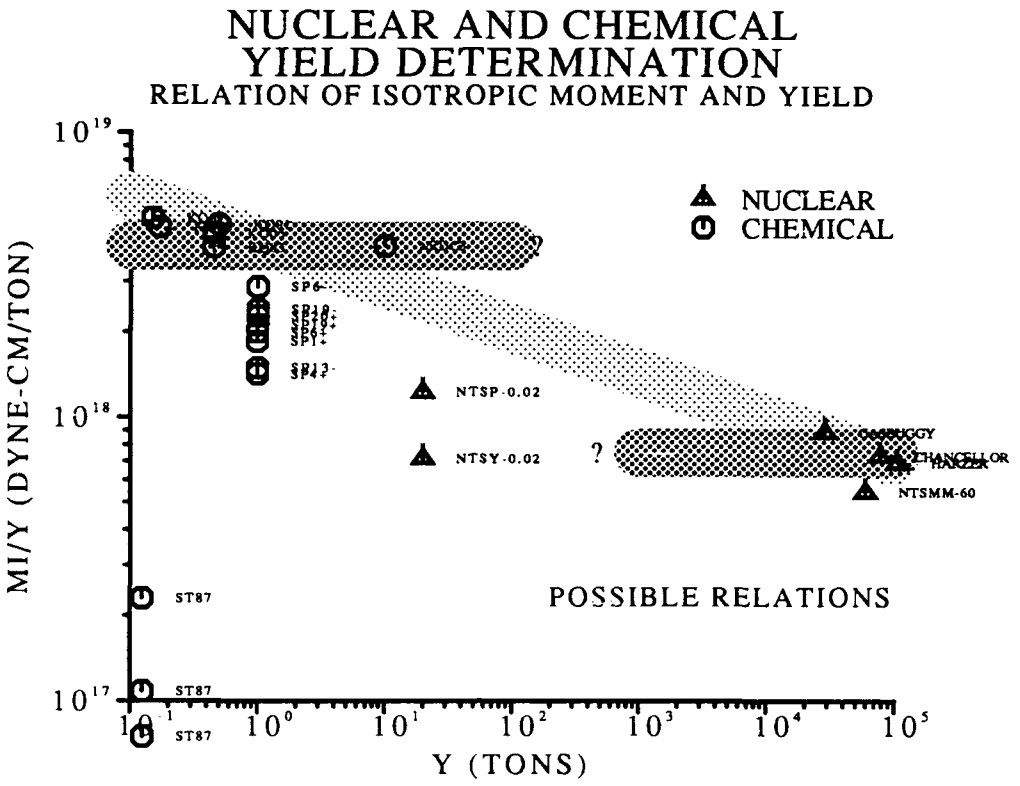


Figure 4. Data sets and possible chemical-nuclear relations

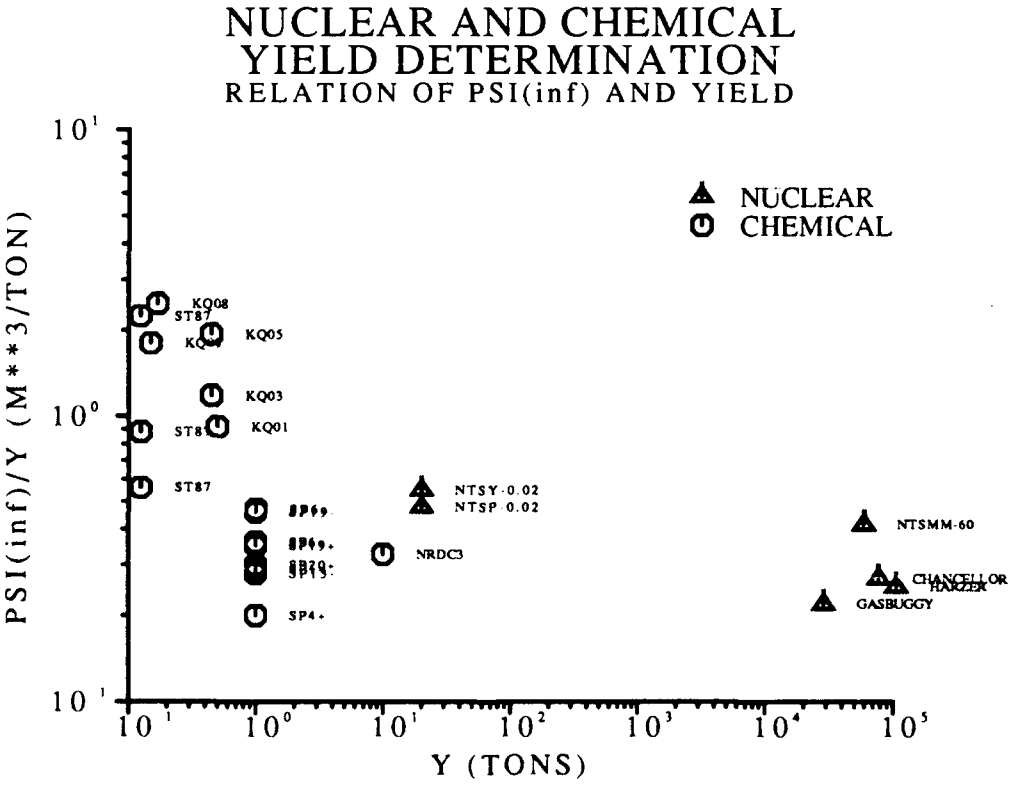


Figure 5.

Finite Difference Wavefield Synthetics –
Understanding Seismic Source Discriminant Features

E.S. Husebye[1] and B.O. Ruud[2]
[1] NTNF/NORSAR, Kjeller, Norway
[2] Dept. of Geology, Oslo University, Oslo, Norway

Grant AFOSR-89-0259

Objectives

Synthetic seismograms which are computed for models derived by structural geophysical mapping of the earth's crust and upper mantle usually lack the complexity seen in real short period records. There are several reasons for this; one is the simplification of the model which is made when interpreting regional reflection and refraction profiles - leaving out all fine scale structures. Another reason for the discrepancy may be due to the methods used to generate synthetic seimograms. Some methods can only be used for models in which the physical properties of the medium vary in the vertical direction solely. Other techniques, like those based on ray-tracing, allow more complicated structures but still usually produce very simple seismograms because the user must specify all rays to include in the computations. Thus crustal guided waves, like P_g and L_g, which are important at regional distances is difficult to model because of their complicated ray-paths.

In order to overcome some of these problems we have, in cooperation with the IBM Science Centre, Bergen, began synthetic seismogram computation using finite diffference (FD) techniques for a 2D elastic medium. The main advantages of this method are that all wavetypes and propagation effects are included and that arbitrary complex models can be used. Large scale structures known from crustal mapping can thus be used in combination with small scale structures generated randomly to produce synthetics that have a striking resemblance with real seismograms - including coda waves.

With this tool at hand we can now start to examine features of regional seismograms that potentially can be used for source classification. By using different source types, various source depths and by changing the statistical properties of the random medium we hope to decide which features of the seismograms that are diagnostic for source type and which are depending on the source depth, ray-path propagation effects, or the medium *per se*.

Research accomplished

In this section we will give a short summary of the computational technique used followed by a description of the models used for testing. Finally, we presents some preliminary results from the experiments performed.

Method

The basic equations governing wave propagation in a continuous elastic medium are the momentum conservation and the stress-strain relation. Following Achenbach (1975), in the velocity-stress formulation, these are given by

$$\rho \frac{\partial}{\partial t} v_j = f_j + \frac{\partial}{\partial x_\ell} \sigma_{j\ell}, \quad j, \ell = 1, \ldots, J \tag{1}$$

$$\frac{\partial}{\partial t} \sigma_{jj} = \lambda \frac{\partial}{\partial x_\ell} v_\ell + 2\mu \frac{\partial}{\partial x_j} v_j, \quad j, \ell = 1, \ldots, J \tag{2}$$

$$\frac{\partial}{\partial t} \sigma_{j\ell} = \mu \left(\frac{\partial}{\partial x_j} v_\ell + \frac{\partial}{\partial x_\ell} v_j \right), \quad j, \ell = 1, \ldots, J, \quad j \neq \ell \tag{3}$$

where Einstein's summation convention is used. J is the dimensionality of the problem, ρ is density, and λ and μ are Lamé's parameters. f_j are body forces and v_j and $\sigma_{j\ell}$ are velocities and stresses, respectively.

Numerical discretization

Spatial partial differentiation is achieved through cost-optimized, dispersion-bounded, high-order finite difference operators on a staggered grid. For time stepping a leap-frog technique is used. The discretization of the elastodynamic equations with two staggered numerical space differentiators, $\delta^{\pm}$, applied as in Levander (1988) to stresses and particle velocities leads to:

$$\rho_j^+ \{V_j^+(t + \Delta t/2) - V_j^+(t - \Delta t/2)\} = \Delta t \{F_j^+(t) + \delta_j^+ S_{jj}(t) + \sum_{\substack{l=1 \\ l \neq j}}^{J} \delta_l^- S_{jl}^{++}(t)\}, j, l = 1, ..., J$$

$$S_{jj}(t + \Delta t) - S_{jj}(t) = \lambda \Delta t \sum_{r=1}^{J} \delta_r^- V_r^+(t + \Delta t/2) + 2\mu \Delta t \delta_j^- V_j^+(t + \Delta t/2), \quad j, l = 1, ..., J$$

$$S_{jl}^{++}(t + \Delta t) - S_{jl}^{++}(t) = \mu_{jl}^{++} \Delta t \{\delta_j^+ V_l^+(t) + \delta_l^+ V_j^+(t)\}, \quad j, l = 1, ..., J, \quad j \neq l$$

$$V_j^+(t) = v_j(\mathbf{x} + \mathbf{h}_j/2, t), \quad F_j^+(t) = f_j(\mathbf{x} + \mathbf{h}_j/2, t),$$

$$S_{jj}(t) = \sigma_{jj}(\mathbf{x}, t), \quad S_{jl}^{++}(t) = \sigma_{jl}(\mathbf{x} + \mathbf{h}_j/2 + \mathbf{h}_l/2, t).$$

$$\rho_j^+ = \rho(\mathbf{x} + \mathbf{h}_j/2), \quad \lambda = \lambda(\mathbf{x}), \quad \mu = \mu(\mathbf{x}) \quad \text{and} \quad \mu_{jl}^{++} = \mu(\mathbf{x} + \mathbf{h}_j/2 + \mathbf{h}_l/2).$$

$$\delta_j^+ q(\mathbf{x}) = \sum_{\ell=1}^{L^+/2} d_{2\ell-1}^+ \frac{q(\mathbf{x} + \ell \mathbf{h}_j) - q(\mathbf{x} - (\ell - 1)\mathbf{h}_j)}{\Delta x_j} \cong \frac{\partial q}{\partial x_j}(\mathbf{x} + \mathbf{h}_j/2),$$

$$\delta_j^- q(\mathbf{x}) = \sum_{\ell=1}^{L^-/2} d_{2\ell-1}^- \frac{q(\mathbf{x} + (\ell - 1)\mathbf{h}_j) - q(\mathbf{x} - \ell \mathbf{h}_j)}{\Delta x_j} \cong \frac{\partial q}{\partial x_j}(\mathbf{x} - \mathbf{h}_j/2).$$

Here $\mathbf{h}_j$ is the unit vector in the jth direction, λ, μ and S_{ij} are defined at the nodes of the Cartesian mesh, ρ_j^+, V_j^+ and F_j^+ and defined at the links connecting the nodes and $S_{j\ell}^{++}$ and $\mu_{j\ell}^{++}$ are defined at the centers of the "plaquettes". $\delta^\pm$ are numerical differentiators of coefficients $d_{2\ell-1}^\pm$. q is here velocity or stress and $L^\pm$ is the length of the operator. For the numerical dispersion relations, the stability limit and bandwidth introduced by the discretization, the reader is referred to Sguazzero *et al* (1990).

Boundary conditions

By necessity, the numerical modeling limits the medium, and to reduce artificial reflections from the numerical boundaries, the velocities and stresses are multiplied by exponentially decreasing terms near the edges (absorbing boundary conditions).

On the top free surface, we use the vanishing stress conditions for a free boundary

$$\vec{n} \cdot \mathbf{T} = 0 \tag{4}$$

(free surface boundary condisions). Here $\vec{n}$ is the outward normal unit vector on the surface and $\mathbf{T}$ is the stress tensor. To get computationally tractable conditions, we assume the free top surface to be locally plane. Then $\vec{n} = \vec{k}$, where $\vec{k}$ is the unit vector in the vertical z-direction. x and y are horizontal coordinates. Eq.(4) then leads to

$$\sigma_{zx} = \sigma_{zy} = \sigma_{zz} = 0 \tag{5}$$

If the constitutive equations (stress-strain relations) (2) and (3) are used together with eq. (5) on the top surface, this leads to a closed system of nine equations for the nine components of velocities and stresses.

In our application a cost-optimized, dispersion-bounded 8th order operator of length 8 is chosen as spatial differentiator. It corresponds to a sampling rate of 3 points per minimum wave length, and it has a relative error-bound of 1.9 % for group velocity. Because of the length of the operator, other devices have to be used on the layers near all boundaries. Second order staggered finite differences given as $\delta_j^\pm$ with $L^\pm = 2$ are therefore employed for all 4 outermost points in the model.

Model

The model used for most of the test runs so far is 200 km × 400 km and with a grid spacing of 0.2 km in both directions. This corresponds to 3 point per minimum wavelength for S-waves with velocity 3.6 km/s and a maximum frequency of 6 Hz. The source function have maximum power at about 2.5 Hz and a duration of less than 2 sec. So far we have used two types of point sources; a P-source with pure divergence and an S-source with pure curl. A double-couple source

for simulation of earthquakes will also be implemented. Due to the absorbing boundaries at the 'walls' of the model the full range of the model can not be used to extract synthetic seimograms. The largest horizontal distance between source and receiver have been 260 km and we have used recording periods up to 90 sec.

Regarding large scale crustal structures we have experimented with different kinds of layering and gradients but for most of the tests we have for simplicity used a one-layered crust over the Moho dicontinuity without velocity gradients. Some experiments have also been done with a 'bump' in the Moho (elevation 2-4 km, width 50 km) in order to simulate the elevated Moho in the Oslo Graben near NORESS. Other tests have been performed with a sinusoidal shaped Moho.

In order to simulate small scale velocity structures we can modify the crustal velocity model by a random field. The autocorrelation function of the random field is specified as a von Kármán function of given order, correlation distance and RMS variation.

Experiments

Example 1: In this test we have used a sinusoidal shaped Moho (wavelength $\sim$ 8 km, amplitude $\sim$ 2 km) separating the crust (V_P = 6.50 km/s, V_S = 3.75 km/s, ρ = 2.85 g/cm^3) from the upper mantle (V_P = 8.20 km/s, V_S = 4.73 km/s, ρ = 3.34 g/cm^3). Average crustal thickness was 30 km. Two runs were made; one with a P-source and the other with an S-source. In Figure 1 a trace (vertical component) from each run is displayed together with semblance velocity analysis. The distance to the source is 160 km and the source depth is 10 km. The semblance analysis was performed at 10 traces with spacing 0.4 km and with a moving time window of 1.0 sec. For the P-source we note the P-to-S converted wave arriving in the time interval 30-42 sec. These waves are generated by scattering/conversion at the corrugated Moho interface (see also Paul and Campillo, 1988) and is absent in models with a flat Moho. For the S-wave source we note the strong sP_MP phase which is generated by S-to-P conversion at the free surface. This phase (or sometimes sP_g) is often the dominating P-phase in seismograms of local earthquakes and is potentially interesting for discrimination when it is properly identified (and not mistaken for P_g as often happens).

Example 2: This is a test for a random medium with P and S velocities having an exponential autocorrelation function (von Kármán medium of order 0.5). The RMS velocity variation was 4% and the correlation distance was 4.0 km. Background velocities were 6.50 km/s for P-waves and 3.75 km/s for S-waves; density was 2.85 g/cm^3 (constant). There was no layering or other large scale structures in the model. Also in this test two runs were made (P and S source). In Figure 2 some traces and results from coherence analysis of the P-coda are shown. The horizontal distance from the source to the nearest receiver is 170 km and the source depth is 100 km. The receivers are situated at the free surface. Coherence was calculated for pairs of filtered traces which were first time shifted according to the expected arrival time for a P-wave from the

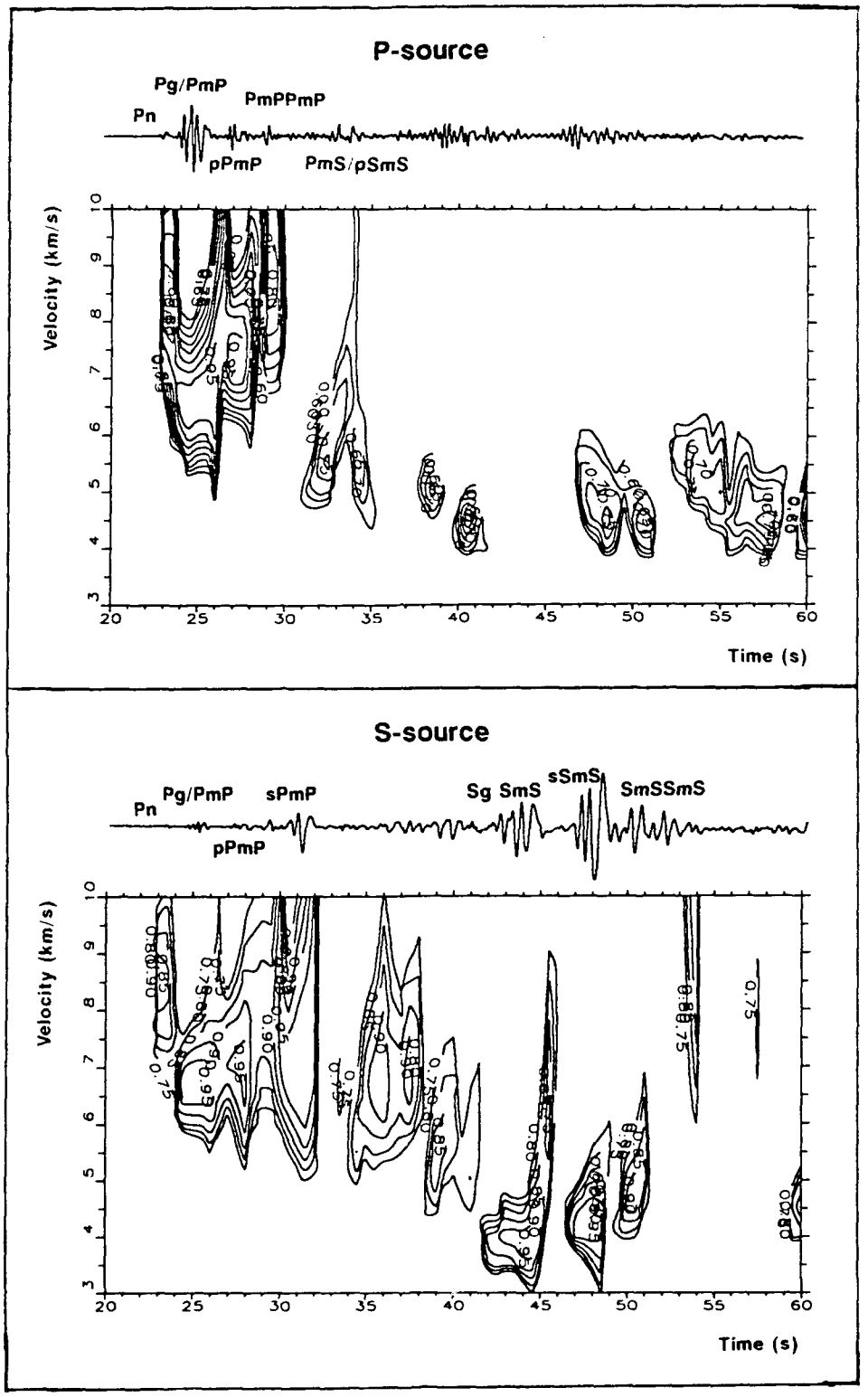


Figure 1: Semblance analysis of synthetic seismograms for a P-source (upper part) and an S-source (lower part) in a crustal model with a sinusoidal Moho interface. Distance is 160 km and depth 10 km.

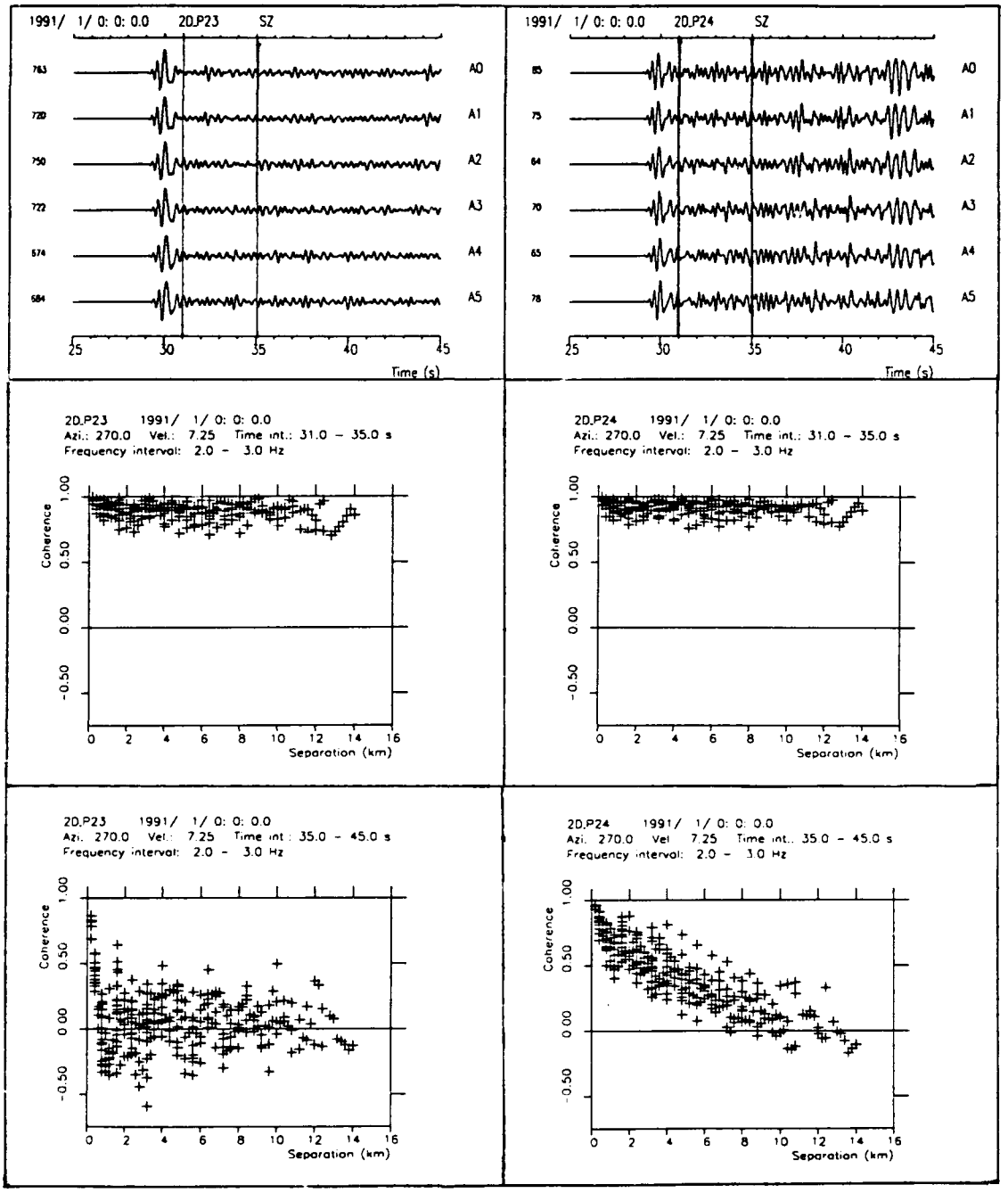


Figure 2: Coherency analysis for a random medium with an exponential autc correlation fu.ction (corr.dist. 4 km, RMS 4%). The left part of the figure is for a P- and the rigth for an S-source. The traces shown in the upper part have an equidistant separation of 0.2 km. The coherence plots in the middle are for the time interval 31-35 sec and the lower plots for the interval 35-45 sec after origin time.

source. Both the P- and S-source produced highly coherent P-coda in the first 4 sec after the source pulse (which is practically identical on all receivers) but in the later part (4-14 sec after the source pulse) the P-coda generated by the S-source is much more coherent than its P-source counterpart. This observation suggest that S-to-P conversion takes place in the source region for a rather long time interval and may explain why the P-coda of teleseismic earthquakes usually have a longer duration than for explosions (the complexity criterion sometimes used in discrimination).

Conclusions and recommendations

The experiments with a bump in the Moho (not shown here), in order to simulate scattering by a graben structure, showed little effect on P_n. An increase in amplitude of up to 50% was seen on some receivers – still the P_n amplitude is small compared to the later P_g/P_MP phases.

Irregular interfaces and random velocity variations are effective in converting energy from P- to S-waves and can produce realistic coda waves (see Example 1 and 2 above).

Given the necessary computational capasity, 2D finite difference modelling of elastic waves have proven to be an excellent tool to generate synthetic seismograms of regional events. All types of waves are automatically included and any type of structures can be handeled. By continuing this work on 2D FD modelling we hope to develop a better physical understanding of regional seismic waveform discriminant features.

References

Achenbach, J.D. (1975): *Wave Propagation in Elastic Solids*, North Holland Publ. Co., The Netherlands.

Levander, A.R. (1988): Fourth-order finite-difference P-SV seismograms, *Geophysics*, 53, 1425–1436.

Paul, A. and Campillo, M. (1988): Diffraction and conversion of elastic waves at a corrugated interface, *Geophysics*, 53, 1415–1424.

Sguazzero, P., M. Kindelan and A. Kamel (1990): Dispersion-bounded numerical integration of the Elastodynamic equations, *Comp. Meth. Appl. Mech. Eng.*, 18.

ANALYSIS OF HISTORICAL USSR SEISMOGRAMS - RMS MAGNITUDES, YIELDS, AND DEPTHS OF EXPLOSIONS AT THE SEMIPALATINSK TEST RANGE

by Hans Israelsson

Center for Seismic Studies, 1300 North 17th, Suite 1450, Arlington, VA 22209

CONTRACT NO. F19628-89-C-0203

OBJECTIVE

A large set of analog recordings from several Soviet in-country seismic stations of a number of underground nuclear explosions have recently become available as a result of bilateral Nuclear Testing Talks. A total of 476 of these recordings obtained at 11 stations, distributed throughout the Western and Central U.S.S.R, for 116 explosions at seven widely separated sites, have been digitized. Figure 1 shows explosion site-station paths, in relation to the major tectonic boundaries, for which digitized data is available. As part of an effort to establish optimized relationships between explosion yields and measurements of Lg-waves, we have analyzed RMS magnitudes calculated for most of the waveforms for explosions at Semipalatinsk and Novaya Zemlya testing grounds. For each waveform these RMS magnitudes were calculated for four consecutive windows: the initial P, the P coda, the S phase with coda, and the Lg phase in the velocity window 3.1 to 3.7 km/s.

RESEARCH ACCOMPLISHED

The analysis has addressed several issues on the quality of explosion yield estimates based on RMS Lg measurements. Results are summarized below and are illustrated by the examples in Figures 2-12.

- Consistency among station magnitudes

Earlier studies of RMS Lg magnitudes have demonstrated the consistency among station magnitudes by comparing them pairwise in scatter diagrams (see e.g. Hansen *et al.* (1990)). Due to the limited number of waveforms for many of the stations from each subregion of the Semipalatinsk Test Range, we combined data for all explosions, regardless of subregion (Balapan, Degelen, Murzhik) in pairwise comparisons of station RMS magnitudes. The misfit errors for RMS Lg appear to be somewhat smaller than for other phases. The errors for most station pairs are above 0.03, a value being typical of the data studied by Hansen *et al.* (1990). However, for many station pairs the difference is only marginal (see example for ARU and OBN in Figure 2). Furthermore, the estimated errors of misfit have estimated standard deviations between 20 and 50% of the point estimate due to the small number of data points. The comparisons of station RMS magnitudes also suggest that values at at least station BOD, for Lg and S coda, scale differently with increasing source strength than those of most of the other

stations.

• RMS magnitudes and explosion yield

Network magnitudes based on a combination of station magnitudes were formed as weighted averages over the station magnitudes and adjusting for differences in scaling with source strength. The number of station magnitudes that contribute to a network magnitude varies between 1 and 5 for the events. Combining the station magnitudes into network magnitudes, although the number of stations is small, reduces scatter in magnitude-yield relations. The correlation between network RMS Lg magnitudes and explosion yield is very high (Figure 3) and the data closely fits a linear relation (logarithm of yield) throughout the yield interval 2-165 kt. The error of misfit for Lg, is less than 0.03 excluding data for the explosion on 72/08/16 (8 kt at 139 m), the yield of which appears high compared to station RMS magnitudes. Compared to other magnitudes like a maximum likelihood m_b based on P wave amplitudes for a world-wide network, the yield of this explosion also appears high.

• Shot depth and RMS Lg

Results from theoretical modelling suggest that the generation of Lg waves can, under some circumstances, be strongly dependent on the shot depth. This would imply that explosions with the same yields, set off at different depths, could also have different RMS Lg magnitudes. The close correlation between RMS Lg network magnitudes and explosion yields obtained here and the fact that many of the explosions were not at scaled depths indicate, however, that depth dependence may not be an important factor. The data in Figure 5 show the RMS Lg magnitudes for groups of explosions with equal or similar yields, 4-8, 12-23, and 90-140 kt, as a function of shot depth, ranging between 124-274, 175-324, and 294-478 m, respectively. There is little scatter in the Lg magnitudes for the three groups; three of the explosions with the same yield, 16 kt, and depths between 175 and 299 are within 0.05 magnitude unit of each other. It therefore appears that the RMS Lg is not sensitive to shot depth (between 125 and 500 m). On the other hand, the data in Figure 4 show that the scatter in RMS P coda magnitudes is more pronounced for the same events: depth may be a contributing factor.

• Relative P and Lg RMS magnitudes

The P-Lg magnitude bias across the Balapan test site at Semipalatinsk that has earlier been demonstrated (Ringdal and Marshall, 1989) was also noted for the U.S.S.R. stations, however, with a distance dependence. Stations at close distances, like ARU, showed little or no bias. Furthermore, for some stations there also appear to be a systematic P-Lg magnitude differences for the Murzhik and Degelen sites with negative and positive bias respectively (Figure 6). Analysis of P-Lg RMS magnitude differences for explosions at Matochkin Shar showed clear systematic variations between explosions separated by the Shumilikha river. These differences were, however, not consistent from station to station (Figures 7 and 8).

• Frequency characteristics in the Lg window

The dominant frequency as a function of travel time in the Lg window was analyzed for most explosion-station paths. The examples in Figure 9 show the dominant frequency from the onset of expected S to a group velocity of about 3.0 km/s for four paths. The velocity windows 3.1 to 3.7 km/s are indicated with vertical bars. The time of the maximum amplitudes are indicated with solid circles. Most paths exhibit characteristics of an Airy phase with an inverse dispersion prior to the arrival of the maximum amplitude (typical group velocity 3.3-3.4 km/s) after which the frequency stayed fairly constant. For the paths from Matochkin Shar to BOD, CHS, and TLY, however, the maximum occurred for higher velocities near 3.7 km/s.

• Attenuation of RMS Lg amplitudes

For the purpose of estimating attenuation with distance of the RMS Lg amplitudes we employed a simple source-path model for the RMS amplitudes. This model assumed that for a given explosion test site (like Semipalatinsk or Novaya Zemlya) the logarithm of the RMS amplitudes at station j from event i could be written in the form:

$$rms_{ij}=s_i+p_j+\epsilon_{ij}$$

where s_i and p_j represent the source and path terms respectively. The Gaussian error terms, ϵ_{ij}, were assumed to independent with zero mean and equal standard deviation. In addition, we imposed the condition that $\sum_j p_j=0$. There is considerable scatter around the general trend of decay with distance for the estimated path terms (Figure 10). However, the path terms can, with surprising accuracy, be separated into a station correction, t_j, and a distance dependent (for Airy phase, see Nuttli, 1973) part: $p_j=t_j+\log_{10}(\Delta_{ij}^{-1/3}\cdot(\sin(\Delta_{ij}))^{-1/2}\cdot e^{-\gamma\Delta_{ij}})$. Station corrections, t_j estimated independently for paths from Novaya Zemlya and Semipalatinsk, assuming the same $\gamma=0.0012\ km^{-1}$, are almost identical (see Figure 11). Apart from the station APA there is also close correlation between station corrections and average station noise levels (Figure 12).

CONCLUSIONS AND RECOMMENDATIONS

The consistency among station RMS Lg magnitudes calculated from hand digitized historical data is comparable to results based on modern high quality digital recordings. Network RMS Lg magnitudes appear more robust than station magnitudes and had estimated standard errors around 0.02 or less (for five stations or more). If we account for magnitude-yield scaling, this translates to uncertainties in *relative* explosion yield of about 15% at the two sigma level for explosions with *similar source coupling*. In addition network RMS Lg magnitudes appear fairly insensitive to shot depth and to subregion of the Semipalatinsk test range. These qualities notwithstanding, the perhaps most encouraging result of this analysis is the simple way in which the attenuation of the RMS Lg amplitudes can be described as the product of a station correction, geometrical spreading, and an anelastic term that decays with the same rate ($\gamma=0.0012\ km^{-1}$) regardless of path.

REFERENCES

Hansen, R., Ringdal, F., and P.G. Richards (1990). The stability of RMS Lg measurements, and their potential for accurate estimation of the yields of Soviet underground explosions *Bull. Seism. Soc. Am.*, **80,** 2106-2126.

Nuttli, O.W. (1973). Seismic wave attenuation and magnitude relations for Eastern North America *J. Geophys. Res.* **78,** 876-885.

Ringdal, F. and P.D. Marshall (1989). Yield determination of Soviet underground nuclear explosions at the Shagan River Test Site, in: *Semiann. Tech. Summ., 1 October -31 March 1989*, **NORSAR Sci. Rep. 2-88/89**, Kjeller, Norway.

FIGURES

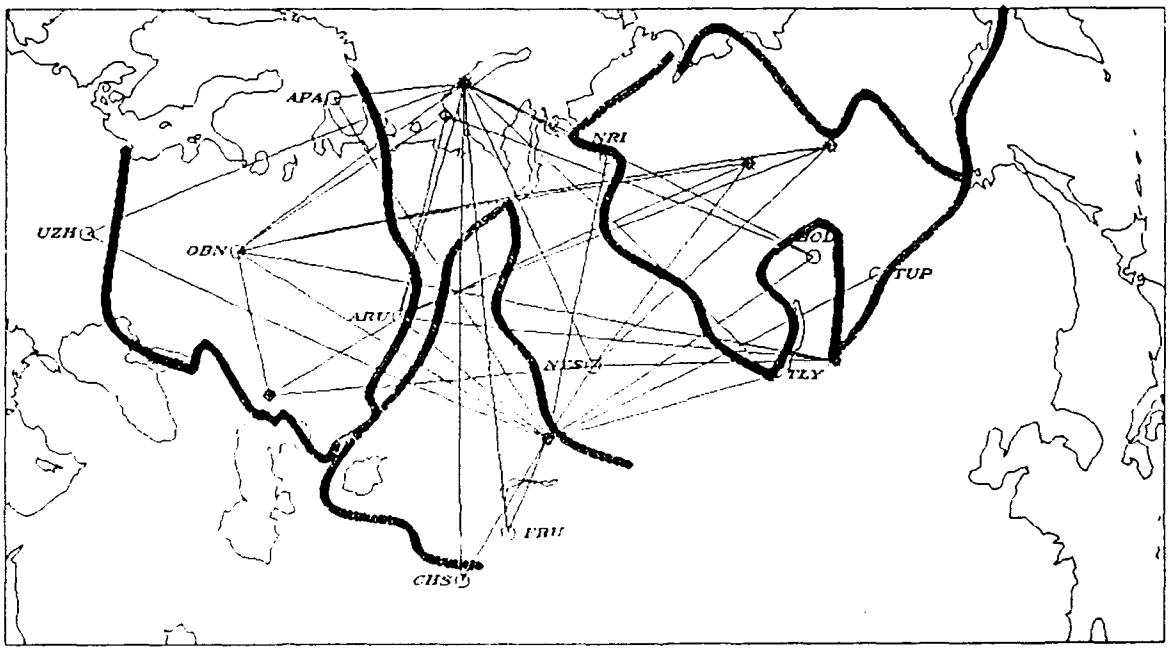


FIGURE 1

Comparison of RMS Lg magnitudes

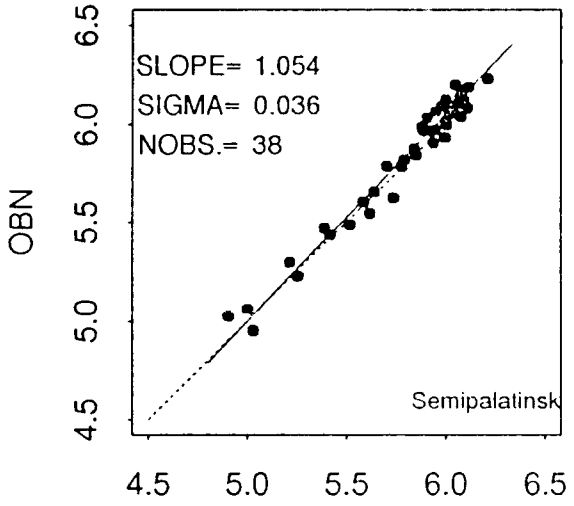


FIGURE 2

RMS Lg and Yield

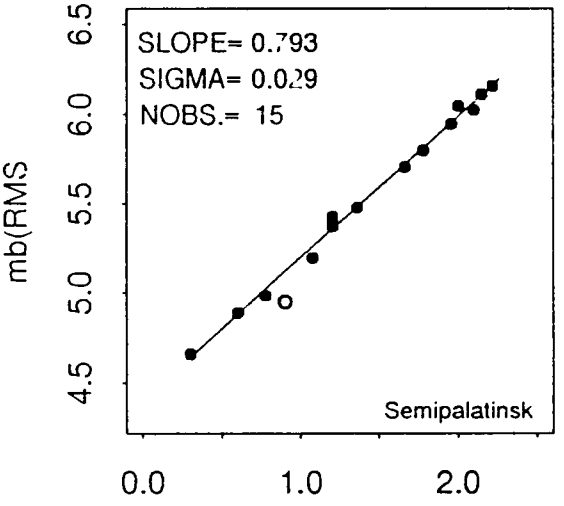


FIGURE 3

Effect of Shot Depth

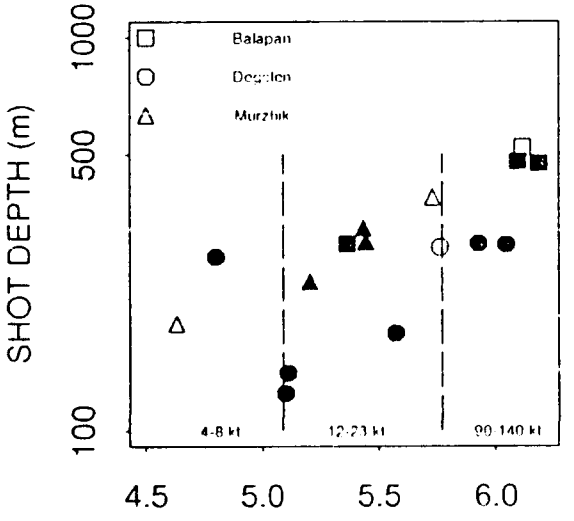


FIGURE 4

Effect of Shot Depth

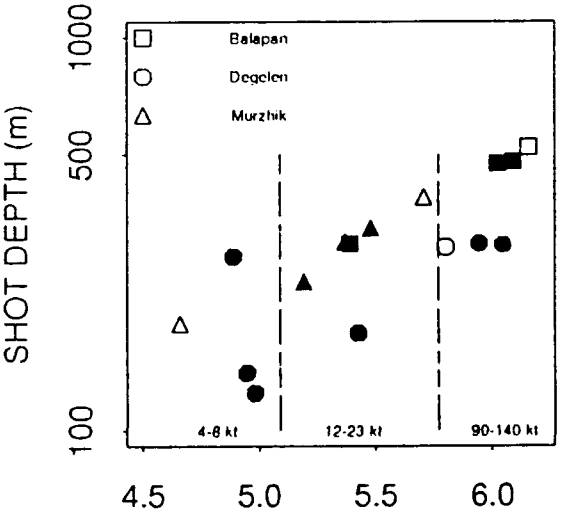


FIGURE 5

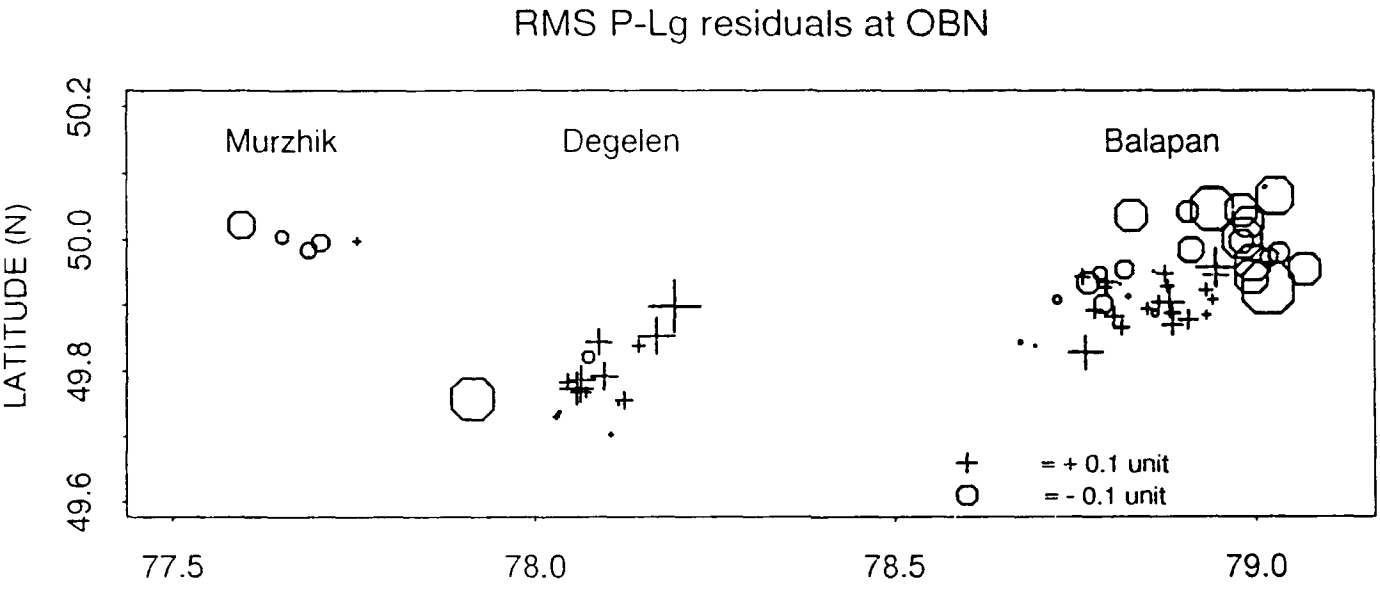


FIGURE 6

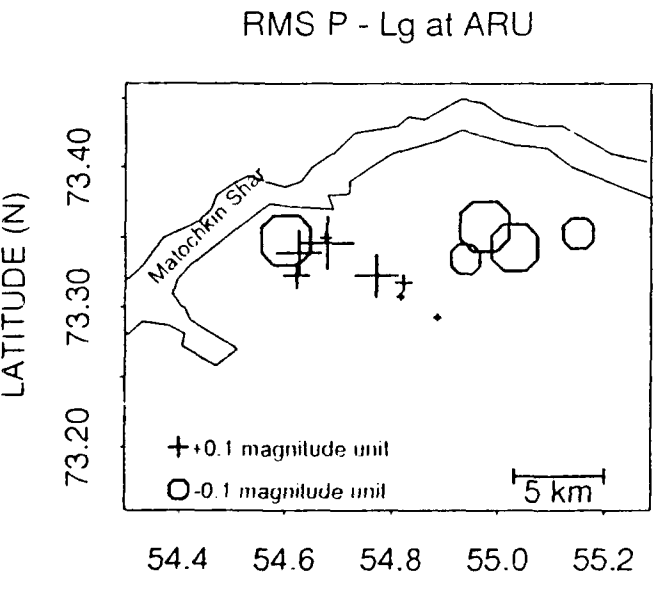


FIGURE 7

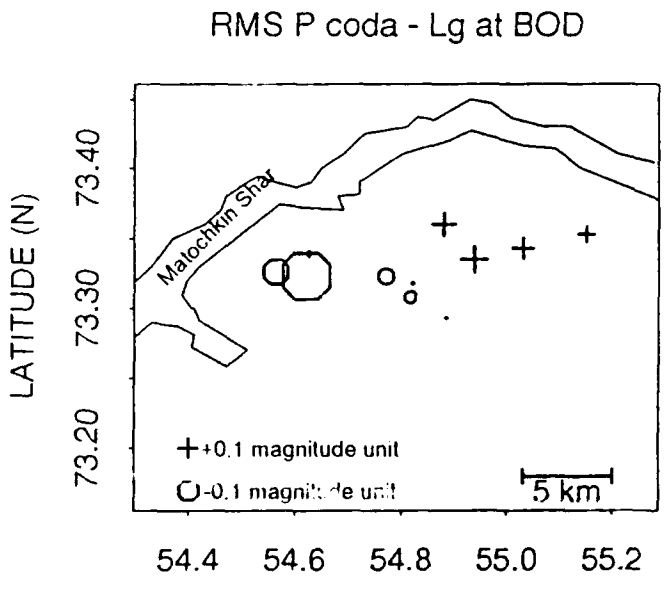


FIGURE 8

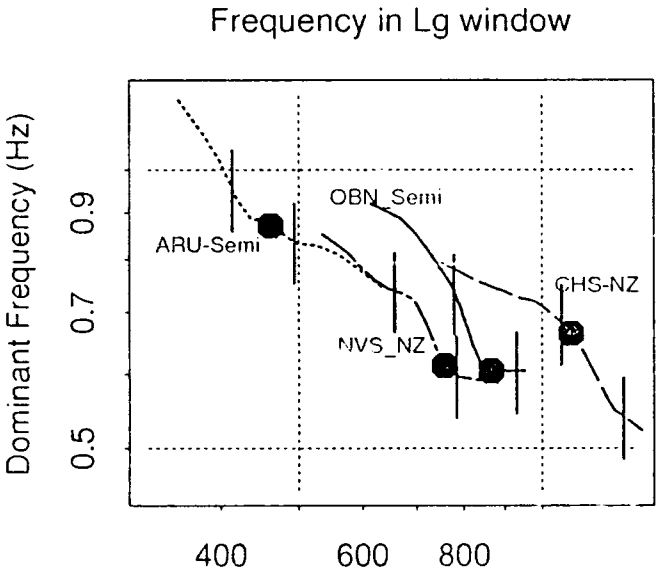


FIGURE 9

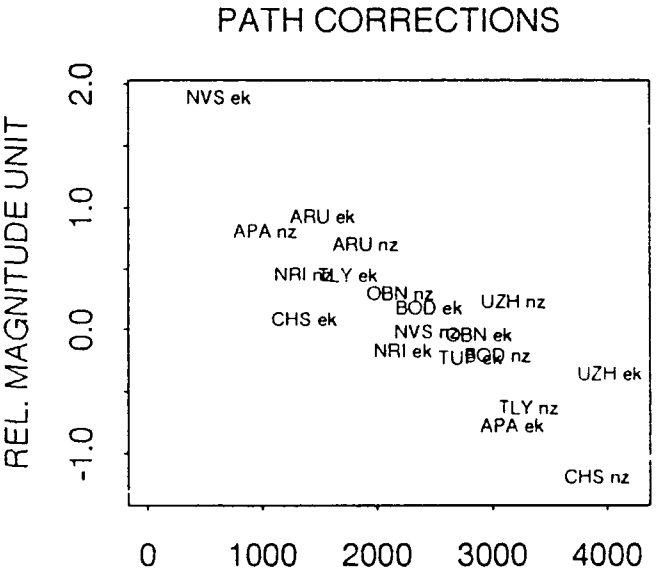


FIGURE 10

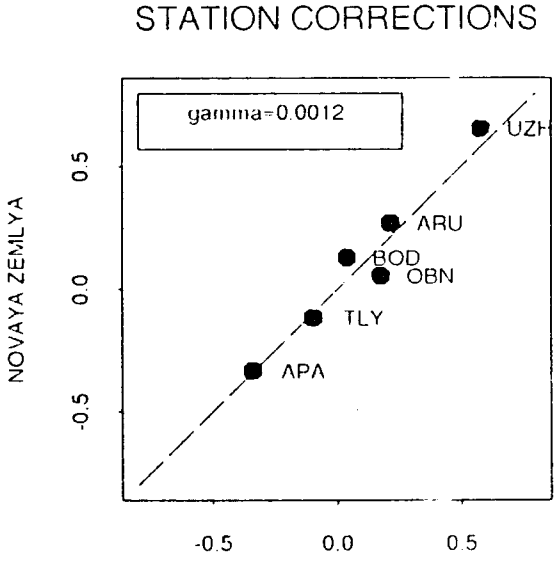


FIGURE 11

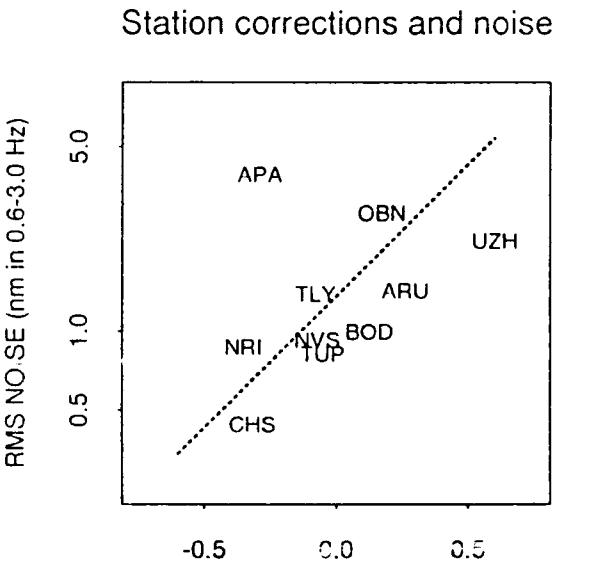


FIGURE 12

EXPLOSION SOURCE SIZE DETERMINATION, DISCRIMINATION AND SPECTRAL CHARACTERISTICS

R.-S. Jih, C. S. Lynnes, I. N. Gupta, R. Baumstark, R. A. Wagner, and R. H. Shumway*
Teledyne Geotech Alexandria Laboratory, 314 Montgomery Street, Alexandria, VA 22314-1581
* Department of Statistics, University of California, Davis, CA 95616

Contract No. F19628-89-C-0063

OBJECTIVES

(A) Improve the fundamental understanding of how energy from explosion and earthquake sources is partitioned into various seismic wave types due to different geological models. The statistical and numerical modeling tools (such as LFD and GLM) will be upgraded and applied to regional phase excitation problems with emphasis on Soviet geological structures.

(B) Test high-frequency phase-ratio discriminants systematically on large data bases from the USA and Canada, and test possible improvements of the discriminants using three-component data.

(C) Analyze teleseismic and regional data to determine and understand the spectral nulls due to cancellation by pP and other secondary arrivals and the scaling of P-wave spectra.

RESEARCH ACCOMPLISHED

(A) Recent Methodological Improvements in Yield Estimation (Jih, Wagner, Shumway)

A recent breakthrough in magnitude determination is the development of a procedure to account for near-source focusing/defocusing effects. Jih and Wagner (1991) propose to compute the station magnitude $m_{2.9}$ for the i-th event recorded at the j-th station as

$$m_{2.9}(i,j) = \log_{10}[A(i,j)/T(i,j)] + B(\Delta(i,j)) - S(j) - F(k(i),j) \qquad [1]$$

where A(i,j) is the displacement amplitude and T(i,j) is the period of the *P* wave. The $B(\Delta)$ is the distance-correction term. S(j) is the station correction, and F(k(i),j) is the near-source focusing correction for explosions from the k(i)-th source region. Testing results with 82 Semipalatinsk events in our WWSSN database indicate that the proposed procedure has the following advantages:

[A] For 96% of the tested events, [1] provides more stable m_b measurements across the whole recording network with a reduction in the fluctuational variation by a factor of up to 3. The 3 anomalous events which do not show significant improvement could have been detonated in environments with different focusing patterns.

[B] The resulting network m_b values are not significantly different from the General Linear Model [GLM] results. Thus if the mean network m_b values derived by GLM or by "Least Squares by Matrix Factorization" [LSMF] are unbiased, then so are the refined results.

[C] The scatter in $\bar{m}_{2.9}$ (*i.e.*, the network-averaged m_b based on $m_{2.9}$) versus log(yield) is smaller than that for conventional GLM or LSMF m_b which are only corrected for the receiver terms.

A simple general regression routine has been developed by Jih and Shumway (1991) to quantify the effects on the yield estimation due to rounding and standard errors [S.E.] in the published yields. For each m_b-yield pair, we use a random number generator to produce a perturbed m_b-yield pair

according to the stochastic distribution of the uncertainty. A standard least-squared regression is then performed for each collection of perturbed pseudo-observations. The procedure is repeated for several hundred iterations, and all the resulting calibration curves are then used to infer the ensemble calibration. This "doubly-weighted least-squares scheme" is an extension to the "ordinary weighted least-squares" in which only errors in the m_b would be used to adjust the inferred parameters.

The "upper 95% confidence limit" of the predicted m_b at a given log(yield) level (say, Y_0) can be computed as follows:

$$\hat{m}_b(\max) + t(\text{D.O.F.}, 0.975)\ [\sigma^2(m_b) + \sigma^2(\text{regression})(\frac{1}{N} + \frac{(Y_0 - \overline{Y})^2}{\sum(Y_i - \overline{Y})^2})]^{0.5} \qquad [2]$$

where N = number of data points used in the regression, D.O.F. = N - 2, $\sigma(m_b)$ = the mean S.E. in the network m_b used in the regression, σ(regression) = the σ of residuals, $\hat{m}_b(\max)$ = estimate of the largest possible mean m_b at the given log(yield) level, $\overline{Y}$ is the mean log(yield) used in the regression, and t(D.O.F., 0.975) is the 97.5 percentile of Student's t distribution at "D.O.F." degrees of freedom. The "lower 95% confidence limit" can be computed in a similar way.

There has been some concern about the accuracy and precision of the Soviet published yields. The 19 Semipalatinsk explosions for which the "exact" yields were published would inevitably be subject to many sources of error. 8 of the announced 19 yields might have been rounded to the nearest 5KT or 10KT. Below 100KT, the rounding errors could overwhelm the presumed standard measurement error --- assuming the announced yields are not otherwise "fudged".

It turns out that, if only the rounding and standard errors are present in the yields, then the uncertainty factor in the predicted yield of future Semipalatinsk events is not very sensitive to the postulated uncertainty in the published yields of the 19 events, provided a good m_b (such as $\overline{m}_{2.9}$) is used. The yields of future underground explosions in the Semipalatinsk area can be estimated seismically with a capability much better than the factor-of-2 uncertainty that is commonly reported. A factor of 1.5 appears to be a reasonable 95%-confidence uncertainty estimate around the 50KT level if $\overline{m}_{2.9}$ is used as the source measure.

Table 1. Inferred Calibration Parameters and Associated Uncertainty Factors

Uncertainty in yield	Slope	Intercept	1KT	10KT	50KT	100KT	150KT
R.E. + 10% S.E.	0.804±0.022	4.288±0.038	3.23	1.82	1.67	1.88	2.04
R.E. + 5% S.E.	0.805±0.020	4.286±0.035	3.11	1.78	1.53	1.64	1.77
R.E. + 2% S.E.	0.806±0.020	4.285±0.035	3.33	1.81	1.53	1.69	1.82
R.E. + 1% S.E.	0.805±0.020	4.287±0.035	3.04	1.80	1.49	1.60	1.75
R.E. Only	0.807±0.019	4.284±0.034	3.04	1.83	1.54	1.60	1.72
10% S.E.	0.807±0.018	4.282±0.027	2.83	1.74	1.60	1.77	1.91
5% S.E.	0.811±0.012	4.277±0.018	2.41	1.62	1.51	1.61	1.71
2% S.E.	0.811±0.009	4.276±0.014	2.33	1.57	1.48	1.57	1.64
1% S.E.	0.812±0.009	4.275±0.014	2.32	1.57	1.49	1.57	1.64
0.1% S.E.	0.812±0.009	4.275±0.014	2.32	1.57	1.49	1.57	1.64

R.E.: Rounding Error ; S.E.: Standard Error

(B) Phase and Spectral Ratio Discrimination in North America (Lynnes, Baumstark)

Phase and spectral ratio discriminants have been studied in a systematic fashion over several frequency bands in 3 regions in North America: the western U.S., the Mid-Atlantic U.S., and southeastern Canada. In the western U.S., path effects have been shown by Lynnes *et al.* (1990) to dominate the *Pg/Lg* ratios measured for earthquakes and underground nuclear tests at station JAS (Jamestown, California). The result is very different trends with distance for events in Nevada and southern California. The *Pg/Lg* discriminant is further complicated by an increase of *Pg/Lg* with shot depth (Lynnes *et al.*, 1990) which may be due to the source velocity: Frankel (1989) has shown that low near-surface velocities increase *Lg* wave generation, especially at high frequencies. Empirical distance corrections were obtained by dividing the earthquakes into northern (> 37° N) and southern (< 37° N) groups and fitting straight lines to the log(*Pg/Lg*) vs. distance. In addition to these corrections, a depth correction was obtained by fitting a line to a plot of log(*Pg/Lg*) vs. shot depth for the explosions and then normalizing to the value at 200 km. When these corrections are made, there is little difference in *Pg/Lg* ratios for explosions and earthquakes at most frequencies (Fig. 1), indicating that the differences observed in the raw values are in fact largely artifacts of the travel paths and deep shot depths.

Similarly, path-dependent distance corrections were applied to the spectral ratios of the *Pg* and *Lg* phases (Fig. 2). These reduce the scatter within the populations by removing much of the effect of attenuation. However, significant differences between explosions and earthquakes remain for the data recorded at JAS. Explosion spectral ratios for both phase types increase with depth down to about 350 m, past which they decrease with depth, possibly due to competing effects of corner frequency and decreasing $Rg \rightarrow P$ and $Rg \rightarrow S$ contributions with depth.

Phase and spectral ratios were also obtained for earthquakes and chemical explosions recorded at the Virginia Polytechnic Institute (VPI) network in the Mid-Atlantic U.S. Network averages were computed for *Pg/Lg* and *Pg* and *Lg* spectral ratios by applying empirical distance corrections obtained from the earthquake data and then computing maximum-likelihood averages. The network average *Pg/Lg* ratios for explosions (Fig. 3) are higher than those for earthquakes in the 4-8 Hz band, but they are not significantly different at lower frequencies. The spectral ratios (Fig. 4) appear to be higher in general for both *Pg* and *Lg* from explosions than from earthquakes.

Similar procedures were applied to data from the Eastern Canada Telemetered Network (ECTN), though the *P* phase measured here is probably a mixture of *Pn*, *P** and *Pg*. The distinction between source types is better at most frequencies for the phase ratio than in the western or Mid-Atlantic U.S. (Fig. 5). However, neither spectral ratio seems to distinguish between source types (Fig. 6).

Simple attenuation can explain many of the trends with distance and frequency that appear in the phase and spectral ratios. The southwestern U.S. generally has the highest attenuation (and strongest distance and frequency trends), whereas southeastern Canada has the lowest attenuation with its attendant weaker distance/frequency trends. The northern area of the southwestern U.S. region studied here is anomalous, as the decay of the *Lg* spectral ratio with distance is similar to that for the VPI network, and it is less than the *Pg* spectral ratio decay. The reason for this is unknown, but it may be related to the relative contributions of scattering and intrinsic Q.

(C) Study of Spectral Nulls and Scaling of P-wave Spectra of Shagan River (USSR) Explosions

(Gupta, Wagner)

An understanding of the spectral nulls in the *P*-wave spectra of underground nuclear explosions is essential for constraining the source depth and for determining the bias in the body wave magnitude resulting from interference with *pP* and later arrivals. Determination of the correct spectral nulls due to *pP* for Shagan River explosions is especially important because of the lack of agreement among various workers and inconsistency of the reported *pP-P* or delay times with what is known about the site conditions and testing practices, which would suggest a delay time for large explosions to be about 0.25 sec.

We examined teleseismic and regional data from 79 underground nuclear explosions at the Shagan River test site. These data included EKA records of 40 events (28 from SW and 12 from NE region). Using a window length of 6.4 sec, starting 2 sec before the onset of direct *P* and with Parzen taper, Fourier spectra were obtained for all data, and a least squares inversion method that isolates the source and receiver terms for each frequency was then used to obtain the source spectra for all 40 events. An examination of these spectra suggested three general trends: (1) a majority of shots have spectral nulls at about 3 Hz, (2) several explosions have spectral nulls at about 4 Hz, and (3) a majority of shots have low-frequency (less than about 2 Hz) nulls which are generally more distinct for smaller explosions and for shots in the northeast Shagan region.

The Shagan River test site is believed to be underlain by about 100 m of unconsolidated sediments with the thickness decreasing gradually towards southwest. The *P*(6.4 sec) source spectra (not corrected for instrument response) of 10 explosions with shot points lying approximately along a SW-NE profile across the test site (Figure 7a) suggests a gradual build-up of the low-frequency nulls as the thickness of sediments increases. Moreover, the peak-amplitude and the null frequencies appear to be decreasing with increasing thickness of sediments. A null at about 3 Hz is also observed in most spectra. Source spectra derived from the *P*(3.2 sec) windows for the same 10 explosions, shown in Figure 7b, indicate almost total absence of the low-frequency nulls and some evidence of nulls at about 4 and 3 Hz. It is therefore clear that the low-frequency nulls are due to secondary (later) arrivals. Moreover, a probable mechanism of generation is greater near-source scattering for explosions under thicker low velocity sediments or shallower shot depths because the near-source environment in both cases is likely to be associated with greater near-source heterogeneity. Thin low velocity sediments may not be "seen" by seismic waves of low frequency or long wavelengths and therefore not make significant contribution to the scattered waves.

In order to compare the observed dependence of *P*-wave spectra on yield or m_b with that predicted by von Seggern and Blandford (1972) and Mueller and Murphy (1971) scaling relationships, synthetic seismograms were made for several assumed t^* and frequency-dependent *pP* reflection coefficient values. The Mueller and Murphy (1971) scaling relationship depends on both shot depth and shot medium whereas the von Seggern and Blandford (1972) relationship is independent of the shot depth. Shot depths for a given value of m_b were estimated by using an empirical relationship derived from the information on shot depths and yields recently released by Bocharov *et al.* (1989). The *P*-wave velocity for the uppermost 0.5 km of the crust in the Shagan River region was assumed to be 5 km/sec. Synthetic seismograms were constructed for several values of m_b and t^*. The observed regional data for *Pn* from 14 Shagan River explosions recorded at WMQ were bandpassed for the frequency bands of 0.5 - 1.0 Hz, 4.0 - 6.0 Hz, and 7.0 - 9.0 Hz by using a three-pole phaseless Butterworth

filter. Log RMS values were computed for the P(12.8 sec) windows with 10% cosine taper and correction for instrument response. Plots of log RMS values versus m_b for the synthetic and the observed data for frequency bands of 0.5 - 1.0 Hz, 4.0 - 6.0, and 7.0 - 9.0 were compared. The synthetics provided results that were not much different whether von Seggern and Blandford or Mueller and Murphy model is used. There is, however, a large discrepancy between the observed and synthetic data with the observations indicating much slower variation with m_b for the lowest frequency band of 0.5 - 1.0 Hz. The discrepancy is considerably reduced for the frequency band of 4.0 - 6.0 Hz and appears further reduced for the frequency band of 7.0 - 9.0 Hz. A comparison of the results for spectral ratios (0.5 - 1.0 Hz)/(4.0 - 6.0 Hz) and (0.5 - 1.0 Hz)/(7.0 - 9.0 Hz) for the two theoretical models and the observed data again indicated the low-frequency spectra to vary more slowly with m_b than expected from either of the two theoretical models.

CONCLUSIONS AND RECOMMENDATIONS

(A) The new magnitude determination scheme (Equation [1]) significantly reduces the fluctuational variation across the recording stations, as illustrated in this study. It is shown that, by applying this scheme to worldwide explosions, it is possible to have a consistent base line in estimating the absolute magnitudes (which is crucial in estimating the test site bias), while the resulting network m_b values can be maintained as precisely as could be achieved by the single-test-site approach. The standard error in most $\overline{m}_{2.9}$ values is 0.02 m.u., about the same as that for *RMS* L_g inferred from in-country regional recordings reported by Israelson (1991) and Hansen *et al.* (1990).

(B) This study shows the importance of accounting for propagation effects when applying high-frequency phase and spectral ratio discriminants to regional phases. Even with the application of regional corrections and network averaging, however, neither the phase ratio nor spectral ratio discriminants appear to be universally transportable. Phase ratios have limited utility in the southwestern U.S., but they appear to do fairly well for the two eastern North America data sets. Spectral ratios do well in the southwestern and Mid-Atlantic U S. but fail in southeastern Canada. Phase ratio discriminants are further complicated by the suggestion that they are dependent on source velocity, which is generally poorly known in a real monitoring situation.

(C) The most important result of this investigation is that, for large Shagan River explosions, spectral nulls due to cancellation by pP occur at about 4 Hz, in agreement with the known geology and testing practice. The lower frequency nulls are probably due to near-source scattering. The observed P spectra vary more slowly with m_b than is predicted by either the Mueller and Murphy (1971) or von Seggern and Blandford (1972) scaling relationships, and these differences are greater at lower than at the higher frequencies.

REFERENCES

---------(A)--------

Hansen, R. A., Ringdal, F. and P. G. Richards (1990). The stability of *RMS* L_g measurements and their potential for accurate estimation of yields of Soviet underground nuclear explosions, *Bull. Seism. Soc. Am.*, **80-6**, 2106-2126.

Israelson, H. (1991). RMS magnitude for Novaya Zemlya events (abstract), *EOS, Trans. A.G.U.*, **72-17**, 193.

Jih, R.-S. and R. A. Wagner (1991). A refined network m_b determination scheme incorporating near-source effects, in *Report PL-TR-91-____ (=TGAL-91-05)*, Phillips Laboratory, Hanscom Air Force Base, MA.

Jih, R.-S. and R. H. Shumway (1991). m_b-yield regression with uncertain measurements: a Monte-Carlo approach *(manuscript in preparation)*.

---------(B)--------

Lynnes, C. S., Baumstark, R., Cessaro, R. K., and W. W. Chan (1990). *Pg/Lg* discrimination in the western United States, *Scientific Report #2, GL-TR-90-0167*, Teledyne Geotech, Alexandria, Virginia. **ADA226819**

Frankel, A. (1989). Effects of source depth and crustal structure on the spectra of regional phases determined from synthetic seismograms, *DARPA/AFTAC Annual Research Review for FY89*, 97-118.

---------(C)--------

Bocharov, V. S., S. A. Zelentsoz, and V. N. Mikhailov (1989). Characteristics of 96 underground nuclear explosions at the Semipalatinsk test site, *Atomic Energy*, **67(3)**.

Mueller, R. A. and J. R. Murphy (1971). Seismic characteristics of underground nuclear detonations, Part I, Seismic spectrum scaling, *Bull. Seism. Soc. Am.*, **61**, 1675-1692.

von Seggern, D. H. and R. R. Blandford (1972). Source time functions and spectra for underground nuclear explosions, *Geophys. J.*, **31**, 83-97.

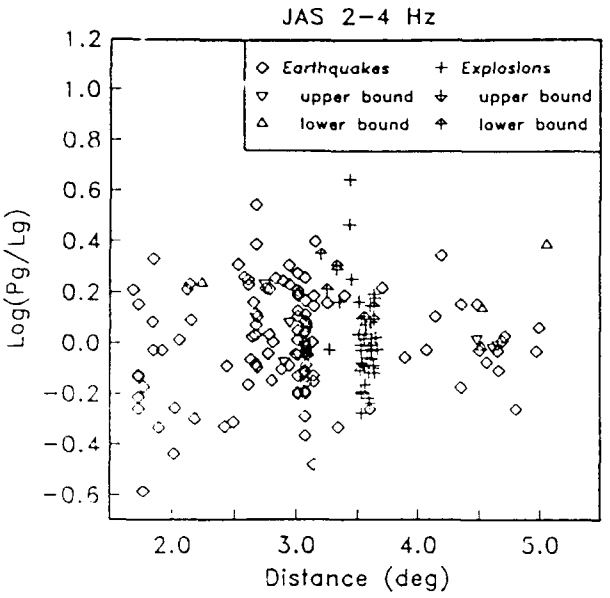


Figure 1. *Pg/Lg* ratios for the 2-4 Hz band at station JAS (Jamestown, California). Path- and frequency-dependent distance corrections have been applied to all events. An additional depth correction has been applied to explosion data to normalize them to a shot depth of 200 m.

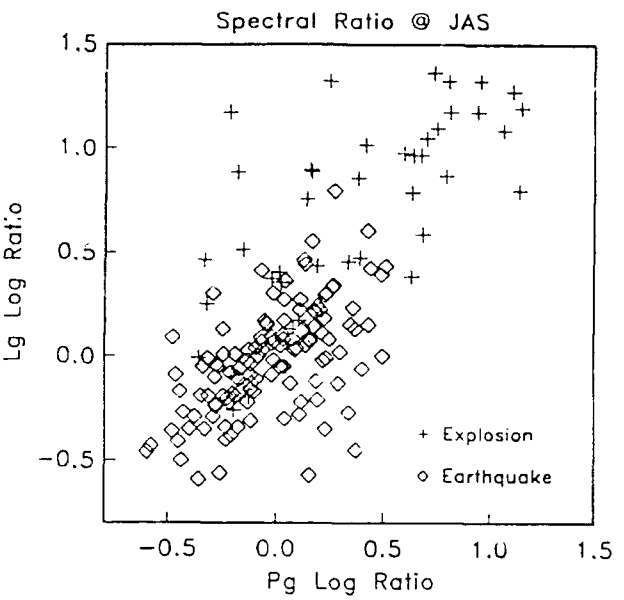


Figure 2. Spectral ratios for *Pg* and *Lg* phases at station JAS. Path-dependent corrections have been applied to all events.

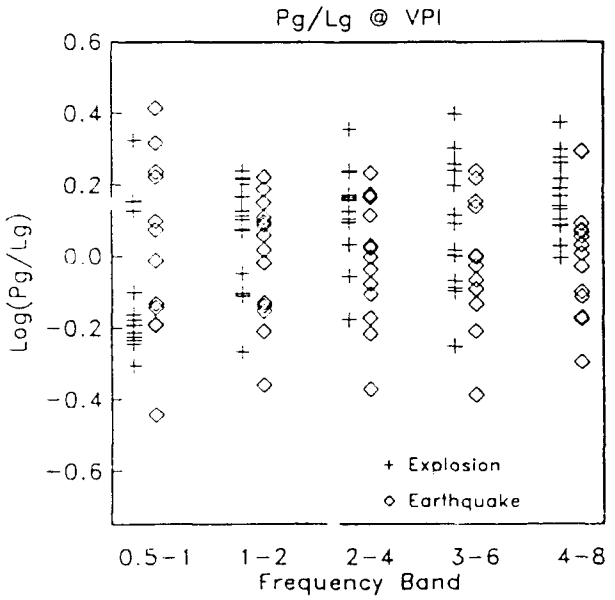


Figure 3. Network average *Pg/Lg* ratios for the Virginia Polytechnic Institute (VPI) network in five frequency bands.

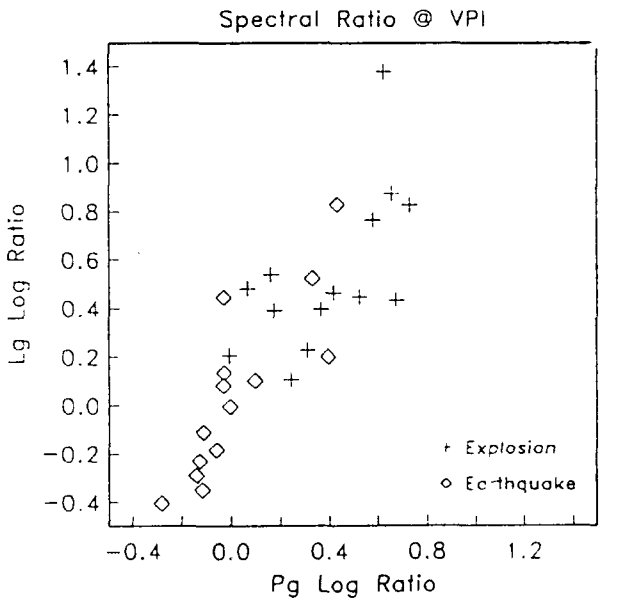


Figure 4. Network average spectral ratios for *Pg* and *Lg* phases at the VPI network.

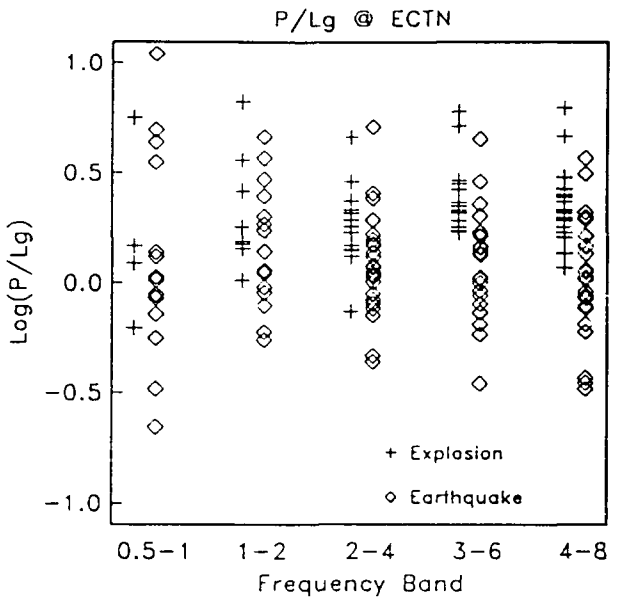


Figure 5. Network average *P/Lg* ratios for the Eastern Canada Telemetered Network (ECTN) in five frequency bands.

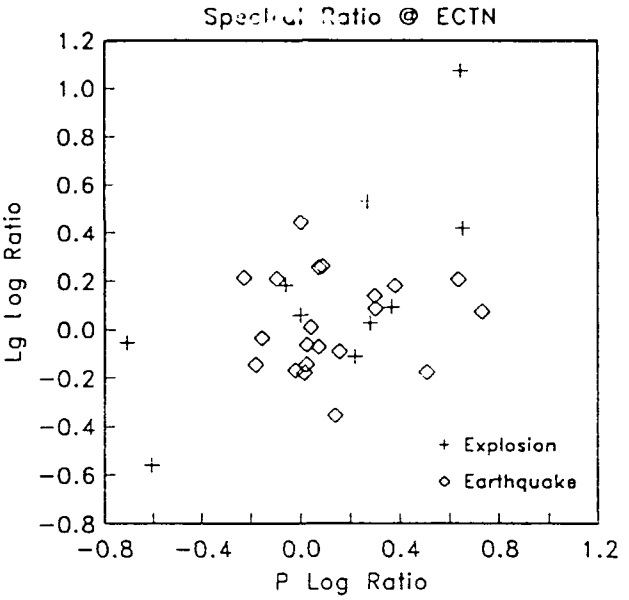


Figure 6. Network average spectral ratios for *Pg* and *Lg* phases at the ECTN.

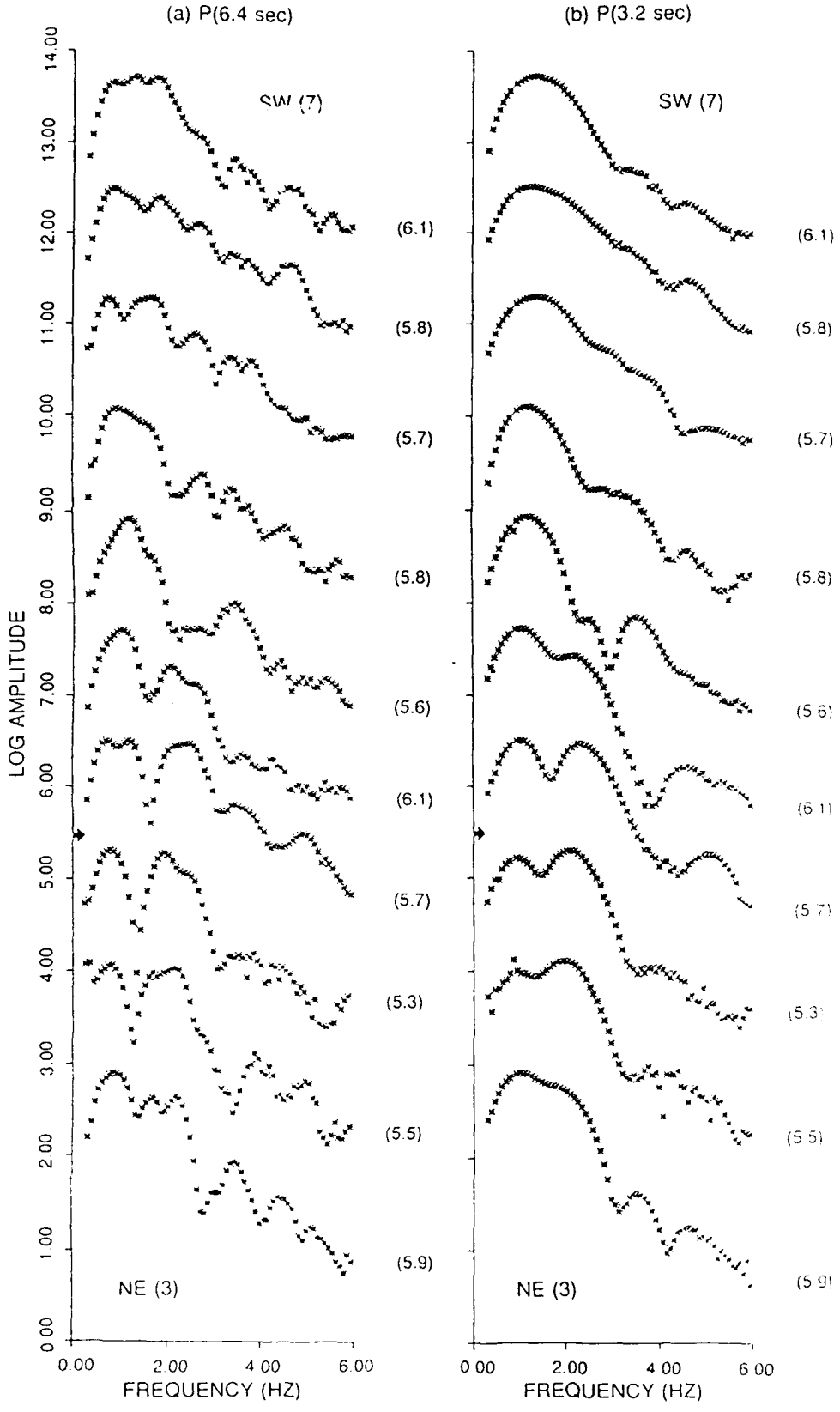


Figure 7. Source spectra (derived from EKA array data) of 10 explosions with shot points lying approximately along a SW-NE profile across the test site, for (a) P(6.4 sec) and (b) P(3.2 sec) windows. Note the gradual build-up of the low-frequency nulls which are more dominant in (a) than in (b). Numbers (in parentheses) next to the spectra indicate m_b.

CHARACTERIZATION OF EXPLOSIVE SOURCES AT NEAR DISTANCES

Lane R. Johnson and T. V. McEvilly

University of California, Berkeley

Contract No. F19628-90-K-0055

OBJECTIVE

One of the important general objectives of this research effort is the collection of critical data sets necessary to test various hypotheses concerning seismic waves generated by explosions and earthquakes. In previous years a number of special experiments have been conducted with the purposes of testing the effects of source depth, source size, and source medium on the seismic yield of explosions. In June of 1991 another such experiment was performed. The OSSY2 (On Site Seismic Yield - 2) experiment was a collaborative effort between scientists at UC Berkeley, the Lawrence Livermore National Laboratory (LLNL), and Southern Methodist University. It was performed in Yucca Valley at the Nevada Test Site (NTS). One of the objectives of this experiment was to demonstrate a method for using chemical explosions to estimate the yield of nuclear explosions.

RESEARCH ACCOMPLISHED

The method of estimating the seismic yield of nuclear explosions consists of four primary stages. First, a VSP survey is used to characterize the material properties in the vicinity of a possible nuclear explosion. Second, surface recordings of small buried chemical explosions are used to calibrate the moment tensor method of inferring source properties from measurements of radiated elastic waves. Third, free field accelerations registered near the chemical explosions are used to provide further checks on the moment tensor inversions and also contribute direct measurements of the coupling of explosive energy into displacements of the surrounding medium. The final stage is the recording of surface displacements when a nuclear explosion is detonated and the use of the moment tensor method to infer the yield of the nuclear explosion.

The experimental phases for the first three stages of this process were completed in June. The analysis of the data collected during these three stages is now underway and preliminary results are given below. The fourth stage is likely to occur in late 1991.

On June 27, 1991, two chemical explosions of 100 pounds each were detonated in hole UE4av of Yucca Valley of the Nevada Test Site. The charges were at depths of 522 and 494 meters below the surface. Free field measurements were made in the

range of between 1.5 and and 52 meters of the first explosion, and between 1.5 and 24 meters of the second explosion. Three component accelerations were measured at the surface along four different azimuths at horizontal ranges between 1.5 and 1600 meters.

Prior to the detonation of the chemical explosions, VSP surveys were performed for three-component receivers in the drilled hole at depths between 40 and 520 meters, with three-component vibrators positioned along four azimuths at distances between 52 and 1600 meters. Because the results from the VSP survey are used in the analysis of data collected from the chemical explosions, the initial analysis has concentrated on the VSP survey.

The experimental arrangement for the VSP part of the experiment is shown in Figure 1. A full nine-component recording was accomplished for each position of source and receiver. The basic purpose of this stage of the experiment is to fully characterize the P and S velocities in the region surrounding the explosions and also to calibrate the propagation paths to the surface receivers during the chemical and nuclear explosions. A sample of the VSP results is shown in Figure 2. This shows all nine components of the seismograms that were obtained for a surface source at a distance of 686 meters and a receiver at a depth of 515 meters. The source has been deconvolved from these traces. The arrival of the P and S waves is fairly easy to determine, given a complete VSP section, and the estimated arrival times are marked in the figure. Note that the S waves from the SH and SV source have different arrival times, indicating some degree of anisotropy in the medium between this source and receiver.

A preliminary analysis of the VSP arrival times has been used to estimate an approximate one-dimensional velocity structure for the medium surrounding the drilled hole. These results are shown in Figure 3. The P velocity shows a general increase in velocity down to a depth of about 270 meters, which is the thickness of the alluvium at this location. At this depth there is a decrease in velocity, which corresponds to the beginning of the tuff section, and then another gradual increase in velocity in the remainder of the tuff section. The VSP survey did not extend into the Paleozoic rocks at this site. The S velocities parallel the P velocity at a lower value, but do not show the marked decrease in velocities near a depth of 270 meters. If further analysis confirms the general validity of these velocity estimates, then we have evidence for rather different values of Poisson's ratio for the alluvium and tuff.

The data collected from the chemical explosions have been inspected and appear to be of excellent quality. The surface accelerations were recorded over a wider bandwidth than in any of our previous experiments, and it will be interesting to determine if useful information is contained in this increased bandwidth. The analysis of these data will proceed as soon as the analysis of the VSP data is completed.

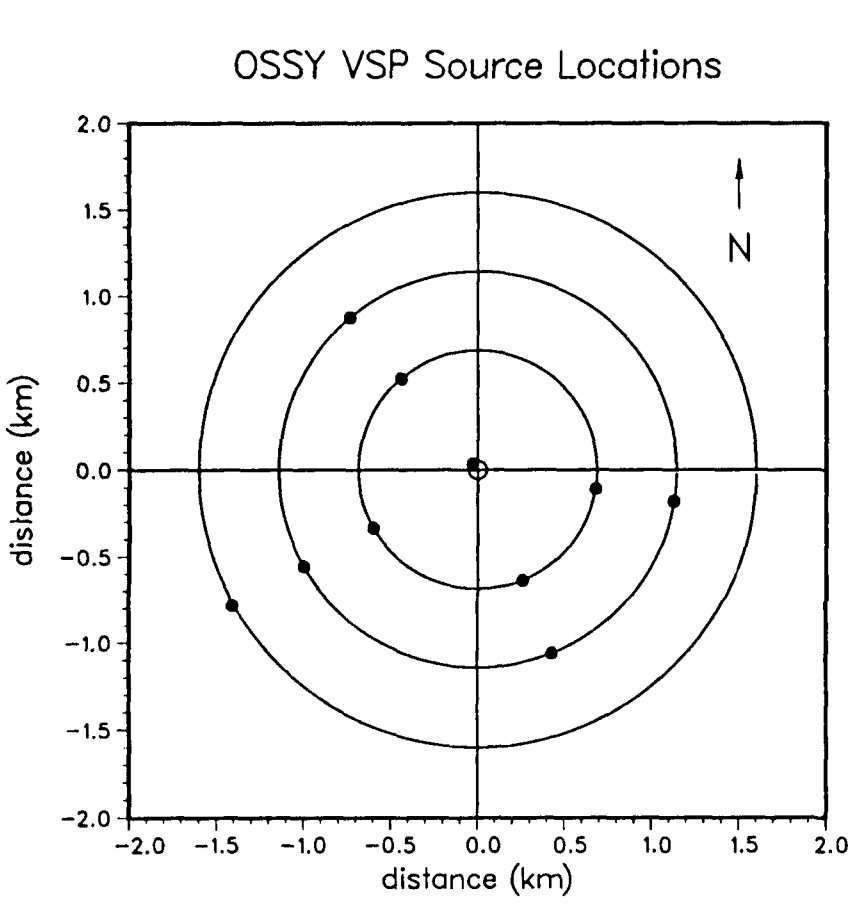
CONCLUSIONS AND RECOMMENDATIONS

The analysis of these data is still in progress so conclusions given at this time must be considered preliminary. However, the following general conclusions seem warranted at the present time:

1) The VSP survey produced high quality data with coverage and resolution sufficient to estimate three-dimensional velocity models for both P and S waves in the medium surrounding the drilled hole.

2) The preliminary analysis of the VSP indicates that there may be significant anisotropy present at this site, as indicated by the difference between the velocities of SV and SH components of S waves. Further analysis will be required to estimate the lateral and vertical extent of this possible anisotropy.

3) Both the surface network and the free-field accelerometer appear to have produced high-quality data from the chemical explosions. The analysis of these data will proceed as soon as the results of the VSP analysis are available.



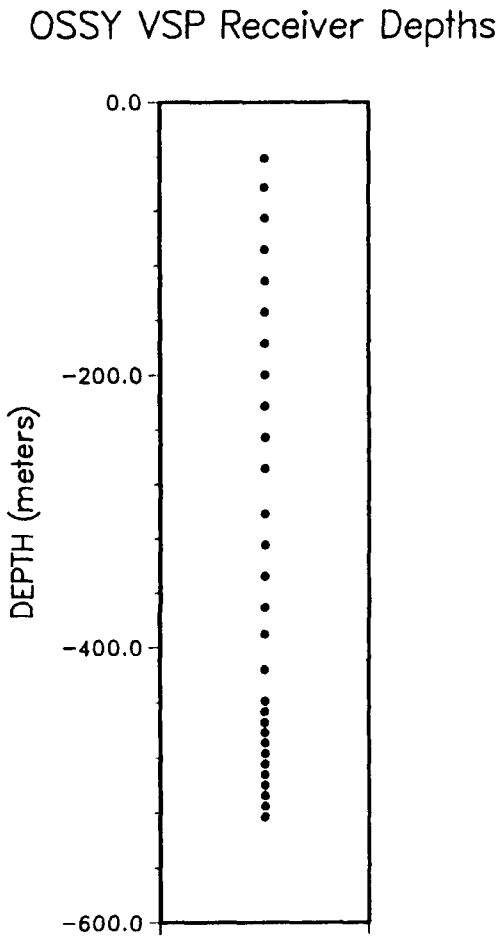


Figure 1. Locations of the VSP vibrator sites (plan view at left) and locations of the VSP receiver sites in the drilled hole (depth section at right). The vibrator sites were arranged along four different azimuths and on four rings having radii of 52, 686, 1143, and 1600 meters, respectively. The surface array of three component receivers occupied the same positions as the VSP vibrator sites during the chemical explosion stage of the experiment.

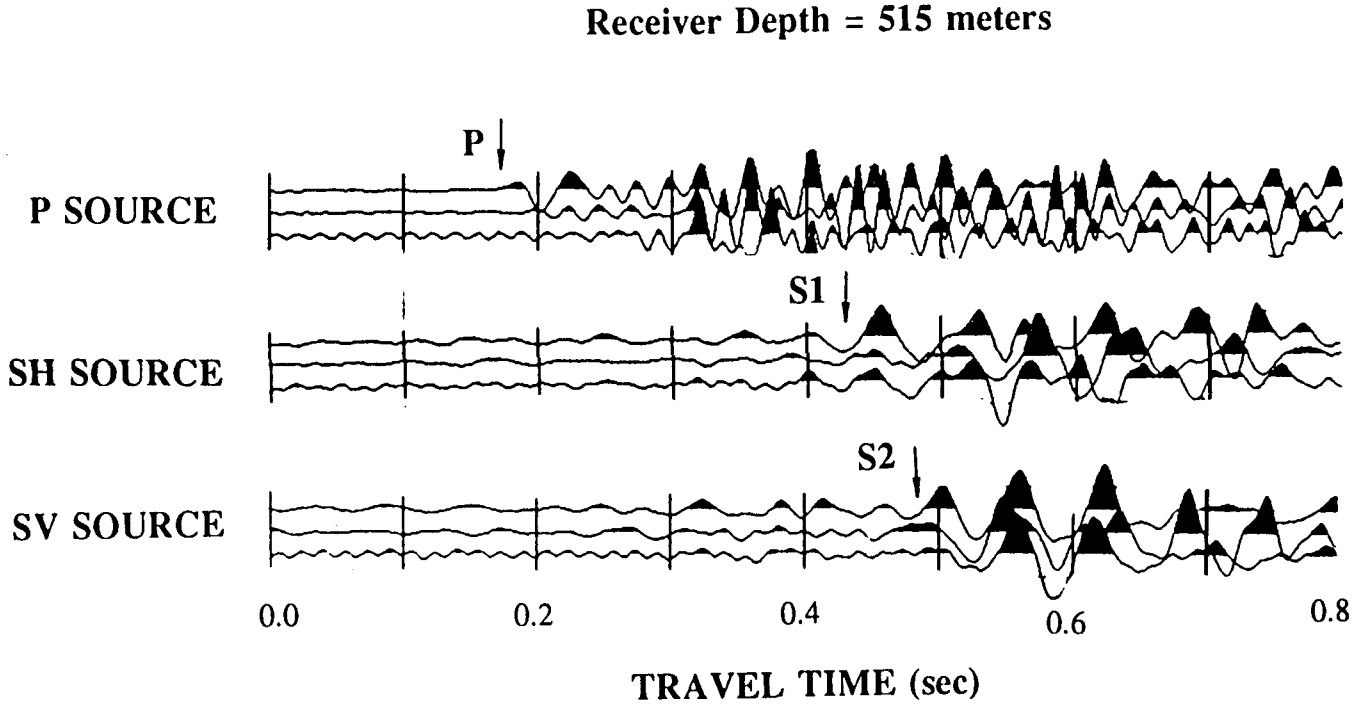


Figure 2. Samples of the deconvolved VSP seismograms that were obtained for one combination of source and receiver location. The source was at a horizontal distance of 686 meters.

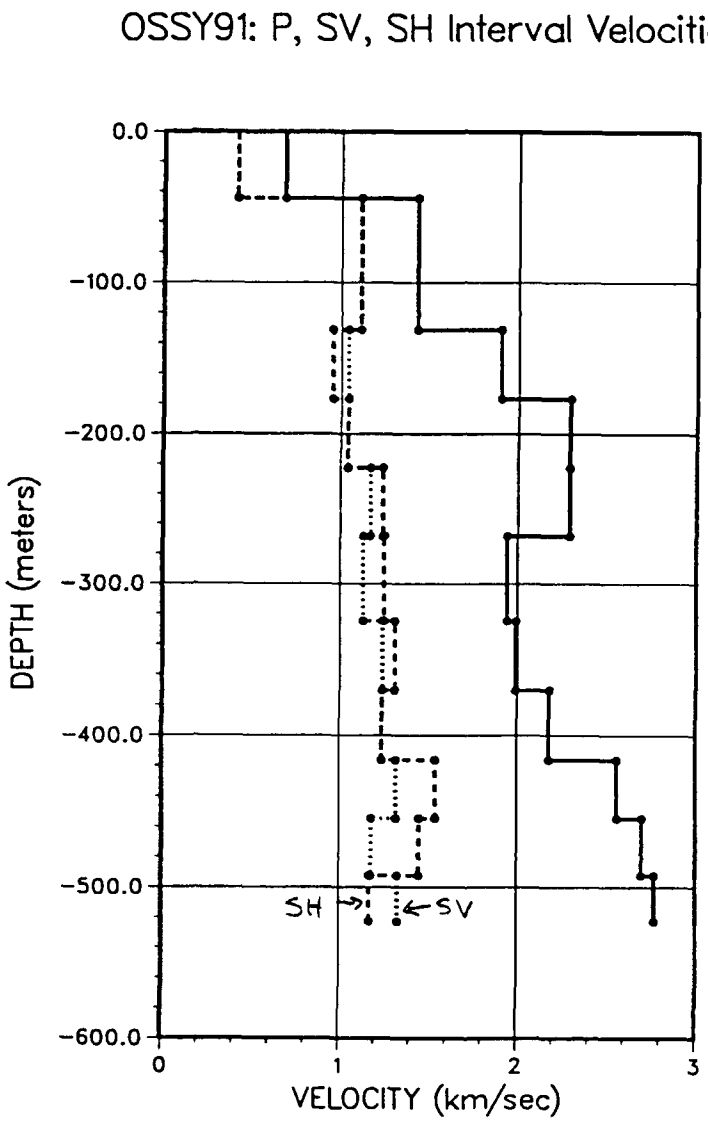


Figure 3 Preliminary one-dimensional velocity sections estimated by calculating interval velocities from the arrival times picked on the VSP seismograms.

PROCESSES CONTRIBUTING TO THE CODA OF REGIONAL SEISMOGRAMS

B.L.N. Kennett, M.G. Bostock

Research School of Earth Sciences,
Australian National University,
G.P.O. Box 4, Canberra ACT 2601
Australia

GRANT: AFOSR-89-0330

OBJECTIVE

A common feature of regional seismograms is an extended coda following Pg and Lg with an approximately exponential decay in time. This energy is usually interpreted as arising from scattering in the neighbourhood of the source and receiver. In some cases portions of the coda have distinctive azimuth and slowness characteristics which can be associated with particular scattering features. We have used a combination of theoretical modelling and observations of regional phases to look at the nature of the scattering processes which influence guided S waves which are particularly prominent on regional seismograms.

We have previously been able to develop techniques for describing the multiple scattering of guided wave trains by distinct scatterers. This approach allows the scattering effect of a number of scatterers to be built up recursively by successive addition of scatterers. The full pattern of multiple scattering can be included as well as interconversion between Love and Rayleigh waves. Such interconversions can be important in changing the balance between the different components of ground motion and so modifying the apparent nature of a source.

We have now been able to extend this type of scattering development to examine the effects of heterogeneity in the neighbourhood of the source or the receiver. The assumption built into into this development is that the heterogeneity in the neighbourhood of the source or receiver, can be locally represented by roughly cylindrical structure modulated by an angular term. The velocity structure has to be smooth but multiple interactions within the structure can be included. This new calculation scheme provides a means of assessing the influence of near-source structure on the polarisation characteristics of the seismic wavefield and hence on the far-field character of the source. This development should be useful in understanding the character and limitations of proposed source discriminants.

RESEARCH ACCOMPLISHED

Widespread observations of wave scattering and multipathing indicate that the propagation of regional seismic phases in the Earth's crust, dominated by fundamental and higher-mode surface waves, is an example of a process which is extremely sensitive to lateral heterogeneity. This heterogeneity can exist in various forms and in efforts to distinguish between the effects of scattering by heterogeneity and the signature of the wavefield imparted at the source it is

desirable to develop techniques which i) model regional phases in appropriate Earth models and ii) provide physical insight into the mechanisms involved.

We have developed a new technique, related to the surface wave T-matrix introduced by Bostock (1990), to model the effect of near source heterogeneity on the radiation patterns of short-period regional phases. The use of a multi-mode representation for the incident and scattered waves, and integral relations describing the interaction of the wavefield with a region of heterogeneity of vanishingly small volume allow us to derive differential equations which describe the scattering response of a regionof arbitrary heterogeneity. By this means we can investigate the interconversion between Rayleigh and Love waves induced by heterogeneity in the near source region.

Our starting model consists of a harmonic source located at some depth within a stratified waveguide. Deviations from lateral homogeneity exist in the vicinity of the source and are defined in terms of perturbations from a reference structure. The presence of this heterogeneity disrupts the propagation of the generated wavefield and affects the dependence of amplitudes as observed in the far field. In particular, it may cause energy transfer between Love and Rayleigh waves and among modes of a common wavetype. Regional seismograms recorded from purely explosive sources, which must in theory generate purely SV-type energy, often exhibit significant energy on the transverse component (Blandford, 1981). The nature of the near field descriptions of Love and Rayleigh waves suggest that this class of near-source heterogeneity may contribute significantly to wavetype conversion.

In order to describe the scattering effects of an arbitrary configuration of near source heterogeneity we locate the source at the origin of a cylindrical coordinate system and investigate the effect of scattering from a thin cylindrical shell of vanishing width centered about the z-coordinate axis. The shell exhibits arbitrary lateral heterogeneity expressed in terms of perturbations from the embedding reference medium The reference medium is taken to be such that the deepest layer has increasing velocity with depth and then the wavefield in this region can be fully described by a superposition of the eigenfunctions of the trapped modes on the stratifications. For each frequency we then represent the incident waves on the scatterer in terms of vector cylindrical harmonics which correspond to waves emerging from the origin. Likewise, the boundary conditions dictate that the scattered waves produced by the heterogeneity must exhibit an outgoing character in the reference medium outside the shell, and so this component of the scattered field is expanded in the same set of vector cylindrical harmonics. The scattered waves in the reference medium within the thin shell are represented by forms of vector cylindrical harmonics which are regular at the origin. These two sets of basis functions need to be indexed by wavetype (Love, Rayleigh), modal order and azimuthal order.

The reflection and transmission characteristics of the wavefield scattered from the shell are then determined using the Born approximation and by employing a basis function expansion for the Green's function of the laterally homogeneous, stratified reference medium. The accuracy of this approximation improves as the magnitude of the heterogeneity perturbations or the volume of the heterogeneity decreases. In the limit of vanishingly small volume the Born approximation is exact. This observation allows us to build up the reflection/transmission response of an arbitrary configuration of near source heterogeneity using

invariant imbedding techniques and considering the heterogeneity as a sequence of individual, laterally heterogeneous, welded shells of vanishing width. The result is a system of matrix differential equations of Ricatti type which describe the evolution of the reflection and transmission matrices for the heterogeneity as additional shell layers are added. This description incorporates all multiple scattering interactions and is in fact the extension of Kennett's (1984) coupled mode treatment to 3-D laterally varying media.

Although strictly speaking, the reflection and transmission matrices have infinite dimensionality, numerical implementation requires truncation to finite sizes. In addition, each matrix element requires the evaluation of a costly 2-D surface integral. It is possible by representing the azimuthal character of the heterogeneity in terms of Fourier components and observing relationships among the various integrand quantities to avoid a significant amount of unnecessary computation and thereby examine a range of near source heterogeneity configurations.

We have assembled two simple models to examine the influence of near source heterogeneity on the character of the transmitted wavefield observed at large distances for single incident Rayleigh modes generated by an explosive source. In each case the heterogeneity is represented by velocity perturbations of both signs and absolute value up to 4% compared with the surrounding 3 layer reference medium, and is distributed over the volume of a thick cylindrical shell. The heterogeneity is tapered so as to vanish at the shell boundaries. The models differ in the azimuthal dependence of the heterogeneity i) a model exhibiting a dominantly $\cos\theta$ variation in properties, and ii) a model comprising equal contributions from $\cos\theta$, $\cos2\theta$, $\cos3\theta$ components (see figure 1).

The radiation patterns for various incident/transmitted mode combinations are presented in figure 2 for model 1. Note the contrast in radiation patterns for the various combinations of unconverted transmitted modes, that is R1-R1, R3-R3, R6-R6, R9-R9. The radiation patterns deviate increasingly from the purely circular case, which we would expect in case of no heterogeneity, as the order of the mode increases. This is because the higher order modes carry a larger proportion of their energy over the depth range where the material perturbations are most significant. Indeed there is a significant reduction in energy levels of the transmitted mode in the positive and negative x-directions for R9-R9 due to reflections within the shell of heterogeneity. For the low order modes these effects are not nearly so pronounced as the perturbations effect them less and we observe more of a focussing/defocussing behaviour. These results may be compared with the radiation patterns for conversion between the same Rayleigh modes and the Love modes with the closest correspondence in character for which relatively complex lobate patterns are commonly found,

Figure 3 shows the partitioning of scattered energy as a function of modal order for incident modes R1, R3 and R6. It indicates that rather continuous lateral variation in material properties of the model i) does not contribute significantly to energy transfer between Love and Rayleigh waves. This does not eliminate the possibility that near source scattering is important in generating Rayleigh-Love conversions but rather that this form of heterogeneity is less effective than scattering from more or less discontinuous structure.

The second model is more complicated in its horizontal description and consists of a large negative velocity perturbation straddling the positive axis and

three less significant positive velocity perturbations over the remainder of the azimuthal range (see figure 1). The radiation patterns for a selection of incident/transmitted mode combinations are shown in figure 4 and we observe that the amplitude of the converted scattered modes is largest in the general direction of the low velocity anomaly, a result which is not unexpected. The characteristics of the unconverted transmitted modes (R1-R1, R4-R4) are also predictable and include increased amplitudes (>10%) and increased phase delays over the angular window encompassed by the low velocity heterogeneity.

A similar development can be made to look at the effect of smooth velocity structure in the neighbourhood of a receiver. Now attention is focussed on the ingoing field which ultimately arrives at the receiver and the transmission effects can again be evaluated via the solution of matrix differential equations of Ricatti type.

CONCLUSIONS AND RECOMMENDATIONS

We have been able to develop a description of near-source or near-receiver propagation processes in the presence of a smooth but fairly rapidly varying velocity structure. The radiation patterns or receiver sensitivity for a given mode of propagation can be significantly modified by the presence of the smooth velocity structure and so distort the apparent magnitude seen in different directions. However, interconversion between Love and Rayleigh waves is not very significant even though the geometry would be favourable for such transfers.

This would suggest that the principal mechanism for modification of the polarisation of the seismic wavefield close to the source arises from scattering from sharp contrasts in seismic parameters. A similar mechanism would operate near a receiver and would be consistent with the observations of scattered arrivals associated with distinct topographic features. However the presence of fairly rapid smooth variations in velocity will be accompanied by focussing and defocussing effects which can modify the sensitivity of the receiver to arrivals from different directions.

REFERENCES

Blandford R., 1981, Seismic discrimination problems at regional distances, in *Identification of Seismic Sources - Earthquake or Explosion?*, pp 695-740, eds Husebye, E.S. & Mykkeltveit, S., D. Riedel Dordrecht.

Bostock, M.G., 1990, Surface wave scattering from discrete obstacles, *Geophys. J. Intl.*, **104**, 351-370.

Kennett B.L.N, 1984, Guided wave propagation in laterally varying media-I. Theoretical development, *Geophys. J R. astr. Soc.*, **79**, 235-255.

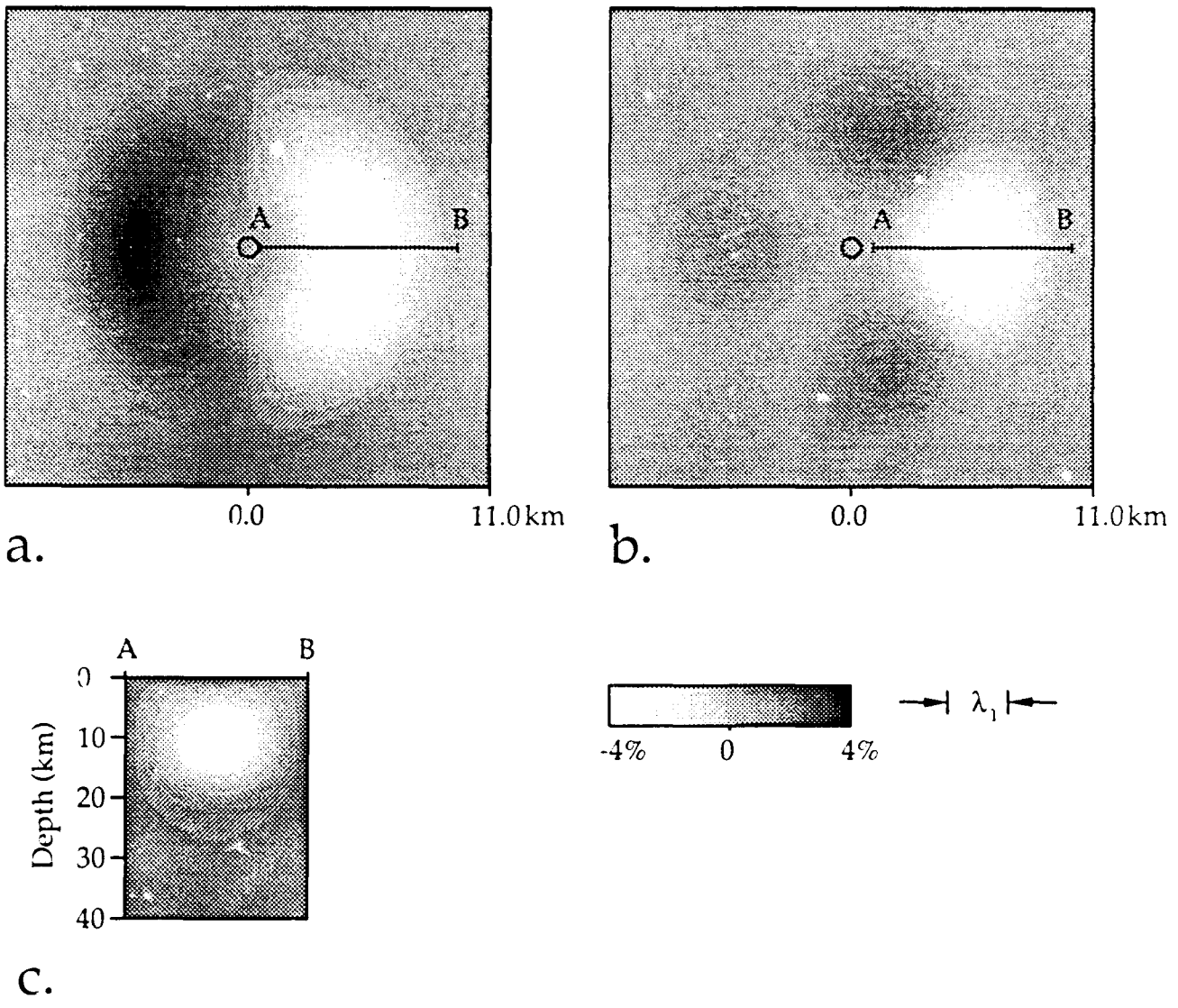


Figure 1. Model descriptions. a) Plan view of velocity perturbations considered in model 1. b) As in a) for model 2. c) Vertical section of velocity perturbations for models 1 and 2 along line A-B. The wavelength of the fundamental Rayleigh mode λ_1 is shown to scale with a) and b).

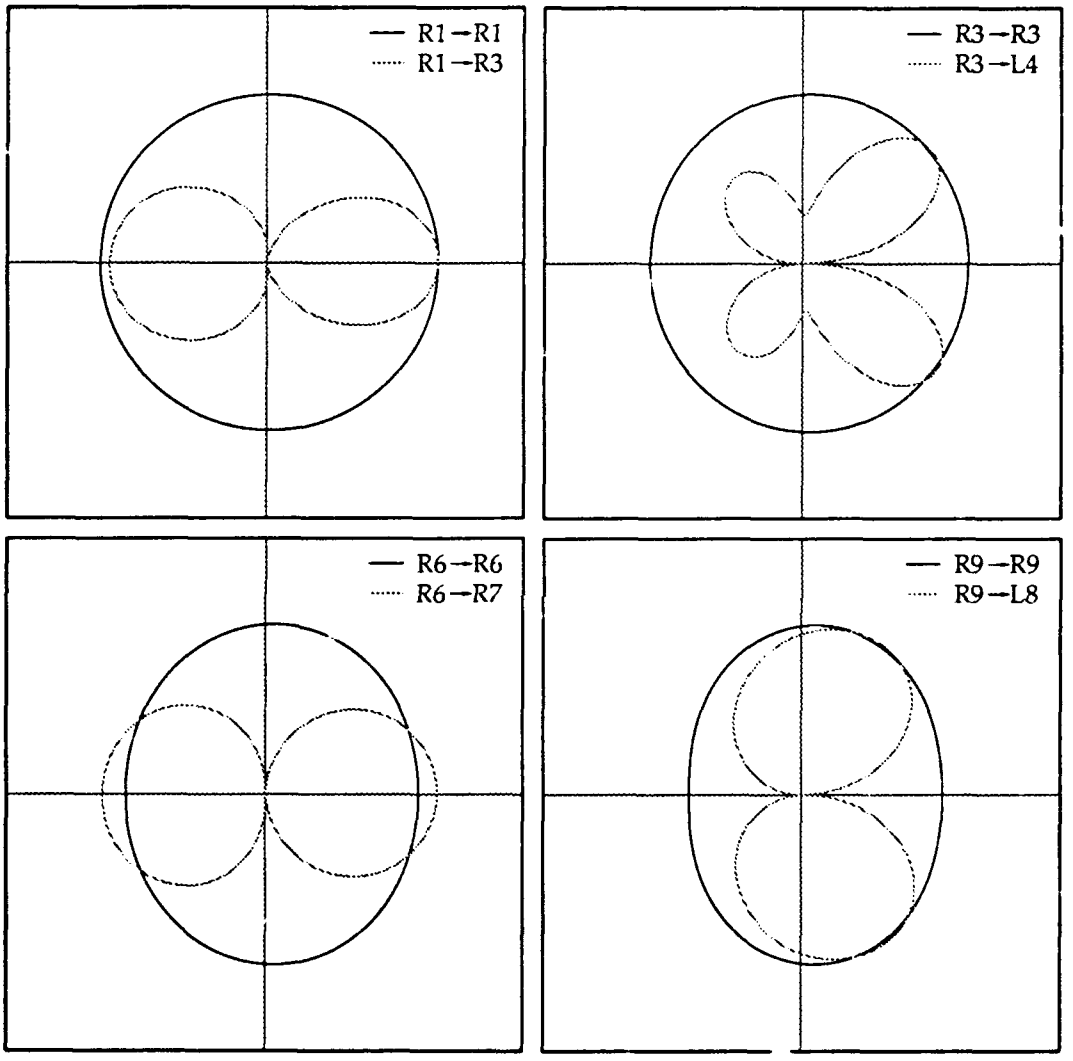


Figure 2. Radiation patterns of transmitted modes in the farfield for model 1. Note increased deviations from isotropy for unconverted modes as modal order is increased.

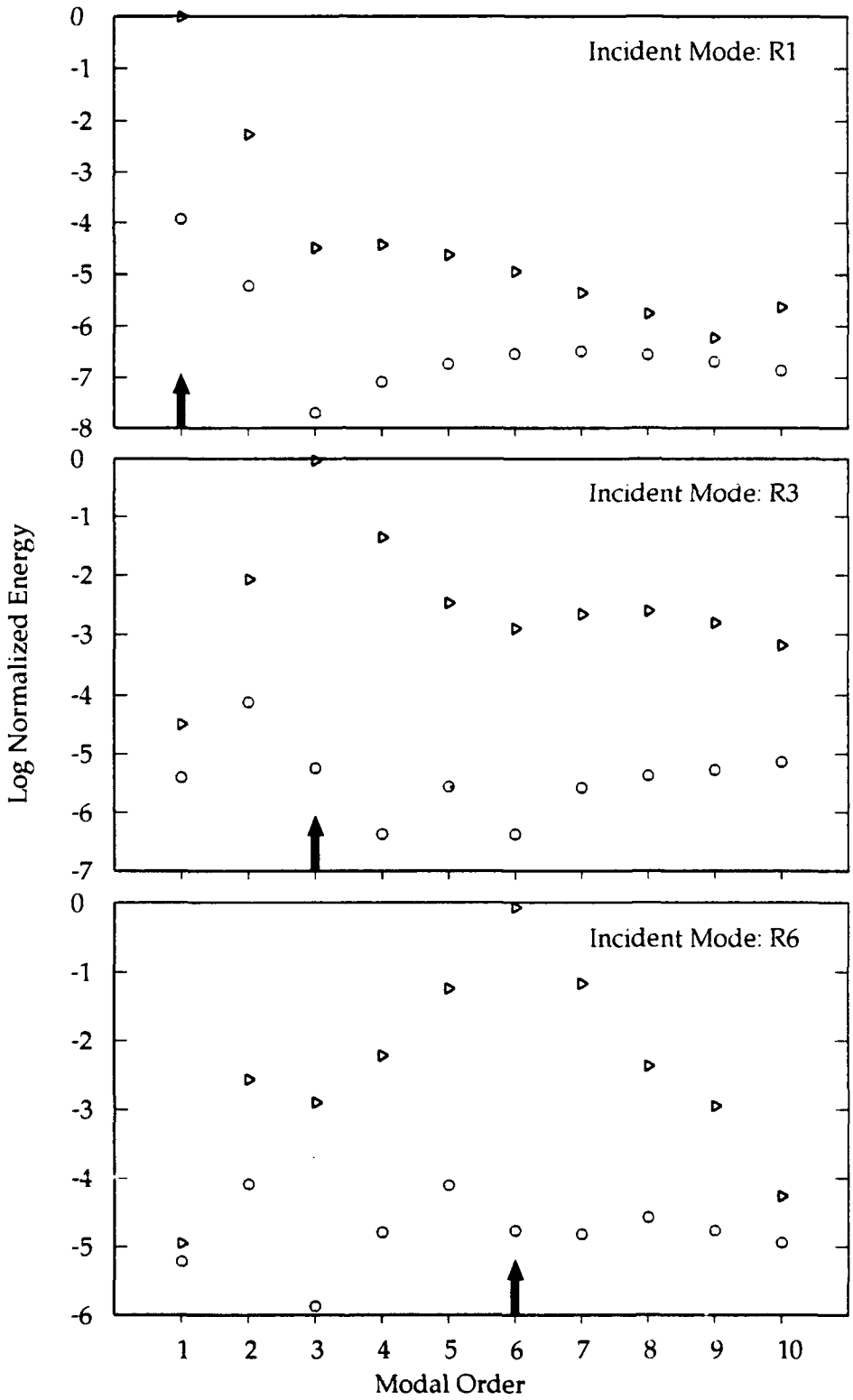


Figure 3. Modal energy spectra for model 1. Note the generally low levels of scattered Love wave energy.

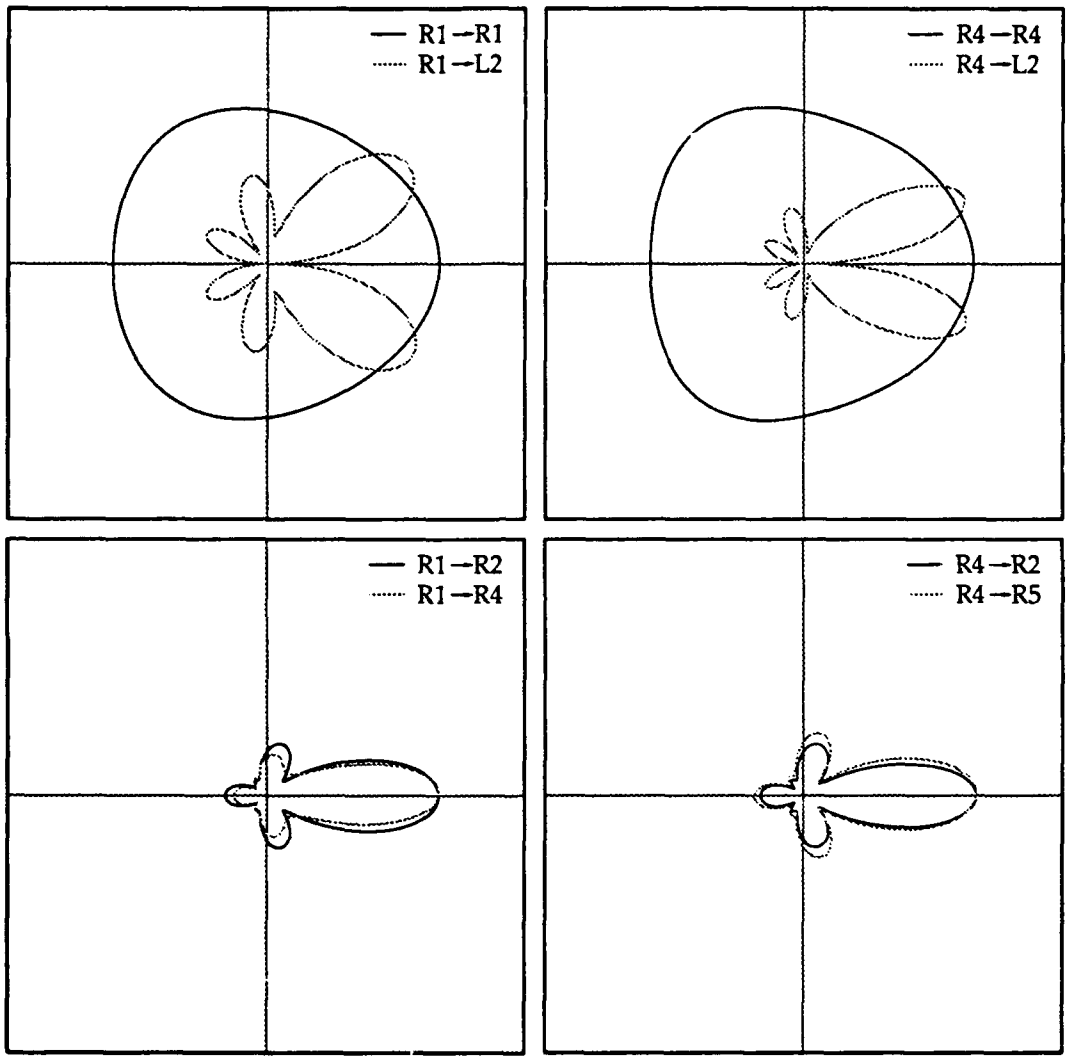


Figure 4. Radiation patterns of transmitted modes in the farfield for model 2.

THE DISTANCE DEPENDANCE OF REGIONAL DISCRIMINANTS

B.L.N. Kennett

Research School of Earth Sciences
Australian National University
G.P.O. Box 4, Canberra ACT 2601
Australia

GRANT: AFOSR-90-0352

OBJECTIVE

A number of the techniques which have been proposed for discriminating between different types of seismic sources at regional distances depend on the relative amplitudes of different P and S phases. Although the phase denoted in discrimination work as Lg is frequently the largest phase on a regional seismogram, it is known to be sensitive to variations in crustal structure. As a result attention has been transferred to Sn as a representative of the S wave radiation from the source, and comparison has been made with the Pn phase to characterise the P radiation.

However, detailed observations of the amplitude behaviour of Pn and Sn frequently show a very different dependence in the range 200 - 300 km away from the source. Whilst Pn is clear and separates distinctly from the rest of the P wavefield, Sn is often not discernable until distances around 300 km. Such behaviour has been observed on refraction surveys in Europe and from regional events in southeastern Australia.

In order to look at the causes of this behaviour and the way in which the Pn and Sn amplitudes vary with distance we have examined a wide range of long-range refraction profiles from the Eurasian area. We have also investigated the influence of topography at the crust-mantle boundary on the amplitude distribution to be expected from mantle phases such as Pn, Sn.

RESEARCH ACCOMPLISHED

A number of authors have noticed that the onset of the Sn phase around 200 km can be difficult to pick by comparison with the equivalent Pn phase even for those situations where the P coda is low. These observations come from a wide range of stable tectonic environments. For example, the phase association procedure used for locating earthquakes in southeastern Australia only declares an Sn phase when the estimated distance is greater than 300 km because of the difficulty in obtaining reliable picks at shorter distances. Such a low amplitude onset building to greater amplitude at longer ranges suggests that the S wave gradient is low in the uppermost mantle and then increases at a depth of 10 or so kilometres below the crust-mantle boundary. Recently Gajewski et al (1990) have

shown that this pattern of slow emergence of Sn is observed on many refraction profiles in western Europe and have noted also differences in the character of the Sg phases compared with the corresponding Pg arrivals.

In order to see whether the pattern of propagation of the mantle phases is consistent from region to region and also to investigate the evolution of the Sn/Pn amplitude ratio with distance we have searched for refraction recordings with good S wave arrivals in the distance range from 100 - 1000 km. Although much of the long-range profiles in Europe were originally recorded with three-component sensors, most of the interpretations have been based on the P wave data from the vertical component records and relatively few S wave sections have been published. However, sufficient S wave data exists for us to be able to make a comparison of the propagation characteristics of the P and S wave field.

As an example we present in figure 1 a comparison of P and S recordings at ranges from 200 - 800 km (Hirn, 1977) from a profile of instruments deployed across France to record a large explosion fired in the sea off Brest. The record sections are phased to concentrate attention on the mantle arrivals which in nuclear monitoring work we would normally term Pn and Sn. However we can see clearly from figure 1 that such phases have significant substructure and the almost constant apparent velocity is built up from a sequence of en-echelon phases which progressively become first arrivals as the distance increases. The interpretation of such arrivals in terms of a one-dimensional velocity model leads to very complex velocity distributions with multiple low-velocity zones (see e.g. Kind 1974), but it is very likely that much of the complexity arises from lateral heterogeneity in the structure in the upper most mantle (Fuchs & Schulz, 1976). A similar pattern of complex structure within the wavegroup characterised by Pn can be seen in the record sections presented by Yegorkin & Chernyshov (1983) from peaceful nuclear explosions in the Soviet Union.

In general the quality of S data from explosive sources is not very good because the P coda is energetic and so we are looking for S arrivals against a relatively noisy background. However some experiments, especially in PreCambrian terrains where the shear velocities are relatively high, do give a very good representation of the S wavefield even on vertical component instruments. Figure 2 shows P and S wave sections from the same shotpoint point A in a Finnish-Polish refraction experiment «Sveka» across part of the Baltic Shield in southern Finland (Luosto et al 1984, Grad & Luosto 1987). The S arrivals are very clear and give a good general agreement with the pattern of the P arrivals. In this case the crust is rather thick and the transition from Moho reflections to refractions occurs at the end of the profile. Interestingly the reflection from the Moho around 160 km offset is clearer on the S wave section. Rg is only visible to 100km.

The quality of the S records in figure 2 is surpassed by the remarkable set of records from a further Finnish-Russian experiment «Baltica» which lay further to the southeast (closer to the Russian border). The data from shot point B is shown in figure 3 and at first sight is difficult to distinguish which is the P and which is the S profile (other than by examining the timing of the Rg phase). The correspondence of the phases is exceptionally close and here, at least, there is a very distinct Sn arrival beyond 200 km. The reversed profile from shotpoint G has less clear Pn and Sn arrivals with a cross over around 3020 km. Despite the

pronounced topography on the Moho good mantle arrivals are seen on these profiles.

In association with the observational studies we have also considered ways of modelling the Pn and Sn phases which can incorporate the effects of lateral heterogeneity. From the Finnish examples, there is a need to be able to include some allowance for topography on the Moho. A promising technique is to replace the effect of the interface by a generalised transmission coefficient so that a single incident plane wave couples into a spray of plane waves on the underside of the interface. Such a scheme can allow for the focussing and defocussing effects associated with the shape of the Moho surface as the waves comprising the Pn and Sn phases enter and leave the upper mantle .

It will be difficult to assess the amplitude behaviour of the Pn and Sn phase for the area around a particular receiver site without careful calibration, and the analysis of regional phases will need to be adapted to take the nature of the particular phases into consideration. The maximum amplitude within a specified group velocity window may not be the best measure of the P or S wave content of the seismogram.

CONCLUSIONS AND RECOMMENDATIONS

We have been able to demonstrate that the amplitude behaviour of Pn and Sn with distance is quite complex and that it is necessary to look at the anatomy of the phases in order to understand the potential performance of some regional discriminants. In detail the Pn and Sn phases tend to break up into a sequence of overlapping branches associated with fine structure in the upper part of the lithosphere. Anomalously low Sn amplitudes can arise between 200 and 300 km away from the source.

The current class of regional phase discriminants based on averaged behaviour of seismic phases such as Pn and Sn could give misleading results in some distance ranges because of the way in which the peak amplitudes in the requisite time windows shift between different wave groups. Such effects are difficult to pick up from isolated earthquakes or mine blasts but are evident in long range refraction profiles.

REFERENCES

Fuchs K. & Schulz K., 1976. Tunneling of low-frequency waves through the subcrustal lithosphere, *J. Geophys.*, **42**, 175-190.

Gajewski D., Stangl R., Fuchs K. & Sandmeier K.J., A new constraint on the composition of the topmost continental mantle - anomalously different depth increases of P and S velocity, *Geophys. J. Int*, **103**, 497-507.

Grad M. & Luosto U., 1987. Seismic Models of the crust of the Baltic shield along the SVEKA profile in Finland, *Annales Geophysicae*, **5B**, 639-650.

Hirn A., 1977. Anisotropy in the continental upper mantle: possible evidence from explosion seismology, *Geophys. J. R. astr. Soc.*, **49**, 49-58.

Kennett B.L.N., 1977, The inversion of long-range refraction profiles, *J. Geophys*, **43**, 243-256.

Kind R., 1974. Long range propagation of seismic energy in the lower lithosphere, *J. Geophys.*, **40**, 189-202.

Luosto U., Lanne E., Korhonen H., Guterch A., Grad M., Materzok R. & Perchuc E., Deep structure of the Earth's crust on the SVEKA profile in central Finland, *Annales Geophysicae*, **2**, 559-570.

Yegorkin, A. V. & Chernyshov, N.M., 1983. Peculiarities of mantle waves from long-range profiles, *J. Geophys.*, **54**, 30-34.

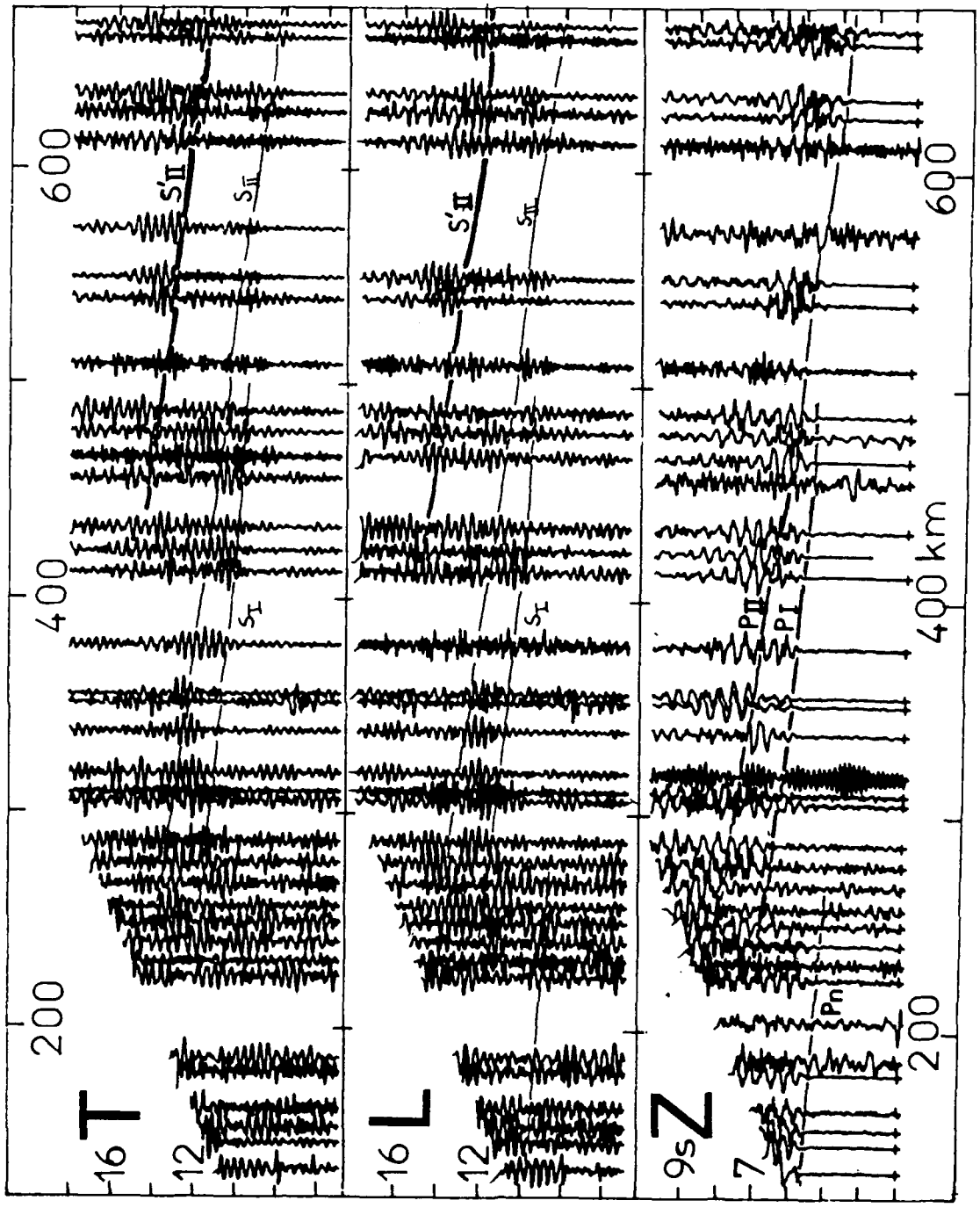


Figure 1: Three component record sections for a large explosive shot off the French coast recorded across a long range profile in France (after Hirn 1977). Reduction velocity for the Z section is 8 km/s, whereas for the L and T sections the velocity is 4.62 km/s



Figure 2: Configuration of the «Sveka» and «Baltica» refraction experiments in Southern Finland

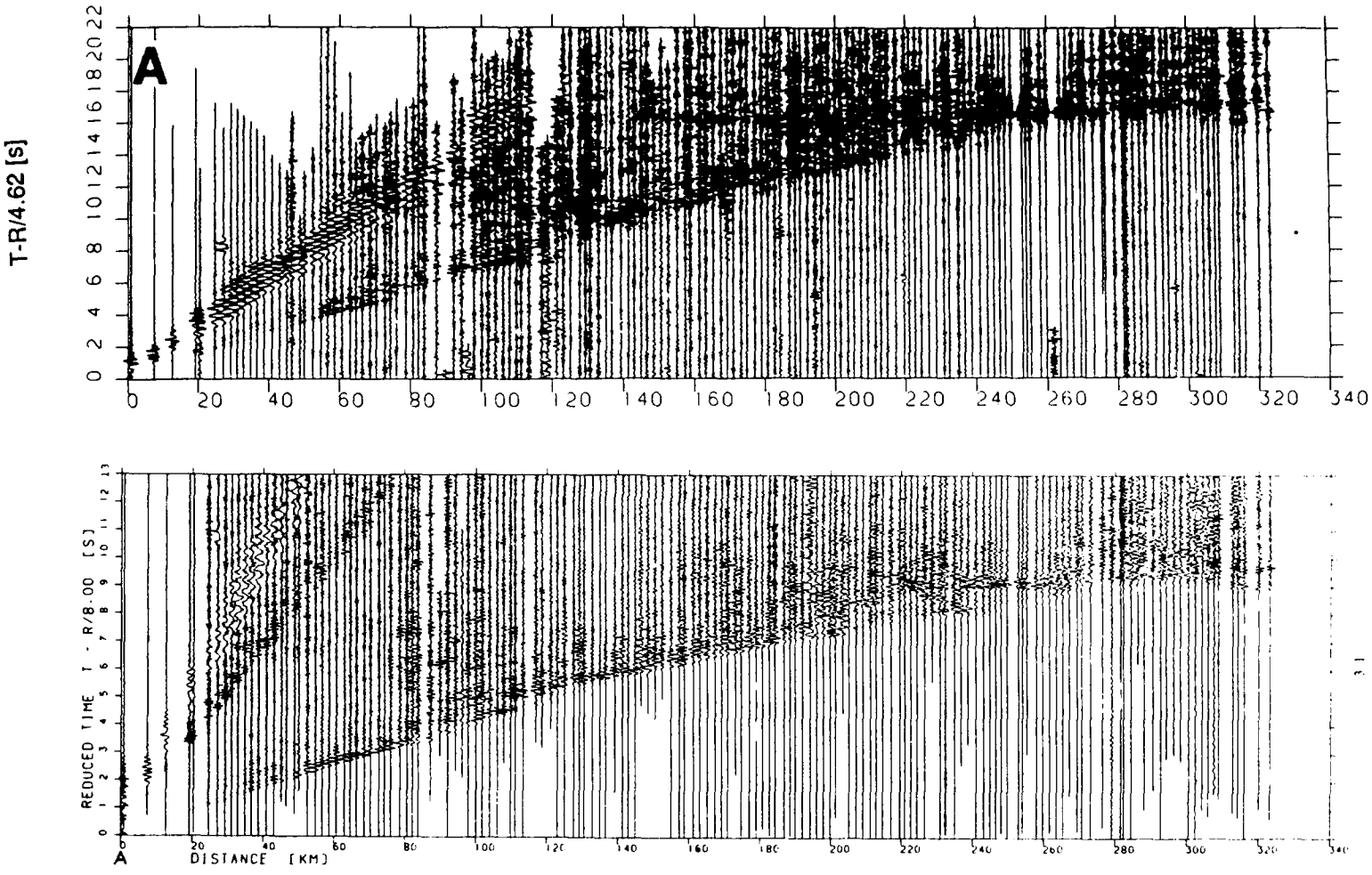


Figure 3: Comparison of P and S record sections from the «Sveka» refraction profile in Finland using vertical component seismometers, the traces are amplitude normalised. The reduction velocity for the P section is 8 km/s, and for the S section it is 4.62 km/s (after Luosto et al 1984, Grad& Luosto 1987).

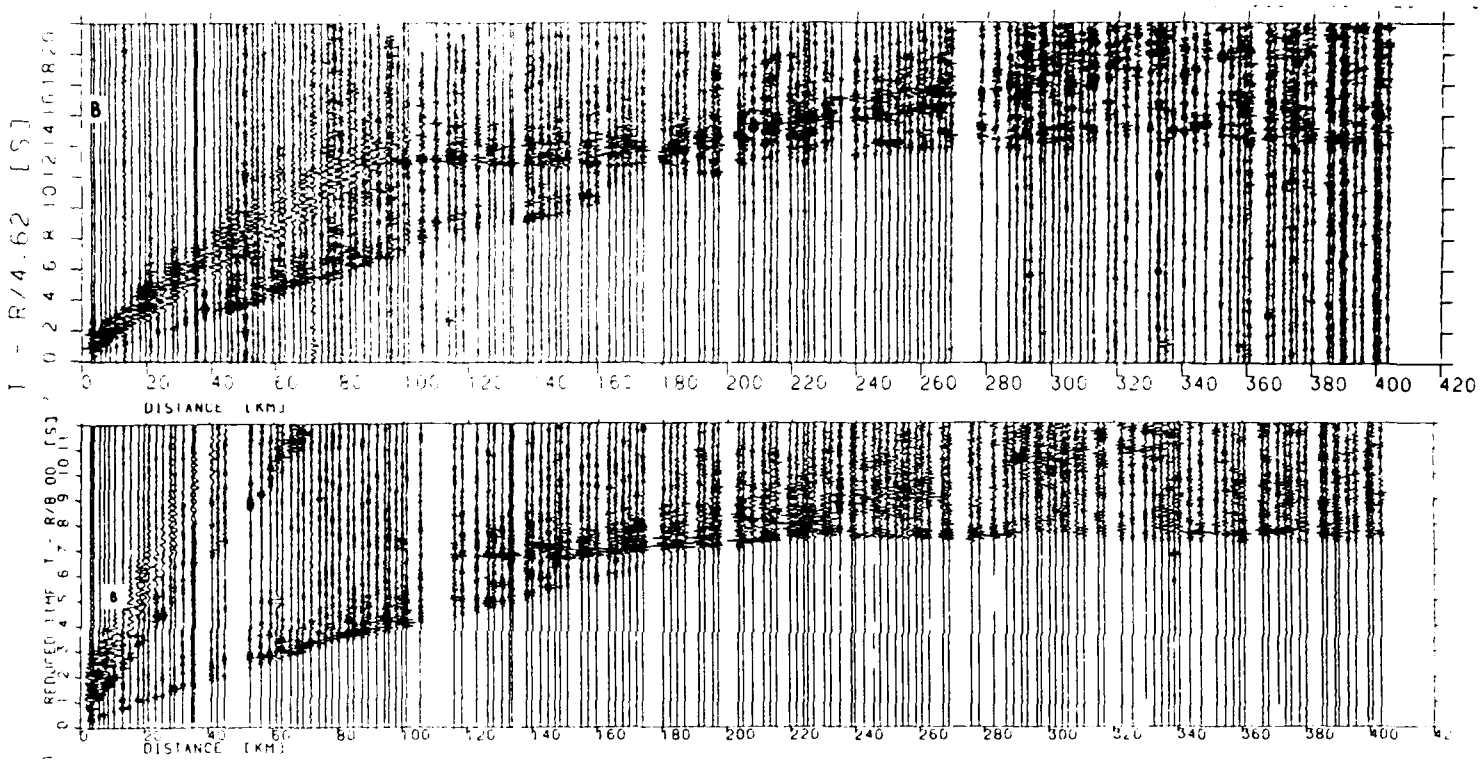


Figure 4: Comparison of P and S record sections from the «Baltica» refraction profile in Finland using vertical component seismometers, the traces are amplitude normalised. The reduction velocity for the P section is 8 km/s, and for the S section it is 4.62 km/s

SEISMIC PHASE AND EVENT LABELING USING ARTIFICIAL NEURAL NETWORKS*

R. T. Lacoss, S. R. Curtis, R. K. Cunningham, M. Seibert
M.I.T. Lincoln Laboratory
CONTRACT: F19628-90-C-0002

August 15, 1991

1 OBJECTIVE AND INTRODUCTION

The overall objective of our research is to develop artificial neural networks to perform specialized recognition functions for nuclear test monitoring systems such as the DARPA IMS. The research this year has concentrated on the labeling of seismic phases, labeling of seismic events, and estimation of arrival times. The goal is to develop networks that will be integrated into the IMS to improve its automatic performance.

During the past year, the greatest amount of work was done on phase labeling, with encouraging results. Initial experiments with event labeling have also been promising. Initial experiments with arrival time estimation were not very promising and that work has been put aside to concentrate on phase and event classification.

The data used for this work are parametric data from the Center for Seismic Studies and an Arcess/Noress waveform data base of over 200 events that was provided to us on optical disk by SAIC.

2 RESEARCH ACCOMPLISHED

2.1 Phase Labeling

Phase labeling consists of attaching a phase label (e.g. Pn, Pg, etc) to a seismic arrival. The information used can be standard parameters computed from the waveform, contextual information such as the ordering of phase arrivals and the time delay between different phases, or non-standard signal features extracted from the waveforms. We have experimented with all of these. We have used the IMS as a source of standard parameters and contextual information. Waveform representation experiments with sonograms and autoregressive modeling have yielded no performance improvements over what could be achieved using only the IMS parametric outputs. Therefore we are presenting only the results obtained using currently available IMS outputs. We began with simple binary labeling problems and worked up to the more complete, multiple phase-type labeling needed by the IMS system. IMS parametric data was obtained from the on-line database at the Center for Seismic Studies (CSS) [1] using the Sequential Query Language (SQL) [2].

The neural networks that gave the results described in this section were single-layer perceptron-like [3] networks. We also experimented with multi-layer perceptrons but found that the additional complexity did not improve performance.

*This work was sponsored by the Department of the Air Force

Table 1: Distinguishing Pn and Pg

	% correct	
Input	Alone	With S-P time diff
detecting beam	52	83
slowness	67	81
period	68	82
rectilinearity	54	82
emergence angle	60	82
short axis angle	52	82
horiz/vert ratio	60	82
max/min ratio	55	83
P-polarization	51	83
only p-type ?	51	81
first p-type ?	57	90
largest p-type ?	53	82
S-P time diff	82	—

2.1.1 Binary Labeling Experiments

We first investigated separating Pn from Pg using a small database of 350 Pn and 350 Pg phases, chosen randomly from the available data. The expert system correctly identified 80% of these phases.

We began by making a list of IMS parameters that might be useful in distinguishing Pn from Pg, and tested each of them individually as inputs to a neural network. After finding the best single input, we experimented with two inputs, and so on, repeating this procedure until the results were not improved by adding more inputs. The results for one and two parameters are shown in Table 1.

In this table, "detecting beam" is a bit indicating whether the phase was detected on a horizontal or vertical beam. Slowness and period are as estimated by the IMS array processing software. Rectilinearity, emergence angle, short-axis angle, horizontal/vertical ratio, maximum/minimum ratio, and P-polarization are IMS three-component parameters. Items such as "only p-type?" are single bits that are set to 1 if this phase is the only p-type phase in this event. The S-P time difference is the difference between the arrival time of the largest S-phase and the first P-phase associated with this event.

The single best parameter for distinguishing Pn from Pg is the S-P time difference, which is reasonable since S-P is a good measure of distance, and a P-phase is more likely to be Pg for a nearby event. When two parameters are used, the best choice for the second parameter is a bit indicating which P-arrival came first. This works because when Pn and Pg are both present, the first arrival is more likely to be Pn and the second is more likely to be Pg.

When all the parameters were used together as inputs, the system achieved about 92% accuracy. We also found that we could achieve 92% accuracy with only 5 parameters: S-P, First P, slowness, P-polarization, and max/min ratio.

Similar experiments were done to distinguish Sn and Lg. The expert system had a 65% success rate and the neural network results for one and three parameters are shown in Table 2.

The parameters in this table are the same as in Table 1, with the addition of "Last S". Last-S binary parameter that is set to 1 if the phase is the last S-phase in the event, or if it is the only S-phase. As can be seen in the table, Last-S is the single most useful parameter in distinguishing Sn from Lg. This parameter is useful because very often if there is only one S-phase, it is Lg, and if there are two S-phases, the last one is Lg. This time we chose to use 2 parameters (Last-S and S-P time) as the basis for further experiments since the difference between results obtained with different inputs was small. Thus, the second column represents results obtained with 3 inputs to the neural network. As can be seen in the table, the best result we obtained with 3 inputs

Table 2: Distinguishing Sn and Lg

	% correct	
Input	Alone	With S-P, Last-S
detecting beam	62	83
slowness	71	85
period	53	84
rectilinearity	62	84
emergence angle	54	82
short axis angle	67	83
horiz/vert ratio	61	81
max/min ratio	61	82
S-polarization	65	84
only s-type ?	65	86
first s-type ?	61	86
last s-type ?	76	—
largest s-type ?	67	85
S-P time diff	71	—

was 86%.

When all the parameters on the list were used together, we got about 89% accuracy. We also found that we could achieve 89% accuracy with 8 parameters: Last S, S-P, First S, slowness, detecting beam, short-axis angle, and rectilinearity.

We also experimented with distinguishing between Rg and Lg. The current version of the IMS expert system does this based on only the estimated period of the arrival. We obtained an 86% success rate using only period, and an 88% success rate using the period and largest S parameters. The addition of other parameters provided only marginal improvement.

2.1.2 Multiple Type Labeling (Pn, Pg, Px, Sn, Lg, Sx, Rg)

After the pairwise experiments, we went on to experiment with the more complete set of the labels used by the IMS expert system, and with a larger data base. We employed a single layer perceptron-like network with seven output nodes, one for each phase label. The input parameters were the ones found useful during the binary classification experiments, augmented as follows. Also, our binary experiments did not include labeling phases as Px or Sx and we added a few parameters that might be useful for these ambiguous phases. For example, we added a parameter "time delay", which measures the difference in arrival times between this phase and the immediately preceding phase of this type (P or S), expressed as a ratio to the S-P time difference. This parameter is occasionally useful because phases that arrive immediately after a preceding phase are more likely to be labeled Px or Sx by the analyst.

The parameters listed in Table 3 were used as network inputs. They are listed in approximate order of importance. Items at the bottom affected the performance by 0.1% or less.

Table 4 shows results for three different time intervals. The time interval boundaries are where the IMS expert system was changed or data from new arrays became available. Data sets for each interval contain 5,000–10,000 arrivals. The arrivals were randomly divided into 2 groups of equal size, with half used for training and half used for testing. The groups then exchanged roles, and the results obtained from the two testing runs were averaged to get the final performance statistics.

As can be seen from the table, the neural network was always able to improve upon the performance of the expert system, regardless of the time interval used. As the expert system improved over time, the performance improvement given by the neural network became somewhat smaller but is still significant in the most recent results. The neural network performance without

Table 3: Input Parameters for Multiple Phase-type Labeling

1 Expert system phase
2 S-P time difference
3 First P/S
4 Last P/S
5 Period
6 Largest P/S
7 Slowness
8 Time Delay
9 Rectilinearity
10 Short-Axis Angle
11 Max/Min Ratio
12 Detecting Beam Type
13 Only P/S
14 Emergence Angle
15 Horiz/Vert Ratio

Table 4: Overall Phase Labeling Performance (%)

	1/90-10/90	11/90-4/91	4/91-6/91
expert system alone (final ID)	79	84	87
neural net alone	82	85	87
neural net with expert system ID input	86	89	90

the expert system input is similar to the expert system performance.

These results demonstrate that a neural network can be used to improve the phase identification performance of the IMS expert system.

2.1.3 Performance at Different Arrays

Performance sensitivity to the arrays used for training is an important issue. To investigate this question, we used the IMS data over the time interval 11/90 - 4/91 to train four different networks, one for each array. We then tested all four networks on data from all four arrays. The results of this experiment are given in Table 5.

Each row in this table indicates the array from which the training data was taken, and each column indicates the array from which the testing data was taken. The performance is best when the training and testing data sets are from the same array, but the performance degradation is small when this is not the case.

Table 5: Performance at Different Arrays(%)

	Testing Array			
Training	ARCESS	FINESA	GERESS	NORESS
ARCESS	87	87	90	89
FINESA	83	90	88	89
GERESS	83	87	90	88
NORESS	85	87	90	89

Table 6: Two-way Event Labeling

Analyst Labels	Neural Network Labels			
	Earthquake	Non-earthquake	Total	Percent
Earthquake	9	5	14	8%
Non-earthquake	1	163	164	92%
Total	10	168	178	
Percent	6%	94%	100%	
Total percent correct was 96.63%.				

2.2 Event Labeling

The goal of our current event labeling research is to develop analysis aids that can be integrated into the IMS. These aids might flag events for more careful analyst review and make the processing of typical events more routine. The hope is that networks might identify certain mines, quarries, or seismic areas on the basis of typical waveforms. An event flagged as atypical would be a candidate for more analysis, independent of the results of other processing elements in the IMS. Disagreements between networks and other elements of the IMS would also be a warning that more analysis is necessary.

Two *preliminary* event labeling experiments have been performed. For an earthquake/not-earthquake classification experiment we achieved a 96.6% success rate. This experiment also provided an example of how networks might flag unusual events for more careful consideration. In another experiment we tried to recognize Kola Peninsula mines without using azimuth or any other parametric information from the expert system and achieved a 91% success rate. Waveform data provided by SAIC were used for event classification experiments.

A *Radial Basis Function* (RBF) neural network [4] classifier was used with feature vectors derived from a multi-channel autoregressive (AR) analysis [5]. The AR analysis for each event wa performed on a single time-window containing all the associated arrivals, starting at the first arrival. Three component beams, steered to the first P arrival speed, as well as single 3-component instruments, were used in the earthquake/non-earthquake experiments. Only single 3-component instruments were used for the Kola Peninsula experiments.

Event classification experiments were performed using *leave-one-out* testing. Given N events, the classifier was trained on $N-1$ of them and tested on the one remaining. The entire training/testing procedure was repeated N times to test on all N events, individually. The total number of events was on the order of 200 and this approach maximized our use of this relatively small number of events.

2.2.1 Earthquakes vs. Non-earthquake

Event labels were provided by SAIC. The labels are best guesses made from all available information. For events that appeared in the Helsinki Bulletin and were labeled there, SAIC accepted the Helsinki classification. SAIC assigned the labels for the remaining events. There were four labels: mine (143 events), earthquake(14 events), explosion(20 events), and unlabeled (1 event). Explosions are events that are probably not earthquakes, but are not located at known mine sites. Many if not all of the explosion events could be mine events. Although we experimented with 4-class labeling the only results we are presenting here are for the 2-class earthquake/non-earthquake problem results. For this purpose, the mine, explosion, and unlabeled events were all treated as non-earthquakes.

The results from our earthquake/non-earthquake experiments are summarized in Table 6. The network was about 97% correct overall but it should be noted that the data distributionis such that a classifier that always selected non-earthquake would have 92% accuracy.

It is interesting to examine the errors made by the neural network in the dichotomous classification problem, listed in Table 7. This table indicates the confidences (between 0 and 1) that

Table 7: Label Confidences for Error Events

Earthquake	Other	ORID	Event Date/Time
0.592	0.408	198311	90 05 23 19:04:24.003
0.001	0.999	191806	90 02 04 01:38.32.571
0.093	0.907	193280	90 04 02 13:46:23.256
0.487	0.513	198272	90 05 20 10:27:07.366
0.494	0.506	128464	89 10 17 20:42:08.973
0.203	0.797	160940	89 11 10 07:06:14.404

Table 8: Kola Peninsula Event Labeling

Analyst Labels	Neural Network Labels			
	Kola Pen	Other	Total	Percent
Kola Pen	32	9	41	19%
Other	10	168	178	81%
Total	42	177	219	
Percent	19%	81%	100%	
Total percent correct was 91.32%.				
Estimated expert system performance was 96.80%.				

the neural network assigned to its labels. The second case stands out because the neural network assigned a confidence of 99.9% to its assessment that this event was not an earthquake as labeled by SAIC. This event was reported in the Helsinki Bulletin, but it was not given an identification which indicates apparently that the analyst was unsure about it. The event occurred at 1:38 AM, and it was not near any catalogued mines. SAIC assigned their own "quake" label a subjective LOW confidence measure. This is a good example of an unusual event the neural network would recommend to the analyst for more careful examination.

The results reported above were obtained using three-component beams steered to the first P arrival. But a single beam cannot be correctly formed for both S and P type phases. Therefore, we also experimented with using a single three-component seismometer. For this, the success rate dropped to about 93%, suggesting that the noise suppression by the beam more than compensated for the information loss due to incorrect steering

2.2.2 Kola Peninsula Mines

The Kola Peninsula is an active mining region that was responsible for approximately 25% of the events in the database we obtained from SAIC. All of the events were labeled as mining explosions and we experimented with networks to discriminate between Kola events and all other events. Azimuth and distance were *not* provided to the neural networks, although the horizontal components of the data were rotated to correspond to the approximate radial and transverse directions estimated by the expert system for the first arrival of the event. Like the experiments in the previous section, the discriminations were made solely on the basis of the coefficients derived from the autoregressive analysis of the waveforms.

Table 8 shows the classification results that were obtained using a single Arcess three-component station. To calculate the expert system performance, the event locations suggested by the expert system were compared to the final locations assigned by an analyst or the Helsinki Bulletin. For this limited data set, the neural network is discriminating mining explosions on the Kola Peninsula from all other events using only an autoregressive representation of a single three-component waveform. The neural network and the expert system did not make errors on the same events. Events for which they differ would be good candidates for additional analysis.

3 CONCLUSIONS AND RECOMMENDATIONS

Simple neural networks can be used to improve upon the phase labeling performance of the current IMS expert system. It is reasonable to assume that, if phase labeling networks were added to the IMS system, improvements in the overall system performance might be achieved. We are working with SAIC to do exactly this. Neural network subroutines are being written and integrated into an experimental version of the IMS. Once that is done, the performance will be evaluated and further improvements made as appropriate.

Event labeling networks are at a much less advanced stage of development. The plan is to continue to develop and evaluate event labeling networks, emphasizing the recognition of characteristic and atypical events, with the goal of developing networks that can be integrated into the IMS and operationally evaluated on large quantities of data. The next step is to experiment with using selected portions of the seismograms rather than a single long data window. We plan to do that, using the IMS outputs to isolate associated phase arrivals, and to ignore quiescent periods between phases as well as unassociated arrivals.

References

[1] Anderson, J., W. E. Farrell, K. Garcia, J. Given, H. Swanger, "Center for Seismic Studies Version 3 Database: Schema Reference Manual", Center for Seismic Studies Technical Report C90-1 (September 1990).

[2] Anderson, J., and H. Swanger, "Center for Seismic Studies Version 3 Database: SQL Tutorial", Center for Seismic Studies Technical Report C90-02 (September 1990).

[3] Lippman, R. P., "Pattern classification using neural networks," *IEEE Communications Magazine*, November, 47–64 (1989).

[4] Broomhead, D. S., and D. Lowe, "Multi-variable functional interpolation and adaptive networks," *Complex Systems* 2, 312–355 (1988).

[5] Jones, R. J., "Prediction of multivariate time series," *J. Appl. Meteorology* 3, 285–289 (1964).

Array Analysis of Regional Pn and Pg Wavefields from the Nevada Test Site

Michael A. Leonard, Lane R. Johnson, and Thomas V. McEvilly

University of California at Berkeley

Contract No. F19628-89-K-0017

Objective

Small-aperture high-frequency regional arrays sited in Scandanavia have proven to be effective in improving the monitoring capability of a regional seismic network. These Scandanavian arrays are located on a geologic shield, which is one of the best propagation environments for high-frequency waves. However, in the tectonically active western United States the crustal structure is profoundly different and one should therefore expect significantly different high-frequency signal characteristics for regional arrays monitoring underground weapons tests from the Nevada Test Site. This study examines the array performance characteristics of Pn and Pg wavefields recorded at three temporary array sites located at regional distances from NTS. This work should aid in the design and deployment of future high-frequency arrays in similar geologic settings. Source and receiver information for this study are shown in Table 1 and Figure 1

Research Accomplished

This research is divided into three parts: I an analysis of spectral characteristics, II an examination of wavefield propagation properties using frequency-wavenumber analysis, and III a contrast of signal correlation properties at each array site and a signal correlation modeling procedure which allows us to simulate array processing characteristics for arbitrary array designs. This simulation procedure can provide a means of more optimally designing an array for a given geologic setting.

I. Spectral Characteristics

To the extent that Pn and Pg can be useful for discrimination and yield estimation, it is important to be aware of the variation in spectral amplitude levels over small distances in receiver location which result from small-scale variations in local geologic structure. At the two larger 4km-aperture arrays the variation in spectral amplitudes reaches as much as an order of magnitude. This large variation reflects the spatially stochastic nature of the wavefields and suggests a need for spectral averaging over short distances. The mean m_b=5.5 Pn and Pg instrument-corrected amplitude spectra recorded at the Savahia Mountain and Rice Valley arrays (explosion SALUT) and at the Ruby Valley array (explosion HARDIN) are shown in Figure 2. The first 2.6 seconds of each wavetype is windowed. The spectra are plotted to the frequency at which the mean spectrum merges with the mean pre-event noise level. Each Pg spectrum can be distinguished from its corresponding Pn spectrum by its larger low-frequency amplitudes. Note the similarity of high-frequency decay among the six spectra, indicating that propagation path effects are less variable at the higher frequencies.

We can use these mean spectra to briefly examine source depth effects. Given the proximity of the SALUT and VILLE detonation sites, spectral ratios of these events will remove the bulk of propagation path effects. In Figure 3 Pn and Pg VILLE/SALUT ratios are shown along with spectral energy ratios predicted by the w^{-2} source model for two events detonated at the same shot point. Adjacent w^{-2} curves are separated by a factor of ten difference in yield. The actual VILLE/SALUT yield ratio is about 0.03, however the observed ratios fall increasingly below this as frequency increases, indicating a relative attenuation of VILLE high-frequency energy relative to SALUT. Given the shallow source depth of VILLE, this suggests that a good deal of high frequency energy is being lost in the upper few hundred meters of the crust.

II. Frequency Wavenumber Analysis at Ruby Valley

The primary functions of an array are to raise the signal to noise ratios of the recorded wavefields and to estimate phase velocity and source azimuth. Using frequency-wavenumber analysis we examine these aspects of array performance at the Ruby Valley array. Examples of the 3-component waveforms used in the analysis, encompassing the first 2.6 seconds of the Pn and Pg wavefields, are shown at the top of Figure 4. Two time windows are examined: Window 1: 0 to 1.3 seconds and Window 2: 1.3 to 2.6 seconds. Note the transition in Pn from essentially vertical ground motion in Window 1 to isotropic ground motion in Window 2, indicating an onset of locally generated scattering. Pg motion is isotropic over both time windows.

A measure of signal correlation, and hence the ability to improve signal to noise ratios, is array gain, which is equal to the ratio of the maximum power in the frequency-wavenumber domain divided by the average power among the array elements. For perfect correlation array gain is equal to 1.0. The array gains for all three components of Pn and Pg in both time windows are also shown in Figure 4. The gains are greatest on the vertical components. Within Window 2 the gain drops significantly, particularly for Pn. Overall, the low signal correlation of the horizontals indicates that any utility of 3-component signal processing is primarily limited to frequencies below about 5 Hz and probably to only the very early portion of Pn. The effect of wavefield distortions due to geologic heterogeneities can also be seen in estimates of phase velocity and source azimuth which display a significant bias and frequency dependence (not shown).

III. Signal Correlation Structure and Array Processing Simulations

It is the spatial correlation of regional wavefields which primarily determines the effectiveness of array processing schemes and hence the suitability of potential regional array monitoring sites. Correlation characteristics of course also affect array design directly. In this part of the study the Pn and Pg correlation properties at the three array sites are quantified in terms of parametric models derived from least squares fits to inter-station coherence estimates. In addition to providing a means of contrasting

array sites, these models can also be used to simulate various array processing characteristics for arbitrary array configurations, thus aiding in array design.

We consider exponential, gaussian, and self-similar forms for the coherence models and for each of these an isotropic model (a function of absolute intersensor separation) and a directional model (a function of intersensor separation in orthogonal directions) are used. Directional models are considered because previous studies have found regional wavefields to have differing correlation properties in directions longitudinal and transverse to the direction of wave propagation. We find significant differences in correlation properties between the array sites in this study. In general, the exponential models fit the coherence estimates best and, for those frequencies where the array gain is sufficiently high, notably better fits are obtained with the exponential directional model with greater decorrelation in the transverse direction, consistent with other studies.

An example of an array processing simulation is shown in Figure 5, which displays the predicted array gain at each of the three array sites based on the model parameters and using the 1.5 km-aperture sub-array configuration and the full 3.0 km-aperture configuration of NORESS. Also included for comparison are similarly derived results for an actual NORESS-recorded m_b=4.2 event located at a distance of 412 km .

Conclusions and Recommendations

This study was undertaken to begin to assess the regional array monitoring characteristics and potential of high-frequency Pn and Pg wavefields from the Nevada Test Site. The following conclusions and recommendations can be made:

1. Though we found significant variations in spectral amplitude over the array apertures, spectral averaging produces mean spectra which are very similar between array sites beyond about 6 Hz. This reveals an advantage to spatial averaging, which cannot be realized by a single-station monitoring site.

2. The VILLE/SALUT spectral ratios indicate that the efficiency of high-frequency propagation is source depth-dependent, and any yield-scaling relationship would have to keep this in mind.

3. If the Ruby Valley site is typical of the Basin and Range, then deployment of a monitoring array will have to be accompanied by site-specific studies aimed at understanding the kinds of wavefield distortion effects we see here.

4. Coherence modeling provides a useful means of contrasting and predicting the relative potential of regional array sites. We find significant differences among the three western U.S. arrays and while NORESS high-frequency Pn gain is greater, that of Pg actually falls within the range of the western U.S. values.

TABLE 1

NTS Explosions					
shot	GMT	latitude	longitude	depth (m)	m_b
SALUT	1985 163:15:15:0.1	37.248	-116.489	608	5.5
VILLE	1985 163:17:30:0.1	37.088	-116.084	293	4.4
HARDIN	1987 120:13:30:0.1	37.233	-116.423	625	5.5

Recording Sites					
site name	latitude	longitude	SALUT Δ	VILLE Δ	HARDIN Δ
Ruby Valley	40.603	-115.191	*	*	387
Rice Valley	34.000	-114.756	385	355	*
Savahia Mountain	34.250	-114.588	371	340	*

* array did not record the explosion

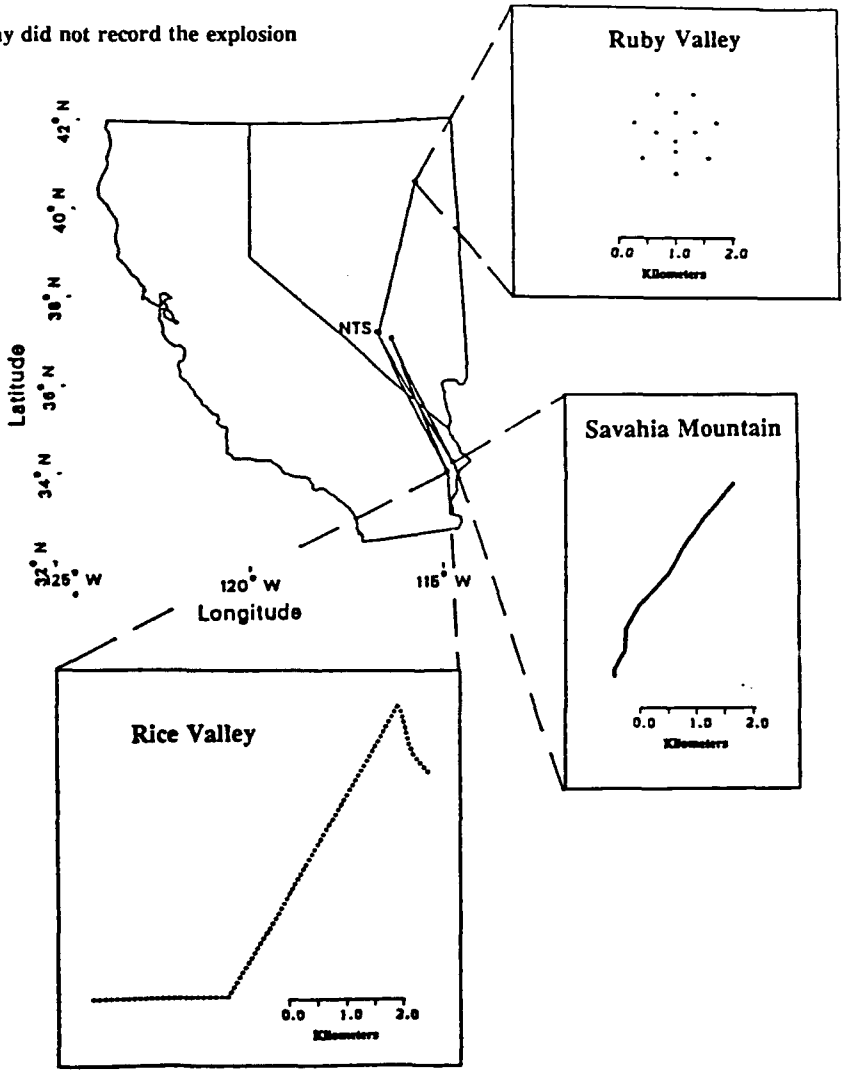


FIGURE 1 Locations of the regional seismic arrays used in this study, connected by solid lines to the locations of explosions each array recorded. The configuration of each array is also shown; each solid dot denotes the placement of one seismometer. The Rice Valley array consisted of 96 vertical-component instruments spaced in 100 meter intervals. The Savahia Mountain array consisted of 145 vertical-component instruments spaced in 25 meter intervals. The Ruby Valley array consisted of 12 3-component instruments over an aperture of 1.5 km.

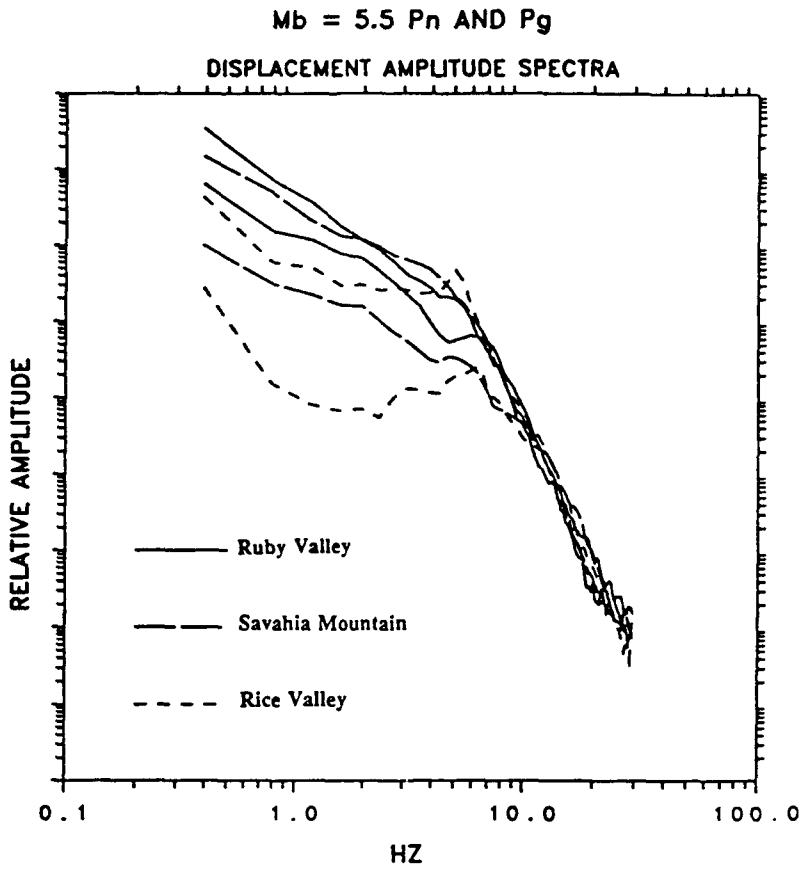


FIGURE 2 Mean Pn and Pg instrument-corrected displacement spectra of the m_b = 5.5 events in this study. Pg can be distinguished from Pn by its larger low frequency values.

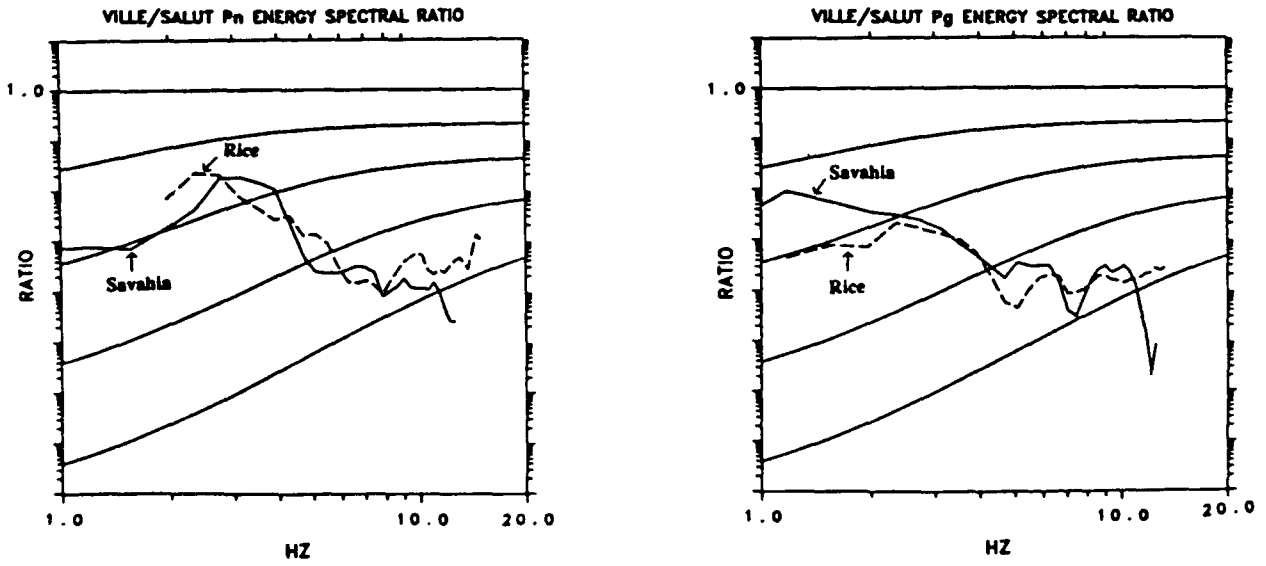


FIGURE 3 VILLE/SALUT Pn and Pg spectral energy ratios at Rice Valley and Savahia Mountain. Also shown are spectral ratio curves predicted by the ω^{-2} source model; adjacent curves are separated by a factor of ten difference in yield.

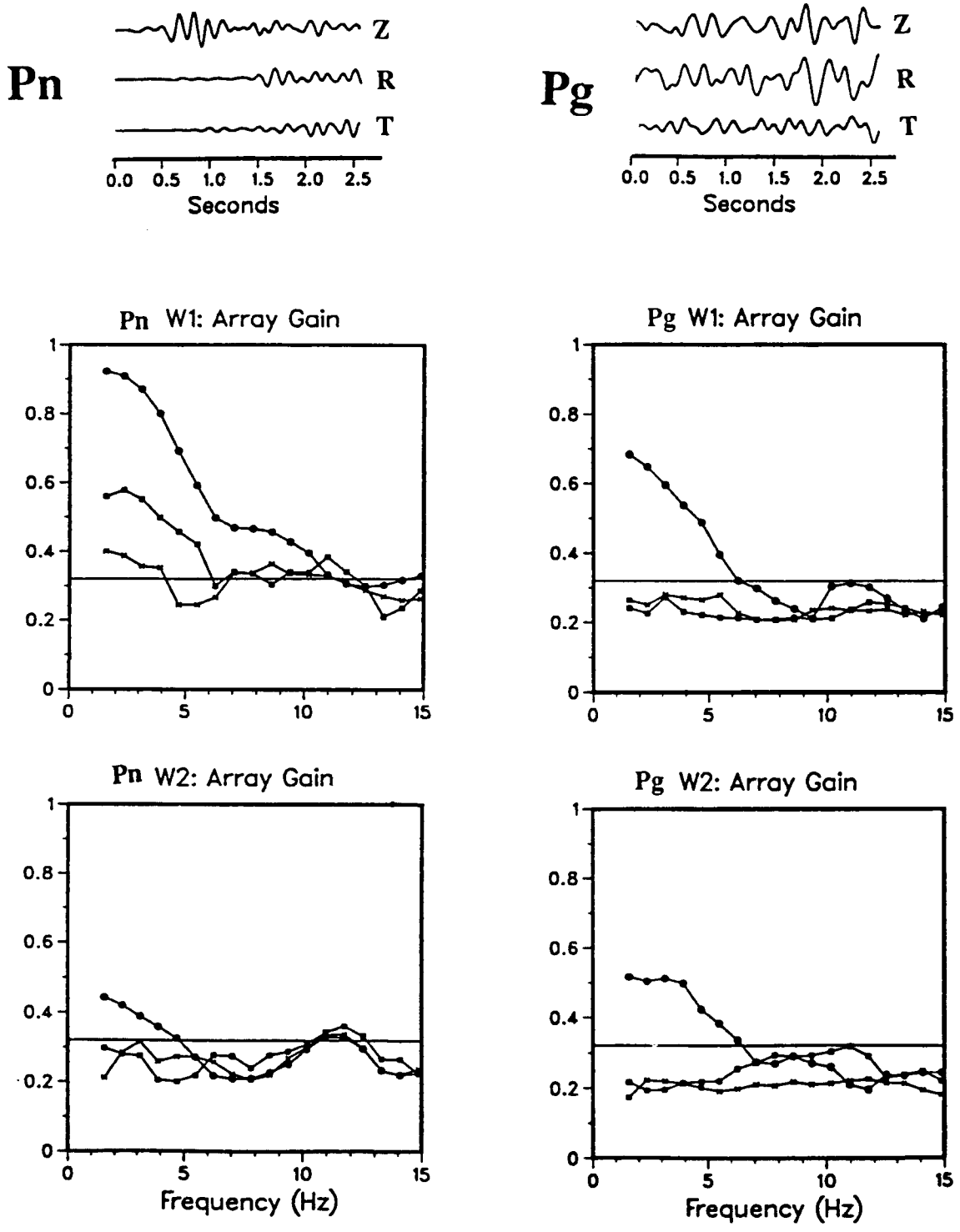


FIGURE 4 Ruby Valley Pn and Pg 3-component array gain for Window 1 (W1: 0 to 1.3 seconds) and Window 2 (W2: 1.3 to 2.6 seconds). The vertical component is denoted by solid circles, the radial by solid squares, and the transverse by crosses. The mean gain level for noise is approximately 0.32. Example 3-component recordings are shown at the top of the figure.

Predicted Array Gains - NORESS Configuration

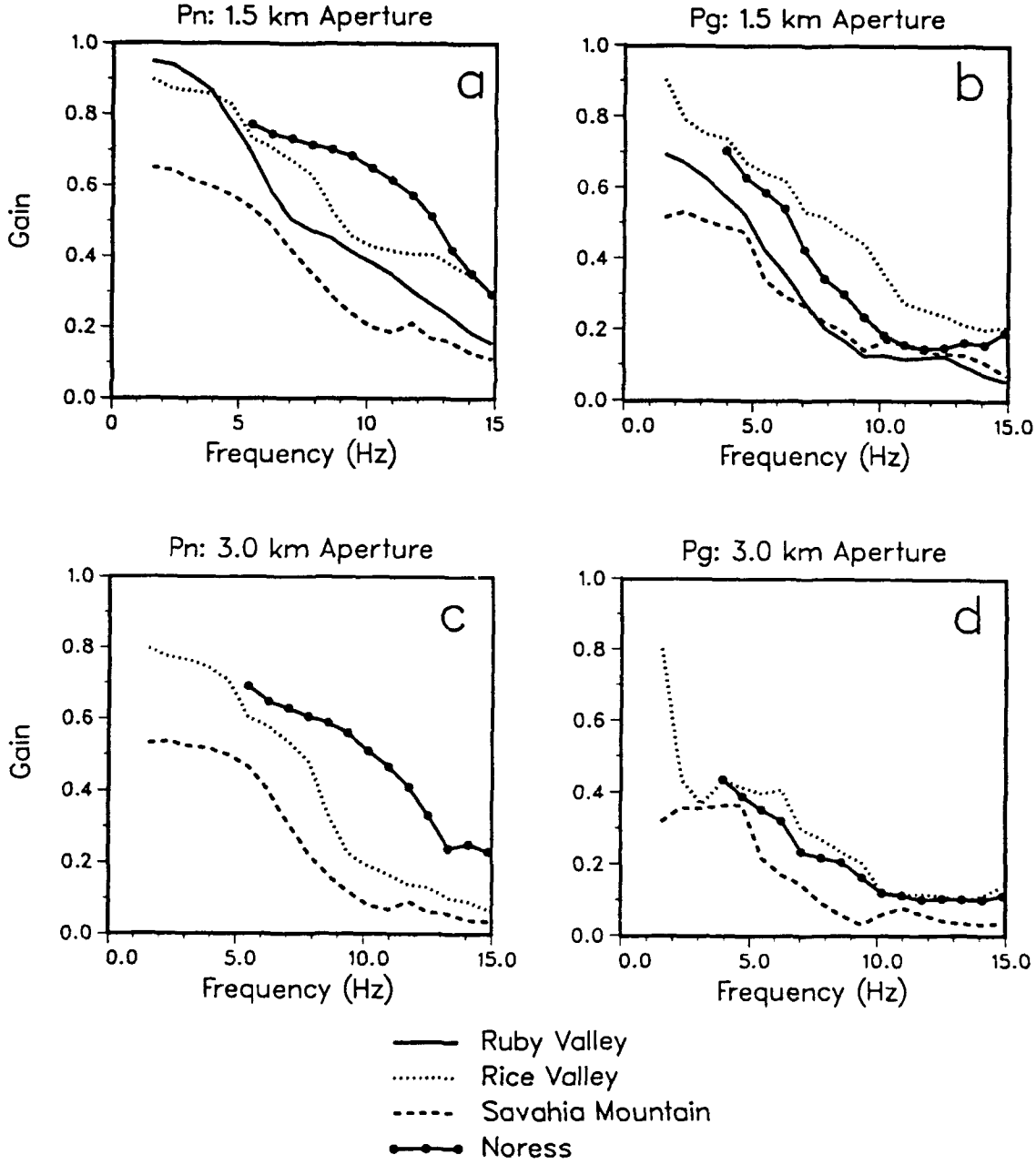


FIGURE 5 Predicted Pn and Pg array gain based on the NORESS array configuration and the coherence models derived in this study. The 15-element 1.5 km aperture configuration includes the center element A_0, and rings A, B, and C. The 24-element 3.0 km aperture configuration includes in addition the D ring. Low-frequency values are omitted at NORESS due to low signal to noise ratios.

A 2 Station and 2 Event Method for Near-Source Attenuation

Peter Malin and Sam Blakeslee[1]
Department of Geology, Duke University
Durham, NC 27706

Contract No. F19628-89-K-0012

Objectives:

The primary objectives of this contract were to understand: (1) how near receiver structure, scattering, and intrinsic attenuation distort the high frequency spectra and spectral ratios of P and S phases, (2) how the vertical and horizontal locations of high frequency 3 component stations affect the individual properties of seismic signals, noise, and their ratios (ie. s, n, and s/n), and (3) the comparative detection and discrimination characteristics of event-triggered, high-frequency 3-component vertical and horizontal arrays. The data used in our study came from microearthquakes along the San Andreas fault at Parkfield, CA, where we operate: (1) a vertical array of seismometers in the 1 km deep Varian well and (2) a network of similar but shallower borehole seismometers nearby. Both observation systems contain 3-component seismometers, and have sampling rates of 500 Hz (Malin, 1989).

In the first part of our project, we completed both a frequency dependent site effects study and a tomographic inversion for along path velocity structure (Malin, 1990). In the course of this study, it became apparent that the P- and S-wave spectra of propagation paths crossing the San Andreas fault were grossly attenuated by the fault itself. To establish the source and character of this attenuation, we developed a 2 station and 2 event spectral ratio method for studying near-source and along path transfer functions (Blakeslee, 1989, Blakeslee et al., 1989).

Research Accomplished:

The 2 station and 2 event spectral ratio technique is illustrated in Figure 1. The procedure shown produces a spectral transfer function that has had source, common path, site, and instrument effects removed. The resulting spectral ratio can be interpreted in terms, for example, of a linear attenuation function. We have applied this method to 2 data sets, one being a cluster of 19 earthquakes located on the fault between the two stations and the other a more general set of 18 earthquakes on the fault as recorded at 6 stations at various points both off and on the fault (Blakeslee et al, 1989; Blakeslee and Malin, in prep).

In the study of 19 earthquakes using two fault-zone stations, amplitudes decay

[1] **Current address: Exxon Production Research Co., PO Box 2189 Houston TX 77252-2189**

exponentially with frequency, over the bandwidth from 1-40 Hz. The severity of attenuation correlates with the length of the propagation path within the fault-zone. Assuming a constant Q attenuation operator, the S-wave quality factor within the fault-zone at a depth of 5-6 kilometers is Q_{fzone}=31 (+7, -5). These results are illustrated in Figure 2.

In the six-station, 18 event study the attenuation is seen to vary significantly depending upon the proximity of the station to the fault-zone. Paths to the stations well away from the fault-trace suffer very little attenuation, the path that produces the most attenuation is to the station within the fault-zone. Q for the fault-zone path is 74, a factor of about 5 less than the non fault-zone paths. These results are investigated and confirmed by calculating *tstar* corrections to the high-frequency portions of the spectra. These results are illustrated in Figure 3.

Conclusions and Recommendations:

The specific value for DARPA in the work we have discussed above is in the ability to evaluate the near source conditions that grossly effect high-frequency signals emitted by seismic sources in a localized region. We used earthquakes along the San Andreas fault, but the methods and conclusions apply equally to a restricted test site area where attempts were being made to deliberately attenuate high frequency signals by placing the source in lossy materials.

In the case of the San Andreas fault zone, the values for fault-zone Q found in the two studies, Q_{fzone}=74 & 39, are a factor of 4-10 lower than Q found for non-fault-zone paths in the same region. This indicates that although the spatial extent of the attenuation is restricted to a zone very near the fault-trace itself the effect of the anomaly may control the high-frequency content of microearthquake spectra recorded downhole. For example, if the San Andreas fault-zone has an average Q of 50, is 1.5 km wide and has a shear-wave velocity of 3 km/s, then an earthquake occurring in the middle of the fault-zone would experience a *tstar* of at least.005 due to propagation within the fault-zone. This level of attenuation is sufficient to artificially lower the apparent corner frequency of even very small earthquakes to approximately 50 hz.

We have not computed practical examples of 2 explosion-2 station test site transfer function (nor consequently linear attenuation values) with our methods at this time. Given that regional data on such events is now more generally available, we recommend that this method be given a try in attempts to establish high-frequency, near source wave propagation effects at test sites. The expected result of such a study will be to localize sites were source parameter calculations will be biased by high-frequency propagation effects.

References:

1989. Blakeslee S. Studies in near-surface, crustal and fault-zone attenuation: Borehole analysis of Parkfield earthquakes, PhD thesis, University of California at Santa Barbara,

1989 Blakeslee, S.N., P.E. Malin, and M.G. Alvarez. Fault-zone attenuation of high-frequency seismic waves. GRL, 16, 1321-1324.

1989 Malin, P.E., Comparative Seismic Observations on Downhole Network verses a Vertical Array, Poster Presentation for DARPA 11th Annual Research Symposium, San Antonio, TX, 5/2-5/4, 1989. Short paper included in DARPA/GL 11th Symposium volume, 6 pp.

1990 Malin, P.E., Results of direct observations of high-frequency site effects with applications to seismic monitoring. Presentation for DARPA 12th Annual Research Symposium, Key West, FL, 9/18-9/20, 1990. Short paper included in DARPA/GL 12th Symposium volume, 6p.

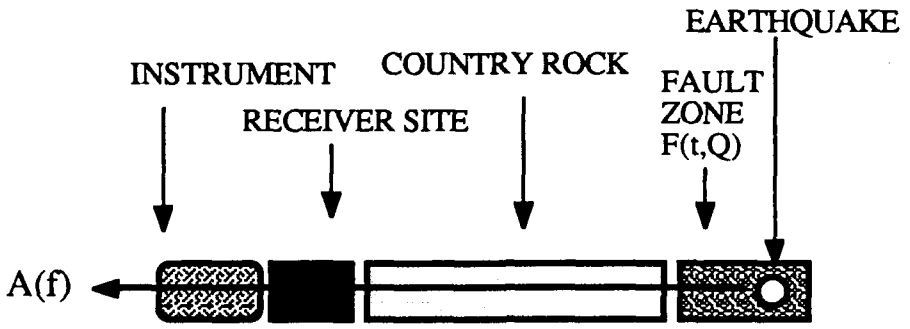
Figure Captions:

Figure 1. *Measurement of Fault Zone Attenuation—a simple case.* Referring to the diagram in Figure 1 showing an arbitrarily placed earthquakes, it can be seen how an observed earthquake spectrum at the earth's surface, A(f), can be viewed as the result of an initial source spectrum that has been subsequently modified by a number of different filters. By using certain combinations of spectra obtained from at least two earthquakes and two stations as shown above, it is possible to formulate the problem so that the attenuation of the portion of fault zone in between the events is obtained. The attenuative effects of the fault zone can now be obtained because of a redundancy in the spectral measures of source spectra, site effects, instrument response, and whole path losses. For this ideal case, the earthquake sources and the receivers would be roughly in a line. This essentially one-dimensional problem can be reduced to the expression at the bottom of the Figure 1.

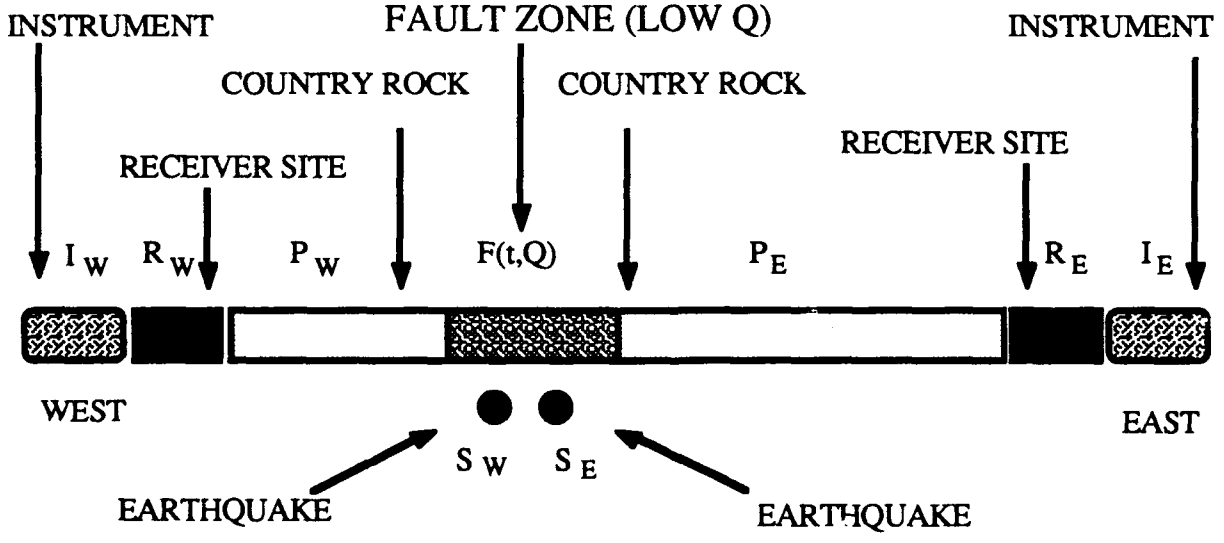
Figure 2. Fault-zone transfer function using spectra from 2 nearly colinear station and earthquake pairs. The least-squares-fit line is shown, the steepness of that slope reflects the severity of high-frequency attenuation.

Figure 3. Transfer functions between 1 station and 5 others at various distances and azimuths along the San Andreas. The transfer functions are the result of stacking together the individual functions for each of the 18 events used in this part of our study. Those paths near or crossing the fault zone at an oblique angle (Middle Mountain and Joaquin North) show the effects of attenuation through the San Andreas fault zone.

FIGURE 1



$$A(f) = I(f)\, R(f)\, P(f)\, F(f,Q)\, S(f)$$



$$\frac{A[R_E,S_W]}{A[R_E,S_E]}\,\frac{A[R_W,S_E]}{A[R_W,S_W]} = \frac{S_W(f)\,F(t/Q(f))}{S_E(f)}\,\frac{S_E(f)\,F(t/Q(f))}{S_W(f)} = F^2(t/Q(f))$$

FIGURE 2

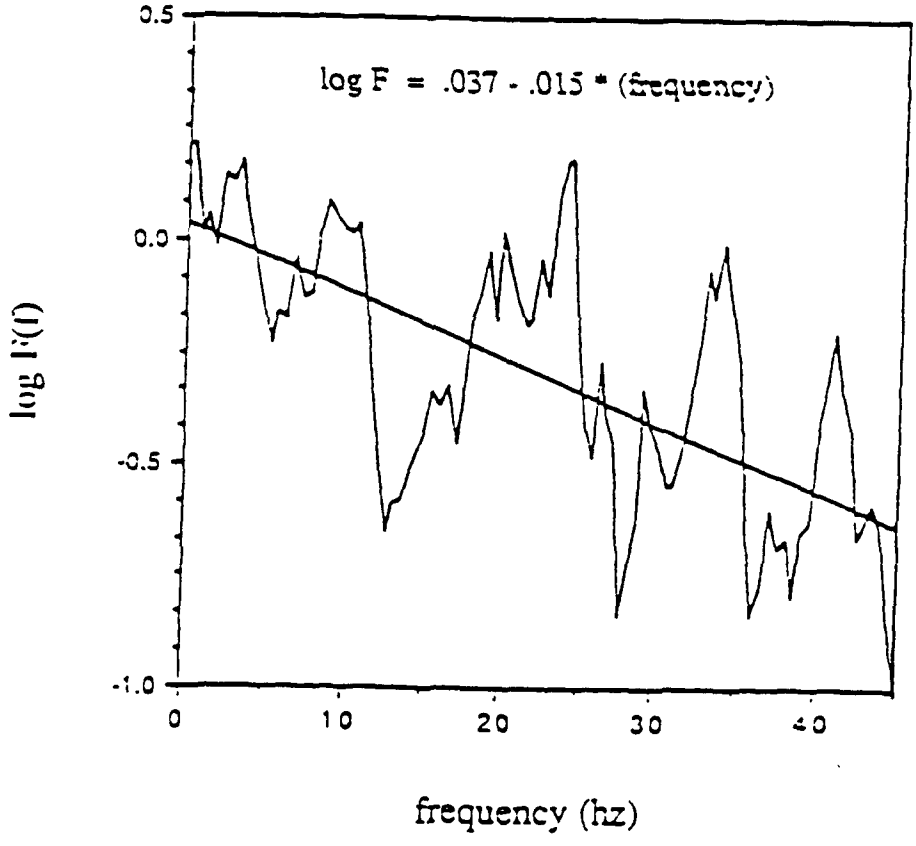
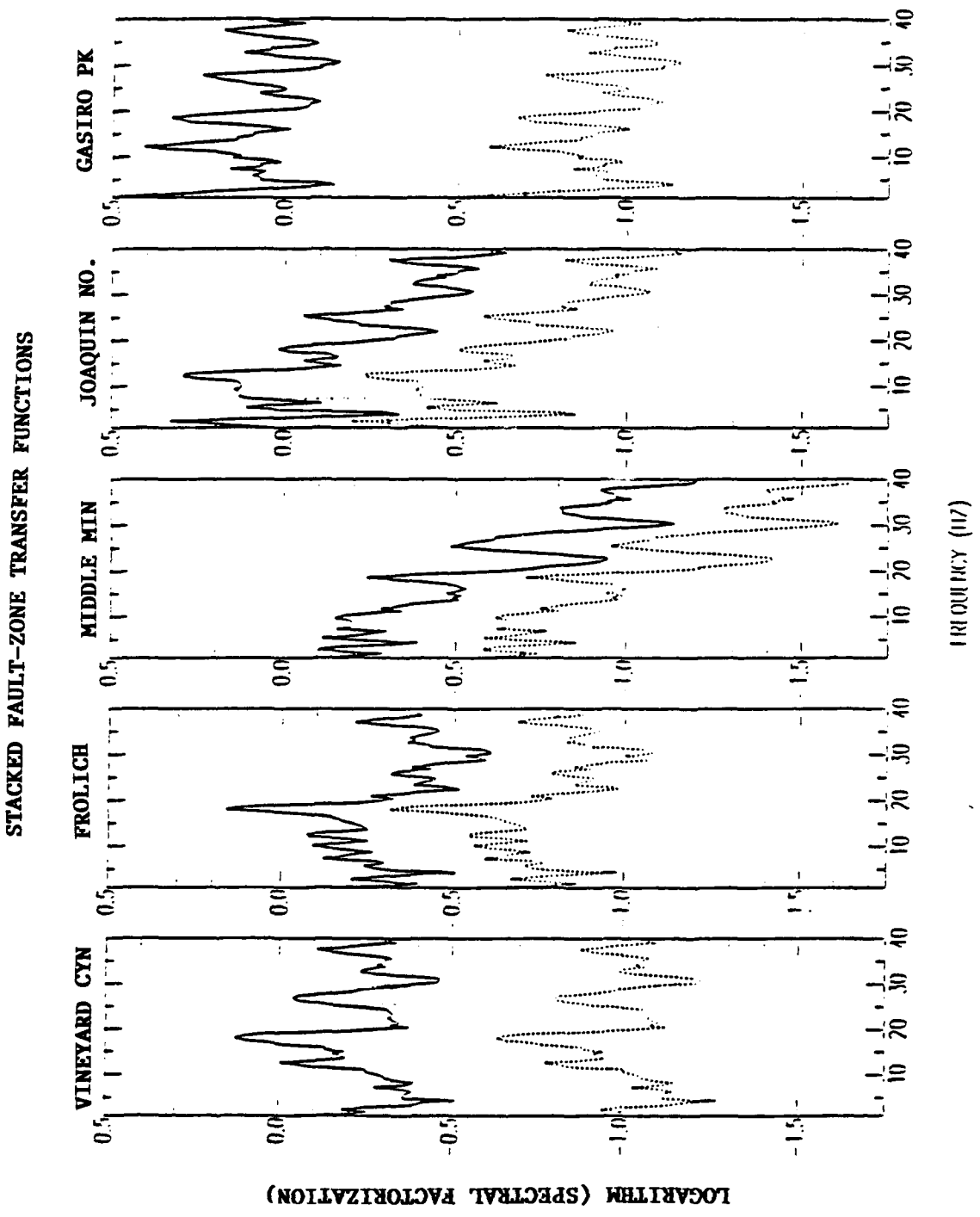

log F = .037 - .015 * (frequency)
0.5
0.0
-0.5
-1.0
0
10
20
30
40
log F(f)
frequency (hz)

FIGURE 3


STACKED FAULT-ZONE TRANSFER FUNCTIONS
VINEYARD CYN
FROLICH
MIDDLE MIN
JOAQUIN NO.
GASIRO PK
LOGARITHM (SPECTRAL FACTORIZATION)
FREQUENCY (HZ)

TITLE: **INVESTIGATIONS OF NONLINEAR EXPLOSION EFFECTS**

AUTHOR AND AFFILIATION: K. L. McLaughlin, J. L. Stevens,T.G. Barker, and B. Shkoller, S-CUBED, A Division of Maxwell Laboratories, Inc.

CONTRACT NO: F19628-89-C-0043

OBJECTIVE: The objective of this project is to reduce uncertainties in discrimination using regional seismic data and to improve the accuracy of explosion yield estimates by developing theoretical models for predicting variations in seismic signals resulting from depth of burial, *in situ* stress, near-source scattering, and scale-dependent rock strength. The study employs state-of-the-art computer models of underground explosions and seismic wave propagation. Predictions are to be compared to Soviet and U.S. contained explosions at regional and teleseismic distances. In this paper, we calculate Lg waveforms and spectra from four explosions beneath flat and sloping surfaces, and with depths of burial ranging from 54 to 120 m/KT $^{1/3.4}$ scaled depth. We find that the Lg waves predicted by the calculations are a very stable yield estimator in spite of the wide range of depth of burial.

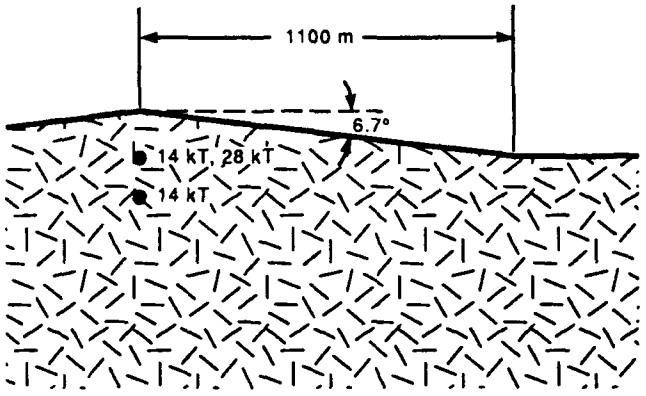
RESEARCH ACCOMPLISHED: Research from this project has previously been reported in Barker, *et al.* (1990a), Barker, *et al.* (1990b), McLaughlin, *et al.* (1990), Day and McLaughlin (1991), and McLaughlin, *et al.* (1988). In these works the authors have concentrated on the analysis of numerical simulations of explosions in the 62 to 125 KT range in tuff and granite. It was found that simulations of normally buried exposions at 125 KT in hard high-velocity rock predict m_b(Lg) consistent with observations. This is contradictory to what is expected from a point explosive source in a high velocty model. The nonlinear free surface interaction (NLFSI) was found to act as a deviatoric seismic source radiating ample SV energy to couple well with the Lg modes in a high velocity crustal model. Models for the NLFSI were proposed in terms of tension cracks and compensated linear vector dipoles (CLVD) at the source. Recent work extends the investigation to lower yields and shallower depths of burial.

We have calculated regional seismograms from a series of four two-dimensional nonlinear axisymmetric finite difference calculations. These calculations simulate 14 and 28 KT explosions in granite at different scaled depths of burial (DOB) ranging from 54 to 120 m/KT $^{1/3.4}$ (see Table 1). The four simulations referred to as SLOPE 1, 2, 3, and 4 are being used to investigate the influence of DOB and free surface slope on the excitation of regional phases. These calculations were intended to model explosions at Degelen Mountain and include the influence of a sloping free-surface above the explosion and are described in detail by Stevens, *et al.* (1990). In the 2D axisymmetric geometry, the explosion is located below a peak (see Figure 1). Analysis of announced (Bocharov, *et al.*, 1989) yields and depths for Soviet explosions indicates that the Soviet scaled DOB's are generally bracketed by these simulated scaled DOB's. Scaled DOB's of 66 and lower are quite shallow and are considered underburied by US testing practices while scaled depths of 120 m/KT$^{1/3.4}$ are generally considered standard depth of burial for US shots. Therefore the depths of burial span a range from underburied to normal burial.

Table 1

	Y(KT)	DOB(m)	DOB(m/KT$^{1/3.4}$)	Slope
SLOPE 1	14	144	66	6.7
SLOPE 2	14	261	120	6.7
SLOPE 3	28	144	54	6.7
SLOPE 4	14	144	66	0.0

Regional seismograms have been computed using the elastic representation theorem. Displacements and tractions from the finite difference calculation are saved on a monitoring surface in the linear region surrounding the nonlinear source. Green's functions based on modal summation were computed up to 1 Hz. Modal summation methods have the advantage that the contribution of each mode to the seismogram can



Slope 1, 2, 3, & 4 Calculations

Figure 1. The 2D axisymmetric SLOPE 1, 2, 3, & 4 calculations were made with and without a sloping surface at depths of 144 and 261 meters and yields of 14 and 28 KT.

be examined separately and the synthetics are inexpensive to compute. In most cases, modal summation accurately models the Lg portion of the seismogram, although it has been found to be inadequate for modeling the Pn and Pg phases (Day, *et al.*, 1989). The crustal model was derived from the Kazakhstan model of McLaughlin, *et al.* (1990). Figures 2 and 3 show the synthetic seismograms for the fundamental mode and for the sum of modes 2 through 15. The fundamental mode surface wave is quite variable and does not correlate well with yield. This is primarily due to the effect of pore crushing on the static displacement. The higher modes, however, are very consistent and correlate remarkably well with yield.

The Rms Lg amplitude normalized to SLOPE 4 is presented in Table 2. Note that the Rms Lg amplitudes for SLOPE 1, 2, and 4 differ by only 11 percent. Furthermore, the amplitude ratio of SLOPE 1 to SLOPE 3 is 2.05 and differs from linear yield scaling by only

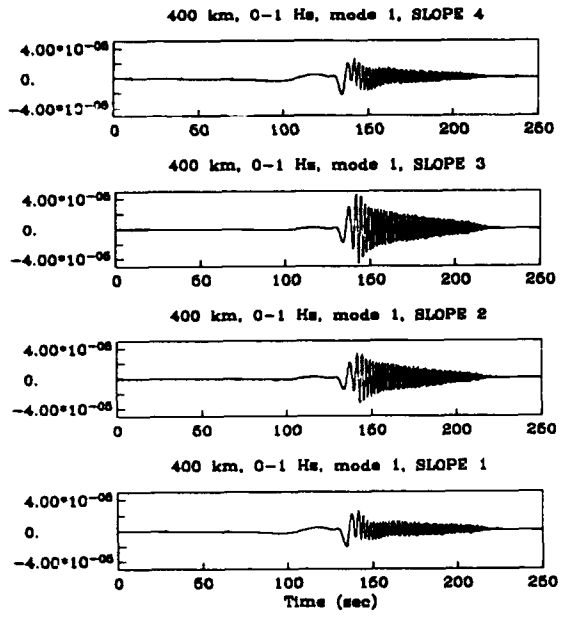


Figure 2a Synthetic seismograms for the fundamental mode in the 0-1 Hz bandwidth at a distance of 400 km by the four SLOPE calculations. Note that SLOPE 1 & 4 (14 KT and underburied) are nearly identical while SLOPE 3 (28 KT and underburied) is about twice as large and SLOPE 2 (14 KT) is larger than the other 14 KT waveforms.

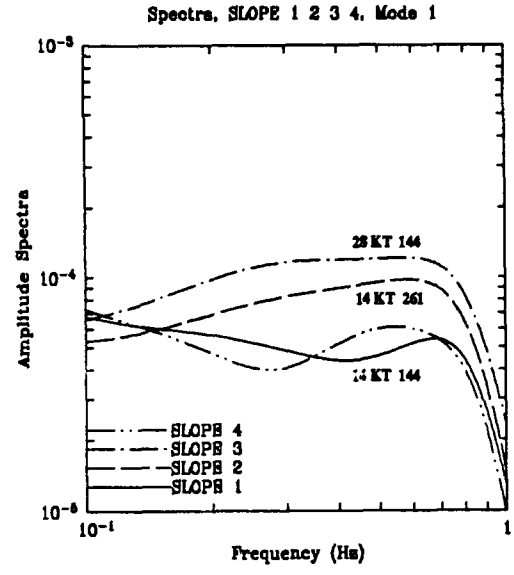


Figure 2b. Spectra of the fundamental mode excited by the four SLOPE calculations. Note that SLOPE 1 & 4 (14 KT and underburied) are nearly identical while SLOPE 3 (28 KT and underburied) is about twice as large and SLOPE 2 (14 KT) is larger than the other 14 KT spectra.

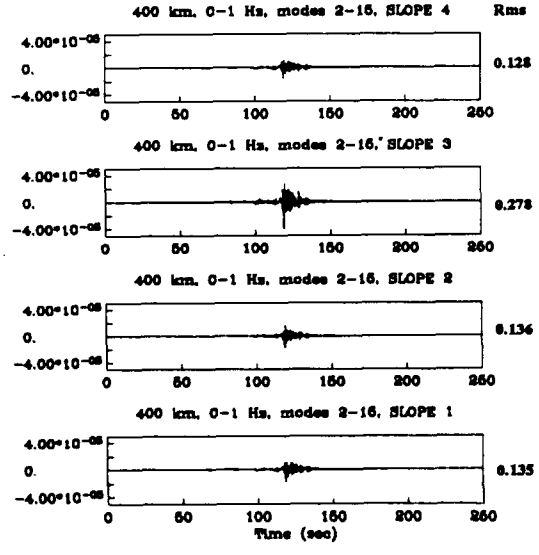


Figure 3a. Synthetic seismograms from modes 2 through 15 in the 0-1 Hz bandwidth at a distance of 400 km by the four SLOPE calculations. Rms Lg amplitude for SLOPE 1, 2, & 4 differ by only 11%. Rms Lg is 2.05 times larger for SLOPE 3 (28 KT) than SLOPE 1 (14 KT).

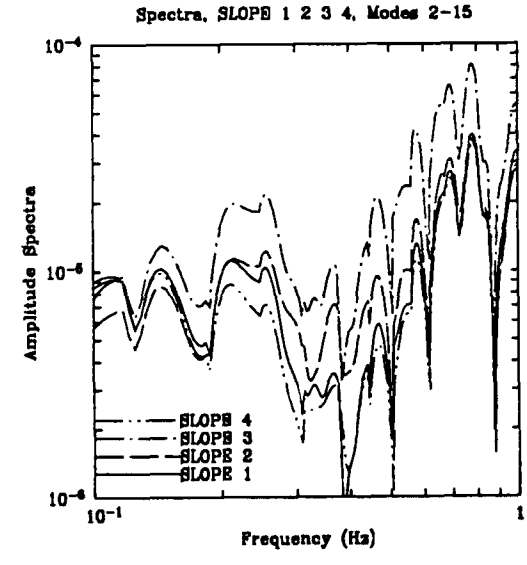


Figure 3b. Spectra of modes 2 through 15 excited by the four SLOPE calculations. Note the similarity of the three 14 KT explosions (SLOPE 1, 2, & 4). Excitation by SLOPE 3 is about twice that of the smaller explosions.

5%. The excitation of the higher modes comprising Lg is very stable with respect to the presence or absence of a free surface slope and for scaled depths of burial between 54 and 120 ($m/KT^{1/3.4}$).

Table 2

	Rms Lg (Normalized)	Scaled Plastic Volume 10^6 m^3/KT	SDOB $m/KT^{1/3.4}$
SLOPE 1	1.10	9.61	66
SLOPE 2	1.11	10.62	120
SLOPE 3	2.26	7.98	54
SLOPE 4	1.00	8.93	66

When we analyzed the finite difference calculations we found that the volume of material that has undergone plastic yielding was very similar regardless of the presence of the slope or the depth of burial (see Table 2). This volume acts as an isotropic source plus a deviatoric source that couples well to the Lg modes. This volume is not spherical due to the presence of the free surface and hydrostatic pressure gradient. The free surface breaks the spherical symmetry of the explosion and the region of deformation has a larger radius near the surface than at depth.

Figure 4 illustrates the volume of material that deformed nonlinearly in the SLOPE 4 simulation. The volume of $1.25 \cdot 10^8 m^3$ corresponds to a sphere of radius 310 m which is very close to the elastic radius of 313 m predicted by 1-D nonlinear simulations. The region of deformation can be divided into two regions. The inner spherically symmetric region corresponds to material that failed under the compressive outgoing wave. Outside this region, the material failed in tension. The non-spherical nature of the failure region is due to 1) reduced overburden near the free surface leads to a weaker rock under tension and 2) the tensile reflection from the free surface (spall). Note that the volume is extended along the free surface and several horizontal "cracks" are evident. This region of non-spherical deformation had a similar shape and scaled volume for all four calculations despite the range in scaled depths of burial (54-120 $m/KT^{1/3.4}$) and presence/absence of a sloping interface.

CONCLUSIONS AND RECOMMENDATIONS:

In this paper we have shown that the Lg excited by explosions in hard rock is insensitive to the scaled depth of burial (50-120 $m/KT^{1/3.4}$) and slope above the source ($\leq 6.7°$) for yields of 1-4-28 KT. In previous reports we have stressed the inefficiency of a point explosive source for exciting Lg in a high velocity medium. We have also found that near-source scattering is not adequate to explain observed Lg from explosions at the Eastern Kazakh-stan test site. This has led to the conclusion that deviatoric source components are required to model the equivalent seismic source. Nonlinear modeling of explosions suggest that the

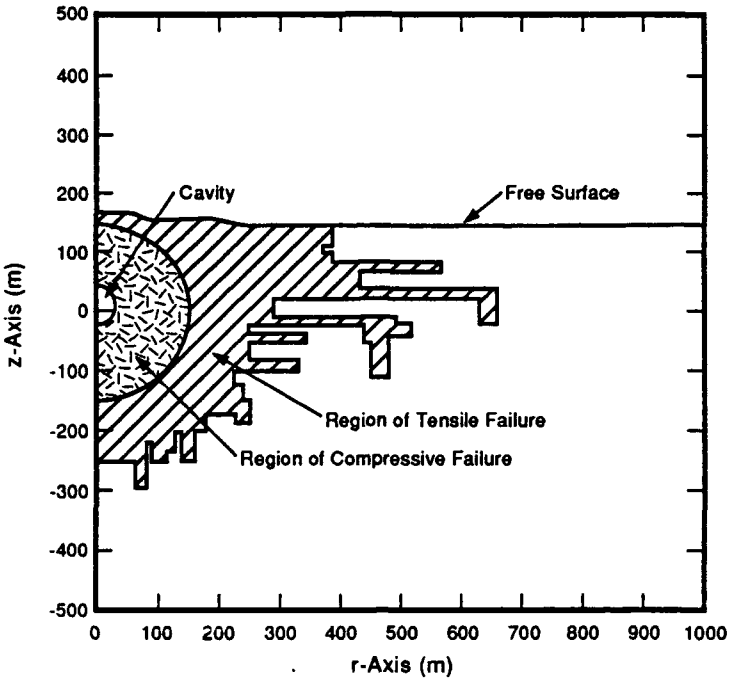


Figure 4. Results from the SLOPE 4 calculation show that the regions that undergo nonlinear deformation may be separated into two regions. A roughly spherical region (radius ~140 m) surrounding the cavity (radius ~30 m) of the material has failed in compression. Outside this region of compressive failure is a non-spherical region where the material fails in tension. This region of tensile failure is responsible for the non-spherically symmetric nature of the seismic source.

nonlinear free surface interaction (NLFSI) is responsible for this deviatoric source, which can be represented at the frequencies of interest here by an equivalent CLVD source. This CLVD source is an efficient exciter of Lg in high velocity structures. In previous reports we have shown that the CLVD model predicts m_b(Lg) consistent with observations for 125 KT explosions at Shagan River. The point explosion + CLVD model serves as a simple model for the simulation of regional seismograms. The model appears to predict m_b(Lg) yield relations consistent with observation. Additional work needs to be done to explore implications for regional Pn and Pg signals.

McLaughlin, *et al.* (1990) demonstrated that the point explosion + CLVD (NLFSI) model predicts Lg has reduced bandwidth compared to Pn and Pg. In comparison to standard earthquake models the explosion Lg should appear depleted in high frequencies with respect to the Pn or Pg. The discrimination potential suggested by this model should be more fully explored. Large industrial blasts also have significant nonlinear free surface

interactions. The techniques used to model contained nuclear explosions are directly applicable to quarry blasts and could be used to investigate chemical explosions and the theoretical basis for discrimination of shallow chemical blasts from earthquakes and contained nuclear explosives.

References

Barker, T. G., S. M. Day, K. L. McLaughlin, B. Shkoller and J. L. Stevens (1990a). An Analysis of the Effects of Spall on Regional and Teleseismic Waveforms Using Two-Dimensional Numerical Modeling of Underground Explosions, GL-TR-90-0126, Scientific Report No. 1. ADA226921

Barker, T. G. and S. M. Day (1990b). A Simple Physical Model for Spall from Nuclear Explosions Based Upon Two-Dimensional Nonlinear Numerical Simulations, GL-TR-90-0189, Scientific Report No. 3. ADA231792

Bocharov, A. S., S. A. Zelentoz, and V. N. Mikhailov (1989). Characteristics of 96 Underground Nuclear Explosions at the Semipalatinsk Test Site, *Atomic Energy, 67, 210-214* (in Russian).

Day, S. M. and K. L. McLaughlin (1991). Seismic Source Representations for Spall, *Bull. Seism. Soc. Amer., 81, 1, 191-201.*

Day, S. M., K. L. McLaughlin, B. Shkoller and J. L. Stevens (1989). Potential Errors in Locked Mode Synthetics for Anelastic Earth Models, *GRL, 16, 203-206.*

McLaughlin, K. L., T. G. Barker, S. M. Day, B. Shkoller and J. L. Stevens (1988). Effects of Depth of Burial and Tectonic Release on Regional and Teleseismic Explosion Waveforms, AFGL-TR-88-0314, S-CUBED Report SSS-R-88-9844. ADA207541

McLaughlin, K. L., T. G. Barker and S. M. Day (1990). Implications of Explosion Generated Spall Models: Regional Seismic Signals, GL-TR-90-0133, Scientific Report No. 2. ADA227273

Stevens, J. L., T. G. Barker, E. J. Halda, J. R. Murphy and N. Rimer (1990). Simulation of Teleseismic Body Waves from Underground Explosions Beneath Sloping and Flat Surfaces Using Nonlinear Axisymmetric Finite Difference Calculations, S-CUBED Technical Report to Defense Nuclear Agency, DNA-TR-91-5, SSS-TR-90-12121, December.

SPHERICAL WAVE PROPAGATION IN FROZEN SATURATED ROCK

S.A. Miller and A.L. Florence
SRI International
Menlo Park California 94025
Contract No. F19628-91-K-0003

OBJECTIVE

The objective of this project is to provide basic experimental data on spherical wave propagation in dry and saturated hard rock under frozen conditions to assist energy coupling characterization by establishing the influence of freezing and ice-filled pores on energy coupling. The approach is to perform laboratory experiments with small, spherical, high explosive charges in a cylindrical core of rock to generate spherical waves that we monitor by particle velocity (PV) gages located at several ranges. Energy coupling is evaluated from the resulting wave forms, and include attenuation of peak velocities and displacements, kinetic energy and strain energy transmission, reduced potentials, and displacement spectra.

RESEARCH ACCOMPLISHED

We conducted spherical wave experiments in 16% porosity Indiana limestone with pore space 'as-received' dry, and with the pore space saturated and frozen. For comparison, we will present these results with experiments where the pore space was room temperature saturated performed under a separate contract. In addition, two experiments were performed in Sierra White granite (less than 1% porosity) under saturated/frozen conditions.

The experimental configuration is shown in Figure 1. In these experiments, a 3/8-g charge of PETN powder, packed to a density of 1 g/cm^3, is placed into machined hemispherical cavities at the center of a 27-cm-diameter by 27-cm-long cylindrical specimen. To perform the experiment, the specimen is placed into a chamber and surrounded by a solenoid and an overburden pressure of 10.7 MPa is applied to the specimen. For the frozen experiments, the overburden fluid is ethylene glycol (anti-freeze) at a testing temperature of -8°C. Particle velocity histories are measured by monitoring the voltage induced by the conducting copper loops as they move at the local particle velocity through the magnetic field. From Faraday's Law, the particle velocity is proportional to the induced voltage, the length of the conductor, and the magnetic field strength. A complete description of the experimental procedure is found in Reference 1.

RESULTS

The particle velocity histories in frozen/dry Indiana limestone at a testing temperature of -8°C are shown in Figure 2(a-c) for one of the two experiments performed. The records show a two-step structure in the rise with an initial linear feature followed by longer duration, rounded rise to the peak. The transition is very distinct in each record and indicates yielding near the source, which is then propagated elastically through the remainder of the limestone specimen. The transition from an initially steep rise to a shallower rise to the peak is not smooth as each record indicates a short reduction in

velocity (deceleration) before continuing the rise to the peak. After the peak, the velocity continues in the outward phase for a total positive pulse duration of about 8 μs. A negative velocity, or rebound phase, in observed for an additional 15 μs. We observe some propagating structure in the negative phase of the pulse. No differences were observed between frozen/dry and room temperature/dry Indiana limestone experiments (Ref. 2).

The particle velocity histories measured in the saturated/frozen Indiana limestone experiments are shown in Figure 3(a-c) for one of the three experiments performed. In these experiments, the wave velocity was measured at about 5.6 mm/μs (c.f.: 4.4 mm/μs for the dry/frozen experiments). A less apparent two-step rise is observed, and the peak particle velocity is greater when compared to dry limestone.

A comparison of the particle velocity histories at the 30-mm range for dry/frozen, saturated/room temperature and saturated/frozen experiments is shown in Figure 4, and a comparison of the corresponding displacements is shown in Figure 5. This comparison shows that filling the pore space has the effect of increased peak velocity, while freezing the pore fluid reduces the pulse width (therefore peak displacement) when compared with the room temperature saturated limestone. Records for the saturated/room temperature experiments are found in Reference 2. Attenuation of peak velocities and displacements are shown in Figures 6 and 7, respectively, and show that the frozen/saturated results fall between the range defined by the dry limestone at the low end and the saturated/room temperature limestone at the high end of the peak values. A comparison of velocity and displacement spectra for the three cases are shown for the 30-mm range in Figures 8 and 9. The low frequency content of the saturated/room temperature is higher in amplitude, followed by the saturated/frozen and dry limestone. The corner frequency is similar in all three cases at a frequency of about 30-40 kHz. Peak values of the reduced velocity potential at the 30-mm range are about 8 $mm^3/\mu s$ for the saturated/room temperature and saturated/frozen limestone and about 4 $mm^3/\mu s$ for the dry/frozen limestone. Peak reduced displacement potential values at the 30-mm range were approximately 85, 50, and 33 mm^3 for the saturated/room temperature, saturated/frozen and dry/frozen experiments, respectively.

We performed two experiments in low porosity (<1%) Sierra White granite where the specimen was first saturated and then frozen. We measured particle velocity histories at nine ranges using the same configuration shown in Figure 1. For brevity, the measured particle velocity histories are not shown here, but attenuations of peak velocity and displacements are shown in Figures 10 and 11. The attenuations show that freezing the pore space in low porosity (<1%) hard rock has no observable effect on wave propagation, and in general, effects of the pore space (i.e., dry, saturated, saturated frozen) on wave propagation can not be separated from experimental uncertainty in the measurement.

CONCLUSIONS

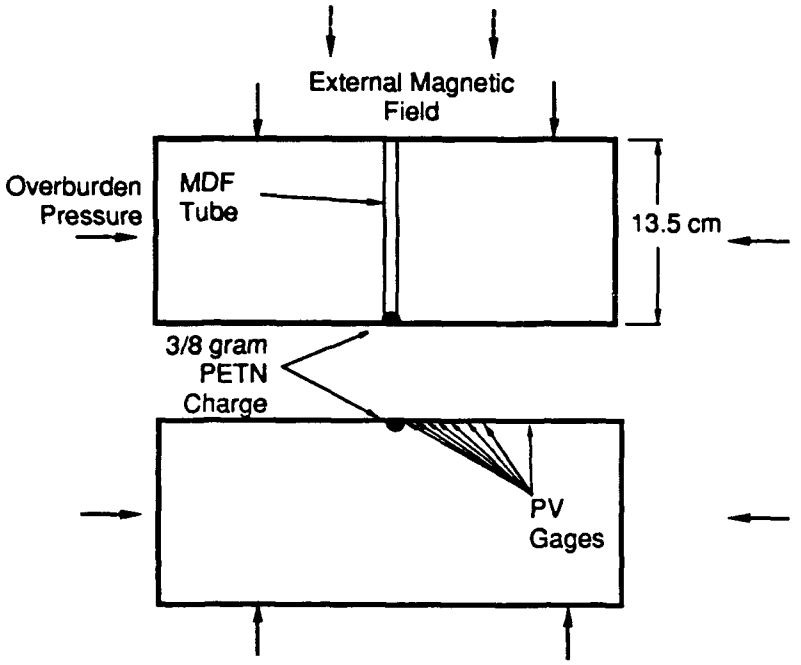
The results from these experiments showed (1) no difference between dry/frozen and dry/room temperature limestone, (2) large differences in the propagated pulse between dry and saturated pore conditions and between saturated/room temperature and saturated/frozen Indiana limestone, (3) attenuation of peak velocity and displacement for the frozen/saturated limestone falls between the saturated/room temperature at the high end and dry at the low end of peak values, (4) The radiated kinetic energy for the dry limestone was about 40J (about 2% of the available chemical energy of the explosive), and about 140J (6.6% of the chemical energy of the explosive) for the saturated/room temperature and saturated/frozen

limestone experiments, and (5) little, if any, effect of freezing the pore fluid in Sierra White granite on wave propagation.

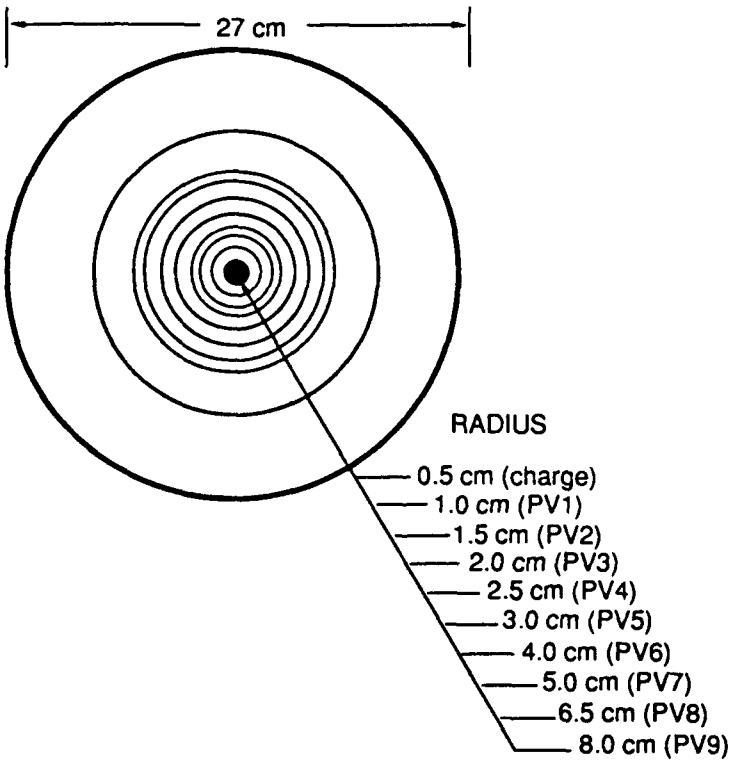
REFERENCES

(1) Miller, S.A.and Florence, A.L., "Spherical Wave Propagation in Frozen Saturated Rock", R&D Status Report No. 1, Contract No. F19628-91-K-0003, SRI International (1991).

(2) Miller, S.A., Gefken, P.R., and A.L. Florence, "Spherical Waves in Jointed Limestone", Bimonthly Progress Report No. 5, Contract No. DNA 001-90-C-0130, SRI International (1991).



(a) Side View



(b) Top View

RM-6645-1H

Figure 1. Configuration of particle velocity experiments in Indiana limestone and Sierra White granite.

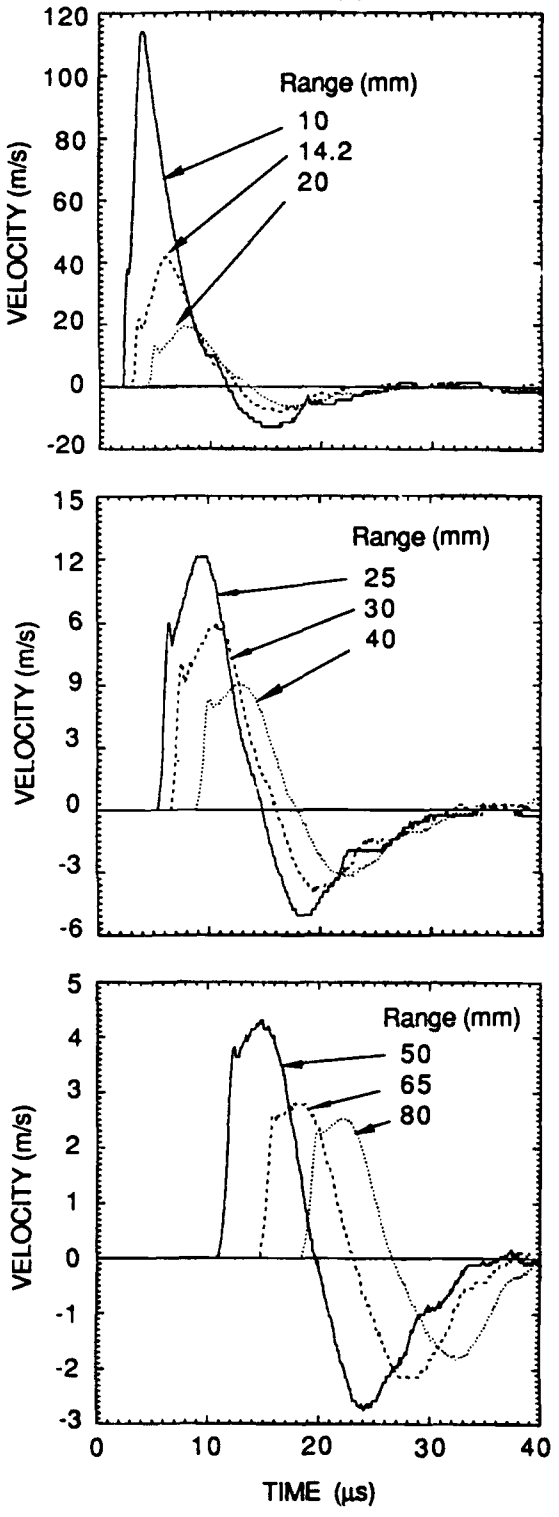


Figure 2. Particle velocity histories measured at three ranges in dry/frozen Indiana limestone, Test 598.

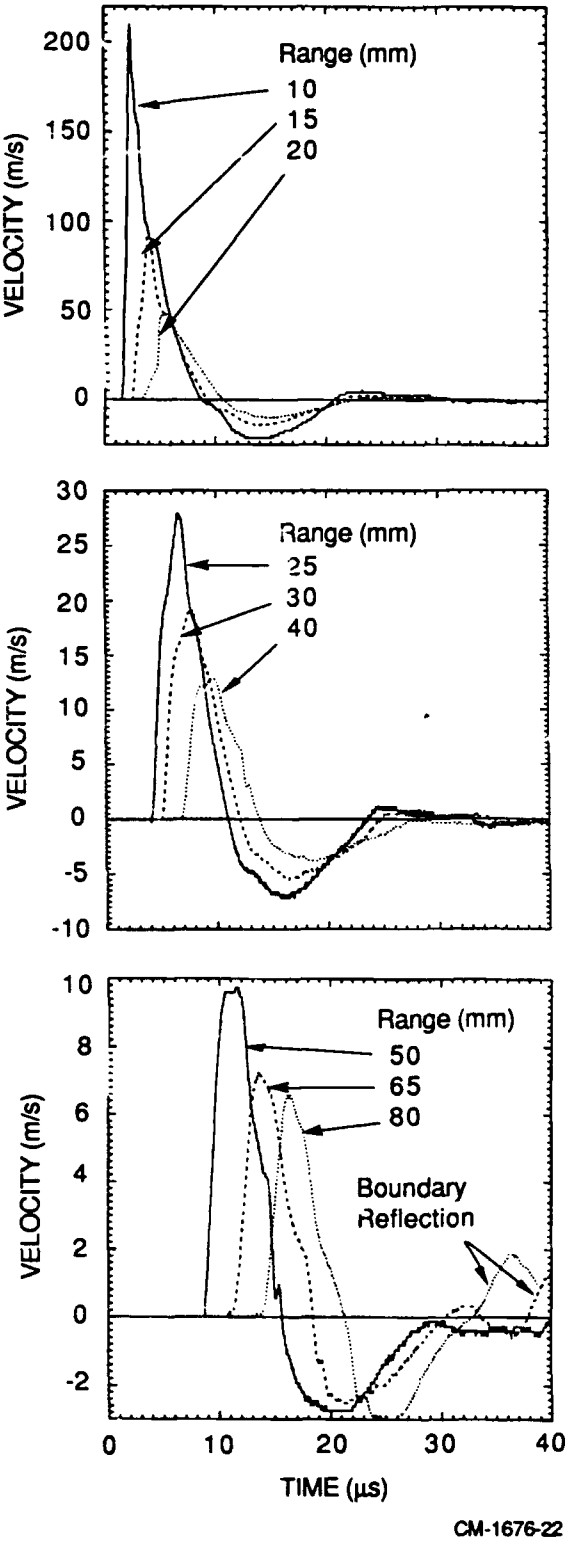


Figure 3. Particle velocity histories measured at three ranges in saturated/frozen Indiana limestone, Test 602.

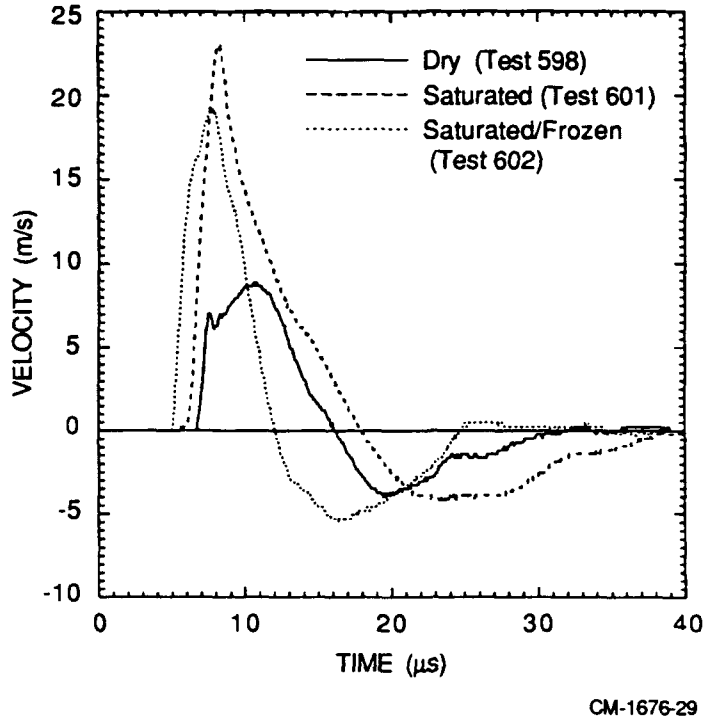


Figure 4. Comparison of velocity histories at 30-mm range in Indiana limestone (16% porosity) for three different pore conditions.

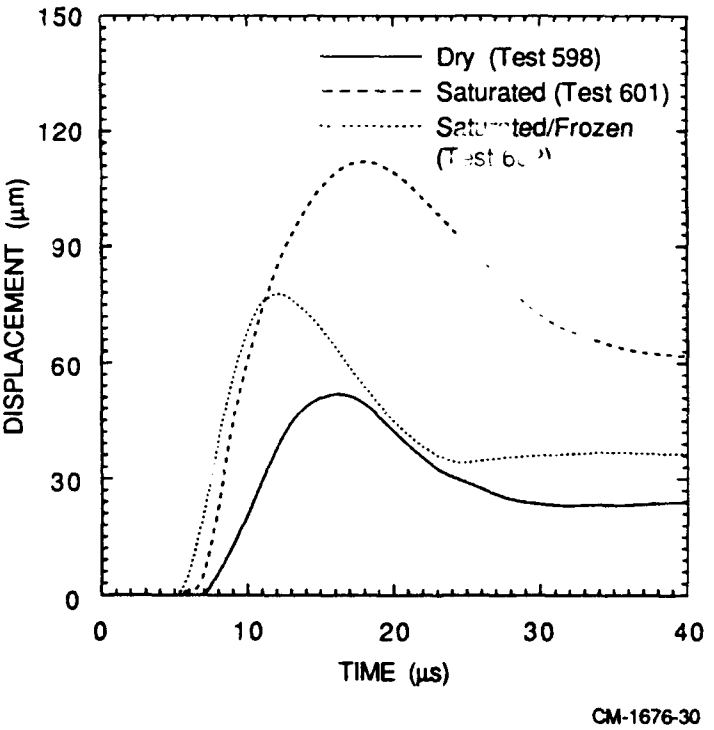


Figure 5. Comparison of displacement histories at 30-mm range in Indiana limestone (16% porosity) for three different pore conditions.

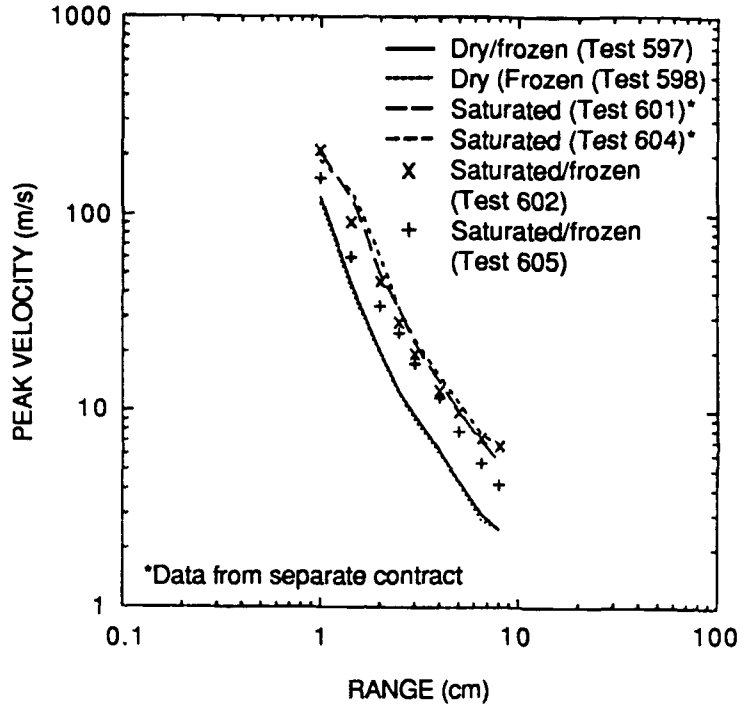


Figure 6. Attenuation of peak particle velocity in dry/frozen, saturated, and saturated/frozen Indiana limestone.

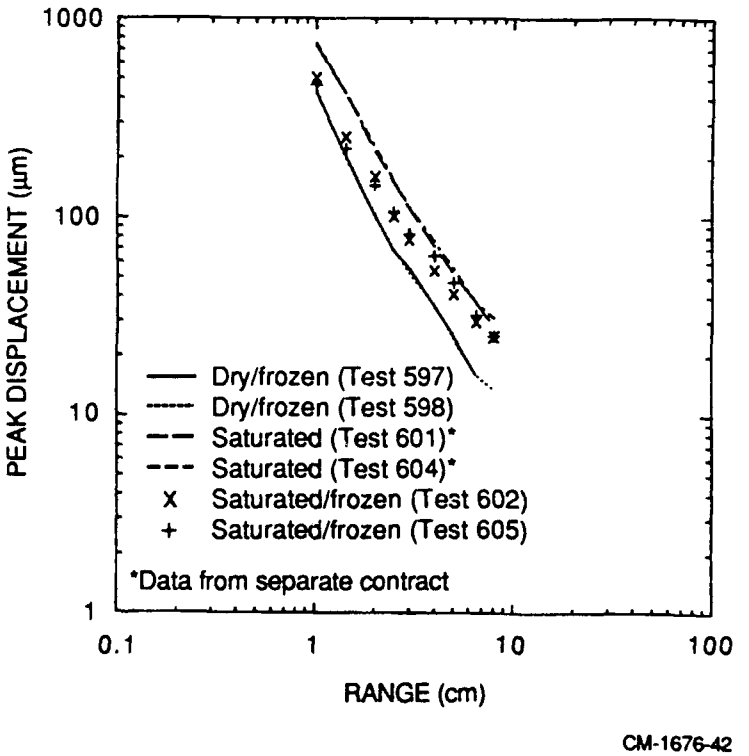


Figure 7. Attenuation of peak displacement measured in dry/frozen, saturated, and saturated/frozen Indiana limestone.

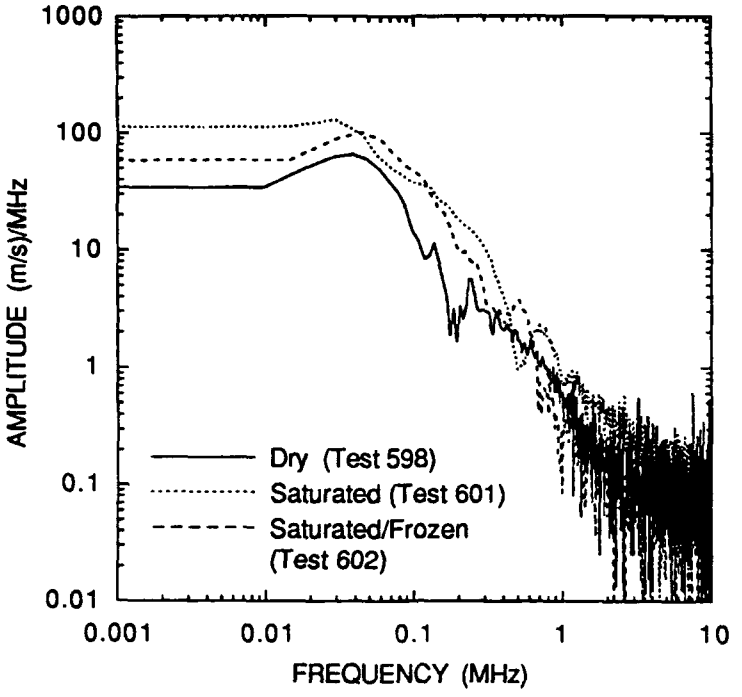


Figure 8. Comparison of velocity spectra at the 30-mm range in Indiana limestone (16% porosity) with three different pore conditions.

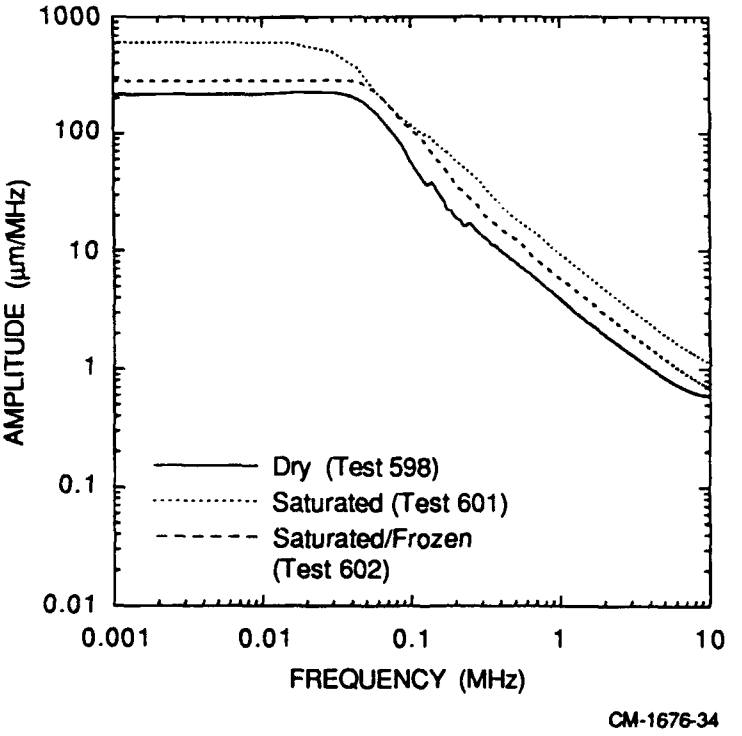


Figure 9. Comparison of displacement spectra at the 30-mm range in Indiana limestone (16% porosity) with three different pore conditions.

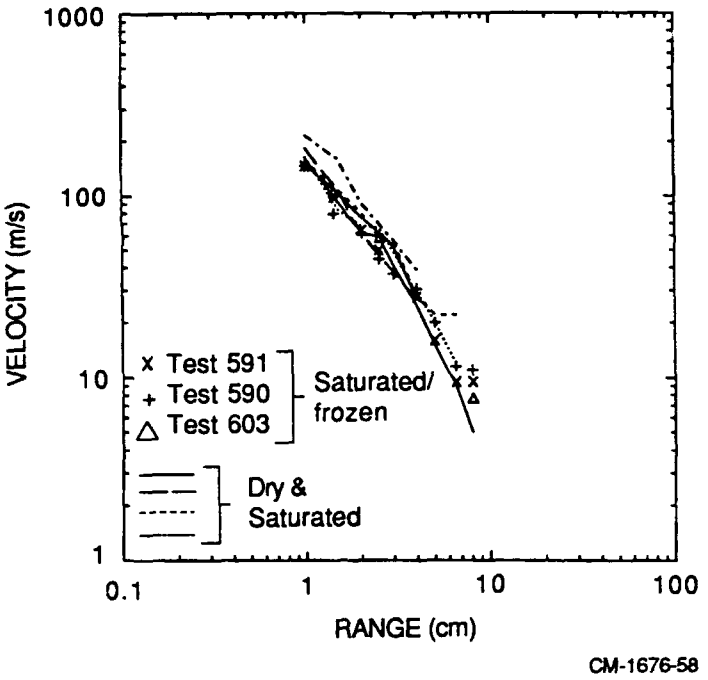


Figure 10. Comparison of velocity attenuation in Sierra White granite with different pore conditions.

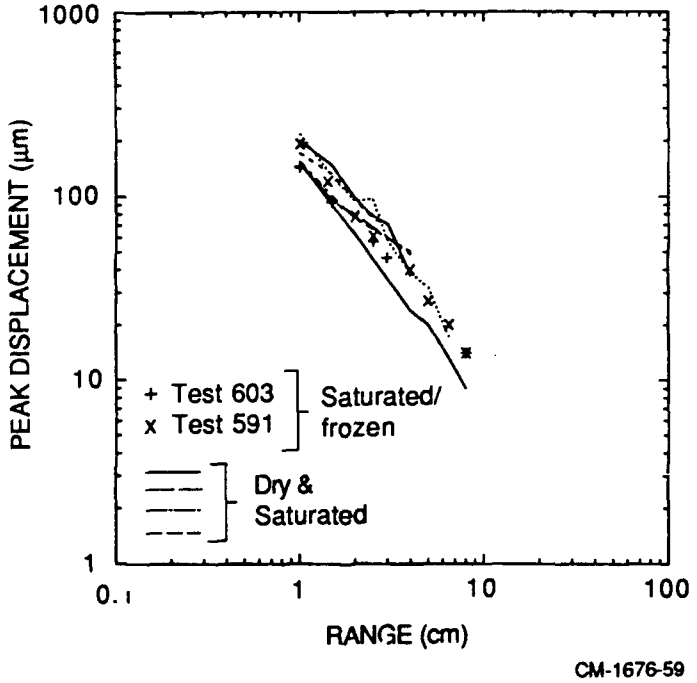


Figure 11. Comparison of displacement attenuation in Sierra White granite with different pore conditions.

FORMATION AND PROPAGATION OF LOVE WAVES FROM A P-WAVE SOURCE

S. A. Miller and A.L. Florence
SRI, International
Menlo Park, CA 94025
Contract No. F19628-89-K-0009

OBJECTIVE

The objective of this research is to investigate experimentally, and support with theoretical calculations, the formation and propagation of Love waves from a P-wave source due to scattering at material heterogeneities. The purpose is to generate experimental data in well-controlled scale model experiments to compare with theoretical calculations. The experiments consist of a scattering surface (i.e., vertical wall) in a surface layer of rock simulant overlying a higher impedance granite substrate representing an infinite half-space. The P-wave source is spherical charge of dilute explosive cast in the surface layer material which generates a known compressional pulse which is propagated elastically beyond a certain radius. Strain gages mounted at the surface of the specimen monitor the surface waves from which the Love wave component is extracted.

In these experiments, lateral heterogeneities of simple geometries (i.e., planar scattering surfaces) are cast into the surface layer, converting incident P-wave energy into shear waves. The horizontally polarized shear waves (SH-wave) trapped in the surface layer wave-guide are the Love waves, we will measure at the free-surface. The sensors at the surface will be distributed so both the undisturbed signals and signals modified by scattering can be monitored.

RESEARCH ACCOMPLISHED

The experimental configuration for the two cases we are investigating with a scattering surface are shown in Figure 1. A third case, not shown, is the case of a layer of rock-simulant over a half-space of granite to establish a baseline measurement on the surface where no Love wave component is present. The sensors on the surface are semi-conductor strain gages and large gage factor conventional strain gages oriented in a rosette so that the principle strains and surface shear strains can be resolved.

Initially we investigated a spherical piezoelectric crystal as the P-wave source. The results of our investigation showed this source to be inadequate for generating signals of high enough amplitude at the longer ranges of interest, especially after scattering, to be easily resolved by measurements at the surface. The piezoelectric crystal approach may still prove useful,;however, a significant effort in development of higher output power supplies is required. Consequently, the source was modified to use a dilute explosive which increases the wave amplitude of the propagated pulse while maintaining elastic wave propagation in the surface layer beyond a certain radius from the source.

The new source consists of a PETN explosive diluted by spherical plastic beads (called microballoons) encased in an acrylic sphere. The density of the dilute explosive is 0.45 g/cm^3, which reduces the detonation pressure of the charge from about 7.5 GPa for our typical 1.0 g/cm^3 charge to about 1.0 GPa for the dilute charge. Another consideration is efficient source installation between experiments. Our plan is to fabricate the surface layer

experimental models using 2C4 grout. However, because this grout has a substantial curing time, 90% strength at 28 days, we will use pourstone to cast the source into the surface layer model because it cures in about 2 hours. Between experiments, we will core out the old source and cast in the new source with pourstone.

We fabricated a model to measure the pulse from the dilute explosive source cast in pourstone and surrounded by 2C4 grout. The configuration is shown in Figure 2. In this experiment the dilute explosive source was cast in a 6.35-cm-diameter cylinder of pourstone grout and then cast in 2C4 grout, resulting in a cylindrical specimen 25.4-cm in diameter and 25.4 cm long. Copper loop particle velocity gages were cast into the midplane of the specimen at radii of 1.5-, 2.5-, 4.0- and 5.0-cm from the center of the source. In the experiments, the models are placed in a solenoid driven by a constant current power supply which provides an axial magnetic field on the specimen. Particle velocity histories are measured by monitoring the induced voltage from the copper loops as they move at the local particle velocity through the magnetic field. The particle velocity is proportional to the induced voltage, the gage length and the magnetic field strength.

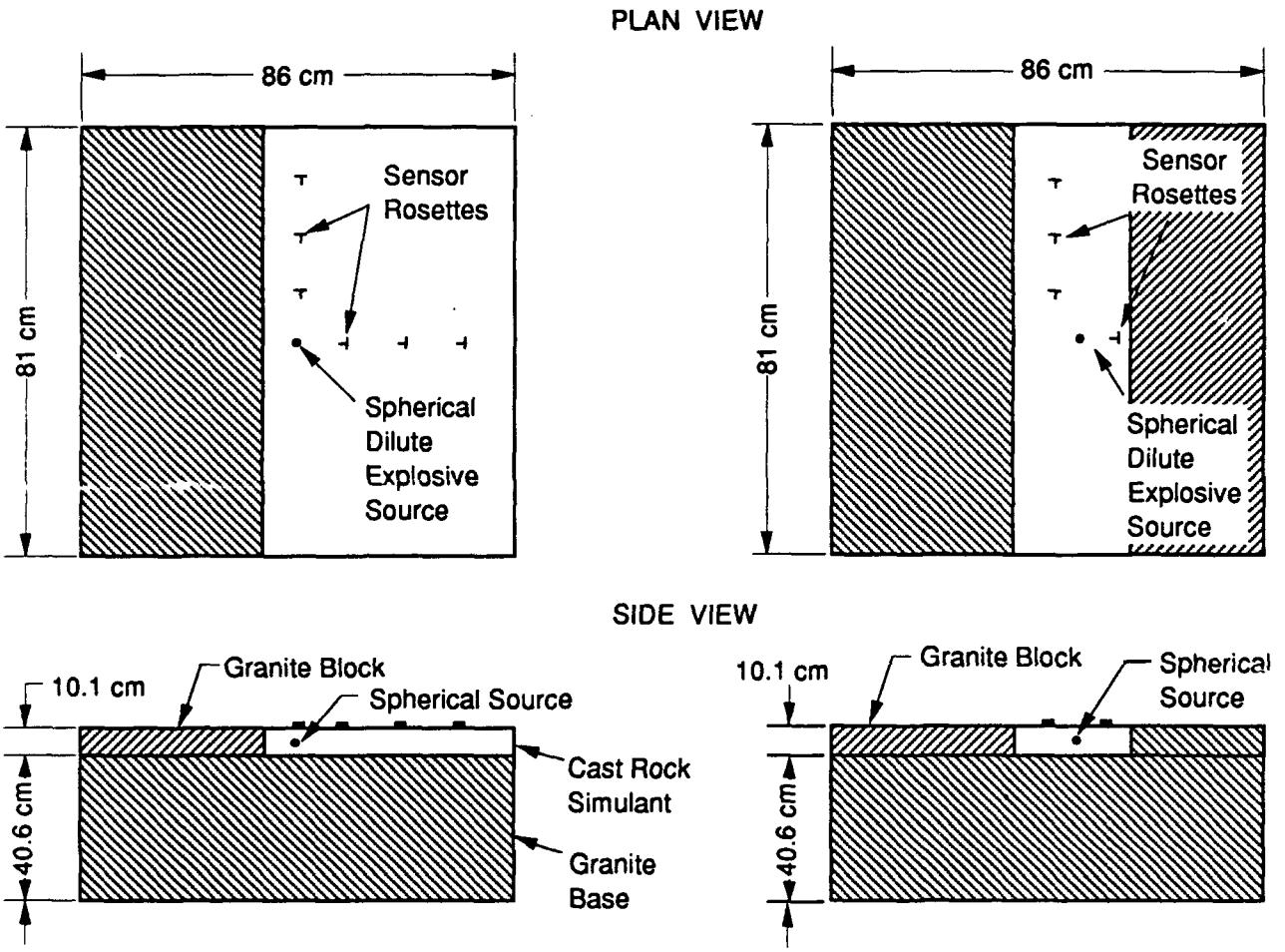
The measured particle velocity histories in the source evaluation experiment are shown superposed in Figure 3. The outward pulse was measured at about 15 μs, followed by about a 12μs negative, or rebound phase. Although plastic deformation occurs around the cavity boundary, at the range of our measurements at the surface, the wave propagation will be elastic. The velocity history at the 1.5-cm range was used as an input velocity boundary condition in finite element calculations of the experimental geometry shown in Figure 1. The results of these calculations will be compared with experimental data when the scale-model tests are conducted.

CONCLUSIONS

The dilute explosive source has been evaluated and provides a known pulse of approximately 15 μs outward motion and the elastic radius is located at approximately 2 cm from the center of the source. We have fabricated the surface wave models and are currently testing. The results will be compared with finite element calculations of the experimental geometries shown in Figure 1.

REFERENCES

Miller, S.A. and A.L. Florence, "Formation and Propagation of Love Waves in a Surface Layer with a P-Wave Source," GL-TR-90-0100, Contract No. F19618-88-K-0051 (April 1990). ADA225559



(a) Model with planar scattering surface.

(b) Model with trough

RM-7206-24

Figure 1. Schematic of scale-model laboratory experiment.

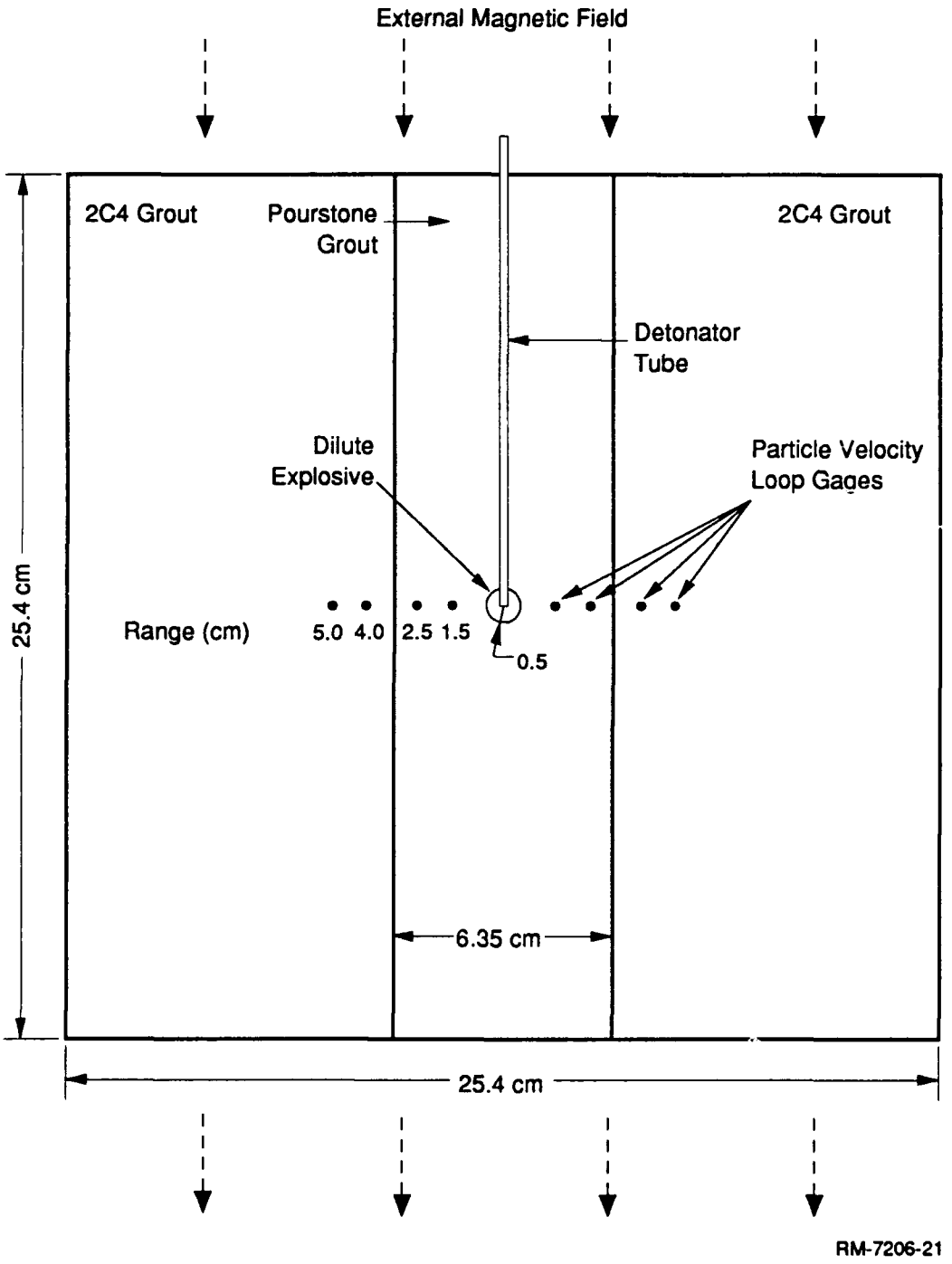


Figure 2. Configuration for low amplitude spherical source using dilute explosive cast in grout.

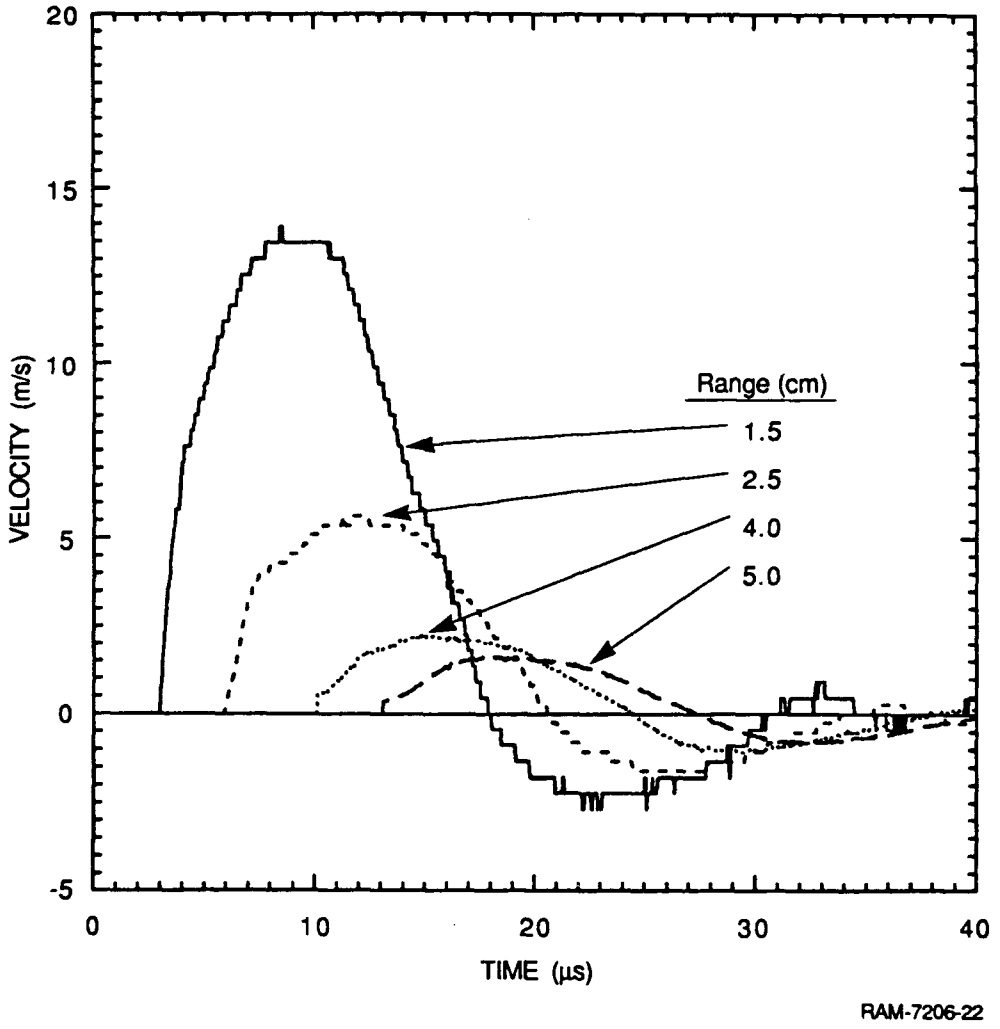


Figure 3. Particle velocity histories measured in dilute explosive source evaluation experiment.

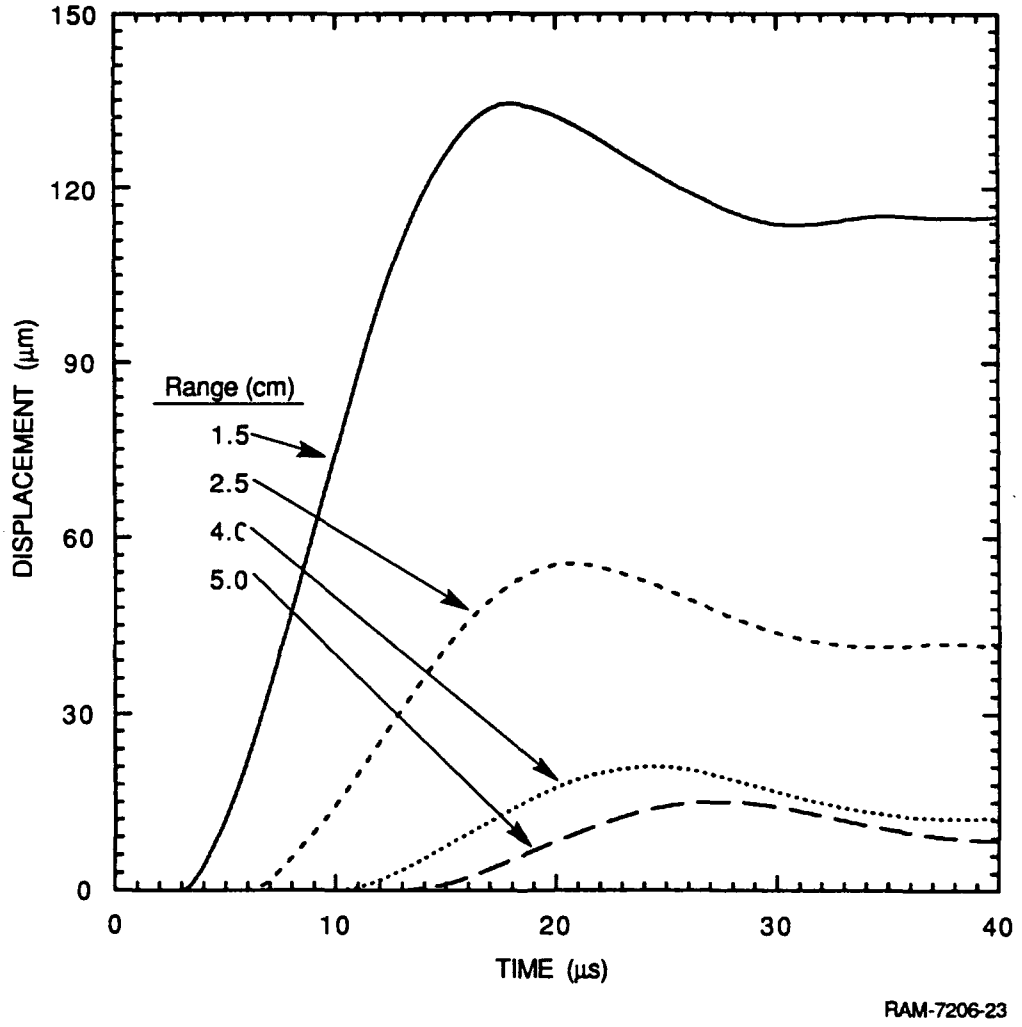


Figure 4. Displacement histories measured in dilute explosive source evaluation experiment.

REGIONAL VARIATION OF Q_{Lg} AND ITS FREQUENCY DEPENDENCE: IMPLICATIONS FOR CRUSTAL STRUCTURE AND EVOLUTION

Brian J. Mitchell

Department of Earth and Atmospheric Sciences
Saint Louis University
St. Louis, MO 63103

OBJECTIVE

Lg has emerged as the phase which may be most useful for determining yields of nuclear explosions at regional distances. Yields derived from Lg are highly dependent upon Q values assumed to occur along the path of travel, values which may vary by nearly two orders of magnitude at crustal depths in continental regions. Since Q values may not be known for some paths of interest, it will be useful to be able to predict them based upon geological criteria such as level of tectonic activity, age, sediment thickness, etc. This paper investigates whether or not there are consistent relationships between Lg coda Q and its frequency dependence for different tectonic provinces and whether those relationships are related to the tectonic evolution of those regions.

RESEARCH ACCOMPLISHED

Introduction

There are now numerous determinations of Q for the phase Lg and its coda. Frequently, the Q determinations are supplemented by determinations of the frequency dependence of Q for those phases, assuming that Q_{Lg} or Q_c (coda Q) is given by $Q_o f^{\eta}$ where Q_o is the value of Q_{Lg} or Q_c at 1 Hz and the exponent η indicates how Q_{Lg} varies with frequency. Both Q_o and η display large regional variations.

Recent work suggests that Q determinations of S-wave coda are dominated by intrinsic anelasticity (Frankel and Wennerberg, 1987) and that intrinsic anelasticity is likely to govern Q_c of Lg waves in the Basin and Range (Xie and Mitchell, 1990b). Pursuing the assumption that Q_c is governed by intrinsic anelasticity, Mitchell (1991) showed that the high values of frequency dependence of Q_{Lg} and Q_c found in the Basin and Range province of the western United States can be explained by a rapid increase in intrinsic shear-wave Q (Q_μ) at mid-crustal depths (from less than 100 to more than 1000) without invoking a frequency-dependence of intrinsic Q_μ for that region. Q_μ values in the eastern United States, on the other hand, must vary with frequency near 1 Hz in order to explain both observed Q_{Lg} values and the attenuation of fundamental-mode Rayleigh waves (Mitchell, 1980).

The frequency dependence observed for Q_{Lg} can therefore be due to both layering of intrinsic shear wave internal friction (Q_μ^{-1}) and to intrinsic frequency dependence of Q_μ in the crust, the relative importance of these two mechanisms being greatly different in high-Q and low-Q regions. In this paper I introduce η-Q plots and apply them to infer Q_μ structure and frequency dependence and their regional variation.

Procedure

Figure 1 shows two relations between η and Q_c, one the western United States, a region currently undergoing active extension, and the other a combination of values from Africa and the eastern United States which are restricted to stable cratonic regions. Most of the western United States values are compiled from maps of Q_o and η compiled by Singh and Herrmann (1983), but one value, with associated standard errors, corresponding to the Basin and Range, is from Xie and Mitchell (1990b). The values from Africa are from Xie and Mitchell (1990a) and are restricted to those cratonic portions of Africa where path coverage was sufficient to provide stable values of Q_o and η with relatively good resolution. Values in the region of the African rift valley were therefore excluded. The shield region of northwestern Africa was also excluded because of poor path coverage.

Two data sets are being considered, one for a low-Q region of the western United States and one corresponding to what we take to be typical cratonic regions. The Q_o values for the western United States are much lower than those for the cratonic regions. Both regions exhibit decreasing values of η with increasing Q_o. My approach will be to attempt to find the simplest sequence of models which will explain those variations of values and to relate those changes to the geologic evolution of the crust.

Theoretical values of Q_o and η were obtained by applying the stacked spectral ratio (SSR) method of Xie and Nuttli (1988) to a suite of synthetic seismograms generated for several distances. The synthetics were computed using model summation using methods of Wang (1981). The process begins by generating synthetics for crustal velocity and Q models appropriate for the region of study. I used the velocity model of Lin (1989) which pertains to the Basin and Range for all computations in the western United States and used the velocity model of Mitchell and Herrmann (1979) for cratonic regions. Variations in the velocity model, unless they are very large, have little effect on the resulting Q_o and η values.

Results

The variations of Q_o and η in the western United States were relatively easy to fit. The fundamental-mode Rayleigh wave data of Lin (1989) were first inverted for a Q_μ structure, assuming various depth distributions for the frequency dependence (ζ) of Q_μ. Several models could be obtained which explain observed Q_o and η values. One example (for 1 Hz) is shown in Figure 3 where ζ is taken to be 0.0 at depths between 0 and 15 km and 0.5 at

greater depths. A suite of 20 synthetic seismograms were generated at distances between 300 and 1250 km at 50 km intervals. The synthetics were all generated at a 45° azimuth from an earthquake source at a depth of 5 km having strike, dip, and slip values of 0°, 90°, and 0°, respectively. A theoretical SSR was then obtained from those synthetics; for the present example it yielded a Q_o value of 267 and an η value of 0.41. These values are consistent with observed values for that region as shown by the dashed line through WUS values in Figure 1. Changes in Q_μ values in the upper crust (Figure 2) were then made and the process was repeated. Few trials were required to explain the trend of the η–Q plot for the western United States in Figure 1.

Explaining the variation of the η–Q values for cratonic regions was more difficult. In these high-Q regions, changes in the layered structure had little effect on η for models in which Q_μ was high. In addition, the models required frequency-dependent Q_μ values throughout much of the crust if both observed Q_{Lg} and the attenuation of fundamental-mode Rayleigh waves are to be explained. The only models which I found which would do that included a low-Q zone at a frequency of 1 Hz at mid-crustal depths (Figure 3). While all models in Figures 3 and 4 suffer from non-uniqueness, it does not appear possible to explain the trend of η–Q values without resorting to very low Q_μ values through the upper crust in the western United States and to z low-Q zone in the middle crust of cratonic regions.

It is interesting that the rapid increase to high Q_μ values in the western United States and the base of the low-Q_μ zone in the cratonic regions of this study both correspond to depths often cited for the brittle-ductile transition in the continental crust. If, as suggested by Mitchell (1975, 1980), low Q_μ values can be attributed to fluids in cracks and interstitial pore space in the crust, then these results indicate a continuing decrease in fluid content throughout the upper crust of tectonically active regions with time since the most recent period of major tectonic activity. This decrease may occur because the fluids have escaped to the surface or have been absorbed in retrograde metamorphic reactions. The models of Figure 3 suggest that in stable areas much of the fluid content has been removed from the upper crust, but that a substantial amount of fluids remain at depth just above the high-Q portion of the crust, either because it had no outlet to the surface or because temperature-pressure conditions, and the mineralogy of the rocks at mid-crustal depth did not permit retrograde metamorphism to absorb all of the fluids.

CONCLUSIONS AND RECOMMENDATIONS

η–Q plots provide a new tool to study Q_μ structure and its evolution in the upper crust of continental regions. They suggest that Q_μ increases with time following tectonic or orogenic activity in the western United States, presumably reflecting a decrerase in crack density and fluid content of the upper crust of that region. An η–Q plot for stable regions of Africa and the eastern United States suggests that a residual fluid layer, producing low Q_μ values at mid-crustal depths in an otherwise high-Q crust, is present in those

regions. Although the low-Q_μ layer is relatively thin, it affects Q values and frequency dependence values of Lg and its coda in those regions.

REFERENCES

Frankel, A., and L. Wennerberg, Energy-flux model for seismic coda: separation of scattering and intrinsic attenuation, *Bull. Seism. Soc. Am., 77,* 1223-1251, 1987.

Lin, W.J., Rayleigh wave attenuation in the Basin and Range province, M.S. thesis, Saint Louis University, 55 pp., 1989.

Mitchell, B.J., Regional Rayleigh wave attenuation in North America, *J. Geophys. Res., 80,* 4904-4916, 1975.

Mitchell, B.J., Frequency dependence of shear wave internal friction in the continent crust of eastern North America, *J. Geophys. Res., 85,* 5212-5218, 1980.

Mitchell, B.J , Frequency dependence of Q_{Lg} and its relation to crustal anelasticity in the Basin and Range province, *Geophys. Res. Lett., 18,* 621-624, 1991.

Mitchell, B.J., and R.B. Herrmann, Shear velocity structure in the eastern United States from the inversion of surface wave group and phase velocities, *Bull. Seism. Soc. Am., 69,* 1133-1148, 1979.

Singh, S.K., and R.B. Herrmann, Regionalization of crustal coda Q in the continental United States, *J. Geophys. Res., 88,* 527-538, 1983.

Wang, C.Y., Wave Theory for Seismogram Synthesis, Ph.D. Diss., Saint Louis University, 235 pp., 1981.

Xie, J., and O.W. Nuttli, Interpretation of high-frequency coda at large distances: stochastic modelling and method of inversion, *Geophys. J., 95,* 579-595, 1988.

Xie, J., and B.J. Mitchell, A back-projection method for imaging large-scale lateral variations of Lg coda Q with application to continental Africa, *Geophys. J. Int., 100,* 161-181, 1990a.

Xie, J., and B.J. Mitchell, Attenuation of multiphase surface waves in the Basin and Range province, part I: Lg and Lg coda, *Geophys. J. Int., 102,* 121-137, 1990b.

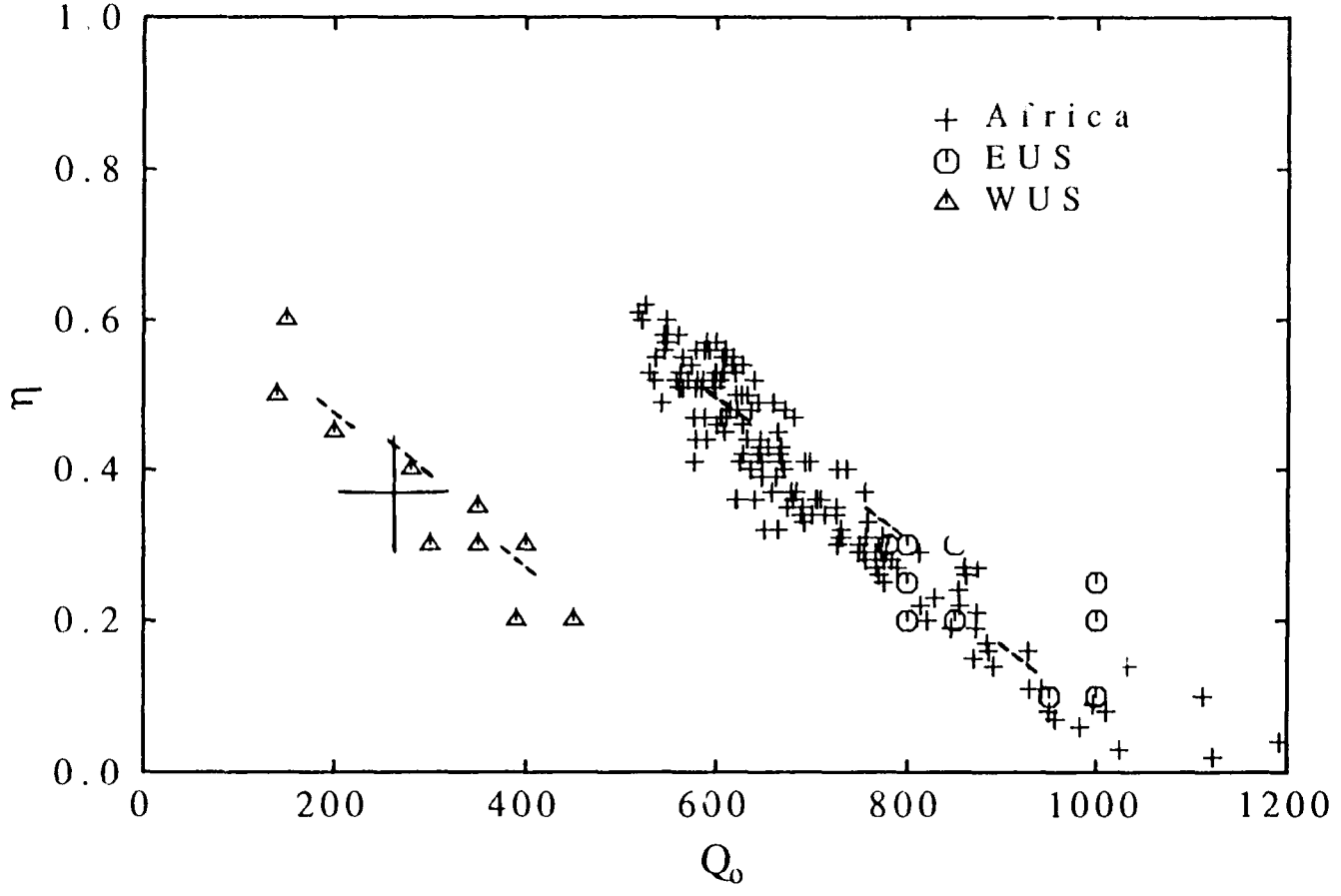


Figure 1. Plots of the frequency dependence of Lg coda Q versus Lg coda Q at 1 Hz for the Basin and Range province and for cratonic regions of Africa and the eastern United States. Basin and Range values and eastern United States values are from Singh and Herrmann(1983). The cross denotes values and standard errors for a Basin and Range path (Xie and Mitchell, 1990b). Values for Africa are from Xie and Mitchell (1990a). Dashed lines denote theoretical values predicted by the evolution models shown in Figures 3 and 4.

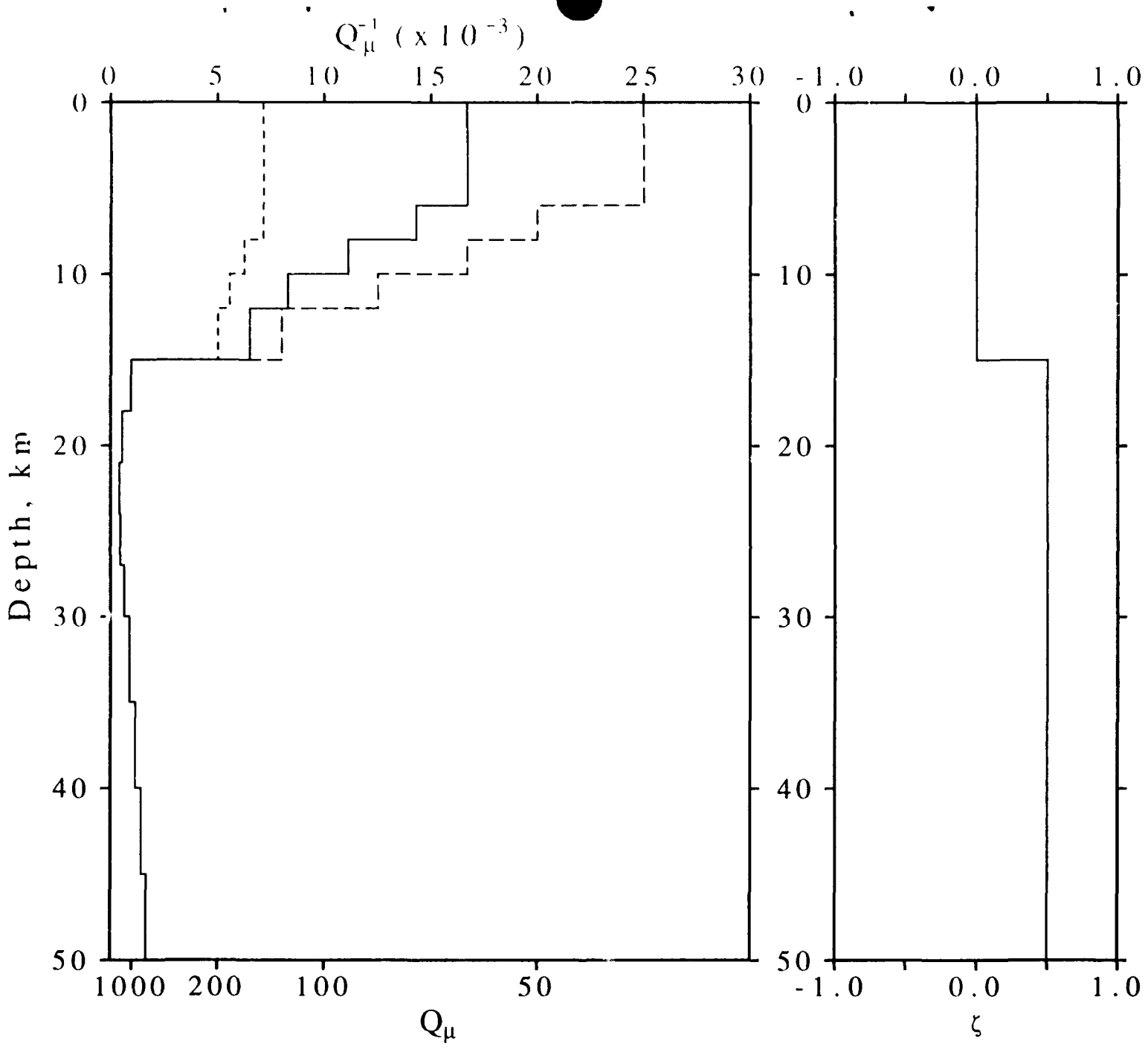


Figure 2. Model of Basin and Range Q evolution which explains the regional patterns of Lg coda Q and its frequency dependence, as well as observed attenuation of fundamental-mode Rayleigh waves.

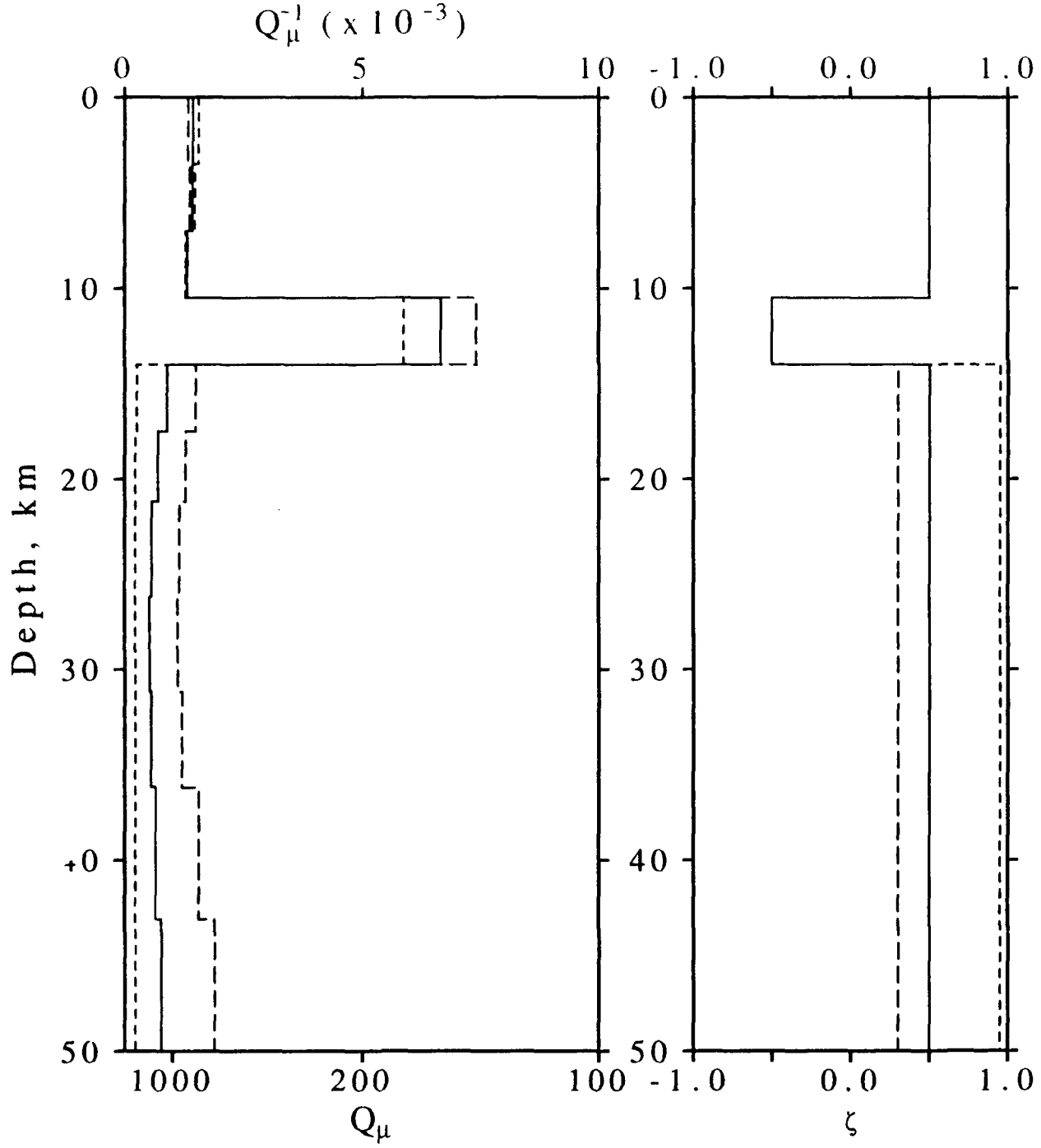


Figure 3. Model of Q evolution for cratonic regions of Africa and the eastern United States which explains pattersn of Lg coda Q and frequency dependence, as well as observed attenuation of fundamental-mode Rayleigh waves.

A New System For Seismic Yield Estimation of Underground Explosions

J. R. Murphy
S-CUBED
11800 Sunrise Valley Dr., Suite 1212
Reston, Virginia 22091
Contract No. F19628-89-C-0026

Objective

Research conducted over the past decade has led to the development of a number of innovative procedures for estimating the yields of underground nuclear explosions based on systematic analyses of digital seismic data recorded from these tests. In addition, a wide variety of new data regarding the geophysical environments at Soviet test locations have now become available as a result of the Joint Verification Experiment (JVE) and associated data exchanges. The objective of this research program is to attempt to integrate all these new capabilities and data into a comprehensive prototype operational system which can be used to provide optimum seismic estimates of explosion yield.

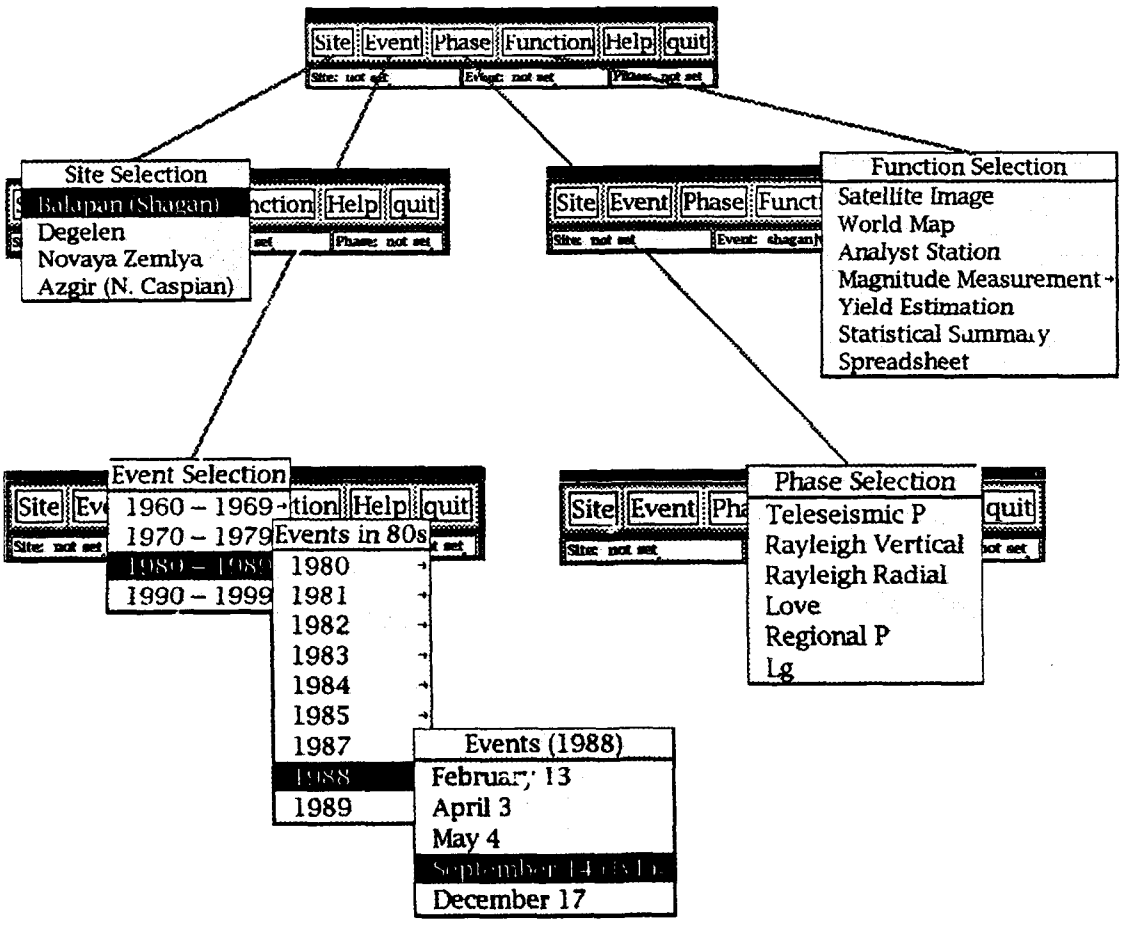
Research Accomplished

A preliminary prototype version of the system designed to achieve the above objectives, designated the Yield Estimation System (YES), has been implemented in a Sun color workstation (SPARCStation) environment at the DARPA Center for Seismic Studies (CSS) using software built upon the framework of the X Window graphics and Oracle relational database management systems. This initial version focuses on explosions at the Soviet Shagan River and Novaya Zemlya test sites and on yield estimates based on five different seismic magnitude measures derived from teleseismic P and surface wave (m_b, M_{Pspec}, M_o) and regional L_g and P wave (M_{Lg}, M_{Pn}) data. Available test site information is presented to the analyst in the context of SPOT™ satellite images of the test regions, in a format which permits the analyst to

interact digitally with the image to easily extract and display information regarding the explosion source environment. A waveform database consisting of more than 10,000 digital seismograms recorded from Shagan River and Novaya Zemlya explosions at stations of the GDSN, USAEDS, CDSN and IRIS networks has been assembled for this project. These data provide the reference base required to support the various seismic analysis options available within the system.

A distinguishing characteristic of the YES is that it is completely menu-driven and mouse-activated and requires no keyboard entry by the user. The principal menu providing access to the system is shown at the top of Figure 1 where it can be seen that it consists of six "buttons" which can be used to initiate (SITE, EVENT, PHASE, FUNCTION) or terminate (QUIT) action within the system, or to view online information regarding the operating characteristics and parameters of the system

Figure 1: *Main menu structure for the YES, illustrating the pulldown access to the individual menu functions.*

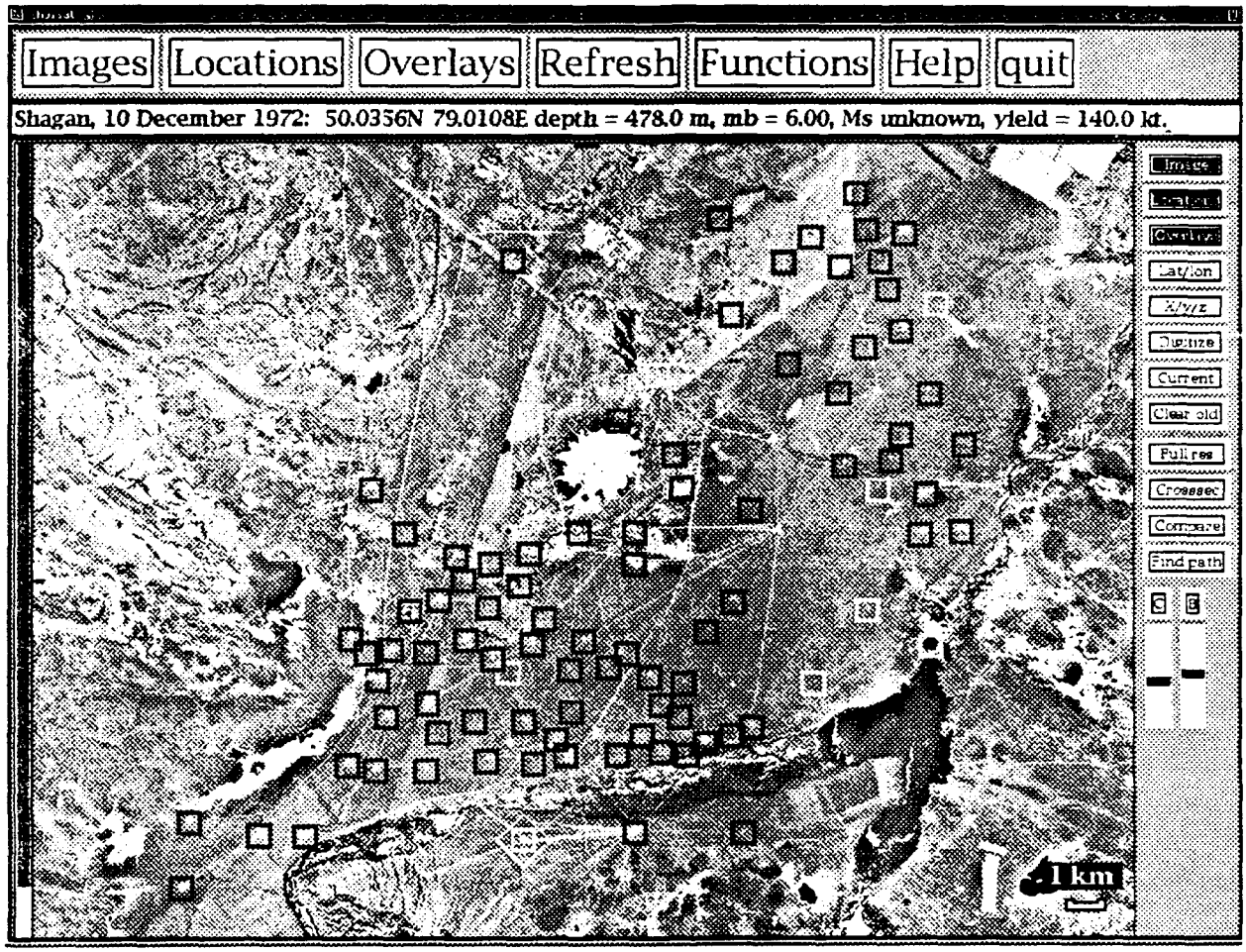


(HELP). As is illustrated in this figure, selection of any of these buttons with the mouse causes a series of pulldown menus to be activated from which more specific options can be accessed. Thus, in the example shown in this figure, the SITE button has been activated to select the Soviet Shagan River (Balapan) test site, and the EVENT button has been activated to select the JVE explosion which was detonated at that test site on 14 September 1988. Subsequent analyst interaction with the system is initiated through the PHASE and FUNCTION buttons. The PHASE button provides the analyst with the capability to choose from among the six different listed seismic phases for which digital waveform data are currently available on the system. The FUNCTION button provides access to the seven principal computational and analysis modules which permit the analyst to:

- view the seismic data within the context of the available information regarding the specific test location under investigation (*Satellite Image, World Map*)
- interact with the recorded seismic data to process it and extract the various magnitude measures of interest (*Analyst Station, Magnitude Measurement*)
- formally combine the seismic measures of source size to obtain an optimum measure of explosion yield and quantitative measures of the uncertainty in that estimate (*Yield Estimation*)
- statistically assess the results with respect to any existing treaty thresholds or other yield levels of particular interest (*Statistical Summary, Spreadsheet*)

Once a test site and a particular explosion have been specified, a typical analysis sequence would normally begin with the selection of the *Satellite Image* option from the FUNCTION menu, which in this case causes the SPOT satellite image of the Shagan River test site to be displayed on the screen in the form shown in Figure 2. Here the locations of previous explosions which have been detonated at this site are shown as square overlays, with the selected JVE event location highlighted by a diamond. Note that this display is dynamic in the sense that the image and overlays to it are formally tied to an extensive online database of supplementary information. Thus, in the example shown here, the operator has pointed with the mouse to one of the squares (arrow), which has initiated a process by which available information about that event has been extracted from the database and displayed on the information line below the menu buttons, indicating that this explosion was detonated at Shagan on 10 December 1972 at the specified latitude and longitude and that the Soviets have reported the depth

Figure 2. *SPOT satellite image of the Shagan River test site with superimposed locations of the historical explosions (squares) and current event (diamond)*



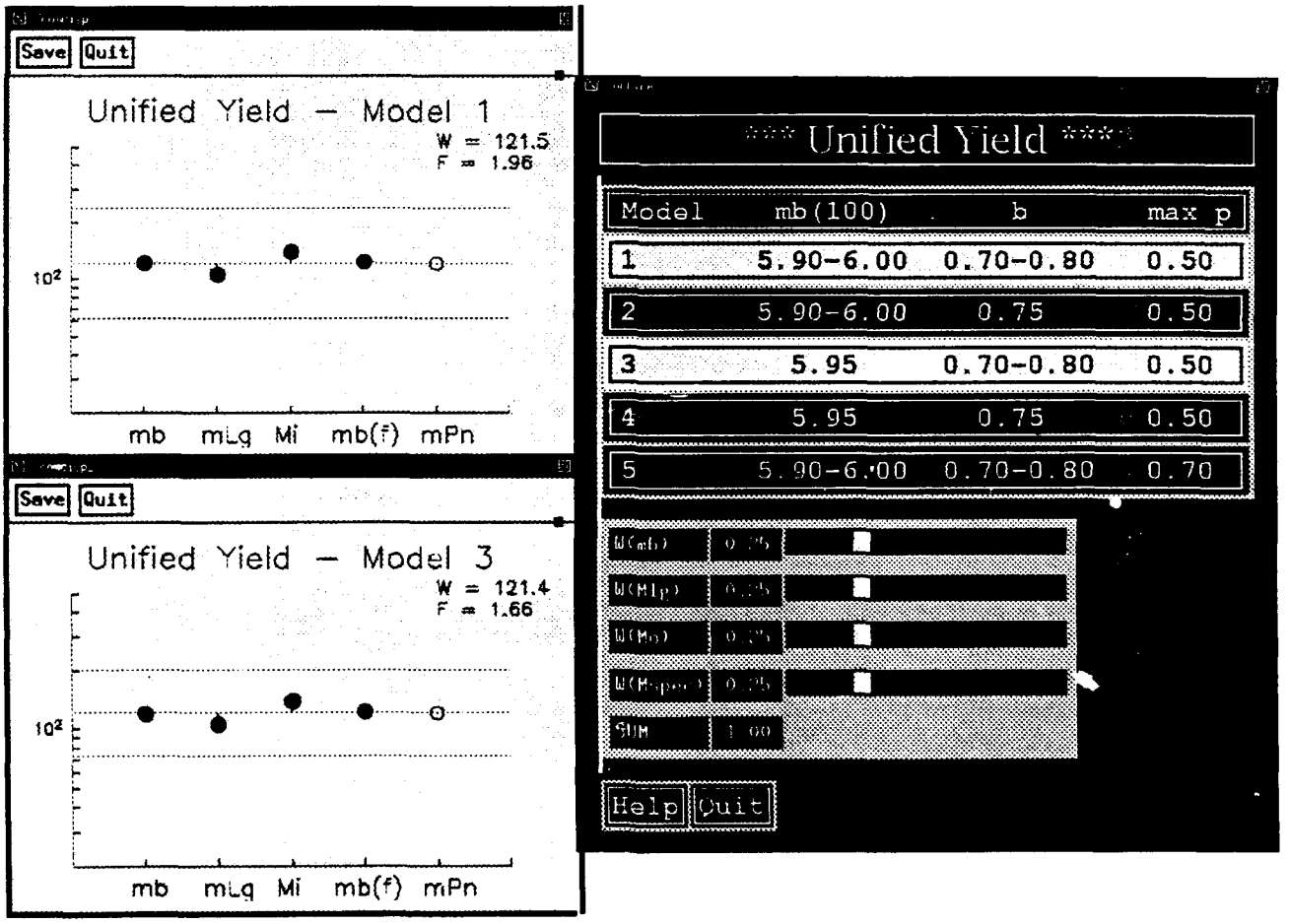
as 478 m and the yield as 140 kt. In addition to the event locations, a number of geologic and topographic databases have been "registered" to this SPOT image and are available for display as overlays or images. These include maps of surface geologic features, Defense Mapping Agency topographic data and subsurface geologic information to a depth of about 1 km.

Having completed an initial review of the available information regarding the explosion source environment, the analyst can proceed to an examination of the corresponding recorded seismic data by accessing the *Analyst Station* and *Magnitude Measurement* modules from the FUNCTION menu. The *Analyst Station* interface provides submenus of commands which can be used by the operator to interactively assign waveform quality, pick arrival times, measure amplitudes and periods, filter the

data, transform to different instrument responses or compare a selected waveform with recordings at that same station from other explosions in the database. Once the required parameters have been extracted, they can be saved to the database and transmitted to the *Magnitude Measurement* module where they are used to compute each of the five network-averaged seismic magnitude measures currently available on the system.

Given these seismic measures of source size, the corresponding explosion yield and associated uncertainty can be estimated by selecting the *Yield Estimation* feature from the FUNCTION menu. This module provides an estimate of explosion yield based on multiple magnitude measures and associated extremal confidence limits corresponding to different sets of constraints specified by the analyst. The menu for the yield estimation module is shown in Figure 3, together with sample output

Figure 3. *Menu structure and sample output for the unified yield estimation module.*



corresponding to the specification of two different sets of constraints (i.e., Models 1 and 3) to the magnitude data determined for the JVE event. In these displays, the resulting unified yield estimates (W) and associated upper bound uncertainty factors (F) are shown together with the yield estimates obtained from the five individual magnitude measures.

Conclusions and Recommendations

A sophisticated working prototype system has now been developed for estimating the yields of underground explosions at the Soviet Shagan River and Novaya Zemlya test sites through systematic analyses of digital seismic data recorded from these tests. This system incorporates a large digital database of over 10,000 seismograms recorded from past explosions at these two sites and provides a simple graphical user interface which permits the analyst to easily access available information regarding the explosion source environment, to estimate a variety of seismic magnitude measures and combine them to obtain a unified estimate of explosion yield and associated uncertainty and to quantitatively evaluate the derived yield with respect to both the TTBT threshold and previous experience at that test site. Future efforts will focus on the incorporation of CORRTEX and DSS data into the system and on the implementation of a semi-automatic report generation module which can be used to fully document YES processing results.

NORSAR research on regional network data processing

Svein Mykkeltveit, Tormod Kværna, Frode Ringdal and Jan Fyen
NTNF/NORSAR, P.O.Box 51, N-2007 Kjeller, Norway

Contract No. F49620-89-C-0038

Objective

The objective of NORSAR's regional array program is to provide data for use in seismological verification research. Specifically, the research in seismic data processing focuses on development and testing of methods to improve the detection, location and identification of low-magnitude events, and techniques that may be useful in the further development of the Intelligent Monitoring system (IMS) are of particular interest. In this regard, much attention has been devoted during the last year to the concept of threshold monitoring (TM). This is a method of monitoring the seismic amplitude levels for the purpose of using this information to assess the largest size of events that might go undetected by a given network.

This paper summarizes the status of development of the regional network in northern Europe that contributes seismic data in real time to the NORSAR Data Processing Center. Also summarized is the current status of development of the IMS. The capabilities of the TM technique for monitoring of specific target sites as well as more extensive geographical regions are demonstrated, using data from NORESS, ARCESS and FINESA.

Research accomplished

The regional network and IMS

The network contributing continuous data to NORSAR is shown in Fig. 1 and currently comprises the NORESS and ARCESS arrays in Norway, the FINESA array in Finland, the GERESS array in Germany, and the two 3-component stations at Ksiaz and Stary Folwark in Poland. A comprehensive description of NORESS and ARCESS is given by Mykkeltveit et al. (1990). These arrays have been in stable and continuous operation since they were installed in 1984 and 1987, respectively. The somewhat smaller and technically less sophisticated, yet very powerful FINESA array in Finland has been described by Uski (1990). The GERESS array in the Bavarian Forest area of Germany has been described by Harjes (1990). Although the quality of GERESS data received at NORSAR is not yet entirely satisfactory, the data are being processed continuously and also used by IMS.

Data from all of these four arrays were provided to the GSETT-2 experiment undertaken by the Geneva Group of Scientific Experts during 22 April-2 June 1991,

along with data from 56 other single stations and arrays worldwide. Inspection of the bulletins from this experiment clearly shows that the four arrays contributed very substantially to the definition of seismic events on a global scale. Furthermore, of the order of 2,000 events in northeastern Europe were determined based on analysis of data from NORESS, ARCESS, FINESA and GERESS during these 6 weeks.

Each of the two stations in Poland are equipped with short period as well as broad band 3-component seismometers. The systems, including satellite links to NORSAR, were operational as of April 1991 and enabled Poland to take part in GSETT-2. Recently (June 1991), a single 3-component staion was installed in Apatity, USSR, in cooperation with the Kola Science Center of the USSR Academy of Sciences. Data from the Apatity station are recorded locally, copied on magnetic tape and mailed to NORSAR. The station is located close to a very active mining area. Fig. 1 shows the records from a presumed double explosion in the Kirovsk mine for both the nearby Apatity station, and ARCESS.

IMS, developed by SAIC and others, is a system for joint processing of data from a regional network of arrays and single 3-component stations. IMS has been described by Bache et al. (1990), and initial results from operating the system are given by Bratt et al. (1990). IMS is distributed between NORSAR and the Center for Seismic Studies (CSS) in Arlington, Virginia. The latest version of IMS has been operated experimentally at CSS since spring of 1991 on data from NORESS, ARCESS, FINESA, GERESS, and the Polish 3-component stations. This new version of IMS will be installed at NORSAR during September 1991, replacing the current version that has been in operation since January 1990 for processing of data from NORESS and ARCESS. IMS will continue to be the prime tool for regional processing and related activities at NORSAR.

Threshold monitoring of the Novaya Zemlya test site; a scaling experiment

During the past two years, the NORSAR staff has conducted extensive research on the development and application of the threshold monitoring method (TM). Using data from the three regional arrays, ARCESS, FINESA and NORESS, Kværna and Ringdal (1990) found that the Northern Novaya Zemlya test site can be consistently monitored at a very low magnitude level (typically $m_b \approx 2.5$). That particular study showed that during a one-week period, every single occurence of the threshold exceeding $m_b = 2.5$ could be explained as resulting from an interfering event signal either from teleseismic or regional distance.

We will attempt to illuminate the concept of threshold monitoring further by describing an experiment, involving down-scaling of recorded signal traces of the 24 October 1990 explosion at Novaya Zemlya and simulating what might have been observed on the threshold traces if such a down-scaled event had in fact occurred.

The explosion of 24 October 1990 had a world-wide $m_b = 5.6$. Our scaling procedure consisted simply of dividing each trace by a factor of 1000 (simulating an $m_b = 2.6$ event) and superimposing these down-scaled traces on actually observed recordings at various points in time.

We selected a typical 24 hour time period (day 104/1991), and added the down-scaled signal at hourly intervals in order to get a picture of the effect under different

noise conditions. A total of 24 identical signals where thus added at different times.

Fig. 2 (top) shows the "actual" threshold trace (day 104) for Novaya Zemlya, devloped exactly as described by Kværna and Ringdal (1990). We note that there is only one peak significantly exceeding $m_b = 2.5$; this corresponds to a large teleseismic earthquake ($m_b = 6.0$) from the Ryuku Islands.

Fig. 2 (bottom) shows the resulting trace for that same day after adding the down-scaled signals and recomputing the threshold trace. We note that all of the 24 occurrences stand out clearly on the plot. Thus, if an explosion of $m_b = 2.6$ had indeed occurred at Novaya Zemlya that day, and assuming that the scaling is representative, there would have been clear indications on the threshold trace of such an explosion.

An interesting observation is the way in which threshold monitoring complements the traditional detection/location type monitoring: Let us assume that an $m_b = 2.6$ explosion had in fact occurred at Novaya Zemlya, and that the resulting signals were similar to the down-scaled signals used here. It might well be that such an explosion would *not* have been detected and located by the regional network. In fact, during daytime noise conditions (see Fig. 3) there would very likely have been only one or two confident phase detections (P_n and possibly S_n at ARCESS), and this is not sufficient to locate in the traditional network sense.

Nevertheless, such an explosion would have been clearly indicated on the network threshold trace. It would not have been possible to explain this peak as resulting from some "different" event (as was always the case for such peaks in the Kværna and Ringdal (1990) study). Thus, a peak of this type would be a prime candidate for further detailed off-line analysis, possibly implying efforts to acquire additional data in order to further elucidate the nature of the event.

Continuous threshold monitoring using "regional threshold displays"

The magnitude calibration factors for the Novaya Zemlya test site were obtained by processing previous events in that area with "known" magnitude. Similarly, we have also obtained "site specific" calibration factors for a number of active mines in Scandinavia and Western Russia. The calibration events enable us to fine tune the TM processing parameters in order to obtain close to optimum monitoring performance.

Extension of the TM method to regions where no calibration events are available requires generic relations for the magnitude calibration factors. Kværna (1991) has developed such initial relations for the P_n and L_g phases for ARCESS, FINESA and NORESS. These relations are applicable to northern Europe and adjacent areas, making possible so-called "regional threshold monitoring" of that geographical region.

The regional threshold monitoring approach lends itself naturally to displays in the form of contoured geographical maps. By using a spatial grid covering the area of interest, interpolation can be applied to get a visual representation of threshold variations over an extended geographical region, and examples of such coloured contour maps will be given in the poster presentation. Examples will be given both in terms of "absolute" TM threhold levels (with m_b units indicated on the colour template) and "relative" thresholds (i.e., thresholds relative to the average thresholds during noise conditions at each geographical point).

Our research has so far shown that the regional approach to threshold monitoring implies a significant enchancement of practical monitoring of underground nuclear explosions. In particular, a computer system with various graphical display features of TM data will provide the analyst with a very useful interactive analysis tool.

Conclusions and recommendations

The deployment of advanced regional arrays and high quality 3-component stations, and the associated development and implementation of automated and increasingly powerful data processing techniques represents one of the major advances in seismic monitoring in recent years. In our judgement, the threshold monitoring technique described in this paper represents a significant enhancement of practical monitoring of underground nuclear explosions. Still, much research remains to be done in further development of this technique and other methods for integrated processing of data from a regional network of arrays and 3-component stations, in order to fully exploit the potential for such data.

References

Bache, T. C., S. R. Bratt, J. Wang, R. M. Fung, C. Kobryn and J. W. Given (1990). The Intelligent Monitoring System, *Bull. Seism. Soc. Am.* 80, Part B, 1833-1851.

Bratt, S. R., H. J. Swanger, R. L. Stead, F. Ryall and T. C. Bache (1990). Initial results from the Intelligent Monitoring System. *Bull. Seism. Soc. Am.* 80, Part B, 1852-1873.

Harjes, H.-P. (1990). Design and siting of a new regional array in central Europe, *Bull. Seism. Soc. Am.* 80, Part B, 1801-1817.

Kværna, T. and F. Ringdal (1990). Continuous threshold monitoring of the Novaya Zemlya test site, *Semiannual Tech. Summary, 1 Apr - 30 Sep 90*, NORSAR Sci. Rep. 1-90/91, NORSAR, Kjeller, Norway.

Kværna, T. (1991). Initial development of generic relations for regional threshold monitoring, *Semiannual Tech. Summary, 1 Oct 90 - 31 Mar 91*, NORSAR Sci. Rep. 2-90/91, NORSAR, Kjeller, Norway.

Mykkeltveit, S., F. Ringdal, T. Kværna and R. W. Alewine (1990). Application of regional arrays in seismic verification, *Bull. Seism. Soc. Am.* 80, Part B, 1777-1800.

Uski, M. (1990). Event detection and location performance of the FINESA array in Finland, *Bull. Seism. Soc. Am.* 80, Part B, 1818-1832.

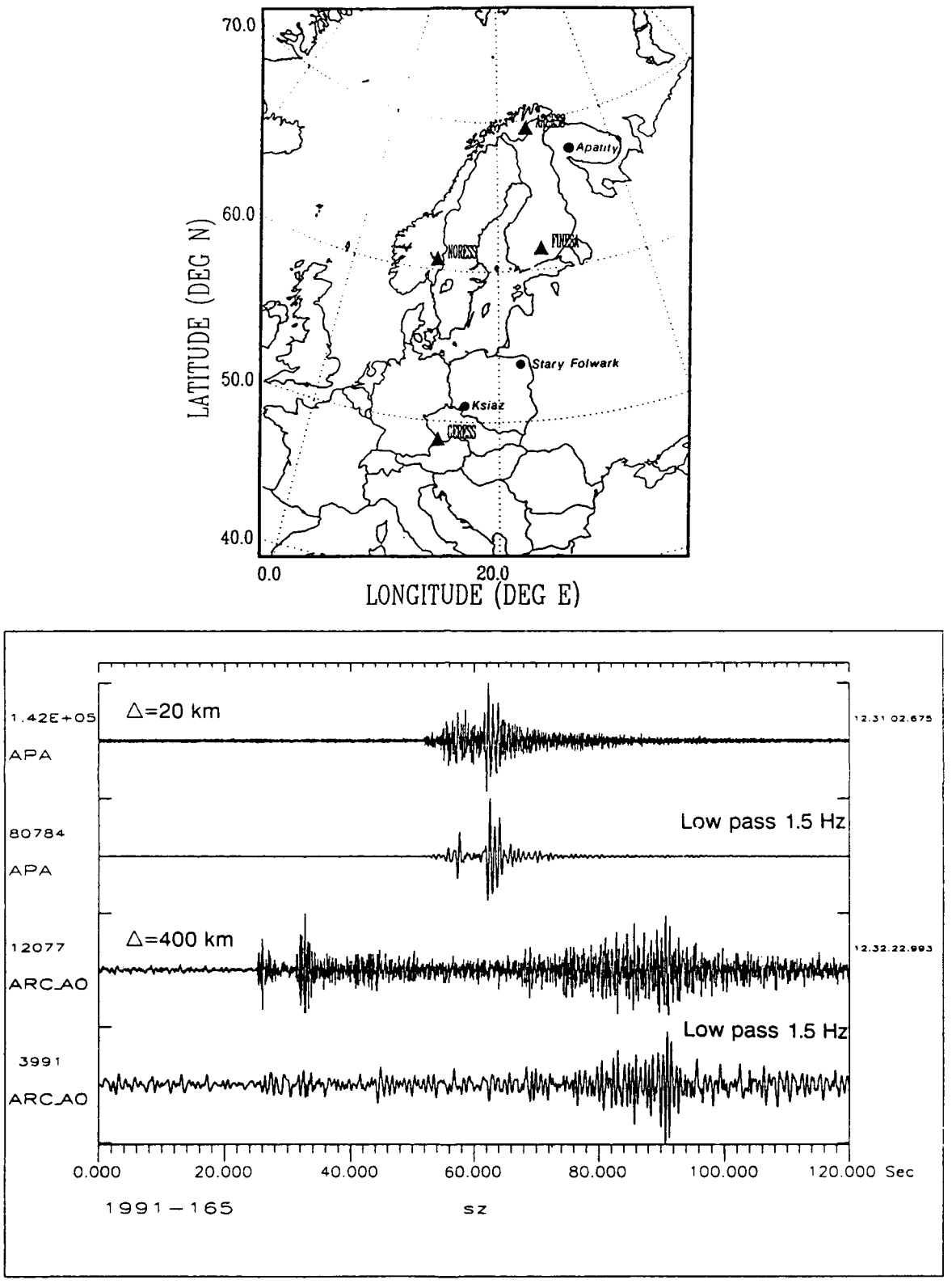


Fig. 1. Top: The map shows the location of the regional arrays NORESS, ARCESS, FINESA and GERESS as well as the 3-component stations Ksiaz and Stary Folwark in Poland, and Apatity in the USSR. Bottom: Apatity and ARCESS recordings of a mining blast at the Kirovsk mine, 20 km from the Apatity station, on 14 June 1991, at 12.31.40 GMT. For each station, data are shown unfiltered and low-pass filtered at 1.5 Hz.

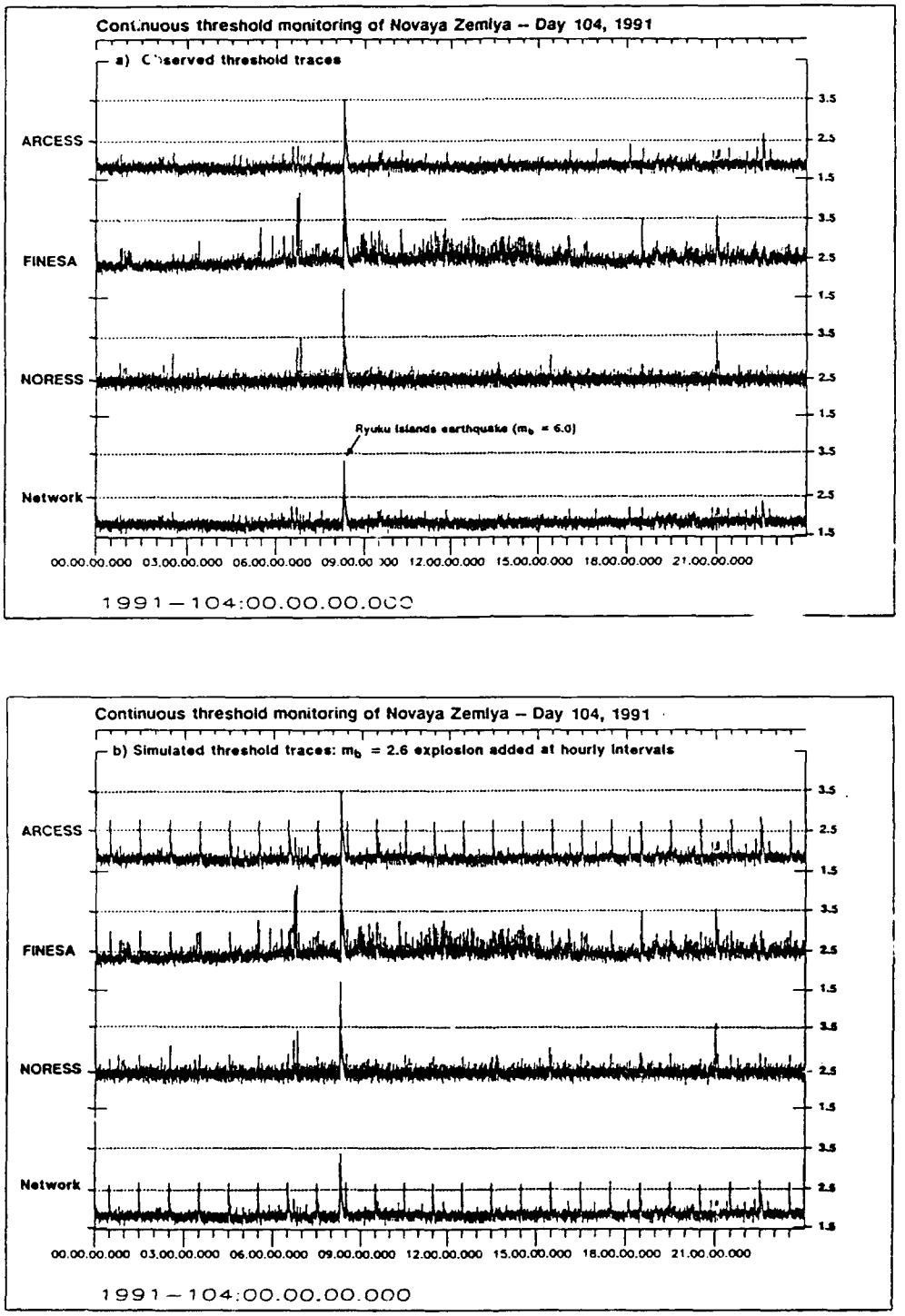


Fig. 2. Top: Threshold monitoring of the Novaya Zemlya test site for day 1991/104 (14 April 1991). The top traces represent thresholds (upper 90 per cent magnitude limits) obtained from each of the three arrays, ARCESS, FINESA and NORESS, whereas the bottom trace shows the combined network thresholds. Bottom: Same as the plot above, but with the down-scaled signals superimposed at hourly intervals. Note that all occurences of the simulated $m_b = 2.6$ events stand out clearly on the combined network trace.

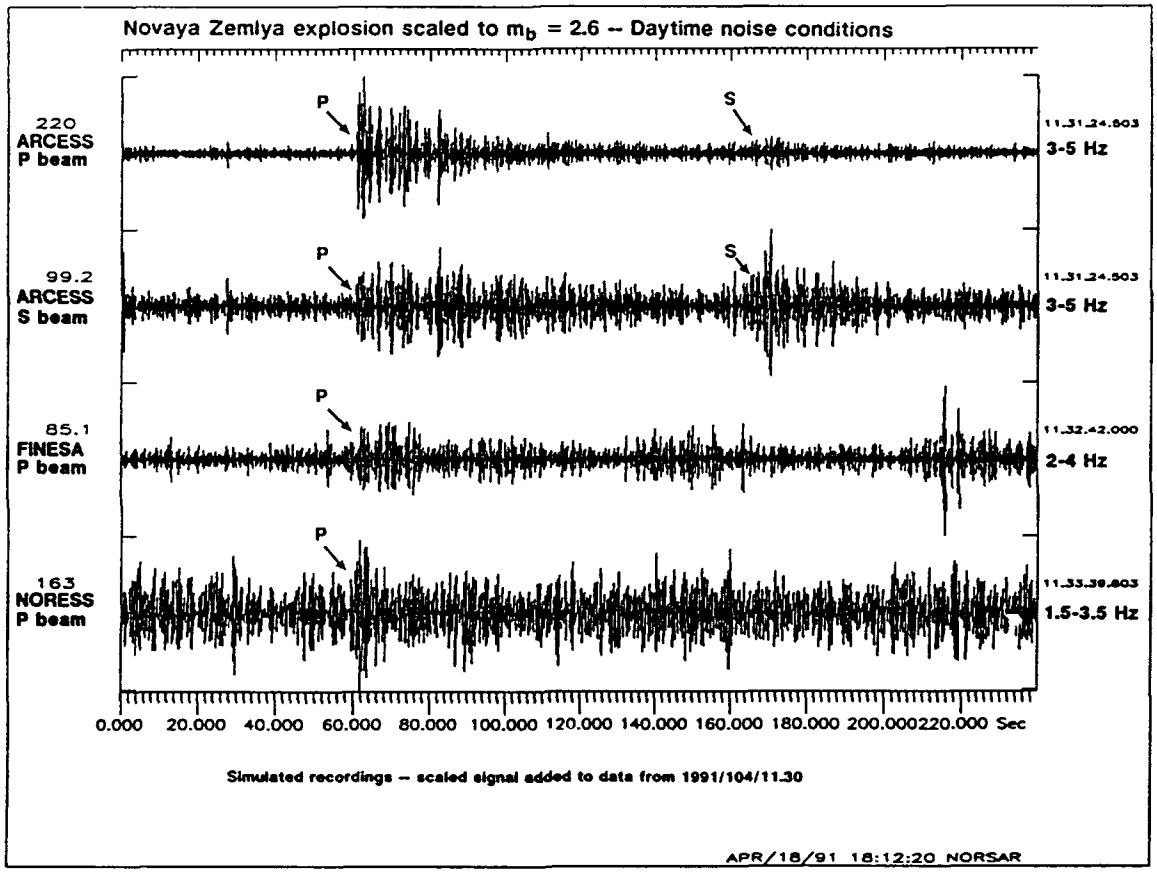


Fig. 3. "Down-scaled" signals from the Novaya Zemlya nuclear explosion of 24 October 1990 superimposed on noise during a "high noise" interval. The origin of the simulated "event" is 1991/101/11.30.00.

TITLE: **A NEURAL NETWORK APPROACH TO INITIAL PHASE IDENTIFICATION FROM THREE-COMPONENT POLARIZATION MEASUREMENTS**

AUTHOR & AFFILIATION: *Gagan B. Patnaik and Thomas J. Sereno, Jr.*
Science Applications International Corporation
10260 Campus Point Drive, San Diego, CA 92121

CONTRACT NO: F-19628-90-C-0156

OBJECTIVE:

The primary objective of this work is to evaluate the applicability of neural network techniques for automated initial identification of seismic phases using 3-component polarization measurements. Accurate estimates of phase velocities from f-k analysis enable nearly perfect identification of P- and S-phases from data recorded by small regional arrays like NORESS and ARCESS. Therefore, the goal of our neural network approach is to improve the performance of automated systems that use data only from single 3-component stations, like the IRIS stations in the Soviet Union. A second objective is to compare the results obtained using these techniques with those obtained using more traditional methods (*e.g.*, multivariate discriminant analysis).

RESEARCH ACCOMPLISHED:

The initial application of our neural network approach is to array-averaged three-component data from NORESS and ARCESS. Polarization attributes of regional P- and S-phases identified by seismic analysts at NORSAR and CSS were used to train the neural networks. These attributes are routinely computed by the Intelligent Monitoring System and are written to an on-line relational database at the CSS (Bache, *et al.*, 1990). The attributes are estimated by solving eigenproblems for the co-variance matrices using windowed three-component waveform data corresponding to phase detections (Jurkevics, 1988). The attributes used in this study are, the center frequency of the band(s) in which a detection was made, signal rectilinearity and planarity, incidence angles of the long-axis and the short-axis of the polarization ellipsoid, ratio of horizontal to vertical power, and the ratio of maximum to minimum horizontal amplitude.

We used these polarization data from more than 2000 detections at NORESS and from more than 4000 detections at ARCESS. An example of the distribution for four of these polarization attributes obtained from ARCESS are shown in Figure 1. These parameters show considerable overlap for P- and S-phases. Neural network classification techniques are well-suited to this type of situation, as they are capable of constructing non-linear decision surfaces across class boundaries.

We used feed-forward neural networks for this study. The networks are fully-connected with three layers (Figure 2). They include 5–8 input nodes (*e.g.*, varying combinations of polarization attributes as input parameters), variable number of nodes in the middle (hidden) layer, and two output nodes that correspond to P- and S-phases. The inputs to each node in the middle layer is a weighted sum of the polarization attributes, and the output of a node is calculated by applying a sigmoidal thresholding function to its input. A similar scheme is applied to the nodes in the output layer. The two weight matrices are initially estimated by an error back-propagation (supervised training) scheme. The ground-truths used for the training were the identified P- and S-phases that were confirmed by the analysts.

The number of nodes in the middle layer is determined empirically. For example, Figure 3 shows the percentage classification accuracy versus the number of nodes for P- and S-phases recorded at NORESS. As seen in Figure 3, networks with more than 4–5 middle nodes in the hidden layer increase complexity without improving classification accuracy. Several neural networks were designed, trained and tested for each array site for differing signal-to-noise conditions (all *snr*, and *snr* >2.0). Training a single network requires approximately 500 presentations of about 2000 samples and it takes less than 2 hours on a SUN4 Sparc Station.

We found that the best performance for NORESS and ARCESS is achieved for networks with seven input attributes and six nodes in the middle layer. The average percentages of correct identification for P- and S-phases for these networks are shown in Table 1. The percentages for the data with *snr* > 2 are 3–5% higher than for all *snr* data. Our estimates of identification accuracy are based on training the networks with 2/3 of the data, and evaluating performance on the remaining 1/3. Stability is established by applying this test three times, each time using a different 1/3 of the data for evaluation. We report the results as the average of the three tests, although we found no appreciable differences for the results for different test sets.

Table 1.

	ALL	SNR > 2.0
ARCESS	92.8%	96.6%
NORESS	91.6%	97.2%

These results for ARCESS and NORESS are 4–8% higher than results obtained by Suteau-Henson (1991) who applied a multivariate linear discriminant analysis to a similar data set. We are currently working with Drs. A. Suteau-Henson and J. Carter to perform a direct comparison of the two methods on the same data. Initial results indicate that there is a slight reduction in this difference for P-phases, but the neural network identification accuracy remains >5% for S-phases.

Having established the validity of our approach on array data, the generalization capability of a trained neural network and its adaptability to handle data from a new site was tested by applying it to data recorded by one of the IRIS stations (Garm) in the the Soviet Union. We found that networks that are trained with NORESS/ARCESS data achieve about 80% classification accuracy when applied directly to data recorded at Garm, without retraining. The classification accuracy increased by about 12% (Table 2) after retraining, using data recorded at Garm (about 1600 detections were used for the retraining).

Table 2.

TRAINED WEIGHTS	TEST GAR (ALL)	TEST GAR (SNR > 2)
ARC	80.8%	81.7%
NOR	80.9%	81.6%

	ALL	SNR > 2
GAR	91.7%	92.6%

We also estimated an empirical confidence measure for the phase identifications determined by the neural networks. This was done by comparing the output activations on each node (P and S) to the true phase identifications (ground-truth). The result is shown in Figure 4 for ARCESS data, which shows that an output activation higher than 0.65 corresponds to greater than 90% confidence in the neural network phase identification. We will apply more rigorous methods to the estimation of probability from the outputs of our neural networks (*e.g.*, Denker and LeCun, 1991).

CONCLUSIONS AND RECOMMENDATIONS:

The proposed neural network technique is applicable to single three-component stations as automated processing for initial phase identification. As seen from the adaptability of a network (to Garm) trained with ARCESS/NORESS data, the technique is transferable to any new site. The time required for retraining is less than two hours, and enough data can be accumulated during two weeks of continuous station operation for retraining. For the IRIS station Garm, a larger data set will be collected and neural network performance will be compared to that of the present automated phase identification process. The technique will be extended to incorporate initial phase identifications from teleseismic signals. This method may also be applied to other IRIS stations within the USSR, and to other single stations within the IMS, GSETT and ADSN networks.

REFERENCES:

Bache, T.C., *et al.*, The Intelligent Array System: Final Technical Report, *SAIC-90/1437*, October, 1990.

Denker, J.S. and Y. Le Cun, Transforming Neural-Net Output Levels to Probability Distributions, *Advances in Neural Information Processing Systems*, **3**, 853-859, 1991.

Jurkevics, A., Polarization Analysis Of Three-Component Array Data, *Bull. Seism. Soc. Am.*, **78**, 1725-1743, 1988.

Suteau-Henson, A., Three-component analysis of regional phases at NORESS and ARCESS: Polarization and phase identification, *Bull. Seism. Soc. Am.*, [to be submitted], 1991.

ARCESS

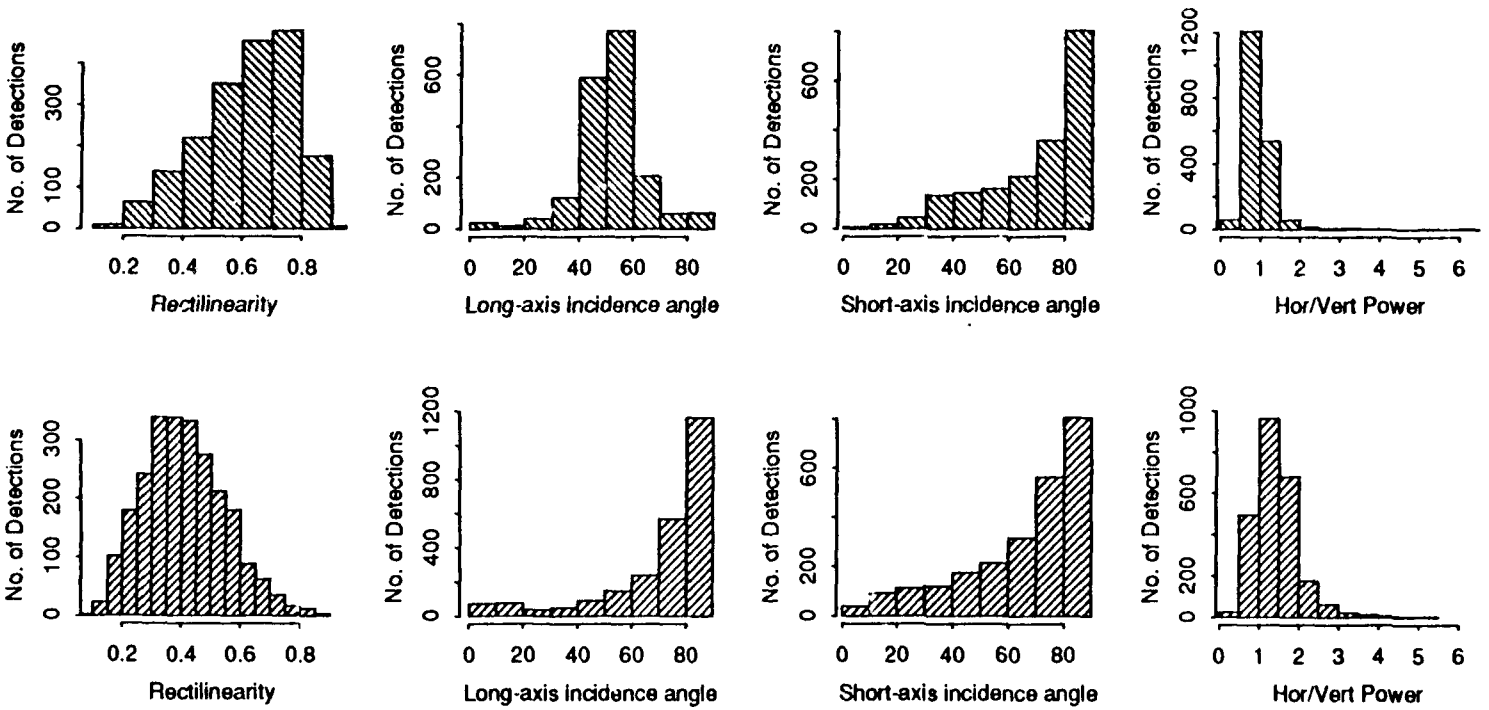


Figure 1. Histograms of four attributes from the polarization measurements of *IMS*, a subset of the seven attributes used, are shown for *P* phases (upper) and *S* phases (lower) recorded at ARCESS. The *P* and *S* populations show overlaps for each attribute.

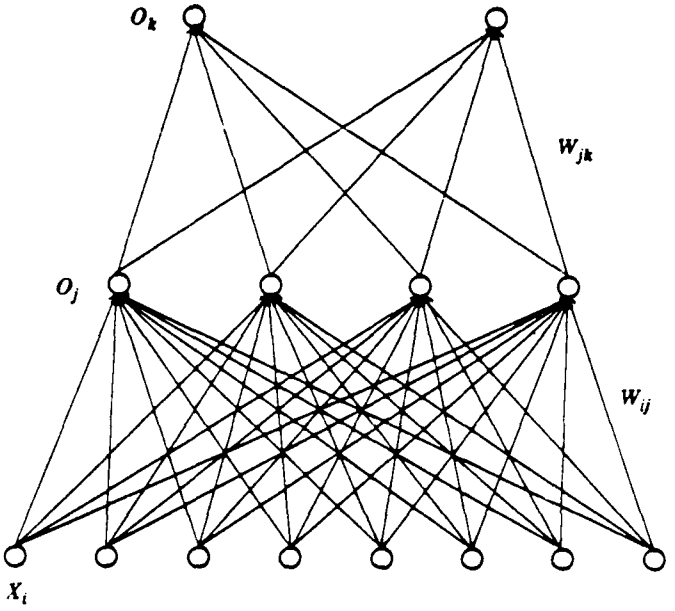


Figure 2. Schematic of a three-layer feed forward neural network (8-4-2). The input nodes are X_i (polarization attributes), W_{ij} are the weights from input to middle (hidden) layer, O_j are the middle-layer nodes, W_{jk} are the weights from middle to output layer, and O_k are the output nodes (P or S).

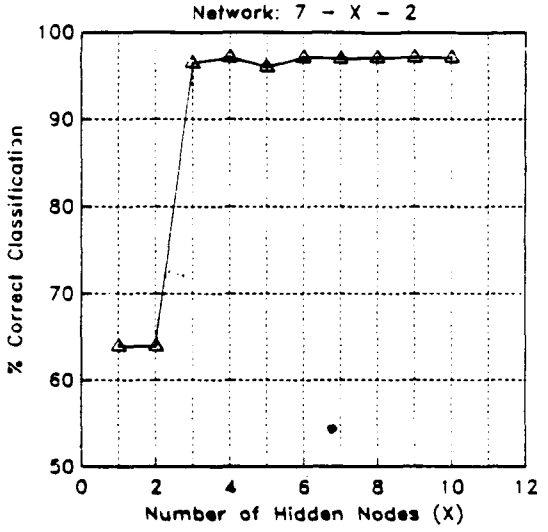


Figure 3. Percentage classification accuracy versus the number of nodes in the hidden layer. This example is for *P* and *S* phases with *snr* > 2.0 recorded at NORESS. The networks are of the form 7-X-2, where 7 is the number of inputs, X is the variable number of nodes in the middle layer, and 2 is the number of output nodes (P or S).

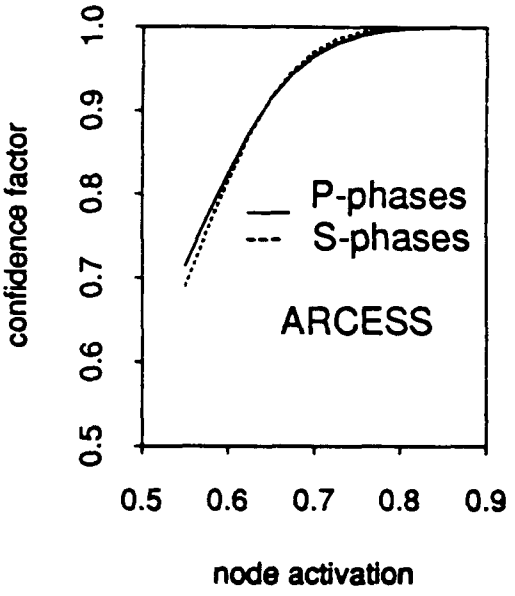


Figure 4. Epirical estimates of the confidence factors for ARCESS P- and S-phases.

Depth dependance of Q beneath the Baltic shield inferred from modeling of short period seismograms

H. Pedersen and *M. Campillo*

Laboratoire de Géophysique Interne et Tectonophysique, Grenoble - France

Grant No: 90 - 0356

OBJECTIVE:

The estimation of seismic hazard requires knowledge of both source mechanisms and the properties of the transmitting medium. The knowledge of the attenuation of seismic waves in the crust is important for the correct modeling of the wave propagation and the amplitude of the different wave phases.

This study is an attempt to estimate the depth distribution of shear wave quality factor Q in the upper crust of a shield area. We first analyse Rg waves (fundamental Raylegh mode) measured by a portable network during the SVEKA-LITHOSCOPE experiment in Finland (Mantyniemi et al. 1991). We next compare synthetic seismograms for different earth models with the seismic records in order to find a simple model of the attenuation in the crust which allows to match correctly all the major phases of the seismograms. Our ultimate goal is to give the thickness and the quality factor of an equivalent surficial attenuative layer that can be used in further applications.

Mokhtar et al. (1988) studied Rg waves in the Arabian Shield and found by a stochastic inversion of the apparent attenuation that Q increases rapidly with depth. In their study the depth distribution of Q was quite different for different parts of the profile under consideration. In Maine, USA, Toksöz et al. (1988) found a depth dependent Q in the crust by the analysis of Rg waves. Considering the quality factor in the upper crust, a general problem for the inversion of Rg wave attenuation is that the resolution of the inversion at depth is poor because of the limited penetration of high frequency Rg waves (about 1-2 Hz). Moreover the measured Q value is a combination of anelastic attenuation and attenuation due to scattering and fluid flow possibly resulting in a frequency dependent apparent Q (Toksöz et al. 1988). It is therefore difficult to eliminate the bias between frequency and depth dependance when studying Rayleigh wave attenuation.

The average shear wave quality factor in the crust is known from the analysis of Lg waves (shear waves trapped in the crust). Q seems to depend on the tectonic activity in the region under consideration. High values of Q were reported in shield areas. Singh and Herrmann (1983) mapped Q in the United States and found that Q_0, the quality factor at 1 Hz, varied between 800 and 1350 in the tectonically stable north Eastern and Central U.S. Dwyer et al. (1983) found a value of about 1500 in central U.S. and Hasegawa estimated a Q_0 of 900 in the Canadian shield.

In the Baltic Shield only little information about the attenuation is available. Kvamme and Havskov (1989) analysed coda waves in southern Norway and found quite a low coda Q_0 (about 120). The higher value (560) found by Sereno et al. (1988) in the same area from the analysis of Lg waves is more consistent with the results obtained in similar areas.

The profile used in this study offers an opportunity to investigate the influence of weathering of an archean basement on the attenuation of short period seismic waves. It was recorded on the Archaean Basement Complex which is a central part of the tectonically stable Baltic Shield. The waves do not cross major structural boundaries and we therefore assume a flat layered earth, an assumption which is necessary for our calculations.

RESEARCH ACCOMPLISHED:

Twenty five digital seismic stations of the LITHOSCOPE portable network (Poupinet et al. 1989) were installed along the SVEKA profile in Finland (Grad and Luosto 1987). The seismometers have a natural period of 1 sec.The main purpose of the experiment was the study, from teleseismic time delays, of the lithosphere in Finland, and especially the deep structures beneath the frontier between the Archaean basement complex and the Svekokarelides (Mantyniemi et al. 1991).

On the 28th of June 1989 10 of the stations situated on the Archaean Basement Complex recorded a quarry blast fired in the Soviet Union near the Finnish border (figure 1). The distance between the source and the stations ranged from 60 to 240 km. The records (figure 2) are dominated by the Rg wave (fundamental mode Rayleigh wave), which shows a clear amplitude decrease as the distance to the source increases. The Pg wave (multiply reflected P waves in the crust) shows quite a small amplitude decrease in the distance interval under consideration. We see a gradual build up of the Lg phase (S waves guided in the upper crust). The energy of the signal is dominated by Rg which has frequencies mainly between 0.5 and 2.0 Hz. The first step of our study is the analysis of the Rg phase that we isolate by time windowing of the seismograms. The limits of the window corresponding to Rg are defined by the group velocities 2.4 km/s and 3.4 km/s.

Velocity model

In order to calculate the group velocity dispersion curves we used the multiple filter analysis as presented by Dziewonski et al. (1969) with the extension proposed by Barker (1988). We used the set of programs of surface wave analysis developed at St Louis University (Herrmann 1985).

We obtained a well defined dispersion curve (figure 3a) The group velocities were calculated with very small standard deviations in the period range between 0.4 and 1.4 sec. The group velocities increased from 2.6 km/s to 3.2 km/s in this interval. There was no evidence of contamination by higher modes in this velocity range.

We used the generalized (stochastic) inversion scheme described by Mokhtar et al. (1988) to infer the shear wave velocity depth distribution, assuming a flat layered earth. We tried to build up a simple velocity model, with a small number of layers, that will be used to study the attenuation. A preliminary study of this method applied on dispersion curves for synthetic seismograms had shown that the results of the inversion are very sensitive to the a-priori thicknesses of the layers. A shear wave velocity inversion for an earth model composed of many horizontal layers and a calculation of the resolution matrix permits one to define a simple earth model: layers with the same depth resolution cannot be individually separated by the inversion, and should therefore be combined into one unit.

We were able to explain the measured dispersion curve by a 3 layer model with shear wave velocities of 3.0 km/s near the surface (0-400 m) and about 3.5 - 3.6 km/s in layers deeper than 1 km (figure 3b). As shown in the figure the observed dispersion curve is well fitted by the model. This implies small standard errors on the velocities of each layer. The simple model allows us to obtain a good resolution of the shear wave velocity in the layers. Due to the limited period band used, we have no information about layers deeper than about 4 km.

Seismic wave attenuation

Rg waves contain information about the shear wave attenuation in the depth interval through which they propagate. We therefore studied their apparent attenuation as a function of frequency.

We assumed an attenuation of the form $\exp(-\gamma r_i)$, where r_i is the distance between the source and the i'th receiver. We corrected the data for geometrical spreading ($1/\sqrt{r_i}$) and calculated the apparent attenuation γ for a number of frequencies by linear regression of the amplitudes measured at the ten stations. This calculation assumes that the attenuation does not change in the area under consideration.

The apparent quality factor Q_a can be calculated because it is a simple function of the attenuation $\gamma(\omega)$ and of the group velocity $u(\omega)$. $Q_a(\omega)$ seemed to have a constant value of about 100 in the frequency interval 0.5 - 2.0 Hz (figure 4).

The depth distribution of the actual shear wave quality factor Q_S in the crust is generally unknown, as is its frequency dependance. It is therefore not possible to separate these two effects with the Rg wave as the only source of information. Due to the narrow frequency content of our data we supposed Q_S to be independent of the frequency in the range of our study and we tried to find its variation with depth.

A stochastic inversion of the Rg wave attenuation did not constrain very well the distribution of Qs with depth. The resolution of the inversion was poor regarding the values of Qs, particularly in deep layers. In order to get quantitative constraints on Qs at depth we therefore compared the observations with synthetic seismograms for different Earth models. The synthetic seismograms were computed by the discrete wavenumber method of Bouchon (1981). This method permits the inclusion of all the seismic phases of a flat layered homogeneous earth.

Based on the seismic studies of Grad and Luosto (1987) we added information about the velocity structure of the deeper crust to our velocity model. The Moho is about 55 km beneath the profile. The crustal model used for the synthetics is given in table 1.We assumed an almost elastic crust (Qs = Qp = 1000) overlain by an attenuative surface layer, and we calculated synthetic seismograms for earth models which were identical except for the thickness of the attenuative layer. We chose a shear wave Q of 100 in the attenuative surface layer, which is equal to the apparent Q of Rg waves at 2.0 Hz.

Figure 5 shows an example of a comparison between data and synthetics. In this case we assumed a shallow (1 km) attenuating layer. The prominant phases (Pg and Rg) are correctly simulated at most stations. One may note the absence of Rg at station 5. This is due to a local effect since Rg is visible at further locations. The case of Lg is more difficult. We do not here address the problem of radiation of S waves during a real explosive experiment.

Figure 6 shows the Rg wave attenuation parameter as a function of frequency both for the data and for several synthetic seismograms. In order to calculate the attenuation we used the method described previously: the Rg wave was separated using a time window defined by the group velocities 2.4 km/s and 3.6 km/s. The signal was corrected for geometrical spreading and the attenuation was measured by linear regression as described above. The attenuation measurement may therefore be contaminated by seismic phases (body waves, Lg waves) other than Rg, which may explain that the curves are not perfectly smooth especially for the high frequencies. The only parameter which changes for the different synthetics is the thickness of the attenuative surface layer. On the figure the bold line corresponds to a thickness of the attenuative layer of 1 km, while the dashed - dotted lines correspond to thicknesses of 0.5 and 2 km respectively. In order to fit the data over the entire frequency interval the thickness of this layer must be bounded in a quite narrow range. We emphasize that our results are obtained under the assumption of a frequency independent Q_S in the frequency interval 0.5 - 2.0 Hz.

CONC USIONS AND RECOMMENDATIONS:

The short period seismological data of this study show evidence of a highly attenuative layer at the surface of the Archaean part of the Baltic shield. We calculated complete synthetic seismograms to constrain the dependance of Q with depth. The thickness of the attenuative layer is found to be about 1 km. This is in good agreement with the velocity structure which indicates a weathered zone of about 1 km thick. The presence of a very strongly attenuative layer above the quasi-elastic shield is an important feature for the quantitative interpretation of the amplitude of seismic waves on shields.

Q_S deduced from regional phases represents a mean attenuation in the crust (Campillo et al. 1985). The clear variation of Q_S with depth shows that it is dangerous to use Lg attenuation measurements to predict ground motion at short distances from the source.

In the narrow frequency window of our data we did not observe evidence of the frequency dependence of the quality factor suggested for shallow layers by Toksöz et al. (1988). We do not, though, deny that a slight frequency dependance may be present.

Acknowledgements. We thank G. Poupinet and the LITHOSCOPE project (INSU/CNRS) for providing the data. Some of the computer programs used in the study were supplied by R. B. Herrmann.

References

Barker, T. (1988), Array processing of Rayleigh waves for shallow shear wave for shallow shear wave velocity structure (abs.),*Seismological research letters*, 59, 12.

Bouchon M. (1981), A simple method to calculate Green's functions for elastic layered media, *Bull. Seis. Soc. Am.*, 71, 959-971.

Campillo, M., Plantet, J.-L., Bouchon, M. (1985), Frequency dependent attenuation in the crust beneath Central France from Lg waves: Data analysis and numerical modeling, *Bull. Seis. Soc. Am.*, 75, 1395 - 1411.

Dwyer, J.J., Herrmann, R.B., Nuttli, O.W. (1983), Spatial attenuation of the Lg wave in the Central United States, *Bull. Seis. Soc. Am.*, 73, 781 - 796.

Dziewonski, A. M., Bloch, S., Landisman, M. (1969), A technique for the analysis of transient seismic signals, *Bull. Seis. Soc. Am.*, 59, 427 - 444.

Grad, M., Luosto, U. (1987), Seismic models of the crust of the Baltic shield along the SVEKA profile in Finland, *Ann. Geophysicae*, 6, 639 - 649.

Hasegawa, H.S.(1985), Attenuation of Lg waves in the Canadian Shield, *Bull. Seis. Soc. Am.*, 75, 1569 - 1582.

Herrmann, R. B. (1985), Computer programs in Seismology, Saint Louis University.

Kvamme, L.B., Havskov., J. (1989), Q in Southern Norway, *Bull. Seis. Soc. Am.*, 79, 1575 - 1588.

Mantyniemi, P.; Poupinet, G., Luosto; U., Korhonen, H. (1991), A teleseismic study of the lithosphere across the Ladoga-Bothnian Bay zone in Finland, *Proceedings of the Finnish Russian Workshop on "Structure and dynamics of the Fennoscandian Lithosphere"*, Series of the Institute of Seismology; University of Helsinki.

Mokhtar, T.A., Herrmann, R.B., Russell, D.R. (1988), Seismic velocity and Q model for the shallow structure of the Arabian shield from short-period Rayleigh waves, *Geophysics*, 53, 1379 - 1387.

Poupinet, G , Fréchet, J., Thouvenot, F. (1989), Portable short period vertical seismic stations, *Digital Seismology and fine modeling of the lithosphere*, Plenum Publishing Corp.

Saikia, C. K., Kafka, A. L., Gnewuch, S. C., McTigue, J. W. (1990), Shear velocity and intrinsic Q structure of the shallow crust in Southeastern New England from Rg wave dispersion, *J. Geophys. Res.*, 95, 8527-8541.

Sereno, T.J., Bratt, S.R., Bache, T.C. (1988), Simultaneous Inversion of Regional Wave Spectra for Attenuation and Seismic Moment in Scandinavia, *J. Geophys. Res.*, 93, 2019 - 2035.

Singh, S., Herrmann, R. B. (1983), Regionalization of Crustal Coda Q in the Continental United States, *J. Geophys. Res.*, 88, 527 - 538.

Toksöz, N., Dainty, A.M., Reiter, E., Wu, R.S. (1988), A Model for Attenuation and Scattering in the Earth's Crust, *PAGEOPH*, Vol. 128, 81 - 100.

(Received: April 15, 1991;
Revised: June 13, 1991;
Accepted: June 21, 1991.)

Fig. 1. Locations of the LITHOSCOPE stations (triangles) and the recorded quarry blast ( ). Both the stations and the source are located on the Archaean Basement Complex (shaded area).

Fig. 2. The unfiltered records of the quarry blast.

Fig. 3. a) Measured dispersion curve. Vertical bars indicate the standard deviation of the measure. The curve which corresponds to the earth model found by inversion of the dispersion curve is superimposed.

b) The S - wave structure found by inversion of the dispersion curve and the resolution of the inversion.

Fig. 4. The apparent quality factor Q_a as a function of frequency, found by linear regression as described in the text.

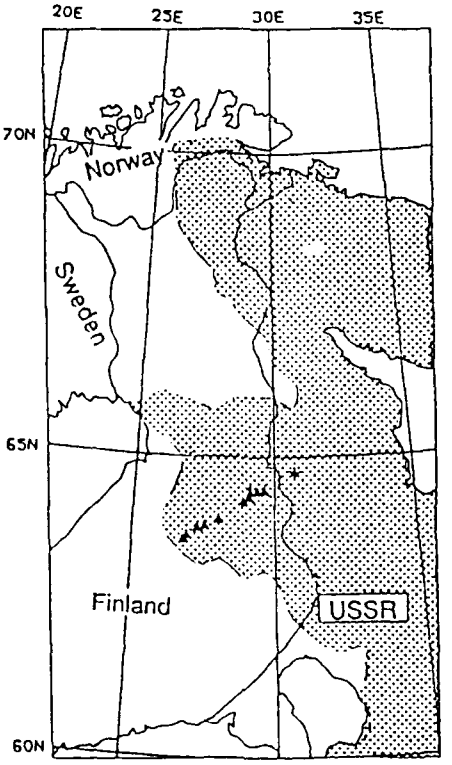
Z -km	Vp - km/s	Vs - km/s
0.0 - 0.4	5.23	2.99
0.4 - 1.0	5.90	3.37
1.0 - 10.0	6.10	3.54
10.0 - 17.0	6.30	3.66
17.0 - 26.0	6.54	3.73
26.0 - 40.0	7.10	4.03
40.0 - 55.0	7.30	4.12
55.0 -	8.00	4.62

Table 1. Earth model used to compute the synthetic seismograms.

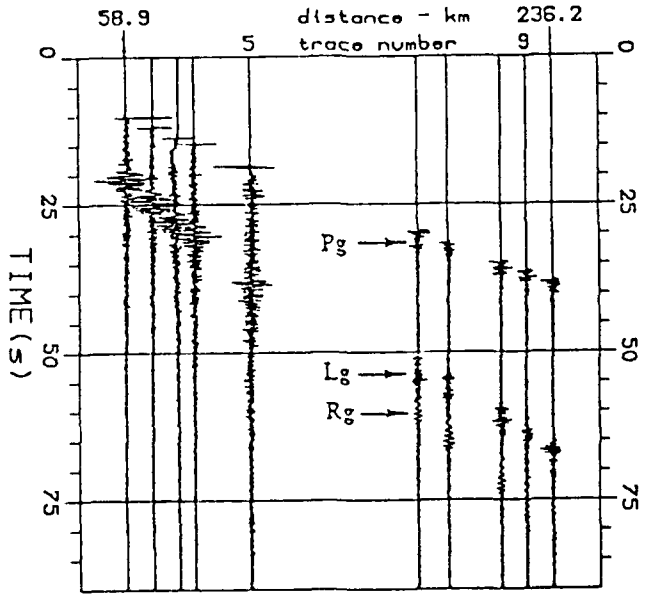
Fig. 5. Data (bold) and synthetic seismograms calculated for a crust with a 1 km thick attenuative surface layer. Both data and synthetic seismograms are bandpass filtered 0.5 - 2.0 Hz.

Fig. 6 Rg wave attenuation as a function of frequency for the data (triangles) and for three synthetic seismograms: model as described in table 1 (bold), models as described in table 1 but with a attenuative layer 0-2000 m (upper dashed - dotted) and 0-500 m (lower dashed - dotted).

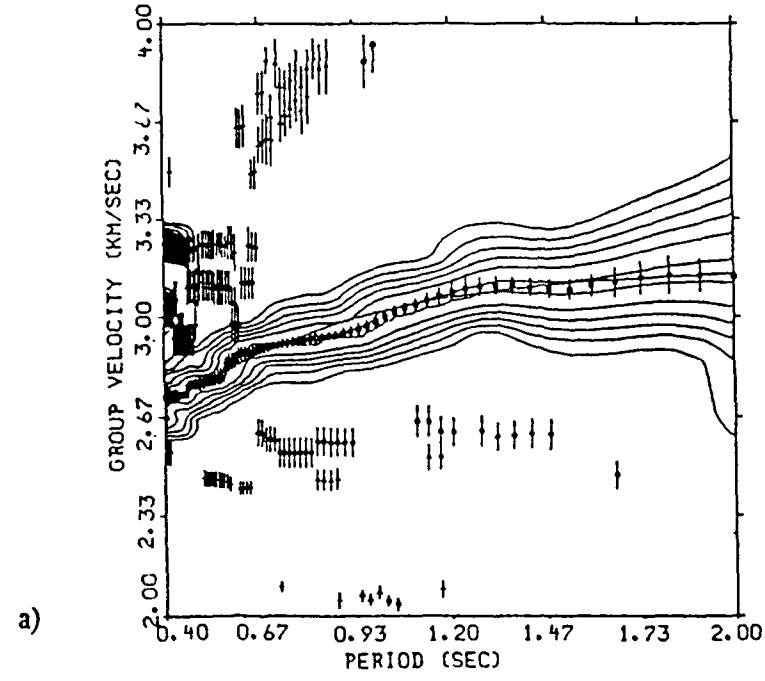
Pedersen and Campillo - Figure 1



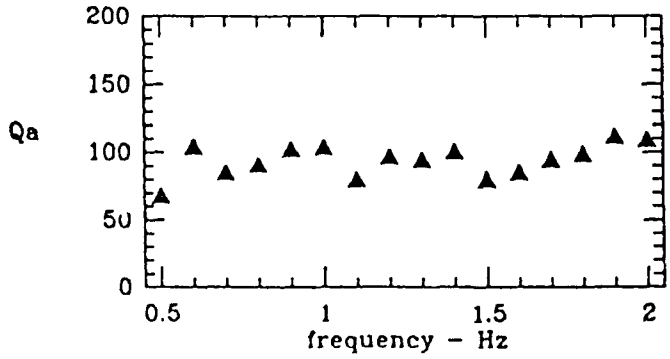
Pedersen and Campillo - Figure 2

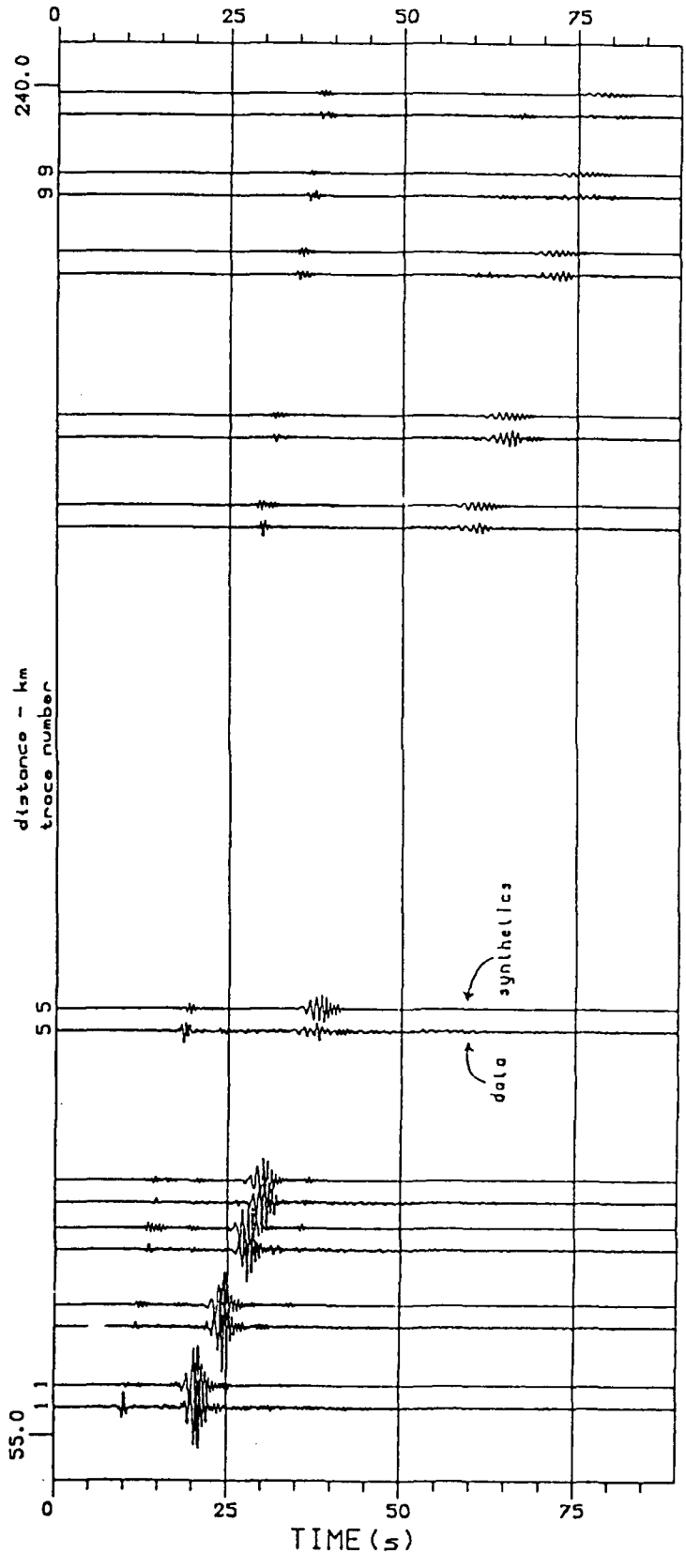


Pedersen and Campillo - Figure 3



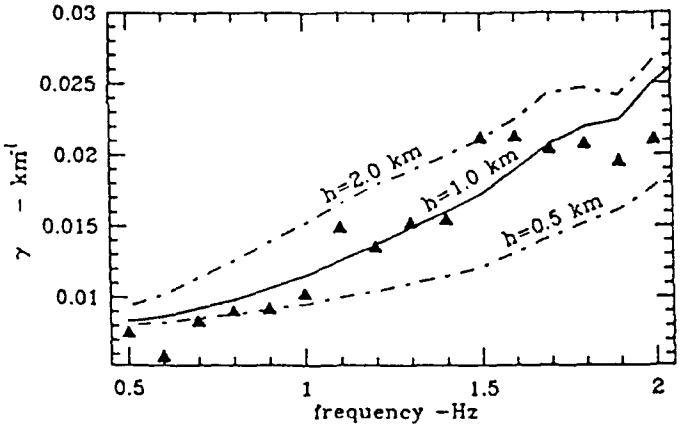
Pedersen and Campillo - Figure 4





Pedersen and Campillo - Figure 5

Pedersen and Campillo - Figure 6



STUDIES OF SEISMIC DATA FROM CENTRAL ASIA

Keith F. Priestley*, William R. Walter+

Seismological Laboratory, University of Nevada,
Reno, Nevada 89557

Contract No. F19628-89-K-0022

OBJECTIVE:

Study of seismic data recorded in the vicinity of the Soviet nuclear test site in Eastern Kazakh.

RESEARCH ACCOMPLISHED:

Regional waveforms offer the potential of increased signal bandwidth for detection and identification, particularly at high (< 1 Hz) frequencies. Various studies [i.e. Pomeroy et al. 1982; Bennett and Murphy, 1986; and Taylor et al., 1989] suggest that spectral ratios of some regional phases hold promise for discrimination. However, as Taylor et al [1989] note, "...a number of uncertainties regarding the lack of a physical understanding of how the spectral discriminants work makes their utilization questionable at this point". Under a CTBT or lower yield TTBT there may be a need to detect and identify events from a geographic region in which we have little or no previous experience. In addition it will be necessary to understand under what circumstances a particular detection and identification method might fail. For these reasons it is important to develop a physical understanding of both the source and the propagation characteristics of regional waves.

In this study we compare spectral amplitude ratios from North American and Central Asian earthquakes and explosions to spectral amplitude ratios predicted by the Sharpe (1942) and Mueller-Murphy (1971) explosion source models and by the Archambeau (1968, 1972) and Brune (1970, 1971) earthquake source models. Figure 1 compares the theoretical far-field displacement amplitude spectra of the Sharpe and Mueller-Murphy (M-M) source models calculated for explosions with yields of 100kt and 1kt, and for the Archambeau and Brune earthquake source models calculated for the same low frequency values. The spectra of the two explosion models and the Brune earthquake model are characterized by a high frequency decay of ω^{-2}. The high frequency decay for the Archambeau earthquake model depends on the rupture velocity. The Archambeau spectrum in Figure 1 is for a rupture velocity equal to the shear wave velocity. This gives maximum high frequency value for the Archambeau model since at higher rupture velocities the spectrum decays at ω^{-2}, and at lower velocities both the corner frequency and spectral amplitudes above the corner frequency decrease. The differences in the high frequency falloff between the four models discussed above predict different *P* wave spectral rations. Figure 2 shows the log of the spectral ratio of 1.0 Hz to 4.0 Hz energy as a function of moment,using the same parameters as Figure 1. For small moments the ratios are unity since both

*Now at Dept. of Earth Science, University of Cambridge, Cambridge, England
+Now at Dept. of Earth Science, LLNL, Livermore, CA

frequencies are on the constant part of the spectrum. For large moments the ratio is a constant value greater than unity, since both frequencies are on the decaying part of the source spectra. For larger moment events the 1.0 to 4.0 Hz ratio for the Archambeau model is larger than for the other models due to the ω^{-3} decay rate, and suggest that for this source model spectral ratio would be a reliable discriminant between earthquakes and explosions. For moments from about 10^{22} to 10^{26} dyne-cm, the frequencies fall on either side of the source corner frequency, and the behavior of the spectral ratio curves in Figure 2 reflect the different corner frequency scaling of each model.

In a previous paper [Walter et al, 1988] we tested some of the predictions of the Sharpe, Archambeau, and Brune source models with data from Western North America. These results are summarized in Figure 3 which displays *P* wave spectral amplitude as a function of moment for a variety of earthquakes and NTS Pahute Mesa underground nuclear explosions. Theoretical curves have been drawn for the Sharpe explosion model and for the Brune (W2P) and Archambeau (W3P) earthquake models. The σ denote the stress drop in bars for each earthquake curve. The earthquake 10 Hz amplitudes are consistent with both earthquake models and the explosions show about an order of magnitude scatter near the theoretical predicted Sharpe amplitude. The earthquakes 30 Hz amplitudes show a continued increase in 30 Hz amplitude with moment consistent with an ω^{-2} falloff model and in disagreement with an ω^{-3} model for larger moments. The explosions in Figure 3b separate into two groups: one showing two orders of magnitude less 30 Hz *P* wave energy than predicted by the Sharpe model, the other closer to the Sharpe prediction. The group with less 30 Hz energy was detonated at depths between 600 and 700 m while the group with more 30 Hz energy was detonated at depths of 800 to 1100 m. Thus the shallower group has a high frequency spectral decay between 10 and 30 Hz that is much greater than the ω^{-2} predicted by the Sharpe model. The shallower explosions were detonated near the level of the water table (about 650 m) at Pahute Mesa and we suggested that the location of the explosion relative to the water table may cause the difference in falloff slope between the deep and shallow events [Walter et al., 1988]. These results are similar to the change in high frequency slope observed by Denny [1990] and used by Taylor and Denny [1990] to model spectral differences observed between NTS and KTS explosions Taylor and Denny [1990] show that for weak porous rock the radiated shock wave divides into a two wave system. In terms of the Sharpe model this is equivalent to introducing a rise time in the pressure function at the elastic radius, so the far-field P spectra then decays as ω^{-3} at high frequencies.

Figures 3a and 3b imply that Western North American earthquakes have more 30 Hz *P* wave energy than NTS Pahute Mesa explosions detonated near the water table. Murphy and Bennett [1982] and Taylor et al., [1988] used low to high frequency spectral ratios for Pn, Pg and Lg and noted that NTS explosions had less high frequency energy than the western U.S. earthquakes. In contrast, Taylor and Marshall [1990] compared teleseismic recordings of KTS events to shallow Asian earthquakes and found that the explosions had more high frequency *P* wave energy than the earthquakes. This raises the questions of what are the corner frequency scaling and high frequency decay slope for Soviet KTS explosions, and, whether Soviet explosions can be discriminated from earthquakes in either the manner of Evernden et al. [1986], or the manner of Chael [1988].

Figure 4 compares instrument-corrected P_n spectra from two earthquakes and two explosions recorded over similar paths in Central Asis. The explosions have a relatively greater high frequency decay compared with the earthquakes. Fitting the log-log spectrum from 5 to 20 Hz with a least squares line we obtain average falloff slopes of about $\omega^{-3.5}$ and $\omega^{-4.0}$ from the earthquake; the explosions have a larger decay, about $\omega^{-5.0}$ between 5 and 15 Hz; the explosions have high apparent corner frequencies, about 5 Hz. The earthquakes do not show a well defined apparent corner frequency but show a gradually larger decay rates with increasing frequency.

Because of the limited Central Asian data set, (6 explosions, 40 earthquakes) any conclusions are of necessity, preliminary. The steeper high frequency *P* wave spectral decay observed for the Soviet explosions compared with those observed for Central Asian earthquakes is similar to that observed for North American earthquakes and explosions [Chael, 1988; Walter et al., 1988]. Recordings of the Soviet explosions show more high frequency energy in the 2-5 Hz band than predicted by the Sharpe or Mueller-Murphy source models. This can also be seen by comparing 1 to 4 Hz spectral ratios with theoretical calculations. We calculated the ratio of the 0.75 - 1.25 Hz to 3.0 - 5.0 Hz energy for the attenuation corrected spectra of the Soviet JVE. The Pn ration is 1.2 and the Pg ratio is 4.3 compared. The Mueller-Murphy and Sharpe models predict larger spectral ratios of 6.6 and 8.3 respectively. For comparison the Brune earthquake model gives a spectral ratio of 7.2 (100 bar stress drop) or 12.3 (10 bar stress drop) , and the Archambeau earthquake model gives a spectral ratio of about 64 (for either 100 or 10 bar stress drop), when constrained to have about the same low frequency level as the Soviet JVE. Overall these observations give similar results to Taylor and Marshall [1990] who found that KTS explosions gave lower 0.5 - 1.0 Hz to 2.0 - 3.0 Hz spectral ratios when compared with shallow Central Asian earthquakes at the United Kingdom teleseismic arrays.

CONCLUSIONS AND RECOMMENDATIONS:

The North American earthquake data are consistent with a constant stress drop ω^{-2} model, and have more high frequency energy than small shallow NTS explosions at Pahute Mesa which show a spectral decay greater that ω^{-3} above 10 Hz. In contrast regional recordings of the Soviet explosions are richer in high frequencies than are regional recordings. These results are consistent with the hypothesis of Taylor and Denny [1990], who found that spectral ratio data from U.S. explosions could be fit by an explosion model that decays as ω^{-3} at high frequencies, KTS (Shagan River) explosion spectral ratios could be fit with a model that decays as ω^{-2}, and both western U.S. and Central Asian earthquake spectral ratios were consistent with an ω^{-2} model. The near regional recordings of the Soviet explosions have a higher corner frequency causing a lower observed explosion 1 to 4 Hz spectral ratio for the Soviet explosions than is predicted by existing explosion models. Comparing the Soviet explosions with earthquakes recorded on similar paths we find a similarly low 1 to 4 Hz spectral ratio for the explosion and a higher ratio for the smaller m_b earthquake. Whether the higher corner frequency for the Soviet explosions require a different explosion scaling relationship at KTS than contained in the models reviewed here, or is due to complications in the simple source models, such as spall and tectonic release, needs to be resolved in order to confidently use a discriminant based on differences between earthquake and explosion spectra.

REFERENCES

Archambeau, C.B., General theory of elastodynamic source fields, *Rev, Geophys., 6,* 241-288, 1968

Archambeau, C.B., The theory of stress wave radiation from explosions is prestressed media, *Geophys. J., 29* 329-366, 1972.

Bennett, T.J. and J.R. Murphy, Analysis of seismic discrimination capabilities using regional data from western United States Events. *Bull. Seism. Soc. Am., 76,* 1069-1086, 1982

Brune, J.N. Tectonic stress and the spectra of seismic shear waves from earthquakes, J. *Geophys. Res., 75,* 4997-5009, 1970

Brune, J.N., Correction, *J. Geophys. Res., 76,* 5002, 1971

Chael, E.P., Spectral Discrimination of NTS Explosions and Earthquakes in the Southwestern United States using High-Frequency Regional Data, *Geophys. Res. Lett., 15,* 625-628, 1988

Evernden, J.F., C.B. Archambeau, and E. Cranswick, An evaluation of seismic decoupling and underground nuclear test monitoring using high-frequency seismic data, *Rev. of Geophys., 24,* 143-215, 1986

Mueller, R.A., and J.R. Murphy, Seismic characteristics of underground nuclear detonations: Part I. Seismic spectrum scaling, Bull. Seism. Soc. Am., 61, 1675-1692, 1971

Pomeroy, P.W., W.J. Best, and T.V. McEvilly, Test ban treaty verification with regional data - a review, *Bull. Seism. Soc. Am. 72,* S89-S129, 1982

Sharpe, J.A., The production elastic waves by explosions pressures, 1. Theory and empirical field observations, *Geophysics, 7,* 144-154, 1942

Taylor, S.R., N.W. Sherman, and M.D. Denny. Spectral discrimination between NTS explosions and western United States earthquakes at regional distances, *Bull. Seism. Soc. Am., 78,* 1563-1579, 1988

Taylor, S.R., M.D. Denny, E.S. Vergino, and R.E. Glaser, Regional discrimination between NTS explosions and western U.S. earthquakes, *Bull. Seism. Soc. Am., 79,* 1142-1176, 1989

Taylor, S.R. and M.D. Denny, An analysis of spectral differences between NTS and Shagan River nuclear explosions, *Rep. UCRL-102276,* Lawrence Livermore Natl. Lab., Livermore, Calif., 1990

Taylor, S.R., and P.D. Marshall, Spectral discrimination between Soviet explosions and earthquakes using U.K. array data, *Geophys. J., in press,* 1990

Walter, W.R., J.N. Brune, K. Priestley, and J. Fletcher, Observations of high-frequency P wave earthquake and explosion spectra compared with ω^{-2}, ω^{-3}, and Sharpe source models, J. *Geophys. Res., 93,* 6318-6324, 1988

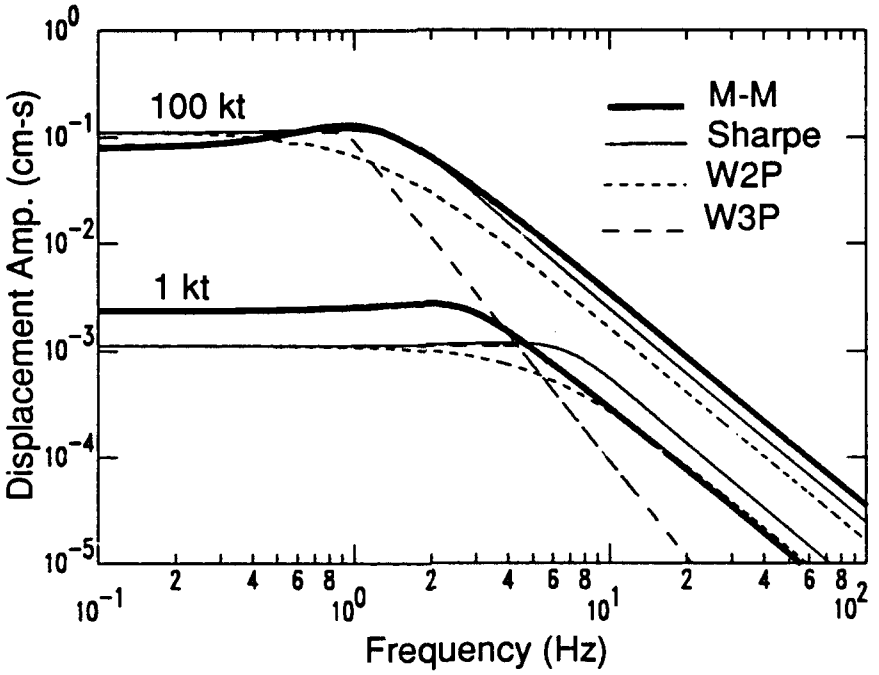


Figure 1 Compaarison of displacement spectra for Sharpe and Muller-Murphy (M-M), and Brune (W2P) and Archambeau (W3P) earthquake models computed for two low frequency levels.

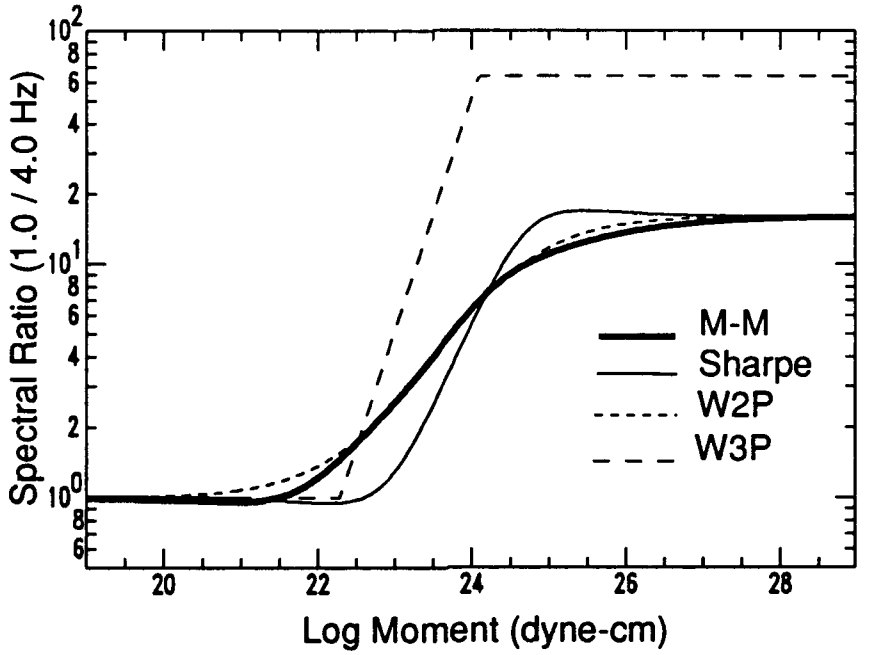


Figure 2 1.0 to 4.0 Hz spectral ratio versus seismic moment for the four source models shown in Figure 1.

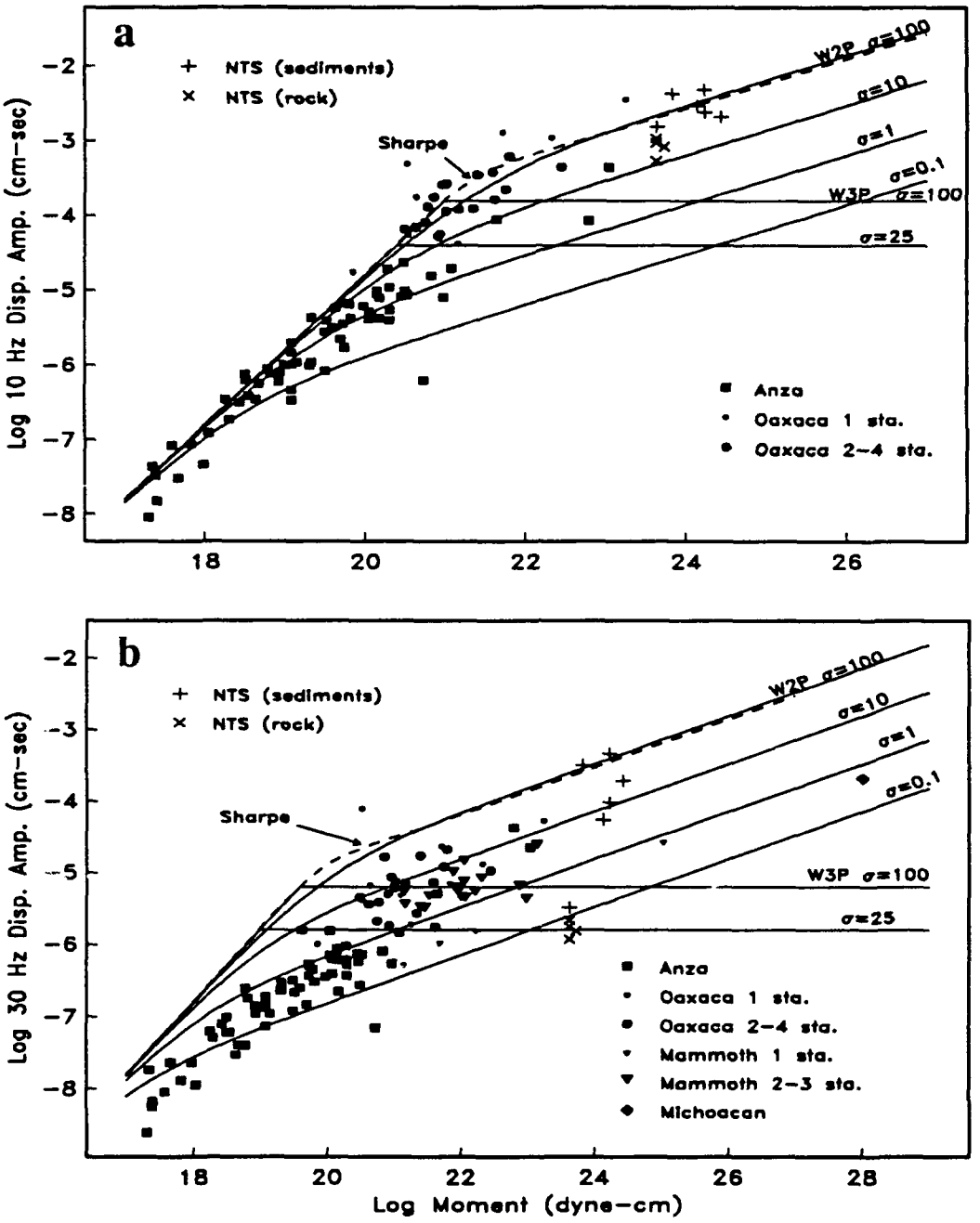


Figure 3 P wave displacement amplitudes for earthquakes and explosions plotted as a function of moment and compared with curves predicted from the Sharpe, Brune, and Archambeau source models. Theoretical curves given for a constant stress drop, denoted by sigma in bars; the Sharpe curve was calculated assuming a pressure step function of 130 bars and a coupling constant of 9.4.

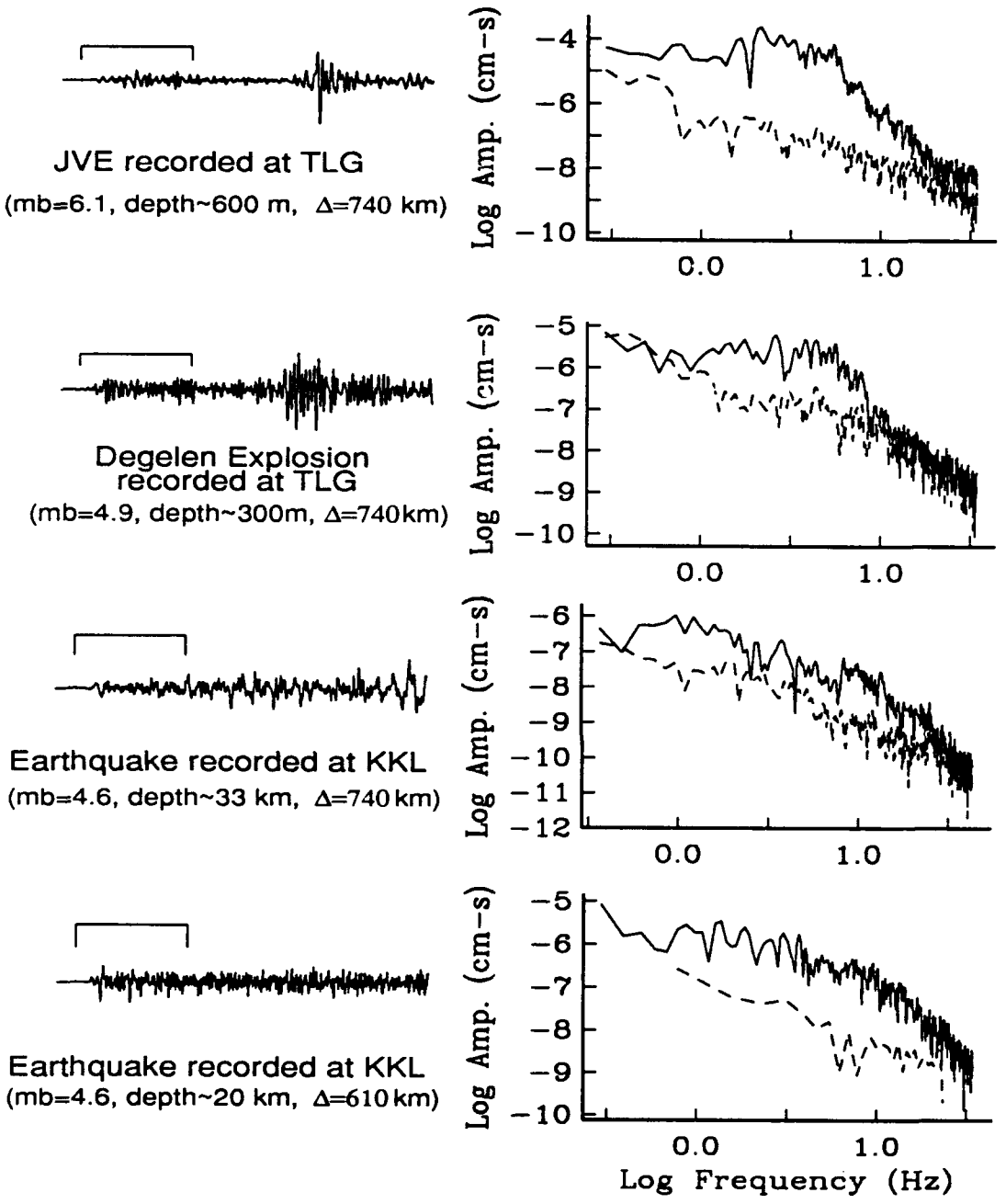


Figure 4 Pn spectra of KTS explosions and two Central Asian earthquakes recorded over similar paths. Earthquake depths are from the NEIS; explosion depths are estimated assuming NTS depth scaling. Note the relatively high corner frequency and steep high frequency falloff of the explosion spectra as compared with the earthquake spectra.

PRELIMINARY ANALYSIS OF THE WESTERN NORILSK - LAKE BAIKAL DEEP SEISMIC SOUNDING PROFILE

K.F. Priestley, University of Cambridge
J. Cipar, Geophysics Directorate, Phillips Laboratory
A.V. Yegorkin, N.I. Pavlenkova, and V. Martynov,
Soviet Academy of Science

Contract No.F19628-90-K-0046

OBJECTIVE:

Study of the velocity structure of the Central Asian upper mantle.

RESEARCH ACCOMPLISHED:

At present there is a great deal of interest in the velocity structure of the upper mantle. Many of the important, unresolved questions concerning upper mantle dynamics will only be answered when a more detailed picture of the upper mantle velocity structure and its lateral variations are attained. For example, some studies (Lerner-Lam and Jordan, 1987) indicate that the structure of the continents extends to upper mantle depths (~400 km) suggesting that the continental lithosphere does not passively drift on the low-velocity asthenosphere. Variations in upper mantle velocity structure also have important implications in a nuclear discrimination/verification context. Regional seismic phases will play a major role in monitoring any future Comprehensive Test Ban Treaty (CTBT) or Low Yield Threshold Test Ban Treaty (LYTTBT). Regional waveforms are more complicated than teleseismic waveforms and can vary greatly between different geologic provinces. Before source contributions (e.g., spall, tectonic release, etc.) to P-wave complexity can be understood, seismic waveform complexities arising from propagation effects must be understood. A knowledge of the seismic velocity and attenuation structure is critical to understanding regional seismic wave propagation characteristics. For example, P_n amplitude behavior as a function of range is strongly influenced by both upper mantle attenuation and by the sub-Moho velocity gradient (Hill, 1971; 1973). The P_n frequency content is also affected by the upper mantle lid thickness (Mellman and Helmberger, 1974). In the stable regions of the Soviet Union where the upper mantle attenuation might be expected to be low, the velocity structure may well be the dominant influence on P_n and S_n propagation. Variations in the lithospheric velocity structure may cause significant variations in the mode of P_n, P_g and L_g propagation resulting in significant differences in the P_n/P_g or P_n/L_g amplitude behavior within the various geological provinces. Thus a seismic discriminant developed in one geologic province may not necessarily be transportable to another geologic province.

During the past 30 years the Soviet Ministry of Geology has conducted an extensive seismic exploration program of the Eurasian crust and upper mantle. Several of these lines (Fig. 1) use

nuclear explosions as seismic sources for recording at large offsets (up to 3000 km) and conventional explosives for shorter offsets. Scheimer and Borg (1984) reviewed the Soviet nuclear DSS program. The energetic sources used on several DSS profiles have permitted recording of significantly longer profiles than typically recorded in U.S. refraction experiments. This has permitted interpretation of velocity structure (from refraction) to upper mantle depths (150-200 km) and of velocity contrast (from reflections) at much deeper depths. The Soviet analysis of the data has been performed using a method analogous to forward raytracing methods. Yegorkin et al, (1977) describe a forward modelling procedure by which travel times are computed for successively deeper penetrating rays and the theoretical travel times for a proposed structure are compared with the observed travel time until they fit to within prescribed error limits (about 0.3-0.5 sec). Soviet seismologists consider wave amplitudes only by comparing observed seismic amplitudes with the density of computed rays. Results for only a few of these profiles are discussed in the western literature (Yegorkin and Pavlenkova, 1981; Pavlenkova and Yegorkin, 1983; Egorkin et al, 1984).

We have recently begun analysis of a 2400 km long profile recorded in 1982 which extends across the Siberian Platform from Norilsk to Lake Baikal (Fig. 1). Data from two shot points are being studied. The first shot point is in western Norilsk within the West Siberian rift on the northwest edge of the Siberian Platform. This failed rift developed in Triassic time (235-215 my) during the initial breakup of Pangea. Following the extinction of extension, the rift was buried beneath approximately 15 km of sediment. Geochemical analysis of the basalts within the rift indicate they have a chemical composition similar to ocean tholeiites. This profiles extends southeast across the Tunguss Basin, a region of Late Paleozoic extension and widespread intraplate flood basalts (1.2×10^6 km^3 in 10 Ma), to the presently active Baikal rift. The second shot point is in western Tura within the Tunguss Basin, approximately 700 km southeast of the first shot point. Data from this shot extends 560 km northwest reversing a section of the profile from the first shot point and extending 1700 km southeast across the Baikal rift. Data for these profiles were obtained in the form of large paper copies (25mm/sec X 2.5mm/km) with station locations accurate to 0.1 km. The traces were commercially digitized and corrected for amplitude scaling to produce a true amplitude record section. Arrival times of first and prominent later arrivals have been measured.

A portion of the data from the distance range 1600-2000 km are shown in record section format in Fig. 2a,b. The first arrival travels through the lithospheric lid while the prominent second arrival is a reflection from the 670 km discontinuity. The lower figure is a blowup of the upper record section illustrating the structure in the wavefield in the 1700-1800 km distance range. First arrival times were read from the digitized seismograms for the West Norilsk shot point (DSS Shot Point 245) and are shown in Figs. 3 and 4. The data are compared to two published models for

the Eurasian upper mantle. Model K8 was derived using long-period seismograms of Soviet nuclear blasts recorded in Europe (Fig. 3) while Section I of Egorkin et al. (1984) was inferred from DSS profiles in central Siberia (Fig. 4). Further discussion of each model is given in the figure caption.

Modeling of this important data set has just begun. We are assembling information on the variations in geology and crustal structure along the profile to correct the travel times for receiver structure beneath each recording site. This will allow us to better isolate upper mantle travel time information. The tau(p) bounds will be inverted for extremal velocity bounds using the computer code developed by Stark et al (1988). Once we have established realistic bounds on the velocity-depth function, we intend to forward model the waveforms using the reflectivity method. This will allow us to constrain specific velocity-depth models within the range of the extremal velocity depth bounds.

CONCLUSIONS AND RECOMMENDATIONS:

The purpose of the proposed investigation is to improve our understanding of the Eurasian crust and upper mantle velocity structure. Improvement of our understanding in these areas will help in evaluating the significant factors controlling the propagation of regional seismic phases; in "calibrating" the IRIS seismographs and the Scandinavian arrays in terms of the seismic wavefield resulting from Kazakh Test Site (KTS) explosions; and in assessing the efficiency of high frequency propagation, and its use in elucidating source characteristics of Central Asian seismic events. An improved understanding of the propagation characteristics of regional seismic phases will facilitate interpretation of source characteristics from the seismograms.

REFERENCES

Egorkin(Yegorkin), A.V., S.K. Ziuganov, and N.M. Chernyshev (1984), The upper mantle of Siberia, Proceeding of the 27th International Geological Congress, 8, 29-56.

Given, J. W. and D. V. Helmberger (1980), Upper Mantle Structure of Northwestern Eurasia, J. Geophys. Res., 85, 7183-7194.

Hill, D.P (1971), Velocity gradients and anelasticity from crustal body wave amplitudes, J. Geophys. Res., 76, 3309-3325.

Hill, D.P. (1973), Critically refracted waves in a spherically symmetric radially heterogeneous earth model, Geophys. J. R. astr. Soc., 34, 149-177.

Lerner-Lam, Arthur L. and Thomas H. Jordan (1987). How Thick are the Continents?, Jour. Geophys. Res., 92, 14007-14026.

Mellman, G.R., and D.V. Helmberger (1974), High-frequency attenuation by a thin high-velocity layer, Bull. Seis. Soc. Am., 64, 1383-1388.

Pavlenkova, N.I., and A.V. Yegorkin (1983), Upper mantle heterogeneity in the northern part of Eurasia, Phys. Earth Planet. Int., 33, 180-193.

Priestley, K.F., G. Zandt, and G.E. Randall (1988), Crustal structure in eastern Kazakh, U.S.S.R. from teleseismic receiver functions, Geophys. Res. Lett., 15, 613-616.

Scheimer, J.F., and I.Y. Borg (1984), Deep seismic sounding with nuclear explosives in the Soviet Union, Science, 226, 787-792

Stark, P.B., R.L. Parker, G. Master, and J.A. Orcutt (1988), Strict bounds on seismic velocity in the spherical Earth, J. Geophys. Res., 91, 13892-13902.

Yegorkin, A.V., V.Z. Ryaboy, L.P. Starobinets, and V.S. Druzhinin (1977), Velocity cross sections of the upper mantle from DSS data on land, Izvesitya, Earth Physics, 13, 467-477.

Yegorkin, A.V., and N.I. Pavlenkova (1981), Studies of mantle structure of U.S.S.R. territory on long-range seismic profiles, Phys. Earth Planet. Int., 25, 12-26.

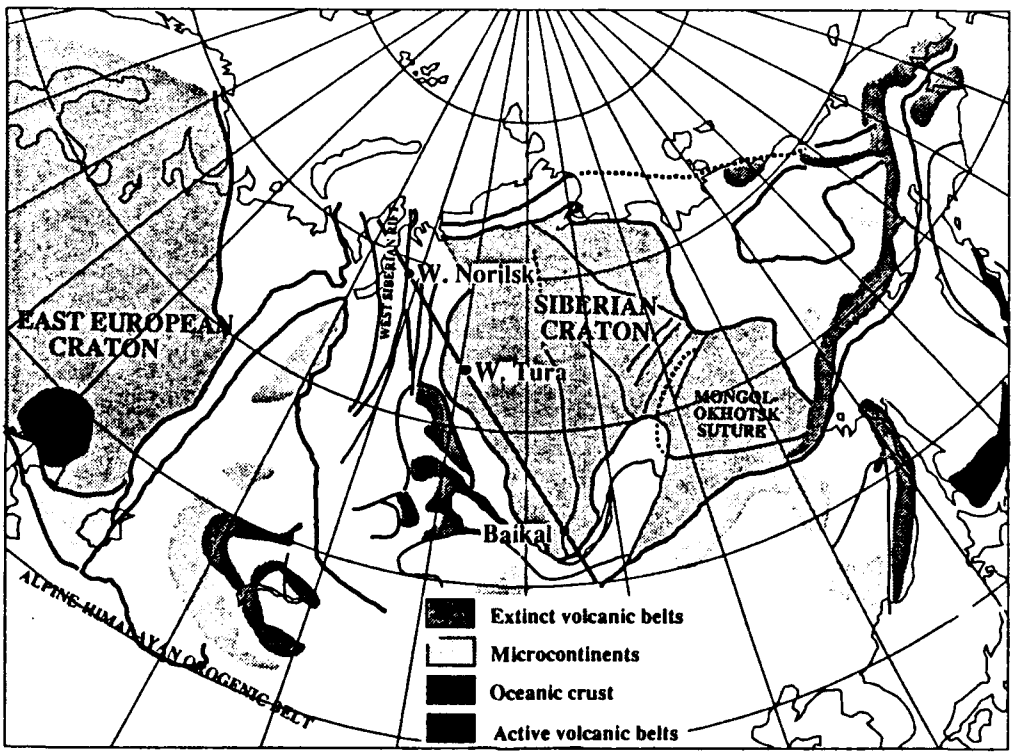
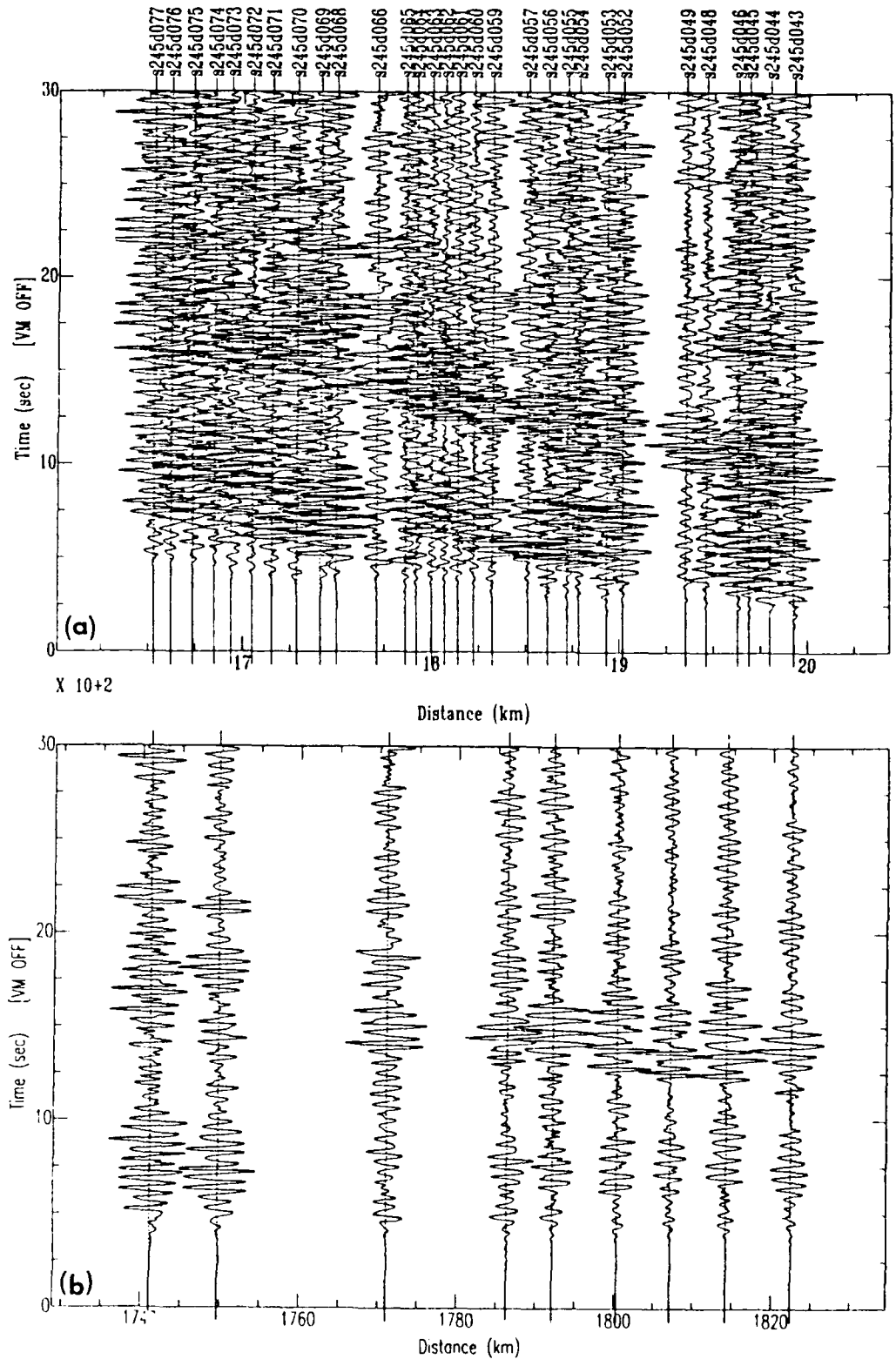


Figure 1. Location of the seismic profile with respect to the simplified geology of Asia. Solid circles denote the W. Norilsk, W. Tura, and Baikal shot points



Figures 2a,b. Seismograms from the DSS shot point at West Norilsk (SP 245) shown in record section format at a reduction velocity of 8.2 km/sec. Note the clear first arrival and the prominent secondary arrival.

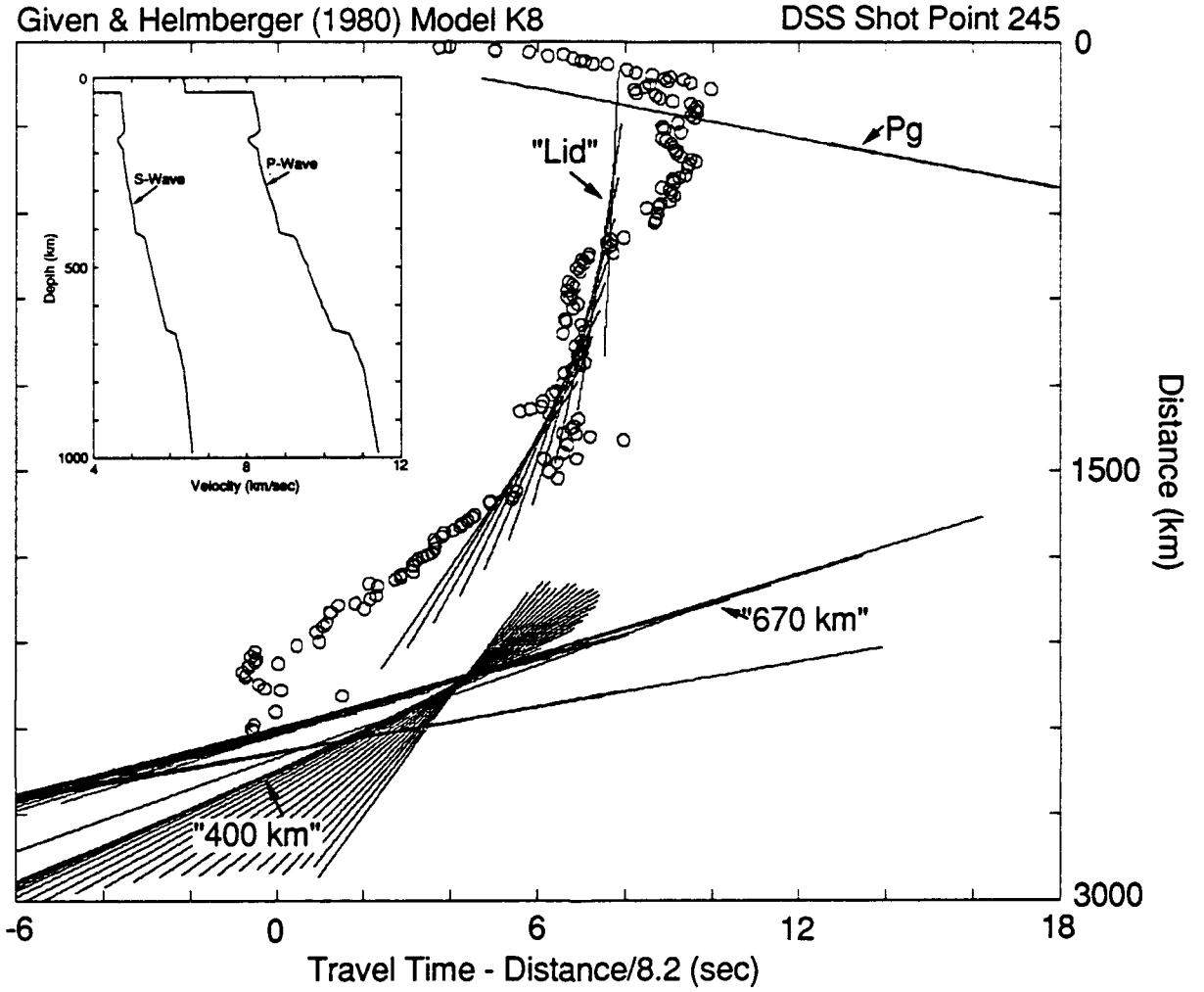


Figure 3. Observed arrival times for DSS shot point 245 (open circles) compared to travel times predicted by Model K8 (Given and Helmberger, 1980). The inset shows the P and S wave velocity model. The model is parameterized by a stack of homogeneous layers in which velocity gradients are approximated by a series of thin layers. The travel time curves are computed as refractions along the tops of these layers. No reflection computations are included. Regions of high gradient such as just above the 400 km discontinuity produce a series of widely spaced travel time curves. Portions of the velocity-depth function with low gradient produce nearly coincident curves (the 670 km arrival). In general, the agreement between K8 and the observed data is fair. The data suggest that the low velocity zone is very weak or absent in central Siberia.

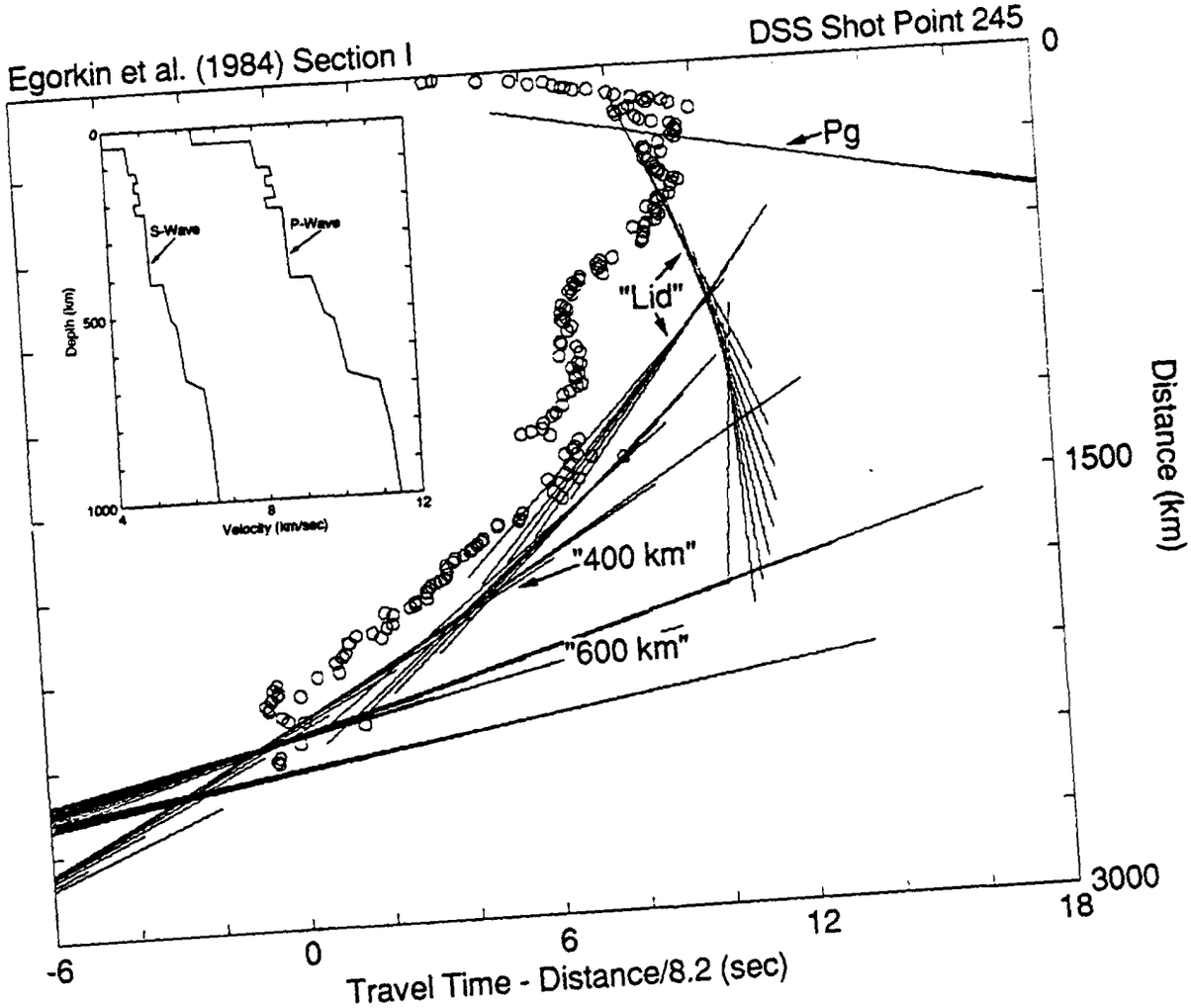


Figure 4. Observed arrival times for DSS shot point 245 (open circles) compared to travel times predicted for model EZC01 (Section I of Table 1 in Egorkin *et al.* (1984). Same format and computations as in Fig. 3. The complex structure in the upper mantle produces several branches to the travel time curve as well as arrivals from the 400 and 670 km discontinuities. Models K8 and EZC01 have similar structures below 400 km depth. The model is in good agreement with the data in the 1500-2400 km range, but is distinctly poorer than K8 at closer ranges. There appears to be no evidence for the alternating high and low velocities between 100 and 250 km.

CLUSTER ANALYSIS METHOD APPLIED TO EVENT LOCATION

Florence Riviere-Barbier, Lori Grant

Center for Seismic Studies
1300N. 17th Street, Suite 1450
Arlington, VA 22209

Contract # F19628-88-C-0159

Objective

A discrimination method that can associate events with a particular mine will reduce the number of events that need to be investigated in more detail. Discrimination has been the subject of numerous studies during the last few years (Bennett *et al.*, 1989; Blanford, 1982; Pomeroy et al. 1982), but associating an event with a particular mine requires ground truth that is not always available. The growing accuracy of location programs has helped in associating events with mining districts but cannot associate events with a particular mine. The ultimate is to discriminate between events from several mines located within a mining district by quantitatively characterizing each mine.

The Intelligent Monitoring System (IMS) that processes data from four arrays (ARCESS, NORESS, FINESA and GERESS) provides a large data set of local and regional events for the baltic shield and the eastern part of the Soviet Union (*Figure 1*). Three different areas with a high concentration of mines were found, all in the Soviet Union. This paper is devoted to the results obtained for a mining district located north of Leningrad and known as the Estonian mines.

Research accomplished

Data

The data set covers a period of time from November, 4 1990 to June 28, 1991. Waveforms recorded at FINESA as well as phase parameters computed and saved during the automatic detection and location of the IMS were utilized in this study. The set of phase parameters extracted from the IMS database was similar to the set used by Baumgardt (1987) in his study: *Lg-P* time, azimuth and velocity computed from f-k analysis for *P* and *Lg*, center period of each phase, and ratio between the short-term average for the *P* and the short-term average for the *Lg*.

IMS locations were compared to the locations provided by the Helsinki bulletin which was used as a reference. Fewer events were reported in the Helsinki bulletin than in the IMS bulletin as the Helsinki bulletin did not report most of the events with an IMS magnitude below 1.0. In addition, most of the events with a magnitude between 1.0 and 2.0 in the Helsinki bulletin had a "manual location" which means that the Finnish analyst attributed them to a particular mine by visual inspection.

Cluster analysis

Cluster analysis is based on the evaluation of either "distance" or "similarity" between data. A measure of the data comparison provided by some processing scheme is used for this

purpose. In a distance scheme, the larger the distance between two data, the more different they are. It is the opposite for the similarity measurement. The representation of the results is a cluster tree (Everitt, 1986). Different methods can be applied to build the cluster tree and the results of these different clusterings can be quite diverse.

Cross-correlation

By assuming that events from the same mine should look very similar, the computation of cross-correlation values provided an easy way to build a numerical link between similar events. A high cross-correlation value between two events would imply a high probability that the events were from the same mine. The maximum value of each cross-correlation was used to build a matrix of similarity that was used in a cluster analysis. The envelope of the signal recorded on the sz components was used to compute the cross-correlation. The envelope included the first arrival as well as the *Lg* and the *Rg* wave. Signals were filtered between 1 and 8 Hz.

Visual classification

In order to better interpret the results along with being to understand the "manual location" of the Helsinki bulletin, a visual classification was performed using recordings of the vertical channel. Waveforms that looked alike were collected into 12 different groups. A total of 22 events were chosen as a reference set to represent the 12 groups. These 22 events were used in the cluster analysis although the results of that analysis showed that two groups of the original reference set should be combined into a single group and that three additional groups should be added. *Figure 2a* shows 14 reference events that have been identified as being from distinct mines. To illustrate the repeatability of mining events, all the events belonging to groups G6 and G9 are displayed in *Figure 2b*. When the signal-to noise ratio was too low, coherent beams were used to group the events.

Application

In addition to the reference events, 124 other events were used in the cross-correlation and cluster analysis computations. These events were split into four data sets, each including the 22 reference events. In *Figure 3*, the cluster tree for the 53 events of the first data set has been plotted. The results of the visual analysis are shown at the top of the figure as groups (G1, G2, etc.). Note that groups G8 and G13 do not have reference events. These are the groups that were identified as a result of cluster analysis and later verified by visual analysis. At the level of the tree corresponding to a cross-correlation value of 0.5, the cluster separates the events into eight groups. At this level, events from groups G2, G4, G6, G10 and G11 become one larger group. These five small groups can be distinguished from one another only at a cross-correlation value of 0.6. Because the events from these groups cluster at a higher level than the events from the other groups, the stability of their shape is greater.

The visual classification differed from the cluster analysis for three of the 53 events and these three events either had a low signal-to-noise ratio or were multiple events. In *Figure 4*, IMS locations of the events are plotted using a unique letter for each group.

Similar results were obtained for the other three data sets. The separation between the group of mines around Lake Ladoga and the mines further south is clear on the cluster trees.

An important feature of the signal is the presence of an *Rg* phase. The events from groups G1, G5, G9 and G14 located in the northern part of the map do not exhibit an *Rg* phase. This may be due to the type of mine (open pit or subterranean), the distance, or the path between

the mines and FINESA.

Among 146 events, the cluster analysis disagreed with the visual classification for 12 of the events and 10 other events had signal-to-noise ratios so low that a visual classification could not be made.

Once the events were clustered, an attempt was made to associate a mine with each group. This was done using the location of the reference events given in the Helsinki bulletin. However, several groups of events clearly belong to mines that were not reported in the Helsinki bulletin. A more thorough analysis of the location of the event clusters is under way using SPOT photos and detailed maps of the area.

The use of f-k parameters (SNR, period, azimuth, slowness, etc.) computed during the automatic process by the IMS in a cluster analysis gives results comparable to those that would be obtained by grouping events based on IMS locations. The addition of polarization parameters from three-component polarization analysis did not improve the results of this cluster analysis because polarization parameters are more characteristic of the receiver than of the source.

A careful study performed on spectra also shows important differences between each group although an attempt to use coherence did not give good results. Differences in the spectral shape can provide an additional source of information in order to classify the events.

Conclusions and recommendations

The set of data includes many events occurring during months for which the Helsinki bulletin has not yet been released. In addition, many events have an IMS magnitude below 1.0 and will probably not be reported in the Helsinki bulletin. This imposes a strong limitation on the comparison of the cluster analysis results and the Helsinki locations. The IMS locations are in general accurate but not enough to assign locations to mines 10km apart.

The main problem in this kind of study remains the lack of reliable ground truth. Reports from each mine giving information such as the origin time, the shooting practice and the size of each event is needed. This information is currently being collected by the researchers at NORSAR, but does not include the time period of this data set and does not include Soviet mines.

This kind of analysis can be easily added to an automatic location process, the location of each new event being used as a key to call master reference events in the area for comparison.

References

Baumgardt, D.R. (1987). Case-based reasoning applied to regional seismic event characterization, *DARPA/AFGL Seismic Research Symposium*, Harbor House, Nantucket, MA, 15-18 June 1987, 173-178.

Bennett, T.J., B.W. Barker, K.L. McLaughlin, J.R. Murphy (1989). Regional Discrimination of Quarry Blasts, Earthquakes and Underground Nuclear Explosions. *S-Cubed Final Report SSS-TR-89-10395.*

Blanford, R.R. (1982). Seismic Event Discrimination. *Bull. Seism. Soc. Am.* 72, 6, S69-S87.

Everitt, Briant (1986). Cluster Analysis. *Halsted Press, Division of John Wiley & Sons, New York* (2nd Edition).

Pomeroy, P.W., W.J. Best, T.W. McEvilly (1982). Test Ban Treaty Verification with Regional Data - A Review. *Bull. Seism. Soc. Am.* **72,** 6, S89-S129.

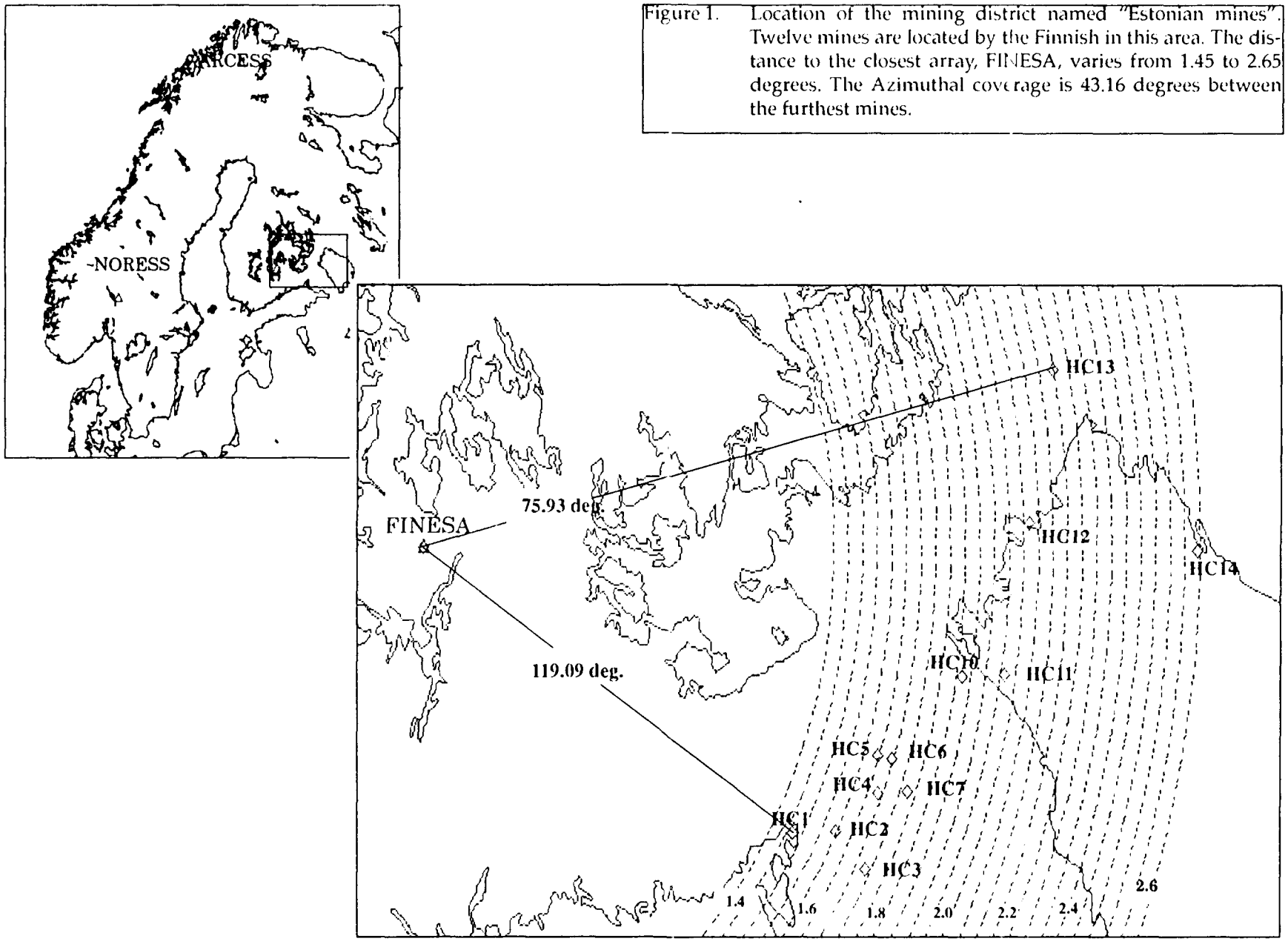


Figure 1. Location of the mining district named "Estonian mines". Twelve mines are located by the Finnish in this area. The distance to the closest array, FINESA, varies from 1.45 to 2.65 degrees. The Azimuthal coverage is 43.16 degrees between the furthest mines.

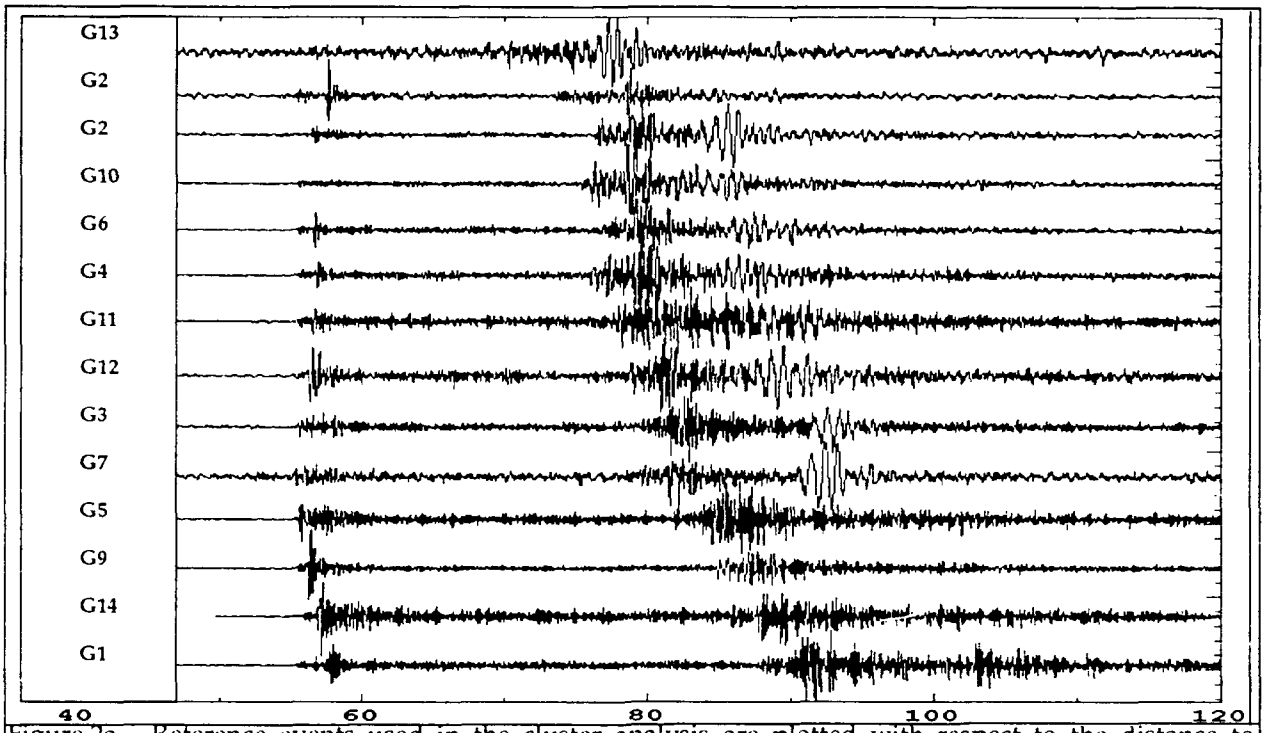


Figure 2a Reference events used in the cluster analysis are plotted with respect to the distance to FINESA. The classification is done visually. Each reference event corresponds to a particular mine. An *Rg* wave is clearly seen in the first ten events but is absent from the last four events which have distances greater than 250 km from FINESA and different azimuthal paths.

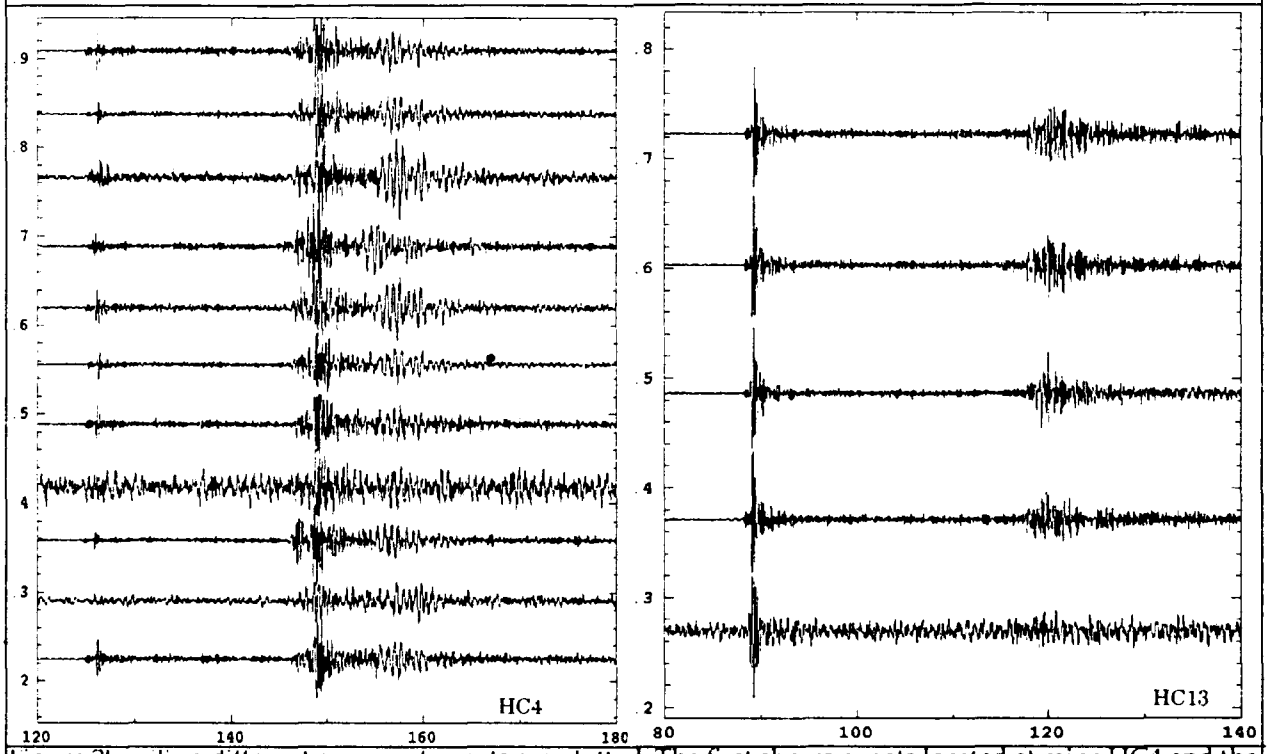


Figure 2b Two different groups of events are plotted. The first shows events located at mine HC4 and the second shows events located at mine HC13. Local magnitudes vary between 1.0 and 2.3 for the first group. The size of the shot does not appear to influence the shape of the waveform as the waveforms are, cycle by cycle, nearly identical, especially the *Rg* phase.

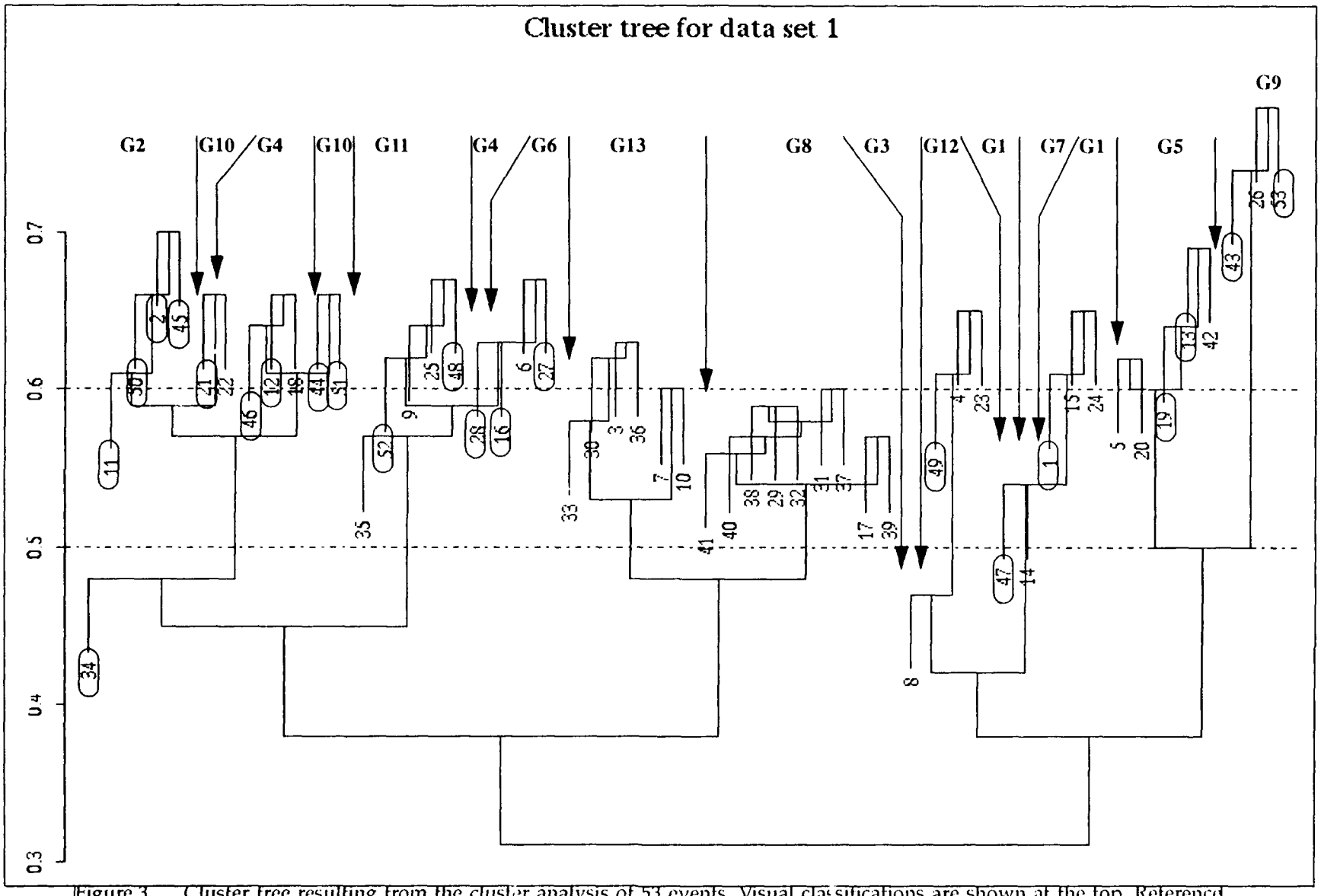


Figure 3 Cluster tree resulting from the cluster analysis of 53 events. Visual classifications are shown at the top. Reference events are circled. Three events do not cluster with the group assigned by the analyst. Even signals with a very low signal-to-noise ratio for which the *P* phase can hardly be seen by the analyst cluster, with their corresponding group.

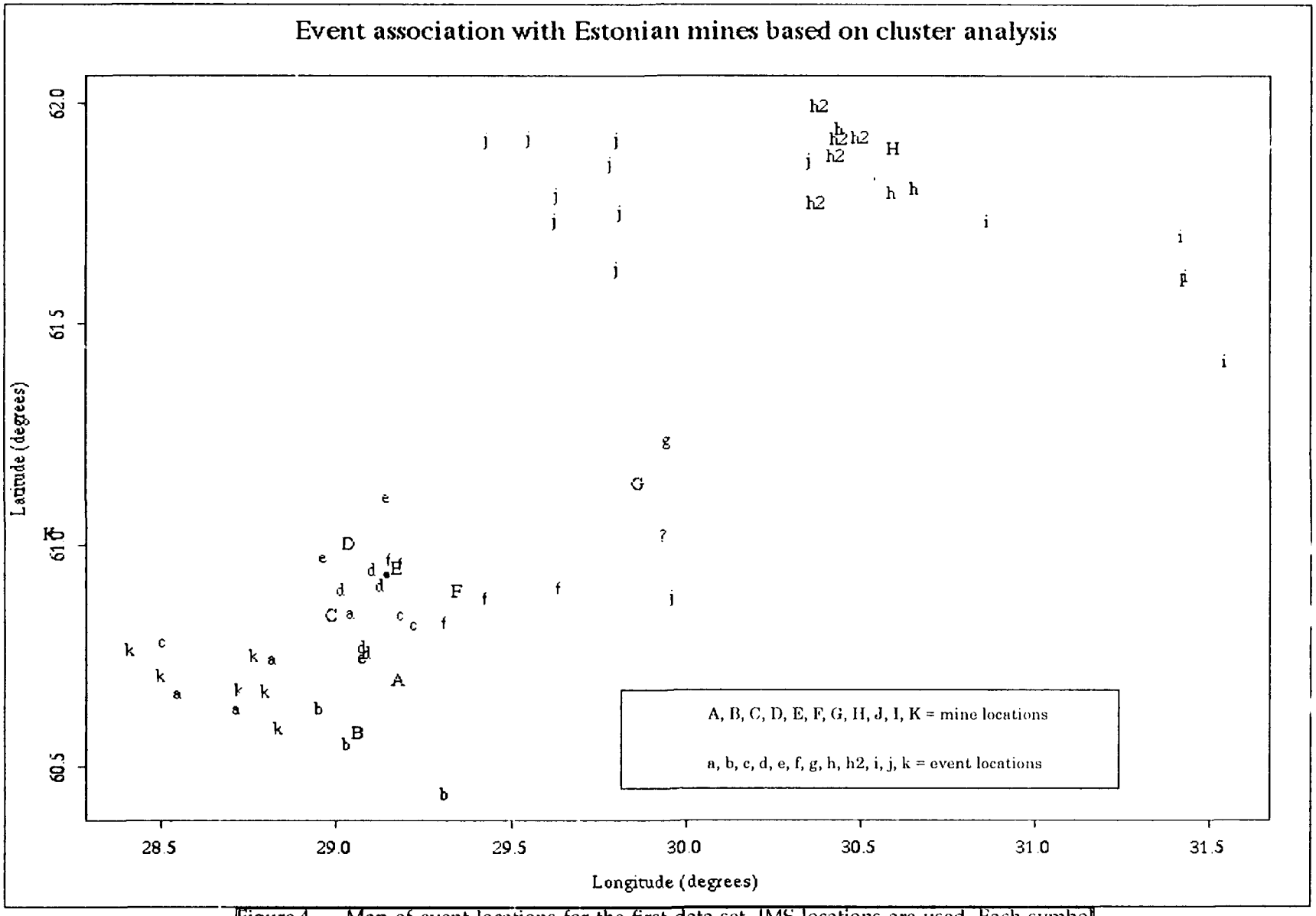


Figure 4 Map of event locations for the first data set. IMS locations are used. Each symbol corresponds to a particular group of events that cluster together.

THE NORILSK DSS PROFILE IN NORTHERN SIBERIA: AN ANALYSIS OF THE 2D CRUSTAL VELOCITY SECTION CONSTRUCTED BY SOVIET SEISMOLOGISTS

V. Ryaboy, H. Benz, J. Unger, and W. Leith
CSS, USGS
Contract No. F19628-89-C-0203

Objective

Under an agreement between the Ministry of Geology of the USSR and the US Geological Survey, data from Soviet and US deep seismic sounding (DSS) profiles were exchanged in early 1991. The Soviet profile is nearly 230 km long, and is located in Northern Siberia, near Norilsk, in a region that has been designated as a site for a joint US/USSR seismic station. Consequently, the accurate characterization of the crust and upper mantle in this region is essential for understanding details of seismic signal propagation recorded at the new station. The objective of this research is to evaluate the Soviet interpretation of the Norilsk DSS profile using theoretical travel times and synthetic seismograms from ray tracing.

Research Accomplished

GEOLOGICAL AND GEOPHYSICAL BACKGROUND

The profile trends NW-SE at the border between the north western part of the Precambrian Siberian platform and the Paleozoic West-Siberian platform plate within the Norilsk uplift (Figure 1). The Norilsk uplift is characterized by a complex geological structure, due partly to the presence of wide-spread trap intrusions within the sedimentary layers and deep faults. This region has been studied extensively because it is rich in a variety of ore deposits. The first crustal studies in Northern Siberia were based on recordings of mine explosions (Tuezov, 1965), but several DSS lines have crossed the area since then. The crustal and upper mantle velocity sections were published for two long-range profiles. The Dikson-Khilok profile crossing the Siberian platform from north to south is located 50-100 km east of the Norilsk profile (Egorkin et al., 1987), and the Vorkuta-Tixie profile (Figure 1) stretching from west to east in the northern areas of Siberia (Egorkin et al., 1980) crosses the northern part of the Norilsk profile. Joint interpretation of geological and geophysical data, including DSS observations, was made for this region and indicate that the crustal thickness in the Norilsk region is less than 40 km, and that the depth to the basement varies from 5 to 10 km (Grichin et al., 1989).

The unpublished Norilsk profile data set consists of three-component analog field recordings from nine reversed and overlapping shots. Recordings of seismic waves were collected from five shot points within the profile and four off-end shots. The shots were recorded up to distances of 250-280 km for off-end shots, and 180-230 km for shots located within the profile. Station spacing varied from 3 to 5 km and the shot spacing averaged 40 km. Three-component portable analog seismic stations provided records in the 1.0-20.0 Hz frequency range. This system of field observations was designed to detect and correlate refracted, reflected, and converted body waves. The analog waveforms were digitized in the USSR at 50 samples per second.

Soviet seismologists interpreted the wave recordings as a complex, two-dimensional (2D) velocity model with crustal thickness varying from 42 to 48 km

and high velocities (6.8 km/s) at depths as shallow as 13-15 km (Figure 2). Their velocity section is characterized by a number of laterally inhomogeneous layers consisting of different size blocks with high and low velocities. The blocks are separated by vertical or subvertical boundaries that were interpretated from reflected and converted waves or interpolated with the help of other criteria developed in the USSR (Egorkin et al., 1989). The linear dimensions of the blocks vary from approximately 10-20 to 50-100 km.

ANALYSIS OF THE CRUSTAL VELOCITY MODEL FOR THE NORILSK PROFILE

Crustal and upper mantle refracted waves were recorded on the Norilsk profile. Apparent velocities vary considerably: 2.0-5.0 (sedimentary layers), 6.0-6.5 (Pg), and 8.0-8.2 (Pn) km/s, respectively. The Pn wave is observed beyond 150-160km from shot points and is typically weak. Reflected waves from crustal boundaries and the Moho (PMP) were recorded as secondary arrivals.

In order to substantiate the crustal velocity model constructed for the Norilsk profile by Soviet seismologists, we calculated theoretical travel-time curves and ray synthetic seismograms for a generalized version of their model. We attempted to accurately parametrize this 2D velocity model (Figure 2) by using a series of 11 laterally-heterogeneous layers, with each layer approximating a layer in the Soviet model. We made calculations for the refracted and reflected P-waves for three reversed and overlapping shot points (SP1, SP17, SP73), using the program Ray84 of J. Leutgert (USGS, Menlo Park), and compared these results with the observed data.

According to the model, a complex group of arrivals from waves refracted in layers of the upper and middle crust up to depths of 20-25 km (Pg) should be recorded as the first arrivals from 40 to 230 km (Figures 3 and 4). Changes in the waveform characteristics of the first arrivals, a break and offset to later time in the travel time curves, and zones of increased and decreased amplitudes caused by vertical and lateral velocity inhomogeneities are observed in the synthetic record sections for these distances. At distances greater than 230 km, Pn refracted in the upper mantle is the first arrival in the synthetic sections. Information about the velocity structure of the lower crust can also be obtained from the analysis of later arrivals. The postcritical reflected wave from the Moho (PMP) is the strongest of the later arrivals of the synthetics, while waves reflected from the intermediate crustal boundaries are very weak.

At distances greater than 100-120 km, theoretical first arrival travel times are consistently 1-2 seconds faster than observed travel times (Figure 4). In this distance range of the observed data, the first arrivals attenuate and are offset to later times in the travel-time curves. Calculations do not predict this observed phenomenon. It is possible that our travel-time picks at distances greater than 100-120 km (Figure 4) are secondary, high amplitude arrivals, and that the true first arrivals are very weak crustal refractions that are not observed. A thorough search was made for these arrivals, but none were detected for SP1, SP17, or SP73 record sections constructed for different frequency ranges and amplifications (Figures 4B and 4C).

Further careful analysis of all record sections should probably more reliably determine if there are weak first arrivals that fit the predicted travel times. It is worth noting that our synthetic analysis does not predict either attenuation or decreased amplitudes of the first arrivals at distances greater than 100-120 km (Figure 4A). There are no large discrepancies between the theoretical and observed travel times for Pn waves. However, the Soviet model predicts a Pn wave cross-over point of 230-240 km (Figures 3 and 4) and observations show that the cross-over occurs at distances of 150-160 km. There is one more important discrepancy

between the synthetics and the observed data. According to calculations, reflected waves from the intermediate crustal boundaries recorded in the later arrivals should be very weak, but these waves are rather intensive on the observed record sections (Figure 4).

Conclusions and Recommendations

Preliminary analysis for three shot points (SP1, SP17, and SP73) of the Soviet crustal velocity model for the Norilsk DSS profile showed discrepancies between calculated and observed travel times and record sections. The major differences are:
1. For distances greater than 100-120 km, theoretical first arrival times were consistently faster than the observed travel times.
2. The Soviet model predicts a Pn cross-over point of 230-240 km, while the Pn wave was observed as a first arrival at distances of 150-160 km.
3. Predicted amplitudes of reflected waves from the intermediate crustal boundaries are very weak, but these waves are rather intensive on the observed record sections.

These discrepancies between the observed and theoretical data for prominent crustal and upper mantle P-waves will help us to construct an alternative two-dimensional crustal velocity model for the Norilsk profile that better fits the observed data. This model should contain lower crustal velocities and probably a thinner crust. At the neighboring Dikson-Khilok and Vorkuta-Tixie long-range profiles (Figure 1), high velocities of 6.8-7.0 km/s were observed at depths as shallow as 25-30 km (Egorkin et al., 1980, 1987). The results of this study indicate the importance of reinterpreting the Norilsk DSS profile.

References

Egorkin, A.V., Chernyshev, N.M., Danilova, Ye. G., Kun, V.V., and Scheglova, L.B., "Regional section across the north of the Asiatic continent (Vorkuta-Tixie profile)," in *Seismic models of the lithosphere for the major geostructures on the territory of the USSR*, pp. 61-66, Nauka (Science) Publisher House (in Russian), Moscow, 1980.

Egorkin, A.V., Zuganov, S.K., Pavlenkova, N.A., and Chernyshev, N.M., "Results of lithospheric studies from long-range profiles in Siberia," *Tectonophysics*, vol. 140, pp. 29-47, 1987.

Egorkin, A.V., Zuganov, S.K., Mikhaltsev, A.V., and Chernyshev, N.M., "Integrated seismic investigations along geotraverses," in *Deep crustal studies of the USSR. Reports of Soviet Geologists*, pp. 226-237, Ministry of Geology of the USSR Publisher House (in Russian), Leningrad, 1989.

Grichin, M.P., Zhero, O.A., Kramnik, V.N., Kuznetsov, V.L., Lotshev, V.I., Smirnov, L.V., and Surkov, V.S., "Deep structure of the Earth crust in platform regions of Siberia," in *Deep crustal studies of the USSR. Reports of Soviet Geologists*, pp. 152-162, Ministry of Geology of the USSR Publisher House (in Russian), Leningrad, 1989.

Tuezov, I.K., "An application of mine explosions for crustal studies within transition zone between Siberian platform and Taimyr depression," *Geology and Geophysics (in Russian)*, no.2, pp. 123-127, 1965.

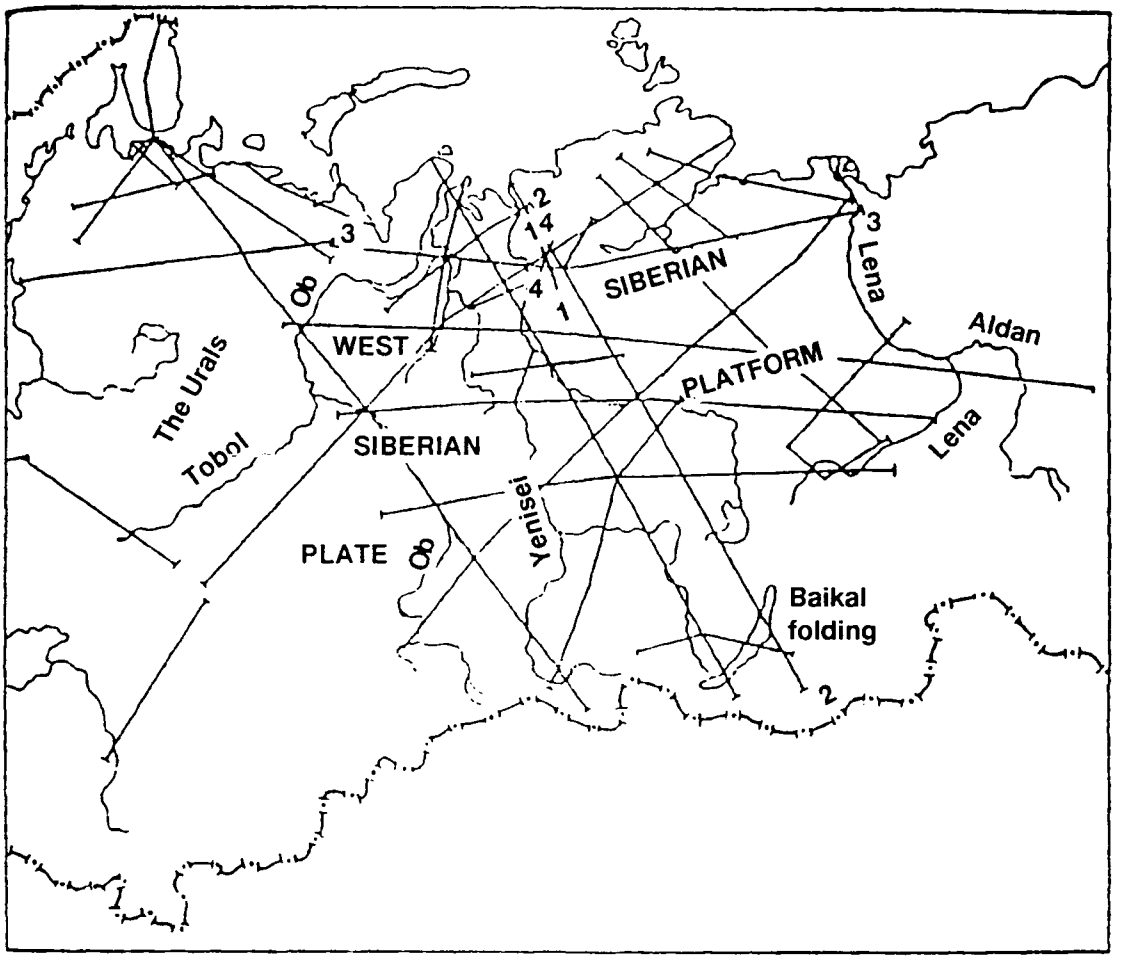


Figure 1. Location map of DSS profiles: 1-1 -- Norilsk crustal DSS profile, 2-2 -- Dikson-Khilok profile, 3-3 -- Vorkuta-Tixsie profile, 4-4 -- a profile based on recordings of mine explosions. Adapted from Egorkin et al., 1989 with additions.

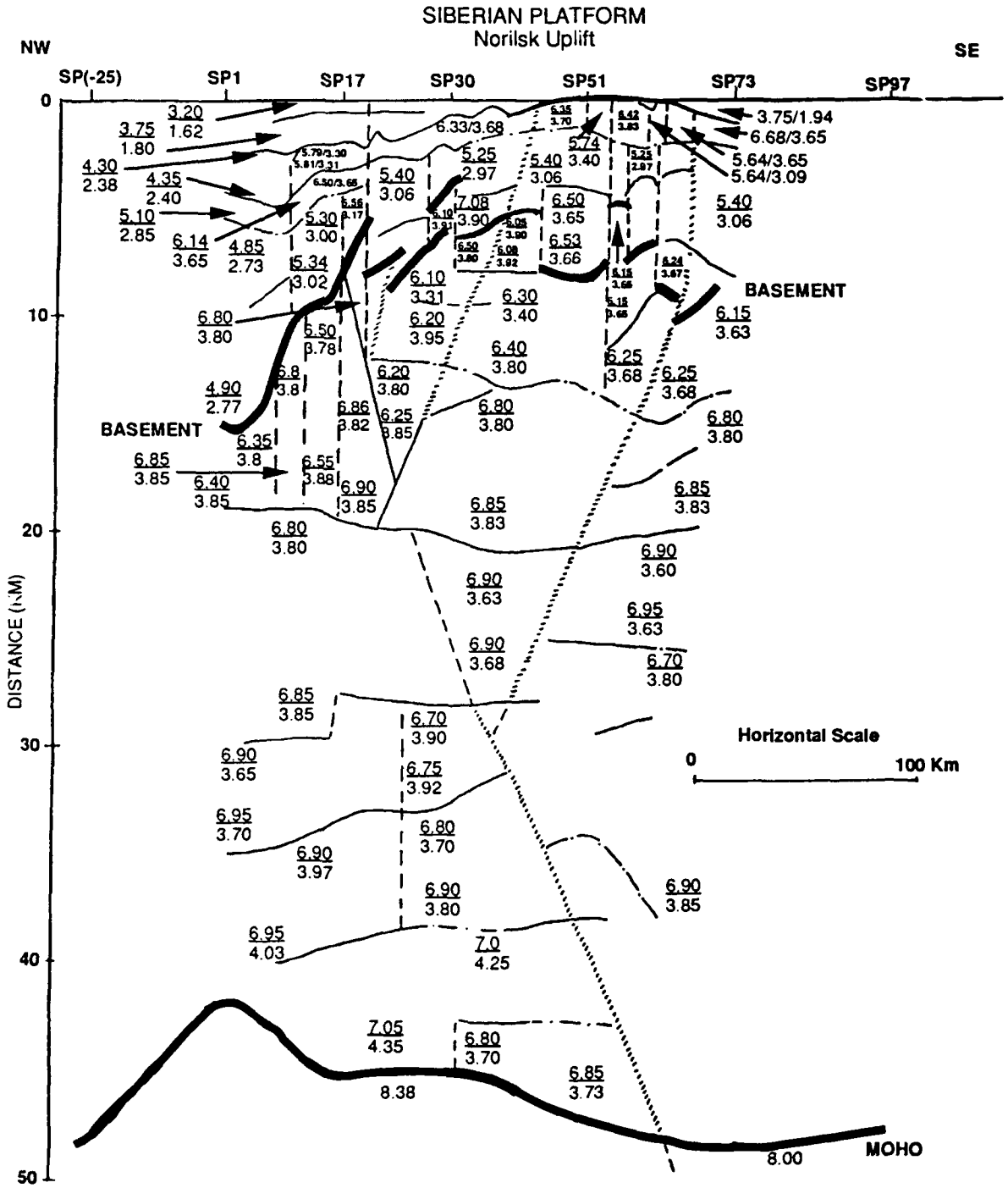


Figure 2. The Norilsk profile crustal velocity section constructed by Soviet seismologists (A.V. Egorkin, L.N. Solodilov et al.). Numbers are velocities of P- and S-wave (above and beneath lines correspondingly). Vertical exaggeration is 10:1.

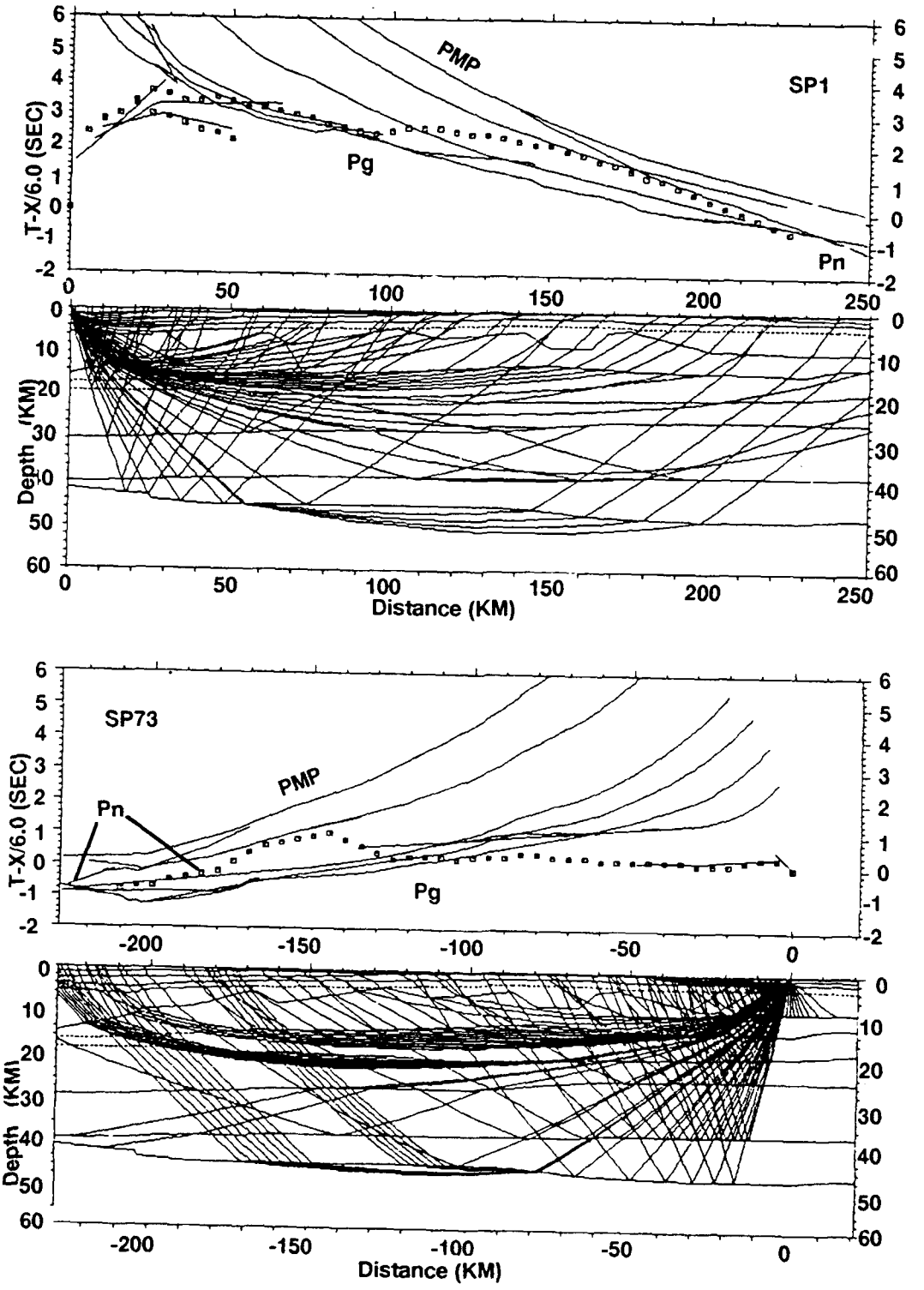


Figure 3. Comparison of first arrival observed travel times (open squares) with theoretical travel time curves of reflected and refracted P-waves (solid lines) and 2-D ray tracing for SP1 (top) and SP73 (bottom).

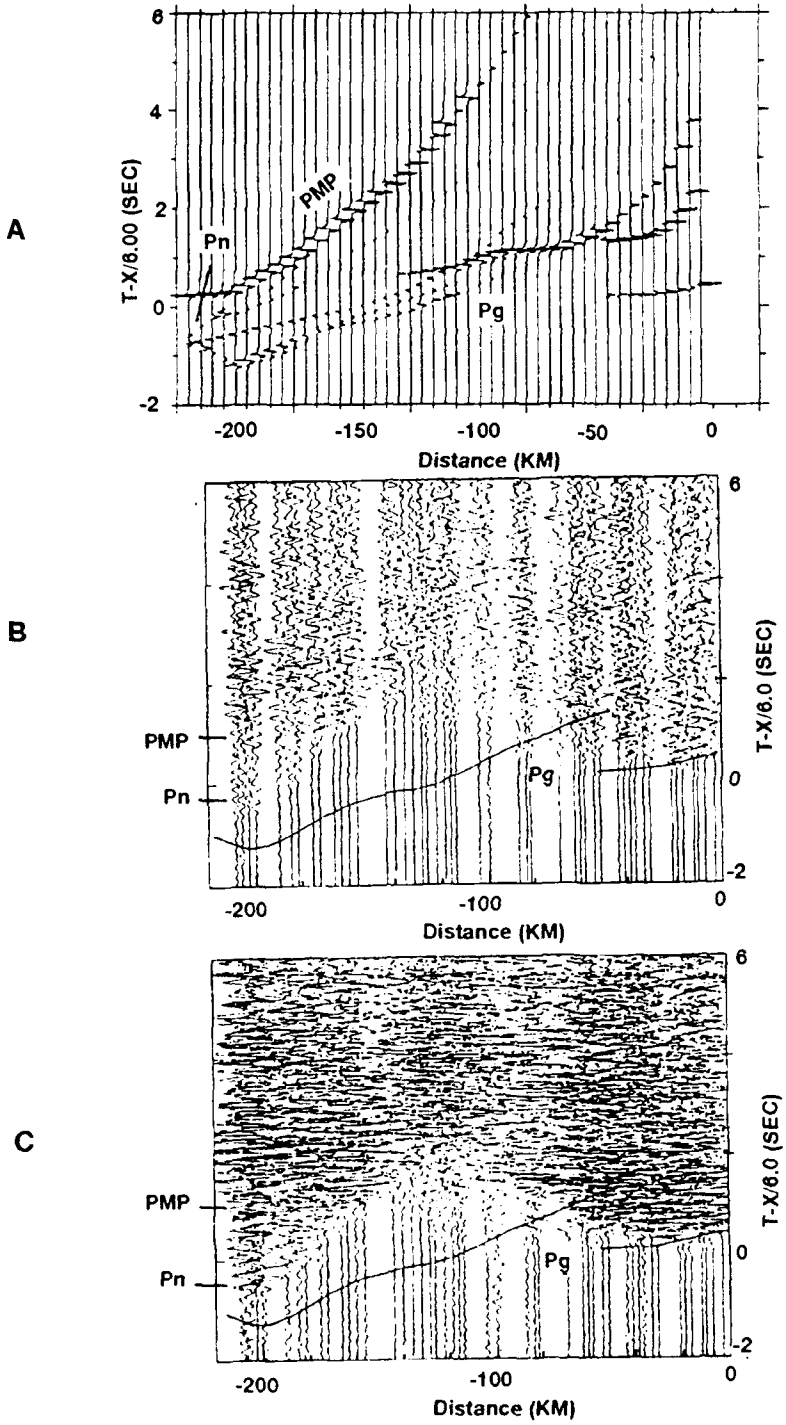


Figure 4. Synthetic seismograms (A) and trace-normalized record sections (B and C) for SP73. Records are bandpass filtered between 3 and 10 Hz. Seismic wave amplitudes for (C) were increased relative to (B) to search for low amplitude arrivals. Solid lines (see Figures B and C) are theoretical travel time curves for first arrivals of SP73.

ANALYSIS OF THE EFFECTS OF EURASIAN CRUSTAL AND UPPER MANTLE STRUCTURE ON REGIONAL PHASES USING BROADBAND SEISMIC DATA: INITIAL PHASE

Susan Y. Schwartz and Thorne Lay
University of California, Santa Cruz

Contract No. F19628-90-K-0041

Objective

A detailed understanding of regional wave propagation in Eurasia is critical for efforts to monitor underground nuclear tests and to discriminate them from earthquakes and chemical explosions. A direct approach to this problem is to analyze regional phases from various Eurasian sources and to empirically characterize useful diagnostics of the regional wavefields. We take an alternative approach to accomplish this objective and use crustal and upper mantle phases to characterize regional Earth structures and then relate regional waveform diagnostics to known structural variations.

Research Accomplished

Due to the success of using SS phases to determine the upper mantle shear wave velocity structure beneath North America (Grand and Helmberger 1984a), the North Atlantic Ocean (Grand and Helmberger 1984b), and the Alpine Front (Rial *et al.*, 1984), we have focussed on evaluating the effectiveness of using the PP phase to determine P wave upper mantle lid structure. The advantages of using multiple bounce phases (SS and PP) over direct observations to determine upper mantle structure arise from the increase in the distance range sampling the upper mantle, a doubling of the time and distance between triplication arrivals, and a reduction in source area anomalies due to local structure or event mislocation, through the use of differential arrival times. Figure 1a shows examples of the long-period S and SS data and synthetics that Grand and Helmberger (1984b) used to determine their North Atlantic upper mantle model ATL. The SS-S times are very well matched and in general, so are the SS waveforms. Lefevre and Helmberger (1989) used PP phases at upper mantle distances, as well as direct P and crustal P_n phases to develop an upper mantle P wave model appropriate for the Canadian Shield. P and PP data and synthetics used in their study are shown in Figure 1b. Careful inspection reveals that although the PP-P travel times are well matched by their model, the synthetic PP waveforms do not strongly resemble the data. This mismatch could arise from either inadequacies in the upper mantle P wave model or in the computation of the synthetic seismograms. To resolve this problem and evaluate the usefulness of the PP phase in determining upper mantle lid structure, we performed a detailed analysis of the PP phase at upper mantle distances. Thus far we have concentrated on understanding the PP phase at periods between about 1 and 50 s, once this is accomplished we will increase our frequency range using broadband data.

The PP phase is more complicated than SS at upper mantle distances due to multiple P-SV conversions from interfaces near the source, receiver, and PP bounce point. LeFevre and Helmberger (1989) computed their PP synthetics using the WKBJ method (Chapman, 1978) including only direct and depth phases, thus approximating the complete layered Earth response. Figure 2 evaluates the accuracy of this approximation by comparing P and PP synthetics calculated with WKBJ, in the same manner as LeFevre and Helmberger (1989), with reflectivity synthetics (Fuchs and Muller, 1971) which include all reflections and conversions arising in a layered Earth. The synthetics are computed for a vertical dip-slip source at 18 km using four different velocity models: a smooth positive velocity gradient with no seismic discontinuities and a low velocity crustal layer (grad), the same model without a crustal layer (grad no crust), increasing velocities with depth, two upper mantle seismic discontinuities and a crust (disc), and the same model without a crust (disc no crust). The correspondence is excellent between

synthetics computed for models that do not contain a low velocity crustal layer (grad no crust and disc no crust), but significantly degrades when synthetics computed with a crustal layer are compared. The largest discrepancy between the synthetics shown in Figure 2 occurs in the later part of the P and PP waveforms, suggesting that the unmodeled energy in the WKBJ synthetics arises from multiple bounces in the crust. The synthetic waveform discrepancy becomes more pronounced for the model that contains upper mantle discontinuities, due to the crustal reverberations of three triplicated arrivals. The inadequacy of the WKBJ synthetics to produce accurate PP waveforms make upper mantle models derived from their use suspect and motivates further investigation of the PP phase. The strong apparent influence of the crust on propagation of the PP phase may prevent its effective use in determining upper mantle lid structure; on the other hand, the sensitivity of the PP phase to the crust may allow it to place constraints on crustal structure.

To determine what phases contribute to the large PP coda not reproduced in the WKBJ synthetics, we added additional rays to these synthetics to see if they would more closely resemble waveforms computed with reflectivity (Figure 3). Synthetics in Figure 3 were computed for the same source as used in Figure 2 and an SNA-like (Grand and Helmberger, 1984a) P wave velocity model. The synthetics in the top row of Figure 3 (WKBJ1) were computed with WKBJ including only direct P and triplicated PP phases and their associated depth phases, pP, sP, pPP, and sPP. In addition to this rayset, the WKBJ2 synthetics include rays having an extra reflection or conversion from the free-surface and the Moho and all corresponding rays that have PP reflections at the Moho rather than the free-surface. Inclusion of the crustal multiples begins to build the large amplitudes observed in the later part of the reflectivity PP waveforms. The P waveforms remain unchanged since the P wave crustal multiples were not included in the synthetic calculations. Inclusion of Moho underside reflections adds amplitude to the beginning of the PP waveforms. Since amplitudes of the underside reflections are small compared with the PP arrivals, their impact is significant out to distances of about 42° where they arrive prior to the PP phase, beyond this distance they have only a small effect on the PP waveform. The comparison between WKBJ and reflectivity synthetics improved with the addition of rays that include an extra bounce in the crust and underside Moho reflections. Additional improvement is expected as more crustal reflections and conversions are added until all possible interactions in a layered Earth have been included. Because of the difficulty identifying and including all significant rays into WKBJ synthetics, we use the reflectivity method to compute all remaining synthetic seismograms.

Figure 4 illustrates the dramatic effect that variations in crustal thickness have on P and PP waveforms. The synthetics are computed using the previously discussed source and mantle structure underlying a single crustal layer varying in thickness between 10 and 40 km. Since the source is located at 18 km, the model having a 10 km thick crust has the source in the higher velocity mantle material (vp=8.2 km/s), all other examples have the source in the crust (vp= 6.4km/s). Both the timing between the P and PP phases and the P and PP waveforms change as the thickness of the crustal layer varies. A thinner crust results in reduced PP-P travel times and PP/P amplitude ratios. Travel time and amplitude variations may also accompany changes in upper mantle lid structure, making it difficult to attribute amplitude and travel time effects to one particular depth range in the Earth.

Figure 5 shows the range in waveform variation expected from three different lid velocity gradients, all producing equivalent travel times through the upper mantle. The differences in waveforms resulting from a reversal in lid gradient are very small, and virtually undetectable in long-period seismograms. We therefore conclude that at the periods studied, the PP phase has little to no sensitivity to the velocity gradient in the lid. However, we do find that P and PP travel times and amplitudes are sensitive to the average velocity structure of the lid. The top row of Figure 6 shows WWSSN long-period P and PP waveforms for paths traversing the Canadian shield (Figure 6a), platform (Figure 6a), and tectonically active (Figure 6b) regions of North America. Below each observed waveform are reflectivity synthetics computed for a suite of P wave lid models with average velocities ranging between the two published models:S25 (shield

model of LeFevre and Helmberger, 1989) and GCA (tectonic model of Walk, 1984). The suite of velocity models is shown in Figure 7a. Variations in lid velocity result in changes in PP-P travel times and PP/P amplitude ratios that are comparable to those produced by variations in crustal thickness (compare Figures 4 and 6). Therefore if *a priori* information on either crustal thickness or average lid velocity is not available, it will be difficult to use the PP phase to uniquely determine either one.

In many regions *a priori* information on crustal thickness is known from refraction profiling. In this case PP-P arrival times and PP waveforms can be modeled using reflectivity synthetics to ascertain the average lid velocity structure. We have accomplished this for North America using values of crustal thickness compiled by Mooney and Braile (1989); our results are shown in Figure 7b. The stars represent the location of earthquakes we modelled recorded at stations indicated by the diamonds. Representative waveforms and synthetics constructed with various lid velocity models (Figure 7a) are shown in Figure 6, with the solid seismograms representing both the data (top row) and the best fit synthetics. The map in Figure 7b summarizes our findings; progressing from north to south, data from each shaded region is best modeled with a lid structure having a slower average velocity then the preceding model. The total range in lid structure spans the two extreme published North American P wave models S25 and GCA.

Conclusions and Recommendations for Future Work

A detailed study of the PP phase at upper mantle distances has revealed that crustal reverberations have a profound effect on PP waveforms giving them sensitivity to both crustal thickness and average lid velocity. Using long-period data sampling North America, we have shown that if crustal thickness is known *a priori* the average lid velocity can be determined. The average lid velocity influences propagation of regional phases, thus it is important to constrain its variation beneath the diverse tectonic provinces of Eurasia. This should be possible given abundant data generated on crustal thickness by the deep sounding experiments in the Soviet Union. Now that we understand the long-period characteristics of the PP phase, the next step is to investigate PP propagation across Eurasia using broadband data with the dual goals of mapping variations in the average lid structure and gaining further insight into PP propagation at higher frequency.

References

Chapman, C.H., (1978). A new method for computing synthetic seismograms, *Geophys. J.R. Astron. Soc., 54,* 481-518.

Fuchs, K. and Muller, G. (1971). Computation of synthetic seismograms with the reflectivity method and comparison with observations, *Geophys. J. R. Astron. Soc., 23*, 417-433.

Grand S.P. and Helmberger, D.V. (1984a). Upper mantle shear structure of North America, *Geophys. J.R. Astron. Soc., 76*, 399-438.

Grand S.P. and Helmberger, D.V. (1984b). Upper mantle shear structure beneath the Northwest Atlantic Ocean, *J. Geophys. Res., 89*, 11,465-11,475.

LeFevre, L.V., and Helmberger, D.V., (1989). Upper mantle P velocity structure of the Canadian Shield, *J. Geophys. Res., 94*, 17,749-17,765.

Mooney, W.D., Braile, L.W. (1989). The seismic structure of the continental crust and upper mantle of North America, in Bally, A.W. and Palmer, A.R., eds., *The Geology of North America-An Overview*, vol. A, 39-52.

Rial, J.A., Grand, S.P., and Helmberger, D.V. (1984). A note on the lateral variation in upper-mantle shear structure across the Alpine front, *Geophys. J.R. Astron. Soc., 77*, 639-655.

Walck, M.C. (1984). The P-wave upper mantle structure beneath an active spreading center: The Gulf of California, *Geophys. J.R. Astron.. Soc., 76*, 697-723.

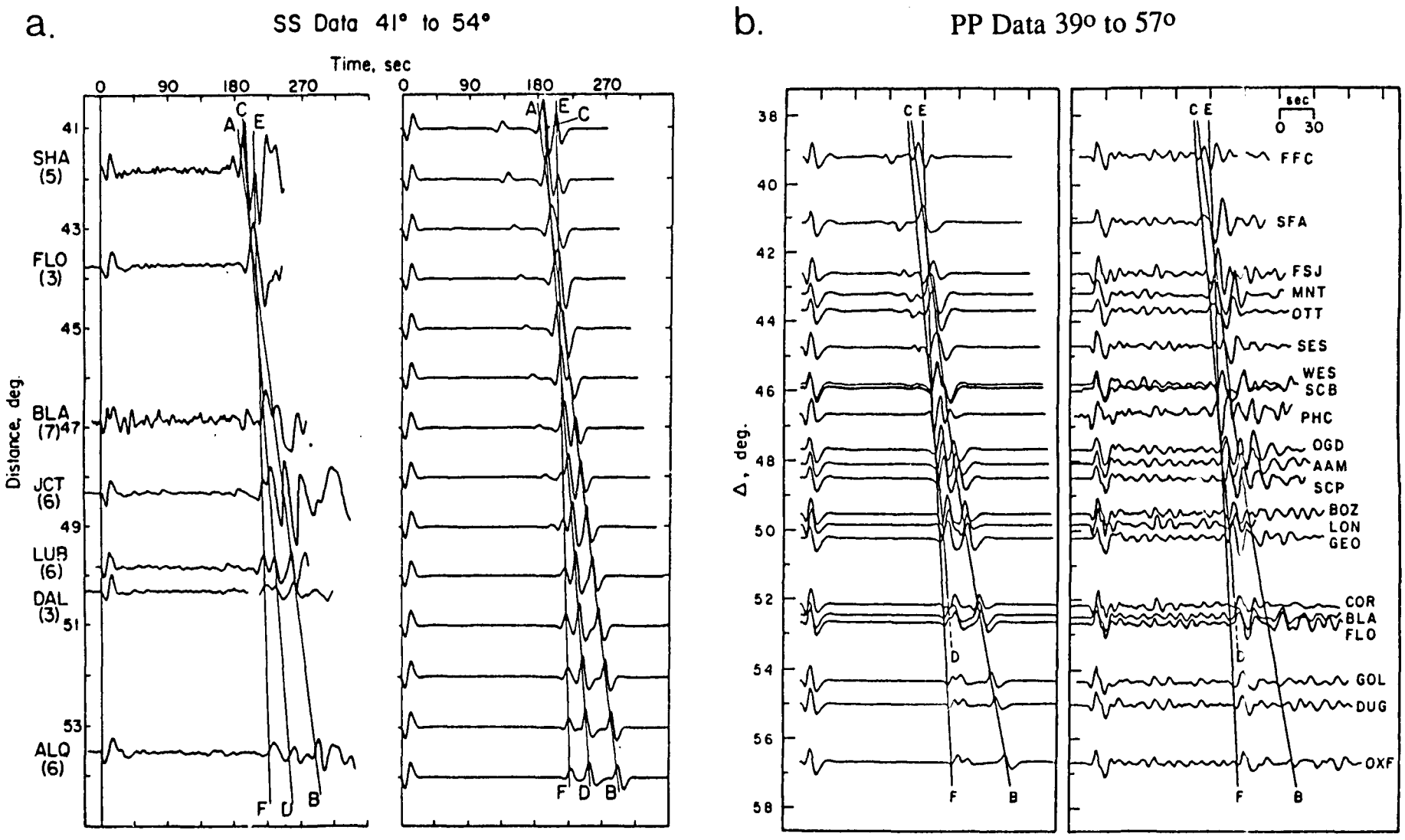


Figure 1. a) S and SS data and WKBJ synthetics from Grand and Helmberger (1984b) for paths traversing old North Atlantic ocean. b) P and PP data and WKBJ synthetics from LeFevre and Helmberger (1989) for paths traversing the Canadian Shield. While the SS data and synthetics show a strong resemblance allowing upper mantle triplicated arrivals to be identified, the comparison of PP data with synthetics is quite poor with large PP coda not satisfactorily reproduced in the synthetics.

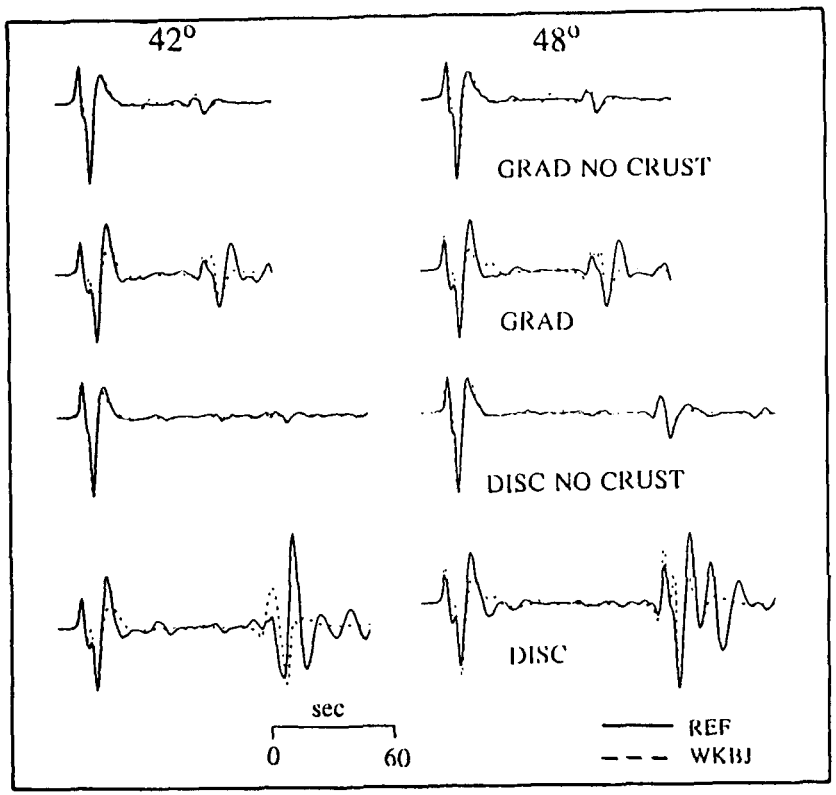


Figure 2. Comparison between synthetic reflectivity and WKBJ P and PP waveforms computed for a shallow (18km) vertical dip-slip source at distances of 42° and 48° for four upper mantle models: smoothly increasing velocities with no discontinuities and no crust (grad no crust), same model with a crust (grad), SNA-like model for P waves with two discontinuities and no crust (disc no crust), and the same model with a crust (disc). Note that both synthetics match when a crust is excluded and the degree of mismatch increases for the model that contains a crust and upper mantle discontinuities.

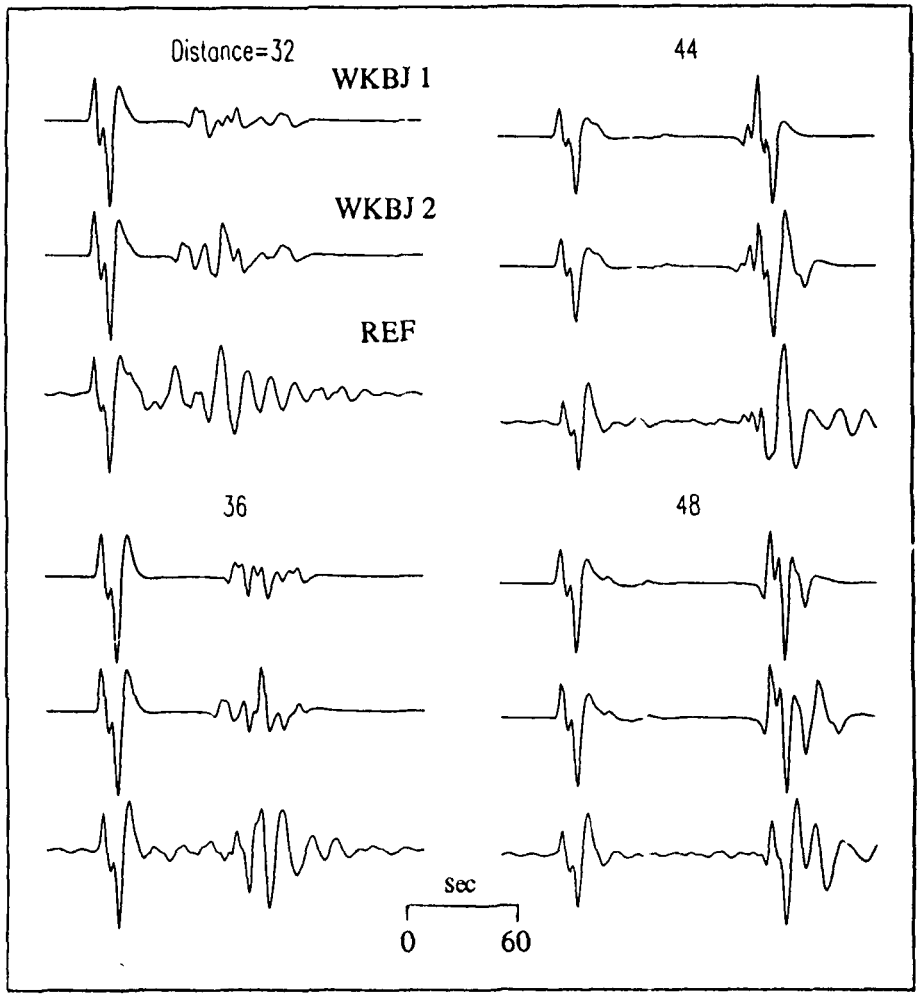


Figure 3. Comparison between synthetic reflectivity and WKBJ P and PP waveforms computed for a shallow (18 km) vertical dip-slip source and an SNA-like P wave upper mantle model with a 40 km two-layered crust. The WKBJ1 synthetics include P,pP,sP,PP,pPP and sPP. In addition to these rays, the WKBJ2 synthetics include all rays having one extra reflection or conversion from the free-surface and the Moho, and all corresponding rays having their PP reflection at the Moho rather than the free surface. Inclusion of the crustal multiples and underside Moho reflections (WKBJ2) causes the WKBJ synthetics to more closely resemble the reflectivity synthetics which include all reflections and conversions in a layered Earth.

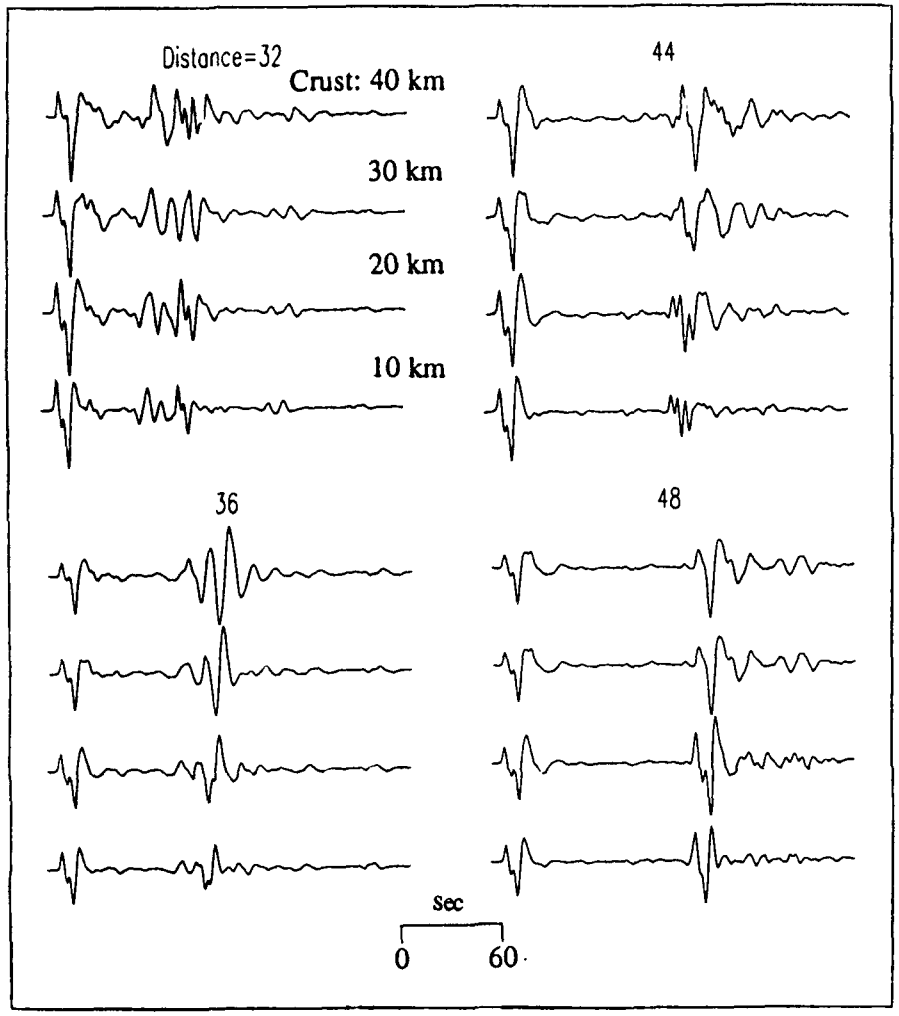


Figure 4. Comparison between reflectivity synthetics for the same source as in Figures 2 and 3 and an SNA-like upper mantle model underlying a one-layer crust of varying thickness. The large variation in the synthetics computed with different crustal thicknesses emphasizes the importance of crustal thickness in the computation of PP seismograms. Comparison between the reflectivity synthetics in Figure 3, computed with a 40 km two-layer crust, with the synthetics computed for the 40 km thick one-layer crust indicate the sensitivity of the synthetics to a one versus two-layer crust. Note that the synthetic computed with a 10 km thick crust has its source (18 km) in the high velocity mantle.

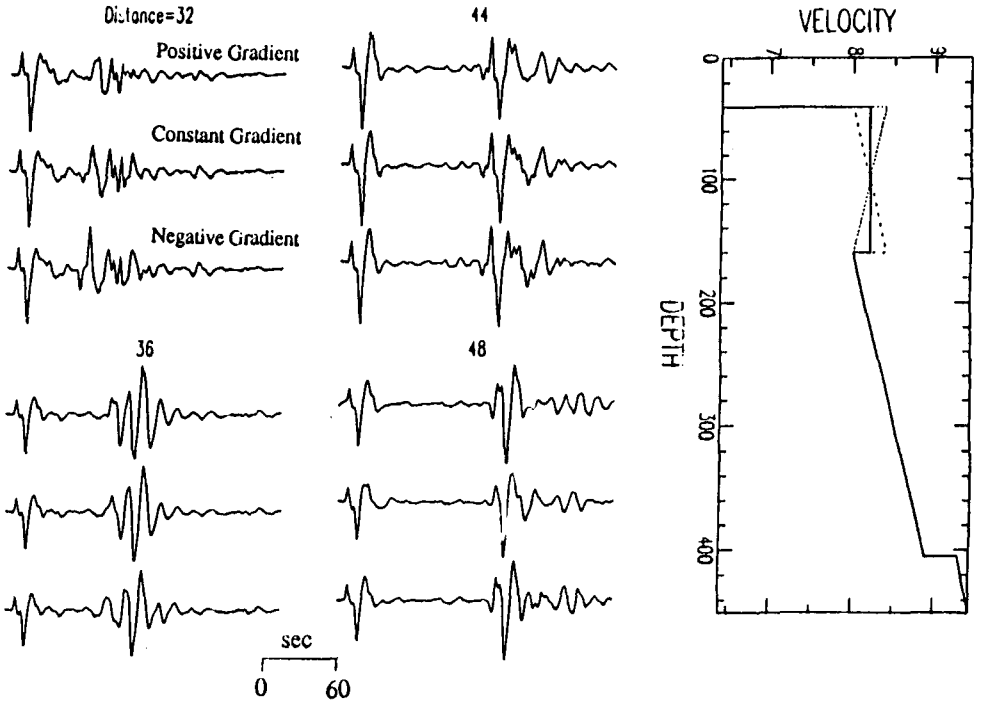


Figure 5. Comparison between reflectivity synthetics for the same source as in Figures 2,3 and 4 and three upper mantle velocity models with positive, constant and negative lid gradients as shown. Changes in the synthetics due to variations in the lid gradient are subtle, indicating that long-period PP seismograms are more sensitive to crustal thickness than lid gradient.

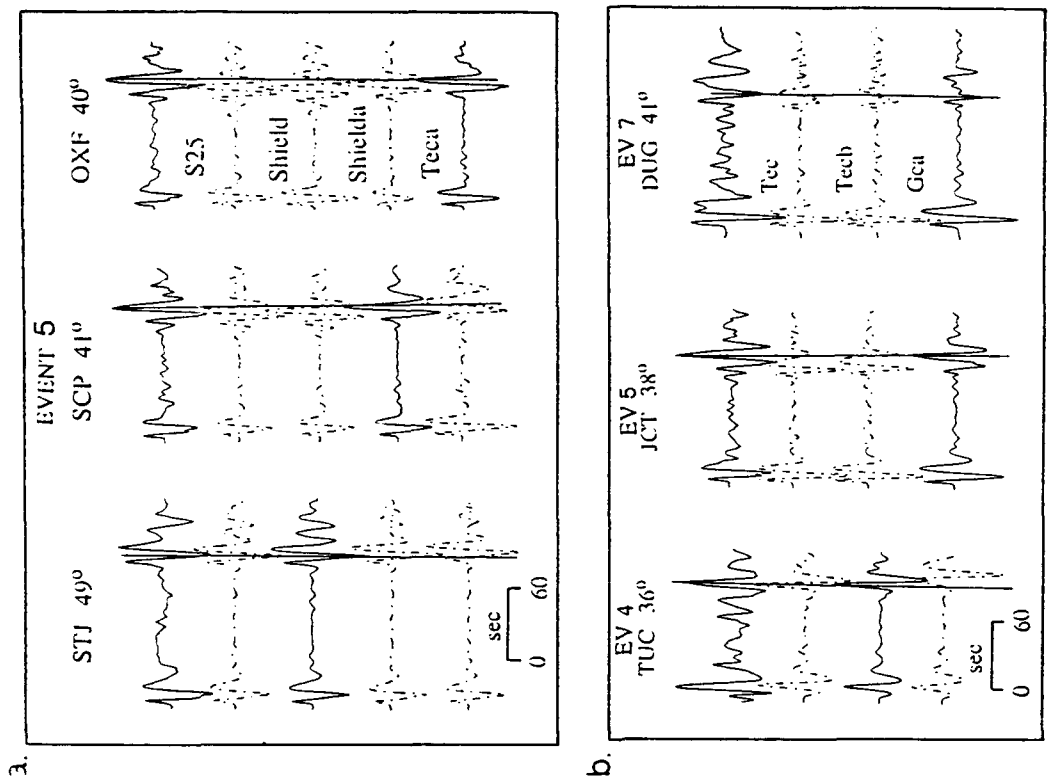


Figure 6. Comparison between long-period P and PP waveforms for paths traversing the shield and platform (a) and tectonically active regions (b) of North America (top row) and reflectivity synthetics computed for a variety of upper mantle P wave models shown in Figure 7a. The synthetic shown with the solid line best matches the observed waveform.

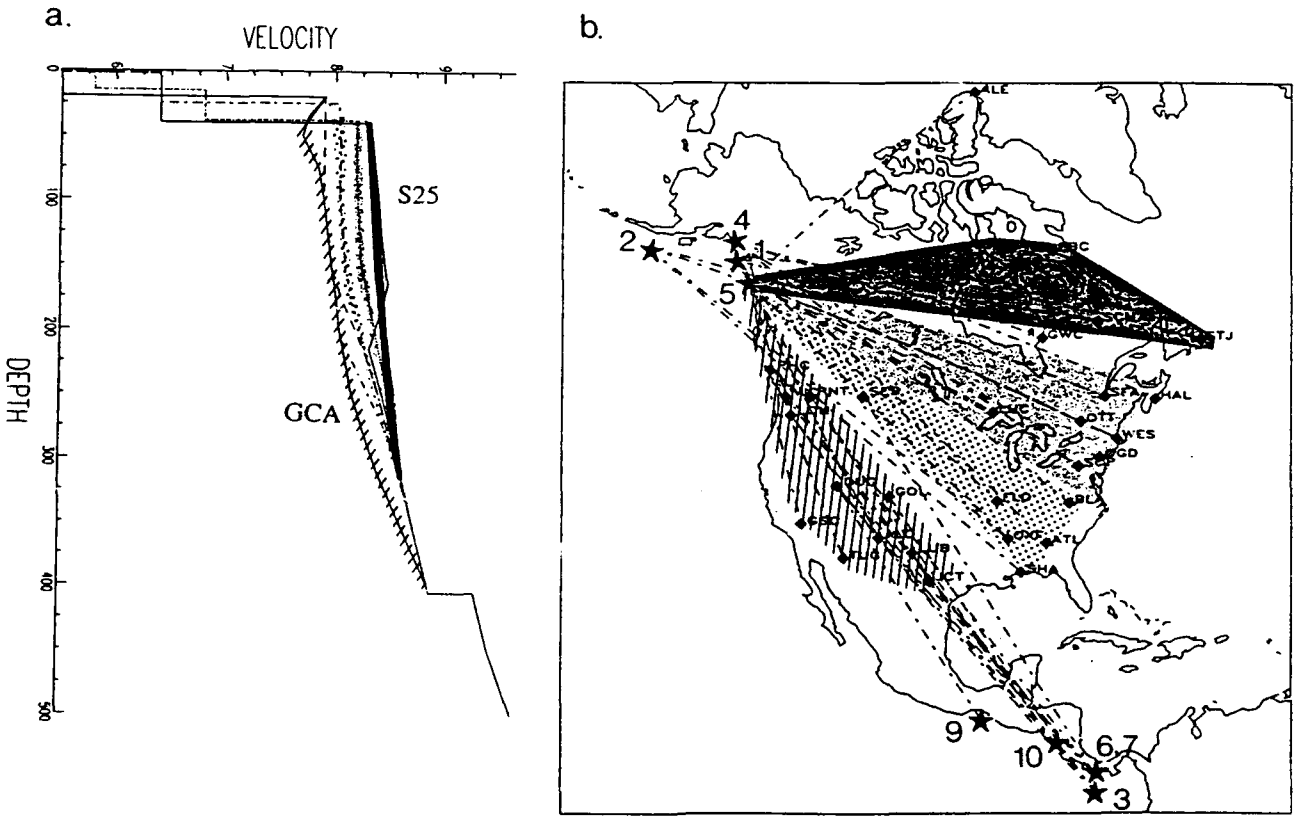


Figure 7. a) Suite of upper mantle velocity models (in order of decreasing average lid velocities: S25, Shield, Shielda, Teca, Tec, Tecb, and Gca) used to model data from North America paths (b). PP waves turning in the northern most portion of the Canadian Shield are fit by the fastest model, with slower models becoming more appropriate as the rays sample the southern shield, platform, and tectonically active portions of North America respectively.

TITLE: PHYSICAL CONSTRAINTS ON SEISMIC WAVES FROM CHEMICAL AND NUCLEAR EXPLOSIONS

AUTHORS & AFFILIATION: B. Stump, S. Reamer, K.-G. Hinzen and G. Min
Southern Methodist University
Department of Geological Sciences
Dallas, Texas 75275-0395

CONTRACT: F19628-89-K-0025

OBJECTIVE:

An experimentally based understanding of coupling of explosive energy into seismic waves is the primary goal of this research. The work is designed to give insight and place constraints on the important physical processes that control the generation of these waves. The explosive sources under study include both large chemical explosions detonated to either fracture rock or remove overburden materials and small to moderate size nuclear explosions.

Three areas have received primary focus in the last year. The first is the development of improved source models for cylindrical chemical charges typical of those used in the blasting industry. Velocity measurements from the near-source region were used to constrain the single shot seismic source model. This model was then compared to multiple source observations in order to quantify the effects of shot time variance on spectral discriminants. A second focus in the last year has been the development of nonlinear inversion schemes for seismic source parameters applied to P wave spectra from explosions. In an attempt to build more quantitative tools for estimating the seismic source function an inversion scheme is under development which is model based. The analysis of the combined free-field and free surface seismic experiments deployed on the MINERAL QUARRY and MISTY ECHO nuclear explosions is the third area of new work. These data sets are used to test the inversion scheme. The resulting source models are then used to predict regional waveforms from these explosions.

RESEARCH ACCOMPLISHED:

In order to quantify the seismic source function from multiple source engineering detonations we have completed an initial analysis of the appropriate model for a single explosion, identical to the elements of one explosive array. Unlike the sources that the nuclear explosion community is familiar with the typical charge is cylindrical in shape with a length that is

many times its width. Velocity waveforms were recovered in the near-source region for the purpose of constraining the source model (Figure 1). As an initial investigation of these sources, we attempted to calculate a modified Mueller-Murphy (1971) source model along with Green's functions appropriate for the test site. The time (Figure 1a) and frequency domain (Figure 1b) fits to the data indicate the degree of success in this exercise. In developing the equivalent source model a number of trade-offs between model parameters were identified. Elastic radius was first estimated using the scaling relations of Perret and Bass (1975) for hard rock which gave a value of 4-8 m for the 68 kg charge. Based on peak velocity decay for production shots in hard rock a modified elastic radius of 16-18 m (Ambraseys and Hendron, 1968) was estimated. This measure also coincides roughly with the length of the borehole (17.5 m). One interpretation of these results is that the elastic radius for a production shot is strongly affected by the source geometry, a conclusion supported experimentally by different scaling relationships for radius of damage from spherical and cylindrical charges (Kutter and Fairhurst, 1971). Cavity radius values were constrained by observational studies that suggest final cavity radius is 2 to 12 times greater than the original borehole radius (Chiappetta et al, 1987). After numerical testing a final cavity radius five times the initial borehole radius was chosen. The finite extent of the source was replicated by convolving the source time function with a series of Green's functions distributed over the depth extent of the source.

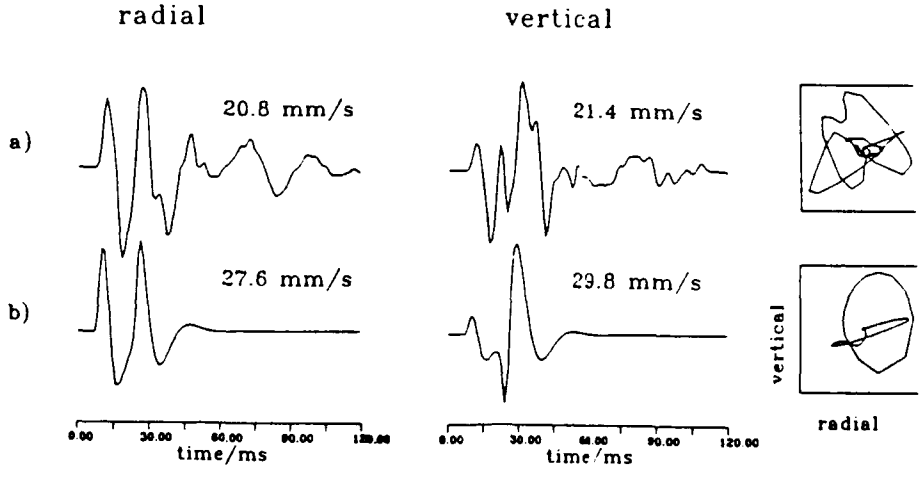


Figure 1a: Observed(a) and modeled(b) velocity waveforms from the 68 kg cylindrical charge. The cavity radius is 0.25 m while the elastic radius is 18 m.

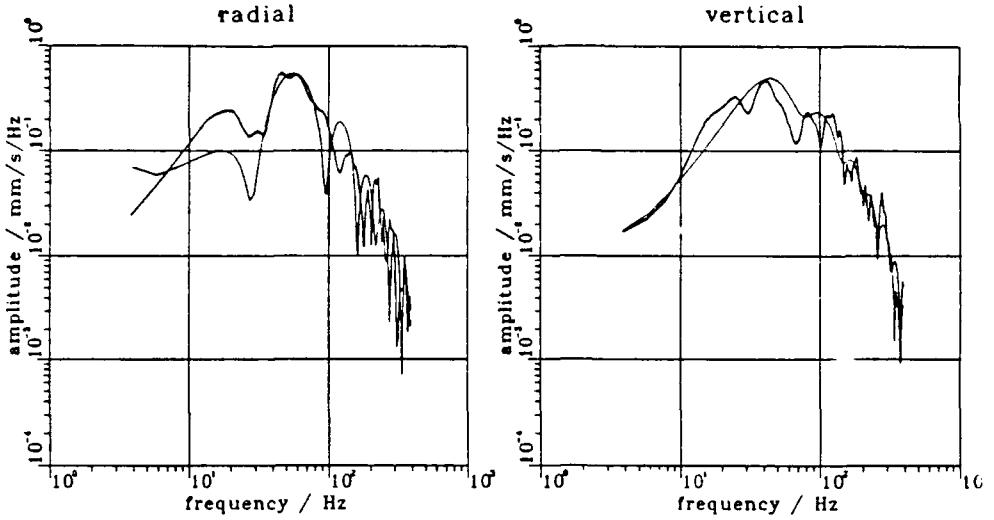


Figure 1b: Amplitude spectra of the observed (thick lines) and modeled (thin lines) single cylindrical charge velocity waveforms. Both data and synthetics have been bandpass filtered between 4.5 to 400 Hz.

This single cylindrical source model was used to create a set of synthetics for a production array of explosions which was recorded at the same test site. These model based synthetics (Figure 2c) which include separate Green's functions to each explosion in the array are compared to the observational data (Figure 2b) at one station. Also included in this figure are a set of seismograms created by simply superposing the observed single source waveform with the appropriate time delays (Figure 2a). The model based synthetics (Figure 2c) do a good job in replicating the peak amplitudes, duration, and general character of the waveforms. As time progress into the shot array (26 holes with 18/27 ms delays) there is some indication that the synthetics overestimate the observations.

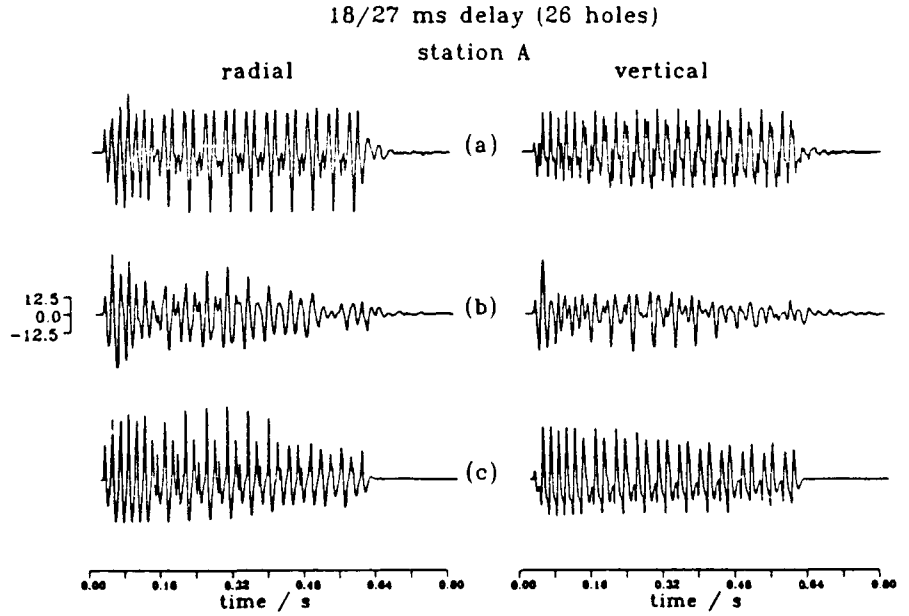


Figure 2: Superpositioning results for the radial and vertical near-source velocity waveforms. (a) Superpositioning with the *measured* single explosion waveforms; (b) Observed production seismograms; (c) Synthetic seismograms constructed with source developed from single explosion waveforms convolved with Green's functions for each source location.

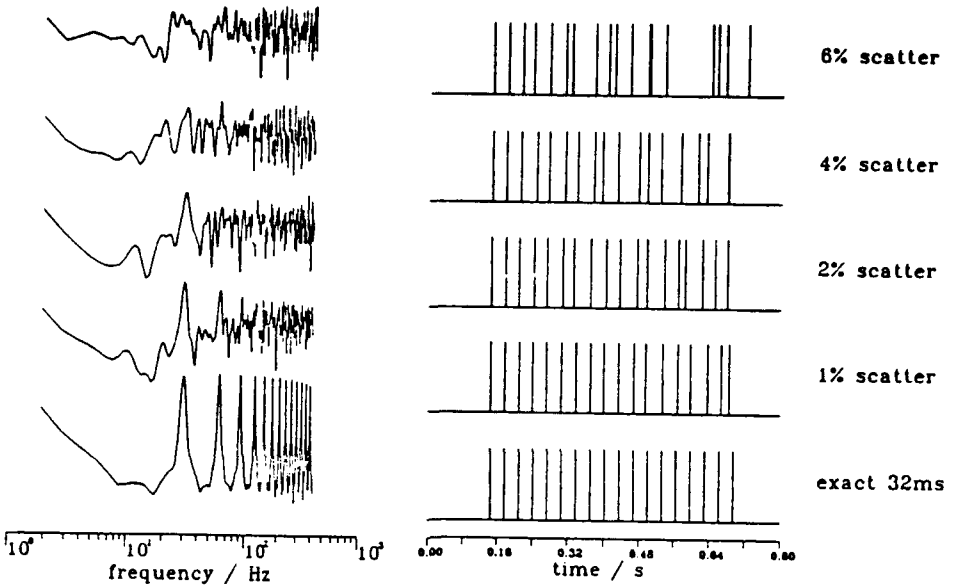


Figure 3: The effect of 18 explosions each delayed by 32 ms is shown in the frequency domain (bottom of figure). The top four spectra show the effect of shot time variances (1-6%) on the observed spectra.

Typically the detonators used in production shots have a scatter associated with their detonation time. This scatter can destroy spectral scalloping that may result from repeated explosions at a constant delay time. In order to test this effect the synthetics developed from the single cylindrical source study were used to replicate seismograms with cap scatter between 1 and 6 %, typical of that found in industry. The multiple source spectra are given in Figure 3 with comparison to the exact sequence. These synthetics illustrate how easy it is to destroy the spectral scalloping with small shot time variations.

The unique determination of explosion source parameters from near-source data generated by contained nuclear has been a second area of work in the last year. Our goal is to simultaneously determine the parameters of the source representation (long period spectral level, overshoot, corner frequency) and attenuation (Q) as well as identify interrelationships that exist between parameters. An inversion method suggested by Tarantola (1987) is used. The variance of the data across the frequency band of interest (0.1-15 Hz) changes dramatically, thus data is pre-whitened with their covariance matrix. The model covariance matrix was used to reduce condition numbers in the analysis. Two source model parameterizations were tested, one with no overshoot resulting in a simple Brune's model, and the other with variable overshoot as parameterized by von Seggern and Blandford.

The data utilized in this study were from near-source observations of underground nuclear explosions at the Nevada Test Site (NTS). One such experiment is that diagramed in Figure 4 which displays the free-field and free surface instrumentation deployed on the MINERAL QUARRY explosion at

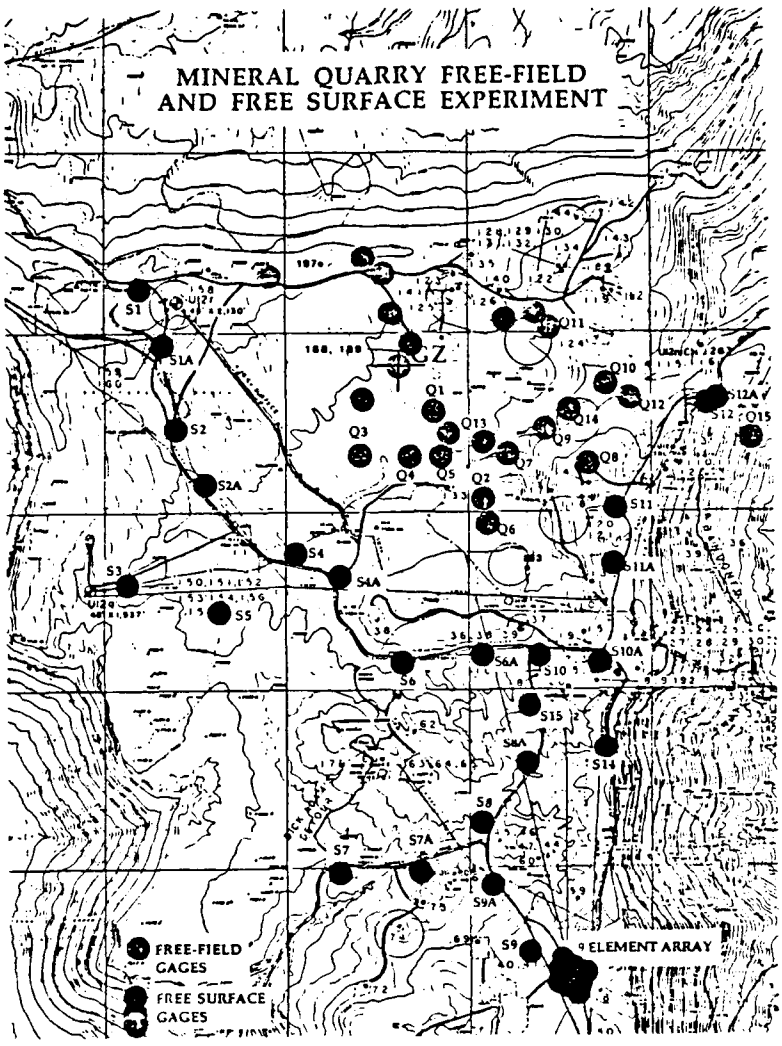


Figure 4: Free-field and free surface instrumentation deployed on the MINERAL QUARRY experiment at Rainier Mesa.

Rainier Mesa. An example of one fit to the observational data in the frequency domain is given in Figure 5a where both the raw displacement spectrum and model fit to the data is given. This analysis has been applied to a number of explosions for the purposes of making relative comparisons of source strength between several events. The long period level (LPL) from four sets of near-source data are given in Figure 5b. No correction for spherical spreading has been applied to the data as indicated by decay rates fit to each explosion in the data set ranging from $r^{-0.7}$ to $r^{-1.2}$. The relative sizes of the four events is well reflected by the static offsets between the four populations. The scatter of each individual explosion around the central decay is small with no more than a factor of 2 difference between near-by measurements. In addition to long-period level the inversions return source corner frequency, overshoot (when appropriate) and attenuation(Q). Source corner frequency is found to be stable parameter while the overshoot is not as well constrained. Q is found to increase with source-receiver distance, reflective of a shallow, high attenuation near surface layer at NTS.

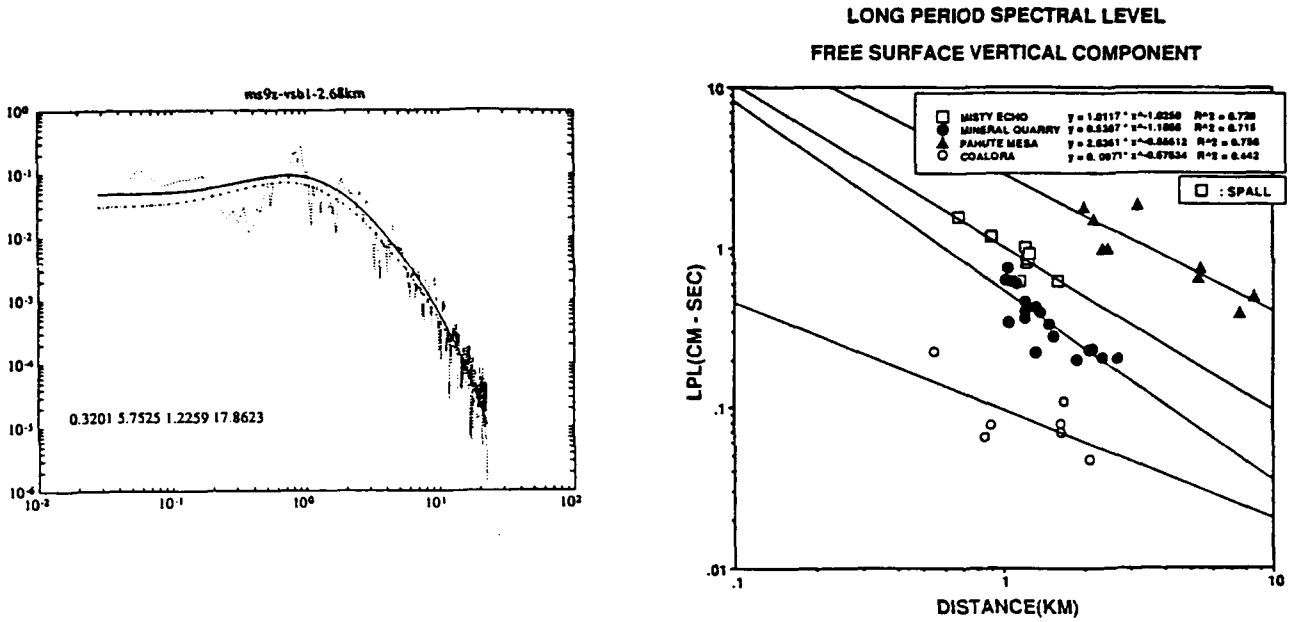


Figure 5: (a) Inversion result from one observed displacement spectra of the MINERAL QUARRY explosion (dotted line). The numbers represent the long period level, overshoot, corner frequency, and Q respectively. (b) Comparison of long period levels determined by inversion for four NTS explosions. A spatial decay (solid lines) is fit to each data set.

The combined free-field and free surface experiments such as MINERAL QUARRY (Figure 4) provide the opportunity to constrain different physical processes around the explosion such as the direct coupling of the explosion as well as the free surface interaction which is most noticeable in the spall zone directly above the explosion. An experiment similar to MINERAL QUARRY was also deployed on the MISTY ECHO explosion. Comparison of the two events indicates free-field peak velocities for MISTY ECHO which are a factor of two greater than those from MINERAL QUARRY while the spall zone peak velocities are nearly identical. The spall zone for the apparently smaller event, MINERAL QUARRY, extends to 500 m while the zone for MISTY ECHO extends to nearly 1000 m. The extent of the spall zone seems to reflect the source size difference while the peak spall zone velocities do not. Explosion and spall seismic source estimates were made from this data and used to generate regional synthetics (600-1400 km). Comparisons between the spall and explosion waveforms indicate that the explosion dominates for most phases although the spall contribution may approach some explosions contributions for the upper bound spall estimate.

CONCLUSIONS/RECOMMENDATIONS:

A modified Mueller-Murphy source function has been shown to be adaptable to cylindrical sources. The adaptation takes into account the large vertical extent of the source with a modified elastic radius and Green's functions distributed over the source extent. These synthetics are successful in reproducing production shots and indicate that shot time variances of 2-6%

can significantly destroy high frequency spectral scalloping.

A nonlinear inversion procedure for recovery of explosion source model parameters directly from near-source observations has been developed and tested. It provides a quantitative tool for comparing long period spectral excitation from explosive sources. The test data set to which the procedure has been applied indicates strong separation of different explosive events.

Future developments will include the application of the cylindrical source model to different surface mining environments. In particular we wish to explore large surface cast blasting used to expose subsurface resources. The effect of charge height and explosive type in the coupling process will also be further investigated. The source inversion work will explore trade-offs between the various model parameters used in the inversion. Attempts will be made to address questions of coupling into body and surface waves. Extension to a full moment tensor inversion is also anticipated. Much work still remains in the free-field and free surface studies. The focus in this case is anticipated to be in assessing the development of the seismic waves as the transition from nonlinear to linear processes occur. Data has been recovered from both the MISTY ECHO and MINERAL QUARRY experiments in this regime.

REFERENCES:

Ambraseys, J. R. and A. J. Hendron, 1968. Dynamic behavior of rock masses in *Rock Mechanics in Engineering Practice*, K. G. Stagg and O. C. Zienkiewicz, eds., John Wiley and Sons, London, 203-227.

Chiappetta, R. F., D. G. Borg and V. A. Sterner, 1987. *Explosives and Rock Blasting*, Atlas Powder Co., Dallas, Texas.

Koch, K. and B. Stump, 1991. Comparative study of explosion and spall source models at regional distances, *Seismological Research Letters, 62*, 17.

Kutter, H. K. and C. Fairhurst, 1971. On the fracture process in blasting, *Int. J. Rock Mech. Min. Sci., B*, 181-202.

Mueller, R. A. and J. R. Murphy, 1971. Seismic characteristics of underground nuclear detonations, I. Seismic spectral scaling, *Bull. Seism. Soc. Am., 61*, 1675-1692.

Tarantola, A., 1987. *Inverse Problem Theory; Methods for Data Fitting and Model Parameter Estimation*, Elsevier, 613p.

YIELDS OF NUCLEAR EXPLOSIONS AT AZGIR AND SHAGAN RIVER AND IMPLICATIONS FOR IDENTIFYING DECOUPLED TESTS IN SALT

by Lynn R. Sykes

Lamont-Doherty Geological Observatory, Columbia University, Palisades NY 10964

CONTRACT NO. F19628-90-K-0059

OBJECTIVES

The detonation of nuclear explosions by the Soviet Union in large underground cavities under either Low-Yield (LYTTBT) or comprehensive test ban treaties would constitute the greatest challenge to U.S. verification efforts.That evasion scenario sets the limit on how low a yield can be verified effectively. The recent OTA Report *Seismic Verification of Nuclear Testing Treaties* found that between 1 to 2 and 10 kilotons (kt) the most critical method of evasion is that of nuclear testing in large cavities in salt domes. It concluded that no method of evading a monitoring network is credible above 10 kt and that several evasion scenarios, including testing in cavities in bedded salt and in hard rocks, are possible below 1 to 2 kt.

Our work address a number of aspects of the problem of clandestine nuclear testing in large cavities in salt domes, bedded salt and hard rock--what types of evasions scenarios are plausable based on geological and engineering constraints, which ones are likely to escape detection by the U.S. and which ones are likely to be identified. Particular attention is given to the Soviet Union and to the critical yield regime from 1 to 10 kt, where scientific research over the next few years seems most likely to have a major impact on the verifiability of a LYTTBT. Several important aspects of decoupling have received little study for more than 20 years. Since then a great deal of experience has been obtained by the U.S. and several European countries on the rheological properties of salt in conjunction with research on radioactive waste disposal and by industry on the construction and stability of large cavities salt. Experience is also available from the construction of large cavities in salt domes to house the U.S. Strategic Petroleum Reserve and from the U.S.S.R. on cavities in salt for gas storage.

Our major research objectives during the first year are:

1) Derive revised m_b values for Soviet underground nuclear explosions in salt and for small explosions at the main Soviet test sites; determine improved magnitude-yield relationships, especially for explosions of small yield;

2) Study numbers, magnitudes and spectral character of small earthquakes and large chemical explosions in and near areas of thick salt deposits in the U.S.S.R.;

3) Evaluate and synthesize data from engineering, rock mechanics and geological sources on the properties of salt, stability of large underground cavities in salt, and the use of cavities in salt for possible clandestine nuclear testing, especially in the yield range 1 to 10 kt;

4) Start work on maps of the U.S.S.R. showing locations suitable for possible decoupled testing of explosions of various yields. Identify areas that have known salt deposits, those that are not known to but conceivably could be such sites, and areas that do not and cannot contain salt deposits of any appreciable thickness (such as old cratonic regions and young volcanic areas).

RESEARCH ACCOMPLISHED

Bodywave magnitudes. m_b values have been recomputed using station corrections for all known Soviet underground nuclear explosions at Shagan River and Azgir for which data are available from the ISC and USGS. Station corrections for Shagan River events were derived for 9 large explosions and applied to all undergroud events for which data were available from the above two sources for that testing area (Sykes and Cifuentes, 1984; Sykes and Davis, 1987; Sykes and Ruggi, 1989; Sykes and Ekstrom, 1989). A major object in our work has been to reduce the standard error of the mean for m_b to values as small as 0.015 to 0.03 by using large numbers of stations (80 to 100 for larger events) and by applying station corrections. Similarly, station corrections were derived for large underground explosions at Azgir, where the testing medium is salt, and applied to other events at Azgir, including the PNE explosions of 1966 and 1968 for which the Soviet Union long ago announed yields of 1.1 and 25 kt respectively.

Small Azgir Explosions. In a special study made for the Azgir explosion of 1.1 kt of 1966, m_b was measured at 16 stations for which unclassified seismograms were available, giving $m_b = 4.52 \pm .06$. Although small in amplitude, P waves could be readily identified at many of the better WWSSN stations of higher gain and good signal-to-noise ratio. The ability to detect such a small event 25 years ago using analog records from simple (non-array) stations reflects the high coupling of a tamped explosion in salt and efficent propagation (high Q) for P waves. A similar study for the 1968 Azgir event gave $m_b = 5.53 \pm .03$.

Magnitude-Yield Curves. The m_b values for explosions of announced yield, Y, in various parts of the world in either hard rock or below the water table were normalized to the SW part of the Shagan River testing area and to Azgir using previously published values of t* and m_b bias. An aim here has been to use as few Soviet announced yields as possible so as to permit the yields of Bocharov et al. (1989) and other recent yields turned over by the U.S.S.R to the U.S. to be verified. The resulting m_b-yield regression (Fig. 1) for the SW part of the Shagan River area, $m_b = 4.48 + 0.79 \log Y$, which includes yields published by Bocharov et al. (1989) for Shagan River, differs very little from a regression that does not include those data but does include the Azgir PNE explosions of 1966 (1.1 kt) and 1968 (25 kt). A similar relationship, $m_b = 4.46 + 0.79 \log Y$, was obtained for Azgir.

Subdivision of Shagan Testing Area for Yield Determination. Magnitudes determined from Lg at NORSAR, m(Lg), and our recalculated values of m_b are now available for large numbers of events at Shagan River. We compare those values for individual explosions, combine data from bodywaves and Lg for yield determination and compare the 95% confidence limits for the average yield estimates.

Fig. 2 shows that the difference between m(Lg) and m_b varies spatially from low values in the southwest (SW) to high values in the northeastern part of the Shagan testing area, much like that found previously by Ringdahl and Marshall (1989). Using m(Lg) as a standard, the Shagan River test site is divided into three subareas. A new magnitude m_b' is defined equal to m_b for the SW area, $m_b + 0.145$ for the NE and $m_b + 0.067$ for the transitional zone between them. Much less scatter is evident for the subregions and for the entire Shagan River area (Figs. 3 and 4) when m(Lg) is compared with m_b'.

Yields for Shagan River obtained from Lg and bodywaves. A new magnitude, $m_b(Lg) = 1.090\ m(Lg) - 0.440$, is defined from the regression shown in Fig. 4 so that yields can

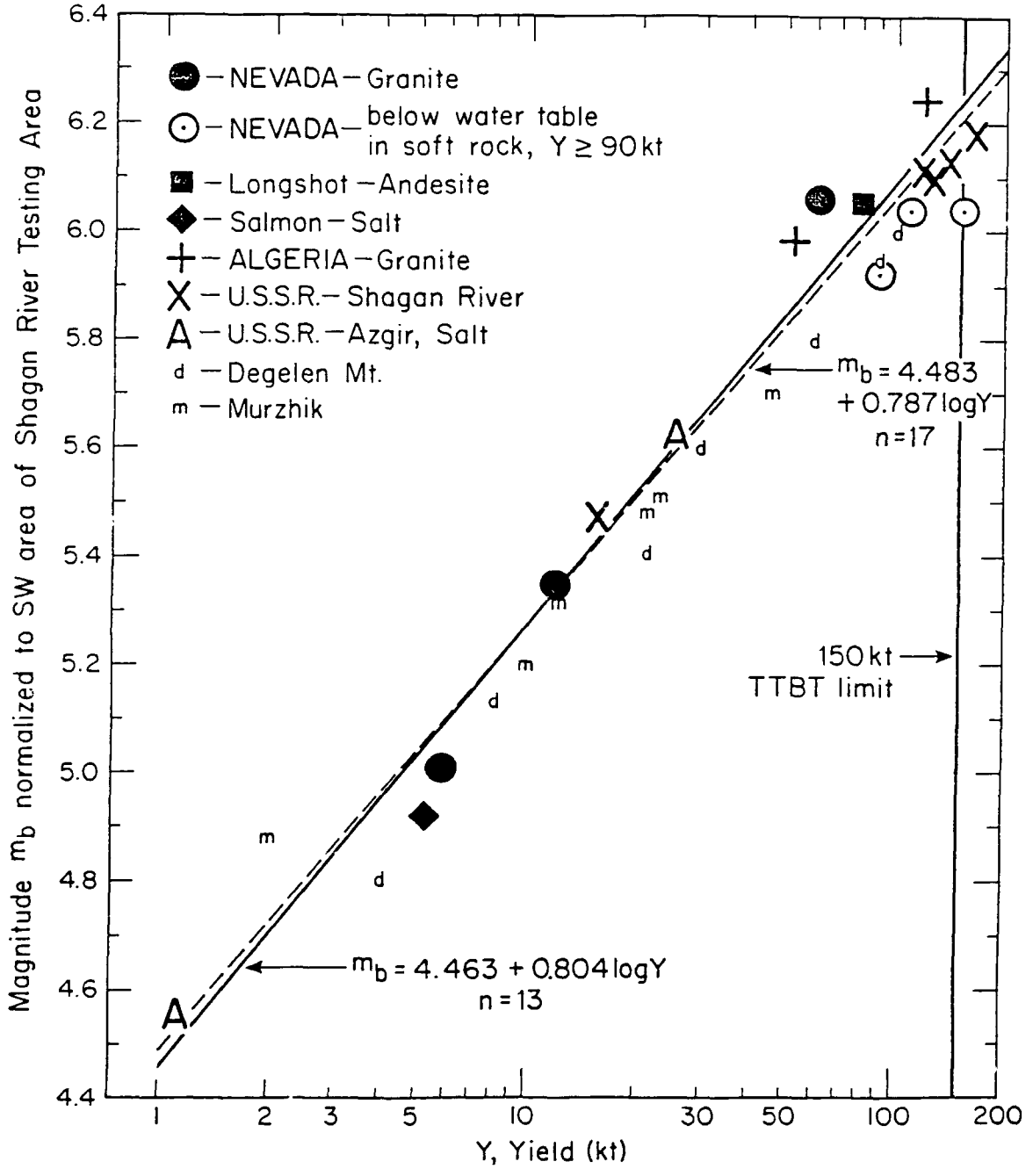


Fig. 1 Calibration curves used for yield estimation as normalized to southwestern portion of Shagan River testing area. Explosions at Degelen and Murzhik were not used in two regressions. Explosions used are those of published yield in either hard rock or below water table.

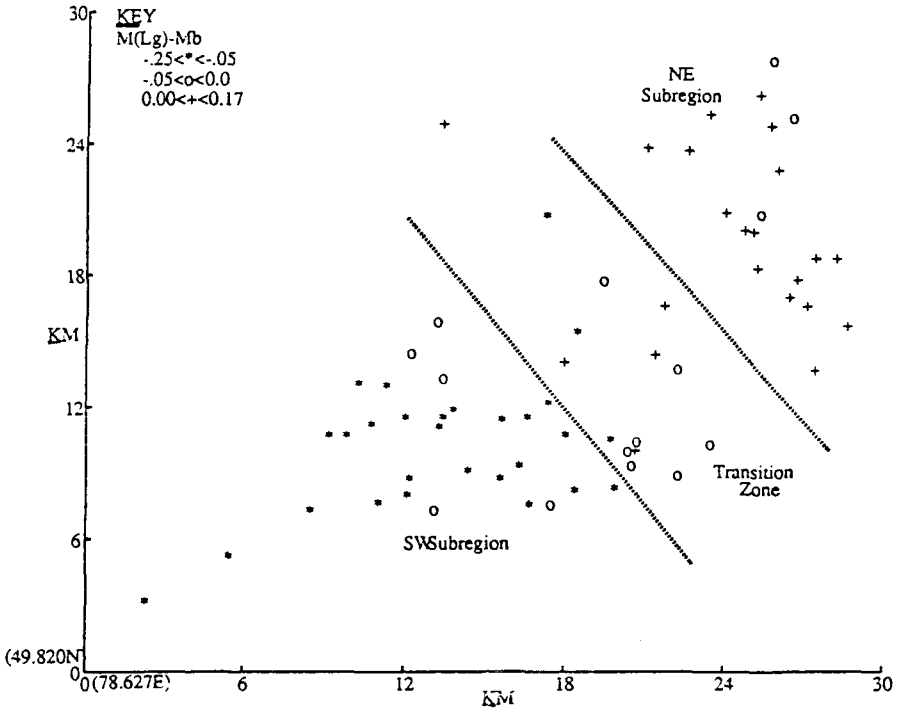


Fig. 2 L_g magnitude minus body wave magnitude as a function of location within Shagan River testing area. Testing area is divided into three parts for better estimates of yield from body waves.

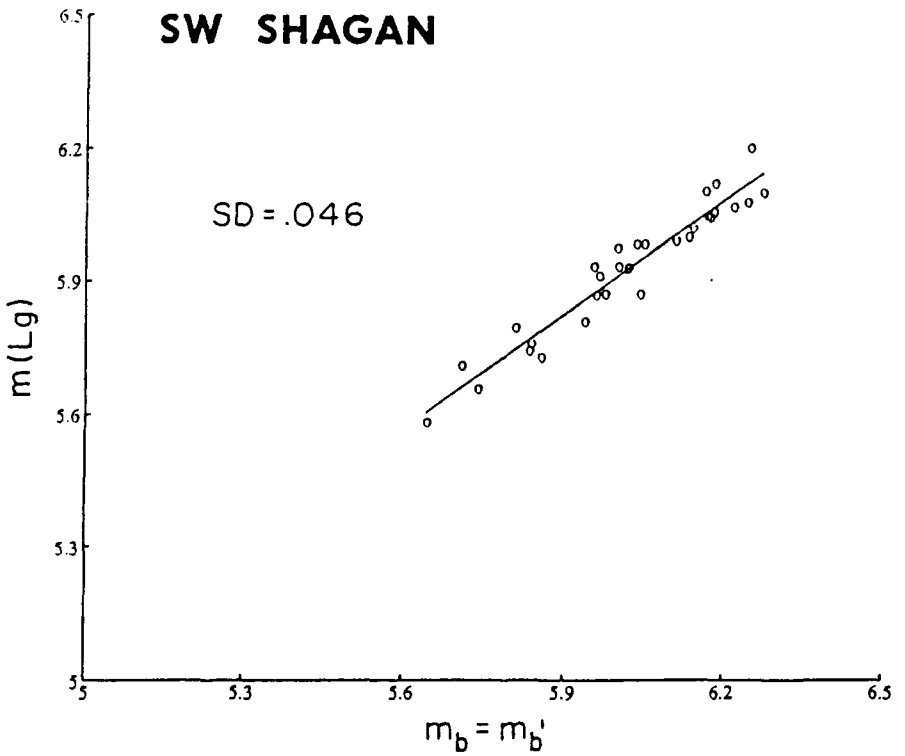


Fig. 3 L_g magnitude as a function of body wave magnitude for southwestern portion of Shagan River testing area. SD = standard deviation.

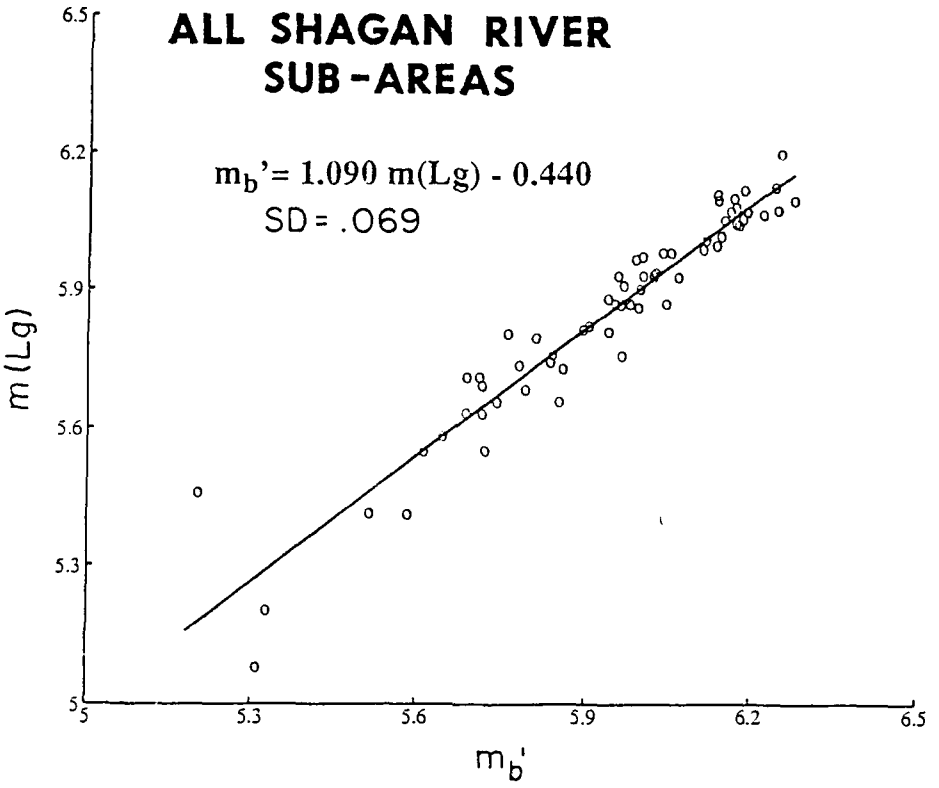


Fig. 4 L_g magnitude as a function of revised body wave magnitude, m_b'. SD = standard deviation.

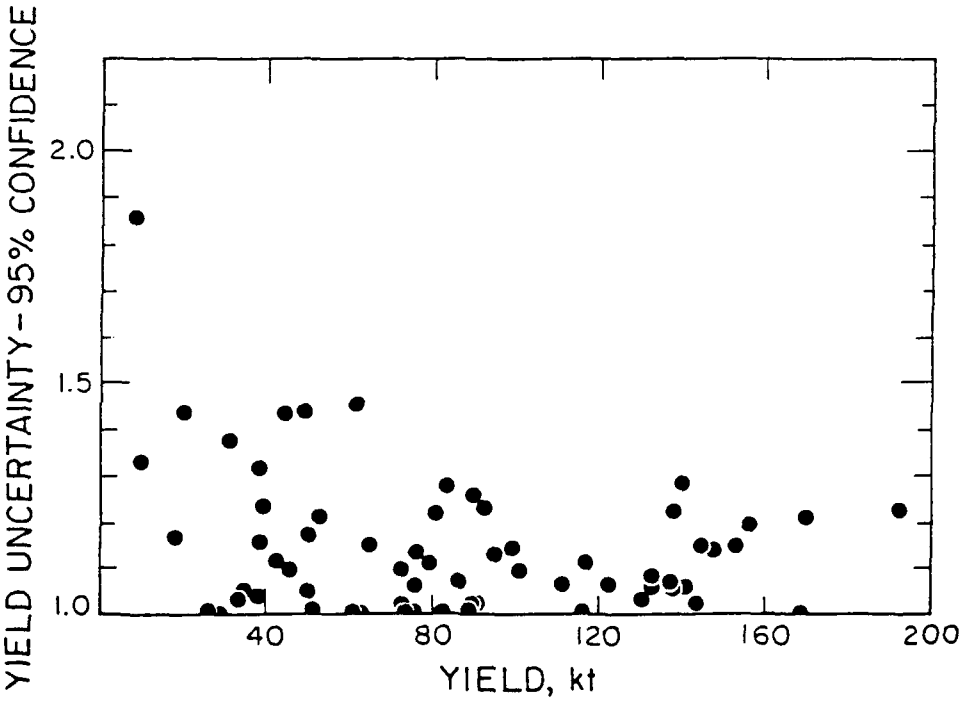


Fig. 5 95% confidence limits on average yield determined from body waves and L_g for Shagan River explosions as a function of calculated yield.

be calculated from m(Lg) using the expression $m_b' = m_b = 4.48 + 0.79 \log Y$, which was derived for SW Shagan (Fig. 1). Yields calculated from m_b' and from $m_b(Lg)$ are much more consistent for the same explosion; each agrees closely with the yields published by Bocharov et al. (1989) for large explosions in 1971 and 1972 in the NE and SW parts of the testing area whereas the yield estimated from m_b alone for the event in the NE area agrees less well and is smaller. The use of $m_b(Lg) = 4.48 + 0.79 \log Y$ permits Lg observations to be used for yield determination using the much larger collection of m_b values that are available for explosions of announced yield on a worldwide basis. Its use also avoids using mainly unverified Soviet yields when calculating yield directly from observations of Lg. Nevertheless, the yields of Bocharov et al. agree closely with those calculated from the regression in Fig. 1 that does not include those data or any other recently released Soviet data. Thus, the published of yields Bocharov et al. for Shagan River must be equal to or close to the actual yields.

Yields calculated by averaging values of log Y obtained from Lg and body waves for 66 Shagan River explosions have a precision at 95% confidence (R value) of a factor of 1.0 to 1.45 (mean value of 1.14) for $Y \geq 10$ kt (Fig. 5). The use of two precise methods of yield estimation permits an assessment to be made of the yields of the three largest underground explosions at Shagan River prior to the Threshold Treaty (TTBT) of 1974 and of the likely missile systems for which those weapons represent testing at full or nealy full yield (Tables 1 and 2). The explosion of 23 July 1973 of Y = 193 kt (R = 1.22) is clearly the largest underground explosion at Shagan River.

The newly calculated yields provide strong evidence of clustering in the distribution of yields of Soviet tests at Shagan River from the start of the TTBT in 1976 to mid 1988 (Fig. 6).

CONCLUSIONS AND RECOMMENDATIONS

Implications for Small Explosions in Salt. For purposes of appreciating the detection capability of a given seismic network, it is important to recognize, using data from Azgir, that a fully-coupled explosion of 1 kt in salt in high-Q areas of the U.S.S.R. has an m_b of 4.46; fully decoupled events of 1 and 10 kt have m_b's of 2.61 and 3.40 respectively (assuming a decoupling factor of 70). These magnitudes are higher than has generally been thought previously. For example, chemical explosions of $m_b \leq 2.6$ in high Q areas need not be considered in monitoring a 1 kt threshold treaty. Most areas of thick salt deposits in the U.S.S.R. are typified by high Q (efficient transmission) for P waves and low natural seismic activity.

Precise Yield Estimates. Yield determinations for Shagan River explosions can be improved by subdividing that testing area into three parts with different m_b-yield relationships and by combining those results with yields calculated from Lg. The calculated yields of many of those explosions since 1976 are clustered in a few specific ranges of yield.

References

Bocharov, V.S., S.A. Zelentsov and V.I. Mikhailov, Atomic Energy, 67 210-214, 1989.

Ringdal, F. and P.D. Marshall, Norsar Semiannual Tech. Summary, pp. 36-67, July 1989.

Sykes, L.R. and I.L. Cifuentes, Proc. Natl. Acad. Sci. USA, 81, 1922-1925, 1984.

Sykes, L.R. and D.M. Davis , Sci. Amer., 256, 29-37, Jan. 1987.

Sykes, L.R. and G. Ekstrom, Proc. Natl. Acad. Sci. USA, 86, 3456-3460, 1989.

Sykes, L.R. and S. Ruggi, Nuclear Weapons Databook, IV, 332-382, Ballanger, New York, 1989.

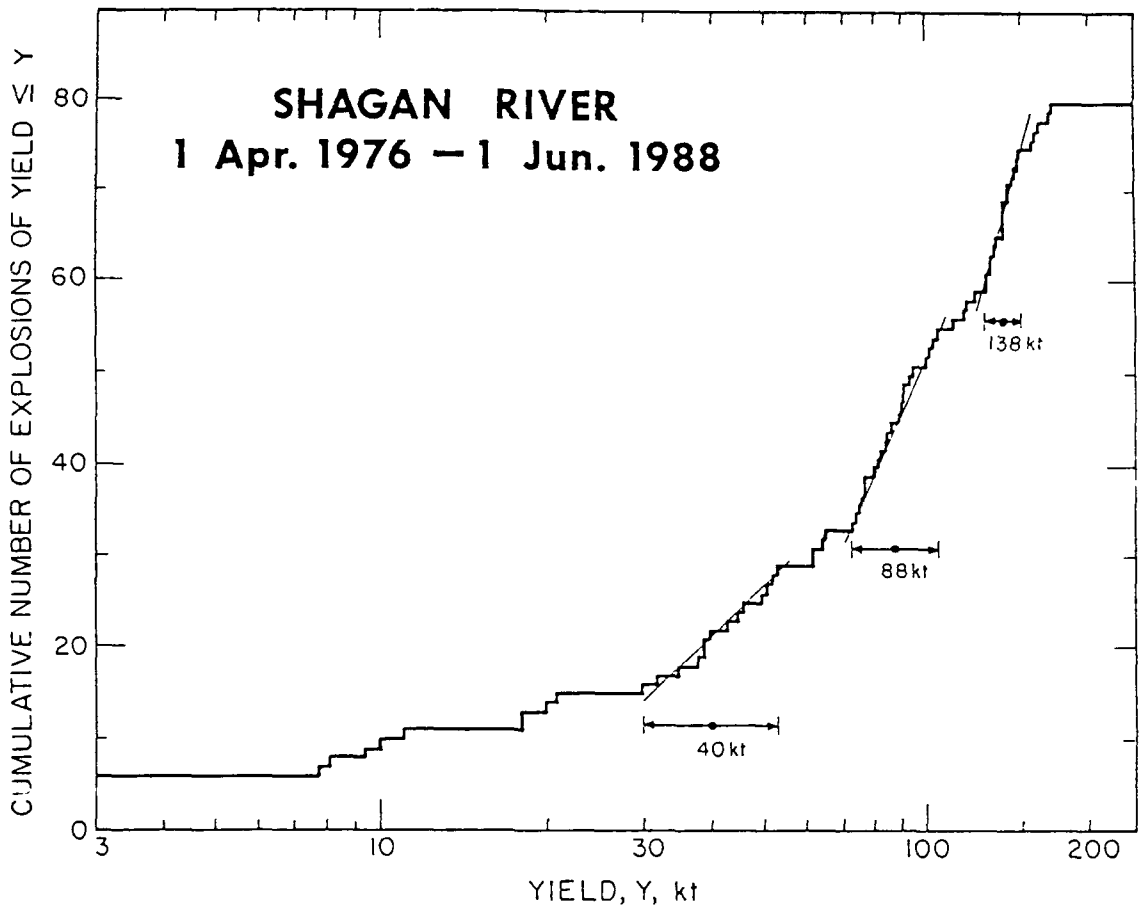


Fig. 6 Cumulative number of all known underground nuclear explosions at Shagan River for time period indicated of calculated yield ≤ Y. Explosions tend to be clustered at a few specific ranges of yields as indicated by the thin lines of steeper slope.

Table 1: Largest Shagan River Underground Explosions prior toJune 1979 of Yield > 125 kt

Date	Yield (kt)	
	Announced	Calculated
02 Nov. 1972	165	154
10 Dec. 1972 II	140	138
23 July 1973	--	193

Table 2: Major Soviet Missile Systems with Throw-weights Appropriate to above Yields

System	First Deployment	#RVs	Comments
SS-20	1977	3	First Soviet MIRVed IRBM
SS-N-18 mod 1	1978	3	First Soviet MIRVed SLBM

TELESEISMIC AND REGIONAL SEISMIC EVENT LOCATION: CONSTRAINTS FROM MASTER EVENTS, SATELLITE IMAGES, AND SYNTHETIC SEISMOGRAMS

Clifford H. Thurber and Howard R. Quin
University of Wisconsin-Madison

Contract #F19628-90-K-0047

OBJECTIVES:

Data from the IRIS Global Seismic Network stations in the Soviet Union and the former NRDC-Soviet Academy of Sciences regional seismic network in Kazakhstan, USSR, present unique opportunities to investigate event location, crustal structure, and wave propagation in the Soviet Union, especially in the area of the Kazakhstan nuclear test site (KTS). We are carrying out a program of detailed analysis of body-wave data from regional events recorded by these stations, in conjunction with other regional and teleseismic network data, with the primary goal of improving event location capability at near-regional, far-regional, and teleseismic distances. The data from events within the Soviet Union are being used in the investigation of the following problems related to regional and teleseismic event location: 1) use of "master event" locations to improve teleseismic and regional location accuracy and precision; 2) observability of regional secondary phase arrivals, from both empirical and theoretical analyses, and their utility for event location. Data from recent Soviet nuclear tests and information released recently on numerous historical Soviet nuclear tests will be of critical value in addressing task 1. Satellite images of KTS and the surrounding area are essential for providing direct information on the absolute locations of events. Improved models for seismic velocity structure are being sought in conjunction with the above tasks.

RESEARCH ACCOMPLISHED:

Event location has traditionally relied on P wave first arrivals at a number of stations. However, in the case of a sparse regional station network (3 stations or less), event location must be done by examining either seismogram polarization, apparent wave azimuth, or timing of secondary arrivals. Thurber et al. [1989] and Li & Thurber [1991] have recently examined the potential for event location using a combination of first arrivals, some secondary arrivals, and arrival azimuths They have determined that epicenters can often be determined to an accuracy of within about 10 kilometers using a combination of these data. An examination of the regional data indicates that additional secondary phases can be picked with considerable accuracy. We therefore have undertaken a study to determine whether or not multiple secondary phases can be accurately picked and epicentral locations determined for a network of three stations or less using a combination of polarization analysis and secondary phase arrival times.

We seek to study the phases Pg, Pn and PmP recorded by the network of three NRDC stations in the Kazakhstan region of the Soviet Union which operated in the years 1987 to 1988 and by the regional IRIS network in the Soviet Union in the years 1989 to 1990. The NRDC network produced high quality, broadband, multiple-station recordings of more than two dozen explosions in the epicentral range 0 to 400 km. In particular, a number of secondary phases arriving between 1 and 4 seconds after the initial P arrival have been observed at the NRDC stations which we believe can be identified as the phases PmP and either Pg or Pn, depending on the epicentral distance. The three IRIS stations in the Soviet Union have produced good quality broadband data for events with epicentral distances between about 900 and 1500 km. We hope to show that secondary phase arrivals can be made on data from these stations as well, with the belief that they can be identified as head waves or wide angle reflections off of various crust or mantle boundaries.

A detailed examination of the waveforms at the NRDC stations indicates a primary crustal arrival (Pg) is usually followed by another distinct secondary arrival at an interval of about 1 to 2 seconds in the regions between 0 and 200 km, and beyond 250 km the primary mantle Pn wave is usually followed by one or two distinct secondary arrivals. A preliminary travel time computation indicates that the secondary arrivals in the 0 to 200 range are primarily the phases PmP and pre-crossover Pn, while in the 250 to 300 km range they are the phases Pg and PmP.

To model the phases observed at the NRDC stations under about 300 km, we utilize a reflectivity synthetic seismogram code described by Mallick and Frazer [1987] which computes complete synthetic seismograms in multi-layered media. This code was written for computing high frequency (up to 10 Hz.) synthetic seismograms over regional distances (0 to 1000 km.) and in particular, near-field P wave arrivals using a large number of layers. This code has been used successfully for a number of different applications, including modeling near source reflection seismograms in the distance range 0 to 100 km and modeling high frequency regional arrivals at distances of up to 1400 km [Mallick and Frazer, 1987]. This code, while relatively simple to use, is extremely C.P.U. intensive, requiring nearly a day of C.P.U. time on a SPARCstation to compute a 512 sample synthetic seismogram at 10 samples/second at 150 km distance for a fifteen layer crustal model. Consequently, we have tried carefully to do as much research in the literature and as much preliminary travel time modeling using computation of regional arrival times before launching into extensive reflectivity calculations. We can calculate a complete set of seismograms for a crustal model for all stations in about a week, which means that over the course of our study we should be able to examine thoroughly between 10 and 15 crustal models. Thus we expect to be able to determine a crustal model which successfully fits a large number of the observations.

Two examples of comparisons between observed seismograms and reflectivity synthetics are shown in Figures 1 and 2. The estimated epicentral distances are 104.6 and 156.5 km from station BAY, based on the results of Thurber et al. [1989]. The vertical bars indicate identifiable phases (Pg and PmP) in both data and synthetics. Absolute travel times and relative amplitudes match surprisingly well for this preliminary modeling effort.

A number of authors have already begun the examination of regional explosion data sets for crust and upper mantle structure using reflectivity and generalized ray calculations. Their work has shown that the crust in this region has a laterally varying structure with the crust-mantle boundary at about 50 km. Leith proposed a crustal structure which is about 50 km thick and has about 5 crustal layers. Starting with an upper crustal layer of about 5 km/sec, his model velocity increases with depth to about 6.95 km/sec, with an upper mantle layer of 8.2 km/sec. Recently, in a study of regional arrivals at station ARU, Goldstein et al. [1991] determined that the upper mantle has a low velocity zone in the depth range 150 to 200 km which is responsible for secondary arrivals at far regional distances (1000 to 1400 km). We will therefore be investigating two sources of secondary arrivals: crustal and upper mantle reflections and refractions in the region between 0 and 300 km depth and an upper mantle low velocity zone for arrivals in the far-regional range (1000 to 1500 km).

To examine the phase arrivals in the far regional case we utilize the generalized ray method as described by Gilbert and Helmberger [1972]. At present we can compute synthetic seismograms for a four layered model using generalized rays. This allows us to model average crustal velocity, an average upper mantle velocity, a low velocity upper mantle layer and a high velocity lower mantle. This simplified model enables us to model the essential features of a number of observed phases and to examine secondary phase arrivals from the lower velocity mantle at the level of complexity exhibited by the waveforms. At present, we have been able to generate synthetic seismograms at far regional distances using this code; however, we have not yet had good success in matching individual waveforms. Experimentation with different crustal models will be needed in order to better match the data.

Our initial work on teleseismic location capability has involved a careful study of previous work combined with preliminary relocation efforts of our own. In Figure 3, we show a comparison of the teleseismic joint relocation (JHD) results for Shagan River of Marshall et al. [1984] (triangles) with those of Lilwall & Farthing [1990] (squares), using the sequence numbers of Marshall et al. [1984] to identify the events. The former study used the 1965 crater event only as a master event, while the latter used the absolute locations of 7 shots reported by Bocharov et al. [1989]. The agreement is quite good except for a small number of events, one of which (07) is from the Bocharov et al. [1989] list. In some areas the locations are adequately constrained and the spacing of events is sufficient that we can uniquely associate individual shots with shot points visible in SPOT satellite images.

We have obtained SPOT satellite images of the Shagan river test site made at various times in the years 1986 to 1989. These photographs clearly show the location of craters from explosions in the Shagan region occurring in the time between successive images. The latitude and longitude of points on these images have been computed by bilinear interpolation of points on the image from a set of well located ground control points consisting of known explosion locations, road junctions, and river crossings. With this image rectification complete, we can accurately determine the location of shot holes to within about 5 seconds of arc. An example image is shown in Figure 4 that includes shot points identified via both time-sequence satellite imagery and teleseismic JHD. We expect that, by combining both seismic and satellite image methods, we can obtain extremely accurate estimates of explosion locations for test ban verification and other seismological purposes.

CONCLUSIONS AND RECOMMENDATIONS:

Our progress in both seismogram synthesis and teleseismic location/satellite image analysis clearly indicates the excellent potential for resolving basic questions regarding crustal structure and P wave propagation in the Kazakhstan region and for determining absolute locations for all or nearly all sizable nuclear explosions at Shagan River. The seismogram synthetics work will provide the firm basis for event location using multiple secondary P arrivals at near-regional distances. Work should be continued to extend this capability to far-regional distances. Once complete, our list of absolute locations for Shagan River nuclear explosions will be beneficial to a number of important investigations, such as reciprocal array analysis of wave propagation [Goldstein et al., 1991].

REFERENCES:

Bocharov, V. S., S. A. Zelentsov, and V. N. Mikhailov, Characteristics of 96 underground nuclear explosions at the Semipalatinsk test site, Atomnaya Energiya, 67, 1989.

Goldstein, P., W. R. Walter, and G. Zandt, Upper mantle structure beneath the Soviet platform using a source array of nuclear explosions, submitted to J. Geophys. Res., 1991.

Gilbert, F., and D. V. Helmberger, Generalized ray theory for a layered sphere, Geophys. J. Roy. Astr. Soc., 27, 57-80, 1972.

Li, Y., and C. H. Thurber, Hypocenter constraint with regional seismic data: A theoretical analysis for the NRDC network in Kazakhstan, USSR, J. Geophys. Res., 96, 10159-76, 1991.

Lilwall, R. C., and J. Farthing, Joint epicentre determination of Soviet underground nuclear explosions 1973-89 at the Semipalatinsk test site, Atomic Weapons Research Establishment Rept. O 12/90, 1990.

Mallick, S., and L. N. Frazer, Practical aspects of reflectivity modeling, Geophysics, 52, 1355-64, 1987.

Marshall, P. D., T. C. Bache, and R. C. Lilwall, Body wave magnitudes and locations of Soviet underground explosions at the Semipalatinsk test site, Atomic Weapons Research Establishment Rept. O 16/84, 1984.

Thurber, C. H., H. Given, and J. Berger, Regional seismic event location with a sparse network: Application to eastern Kazakhstan, USSR, J. Geophys. Res., 94, 17767-80, 1989.

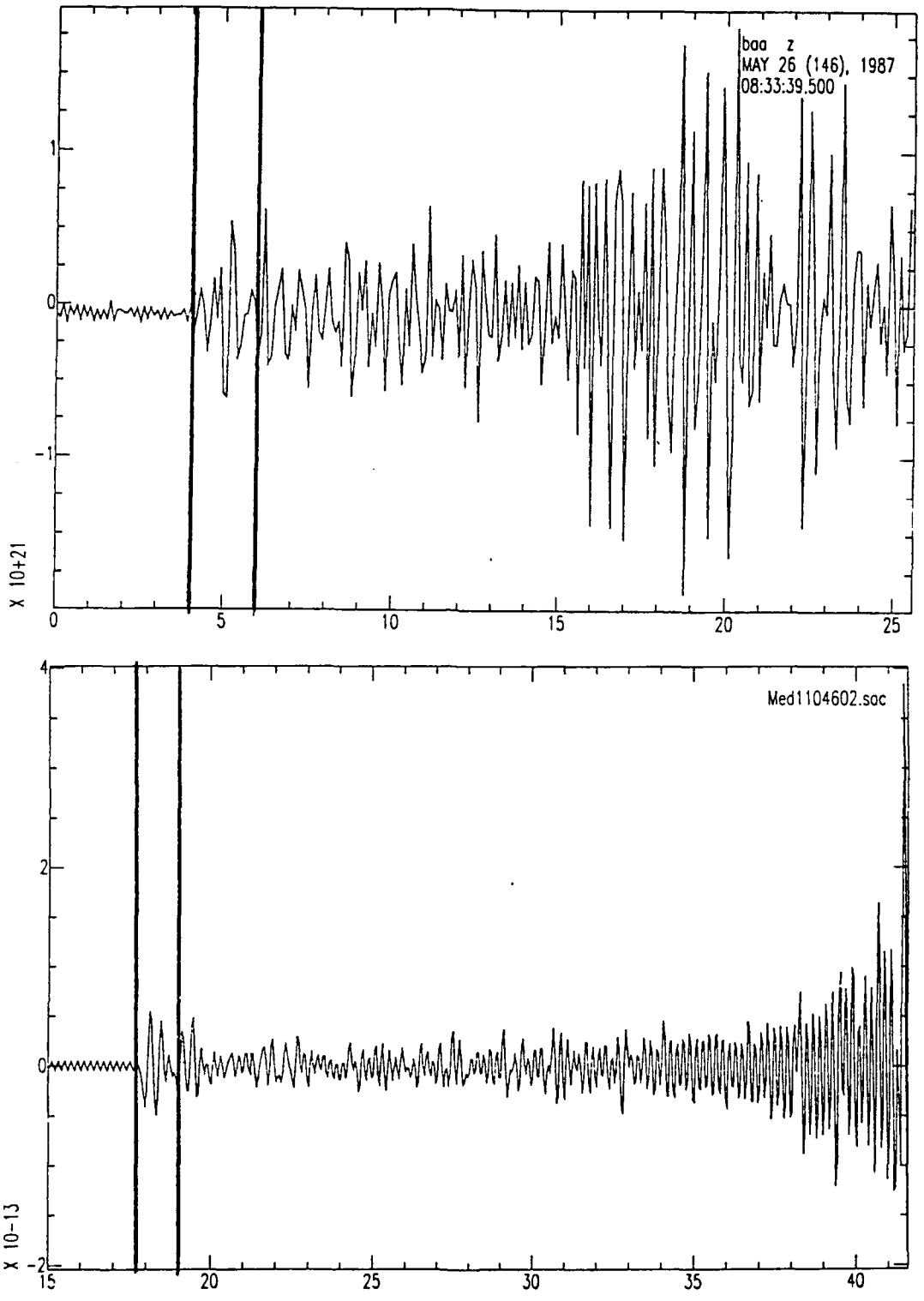


Figure 1. Comparison of vertical-component seismogram from an event studied by Thurber et al. [1989] estimated to be located at an epicentral distance of 104.6 km from station Bayanaul (BAY) of the former NRDC network (top panel) with a reflectivity synthetic in our "Med1" crustal model for that same distance (bottom panel). The vertical lines mark the distinct arrivals Pg and PmP in both data and synthetics.

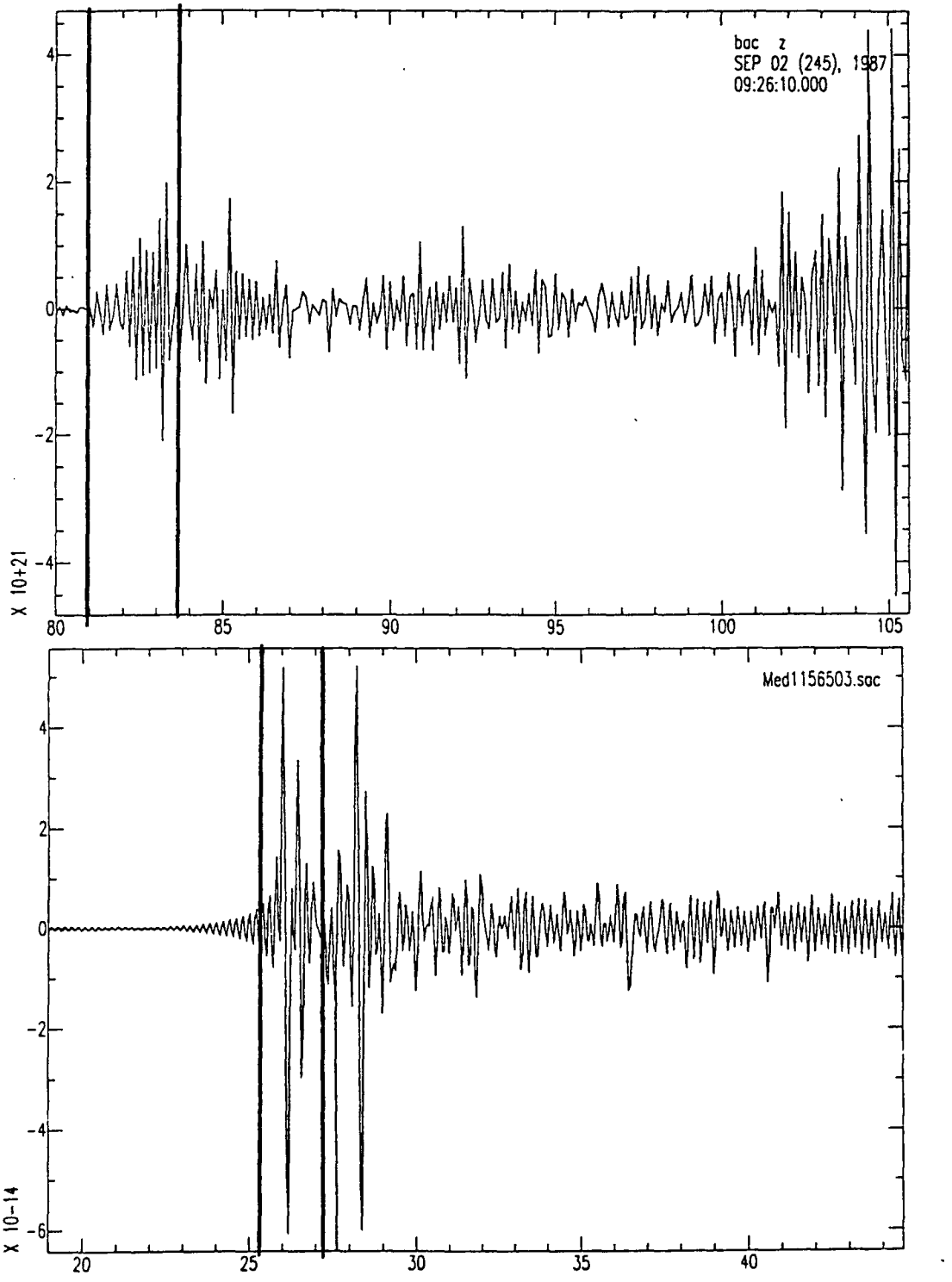


Figure 2. Comparison of vertical-component seismogram from an event studied by Thurber et al. [1989] estimated to be located at an epicentral distance of 156.5 km from station Bayanaul (BAY) of the former NRDC network (top panel) with a reflectivity synthetic in our "Med1" crustal model for that same distance (bottom panel). The vertical lines mark the distinct arrivals Pg and PmP in both data and synthetics.

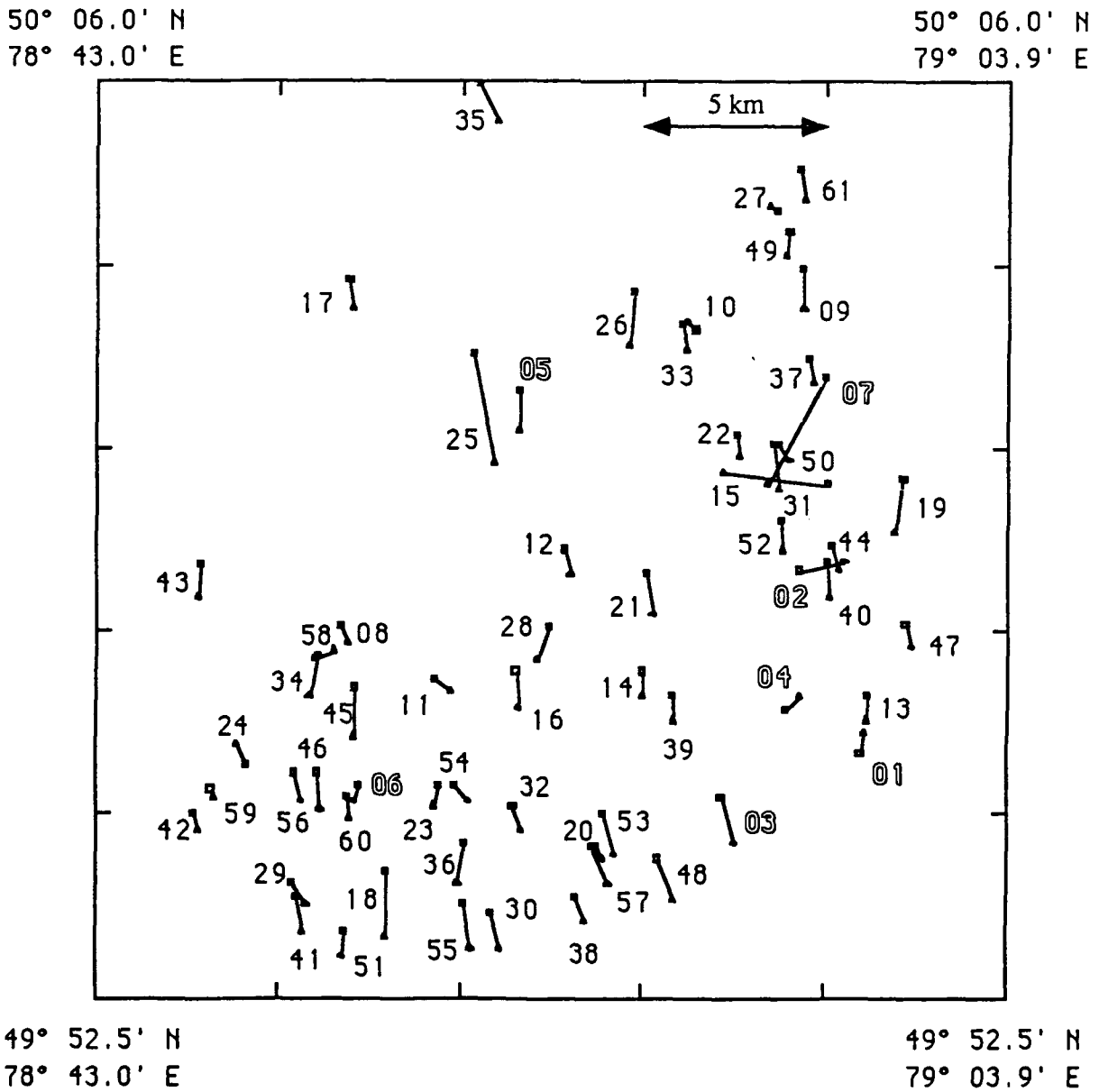


Figure 3. Comparison of JHD locations of 61 Shagan River nuclear explosions (1965 to 1982) computed by Marshall et al. [1984] (triangles) versus those of Lilwall & Farthing [1990] (squares). Disagreement is greatest for events 07, 15, 18, and 25. The numbers for the events included in the listing by Bocharov et al. [1989] are in outline (01 to 07), and were used as master events by Lilwall & Farthing [1990]. Combining these results with our satellite image analysis has allowed us to determine absolute locations for a number of additional events (see Figure 4). We have also used this set of 7 events to derive improved station corrections for Shagan River.

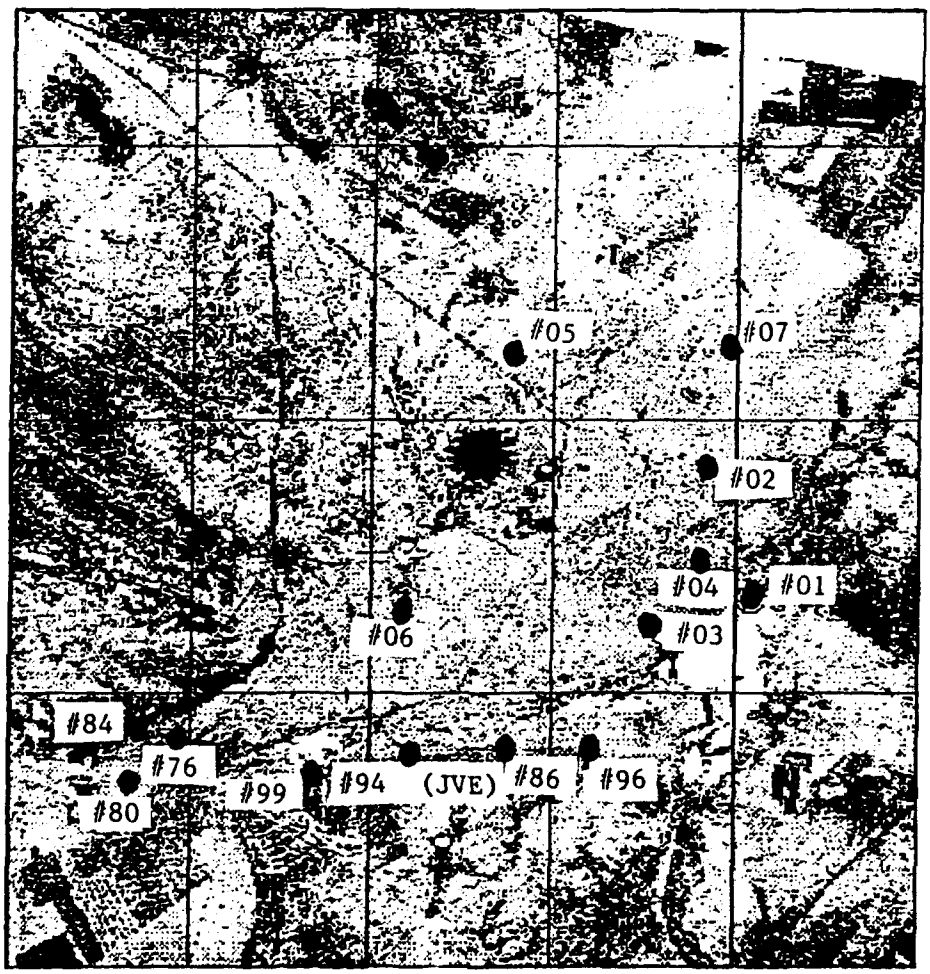


Figure 4. Rectified and annotated portion of a SPOT satellite image from the Shagan River section of the Kazakhstan test site (contrast-enhanced negative image) showing shot points identified for 14 nuclear explosions at Shagan River, including the group of 7 reported by Bocharov et al. [1989] (#01 to #07) and the 1988 Soviet JVE (#94). We believe we can immediately identify an additional 15 to 20 shot points, and eventually expect to be able to identify uniquely the vast majority of shot points from explosions at Shagan River detected at teleseismic distances.

RESEARCH IN REGIONAL SEISMOLOGY: THE EFFECT OF ANISOTROPY

M.N. Toksöz, B. Mandal, R.L. Gibson, Jr., and A.M. Dainty

Earth Resources Laboratory
Department of Earth, Atmospheric, and Planetary Sciences
Massachusetts Institute of Technology
Cambridge MA 02139

Contract No. F19628-90-K-0057

OBJECTIVE

The objective of this study is an examination of the influence of fracturing and anisotropy in the source medium or near the source on radiation patterns from explosions, including the generation of SH waves. Specific objectives are: (1) study of radiation patterns of P and S waves for explosions set off in anisotropic media, especially for cases that mimic earthquakes and/or generate SH waves; (2) elucidating the effects of scattering from fractured zones of material, such as might be found near the source; (3) reexamining the question of the effective medium that results from fracturing rock, especially in a near-surface environment.

RESEARCH ACCOMPLISHED

Introduction

Transverse shear energy (SH) is observed in seismic records from explosions. Various mechanisms have been proposed to account for this, such as tectonic release, but the problem is still not resolved, especially at short periods. The problem is critical for seismic monitoring of underground nuclear explosions because the essential question being asked is, what is the source? Before an assessment can be made of the causes of shear radiation from explosions, all possible mechanisms need to be studied. We are studying two specific possibilities. One is anisotropy of the source medium within which the explosion is detonated. Because of the non-isotropic compliance of the medium, generation of shear can occur. The second is scattering from heterogeneity likely to be present at a test site. One strong candidate for heterogeneity is fractured rock, either naturally present or due to previous explosions. Both of these topics have a strong connection with the influence of fracturing on rock properties. A major source of anisotropy in the crust is fracturing aligned in a preferred direction because of geologic history or in-situ tectonic stress. This has led us to a third topic, a reexamination of the effective anisotropic medium produced by fracturing. Most investigators in this area have used a model based on microcracks, but large scale fractures or joints are more likely in the upper crust where explosions are detonated.

Radiation Patterns in Anisotropic Media

An explosion in a vertically stratified isotropic medium will not exhibit azimuthally dependent radiation patterns of P, SV, and Rayleigh waves, and will not generate SH and Love waves (see

papers in the AGU Monograph "Explosion Source Phenomenology", 1991). Underground nuclear tests have exhibited all of these phenomena. Such mechanisms as tectonic release, dislocation across cracks, and spallation and "slapdown" have been proposed and can explain some of the data, but no single explanation has been found for all of the data (Massé, 1981; Johnson, 1988). We are conducting a theoretical investigation of the effect of seismic anisotropy of the medium in which the explosion takes place on the radiation of seismic waves. It is generally expected that upper crustal rocks will be anisotropic due to the influence of non-uniform tectonic stress on randomly distributed fractures (Crampin, 1984; Thomsen, 1986; Martin, 1990).

The problem has been solved both exactly and in the asymptotic ray-theory limit (Mandal and Toksöz, 1989; Ben-Menahem and Sena, 1990; Mandal and Toksöz, 1990, 1991). An example of radiation patterns for an explosion in an anisotropic medium with a horizontal symmetry axis is shown in Figure 1, from Mandal and Toksöz (1991). The patterns were computed using the exact theory, and the top part of the Figure shows the geometry: receivers are distributed at equal radial distance from the source in a vertical plane at an azimuthal angle ϕ to the plane at right angles to the symmetry axis. Radiation patterns of P and S waves at five different azimuthal vertical planes are shown, measured from time domain responses of the complete waveforms, as well as a solid circle which is the P radiation pattern for an isotropic medium (there is of course no S for this case). We see that the P radiation pattern (dashed line) is little affected for this case, but significant S is generated (chained line) and has a similar form to that expected from a double couple for measurements in planes near $\phi = 90°$.

Scattering from Fractured Inclusions

Scattering from inclusions of fractured rock can be studied by treating the inclusion as an effective medium, i.e., a medium with new properties. These properties may be anisotropic due to orientation of the fractures, as discussed above. We have solved the problem of scattering from any fractured inclusion, whether the cracks are oriented or not, using the Born approximation (Ben-Menahem and Gibson, 1990; Gibson, 1991). This formalism has been integrated into a Ray-Born code allowing seismograms to be calculated using the scattering theory for the fractured inclusions and ray theory for an isotropic background model of any desired degree of complexity (Gibson, 1991). The theory now exists to extend ray tracing for both P and S waves to an anisotropic background model (Coates and Chapman, 1990). Figure 2 shows an illustrative model and a source-receiver geometry. Although only a 2-D cross-section is shown, the code is 3-D. Figure 2 also shows vertical and radial seismograms for an explosive source and a fracture zone with isotropic, randomly oriented, dry cracks. Scattered arrivals of both P and S waves are marked by arrows on Figure 2. Although the case of randomly oriented cracks is shown, the code will accomodate any orientation or combination of orientations of cracks. It has been shown that scattered SH can be produced from incident P if the cracks are suitably oriented.

Velocity Anisotropy for Micro-Fractures and Parallel Joints

The theory presented in the preceeding sections relies on the concept of an equivalent medium, namely, that the two-phase medium of host rock and dry or fluid-filled fractures may be replaced

by an anisotropic medium. This has led us to examine the theories used to find the relationship between the real fractured medium and the equivalent anisotropic medium. These theories fall into two classes: micro-fracture theories, which assume the cracks are small, and macro-fracture theories, which do not. Micro-fracture theories have been used in most investigations of which we are aware. Macro-fracture theories can be applied to systems of parallel joints, faults, etc., common in the very shallow crust. This is especially relevant to quarry blasts and nuclear explosions. Theoretical calculations have been made to compare the anisotropic velocity variations for rock masses having micro-fractures and sets of parallel joints.

We use different hypotheses in computing elastic moduli in the two cases. For the micro-fracture models fracture dimensions are assumed very small compared to the wavelength (Hudson, 1980, 1981). For a rock mass with macro-fractures or joints, the stresses are continuous across the fracture but displacements are discontinuous (e.g. Schoenberg, 1980, 1983; Pyrak-Nolte *et al.*, 1990). Both cases show anisotropic velocity variation but differ in nature. For the micro-fracture model, the crucial parameters are the fracture density (CD = $N\ a^3/V$) and aspect ratio (AR = d/a), where N is the number of fractures of radius a and thickness d in volume V. The macro-fracture model is controlled by the fracture spacing (number of fractures per unit length) and the specific stiffness of the fractures (the ratio of the incremental stress across the fracture to the incremental displacement that the stress produces). The value of specific stiffness determines the seismic properties of the joints, including the effect of the mechanical coupling between the the joint surfaces on the transmission properties across the joint. For example, an infinite specific stiffness refers to a welded contact and a zero stiffness represents a free surface.

In the micro-fracture model, for a fixed crack density the qSH velocity does not depend on the aspect ratio. There are smaller velocity variations for qSV and larger variations for qP with increase in aspect ratio. Velocity variations for all velocities increase with increasing fracture densities. The qP and qSH velocity variations for the joint model are some what similar to the micro-fracture model. The joint model does not produce azimuthal velocity variations of qSV but gives the (constant) velocity for different specific stiffnesses. Figure 3 shows a comparison of two models chosen so that the total range of azimuthal qP variation is the same; it is seen that the joint model predicts no anisotropy for qSV and less anisotropy in qSH than the micro-fracture model in this case.

CONCLUSIONS AND RECOMMENDATIONS

Work on the ability of fractured and anisotropic material to generate shear energy for an explosive source is being conducted using theoretical calculations of seismograms and radiation patterns, and developing theoretical formulations for realistic fractured media appropriate for quarry blasts and shallow explosions. Because of the directional dependence of the compliance of the material, an explosion detonated in an anisotropic medium will have a non-isotropic radiation pattern and can generate significant amounts of shear waves, including transverse components. Scattering from zones of fractured material can also produce significant shear energy. For tranverse shear to be produced from scattering of the incident P expected from an explosion, the fractures must be aligned preferentially. An equivalent anisotropic medium model of macro-fractured rock, such as near-surface rock with a parallel joint system, has been compared to the conventional microfracture theory; it has been shown that they give rise to different anisotropic media in general. For future efforts we recommend:

1. Continue theoretical investigation of explosive sources in anisotropic media. Specifically, investigate a sufficient number of practical cases to determine how the effects of anisotropy may be separated from those of tectonic strain release and source region heterogeneity.

2. Determine the scattering response of an inclusion of fractured rock for incident P and S waves. The P wave case is particularly interesting for explosions and a suitable number of practical cases should be investigated.

3. Examine new models relating a fractured medium to an equivalent anisotropic medium, and determine their implications in terms of characterization of the near-source region.

4. Improve the ultrasonic laboratory models we presented last year to look at realistic cases. and compare results with theory and field data.

REFERENCES

Ben-Menahem, A., and R.L. Gibson, Jr. (1990). Scattering of elastic waves by localized anisotropic inclusions. *J. Acoust. Soc. Am., 87*, 2300–2309.

Ben-Menahem, A., and A.G. Sena (1990). Radiation patterns of point sources in anisotropic media. *J. Geophys. Res., 95*, 15,395–15,427.

Coates, R.T., and C.H. Chapman (1990). Quasi-shear wave coupling in weakly anisotropic 3-D media. *Geophys. J. Int., 103*, 301–320.

Crampin, S. (1984). Effective elastic constants for wave propagation through cracked solids. *Geophys. J. R. Astr. Soc., 78*, 691–710.

Gibson, Jr., R.L. (1991). *Elastic Wave Propagation and Scattering in Anisotropic Fractured Media.* Ph.D. Thesis, Massachusetts Institute of Technology.

Hudson, J.A. (1980). Overall properties of a cracked solid. *Math. Proc. Cambridge Philos. Soc., 88*, 371–384.

Hudson, J.A. (1981). Wave speeds and attenuation of elastic waves in material containing cracks. *Geophys. J. R. Astron. Soc., 64*, 133–150.

Johnson, L.R. (1988). Source characteristics of two underground nuclear explosions, *Geophys. J., 95*, 15–30.

Mandal, B., and M.N. Toksöz (1989). Radiation patterns from explosions in anisotropic med *Proceedings of the DOE/LLNL Symposium on Explosion-Source Phenomenology*, 215–230.

Mandal, B., and M.N. Toksöz (1990). Computation of complete waveforms in general anisotropic media—results from an explosion source in anisotropic medium. *Geophys. J. Int., 103*, 33–45.

Mandal, B., and M.N. Toksöz (1991). Explosive source in an anisotropic medium. *AGU Mon. "Explosion Source Phenomenology"*, in press.

Martin, R.M. (1990). Anisotropy of Topopah Spring Member Tuff. *New England Research Report.*

Massé, B.P. (1981). Review of seismic source models for underground nuclear explosions, *Bull. Seismol. Soc. Am., 71*, 1249–1268.

Pyrak-Nolte, L.J., L.R. Myer and N.G.W. Cook (1990). Anisotropy in Seismic Velocities and Amplitudes from Multiple Parallel Fractures. *J. Geophys. Res., 95*, 11,345–11,358.

Schoenberg, M. (1980). Elastic wave behavior across linear slip interfaces. *J. Acoust. Soc. Am., 68*, 1516–1521.

Schoenberg, M. (1983). Reflection of elastic waves from periodically stratified media with interfacial slip. *Geophys. Prospect., 31*, 265–292.

Thomsen, L. (1986). Weak elastic anisotropy, *Geophysics, 51*, 1954–1966.

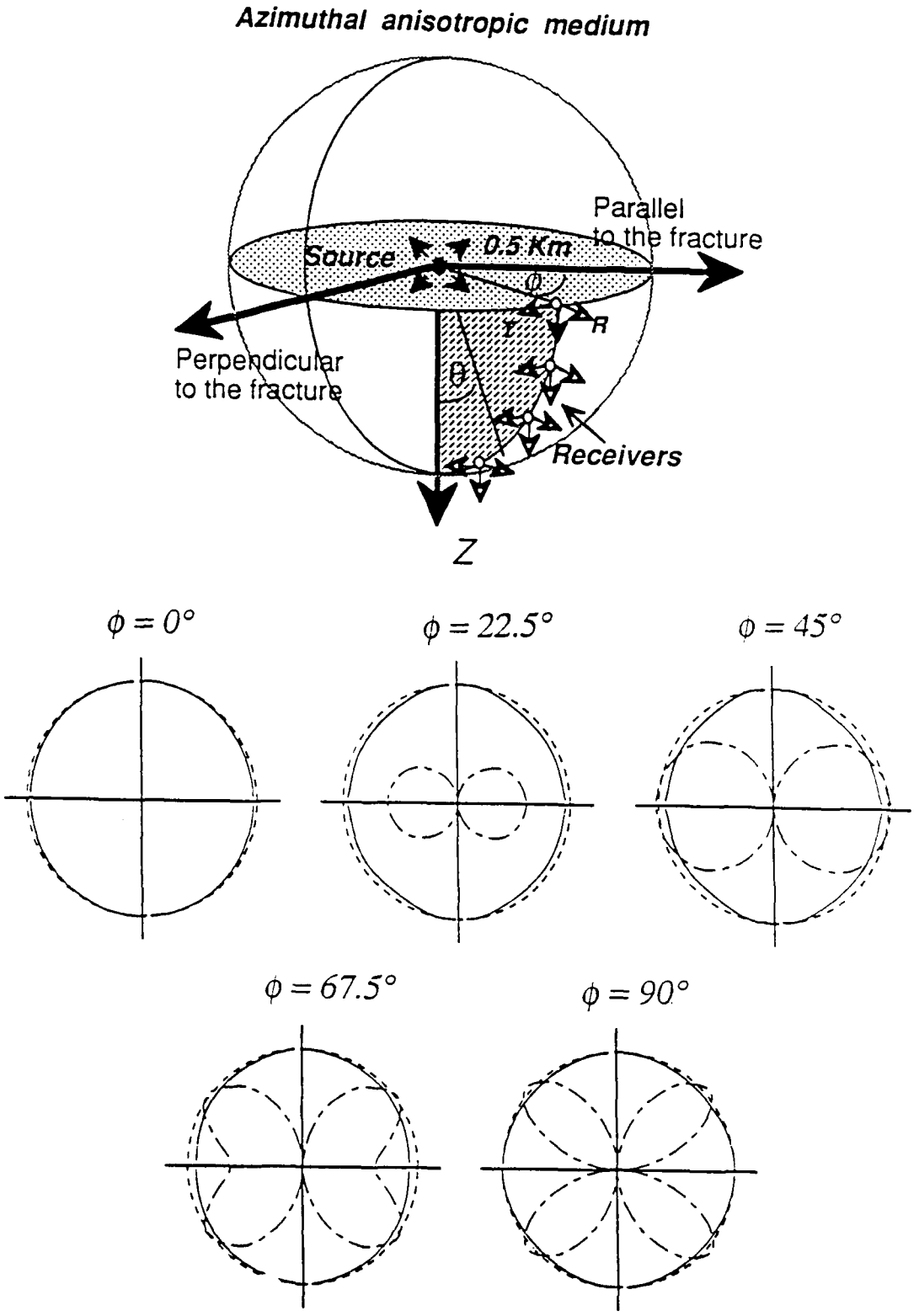


Figure 1: (Top) Geometry for an explosive source in an azimuthally anisotropic medium due to aligned vertical cracks. (Bottom) Radiation patterns for P and S in five vertical planes. The model has a background velocities V_P = 6.132 km/s, V_S = 3.266 km/s, ρ = 2.7 gm/cc, a fractional crack density of 0.1 and an aspect ratio of 0.001. From Mandal and Toksöz (1991).

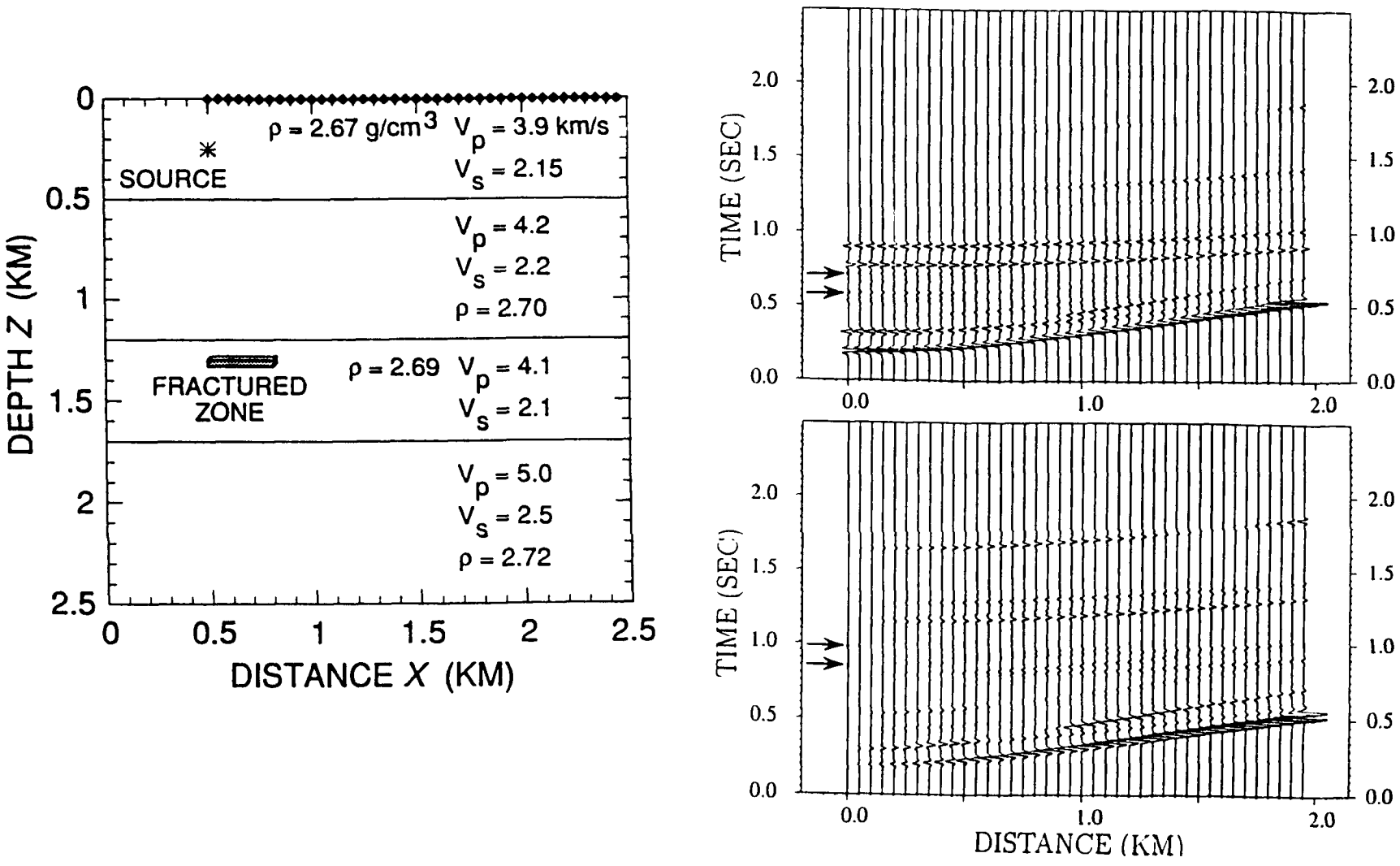


Figure 2: (Left) Model used to calculate synthetic seismograms including the effect of a thin fractured zone. Receivers are indicated by black diamond symbols. (Right) Vertical (top) and radial (bottom) component total wavefield synthetic seismograms from an explosive source for a fractured zone containing isotropic, randomly oriented and dry cracks. Arrows mark the positions of scattered P waves on the vertical component and scattered S waves on the radial component. From Gibson (1991).

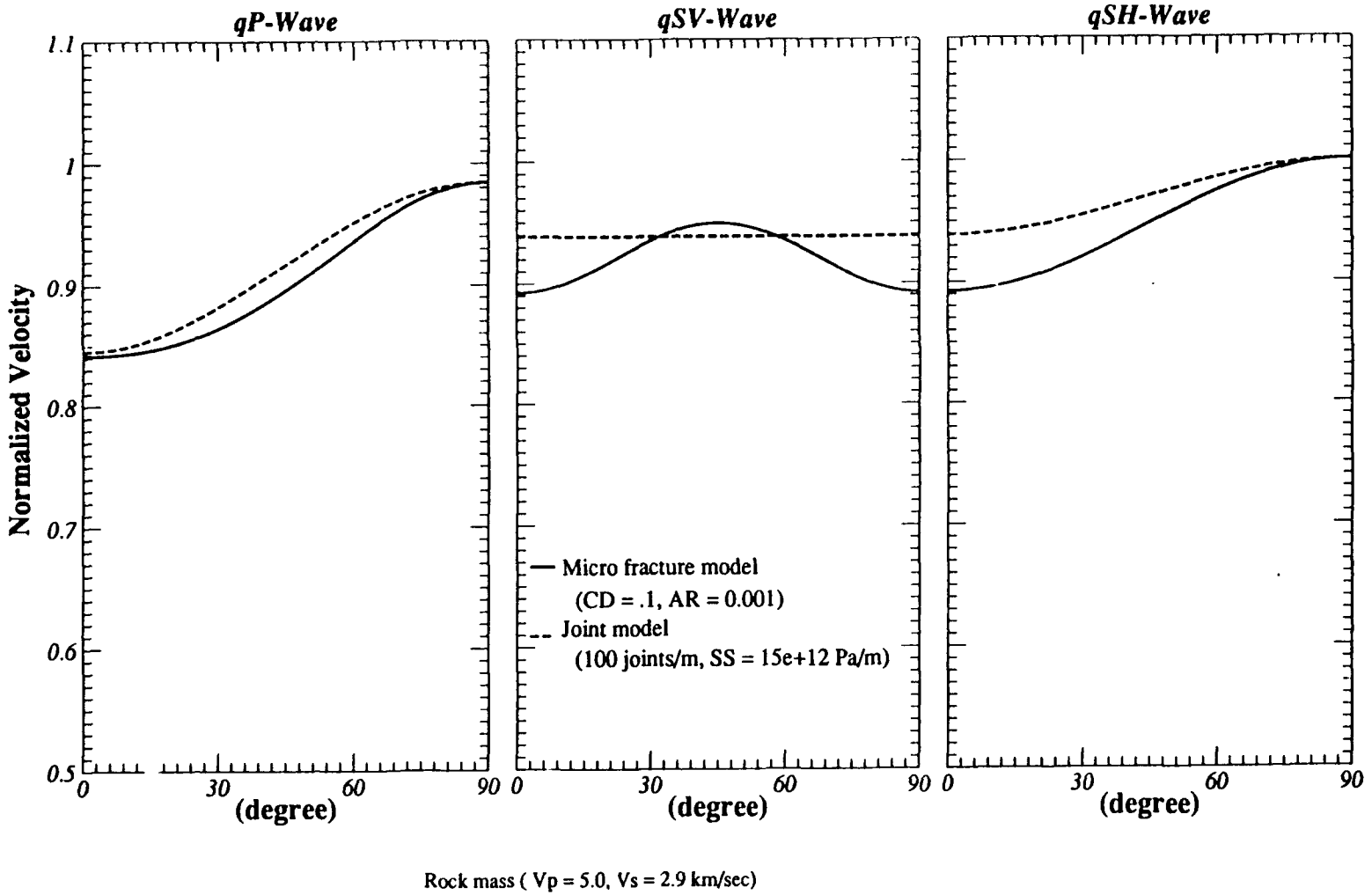


Figure 3: Azimuthal velocity variation for a micro-fracture and a joint model. Azimuth 0° refers to the symmetry axis (perpendicular to the fractures) and 90° parallel to the fractures. Parameters of the medium and the model are given on the Figure. The two models were chosen to give a similar variation of the qP velocity.

REGIONAL SEISMOGRAMS: ATTENUATION AND SCATTERING

M.N. Toksöz, A.M. Dainty, B. Mandal, N. Cheng, E.E. Charrette and C. Schultz

Earth Resources Laboratory
Department of Earth, Atmospheric, and Planetary Sciences
Massachusetts Institute of Technology
Cambridge MA 02139

Contract No. F19628-89-K-0020

OBJECTIVE

The primary objective of this study was to examine the effects of attenuation and scattering on seismic waves propagating over regional (200–2000 km) distances and the implications for detection and characterization of nuclear explosions. To help achieve the primary objective, studies of scattering in the lithosphere and scattering from rough surfaces have been added as secondary objectives. Specific objectives include: (1) fitting a physical model of crustal attenuation to specific regions in Eurasia by comparing complete seismograms for layered anelastic media with observed seismograms; (2) investigating the effect of scattering on the seismic phase Lg both by large scale crustal structure (Lg blockage) and by small scale heterogeneity through the method of coupled modes; (3) determining the heterogeneity spectrum in the lithosphere under the NORSAR array; (4) theoretical and ultrasonic investigation of scattering from a rough interface.

RESEARCH ACCOMPLISHED

Introduction

Under this contract we are examining the effect of attenuation (including structural effects) and scattering on regional seismic propagation. This is important for monitoring low-yield underground nuclear tests because seismic waves from such tests will only be observed at regional distances. The methods used include theoretical calculations, comparisons to observed seismograms, and ultrasonic modeling. The ultimate goal is a complete understanding of the way propagation and structure govern the characteristics of regional seismograms. One focus of our work has been calculation of complete seismograms in flat layered structures, with the affect of attenuation in each layer included, and then comparing them with observed seismograms from Eurasia to determine the velocity and attenuation structure that best fits the seismograms in a given area. Another focus has been the phase Lg, commonly the most prominent regional phase over continental paths, and perhaps the most useful and reliable phase for estimating the yield of underground nuclear tests. This phase is subject to scattering by both large scale and small scale structures. We present here work using the theory of coupled modes to examine the blockage of Lg by zones of crustal extension. Also, an analysis using Scandinavian data of whether the theory of coupled modes can explain some general characteristics of Lg has been carried out. A third topic is the determination of the heterogeneity structure of the lithosphere under the NORSAR array in Scandinavia. The final topic reported here is a general study of scattering from rough interfaces using theoretical and ultrasonic methods. This was undertaken because there is increasing evidence that this is an

important effect for regional seismic phases, which often involve reflections from interfaces, and there is no good theory for the strong roughness case. Below, we give brief summaries of results in each area.

Attenuation and Structure in Eurasia

In work under previous contracts, we proposed a general physical model of attenuation in stable crust with a low Q in the uppermost one or two km (Toksöz *et al.*, 1988). The utility of this model was confirmed in studies of the velocity and attenuation structure of the crust in New England and Scandinavia (Toksöz *et al.*, 1990a). In these studies we compared complete synthetic seismograms for candidate crustal structures with observed seismograms from dynamite explosions over short (1–30 km) distances and major quarry blasts over longer (up to 300 km) distances. While subsequent work has raised some questions at longer ranges (Toksöz *et al.*, 1990b), as discussed below, the method yields good results at the ranges given above. Figure 1 shows a preliminary comparison for waveforms recorded at the NRDC station KKL (Karkaralinsk) at ranges of 190–260 km, with the synthetics calculated for a preliminary model based on DSS soundings compiled by Leith and reported in Priestley *et al.* (1988). We see that the seismogram at 217 km is quite well fit in general amplitude of the phases, although as usual in these models the synthetic is simpler than the observed. The synthetic at 194 km suggests that some adjustment in near surface structure is needed to increase Rg amplitude and improve the timing, whereas the explosion synthetic at 254 km needs a more complex source with spall slapdown to increase the amplitude of Lg, and a decrease in Rg. While this model needs refinement, it seems to confirm our experience in New England and Scandinavia that relatively simple flat layered models can explain gross features of seismograms at these ranges.

The Effect of Scattering on Lg

In regional propagation over continental paths, the Lg phase is usually prominent and shows great promise for estimating source size (magnitude and yield). This phase is made up of shear energy trapped in the crustal waveguide, the trapping providing a ready explanation for the efficiency of propagation. However, it is clear that Lg is subject to scattering during propagation. We have investigated two scattering effects by the method of coupled modes (Kennett, 1984; Marcuse, 1974). In this method, the waveguide nature of the propagation is retained with scattering causing energy to be transferred between modes (coupling) or lost from the waveguide (attenuation); intrinsic attenuation of the modes may also be accomodated. One problem that we have looked at is the attenuation and blockage of Lg across crustal extension zones such as the North Sea graben. Kennett and Mykkeltveit (1984) present data for this structure demonstrating the blockage and theoretically examined the Love modes without computing theoretical seismograms. In Figure 2 we show theoretical seismograms of the Lg phase for the P-SV modes (vertical and radial components) showing the effect of the graben structure, i.e., Moho shallowing and a sedimentary basin, from a forthcoming paper (Cheng and Toksöz, 1991). Figure 2 clearly demonstrates that these alone could explain the blockage observed.

Another problem that has been examined using coupled modes is the overall shape of Lg, as

expressed by the width at the $1/e$ power level, and the effect of scattering upon it. A theoretical consequence of the energy transfer between modes in coupled mode theory is the existence of collections of modes, known as statistical modes (Marcuse, 1974), that are in radiative equilibrium with each other. At long ranges, the statistical mode with the lowest attenuation will dominate; a consequence of this is that the width of the Lg pulse should be proportional to the square root of range. A data set of mine blasts and earthquakes recorded at NORESS in Scandinavia shows considerable scatter of measurements of Lg width. A square root dependence on range may, however, be fit to data at ranges greater than about 400 km, suggesting that the concept of radiative equilibrium may be useful beyond 400 km

Volume Heterogeneity of the Lithosphere

The preceeding section indicates the importance of crustal, and more generally lithospheric, heterogeneity and the attendant scattering in the propagation of regional phases. Accordingly, an understanding of the physical nature and causative structures of the scattering is important. These may be divided into volume scattering from inclusions and interface scattering from rough boundaries. In this section we discuss our work on determining volume heterogeneity and discuss interface scattering in the next section.

In seeking to determine the nature of lithospheric heterogeneity, analysis of teleseismic data at large arrays has proven useful because the near-vertical incidence of the initial wavefield reduces the complexities of the analysis (see Flatté and Wu, 1988, for recent work). We have used finite difference calculations of the first P and the first 15 seconds of the P coda from Semipalatinsk explosions to construct a model of lithospheric heterogeneity under the NORSAR and NORESS arrays in Norway (Charrette, 1991). This study is the first on this problem to compute complete waveforms for the proposed model and to match the P coda level to first P. A three-layered model random medium model was derived for heterogeneity scales between 5 and 125 km, the limits allowed by the data. In the upper 3 km, the spatial spectrum of the heterogeneity is white with an rms deviation of 2% in velocity. This near surface layer produces the incoherence often seen between seismograms at different array sensors. In the rest of the crust, down to 35 km depth, a zeroth order von Karman spectrum is used with a 3% rms deviation and a correlation length of 10 km. This part of the medium has an important effect in providing the correct level of coda relative to first P. Heterogeneity in the mantle (to 250 km depth) has an anisotropic Gaussian spectrum with a 2% rms deviation. The spatial correlation length in the mantle is 20 km horizontally and 5 km vertically.

In addition to the work on determining heterogeneity, we have carried out joint work with Mission Research Corporation to compare their phase screen method with finite difference.

Reflection from Rough Interfaces

In a previous report (Toksöz *et al.*, 1990b), we have presented work suggesting that Lg consists of multiple S to S bounces in the crust. Scattering from rough interfaces such as the Moho or the free surface is clearly a possibility that must be considered, and indeed could be the most important

form of scattering. However, the theory of such scattering is less well developed than for volume scattering, and we have commenced our attack on the problem with some fundamental studies prior to proceeding to the computation of seismograms. In previous work we have investigated interface scattering by the Born approximation and finite difference (Prange and Toksöz, 1990). This three-dimensional study has shown that energy will be scattered at angles other than the Snell's law angle in both reflection and transmission, and that there are phase shifts (i.e., travel time shifts and/or waveform distortion) in the wavelet, effects that may be present in Lg. In addition to continuing the finite difference, we are now using ultrasonic modeling. Figure 3 shows reflections at different offsets obtained from the surface of an aluminum block in a water tank. Figure 3a shows the case of a smooth surface, with a head wave starting at 0.15 m offset. Figure 3b shows the case of a rough surface. The head wave is greatly weakened and scattered energy appears as a coda after the direct reflection in a manner very reminiscent of Lg. We have successfully modeled this data using finite difference methods; all orders of scattering must be included for this high-contrast case.

CONCLUSIONS AND RECOMMENDATIONS

Work on understanding regional seismograms as they are affected by propagation is being conducted using theoretical calculations, analysis of observed seismograms, and ultrasonic laboratory modeling. Calculations of complete synthetic seismograms in simple layered crustal models in Eurasia based on DSS profiles and our previous general attenuation model have been compared to observed seismograms with general agreement, demonstrating the effectiveness of the approach. Coupled mode theory has shown that Lg will be attenuated to the point of blockage across crustal extension zones of suitable width (tens of km), independently of any effects of anelastic attenuation. An analysis of the implications of coupled mode theory for Lg has been carried out using data recorded at NORESS and indicates that a steady state (radiation balance between coupled modes) may occur at ranges greater than 400 km. The heterogeneity structure under the NORSAR and NORESS arrays has been determined using finite difference to compute complete waveforms for proposed models, the resulting three-layer model explaining the observed incoherency between seismograms and the relative level of P coda and first P. Ultrasonic modeling and finite difference calculations have demonstrated the degradation of the reflection from rough boundaries with high contrast and the production of coda. For future work on the topics discussed here, we recommend

1. Determine Q and velocity structure of the crust in Eurasia by comparing data from CDSN, IRIS and NRDC stations with synthetic seismograms in the distance range 150–300 km.

2. Assess the geometrical attenuation of Lg due to areas of crustal thinning such as the Barents, Black and Caspian Seas by theoretical computations using coupled modes, compared to observed seismograms.

3. Use finite difference to investigate problems in volume scattering of seismic waves, including the use of fluctuations to determine lithospheric variability, computation of two-dimensional models at near-regional distances, and three-dimensional models for near-source problems.

4. Investigate interface scattering theoretically by perturbation and finite difference techniques, and experimentally by ultrasonic modeling; integrate the results into realistic codes to compute theoretical seismograms.

5. Investigate the influence of crustal reflections in the P coda and especially the Lg phase in the distance range 300–1000 km by comparing closely (1–10 km) spaced data with theoretical computations, including ray theory; if successful, look at recordings of Soviet tests from the CDSN, IRIS and Soviet Analog networks.

REFERENCES

Charrette, III, E.E. (1991). *Elastic Wave Scattering in Laterally Inhomogeneous Media.* Ph.D. Thesis, Massachusetts Institute of Technology.

Cheng, N., and Toksöz (1991). An analysis of the nature and attenuation of Lg waves. *Submitted to* Geophys. J. Int.

Flatté, S.M., and R.S. Wu (1988). Small scale structure of the lithosphere and asthenosphere deduced from arrival-time and amplitude fluctuations at NORSAR. *J. Geophys. Res., 93*, 6601–6614.

Kennett, B.L.N. (1984). Guided wave propagation in laterally varying media—I. Theoretical development. *Geophys. J. R. Astr. Soc., 79*, 235–255.

Kennett, B.L.N., and S. Mykkeltveit (1984). Guided wave propagation in laterally varying media—II. Lg-waves in north-western Europe. *Geophys. J. R. Astr. Soc., 79*, 257–267.

Marcuse, D. (1974). *Theory of Optical Dielectric Waveguides.* Academic Press.

Prange, M., and M.N. Toksöz (1990). Perturbation approximation of 3-D seismic scattering. *Geophys. J. Int., 101*, 713–738.

Priestley, K.F., G. Zandt and G. Randall (1988). Crustal structure in eastern Kazakh, U.S.S.R. from teleseismic receiver functions. *Geophys. Res. Lett., 15*, 613–616.

Toksöz, M.N., A.M. Dainty, E. Reiter and R.-S. Wu (1988). A model for attenuation and scattering in the earth's crust. *PAGEOPH, 128*, 81–100.

Toksöz, M.N., B. Mandal and A.M. Dainty (1990a). Frequency dependent attenuation in the crust. *Geophys. Res. Lett., 17*, 973–976.

Toksöz, M.N., N. Cheng, A.M. Dainty and B. Mandal, 1990c. Regional seismograms: attenuation, scattering and anisotropy. Papers presented at 12th Ann. DARPA/GL Seismic Res. Symp., 166–176.

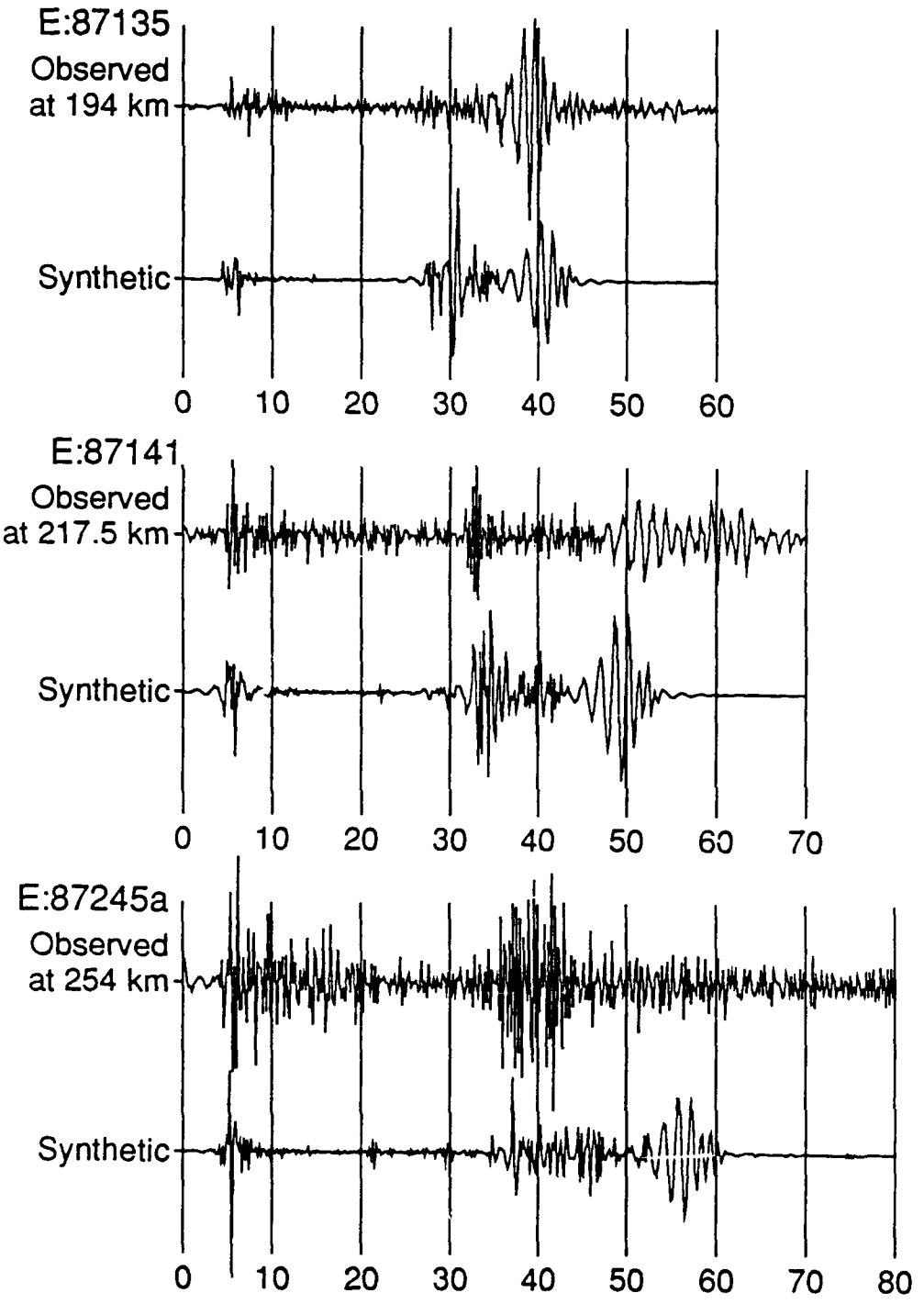


Figure 1: Preliminary matches of synthetics with NRDC data at station Karkaralinsk. Vertical components shown. Top two events are quarry blasts modeled as point vertical forces, bottom is an explosion.

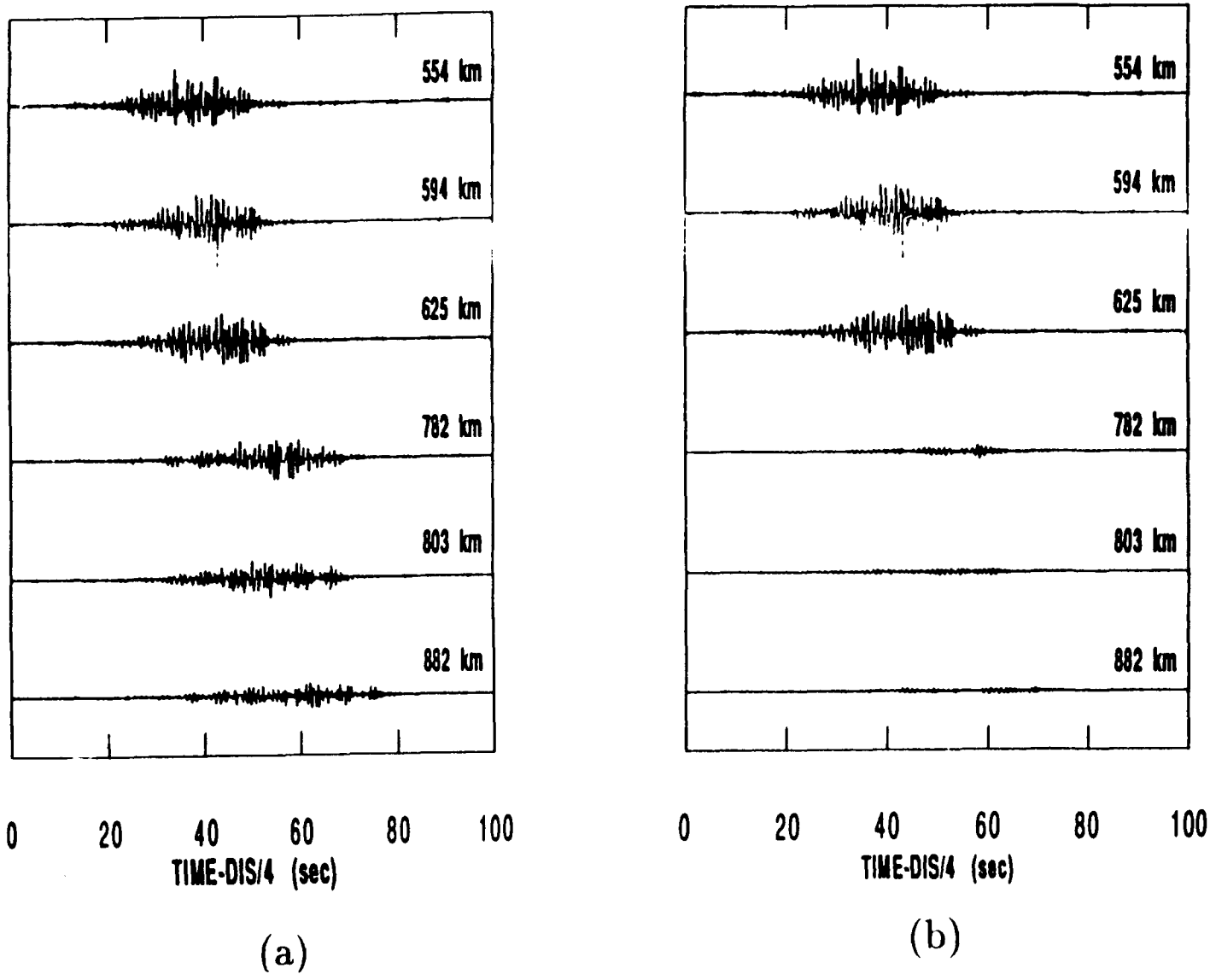


Figure 2: Synthetic seismograms in the North Sea area. (a) Without the Central Graben. (b) With a 60 km wide Central Graben.

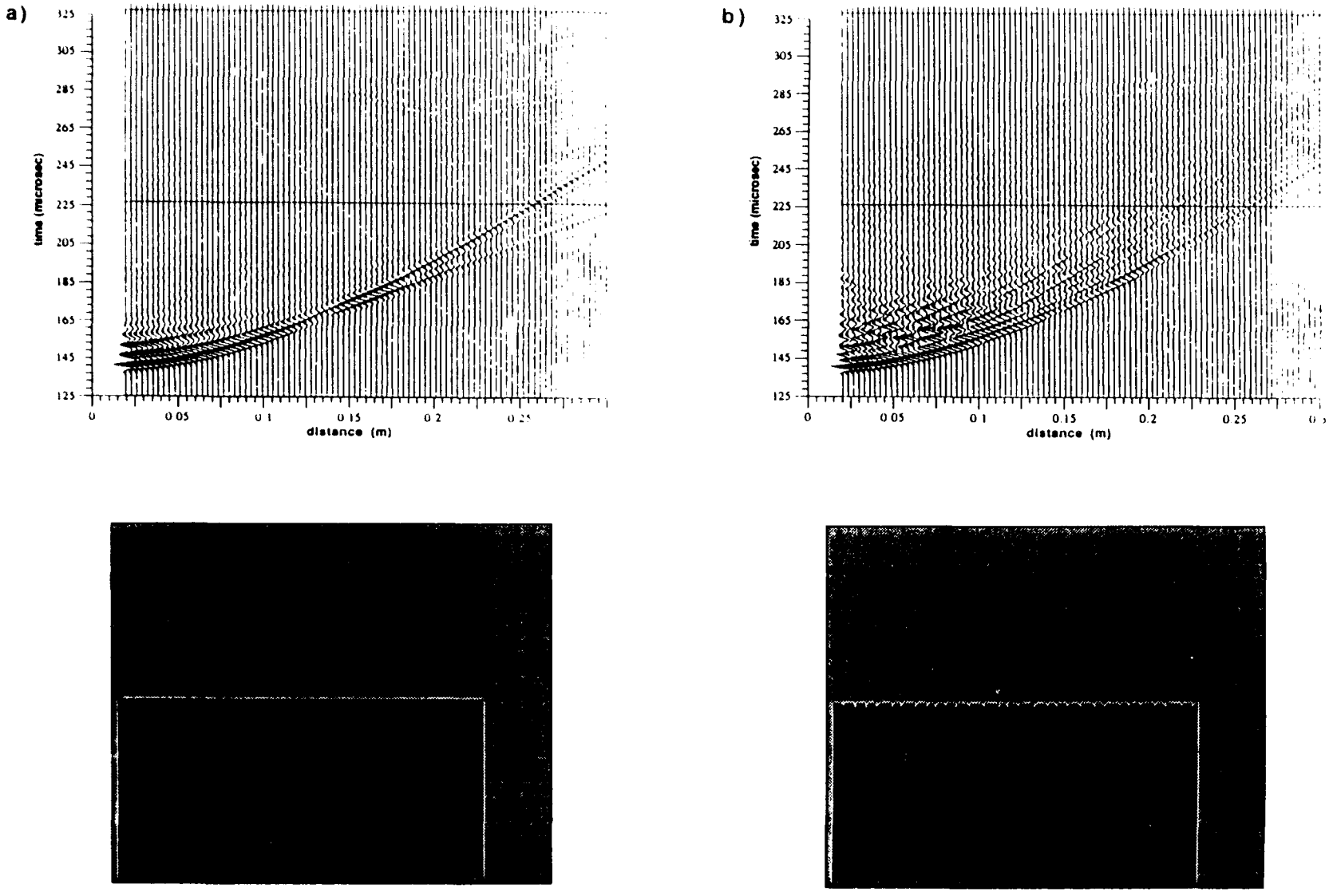


Figure 3: Seismic waves observed in an ultrasonic water tank experiment designed to observe reflections from an aluminum block: (a) with a flat surface; (b) with the surface of the block randomly grooved. Schematic of models below seismograms; source and receivers in water (light grey).

FRACTURE LENGTH AND APERTURE: A GENERAL RELATIONSHIP

JAN VERMILYE AND C. H. SCHOLZ - LAMONT-DOHERTY GEOLOGICAL OBSERVATORY, COLUMBIA UNIVERSITY

CONTRACT # LLNL B157348

OBJECTIVE:

The effect of natural fractures on near field seismic attenuation is being addressed in a field study of fracture networks. General statistical properties of natural fracture geometry must be determined in order to scale up from laboratory models to field scale phenomena. While the size distribution of fractures, defined by length, within a pre-existing network has been defined (Barton and Larsen 1985; Hirata, 1989; Scholz and Cowie, 1990) the relationship between fracture length and aperture has not. Since joint aperture is an important factor in the attenuation mechanism, the objective of this study is too define a general relationship between the length and aperture of fractures within a rock body at depth.

In order to eliminate the possibility of alteration of the geometry of open fractures formed at depth by near surface distortion, caused by unroofing and/or weathering, fractures that have been mineralized at depth (veins) have been selected for study. Observation of cross-cutting relationships and the morphology of the vein filling are used to distinguish undeformed extensional veins that accurately represent the geometry of the original fractures.

RESEARCH ACCOMPLISHED:

The trace geometry of selected vein systems on large exposed bedding planes has been recorded in the field with detailed measurements of length and aperture. When possible, measurements have been made perpendicular to the traces, extending the predominantly two-dimensional data set into three dimensions. Seven field locations representing a variety of rock types (limestone, siltstone, quartz conglomerate, fine grained mafic intrusive, slate and shale) and tectonic environments have yielded a combined data set of 750 veins. Four of these locations contain the

bulk of the data with measurements of length, aperture, segmentation, spacing and selected profiles for 650 veins. Two typical vein profile plots are shown in fig. 1. The profiles, along with spacing and segmentation data are used to define the connectedness of individual veins within a system. All locations indicate a positive correlation between length and aperture with an aspect ratio (aperture/length) of about 10^{-3}.

An excellent bedding plane exposure of Balls Bluff calcareously cemented siltstone (Culpeper Crushed Stone Quarry, Stevensburg, Virginia) contains a NE-SW trending, vertical system of calcite filled fractures. This orientation is compatible with the NW-SE extension direction postulated for the formation of Culpeper and associated Early Mesozoic rift basins (Olsen, P.E. and Schlische, R.W., 1989). The length-aperture plot (fig.2. a.) shows a positive correlation with clustering of data near the origin. This clustering is seen in the plots for all data sets and reflects the greater frequency of small fractures, a consequence of the power-law size distribution typically observed for fracture populations (eg. Scholz and Cowie, 1990).

An outcrop of Upper Ordovician carbonates in the Ganister Quarry, Williamsburg, Pennsylvania, contains calcite, dolomite and quartz filled mode I fractures, in exposures of Coburn Formation limestone. Data was collected for all veins intersecting a 80 M^2 bedding plane. Since some veins showed evidence of shear deformation and/or crack-seal morphology (Ramsay, 1980), indicating incremental growth events, a subset of undeformed, single event fractures was selected from the larger data set. Formation of these NW-SE oriented, bedding perpendicular veins is consistent with strike parallel stretching of beds during Appalachian thrusting (Srivastava and Engelder, 1990). Length-aperture plots for both data sets are in fig. 2. b.

Mineralized fractures were measured on the horizontal, glacially polished surface of a post-Ordovician, mafic dike near Whitehall, New York. These joints do not effect the surrounding country rock but are restricted to the intrusion. Figure 2.c shows the length-aperture plot for this data set.

Horizontal beds of Late-Ordovician Cumberland Head Argillite and overlying Stony Point Shale are found in wave polished outcrops along the west shore of Lake Champlain near Plattsburgh, New York and on South Hero Island, Vermont. A system of vertical, N-S striking, calcite veins cuts both formations. Though the veins in this set consistently offset the first and most dominant cleavage in the rocks, they are offset by a later, less well developed widely spaced pressure solution cleavage, indicating syn-tectonic formation. The tectonic history of the Champlain Valley is complex and the significance of the veins orientation in relation to other tectonic structures is not clear (Fisher, 1968). The plot for this last data set is shown in fig. 2. d.

CONCLUSIONS AND RECOMMENDATIONS:

While all data sets show a positive correlation between length and aperture this relationship can be seen more quantitatively in fig. 3. Here the frequency distribution of aspect ratio for veins in all four data sets has been plotted. There is a strong peak, with an aspect ratio of $1x10^{-3}$ for 43% of the veins measured.

The length of veins measured in this study range from 7 to 8895 mm, covering almost three orders of magnitude in length. This range can be extended by three orders of magnitude with the addition of data from extensional igneous dikes in northwestern Iceland (Gudmundsson,1984). The difference in fracture filling materials (magma in dikes as opposed to water in veins) and the evidence for incremental growth, noted in some of the dikes, give cause for caution, yet in the logarithmic length-aperture plot of fig. 4 Gudmundsson's data helps to define a possible linear relationship in which: APERTURE = 10^{-3} x LENGTH.

Continued field work will concentrate on expanding the data set upward by locating more, longer fractures and downward by collecting samples for micro-crack examination. More three dimensional data will be recorded in order to determine if the preliminary indication that bedding perpendicular aspect ratios are larger than bedding parallel ratios is correct. Segmentation, spacing and profile information will be used to determine more accurately if

vein segments are individual veins or segments of a single vein connected at depth. This, as well as careful examination for indication of incremental growth will be used reduce scatter in the data sets.

REFERENCES:

Barton, C.C. and Larsen. E., 1985, Fractal geometry of two-dimensional fracture networks at Yucca Mountain, Southwest Nevada, in Proceedings, International Symposium on Fundamentals of Rock Joints, edited O. Stephansson p. 77-84, Centek Publishers, Lulea, Sweden.

Fisher, D.W., 1968 Geology of the Plattsburgh and Rouses Point, New York-Vermont, Quadrangles: New York State Museum and Science Service, map and chart series no. 10, p. 1-51.

Gudmundsson, A., 1984, Tectonic aspects of dykes in northwestern Iceland: Jokull, 34, p. 81-96.

Hirata, Takayuki, 1989, Fractal Dimension of fault systems in Japan: Fractal Structure in Rock fracture geometry at various scales: PAGEOPH, v. 131, no. 1/2, p. 157-1170.

Olsen, P.E. and Schlische, R.W., 1989, Tectonic history: in Tectonic, depositional, and paleocological history of Early Mesozoic rift basins, Eastern North America, eds. Olsen, P.E., Schlische, R.W. and Gore, P.J.W., Field trip guide book T351, American Geophysical Union, p. 12-14.

Ramsay, J.G., 1980, The crack-seal mechanism of rock deformation: Nature, v. 284, p. 135-139.

Scholz, C.H. and Cowie, P.A., 1990, Determination of total strain from faulting using slip measurements: Nature, v. 346, p. 837-839.

Srivastava D.C. and Engelder,T., 1990, P-T conditions for progressive development of a brittle-ductile shear zone in the Coburn Formation: Appalachian Valley and Ridge, Pennsylvania: preprint.

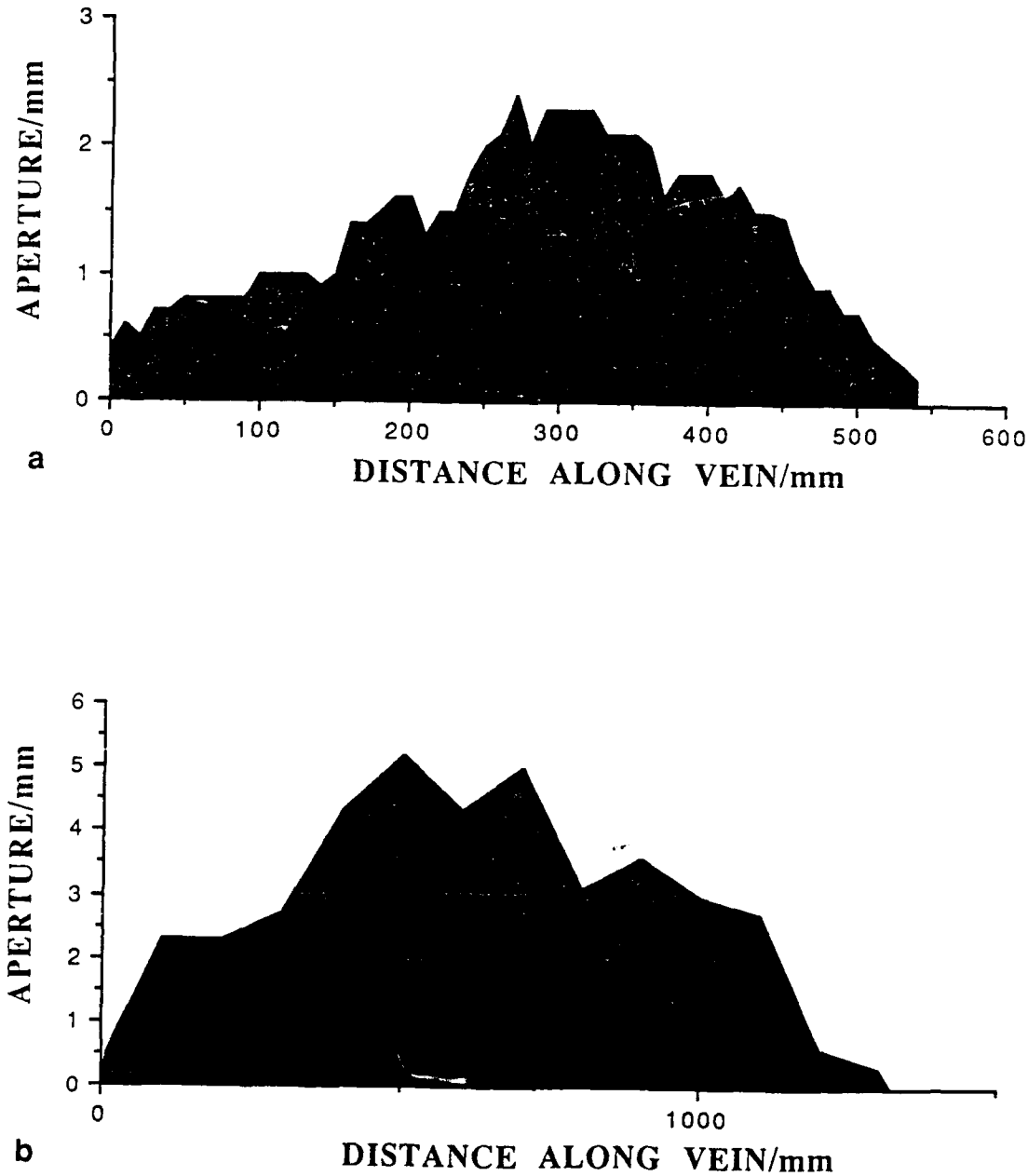


Fig. 1. Profile plots of two typical extension veins. a. Quartz vein in sandstone. b. Calcite vein in limestone. Note the vertical exaggeration.

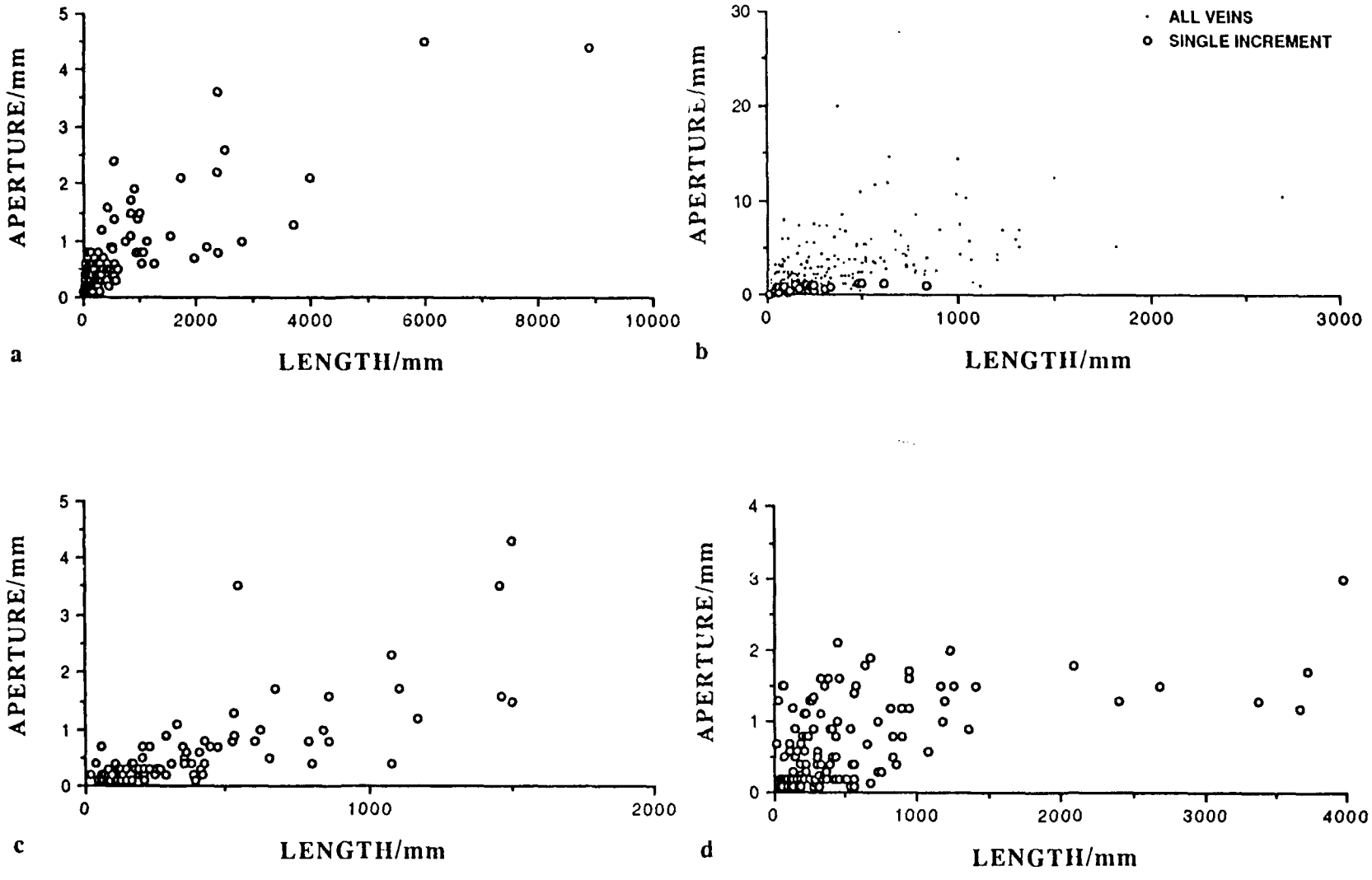


Fig. 2. Length-aperture plots for veins from: a. Culpeper Stone Quarry. b. Ganister Quarry. c. Whitehall dike. d. Lake Champlain.

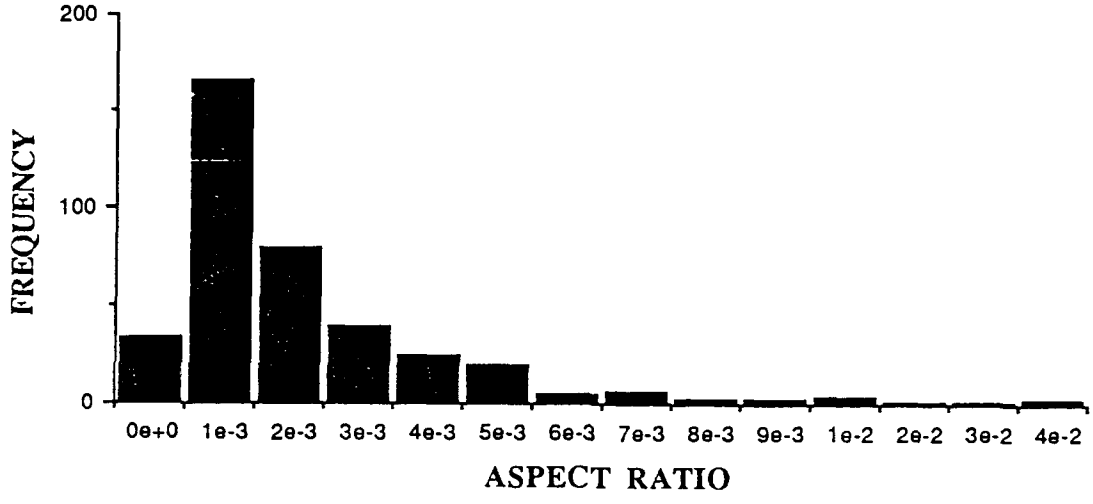


Fig. 3. Frequency distribution of aspect ratios for veins in the four locations discussed in the text.

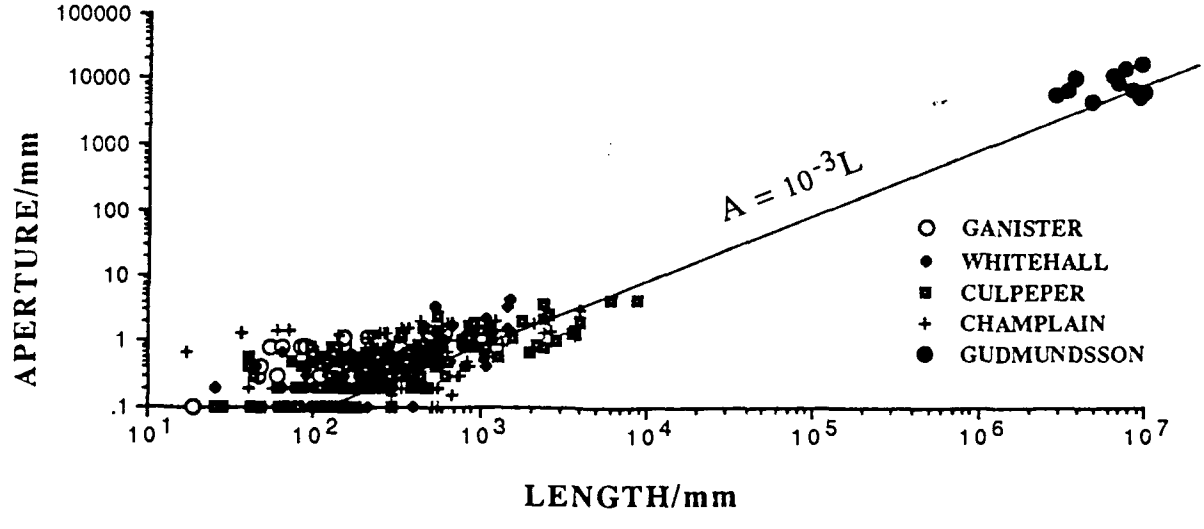


Fig. 4. Logarithmic plot of fracture length against fracture aperture for the four data sets discussed in the text along with Gudmundsson's data for Icelandic dikes.

ARRAY STUDIES OF SEISMIC SCATTERING

John E. Vidale
University of California at Santa Cruz
Contract F19628-89-K-0048
Objectives: Characterize scattering of seismic waves with dense arrays

Research Accomplished:

We are engaged in two projects. The first, which emphasized the strong effect of near-surface geology on the seismic wavefield, has been published in Vidale and Bonamassa (1991), Bonamassa et al. (1991), and Bonamassa and Vidale (1991). In this work, we find that the duration of ground motion, the amplitude of motion, and the direction of strongest motion depend on the observation point. We further find that the details of the seismic source are less important than the observation point in determining the ground motion, particularly the direction of strongest shaking. We find a transition at 1 Hz frequency (for propagation distances from 30 to 150 km in the San Francisco area), where at higher frequencies the above observations are valid, but at lower frequencies the seismic source is the main determinant of ground motion (Vidale, 1991).

The second half of our research is the study of large aperture array recordings. This project, which will require the assembly of seismograms from more than 1000 stations ranging from southern California to Alaska, is still in its infantcy. We present below an example of its potential (see Vidale and Benz, 1991 for more details). Once the assembly of data from the entire array is made routine, study of regional wave propagation and beamforming of teleseismic events can be conducted on an array of unprecedented aperture and station density.

Introduction

Our understanding of the constitution, convective pattern, and temperature field within the Earth's mantle is based on many kinds of evidence. Seismology, however, generally provides the highest resolution picture of the current state of the world. At least two depths within the mantle, 415 and 660 km, are known from seismology to be the location of transitions in rock properties. Near 415 km depth there is an about 5% increase with depth in seismic shear (S) and compressional (P) velocity and density, hereafter referred to as the "415", that is generally interpreted to signal the transition from olivine to the higher pressure phase spinel.

This section will focus on the "415". The majority of studies suggest that the olivine <-> spinel transition occurs near 400 km depth and accounts for the observed velocity increase at the "415". Some mantle geochemical models, however, suggest alternative interpretations for the "415". W expect from mineral physics studies that an equilibrium olivine <-> spinel boundary would be elevated because of lower temperatures by tens of km near subducting slabs (Akaogi *et al.*, 1989). Thus, a higher resolution measurement of the olivine-spinel boundary elevation near slabs can tell us the temperature in subducting material. It has also been proposed that the cold temperature in subducting material would kinetically inhibit the transformation, perhaps for the millions of years the slab requires to sink

to depths near the "660". Such a mechanism, which would depress the "415" elevation observable near subduction, would allow for the initiation of faulting by the phase transition as the sinking slab warms in the depth range 400 to 660 km (Green and Burnley, 1989).

We will show below that our observations support an elevated, not depressed "415", and support a relatively level, broad elevation consistent with the equilibrium phase transition prediction.

Seismological background

Seismic velocities increase rapidly with depth near 400 and 660 km depth. These features were first discovered by the investigation of body waves that turn near the depths of 400 and 660 km (Jeffreys, 1936). Shearer (1991) and others have produced precise and global measurements of these features with 25 to 100 sec period reflected waves, finding a prominent reflectors in the mantle at a depth of 415 km. The 150 to 1000 km wavelengths preclude either estimates of discontinuity sharpness or detailed study of depth variations near subduction zones, where temperature is expected to vary over short distances. Such studies cannot resolve topography on the "415", but shows that it is small at long wavelengths. The Fresnel zone of these waves on upper mantle layers is hundreds of kilometers.

Studies of traveltimes, reflected phases, S to P conversions from layers beneath the seismometer, and the reflected phase P'P' and its precursors have also been analyzed to learn the structure near 400 km depth (see Shearer (1991) for a summary), but have failed to resolve topography on the "415".

This study differs from previous work in the use of extremely low amplitude signals that are detectable only by analyzing many-element, wide-aperture array recordings. Since we examine individual earthquakes and find high-frequency mantle reflections that leave the source region in a fairly narrow cone of take-off angles, our measurements sample mantle structures with lateral sampling of tens of kilometers or less.

Data

We are currently examining seismograms from the 1980's recorded on the Northern California Seismic Network (NCSN) and University of Utah Seismic Station (UUSS) to characterize the arrivals that reflect from near 400 km depth. The NCSN data provides depths to a reflector near 400 km in 4 locations. We then reinterpret as reflections near 400 km depth 28 arrivals from 24 events timed by Lin (1974) from earthquakes between 1965 and 1973 recorded on the LASA array in Montana.

NCSN has more than 350 short-period vertical seismometers in central and northern California (Eaton, 1989). The array spans an area that is 900 by 250 km. Frequencies from 0.2 to well above 2 Hz are recorded with good signal-to-noise. The UUSS adds more than 60 stations, and extends the long axis of the array to 1500 km. Although no examples of UUSS data are presented in this report, its addition appears to double the slowness resolution in the slant-stacks. Our slant stacks have 3 times better resolution (about 0.002 sec/km) at 1 Hz than LASA Vespagrams (found in Lin, 1974, for example,) due to the unprecedented aperture. We expect

further improvement with the addition of the short-period, vertical arrays from Nevada, Southern California, Washington, and Alaska.

With so many stations and such a large aperture, we can nearly eliminate the energy scattered near the stations by stacking in search of incident plane waves, as described below. The scattering near the source is also minimized by considering the part of the wavefield from deep earthquakes before pP, which is the earliest arriving energy scattered off the Earth's surface above the earthquake.

We start the processing by anti-alias filtering the NCSN records, which are digitized at 100 samples per second, and resampling at 2.5 samples per second. We resample because it is difficult to align traces at high frequency, there is little energy above 2 Hz in these teleseisms, and the size of the data files is cumbersome. Then, we visually examine every trace and reject the 20-60% that are too noisy, very dissimilar to nearby stations, or reversed in polarity. A time in the P arrival is picked, either the onset time or a prominent early peak, depending on the character of the earthquake. Finally, the traces are shifted in time so that the picked phase arrives at the same time for all traces, normalized to a peak amplitude of unity, and slant-stacked to search for plane wave arrivals.

Figure 1 shows the slant stack of an event near 481 km depth in the Bonin subduction zone. For clarity, this figure shows the logarithm of the envelope of the true slant stack. This is one of the cleanest events we have examined since the direct (downgoing) P wave is much weaker than the upgoing P and S waves that scatter above the event, so the scattering locally generated around the array from the direct P wave is also weak. Two clear, early arrivals appear, one 20 sec and the other 32 sec after the P wave. Two additional arrivals also appear 50 and 60 seconds after the P wave, but these arise either from layers in the upper 300 km or completely unexpected structures. These arrivals must be P waves, since they are vertical motions, emanating from the region of the earthquake, and arriving just after the direct P wave. These arrivals are most likely S-to-P conversions. The next likeliest alternative is P-to-P reflections, but the S-to-P conversions are expected to be three times larger since the conversion coefficient is similar while earthquakes radiate much more S wave energy.

Figure 2 shows the stacked waveforms of the direct P wave, the surface reflection pP, and the S-to-P conversions from the "415" and the "660". Note that the two phases which initially leave the source upward, pP and s360P, have similar waveforms, as do the two that leave downwards, P and S670P. These similarities in waveform argue against aftershocks causing the arrivals labeled S670P and s360P. Note the very small amplitude in the mantle reflections, which necessitated many widely spaced seismometers to suppress the noise.

Inspection of Figure 1 shows that the 20 sec arrival has a slowness that is less than the direct P wave, while the 32 sec arrival has a slowness about one third of the way from P to pP. As shown in Vidale and Benz (1991), the likely 32 sec reflector is nearly horizontal and at 360 km depth. The reflector cannot dip more than 15°. A dip on the reflector will result in our underestimating the depth of the reflector, but this is a small effect. A similar analysis shows that the 20 sec arrival is probably due to an S-to-P conversion in transmission through a horizontal boundary at 670 km

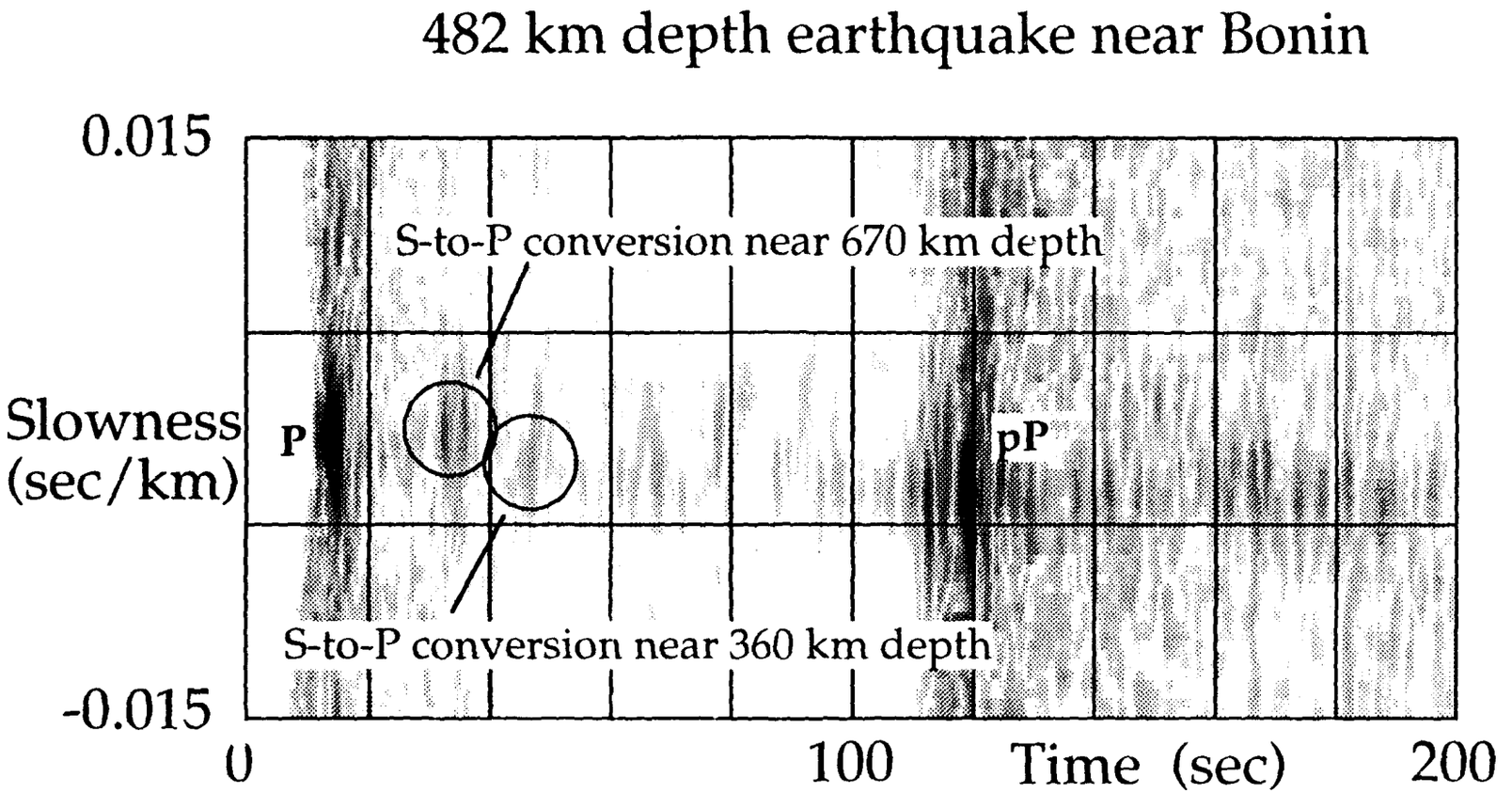


Figure 1. Slant stack of April 3, 1985 earthquake, which occurred at 482 km depth beneath the Bonin Islands. 254 NCSN seismograms are aligned on the P wave, decimated to 2.5 samples per second, and stacked for delay times ranging from before P until after pP, and for a range of slownesses ranging from more steep angles of incidence than the P arrival to more shallow than pP. The envelopes of the stacks are shown. Darker color indicates more energy in the stack, but both P and pP are clipped. Note, for example, that pP arrives 106 sec after P and differs in slowness across the array by 0.003 sec/km. This difference in slowness corresponds to a difference in angle of incidence of about 1°, or a difference of 3 sec between the pP minus P times at the opposite ends of the NCSN array. Such array recordings of distant earthquakes may reveal subtle features of the crust, mantle, and core of the Earth.

depth. The rest of this section will focus on the reflections from near 400 km depth, except to note that conversions from near 670 are often observed in our slant stacks.

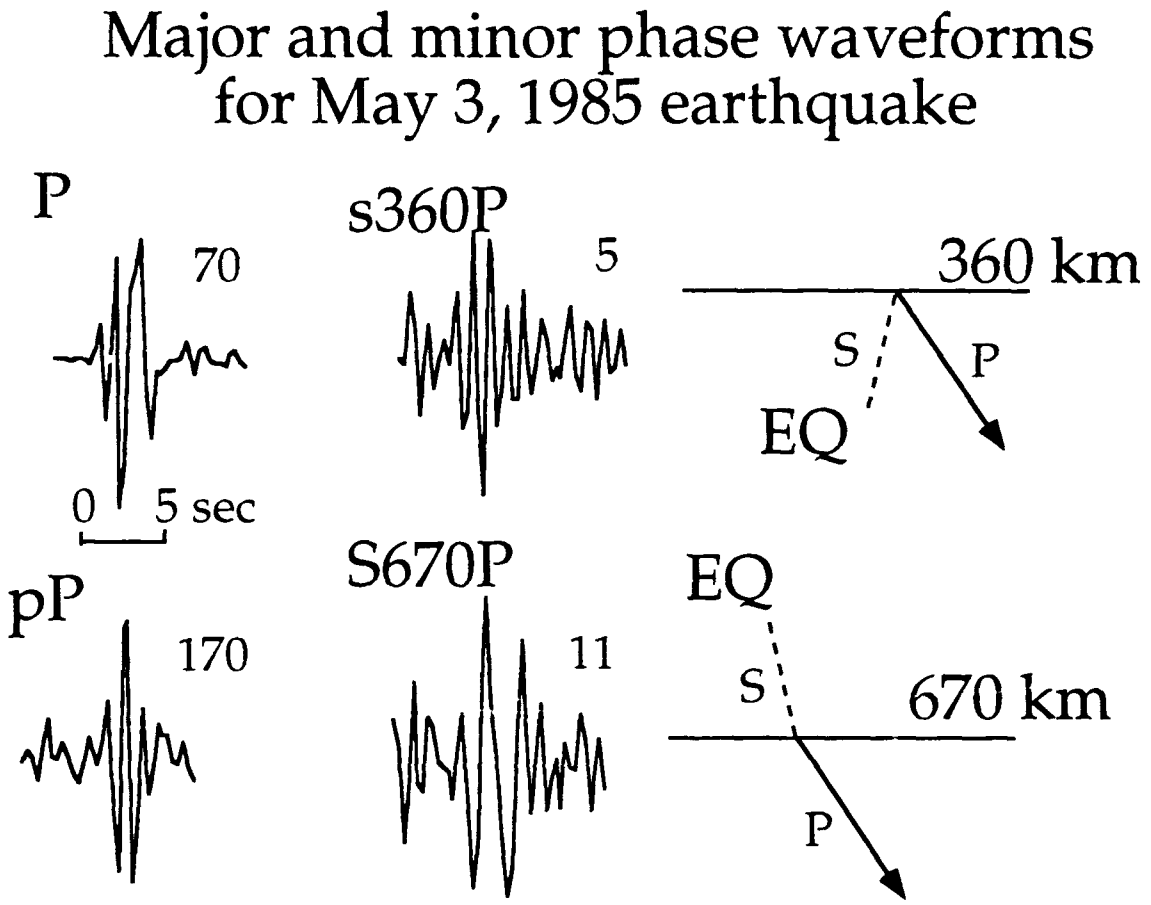


Figure 2. The stacked waveforms of P, pP, S670P, and s360P. The peak amplitude in each phase is shown to the upper right of each trace.

Since the differential time between P and the reflected phases is precisely known, and the seismic velocity profile between the earthquake and the reflector is fairly well known, most of the uncertainty about the depths of the reflectors arise from uncertainty about the depth of the earthquake itself. We restrict our study to events for which ISC pP-P depth measurements (~15 km uncertainty) are available. Unfortunately, ISC pP-P depths are available for only four of the NCSN events, although this reflection from near 400 km depth is present for most of 16 NCSN recordings we have examined.

Lin (1974) has made similar measurements. He noticed that reflected energy is present between P and pP for deep earthquakes by examining seismograms from the LASA array for earthquakes from 1965 to 1973. He interpreted the arrivals as P-to-P reflections, which placed the reflectors much shallower. However, as we discussed above, S-to-P conversions are a more likely explanation.

Figure 3 shows the depths for 4 events captured by NCSN and 24 by LASA. There is a clear peak in the 350 to 375 km depth range, although a significant number of

normal mantle (Akaogi, 1989). Our observation points range from the middle of the seismicity at 400 km depth to about 200 km to the side of the seismicity. However, the earthquake depth uncertainty precludes the interpretation of differences in reflector depth with distance from the slab, with age of the subducting lithosphere, or age of the subduction zone without further study.

Mineral physics experiments suggest that the conversion from olivine to spinel is kinetically hindered at temperatures below 520 to 900° C, at least on laboratory time scales (Sung and Burns, 1976). Some seismic studies suggest that this transition is depressed near slabs, others suggest that it is elevated. Our observations of a transition generally elevated by 30 to 60 km suggests that olivine can convert to spinel at temperatures more than 500° C colder than ambient mantle (Akaogi, 1989). It is still possible that isolated pockets of olivine remain untransformed, or a very cold center of the slab forms a thin, untransformed tongue of metastable olivine. However, if laboratory estimates of the Clapyron slope are accurate, olivine can transform at a temperature several hundred degrees colder than ambient mantle.

Recent work suggests that the olivine-to-spinel transition may initiate and lubricate deep earthquakes, overcoming the high friction theoretically expected to prevent seismic faulting (Burnley and Green, 1989). Our results preclude models that predict olivine metastability at temperatures only 100 or 200° colder than the normal mantle geotherm, and require either extreme temperature contrasts or some compositional or grain-size influence on metastability for the penetration of olivine to the depths of the deepest earthquakes, which is unlikely.

References

Akaogi, M., E. Ito, and A. Navrotsky, 1989. Olivine-modified spinel-spinel transitions in the system Mg_2SiO_4-$FeSiO_4$: Calorimetric measurements, thermochemical calculations, and geophysical applications, *J. Geophys. Res.*, **94**, 15,671-88.

Bonamassa, O., J.E. Vidale, 1991. Observations of directional site resonances from the Loma Prieta earthquake sequence, in press, *Bull. Seism. Soc. Am.*

Bonamassa, O., J.E. Vidale, H. Houston, and S.Y. Schwartz, 1991. Directional site resonances and the strong influence of near-surface geology on ground motion, *Geophys. Res. Lett.*, **18**, 901-904.

Eaton, J.P., 1989. Dense microearthquake network study of northern California earthquakes, in *Observational Seismology*, J.J. Litehiser, ed., University of California Press, Berkeley, 199-224.

Green, H.W., and P.C. Burnley, 1989. A new, self-organizing mechanism for deep-focus earthquakes, *Nature*, **341**, 733-737.

Lin, M.T., 1974. Reflectors in the upper mantle above the deep earthquakes, Master's Thesis, Massachusetts Institute of Technology, 124 p.

Richards, M.A. and C.W. Wicks, Jr., 1990. S-P conversion from the transition zone beneath Tonga and the nature of the "650 km" discontinuity, *Geophys. J.*, **101**, 1-35.

Shearer, P., 1991. Constraints on upper mantle discontinuities from observations of long-period reflected and converted phases, in press, *J. Geophys. Res.*

Sung, C.M., and R.G. Burns, 1976. Kinetics of the olivine-spinel transition: Implications to deep-focus earthquake genesis, *Earth Planet. Sci. Lett.*, **32**, 165-170.

Vidale, J.E., 1991. Strong path effects on the way from Loma Prieta to San Francisco, in preparation for USGS Professional Paper on the Loma Prieta Earthquake.

Vidale, J.E., O. Bonamassa, and H. Houston, 1991. Directional Site Resonances Observed from the 1 October 1987 Whittier Narrows Earthquake and the 4 October Aftershock, appeared in February, 1991 issue of *Earthquake Spectra*.

Vidale, J.E., and H Benz, 1991. High-resolution sounding of the "415" km depth seismic reflector: A sharp, elevated boundary near subduction Zones, submitted to *Nature*.

Composition of Short-Period Regional Phases Inferred from Fennoscandian Array Data

Kristín S. Vogfjörd, Ben Yan and Charles A. Langston
Department of Geosciences
Pennsylvania State University
University Park, PA 16802

Contract No. F19628-90-K-0044

Objective:

The general objective of the study is to understand the composition of short-period seismograms from regional events. Timing, amplitude and phase velocities of the dominant phases observed on regional seismograms are influenced by crustal and upper mantle structure. In order to properly identify these dominating phases in the seismograms, and thus reliably locate local and regional events, the gross crustal and upper mantle structure around the recording site must be obtained. By studying regional events at various distances and backazimuths from the recording site, critical information is obtained which can then be used to reliably locate future events and determine source depth. Receiver function analysis of teleseismic events can also aid in identifying velocity contrasts under the recording site. The focus of the present study are events from local and regional distances recorded at the ARCESS array, and teleseismic events recorded at NORESS and ARCESS.

Research Accomplished:

Thirty three events at regional distances from ARCESS have already been chosen from the IMS bulletin at CSS, based on location and magnitude. The events range in local magnitude (*Ml*) from 2.0 to 3.2, and in distance from 190 to 510 km. Event locations are shown in Figure 1.

Phases in the Seismograms are identified with f-k analysis in sliding time windows, beams are formed for the major phases, and time sections of the beams then pieced together to form a composite seismogram for each event. By plotting the events in record sections, as a function of distance the moveout and phase velocity of the various phases can be observed and identified. Travel-time curves calculated for the major turning and reflecting crustal waves, P_g, S_g, P_mP, S_mS, $2\times P_mP$, and $2\times S_mS$, as well as for the upper mantle waves, P_n and S_n, aid in identifying the phases. The starting velocity model for the crust and upper mantle is based on the average structure under the northern end of the POLAR Profile shown in Figure 1 (Luosto et al., 19[illegible]); the crust is assumed 42-km thick. The P-wave velocity structure is plotted in Figure 2. S-wave velocity is assumed $1/\sqrt{3}$ of the P-wave velocity. A record section of three events located on the Kola peninsula is shown in Figure 3, together with travel-time curves for the major phases of the POLAR-Profile model. Phase velocities of the dominant phases, used to form the beams, are indicated above each trace.

At 200 km distance the seismogram is dominated by Moho reflections (P_mP, S_mS) and waves turning in the lower crust, while at 350 and 400 km distance, the double Moho

reflections ($2\times P_mP$, $2\times S_mS$) and turning waves dominate. The apparent absence of P_mP at 350 and 400 km distance is probably due to the high velocity gradient at the base of the crust (Figure 2), causing most of the energy of P_mP and S_mS to be concentrated around 200 km distance. Waves from the upper mantle (P_n, S_n) probably arrive ahead of the crustal waves at 200 km distance, but can not be discerned. At 350 and 400 km however, P_n is a clear first arrival and both P- and S-wave amplitudes of the upper mantle phases are significant. R_g is clearly detected at 200 and 400 km distances, but is absent or of small amplitude in the event at 350 km distance.

Phase velocity at the dominant frequency in the R_g wave is 3.2 km/s, reflecting the average velocity in the top 3 km of the crust. Phase velocities of the upper mantle waves, are lower than predicted by the model. This may indicate a down-dip in the Moho interface towards ARCESS. Undulations on the order of a few kilometers were observed on the POLAR profile (Luosto et al., 1989). Variations in backazimuth among the phases of the two farthest events also suggest an undulating Moho.

Parameter data (phase velocities, relative travel times) from events around NORESS, located by IMS suggests that misidentified phases and missed detection of P_n is still causing mislocations of local and regional events in southern Norway. A previous study of regional events around NORESS, recorded prior to the istallation of the Intelligent Monitoring System, revealed such mislocations (Vogfjörd and Langston, 1991). A closer look at the few IMS-waveform data available from the region may confirm this.

Structure directly under NORESS and ARCESS is being investigated using the receiver function technique and f-k analysis of coda from teleseisms. The receiver function technique is described by Langston (1979) and Owens et al. (1987), among others. The principal idea is to observe S-to-P conversions on the horizontal components of the teleseismic P wave to infer velocity contrast, and if an estimate of absolute velocity is available, depth to the conversion interface. When used with broad-band data, a source equalization technique is performed by deconvolving the vertical component of motion from the radial component. This removes the common effect of the instrument response and effective source function. Resulting Sp conversions on the deconvolved radial component are then modeled.

Some broad-band, three-component, teleseismic waveforms recorded at the NRE0 element of the NORESS array, have been collected. The data are from events of $Mb \geq 6.0$, at epicentral distances of 30° to 90°, recorded during the time period of January, 1984 to December, 1988. The data were selected from both the CSS and NRSS databases, and NEIC event CD-ROMs. Table 1 lists the event information and Figure 4 shows the distribution map of these events.

More recent teleseismic data (from January, 1989 to June 30, 1991) are being collected. We have searched the NEIC/PDE bulletins for data which satisfy the above criterion. Waveform data from the E0 element at NORESS and ARCESS are not yet available from CSS. In the meantime, we have requested the data directly from Norway. Once available,

these data will also be used in the receiver function analysis.

Conclusions and Recommendations:

From the regional events studied so far it is evident that crustal and upper mantle structure near ARCESS differs from the structure near NORESS. The velocity gradient above and below the Moho appears higher near ARCESS, than near NORESS, and the crust is also thicker in northern Fennoscandia. Undulations in the Moho interface near ARCESS are apparent from the backazimuths and phase velocities of the Moho reflections and the upper mantle waves. Events at distances ≤ 190 km from ARCESS are needed to constrain structure within the crust. The ARCESS database will be searched for such events.

Current practice at CSS is to save waveform files from the arrays for events greater than *Ml* 2.0. With the possibility of mislocations, and the small number of events near NORESS with *Ml*≥2.0, we suggest that all IMS-located events be saved for further refinement of phase interpretation and source location.

References

Langston, C. A. (1979). Structure under Mount Rainier, Washington, inferred from teleseismic body waves, *J. Geophys. Res.*, **84**, 4749-4762.

Luosto, U., E. R. Flueh, C.-E. Lund and Working Group (1989). The crustal structure along the POLAR Profile from seismic refraction investigations, *Tectonophysics*, **162**, 51-85.

Owens, T. J., R. Taylor and G. Zandt (1987). Crustal structure at regional seismic test network stations determined from inversion of broadband teleseismic P waveforms, *Bull. Seism. Soc. Am.*, 77, 631-662.

Vogfjörd, K. S. and C. A. Langston (1991). Analysis of regional events recorded at NORESS, *Bull. Seism. Soc. Am.*, **80**, 2016-2031.

Table 1.

Selected Events for Mb>=6.0 and
distance 30° ~ 90° from NORESS

Date	Time UT	Latitude deg	Longitude deg	M_b	Depth km	Distance deg	Back Azimuth deg
1984 12 02	06:20: 40.8	20.357	-115.765	6.0	10.	88.8	311.7
1984 12 28	10:46: 13.5	56.194	163.460	6.2	33.	61.3	17.5
1985 10 05	15:31: 21.3	62.237	-124.266	6.5	10.	52.8	335.8
1985 12 23	05:23: 22.5	62.222	-124.239	6.4	6.	52.8	335.8
1986 06 11	13:48: 03.3	10.602	-62.949	6.0	34.	73.2	261.6
1986 06 19	09:09: 12.3	56.418	-152.729	6.0	33.	62.5	350.2
1986 06 20	17:12: 46.5	31.221	86.862	6.0	33.	56.2	85.6
1986 06 24	02:53: 09.4	34.733	140.502	6.1	48.	76.1	41.3
1986 07 07	16:26: 56.9	10.421	56.764	6.4	10.	60.2	126.4
1986 07 21	14:42: 26.6	37.537	-118.447	6.0	9.	73.9	320.7
1986 08 26	09:43: 4.2	37.686	101.412	6.1	33.	57.9	69.4
1986 11 14	21:20: 4.7	23.963	121.817	6.1	33.	78.7	61.1
1987 03 21	10:50: 35.3	52.008	-177.444	6.0	97.	67.4	6.0
1987 05 07	03:15: 15.5	46.740	139.230	6.0	430.	64.8	37.0
1988 02 07	18:15: 05.6	50.785	173.465	6.2	33.	67.9	12.3
1988 02 24	03:52: 03.2	13.477	124.616	6.0	25.	89.2	63.5
1988 02 29	05:31: 41.4	55.149	167.430	6.1	33.	62.9	15.3
1988 03 06	22:35: 38.1	56.953	-143.032	6.8	10.	61.0	344.4
1988 03 10	06:17: 23.3	10.402	-60.587	6.2	56.	72.3	259.4
1988 03 21	23:31: 21.6	77.601	125.451	6.0	10.	36.2	19.6
1988 03 25	19:36: 46.4	62.154	-124.182	6.1	10.	52.9	335.7
1988 04 03	01:33; 05.8	49.917	78.945	6.1	0.	38.1	75.1

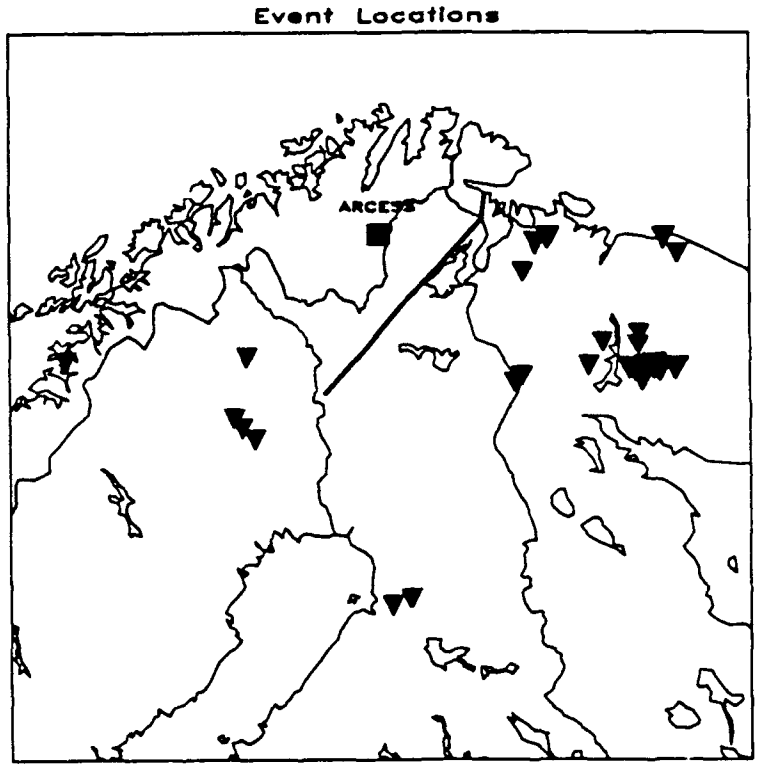


Figure 1 Map showing location of events with respect to ARCESS. The thick line shows the location of the POLAR profile.

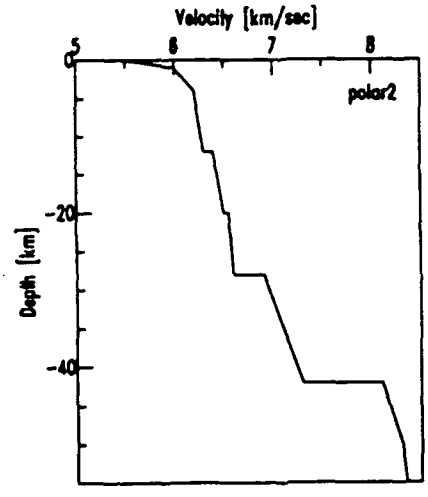


Figure 2 Average P-wave velocity model for the northern part of the POLAR profile.

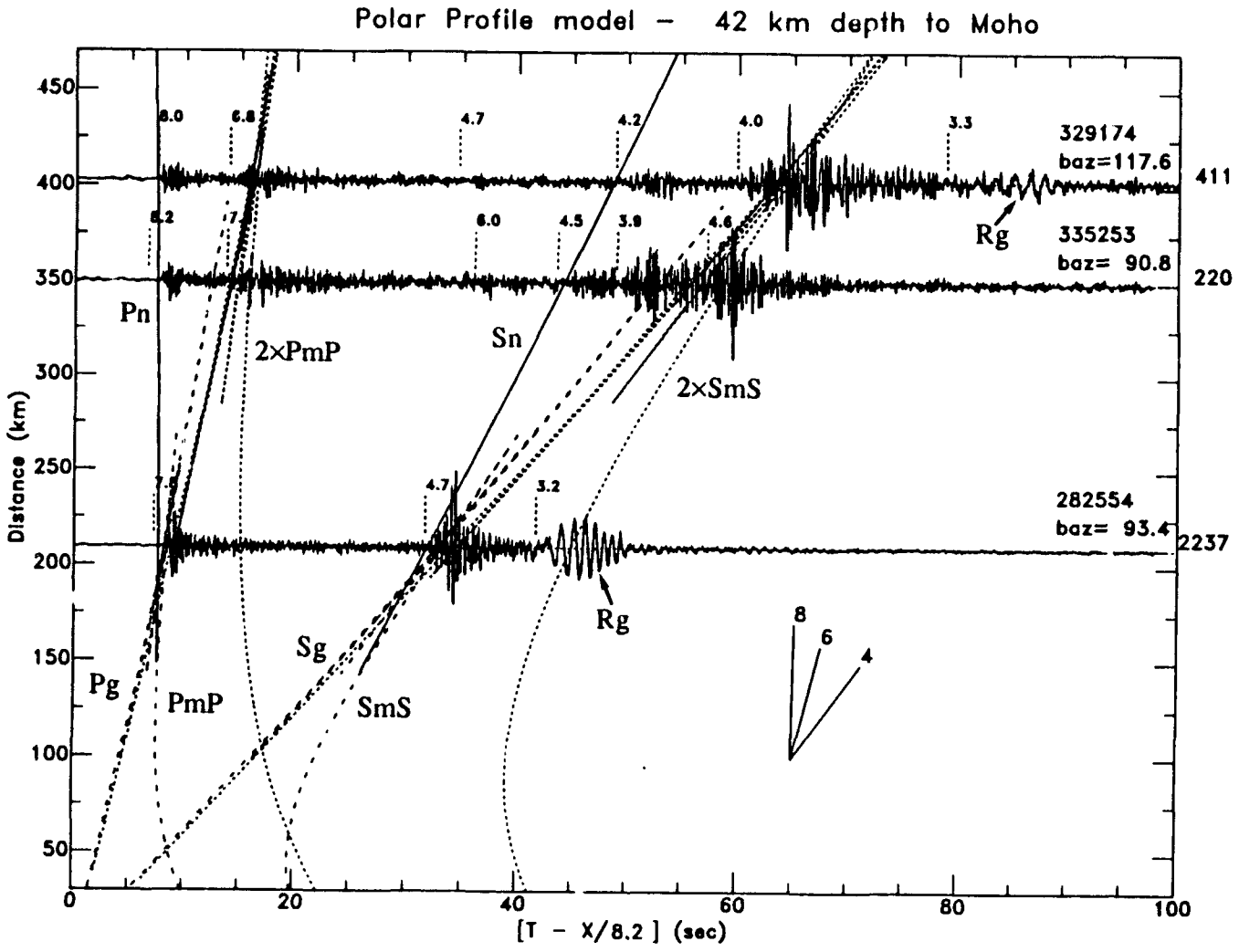


Figure 3 Composite seismogram for three events on the Kola peninsula, plotted at their respective source distances; backazimuth is shown above each trace. The seismograms are normalized to their maximum amplitude, which is shown at the end of each trace. Stacking velocities of individual beams in the composites are indicated. Travel-time curves for the major phases in the POLAR profile model are overlaid on the record section. Phase velocities on the travel-time curves can be read from the velocity template.

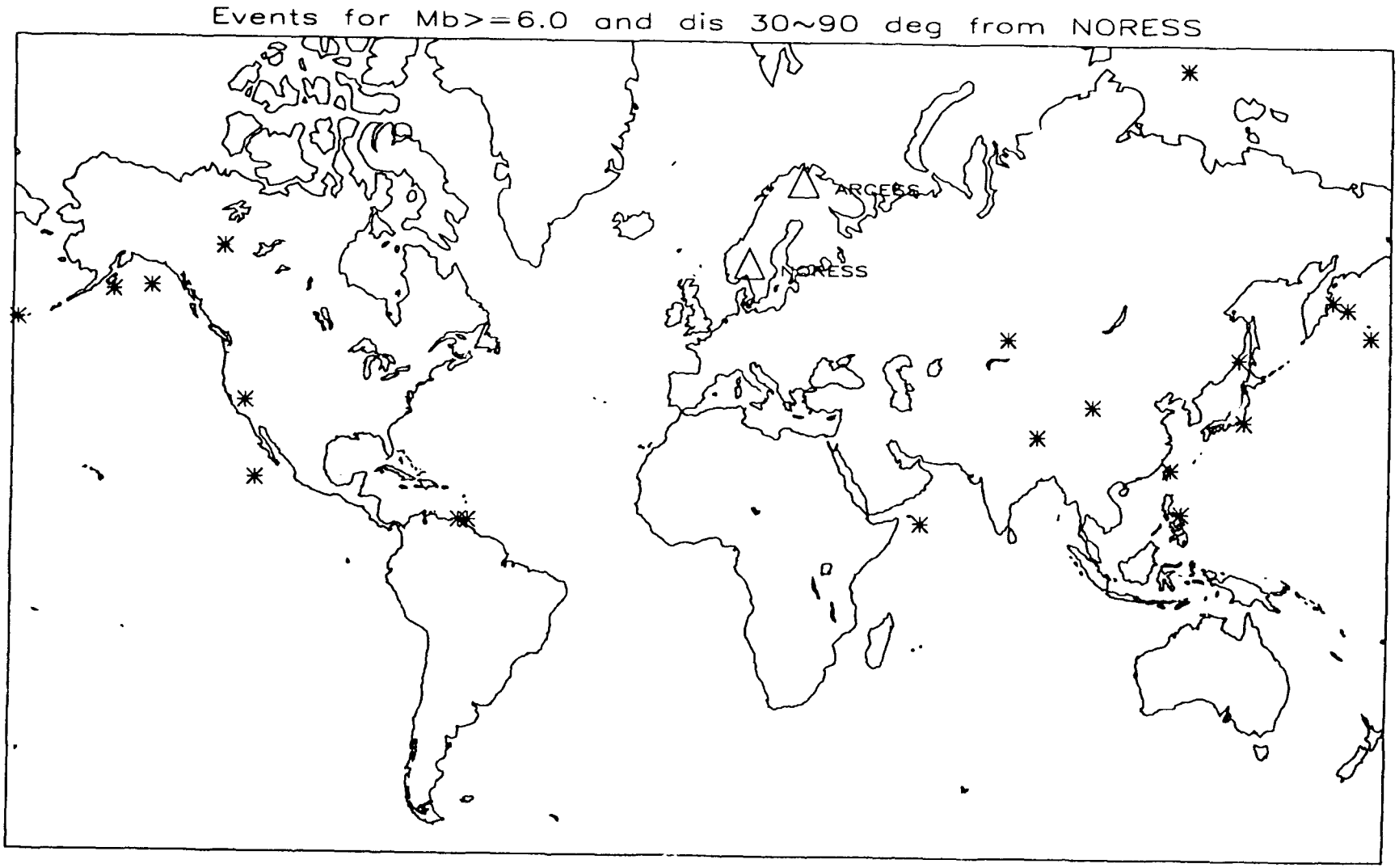


Figure 4 Map showing teleseismic events used for receiver-function studies.

Theoretical Studies of Scattering for Teleseismic P waves and Regional S waves

Gregory Wagner, Robert Clouser and Charles Langston
Department of Geosciences
Pennsylvania State University
University Park, PA 16802

Contract No. F19628-89-K-0013

Objectives

The source of seismic coda and its characteristics are controlled by scattering processes within the lithosphere. Teleseismic P wave coda generation is studied by using 2D finite difference solutions to the acoustic and elastic wave equations for models simulating a scattering crust over a homogeneous elastic halfspace. These simulations were performed to determine the relationship between types of stochastic structure models and resulting coda decay rates and coda levels. Observation of coda decay rate and level may yield information on the distribution and character of scatterers within the lithosphere. Teleseismic P waves recorded at NORESS were examined to examine the nature of scattering under the array. Research on scattering from irregular boundaries between homogenous layers was performed to investigate this alternative scattering mechanism in heterogeneous media.

Research Accomplished

A complete statistical description of a randomly varying media can be obtained by specifying a correlation function, correlation distance and a standard deviation of the velocity perturbations. A total of more than 150 acoustic and elastic models of a scattering layer over homogeneous halfspace were constructed to investigate scattering of teleseismic P. The basic wave geometry consisted of an incident P plane wave under the scattering layer. Velocity perturbations within the scattering layer consisted of both isotropic and anisotropic distributions of scatterers. Scatterer anisotopy was specified by allowing the vertical and horizontal correlation distances to be different.

Figure 1 shows three realizations of velocity models used in the finite difference calculations. The figure shows a gradation in scatterer geometry from a nearly isotropic distribution of scatterers to one where the media appears to be nearly plane-layered. Acoustic synthetic seismograms were computed to investigate coda where the wave propagation is relatively simple. Elastic models were investigated to understand the interaction of P and S waves in random media. The basic observables that were studied were the decay rate and level of coda behind the direct P arrival. These are the robust observables in studies of real seismic data. In particular, we wanted to find out how the scattering parameters of the medium

affected coda decay rates. Coda decay rate has been related to both scatterer density and anelasticity. We wanted to find out if scatterer geometry was also important.

Figures 2 and 3 show the results of all the acoustic and elastic finite difference calculations for coda decay rate (log amplitude per second) and level (log amplitude relative to the direct wave amplitude). The principal result was that coda decay rate was largely independent of the amplitude of scatterers for isotropic distributions of scatterers. It was also independent of layer thickness, contrary to the behavior of plane waves in 1D scattering media. Remarkably, scatterer anisotropy was found to be the largest factor in controlling coda decay rates. The rate of coda decay increased when the media became more anisotropic approaching plane layered structure. This effect can mimic the effect of anelasicity but is due only to the scattered field being radiated into the halfspace. Coda levels were primarily affected by how close the wavelength of the incident wave was to the scatterer correlation distance and by scatterer amplitude.

Frequency-wavenumber analysis of the elastic case synthetic seismograms showed that P-to-S and P-to-Rayleigh scattering into the horizontal direction were important for isotropic distributions of scatterers. As the media became anisotropic (more plane layered), vertically propagating body waves became dominant. These observations suggest that the degree of scatterer anisotropy can be inferred from array observations. These results are described in detail in Wagner and Langston (1991a).

Teleseismic NORESS array data were investigated to study coda. It was found that stucture near NORESS appeared to be plane layered-like except for a discrete P to Rg conversion which was caused by topographic scattering near Lake Mjosa (Wagner and Langston, 1991b).

Since complete regional seismograms can be constructed from a sum of plane waves, it is helpful to first examine scattering effects on plane waves. The scattering theory employed for irregular interfaces is the scalar T-matrix, or extinction theorem, method applied to scattering from periodic interfaces (Waterman, 1975). For plane SH-waves with displacement parallel to the 2D periodic interface corrugation direction, the problem is totally scalar. This method has been applied to SH-wave propagation in a layer-over-halfspace earth model by Varadan et al. (1987) for a sinusoidally undulating free surface.

This approach assumes a plane wave decomposition of the incident and scattered fields above and below the scattering interface. Figure 4 shows the problem geometry and parameters. The scalar coefficients for the reflected and transmitted field expansions are expressible, after utilization of Huygens' principle, interface periodicity, and boundary conditions, as integrals of the surface field and normal gradient over the interface. These being unknown, they are expanded in a set of plane wave basis functions, yielding another set of coefficients. The type of expansion employed here limits the maximum interface slope that can be modeled to less than 0.448 (Millar, 1969).

We investigate some reflected and transmitted seismograms computed for a Moho-type welded interface. Medium parameters are given in Figure 4. The incident wave for the synthetics has a Ricker wavelet time history with a peak frequency of 0.25 Hz. Figure 6 show the reflected (plus incident) and transmitted

waveforms for an incidence angle 20°, as recorded by horizontal lines of receivers above and below the interface. The reflected pulse varies noticeably in amplitude, being largest over the "valleys" , due to focussing. There is also a slight reflected wave time delay. It arrives about 1.8 sec later, relative to the incident wave, under the "valley". Post-reflected wave coda also becomes important with the specular reflection being "lost" at most receivers.

Figure 6 also shows results for an angle of incidence of 60°, which is post-critical. More interesting is the transmitted wavefield. The amplitude of the "transmitted" evanescent wave for a planar interface is about 0.025 at 30 km below the interface, and is severely depleted in high frequencies relative to the incident wave. However, the transmitted maximum amplitude is about 0.1, about 4 times the planar value. What this implies is that, for post-critical reflections from irregular interfaces, energy partitioning is severely perturbed from the planar boundary case. This would distort the spectral content of the reflected wave, and lead to "leakage" of energy into the lower medium. As a result, spectra of guided regional phases in the crust will be affected in a manner not predicted by planar interface theory. Figure 5 shows the energy partitioning of reflected and transmitted fields for the two cases of angle of incidence. Note the equal partitioning of energy at high frequency for the post-critical case.

Conclusions and Recommendations

P wave coda decay rate can be controlled by scatterer anisotropy, with large decay rates associated with highly anisotropic (near plane layered) structure. Coda levels are sensitive to the match between incident wavelengths and media correlation distances and perturbation amplitude. Irregular interfaces serve to produce leaky waveguides. This will affect attenuation of the Lg wave at regional distances.

References

Wagner, G.S., and C.A. Langston(1991a). Scattering effects for teleseismic plane wave propagation in a heterogeneous layer over a homogeneous half-space, Geophys. Joun. Int., in press.

Wagner, G.S., and C.A. Langston(1991b). Body-to-Surface wave scattered energy in teleseismic coda observed at the NORESS seismic array, Bull. Seism. Soc. Am., in press.

Millar, R. F. (1969). On the Rayleigh assumption in scattering from periodic surfaces, Proc. Camb. Phil. Soc. 65, 773.

Varadan, V. K., A. Lakhtakia, V. V. Varadan, and C. A. Langston (1987). Radiation characteristics of elastodynamic line sources buried in layered media with periodic interfaces. I. SH-wave analysis, Bull. Seism. Soc. Am., 77, 2181.

Waterman, P. C. (1975). Scattering by periodic surfaces, Acoust. Soc. Am., 57, 791.

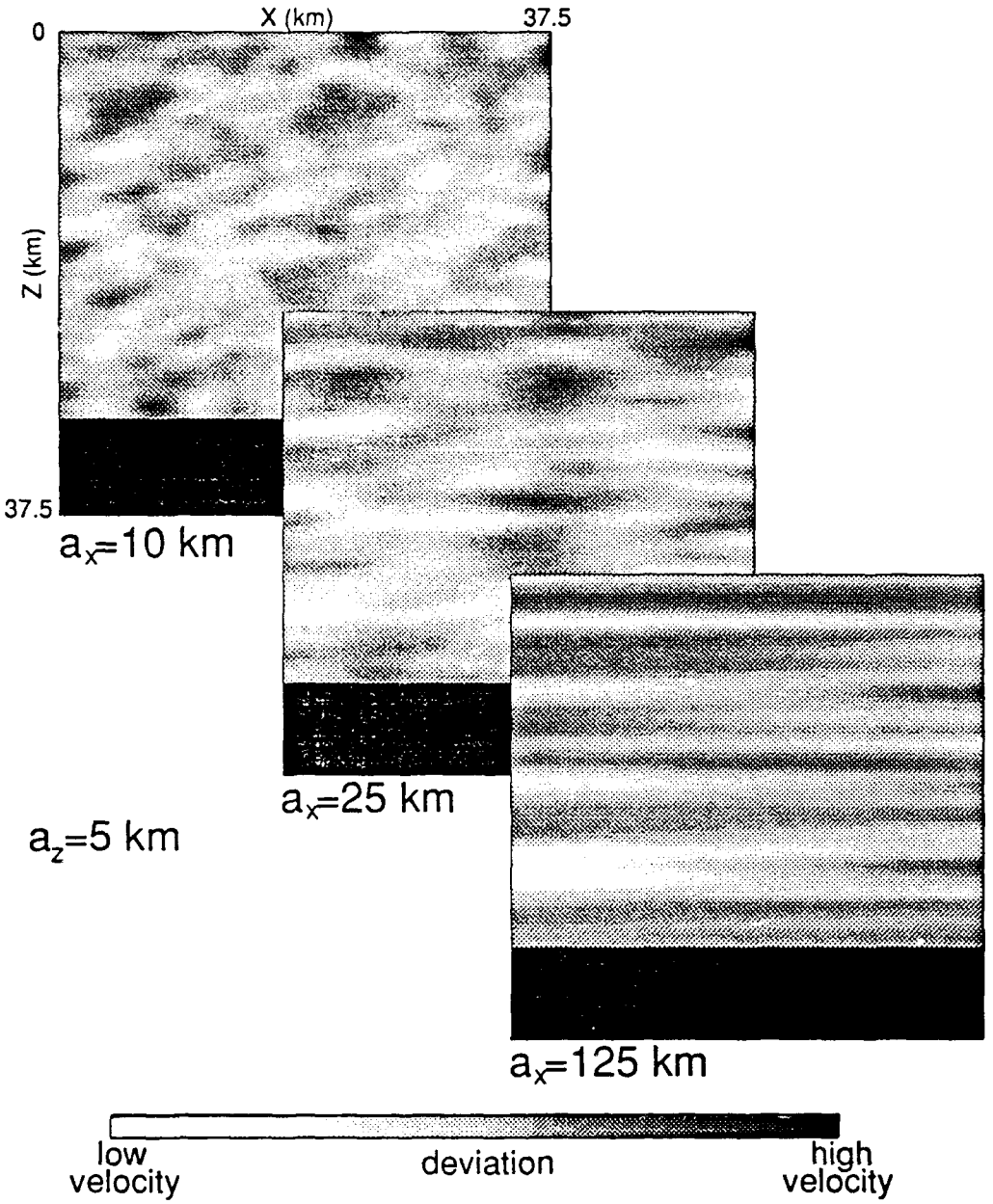


Figure 1: Spatially anisotropic velocity perturbations generated using an anisotropic Gaussian correlation function. All three models use a_z=5 km and a_x=10, 25 and 125 km.

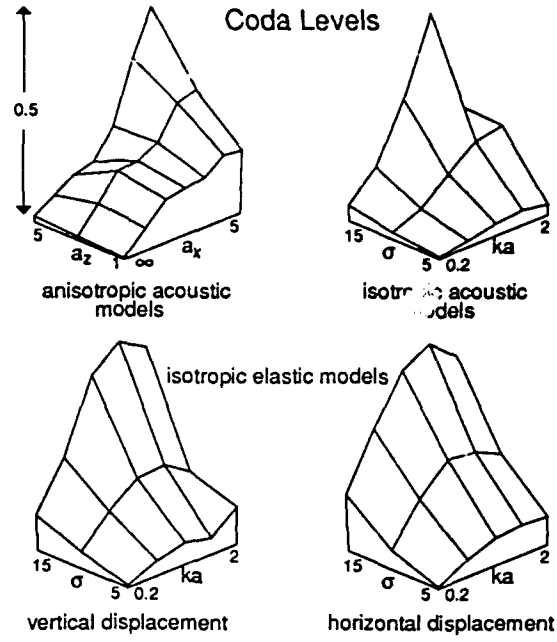


Figure 2 : Relative coda levels for a large range of models. The spatially isotropic heterogeneity plots are for 1 Hz data for a 30 km thick scattering layer. The anisotropic data are 1 Hz pass-band data for a model with 10% standard deviation and a 30 km thick scattering layer; ka is the normalized wavenumber, a_x and a_z are the correlation distances in x and z, respectively (in km), and σ is the standard deviation in percent of the mean.

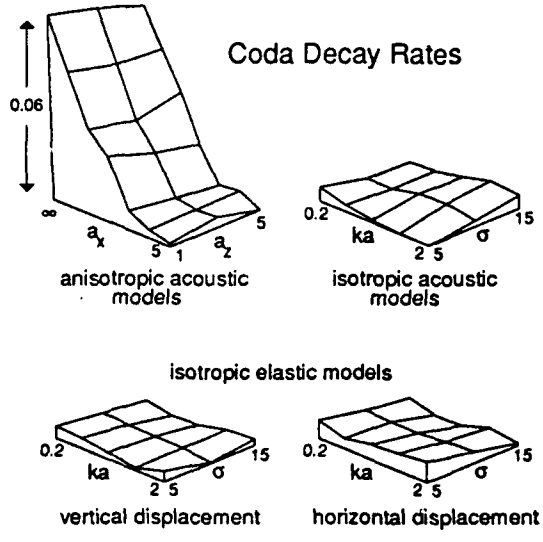


Figure 3: Relative coda decay rates for a large range of models. The spatially isotropic heterogeneity plots are for 1 Hz data for a 30 km thick scattering layer. The anisotropic data are 1 Hz pass-band data for a model with 10% standard deviation and a 30 km thick scattering layer; ka is the normalized wavenumber, a_x and a_z are the correlation distances in x and z, respectively (in km), and σ is the standard deviation in percent of the mean.

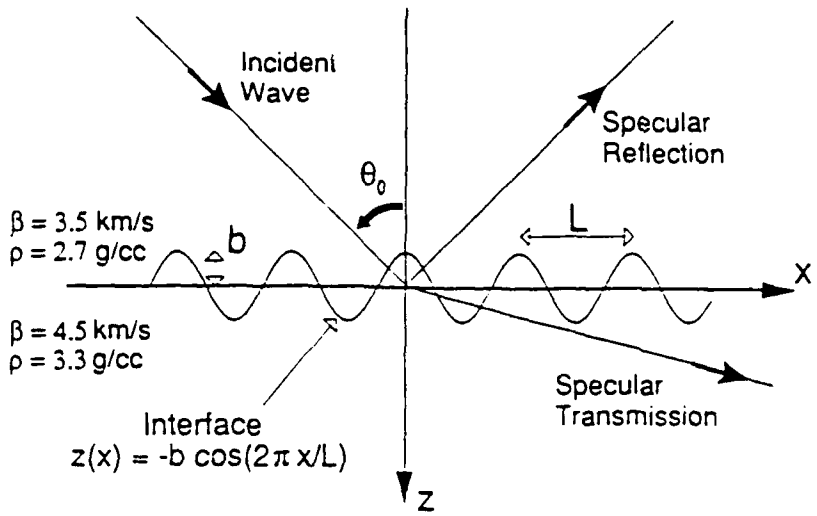


Figure 4: Geometry and parameters for scattering from a sinusoidal welded boundary.

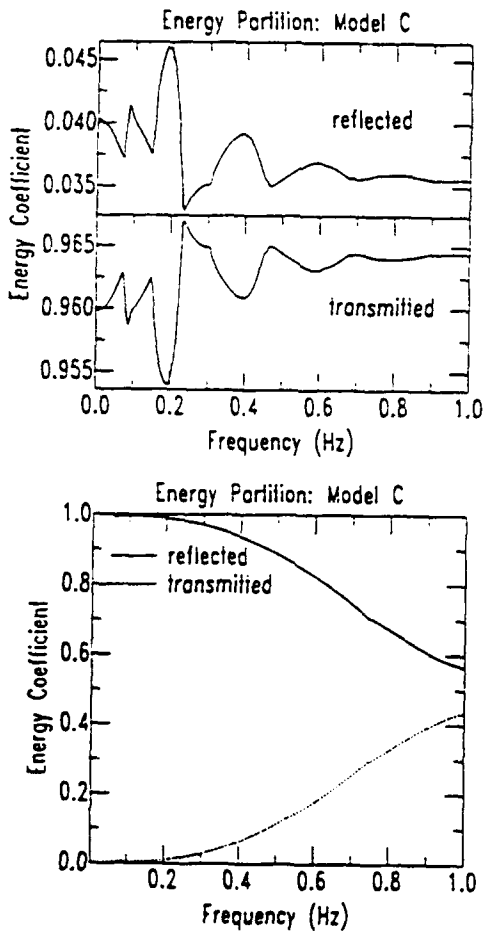


Figure 5: Curves showing energy partitioning versus frequency for Model C. Upper curves are for an angle of incidence of 20°. Lower curves are for an angle of incidence of 60°. The curves are mirror images of each other because they must sum to one to satisfy energy conservation.

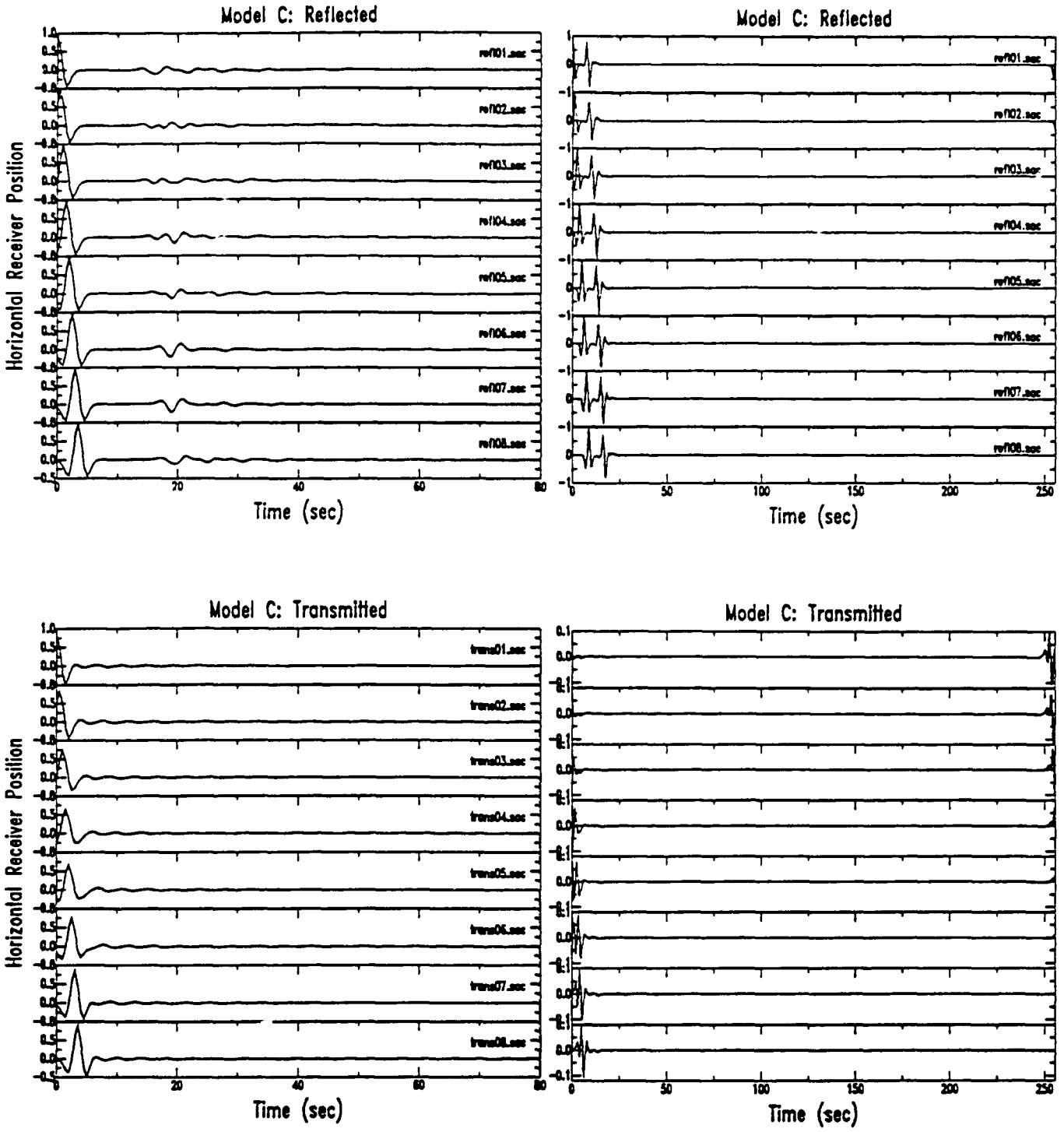


Figure 6: Reflected and transmitted wave fields for an incident plane SH wave on a sinusoidal interface with a wavelength of 35 km and amplitude of 3 km. Angles of incidence are 20° and 60° for the the left-hand and right-hand sides of the figure, respectively.

REGIONAL DISTANCE RECORDINGS OF LARGE MINING EXPLOSIONS IN THE SOUTHWESTERN U.S.

Terry C. Wallace

Department of Geosciences
University of Arizona
Tucson, Arizona 85721

Contract: F19628-90-K-0038

Objective:

It has long been recognized that seismic monitoring at regional distances is essential for the implementation of a low-yield threshold test ban treaty or comprehensive test ban. The discrimination of large chemical explosions from underground nuclear explosions is of major importance for any regional monitoring scheme. It has been shown that most large mining explosions have a unique signature in the frequency domain due to the "ripple fire" detonation of explosions separated by small distances and times. Ripple fire produces a unique spectral signature which is strongly scalloped, and this signature can be used to discriminate chemical explosions from nuclear explosions (Smith, 1988; Baumgardt and Ziegler, 1988; Hedlin et al., 1988; Suteau-Henson and Bache, 1988). This nuclear/chemical explosion discriminant is best at very high frequencies (> 20 Hz), but many of the GSN and Soviet-IRIS stations are limited by a sampling rate of 20 sps. We are attempting to better quantify the signature of ripple fire explosions as a function of travel path, propagation distance and shot configuration by studying chemical explosions recorded at ANMO from copper, coal and uranium mines in New Mexico and Arizona.

Research Accomplished:

Much of the recent work in seismic yield determination and discrimination has emphasized the use of regional distance data. There are several advantages to using regional distance data. First, regional distance seismic stations can significantly reduce the detection threshold over that achieved by teleseismic monitoring. The Lg amplitude recorded at regional distances provides a very stable yield estimate. Finally, spectral discriminate based on the fact that earthquakes produce more high frequency seismic energy than explosions can be used with a high degree of confidence to small magnitudes ($m_b \sim 3.5$). Although much work remains to be done on quantifying the effects of travel path on discrimination and yield determination, the outstanding problem in regional distance verification is the identification and characterization of large chemical explosions. Is it possible to always discriminate between nuclear and chemical explosions? Is it feasible to develop an evasion scenario in which a nuclear explosion is fired in conjunction with a series of chemical explosions? The only way to answer these questions is to develop a data base of observations which can be analyses in terms of travel path, explosion configuration and recording instrumentation. We have begun to develop such a data base for large mining explosions in New Mexico and Arizona recorded at ANMO.

Figure 1 shows the location of 16 mines or quarries which have produced at least one usable seismogram at ANMO. We have collected 117 recordings, with travel distances ranging from 118 to 1292 km. The size of the explosions ranges from 17,000 to 171,000 pounds. The travel paths cross several different geologic provinces (the Rio Grande Rift, the Colorado Plateau, the Datil Plains), and attenuation (Q_β) probably varies by a factor of 3. The mines in northern New Mexico and Arizona are primarily coal; the mines in southern New Mexico and Arizona are open pit copper mines. In general, the coal mines have larger explosions but the signal amplitude corrected for distance is smaller than those explosions from copper mines. The frequency content is higher, suggesting that attenuation is not responsible for the reduction in amplitude, but rather, it is the result of the explosion medium.

Preliminary analysis of waveforms from mine explosions southwest of ANMO (travel paths are dominated by regions of late Cenozoic volcanism) indicates that characteristic spectral scalloping disappears beyond distances of 890 km. This is the result of the attenuation of the high frequencies; we also document this effect in the spectral ratio of Pn and Pg phases. Using Taylor et al. (1988) algorithm which compares a high frequency and a low-frequency pass band (6 to 8 Hz and 1 to 2 Hz, respectively), the Pn and Pg phases both behave similar to earthquakes with like travel paths.

Conclusions and Recommendations:

At this early stage of research we have only completed the construction of the explosion waveform archive and begun preliminary analysis. In the next year we have planned an experiment with the cooperation of Phelps Dodge in which we will record both in the near and far field.

References:

Baumgardt, D.R. and K. A. Ziegler (1988). Spectral evidence for source multiplicity in explosions: application to regional discrimination of earthquakes and explosions, Bull. Seism. Soc. Am., 78, 1773-1795.

Hedlin, M., J. Orcutt, B. Minster and H. Gurrola (1989). The time-frequency characteristics of quarry blasts, earthquakes and calibration explosions recorded in Scandinavia and Kazakhstan, USSR, in 11th DARPA/AFGL SESIMIC RESEARCH SYMPOSIUM, P 40-48.

Smith, A.T. (1988). High-frequency seismic observations and models of chemical explosions: implications for the discrimination of ripple-fired mining blasts, Bull. Seism. Soc. Am.

Suteau-Henson, A. and T.C. Bache (1988). Spectral characteristics of regional phases recorded at NORESS, Bull. Seism. Soc. Am., 78, 708-725.

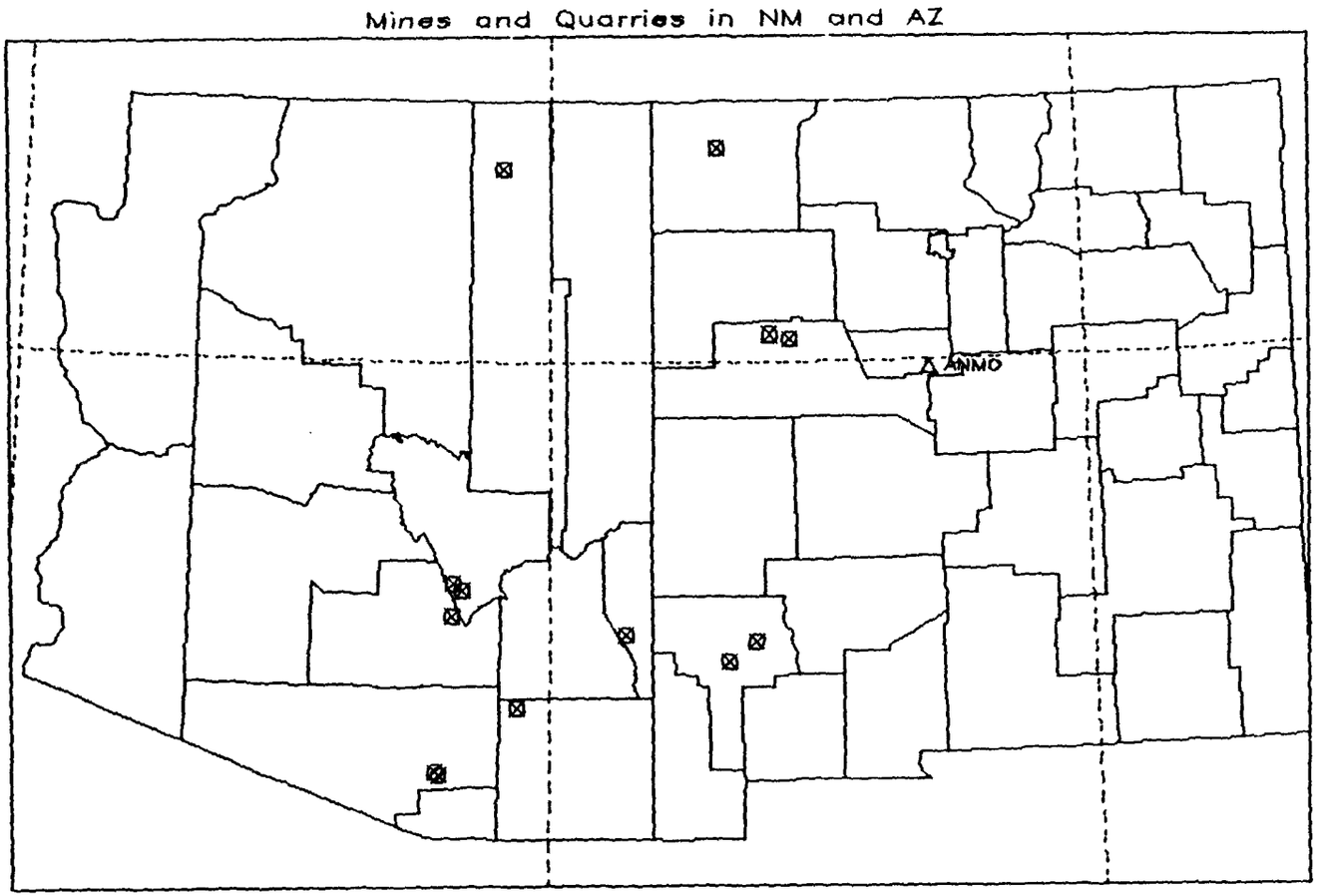


Figure 1: Mines (squares) which have produced at least 2 recordings at ANMO (triangle). The travel paths vary from 124 km to over 1200 km.

THE EFFECTS OF CRUSTAL STRUCTURE ON SPECTRAL DISCRIMINATES

Terry C. Wallace

Department of Geosciences
University of Arizona
Tucson, Arizona 85721

Contract: F19628-89-K-0023

Objective:

A comprehensive or low yield threshold test treaty will require monitoring at regional distances, and the seismograms at these distances are very difficult to deterministically model. The character of the phases Pg and Lg show a very strong dependence on travel path. Although scattering is apparently very important in controlling the character of these phases, the gross features of the crustal waveguide, such as crustal thickness, Pn velocity and "continuity" of the waveguide have a strong signature on the efficiency of Pg and Lg propagation. It has been shown that Lg (and to a lesser extent, Pg) can be blocked by certain geologic structures such as grabens or mountain ranges. Further, the efficiency of Pn propagation is strongly dependent on the upper most mantle velocity structure. For these reasons it is important to empirically characterize the efficiency of regional distance propagation in areas in which seismic monitoring is important.

Research Accomplished:

In the final phase of this research we have concentrated on regionalizing the crustal structure in area around the Western Himalayan syntaxis (Iran, Afghanistan, Pakistan and north western India). The crustal structure in this region is extremely heterogeneous; there are signatures of the India-Eurasian collision and the Arab-Eurasian collision. The method we used to invert for the gross crustal structure is that of Wallace (1986) and Holt and Wallace (1990). The P_{nl} waveforms from explosions and earthquakes are strongly affected by the waveguide nature of the crust. If the source terms of the waveform are understood, then a P_{nl} waveform can parameterized in terms of the average crustal thickness and Pn velocity along a travel path. It is possible to determine these gross parameters using an iterative, linear inversion which minimizes the differences between an observed and a synthetic P_{nl} waveform. The norm, or error function, used for the inversion is given by:

$$e_i = 1 - \left| \frac{\int fg}{\left\{\int f^2\right\}^{1/2}\left\{\int g^2\right\}^{1/2}} \right|$$

where f is the observed P_{nl} waveform and g is the corresponding synthetic waveform. The limits of integration correspond to the starting and ending time of the window over

which the waveform was inverted (these window are typically 60-100 seconds). This error function is minimized in terms of average crustal thickness and Pn velocity by using numerical derivatives.

Figure 1 shows the study area, the seismic stations, the earthquakes used and a series of blocks used to regionalize the region. The blocks were partitioned on the basis of topography, geology and path coverage. A total of 32 earthquakes in the Hindu Kush, Pamirs, Zagros, Turkey and the Quetta syntaxis recorded at 4 WWSSN stations were used for the regionalization. The average crustal thickness and upper mantle velocity were determined for each block by performing a linear weighted least squares inversion using the crustal thickness and Pn velocity results for the individual paths. The average thickness and slowness (1/Pn) of a given path are assumed to be the sum of the fraction of path length in a given block multiplied by the thickness or slowness of the block:

$$X_j = \sum_{i=1}^{n} X_i d_{ij}/D_j$$

where X_j is the average crustal thickness or slowness obtained from each inversion of the P_{nl} waveform that travel path j, X_i is the same parameter for block i, d_{ij} is the distance travel in block i by raypath j, and D_j is the total raypath length. The *a priori* variance-covariance matrix is assumed to be a diagonal matrix composed of the variance from crustal thickness and the slowness obtained from the individual inversions for each path. Holt and Wallace (1990) have determined that errors in crustal velocity of $\pm$ 0.1 km/s can lead to errors in crustal thickness estimates of $\pm$ 5% of the true thickness. On the basis of experience with inversions in the Tibet and China region, it is assumed that the average standard deviations for crustal thickness and Pn velocity are $\pm$ 2.5 km and $\pm$ 0.1 km/s respectively. Uncertainties in Pn velocity are due to errors in origin time of hypocenter location.

Figures 2 and 3 summarize the results of the regionalized inversion. The standard deviation of each parameter was obtained from a *posteriori* model variance-covariance matrix after the inversion was performed. Block 1, which is dominantly south of the Zagros has a crustal thickness of 33 km. Block 2 is in central Iran and is associated with the Zagros. Although the crustal thickness is the most poorly resolved of any block, the value of 60 km is consistent with the collision zone. Central Iran is believed to relatively rigid (Jackson and McKenzie, 1984), with a very low level of seismicity. There is considerable evidence for crustal shortening in the Kopet Dag. If thickening accompanies this shortening, the crust should be overthickened. The Pn velocity is very high for this region, and, as will be discussed later, the Pn and Sn propagation appears to be very efficient, but the Lg propagation is at least partially blocked.

Block 3 is a region known as the Makran, and the is documented subcrustal seismicity in this region indicating that the Arabian plate is being underthrust beneath Eurasia (Ni and Baraznagi, Quitmeyer *et* al., 1979). This underthrusting is consistent with the value of 56 km we obtained for the crustal thickness; the low Pn velocity indicates that the upper most mantle is at elevated temperatures. Block 4 encompasses the Helmond Basin (in regions into the southern USSR), and the inversion results are similar to those obtained for the Markran. Block 5 is the Quetta Syntaxial region. The crust here is relatively thin (30 km) and the Pn velocity is very low (7.5 km/sec). At first glance this would seem inconsistent with a zone of convergence, but the Chaman fault is a major left-

lateral fault which may accommodate the collision. Finally, block 6 which is in the Hindu Kush and Pamirs, has an extremely thick crust (75 km) and a high Pn velocity (8.2 km/sec). This is consistent with other studies of the region (for example, Holt and Wallace, 1990).

We investigated the efficiency of the propagation of Lg and Pg several ways. The first method is based on the empirical algorithm of Kennet et al. (1985). Each Lg train is assigned a numerical code on the basis of Lg appearance. Although the size of the Lg packet is not simply related to the nature of the crustal structure along the path, the largest effects (such as blockage) come from prominent structural heterogeneity. A similar empirical approach is used to asses Pg efficiency. The installation of two very broad band seismic stations in the Soviet Union allowed us to also asses the efficiency of propagation more rigorously. An envelope function was fit to Pn, Sn, Pg and Lg; these envelopes were calculated at 1, 3 and 5 Hz. The ratio of the envelope functions for Pg and Pn was used to calculate the relative efficiency of Pg. Similarly, the ratio of Lg to Sn was used to calculate the efficiency of Lg.

Figure 4 summarizes the Lg efficiency. Paths which traveled through relatively constant thickness crust (for example, blocks 2, 4 and 3) were fairly efficient. As expected, when paths crossed regions of rapidly varying crustal thickness the Lg was much diminished. For example, ray paths from the Hindu Kush to Quetta syntaxis were nearly devoid of Lg. Similarly, earthquakes in southern Iran recorded at ASH (only two events studied thus far), had poorly developed Lg. Figure 5 summarizes the Pg efficiency. Again, crustal thickness heterogeneity plays a role in the efficiency of propagation, although the correlation is much less well developed. For example, the Pg phase is much more efficiently propagated for the Hindu Kush to the Quetta syntaxis than Pn. This is probably the result of very low Pn velocities in block 5 (as associated high attenuation of the upper most mantle).

Conclusions and Recommendations:

The crustal thickness has a strong effect on the character of short-period regional phases. With the improved models developed from crustal and upper mantle structure presented in the Western Syntaxial region presented here, it is possible to predict the character is signals for events of interest in the Soviet Union or India and Pakistan. Clearly Lg and Pg do not necessarily have similar propagation characteristics, and spectral discriminate methodologies should take this into consideration.

Future work will rely on the digital data from the GSN and the new Soviet stations. The envelop function developed for this study appears to yield a very good measure of the efficiency of propagation for regional distance phases.

References:

Holt, W.E. and T.C. Wallace (1990). Crustal thickness and upper mantle velocities in the Tibetan Plateau from the inversion of regional P_{nl} waveforms: evidence for a thick upper mantle lid beneath southern Tibet, J. Geophys. Res., 95, 12,499 -12,525.

Jackson, J.A. and D.P. McKenzie (1984). Active tectonics of the Alpine-Himalaya Belt between western Turkey and Pakistan, Geophys. J.R. astr. Soc., 77, 185-264.

Kennett, B.L.N., S. Gregersen, S. Mykkeltveit and R. Newmark (1985). Mapping of crustal heterogeneity in the North Sea Basin via the propagation of Lg waves, Geophys. J. R. astr. Soc., 83, 299-306.

Ni, J. and M. Barazangi (1986). Seismotectonics of the Zagros continental collision zone and a comparison with the Himalayas, J. Geophys. Res., 91, 8205-8218.

Quitmeyer, R.C., A. Farah and K. Jacob (1979). The seismicity of Pakistan and its relation to surface faults, in *Geodynamics of Pakistan*, editors, A. Farah and K. Delong.

Wallace, T.C. (1986). The inversion of long-period regional distance body waves for crustal structure, Geophys. Res. Let., 13, 749-752.

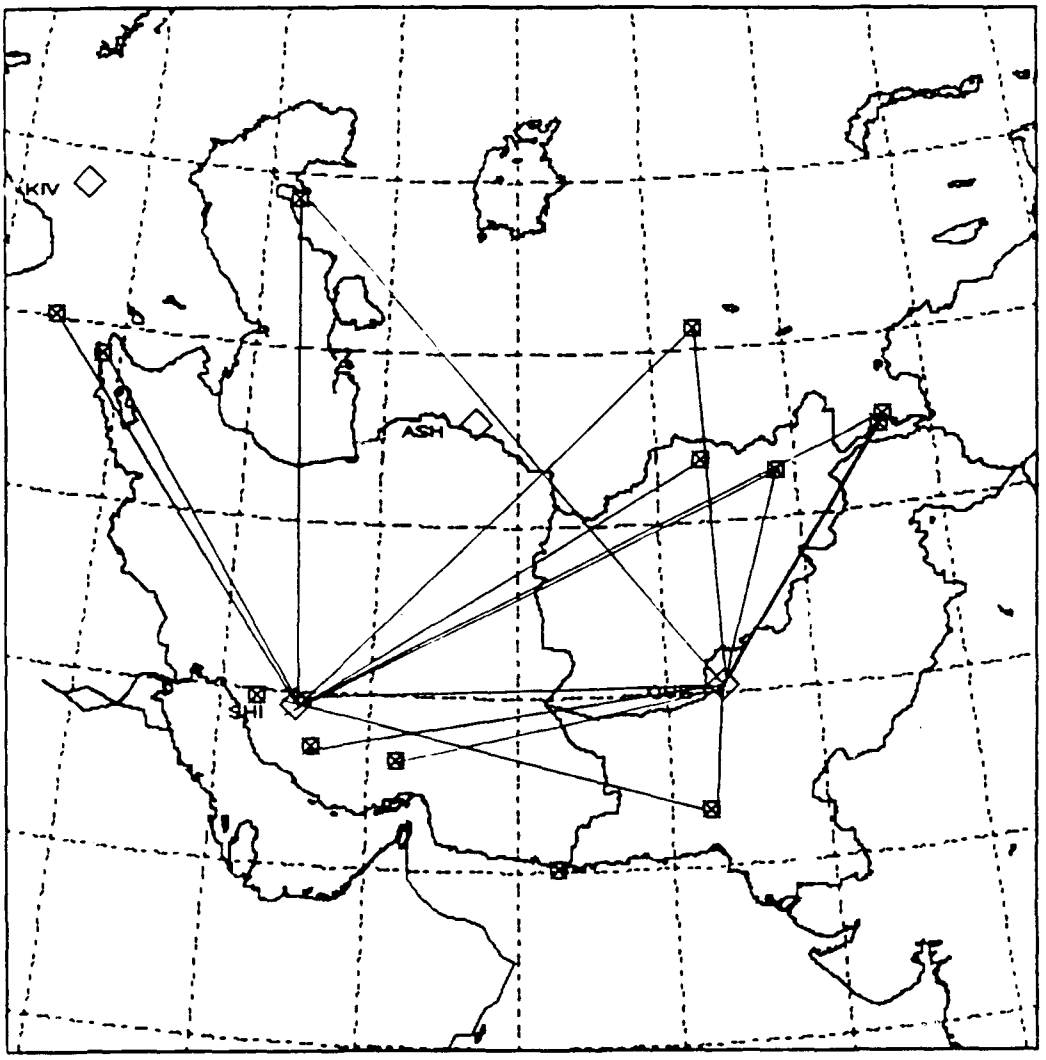


Figure 1: Stations (diamonds), earthquakes (squares) and raypaths used to regionalize the gross crustal strucute in the region around the western Himalayan syntaxis.

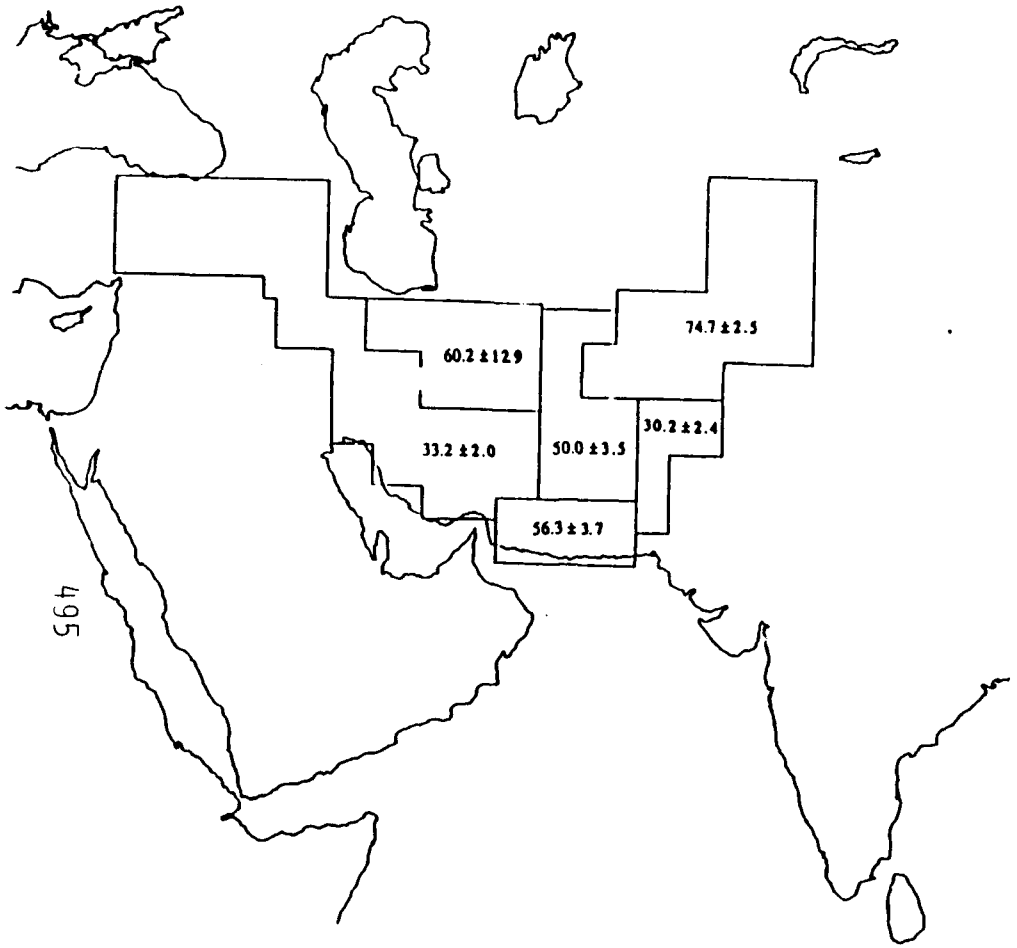


Figure 2: Crustal thickness estimates for the 6 blocks of the regionalization. Standard deviation is a formal estimate obtained from the model variance-covariance matrix.

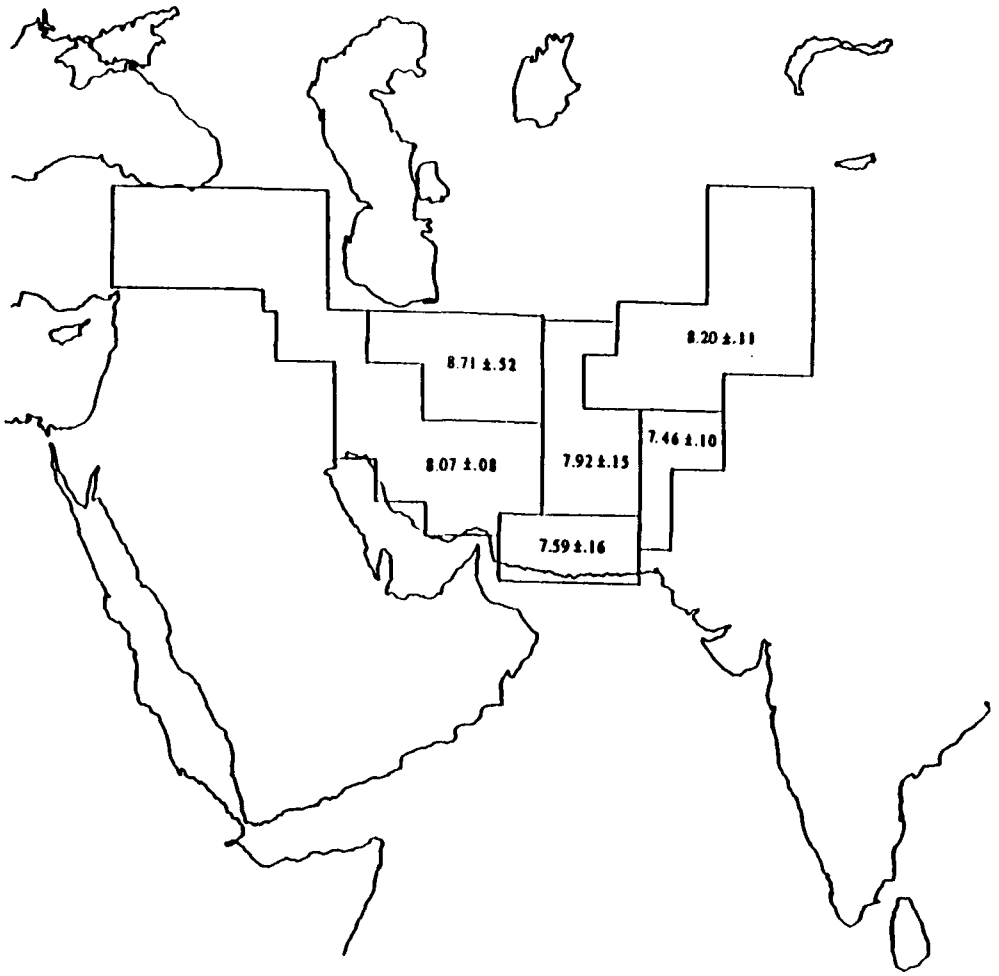


Figure 3: Pn velocity estimates for the 6 blocks of the regionalization. As before, standard deviation is from the variance-covariance matrix.

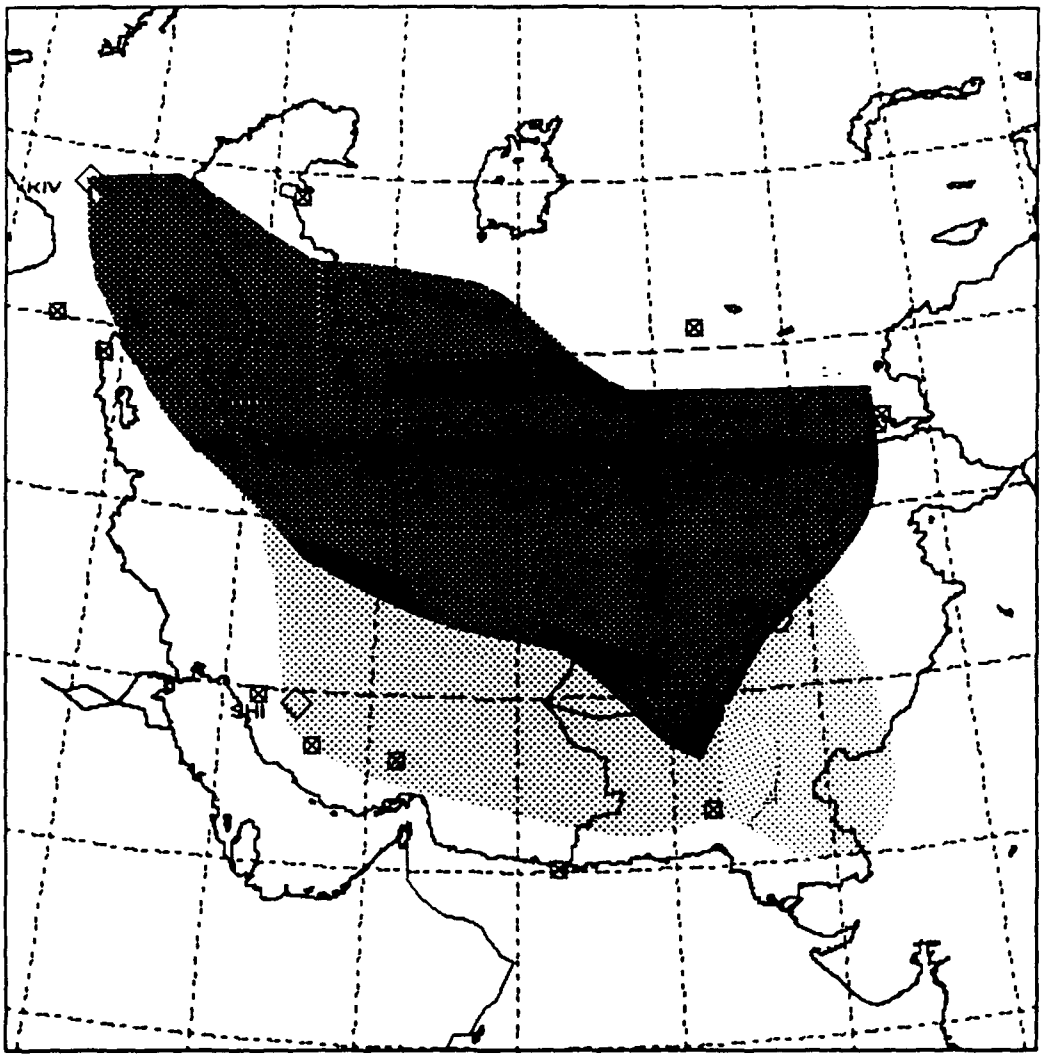


Figure 4: Efficiency of Lg propagation. Density of dotting indicates the efficiency of Lg progation (the darkest regions represent the most efficient paths).

NTS SURFACE WAVE MAGNITUDES FROM A REGIONAL NETWORK

B. B. WOODS and D. G. HARKRIDER
Seismological Laboratory, California Institute of Technology,
Pasadena, California, 91125
F19628-89-K-0028

OBJECTIVE

The objective of this research is to determine surface wave magnitudes from regional stations, which may have the only seismic data available for small events. The regional determination is designed to be compatible with teleseismic determinations for large events. Surface wave magnitudes are especially important in estimating biases at new test sites for which there may be no calibration event. Great effort went towards making the data set comprehensive and diverse in terms of yield, source location and shot medium in order to determine the portability of seismic measuring scales. In particular we examine Pahute Mesa, Rainier Mesa and Yucca Flat explosions detonated above and below the water table.

RESARCH ACCOMPLISHED

We re-examine the use of surface-waves for underground nuclear explosion magnitude determinations, particularly for smaller yield (Y $<$ 20Kt) events. The surface wave magnitude-yield scaling law for such low-yield events, until now, was not known well. The data used are long-period North American station vertical records for 102 specified Nevada Test Site (NTS) events. The stations used are from several networks. Their respective instruments all have pass bands that lie within the 10 to 60 second range. Surface waves are very useful for yield estimation purposes, for M_s is determined from relatively long-period seismic waves which are insensitive to high frequency near-source effects, which, along with several other possible mechanisms, may be caused by asymmetries in the shot cavity, see Zhao and Harkrider (1991). These high frequency source effects may cause appreciable bias in magnitudes that are based on higher frequency waves, such as the m_b and L_g scales.

For the lower yield events it becomes necessary to include the data from regional stations ($\Delta<25^\circ$) , for teleseismic recordings have too low a signal to noise ratio, which makes them unusable. At regional distances surface waves are not well dispersed, having a prominant Airy phase pulse with a period between 6 and 20 seconds (Alewine, 1972), so that it is not possible to measure M_s conventionally (that is measuring the amplitude of the 20 sec. wave). For North America in general, there is mininum in the goup velocity curve near 12 seconds for the fundamental Rayleigh-wave (Marshall *etal* 1979).

To measure M_s we employ a technique whereby theoretical seismograms in conjunction with the surface wave data are employed to indirectly calculate it. In using this procedure several propagation path models were tested to determine the effect of attenuation and seismic velocity structure upon the M_s values. These calculated M_s values remain stable, have reasonably small errors and correlate well with associated m_b maginitudes and log yield for the event data set. The M_s—m_b relationships are determined by a weighted least-squares linear regression.

Besides comparing the M_s results with several different independent magnitude scales, the data have also been separated with respect to source region and shot material. M_s values at Yucca Flat tend to be larger than those at Rainer Mesa by 0.09 magnitude units for a given m_b. There also appears to be some difference in waveforms between events of these two source regions. Pahute Mesa events are 0.22 magnitude units larger than those at Yucca flat for explosions set-off below the water table and with the same m_b.

We do not account for tectonic release effects upon the magnitude measurments. Such effects are best accounted for with moment tensor inversions of sources which involves more sophisticated data analysis. Standard M_s measurement techniques ignore this factor as well.

The data are long-period vertical seismograms recorded at North America stations for 102 explosions at NTS and consist of digitized World Wide Seimic Network (WWSN) and Canadian Seismographic Network (CSN) records, Digital World Wide Seismic Network (DWWSN), Lawrence Livermore Regional Seismic Network (LNN) and Regional Test Seismic Network (RSTN) digital data for events occurring later than 1981. The analog WWSN and Canadian station data were digitized by ENSCO. Fifty-eight stations comprise the network, although fewer than 60 percent of the stations had data available for any single event. Epicentral distances range from 220 km for NTS to GSC (Goldstone, California), to 5200 km for NTS to STJ (Saint Johns, Newfoundland). For the smaller events, particularly Rainer Mesa explosions, only the nearer stations (distance $<$ 1000 km) had either data available or reasonable signal to noise ratios. Station coverage varies widely between events. Five of the smaller events only had one viable station seismogram each, while some events had over 30. The average number of stations reporting per event is 10.

Surface waves that propagate across oceanic/continental margins undergo significant modification in their waveforms because of the great lateral variation in crustal and upper mantle structure at such boundaries. These propagation effects are not straight forward to model, hence appropriate Green's functions, or transfer functions, are difficult to obtain. Without robust Green's functions it is hard to infer accurate source information from the data. Smaller events also are not likely to be observed at the distant stations, which often include oceanic structure along their propagation path, and make these longer paths even less attractive to include in the monitoring network. Hence, we chose to confine our study to surface waves travelling solely along continental paths, *i.e.* within North America.

Of the 102 events, 27 are from Pahute Mesa, 16 are from Rainer Mesa, 58 from Yucca Flat and one, Piledriver, is located at Climax Stock. We consider these to be 4 distinct source regions. For some specific stations, waveforms varied somewhat between events, depending upon source location.

The Piledriver data from a given station look appreciably different from that of any other events recorded at that same station. This was true for every station recording Piledriver and probably is caused by differences in the source region for this explosion. Piledriver was detonated in a granitic source region, north of the other sites. The source to receiver geometries for this event are approximately the same as those as the other NTS events, so the difference in waveforms doesn't appear to be attributable to dispersive effects caused by differences in propagation path length. Piledriver was the only Cliamx Stock event with readily available data, so no further examination of this source was carried out.

At some of the nearer regional stations (distance $<$ 9 $^\circ$), there are also subtle differences between the Yucca Flat and Rainer Mesa event waveforms. At DUG (Dugway, Utah), for example, the Rainer event waveforms look as if the Airy phase has been Hilbert transformed (equivalent to a 90 $^\circ$ phase shift) relative to the Yucca Flat waveforms. The DUG Rainer waveforms also contain more high frequency coda energy than those from Yucca Flat. Pahute events are similar in waveform to Rainier events and have less high frequency content than Yucca events.

The seismograms were band-passed filtered between 6 and 100 seconds to get rid of the long period and short period noise which would otherwise affect the peak to peak measurement of the Rayleigh pulse. The absolute amplitudes of the data were verified by choosing several different stations and comparing the peak to peak amplitude of the digitized record to that measured directly from the respective analog WWSSN film chip. From this step we ascertained

that the station gain factor had been correctly factored out of the seismograms.

Yield information was available for 97 of the events (Fig. 1). The yields for this data set range over three orders of magnitude in size. The greatest scatter, as in the case of M_b vs. log yield, is due to shots above the water table. It should also be be kept in mind that the scatter would be further reduced if the data were separated into populations based on their location at NTS, *i.e.* Pahute Mesa, Rainier Mesa and Yucca Flat). Because of the classified nature of some the yields, it is not possible, here, to closely examine these effects with respect to yield.

Since our magnitude values are based on theoretical continental structures, as well as the particular network used, we wanted to compare our M_s values to those obtained from standard methods. One such standard data set is that of Marshall *etal* (1979). There is a overlap of 14 events betwen studies. We preformed a fixed-slope (slope=1.0), regression of our M_s values to theirs. The correlation is very good; scatter is small for events above and below the water table. It's important to note that with our method we are able to measure M_s for events 0.75 units smaller than the smallest Marshall values after the off-set adjustment is made. We are able to measure M_s for these smaller events, because we are able to make use of near-regional ($<$ 500 km) records with the method described in this paper. The offset in M_s between scales is 0.53 with mean standard error of 0.03 magnitude units. This offset is due in part to the difference in definition of M_s. At 40 $^\circ$ the offset in magnitude is 0.15, thus reducing the offset to 0.38 units. However, for the method decribed in this study, M_s is based upon a theoretical network average M_s, so it will have a bias attached to it which is dependent upon the network used. This network bias can be assumed to be responsible for part of the offset, as well.

To determine the portabiltiy of this M_s calculation method the events need to be separated into groups based on their source regions and then compared, one group to another, in order to see if there are systematic differences in M_s values relative to any other magnitude scale. Three main geographic source regions comprise the event data set: Pahute Mesa, Rainier Mesa and Yucca Flat.

Whether or not a shot occurs within saturated material is another criterion by which to separate events in order to look for systematic differences in M_s values. Other studies have found significant seismic coupling differences between explosions detonated above and below the water table (Gupta, 1989), so it a reasonable parameter to study. Reviewing Fig. 1, it is also apparent that for shots fired-off below the water table have a larger seismic magnitude than those detonated above the water table.

Fig. 2a shows the relationship between M_s vs. Lilwall m_b for all NTS events. The surface-wave maginitudes were all calculated using mixed-path Green's functions and path corrections. Fig.'s 2b and 2c divide the data populations into above and below the water table, respectively; shots for which water table information was not available were left out. There is no appreciable difference between the above water table and below water table curves. This is not surprising; refering to Fig. 1 it is apparent that both seismic magnitude-yield curves show that for a given yield an event below the water table has a larger magnitude than a shot above the water table. It follows that the M_s - m_b relationship may not show the same discrepancy between shots detonated above and below the water table, for the effect of the water content in the shot medium should affect surface waves and body wavesin the same manner. All three regression curves are essentially the same within the error bounds. There is considerable scatter in all three figures, but that is not surprising considering the diversity of the sampled populations. Even with this scatter, the best-fitting M_s- m_b line is well constrained, for the population covers a wide range of magnitudes.

Fig. 3a gives the M_s- m_b relationship for all Yucca events. The regression curve is signifcantly different from that of Fig. 2a. The scatter in the data is reduced by 25 percent over

that of the general population. Separating the events with respect their relation to the water table yields two distinct curves, unlike the case where shots from all sites are grouped together. For the Yucca events below the water table (Fig. 3b) the regression curve fit is, within the errors, is not greatly different from the case of all NTS events below the water table (Fig. 2b). In Fig. 2c, for shots in dry medium, the M_s- m_b curve is significantly different from the NTS above water table curve (Fig. 2c). The significance of this curve is questionable, however, due to the paucity of data used to establish it.

Fig. 3c plots all Pahute event M_s's vs. their respective m_b's. The realtionship is essentially the same as for the aggregate NTS plot (Fig. 2a). Fig. 11b shows the relationship for Pahute shots below the water table. The slope of this curve is nearly the same as that for Yucca below water table shots, although the intercept differs appreciably. This result implies that for a given m_b, surface wave magnitudes for events at Pahute Mesa are larger than those at Yucca Flat. Fig. 3f shows the M_s- m_b relationship for Pahute events above the water table. Because events in this category are clustered around $m_b = 5.5$, a well constrained line cannot be obtained, so we applied a fixed-slope regression, using a slope of 0.82 (that of the below water table case). Comparing Fig.'s 3e and 3f, an off-set in M_s- m_b of 0.09 with a mean standard error of 0.04 is obtained, implying some degree of difference in seismic coupling between body and surface waves.

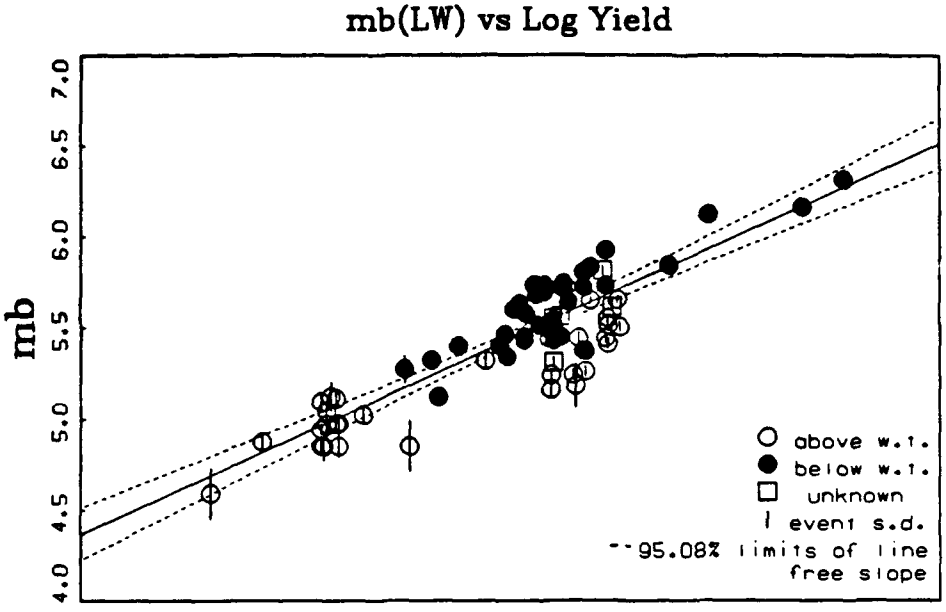
Fig. 2d displays the M_s- m_b regresssion curve and data for Rainier Mesa events, all of which are above the water table. Although the clustering of data near $m_b = 5.0$ causes the curve to be poorly constrained, a slope close to that for Pahute events and Yucca (below the water table) is obtained. Constraining the slope to be 0.82, as in the case of Pahute events yields Fig. 2e. Comparision of the equations of Fig.'s 2e and 3e give an off-set of 0.31, with a mean standard error of 0.04, m_b units, so that for a given m_b, shots at Pahute produce larger M_s values than at Rainier Mesa. Either the Pahute site is more efficient at producing surface waves or the Rainier site is less efficient at coupling body-wave energy. Rainier events are tunnel shots. The immediate source region (R $<$ 20C m) may behave like an asymmetric cavity, resulting in a source that is non-isotropic (Zhao and Harkrider, 1991) and/or seismic coupling that has strong frequency dependence.

CONCLUSIONS

The method used herein to calculate surface wave magnitudes allows the measuring of M_s for nuclear explosions over a wide magnitude distribution. Using this technique, it is now possible to use near-regional ($\Delta<15$ °), long period records in conjunction with the far- regional ($\Delta>15$ °) } and teleseismic records, that have previously been used to make conventional M_s measurements, in order to measure surface wave magnitudes. This increase in observations has two advantages. First, for any event the station network coverage is enhanced in terms of overall numbers as well as in azimuthal coverage, in particular stations only several hundred miles away from NTS in California, Nevada and Utah can be included in a network that otherwise would have no coverage to the west or southwest. These improvements make the network M_s's more stable and statistically robust. Secondly, smaller events with surface waves that haven't been analyzed will now have such observations available, so that their surface wave magnitudes now can be calculated. The method produces stable M_s values that are consistent with other seismic magnitude scales. Thirdly, the effect of inaccuracies in estimating Q are negligible for very near-regional recordings ($<$ 500 km). With the M_s calculation technique used here, one can take advantage of such nearby recordings. Lastly this method makes it very easy to use historical analog data sets more easily, for it is not necessary to use digitized data if only the maximum peak to peak amplitude needed to calculate M_s's in this fashion.

In order to do a thorough investigation of source effects discussed above, a more complete data set of events with different pertinent source parameters is needed for observation. Specifically, events chosen for any one site location should cover a wide range of yields or magnitudes and comprise events detonated both above and below the water table. Obviously, at some site locations, it may not be possible to come up with such a comprehensive, ideal data set. This is particularly true of Rainier Mesa where most all events have yields less than 20Kt. From the results obtained with the data set used here, there does appear to be signicant differences in seismic coupling between NTS sub-sites, with events at Pahute Mesa producing larger surface-wave magnitudes for a given m_b than at Rainier Mesa or Yucca Flat. This discrepancy is largest for Rainier Mesa events.

As stated earlier the method used here to obtain M_s values lends itself to such a diverse data set, for the measurement of the smallest events is facilitated with near-regional observations.


mb(LW) vs Log Yield
mb
7.0
6.5
6.0
5.5
5.0
4.5
4.0
above w.t.
below w.t.
unknown
event s.d.
95.08% limits of line
free slope
Log Yield
(s.d.=0.16)

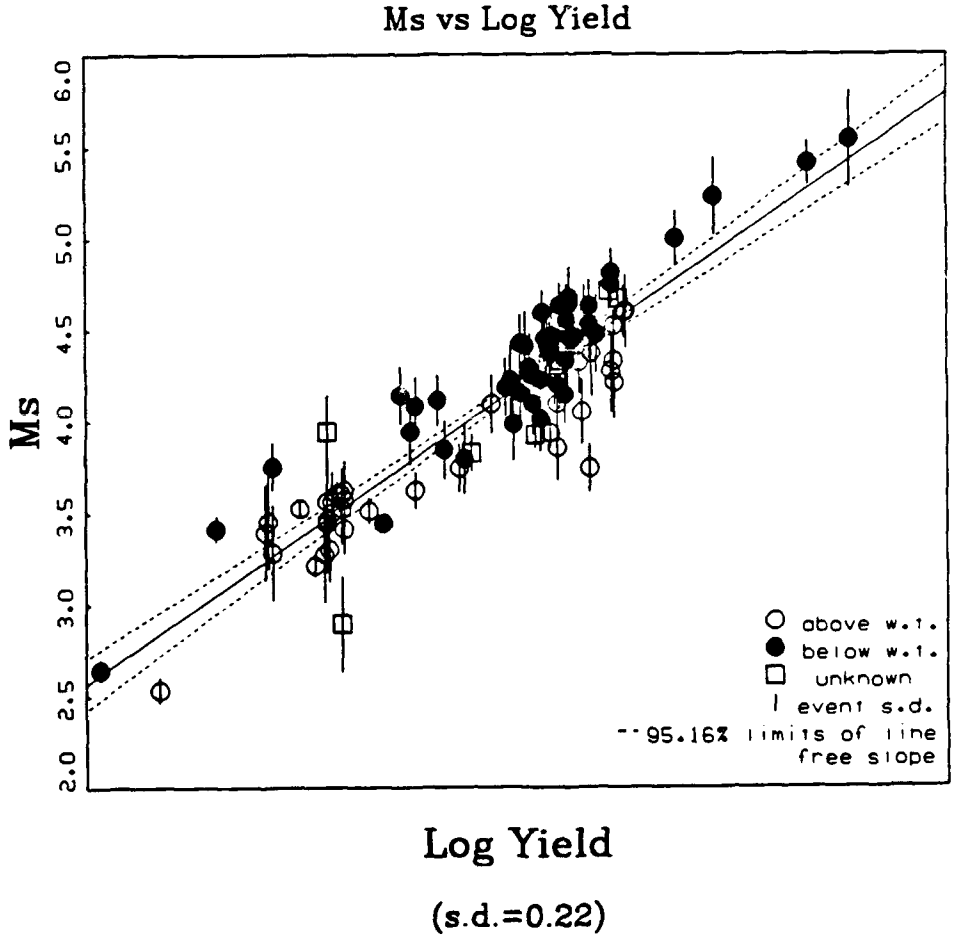

Ms vs Log Yield
Ms
6.0
5.5
5.0
4.5
4.0
3.5
3.0
2.5
2.0
above w.t.
below w.t.
unknown
event s.d.
95.16% limits of line
free slope
Log Yield
(s.d.=0.22)

Figure 1

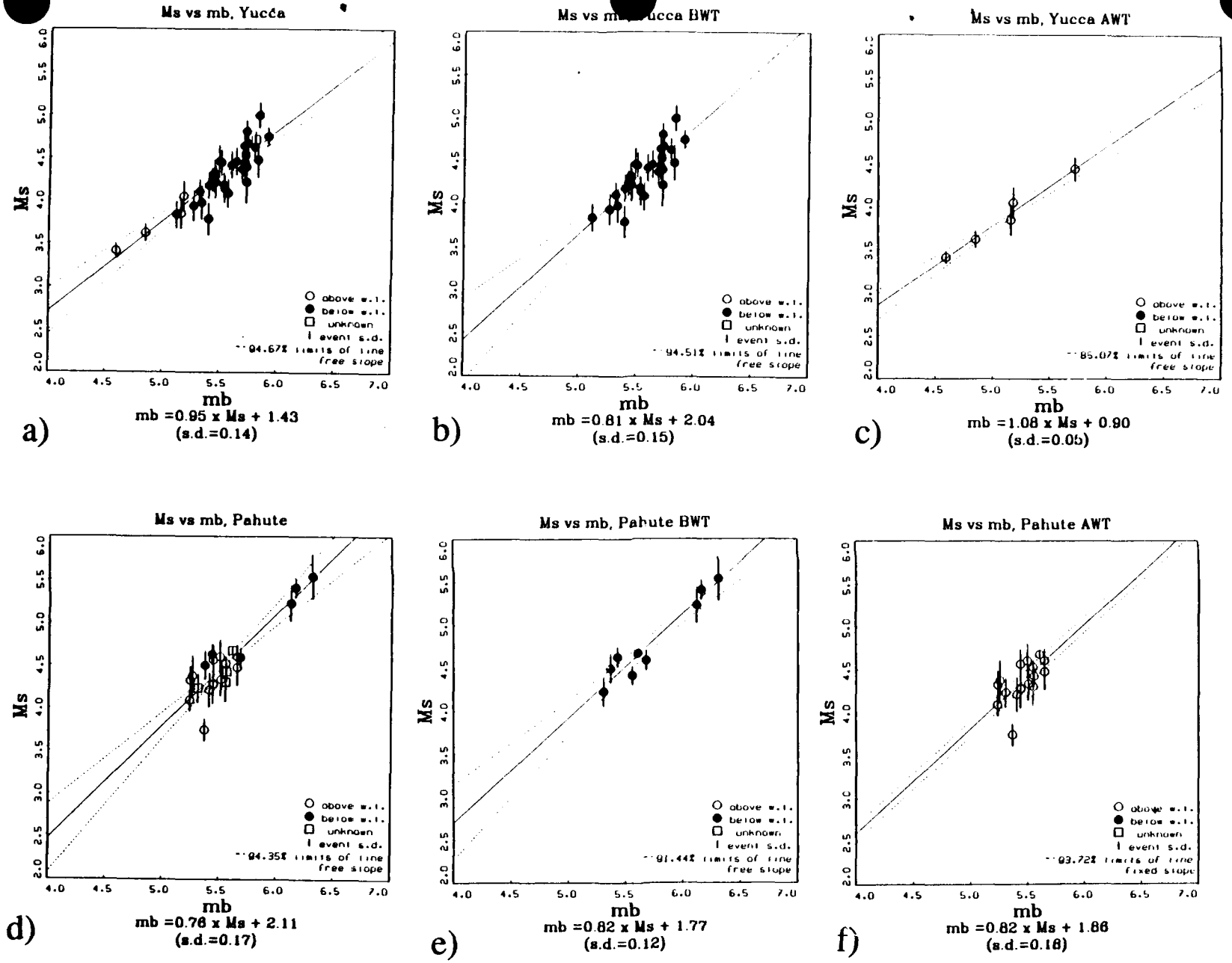

Ms vs mb, Yucca
Ms vs mb, Yucca BWT
Ms vs mb, Yucca AWT
Ms vs mb, Pahute
Ms vs mb, Pahute BWT
Ms vs mb, Pahute AWT
Ms
mb
above w.t.
below w.t.
unknown
event s.d.
94.67% limits of line
free slope
94.51% limits of line
free slope
85.07% limits of line
free slope
94.35% limits of line
free slope
91.44% limits of line
free slope
93.72% limits of line
fixed slope
a)
mb =0.95 x Ms + 1.43
(s.d.=0.14)
b)
mb =0.81 x Ms + 2.04
(s.d.=0.15)
c)
mb =1.08 x Ms + 0.90
(s.d.=0.05)
d)
mb =0.76 x Ms + 2.11
(s.d.=0.17)
e)
mb =0.82 x Ms + 1.77
(s.d.=0.12)
f)
mb =0.82 x Ms + 1.86
(s.d.=0.18)

Figure 2

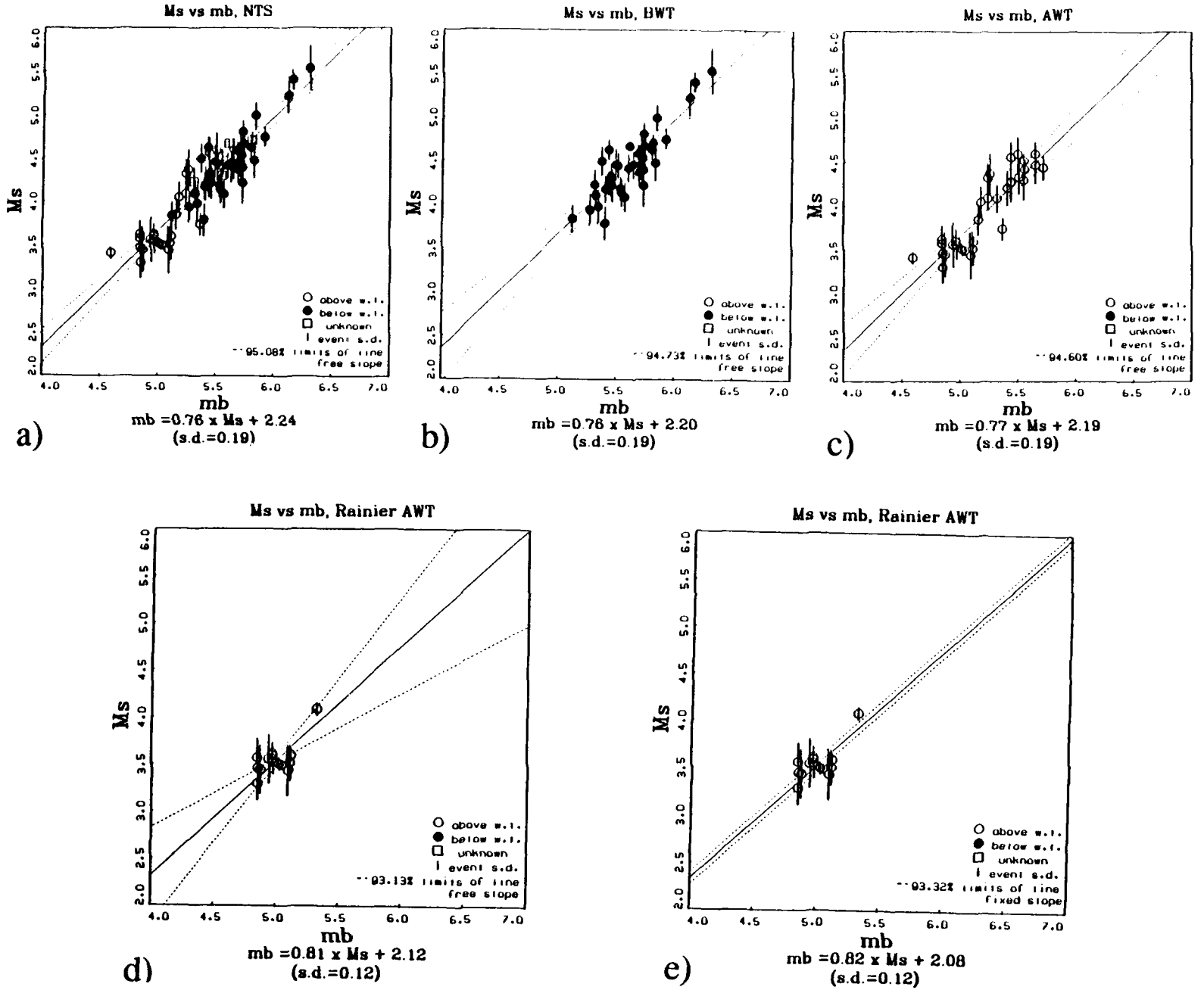

Ms vs mb, NTS
Ms
mb
above w.l.
below w.l.
unknown
event s.d.
95.08% limits of line
free slope
mb =0.76 x Ms + 2.24
(s.d.=0.19)
a)
Ms vs mb, BWT
Ms
mb
above w.l.
below w.l.
unknown
event s.d.
94.73% limits of line
free slope
mb =0.76 x Ms + 2.20
(s.d.=0.19)
b)
Ms vs mb, AWT
Ms
mb
above w.l.
below w.l.
unknown
event s.d.
94.60% limits of line
free slope
mb =0.77 x Ms + 2.19
(s.d.=0.19)
c)
Ms vs mb, Rainier AWT
Ms
mb
above w.l.
below w.l.
unknown
event s.d.
93.13% limits of line
free slope
mb =0.81 x Ms + 2.12
(s.d.=0.12)
d)
Ms vs mb, Rainier AWT
Ms
mb
above w.l.
below w.l.
unknown
event s.d.
93.32% limits of line
fixed slope
mb =0.82 x Ms + 2.08
(s.d.=0.12)
e)

Figure 3

Velocity Structures Of Different Tectonic Provinces Of China

Francis T. Wu, Alan L. Jones and Zhaoming Ke
Department of Geological Sciences
State University of New York
Binghamton, New York 13902-6000
F19628-90-K-0042

Objective

The objective of the present research is to determine the crustal structures of eastern Asia using surface waves recorded at the newly installed high quality digital stations in that region. The work includes the following aspects:

1. Tectonic regionalization.
2. Determination of the dispersion curves for the different tectonic regions.
3. Determination of the crustal structures corresponding to different region so that they can be used in waveform studies in China (see Barker, 1991).

Research Accomplishment

Regionalization of China

Modern reflection and refraction methods for crustal studies can provide fundamental data needed to predict surface and body waveforms at distances from seismic sources. It is not possible to perform such studies in all parts of the world. In fact, in most regions we have to resort to waves recorded only at a few seismic stations. Fortunately the number of high quality stations has increased dramatically around the world. However, with sparsely distributed stations separated by distances of more than one thousand kilometers, we have to resort to methods that can produce average models with as much details as can be justified. We have resorted to the use of surface wave regionalization method that have been applied in studying large scale velocity structures (with dimensions > 1000 km) (e.g., Yu and Mitchell, 1979; Wu,1972; Nishimura and Forsyth,1988) using stations that are spaced several thousand kilometers apart or single stations. In this research, we use stations roughly 1000 km apart to determine structures with dimensions as small as one hundred km.

The choice of a particular regionalization scheme is necessarily somewhat subjective. The purpose of regionalization is to separate crusts with different velocity structures, such that we can use waves travelling through different subregions to decipher these structures. Let us consider two regions. Certainly if the velocity structures for different regions are known from other sources, then our problem is solved. For most areas we studied, little or no refraction or reflection data exists. Other geophysical data of importance is gravity maps; only small scale maps are available, however. Lacking data concerning deep structures we have to depend on surface geology; if it is different for two areas (e.g., one covered by Pre-Cambrian metamorphic complex and the other by Mesozoic sedimentary rocks), the crustal structures can be expected to be different. If the shallow structures are very similar, it does not imply that the deep structures are the same but we have no basis to differentiate a region further without additional data. The tectonic history of a region can also be very useful.

If regions with different velocity structures are lumped together, an average dispersion of this combined region will be determined, similar to other surface dispersion analysis. In principle, if one region with uniform velocity structure is divided into two regions, the same dispersion should be derived for both regions. Thus, more detailed regionalization should yield better results. Since regionalization analysis is an inverse problem, increasing the number of regions means the addition of parameters. By dividing the areas into more regions we may not able to resolve well some of the parameters. Therefore, in our analyses, we have to adjust our regionalization scheme until the regions of interest can be resolved with available data. By enlarging our dataset in the future, more regions can be resolved.

Dispersion for various regions

By dividing the region of interest into "homogeneous" subregions, the group velocities traversing N subregions can be approximated, to the first order, as:

$$t_k = \sum_{i=1}^{N} \frac{\Delta_{ik}}{U_i}$$

t_k is the travel time of a particular group for the kth event-station pair. After a regionalization scheme is adopted in which the area in which the wave paths traverse is divided into blocks, Δ_{ik} can be readily determined and the group velocities U_i for each block can be obtained by solving the set of linear equations as defined above. The solution is repeated for each period.

An SVD algorithm (Press et al., 1986) is used in solving the set of linear equations above. Small eigenvalues are truncated at various levels (1-5%) while monitoring the resolution and the resulting dispersion curves. The appropriate number of parameters to use in the inversion can be determined using Akaike's (1969) final prediction error (FPE). Regions that are ill resolved can be combined with others to improve resolution, if it can be justified; otherwise the results are ignored.

We have also made tests to see whether significant azimuthal anisotropy in group velocity can be determined. Following Smith and Dahlen (1973) and Nishimura and Forsythe (1988), we shall express U as a function of azimuthal angle ϕ:

$$U = U_0 + C_1 \cos 2\phi + C_2 \sin 2\phi$$

For slightly anisotropic medium, we may express the travel time in each anisotropic region as (Nishimura and Forsyth, 1988):

$$t_k = \sum_{i=1}^{N} \frac{L_{ki}}{U_i}\left\{1 - \left(\frac{a}{U}\right)_i CS_{ki} - \left(\frac{b}{U}\right)_i SN_{ki}\right\}$$

where a and b are anisotropic coefficients associated with the $\cos 2\phi$ and $\sin 2\phi$ terms and U_i is the average velocity for each block. One of the most important questions for this problem is the significance of the result. We view this matter on the basis the F-test and Akaike information criteria (Akaike, 1969; Jones, 1976).

Isotropic analyses

Fig. 1a shows the detailed regionalization we have adopted for China. Software was written such that the regions can be combined easily; we can thus investigate the effect of different schemes of regionalization on the resolution and dispersion results. There are altogether 200 paths with both Love and Rayleigh data. It is evident that some regions are poorly sampled, for example, regions 2, 5, and 6; in general, western China is much better sampled than eastern China.

Fig. 2 shows the Love wave dispersion of the best resolved regions, while Fig. 2b shows the resolution matrix for the thirty one regions. Although we have determined the Rayleigh dispersion also, we shall only show Love wave results because of limited space. The Region 1 dispersion (for southern Tibet) has a relatively flat shape, hovering around 3.2 km/sec, for Region 10 (Tarim basin) the velocity increases from 2.8 to 3.4 km/sec in the 28-70 second period range. The former corresponds to a thick relatively low velocity crust while the latter corresponds to low velocity upper crust (sediments) and high velocity crystalline basement. Similar interpretation can be made of other regions shown in Fig. 2. Fig. 3a shows the resolution matrix corresponding to the 31 regions and Fig. 3b the variances. By comparing Fig. 1b and Fig. 3a and b, it is clear that the amount of path coverage determines the resolution and the variances of parameters.

Short of conducting direct field tests, we can study data that have travelled through one "uniform" region. For example, an event in western Tibet recorded at KMI (Kunming), yields dispersion curves very close to the regionalization results. More verification is needed.

Anisotropic analyses

Anisotropic upper mantle seismic velocities have been found to exist, especially in the mantle under the oceans. We wish to detect any significant anisotropy in the crust of China. Regions with old crystalline basement or in Tibet where recent tectonics may have created a definite fabric are areas of interest.

Fig. 4 shows the anisotropic result for the same regions as those in Fig. 2. We have only retained 35 of the 93 eigenvalues (corresponding to those regions with enough path coverage). It is interesting to note that the orientation of the maximum velocity in southern Tibet is N 50 E, nearly parallel to the direction of compression in the region.

Velocity Inversion

For velocity inversion, we have implemented the following features in the inversion programs:

(a) Forward calculation of Rayleigh and Love group (and phase) velocities using Saito's (1988) algorithm.

(b) For group velocity partials we adopt the algorithm of Rodi et al. (1975).

(c) For inversion of the group velocity dispersion data, the "Jumping" method (Ammon et al., 1990) is coupled with smoothness constraints applied to the layer parameters. SVD is used for solution.

Only preliminary results have been obtained for a few regions; details will be provided in the poster.

Conclusions

We have derived what appear to be valid dispersion curves for many regions in China. It is to be tested whether the crustal structures derived from these dispersion curves can be used effectively in waveform synthesis for this part of the world where crustal structure information is scarce. We are processing more data in Taiwan and neighboring areas in order to improve path coverage in eastern China. We are also extending similar studies to Soviet Union.

Recommendations

One of the most effective ways to test the validity of the results contained in this report is to use actual data. To perform the test in the United States is not possible at the moment because of the lack of wide dynamic range digital stations. Testing in China or the Soviet Union is possible. By establishing temporary stations in these countries for a few months, we may have enough data. It is also possible to use limited data from China recorded on Chinese-made long period seismographs.

Acknowledgement

We wish to acknowledge the beneficial discussions we had with Jeff Barker of SUNY Binghamton on aspects of the inversion problems and R. H. Jones of University of Colorado on the statistical test of significance.

References

Akaike, H., Fitting autoregressive models for prediction, Annals Inst. Statis. Math., **21**, 243-247, 1969.

Ammon, C.J., G.E. Randall, G. Zandt, On the nonuniqueness of receiver function inversion, Jour. Geophys. Res., **95**, 15303-15318, 1990.

Barker, J.,Analysis of regional bodywave phases from earthquakes and explosions in eastern Asia, This volume, 1991.

Jones, R.H., Autoregressive order selection, Geophysics, **41**, 771-773, 1976.

Nishimura, C.E., And D. W. Forsyth, Rayleigh wave phase velocities in the Pacific with implications for azimuthal anisotropy and lateral heterogeneities, Geophysical Jour., **94**, 479-501, 1988.

Press, W.H., B.P. Flannery, S.A. Teukolsky, and W.T. Vetterling, Numerical Recipes, Cambridge University Press, New York, pp 797, 1986.

Rodi, W.L., P. Glover, T.M.C. Li, and S.S. Alexander, A fast, accurate method for computing group-velocity partial derivatives for Rayleigh and Love modes, Bull. Seism. Soc. of Am., **65**, 1105-1114, 1975.

Saito, M., DISPER80: A subroutine package for the calculation of seismic normal mode solutions, Seismological Algorithms (edited by Doornbos), Academic Press, 1988.

Zonenshain, L.P., J. Verhoef, R. Macnab and H. Meyers, Magnetic imprints of continental accretion in the U.S.S.R., EOS, **72**, 305, 1991.

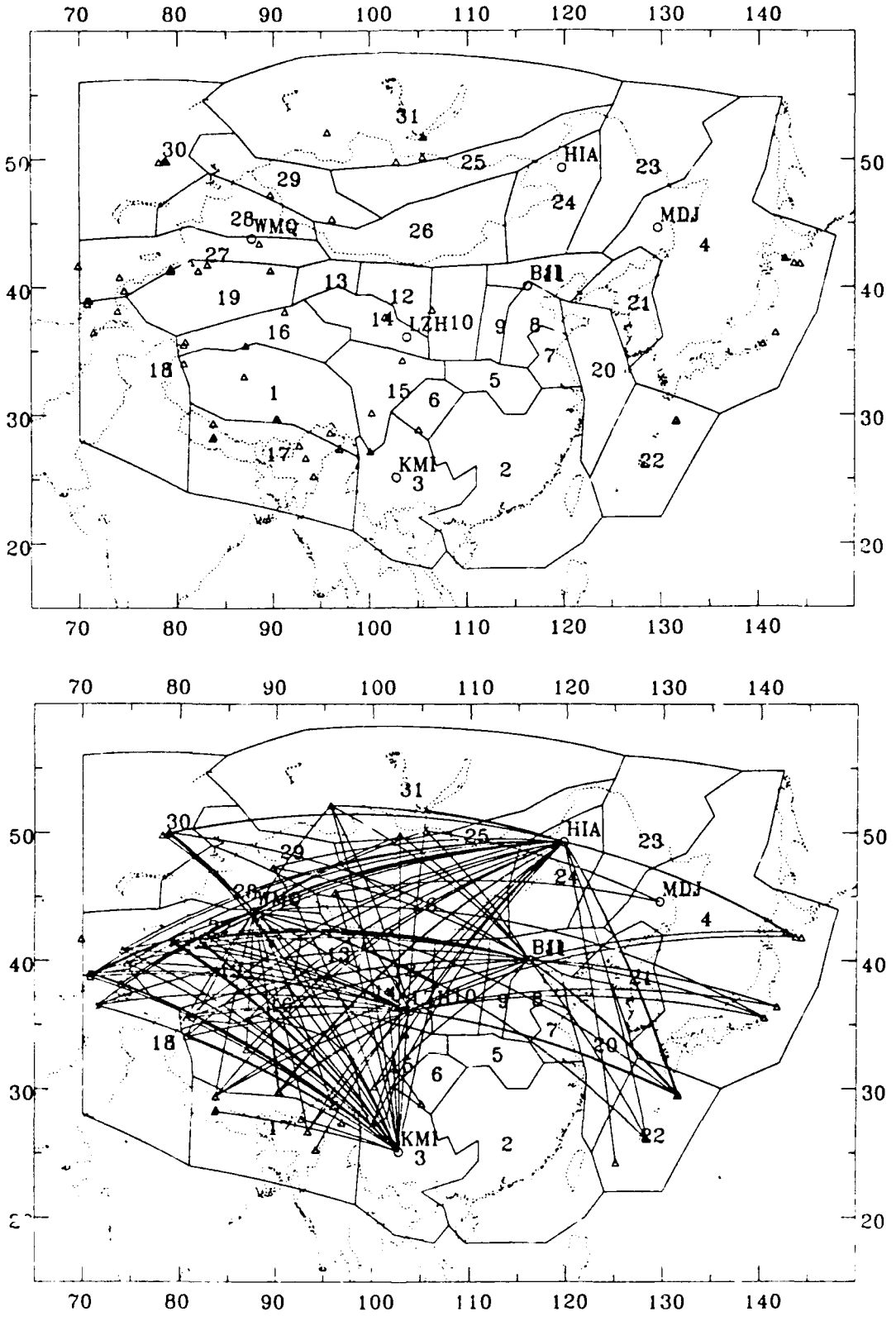


Figure 1. (a) Detailed regionalization of China based on geophysical and geological data. The circles show the location of the Chinese Digital Seismic Network stations and triangles show the location of the events used. The numbers denote the regions. Dotted lines show geographic features. (b) The paths of Rayleigh and Love waves used in the study. It is evident that the regions in western China are much better covered by the available paths.

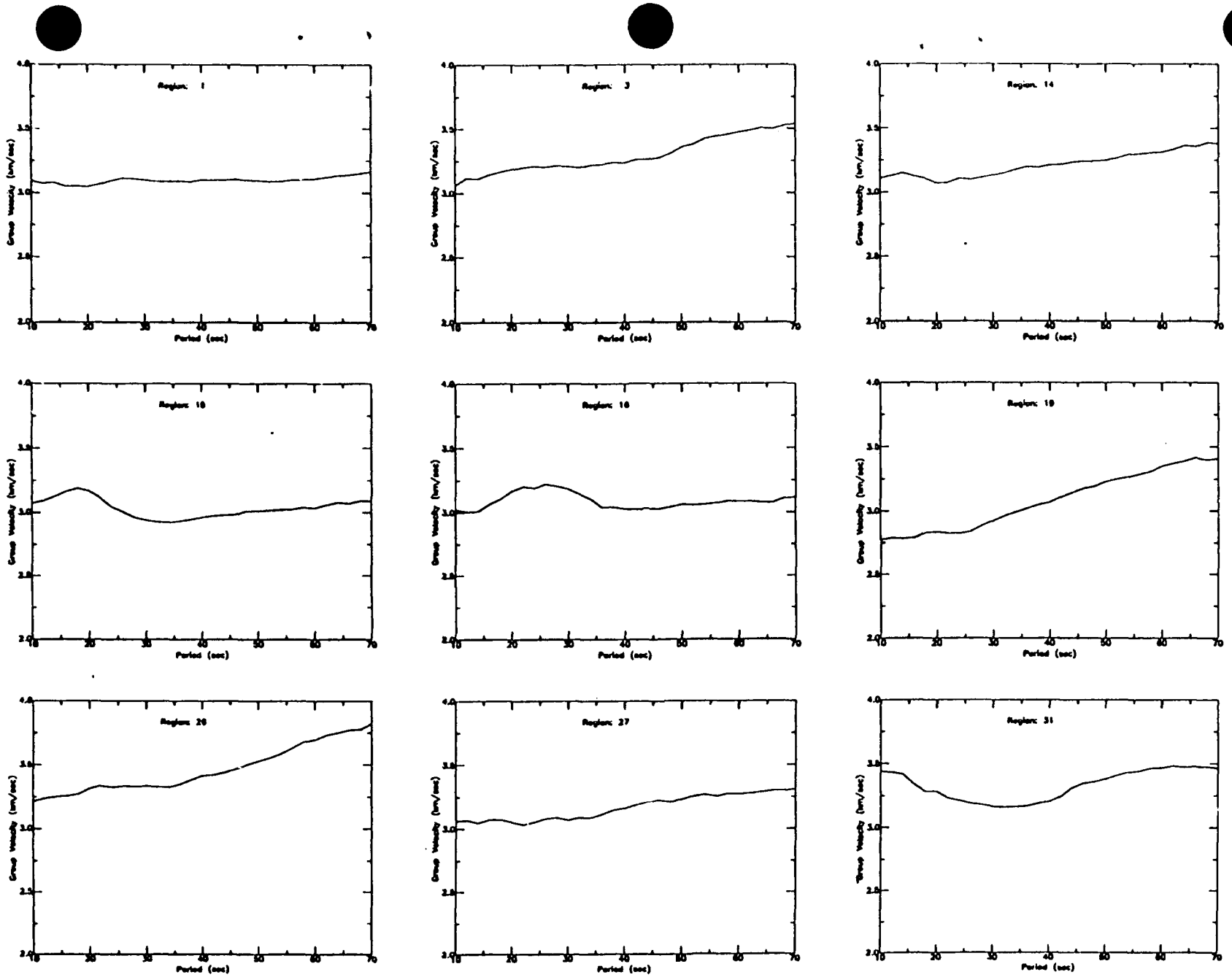


Figure 2. Dispersion results for Tibet (Region #1), Yunnan (# 3), Gansu (#14), Eastern Tibet (#15), Northern Tibet (#16), Tarim Basin (#19), Southern Mongolia (# 26), Tianshan (#27), and Southern Siberia (#31).

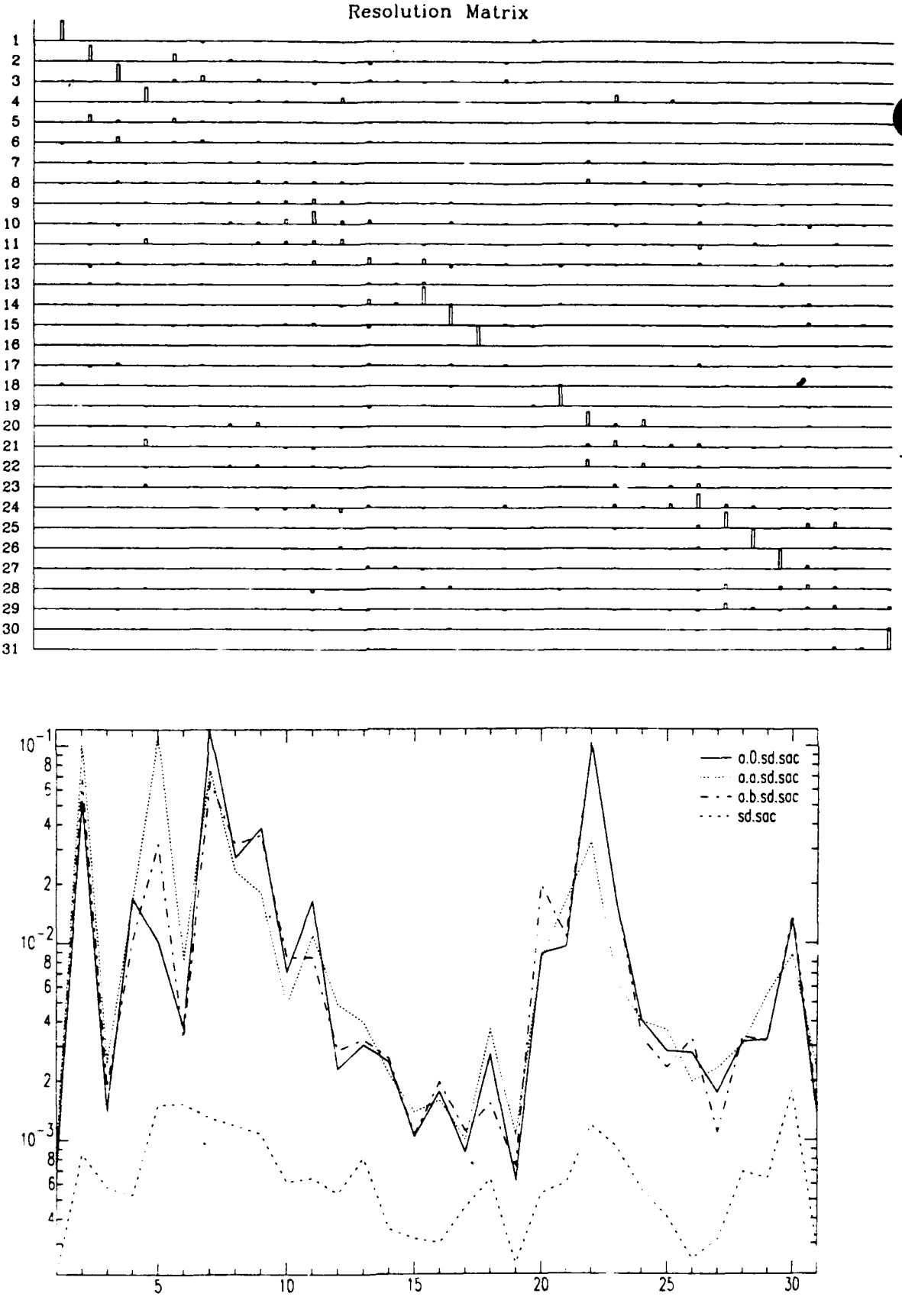


Figure 3. (a) Resolution matrix and (b) variance of parameters corresponding to the 31 regions.

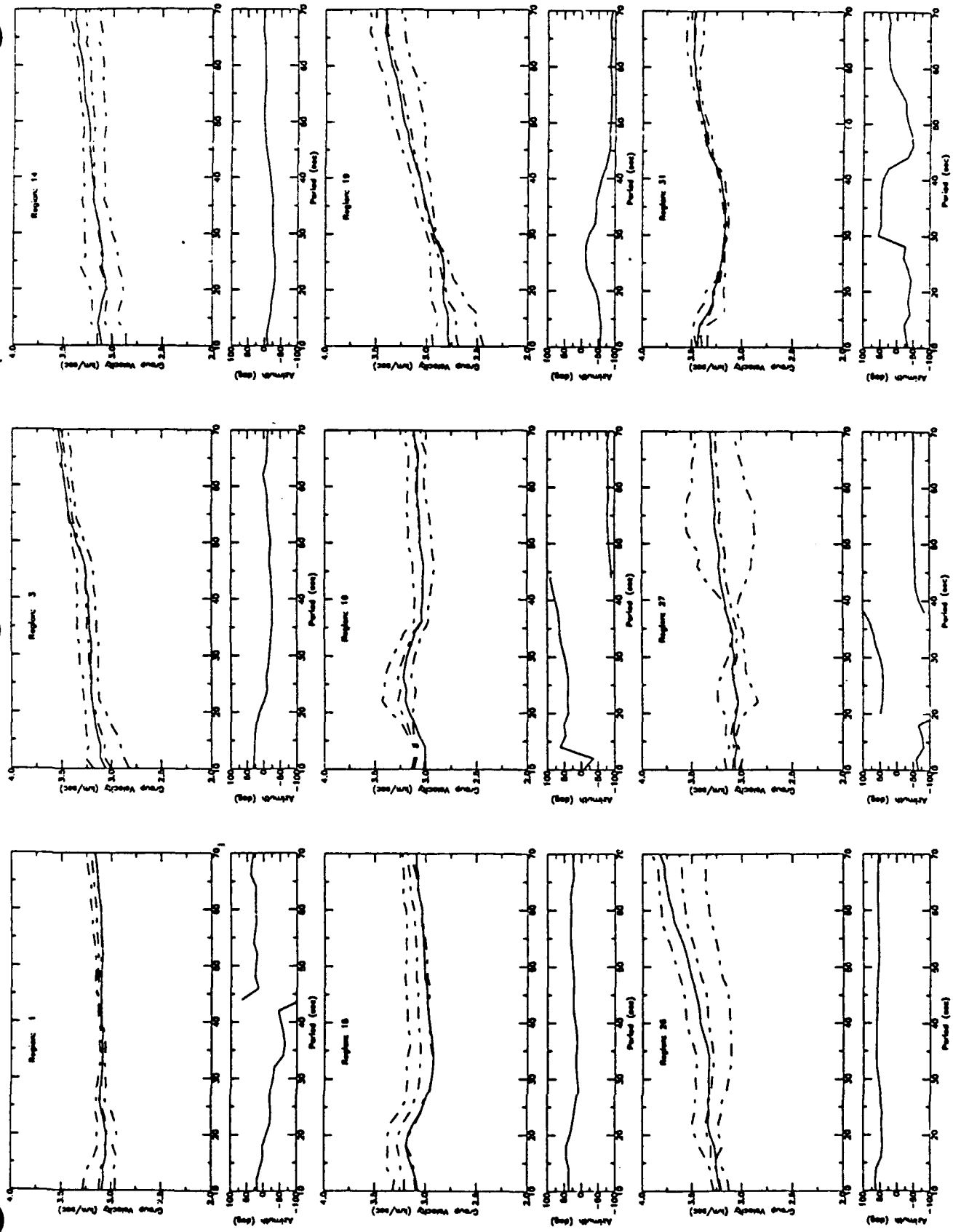


Figure 4. Experiment on the determination of anisotropy. The regions shown are the same as in Fig. 2. The solid lines are the isotropic results shown in Fig. 2 and the three dashed lines in each panel are the maximum (top), the isotropic component (middle) and the minimum (bottom) velocities. The small figure below each dispersion curve shows the orientation of maximum velocity.

TITLE:
Signal-to-Noise Enhancement with Depth in a Borehole near Amarillo, TX

AUTHORS & AFFILIATIONS:
Chris Young and Eric Chael, Sandia National Laboratories
Jerry Carter, Center for Seismic Studies

CONTRACT NO:
ARPA Order No. 4554

OBJECTIVES:

The primary objective of this study is to investigate the potential advantages of installing seismometers in deep boreholes. It is a well-established fact that placing seismic instruments below the surface of the Earth will lead to improvements in the signal-to-noise ratio (SNR) at any given site for two basic reasons. First, a significant portion of the noise commonly seen on seismograms comes from nearby surface sources (e.g. wind, industrial activity, etc.). For this reason, almost regardless of site location, noise levels decrease downhole relative to the surface (e.g. Galperin et. al., 1986; Berger et al., 1988; Barstow et. al., 1990; Gurrola et. al, 1990). The second reason for SNR improvements with depth is that signals lose energy as they propagate, particularly in low-Q (high attenuation) regions such as the near-surface. Hence, a disproportionately large amount of the total energy loss along the propagation path may occur in the relatively short final upward leg immediately beneath the seismometer.

Many previous shallower studies have found increases in SNR with depth for the near surface using data including frequencies up to 200 Hz (e.g. Fletcher et al., 1990; Aster and Shearer, 1991; Blakeslee and Malin, 1991), but deeper studies have been limited to much lower frequencies due to instrumental constraints (e.g. Hauksson et al., 1987). The availability of a very deep borehole near Amarillo, Texas, along with the relatively recent advent of broadband instrumentation which can operate under the required conditions, allowed us to conduct an experiment to investigate whether improvements in signal-to-noise continue downhole at greater depths, and if so, over what frequency bands. The answers to these questions are of great interest to the treaty verification community for a variety of reasons. First, an increase in SNR means a lower detection threshold. Second, it has been suggested that high-frequency data may be the key to identifying decoupled explosions (Evernden et al., 1986). Third, despite the tremendous number of borehole instruments now in operation, very little quantitative information is available on the increase in SNR with depth. It is important to know what the potential gains are so that they can be weighed against the various constraints (money, time, etc.) to arrive at the optimal sensor depth for a given site.

RESEARCH ACCOMPLISHED:

Our site, 50 km from Amarillo, Texas, was chosen due to the presence of a cased borehole with a total depth of nearly 2000 m. In order to be able to make simultaneous recordings at different depths, a second (370 m) hole, 8 m away from the other, was drilled and cased. A Teledyne Geotech GS21 seismometer was fixed at the bottom of the second (shallower) hole for the duration of the experiment. In the deeper hole, a GS28 seismometer was deployed at a depth of 1951 m and subsequently moved up to a depth of 1219 m (the majority of the data was recorded in the former configuration due to a variety of technical

problems). Eventually this instrument will be moved up to the surface to investigate the changes in SNR above 367 m. Both instruments are single (vertical) component, and they have identical response curves. The site is shown schematically in Figure 1a.

250 sample/sec data were recorded in both timed (noise samples every 2 hrs) and triggered (events) modes from November through December of 1989, and March through June of 1990 using a Ref-Tek portable digital data acquisition system. Surface wind velocity was also recorded to test for correlation with the noise samples. Although the Nyquist frequency of the seismic data is 125 Hz, spectral analysis was restricted to frequencies up to only 80 Hz because the responses of the instruments are unreliable for frequencies above this (P. Leahy, personal comm.).

Noise Samples and Wind

The majority of the noise sample data was taken when the deeper instrument was at 1951 m depth, so discussion of this data will be limited to that configuration. The large volume of data collected in this configuration allows us to make robust estimates of the long term noise levels at both the 367 m and 1951 m levels, and several general observations can be made.

First, the 1951 m level shows no correlation with wind at any frequency. This is somewhat surprising given the results from a similar experiment in the Balmat mine in upstate New York (Barstow, et al., 1990), where low-frequency wind noise was observed at a depth of 945 m below the surface. A possible explanation for the disagreement is that at Balmat the large shaft diameter provides enough surface area for pressure changes to load the rocks at all depths, whereas at Amarillo the narrow-diameter capped borehole does not. It may also be that the attenuation between 367 m and 1951 m at Amarillo is simply too strong to allow even low-frequency noise to penetrate to the deeper instrument. Indeed, we found that the overall (irrespective of wind) 1-3 Hz noise levels at 1951 m were up to 6 db less than at 367 m, suggesting that low-frequency noise can penetrate to 367 m, but not to 1951 m.

Wind effects can be seen at 367 m, though, again, not at the lower frequencies as was the case at Balmat. At Amarillo, times of high wind correlate with broad bands of noise from 15-60 Hz. Again, this noise is not seen at 1951 m, presumably due to attenuation.

Diurnal trends are apparent at both depths. 8 hour intervals of very broadband noise are clearly visible at both 367 m and 1951 m, and these correlate with local mining activity. Presumably the presence of this noise at 1951 m reflects a strong body wave component. It is certainly possible that the mining may emit strong surface wave components as well: if so, we would expect to see a dramatic increase in diurnal noise levels in surface data relative to the 367 m data.

Triggered Events

Some difficulty was encountered in assembling a catalogue of events with which to look for SNR changes at the shallow and deep instruments. Figure 1b shows the region around Amarillo. We quickly found that the teleseismic distance events that were recorded at Amarillo showed no changes in SNR at the shallow and deep levels due to a lack of high frequencies. Unfortunately this includes events at the Nevada Test Site (NTS -- 11.1° away). During the time of our experiment, two NTS explosions were recorded (Metropolis, 3/10/90, m_b = 5.0 and Bullion, 6/13/90, m_b = 5.7), but neither showed signal above noise level for

frequencies greater than 4 Hz. Similar observations have been made for NTS explosions recorded in Oklahoma (J. Lawson, pers. comm.), so it is apparent that the attenuation of higher frequencies is not local. Apparently the high-frequency energy from NTS shots is lost during propagation through the highly attenuating shallow mantle structure of the western U.S. We also examined recordings of teleseismic earthquakes but found the situation to be little better. For example, 13 m_b = 4.0-5.8 Mexican subduction zone events were recorded, but none had signal above noise levels beyond 10 Hz.

From this one might conclude that the deep borehole has very limited utility for teleseismic events, but we must urge extreme caution in forming such an opinion: our limited (6 non-consecutive months) period of operation hardly provides a thorough sampling of the various possible sources around Amarillo. In particular, we recorded no events from the eastern U.S., and this is very significant because it is well-known that signals traveling from the eastern U.S. to the western U.S. experience far less attenuation than the converse. Thus, it seems quite possible that the spectra for eastern U.S. events recorded at Amarillo might have significantly more power at high-frequencies, and, as we shall show subsequently, this could well lead to significant SNR improvement below 367 m.

We next turned our attention to regional events, of which there are not a great many in the Texas Panhandle. Nor is there is much in the way of other instrumentation to help locate and identify triggered events. We were able to independently verify only one event (with the quarterly bulletin of the Oklahoma Geological Survey, which runs an 11 element seismic network in Oklahoma); all other events had to be identified and assigned distances based solely on identification of regional phases (Pn,Pg,Sn,Lg) on our vertical component recordings. By far the most common type of event we triggered on was 10 km or less away, most likely due to nearby mining activity, but we chose not analyze this type of event because of the very realistic possibility of dissimilar propagation paths to the shallower and deeper instruments. We wanted to focus on the affects of attenuation on the signal as it propagates upward along the borehole. After eliminating the very local events and those that were too distant to have appreciable signal, we were left with 13 events, spanning distances from 60 to 440 km.

For both noise and signal samples, power density spectra were calculated using Welch's method (1961) with 50% overlapping sample windows. Noise samples were always taken preceding the first arrival; signal samples begin just before first arrival (Pg or Pn depending on the distance) and end before the Lg/Sn arrival. SNR's were calculated for the shallow and deep levels for each event, and we then took ratios of these ratios, i.e. $SNR_{deep}/SNR_{shallow}$. Although it might seem superfluous, this ratio of ratios is quite useful in highlighting changes in SNR with depth.

The SNR ratios for the regional events at distances greater than 220 km are shown in Figure 2a. These curves are all essentially flat, indicating no change in SNR across the range of frequencies (the curves have been offset to facilitate comparison: actually, each would plot at 0 db). We should point out that in fact none of these events has signal above noise out to 80 Hz, and the worst of them has signal above noise only out to 10 Hz, so much of what is really shown is a noise-to-noise ratio. This is a very important point, because as we shall show, the lack of any improvement in SNR for these events is almost certainly a direct result of their lack of high-frequency signal, as was the case with teleseismic events. There are some slight deviations from horizontality due to variations in the noise spectra, but no general trend is apparent to indicate that the noise is consistently different at either depth.

SNR ratios for events at distances within 220 km of our site are shown in Fig. 2b. Again, these curves have been offset for comparison. All of these events have signal above noise level out to 80 Hz, except the uppermost one which falls to noise level at 60 Hz. Thus, these events have significantly more high-frequency power than the previous ones, and it is precisely this power which should be preferentially attenuated out as the signal propagates upward, and this should be reflected as changes in SNR. In fact, clear changes in SNR are apparent: the curves are not simply horizontal and flat as was the case in Figure 3a. Careful examination reveals two important trends. First, several of the curves show a broad upwarp between 15 and 60 Hz. Second, all of the curves show a general increase in $SNR_{deep}/SNR_{shallow}$ with increasing frequency (compare left and right intercepts). In order to better see these trends, and to understand their causes, we form separate ratios of noise-to-noise (NNR) and signal-to-signal (SSR).

The NNR's for the same events, in the same order are shown in Figure 2c. 3 (4?) of the 6 curves show broad downwarping between 15 and 60 Hz, and comparison with Fig. 2b demonstrates that this feature corresponds directly with the upwarping noted above. The downwarping here indicates decreased noise levels at 1951 m (1219 m for one event) relative to those at 367 m in the range 15-60 Hz. Noting the intermittent nature of this feature, and recalling that 15-60 Hz wind noise was observed at 367 m but not at 1951 m, it seems reasonable to conclude that this feature and the corresponding one in Figure 2b may be due to wind noise. Thus, for this site on windy days, the deeper level may show broadband gains in SNR due to decreased noise levels. Returning to Figure 2c and comparing with 2b, it is apparent that the second trend alluded to, the general increase in ratio with frequency, is not present in Figure 2c. In fact, comparison with Figure 2b makes this trend much more apparent. Evidently, this feature is not related to noise.

The SSR's are shown in Figure 2d. Note that the upward/downward warping of the curves is not present, but that the positive slope is, and is now easier to see as a result. This simple linear trend in the SSR is, of course, indicative of attenuation of a signal by a frequency independent Q, and the slope of the best fitting line for each curve can be used to solve for the appropriate Q (spectral ratio method):

$$Q = \frac{-\pi(t_{deep} - t_{shallow})}{\text{slope}}$$

Where t_{deep} and $t_{shallow}$ are the measured arrival times at the deep and shallow instruments. Using this formula for the 6 events within 220 km, we find $Q_{ave} = 35.5$, with a standard deviation of 8.3. Predicted slopes for this value of Q for both 1951/367 and 1219/367 are indicated with dashed lines in Figure 2d. Clearly the fit is quite good.

CONCLUSIONS AND RECOMMENDATIONS:

We have found that for regional events within 220 km of a deep borehole near Amarillo, Texas, significant improvements in SNR at depths beneath 367 m are present. 15-60 Hz wind noise can be seen at 367 m but not at 1951 m, and this leads to broadband increase in SNR at the deeper level relative to the shallower level on windy days. More importantly, regardless of the presence or absence of wind, events with high-frequency content show a definite increase in signal power with frequency at the deeper instrument (1219 m or 1951 m) relative to the shallower. This increase can be explained by energy loss as signals propagate upward in a low-Q (35.5) attenuating layer beneath 367 m.

Highly attenuating structure in the near-surface is common, so presumably similar increases in SNR should be seen at other sites, and, indeed, this seems to be the case. In a study of local and regional events recorded in two 300 m deep boreholes in the San Jacinto fault zone, Aster and Shearer (1991) found "significantly improved seismic bandwidth due to both a reduction in ambient noise levels and (especially) to dramatically increased levels of high-frequency signal. Both effects are attributable to very high near-surface attenuation..."

Future efforts should focus on finer scale quantification of these SNR gains, and on their dependence on geologic setting. These are very important issues for determining optimal sensor depth. As the Amarillo experiment draws to a close, we will bring the deep instrument to the surface so that we can extend our analysis to the region above 367 m. Also, we will soon begin recording data in another deep borehole in Pinedale, Wyoming, a region which is characterized by a much different crustal structure.

REFERENCES:

Aster, R. C., and P. M. Shearer, 1991. High-frequency borehole seismograms recorded in the San Jacinto fault zone, southern California, part 2: attenuation and site effects, *Bull. Seism. Soc. Amer.*, **81,** 1081-1100.

Barstow, N., J. A. Carter, P. W. Pomeroy, G. H. Sutton, E. P. Chael, and P. J. Leahy, 1990. High Frequency (1-100 Hz) noise and signal recorded at different depths in a mine, northwest Adirondacks, NY, *Geophys. Res. Lett.*, **17,** 681-684.

Berger, J., H. K. Eissler, F. L. Vernon, I. L. Nersesov, M. B. Gokhberg, O. A. Stolyrov, and N. T. Tarasov, 1988. Studies of high-frequency seismic noise in eastern Kazakhstan, *Bull. Seism. Soc. Amer.*, **78,** 1744-1758.

Blakeslee, S., and P. Malin, 1991. High-frequency site effects at two Parkfield downhole and surface stations, *Bull. Seism. Soc. Amer.*, **81,** 332-345.

Evernden, J. F., C. B. Archambeau, and E. Cranswick, 1986. An evaluation of seismic decoupling and underground nuclear test monitoring using high-frequency seismic data, *Rev. of Geophys.*, **24,** 143-215.

Fletcher, J. B., T. Fumal, H. Liu, and L. C. Carroll, 1990. Near surface velocities and attenuation at two boreholes near Anza, California, from logging data, *Bull. Seism. Soc. Amer.*, **80,** 807-831.

Galperin, E. I., I. L. Nersesov, and R. M. Galperina, 1986. Borehole seismology and the study of the seismic regime of large industrial centers, Reidel, Dordrecht, 315 pp.

Gurrola, H., J. B. Minster, H. Given, F. Vernon, J. Berger, and R. Aster, 1990. Analysis of high-frequency seismic noise in the western United States and eastern Kazakhstan, *Bull. Seism. Soc. Amer.*, **80,** 951-970.

Hauksson, E., T. Teng, and T. L. Henyey, 1987. Results from a 1500 m deep, three-level downhole seismometer array: site response, low Q values and f_{max}, *Bull. Seism. Soc. Amer.*, **77,** 1883-1904.

Welch, P. D., 1961. A direct digital method of power spectrum estimation, *IBM J. Res. Develop.*, **5,** 141.

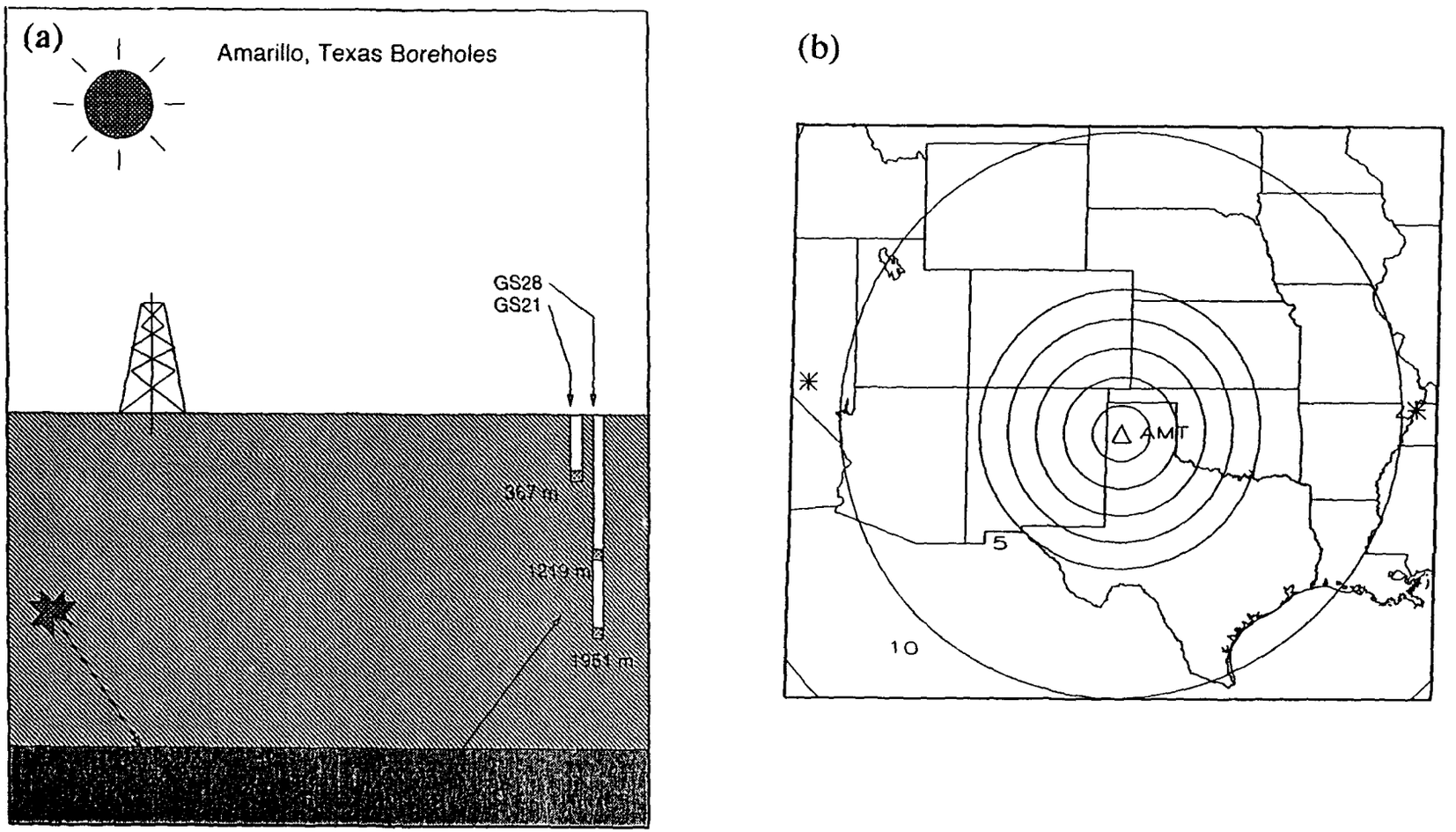


Figure 1. (a) Schematic of Amarillo, Texas borehole site. (b) Regional distance map of area around Amarillo. Circular contours indicate distance from Amarillo (1-5°, 10°). NTS and New Madrid, Missouri are marked with crosses.

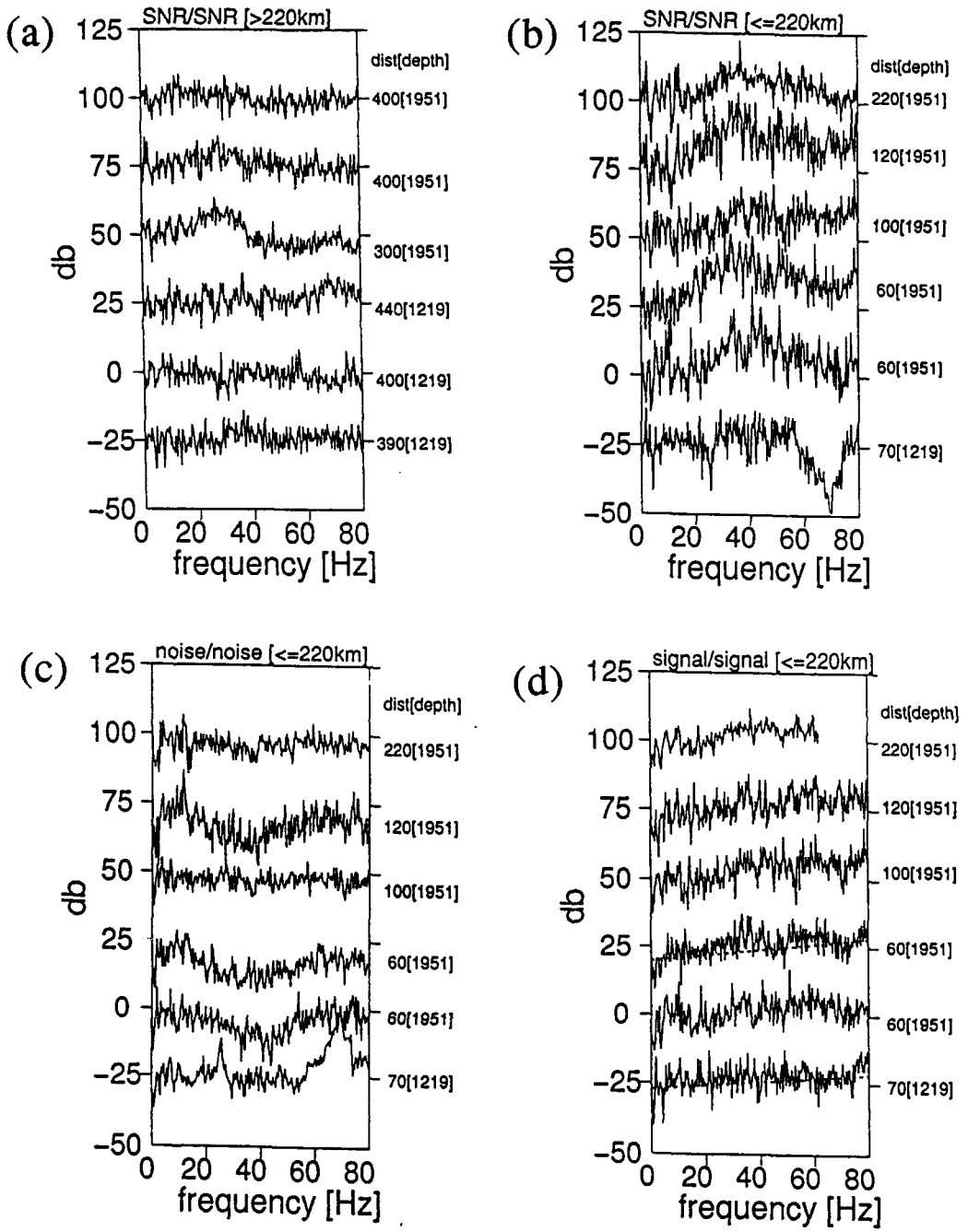


Figure 2. (a) Ratio of SNR's for regional events >220 km distance from Amarillo. Spectra have been vertically offset, so vertical scale is for relative comparison only. Numbers to the right indicate distance in kilometers, and depth of the deeper instrument in meters. (b) Same as "a", but for events within 220 km. (c) As in "b", but noise/noise (same events, same order). (d) As in "b", but signal/signal. Dashed lines indicate predicted trends for frequency independent Q of 35.5 for 1219/367 and 1951/367.

Regional Phase Propagation in Central Asia

C. S. Lynnes
R.-S. Jih

Teledyne Geotech, 314 Montgomery, Alexandria, VA 22314

Contract No. F19628-90-C-0158

OBJECTIVE

Obtain 1-d and 2-d velocity structure in Central Asia, near Garm, U.S.S.R.

RESEARCH ACCOMPLISHED

Introduction

The propagation of regional phases is still problematic: amplitudes and even the observability of phases can be highly variable. This has important implications for the application and efficacy of earthquake/explosion discriminants and event size estimation. At least some of this variation is likely due to the effects of lateral heterogeneity, particularly in the waveguides and near the boundaries along which regional phases such as *Pg, Pn, Sn,* and *Lg* propagate. The effects of lateral heterogeneity on regional phase propagation can be modeled using finite-difference methods.

In order to employ these methods, a realistic velocity model is required. Block inversion of travel times is a well-established technique for deriving laterally heterogeneous velocity structures. In order to simplify the problem and improve ray coverage, a two-dimensional geometry is sought: the high seismicity rate in the vicinity of the IRIS station GAR provides such an opportunity. The first step in this process is the derivation of a spherically symmetric structure for the crust and upper mantle in this region. This model will then be the starting model for a two-dimensional velocity inversion in the vertical plane.

Methodology

The inversion method used herein is based on the joint inversion of hypocenters and velocity structure outlined by Crosson (1976). Beginning with a starting model, perturbations ($\Delta\mathbf{m}$) to the previous model $\mathbf{m}$ are sought to minimize the travel time residual vector $\mathbf{d} = \mathbf{T}^{pred} - \mathbf{T}^{obs}$. The model perturbations include both hypocentral parameters and velocity structure.

The above method requires computations of theoretical travel times, ray parameter and $\partial T/\partial z$ for all source-station pairs in an arbitrary velocity structure. As the solution of the two-point problem can be lengthy and unstable in the presence of low-velocity zones or strong gradients, we use Vidale's (1988) finite-difference technique to compute the travel times throughout a two-dimensional grid for a source at the surface. The various hypocentral partial derivatives are computed numerically, interpolating from the grid points at the corresponding to the focal depth and epicentral distance. Rays are also traced by following the travel time gradient back to the source at the surface in order to compute the velocity structure derivatives.

The resulting matrix equation $\mathbf{A\Delta m = d}$ is inverted by forming the square matrix equation $\mathbf{A^T A\Delta m = A^T d}$. The matrix $\mathbf{A^T A}$ is a doubly-bordered block-diagonal sparse matrix. Consequently, it lends itself well to the Sherman-Morrison inversion method (Press *et al.*, 1986), in which the matrix inverse is found for the purely block-diagonal matrix, and then successively modified for each row and column making up the borders. Increasing the number of events thus results in an increase of only order N^2 for the inversion of the normal equations.

Data and Results

The travel time data consist of the primary arrivals reported by the International Seismological Center (ISC) from 1971-1982 at stations less than 1000 km (9°) away. The ISC locations (Figure 1) are used as the initial guesses for hypocentral parameters. Events were selected carefully to include close stations so that the tradeoff between depth, origin time and source layer velocity could be resolved.

Several studies (*e.g.*, Carter *et al.*, 1991) indicate the crust to be very thick in this region. Figure 2 shows reduced travel time residuals for events with ISC depths of 10-15 km. The travel time curve for the Soviet GAR model (which has a mantle velocity of about 8.22 km/s) is superimposed. The match is fairly good at this depth, with the thick crust confirmed by the large crustal-mantle phase crossover distance. Figure 3 shows the residuals for events with ISC depths between 40 and 45 km. The deterioration at depth may indicate that ISC depths are systematically overestimated due to the velocity model.

A starting model similar to the GAR model was used in the inversion. The mantle velocity was fixed at 8.2 km/s in order to stabilize the layer directly abov However, this velocity appears to be well constrained by the travel time slope from 400-1000 km (Figures 2-3). The crustal depth was fixed at 65 km. Figure 4 shows the results of the joint inversion. The resulting model is similar to the GAR model. The velocity gradient is slightly steeper in the upper crust. Below this is a 35-km thick lower crust of about 7 km/s, slightly lower than the GAR model velocity. The relocated depths are plotted against the ISC depths in Figure 5. As indicated in Figure 3, the relocated depths are generally less than the ISC depths.

Conclusions and Recommendations

A joint inversion algorithm for hypocenters and velocity structure has been developed based on the algorithm of Crosson (1976). Vidale's (1988) finite-difference travel time algorithm and the Sherman-Morrison inversion of sparse matrices have been used to speed execution for large numbers of events. A joint inversion for hypocenters and velocity structure in Central Asia yields a 1-dimensional model with a thick crust consisting a 30-km upper crust with a steep gradient and a roughly homogeneous 35-km lower crust of about 7 km/s. Focus depths appear to be systematically overestimated by the ISC. This model will be used as the starting model for a 2-dimensional tomographic inversion of a profile in central Asia.

References

Carter, J., Coyne, J., Israelsson, H., Riviere-Barbier, F., Ryaboy, V., and A. Suteau-Henson (1991). Nuclear monitoring research at the Center for Seismic Studies, *Scientific Report No. 1., PL-TR-91-2127*, SAIC, Arlington, Virginia.

Crosson, R. S. (1976). Crustal structure modeling of earthquake data 1. Simultaneous least squares estimation of hypocenter and velocity parameters, *J. Geophys. Res.*, **81**, 3036-3046.

Given, J. W. and D. V. Helmberger (1980). Upper mantle structure of northwestern Eurasia, *J. Geophys. Res.*, **B12**, *7183-7194*.

Press, W. H., Flannery, B. P., Teukolsky, S. A., and W. T. Vetterling, (1986). *Numerical Recipes*, New York: Cambridge University Press, 818 p.

Vidale, J. (1988). Finite-difference calculation of travel times, *Bull. Seism. Soc. Am.*, **78**, 2062-2076.

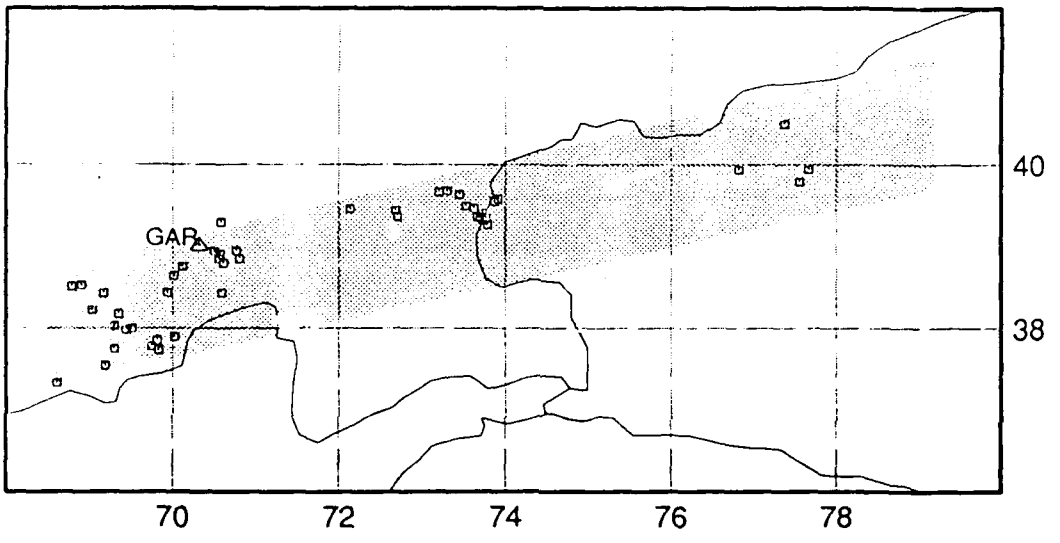


Figure 1. Index map showing the events used in the inversion, and station GAR.

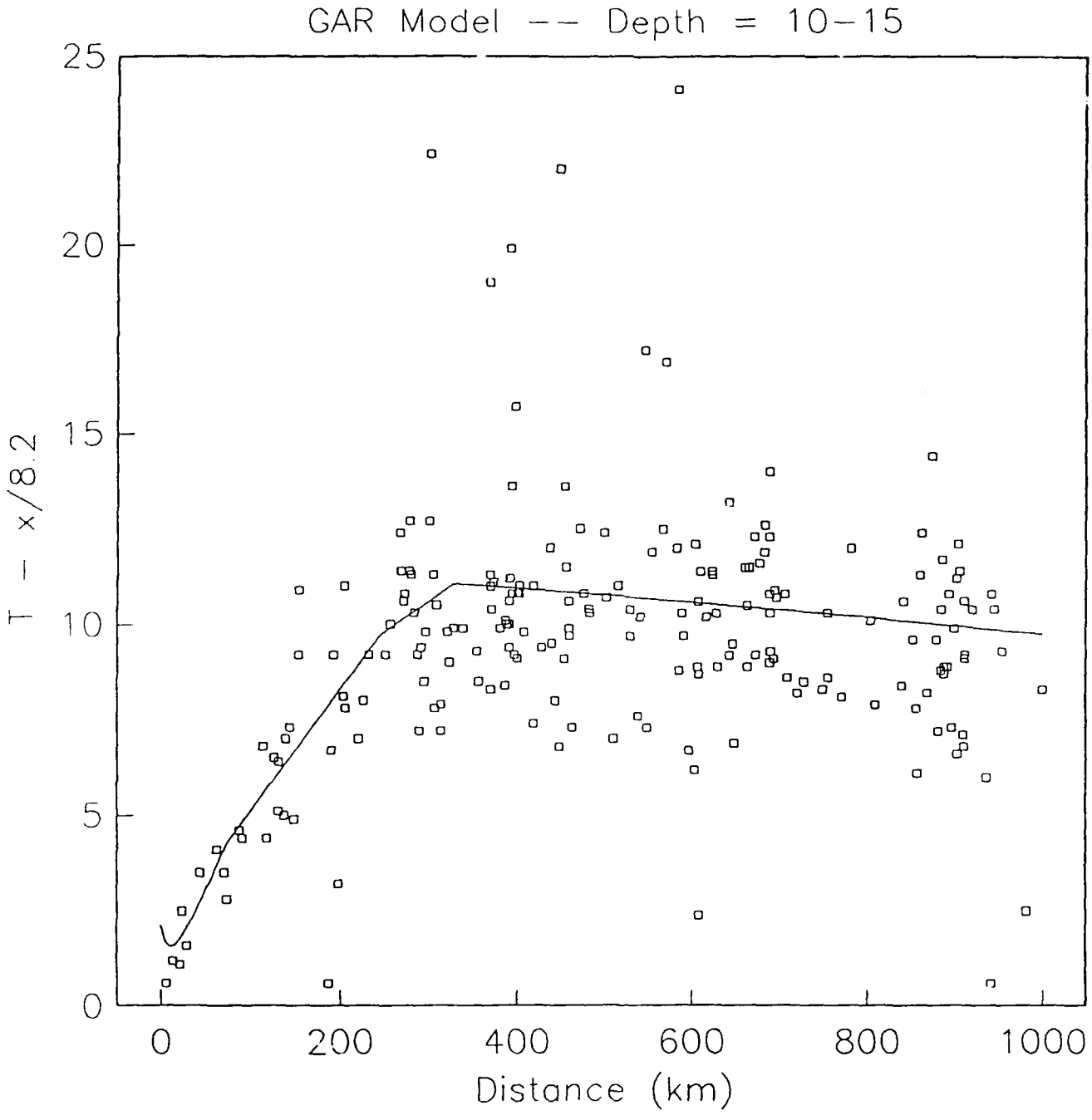


Figure 2. Reduced travel times for events 10-15 km in the shaded region of Figure 1 with ISC depths of 10-15 km. (The inversion events in this depth range are a subset of this set). The predicted travel time curve for the Soviet GAR model reported by Carter *et al.* (1991) is superimposed.

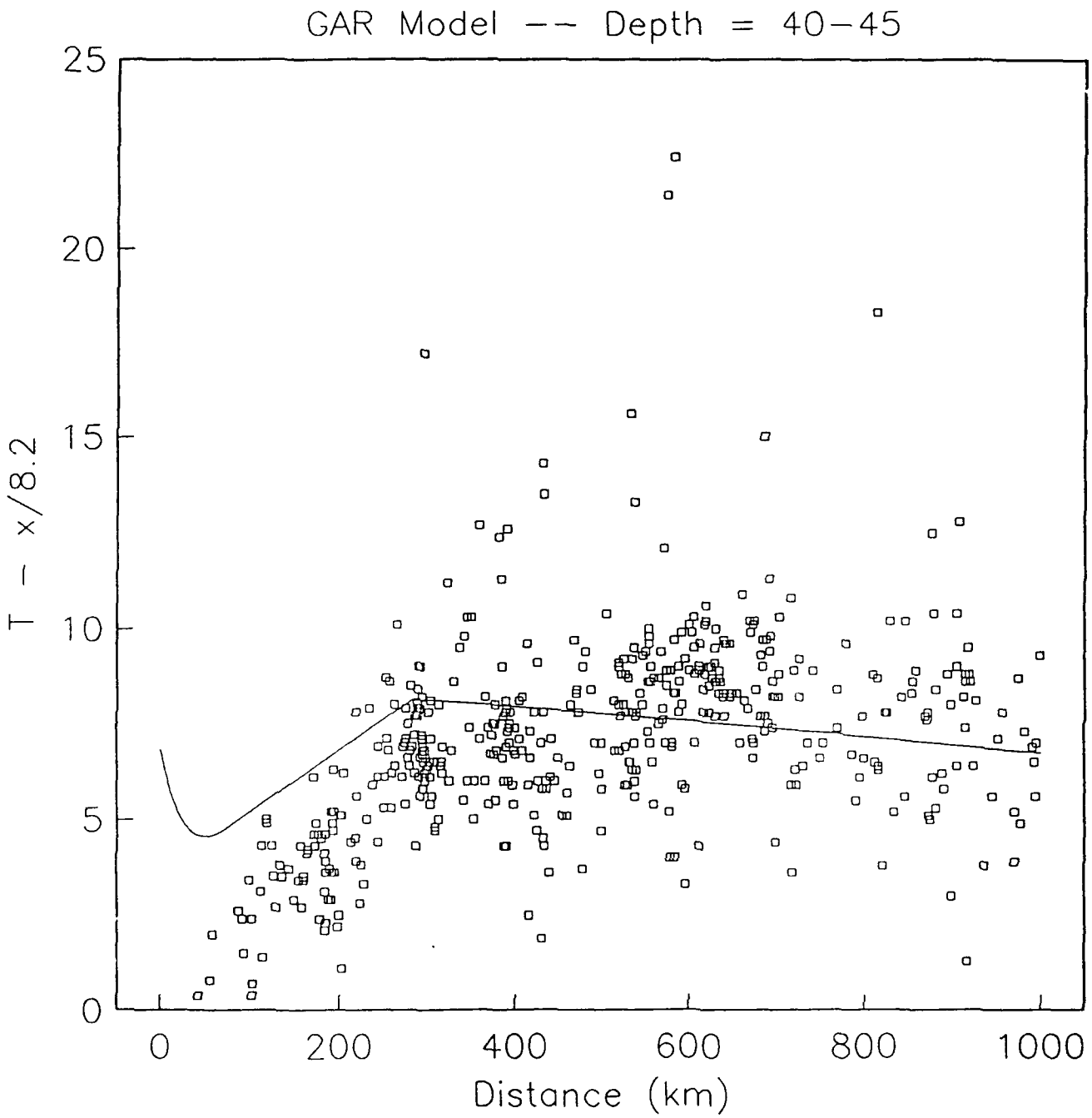


Figure 3. Same as Figure 2 for a depth range of 40-45 km. The small reduced travel times for close stations suggests the ISC depths are systematically overestimated.

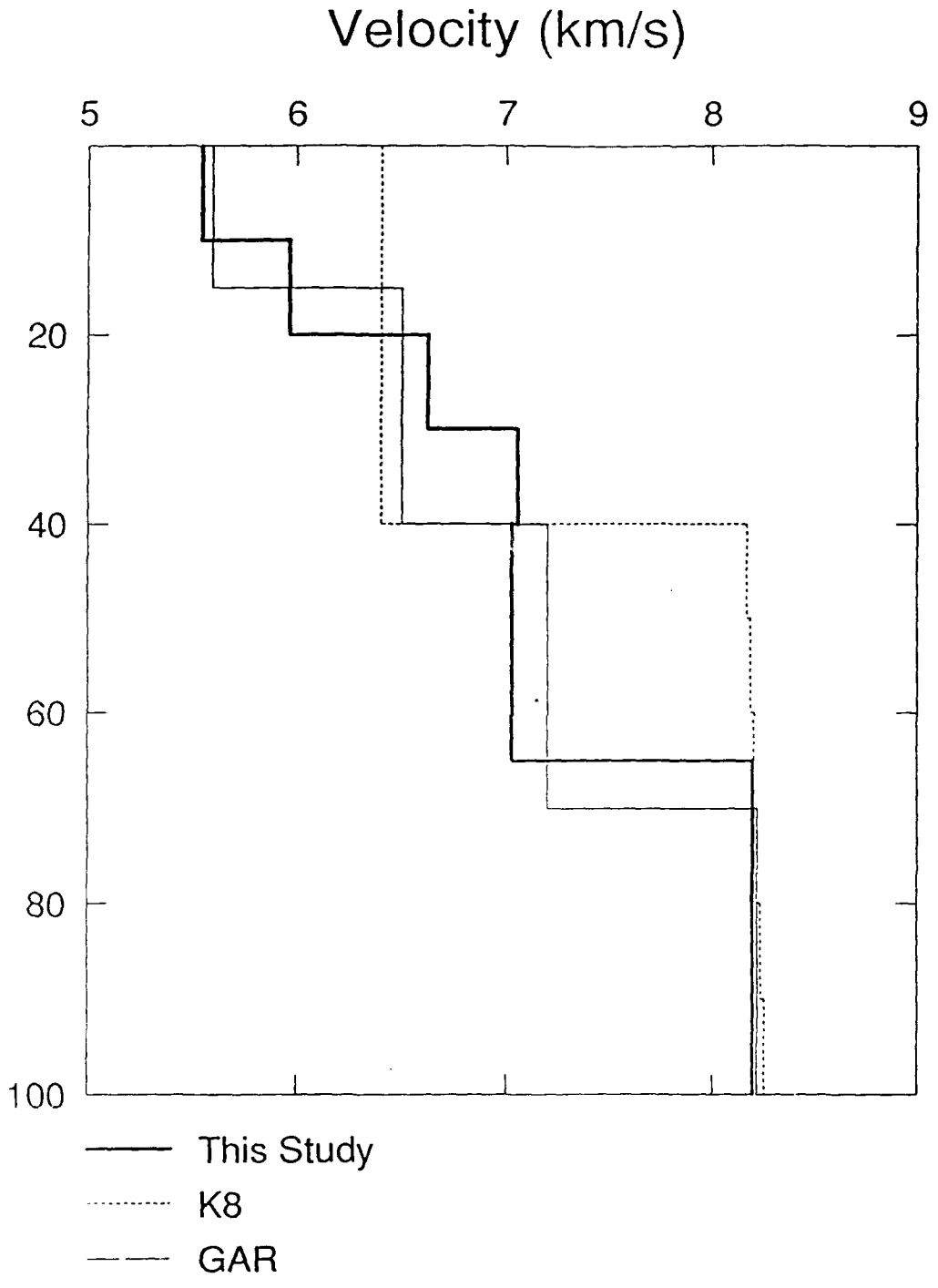


Figure 4. The final velocity model from the joint inversion is shown as the thick line. The Soviet model for station GAR (Carter *et al.*, 1991) and K8 model (Given and Helmberger, 1980) for NW Eurasia are shown for comparison.

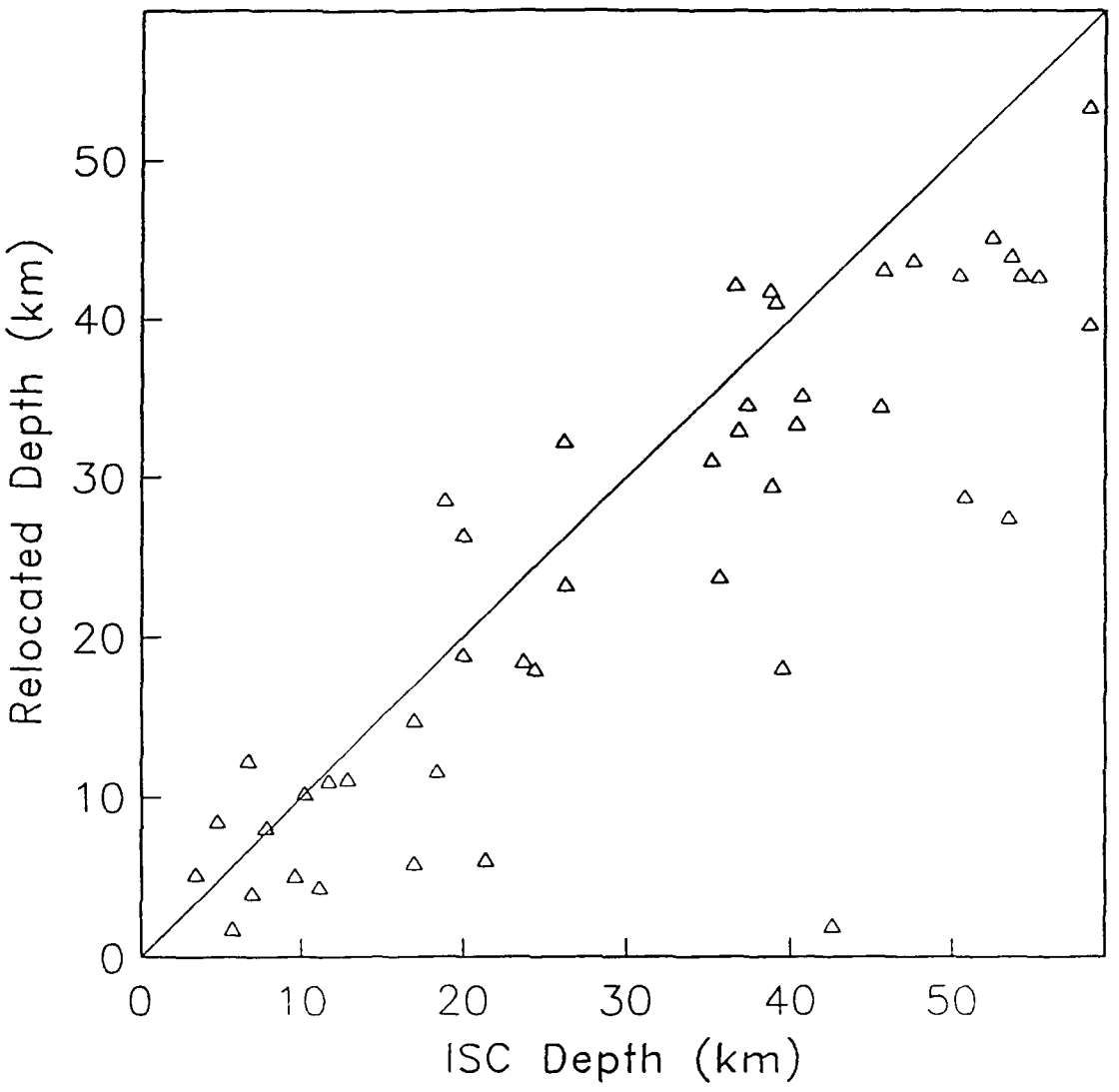


Figure 5. Hypocentral depths obtained from joint inversion plotted vs. those from the ISC. The inversion yields systematically shallower depths.

Modulus Dispersion and Seismic Wave Attenuation Related to the Seismic Source Region

R.W. Haupt, R.J. Martin, III, X. Tang, W.J. Dupree

New England Research, Inc.
White River Junction, VT

Yield determinations for large explosions computed from teleseismic data are strongly dependent on the lithological properties in the source region. The most significant changes in the seismic pulse occur within a few wavelengths of the source. Equal magnitude explosions hosted in different rock types can generate very different teleseismic waveform signatures. Essential rock properties characteristic of different sites can be measured in the laboratory. The benefit of obtaining laboratory measurements is that a variety of rock types similar to those in the source region can be readily studied and analyzed.

It is important to determine the correlation between rock properties measured in the laboratory and *in-situ* conditions. Elements that must be considered in determining this correlation include frequency, lithologic variations, fluid saturation, fractures, and strain amplitude. The effect of each variable must be studied separately to define its relative contribution to *in-situ* rock properties. In this study, the effects of frequency on the observed elastic and inelastic properties are addressed. The physical mechanisms of modulus dispersion and seismic wave attenuation are examined for three different rock types; Sierra White granite, Berea sandstone, and the Topopah Spring Member tuff.

Four laboratory techniques are used to determine Young's modulus and the extensional quality factor, Q_E (attenuation), spanning frequencies from 0.01 Hz to 700 kHz. These techniques differ substantially in experimental arrangement. A serious attempt was made to minimize the variations in strain amplitude between the techniques. This enabled meaningful comparisons of the measured data. These techniques and frequency ranges are listed below.

hysteresis loop (cyclic loading)	0.01 - 50 Hz
waveform inversion	10 - 80 kHz
resonant bar	1-100 kHz
ultrasonic	1 MHz

At frequencies less than 100 Hz, Young's modulus and Q_E were determined from stress and strain measured during cyclic loading experiments. Young's modulus was determined from the slope of the stress-strain data. Attenuation was computed from the phase angle between stress and strain. Special attention was given to minimize the strain

amplitude for the cyclic loading measurements. Strain amplitudes as low as 10^{-6} to 10^{-5} were achieved. Extrinsic mechanical and electronic system losses of the loading apparatus were determined from a low loss standard (aluminum). The aluminum sample had the same cross-sectional area, length, and loading conditions of those of the rock samples. The system phase lag was then subtracted from the measured phase angle for the rock sample.

The waveform inversion technique was also used to measure attenuation. The technique consists of propagating low-frequency waveforms through cylindrical bars of the same rock, but of different lengths. The procedure consists of two steps. First, the waveform received from the short bar is theoretically propagated to the distance of the long bar, in which the dispersion effect on the waveform due to the waveguide is removed. Second, the inversion of the attenuation in the rock sample is computed by minimizing the difference between the propagated waveform and the actually measured waveform with the long bar.

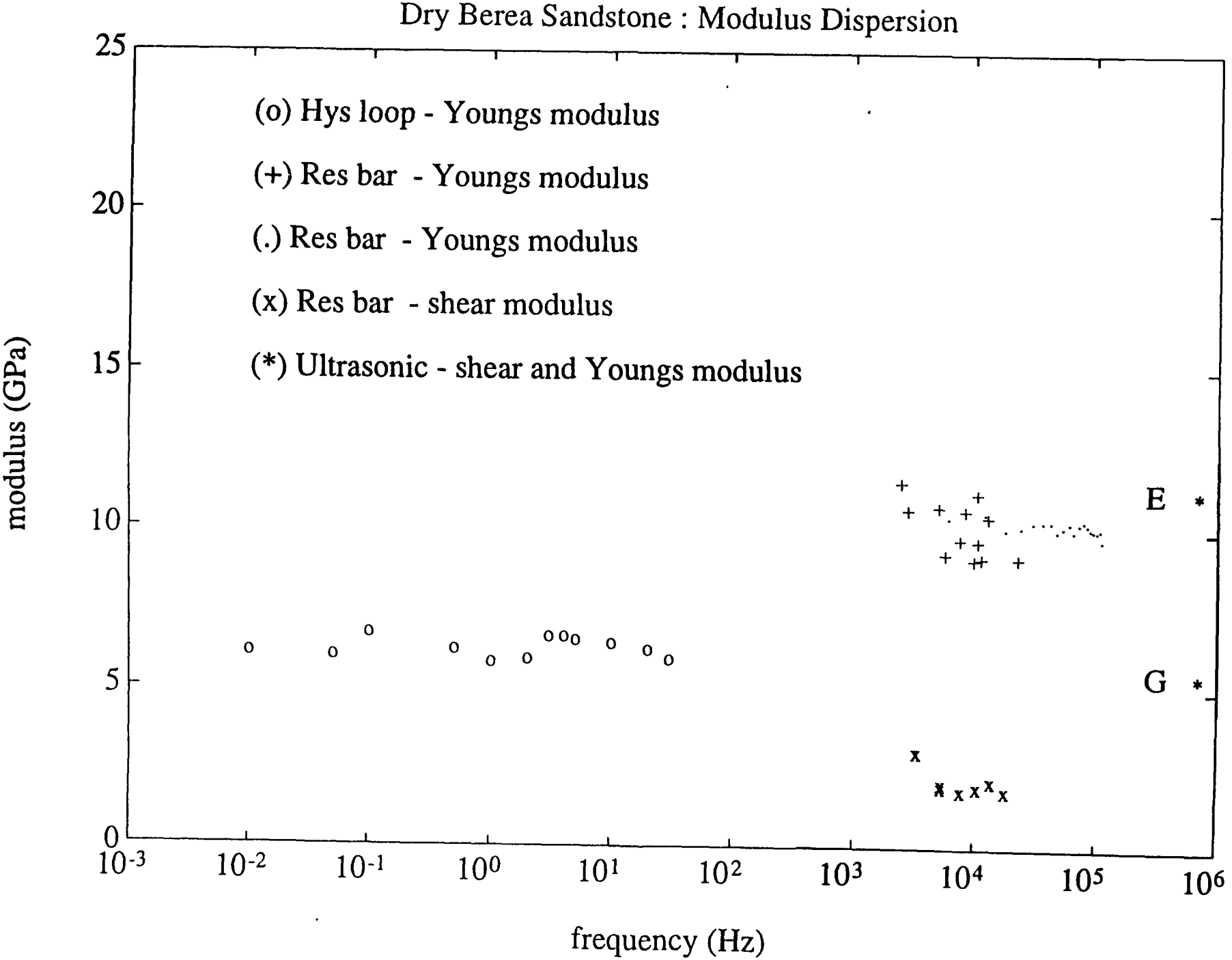
The resonant bar technique is used over the frequency band from 1 to 100 kHz. A standing extensional wave is generated from piezoelectric crystals mounted to the sample ends. Extensional velocity was computed from the center frequency of the resonant peak and bar length. Young's modulus was then computed from the velocity and bar density. Q_E is computed from the center frequency and half-power bandwidth of the resonance.

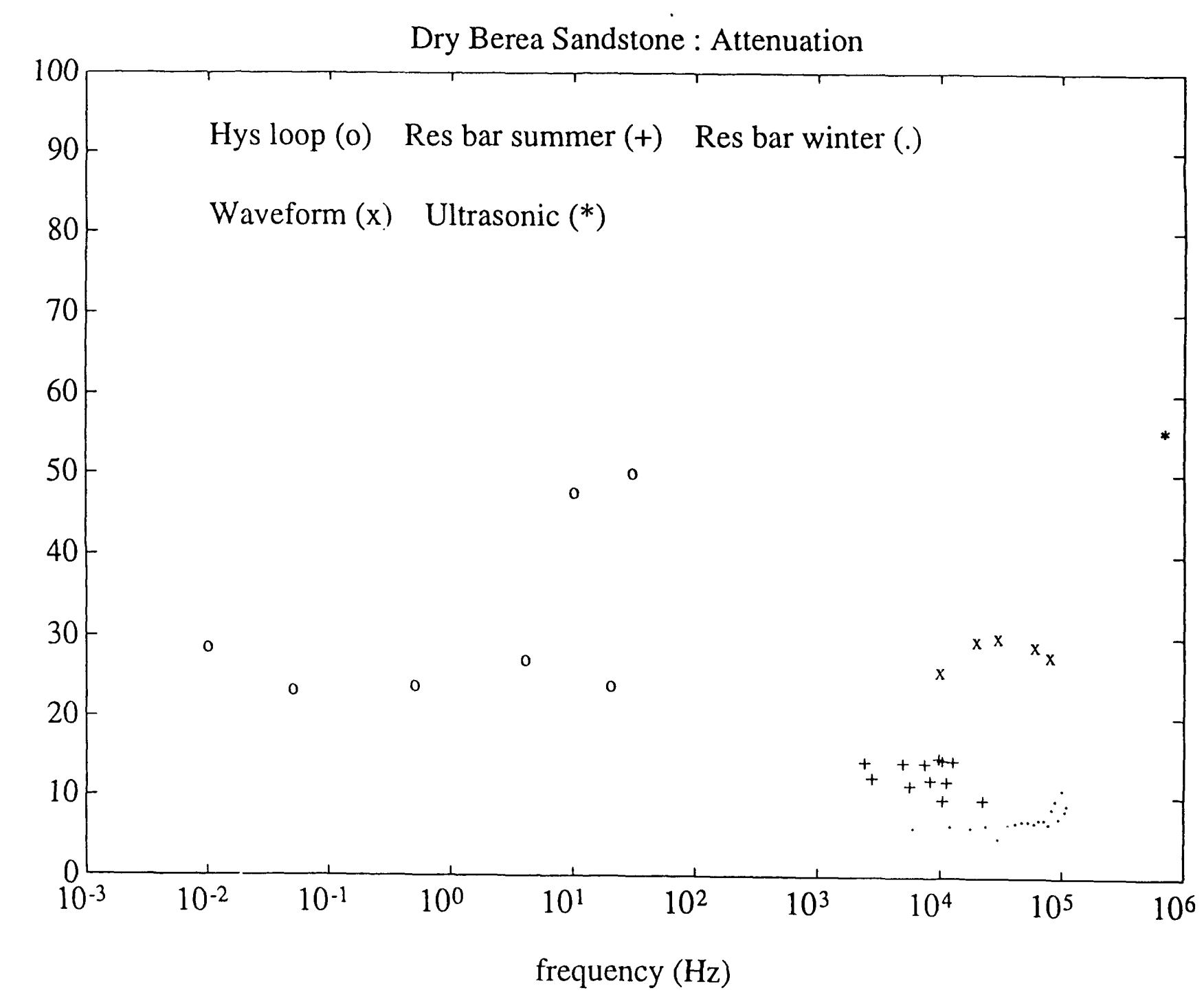
Ultrasonic compressional and shear wave velocities were measured to determine Young's modulus at 700 kHz. Attenuation was computed from values of Q_p, Q_S and Q_E determined from the spectral ratio technique of a low loss standard (aluminum) to that of the rock sample.

The suite of measurements was performed on the three rock types at ambient pressure and temperature for room dry conditions. For all three rock types, Young's modulus exhibits an increase with increasing frequency. The largest change observed approached 33% for the dry Berea sandstone sample. Some of the change is attributable to differences in strain amplitude. Strain amplitudes developed for the cyclic loading were on the order of 10^{-6} to 10^{-5}, whereas wave propagation and bar resonance were associated with strains of 10^{-8} to 10^{-7}. Results on dry Berea sandstone show that the Young's modulus increases from 7.8 GPa at a frequency of 0.01 Hz to 11.7 GPa at 700 kHz. The attenuation for dry Berea sandstone appears to be independent of frequency up to 100 kHz and then increases above this point. The resonant bar measurements exhibit Q_E values approximately double those of the other techniques. Modulus dispersion and attenuation for Berea sandstone are shown as a function of frequency in Figures 1 and 2. The attenuations for dry Sierra White granite and Topopah Spring Member tuff also appear relatively independent of frequency. There was better agreement between the resonant bar and the waveform inversion technique for Sierra White granite; in fact, attenuation was equivalent where the frequencies overlap.

A comprehensive investigation is continuing on the characterization of the these rocks in a water saturated condition. Moduli and attenuation are strongly affected by water saturation. Results show that modulus and attenuation vary more for the saturated samples than the dry.

This is the first comprehensive study of modulus dispersion and attenuation from quasi-static to ultrasonic frequencies for granite, sandstone, and tuff. These experiments indicate that the elastic moduli and attenuations of rocks do vary as a function of frequency.


Dry Berea Sandstone : Modulus Dispersion
(o) Hys loop - Youngs modulus
(+) Res bar - Youngs modulus
(.) Res bar - Youngs modulus
(x) Res bar - shear modulus
(*) Ultrasonic - shear and Youngs modulus
E
G
modulus (GPa)
frequency (Hz)
25
20
15
10
5
0
10-3
10-2
10-1
100
101
102
103
104
105
106


Dry Berea Sandstone : Attenuation
Hys loop (o) Res bar summer (+) Res bar winter (.)
Waveform (x) Ultrasonic (*)
attenuation (1000/Qe)
frequency (Hz)
100
90
80
70
60
50
40
30
20
10
0
10-3
10-2
10-1
100
101
102
103
104
105
106

A Systematic Study of the Effects of Crust and Upper Mantle Structure on Regional Seismograms

by

Danny J. Harvey
University of Colorado/CIRES
Campus Box 449
Boulder, CO 80309

Roger A. Hansen
AFTAC
Patrick AFB, FL

Contract No. F19628-90-K-0050

Objective

As part of a broader effort to invert for Eurasian crust and upper mantle structure, a study has been undertaken to investigate the effects of structural model variations on regional synthetic seismograms. The intent of this study is to produce regional synthetic seismograms that approximately match the observed data so that the inferred structural models can be used as starting points in a formal inversion procedure. Another purpose for this study is to identify to what extent different modeling techniques can be used to adequately represent the observations.

We are particularly interested in using laterally homogeneous modeling procedures since they are computationally efficient and accurate, given the assumption of 1D structure. This issue of computational efficiency is not a minor point. The process of inferring source and structural parameters, whether using formal inversion procedures or systematic studies, requires a large number of forward evaluations. On the other hand, we know that the earth is not laterally homogeneous and it is important to identify the inadequacies of full waveform modeling using 1D structures. In this study we hope to gain understanding about the basic physical processes that are important for regional seismic wave propagation and we want to determine the fundamental limitations of 1D modeling techniques.

Research Accomplished

The data we used in this study comes from three sources and we have concentrated on the USSR Joint Verification Experiment (JVE) nuclear shot that took place on September 14, 1988 at the Semipalatinsk test site in Kazakhstan. The first set of data sources are the IRIS high frequency surface instruments at Chusal (CHS), Arti (ARU) and Obninsk (OBN). The second set of sources were portable high frequency instruments that were placed at Karasu (KSU), Karkaralinsk (KKL) and Bayanaul (BAY) and the third data source consists of hand digitized analog records recorded by Soviet observatories at

ARU, OBN, Talaya (TLY) and Norilinsk (NRI).[1] Figure 1 shows a record section plot of the vertical component IRIS and portable digital instrument recordings after application of a low pass filter and decimation to 1 Hz nyquist frequency. The useful frequency range is 0.1 to 1.0 Hz. The digitized Soviet data after similar filtering and decimation is shown in figure 2.

Although the instrument responses for the analog records are somewhat different from those of the digital instruments, we can still see certain basic characteristics of the waveforms.

1. Other than the first P arrival, the only consistent arrival is L_g which is characterized as an emergent arrival with a long coda. We should point out that L_g is not always apparent from other test sites or at stations from the Kazakh test site that are further away.
2. The S_n arrival, which becomes the direct upper mantle S arrival at the longer distances, can be seen on some of the records (CHS and ARU), but it is small.
3. There is no obvious P_g arrival. It could be hidden in, or contributing to, the coda associated with the first P arrival.
4. There is no appreciable Rayleigh wave in this frequency band for the stations at distances greater than 250 km.

We used three methods for computing synthetic seismograms for comparison with the data: the locked mode method of Harvey,[2] the reflectivity method[3] and the WKBJ ray theoretical method of Chapman and Dey-Sarkar.[4] Most of the complete seismograms were computed with the locked mode method with the reflectivity method used for periodic checks. The WKBJ ray theory was meant to be used as a very rapid initial check of candidate structural models. The synthetic seismograms were all computed to 1 Hz nyquist frequency and were filtered with the instrument responses and the same anti-aliasing filter used in the decimation of the data.

The structural models used in this study are shown in figure 3. We started with a "crude" model, shown in figure 3a, which consists of six homogeneous layers with discontinuities at 10, 50, 220, 410 and 700 km depth. The Q model for the "crude" structure was Q_α = 2000 and Q_β = 950 in every layer except the topmost layer where Q_α = 200 and Q_β = 95. A synthetic record section using the crude model is shown in figure 4a. If we compare this with the data we can see that the crude model produces no appreciable L_g and it produces a direct S arrival that is much larger than in the data. If we try to increase the Q values in the topmost layer, a large Rayleigh wave appears and L_g is still much smaller than in the data.

Figures 4b through 4g show the synthetic record sections corresponding to the structural models shown in figures 3b through 3g. The base1 model is a layerized version of a model with smooth gradients within the crust, at the Moho and in the upper mantle. The base2 model is similar to base1 except that a weak low velocity zone has been introduced at about 100 km depth, the upper mantle gradients have been decreased and gradients at the upper mantle discontinuities have been added. The base3 model, although unrealistic,

---

[1] The digitized analog Soviet data was obtained through a joint US-Soviet seismic data exchange agreement. These data were originally heliocorder records that were hand digitized by a US contractor.

[2] Harvey, D. (1981). Seismogram synthesis using normal mode superposition: the locked mode approximation. *Geophys. J. R. Astr. Soc.* **66**, 37-61.

[3] Luco, J. and Apsel, R. (1983). On the Green's functions for a layered half-space: Part I. *Bull. Seismol. Soc. Am.* **73**, 909-929.

[4] Dey-Sarkar, S. K. and Chapman, C. H. (1978). A simple method for the computation of body-wave seismograms. *Bull. Seismol. Soc. Am.* **68**, 1577-1593.

was an attempt to minimize the direct S phase by using a completely smooth V_s distribution throughout the upper mantle.

In a previous study we determined that using a vertically randomized velocity distribution in the crust produced synthetic seismograms that show many of the features that we see in the data especially in the early parts of the wavetrain. The ran1-base1, ran1-base2 and ran1-base3 (figures 3e, 3f and 3g) structural models are combinations of the upper mantle structures of base1, base2 and base3 with a vertically randomized version of the crust.

If we look at the synthetic record sections of figures 4a, 4b, 4c and 4d, which all correspond to smooth or large-scale blocky structural models, we see many large amplitude impulsive arrivals. The direct upper mantle S arrival is particularly large and we took some time to understand the nature of this arrival in the synthetic seismograms. We were using pure explosion sources at 630 m depth for all of the synthetic seismograms so the S arrival is generated entirely by P toS conversions predominately at the free surface. By comparing ray theoretical arrivals with those from the complete seismogram synthesis codes we were able to determine that the direct S arrival is a combination of a normal P to S conversion at the free surface along with a strong diffraction arrival that is generated by the small radius of curvature of the P wave front as it is reflected at the free surface. In order to represent this diffraction arrival in the ray theoretical code we added a vertical vector point force at the free surface that was time delayed by the P travel time from the explosion source at 630 m depth to the surface.

The data shows weak or nonexistent direct S arrivals which represents a major discrepancy between the data and the synthetics. From previous studies we know that there is evidence that underground nuclear explosion arrivals generated by free surface conversions are weaker in the near source region than theory predicts.[5] However, this effect is not normally strong enough to explain the difference the we see here between the synthetic seismograms and the data. If we look to upper mantle intrinsic attenuation, a simple calculation yields a Q_β value of about 100 that would be necessary to bring down the direct S arrival amplitudes to be consistent with the data and this value of upper mantle Q is probably unreasonable and at odds with the Q estimates from whole earth inversion studies for the central Asian shield region.

As an alternative mechanism for the reduction of the direct S arrival amplitude we have investigated near surface linear elastic scattering by introducing a large number of thin crustal layers with a random component to the velocity distribution which presents a broad-scale vertical scattering environment to the upper mantle arrivals as they pass through the crust. Figures 4e, 4f and 4g show synthetic record sections with crustal randomized versions of the structures represented in figures 4b, 4c and 4d respectively. The crustal scattering in the randomized models has caused a number of effects.

1. The direct S arrival is consistently reduced in amplitude. In some cases, such as at CHS, this reduction is substantial and the seismograms for the randomized models conform to what we see in the data.
2. The direct P arrival is able to pass through the randomized crustal layers with only a small reduction in amplitude which is consistently with the data.
3. There is a tendency for all impulsive arrivals to be "blurred" out to produce wavelet groupings followed by coda. This is a characteristic that we see in the data.
4. Although it is not readily apparent in the figures, the total L_g energy level increases with the randomized models.

[5] This is normally attributed to non-linear effects in the region above the explosion which effectively create an extremely low Q zone between the explosion and the surface.

A closer comparison of the data with all of the synthetic seismograms at four stations can be seen in figure 5. The crustal randomization mitigates, at least to some extent, the problem with the direct S arrival, however there remain substantial differences between the data and the synthetics especially regarding L_g and the Rayleigh surface wave. By using differential seismograms we have determined that L_g for these crustal models propagates in the upper 10 km of the crust, in the same general region where the 0.5 Hz Rayleigh wave is appreciably energetic. All attempts to attenuate the Rayleigh wave with suitable Q models also causes L_g to be attenuated. This can be clearly seen when we compare the crude model, where the Q values were low all the way down to 10 km depth, to the basel model, where the Q values were low only to several km depth. If we compare L_g to P amplitude ratios of the data to those of the synthetics we find that except for station KKL, the data has consistently higher values than the synthetics suggesting that, if anything, the upper crust Q values for the synthetics are too low. At the same time the data shows no sign of 0.5 Hz Rayleigh waves for the stations at distances more than 1000 km, suggesting that the upper crust Q values for the synthetics are too high.

If we look at the comparison for station KKL (figure 5a), which is at a distance of about 250 km, the data shows a large and dispersed Rayleigh wave and a small L_g arrival. This is a station where the L_g to P amplitude ratio is higher for the synthetics than for the data and where the data shows a Rayleigh wave that has approximately the same amplitude as that of the synthetics. The big difference between the data and the synthetics is the dispersed nature of the Rayleigh wave in the data compared to the relatively impulsive nature of the Rayleigh wave in the synthetics. The group velocity range corresponding to the observed Rayleigh wave dispersion is about 3.0 to 2.4 km/sec. This sort of dispersion at such a small distance is difficult, if not impossible, to produce with laterally homogeneous modeling techniques using reasonable structural models. We think that the observed dispersion in the Rayleigh wave at KKL is likely due to lateral scattering mechanisms that fall into two basic categories: 1) large scale multi-pathing of the fundamental Rayleigh wave from different azimuths at the receiver and 2) small to medium scale scattering of the fundamental Rayleigh wave into higher modes along the entire propagation path.

If small scale scattering of the Rayleigh wave is not important, then we would expect to see the Rayleigh wave at the larger distances except with "scrambled" dispersion characteristics, like we do at KKL. If small scale scattering is important, then the Rayleigh wave would be continuously scattered into other modes along its propagation path which would effectively attenuate it as it propagates. When the Rayleigh wave impinges upon a small subsurface scattering region, body wave energy would be radiated which would likely be at the S wave velocity of the upper crust, i.e. the L_g velocity. We think that there is a strong tendency for the high frequency Rayleigh wave to be scattered into L_g which attenuates the Rayleigh wave and boosts the L_g arrival and this hypothesis is consistent with the differences we see between the data and the laterally homogeneous modeling results.

The lateral scattering of a well organized surface wave into a highly focused waveguide arrival points out the inadequacies of representing random scattering with an effective "scattering" Q value. The scattering Q value necessary to reduce the Rayleigh wave amplitude consistent with the data also clobbers L_g. In this case the effective scattering Q value is different for the Rayleigh wave and L_g even though they occupy the same depth and frequency range. In fact it may be that the scattering Q for L_g is negative, since L_g is the beneficiary of Rayleigh wave energy along with other forms of scattered energy. If this representation of L_g is accurate then we could consider L_g to be a sort of "garbage can" arrival that picks up energy scattered from other arrivals and focuses it along the upper crust waveguide.

Conclusions and Recommendations

We have compared regional data recorded during the Soviet JVE with synthetic seismograms for a number of hypothetical structural models using laterally homogeneous modeling techniques. Our intent was to determine which parts of the waveforms could be adequately represented by these techniques, to identify where lateral scattering plays a critical role in the wave propagation and to infer structural models that can be used as starting values in a formal inversion procedure. Out conclusions from this study are as follows.

1. The only clear and consistent arrivals in the data are the first P arrival and L_g. A weak direct S arrival can be seen occasionally. There is no evidence of a Rayleigh wave at distances above 1000 km.
2. Laterally homogeneous modeling does a fairly good job of representing the first P arrival and, to a lesser extent, the first S arrival.
3. Vertical randomization of the crust is necessary to smooth out impulsive arrivals that we do not see in the data and to help capture S energy within the crust before it has a chance to propagate into the mantle.
4. Although most reasonable laterally homogeneous structural models will produce an L_g arrival, it is difficult to match the observed amplitude. Attempts to adjust upper crust Q values to boost L_g has the undesirable side effect of boosting the Rayleigh wave amplitude.
5. A plausible hypothesis to explain the differences in L_g and Rayleigh wave amplitudes between the synthetics and data is that small to medium scale lateral scattering of the Rayleigh wave into L_g is occurring along the entire Rayleigh wave propagation path.
6. The L_g arrival may be a seismic "garbage can" that naturally picks up and focuses energy that has been scattered, either vertically or laterally, from all other waves that pass through the upper crust.

Our recommendations for future work are as follows.

1. In order to explain Rayleigh wave and L_g amplitudes at regional distances, Rayleigh wave to L_g lateral scattering needs to be investigated. It is likely that either a mode coupling method must be used to model this or numerical modeling methods, such as 2D or 3D finite difference, must be used.
2. The role of vertical randomization in the upper mantle needs to be studied. Although we would not expect the random characteristics of upper mantle velocity distributions to be the same as those in the crust, it would be reasonable to expect some effectively random component to the velocity distributions. Upper mantle randomization would help to further smooth out impulsive arrivals and to effectively defocus strong triplications.
3. It will be highly desirable to develop methods for mapping structural and source statistical parameters into observed statistics, such as RMS L_g measurements.

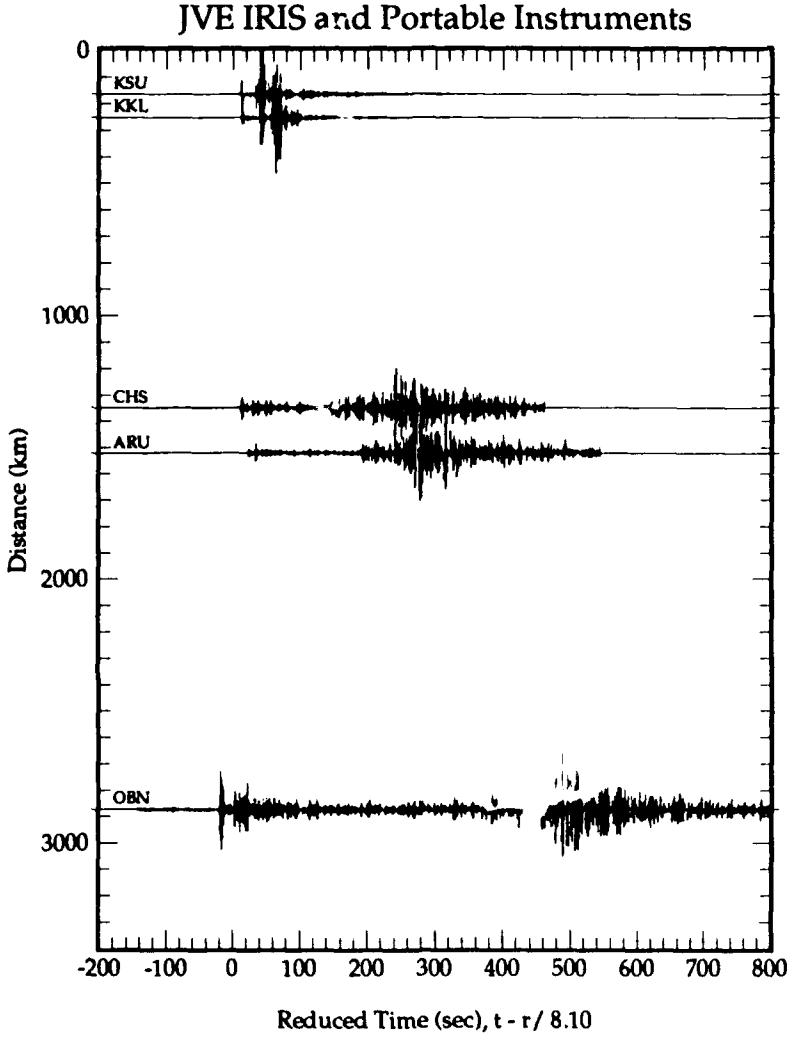


Figure 1. Digital vertical component records from the IRIS and portable instruments for the JVE after decimation to 1 Hz.

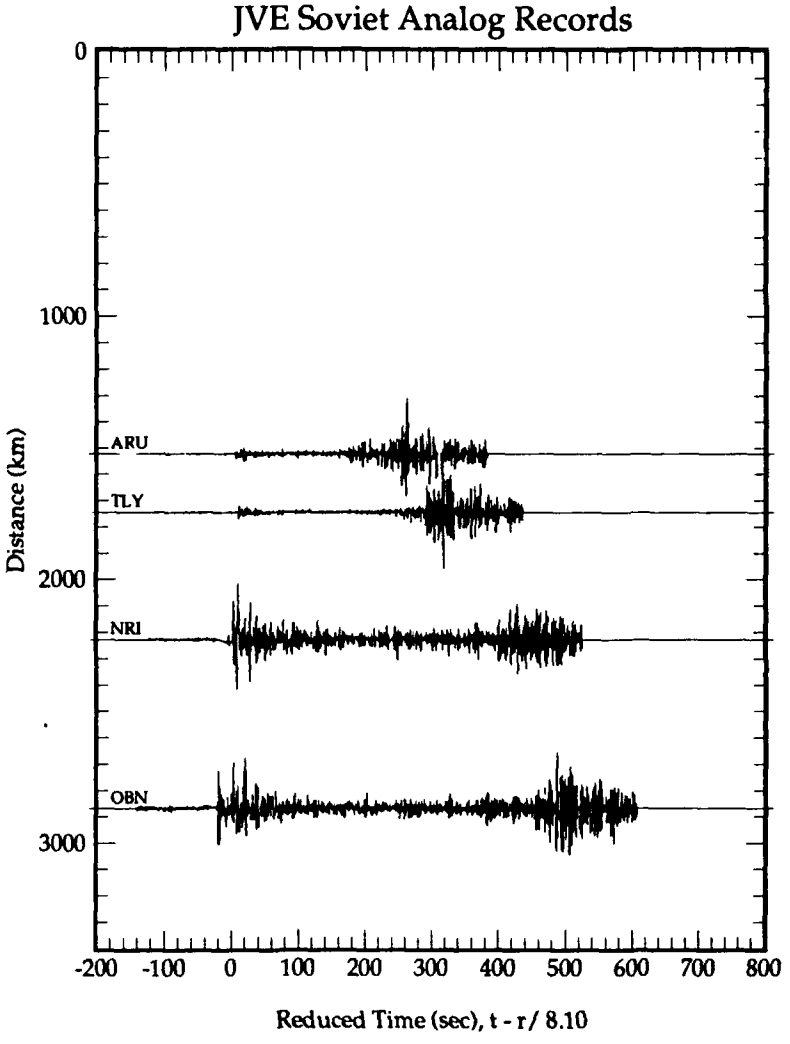


Figure 2. Analog vertical component records from the Soviet instruments for the JVE after decimation to 1 Hz.

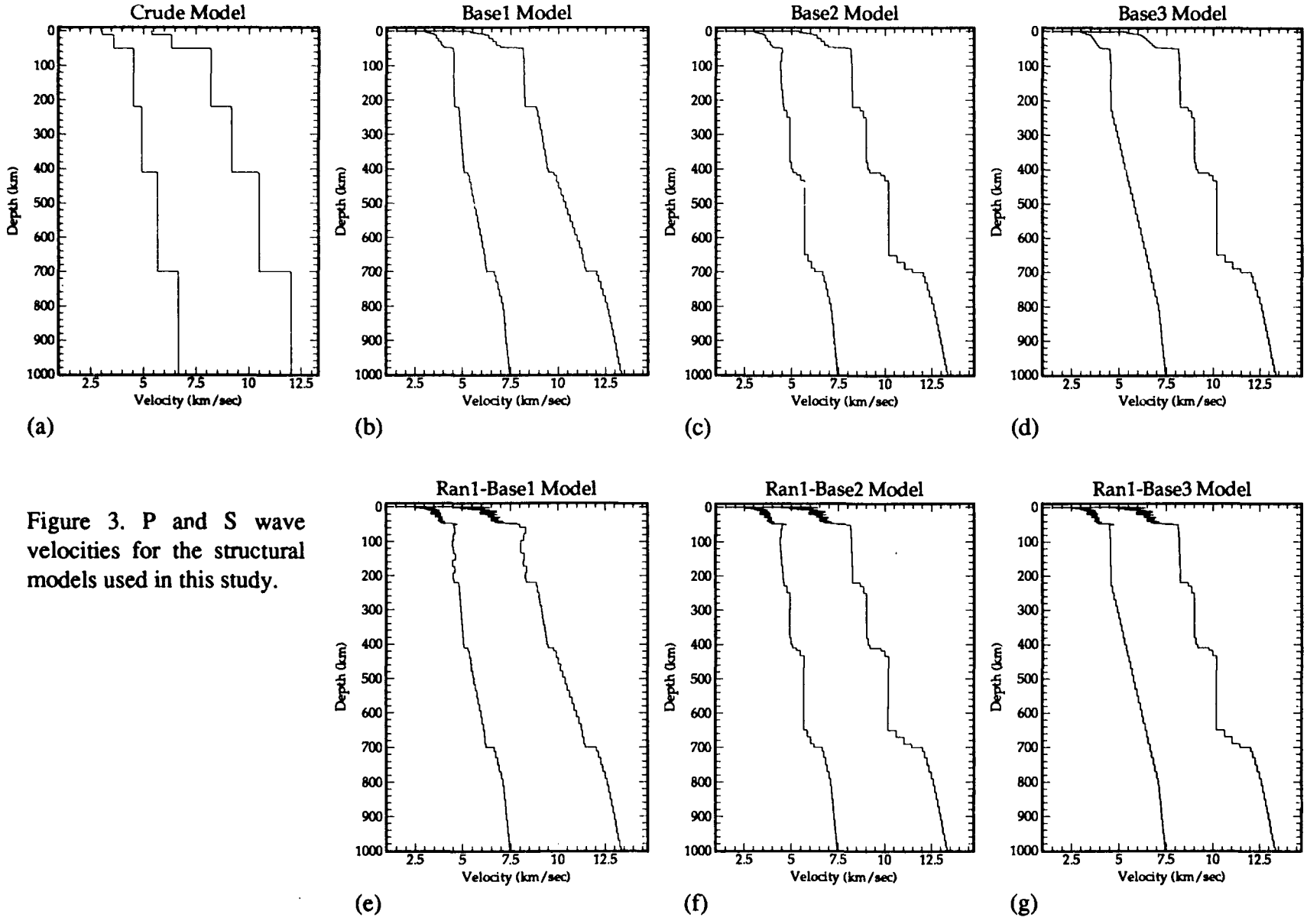


Figure 3. P and S wave velocities for the structural models used in this study.

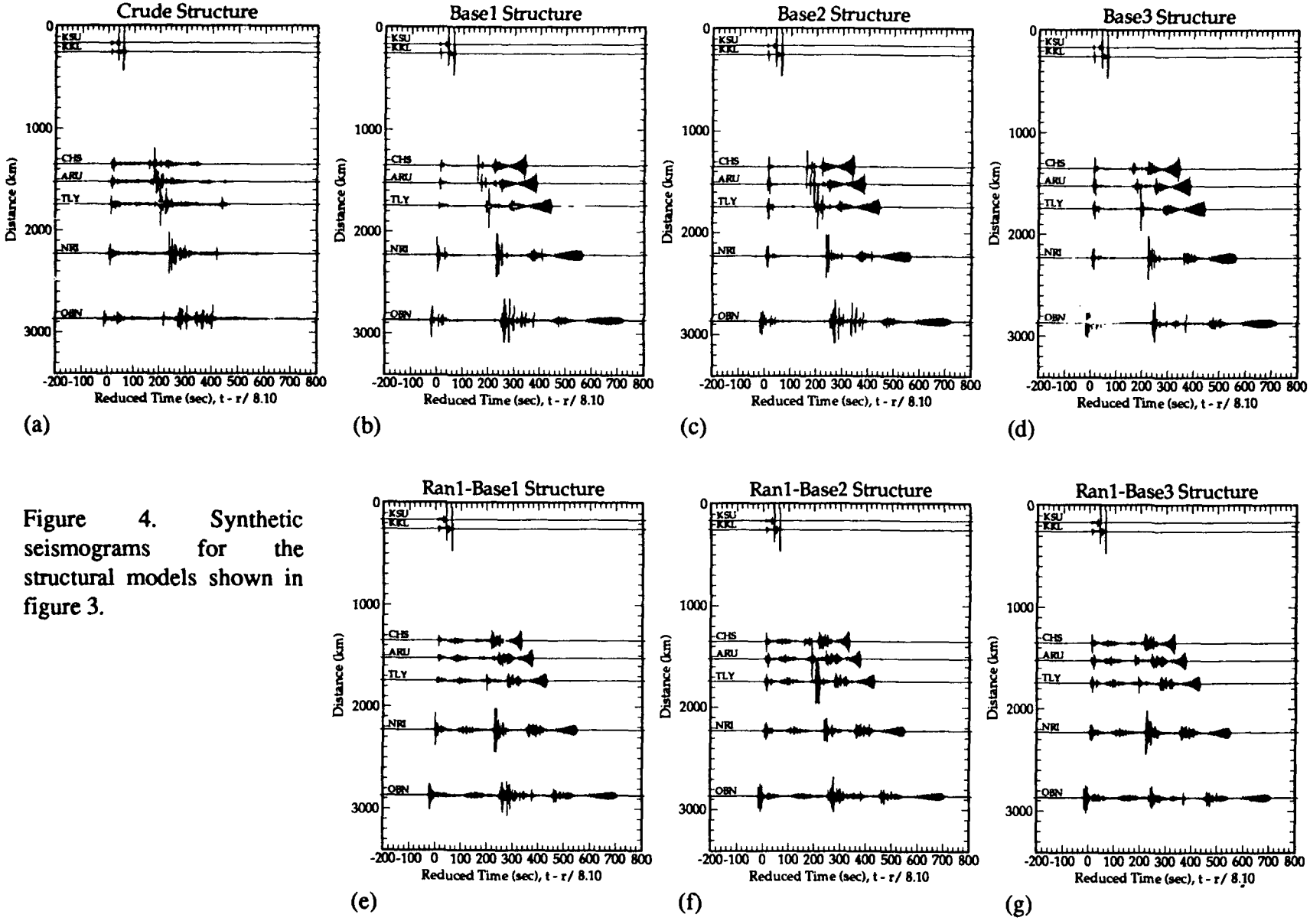


Figure 4. Synthetic seismograms for the structural models shown in figure 3.

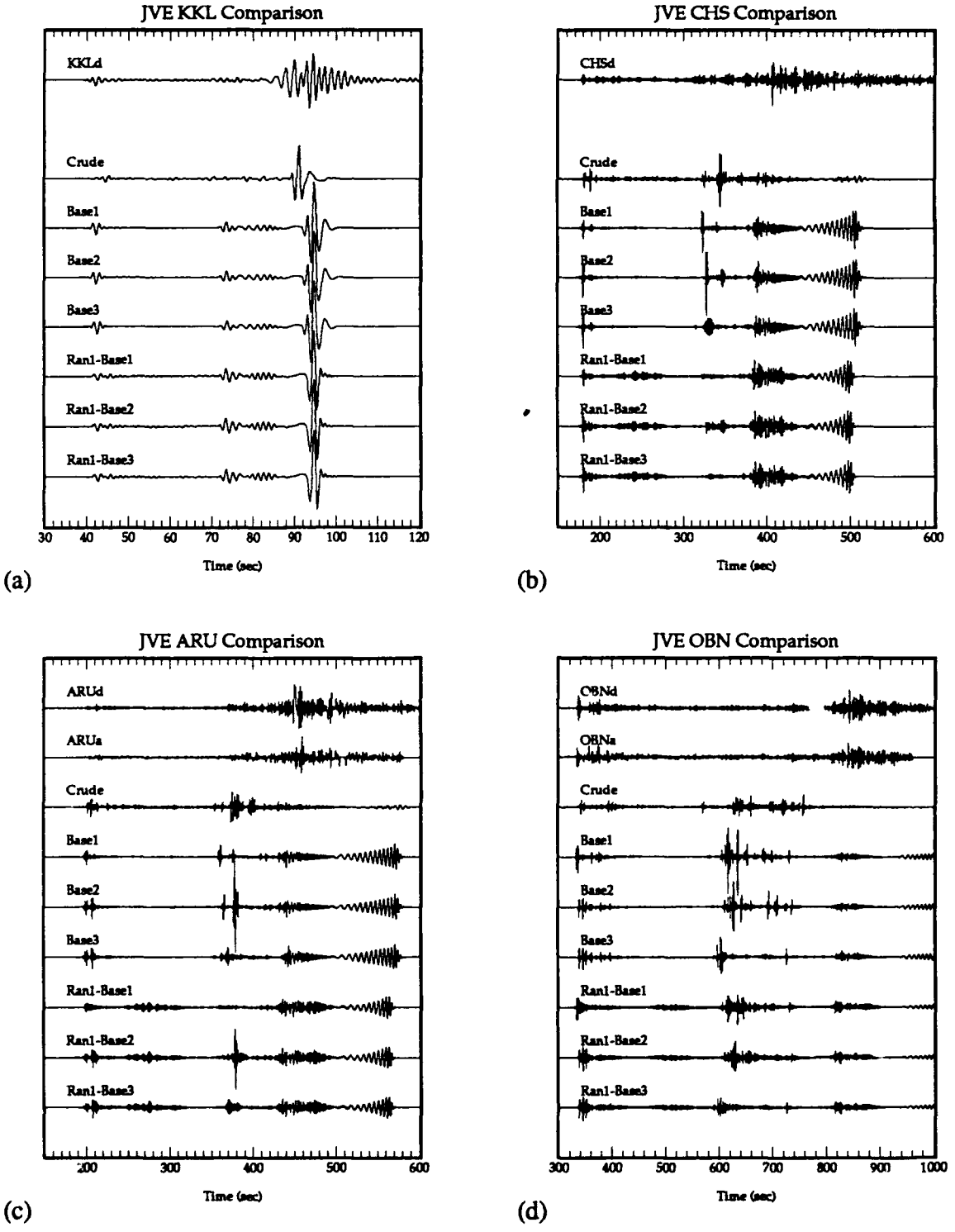


Figure 5. Comparisons of data with synthetic seismograms at four stations. The data station names end in "d" to signify the digital data or "a" to signify the analog data.

A View of the Department of Energy's Test Ban Verification Program*

Willard J. Hannon
Lawrence Livermore National Laboratory

Abstract

The Department of Energy carries out a diverse program of research and development related to the detection, characterization and identification of underground nuclear explosions at its National Laboratories. In addition it currently sponsors a limited amount of university research in conjunction with the Phillips Laboratory. The results of these efforts are used to develop U. S. monitoring capabilities and advise the U.S. government about the ability to enter into and verify treaties limiting the testing of nuclear explosives. This talk will describe the efforts currently being carried out at the National Laboratories -- the work in progress and the data bases being used. Future directions will also be described.

*Work performed under the auspices of the U.S. Department of Energy by the Lawrence Livermore National Laboratory under contract W-7405-ENG-48.

What Machines Must Learn ... and Why

Roy A. Maxion

School of Computer Science
Carnegie Mellon University
Pittsburgh, PA 15213 USA
InterNet: maxion@cs.cmu.edu

Machines that learn would be a great boon to humans, who are increasingly unable to cope with emerging monitoring and computing regimes of ever higher scale and complexity, wider geographic distribution, faster context changes, expanded data rates, growing environmental uncertainties, and greater system autonomy. Critical systems such as hospital patient monitors, air traffic control systems, and global surveillance telemetry systems are at risk because we cannot react quickly and intelligently enough to their continuous, voluminous and constantly varying signals; data and opportunities are lost. That machines should evolve autonomously to deal with the variation and volume of data in these environments, without being taught or programmed specifically to acquire new capabilities, seems a foregone conclusion, but what does this really imply? If we need or expect machines to become our colleagues as co-investigators in the discovery, monitoring, interpretation and control of routine, novel, interesting or important phenomena, we need first to understand what a machine must learn, and why. What -- so we can implement it; why -- so we can understand how the architecture for such a machine must be constituted.

An example of a task that machines might learn is interpretation of time-based signals from cardiograms, satellite telemetry, surveillance data, process control information or event logs, perhaps requiring coordinated activity from thousands of sensors in hundreds of locations. Typically, task conditions are constantly changing, data streams are too swift and complex for humans to apprehend, and no supervisors are available for teaching (although the opportunity for imbuing intelligent systems with existing knowledge should be needed when knowledge is available). For machines to perform competently in learning about and understanding such environments, they will, at minimum, be required to: orient (have their attention drawn to new, useful, interesting and important events); habituate (adapt or accommodate to unusual, but benign, conditions in the environment); discriminate (determine that one event is different from, or similar to, another); classify (sort objects or events into abstract taxonomic hierarchies); represent (internalize conditions, objects, events and temporal constructs from the external environment); set goals (know what it is supposed to do); remember (organize past information so it is accessible in timely and useful ways); and communicate (share a community of externalized symbols for interacting effectively with the environment and with other intelligent organisms, whether computational or biological). These are a few of the considerations necessary for a computational organism that must discover

patterns, search for regularities, form relationships, construct internal representations, explore and survive in novel environments and communicate with others. This talk will attempt to clarify these and other preconditions for a truly competent autonomous agent whose task is to interpret and control continuously, without human intervention, the ebb and flow of monitored data streams and their concomitant environments. A research approach for open problems will be outlined.